Welcoming Address

Dear Colleague,

It is a pleasure to welcome you in Salt Lake City for the second edition of The International Conference on Image Formation in X-ray Computed Tomography, also known as “The CT meeting”.

The idea for this meeting came about four years ago, following a wish from many to have a venue where CT scientists could meet together to discuss in depth all aspects that impact the image formation process in CT. These aspects include dose evaluation and dose reduction strategies, non-linearity effects and compensation schemes for these effects, image reconstruction algorithms, spectral decomposition, dynamic effects, geometrical calibration, phase-contrast physics, and image quality assessment. Both medical imaging and non-destructive testing applications are of interest, along with emerging breast imaging techniques, and the attractive micro- and nano-CT technology.

Pleasantly, the meeting is quickly becoming an attractive venue. Whereas 57 presentations were given at the first meeting, in 2010, 104 presentations will be given this year, including a special session on homeland security applications. As you will see, the breadth of the topics being covered is amazing. I am grateful to all authors for submitting their work for presentation at this conference. As in 2010, oral presentations have been allocated significant time to allow for in-depth discussion between the attendees. Also, comfortable poster sessions have been planned, and attractive locations have been selected to promote discussion during the meals.

The meeting could not be a success either without a great scientific committee. I would like to take the opportunity here to once again thank the following scientists, for their support, as well as for their help with the evaluation of submitted abstracts which was critical in shaping the scientific program:

Samit Basu	Morpho Detection, CA, USA
Guang-Hong Chen	University of Wisconsin, Madison, WI, USA
Carl Crawford	Csuptwo, LLC, WI, USA
Michel Defrise	Vrije Universiteit of Brussels, Belgium
Bruno DeMan	GE Global Research Center, NY, USA
Frank Dennerlein	Siemens Healthcare Sector, Germany
Idris Elbakri	CancerCare Manitoba, Winnipeg, Manitoba, Canada
Rebecca Fahrig	Stanford University, Stanford, CA, USA
Jeff Fessler	University of Michigan, MI, USA
Thomas Flohr	Siemens Healthcare Sector, Germany
Stephen Glick	UMass Medical School, MA, USA
Michael Grass	Philips Research Laboratories, Germany
Joachim Hornegger	University of Erlangen, Germany
Jiang Hsieh	GE Healthcare, WI, USA
Steve B. Jiang	University of California, San Diego, USA
Marc Kachelriess	German Cancer Research Center (DKFZ), Heidelberg, Germany
Alexander Katsevich	University of Central Florida, FL, USA
Thomas Koehler	Philips Research Laboratories, Germany

Hiroyuki Kudo	University of Tsukuba, Japan
Patrick La Riviere	University of Chicago, IL, USA
Guenter Lauritsch	Siemens Healthcare Sector, Germany
Michael McNitt-Gray	David Geffen School of Medicine at UCLA, CA, USA
Kyle Myers	Office of Science and Engineering Labs, CDRH, FDA, MD, USA
Johan Nuyts	Katholieke Universiteit, Belgium
Xiaochuan Pan	University of Chicago, IL, USA
Roland Proksa	Philips Research Laboratories, Germany
Leng Shuai	Mayo Clinic, MN, USA
Jeff Siewerdsen	Johns Hopkins University, MD, USA
Mike Silver	Toshiba Medical Research Institute, IL, USA
Josh Star-Lack	Varian Medical Systems, CA, USA
Karl Stierstorfer	Siemens Healthcare Sector, Germany
Katsuyuki Taguchi	Johns Hopkins University, MD, USA
Xiangyang Tang	Emory University, GA, USA
Srinivasan Vedantham	UMass Medical School, MA, USA
Ge Wang	Virginia Tech University, VA, USA
Bruce Whiting	University of Pittsburgh, PA, USA
Hengyong Yu	Wake Forest University Health Sciences, NC, USA
Lifeng Yu	Mayo Clinic, MN, USA
Alex Zamyatin	Toshiba Medical Research Institute, IL, USA
Yoram Bresler	InstaRecon Inc., Champaign, IL, USA & University of Illinois at Urbana-Champaign

Once again, we were also fortunate to receive generous support from

- ✓ Siemens AG, Healthcare Sector
- ✓ Toshiba Medical Systems Corporation
- ✓ GE Healthcare

This financial support is essential to accommodate a lower registration fee for graduate students. This year, we have 151 attendees out of which a full third are students.

Finally, I am thankful to Andrew Karellas for his continuous support and advices. Also, without his help, there would most likely be no special issue of Medical Physics. I am grateful to Dominic Heuscher, Jeremy Jorgensen, Yanfei Mao, Katharina Schmitt, Adam Wunderlich, and Zhicong Yu for providing a strong hand. And, of course, there was my colleague, Larry Zeng, helping me at each step; I cannot imagine how one could run such a conference without Larry.

I wish you all a pleasant meeting.

Frederic Noo, Ph.D.
General Chair
Utah Center for Advanced Imaging Research (UCAIR)
Department of Radiology
University of Utah
E-mail: noo@ucair.med.utah.edu

Table of contents

Session M1: Cardiac imaging
Moderated by X. Pan (The University of Chicago) and J. Pack (GE Global Research Center)

Improving best-phase image quality in cardiac CT by motion correction with MAM optimization 1
Rohkohl C, Bruder H, Stierstorfer K, Flohr T
Siemens AG, Healthcare Sector, Forchheim, Germany

Evaluation of interpolation methods for motion compensated tomographic reconstruction for cardiac angiographic C-arm data 5
Müller K, Zheng Y, Lauritsch G, Rohkohl C, Schwemmer C, Maier A K, Fahrig R, Hornegger J
Pattern Recognition Lab, Dept. of Computer Science, Universität Erlangen-Nürnberg, Erlangen, Germany; Erlangen Graduate School in Advanced Optical Technologies (SAOT), Universität Erlangen-Nürnberg, Erlangen, Germany; Siemens AG, Healthcare Sector, Forchheim, Germany; Image Analytics and Informatics, Siemens Corporate Research, Princeton, NJ, USA; Dept. of Radiology, Stanford University, Palo Alto, CA, USA

Second-pass stent reconstruction 9
Oishi S, Chang Y-B, Silver M D, Yamada M, Yokoyama H, Satow T
X-ray Systems Development Dept., Toshiba Medical Systems Corp., Otawara, Japan; Toshiba Medical Research Institute USA, Vernon Hills, IL, USA; National Cerebral and Cardiovascular Center, Suita, Japan

Diaphragm tracking for respiratory motion compensated cardiac C-arm CT 13
Bögel M, Maier A, Hofmann H G, Hornegger J, Fahrig R
Pattern Recognition Lab, Universität Erlangen-Nürnberg, Germany; Erlangen Graduate School in Advanced Optical Technologies (SAOT), Universität Erlangen-Nürnberg, Germany; Dept. of Radiology, Lucas MRS Center, Stanford University, Palo Alto, CA, USA

Session M2: Image reconstruction with physical effects modeling
Moderated by P. La Riviere (The University of Chicago) and P. Kinahan (The University of Washington)

Effects of ray-modeling: simulation study 17
Hofmann C, Knaup M, Kachelrieβ M
Institute of Medical Physics, University of Erlangen–Nürnberg, Erlangen, Germany; German Cancer Research Center (DKFZ), Heidelberg, Germany

Patchwork reconstruction with resolution modeling for digital breast tomosynthesis 21
Michielsen K, Van Slambrouck K, Jerebko A, Nuyts J
Dept. of Nuclear Medicine, KU Leuven, Belgium; Siemens AG, Healthcare Sector, Erlangen, Germany

Comparative studies on distance-driven and finite-detector-based projection models for iterative image reconstruction 25
Miao C, Liu B, Xu Q, Yu H
Biomedical Imaging Division, VT-WFU School of Biomedical Engineering and Sciences, Wake Forest University Health Sciences, Winston-Salem, NC, USA; Dept. of Radiology, Division of Radiologic Sciences, Wake Forest University Health Sciences, Winston-Salem, NC, USA; Institute of Image Processing and Pattern Recognition, Xi'an Jiaotong University, Xi'an, Shanxi, P.R. China

A new method for metal artifact reduction in CT 29
Koehler T, Brendel B, Brown K M
Philips Technologie GmbH, Innovative Technologies, Research Laboratories, Hamburg, Germany; Philips Healthcare, Cleveland, OH, USA

Session M3A: Premium posters – Iterative reconstruction techniques
Moderated by L. Desbat (Grenoble University) and E. Sidky (The University of Chicago)

Parallelizable algorithms for X-ray CT image reconstruction with spatially non-uniform updates 33

Kim D, Fessler J A

Dept. of Electrical Engineering and Computer Science, Univ. of Michigan, Ann Arbor, MI, USA

Combined shearlet and TV regularization in sparse-view CT reconstruction 37

Vandeghinste B, Goossens B, Van Holen R, Vanhove C, Pižurica A, Vandenberghe S, Staelens S

Medical Image and Signal Processing (MEDISIP) research group, Ghent University–IBBT, Gent, Belgium; Image Processing and Interpretation (IPI) research group, Ghent University–IBBT, Gent, Belgium; Molecular Imaging Centre Antwerp, University of Antwerp, Edegem, Belgium

Low-dose CT image reconstruction by adaptive-weighted TV-constrained penalized weighted least-squares approach 41

Liu Y, Ma J, Zhang H, Wang J, Liang Z

Depts. of Radiology, Electrical and Computer Engineering, and Biomedical Engineering, Stony Brook University, Stony Brook, NY, USA; School of Biomedical Engineering, Southern Medical University, Guangzhou, China; Dept. of Radiation Oncology, The University of Texas Southwestern Medical Center, Dallas, TX, USA

Algebraic tomosynthesis reconstruction with spatially adaptive updating term 46

Levakhina Y M, Mueller J, Duschka R L, Vogt F M, Barkhausen J, Buzug T M

Graduate School for Computing in Medicine and Life Sciences and Institute of Medical Engineering, University of Luebeck, Luebeck, Germany; Institute of Medical Engineering, University of Luebeck, Luebeck, Germany; Klinik für Radiologie und Nuklearmedizin, Universitaetsklinikum Schleswig-Holstein, Luebeck, Germany

Initial experience in constrained-TV-minimization image reconstruction from diagnostic-CT data 50

Zhang Z, Bian J, Han X, Shi D, Zamyatin A, Rogalla P, Sidky E Y, Pan X

The University of Chicago; Toshiba Medical Research Institute USA; University of Toronto; UHN Mount Sinai Hospital, Canada

Total variation regularized weighted simultaneous algebraic reconstruction technique – a parallel scheme 57

Shi D, Zamyatin A A, Dinu M P

Toshiba Medical Research Institute of USA, Inc., Vernon Hills, IL, USA.

Session M3B: Premium posters – Tools for image quality assessment
Moderated by L. Desbat (Grenoble University) and E. Sidky (The University of Chicago)

A low-dose simulation tool 61

Žabić S, Wang Q, Brown K M

Philips Healthcare; Cornell University

A realistic CT/Human-model simulation package 66

Fung G S K, Stierstorfer K, Taguchi K, Segars W P, Flohr T G, Tsui B M W

Russell H. Morgan Dept. of Radiology, Johns Hopkins University, Baltimore, MD, USA; Siemens AG, Healthcare Sector, Forchheim, Germany; Dept. of Radiology, Duke University, Durham, NC, USA

Dedicated breast CT: anatomic power spectrum 70

Vedantham S, Shi L, Karellas A, O’Connell A M, Conover D

Dept. of Radiology, University of Massachusetts Medical School, Worcester, MA, USA; Dept. of Radiology, University of Rochester Medical Center, Rochester, NY, USA; Koning Corporation, West Henrietta, NY, USA

Prediction of human observer performance in a low-contrast detection task using channelized Hotelling observer: impact of radiation dose and reconstruction algorithms 74
Yu L, Leng S, Chen L, Kofler J M, McCollough C H
Dept. of Radiology, Mayo Clinic, Rochester, MN, USA

Noise and bias properties of PET images using DECT based attenuation correction 79
Xia T, Alessio A M, Kinahan P E
Imaging Research Laboratory, Dept. of Radiology, University of Washington

On the statistical analysis of image quality metrics based on alternative forced-choice experiments 83
Noo F, Wunderlich A, Heuscher D J, Schmitt K, Yu Z
Dept. of Radiology, University of Utah, Salt Lake City, UT, USA

Session M3C: Premium posters – Dynamic CT
Moderated by L. Desbat (Grenoble University) and E. Sidky (The University of Chicago)

Temporal interpolation of partial scan sinograms in myocardial CT perfusion 87
Ramirez-Giraldo J C, Crane J A, Yu L, Leng S, Lerman L O, McCollough C H
CT Clinical Innovation Center, Dept. of Radiology, Mayo Clinic, Rochester MN, USA;Division of Nephrology and Hypertension, Mayo Clinic, Rochester, MN, USA

A new registration algorithm for motion-compensated computed tomography for image-guided radiation therapy 91
Brehm M, Paysan P, Oehlhafen M, Kunz P, Kachelrieβ M
Institute of Medical Physics, University of Erlangen–Nürnberg, Erlangen, Germany; German Cancer Research Center (DKFZ), Heidelberg, Germany; Varian Medical Systems, Baden–Dättwil, Switzerland

Cardiac function analysis with four-dimensional CT image 95
Tang Q, Kigure T, Higuchi T, Fung G S K, Fishman E K, Taguchi K
The Johns Hopkins University School of Medicine, Baltimore, MD, USA; Tokyo Institute of Technology, Tokyo, Japan; University of Würzburg, Würzburg, Germany

High-speed dynamic imaging with a real time tomography system 99
Thompson W M, Lionheart, W R B, Morton E J
Henry Moseley X-ray Imaging Facility and School of Mathematics, University of Manchester. UK; Rapiscan Systems

Session M4: Hardware and software techniques for dose reduction
Moderated by Srinivasan Vedantham (UMass Medical School) and Bruce Whiting (University of Pittsburgh)

View-based noise modeling in the filtered backprojection MAP algorithm 103
Zeng G L
Dept. of Radiology, University of Utah, Salt Lake City, UT, USA

Bi-modal CT reconstruction (BMR) 107
Bruder H, Raupach R, Petersilka M, Sunnegårdh J, Stierstorfer K
Siemens AG, Healthcare Sector, Forchheim, Germany

Database-Assisted Low-Dose CT Image Restoration 111
Xu W, Ha S, Mueller K
Visual Analytics and Imaging (VAI) Lab, Computer Science Dept., Stony Brook University, NY, USA

CT dose reduction using dynamic collimation 115
Heuscher D J, Noo F
Dept. of Radiology, University of Utah, Salt Lake City, UT, USA

Fluence field modulated computed tomography 119
Bartolac S, Jaffray D
Dept. of Medical Biophysics, University of Toronto, Toronto, Canada; Radiation Medicine Program, Princess Margaret Hospital/Ontario Cancer Institute, Toronto, Canada

Session T1: Dynamic CT imaging
Moderated by M. Silver (Toshiba Medical Research Institute USA) and X. Tang (Emory University)

Evaluation of a tight frame reconstruction algorithm for perfusion C-arm CT using a realistic dynamic brain phantom 123
Manhart M, Fieselmann A, Deuerling-Zheng Y
Pattern Recognition Lab, FAU Erlangen-Nürnberg, Germany; Siemens AG, Angiography & Interventional X-Ray Systems, Forchheim, Germany

Phase–correlated perfusion imaging of free–breathing rodents 127
Sawall S, Kuntz J, Socher M, Bartling S, Knaup M, Kachelrieß M
Institute of Medical Physics, University of Erlangen-Nürnberg, Erlangen, Germany; German Cancer Research Center (DKFZ), Heidelberg, Germany

Improving motion accuracy for the McKinnon-Bates 4D-CBCT reconstruction algorithm 131
Sun M, Oelhafen M, Carvalho L, Pavkovich J, Berkus T, Star-Lack J
Varian Medical Systems, Ginzton Technology Center, Palo Alto, CA, USA; Varian Medical Systems, Imaging Laboratory, Baden-Daettwil, Switzerland

Temporal resolution and motion artifacts in dual-source cardiac CT and single-source CT with iterative reconstruction 135
Schoendube H, Allmendiger T, Kappler S, Bruder H, Stierstorfer K
Siemens AG, Healthcare Sector, Forchheim, Germany

Session T2: Task-based assessment of image quality
Moderated by B. Tsui (The Johns Hopkins University) and J. Nuyts (Katholieke Universiteit Leuven)

Evaluation of low dose CT perfusion using a reproducible biological phantom 140
Ramirez-Giraldo J C, Thompson S, Knudsen B, Yu L, Woodrum D A, Callstrom M R, McCollough C H
CT Clinical Innovation Center, Dept. of Radiology, Mayo Clinic, Rochester, MN, USA; Center for Translational Science, Mayo Clinic, Rochester MN, USA; Vascular Interventional Radiology Dept., Mayo Clinic, Rochester MN, USA

Guiding decisions in CT image reconstruction algorithm design via the Hotelling template 144
Sanchez A A, Sidky E Y, Pan X
The University of Chicago, Dept. of Radiology, Chicago, IL, USA; The University of Chicago, Dept. of Radiation and Cellular Oncology, Chicago, IL, USA

CT image assessment by low contrast signal detectability evaluation with unknown signal location 148
Popescu, L M, Myers K J
Food and Drug Administration, Center for Devices and Radiological Health, Office of Science and Engineering Laboratories, Division of Imaging and Applied Mathematics, Silver Spring, MD, USA

New results for efficient estimation of CHO performance 153
Wunderlich A, Noo F, Heilbrun M
Dept. of Radiology, University of Utah, Salt Lake City, UT, USA

Session T3: Classical posters -- New directions

A B-spline based and computationally performant projector for iterative reconstruction in tomography: application to dynamic X-ray gated CT 157
Momey F, Denis L, Mennessier C, Thiebaut E, Becker J-M, Desbat L
Centre de Recherche Astrophysique de Lyon - Observatoire de Lyon, France; Laboratoire Hubert Curien, Université Jean Monnet, Saint-Etienne, France; CPE, Lyon, France; TIMC-IMAG, Grenoble, France

Toward quantifying admissible undersampling of sparsity-exploiting iterative image reconstruction for X-ray CT 161
Jorgensen J H, Sidky E Y, Pan X
Dept. of Informatics and Mathematical Modeling, Technical University of Denmark, Denmark; Dept. of Radiology, The University of Chicago, Chicago, IL, USA

A preliminary study of optimization-based image reconstruction from offset-detector CBCT 165
Bian J, Wang J, Han X, Sidky E Y, Shao L, Pan X
The University of Chicago; Philips Healthcare

Spatial variations in reconstruction methods for CT 170
Plantagie L, Palenstijn W J, Sijbers J, Batenburg K J
Centrum Wiskunde & Informatica (CWI), Amsterdam, The Netherlands; IBBT-Vision Lab, University of Antwerp, Wilrijk, Belgium

Effective CT scattering simulation with bi-directional ray tracing on GPU 174
Pi J, Ha S, Mueller K
Center for Visual Computing, Computer Science Dept., Stony Brook University, NY, USA

GPU-accelerated first-order scattering simulation for x-ray CT image reconstruction 178
Ha S, Pi J, Mueller K
Center for Visual Computing, Computer Science Dept., Stony Brook University, NY, USA

Searching effective parameters for low-dose CT reconstruction by ant colony optimization 182
Zheng Z, Papenhausen E, Mueller K
Computer Science Dept., Stony Brook University, Stony Brook, NY, USA

Spectral response compensation for photon counting clinical x-ray CT and application to coronary vulnerable plaque detection 186
Cammin J, Srivastava S, Fung G S K, Taguchi K
Russell H. Morgan Dept. of Radiology and Radiological Science, The Johns Hopkins School of Medicine, Baltimore, MD, USA

Noise reduction using coupled projections in helical computed tomography 190
Fan Y, Ma J, Liu Y, Lu H, Liang Z
Dept. of Radiology, State University of New York, Stony Brook, NY; Dept. of Biomedical Engineering, Fourth Military Medical University, Xi'an , Shaanxi, China

Perturbation-based error analysis of iterative image reconstruction algorithm for x-ray computed tomography 194
Kim J K, Fessler J A, Zhang Z
EECS Dept., University of Michigan, Ann Arbor, MI, USA

One-dimensional study of methods for improving resolution in CT model-based iterative reconstruction Choi K, Fu L, Zeng K, Rui X, De Man B *CT Systems and Applications Laboratory, GE Global Research, Niskayuna, NY, USA*	198
Estimating X-ray spectrum of a clinic CT scanner from transmission measurements Duan X, Wang J, Yu L, McCollough C H *CT Clinical Innovation Center, Radiology, Mayo Clinic, Rochester, MN, USA*	202
4D-CT reconstruction using sparsity level constrained compressed sensing Wu H, Maier A, Hofmann H, Fahrig R, Hornegger J *Pattern Recognition Lab (LME), University Erlangen- Nürnberg; Graduate School in Advanced Optical Technologies (SAOT), University Erlangen-Nürnberg; Dept. of Radiology, Stanford University*	206
An open database of metal artifacts cases for clinical CT imaging Mueller J, Kaiser F, Levakhina Y, Stille M, Weyers I, Buzug T M *Institute of Medical Engineering, University of Luebeck, Luebeck, Germany; Graduate School for Computing in Medicine and Life Sciences University of Luebeck, Luebeck, Germany; Institute of Medical Engineering, University of Luebeck, Luebeck, Germany; Institute of Anatomy, University of Luebeck, Germany*	210
Low–Contrast visibility in flat detector CT: a simulation study Knaup M, Ritschl L, Kachelrieβ M *Institute of Medical Physics, University of Erlangen–Nurnberg, Erlangen, Germany; German Cancer Research Center (DKFZ), Heidelberg, Germany*	214
Optimizing the antiderivative of X-ray differential phase contrast data for tomographic reconstruction Ritschl L, Sawall S, Schüller S, Ritter A, Bayer F, Weber T, Pelzer G, Wucherer L, Rieger J, Gödel K, Durst J, Michel T, Anton G, Haas W, Bäuerle T, Kachelrieβ M *Institute of Medical Physics (IMP), University of Erlangen-Nürnberg, Erlangen, Germany; Radiation Physics Group at the Erlangen Centre for Astroparticle Physics (ECAP), University of Erlangen-Nürnberg, Erlangen, Germany; Pattern Recognition Lab, University of Erlangen-Nürnberg, Erlangen, Germany; German Cancer Research Center (DKFZ), Heidelberg, Germany*	218
A multi-modality software platform for image reconstruction Johnston S M, Johnson G A, Badea C T *Center for In Vivo Microscopy, Duke University, Durham, NC, USA*	222
Super resolution CT imaging based on the collimator Zhu Y, Chen D, Zhang P *The CT Laboratory, School of Mathematics, Capital Normal University,Beijing, China*	226
Fat and iron quantification of the liver with dual-energy computed tomography in the presence of high atomic number elements Kis B J, Sarnyai Z, Kakonyi R, Erdelyi M, Szabo G *Dept. of Optics and Quantum Electronics at the University of Szeged, Szeged, Hungary*	230
Evaluation of mA switching method with penalized weighted least-square noise reduction for low-dose CT Lee Y, Chung H, Cho S *Dept. of nuclear and quantum engineering at KIAST, Korea*	234

Ultra-high resolution imaging by Archimedian Spiral on Radon space 238
Do S, Gupta R, Brady T, Karl W C
Dept. of Radiology, Massachusetts General Hospital and Harvard Medical School, Boston, MA, USA; Dept. of Electrical and Computer Engineering, Boston University, Boston, MA, USA

Curvelet-based inpainting for metal artifact reduction in computed tomography 242
Kleine M, Buzug T M
Graduate School for Computing in Medicine and Life Sciences, University of Luebeck, Luebeck, Germany; Institute of Medical Engineering, University of Luebeck, Luebeck, Germany

A translation-based data acquisition for industrial computed tomography 246
Schön T, Fuchs T, Hanke R, Dremel K
Process Integrated Inspection Systems, a Dept. of the Fraunhofer Institute for Integrated Circuits, Fürth, Germany; Development Center for X-ray Technology (Fraunhofer-EZRT), a common Dept. of the Fraunhofer Institute for Integrated Circuits, Saarbrücken, Germany; Fraunhofer Institute for Non-destructive Testing, Fürth, Germany; Chair for X-ray microscopy, Julius-Maximilians-University, Würzburg

GPU implementation of exact FBP and BPF algorithms for saddle and circle-plus-line CT 250
Lee M, Kim K S, Ye J C
Dept. of Bio & Brain Engineering, Korea Advanced Institute of Science & Technology (KAIST), Daejeon, Korea

Iterative image reconstruction with variable resolution in diagnostic CT 254
Zhang Z, Bian J, Han X, Shi D, Zamyatin A, Rogalla P, Sidky E Y, Pan X
The University of Chicago; Toshiba Medical Research Institute USA; University of Toronto; UHN Mount Sinai Hospital, Canada

Residual motion compensation in ECG-gated cardiac vasculature reconstruction 259
Schwemmer C, Rohkohl C, Lauritsch G, Müller K, Hornegger J
Pattern Recognition Lab, Dept. of Computer Science, Universität Erlangen-Nürnberg, Erlangen, Germany; Erlangen Graduate School in Advanced Optical Technologies (SAOT), Universität Erlangen-Nürnberg, Erlangen, Germany; Siemens AG, Healthcare Sector, Forchheim, Germany

Noise reduction with low dose CT data based on a modified ROF model 263
Zhao M, Zhu Y, Li H, Zhang P
The CT Laboratory, School of Mathematics, Capital Normal University, Beijing, China

Robust automated regularization factor selection for statistical reconstructions 267
Bergner F, Brendel B, Noel P B, Dobritz M, Koehler T
Philips Technologie GmbH, Innovative Technologies, Research Laboratories, Hamburg, Germany; Dept. of Radiology, Technische Universität München, Germany

The potential imaging performance of differential phase-contrast CT -- NPS(k), MTF(k) and NEQ(k) 271
Tang X, Yang Y, Tang S
Dept. of Radiology and Imaging Sciences, Emory University School of Medicine, Atlanta, GA, USA

Mobile C-arm CT for minimally invasive surgery 275
Braun-Jones T, Duncan W, Cheryauka A
GE Healthcare-Surgery, Salt Lake City, UT, USA

Distortion correction, geometric calibration, and volume reconstruction for an isocentric C-arm X-ray system: preliminary studies Spencer B, Clackdoyle R, Mennessier C, Xu T *Carleton University, Ottawa, Ontario, Canada; Laboratoire Hubert Curien, CNRS Unité Mixte de Recherche 5516, Saint Etienne, France; Ecole de Chimie Physique, Lyon, Villeurbanne, France*	279
Low dose perfusion CT Heuscher D J, Zhang J, Žabić S, Noo F *Dept. of Radiology, University of Utah, Salt Lake City, UT, USA; Philips Medical Systems, Cleveland, OH,USA*	284
Analysis of bias induced by various forward projection models in iterative reconstruction Schmitt K, Schoendube H, Hornegger J, Stierstorfer K, Noo F *Patter Recognition Lab, University of Erlangen-Nürnberg, Erlangen, Germany; Dept. of Radiology, University of Utah, Salt Lake City, UT, USA; Siemens AG, Healthcare Sector, Germany*	288

Session T4: Homeland security applications
Moderated by C. Crawford (Csuptwo, LLC, Milwaukee, Wisconsin) and H. Martz (Lawrence Livermore National Laboratory)

Visualizing the segmentation error of a tomogram using the residual projection error Roelandts T, Batenburg K J, Sijbers J *IBBT-Vision Lab, University of Antwerp, Wilrijk, Belgium; Centrum Wiskunde & Informatica (CWI), Amsterdam, The Netherlands*	293
A Model-Based 3D Multi-slice Helical CT Reconstruction Algorithm for Transportation Security Application Jin P, Haneda E, Bouman C A, Sauer K D *School of Electrical and Computer Engineering, Purdue University, West Lafayette, IN, USA; Dept. of Electrical Engineering, University of Notre Dame, Notre Dame, IN, USA*	297
Design of the discrete skew geometry and iterative reconstruction of the MV3D scanner Foland A D L-3 Communications, Security and Detection Systems, Woburn, MA, USA	301
Ray-weighted constrained-conjugate-gradient tomographic reconstruction for security applications Kallman J S, Azevedo S G *Lawrence Livermore National Laboratory, CA, USA*	305
Automatic segmentation of CT scans of checked baggage Wiley D F, Ghosh D, Woodhouse C *Stratovan Corporation, Sacramento, CA, USA*	310
An iterative reconstruction method for spectral CT with tensor-based formulation and nuclear norm regularization Semerci O, Miller E L *Dept. of Electrical and Computer Engineering, Tufts University, Medford, USA*	314
Model-based CT reconstruction from sparse views Kisner S J, Haneda E, Bouman C A, Skatter S, Kourinny M, Bedford S *School of Electrical and Computer Engineering, Purdue University, West Lafayette, IN, USA; Morpho Detection Inc., Newark, CA, USA; Astrophysics Inc., City of Industry, CA, USA*	444

Session W1: Motion estimation and compensation techniques
Moderated by K. Taguchi (The Johns Hopkins University) and H. Schoendube (Siemens AG, Healthcare Sector)

Dynamic tomography, mass preservation and ROI reconstruction 318
Desbat L, Mennessier C, Clackdoyle R
UJF-Grenoble 1, CNRS, TIMC-IMAG UMR 5525, Grenoble University, France; LHC, UMR, St Etienne University, France; CPE, Lyon, France

An analysis of motion artifacts in CT and implications for motion compensation 322
Pack J D, Claus B
GE Global Research Center, Niskayuna, NY, USA

A novel motion estimation algorithm 326
Katsevich A, Zamyatin A, Silver M
Dept. of Mathematics, University of Central Florida, Orlando, FL, USA; Toshiba Medical Research Institute USA, Vernon Hills, IL, USA

Motion-compensated image reconstruction with alternating minimization 330
Cho J H, Ramani S, Fessler J A
Dept. of Electrical Engineering and Computer Science, University of Michigan, Ann Arbor, MI, USA

Session W2: Iterative reconstruction methods
Moderated by T. Koehler (Philips Research Laboratories) and B. De Man (GE Global Research Center)

Information propagation in prior-image-based reconstruction 334
Stayman J W, Prince J L, Siewerdsen J H
Dept. of Biomedical Engineering, Johns Hopkins University, Baltimore, MD, USA; Dept. of Electrical and Computer Engineering, Johns Hopkins University, Baltimore, MD, USA

Iterative helical cone-beam CT reconstruction using fast hierarchical backprojection/reprojection operators 339
Brokish J, Guo H, Sack P, Keesing D B, Bresler Y
InstaRecon, Inc., Champaign, IL, USA; Dept. of Electrical and Computer Engineering, University of Illinois at Urbana-Champaign

Convex optimization prototyping for iterative image reconstruction in X-ray CT 343
Sidky E Y, Jorgensen J H, Pan X
The University of Chicago, Dept. of Radiology, Chicago IL, USA; Dept. of Informatics and Mathematical Modeling, Technical University of Denmark

A hybrid regularizer combining orthonormal wavelets and finite differences for statistical reconstruction in 3-D CT 348
Ramani S, Fessler J A
EECS Dept., University of Michigan, Ann Arbor, MI, USA

Statistical CT reconstruction from limited views with probabilistic atlas prior 352
Rashed E A, Kudo H
Division of Information Engineering, University of Tsukuba, Tsukuba, Japan; Department of Mathematics, Suez Canal University, Ismailia, Egypt

Session W3A: Premium poster -- Advanced imaging techniques
Moderated by G. Lauritsch (Siemens AG, Healthcare Sector) and A. Zamyatin (Toshiba Medical Research Institute USA)

Coding ants: using ant colony optimization to accelerate CT reconstruction 356
Papenhausen E, Zheng Z, Mueller K
Computer Science Dept., Stony Brook University, Stony Brook, NY, USA

An inversion formula for the cone-beam transform for arbitrary source trajectories 360
Yazıcı B, Li Z, Pack J
Dept of Electrical, Computer and Systems Engineering & Dept of Biomedical Engineering, Rensselaer Polytechnic Institute,Troy, NY, USA; GE Global Research Center,Niskayuna, NY, USA

First experimental results on long-object imaging using a reverse helical trajectory with a C-arm system 364
Yu Z, Maier A, Schönborn M, Vogt F, Köhler C, Lauritsch G, Hornegger J, Noo F
Dept. of Radiology, University of Utah, Salt Lake City, UT, USA; Siemens AG, Healthcare Sector, Forchheim, Germany; Pattern Recognition Lab, University of Erlangen-Nuremberg, Erlangen, Germany

Cone beam X-ray luminescence computed tomography: a preliminary experimental study 369
Zhu S, Chen D, Yi H, Zhang X, Liang J, Tian J
Life Sciences Research Center, School of Life Sciences and Technology, Xidian University, Xi'an, Shaanxi, China; Intelligent Medical Research Center, Institute of Automation, Chinese Academy of Sciences, Beijing, China

A small-animal phase-contrast CT scanner 373
Bruyndonckx P, Pauwels B, Liu X, Tapfer A, Bech M, Velroyen A, Sasov A, Pfeiffer F
Skyscan, Kontich, Belgium; Technische Universität München, Garching bei München, Germany; Medical Radiation Physics, Clinical Sciences, Lund University, Lund, Sweden

Improved ordered subsets algorithm for 3D X-ray CT image reconstruction 378
Kim D, Pal D, Thibault J-B, Fessler J A
Dept. of Electrical Engineering and Computer Science, University of Michigan, Ann Arbor, MI, USA; GE Healthcare, Waukesha, WI, USA

Distance-driven binning for proton CT filtered backprojection along most likely paths 382
Rit S, Freud N, Sarrut D, Létang J-M
Université de Lyon, CREATIS, France; CNRS UMR5220, France; Inserm U1044, France; INSA-Lyon, France; Université Lyon 1, France; Centre Léon Bérard, France

Session W3B: Premium poster – Physical effects modeling
Moderated by G. Lauritsch (Siemens AG, Healthcare Sector) and A. Zamyatin (Toshiba Medical Research Institute USA)

Micro-CT artifacts reduction based on detector random shifting and 3D-data inpainting 386
Zhu Y, Zhao M, Li H, Zhang P
The CT Laboratory, School of Mathematics, Capital Normal University,Beijing, China

Optimization-based extrapolation for truncation correction 390
Maier A, Scholz B, Dennerlein F
Siemens AG, Healthcare Sector, Forchheim, Germany

Comparison of image features for misalignment correction in flat-detector CT 395
Wicklein J, Kunze H, Kalender W A, Kyriakou Y
Institute of Medical Physics (IMP), University of Erlangen–Nürnberg, Erlangen, Germany; Siemens AG, Healthcare Sector, Forchheim, Germany

An analytical geometric calibration method for circular cone-beam CT geometry 399
Xu J, Tsui B M W
Russell H. Morgan Dept. of Radiology and Radiological Science, The Johns Hopkins School of Medicine, Baltimore, MD, USA

Hybrid scatter correction for CT imaging 404
Baer M, Kachelrieβ M
Institute of Medical Physics, University of Erlangen-Nürnberg, Erlangen, Germany; German Cancer Research Center (DKFZ), Heidelberg, Germany

Calculation and comparison of figures of merit for spectral CT 409
Rigie D, La Rivière P J
Radiology Dept., University of Chicago, Chicago, IL, USA

Multi-material decomposition using statistical image reconstruction in X-ray CT 413
Long Y, Fessler J A
Dept. of Electrical Engineering and Computer Science, University of Michigan, Ann Arbor, MI, USA

Quantitative soft tissue characterization from multi-energy photon counting CT 417
Alessio A, MacDonald L R
University of Washington, Seattle, WA, USA

Image reconstruction for hybrid true-color micro-CT 421
Xu Q, Yu H, Bennett J, He P, Zainon R, Doesburg R, Opie A, Walsh M, Shen H, Butler A, Butler P, Mou X, Wang G
Institute of Image Processing and Pattern Recognition, Xi'an Jiaotong University, Xi'an, Shaanxi, P.R. China; Division of Radiologic Sciences, Wake Forest University Health Sciences, Winston-Salem, NC, USA; School of Biomedical Engineering and Sciences, Virginia Tech, Blacksburg, VA, USA; Dept. of Physics and Astronomy, University of Canterbury, Christchurch, New Zealand; Dept. of Radiology, University of Otago, Christchurch, New Zealand; European Organization for Nuclear Research (CERN), Geneva, Switzerland

Session W4: Spectral CT imaging
Moderated by J. Fessler (The University of Michigan) and H. Kudo (University of Tsukuba)

Differentiation of uric acid vs non uric acid urinary stones in the presence of iodine constrast using dual energy CT 425
Wang J, Qu M, Duan X, Takahashi N, Kawashima A, Leng S, McCollough C H
Dept. of Radiology, Mayo Clinic, Rochester, MN, USA

Incorporation of bone beam harderning correction into statistical iterative CT reconstruction 430
Brendel B, Koehler T, Yagil Y, Thomson R
Philips Technologie GmbH, Innovative Technologies, Research Laboratories, Hamburg, Germany; Philips Healthcare, Haifa, Israel; Philips Healthcare, Cleveland, OH

CT reconstruction using spectral and morphological prior knowledge: application to imaging the prosthetic knee Zbijewski W, Stayman J W, Muhit A, Yorkston J, Carrino J A, Siewerdsen J H *Dept. of Biomedical Engineering, Johns Hopkins University, Baltimore, MD , USA; Carestream Health, Rochester, NY, USA; Dept. of Radiology, Johns Hopkins University, Baltimore, MD, USA*	434
A model-based iterative algorithm for dual-energy X-ray CT reconstruction Zhang R, Thibault J-B, Bouman C A, Sauer K D, Hsieh J *School of Electrical and Computer Engineering, Purdue University, West Lafayette, IN, USA; GE Healthcare technologies, Waukesha, WI, USA; Dept. of Electrical Engineering, University of Notre Dame, Notre Dame, IN, USA*	439

Improving Best-Phase Image Quality in Cardiac CT by Motion Correction with MAM Optimization

Christopher Rohkohl, Herbert Bruder, Karl Stierstorfer and Thomas Flohr

***Abstract*—Despite the latest hardware developments in high-end cardiac CT (e.g. dual source), there exist clinical scenarios where the temporal resolution is not sufficient and motion artifacts affect the image quality mainly of the coronary arteries. Latest research claims motion correction in cardiac CT to be a solution to improved image quality in such scenarios. However, yet it could only be shown that the motion information inferred by 3-D / 3-D registration from quiescent heart phases of a 4-D cardiac CT acquisition can be used to increase the image quality during rapid phases of motion.**

In this paper we propose a novel method for motion estimation and compensation, which for the first time allows a significant improvement of the clinical relevant best-phase image quality and does not rely on a multiple phase (4-D) data acquisition. For image reconstruction the motion compensated version of the ECG-gated FDK-algorithm is utilized. The motion is modeled by a sub-sampled 4-D motion vector field which is parameterized by the acquisition time of the contributing projection data. Motion estimation is formalized as a high-dimensional optimization problem. The cost function is based on the definition of motion artifact metrics (MAM) which allow the quantification of motion artifacts in a 3-D reconstructed image. By adjusting the motion field parameters the MAM of the resulting motion compensated reconstruction is optimized (motion artifacts are minimized) using a gradient descent procedure. Since for motion estimation and compensation only analytical methods (FDK-algorithm) are utilized, the derivatives can be easily computed, which in turn allows a fast and practical implementation.

I. INTRODUCTION

THE imaging of cardiac structures, in particular the coronary arteries, using CT is a clinically important and at the same technically challenging problem. Cardiac vessels are small, rapidly moving structures and therefore require a high temporal resolution of the reconstructed image. Naturally the temporal resolution is limited by hardware constraints which evolved into the latest high-end dual-source systems with a temporal resolution of less than 90 ms [1]. Clinical imaging is usually performed in phases of low motion. The duration of that quiescent heart phases shortens with increasing heart rate and at the same time lead to higher vessel velocities [2]. This circumstance causes image quality problems due to motion artifacts especially in older or cheaper systems, and can even bring high-end systems to their limits.

That's the reason why the research community is actively trying to increase the temporal resolution by means of novel reconstruction algorithms. In essence there exist two different strategies. One research direction is to use less data than theoretically required for image reconstruction. In order to overcome limited data artifacts, constraints need to be incorporated into an iterative algorithm, e.g. a prior image and smoothness constraint in TRI-PICCS [3] or a positivity constraint in TRIM [4]. The quantification of the temporal resolution of those algorithms is difficult and latest results suggest only minor improvements for TRI-PICCS [5], [6]. For TRIM no quantitative or clinical results have been reported yet.

The second research direction is to estimate the cardiac motion by 3-D / 3-D registration of the relevant structures at different heart phases [7]–[10]. The estimated motion is then used to reconstruct an image with improved image quality by compensating the object motion in the image reconstruction algorithm, e.g. [11]. While theoretically appealing, estimating the unknown heart motion proofs to be a challenging problem. Promising results have been presented for coronary CT which show that phases of rapid motion benefit from motion correction [8]–[10]. However, to our best knowledge, yet no publication reported an increased image quality for the *best* motion phase available in a particular dataset and threfore no increase of temporal resolution could be actually demonstrated for 3-D / 3-D or tracking based motion correction algorithms. In literature this aspect has not received attention yet. We hypothesize that one main reason is the accurracy of the registration or tracking. The image quality of the coronaries drastically decreases in non best-phase images and thus can render a perfect tracking or registration highly difficult.

Due to that we believe that a new approach towards solving this problem is required. For C-arm systems latest research suggests, that the quality (artifact level) of a reconstructed image can be estimated directly from the image by computing an image metric, e.g. the Entropy [12]. This observeration was used to correct the geometric calibration of the wobbling C-arm trajectory by seeking a geometry which minimizes the image quality metric. We propose to use a similar approach for correcting artifacts caused by local motion of the heart during the data acquisition. The novel approach requires only the data that is used for image reconstruction. This allows saving dose as no additional data needs to be acquired and further – for the first time shown – allows a significant improvement of the best phase image quality by motion correction. The detailed algorithm along with the motion artifact metrics is presented in the remainder of this paper.

II. MOTION CORRECTED RECONSTRUCTION

A. Motion Model

One important building block of the proposed framework is the ability to perform a motion compensated 3-D image

---

The authors are with the Siemens AG, Healthcare Sector, Forchheim, Germany. Corresponding author: C. Rohkohl (christopher.rohkohl.ext@siemens.com).

reconstruction. Therefore we need to define a motion model that formally describes the motion. There exists a variety of different possibilities for describing a time-continuous local motion. Mostly a set of control points is placed in space and time. Each control point is assigned a motion vector. The motion at a certain point and time is then computed by a linear combination of the neighboring control points, e.g. using B-splines [13].

In this paper we will follow the same approach and use a linear interpolation of a sub-sampled time-resolved motion vector field. However, in theory any other motion model would be applicable. For simplicity, we denote the parameters of the motion model to be the parameter vector $\boldsymbol{s}$ where $\boldsymbol{s}_{t,\boldsymbol{x}} \in \mathbb{R}^3$ is the linearly interpolated motion vector from the control points in $\boldsymbol{s}$ for a spatial location $\boldsymbol{x} \in \mathbb{R}^3$ at the acquisition time t. The formula for the motion model function is then given by

$$M(t, \boldsymbol{x}, \boldsymbol{s}) = \boldsymbol{x} + \boldsymbol{s}_{t,\boldsymbol{x}} \ . \tag{1}$$

It computes for any time t and any location $\boldsymbol{x}$, the novel (displaced) location from a particular parameter vector $\boldsymbol{s}$.

B. Reconstruction Algorithm

For computing a motion compensated image from the parametric motion model we propose to use the approximate algorithm introduced by [11] based on the FDK-algorithm. It is fast and gives reasonable improvements of image quality if provided with correct motion information. The ony difference to the standard algorithm is the backprojection along a new trajectory which is defined by the motion model function M. Formally, the analytical formular for a reconstructed image value at location $\boldsymbol{x}$ is given by the summation of the backprojection onto each acquired detector data i, i.e.

$$f(\boldsymbol{x}, \boldsymbol{s}) = \sum_i Q(i, \boldsymbol{x}')\, p(i, A(i, \boldsymbol{x}')) \tag{2}$$

with $\boldsymbol{x}' = M(t_i, \boldsymbol{x}, \boldsymbol{s})$. Here, t_i is the acquisition time for detector image i, the function Q is a redundancy weight, $p(i, \boldsymbol{u})$ returns the ramp-filtered detector value at detector bin $\boldsymbol{u}$ and $A(i, \boldsymbol{x}) = \boldsymbol{u}$ is the geometric mapping (backprojection) of the voxel $\boldsymbol{x}$ to the detector coordinate $\boldsymbol{u}$.

In [13] it was demonstrated that the analytical algorithm has various benefits, e.g. the derivative $\frac{\partial f(\boldsymbol{x},\boldsymbol{s})}{\partial \boldsymbol{s}}$ of the reconstruction with respect to the motion model can be analytically determined and be computed in a backprojection-like operation. This enables fast and efficient schemes for motion estimation and will be exploited in the herein proposed algorithm.

III. NOVEL MOTION ESTIMATION ALGORITHM

The novel motion estimation algorithm is composed of three major components which will be detailed in the following. First, different motion artifact metrics (MAM) are defined which allow the relative quantification of local motion artifacts. Locality of the motion artifacts requires the identification of corrupted volume areas (volume of interest) which we denote motion maps. As last component, an optimization algorithm for the MAMs is required which actually estimates the unknown parameters of the motion model.

A. Motion Artifact Metrics (MAM)

Local motion of contrasted structures causes streaks and blurring in the reconstructed images caused by data inconsistencies. We propose different metrics which can be used to assess the relative amount of motion artifacts. The metrics are formally described by a function $\mathcal{L}(\boldsymbol{s})$ which computes the MAM value for the motion compensated reconstruction corresponding to the motion model parameters $\boldsymbol{s}$ in a volume of interest (motion map) denoted Ω.

1) Entropy: Entropy is an information theoretic measure quantifying the amount of information encoded in the volume. The over- and undershoots caused by motion artifacts therefore increase entropy values which in turn may allow a relative quantifaction of the artifact level [12]. Formally it is given by

$$\mathcal{L}_{\text{ent}}(\boldsymbol{s}) = -\sum_h P(h, \boldsymbol{s}) \ln P(h, \boldsymbol{s}), \tag{3}$$

where $P(h, \boldsymbol{s})$ is the probability of the intensity value h in the reconstructed volume. An estimate of the probability values can be computed using various kernel density estimation techniques, e.g. Parzen-windowing [14]:

$$P(h, \boldsymbol{s}) = \frac{1}{|\Omega|} \sum_{\boldsymbol{x} \in \Omega} K(f(\boldsymbol{x}, \boldsymbol{s}) - h) \tag{4}$$

with some kernel function K, e.g. a Gauß-kernel.

2) Positivity (No-Undershoots): With the introduction of the TRIM-algorithm [4] a constraint for iterative reconstruction algorithms was proposed which punishes undershoots, i.e. enforces positivity against an average value T of the structure of interest. This constraint can be easily transformed into an MAM by

$$\mathcal{L}_{\text{pos}}(\boldsymbol{s}) = \sum_{\boldsymbol{x} \in \Omega} \left(\begin{cases} 0 & \text{if } f(\boldsymbol{x}, \boldsymbol{s}) \geq T \\ (f(\boldsymbol{x}, \boldsymbol{s}) - T)^2 & \text{otherwise} \end{cases} \right) \tag{5}$$

which becomes minimum if there are no reconstructed values in Ω which are below the undershoot threshold T.

3) Total Variation: Another MAM cab be derived from the smoothness constraint of iterative reconstruction algorithms. Those algorithms assume that artifacts caused by motion increase the total variation of the image. This constraint can be easily transformed into an MAM by

$$\mathcal{L}_{\text{tv}}(\boldsymbol{s}) = \sum_{\boldsymbol{x} \in \Omega} \sqrt{\sum_{j=1}^{3} \left(\frac{\partial f(\boldsymbol{x}, \boldsymbol{s})}{\partial x_j} \right)^2} \ . \tag{6}$$

B. Motion Maps

In the previous definition of the MAM the computation was restricted to a volume of interest Ω. This set of voxels describes the image regions that show motion artifacts and hence will be named a motion map. We propose to utilize an automatic segmentation algorithm for the motion map computation. There have been enormous efforts to make automatic segmentation of the coronaries feasible in recent years and various algorithmic solutions are available with a high accurracy and reliability. For our results the algorithm presented in [15] was utilized for extracting the coronary centerlines. Further the segmented region was dilated by several millimeters in order to capture the whole range of motion related artifacts originating from the contrasted vessels.

C. Optimization Algorithm

Motion estimation corresponds to finding a set of motion parameters $\boldsymbol{s}$ that minimizes one or more of the selected MAMs. For minimization a simple gradient descent algorithm with adaptive step size is utilized. This requires the derivative of the MAM with respect to the motion parameters. This derivative $\frac{\partial \mathcal{L}(\boldsymbol{s})}{\partial \boldsymbol{s}}$ can be analytically computed for all presented MAMs. It further requires the determination of $\frac{\partial f(\boldsymbol{x},\boldsymbol{s})}{\partial \boldsymbol{s}}$ which was shown in [13] to be feasible in a backprojection-like operation. The optimization is stopped after a fixed number of iterations. If multiple MAMs are to be optimized, they are alternated in fixed order.

IV. EXPERIMENTS

A. Experimental Setup

It is the aim of this paper to show a proof of concept for a novel algorithmic approach to motion estimation. Therefore we provide results for four clinical datasets. The spatial spacing of the motion model control points was set to 7.5 mm in each direction. The temporal spacing was set to 2.5% of the heart beat duration. The specification of the dataset and of the optimization algorithm were varied in order to demonstrate the flexibility of the introduced concepts. Further dataset specific details can be found in the corresponding figures Fig. 1 to Fig. 3. The reconstruction was parameterized to cover the complete heart, i.e. the field of view was 150 mm with a matrix size of 512 pixels, a slice thickness of 0.6 mm and a slice spacing of 0.3 mm. Motion estimation was carried out at a reduced resultion with a matrix size of 128 pixels for accelerating the computation.

B. Results and Discussion

The reconstruction results from the four clinical cases are depicted in Fig. 1 to Fig. 4. It can be observed that the image quality drastically improves for dual source and single source datasets, i.e. the motion artifacts are clearly reduced by the novel algorithm. In Fig. 2 it can be seen how the proposed algorithm can significantly improve the best phase image quality even in datasets with a very good temporal resolution of 75 ms. Further the algorithm is capable to improve image quality reconstructed in non-ideal phases (cmp. Fig. 1) and in datasets with a lower temporal resolution (cmp. Figs. 3–4). This demonstrates the generality of the proposed approach and that it can fully automatically optimize image quality without relying on image data from other heart phases as it is the case in 3-D-3-D registration or tracking algorithms.

V. CONCLUSIONS AND OUTLOOK

In this paper a novel approach for motion estimation and correction was proposed. It is based on the definition and optimization of motion artifact metrics (MAMs). For first clinical datasets it was demonstrated that with the new approach the quality of the best-phase image can be drastically improved. Yet, the results are only qualitatively and a quantitative evaluation of temporal resolution improvement and a comparison of different MAMs remains to be investigated in future work. Due to the encouring results we show great promise that image quality of the coronary arteries can be drastically increased without exposing the patient to more dose and without requiring the latest hardware. However, we are convinced that the software-based approaches cannot make hardware developments like dual source CT mandatory, but rather extend their applicability to a wider range of patients. One example for this are dual source CT protocols which image the complete heart during a single cardiac cycle [16]. With novel motion estimation and compensation approaches as the one presented, such protocols could be applied to patients with high heart rates.

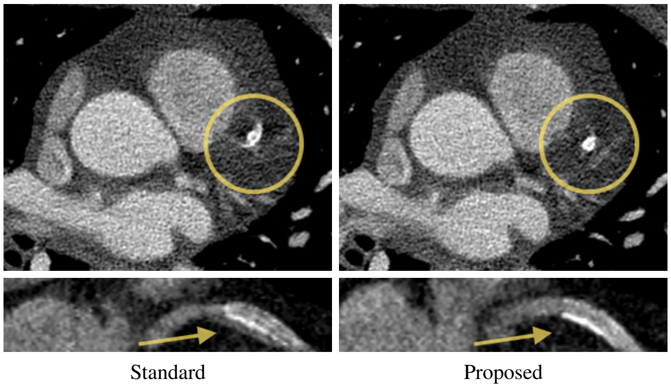

Fig. 1: Results for a clinical case with a stent. It is a single-source dataset with a temporal resolution of 143 ms at a heart rate of 66 bpm reconstructed in a heart phase centered at 66%. The MEM $\mathcal{L}_{\text{ent}}$ was optimized over 20 iterations.

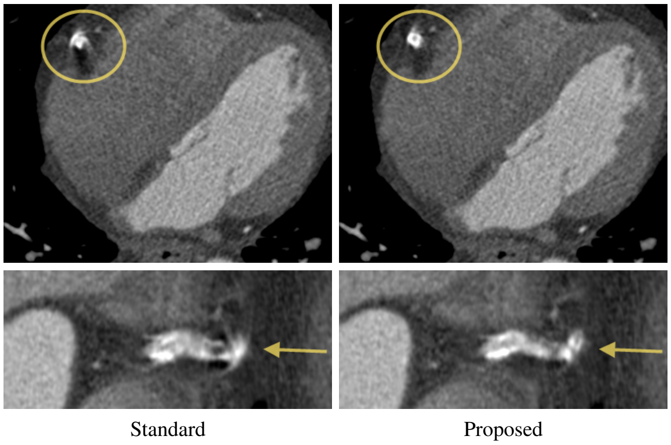

Fig. 2: Results for a clinical case. It is a dual-source dataset with a temporal resolution of 75 ms at a heart rate of 73 bpm reconstructed in the best heart phase centered at 75%. The MEMs $\mathcal{L}_{\text{ent}}$ and $\mathcal{L}_{\text{pos}}$ were optimized over 30 iterations.

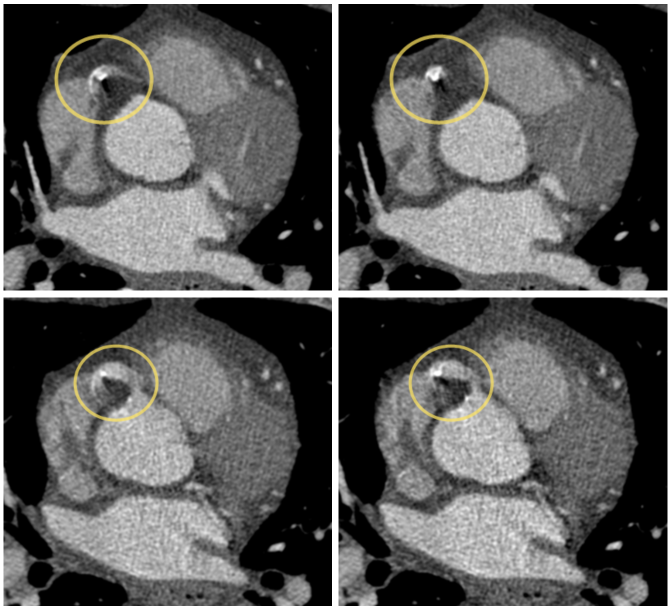

Fig. 3: Results for a clinical case. It is a single-source dataset with a temporal resolution of 143 ms at a heart rate of 73 bpm reconstructed in the best heart phase centered at 76%. The MEMs $\mathcal{L}_{\text{ent}}$ and $\mathcal{L}_{\text{pos}}$ were optimized over 30 iterations.

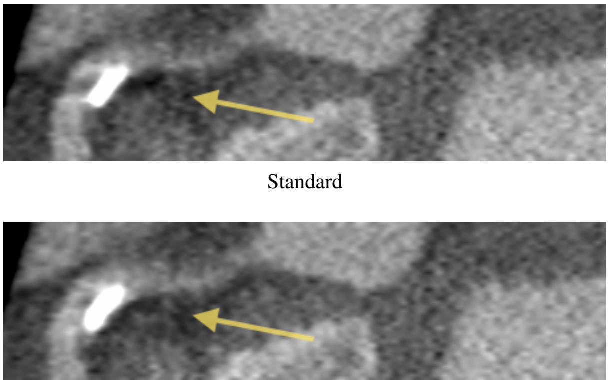

Fig. 4: Results for a clinical case. It is a dual-source dataset with a temporal resolution of 75 ms at a heart rate of 60 bpm reconstructed at a heart phase centered at 60%. The MEMs $\mathcal{L}_{\text{ent}}$ and $\mathcal{L}_{\text{pos}}$ were optimized over 30 iterations.

REFERENCES

[1] T. G. Flohr, H. Bruder, K. Stierstorfer, M. Petersilka, B. Schmidt, and C. H. McCollough, "Image reconstruction and image quality evaluation for a dual source CT scanner," *Medical Physics*, vol. 35, no. 12, pp. 5882–5897, 2008.

[2] L. Husmann, S. Leschka, L. Desbiolles, T. Schepis, O. Gaemperli, B. Seifert, P. Cattin, T. Frauenfelder, T. G. Flohr, B. Marincek, P. A. Kaufmann, and H. Alkadhi, "Coronary Artery Motion and Cardiac Phases: Dependency on Heart Rate Implications for CT Image Reconstruction," *Radiology*, vol. 245, no. 2, pp. 567–576, 2007.

[3] G.-H. Chen, J. Tang, and J. Hsieh, "Temporal resolution improvement using piccs in mdct cardiac imaging," *Medical Physics*, vol. 36, no. 6, pp. 2130–2135, 2009.

[4] H. Schöndube, H. Kunze, H. Bruder, and K. Stierstorfer, "Using the positivity constraint to enhance temporal resolution in CT," in *Proceedings of the first international conference on image formation in x-ray computed tomography*, Salt Lake City, Utah, USA, June 2010, pp. 189–193.

[5] C. Maass, C. Hofmann, and M. Kachelriess, "TRI-PICCS in single source and dual source CT," in *IEEE NSS-MIC (Nuclear Science Symposium-Medical Imaging Conference)*, Knoxville, USA, October 2010, pp. 2805–2810.

[6] C. Maass and M. Kachelriess, "Quantification of temporal resolution and its reliability in the context of TRI-PICCS and dual source CT," N. J. Pelc, E. Samei, and R. M. Nishikawa, Eds., vol. 7961, no. 1. Lake Buena Vista, USA: SPIE, 2011, p. 79611M.

[7] M. Prümmer, J. Hornegger, G. Lauritsch, L. Wigström, E. Girard-Hughes, and R. Fahrig, "Cardiac c-arm CT: A unified framework for motion estimation and dynamic CT," *IEEE Transactions on Medical Imaging*, vol. 28, no. 11, pp. 1836–1849, 2009.

[8] A. A. Isola, M. Grass, and W. J. Niessen, "Fully automatic nonrigid registration-based local motion estimation for motion-corrected iterative cardiac CT reconstruction," *Medical Physics*, vol. 37, no. 3, pp. 1093–1109, 2010.

[9] J. Cammin, P. Khurd, A. Kamen, Q. Tang, K. J. Kirchberg, C. Chefd'Hotel, H. Bruder, and K. Taguchi, "Combined motion estimation and motion-compensated FBP for cardiac CT," in *11th Int. Meeting on Fully 3D Image Reconstruction in Radiology and Nuclear Medicine*, Potsdam, Germany, July 2011, pp. 136–139.

[10] Q. Tang, J. Cammin, and K. Taguchi, "A fully four-dimensional, iterative motion estimation and compensation for cardiac x-ray computed tomography," in *11th Int. Meeting on Fully 3D Image Reconstruction in Radiology and Nuclear Medicine*, Potsdam, Germany, July 2011, pp. 470–473.

[11] D. Schäfer, J. Borgert, V. Rasche, and M. Grass, "Motion-compensated and gated cone beam filtered back-projection for 3-d rotational x-ray angiography." *IEEE Transactions on Medical Imaging*, vol. 25, no. 7, pp. 898–906, July 2006.

[12] Y. Kyriakou, R. M. Lapp, L. Hillebrand, D. Ertel, and W. A. Kalender, "Simultaneous misalignment correction for approximate circular cone-beam computed tomography," *Physics in Medicine and Biology*, vol. 53, no. 22, pp. 6267–6289, 2008.

[13] C. Rohkohl, G. Lauritsch, L. Biller, M. Prümmer, J. Boese, and J. Hornegger, "Interventional 4D motion estimation and reconstruction of cardiac vasculature without motion periodicity assumption," *Medical Image Analysis*, vol. 14, no. 5, pp. 687–694, 2010.

[14] E. Parzen, "On estimation of a probability density function and mode," *The Annals of Mathematical Statistics*, vol. 33, no. 3, pp. 1065–1076, 1962.

[15] M. Gülsün and H. Tek, "Robust vessel tree modeling," in *Medical Image Computing and Computer-Assisted Intervention - MICCAI 2008*, ser. Lecture Notes in Computer Science, D. Metaxas, L. Axel, G. Fichtinger, and G. Székely, Eds. Springer Berlin / Heidelberg, 2008, vol. 5241, pp. 602–611.

[16] S. Achenbach, M. Marwan, T. Schepis, T. Pflederer, H. Bruder, T. Allmendinger, M. Petersilka, K. Anders, M. Lell, A. Kuettner, D. Ropers, W. Daniel, and T. Flohr, "High-pitch spiral acquisition: a new scan mode for coronary CT angiography." *Journal of cardiovascular computed tomography*, vol. 3, no. 2, pp. 117–121, 2009.

Evaluation of Interpolation Methods for Motion Compensated Tomographic Reconstruction for Cardiac Angiographic C-arm Data

Kerstin Müller, Yefeng Zheng, Günter Lauritsch, Christopher Rohkohl, Chris Schwemmer,
Andreas K. Maier, Rebecca Fahrig and Joachim Hornegger

***Abstract*—Anatomical and functional information about the cardiac chambers is a key component of future developments in the field of interventional cardiology. With the technology of C-arm CT it is possible to reconstruct intraprocedural 3-D images from angiographic projection data. Some approaches attempt to add the temporal dimension (4-D) by electrocardiogram (ECG)-gating in order to distinguish physical states of the heart. However, for the left heart ventricle scanned during one single C-arm sweep, this approach leads to insufficient projection data and thus to a degraded image reconstruction quality.**

In this paper, we evaluate the influence of different interpolation methods for a motion compensated reconstruction approach for the left heart ventricle based on a recently presented 3-D dynamic surface model. The surface model results in a sparse motion vector field (MVF) defined at control points. However, to perform a motion compensated reconstruction a dense MVF is required. The dense MVF can be determined by different interpolation methods. In this paper, we evaluate thin-plate splines (TPS), the Shepard's method, simple averaging, and a smoothed weighting function as interpolation functions. The 2-D overlap of the forward projected motion compensated reconstructed ventricle and the segmented 2-D ventricle blood pool is quantitatively measured with the Dice similarity coefficient and the mean deviation between extracted ventricle contours. Preliminary results on heart ventricle phantom data, as well as on clinical human data show the best results with the TPS interpolation.

I. INTRODUCTION

A. Purpose of this Work

There is increasing interest in three-dimensional imaging of dynamic cardiac ventricular shapes, e.g. left ventricle (LV) motion, for quantitative evaluation of cardiac function such as ejection fraction measurements and wall motion analysis. Typically these parameters are estimated based on 2-D projections from two or less views [1]. The 2-D approach lacks information about the 3-D shape of the LV. A 3-D reconstruction with projection data from a short-scan permits the physician to assess the LV in all spatial dimensions. Due to the long acquisition time (a few seconds) of the C-arm, the dynamics of the ventricle need to be taken into account. A standard cone-beam reconstruction (FDK) [2] averages over all heart phases and has no temporal resolution. Therefore, a motion compensated tomographic reconstruction for the heart ventricle should be developed. An accurate estimate of the motion would also provide a direct analysis of the temporal characteristics of the ventricle.

B. State-of-the-Art

Different approaches for recovering ventricular shapes from angiographic data using biplanar angiographic systems can be found in the literature [1], [3]. These systems can acquire two orthogonal projection images simultaneously. However, such a biplanar system is not accessible to all cardiologists.

Another approach records an ECG signal during acquisition and a relative heart phase is assigned to each projection. Commonly, the heart phases are then denoted as a percentage between two successive R-peaks. In order to improve temporal resolution, the reconstruction is performed with the subset of the projections that lie inside a certain ECG window centered at the favored heart phase [4]. As an example, for a 5 s acquisition time and 60 bpm five intervals contribute to one heart phase. The ECG-gated approach works well for the sparse and high contrasted structure of the coronaries [5]–[7]. However, for the heart chambers an insufficient number of projections are acquired in a single scan. Consequently, multiple sweeps of the C-arm have to be performed in order to acquire enough projections for each heart phase [8], [9]. The longer imaging time results in a higher contrast burden and radiation dose for the patient.

In this paper, we perform a motion compensated tomographic reconstruction with projection data from one single C-arm sweep. As a first step, a dynamic surface model of the LV is generated to extract a sparse MVF [10]. The LV surface model is reconstructed from a set of ECG-gated 2-D X-ray projections such that the forward projection of the reconstructed LV model matches the 2-D blood pool segmentation of the ventricle. In the second step, a motion compensated tomographic reconstruction is performed. This requires a dense MVF [11]. Thus, the sparse motion field on the surface has to be interpolated. In order to generate a dense MVF from scattered data several interpolation methods can be applied

---

K. Müller, C. Schwemmer and J. Hornegger are with the Pattern Recognition Lab, Department of Computer Science and the Erlangen Graduate School in Advanced Optical Technologies (SAOT), Friedrich-Alexander-Universität Erlangen-Nürnberg, Erlangen, Germany. Email:kerstin.mueller@cs.fau.de. G. Lauritsch, C. Rohkohl and A. K. Maier are with the Siemens AG, Healthcare Sector, Forchheim, Germany. Y. Zheng is with Image Analytics and Informatics, Siemens Corporate Research, Princeton, NJ, USA. R. Fahrig is with the Department of Radiology, Stanford University, Stanford, CA, USA.

[12]. For computed tomography (CT) image reconstruction, different interpolation methods for cardiac motion were investigated by Forthmann et al [13]. However, the main focus of the reconstruction was on the sharpness of the coronaries. Furthermore, C-arm projection data displays different contrast conditions and suffers from a lower temporal resolution than a conventional CT scanner. Therefore, it is not evident that the same interpolation methods yield the same results.

C. *Outline*

In this paper, we investigate different interpolation methods: a thin-plate spline (TPS) interpolation [14], [15], the Shepard's method [16], a simple averaging, and a weighting function based interpolation method. The interpolation methods were evaluated by comparing the image results of the motion compensated tomographic reconstructions with the gold standard of the segmented original projection data.

II. SURFACE BASED MOTION COMPENSATED RECONSTRUCTION

A. *Surface Model*

The basis of the motion compensated reconstruction is the dynamic 3-D surface of the ventricle with its control points $\boldsymbol{p}_i(\phi_k) \in \mathbb{R}^3$, with $i = 1, \ldots, N$ where N is the number of control points for each heart phase ϕ_k [10]. For reconstruction a reference heart phase ϕ_0 is selected. Displacement vectors $\boldsymbol{d}_i(\phi_k) \in \mathbb{R}^3$ between the control points in the reference heart phase ϕ_0 and the current heart phase ϕ_k can then be computed.

B. *Interpolation Methods*

In order to perform a motion compensated tomographic reconstruction, a dense MVF needs to be generated from the sparse MVF. Therefore, different interpolation methods were evaluated.

1) Thin-Plate Splines (TPS): The deformation of the control points over time can be represented by a TPS transformation. The TPS approach assumes that the bending and stretching behavior of the left ventricle is similar to the bending of a thin plate. TPS have already been applied to estimate cardiac vascular motion of CT data [17] and ventricular motion of MRI data [18].

The TPS coordinate transformation with its displacements for an arbitrary point $\boldsymbol{x} \in \mathbb{R}^3$ is given as:

$$\boldsymbol{d}(\boldsymbol{x}, \phi_k) = \sum_{i=1}^{N} \boldsymbol{G}(\boldsymbol{x} - \boldsymbol{p}_i(\phi_k)) c_i(\phi_k) + \boldsymbol{A}(\phi_k)\boldsymbol{x} + \boldsymbol{b}(\phi_k), \quad (1)$$

where the spline coefficients $c_i(\phi_k) \in \mathbb{R}$ of the TPS are determined by the control points $\boldsymbol{p}_i(\phi_k) \in \mathbb{R}^3$ and the displacements $\boldsymbol{d}_i(\phi_k) \in \mathbb{R}^3$ of the control points. $\boldsymbol{A}(\phi_k) \in \mathbb{R}^{3\times3}$, $\boldsymbol{b}(\phi_k) \in \mathbb{R}^3$ specify an additional affine transformation to which the spline reduces farther away from the control points. The transformation's kernel matrix $\boldsymbol{G}(\boldsymbol{x}) \in \mathbb{R}^{3\times3}$ of a point $\boldsymbol{x} \in \mathbb{R}^3$ for a 3-D TPS is given according to [15]:

$$\begin{aligned} \boldsymbol{G}(\boldsymbol{x}) &= r(\boldsymbol{x}) \cdot \boldsymbol{I}, & (2) \\ r(\boldsymbol{x}) &= ||\boldsymbol{x}||_2 = \sqrt{x_1^2 + x_2^2 + x_3^2}, & (3) \end{aligned}$$

where $\boldsymbol{I} \in \mathbb{R}^{3\times3}$ is the identity matrix. In order to solve Equation 1 for each ϕ_k, set $\boldsymbol{d}(\boldsymbol{x}, \phi_k) = \boldsymbol{d}(\phi_k)$ for $\boldsymbol{x} = \boldsymbol{p}_i(\phi_k)$. Since Equation 1 is linear in $c_i(\phi_k)$, $\boldsymbol{A}(\phi_k)$, and $\boldsymbol{b}(\phi_k)$ it can be solved in a straightforward manner [15].

The resulting spline coefficients and affine parameters are inserted in Equation 1 in order to evaluate the spline at any arbitrary 3-D point. A motion vector can therefore be computed for every voxel in the reconstructed volume.

2) Linear Interpolation: All surface control points inside a radius R (here: 2 cm) around the point $\boldsymbol{x}$ are determined and the resulting displacement vector $\boldsymbol{d}(\boldsymbol{x}, \phi_k)$ is a weighted sum of the corresponding displacement vectors:

$$\begin{aligned} \boldsymbol{d}(\boldsymbol{x}, \phi_k) &= \sum_{i=1}^{N} \boldsymbol{G}^*(\boldsymbol{x} - \boldsymbol{p}_i(\phi_k)) \boldsymbol{d}_i(\phi_k), & (4) \\ \boldsymbol{G}^*(\boldsymbol{x}) &= f(\boldsymbol{x}) \cdot \boldsymbol{I}, & (5) \end{aligned}$$

where f is a weighting function. Function f weights the displacement vectors according to the distance of the control point $\boldsymbol{p}_i(\phi_k)$ to the point $\boldsymbol{x}$.

a) Simple Averaging: Here the resulting displacement vector $\boldsymbol{d}(\boldsymbol{x}, \phi_k)$ is a simple average of the displacement vectors at the surrounding control points. Thus the function f, with M denoting the number of control points used is defined as:

$$f(\boldsymbol{x}) = \begin{cases} \frac{1}{M} & |\boldsymbol{x}| \leq R \\ 0 & \text{else} \end{cases} \quad (6)$$

b) Weighting Function: Here the function f is a cosine-based smoothing function:

$$f(\boldsymbol{x}) = \begin{cases} \frac{1}{\mathcal{N}}(1 + \cos(\frac{\boldsymbol{x} \cdot \pi}{R})) & |\boldsymbol{x}| \leq R \\ 0 & \text{else,} \end{cases} \quad (7)$$

where $\mathcal{N}$ denotes a normalization constant such that $\sum_{j=1}^{M} f(\boldsymbol{x}_j) = 1$.

c) Shepard's Method: Here an inverse distance weighting is applied according to the distance from the considered point to the n closest control points [16]. The function f is therefore defined as:

$$f(\boldsymbol{x}) = \frac{||\boldsymbol{x}||_2^{-1}}{\sum_{j=1}^{n} ||\boldsymbol{x}_j||_2^{-1}}. \quad (8)$$

We set n empirically to 30 in this paper.

C. *Cutting*

In order to reduce the computational complexity we assume that the left ventricle is the central moving organ inside the scan field of view. Therefore, a dense MVF is computed inside the ventricle and within a neighborhood around the extracted surface of the first section of the ascending aorta and the ventricle. Hence, the considered set of points $\mathcal{P}$ is given as:

$$\mathcal{P} = \{\boldsymbol{x} \mid ||\boldsymbol{x} - \boldsymbol{p}_{\boldsymbol{x}}(\phi_k)||_2 \leq l\}, \quad (9)$$

where $\boldsymbol{p}_{\boldsymbol{x}}(\phi_k)$ is the closest surface control point to the current point $\boldsymbol{x}$. The distance l was heuristically set to 2 cm.

III. EXPERIMENTS

A. Phantom Data

The presented algorithm has been applied to a ventricle data set comparable to the XCAT phantom [19]. We simulated data using a clinical protocol with the following parameters: 395 projection images simulated equi-angularly over an angular range of 200° in 8 s with a size of 620 × 480 pixels at an isotropic resolution of 0.62 mm/pixel (≈0.4 mm in isocenter). The heartbeat was simulated with 75 bpm. The surface model consisted of 40 heart phases and 957 control points uniformly distributed over the left ventricle. The image reconstruction was performed on an image volume of $(25.6\,\text{cm})^3$ distributed on a 256^3 voxel grid.

B. Clinical Data

The dataset was acquired on an Artis Zee C-arm system (Siemens AG, Healthcare Sector, Forchheim, Germany). It consists of 133 projection images acquired over an angular range of 200° in 5 s with a size of 960 × 960 pixels at an isotropic resolution of 0.18 mm/pixel (≈0.12 mm in isocenter). The patient had a heart rate of ≈60 bpm. The surface model consisted of 26 heart phases and 961 control points equally distributed over the first section of the ascending aorta and left ventricle. Image reconstruction was performed on an image volume of $(14.1\,\text{cm})^3$ distributed on a 256^3 voxel grid.

C. Quantitative Evaluation

In order to compare the reconstruction quality of the motion compensated reconstruction algorithm, the maximum intensity forward projections (MIP) of the compensated LVs were generated. Binary mask images were created from the MIPs where a value equal to zero defines background and a non-zero value defines the ventricle shape. These binary images were compared to the segmented 2-D projections from which the original surface model was built. The overlap of the binarized image and the segmented 2-D projections was analyzed with the Dice similarity coefficient (DSC) [20]. The DSC is defined in the range of $[0, 1]$, where 0 means no overlap and 1 defines a perfect match between the two compared images. Since the motion compensated reconstruction improves the sharpness of the ventricle contour, the similarity of the contours of the projection images were evaluated with the mean deviation between the contours denoted by ϵ, where a small ϵ denotes a similar contour. The results were averaged over all heart phases.

IV. RESULTS AND DISCUSSION

In Figure 1, an MVF of the human data set between the reference heart phase at end-diastole and the current heart phase at end-systole are illustrated for the TPS.

A. Phantom Data

In Table I the results for the phantom left ventricle are reported. The best results were obtained with the TPS interpolation method. The contour deviation (ϵ) improved by ≈2 pixel which corresponds to 1.24 mm compared to the standard FDK. The standard deviation is also much smaller with the TPS compared to the standard reconstruction. The widely used Shepard's method and the weighting function provide slightly inferior results compared to the TPS. The Dice coefficient shows similar results between all interpolation methods as well as for the FDK reconstruction.

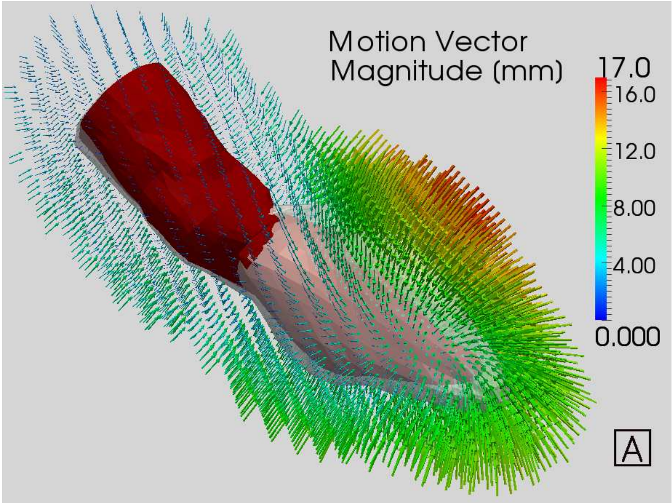

Fig. 1. Illustration of a dense MVF of the human data set computed with TPS between reference heart phase 70% and current phase 20%. Undersampled for illustration purposes.

TABLE I
RESULTS FOR THE LEFT VENTRICLE.

	Dice [pixel]	ϵ [pixel]	ϵ [mm]
Phantom			
TPS	0.95 ± 0.03	3.26 ± 0.37	2.02 ± 0.23
Shepard	0.95 ± 0.02	3.33 ± 0.31	2.06 ± 0.20
Weighting Fct.	0.95 ± 0.02	3.33 ± 0.27	2.06 ± 0.17
Simple Averaging	0.94 ± 0.02	3.64 ± 0.33	2.26 ± 0.20
Standard	0.94 ± 0.03	4.66 ± 1.91	2.89 ± 1.18
Human			
TPS	0.93 ± 0.01	9.15 ± 1.22	1.65 ± 0.22
Shepard	0.91 ± 0.02	10.29 ± 2.07	1.85 ± 0.33
Weighting Fct.	0.91 ± 0.02	10.92 ± 3.02	1.97 ± 0.54
Simple Averaging	0.91 ± 0.03	11.74 ± 2.81	2.11 ± 0.51
Standard	0.88 ± 0.03	17.60 ± 10.0	3.17 ± 1.80

B. Clinical Data

In Table I the results for the human left ventricle are listed. The best motion compensated reconstruction is again performed with the TPS interpolation method. The contour deviation (ϵ) improved by ≈9 pixel which corresponds to 1.62 mm compared to the standard FDK. The patient had a healthy ejection fraction of ≈75%. The standard deviation is also much smaller with the TPS compared to the standard reconstruction. The widely used Shepard's method and the weighting function provides slightly inferior results compared to the TPS. The Dice coefficent again shows similar results between all interpolation methods as well as for the FDK reconstruction.

In Figure 2 the results of different reconstructions are illus-

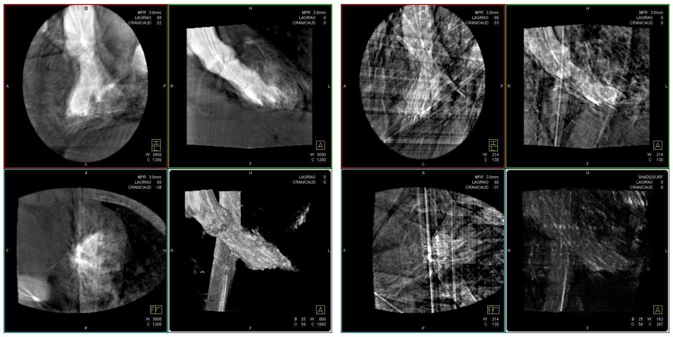

(a) Standard FDK reconstruction. (b) Nearest-Neighbor ECG-gated reconstruction for 20% heart phase (5 views).

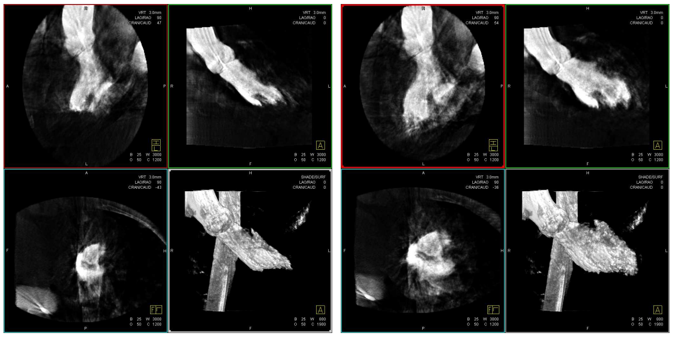

(c) Motion compensated reconstruction for 20% heart phase. (d) Motion compensated reconstruction for 70% heart phase.

Fig. 2. Reconstruction results of the human left ventricle with the TPS interpolation (W 3000, C 1200, Slice Thickness 3.0 mm). The ECG-gated reconstruction was windowed to be visually comparable.

trated. The standard reconstruction in Figure 2(a) exhibits blurring around the LV. In Figure 2(b) it can be observed that the ECG-gated reconstruction lacks LV structure. In comparison, the motion compensated reconstruction shows an expansion in diastole and contraction in systole of the LV, respectively (Fig.2(c),2(d)).

V. CONCLUSION

In this paper, we investigated the influence of different motion interpolation methods for a left ventricle motion compensated tomographic reconstruction. The best quantitative results (Dice coefficient, mean contour deviation) of a phantom and human data set were achieved with the TPS interpolation approach. The Shepard's method and the weighting function might be a good compromise between computational efficiency and accuracy. In conclusion, motion compensated reconstruction improved the reconstruction results compared to a standard reconstruction.

ACKNOWLEDGMENT

The authors would like to thank Drs. Patrick W. Serruys, Carl Schultz, Peter de Jaegere, and Robert van Geuns, Thorax Center, Erasmus MC, Rotterdam, The Netherlands for acquiring clinical data. Furthermore, the authors gratefully acknowledge funding of the NIH grant R01 HL087917 and of the Erlangen Graduate School in Advanced Optical Technologies (SAOT) by the German Research Foundation (DFG) in the framework of the German excellence initiative.

Disclaimer: The concepts and information presented in this paper are based on research and are not commercially available.

REFERENCES

[1] M. Moriyama, Y. Sato, H. Naito, M. Hanayama, T. Ueguchi, T. Harada, F. Yoshimoto, and S. Tamura, "Reconstruction of time-varying 3-D left-ventricular shape from multiview x-ray cineangiocardiograms," *IEEE Trans. Med. Imag.*, vol. 21, no. 7, pp. 773–785, 2002.

[2] L. Feldkamp, L. Davis, and J. Kress, "Practical cone-beam algorithm," *J. Opt. Soc. Am. A*, vol. 1, no. 6, pp. 612–619, 1984.

[3] R. Medina, M. Garreau, H. Lebreton, and D. Jugo, "Three-dimensional reconstruction of the left ventricle from two angiographic views," in *IEEE EMBS*, October 1997, pp. 569–572.

[4] B. Desjardins and E. Kazerooni, "Ecg-gated cardiac ct," *Am. J. Roentgenol.*, vol. 182, no. 4, pp. 993–1010, 2004.

[5] C. Blondel, G. Malandain, R. Vaillant, and N. Ayache, "Reconstruction of coronary arteries from a single rotational x-ray projection sequence," *IEEE Trans. Med. Imag.*, vol. 25, no. 5, pp. 653–663, 2006.

[6] E. Hansis, D. Schäfer, O. Dössel, and M. Grass, "Projection-based motion compensation for gated coronary artery reconstruction from rotational x-ray angiograms," *Phys. Med. Biol.*, vol. 53, no. 14, pp. 3807–3820, 2008.

[7] C. Rohkohl, G. Lauritsch, L. Biller, M. Prümmer, J. Boese, and J. Hornegger, "Interventional 4D motion estimation and reconstruction of cardiac vasculature without motion periodicity assumption," *Medical Image Analysis*, vol. 14, no. 5, pp. 687–694, 2010.

[8] G. Lauritsch, J. Boese, L. Wigström, H. Kemeth, and R. Fahrig, "Towards cardiac c-arm computed tomography," *IEEE Trans. Med. Imag.*, vol. 25, no. 7, pp. 922–934, 2006.

[9] M. Prümmer, J. Hornegger, G. Lauritsch, E. Wigström, L. Girard-Hughes, and R. Fahrig, "Cardiac c-arm ct: A unified framework for motion estimation and dynamic ct," *IEEE Trans. Med. Imag.*, vol. 28, no. 11, pp. 1836–1849, 2009.

[10] M. Chen, Y. Zheng, K. Müller, C. Rohkohl, G. Lauritsch, J. Boese, G. Funka-Lea, J. Hornegger, and D. Comaniciu, "Automatic extraction of 3D dynamic left ventricle model from 2D rotational angiocardiogram," in *MICCAI 2011*, September 2011, pp. 471–478.

[11] D. Schäfer, J. Borgert, V. Rasche, and M. Grass, "Motion-compensated and gated cone beam filtered back-projection for 3-D rotational x-ray angiography," *IEEE Trans. Med. Imag.*, vol. 25, no. 7, pp. 898–906, 2006.

[12] I. Amidror, "Scattered data interpolation methods for electronic imaging systems: a survey," *J. Electron. Imaging*, vol. 11, no. 2, pp. 157–176, 2002.

[13] P. Forthmann, U. Stevendaal, M. Grass, and T. Köhler, "Vector field interpolation for cardiac motion compensated reconstruction," in *IEEE NSS-MIC*, October 2008, pp. 4157–4160.

[14] F. Bookstein, "Principal warps: Thin-plate splines and the decomposition of deformations," *IEEE Trans. Pattern Anal. Mach. Intell.*, vol. 11, no. 6, pp. 567–585, 1989.

[15] M. Davis, A. Khotanzad, D. Flamig, and S. Harms, "A physics-based coordinate transformation for 3-D image matching," *IEEE Trans. Med. Imag.*, vol. 16, no. 3, pp. 317–328, 1997.

[16] D. Shepard, "A two-dimensional interpolation function for irregularly-spaced data," in *ACM 1968*, 1968, pp. 517–524.

[17] A. Isola, C. Metz, M. Schaap, S. Klein, W. Niessen, and M. Grass, "Coronary segmentation based motion corrected cardiac ct reconstruction," in *IEEE NSS-MIC*, October 2010, pp. 2026–2029.

[18] D. Suter and F. Chen, "Left ventricular motion reconstruction based on elastic vector splines," *IEEE Trans. Med. Imag.*, vol. 19, no. 4, pp. 295–305, 2000.

[19] W. Segars, M. Mahesh, T. Beck, E. Frey, and B. Tsui, "Realistic ct simulation using the 4D xcat phantom," *Med. Phys.*, vol. 35, no. 8, pp. 3800–3808, 2008.

[20] K. Zou, A. Warfield, A. Bharatha, C. Tempany, M. Kaus, S. Haker, W. Wells, F. Jolesz, and R. Kikinis, "Statistical validation of image segmentation quality based on a spatial overlap index: Scientific reports," *Acad. Radiol.*, vol. 11, no. 2, pp. 178–189, 2004.

Second-pass Stent Reconstruction

Satoru Oishi, Yu-Bing Chang, Michael D. Silver, Masanobu Yamada, Hiromichi Yokoyama, Tetsu Satow

Abstract—**A new self-calibration technique is developed for reconstructing stents used for stent-assisted coiling. It is valuable to clearly visualize the struts of the stents after stent deployment and before starting coiling in the cases of wide-neck aneurysms. Phantom studies show the technique is robust for irreproducible factor of C-arm wobble. The same technique can be used in cases of slight patient motion such as pulsatile of the vessel supporting the aneurysm.**

Keywords-coiling; stent-assist technique; intra-cranial stent; self-calibration; reconstruction; CT; cone-beam CT; C-arm gantry

I. INTRODUCTION

Coiling is a treatment technique for intra-cranial aneurysms. The number of coiling cases is increasing dramatically year by year because it is less invasive than surgical clipping. However, clipping has been preferred in the wide-neck aneurysm case illustrated in Fig. 1(b). Here the aneurysm neck is wide compared to the aneurysm dome and there is a risk that a coil could escape to occlude major vessels. On the other hand, the open-skull treatment technique for surgical clipping is also risky, especially for elderly patients, often leaving such patients with few options.

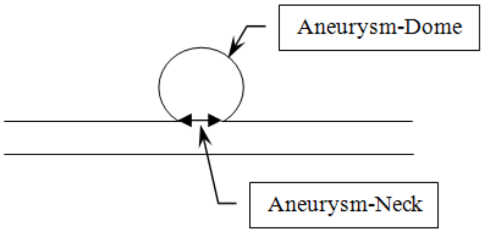

(a) Definition of aneurysm dome and neck.

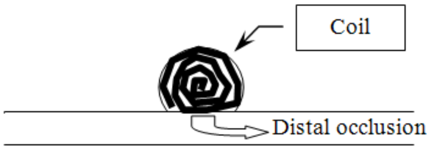

(b) Wide-neck aneurysm.

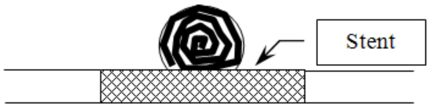

(c) Stent-assisted coiling.

Figure. 1 Aneurysms, coiling, and stent-assisted coiling.

The answer is the stent-assisted coiling technique [1] as cartooned in Fig. 1(c). First, the stent is deployed to cover the aneurysm-neck and then the coils are inserted. Stent struts prevent coils from escaping the aneurysm. In this technique, it is essential to check stent deployment before starting coiling. But it is too hard to see struts on fluoroscopy or acquisition images. The two most used stents for this purpose are the Enterprise VRD from Codman & Shurtleff and Neuroform3 from Boston Scientific Corporation. Diameter of the struts of these two stents is 60 μm; that is much smaller than for other types of stents. Only four markers at each end are visible on the fluoro or acquisition images as seen on Fig. 2.

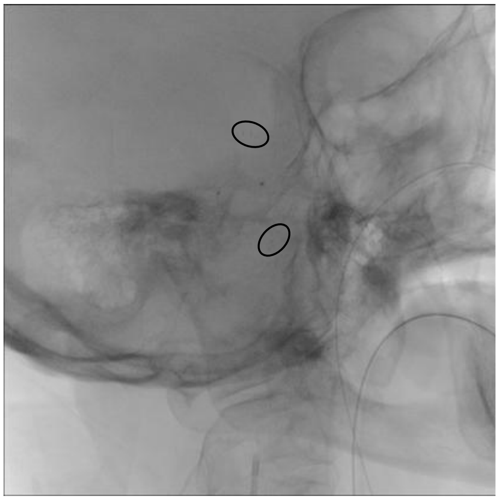

Figure. 2 Acquisition image. Four markers at proximal and distal ends are circled.

We propose to use cone-beam CT (CBCT) from a C-arm gantry to see the stent struts. There are several factors working against us besides the usual spatial resolution restrictions:

- motion of aneurysm and stent due to pulsatile blood pressures
- irreproducible C-arm wobble.

Our CBCT method calibrates C-arm wobble with data from a previously performed calibration scan. This works fine for vessels or aneurysms, but it is sometimes difficult to control irreproducible factor of C-arm wobble within 100 μm or less.

To solve this problem, which also works in principle to correct for pulsatile motion, we have developed a 2nd

SO is with Toshiba Medical Systems Corporation, Otawara, Japan
Y-BC and MDS are with Toshiba Medical Research Institute USA
MY, HY and TS are with the National Cerebral and Cardiovascular Center, Suita, Japan

pass reconstruction technique using a new self-calibration technique.

II. SECOND PASS RECONSTRUCTION TECHNIQUE

The flowchart of the technique is shown in Fig 3.

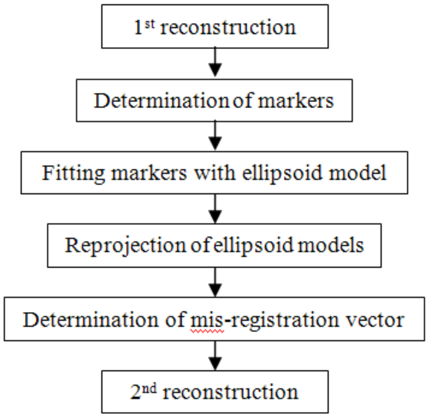
1st reconstruction
Determination of markers
Fitting markers with ellipsoid model
Reprojection of ellipsoid models
Determination of mis-registration vector
2nd reconstruction

Figure. 3 Flowchart of 2nd pass reconstruction technique.

A. 1st reconstruction

The first reconstructed image uses a modified Feldkamp method [2], which assumes perfect reproducibility of the C-arm wobble. The acquisition data is often truncated due to the limited size of the flat panel detector (FPD) so a water cylinder data extrapolation method is used to assure good image quality within the region-of-interest of the aneurysm and stent.

B. Dertermination of markers

The volume image from the 1st reconstructed image undergoes a threshold segmentation to isolate the eight markers. Implants or guide-wires are also extracted but these are removed from the image volume using *a priori* knowledge of the volumetric differences among markers, implants, and guide-wires.

C. Fitting markers with ellipsoid model

Marker positions and inclinations are determined accurately by fitting each individual marker with an ellipsoid model. The dimensions of the model are automatically determined to fit the surfaces of the markers, which were calculated by the marching cube algorithm [3].

D. Reprojecting of ellipsoid models

Four ellipsoid models at one end of the stent are reprojected onto detector plane by using same calibration data used in the 1st reconstruction. The reprojected models are expressed as $E_\theta(u,v)$, where u,v are the horizontal and vertical axes on detector plane, and θ is projection angle. If the reprojection area of our markers at the proximal end is close to the reprojection area of four markers at distal end, the eight ellipsoid models are reprojected as one set of markers instead of treating the distal and proximal separately.

If the markers overlap in the reprojected projections, we treat them as a single unit.

E. Determination of mis-registration vector

Cross-correlation coefficients between the original projection data $p_\theta(u,v)$ and the reprojected models $E_\theta(u+\Delta u,v+\Delta v)$ are carried out by changing $(\Delta u,\Delta v)$ at certain intervals within a certain area. The mis-registration vector $\Delta u_0(\theta), \Delta v_0(\theta)$ derives from the maximum correlation coefficient; it is determined for each projection and at each end of the stent. Mis-registration vector is finally calculated by averaging two the mis-registration vectors at the two ends.

F. 2nd reconstruction

Our backprojection equation was derived in [2]; it is given by

$$\left.\begin{aligned} u_\theta(x,y,z) &= \frac{m_{1,\theta}x+m_{2,\theta}y+m_{3,\theta}z+m_{4,\theta}}{1+m_{9,\theta}x+m_{10,\theta}y+m_{11,\theta}z}\times\frac{1}{\Delta s} \\ v_\theta(x,y,z) &= \frac{m_{5,\theta}x+m_{6,\theta}y+m_{7,\theta}z+m_{8,\theta}}{1+m_{9,\theta}x+m_{10,\theta}y+m_{11,\theta}z}\times\frac{1}{\Delta s} \end{aligned}\right\} \qquad (1)$$

where $m_{n,\theta}$ are the coefficients that map from 3D-space to 2D-space with Δs as the pitch of the sensor cells in the FPD. These coefficients are given by calibration and assumed repeatable for non-stent imaging.

For the second reconstruction, we assume the stent is reasonably close to isocenter so we only need to update m_4 and m_8:

$$\left.\begin{aligned} m_{4,\theta} &\to m_{4,\theta}+\Delta u_0(\theta) \\ m_{8,\theta} &\to m_{8,\theta}+\Delta v_0(\theta) \end{aligned}\right\}. \qquad (2)$$

III. PHANTOM STUDIES

The experimental setup for the phantom studies, Fig. 4

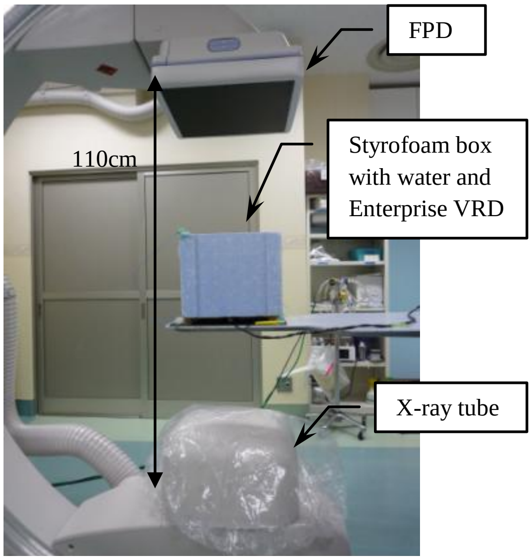

Figure 4. Experimental setup for phantom studies.

contained a Styrofoam box, about 18 cm on each side.

A. Acquisitions

Five phantom data sets were acquired with conditions shown in Table 1. Projections of 607 frames were acquired covering 200°. The FPD pitch is 194 μm and the focal spot size is 300 μm. Magnification was 1.57.

TABLE I. ACQUISITION CONDITIONS OF PHANTOM DATA

DATA	**ACQUISITION CONDITIONS**				
	***Voltage* [kV]**	***Current* [mA]**	***Pulse width* [msec.]**	***Beam filter***	***Angular sampling* [deg./frame]**
1	120	200	10.4	Cu 0.2 mm	0.33
2	110	250	9.6	Cu 0.2 mm	0.33
3	100	250	11.7	Cu 0.2 mm	0.33
4	90	320	8.2	Cu 0.2 mm	0.33
5	80	320	9.7	Cu 0.2 mm	0.33

B. Reconstructions

Two image volumes were reconstructed for each data set, one using the existing method and the other using the new 2^{nd} pass stent reconstruction technique.

C. Evaluations

We measure the full-width at half maximum (FWHM) from profiles through the struts. Our procedure, for the *before* (first-pass reconstruction only) and the *after* (second-pass reconstruction), is listed below:

1) We use zoom mode reconstruction with a voxel size of 7 μm in order to have enough points in the profiles.
2) Make two coronal MIPs (max intensity projections)
   a) One MIP is the front half of the stent
   b) The other MIP is the backhalf of the stent

   This is to avoid overlapping structs in the MIPs.
3) A total of 120 locations were manually selected for the center of each profile in the MIPs. Each location was midway between strut crossings.
4) All 120 of the 101-point profiles were averaged together.
5) FWHM calculated from the before and after images along with the percent improvement.

We also check the contrast improvement by comparing the profile amplitude above background *before* and *after* for each of the five data sets.

IV. RESULTS

Fig. 5 shows some examples of the full coronal MIPs, comparing the standard, first-pass reconstruction with the second-pass reconstruction that uses the self-calibration technique. All data sets were first reconstructed with the same set of wobble coefficients and then again with the self-calibration. It is evident from comparing data set 1 images with data set 5 images that the C-arm gantry geometry was very similar between set 5 and the calibration while for set 1, the gantry wobble was somewhat different. This is verified in Fig. 6 where the mis-registration vector, $\Delta u_0\ \ \theta$ is shown ($\Delta v_0\ \ \theta$ is less interesting). We see that all five data sets think there was something different about the gantry rotation at -20° from calibration but that there is a range of mis-registrations at other angles from the most mis-registration for data set 1 (black) to the least for data sets 4 and 5 (cyan and red).

Fig. 7 shows the averaged profiles for data sets 1, 3, and 5 while Table II gives the FWHM and contrast improvement results for all five data sets. Because the struts are thin (60 μm) compared with the beam width as defined by the FPD pitch and focal spot (~200 μm), spatial resolution is dominated by the sampling beam. FWHM might not be a good metric in such cases.

On the other hand, contrast is clearly improved in all five cases, more in line with our visual assessment. Contrast improvement is the difference in profile (maximum – minimum) between the *before* and *after* images divided by background and converted to percent.

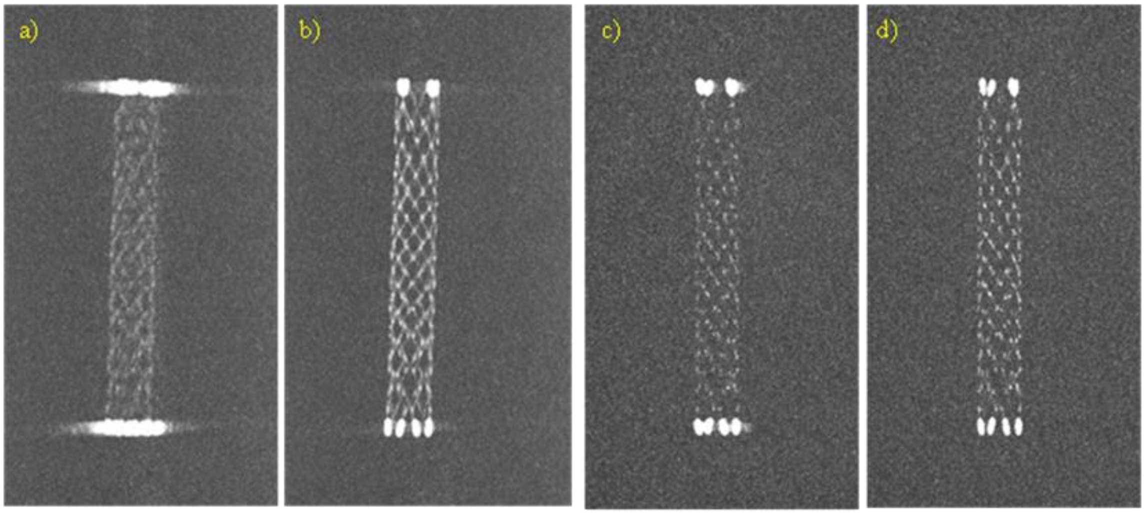

Figure 5. MIP displays of volume reconstructed images. a,b) Data Set 1, a) 1^{st} reconstruction and b) 2^{nd}-pass reconstruction; c,d) Data Set 5. c) 1^{st} reconstruction and d) 2^{nd} –pass reconstruction.

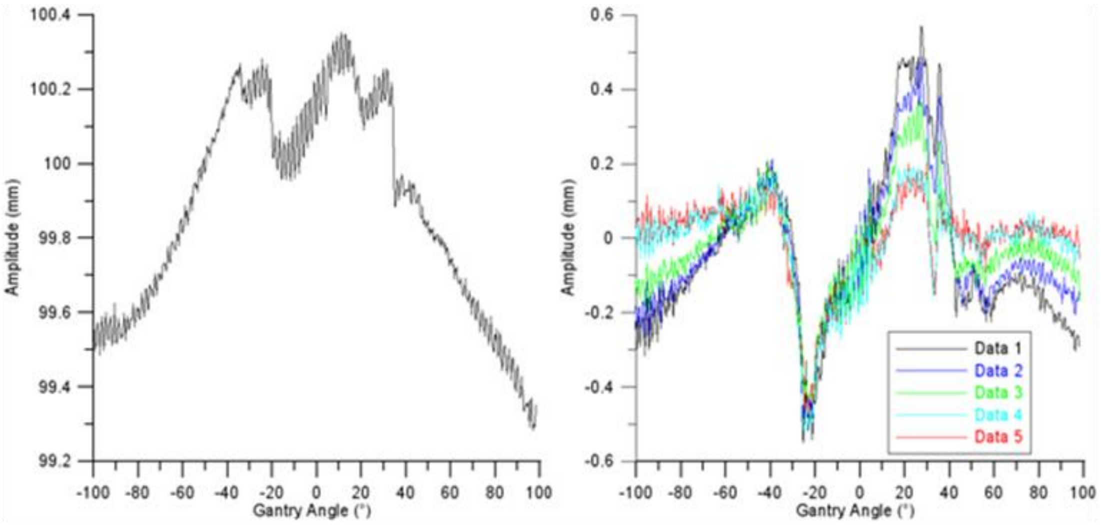

Figure 6. Left is the m_4 wobble coefficient as determined by calibration. Right is the mis-registration vector for m_4 for all five data sets. The irreproducible factor of this C-arm gantry is of the order of a few 0.1 mm.

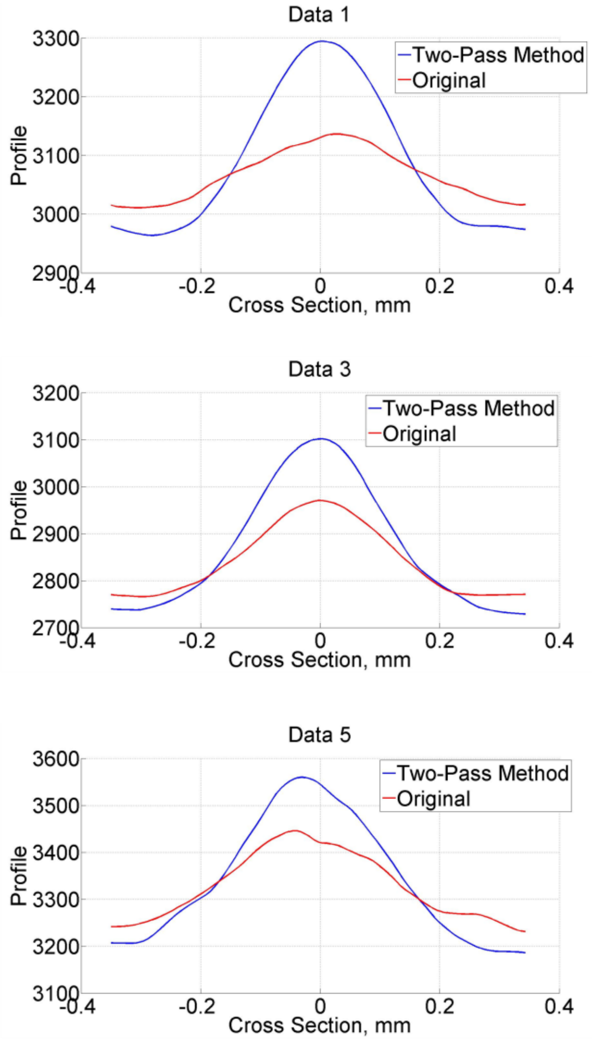

Figure 7. Profiles through the struts. Each profile is an average of 120 profiles and were sampled every 7 μm.

TABLE II. RESOLUTION AND CONTRAST IMPROVEMENT

	FWHM			**Contrast Improvement**
Data Set	***Before***	***After***	**Improvement**	
1	0.301	0.249	17%	6.8%
2	0.294	0.255	13%	7.1%
3	0.245	0.245	0	6.1%
4	0.297	0.262	12%	5.5%
5	0.296	0.273	8%	5.0%

V. CONCLUSIONS

Phantom studies demonstrate accurate self-calibration for stent struts by using stent markers against irreproducible factor of C-arm wobble.

We have started to use this technique in a few clinical cases and observed an improvement in image quality of the stent. Thus, the self-calibration does correct against motion of aneurysms and stents due to pulsatile blood pressures. However, it is too soon to say whether this imaging method improves patient outcomes.

Ultimately, spatial resolution is limited by the sensor pitch of the FPD, here 194 μm, and focal spot size, here 300 μm.

REFERENCES

[1] Szikora, L.R. Guterman, K.M. Wells, L.N. Hopkins, “Combined use of stents and coils to treat experimental wide-necked carotid aneurysms: preliminary results,” Am. J. Neuroradiol., 15, pp. 1091-1102, 1994.

[2] M.D. Silver, A. Sen, S. Oishi, “Determination and correction of the wobble of a C-arm gantry,” SPIE 3979-163, 2000.

[3] W.E Lorensen and H.E. Cline, “Marching cubes: A high resolution 3D surface construction algorithm,” Computer Graphics, 21, pp. 163-169, 1987.

Diaphragm Tracking for Respiratory Motion Compensated Cardiac C-Arm CT

Marco Bögel*, Andreas Maier*, Hannes G. Hofmann*, Joachim Hornegger*,† and Rebecca Fahrig‡

***Abstract*—Long acquisition times of several seconds lead to image artifacts in cardiac C-arm CT. While ECG gating is able to select a certain heart phase, residual artifacts are mostly caused by respiratory motion. In order to improve image quality, it is important to accurately estimate the breathing motion that occurred during image acquisition. It has been shown that diaphragm motion is correlated to the respiration-induced motion of the heart.**

We present a motion estimation and compensation method based on the tracking of the diaphragm contour in projection space. The approach utilizes a 2-D quadratic curve model to estimate and track the diaphragm with sub-pixel accuracy. Based on the tracking results, we use a motion corrected triangulation algorithm to estimate the 3-D motion of the diaphragm top. The resulting signal is used to compensate for superior-inferior respiratory motion during the reconstruction.

***Index Terms*—C-arm CT; reconstruction; respiratory motion; diaphragm tracking; motion compensation;**

I. INTRODUCTION

Cardiac C-arm CT enables reconstruction of 3-D images during medical procedures. However, the long acquisition time of several seconds, during which the heart is beating and the patient might breathe, may lead to artifacts, such as blurring or streaks. A commonly used technique to reduce breathing motion is the single breath-hold scan. The physician instructs the patient to hold his breath after exhalation. The data is then acquired during the breath-hold. Although this approach is widely used, several studies have shown that breath-holding does not eliminate breathing motion entirely. Monitoring the position of the right hemidiaphragm during breath-hold, Jahnke et al. observed residual breathing motion to a certain extent in almost half of their test group [1]. Therefore, it is necessary to develop more sophisticated methods to estimate and compensate for respiratory motion in cardiac C-arm CT.

There are many ways to acquire respiratory signals. Most are based on additional equipment, e.g. Time-of-Flight or stereo vision cameras. Other techniques aim to extract the respiratory signal directly from the projection images. Using this approach the extracted breathing signal is perfectly synchronized with the projection images. Image-based respiratory motion extraction often relies on tracking of fiducial markers in the projection images [2], [3]. Wang et al. have shown that the motion of the diaphragm is highly correlated to respiration-induced motion of the heart [4]. Sonke et al. propose to extract a 1-D breathing signal by projecting diaphragm-like features on the superior-inferior axis and selecting the features with the highest temporal change [5]. However, the downside of this approach is that the extracted signal is not the real respiration signal. Due to perspective projection, the projected amplitude depends on the C-arm rotation angle.

In this work, we propose to estimate respiratory motion by tracking the diaphragm in a set of rotational projection images. The tracked position of the diaphragm top is used to compute a 1-D respiration signal, which is then incorporated into the reconstruction algorithm to compensate for respiratory motion.

II. METHODS AND MATERIALS

The proposed method is composed of three major steps that are each discussed in the following sections. In the first step, the contour of the diaphragm is tracked throughout the entire projection image sequence. Based on this tracking, we are able to obtain the 2-D projection of the diaphragm top for each image. In the second step, a motion corrected triangulation approach is used to compute the 3-D position of the diaphragm top for each projection. Assuming superior-inferior breathing motion, the 1-D respiration signal is extracted. In the final step, the respiration signal is used to compensate for respiratory motion during reconstruction.

A. Diaphragm Tracking

We introduced a model-based tracking method that is able to accurately track the contour of a user-selected hemidiaphragm in a set of rotational projection images [6]. Compared to other tracking-based methods, e.g. fiducial markers, the shape we want to track is not unique. The diaphragm appears as two similar shaped hemidiaphragms. Therefore, it is necessary for the user to select the one to be tracked. The user selects a point roughly located at the top of the desired contour. Subsequently, we define a rectangular Region of Interest (ROI) symmetrically around the selection. The image is then preprocessed using a gaussian low-pass filter and the Canny edge detector.

In the next step, the Random Sample Consensus (RANSAC) [7] is used to fit a parabolic curve to the obtained set of edge points. RANSAC can deal with datasets with large percentages of gross errors, and is thus the ideal choice to fit a model to our very noisy set of points. The aim of this method is to model the diaphragm as a quadratic function $v = au^2 + bu + c$, where u and v are the detector coordinates. Thus, RANSAC has to estimate the three parameters a, b, and c. In the first step, three random points are selected. The model estimation is then formulated as the following optimization

---

*Pattern Recognition Lab, Universität Erlangen-Nürnberg, Germany
†Erlangen Graduate School in Advanced Optical Technologies (SAOT)
‡Dept. of Radiology, Lucas MRS Center, Stanford University, CA, USA

problem:

$$\sum_{i=1}^{3}(a \cdot u_i^2 + b \cdot u_i + c - v_i)^2 \rightarrow min. \tag{1}$$

A total of N models are estimated and evaluated to determine the best one. A model's quality is defined by the number of inliers. An inlier is a point that lies within a predefined distance to the model. Since an accurate model is desired, we only consider points with a one pixel distance to the model inliers. Assuming small motion between subsequent frames, the contour is tracked by calculating the current contour's vertex and using it as the start point in the subsequent frame.

One additional important optimization is made. Instead of continuing to use the rectangular ROI, we restrict it to a parabolic ROI based on the model from the previous frame. This approach decreases the number of points we have to consider in the model estimation.

To guarantee accurate tracking in projections where both hemidiaphragms are visible in the ROI, we propose additional constraints based on the small motion assumption and prior knowledge: (i) the horizontal motion of the contour is limited by the average motion, (ii) deformation of the contour is limited to 5% compared to the previous model, and (iii) the direction of horizontal motion can be derived from patient positioning and C-arm rotation.

B. Triangulation and Signal Extraction

The result of the diaphragm tracking is a parabolic model of the hemidiaphragm for each image. Our approach relies on the assumption that the projection of the 3-D diaphragm top coincides with the top of the 2-D diaphragm contour. However, this assumption is quite restrictive. Based on this assumption, we are able to reconstruct the 3-D position using multi view triangulation. However, triangulation algorithms are designed for static scenes and yield inaccurate results when used for dynamic scenes. For triangulation of dynamic scenes we propose the following four step process:

1) Select image pair
2) Rectification of the image planes [8]
3) Motion correction
4) Triangulation [9]

First, we select two images with the contour vertices $\tilde{\mathbf{g}} = (\tilde{g}_u, \tilde{g}_v, 1)^T$ and $\tilde{\mathbf{g}}' = (\tilde{g}'_u, \tilde{g}'_v, 1)^T$. Ideally, the selected images should be acquired from orthogonal views. The second step is essential for the subsequent motion correction. The rectification algorithm by Fusiello et al. transforms the image planes such that they become coplanar and their epipolar lines become parallel and horizontal [8]. The transformed images have then one very important feature: the projections of a point have the same vertical coordinate in both image planes. Thus, after transforming the point correspondences, any residual difference in their vertical coordinates must be caused by respiratory motion during image acquisition. Therefore, we can eliminate the respiratory motion of this image pair in the third step. We choose the first point $\tilde{\mathbf{g}}$ as the reference and the corresponding point in the second image is set to

$$\tilde{\mathbf{g}}' = (\tilde{g}'_u, \tilde{g}_v, 1)^T. \tag{2}$$

Algorithm 1: Motion compensated reconstruction. Respiratory motion is compensated in line 8.

```
1  forall the projections $i \in [1, N_p]$ do
2      forall the voxels $(x, y, z)$ do
3          Project voxel $(x, y, z)$ onto detector plane
4          if point on detector plane then
5              Get update value
6          else
7              Next voxel
8          $z_{corr} \leftarrow z + \hat{r}_i$
9          if $(x, y, z_{corr})$ in volume then
10             Update voxel $(x, y, z_{corr})$
```

Finally, we use the transformed and motion corrected point correspondences to triangulate the corresponding 3-D point. In this work a simple iterative Linear-Eigen approach, as proposed by Hartley [9], has yielded excellent results.

After we triangulate a 3-D point corresponding to each image, we can now compute the respiration signal. Since respiratory motion is generally considered as a mainly translational motion along the superior-inferior axis, we compute the 1-D respiration signal $\hat{\mathbf{r}}$ as

$$\hat{r}_i = z_{ref} - z_i, \tag{3}$$

with z_{ref} as the z-coordinate of the reference point, and z_i as the z-coordinate of the triangulated point corresponding to image i. Finally, the resulting signal is smoothed using a gaussian low-pass filter.

C. Motion Compensated Reconstruction

The signal is now included in the reconstruction process. Algorithm 1 shows the motion compensated reconstruction algorithm. For each projection, each voxel is projected on the detector to get the update value. Instead of regularly updating the volume, we first compensate for respiratory motion by shifting the voxel back to its reference position using the estimated signal. Then, we update the corrected voxel. Therefore, we are able to obtain a reconstruction at the reference time we selected for the respiration signal. The proposed method assumes a constant shift for the whole heart. For clinical data more sophisticated motion models are required, as the deformation of the heart is not rigid.

III. EXPERIMENTAL RESULTS

The evaluation of this work was carried out on a simulated XCAT phantom [10]. The XCAT phantom was created with breathing motion only. We simulated an acquisition time of four seconds with one full respiration cycle. Both heart and diaphragm moved about 2.3 cm along the superior-inferior axis, the rest of the scene was static. A detector of size 640×480 px was simulated with a resolution of 0.616 mm/px. 200 projections were acquired with an average angular increment of $1.0°$. As ground truth we used the reconstruction of an XCAT dataset that was simulated without respiratory motion.

Fig. 1. Comparison of the extracted diaphragm motion signal and the actual breathing signal. The amplitude of the signal can not be estimated accurately, as the projections of the diaphragm top do not coincide with the 2-D contour.

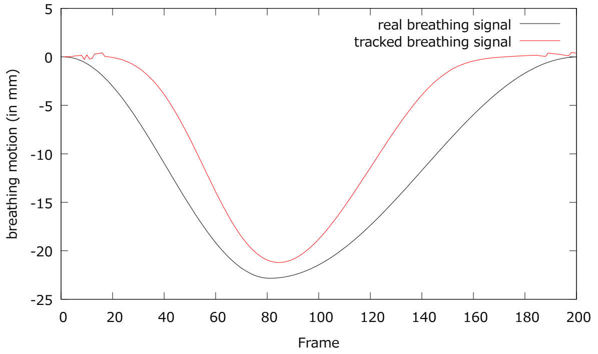

TABLE I

TRIANGULATION ERRORS (IN MM) BASED ON PROJECTIONS OF THE REAL DIAPHRAGM TOP. ANGULAR OFFSET OF THE IMAGE PAIR IN BRACKETS.

	Mean 3-D	Std. Dev. 3-D	Mean Z	Std. Dev. Z
Rect. Iter. (90°)	0.20	0.06	0.10	0.06
Rect. Iter. (30°)	0.32	0.15	0.10	0.06
Rect. Iter. (10°)	0.89	0.60	0.11	0.08
Iterative (90°)	2.22	0.97	2.22	0.96

The diaphragm tracking method was evaluated on the left and right hemidiaphragms in XCAT projection data [6]. We were able to track the vertex of the diaphragm contour with sub-pixel accuracy. We observed a Euclidean distance of the right vertex to the correct vertex of 0.45 ± 0.56 pixels, and 0.75 ± 0.84 pixels for the left vertex respectively.

Figure 1 shows the extracted signal based on the diaphragm tracking results. As previously noted, our approach depends on the assumption that the projection of the diaphragm top lies on the 2-D contour. However, this is a strong assumption that is not always fulfilled. In fact, the correct projection of the diaphragm top is often located below the contour, due to perspective projection. This results in inaccuracies in the estimated amplitude of the signal, caused by triangulation with false point correspondences. In order to assess the accuracy of the triangulation approaches without the effect of false point correspondences, we tested the methods using the correct projections of the diaphragm top as input. Therefore, we can test the performance of our algorithm if the assumption is met. As results in TABLE I show, our rectified iterative approach provides sub-millimeter accuracy even for image pairs with low angular offset, whereas the average error of the standard approach without rectification and motion correction is about 10% of the total breathing motion.

For the evaluation of reconstruction quality we used the structural similarity index (SSIM) by Wang et al. [11]. SSIM measures the similarity of two images based on structural information. Two images are compared and a value between -1.0 and 1.0 is returned, with 1.0 for a perfect match and -1.0 for completely different images. In order to reduce the influence of the static background on the quality evaluation, the reconstructed volume was cropped to the bounding box that contains the heart. In total, we evaluated the quality of three different reconstructions: (i) a compensated reconstruction using the proposed tracking methods, (ii) a compensated reconstruction with the correct 2-D projections of the diaphragm top (simulating an optimal diaphragm tracking), and (iii) an uncompensated reconstruction. Figure 2 shows the evaluation results for xy and xz-slices. Both compensated reconstructions show highly improved image quality. As expected, the diaphragm tracking approach is slightly below the quality of the optimal reconstruction. However, it shows significant improvement when compared to the uncompensated reconstruction. The uncompensated reconstruction seems to be superior in the first and last slices. The heart is only of small size in these slices. Therefore, the static background has a larger influence on the evaluation. Compensation blurs the static background, whereas it is perfectly reconstructed without compensation. Figures 3 and 4 show the results for two example slices.

Fig. 2. Structural similarity index of the heart volume for xy and xz-slices. The uncompensated reconstruction shows better results in the beginning and the end, as the heart is only of small size in these slices.

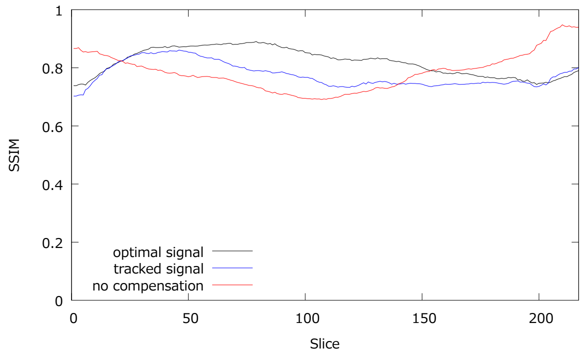

(a) xy-slices

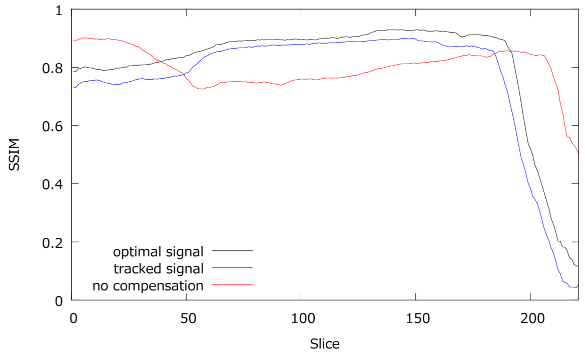

(b) xz-slices

IV. CONCLUSION AND OUTLOOK

Results of respiratory motion compensated reconstruction already show promising results in image quality improvement close to the optimal solution. Still, there is one important issue that has to be solved. The proposed method works on the very restrictive assumption that the projection of the 3-D diaphragm top coincides with the top of the 2-D contour.

Future work will be focused on this problem. Due to perspective projection, this assumption is not always fulfilled.

Fig. 3. Comparison of xy-slice 70 of compensated and uncompensated volumes (cf. Fig. 2a). Simulated high-contrast heart lesions further illustrate the improved image quality.

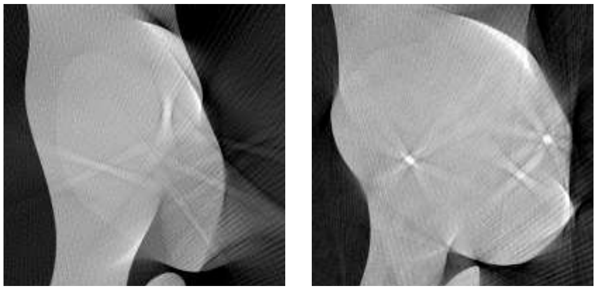

(a) No compensation. SSIM: 0.75

(b) Compensation with tracked signal. SSIM: 0.86

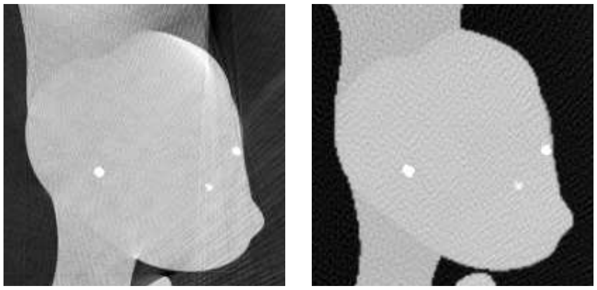

(c) Compensation with optimal signal. SSIM: 0.90

(d) Ground truth

Fig. 4. Comparison of xz-slice 60 of compensated and uncompensated volumes (cf. Fig. 2b).

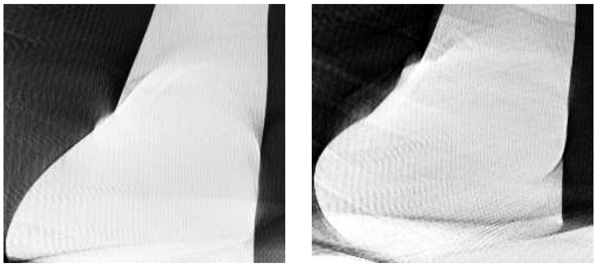

(a) No compensation. SSIM: 0.76

(b) Compensation with tracked signal. SSIM: 0.84

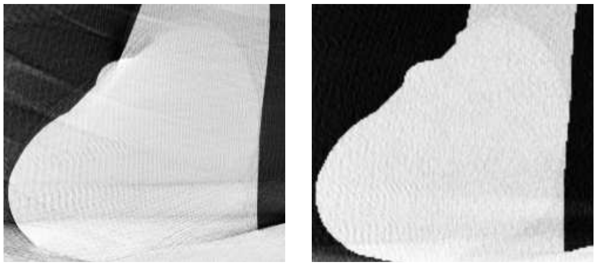

(c) Compensation with optimal signal. SSIM: 0.88

(d) Ground truth

This results in inaccurate amplitudes of the extracted respiration signal. One interesting approach would be to combine the current approach with other existing methods to estimate respiratory motion, e.g. Time-of-Flight cameras. This way, we could possibly improve the extracted diaphragm motion signal by correlating it to the externally measured respiration signal.

ACKNOWLEDGEMENT

This work is supported by NIH grant R01 HL087917.

REFERENCES

[1] C. Jahnke, I. Paetsch, S. Achenbach, B. Schnackenburg, R. Gebker, E. Fleck, and E. Nagel, “Coronary MR Imaging: Breath-hold Capability and Patterns, Coronary Artery Rest Periods, and beta-Blocker Use,” *Radiology*, vol. 239, no. 1, pp. 71–78, 2006.

[2] S. Wiesner and Z. Yaniv, “Respiratory Signal Generation for Retrospective Gating of Cone-Beam CT Images,” *Proc SPIE*, vol. 6918, pp. 691 817–1 – 691 817–12, 2008.

[3] T. Marchant, G. Price, B. Matuszewiski, and C. Moore, “Reduction of motion artefacts in on-board cone beam CT by warping of projection images,” *Br J Radiol*, vol. 84, no. 999, pp. 251–264, March 2011.

[4] Y. Wang, S. Riederer, and R. Ehman, “Respiratory motion of the heart: Kinematics and the implications for spatial resolution in coronary imaging,” *Magn Reson Med*, vol. 33, pp. 716–719, 1995.

[5] J.-J. Sonke, L. Zijp, P. Remeijer, and M. van Herk, “Respiratory correlated cone beam CT,” *Med Phys*, vol. 32, no. 4, pp. 1176–1186, 2005.

[6] M. Bögel, A. Maier, H. G. Hofmann, J. Hornegger, and R. Fahrig, “Diaphragm Tracking in Cardiac C-Arm Projection Data,” *Proc BVM*, pp. 33–38, 2012.

[7] M. A. Fischler and R. C. Bolles, “Random sample consensus: a paradigm for model fitting with applications to image analysis and automated cartography,” *Commun ACM*, vol. 24, pp. 381–395, June 1981.

[8] A. Fusiello, E. Trucco, and A. Verri, “A compact algorithm for rectification of stereo pairs,” *Mach Vis Appl*, vol. 12, no. 1, pp. 16–22, 2000.

[9] R. I. Hartley and P. Sturm, “Triangulation,” *Comput Vis Image Underst*, vol. 68, no. 2, pp. 146–157, 1997.

[10] W. P. Segars, M. Mahesh, T. J. Beck, E. C. Frey, and B. M. W. Tsui, “Realistic CT Simulation Using the 4D XCAT Phantom,” *Med Phys*, vol. 35, no. 8, pp. 3800–3808, 2008.

[11] Z. Wang, A. C. Bovik, H. R. Sheikh, and E. P. Simoncelli, “Image Quality Assessment: From Error Visibility to Structural Similarity,” *IEEE Trans Image Process*, vol. 13, no. 4, pp. 600–612, 2004.

Effects of Ray-Modeling: Simulation Study

Christian Hofmann, Michael Knaup, and Marc Kachelrieß

Abstract—**In the recent years iterative reconstruction regained more and more interest to several applications in computed tomography such as cardiac CT imaging. This is mainly due to the fact that modern compute hardware makes acceptable reconstruction times feasible. Furthermore much research has been done to push the potential of iterative reconstruction and to benefit most of its advantages. In this context one must mention image representation by spherically symmetric Kaiser Bessel functions, regularization methods and ray modeling of the physical acquisition process. We want to focus on the last aspect, the ray modeling process. This paper aims at investigating the possible improvements by exactly modeling the forward projection in an iterative reconstruction by a simulation study.**

A thorax phantom with resolution line pairs in the region of the heart is simulated. Simulations are performed in 2D. An FBP reconstruction with a Ram-Lak kernel is used as a reference reconstruction. This is compared with an OSSART (Ordered Subset SART) algorithm without any ray modeling and with an OSSART in which the forward projection is modeled concerning the finite focal spot, detector size and angular blurring (OSSART-RM). For the regularized iterative scheme proposed in this paper a bilateral filter (BF) is used as a regularization.

The simulation and the patient data show that the signal-to-noise ratio cannot be improved significantly by the ray modeling process compared to the FBP and the OSSART reconstructions. The modeling in OSSART-RM affects the convergence speed in terms of iterations compared to OSSART but not in terms of time due to the increased computational effort. The point of convergence is different in OSSART and OSSART-RM but there is no improvement in signal-to-noise ratio. By using this knowledge the iterative reconstruction scheme utilizes the edge preserving bilateral filter in combination with the iterative algorithms to achieve a higher resolution at identical noise level as in the FBP image. The differences in the results of the schemes in the simulation case with OSSART and OSSART-RM are minor.

Ray modeling is an expensive task. The benefits are only minor and bear in no relation to the additional computational effort. The regularization seems to be a crucial part of an iterative reconstruction. The iterative scheme is promising but a clinical study has to confirm this from a diagnostic point of view.

Index Terms—**Computed Tomography (CT), Cardiac, Region of interest imaging, Iterative reconstruction**

I. INTRODUCTION

CLINICAL applications of CT diagnosis demand for consistent improvement of computer tomographs. Analytical reconstruction algorithms are based on approximation approaches for cone beam reconstructions which introduces cone beam artifacts among others. This issue of image quality can be addressed by iterative reconstruction algorithms which do not underlie this problem. On the contrary, iterative reconstruction algorithms offer the possibility to incorporate non idealities in the problem description. Prior knowledge such as positivity or smoothness can be considered in an iterative algorithm by different regularization approaches. Furthermore the forward projection step of iterative algorithms offers the possibility of modeling the physical acquisition process [1], [2]. One can account for angular blurring, finite focal spot and detector sizes thus avoiding inaccuracies which can lead to a loss of resolution in the reconstructed images.

This paper aims at investigating the effects of modeling forward projection in a highly accurate way. A simulation study is done to investigate the effects of ray modeling on high contrast objects and noise properties. The simultaneous algebraic reconstruction method (SART) [3] has proven to be a suitable choice and can be improved in performance by using ordered subsets (OSSART) [4]. Furthermore the gained knowledge of the simulations induced us to develop a new iterative scheme consisting of an OSSART regularized with a bilateral filter [5]. This scheme will also be presented in the context of this paper as it was developed as a integral part of the analysis of the simulation study.

II. MATERIALS AND METHODS

The simulations are based on the Siemens Definition Flash scanner geometry, using a simulated thorax phantom containing the heart region. Iterative reconstruction algorithms like OSSART need a preprocessing step of the rawdata for an iterative region of interest reconstruction (IROI) which is based on a method presented in [6]. Details of the employed reconstruction algorithms, realization of the ray modeling procedure, the phantom study and the iterative reconstruction scheme are explained in detail in the following.

A. ROI Reconstructon Methods

The analytical reference reconstruction is an FBP with a Ram-Lak kernel for the simulations. The OSSART is an established iterative algebraic reconstruction method which offers an approximate solution by finding an image represented by a vector $\boldsymbol{f}$ which minimizes the rawdata fidelity term $||\boldsymbol{A}\boldsymbol{f}-\boldsymbol{p}||_2^2 < \epsilon$. $\boldsymbol{A}$ is the system matrix which represents the forward projection process. The transpose of $\boldsymbol{A}$, $\boldsymbol{A}^T$, can then be seen as the backprojection operation. The measured rawdata are represented by the vector $\boldsymbol{p}$. The parameter ν indicates the ν-th subset that is being processed. The update equation, taken from [7], for the OSSART algorithm then is:

$$\boldsymbol{f}^{(n+1)} = \boldsymbol{f}^{(n)} + \lambda \cdot \frac{1}{\boldsymbol{A}_\nu^T 1} \boldsymbol{A}_\nu^T \frac{(\boldsymbol{p}^{(\nu)} - \boldsymbol{A}_\nu \boldsymbol{f}^{(n)})}{\boldsymbol{A}_\nu 1}$$

The parameter $\lambda \in]0,1[$ is called the relaxation parameter. It determines how strong the update is incorporated in each iteration.

Christian Hofmann, Dr. Michael Knaup and Prof. Dr. Marc Kachelrieß, Friedrich–Alexander–Universitt (FAU), Henkestr. 91, 91052 Erlangen, Germany.

Prof. Dr. Marc Kachelrieß: German Cancer Research Center (DKFZ), Im Neuenheimer Feld 280, 69120 Heidelberg, Germany.

Corresponding author: marc.kachelriess@dkfz.de

Preprocessing has to be done with the rawdata to perform an iterative region of interest (IROI) reconstruction. The basic idea is taken from reference [6].One has to perform an initial FBP reconstruction of the full field of view (FOV). Then the desired ROI is being clipped from this volume. This volume is being forward projected and then subtracted from the measured data resulting in the sinogram for the IROI reconstruction.

We aim at having an as fair comparison as possible between the analytical reconstruction and the iterative reconstruction with and without ray modeling. The OSSART algorithm incorporates no further knowledge about the noise structure as for example the OSC algorithm which is based on a Poisson noise model. Furthermore no postprocessing was performed on both the analytical reconstructions and the iterative reconstructions. Thus the investigated effects are the effects of the ray modeling process.

B. Phantom simulations

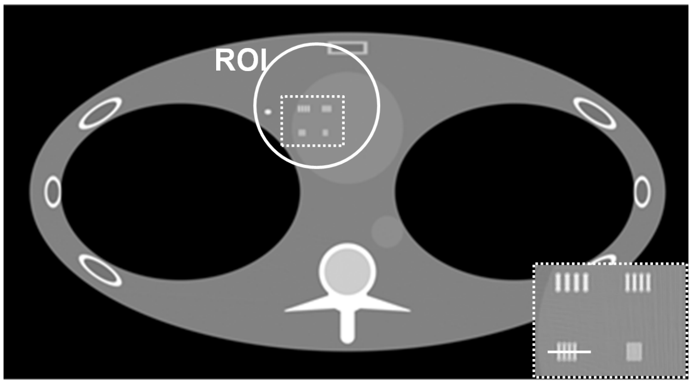

Fig. 1. The Simulated FORBILD thorax phantom. The circle shows the reconstructed ROI, the dashed box shows the the section with the resolution patterns. In the enlarged section the line profile through the lower pattern line is indicated.

To investigate the effects of ray modeling, high contrast resolution line profiles are used which were simulated into a FORBILD thorax phantom [8]. We use four pairs of profiles with successive smaller dimensions. The rawdata for the simulations were simulated analytically. Poisson noise was simulated resulting in 20 HU noise in the FBP reconstruction. The finite focal spot and detector were realized by simulating and averaging of 27 lines. The angular blurring is taken account for by averaging within the range of the angular increment $\partial\alpha$. The finite focal spot is a line of 10 mm length perpendicular to the direction from source to center of rotaion. The ray modeling was performed in the same manner like it is handled later in the forward projection with the difference that a very fine sampling used for the detector, the focal spot and the angular increment $\partial\alpha$. An FBP reconstruction with a Ram-Lak kernel is used as a reference reconstruction. The analytical reconstruction is compared with the OSSART reconstructions without any ray modeling and with OSSART in which the forward projection is modeled in the same manner like in the rawdata generation (OSSART-RM). The forward projection algorithm used in the iterative algorithms is of Joseph type [9].

The simulation is based on three different approaches to analyze the effects of ray modeling. In the first case the iterative algorithms are stopped when the same noise level is reached as in the reference FBP reconstruction to conclude on the influence on the signal-to-noise ratio. For the second case a fixed number of iterations is chosen for both iterative algorithms. Thus one can draw conclusion on the effect ray modeling can have on the convergence speed in terms of number of iterations. The third case investigates the results of OSSART and OSSART-RM in the region of convergence and how this is being affected by the ray modeling. Convergence here means that a certain threshold is underrun by the update of the iterative algorithms.

For the 2D simulations a circular scan with 1150 projections was simulated. The FORBILD thorax phantom was used. Four resolution line profiles were simulated into the region of the heart. All lines have a height of 4 mm. The thickness and distance d of the lines is equal and follow the relation $d = 0.75^n$ mm for $n \in [0, 3]$. All lines have the same attenuation value equivalent to 400 HU. The distance from the focus to the center of rotation is 595.0 mm and the distance from the center to the detector is 490.6 mm. The detector has 736 elements in fan direction.

For the ROI reconstruction first an FBP reconstruction of the whole FOV with radius of 250 mm is reconstructed with 830×830 voxels resulting in a 0.6 mm voxel grid. The reconstructed ROI has a radius of 60 mm reconstructed with a voxel size of 0.2 mm which is equivalent to 512×512 voxels. The ROI is centered at (-15 mm, 40 mm).

C. Iterative Scheme

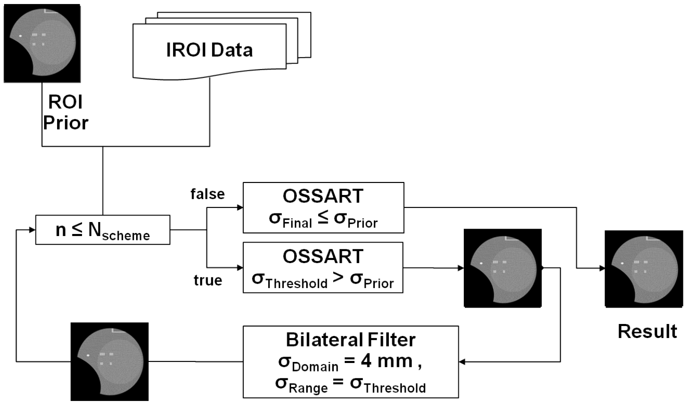
IROI Data
ROI Prior
$n \leq N_{scheme}$
false
true
OSSART $\sigma_{Final} \leq \sigma_{Prior}$
OSSART $\sigma_{Threshold} > \sigma_{Prior}$
Bilateral Filter $\sigma_{Domain} = 4$ mm , $\sigma_{Range} = \sigma_{Threshold}$
Result

Fig. 2. Illustration of the iterative scheme. The scheme is initialized with the ROI prior image and the preprocessed IROI data. The scheme is composed of an iterative algorithm like the OSSART and an edge preserving bilateral filter.

The results of the ray modeling investigation induced us to develop an iterative scheme which was evaluated with simulations. Figure 2 illustrate the iterative scheme. The scheme is initialized with the ROI prior image (ROI Prior), which has the same reconstruction grid as the IROI reconstruction.

The iterative scheme is composed of an iterative algorithm like the OSSART and an edge preserving regularization like the bilateral filter (BF-OSSART). To define the bilateral filter we restrict to one dimension. Bilateral filtering of a function $f(x)$ is defined as

$$\mathrm{B}f(x) = \frac{\int dt D(x,t) R(x,t) f(t)}{\int dt D(x,t) R(x,t)}$$

with B denoting the bilateral filtering operator and

$$D(x,t) = e^{-(\frac{x-t}{\sigma_x})^2}$$
$$R(x,t) = e^{-(\frac{f(x)-f(t)}{\sigma_f})^2}$$

being the domain and the range filter, respectively. The parameters σ_x and σ_f are the widths of the Gaussian domain and range filters, respectively.

The OSSART could be replaced by another iterative reconstruction algorithm like the OSC which takes the noise structure into account. The iterative reconstruction is done until higher resolution than in the ROI prior is reached which is equivalent to $\sigma_{\text{Threshold}} > \sigma_{\text{Prior}}$ were σ_{Prior} is the noise in an ROI in the prior image. This is controlled by fixed parameter $\sigma_{\text{Threshold}}$ which is chosen to be 100 HU. Depending on this noise threshold the bilateral filter is used to suppress noise to a lower value than in the ROI prior by setting $\sigma_{\text{Domain}} = 4$ mm and $\sigma_{\text{Range}} = \sigma_{\text{Threshold}}$. In the final iteration step of the iterative scheme the stopping criteria for the OSSART is a noise less or equal to the noise of the initial analytical reconstruction $\sigma_{\text{Final}} \leq \sigma_{\text{Prior}}$. In the simulations three iterations ($\text{N}_{\text{scheme}} = 3$) were enough to get satisfying results.

III. RESULTS

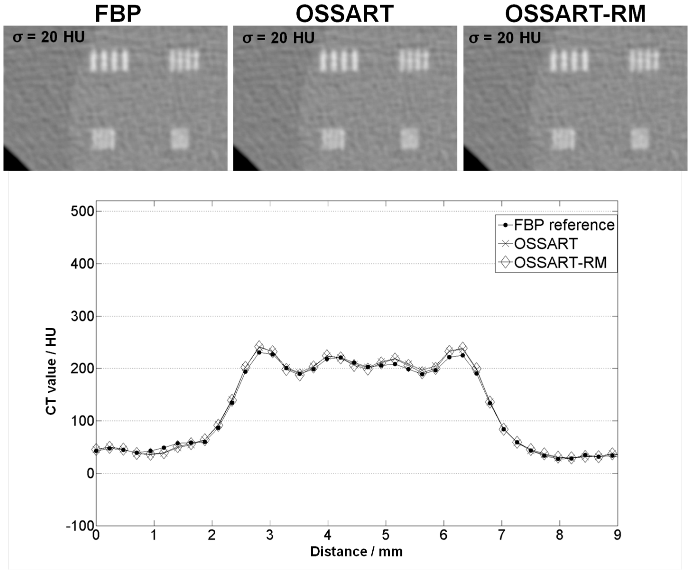

Fig. 3. The simulation results with matched noise. The reconstructions from left to right are FBP, OSSART and OSSART-RM. The images on top show a small region containing the resolution line patterns of the transversal view. The corresponding profile through the lower left line pair is presented at the bottom. The images are shown at a grayscale window of C/W = 0/1000 HU.

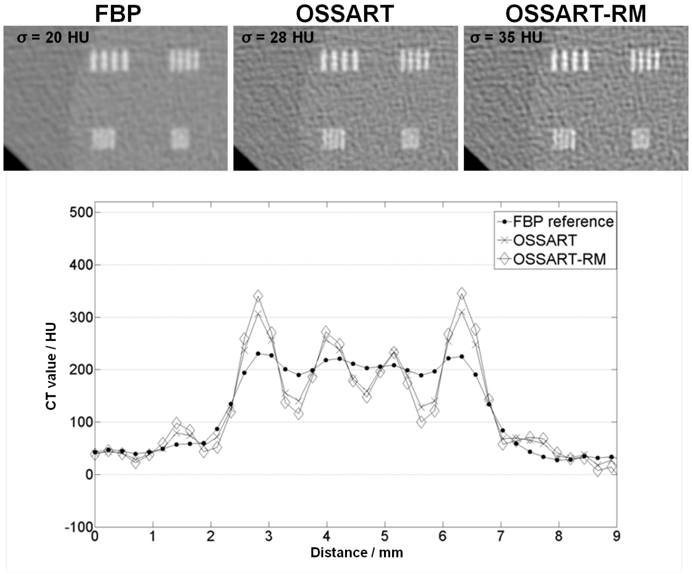

Fig. 4. The simulation results with fixed number of iterations for the iterative reconstructions. The reconstructions from left to right are FBP, OSSART and OSSART-RM. The images on top show a small region containing the resolution line patterns of the transversal view. The corresponding profiles of the lower left line pair is presented at the bottom. The images are shown at a grayscale window of C/W = 0/1000 HU.

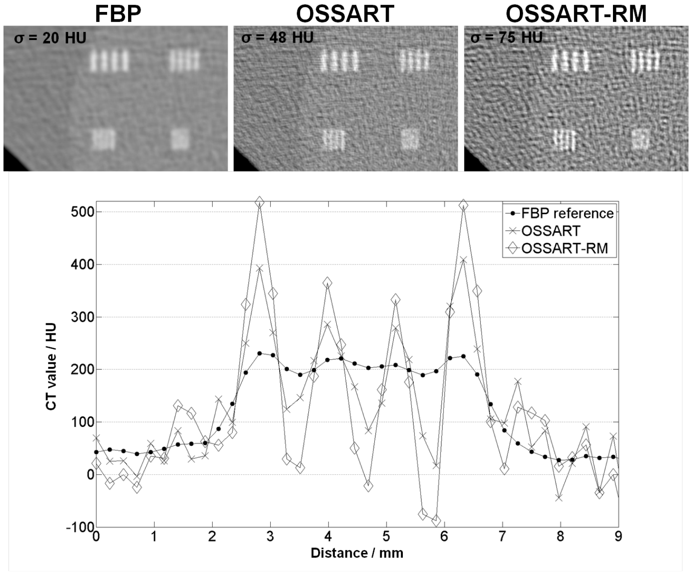

Fig. 5. The simulation results at convergence. The reconstructions from left to right are FBP, OSSART and OSSART-RM. The images on top show a small region containing the resolution line patterns of the transversal view. The corresponding profile through the lower left line pair is presented at the bottom. The images are shown at a grayscale window of C/W = 0/1000 HU.

To conclude on the signal-to-noise ratio, we first matched the noise of the FBP, OSSART and OSSART-RM. The results can be seen in figure 3. The profiles are drawn through the lower left line pair as can be seen in figure 1 in the enlarged dashed box. In figure 3 no major differences can be seen between the three cases. This means that no significant benefit in signal-to-noise ratio can be achieved with the ray modeling

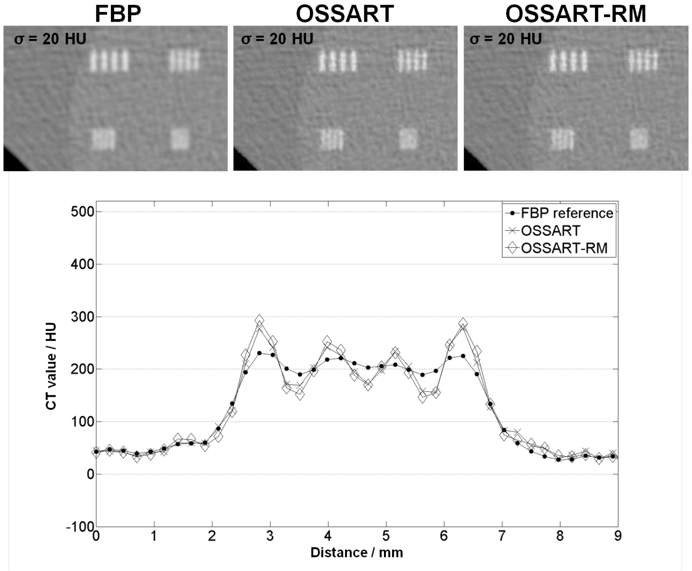

Fig. 6. The simulation results with the iterative scheme. The reconstructions from left to right are FBP, iterative scheme with OSSART and iterative scheme with OSSART-RM. The images on top show a small region containing the resolution line pattern of the transversal view. The corresponding profile through the lower left line pair is presented at the bottom. The images are shown at a grayscale window of C/W = 0/1000 HU.

approach without additional means.

Next we investigated the behavior of the iterative algorithms with a fixed number of iterations. The results are shown in figure 4. The iterative algorithms show a better resolution compared to the FBP which can be seen in the profiles with the downside of higher noise ($\sigma_{\text{FBP}} < \sigma_{\text{OSSART}} < \sigma_{\text{OSSART-RM}}$). Comparing the OSSART with OSSART-RM the same can be seen here. With a fixed number of iterations the OSSART-RM results in an image with better resolution but also higher noise as in the OSSART reconstruction. From this one can conclude on faster convergence speed in terms of iteration number in the ray modeling case.

The last case of interest is to investigate the results of OSSART and OSSART-RM in the region of convergence. Convergence here means that a certain threshold is underrun by the update. The results can be seen in figure 5. Here one can again see that OSSART and OSSART-RM result in images with higher resolution and higher noise. The interesting observation that can be done comparing the OSSART with OSSART-RM is that they both converge to different results due to the ray modeling. This can be seen comparing the profiles in figure 5. Again this is at the expense of higher noise which increases in the same degree the contrast of the line profile. Thus so far no clear benefit can be seen through ray modeling.

One can now think of a regularization approach which takes advantage of the OSSART and OSSART-RM by suppressing noise and maintaining resolution so that the reconstruction can profit from the higher resolution of the iterative algorithms. We use a bilateral filter incorporated in an iterative scheme. This scheme utilizes the fact that iterative algoritms result in a higher resolution as the analytical reconstructions.

The simulation results of the iterative scheme can be seen in figure 6. Here the stopping criterion was $\sigma_{\text{Final}} = \sigma_{\text{Prior}} = \sigma_{\text{FBP}}$ That means the iteration was stopped when the noise is matched with the noise of the reference FBP reconstruction. Looking at the profiles one can see that the line profile in the lower left can now be resolved in the BF-OSSART and in the BF-OSSART-RM case. Thus the signal-to-noise ratio could be improved. Comparing the results with and without ray modeling one can see that the result with ray modeling is slightly better but bears in no relation to the additional computational effort.

IV. SUMMARY

We have examined the effects that are introduced by modeling the ray acquisition process in the forward projection of an iterative OSSART algorithm in a simulation study. Comparing it to a reference FBP reconstruction and a normal OSSART, we could not recognize any benefits in signal-to-noise ratio. The main difference was found in the convergence behavior of the OSSART and OSSART-RM. From these findings we derived an iterative scheme which utilizes an bilateral filter as an edge preserving regularization leading to a better signal to noise ratio. Our overall finding is that ray modeling is an expensive task and the benefits are only minor and bear in no relation to the additional computational effort. However iterative reconstruction schemes with appropriate regularization seem to be promising.

ACKNOWLEDGMENTS

This work was funded by the Deutsche Forschungsgemeinschaft DFG under grant KA 1678/3-1. Parts of the reconstruction software were provided by RayConStruct® GmbH, Nürnberg, Germany. We thank the Intel Corporation and Fujitsu Siemens Computers GmbH for providing the highly performant computing hardware.

REFERENCES

[1] K. Zeng, B. De Man, and J.-B. Thibault, "Spatial resolution enhancement in CT iterative reconstruction," *Nuclear Science Symposium Conference Record (NSS/MIC), 2009 IEEE*, pp. 3748–3751, Oct. 2009.

[2] S. Do, S. Cho, W. Karl, M. Kalra, T. Brady, and H. Pien, "Accurate model-based high resolution cardiac image reconstruction in dual source CT," *Biomedical Imaging: From Nano to Macro, 2009. ISBI '09. IEEE International Symposium on*, pp. 330–333, Jul. 2009.

[3] T. Nielsen, R. Manzke, R. Proksa, and M. Grass, "Cardiac cone-beam CT volume reconstruction using ART," *Med. Phys.*, vol. 32, no. 4, pp. 851–860, Apr. 2005.

[4] C. Kamphuis and F. Beekman, "Accelerated iterative transmission ct reconstruction using an ordered subsets convex algorithm," *IEEE Transactions on Medical Imaging*, vol. 17, no. 6, pp. 1101–1105, 1998.

[5] C. Tomasi and R. Manduchi, "Bilateral filtering for gray and color images," *Proc. 6th Int. Conf. Computer Vision*, pp. 839–846, 1998.

[6] A. Ziegler, T. Nielsen, and M. Grass, "Iterative reconstruction of a region of interest for transmission tomography," *Med. Phys.*, vol. 35, no. 4, pp. 1317–1327, Apr. 2008.

[7] A. Andersen and A. Kak, "Simultaneous algebraic reconstruction technique (SART): A superior implementation of the ART algorithm," *Ultrasonic Imaging*, vol. 6, pp. 81–94, 1984.

[8] M. Kachelrieß, "The FORBILD CT–simulation phantoms," *Proc. of the 1999 Int. Meeting on Fully 3D Image Reconstruction*, p. 383, Jun. 1999.

[9] P. M. Joseph, "An improved algorithm for reprojecting rays through pixel images," *IEEE Transactions on Medical Imaging*, vol. MI–2, no. 3, pp. 192–196, Nov. 1982.

Patchwork Reconstruction with Resolution Modeling for Digital Breast Tomosynthesis

Koen Michielsen, Katrien Van Slambrouck, Anna Jerebko and Johan Nuyts

***Abstract*—Visualizing micro-calcifications adequatly remains a challenge in digital breast tomosynthesis. We propose a maximum a posteriori algorithm which uses a plane by plane updating scheme for faster convergence. The scheme enables efficient implementation of an approximate model for position dependent resolution. An observer study shows an improvement in detection of micro-calcifications compared to the filtered backprojection method currently in use.**

I. INTRODUCTION

Early detection of breast cancers by mammography screening has been shown to improve patient outcome [1]. However, some lesions, like masses in dense breasts, remain difficult to detect due to the amount of anatomical noise [2]. A three dimensional imaging technique, like digital breast tomosynthesis (DBT), may be able to solve this problem by removing interference from overlapping dense tissue [3]. DBT provides a limited angle set of projections. These projections are usually reconstructed with filtered backprojection (FBP). However, because of the limited angular range and low dose acquisitions, reconstruction by FBP is not always optimal [4], [5], especially for small angular range [6].

Using the more accurate acquisition model of the Maximum Likelihood for Transmission (MLTR) algorithm proposed in [7] could improve reconstruction for DBT, but this algorithm (like all iterative methods) is quite slow in comparison to FBP. We try to improve the convergence speed of the algorithm by applying a grouped coordinate ascent (GCA) algorithm [8], [9], where groups of voxels are updated sequentially instead of simultaneously. By choosing the reconstruction planes parallel to the detector as these groups, we can simultaneously introduce a resolution model which is dependent on the height above the detector.

II. MATERIALS AND METHODS

A. Patchwork Reconstruction

In the MLTR algorithm, attenuation distribution $\vec{\mu}$ is obtained by maximising log-likelihood function L. The log-likelihood can be written as

$$L = \sum_i y_i \ln \hat{y}_i - \hat{y}_i \tag{1}$$

with y_i the measured transmission scan, $\hat{y}_i$ the estimated transmission scan and i the index of the projection line. In the simplest case the acquisition process can be written as:

$$\hat{y}_i = b_i e^{-\sum_j l_{ij}\mu_j} \tag{2}$$

with b_i the blank value for projection line i and l_{ij} the intersection lenght between projection line i and voxel j. With this information, one can construct a gradient ascent algorithm, with following update step:

$$\mu_j^{\text{new}} = \mu_j^{\text{old}} + \frac{\alpha_j \sum_i l_{ij}(y_i - \hat{y}_i)}{\sum_i l_{ij}\hat{y}_i \sum_h \alpha_h l_{ih}} \tag{3}$$

Choosing $\alpha_j = 1$ in equation 3 results in the MLTR algorithm and $\alpha_j = \mu_j^{\text{old}} + \epsilon$, with ϵ a small positive constant to make sure $\alpha_j > 0$, gives the convex algorithm [10].

For a patchwork reconstruction, the image is divided into regions (patches) that are updated separately and sequentially [11]. Accelerated convergence is partly due to the sequential updates but mainly due to an increased step size in the update. In equation 3 we can consider a patch update as an update with $\alpha_j = 0$ everywhere except in the current patch. Therefore the sum $\sum_h \alpha_h l_{ih}$ in the denominator will be smaller and the step size for updates will be larger for smaller patches. We choose to use each plane (parallel to the detector surface) in the reconstruction volume as a separate patch. This is both the logical choice, since this is how tomosynthesis images are visualized, and close to optimal, since it minimises the denominator in equation 3, indicating that voxels in one plane share little information in the projection.

Because of the limited angular sampling, there is little to no information on the distribution of attenuation values in the direction perpendicular to the detector surface. The patchwork algorithm tends to accumulate all low frequency information in the first patch. To ensure that low frequency information will be uniformily distributed over all patches, we initialize the reconstruction volume with a rough estimate of the attenuation and divide the update step for each patch in the first two iterations by the number of patches that still need to be updated in the current iteration. Because this creates a non-uniform noise distribution in the volume, the update order of the patches is reversed in the second iteration.

B. Resolution Modeling

While the detectors in mammography tomosynthesis systems have good resolution, tube motion during the acquisition causes additional blurring in the acquisition of tomosynthesis data. Mathematically this blurring can be added to the simple aqcuisition model in equation 2 as follows:

$$\hat{y}_i = b_i \sum_n A_{in} \int_{\theta_1}^{\theta_2} w(\theta) e^{-\sum_j l_{nj}(\theta)\mu_j} d\theta + s_i \tag{4}$$

K. Michielsen, K. Van Slambrouck and J. Nuyts are with the department of Nuclear Medicine, KU Leuven, Belgium

A. Jerebko is with Siemens AG, Erlangen, Germany

This work is supported by Siemens AG and by SBO project QUANTIVIAM (060819) of the Institute for Promotion of Innovation through Science and Technology in Flanders (IWT-Vlaanderen).

Corresponding author: koen.michielsen@uzleuven.be

With the angles θ representing the tube motion during one of the acquisitions of the tomosynthesis series, $w(\theta)$ is the relative weight of each angle within a single exposure. The scatter is represented by s_i, and the kernel with coefficients A_{in} represents the intrinsic detector blurring.

Although equation 4 describes the acquisition process adequatly, the derived update step would be too complex for an efficient reconstruction. Therefore we introduce the following approximation, making use of the fact that the volume is already split in patches parallel to the detector plane:

$$\hat{y}_i = b_i \prod_p \sum_n A^p_{in} e^{-\sum_{j \in p} l_{nj}\mu_j} + s_i \tag{5}$$

In essence, the motion blur, which is dependent on the height above the detector plane, is included in the detector blur A^p_{in} for each patch p.

Using the following notation, we can derive the update step for an MLTR algorithm using this model for the acquisition.

$$\hat{y}_i = b_i \prod_p \bar{\psi}^p_i + s_i \tag{6}$$

$$\bar{\psi}^p_i = \sum_n A^p_{in} \psi^p_n \tag{7}$$

$$\psi^p_i = e^{-\sum_{j \in p} l_{ij}\mu_j} \tag{8}$$

The patches appear in equation 8 in the form of the sum over j: $\sum_{j \in p} l_{ij}\mu_j = \sum_j \alpha_j l_{ij}\mu_j$ with $\alpha_j = 1$ for $j \in p$ and $\alpha_j = 0$ for $j \notin p$. With this we can calculate the update step in eq. 9.

$$\Delta\mu_j = \frac{-\frac{\partial L}{\partial \mu_j}}{\sum_k \frac{\partial^2 L}{\partial \mu_j \partial \mu_k}} \tag{9}$$

$$-\frac{\partial L}{\partial \mu_j} = \sum_i l_{ij} \psi^{p(j)}_i \sum_n A^{p(j)}_{in} \frac{y_n - \hat{y}_n}{\bar{\psi}^{p(j)}_n} \frac{\hat{y}_n - s_n}{\hat{y}_n} \tag{10}$$

$$\begin{aligned}\sum_k \frac{\partial^2 L}{\partial \mu_j \partial \mu_k} \approx -\sum_i l_{ij} \psi^{p(j)}_i \cdot \sum_k l_{ik} \cdot \\ \sum_n A^{p(j)}_{in} \frac{\hat{y}_n - s_n}{\bar{\psi}^{p(j)}_n} \left(1 - \frac{y_n s_n}{\hat{y}^2_n}\right)\end{aligned} \tag{11}$$

The approximation for the second derivative comes from the assumption that the intersection lengths are smooth on the scale of the kernel A^p_{in}:

$$\sum_n A^p_{in} \psi^p_n \sum_{k \in p} l_{nk} \approx \sum_{k \in p} l_{ik} \sum_n A^p_{in} \psi^p_n \tag{12}$$

C. Phantom Simulation and Reconstruction

To test the reconstruction method, we simulated background images with stochastical noise by filtering white noise with a power law filter $f(\nu) = \kappa/\nu^\beta$, with ν the frequency, $\beta = 3$ and $\kappa = 10^{-5}\ \mathrm{mm}^{-1}$ [12], [13]. The resulting images were reduced to 500 by 500 by 200 isotropic voxels with sides of 85 μm. This background volume was placed in one of three possible locations, always with one side above the chest-side detector edge: central at 27 mm above the detector plane, central at 67 mm above the detector plane, and 75 mm off center at a height of 47 mm.

We used the background images to generate two data sets: in the first set we added a random number of clusters to each background image, Poisson distributed with a mean of 1.0 per image, and placed at a random location within the volume (but not on the edge). Each cluster consisted of a random number of calcifications, with a mean of 2.5 per cluster (again Poisson distributed), but with a minimum of a single calcification per cluster. The individual calcifications were spherical, with a diameter between 100 and 200 μm, spaced 0.5 to 1.5 mm apart in a random direction and set in a volume with isotropic voxel spacing of 5 μm.

For the second set we created two series of micro-calcifications (smooth, corresponding to Le Gal II and irregular, corresponding to Le Gal IV) according to the recipe of Näppi [14]. These micro-calcifications were rescaled to diameters between 200 and 600 μm. The volume in which they were set had isotropic voxel spacing between 6 and 18 μm, depending on the rescaling.

Projections of these volumes were simulated according to the acquisition model described in eq. 4 and with increased detector sampling. Multiple source positions were sampled for each exposure angle, corresponding to an exposure time of 120 ms per projection, x-ray energy was set to 20 keV and Poisson noise was generated with a blank scan of 1500 photons per pixel (12.5 μGy detector dose after attenuation).

The geometric blurring parameters for our model were determined for the Mammomat Inspiration[1] system (Siemens, Erlangen, Germany), which is in clinical use on site. Therefore the Siemens iFBP method [15] without detector binning, with slice thickness filter and with a filter designed so that resulting reconstructed slices resemble 2D mammography images was used as the point of reference. The two reconstructions to be compared to the point of reference were 3 iterations of our patchwork reconstruction with resolution modelling, with prior and without prior. The Huber prior (equation 13) was used, with $\beta = 3.0 \cdot 10^{-4}$ and $\delta = 2.5 \cdot 10^{-4}\ \mathrm{mm}^{-1}$. Since the average reconstructed attenuation is about 0.06 mm^{-1}, the prior function is mostly active in linear mode.

$$\begin{aligned}|\mu_j - \mu_k| < \delta :\ \ P(\vec{\mu}) = \sum_{j,k} w_{jk} \frac{(\mu_j - \mu_k)^2}{2\delta^2} \\ |\mu_j - \mu_k| \geq \delta :\ \ P(\vec{\mu}) = \sum_{j,k} w_{jk} \frac{|\mu_j - \mu_k| - \delta/2}{\delta}\end{aligned} \tag{13}$$

Figure 1 shows an example of the three reconstruction methods for two simulated calcifications.

We compare the convergence speed of the two patchwork iterative methods used in the observer study with the MLTR and Convex algorithms by plotting, $L_{max} - L$ in function of iteration number for the reconstruction of a mathematical phantom [16].

---

[1] Breast tomosynthesis with Siemens MAMMOMAT Inspiration is an investigational practice and is limited by U.S. law to investigational use. It is not commercially available in the U.S. and its future availability cannot be ensured.

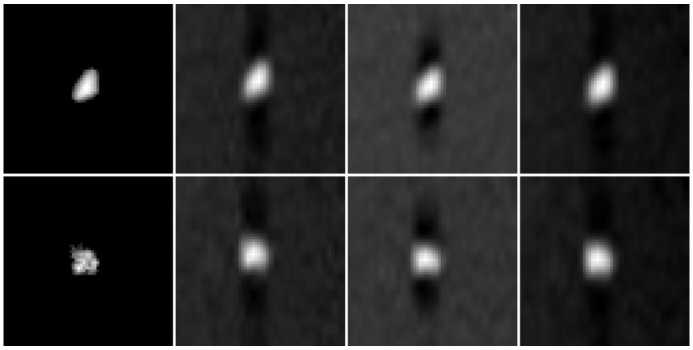

Fig. 1: Two simulated calcifications with a diameter of 400 μm. Window is set from minimum to maximum pixel value. Top: smooth, bottom: irregular; from left to right: true slice, iFPB, patchwork iterative without prior and with prior.

D. Reconstruction Comparison

The comparison was split in two distinct observer experiments: first, a free search study to check the detectability of small spherical micro-calcifications and second, a two-alternate forced choice (2AFC) study to check the discrimination between smooth (Le Gal II) and irregular (Le Gal IV) micro-calcifications.

For the detection study, 7 readers performed a free search on 120 cases for each reconstruction (with 40 images used for initial training) and scored detected lesions on a 4 point scale as shown in table I. Results were analyzed using the weighted JAFROC method [17].

Score	Description
1	I see a hint of a calcification
2	This might be a calcification
3	This is probably a calcification
4	I am sure this is a calcification

TABLE I: Evaluation scale for the detection experiment.

For the 2AFC study, 5 readers evaluated 300 cases for each reconstruction (of which 100 cases were used as initial training) by classifying them as smooth or irregular and providing their certainty of this classification (low, medium or high certainty). Results were analysed using the DBM MRMC method [18].

III. RESULTS

Figure 2 shows results for the detection study. The extension from the point of the lowest confidence score (1 in table I) is shown in grey. There are significant differences between the iFBP and the patchwork reconstruction with prior ($p = 0.029$) and between both patchwork reconstructions ($p = 0.022$) for detecting the smallest micro-calcifications (<200 μm). There is no difference between the iFBP and the patchwork reconstruction without prior ($p = 0.893$).

Table II shows the results for the shape discrimination study with the area under the ROC curve (AUC) as the figure of merit (FoM). The p-value of 0.935 indicates that the three reconstruction methods have identical performance when considering shape discrimination of small lesions.

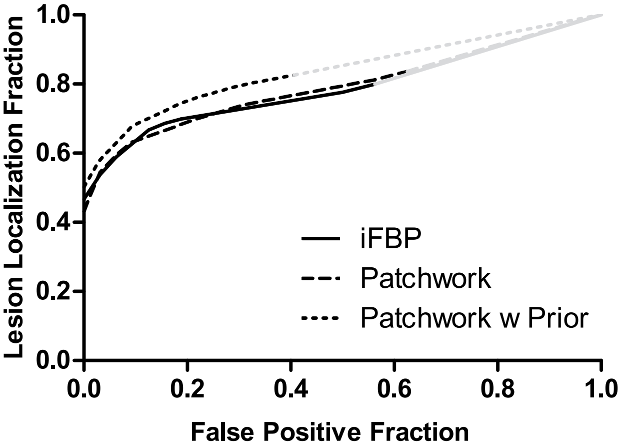

Fig. 2: AFROC curve of detection study results.

Reconstruction	Figure of Merit
iFBP	0.774
Patchwork	0.773
Patchwork w Prior	0.769
p-value	0.935

TABLE II: Results of the 2AFC study.

Figure 3 shows the likelihood as a function of the iteration number. The patchwork reconstruction with prior is not shown since its curve would overlap that of the normal patchwork reconstruction on the graph. The patchwork reconstructions reach a better likelihood value than the MLTR reconstruction at 10 and 20 iterations after only 5 and 7 iterations respectively.

IV. DISCUSSION

The initial evaluations show that the patchwork reconstruction with resolution modelling and smoothing prior can improve upon iFBP after only 3 iterations for detecting very small micro-calcifications while performing at the same level for classifying slightly larger micro-calcifications.

The new algorithm currently results in a limited improvement on the clinical image quality, as shown in a comparison with iFBP in figure 4. This makes sense when considering the fact that the iFBP algorithm has been specifically optimised for the Mammomat Inspiration system. We expect further

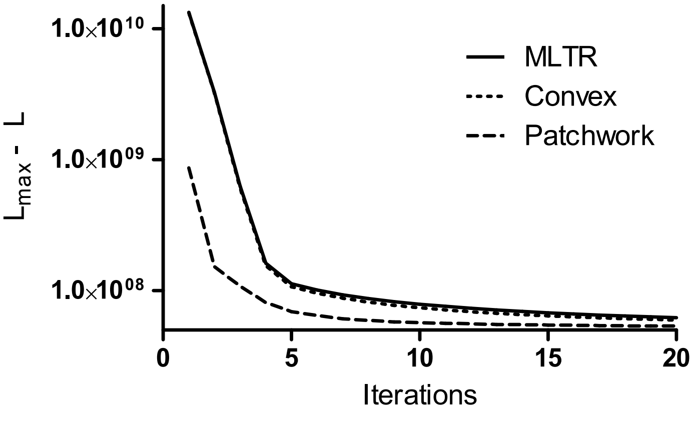

Fig. 3: Likelihood ($L_{max} - L$) curve.

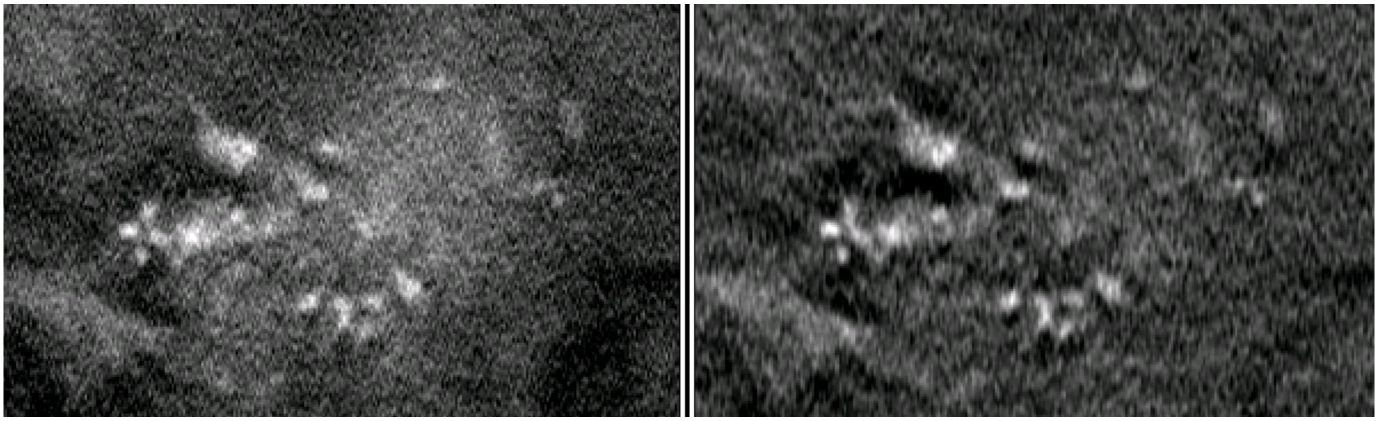

Fig. 4: A cluster of micro-calcifications (left: iFBP, right: patchwork reconstruction with resolution modelling).

improvements in our algorithm when including the measured point spread functions of the system in the resolution model instead of a Gaussian approximation.

An important advantage in comparison to other iterative methods is the improved convergence speed that comes from applying a grouped coordinate ascent algorithm. The much faster convergence speed per iteration step reduces one of the most critical factors that keeps iterative reconstruction from being used in the clinic: reconstruction time. In our results we only used 3 iterations while typically we would use 8-10 iterations without the GCA algorithm.

V. CONCLUSIONS

The described method greatly increases convergence rate per iteration of DBT reconstruction while including an accurate resolution model. Adding a Huber-prior to the algorithm limits the noise in the image and allows reconstruction of clinical images in only 3 iterations while increasing detection performance in comparison to iFBP and maintaining the same level of lesion discrimination performance.

ACKNOWLEDGEMENTS

The authors would like to thank Nicholas Marshall for providing the MTF measurements for the resolution model; Federica Zanca for her advice on designing the observer study; and Joke Bints, Gregory Cieters, Lesley Cockmartin, Annelies Jacobs, Xochitl Lopez Rendon, Ahmadreza Rezaei, Elena Salvagnini, Eman Shaheen and Lin Zhou for their participation in the observer study.

REFERENCES

[1] L. Nyström, I. Andersson, N. Bjurstam, J. Frisell, B. Nordenskjöld, and L. E. Rutqvist, "Long-term effects of mammography screening: updated overview of the Swedish randomised trials." *Lancet*, vol. 359, no. 9310, pp. 909–19, Mar. 2002.

[2] R. E. Bird, T. W. Wallace, and B. C. Yankaskas, "Analysis of cancers missed at screening mammography." *Radiology*, vol. 184, no. 3, pp. 613–617, Sep. 1992.

[3] J. A. Baker and J. Y. Lo, "Breast tomosynthesis: state-of-the-art and review of the literature." *Academic Radiology*, vol. 18, no. 10, pp. 1298–1310, Oct. 2011.

[4] T. Wu, R. H. Moore, E. A. Rafferty, and D. B. Kopans, "A comparison of reconstruction algorithms for breast tomosynthesis," *Medical Physics*, vol. 31, no. 9, pp. 2636–2647, 2004.

[5] Y. Zhang, H.-P. Chan, B. Sahiner, J. Wei, M. M. Goodsitt, L. M. Hadjiiski, J. Ge, and C. Zhou, "A comparative study of limited-angle cone-beam reconstruction methods for breast tomosynthesis," *Medical Physics*, vol. 33, no. 10, pp. 3781–3795, 2006.

[6] T. Mertelmeier, J. Ludwig, and B. Zhao, "Optimization of tomosynthesis acquisition parameters: angular range and number of projections," in *LNCS Proceedings of the IWDM*, J. Marti, A. Oliver, J. Freixenet, and R. Marti, Eds., 2008, pp. 220–227.

[7] J. Nuyts, B. De Man, P. Dupont, M. Defrise, P. Suetens, and L. Mortelmans, "Iterative reconstruction for helical CT: a simulation study." *Physics in Medicine and Biology*, vol. 43, no. 4, pp. 729–737, Apr. 1998.

[8] J. A. Fessler, E. P. Ficaro, N. H. Clinthorne, and K. Lange, "Grouped-coordinate ascent algorithms for penalized-likelihood transmission image reconstruction." *IEEE Transactions on Medical Imaging*, vol. 16, no. 2, pp. 166–175, Apr. 1997.

[9] J. A. Fessler and D. Kim, "Axial block coordinate descent (ABCD) algorithm for X-ray CT image reconstruction," in *Proceedings of Fully3D*, 2011, pp. 262–265.

[10] K. Lange and J. A. Fessler, "Globally convergent algorithms for maximum a posteriori transmission tomography." *IEEE Transactions on Image Processing*, vol. 4, no. 10, pp. 1430–1438, Jan. 1995.

[11] K. Van Slambrouck and J. Nuyts, "A patchwork (back)projector to accelerate artifact reduction in CT reconstruction," in *IEEE Nuclear Science Symposium Conference Record*, no. 060819. IEEE, 2010.

[12] K. G. Metheany, C. K. Abbey, N. Packard, and J. M. Boone, "Characterizing anatomical variability in breast CT images," *Medical Physics*, vol. 35, no. 10, pp. 4685–4694, 2008.

[13] E. Engstrom, I. S. Reiser, and R. M. Nishikawa, "Comparison of power spectra for tomosynthesis projections and reconstructed images," *Medical Physics*, vol. 36, no. 5, pp. 1753–1758, 2009.

[14] J. Näppi, P. B. Dean, O. Nevalainen, and S. Toikkanen, "Algorithmic 3D simulation of breast calcifications for digital mammography." *Computer Methods and Programs in Biomedicine*, vol. 66, no. 1, pp. 115–124, Jul. 2001.

[15] J. Ludwig, T. Mertelmeier, H. Kunze, and W. Harer, "A Novel Approach for Filtered Backprojection in Tomosynthesis Based on Filter Kernels Determined by Iterative Reconstruction Techniques," in *LNCS Proceedings of the IWDM*. Springer, 2008, pp. 612–620.

[16] P. R. Bakic, C. Zhang, and A. D. A. Maidment, "Development and characterization of an anthropomorphic breast software phantom based upon region-growing algorithm," *Medical Physics*, vol. 38, no. 6, pp. 3165–3176, 2011.

[17] D. P. Chakraborty and K. S. Berbaum, "Observer studies involving detection and localization: modeling, analysis, and validation." *Medical physics*, vol. 31, no. 8, pp. 2313–2330, Aug. 2004.

[18] D. D. Dorfman, K. S. Berbaum, and C. E. Metz, "Receiver operating characteristic rating analysis. Generalization to the population of readers and patients with the jackknife method." *Investigative radiology*, vol. 27, no. 9, pp. 723–31, Sep. 1992.

Comparative Studies on Distance-driven and Finite-detector-based Projection Models for Iterative Image Reconstruction

Chuang Miao, Baodong Liu, Qiong Xu, Hengyong Yu[*]

Abstract

Fast and accurate image reconstruction is the ultimate goal of iterative methods for limited-angle, few-view, interior problems, etc. Recently, we proposed a finite-detector-based area integral model (AIM) to model the projection procedure of a discrete imaging object. On the other hand, the distance-driven model (DDM) is the state-of-the-art technology to model forward projection and backprojection. In an ordered-subset simultaneous algebraic reconstruction technique (OS-SART) framework, both of the AIM and DDM are implemented and evaluated using a sinogram from a phantom experiment on a Discovery CT750 HD scanner. The results show that the DDM-based method is 6 to 10 times faster than the AIM-based method assuming the same number of times of iterations. The spatial resolution of the AIM-based method can have ~10% improvement compared to the DDM-based method in terms of full-width-of-half-maximum (FWHM).

***Index Terms*---** computed tomography (CT), image reconstruction, area integral model, distance-driven model, OS-SART.

1. Introduction

Computed tomography (CT) reconstruction is a process of recovering *n*-dimensional (*n*D) image data from a set of integrals of that data over lower-dimensional subspaces. The projection and/or backprojection model is required for image reconstruction, artefact correction, or simulation purposes. In the continuous domain, the well known Radon transform is accepted as the projection model, in which line integrals of the imaging object are calculated. The backprojection model, generally defined as the transpose (or adjoint) of the projection model. The most prevalent application of the backprojection operation is in the filtered backprojection (FBP) reconstruction algorithms, which are based on analytic inversion formulae for the Radon transform [1]. Parallel to the development of analytic reconstruction algorithms, the iterative reconstruction methods are proposed, in which repeated applications of the projection and backprojection are used to approximate the image that best fits the measurements according to an appropriate objective function [2].

There are many methods to model the projection and backprojection procedures for a discrete imaging object. All of those models compromise between computational complexity and accuracy. To our best knowledge, the current projection and backprojection models can be divided into three categories[3]. The first is the *pixel-driven* model, which is usually used for implementations of backprojection. By connecting a line from the focal spot, a location of intersection on the detector is determined on a detector array. A value is obtained from the detector via interpolation, and the result is accumulated in the pixel [4-6]. The second is the *ray-driven* model, which is used for forward projection. It connects a line from the focal spot through the image to the detector centre. A value is obtained via interpolation from the image pixel values, and the result is accumulated on the detector cell. The third is called the *distance-driven* model (DDM), which combines the advantages of the pixel-driven and ray-driven models [7, 8]. The key is to calculate the length of overlap between each image pixel and each detector cell, and then use the normalized length of overlap to calculate the weight used in projection and backprojection. Recently, a finite-detector-based projection model was proposed for iterative CT reconstructions by H.Y. Yu and G. Wang [9], which was also called area integral model (AIM). This model is different from all the aforementioned projection models without any interpolation.

It is our understanding that the AIM-based method can be simplified to the DDM-based method under some approximation. Compare to the distance-driven method, the AIM-based method is more accurate but on the other hand more time-consuming due to the high computing

Chuang Miao is with the Biomedical Imaging Division, VT-WFU School of Biomedical Engineering and Sciences, Wake Forest University Health Sciences, Winston-Salem, NC, 27157, USA.

Baodong Liu and Hengyong Yu are with the Biomedical Imaging Division, VT-WFU School of Biomedical Engineering and Sciences, Wake Forest University Health Sciences, Winston-Salem, NC, 27157, USA & the Department of Radiology, Division of Radiologic Sciences, Wake Forest University Health Sciences, Winston-Salem, NC, 27157, USA. (e-mail: Hengyong-yu@ieee.org).

Qiong Xu is with the Biomedical Imaging Division, VT-WFU School of Biomedical Engineering and Sciences, Wake Forest University Health Sciences, Winston-Salem, NC, 27157, USA & the Institute of Image Processing and Pattern Recognition, Xi'an Jiaotong University, Xi'an, Shaanxi, 710049, P.R. China.

cost of the system matrix. In this paper, we will perform extensive numerical experiments to quantitatively evaluate the DDM-based and the AIM-based methods assuming a fan-beam geometry of a typical GE CT scanner. This work will have a direct impact on several applications including the development of fast and accurate iterative CT reconstruction for super resolution. The rest of this paper is organized as follows: In Section II, we will briefly summarize the AIM and DDM; In Section III, numerical experiments will be performed and the results will be presented; In Sec. IV, we will discuss some related issues and conclude the paper.

2. Method

2.1. Discretized Description of a CT Imaging System

Many imaging system, such as CT scanners can be modeled by the following linear equations [10]:

$$Wf = p, \tag{1}$$

where $p \in P$ represents projection data, $f \in F$ represents an unknown image, and the non-zero matrix $W : F \rightarrow P$ is a projection operator. For practical applications, the discrete-discrete model is assumed. In other words, f and p are vectors. The projection data p is usually measured by detector cells, which implies that p is already discrete. For the two-dimensional (2D) case, an image can be discretized by superimposing a square grid on the image. Usually$f$ is assumed as constant in each grid cell, which is referred to as a pixel. As a result, we have a 2D digital image $f = \left(f_{i,j}\right) \in R^I \times R^J$, where the indices $1 \leq i \leq I$, $1 \leq j \leq J$ are integers. Define

$$f_n = f_{i,j}, n = (i-1) \times J + j, \tag{2}$$

with $1 \leq n \leq N$, and $N = I \times J$, we can re-arrange the image into a vector $f = [f_1, f_2, \ldots, f_N,]^T \in R^N$. We may use both the signs f_n and $f_{i,j}$ to denote the image.

Let p_m be the m^{th} measured datum with m^{th} ray. Eq.(1) can be rewritten as

$$p_m = \sum_{n=1}^{N} \omega_{mn} f_n, \; m = 1, 2, \ldots, M. \tag{3}$$

where M is the total number of rays and ω_{mn} is the weighting coefficient that represents the relative contribution of the n^{th}pixel to the m^{th} measured datum. Therefore, we have a system matrix $W = (\omega_{mn})_{M \times N}$ and two vectors $f = [f_1, f_2, \ldots, f_N,]^T \in R^N$ and $p = [p_1, p_2, \ldots, p_M,]^T \in R^M$ for the discrete-discrete model. The major difference between the AIM and DDM is how to calculate the weighting coefficient ω_{mn}.

2.2. AIM

As shown in Fig. 1, the AIM considers the rays as 'fat' lines or narrow fan-beam [9], which covers a region connecting the x-ray source and two endpoints of the detector cell. The coefficient ω_{mn} can be expressed as:

$$\omega_{mn} = \frac{S_{m,n}}{L_{m,n}}, \tag{4}$$

where $S_{m,n}$ represents the interaction area between the n^{th} pixel and the m^{th} ray, and $L_{m,n}$ represents the product of the narrow fan-beam angle γ and the distance from the center of the n^{th} pixel to the x-ray source. For the details of the derivation, please refer to [9].

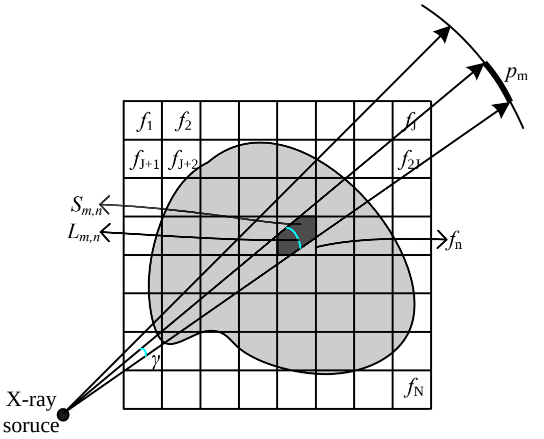

Fig.1: Area-integral model

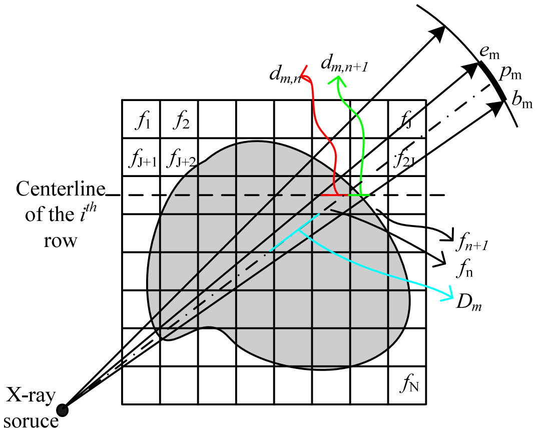

Fig. 2: Distance-driven model

2.3. DDM

The DDM combines the advantages of the pixel-driven and ray-driven methods. The key step for calculating the weighting coefficient is to calculate the length of overlap between each image pixel and each detector cell [3]. To calculate the overlapped length, we need to map all the detector cell *boundaries* onto the centerline of the image row of interest. One can also map all pixel *boundaries* in an image row of interest onto the detector. Or map both sets of boundaries onto a common line. In Fig. 2, we map the two boundaries of the m^{th} detector onto the centerline of the i^{th} image row, e_m and b_m are the ending boundary and the beginning boundary of the m^{th} detector, respectively. Let f_n and f_{n+1} are the n^{th} and $n+1^{th}$ pixels locate at the i^{th} row of the image, which are the only two pixels that intercept with the m^{th} detector in the i^{th} row of the image. $d_{m,n}$ and $d_{m,n+1}$ are the length of overlap between the two image pixels and the m^{th}

detector in this row. D_m is the interception length between every image row and the m^{th} ray. The normalized weighting coefficient can be computed by,

$$\omega_{mn} = D_m \cdot \frac{d_{m,n}}{d_{m,n}+d_{m,n+1}}, \qquad (5)$$

ω_{mn} is the weighting coefficient that represents the relative contribution of the n^{th} pixel to the m^{th} measured datum, and will be used in projection and backprojection (symmetric). For details of the DDM, please refer to [3].

2.4. OS-SART Reconstruction

In the ordered-subset simultaneous algebraic reconstruction (OS-SART) framework [11], we implemented each projection model assuming an equiangular fan-beam geometry. The fast iterative shrinkage thresholding algorithm (FISTA) [12] was employed to accelerate the convergence.

3. Results

A phantom experiment was performed on a GE Discovery CT750 HD scanner at Wake Forest University Health Sciences with a circular scanning trajectory. After appropriate pre-processing, we obtained a sinogram of the central slice in typical equiangular fan-beam geometry. The radius of the scanning trajectory was 538.5 mm. Over a 360° range, 984 projections were uniformly acquired. For each projection, 888 detector cells were equiangularly distributed, which defines a field of view of 249.2 mm in radius and an iso-center spatial resolution of 584 μm. Using the aforementioned sinogram, the DDM and AIM were evaluated and compared quantitatively according to the following criteria:

(a). Computational cost: the total computational times were compared assuming the same number of iteration times. The algorithms were implemented in Visual C++ and tested on a platform of PC (4.0 GB memory, 3.2 GHz CPU).

(b). Image noise: the standard variance of the pixel values within a homogenous region were computed to measure the image noises using Eq. (6),

$$\sigma = \sqrt{\frac{1}{B}\sum_{j=1}^{B}\left(f_j - f_m\right)^2} \qquad (6)$$

where B is the total number of pixels in the selected flat region, f_m is the mean of the total image pixel values in the region.

(c). Spatial resolution: Full-width-of-half-maximums (FWHMs) were calculated in a red square (showed in Fig. 3 within red square) to compare the spatial resolution [13].

For different projection models, the same parameters were used in the OS-SART algorithms. The initial image was set to zero and the size of all the subsets of OS-SART was set to 41. We reconstructed image matrixes of 512x512 (40 iterations) and 2048x2048 (20 iterations) to cover the whole field of view (FOV), and each pixel covered an area of $973.3 \times 973.3\ \mu m$ and $243.3 \times 243.3\ \mu m$, respectively.The full view of the phantom is shown in Fig. 3, and the selected sub-regions of the four reconstructed results were magnified as shown in Fig. 4. The results are summarized in Table 1.

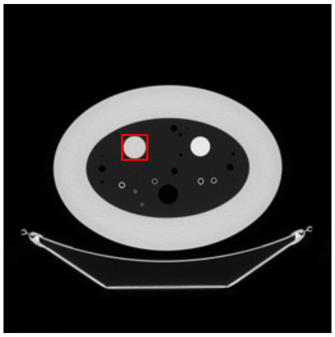

Fig. 3: The full view of the phantom

From Fig. 4 and Table 1, we can conclude that: the reconstruction speed of DDM-based OS-SART is about 6.3 (512x512, 40 iterations) and 9.4 (2048x2048, 20 iterations) times faster than the AIM-based OS-SART. While the image noise of DDM-based method is lower than that of AIM-based method, the AIM-based method has a better spatial resolution than that of DDM-based method.

4. Discussion and Conclusion

Compared to the AIM-based method, the DDM-based method is faster. This is because most of the computational cost in AIM-based method is to compute the system matrix W analytically. On the other hand, the system matrix computation in DDM-based method is more efficient because of the low computation complexity. In conclusion, we have numerically compared the AIM and DDM in an OS-SART framework. While the AIM-based method has a better performance, it requires higher computational cost. When the requirement of spatial resolution is not high, we can choose DDM-based method for lower computational cost.

5. References

[1] Suetens P, "*Fundamentals of Medical Imaging* (Cambridge: Cambridge University Press)", 2002.

[2] Hsieh J, Molthen R, Dawson C and Johnson R, "An iterative approach to the beam hardening correction in cone beam CT", *Med. Phys.* **27** 23–9.

[3] B. De Man and S. Basu, "Distance-driven projection and backprojection in three dimensions", *Phys. Med. Biol.,* vol. 49, p. 13, 2004.

[4] Herman G, "*Image Reconstruction from projections* (Orlando: Academic)", 1980.

[5] Peters T, "Algorithms for fast back- and re-projection in computed tomography", *IEEE Trans. Nucl. Sci.* **28** 3641–7, 1981.

[6] Zhuang W, Gopal S and Hebert T, "Numerical evaluation of methods for computing tomographic projections", *IEEE Trans. Nucl. Sci.* **41** 1660–5,1994.

[7] De Man B and Basu S, “Distance-driven projection and backprojection”, *IEEE Nuclear Science Symp. Medical Imaging Conf. (Norfolk),* 2002.

[8] De Man B and Basu S, “3D distance-driven projection and backprojection”, *Proc. 7th Int. Conf. on Fully 3D Reconstruction in Radiology and Nuclear Medicine (Saint Malo),* 2003.

[9] Yu H and Wang G, “Finite detector based projection model for super resolution CT”, *11th Int. Meeting on Fully Three-Dimensional Image Reconstruction in Radiology and Nuclear Medicine (Potsdam, 2011)* pp 387–90, 2011.

[10] Kak A C and Slaney M, “Principles of Computerized Tomographic Imaging*”, New York: IEEE Press,* 1999.

[11] G. Wang and M. Jiang, "Ordered-Subset Simultaneous Algebraic Reconstruction Techniques (OS-SART)", *Journal of X-ray Science and Technology,* vol. 12, pp. 169-177, 2004.

[12] A. Beck and M. Teboulle, "A Fast Iterative Shrinkage-Thresholding Algorithm for Linear Inverse Problems", *Siam Journal on Imaging Sciences,* vol. 2, p. 183, 2009.

[13] F. J. Schlueter, G. Wang, P. S. Hsieh, J. A. Brink, D. M. Balfe, and M. W. Vannier, "Longitudinal Image Deblurring In Spiral Ct", *Radiology,* vol. 193, pp. 413-418, Nov 1994.

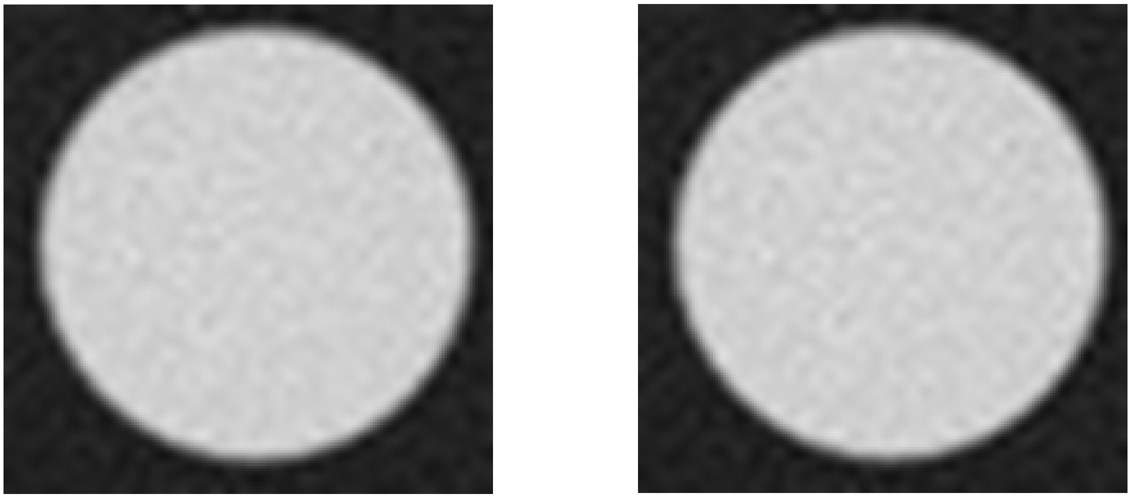

(a) DDM (512×512) *(b) AIM (512×512)*

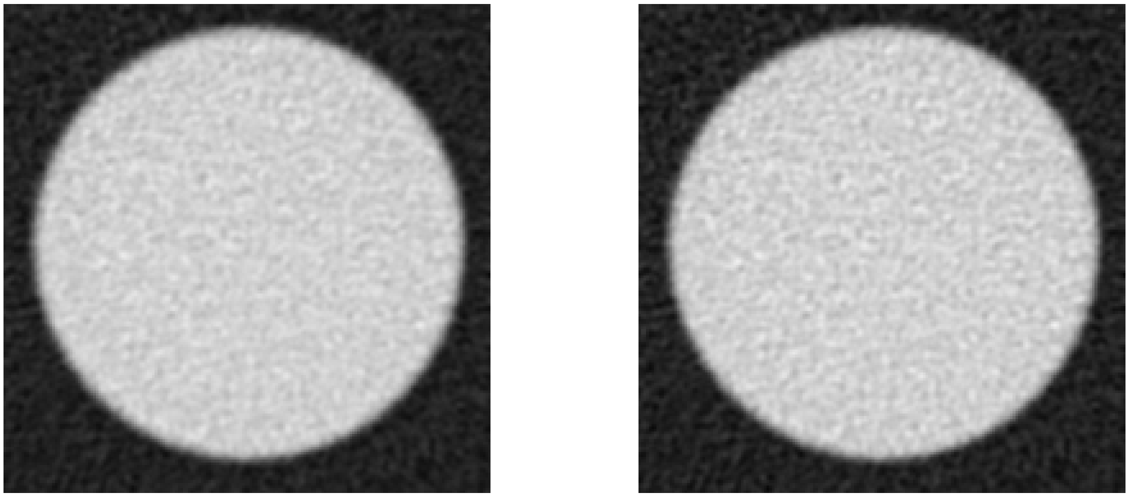

(c) DDM (2048×2048) *(d) AIM (2048×2048)*

Fig. 4: Magnifications of the selected regions in Fig. 3. (a)-(d) correspond to the reconstructed images by DDM and AIM with different image matrixes, respectively.

Table 1: Performance comparison between the DDM- and AIM-based methods.

OS-SART +FISTA	Image size	# of Iteration	Computational Cost (hrs)	Noise (HU)	Spatial Resolution (mm)
DDM	512×512	40	0.4335	32.4945	1.8481
AIM	512×512	40	2.7648	35.3084	1.6904
DDM	2048×2048	20	1.3652	41.9767	0.4228
AIM	2048×2048	20	12.7951	49.0495	0.3720

A New Method for Metal Artifact Reduction in CT

Thomas Koehler,[a] Bernhard Brendel,[a] and Kevin M. Brown[b]

***Abstract*—In this work, we present a new method for metal artifact reduction in computed tomography (CT), which is based on a sinogram interpolation technique. The method further comprises an adaptive application of the correction image which is specifically designed to avoid that the correction introduces new artifacts. The method is evaluated using clinical data.**

I. INTRODUCTION

The presence of metal within the field of view of a CT scanner can create severe artifacts in the reconstructed images. There are several different physical origins of these artifacts and the appearance of the artifacts can be very different, too [1]: Metal causes beam-hardening, resulting in dark and bright shading artifacts, in particular dark shading between metal objects, e. g., between two hip implants. Metal has a large linear attenuation coefficient leading to photon starvation in the shadow of the metal object, which can result in severe noise streaks. The large contrast of metal objects makes the CT imaging chain more sensitive to patient motion, which can lead to streak-shaped or arc-shaped artifacts for axial or helical acquisitions, respectively [2]. Furthermore, the contribution of scattered photons to the detected signal in the metal shadow is typically large, resulting also in dark and bright shading artifacts.

There are a lot of methods for metal artifact reduction (MAR): Noise streaks due to photon starvation can be suppressed by adaptive filtering [1], [3]. Beam hardening can be addressed by beam hardening correction algorithms [1], [4].

Another common and completely different approach for MAR is to replace data in the metal shadow in the sinogram by something more meaningful. The shadow is typically identified by segmentation in image domain followed by a forward projection. The replacement can be done by interpolation [2], [3], [5]–[9], or by a re-projection of a segmented image [10]–[13].

More recently, several iterative methods for MAR have been proposed [14]–[16]. Although statistical iterative methods are in general less sensitive to metal artifacts since the statistical weight for data in the metal shadow are small due to their bad statistics, they cannot reduce beam-hardening artifacts unless they contain a metal segmentation step.

MAR has been an area of active research for more than 30 years now, indicating that it is in fact a very tough problem. From our point of view, the major problem with MAR algorithms is robustness: Since the effects which lead to the artifacts and the appearance of the artifacts can be quite different, it is hard to set up an algorithm that handles every case well. Furthermore, many of the advanced methods contain a segmentation step in the processing chain. However, we observed that the artifacts in the original images can be so severe that a reliable segmentation is not possible, often leading not only to an imperfect correction of the metal artifacts but rather to the introduction of new artifacts. While an imperfect or incomplete correction of the metal artifacts may be acceptable in a clinical use case, the introduction of new artifacts is not.

This work contains two new contributions to the art of MAR: The first one is a further improvement of the algorithm proposed by Timmer [11]. The second is a general idea related to artifact correction methods in CT that aims specifically at preventing the introduction of new artifacts.

II. METHOD

First, we briefly review the method described by Timmer [11] and discuss its shortcomings.[1] The basic idea of the algorithm is to replace the data in the metal shadow by something more meaningful than the linear interpolation used by Kalender et al. [6]. In detail, the method comprises the following steps:

1) generation of an initial image using filtered back-projection,
2) classification of the pixels in the initial image into metal, bone, soft tissue, and air by thresholding,
3) generation of a metal only sinogram by forward projecting the pixels classified as metal,
4) generation of a synthetic image by replacing the pixels belonging to the soft tissue class by their mean pixel value (keeping bone and metal pixels unchanged),
5) generation of a synthetic sinogram by forward projecting the synthetic image,
6) replacing the line integrals in the metal shadow by the synthetic sinogram values (including a linear baseline shift to ensure that the replacement fits continuously to the data), and

---

[a] Philips Technologie GmbH, Innovative Technologies, Research Laboratories, Hamburg, Germany
[b] Philips Healthcare, Cleveland, OH, USA

[1] We always use additionally an adaptive filtering step in order to suppress high frequency streak patterns.

7) generation of the corrected image by filtered back-projection of the new sinogram.

The use of the forward projected synthetic image to fill the metal shadow gives a realistic estimate of the missing data. The classification step is intended to avoid that streak or shading artifacts propagate through the processing chain into the corrected image.

The first shortcoming of this algorithm is that the classification procedure sometimes fails in the presence of severe beam-hardening artifacts. This issue was addressed by Schmitt et al. [17] by performing the classification step on an image that is already corrected by Kalenders algorithm.

Another shortcoming is that the linear baseline correction in the metal shadow replacement step ensures a continuous fit of the synthetic sinogram data but not a smooth fit. Consequently, there is still a fair likelihood that streak artifacts are generated. This problem is addressed in the new algorithm by the introduction of a smooth fading of the synthetic sinogram data into the metal shadow. Another minor change is that we do not explicitely interpolate across the shadow, but rather calculate a correction sinogram. These changes lead to the following processing scheme, which is also illustrated in Fig. 1:

1) Initial MAR:
    a) generation of an *initial image* by an FBP reconstruction,
    b) generation of a *metal only image* by thresholding,
    c) generation of a *metal mask sinogram* by forward projection of the metal only image followed setting all non-zero values to one,
    d) generation of a *metal replaced sinogram* by linear interpolation across the metal shadow in the original sinogram, and
    e) generation of a 1^{st} *MAR image* by filtered back-projection of the metal replaced sinogram.
2) 2^{nd} pass MAR:
    a) generation of a *synthetic image* as in the original method by Timmer from the 1^{st} MAR image,
    b) generation of a *synthetic sinogram* by forward projection,
    c) generation of an *error sinogram* as the difference of the synthetic sinogram and the original sinogram,
    d) generation of a *correction sinogram* by multiplying the error sinogram with a smoothed version of the metal mask sinogram,
    e) generation of a *correction image* by filtered back-projection of the correction sinogram, and
    f) generation of the 2^{nd} *MAR image* by subtracting the correction image from the original image.

We note that the artifact reduction can be further improved by running a 3^{rd} pass with the 2^{nd} MAR image as input. The original sinogram can be either the acquired sinogram or a synthesized one re-projected from the original image. Using the synthesized sinogram results typically in only slightly worse results, but the processing is much faster since 2D processing can be used. For the images in this paper, the second method is used.

Even though the smoothed metal mask sinogram is used to generate the correction sinogram, we still observe occasionally some newly introduced streak artifacts. Furthermore, inaccuracies in the segmentation and classification can lead to some artificial dark or bright shading in the final image. These remaining problems can be addressed by the following idea of *adaptive application of the correction image*: The starting point for the idea is the fact that the correction image is supposed to show just the artifacts which are present in the initial image. In other words, the intention of the last processing step, namely the image subtraction, is to remove structured features from the initial image. This observation leads to the idea of performing the last step locally, if and only if, the amount of structure in the obtained image is reduced. One straight forward realization of this idea is to locally weight the correction image with a weighting factor. If this weighting factor is allowed to take values smaller or larger than one, the method can also correct locally an over- or under-estimation of the strength of the metal artifacts.

We formulate this method using the following definitions: The $N \times N$ initial image is denoted as I with individual pixels I_{ij}. The correction image and its pixels are denoted as C and C_{ij}, respectively. For a given index pair (k, l) we denote a sub-image of I containing the neighborhood of the image pixel I_{kl} as $\mathcal{N}_{kl}(I)$. We further assume to have a structure measure S that gives for any image a quantitative measure for the amount of structure in the image. Details about the neighborhood and the structure measure will be given later. Using these definitions we can formulate the calculation of a weighting image W by

$$W_{kl} = \arg\min_{w} S\left(\mathcal{N}_{kl}(I) - w\mathcal{N}_{kl}(C)\right) \tag{1}$$

and the final image metal artifact corrected image F is defined by

$$F_{kl} = I_{kl} - W_{kl}C_{kl}\,. \tag{2}$$

For the evaluation of this approach we need to pick a structure measure and a certain neighborhood. Several options are at hand for the structure measure like the variance of the image values or their total variation. Here, we use the entropy of the normalized histogram of the image as structural measure. The default bin size for the histogram is 10 HU. The neighborhood $\mathcal{N}_{kl}(I)$ of the pixel I_{kl} is by default a 11×11 patch centered around the pixel I_{kl}. In a few special cases, we observed that the shading artifacts in the correction image are so large and smooth that the default neighborhood of 11×11 is too small in order to be able to calculate appropriate weighting factors using Eq. (1) since the structure measure is insensitive to just changing all pixel values by the same correction value. In this case, the neighborhood can be adaptively enlarged in order to ensure that $\mathcal{N}_{kl}(C)$ has sufficient structure.

III. RESULTS

The proposed method was tested on a couple of clinical cases. Fig. 2 shows the performance of the new algorithm

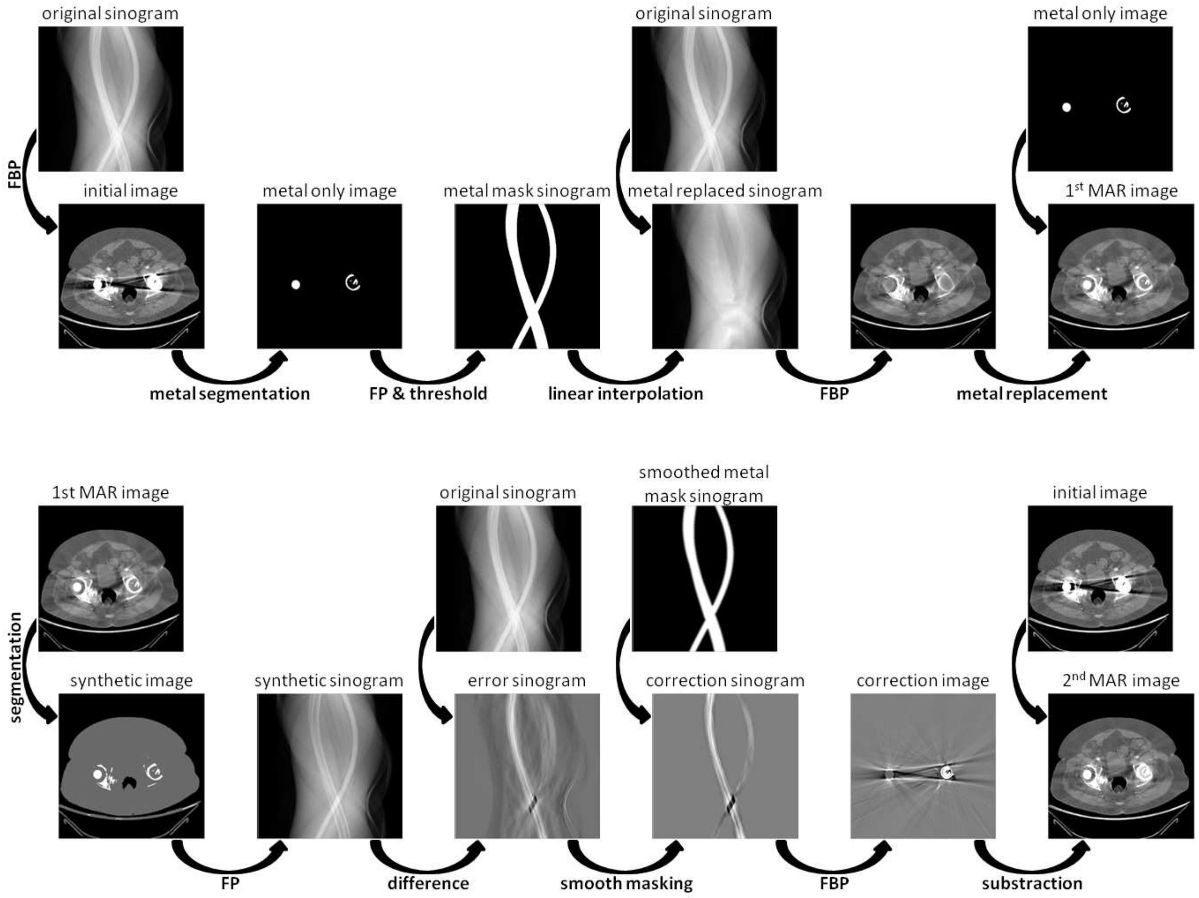
original sinogram
original sinogram
metal only image
FBP
initial image
metal only image
metal mask sinogram
metal replaced sinogram
1st MAR image
metal segmentation
FP & threshold
linear interpolation
FBP
metal replacement
1st MAR image
original sinogram
smoothed metal mask sinogram
initial image
segmentation
synthetic image
synthetic sinogram
error sinogram
correction sinogram
correction image
2nd MAR image
FP
difference
smooth masking
FBP
substraction

Fig. 1. Flow chart of the proposed MAR algorithm. The lower processing may be executed multiple times.

applied to a few example cases. For illustration purpose, we show in addition to the initial, uncorrected image and the final, fully corrected image also the result of the algorithm without the last step of adaptive application of the correction image, i. e. the images obtained using a weighting image W that is a constant unity image. Please note that we selected only examples, where the algorithm without adaptive application of the correction image does in fact introduce some new artifacts, which happens only in rare cases. However, we selected these examples to show the importance and effectiveness of the additional step of adaptive application of the correction image.

The top row of Fig. 2 shows a case with bilateral hip replacement. The dominant artifact in the initial image is the dark broad streak between the two hips. This dominant artifact is well reduced using the plain MAR algorithm. However, it also introduces a few minor streak artifacts (indicated by arrows). The use of the adaptive application of the correction image avoids the introduction of these artifacts while still removing the dominant ones.

The middle row of Fig. 2 shows a case with a ventricular assist device. The dominant artifacts in the initial image are streaks emanating from the electrode and the battery. Again, the plain MAR algorithm reduces the dominant artifacts substantially. However, it also introduces a lot of low frequency artifacts, in this case most likely because the contrast agent in the ventricle and the aorta is classified as soft-tissue. As in the first case, the adaptive application of the correction image avoids the introduction of these artifacts while still removing the dominant one.

The bottom row of Fig. 2 shows another slice of the same case as in the middle row. The dominant artifact in the initial image are two streaks connecting the metal objects. These streaks are reduced considerably by the plain MAR algorithm (although not completely, see arrow), but some shading artifacts are introduced (indicated by a circle in the middle column). Again, the adaptive application of the correction image preserves the suppression of the metal artifacts while at same time it does not introduce new artifacts.

IV. DISCUSSION

MAR has been a field of active research for more than 30 years now. This long history and the fact that it was only recently introduced commercially on a clinical scanner indicates that MAR is a very difficult problem. We presented in this work two new contributions to the art of MAR. The first one is a basic MAR algorithm that works well already in most cases. The second one is the idea of adaptive application of the correction image, which is specifically

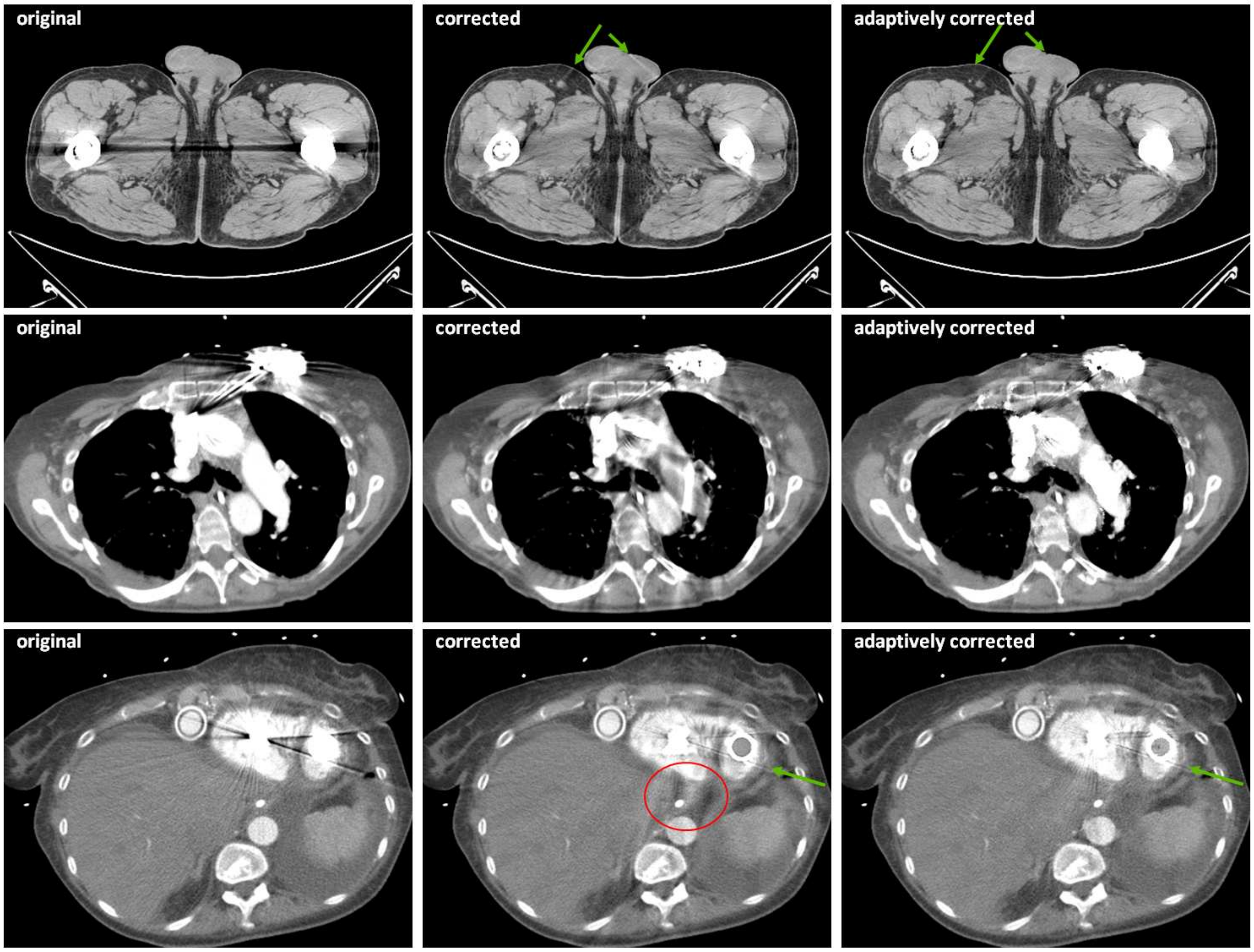

Fig. 2. Results of the proposed method. Left column: initial images with metal artifacts. Middle column: Result of the proposed method without adaptive application of the correction image. Right column: Result of the proposed method with adaptive application of the correction image. Level and window are 0 HU and 500 HU, respectively.

designed to avoid the introduction of new artifacts in the image after application of MAR. We would like to stress that the second idea can be applied to any MAR algorithm as long as this algorithm can be formulated as a subtraction of an correction image from an initial image, which is in most cases possible, at least in FBP based methods.

The idea of adaptive application of the correction image requires a choice for a structure measure and for a neighborhood. So far we obtained decent results using the entropy as a structure measure and a 11×11 neighborhood that can be further enlarged if the sub-image of the correction image does not contain sufficient structure. However, the optimization of this structure function is rather slow since a lot of evaluations of the logarithm are required. Thus, further investigations in this area comparing effectiveness and speed of different structure measures are desirable.

REFERENCES

[1] J. Hsieh, *Computed Tomography - Principles, Design, Artifacts, and Recent Advances*, SPIE, Bellingham, Washington, 2003.
[2] G. H. Glover and N. J. Pelc, *Med. Phys.*, vol. 8, no. 6, pp. 799–807, 1981.
[3] O. Watzke and W. A. Kalender, *European Radiology*, vol. 14, no. 5, pp. 849–856, 2004.
[4] B. De Man, J. Nuyts, P. Dupont, G. Marchal, and P. Suetens, *IEEE Trans. Med. Imag.*, vol. 20, no. 10, pp. 999–1008, 2001.
[5] R. M. Lewitt, *Med. Phys.*, vol. 6, no. 5, pp. 412–417, 1979.
[6] W. A. Kalender, R. Hebel, and J. Ebersberger, *Radiology*, vol. 164, pp. 576–577, 1987.
[7] A. H. Mahnken, R. Raupach, J. E. Wildberger, B. Jung, N. Heussen, T. G. Flohr, R. W. Günther, and S. Schaller, *Investigative Radiology*, vol. 38, no. 12, pp. 769–775, 2003.
[8] J. Wei, L. Chen, G. A. Sandison, Y. Liang, and L. X. Xu, *Phys. Med. Biol.*, vol. 49, no. 24, pp. 5407–5418, 2004.
[9] E. Meyer, R. Raupach, M. Lell, B. Schmidt, and M. Kachelriess, *Med. Phys.*, vol. 37, no. 10, pp. 5482–5493, 2010.
[10] H. K. Tuy, *European Radiology*, vol. 3, pp. 129–143, 1993.
[11] J. Timmer, "Metal artifact correction in computed tomography," 2003, US 7340027 B2.
[12] M. Bal and L. Spies, *Med. Phys.*, vol. 33, no. 8, pp. 2852–2859, 2006.
[13] D. Prell, Y. Kyriakou, M. Beister, and W. A. Kalender, *Phys. Med. Biol.*, vol. 54, no. 21, pp. 6575–6591, 2009.
[14] T. Buzug and M. Oehler, *Methods Inf. Med.*, vol. 46, no. 3, pp. 261–269, 2007.
[15] C. Lemmens, D. Faul, and J. Nuyts, *IEEE Trans. Med. Imag.*, vol. 28, no. 2, pp. 250–260, 2009.
[16] H. Xui, L. Zhang, Y. Xing, and Z. Chen, in *Proceedings of the Fully3D/HPIR*, 2011, pp. 199–202.
[17] H. Schmitt, J. Timmer, and T. Köhler, in *Medical Physics*, 2007, vol. 34(6), p. 2571.

Parallelizable algorithms for X-ray CT image reconstruction with spatially non-uniform updates

Donghwan Kim and Jeffrey A. Fessler

***Abstract*—Statistical image reconstruction methods for X-ray CT provide good images even for reduced dose levels but require substantial compute time. Iterative algorithms that converge in fewer iterations are preferable. Spatially non-homogeneous iterative coordinate descent (NH-ICD) accelerates convergence by updating more frequently the voxels that are predicted to change the most between the current image and the final image. However, the sequential update of NH-ICD reduces parallelism opportunities.**

This paper focuses on iterative algorithms that are more amenable to parallelization, namely the axial block coordinate descent (ABCD) algorithm and an ordered subsets algorithm based on separable quadratic surrogates (OS-SQS), because these have the potential to be faster than ICD in multiprocessor implementations. We first adapt the "non-homogeneous" approach to ABCD, which simply requires updating more frequently the axial blocks that are predicted to change the most during convergence. More interestingly, we derive a new version of the OS-SQS algorithm that leads to *spatially non-uniform updates* with larger step sizes for the voxels that are predicted to change the most between the current image and the final image. The single subset version of this algorithm is still guaranteed to converge monotonically.

We use a 3D patient CT scan to demonstrate that the proposed algorithms with spatially non-uniform updates converge faster than the ordinary algorithms. In particular, the NU approach accelerated the OS-SQS algorithm by a factor of three.

I. INTRODUCTION

Statistical image reconstruction for X-ray CT can provide good images even with reduced dose levels [1]. However, the substantial compute time required for the iterative algorithms is a drawback. This paper describes acceleration methods for parallelizable algorithms for penalized weighted least-squares (PWLS) image reconstruction.

Iterative coordinate descent (ICD) is a convergent method that can converge to a reconstructed image that is close to the minimizer of the PWLS cost function in a small number of iterations when initialized appropriately [1]. However, ICD updates each voxel sequentially so it is relatively difficult to parallelize. To accelerate ICD, one can try to predict which voxels will change the most between the current image and the final image, and then update those voxels more frequently. This non-homogeneous (NH) approach to ICD, called NH-ICD [2], can reduce the number of iterations needed but does not affect the parallelizability.

Considering the modern parallel computing architecture, we focus on two parallelizable algorithms: axial block coordinate descent (ABCD) [3] and an ordered subsets (OS) algorithm based on separable quadratic surrogates (SQS) called OS-SQS [4]. When appropriately parallelized, these algorithms should require less time per iteration, but need more iterations to converge than NH-ICD. (ABCD needed a similar number of iterations as ICD in one preliminary simulation [3], whereas OS-SQS needed far more iterations than ICD [5].) Inspired by the success of NH-ICD, in this paper, we develop similar acceleration methods for ABCD and OS-SQS. Applying the NH idea to ABCD is straightforward; we simply update more frequently the axial blocks that we predict will change the most during convergence. However, the original NH idea is not directly applicable to OS-SQS because it updates all voxels simultaneously. In this paper we derived a new version of the OS-SQS algorithm that leads to spatially non-uniform (NU) updates. Specifically, we design the surrogate functions so that the resulting iterations take larger step sizes for voxels that are predicted to change the most during convergence. Importantly, the theoretical derivation ensures that the new SQS algorithm (the one-subset version of the OS-SQS algorithm) is still guaranteed to converge monotonically. The derivation uses a modification of De Pierro's approach [6]. The resulting algorithm still updates all voxels simultaneously and thus is amenable to parallelization.

NH-ABCD and NU-OS-SQS are designed to work efficiently with the separable footprint (SF) projector [7]. The axial/transaxial separability of the SF projector facilitated the proposed algorithm to be highly efficient and parallelizable. We examined the performance of the proposed algorithms using a 3D patient CT scan. The results show that the proposed spatially non-uniform algorithms converge much faster than the ordinary algorithms. The proposed NU approach accelerated the OS-SQS algorithm by about a factor of three.

II. PROBLEM

We reconstruct an image $x \in \mathbb{R}^N$ from a noisy CT measurement data $y \in \mathbb{R}^M$ by finding the minimizer $\hat{x}$ of the following PWLS cost function [1]:

$$\begin{aligned}\Psi(x) = Q(x) + \beta R(x) &= \frac{1}{2}||y - Ax||_W^2 + \beta R(x) \\ &= \sum_{i=1}^M q_i([Ax]_i) + \beta \sum_{r=1}^K \psi_r([Cx]_r), \end{aligned} \tag{1}$$

where A is a system matrix (projector), C is a finite differencing matrix, $W = \mathsf{diag}\{w_i\}$ is a statistical weighting for measurement data, $q_i(t) = \frac{1}{2}w_i(t - y_i)^2$, each $\psi_r(t)$ is a (edge preserving) potential function, and β is a regularization parameter. Our goal is to find the minimizer $\hat{x}$ more efficiently.

Dept. of Electrical Engin. and Computer Science, Univ. of Michigan, Ann Arbor, MI 48109 USA (e-mail: kimdongh@umich.edu, fessler@umich.edu).
Supported in part by NIH grant 1-R01-HL-098686.

III. SPATIALLY NON-HOMOGENEOUS AXIAL BLOCK COORDINATE DESCENT (NH-ABCD)

A. Algorithm

ABCD sequentially updates each axial block of voxels [3]. The low coupling between voxels within an axial block simplifies the update [3]. Traditional ABCD updates the axial block sequentially, but the update order is flexible so we can easily adapt the NH idea of NH-ICD for the ABCD algorithm.

Let $x_k^{(n)}$ denote the vector of voxel values along the kth axial block at the nth iteration, and let $x_k^{(\infty)}$ denote the corresponding converged values, where k ranges from 1 to the number of voxels in one transaxial plane. One way to describe how much the voxels change between the nth iteration and the converged image is by this "*update-needed factor*" [2]:

$$\hat{u}_k^{(n)} = \left|\left|x_k^{(n)} - x_k^{(\infty)}\right|\right|_1.$$

Ideally NH-ICD would order the voxel updates based on $\hat{u}_k^{(n)}$, updating more frequently voxels within axial blocks having larger values of $\hat{u}_k^{(n)}$, accelerating convergence. However, $\hat{u}_k^{(n)}$ is unavailable at the nth iteration in practice, so NH-ICD uses the following factor instead:

$$u_k^{(n)} = \left|\left|x_k^{(n)} - x_k^{(n-1)}\right|\right|_1, \tag{2}$$

which is the difference between the current and previous kth axial block. (In addition $u_k^{(n)}$ is low-pass filtered to try to improve $u_k^{(n)}$.) In practice, the NH-ICD approach uses both homogeneous update orders and non-homogeneous update orders based on $u_k^{(n)}$ for fast convergence overall.

We adapted these NH ideas to the ABCD algorithm, yielding NH-ABCD, by non-uniformly updating axial blocks. We implemented a SQS version of NH-ABCD (NH-ABCD-SQS) that we expected to converge faster than ABCD-SQS.

IV. SPATIALLY NON-UNIFORM SEPARABLE QUADRATIC SURROGATE (NU-SQS) APPROACH

A. SQS Algorithm

SQS for PWLS has the benefit of low computation per iteration and high parallelizability [4]. However, it needs many iterations to converge. This section presents a new SQS algorithm that uses spatially non-uniform updates to accelerate convergence without reducing parallelizability.

In a simultaneous update algorithm like SQS, the idea of updating certain voxels more frequently is unnatural. Instead, we re-derive the algorithm to increase the *step size* of voxels that are predicted to need to change more during convergence. Simply weighting the step size arbitrarily would break the monotonicity of optimization, so instead we derive an appropriate weighting scheme that preserves the monotonicity (in the one subset version) by adapting De Pierro's approach [6].

For completeness, we repeat De Pierro's argument in [4]. We first rewrite forward projection $[Ax]_i$ as follows:

$$[Ax]_i = \sum_{j=1}^{N} a_{ij}x_j = \sum_{j=1}^{N} \pi_{ij}^{(n)} \left(\frac{a_{ij}}{\pi_{ij}^{(n)}}(x_j - x_j^{(n)}) + [Ax^{(n)}]_i \right),$$

where $\sum_{j=1}^{N} \pi_{ij}^{(n)} = 1$ and $\pi_{ij}^{(n)}$ is zero only if a_{ij} is zero. Using the convexity of $q_i(\cdot)$ and the convexity inequality:

$$q_i([Ax]_i) \leq \sum_{j=1}^{N} \pi_{ij}^{(n)}\, q_i\left(\frac{a_{ij}}{\pi_{ij}^{(n)}}(x_j - x_j^{(n)}) + [Ax^{(n)}]_i \right).$$

Thus we have the following separable quadratic surrogate $\phi_Q^{(n)}(x)$ for the data-fit term $Q(x)$:

$$\begin{aligned} Q(x) \leq \phi_Q^{(n)}(x) &\triangleq \sum_{j=1}^{N} \phi_{Q,j}^{(n)}(x_j) \\ &= \sum_{i=1}^{M}\sum_{j=1}^{N} \pi_{ij}^{(n)}\, q_i\left(\frac{a_{ij}}{\pi_{ij}^{(n)}}(x_j - x_j^{(n)}) + [Ax^{(n)}]_i \right). \end{aligned} \tag{3}$$

The second derivative of the surrogate $\phi_{Q,j}^{(n)}(x_j)$ is

$$d_j^{Q,(n)} \triangleq \frac{\partial^2}{\partial x_j^2}\phi_{Q,j}^{(n)}(x_j) = \sum_{i=1}^{M} w_i a_{ij}^2/\pi_{ij}^{(n)}.$$

Then the step size $\Delta_j^{(n)}$ of SQS [4] has this relationship:

$$\Delta_j^{(n)} \triangleq x_j^{(n+1)} - x_j^{(n)} \propto \frac{1}{d_j^{Q,(n)}} \propto \pi_{ij}^{(n)}, \tag{4}$$

where small $d_j^{Q,(n)}$ and large $\pi_{ij}^{(n)}$ values lead to larger steps. Therefore we should encourage $\pi_{ij}^{(n)}$ to be large to accelerate the SQS algorithm, subject to the condition $\sum_{j=1}^{N} \pi_{ij}^{(n)} = 1$.

The standard choice [4], [8] is $\pi_{ij}^{(n)} = \frac{a_{ij}}{\sum_{l=1}^{N} a_{il}}$, leading to

$$d_j^{Q,(n)} = \sum_{i=1}^{M} w_i a_{ij} \left(\sum_{l=1}^{N} a_{il} \right). \tag{5}$$

This choice does not exploit the relationship (4). Thus, we propose to choose $\pi_{ij}^{(n)}$ to be larger if the jth voxel is predicted to need more update based on the following "update-needed factor" after the nth iteration:

$$u_j^{(n)} = \left|x_j^{(n)} - x_j^{(n-1)}\right|. \tag{6}$$

We select $\pi_{ij}^{(n)} = \frac{a_{ij}u_j^{(n)}}{\sum_{l=1}^{N} a_{il}u_l^{(n)}}$ which is proportional to $u_j^{(n)}$ and satisfies the conditions for $\pi_{ij}^{(n)}$. This choice for $\pi_{ij}^{(n)}$ leads to the following NU-based denominator:

$$\tilde{d}_j^{Q,(n)} = \frac{1}{u_j^{(n)}} \sum_{i=1}^{M} w_i a_{ij} \left(\sum_{l=1}^{N} a_{il}u_l^{(n)} \right), \tag{7}$$

which leads to spatially non-uniform updates $\Delta_j^{(n)} \propto u_j^{(n)}$. Computing (7) requires one forward and back projection which increases computation, but Sec. IV-B explains how to minimize this effect. The NU-based denominator (7) reduces to the standard denominator (5) when $u_j^{(n)}$ is uniform.

Recall that NH-ICD balanced between the uniform and non-uniform voxel ordering to provide fast convergence. Likewise, using values for $u_j^{(n)}$ with too large of dynamic range that would focus most of the updates on a few voxels would likely be undesirable. Therefore we modified the "update needed

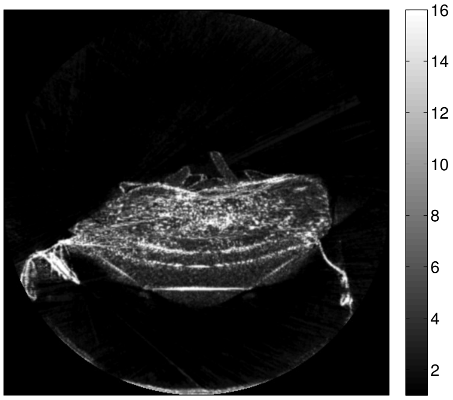

Fig. 1. Dynamic range compression (DRC) applied $u_j^{(4)}$ for NU-OS-SQS. In each case we map $u_j^{(n)}$ to 16 for the largest 5% voxels, to [8 4 2] for next [10% 20% 40%] voxels, and to 1 for the rest of the voxels, followed by low-pass filtering. NU-OS-SQS updates more the bright voxels, whereas ordinary OS-SQS updates all voxels equivalently.

factors" $u_j^{(n)}$ to have a reasonable dynamic range (see Fig. 1), which we call dynamic range compression (DRC).

Similar to the data-fit term, we derive the denominator of NU-SQS for the regularizer term to be:

$$\tilde{d}_j^{R,(n)} = \frac{1}{u_j^{(n)}} \sum_{r=1}^{K} \ddot{\psi}_r(0)|c_{rj}| \left(\sum_{l=1}^{N} |c_{rl}| u_l^{(n)} \right), \tag{8}$$

by using the choice $\pi_{rj}^{(n)} = \frac{|c_{rj}| u_j^{(n)}}{\sum_{l=1}^{N} |c_{rl}| u_l^{(n)}}$ and using the maximum curvature $\ddot{\psi}_r(0) = \max_t \ddot{\psi}_r(t)$ for efficiency [4]. The computation of (8) is negligible compared to that of data-fit term.

Combining the above derivations leads to the following simple and parallelizable NU-SQS iteration:

$$x^{(n+1)} = x^{(n)} - \mathsf{diag}\left\{ \frac{1}{\tilde{d}_j^{Q,(n)} + \beta \tilde{d}_j^{R,(n)}} \right\} \nabla \Psi(x^{(n)}).$$

This algorithm monotonically decreases $\Psi(x)$ and is provably convergent [9]. We can further accelerate NU-SQS by using ordered subsets (OS) of projection views [4], [10] which we call NU-OS-SQS.

B. Implementation

The dependence of $\pi_{ij}^{(n)}$ on $u_j^{(n)}$ increases computation, but we found two practical way to reduce the burden. First, we found that it suffices to update $u_j^{(n)}$ every few iterations instead of every iteration. Second, in 3D CT we use forward and back-projectors that compute elements of the system matrix A on the fly, and as those elements are computed for gradient of $Q(x)$, which requires one forward and back projection, we simultaneously compute the forward and back-projection needed for the NU-based denominator (7). For the results shown below, we computed $u_j^{(n)}$ during one iteration and computed the NU-based denominator (7) during the next iteration, and then used it for several iterations. For the first iteration we form $u_j^{(0)}$ using a combination of edge and intensity detector. This is reasonable as the initial FBP is a good low-frequency estimate, so $\hat{u}_j^{(0)}$ will be bigger for voxels near edges.

C. Application of NU-SQS in ABCD algorithm

We also tried to further accelerate the ABCD algorithm by applying the NU-SQS principle to ABCD using the following NU-based denominator:

$$\tilde{d}_j^{Q,(n)} = \frac{1}{u_j^{(n)}} \sum_{i=1}^{M} w_i a_{ij} \left(\sum_{l \in \mathcal{B}_k} a_{il} u_l^{(n)} \right), \quad j \in \mathcal{B}_k, \tag{9}$$

where $\mathcal{B}_k$ denotes the indices of the voxels in the kth axial block. For a typical multi-slice CT geometry, the set $\{l : a_{il} > 0,\ l \in \mathcal{B}_k\}$ contains at most three (adjacent) voxels with similar $u_l^{(n)}$ values, and the resulting acceleration was minimal. However, block coordinate descent (BCD) algorithms [11] that group voxels in transaxial plane could exploit non-uniformity.

V. RESULT

We implemented the proposed algorithms in C and applied them to a helical patient CT scan. We examined spatially nonuniform approaches for ABCD and OS-SQS algorithms in terms of convergence rate and compute time per iteration. Our implementations are not optimized in terms of run time, so we show the results of each method separately. Fig. 2 and Fig. 4 show the root mean squared (RMS) difference (in HU) from the converged image[1] versus normalized run time for NH-ABCD and NU-OS-SQS. The run time of the algorithms are normalized in time by one iteration of ABCD-SQS and OS-SQS respectively, and the plot markers show each iteration. Image reconstruction included the nonnegativity constraint.

In Fig. 2, NH-ABCD converged 3× faster than ABCD, similar to the acceleration of NH-ICD in [2]. Using the NH idea in the ABCD algorithm increased compute time per iteration by only 3%.

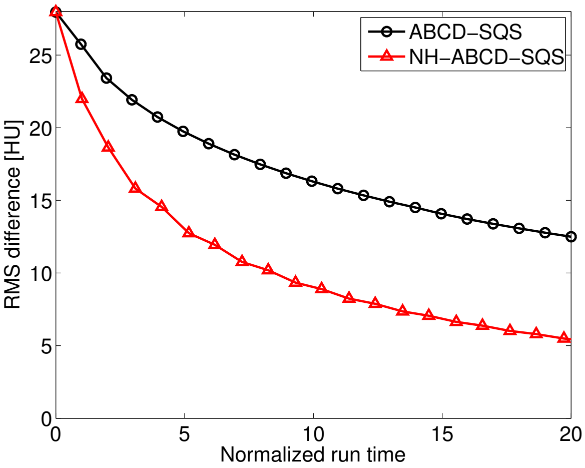

Fig. 2. RMS difference [HU] from converged image vs. normalized compute time for previous ABCD-SQS [3] and proposed NH-ABCD-SQS. Compute time is normalized by the elapsed time for one iteration of ABCD-SQS.

---

[1] We generated an (almost) converged image by running 100 iterations of NH-ABCD-SQS followed by 2000 iterations of SQS.

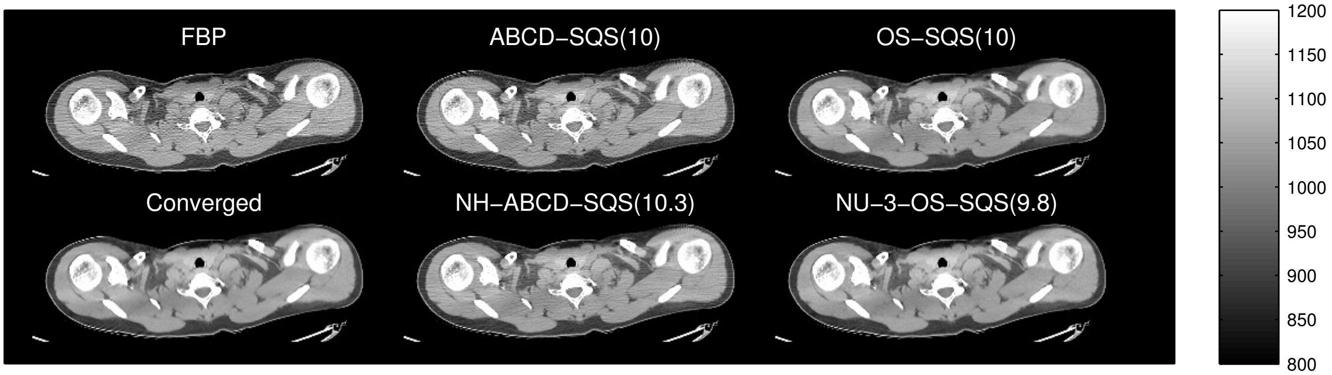

Fig. 3. FBP image $x^{(0)}$, converged image $\hat{x}$, and reconstructed images by ABCD and OS-SQS algorithms. Numbers in parentheses represent normalized compute time; ABCD and OS-SQS have different normalized compute time. The proposed NH and NU methods each accelerate convergence to $\hat{x}$.

In Fig. 4, the NU approach accelerated the OS algorithm by a factor of three. Incorporating the computation of the NU-based denominator (7) simultaneously with the gradient increased run time by 25%, but this increase was amortized by updating the NU-based denominator only every few iterations. Fig. 4 suggests that every 3-5 iterations is enough.

Compressing the dynamic range of $u_j^{(n)}$, as shown in Fig. 1, was essential to accelerate convergence compared with solely using (6). The DRC approach in Fig. 1 is just one of many possibilities, and we expect to find other candidates that will lead to even faster convergence.

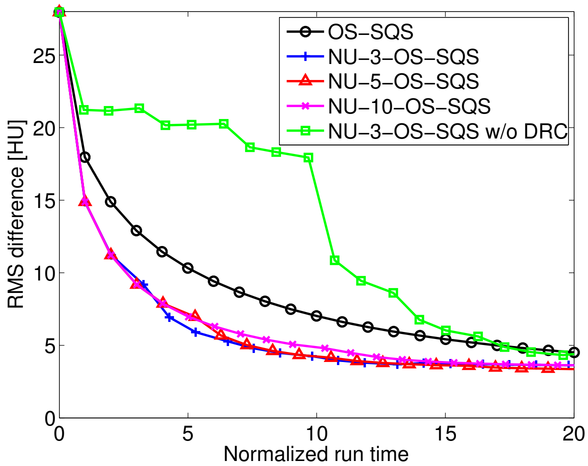

Fig. 4. RMS difference [HU] to converged image vs. normalized compute time for NU-OS-SQS with 246 subsets. Compute time is normalized by the elapsed time of one iteration of OS-SQS. Number in the legend indicates how often we update the NU-based denominator.

Fig. 3 shows the center slice of FBP, the converged image $\hat{x}$, and reconstructed images by ABCD and OS-SQS methods. The quality of $\hat{x}$ compared to FBP reaffirms the benefits of statistical image reconstruction. The reconstructed images with the proposed spatially non-uniform approaches are closer to the converged image $\hat{x}$ than the ordinary ABCD and OS-SQS reconstructed images.

VI. DISCUSSION

We have used spatially non-uniform updates to accelerate parallelizable iterative algorithms ABCD and OS-SQS. In particular, we derived a new spatial non-uniformity approach for SQS, a simultaneous update algorithm, which improved the convergence rate by about a factor of three. The next step is to optimize the implementation in terms of compute time and parallelization, and compare the proposed algorithms with other algorithms such as NH-ICD.

REFERENCES

[1] J-B. Thibault, K. Sauer, C. Bouman, and J. Hsieh, “A three-dimensional statistical approach to improved image quality for multi-slice helical CT,” *Med. Phys.*, vol. 34, no. 11, pp. 4526–44, Nov. 2007.

[2] Z. Yu, J-B. Thibault, C. A. Bouman, K. D. Sauer, and J. Hsieh, “Fast model-based X-ray CT reconstruction using spatially non-homogeneous ICD optimization,” *IEEE Trans. Im. Proc.*, vol. 20, no. 1, pp. 161–75, Jan. 2011.

[3] J. A. Fessler and D. Kim, “Axial block coordinate descent (ABCD) algorithm for X-ray CT image reconstruction,” in *Proc. Intl. Mtg. on Fully 3D Image Recon. in Rad. and Nuc. Med*, 2011, pp. 262–5.

[4] H. Erdoğan and J. A. Fessler, “Ordered subsets algorithms for transmission tomography,” *Phys. Med. Biol.*, vol. 44, no. 11, pp. 2835–51, Nov. 1999.

[5] B. De Man, S. Basu, J-B. Thibault, J. Hsieh, J. A. Fessler, C. Bouman, and K. Sauer, “A study of different minimization approaches for iterative reconstruction in X-ray CT,” in *Proc. IEEE Nuc. Sci. Symp. Med. Im. Conf.*, 2005, vol. 5, pp. 2708–10.

[6] A. R. De Pierro, “A modified expectation maximization algorithm for penalized likelihood estimation in emission tomography,” *IEEE Trans. Med. Imag.*, vol. 14, no. 1, pp. 132–7, Mar. 1995.

[7] Y. Long, J. A. Fessler, and J. M. Balter, “3D forward and back-projection for X-ray CT using separable footprints,” *IEEE Trans. Med. Imag.*, vol. 29, no. 11, pp. 1839–50, Nov. 2010.

[8] H. Erdoğan and J. A. Fessler, “Monotonic algorithms for transmission tomography,” *IEEE Trans. Med. Imag.*, vol. 18, no. 9, pp. 801–14, Sept. 1999.

[9] M. W. Jacobson and J. A. Fessler, “An expanded theoretical treatment of iteration-dependent majorize-minimize algorithms,” *IEEE Trans. Im. Proc.*, vol. 16, no. 10, pp. 2411–22, Oct. 2007.

[10] H. M. Hudson and R. S. Larkin, “Accelerated image reconstruction using ordered subsets of projection data,” *IEEE Trans. Med. Imag.*, vol. 13, no. 4, pp. 601–9, Dec. 1994.

[11] J. A. Fessler, E. P. Ficaro, N. H. Clinthorne, and K. Lange, “Grouped-coordinate ascent algorithms for penalized-likelihood transmission image reconstruction,” *IEEE Trans. Med. Imag.*, vol. 16, no. 2, pp. 166–75, Apr. 1997.

Combined shearlet and TV regularization in sparse-view CT reconstruction

Bert Vandeghinste, Bart Goossens, Roel Van Holen, Christian Vanhove, Aleksandra Pižurica,
Stefaan Vandenberghe and Steven Staelens

***Abstract*—Preclinical in vivo micro computerized tomography suffers from high image noise, due to limitations on total scanning time and the small pixel sizes. A lot of different noise minimization algorithms have already been proposed to reconstruct images acquired in low dose settings. Sparse-view reconstruction amongst others can reduce acquisition dose significantly, by acquiring only a small subset of projection views. These low-view datasets can then be reconstructed by using Total Variation minimization. However, the performance of TV is suboptimal for complex images, compared to simple images with little texture. This is mainly due to the underlying piecewise constant image model imposed by TV.**

A recent efficient solver was developed for convex problems, able to incorporate regularization terms different from TV. The work presented here is a proof-of-concept study combining both isotropic TV as well as shearlets as regularization terms into one general CT reconstruction algorithm. Shearlets, closely related to wavelets, take edges into account in a multitude of directions at different scales, and have good compaction properties. This makes shearlets a better candidate than TV for compressed sensing problems. The resulting reconstructions were compared to TV minimization and to shearlet minimization. The combination of both shows benefits for sparse-view CT imaging, and leads to edge-preserved image denoising. Difference images show a very small loss in resolution, which may be caused by difficult parameter selection.

***Index Terms*—Computed Tomography, Iterative Algorithms, Noise, Reconstruction Algorithms**

I. INTRODUCTION

PRECLINICAL in vivo micro computerized tomography (μCT) suffers from high image noise, as a result of the small detector pixel sizes, a high scatter-to-primary noise ratio [1], and the limited time animals can be safely kept under anesthetics. This results in limited soft tissue contrast. Reducing the dose without sacrificing image quality could offer significant benefits for longitudinal preclinical research, where the small animals receive a large dose within a timeframe of several days to weeks.

Total variation (TV) minimization has been extensively investigated in the last decade for image denoising in general and sparse-view reconstruction in particular [2]–[5]. These methods have been shown to have superior denoising performance in simple classes of images. However, TV minimization produces cartoon-like approximations due to its underlying image model. This model biases the results towards distorted images, which may be less suitable for medical images used in diagnostics [3].

In the search for objective functions different from TV, a recent efficient solver was developed, based on a split-Bregman approach. With this solver, other regularization terms can easily be tested. One possibility is the shearlet [6], [7], closely related to wavelets, which has better directional sensitivity, better ℓ_1-norm sparsity and, because of a different underlying image model, does not lead to the staircasing effect. We have previously shown that shearlet-regularized reconstructed images show no staircasing and exhibit small aliasing artifacts. However, these reconstructions did not outperform TV-based regularization for all datasets [8], as the anisotropic nature of shearlets tends to not work optimally for isotropic image features. In the research presented here, we investigate if combining isotropic TV and shearlets can combine their benefits and reduce the small artifacts induced by both methods in CT reconstruction. This combination has already been shown effective in Magnetic Resonance Imaging reconstruction [9]–[11].

The remainder of this paper is organized as follows. In Sec. II, we introduce the problem formulation and quickly reiterate the mathematical background for using the split-Bregman approach in CT. Section III describes the set-up for the evaluation on simulated and measured preclinical in vivo μCT data. In Sec. IV we compare the combination of shearlets and TV to conventional algebraic reconstruction and to reconstruction with only one of these terms, for sparse-view data. These results are then discussed in Sec. V, where suggestions are also made for further research. Our conclusions are in Sec. VI.

II. PRELIMINARIES

Previously, we have developed the split-Bregman framework for regularized CT reconstruction [8], [12], [13]. We denote an ℓ_1-norm by $|.|_1$ and an ℓ_2-norm by $\|.\|_2$. The following minimization problem is solved:

$$\hat{\mathbf{x}} = \arg\min_{\mathbf{x}} E(\mathbf{x}) + \lambda \left\| \mathbf{C}^{-1/2} \left(\mathbf{y} - \mathbf{W}\mathbf{x} \right) \right\|_2^2, \qquad (1)$$

This work was supported in part by a PhD grant to Bert Vandeghinste of the Institute for the Promotion of Innovation through Science and Technology in Flanders (IWT-Vlaanderen). B. Goossens and R. Van Holen are postdoctoral research fellows with FWO, Flanders. C. Vanhove is supported by the GROUP-ID consortium. *Asterisk indicates corresponding author.*

*B. Vandeghinste, R. Van Holen, C. Vanhove, S. Vandenberghe and S. Staelens are with the Medical Image and Signal Processing (MEDISIP) research group, Ghent University–IBBT, 9000 Gent, Belgium. (e-mail: bert.vandeghinste@ugent.be).

B. Goossens and A. Pižurica are with the Image Processing and Interpretation (IPI) research group, Ghent University–IBBT, Sint-Pietersnieuwstraat 41, 9000 Gent, Belgium.

S. Staelens is also with the Molecular Imaging Centre Antwerp, University of Antwerp, 2650 Edegem, Belgium.

with $\mathbf{x}$ the unknown reconstructed image, $E(\mathbf{x})$ the penalty term, λ a constant which determines the contribution of the regularization to the total cost, $\mathbf{C}$ a prewhitener to decorrelate the noise, $\mathbf{y}$ the measured data and $\mathbf{W}$ the system matrix.

The penalty term $E(\mathbf{x})$ can include different regularizers. Previously, the ℓ_1-norm of the discrete gradient operator has already been used in anisotropic fasion [13], as well as a case where shearlets were used [8]. In this study, we will use a penalty term combining the isotropic TV with shearlets:

$$E(\mathbf{x}) = \gamma_{TV} \sqrt{(\nabla_x \mathbf{x})^2 + (\nabla_y \mathbf{x})^2} + \gamma_{SH} \left| \mathbf{S}\mathbf{x} \right|_1 , \quad (2)$$

with ∇ the discrete gradient operator, $\mathbf{S}$ the shearlet transform and constants γ_{TV} and γ_{SH} weighting the influence of the two components. This cost function can be minimized by using Bregman iterations and variable splitting [12], effectively splitting the ℓ_1- and ℓ_2-norm into subproblems which are easier to solve [13]. This results in Algorithm 1.

III. MATERIALS AND METHODS

A. Simulated data

Fan-beam data was simulated using MC-GPU v1.2 [14][1], a GPU-accelerated x-ray transport simulator. A high resolution phantom was built based on the work of the FORBILD group[2] (Fig. 1a). The resolution rods were simulated as containing air, surrounded by soft tissue. One 3.6864 cm × 3.6864 cm × 0.1395 cm thick slice was generated, containing 8192×8192 voxels, to get sufficient subsampling in the holes with smallest diameter. The detector was simulated as a perfect detector with 100% efficiency, and consists of 296 elements with a pixel pitch of 0.14 mm, acquiring 360 uniformly spaced projection views over 2π. All data was generated using a 60 keV monoenergetic x-ray source with 10^8 photons per ray. The sinogram includes scattered photons.

B. Measured data

The X-O CT system (Gamma Medica Ideas, Northridge, California, USA) was used to obtain preclinical data of one in vivo contrast-enhanced mouse study. This flat-panel cone-beam system consists of a 1280×1120 detector with a 100 μm pixel pitch. The tube current is determined automatically during calibration to ensure that the dynamic range of the detector is optimally used. Fan-beam data were generated by retaining only the central detector row. 2048 projection views were obtained over 2π. A new dataset was generated from this projection data, by removing all but every 16th projection (128 views).

C. Data reconstruction and analysis

All datasets were reconstructed using 4 methods: SIRT, split-Bregman using isotropic TV (SpBR-TV), split-Bregman using shearlets (SpBR-SH) and split-Bregman using both shearlets and isotropic TV (SpBR-SHTV). In SpBR, $\mathbf{x}^{(i+1)}$ was minimized using 30 iterations of conjugate gradient on the normal equations. Matrix $\mathbf{W}$ was implemented as the 2D Distance Driven projector [15]. The shearlet transform $\mathbf{S}$ was implemented as previously proposed by Goossens et al. [16], based on the Meyer wavelet. Soft-shrinkage [12] was used to implement the minimization to find $\mathbf{d}^{(i+1)}$. The Bregman update step used to find $\mathbf{b}^{(i+1)}$ is trivial to solve. All regularized reconstructions converged and were stopped at iteration 20. All SIRT reconstructions were stopped when $\left\| \mathbf{x}^{(i+1)} - \mathbf{x}^{(i)} \right\|_2^2 / \left\| \mathbf{x}^{(i+1)} \right\|_2^2 < 10^{-4}$.

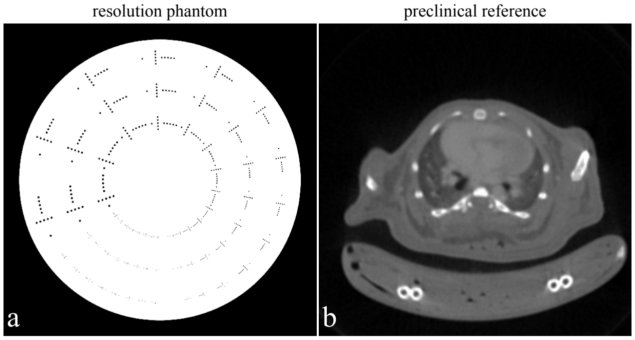

Fig. 1. Reference images for the simulated data (resolution phantom converted to 60 keV attenuation values) and the preclinical data (converged SIRT reconstruction of 2048 projection views).

The simulated data was reconstructed to a 256^2-grid with voxel pitch 0.16 mm, the preclinical data was reconstructed to a 256^2-grid with 0.13 mm voxel pitch. The diagonal elements of $\mathbf{C}$ were set to $c_{ii} = e^{-y_i}$ [17] with y_i the measured counts, serving as an estimator for the mean number of counts.

For each regularized reconstruction, parameter λ was empirically chosen, by reconstructing with different λ values and gradually making the search interval smaller, fine tuning the amount of denoising. This generally results in 5 to 10 reconstructions needed to determine a good λ value for the case of only one regularizer. When SH and TV were combined, γ_{SH} and γ_{TV} also had to be empirically determined. The parameter μ was always set to 0.025λ, which was empirically determined.

The peak signal-to-noise ratio (PSNR) was determined to objectively evaluate the preclinical images. The SIRT reconstruction of 2048 projection views was used as the reference many-view image (Fig. 1b).

IV. RESULTS

Figure 2 shows the resolution phantom reconstructed with the different methods, zoomed in to the low resolution part of the resolution phantom. For SpBR-TV, noise patches become apparent in the image with little denoising ($\lambda = 4000$), compared to more denoising ($\lambda = 1600$). However, a slight increase in resolution can be noted when only a small amount of denoising is applied. Furthermore, the rods are shaped irregularly and are not perfectly round.

In the SH reconstruction, denoising with a low λ factor does not eliminate all noisy patches in between of the rods. The resolution increases when less denoising is used, also increasing the noise in the background. However, when SH

---

[1] Freely available from http://code.google.com/p/mcgpu/

[2] http://www.imp.uni-erlangen.de/phantoms/highcontrast/highcontrast.html

Algorithm 1 The proposed split-Bregman reconstruction algorithm, solving Eq. (1).

```
initialize $\mathbf{d}^{(0)} = \mathbf{0},\ \mathbf{b}^{(0)} = \mathbf{0},\ i = 0$
repeat
$\mathbf{x}^{(i+1)} = \arg\min_{\mathbf{x}} \frac{\lambda}{2} \left\|\mathbf{C}^{-1/2}(\mathbf{y} - \mathbf{W}\mathbf{x})\right\|_2^2 + \frac{\mu}{2} \left\|\mathbf{d}^{(i)}_{TV,x} - \nabla_x(\mathbf{x}) - \mathbf{b}^{(i)}_{TV,x}\right\|_2^2 + \frac{\mu}{2} \left\|\mathbf{d}^{(i)}_{TV,y} - \nabla_y(\mathbf{x}) - \mathbf{b}^{(i)}_{TV,y}\right\|_2^2$
        $+ \frac{\mu}{2} \left\|\mathbf{d}^{(i)}_{SH} - \mathbf{S}\mathbf{x} - \mathbf{b}^{(i)}_{SH}\right\|_2^2$
$\mathbf{s} = \sqrt{\left|\nabla_x \mathbf{x}^{(i+1)} + \mathbf{b}^{(i)}_{TV,x}\right|^2 + \left|\nabla_y \mathbf{x}^{(i+1)} + \mathbf{b}^{(i)}_{TV,y}\right|^2}$
$\mathbf{d}^{(i+1)}_{TV,x} = \max\left(\mathbf{s} - \frac{1}{\mu}, 0\right) \frac{\nabla_x \mathbf{x}^{(i+1)} + \mathbf{b}^{(i)}_{TV,x}}{\mathbf{s}}, \quad \mathbf{d}^{(i+1)}_{TV,y} = \max\left(\mathbf{s} - \frac{1}{\mu}, 0\right) \frac{\nabla_y \mathbf{x}^{(i+1)} + \mathbf{b}^{(i)}_{TV,y}}{\mathbf{s}}$
$\mathbf{d}^{(i+1)}_{SH} = \arg\min_{\mathbf{d}} |\mathbf{d}|_1 + \frac{\mu}{2} \left\|\mathbf{d} - \mathbf{S}\mathbf{x}^{(i+1)} - \mathbf{b}^{(i)}_{SH}\right\|_2^2$
$\mathbf{b}^{(i+1)}_{TV,x} = \mathbf{b}^{(i)}_{TV,x} + \left(\nabla_x \mathbf{x}^{(i+1)} - \mathbf{d}^{(i+1)}_{TV,x}\right), \quad \mathbf{b}^{(i+1)}_{TV,y} = \mathbf{b}^{(i)}_{TV,y} + \left(\nabla_y \mathbf{x}^{(i+1)} - \mathbf{d}^{(i+1)}_{TV,y}\right)$
$\mathbf{b}^{(i+1)}_{SH} = \mathbf{b}^{(i)}_{SH} + \left(\mathbf{S}\mathbf{x}^{(i+1)} - \mathbf{d}^{(i+1)}_{SH}\right)$
$i \leftarrow i + 1$
until $i = \text{iterations} + 1$
```

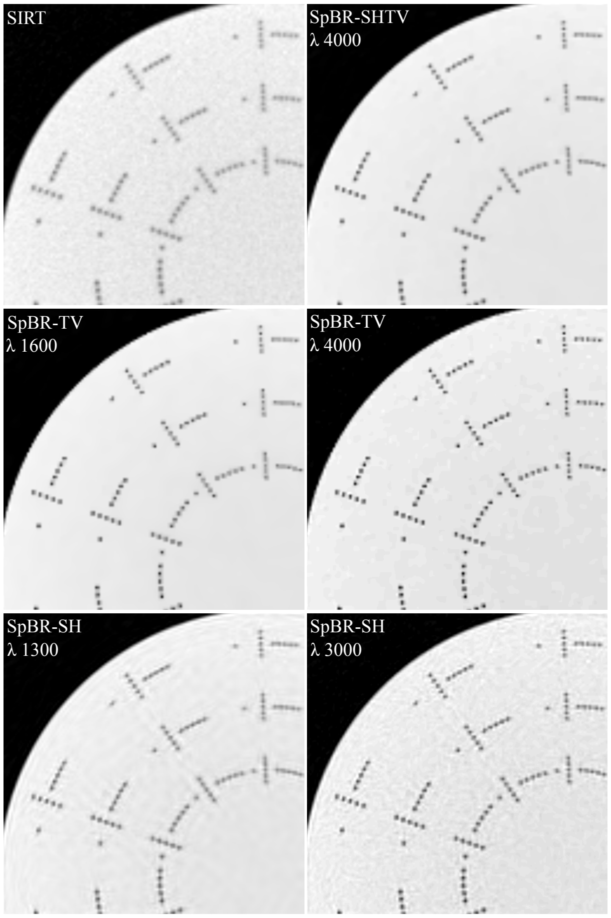

Fig. 2. Comparison of SIRT of noisy data, combined SH and TV ($\gamma_{SH} = 1.0$, $\gamma_{TV} = 0.45$), TV with low and high λ, SH with low and high λ. All images were normalized to the same window.

and TV are combined ($\gamma_{SH} = 1.0$ and $\gamma_{TV} = 0.45$), round rods are obtained, whilst still perfectly minimizing the noise in the background.

Figure 3 compares SpBR-TV, SpBR-SH and SpBR-SHTV to the reference high-dose SIRT reconstruction in the case of measured preclinical data. Parameter λ was set to 2000 for SpBR-SHTV, with $\gamma_{SH} = 0.25$ and $\gamma_{TV} = 1.0$. Plotted on the right are the absolute difference images between the reconstruction and the reference image. SIRT shows streaking artifacts when only 128 views are used. All regularized reconstructions lead to higher PSNR compared to SIRT.

The difference image for SpBR-TV shows some resolution loss at the edges of the animal bed and at the body contour, primarily at edges which are not mainly horizontally or vertically oriented. For SH, these edges are not visible. However, there are some streaking artifacts left, which could not be minimized with a different λ choice without sacrificing resolution. When SH and TV are combined, good denoising properties are obtained with a small amount of resolution loss. This is primarily visible at the sternum, where the spongious bone is more difficult to distinguish on SpBR-SHTV reconstructions than on SIRT or with TV alone.

V. DISCUSSION

Combining TV and SH regularization into one algorithm shows benefits for sparse-view CT imaging. Previous research has shown that shearlets do not lead to any form of piecewise-constant behavior, but on the other hand do not tend to approximate uniform regions as well as TV [8]. The preliminary results presented here show that a combination of both regularization terms combines the benefits of both SH as well as TV.

One tricky and very sensitive area is parameter selection in iterative algorithms. Next to determining λ empirically, there is now also the difficulty of weighing the contribution of SH against the contribution of TV with γ_{SH} and γ_{TV}. Special care has to be taken to not let TV overpower SH, as this will result in piecewise constant behavior. In theory, we would like to use shearlets to minimize the cost function in general, and use a little bit of TV to minimize the introduced artifacts, such as Gibbs phenomena next to jump discontinuities, or remaining streaking artifacts. We have shown that this works sufficiently in the case of preclinical data, although with a small loss of resolution. This may be due to parameter selection.

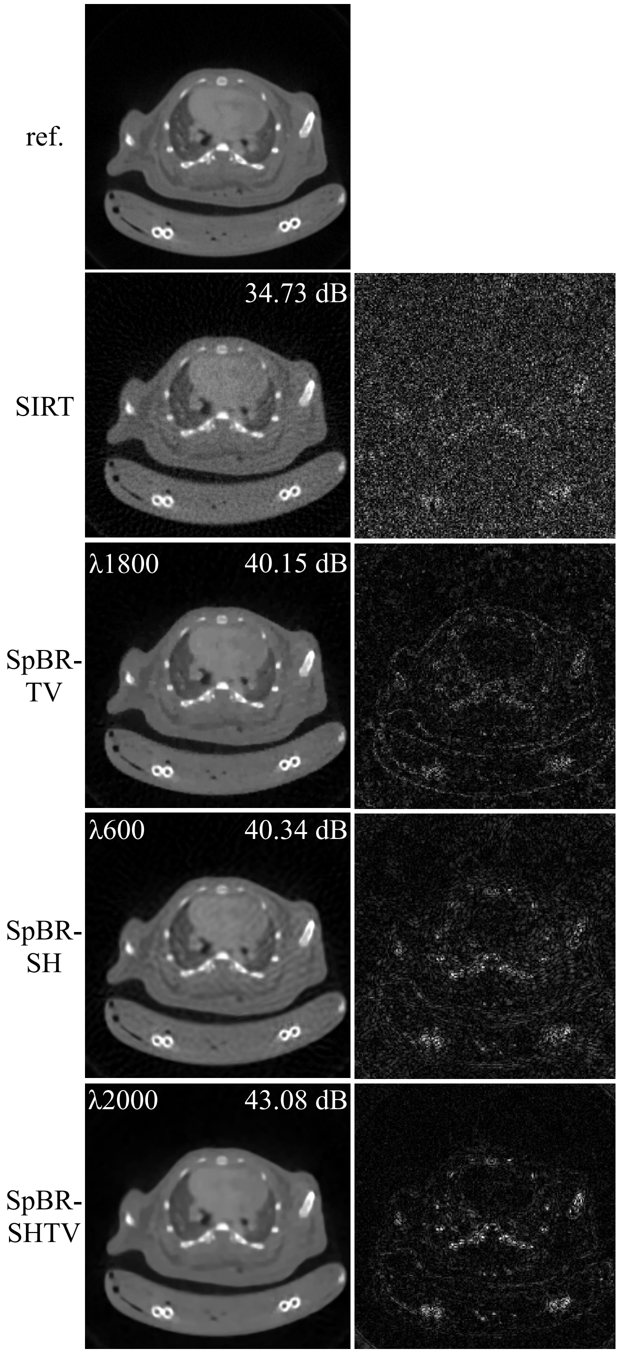

Fig. 3. Preclinical sparsified data reconstructed from 128 projection views with SIRT, SpBR-TV, SpBR-SH and SpBR-SHTV ($\gamma_{SH} = 0.25$, $\gamma_{TV} = 1.0$). All images were normalized to the same window. Difference is the absolute difference between reconstruction and reference.

On the other hand, a larger γ_{TV} than γ_{SH} is needed when phantom data is reconstructed. Shearlets can not reconstruct the uniform areas in phantoms accurately, as was demonstrated with the resolution phantom in Fig. 2. However, these cases are not realistic when doing (pre)clinical measurements. Optimal selection of these parameters will be subject to future research, as well as task-based observer studies to determine if SpBR-SHTV has better diagnostic value than simple TV minimization.

VI. CONCLUSION

We have combined TV and shearlet minimization into one reconstruction algorithm, and have shown its benefits for sparse-view CT imaging in a proof-of-concept study. A small loss of resolution is apparent, probably due to suboptimal parameter selection.

REFERENCES

[1] D. Gutierrez and H. Zaidi, “Assessment of scatter for the micro-CT subsystem of the trimodality FLEX Triumph^{TM} preclinical scanner,” *Medical Physics*, vol. 38, no. 7, pp. 4154–4165, 2011.

[2] L. I. Rudin, O. Stanley, and E. Fatemi, “Nonlinear total variation based noise removal algorithms,” *Physica D*, vol. 60, no. 1-4, pp. 259–268, Nov. 1992.

[3] G. T. Herman and R. Davidi, “On Image Reconstruction from a Small Number of Projections.” *Inverse Problems*, vol. 24, no. 4, pp. 45 011–45 028, Aug. 2008.

[4] M. Lustig, D. Donoho, and J. M. Pauly, “Sparse MRI: The application of compressed sensing for rapid MR imaging,” *Magnetic Resonance in Medicine*, vol. 58, no. 6, pp. 1182–1195, 2007.

[5] M. Defrise, C. Vanhove, and X. Liu, “An algorithm for total variation regularization in high-dimensional linear problems,” *Inverse Problems*, vol. 27, no. 6, p. 065002, May 2011.

[6] G. Kutyniok and D. Labate, “Resolution of the Wavefront Set Using Continuous Shearlets,” *Transactions of the American Mathematical Society*, vol. 361, no. 5, pp. 2719–2754, 2009.

[7] K. Guo, D. Labate, and W.-Q. Lim, “Edge analysis and identification using the continuous shearlet transform,” *Applied and Computational Harmonic Analysis*, vol. 27, no. 1, pp. 24–46, 2009.

[8] B. Vandeghinste, B. Goossens, R. Van Holen, C. Vanhove, A. Pižurica, S. Vandenberghe, and S. Staelens, “Iterative CT reconstruction using shearlet-based regularization,” *Proc. of SPIE*, pp. 1–7, 2012.

[9] A. Pižurica, J. Aelterman, F. Bai, S. Vanloocke, H. Quang Luong, B. Goossens, and W. Philips, “On structured sparsity and selected applications in tomographic imaging,” *Proc. of SPIE Conference Wavelets and Sparsity XIV*, p. 81381D, 2011.

[10] L. He, T.-C. Chang, S. Osher, T. Fang, and P. Speier, “MR image reconstruction from undersampled data by using the iterative refinement procedure,” *PAMM*, vol. 7, no. 1, pp. 1 011 207–1 011 208, Dec. 2007.

[11] J. Huang, S. Zhang, H. Li, and D. Metaxas, “Composite splitting algorithms for convex optimization,” *COMPUTER VISION AND IMAGE UNDERSTANDING*, pp. 1–13, Sep. 2011.

[12] T. Goldstein and S. Osher, “The split Bregman method for L1 regularized problems,” *SIAM Journal on Imaging Sciences*, vol. 2, no. 2, pp. 323–343, 2009.

[13] B. Vandeghinste, B. Goossens, J. De Beenhouwer, A. Pižurica, W. Philips, S. Vandenberghe, and S. Staelens, “Split-Bregman-based sparse-view CT reconstruction,” *Proceedings of the 11th International Meeting on Fully 3D Image Reconstruction*, pp. 431–434, 2011.

[14] A. Badal and A. Badano, “Accelerating Monte Carlo simulations of photon transport in a voxelized geometry using a massively parallel graphics processing unit,” *Medical Physics*, vol. 36, no. 11, p. 4878, 2009.

[15] B. de Man and S. Basu, “Distance-driven projection and backprojection in three dimensions.” *Physics in Medicine and Biology*, vol. 49, no. 11, pp. 2463–2475, 2004.

[16] B. Goossens, J. Aelterman, H. Luong, A. Pižurica, and W. Philips, “Efficient design of a low redundant discrete shearlet transform,” *Proc. of the 2009 Int. Workshop on Local and Non-Local approximation in Image Processing*, pp. 112–124, 2009.

[17] K. Sauer and C. Bouman, “A local update strategy for iterative reconstruction from projections,” *Signal Processing, IEEE Transactions on*, vol. 41, no. 2, pp. 534–548, 1993.

Low-dose CT image reconstruction by adaptive-weighted TV-constrained penalized weighted least-squares approach

Yan Liu, Jianhua Ma, Hao Zhang, Jing Wang and Zhengrong Liang

Abstract–**Previous work has shown that computed tomography (CT) image can be reconstructed satisfactorily from sparse-view or under-sampled projection data by minimizing the total variation (TV) of the desired image with some data constraints without considering the data statistical properties. However, the data statistical properties play an important role for CT image reconstruction, especially for the data acquired from low-mAs or low-dose protocols. Inspired by previous works in statistical iterative reconstruction (SIR), this paper introduces a novel method to integrate the data statistical properties for an adaptive-weighted TV-constrained penalized re-weighted least-squares (AwTV-PRWLS) approach with comparison to the conventional TV-constrained PRWLS method (i.e., TV-PRWLS). It further compares the above approaches to the previous TV minimization with projection onto convex sets approaches (i.e., AwTV-POCS and TV-POCS). All these four approaches were tested by cone-beam projection data from an anthropomorphic head phantom. The results indicate that when the current normal dose acquisition becomes sparse, i.e., the noise level is very low in each projection view and the number of projection views is reduced, both the AwTV-POCS and TV-POCS methods can reconstruct images satisfactorily, while the AwTV-PRWLS and TV-PRWLS algorithms may produce inferior results. When the data sparsity is not severe and the noise level is relatively high as in low-mAs acquisitions, the AwTV-PRWLS and TV-PRWLS algorithms may be advantageous over the AwTV-POCS and TV-POCS methods. In the case of both sparse sampling and low-mAs acquisition, all the four approaches couldn't satisfactorily reconstruct the images. In addition, the results show that AwTV-based approaches can outperform TV-based approaches. AwTV-PRWLS has advantage in non-sparse and low-mAs acquisition, while AwTV-POCS has advantage in sparse and high-mAs acquisition. Both AwTV-PRWLS and AwTV-POCS have the potential for low-dose CT imaging via reducing the X-ray exposure and further evaluation is needed.**

Index Terms–**Adaptive-weighted total variation, penalized re-weighted least squares, anisotropic weights, image reconstruction, noise reduction, low-dose computed tomography**

I. INTRODUCTION

Nowadays, in clinical practice, around thousand of projection views are performed for computed tomography (CT) image reconstruction, and such high X-ray exposure will cause potential negative effects to the patients. Previous works have shown that it is possible to reconstruct CT image from sparse-view or angularly under-sampled projections by minimizing the total variation (TV) of the desired image with some data constraints. A typical example is the TV minimization with projection onto convex sets (TV-POCS) approach [1], and its upgraded computing algorithm, i.e., the adaptive-steepest-descent-POCS (ASD-POCS) algorithm [??]. Both algorithms are based on the assumption of piecewise constant source intensity distribution and showed good ability to reconstruct piecewise smooth image without introducing noticeable artifacts. Considering the anisotropic property of edges in the image domain, an adaptive-weighted total variation (AwTV) model and its associated computing algorithm, i.e., AwTV-POCS, was introduced by Liu *et al*. [2] as another example in the field. The AwTV model showed noticeable gain in edge preservation by incorporating the edge characteristics in the reconstruction.

Although the above algorithms (i.e., TV-POCS and AwTV-POCS) showed effective reconstruction from sparse projection views, they do not consider the statistical properties of the projection data and, therefore, demand a high fidelity between the projection data and the anticipated data, which may limit further reduction for low-dose CT (LDCT) imaging. On the other hand, remaining sufficient angular-sampling rate while reducing the X-ray tube current-milliampere-seconds (mAs) or voltage-kilovoltage-peak (kVp) for data acquisition at all views has been investigated as an alternative means for LDCT imaging via statistical image reconstruction strategies [3]. Based on repeated data-scanning experiments, a nonlinear relationship between the variance and mean of the acquired low-mAs projection data was determined, which provides a reasonable theoretical prediction of the variance of the projection data. Based on the nonlinear relationship, Wang *et al*. [3] investigated a framework of penalized re-weighted least-squares optimization (PRWLS) to reconstruct the low-mAs data for LDCT imaging. More general description on CT image reconstruction methodologies can be found in [4, 5]. This alternative means for low-dose CT imaging may also encounter limitation because the mAs or kVP level cannot be lowered unlimitedly.

By considering the advantages of both the TV minimization approaches and the statistical reconstruction

---

This work was supported in part by the NIH/NCI under Grant #CA143111 and Grant #CA082402. *Asterisk indicates corresponding author.*

Y. Liu is with the Departments of Radiology and Electrical and Computer Engineering, Stony Brook University, Stony Brook, NY, 11794, USA (telephone: 631-444-2508, e-mail: yanliu@mil.sunysb.edu).

J. Ma is with the School of Biomedical Engineering, Southern Medical University, Guangzhou, 510515, China.

H. Zhang is with the Departments of Radiology and Biomedical Engineering, Stony Brook University, Stony Brook, NY, 11794, USA.

J. Wang is with the Department of Radiation Oncology, The University of Texas Southwestern Medical Center at Dallas, Dallas, TX, 75390,USA.

* Z. Liang is with the Departments of Radiology, Computer Science and Biomedical Engineering, Stony Brook University, Stony Brook, NY 11794, USA (telephone: 631-444-7837, e-mail: jerome@mil.sunysb.edu).

strategies, we consolidate the statistical property of the projection data with the constraints of TV on the image intensity distribution for LDCT image reconstruction in this study. While similar concepts have been recently presented in [6, 7], two distinctions differentiate our work from theirs. (1) In their data statistics description or WLS term, the weight is related to the acquired random data and does not reflect the truth. Our weight reflects the truth on the first and second statistical moments of the data and, therefore, results in the re-weighted LS minimization. (2) Their TV term remains the conventional definition, while ours incorporates additional anisotropic property of edges in the TV definition on the image and, therefore, results in the AwTV model. By consolidating the advantages, we will focus, in this paper, on the comparison between AwTV/TV-PRWLS strategy and AwTV/TV-POCS approach.

The remainder of this paper is organized as follows. In section II, the noise model described in [8] will be presented for the WLS term, followed by presentation of the AwTV model described in [2] to establish the AwTV-PRWLS framework where TV-PRWLS is a simplified version. In section III, preliminary experimental results will be reported with comparison to the AwTV/TV-POCS approach. Finally, discussions and conclusions will be given in Section IV.

II. MATERIALS AND METHODS

A. *Penalized Re-weighted Least-squares Approach*

Practically, the measured transmission data *I* can be assumed to statistically follow the Poisson distribution upon a Gaussian distributed background noise:

$$I = \text{Poisson}(\lambda) + \text{Normal}(m_e, \sigma_e^2) \tag{1}$$

where λ is the mean of Poisson distribution and m_e and σ_e^2 are the mean and variance of the Gaussian distribution.

Based on the signal model (1), Ma *et al.* [8] recently derived a new formula for the mean-variance relationship in CT projection domain by considering the effect of the Gaussian distributed electronic noise background at different mAs levels:

$$\sigma_{p_i}^2 = \frac{1}{I_{i0}} \exp(p_i) \left(1 + \frac{\sigma_{e,i}^2 - 1.25}{I_{i0}} \exp(p_i) \right) \tag{2}$$

where I_{i0} is the mean number of incident photons along projection path *i*, p_i denotes the log-transformed ideal projection datum along path *i* and is usually called the line integral of the attenuation coefficients along the projection ray, $\sigma_{e,i}^2$ is the variance of the electronic noise associated with the measurement on p_i , and $\sigma_{p_i}^2$ represents the variance of measuring the projection datum p_i. From Eq. (2), it can be observed that a larger line integral p_i value, indicating less X-ray photons being detected in the detector, will have a larger variance. Thus, a smaller signal-to-noise ratio (SNR) is expected due to the Poisson noise nature of the detected photons. On the contrary, a smaller line integral p_i value will result in a higher SNR. Due to this property, the $\sigma_{p_i}^2$ of (2) shall be used as the weights for the WLS term, i.e., a lower SNR shall contribute less for the estimate of the ideal projection and a higher SNR will contribute more for the estimation. This expectation is mathematically proved by Taylor expansion on the signal model (1) as described in [8].

Using the terminologies in the previous study [3], the cost function of PRWLS can mathematically be written as:

$$\Phi(\mu) = (\hat{p} - A\mu)^T \Sigma^{-1} (\hat{p} - A\mu) + \beta R(\mu) \, . \tag{3}$$

The first term in the right hand side is the re-weighted least-squares (RWLS) measure, where $\hat{p}$ is the acquired projection data and *A* represents the system transfer matrix, which depends on the projection geometry, and its elements of $a_{i,j}$ can be the length of the intersection of projection ray *i* with voxel *j*, μ is the vector of the attenuation coefficients to be reconstructed. The matrix Σ is a diagonal matrix and its *i*th element denotes the variance of the projection datum at detector *i* as defined by Eq. (2). This definition distinguishes the RWLS from the conventional WLS. Minimizing only the first term, similar to the maximum-likelihood (ML) approach, usually leads to unacceptable results [4], thus a penalty *R* (the second term in the right hand side) is desired for a penalized solution. The parameter $\beta > 0$ is designed to control the weight of the penalty. The desired image can be calculated by minimizing the cost function (4), which can be written as:

$$\mu = \arg \min_{\mu \geq 0} \Phi(\mu) \, . \tag{4}$$

For LDCT image reconstruction, the resulting image always suffers noticeable artifacts due to the low SNR property of the signals. To eliminate the effects of the noise, many penalty forms have been used as an *a priori* constraint to regularize the weighted least-squares solution, such as isotropic quadratic term in [3] and anisotropic quadratic term in [9]. In this work, we adapt both the AwTV term introduced in [2] and the conventional TV term in [1] as a penalty respectively. By solving Eq. (4) iteratively with the penalty, a desired resulting image can be obtained. Their related computing algorithms are presented in the next two sections.

B. *Iterative Algorithm for TV-PRWLS Minimization*

From the previous work [1], the definition of TV is given as:

$$\|\mu\|_{AwTV-3D} = \sum_{s,t,z} \sqrt{(\mu_{s,t,z} - \mu_{s-1,t,z})^2 + (\mu_{s,t,z} - \mu_{s,t,z-1})^2 + (\mu_{s,t,z} - \mu_{s,t-1,z})^2} \tag{5}$$

where *s* and *t* are the indices of the location of the attenuation coefficients along in-plane domain (slice), *z* is the indices of the attenuation coefficients along the axis direction. Thus, the cost function of PRWLS-TV is:

$$\Phi_{TV}(\mu) = (\hat{p} - A\mu)^T \Sigma^{-1} (\hat{p} - A\mu) + \beta \|\mu\|_{TV} \, . \tag{6}$$

In practice, several schemes can be implemented to solve such optimization problem, for example the PWLS ordered subsets (PWLS-OS) method was introduced in [5]. In our study, the conventional Gauss-Seidel method as described in [3] was used to solve this problem. Simply, the proposed algorithm was termed as "TV-PRWLS".

C. Iterative Algorithm for AwTV-PRWLS Minimization

Based on the definition of AwTV in [2], anisotropic weights are added to the conventional TV term and the addition can mitigate the over-smooth effects of the conventional TV term. Simulation results have shown that the AwTV model can more accurately reconstruct image as compared to the conventional TV model [2]. Inspired by the motivation of AwTV-POCS approach, the AwTV model is adapted to the PRWLS strategy here. The definition of AwTV can be written as:

$$\|\mu\|_{AwTV-3D} = \sum_{s,t,z}\Big[w_{s,s-1,t,t,z,z}(\mu_{s,t,z}-\mu_{s-1,t,z})^2 + w_{s,s,t,t,z,z-1}(\mu_{s,t,z}-\mu_{s,t,z-1})^2 + w_{s,s,t,t-1,z,z}(\mu_{s,t,z}-\mu_{s,t-1,z})^2\Big]^{\frac{1}{2}} \quad (7)$$

$$w_{s,s-1,t,t,z,z} = \exp\left[-\left(\frac{\mu_{s,t,z}-\mu_{s-1,t,z}}{\delta}\right)^2\right],$$

$$w_{s,s,t,t-1,z,z} = \exp\left[-\left(\frac{\mu_{s,t,z}-\mu_{s,t-1,z}}{\delta}\right)^2\right] \text{ and}$$

$$w_{s,s,t,t,z,z-1} = \exp\left[-\left(\frac{\mu_{s,t,z}-\mu_{s,t,z-1}}{\delta}\right)^2\right] \quad (8)$$

where δ in the weights is a scale factor which controls the strength of the diffusion during each iteration. Then, the cost function for AwTV -PWRLS can be written as:

$$\Phi_{AwTV}(\mu) = (\hat{p}-A\mu)^T\Sigma^{-1}(\hat{p}-A\mu) + \beta\|\mu\|_{AwTV}. \quad (9)$$

Since the weights in AwTV depend on the local intensity of the image, it is numerically difficult to utilize directly the second-order derivative for the purpose of effectively minimizing the objective function (9), the weights will be separately pre-computed before each iteration step. By executing such iterative reconstruction, a desired image can be obtained.

III. RESULTS

To estimate the incident X-ray intensity over the field of view (FOV), an air scan was performed at a specific mA level. In this study, the tube voltage was set to 125 kVp. Figure 1 shows an example of the incident X-ray intensity in low-dose case. The X-ray tube current was set at 10 mA and the duration of the X-ray pulse at each projection view was set to be 10 ms. For the corresponding high-dose case, the tube current was set at 80 mA and the duration of the X-ray pulse at each projection view was 12 ms. A total of 678 projection views were collected for a full 360 rotation. The dimension of each projection image is 1024×768 pixels. To reduce computational time, the projection data were down-sampled by a factor of 2. Only 8 out of 768 slices from the projection image were selected for image reconstruction. The distance of source-to-axis is 100 cm and source-to-detector distance is 150 cm. The pixel size in the reconstructed image is $0.776\times0.776\times0.776$ mm^3.

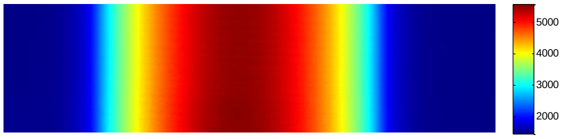

Fig. 1: Incident X-ray intensity profile across the field of view with 10 mA tube current and 10 ms pulse time for fan-beam geometry.

A. Noise Reduction

In this study, the above presented TV-PRWLS and AwTV-PRWLS reconstruction algorithms were tested by cone-beam projection data acquired from an anthropomorphic head phantom. An image reconstructed by the Feldkamp–Davis–Kress (FDK) method with Hamming window at Nyquist frequency cutoff in 80 mA protocol was used as a reference for comparison purpose.

Figure 2 shows that the reconstructed images by TV-PRWLS and AwTV-PRWLS can noticeably reduce the noise for 10 mA data. In addition, because of the anisotropic property of the AwTV model, the result of AwTV-PRWLS shows more some improvement (as indicated by arrows) compared to the result of the TV-PRWLS.

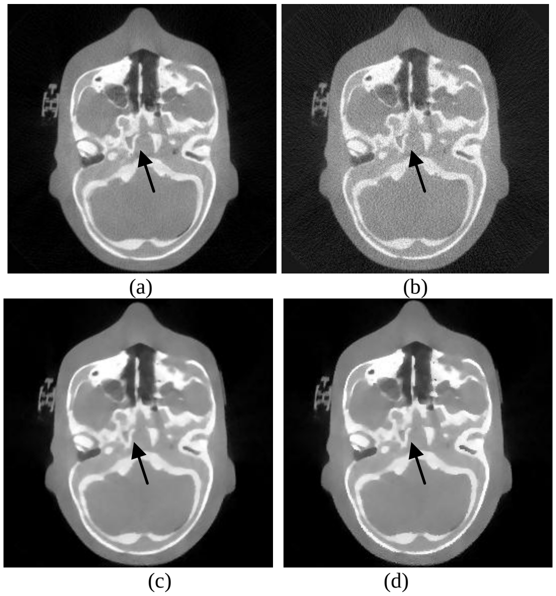

Fig. 2: Transverse reconstructed images of the head phantom: (a) The reconstruction with 80 mA tube current by FDK method. (b) The reconstruction with 10 mA tube current by FDK method. (c) The reconstruction with 10 mA tube current by TV-PRWLS approach. (d) The reconstruction with 10 mA tube current by AwTV-PRWLS approach. The display window is [0, 0.03].

To further visualize the difference between the two approaches for image reconstruction in low-dose case, profiles of the resulting images were drawn across the 108th row and 127th-227th column for each approach and are shown in Fig. 3.

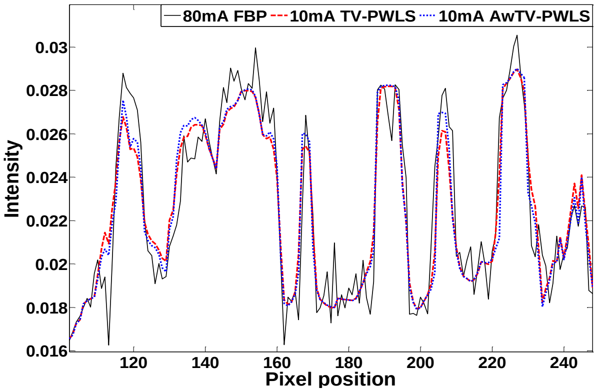

Fig. 3: Horizontal profiles of the reconstructed images.

B. Image Reconstruction from Sparse-view Projections

Previous works have shown that the gain of implementing the TV or AwTV term as an objective function with data constrains for image reconstruction from sparse projection views is significant [1, 2]. The results show that both TV-POCS and AwTV-POCS can reconstruct image very well by sparse number of projection views. Moreover, the improvement by considering the edge properties in the AwTV model over the conventional TV model was noticeable for LDCT image reconstruction [2]. In order to further insight the possibility of extending the PRWLS strategy for LDCT image reconstruction from sparse projection views, we performed a comparison study among AwTV/TV-PRWLS strategies and AwTV/TV-POCS approaches. The TV-POCS algorithm introduced in [1] and the AwTV-POCS algorithm introduced in [2] were implemented. A total of 113 projections were selected from the original 678 views in different protocols (i.e., 80mA and 10mA) to mimic the sparse data. The reconstruct image results are shown in Fig. 4 and Fig. 5.

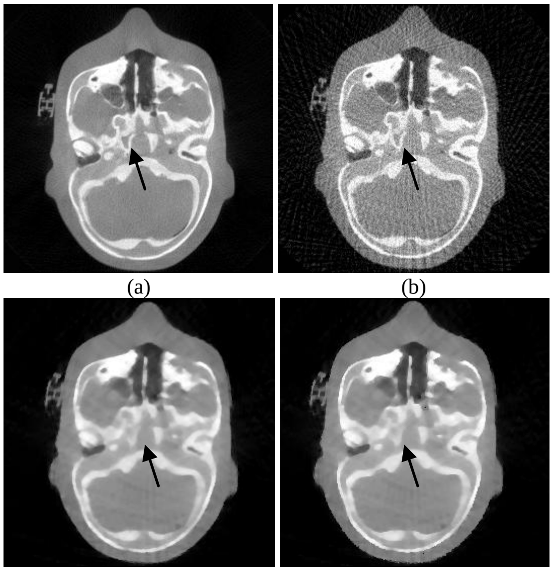
(a) (b)

(c) (d)

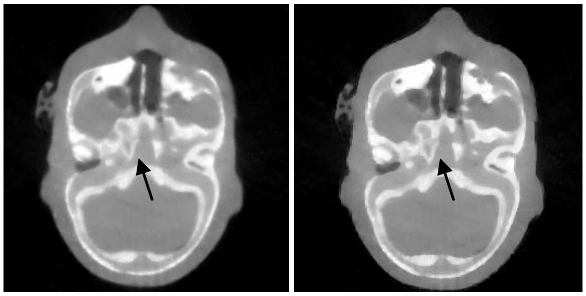
(e) (f)

Fig. 4: Comparison study between AwTV/TV-PRWLS strategy and AwTV/TV-POCS approach in high-dose case. (a) The reference or high dose FDK image from 80 mAs data. (b)-(f): The reconstructions from 113 (or sparse) projection views with 80 mA tube current, where (b) from FDK method, (c) from TV-PRWLS approach, (d) from AwTV-PRWLS approach, (e) from TV-POCS approach, and (f) from AwTV-POCS. The display window is [0, 0.03].

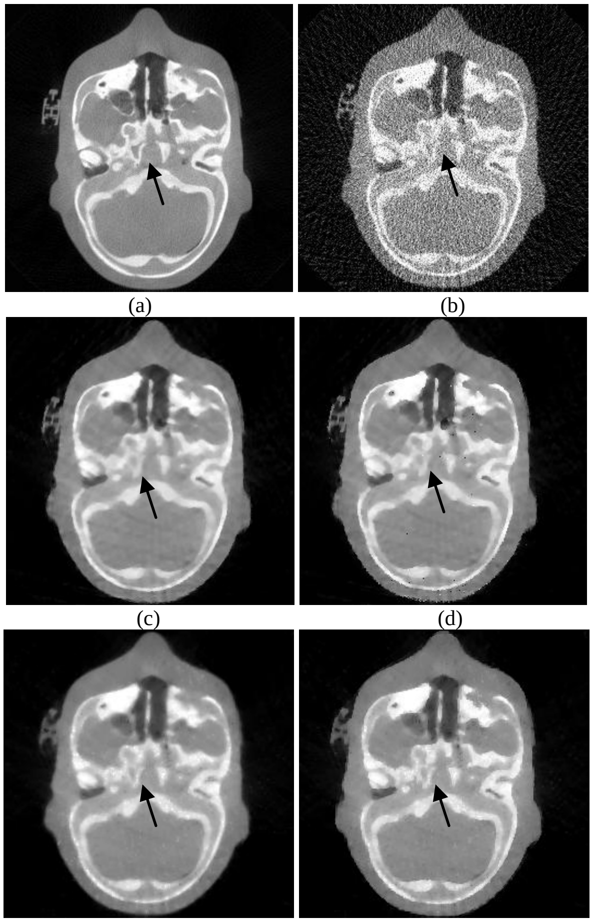
(a) (b)

(c) (d)

(e) (f)

Fig. 5: Comparison study between AwTV/TV-PRWLS strategy and AwTV/TV-POCS approach in low-dose case. (a) The reference or high dose FDK image from 80 mAs data. (b)-(f): The reconstructions from 113 (or sparse) projection views with 10 mA tube current, where (b) from FDK method, (c) from TV-PRWLS approach, (d) from AwTV-PRWLS approach, (e) from TV-POCS approach, and (f) from AwTV-POCS. The display window is [0, 0.03].

From Figure 4, it can be observed that both the TV-POCS and AwTV-POCS have higher ability to reconstruct image from sparse projection views in the high-dose 80 mA protocol. Because a scalar parameter δ was introduced to the AwTV-POCS, the resolution and noise level can be controlled by selecting different values of δ. Thus, the result from the AwTV-POCS has a better resolution than the TV-POCS as indicated by arrows in Fig. 4(e) and Fig. 4(f).

In the low-mA (i.e., 10 mA protocol) and sparse case, as shown at Fig. 5, we can conclude that all the four algorithms produced weaker results. For the PRWLS strategy, the sampling rate is not sufficient. When the rate was increased, better result was obtained, as seen in Fig. 2. For the TV-POCS approach, the data constraint is not sufficient. When the data noise was decreased in the high-dose case, better result was obtained, as seen in Fig. 4.

IV. CONCLUSION AND DISCUSSION

In this work, we presented the PRWLS strategy with incorporation of the TV image model. Two related algorithms, AwTV-PRWLS and TV-PRWLS, were formulated and tested for LDCT image reconstruction. The visual comparison of these two algorithms indicates that both algorithms can mitigate the noise effect in the 10 mA protocol (i.e., about 1/8 of the high-dose case) for full angular scanning protocol. Because of the consideration of the anisotropic property of edges in the AwTV model, reconstruction resolution can be improved by selecting a proper value of δ in the AwTV model. Thus, a higher quality of image can be obtained by using the AwTV - PRWLS algorithm.

We also compared these two algorithms with the previous works (i.e., TV-POCS and AwTV-POCS) for image reconstruction from sparse-view projections (i.e., the number of views was about 1/6 of the original views). In such sparse case, the TV-POCS and AwTV-POCS can have a higher ability than the TV-PRWLS and AwTV-PRWLS for reconstruction of the high-dose data from the 80 mA protocol. We further observed the gain of the AwTV model as compared to the conventional TV model. In the low-dose (10 mA protocol) and sparse-view (1/6 views) case, all the four algorithms could not produce satisfactory results.

Based on experimental results above, we can draw the conclusions as follows. For sufficient angular sampling and low-dose on each view, the PRWLS strategy has advantage. For sparse sampling (low-dose) and high counts on each view, the TV approach has advantage. Further evaluation on these two alternative approaches to LDCT imaging is needed and is under progress.

REFERENCES

[1] E. Sidky, C. Kao, and X. Pan, “Accurate image reconstruction from few-views and limited angle data in divergent-beam CT,” *Journal of X-Ray Science and Technology*, vol. 14, no. 2, pp. 119–139, 2006.

[2] Y. Liu, J. Ma, Y. Fan and Z. Liang: “Low-dose computed tomography image reconstruction from under-sampling data based on weighted total variation minimization,” *Proceedings of SPIE Medical Imaging*, vol.8313, 83133H, February, 2012.

[3] J. Wang, T. Li, H. Lu, and Z. Liang, “Penalized weighted least-squares approach to sinogram noise reduction and image reconstruction for low-dose X-ray CT,” *IEEE Transactions on Medical Imaging*, vol. 25, no. 10, pp. 1272–1283, October, 2006.

[4] P. J. La Rivière, J. Bian, and P. A. Vargas, “Penalized-likelihood sinogram restoration for CT,” *IEEE Transactions on Medical Imaging*, vol. 25(8), 1022–1036, August, 2006.

[5] I. A. Elbakri, and J. A. Fessler, “Statistical image reconstruction for polyenergetic X-ray CT,” *IEEE Transactions on Medical Imaging*, vol. 21, no. 2, pp. 89–97, February, 2002.

[6] Q. Xu, X. Mou, G. Wang, J. Sieren, E. Hoffman, and H. Yu, “Statistical interior tomography,” *IEEE Transactions on Medical Imaging*, vol. 30, no. 5, pp. 1116–1128, May, 2011.

[7] M. Defrise, C. Vanhove, and X. Liu, “An algorithm for total variation regularization in high-dimensional linear problems,” *Inverse Problem*, vol. 27, no. 6, pp. 65002–65017, June, 2011.

[8] J. Ma, Z. Liang, Y. Fan, Y. Liu, J Huang, L. Li, W. Chen and H. Lu: “Variance estimation of X-ray CT sonogram in Radon domain,” *Proceedings of SPIE Medical Imaging*, vol.8313, 83132G, February, 2012.

[9] J. Wang, T. Li, and L. Xing, “Iterative image reconstruction for CBCT using edge-preserving prior,” *Medical Physics*, vol.36, no. 1, pp. 252–260, January, 2009.

Algebraic Tomosynthesis Reconstruction with Spatially Adaptive Updating Term

Yulia M. Levakhina, Jan Mueller, Robert L. Duschka, Florian M. Vogt, Joerg Barkhausen, Thorsten M. Buzug

***Abstract*—Digital Tomosynthesis (DT) is an attractive low-dose alternative to Computed Tomography (CT) in certain medical imaging applications. In contrast to CT, an accurate image reconstruction in DT is a challenging task due to the incompleteness of the projection data. In the current work, an adaptive weighting for the back-distribution of the updating term in the Simultaneous Algebraic Reconstruction Technique (SART) is proposed. It is designed for tomosynthesis imaging of objects with high-contrast features. The weights are spatially adaptive and calculated based on the dissimilarity evaluated in a space called "backprojected space". The proposed approach is evaluated on real three-dimensional tomosynthesis data. The reconstruction results demonstrate the feasibility of the proposed algorithm to reduce out-of-focus artifacts and black shadows produced by the dense features. The proposed algorithm can potentially be included into various iterative reconstruction algorithms with an additive updating strategy and it can also be extended to the a CT scan with full data..**

I. INTRODUCTION

Digital Tomosynthesis (DT) is a limited angle X-ray imaging technique for producing a three-dimensional stack of cross-sectional images of an object. Nowadays, it is an attractive low-dose alternative to Computed Tomography (CT) in certain imaging applications e.g. breast imaging [1], chest imaging [2], dental imaging [3] or musculoskeletal imaging of hands [4]. In contrast to CT, an accurate image reconstruction in DT is a challenging task since only limited number of projections acquired over limited angular range is available. The incompleteness of the projection data results in several problems. First, tomosynthesis provides images with limited in-depth resolution. Only the planes parallel to the detector can be reconstructed with high resolution. Second, the in-plane images are typically affected by out-of-focus artifacts and black shadows. Out-of-focus artifacts are produced by structures located above and below the plane of interest and appear as "ghosting" copies of those structures. It is known that an intensity of out-of-focus artifacts is proportional to the size and density of the artifact-causing object [5]. Black shadows are produced by high-contrast boundaries which are perpendicular to the tube movement direction. High-absorption features with clearly visible boundaries like bones, microcalcifications or metal objects create both type of artifacts at the same time. Various reconstruction methods have been proposed so far in order to reduce artifacts and obtain tomosynthesis images with good quality [6].

The tomosynthesis measurement process is schematically shown in Fig. 1 (left) and the simple backprojection is shown in Fig. 1 (right). The selected plane of interest with the green triangle feature is marked by a dashed gray line. It can be seen that after the backprojection step the green triangle feature appears sharp in this plane. At the same time the red circle feature produces blur in this plane, i.e. it appears as multiple "ghosting" copies. This happens because the green triangle belongs to the selected plane and the corresponding projection value is always back-projected onto the "correct" location. The red circle does not belong to the selected plane and therefore it is always back-projected onto the "wrong" location. Taking into account the blur formation principle, it is possible to introduce the weighting coefficients into reconstruction algorithms for DT in order to suppress contributions from high-contrast structures when they are backprojected onto wrong geometrical locations. As it will be discussed in the Section 2, the blur formation can be decomposed into angular components when considering a so-called backprojected space (also known as a stackgram representation [7] in two-dimensional case).

An empirical adaptive weighting scheme which allows for the reduction of the simple backprojection blur in musculoskeletal tomosynthesis has been presented recently [8]. The scheme is based on the evaluation of the dissimilarity in the backprojection space. In this scheme the weighting coefficients are calculated for each pixel and each angular view individually based on the ensemble of the measured projection data. Extending this idea, the weighting can be used in an iterative reconstruction. In the current work an algorithm for using the adaptive weighting for the back-distribution of the updating term in the Simultaneous Algebraic Reconstruction Technique (SART) is proposed. The proposed algorithm does not need any segmentation step or decisions done by thresholding. An algebraic reconstruction (SART) was chosen as an example to show the capability of the proposed algorithm to reduce artifacts. The proposed algorithm is not only limited to the algebraic reconstruction and can potentially be included into various iterative reconstruction algorithms with an additive updating strategy. The scheme is also not only limited to tomosynthesis geometry but can be extended to the full scan CT case and applied, for example, to the metal artifact

---

This work is supported by the Graduate School for Computing in Medicine and Life Sciences funded by Germanys Excellence Initiative [DFG GSC 235/1]

Y. M. Levakhina is with the Graduate School for Computing in Medicine and Life Sciences and Institute of Medical Engineering, University of Luebeck, Luebeck, Germany (e-mail: levakhina@imt.uni-luebeck.de)

J. Mueller and T. M. Buzug are with the Institute of Medical Engineering, University of Luebeck, Luebeck, Germany (e-mail: buzug,mueller@imt.uni-luebeck.de)

R. L. Duschka, F. M. Vogt and J. Barkhausen are with the Klinik fuer Radiologie und Nuklearmedizin, Universitaetsklinikum Schleswig-Holstein, Luebeck, Germany (e-mail: Robert.Duschka, Florian.Vogt, Joerg.Barkhausen@uk-sh.de)

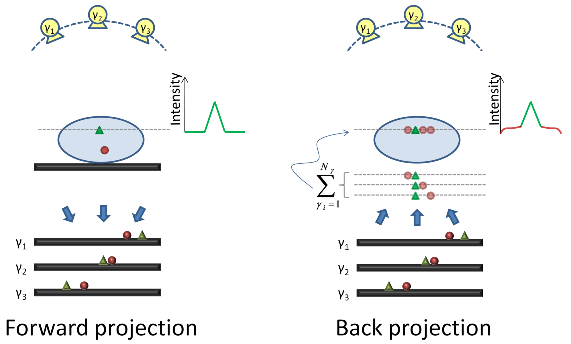

Figure 1: The principle of blur formation in tomosynthesis and a motivation for the weighted backprojection.

reduction problem or data truncation problem.

The paper is organized as follows. In the second section, a short description of the SART algorithm will be given. Then, an idea of the backprojection space is explained followed by the scheme for weighing coefficients calculation. In the third section, the materials and the used tomosynthesis acquisition system are described. In fourth section, the reconstruction results are presented and discussed. Finally, the fifth section presents the conclusion and the outlook.

II. METHODS

In the current work an algorithm for weighting coefficients calculation for an additive iterative tomosynthesis reconstruction on an example of Simultaneous Algebraic Reconstruction Technique (SART) is proposed. The process of coefficients calculation is called adaptive because it is based on the ensemble of the projection data and it is spatially adaptive because an individual weighting coefficient is assigned to each updating term and each image voxel.

A. *SART*

The tomographic reconstruction problem can be considered as a system of linear equations, which is undetermined in case of limited angle tomosynthesis acquisition. Let $\mathbf{f}$ be a discrete representation of an object to be reconstructed, $\mathbf{A}$ be a system matrix describing the measurement process and acquisition geometry and $\mathbf{p}$ be the measured data. The algebraic reconstruction is searching for a solution of a system $\mathbf{Af} = \mathbf{p}$ in therms of L_2 norm minimization $\mathbf{min}\,|\mathbf{Af} - \mathbf{p}|_\mathbf{2}$, i. e. it iteratively minimizes the residual error between the measured data and the calculated forward projection of the estimated image. It works as follows: in i-th iteration a forward projection of the current solution is calculated. Afterwards it is compared with the measured data and based on this an updating term is calculated. Then, the updating term is homogeneously projected back into image domain according to the system matrix $\mathbf{A}$. If an updating term is applied considering each single ray, the method corresponds to the classical ART scheme, if an updating term is applied considering a complete view, the method is called Simultaneous ART (SART). In the presence of high density features such as bones or metal the corresponding measured projection value will be relatively high. Consequently, an updating term calculated based on these projection values will be "too large" for certain voxels, contributing this way to the formation of the out-of-focus artifacts and black shadows.

B. *Backprojected space*

A backprojected space representation allows for easily identifying which voxels will get "too large" updating term and for calculatingthe corresponding weighting coefficients.

The stackgram representation is a sinusoid-like curve decomposition of the sinogram [7] . In case of the two-dimensional imaging geometry it is an intermediate step between the sinogram domain and the image domain. In order to construct this representation, the integral (summation) in the backprojection operator is replaced by a stack operator. The stack operator $\mathbf{S}$ maps the projection $p\,(l,\theta)$ onto the three-dimensional function $h\,(x,y,\theta)$. In case of the 2D parallel beam geometry h is defined as:

$$h\,(x,y,\theta) = \mathbf{S}p\,(l,\theta) = p\,(x\sin\theta + y\cos\theta,\theta)\,. \qquad (1)$$

In the two-dimensional case $h_{xy}\,(\theta)$ represents the data on the sinus, which the image-point (x,y) produces in the sinogram. In case of the three-dimensional imaging geometry, a similar operator $\mathbf{S}$ can be defined for each point (x,y,z) within the reconstructed volume, resulting in the four-dimensional backprojected space $h\,(x,y,z,\theta)$:

$$h\,(x,y,z,\theta) = \mathbf{S}p\,(u,v,\theta)\,. \qquad (2)$$

The angle θ describes the X-ray tube position and (u,v) are coordinates describing a point on the detector. In contrast to the simple two-dimensional parallel beam geometry where the $\mathbf{S}$ is easily defined, in the three-dimensional case it can not be easily described and depends on the specific geometry of the scanner. A vector $h_{xyz}\,(\theta)$ contains all backprojected values contributing to the current point (x,y,z) from different angular views. In case if a volume contains only one feature located at the position (x,y,z), the corresponding projection data $p\,(u,v,\theta)$ will contain exactly one three-dimensional sinusoidal-like curve. Therefore, all entries of the corresponding θ-vector $h_{xyz}\,(\theta)$ in the backprojected space have the same value. In the case of medically relevant images (volumes), the projection data contains multiple overlying sinusoidal-like curves and each entry in the θ-vector might have a different value. When an object contains a high-contrast feature, the sinusoidal-like curves produced by this feature will cross the sinusoidal-like curve produced by the (x,y,z) point. The values on the crossing location will be relatively large when comparing to the rest of the values. One can assign a dissimilarity degree to each value in the θ-vector and identify outliers. The outliers come from the high-contrast features and potentially produce artifacts. It allows for introducing the spatially-depended adaptive weighting coefficients to suppress non-similar values based on their dissimilarity degree.

C. Weighting scheme and ωSART

The same principle can be used to correct for "too large" updating terms in the algebraic reconstruction when the updating term is calculated using a large projection value and is back-distributed onto the "wrong" geometrical location. First, for each voxel (x, y, z) within the reconstructed volume the backprojected space representation is constructed (eq. 3, first step). Then, for each element of each θ-vector a dissimilarity is assigned (eq. 3, second and third steps). The dissimilarity can be, for example, calculated as a mutual cross-difference between all values in the θ-vector. It can also be defined as an appropriately normalized L_p-distance measure to a reference value M. The trade-off between noise-sensitivity and artifact amplitude defines the choice of the reference value. The reference value can be chosen as a mean, min, median or other values based on the statistics of the θ-vector. It is important to note, that the reference value M is not considered as an expected solution and the algorithm is not converging to this value. The relation between the dissimilarity and the weighting coefficients can be assumed to be a non-increasing convex function, see the eq. 3, the fourth step as an example. Here, the α and the β are two parameters defining the steepness of the function.

$$\begin{array}{l}
1.\ \forall\ (x, y, x) \in V,\ \forall\, \gamma \in \Gamma : h\,(x, y, z, \theta) = \mathbf{S}p\,(u, v, \theta) \\
2.\ \forall\ h_{xyz}\,(\theta)\ \text{select the reference value}\ M_{xyz} \\
3.\ d_{xyz}\,(\theta) = \left\| h_{xyz}\,(\theta) - M_{xyz} \right\|_p,\ 0 \le d \le 1 \\
4.\ \omega_{xyz}\,(\theta) = f\,(d_{xyz}\,(\theta)),\ \text{e.g. } \omega = \left(\frac{1-d}{1+\alpha d}\right)^{\beta}
\end{array} \tag{3}$$

Now, the weighting coefficients $\omega\,(x, y, z, \theta)$ can be used in the SART reconstruction as a weighting of the back-distribution of the updating term.

III. MATERIALS

All measured data have been acquired with the Siemens Mammmomat Inspiration tomosynthesis device. The device is equipped with a half-cone X-ray tube, a fixed flat-panel detector and a compression paddle. The X-ray tube moves along 50^o-arc taking 25 projections. The detector total size is 24 cm x 30 cm and the detector element size is 85 μm. The compression paddle is used for object fixation. All measurements were done with the tube voltage 35 kV and the tube current 152 mAs. An apple with metal needles and a hand from a body donor were used in the current work. The apple height is 60 mm. Ten needles have been manually inserted into the apple at approximately half of its height (30 mm) forming the plane of interest. The needles have been inserted in two perpendicular directions and distributed in the following fashion: one needle is on the frontal side, two needles are on the right-hand side, three needles are on the back side and four needles are on the left-hand side. They are oriented such that some of the needles are parallel and some of the needles are perpendicular to the tube rotation axis. The needles were used to visually demonstrate the formation of the out-of-focus artifacts and black shadows. The hand is from a body donor who gave a permission to use its body for medical education and research. The hand is approximately 44 mm thick and has been placed on the detector in the prone position. The hand was used to demonstrate the artifacts formation in the clinically relevant case.

IV. RESULTS AND DISCUSSION

To determine the efficacy of the proposed weighting algorithm to reduce the out-of-focus artifacts and black shadows, several experiments were conducted. Two objects have beenused: a hand and an apple with metal needles. For each object a stack of slices with 1 mm thickness was reconstructed. All images in the stack are parallel to the detector plane. Reconstruction is done using Simultaneous Algebraic Reconstruction Technique (SART) with and without the adaptive weighting. The SART reconstruction parameters have been chosen: zero-valued initial guess and the random projection access order. For the weighting coefficients calculation the reference value has been chosen as a minimum value, L_1-norm has been chosen as the dissimilarity measure and the damping function parameters were $\alpha = 2$, $\beta = 2$. The reconstructed volume of the apple contains 60 slices, the needles appear in-focus at slices 29-31. When discussing the reconstructed images, the frontal side of the apple is referred to the bottom side of the image and the back side is referred to the top side of the image. The reconstructed volume of the hand contains 44 slices. For all images presented below, the visualization parameters, i.e. the window width and the window level have been adjusted in order to emphasize artifacts. The minimum value of the window width was chosen slightly negative. The tube movement direction is from the left to the right with respect to all presented tomosynthesis images.

A. Apple with needles

The apple with needles visually shows the formation of the out-of-focus artifacts and black shadows. Slice number 29 is presented in Fig. 2. The reconstruction using SART without weighting is shown in Fig. 2a. The reconstruction using SART with weighting and convex-shaped correction function is shown in Fig. 2b. In the presented slice, the bottom needle and one of the top needles are in-focus. Only one of the top needles is in-focus due to the fact that the needles are slightly angulated with respect to the slice orientation. All discussed in-focus features are marked with dashed ellipsoids and all discussed artifacts are marked with dashed arrows. In the Fig. 2a one can see the shadows around the bottom needle and multiple "ghost" copies of the top needles. Similar artifacts can be noticed near the horizontally-oriented needles. They are oriented parallel to the tube rotation axis and produce less artifacts in the selected slice. Beside this, the apple boundary is also surrounded by out-of-focus artifacts (marked with double arrow). In the Fig. 2b one can see an improvement in the image quality. The ghosting artifacts produced by needles and the apple itself are reduced. The black shadows produced by needles are almost completely eliminated. In Fig. 3 slice number 40 is presented. In this slice all needles are out-of-focus. SART reconstruction shows "ghost" copies of the top and bottom needles and black shadows around them. At the same time the ωSART is able to reduce artifacts and shadows considerably. Needles which are parallel to the tube rotation axis produce the strongest artifacts in this slice. The ωSART notably reduces them.

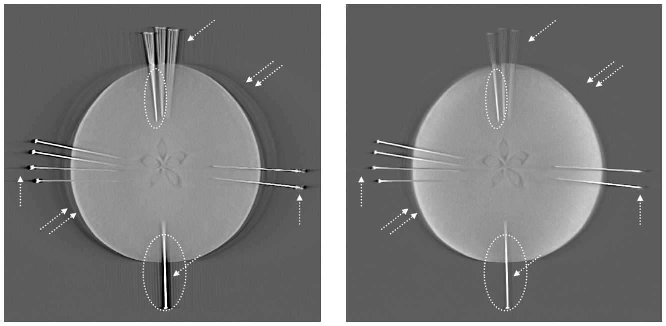
(a) SART (b) ωSART

Figure 2: Apple, slice 29. (Almost all) needles are in-focus.

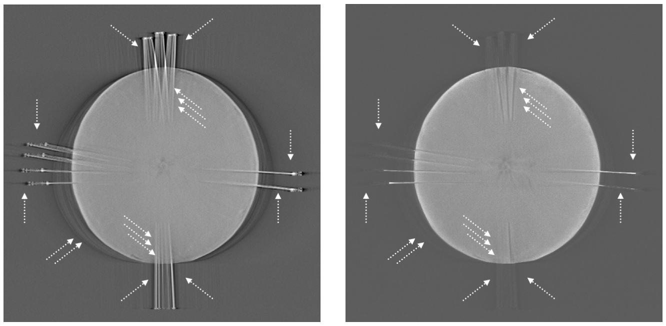
(a) SART (b) ωSART

Figure 3: Apple, slice 40. All needles are out-of-focus.

B. *Hand*

The hand from a body donor represents a clinically relevant case. An arbitrary selected slice is presented in Fig. 4. Reconstruction using SART without weighting is shown in Fig. 4a. Reconstructions using SART with weighting and convex-shaped correction function is shown in Fig. 4b. In the presented slice, three proximal phalanges (forefinger, middle finger, ring finger), one metacarpals (little finger) and carpals are in-focus. At the same time, the thumb, the proximal phalange (little finger), three metacarpals (forefinger, middle finger, ring finger) and all distal phalanges are out-of-focus. The typical out-of-focus artifacts and the black shadows are marked with the dashed arrows. As in the previous example, one can see that the artifacts are successfully suppressed when using the proposed weighting scheme.

V. CONCLUSIONS AND OUTLOOK

In the current work, an adaptive weighting for the back-distribution of the updating term of the Simultaneous Algebraic Reconstruction Technique (SART) in the application to tomosynthesis of objects with high-contrast features was proposed. Coefficients are spatially varying and calculated based on the dissimilarity in the backprojected space. The proposed approach was evaluated on real three-dimensional tomosynthesis data. The reconstruction results of the apple with metal needles and the hand demonstrate the feasibility of the proposed algorithm to reduce the out-of-focus artifacts and the back shadows produced by dense features.

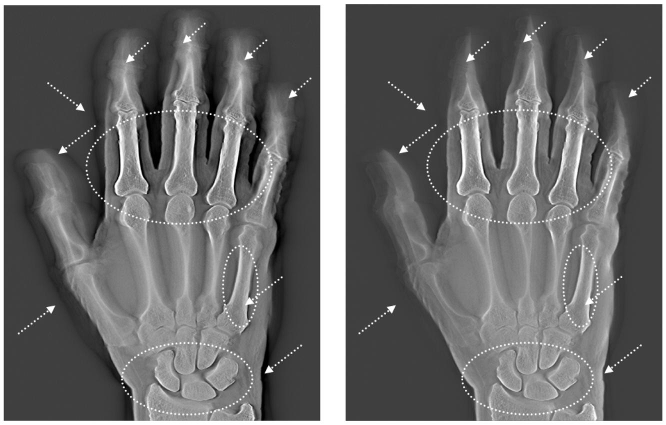
(a) SART (b) ωSART

Figure 4: A hand reconstruction, slice 24.

The proposed algorithm does not need any segmentation step or decisions done by thresholding. An algebraic reconstruction (SART) was chosen as an example to show the capability of the proposed algorithm to reduce artifacts. The proposed algorithm is not only limited to the algebraic reconstruction and can potentially be included into various iterative reconstructions with an additive updating strategy. The algorithm is also not only limited to tomosynthesis geometry but can be extended to the full scan CT case and applied, for example, to the metal artifact reduction problem or data truncation problem.

REFERENCES

[1] A. Tingberg, "X-ray tomosynthesis: a review of its use for breast and chest imaging," *Radiat. Prot. Dosim.*, vol. 139, no. 1-3, pp. 100–107, 2010.

[2] J. T. Dobbins, III, H. P. McAdams, J.-W. Song, C. M. Li, D. J. Godfrey, D. M. DeLong, S.-H. Paik, and S. Martinez-Jimenez, "Digital tomosynthesis of the chest for lung nodule detection: Interim sensitivity results from an ongoing NIH-sponsored trial," *Med. Phys*, vol. 35, no. 6, pp. 2554–2557, 2008.

[3] K. Ogawa, R. P. Langlais, W. D. McDavid, M. Noujeim, K. Seki, T. Okano, T. Yamakawa, and T. Sue, "Development of a new dental panoramic radiographic system based on a tomosynthesis method," *Dentomaxillofac Radiol.*, vol. 39, no. 1, pp. 47–53, 2010.

[4] J. Duryea, J. Dobbins, and J. Lynch, "Digital tomosynthesis of hand joints for arthritis assessment," *Med. Phys*, vol. 30, no. 3, pp. 325–333, 2003.

[5] T. Svahn, M. Ruschin, B. Hemdal, I. Andersson, P. Timberg, , and A. Tingberg, "In-plane artifacts in breast tomosynthesis quantified with a novel contrast-detail phantom," *Proc. SPIE*, vol. 6510, p. 65104R, 2007.

[6] J. T. Dobbins, III, "Tomosynthesis imaging: At a translational crossroads," *Med. Phys.*, vol. 36, no. 6, pp. 1956–1967, 2009.

[7] A. Happonen, "Decomposition of Radon Projections into Stackgrams for Filtering, Extrapolation, and Alignment of Sinogram Data," Ph.D. dissertation, Departmen of Information Technology, Tampere University of Technology, 2005.

[8] Y. M. Levakhina, R. L. Duschka, , J. Barkhausen, F. M. Vogt, and T. M. Buzug, "Adaptive spatially dependent weighting scheme for tomosynthesis reconstruction," *Proc. SPIE*, vol. to be published, 2012.

Initial Experience in Constrained-TV-minimization Image Reconstruction from Diagnostic-CT Data

Zheng Zhang, Junguo Bian, Xiao Han, Daxin Shi, Alex Zamyatin, Patric Rogalla, Emil Y. Sidky and Xiaochuan Pan

***Abstract*—Advanced diagnostic CT scanners typically acquire a large number (>1000) of projections, and employ analytic-based algorithms for image reconstruction. Optimization-based algorithms can reconstruct images of potentially enhanced quality, and has the flexibility in accommodating non-conventional data-acquisition configurations, such as data collected at sparse views. In this work we focus on reconstructing CT images by tailoring and applying one of such algorithms, the adaptive-steepest-descent-projection-onto-convex-sets (ASD-POCS) algorithm from patient and swine data sets collected at 1200 views by use of a Toshiba 320-slice scanner. We first studied ASD-POCS reconstructions from 1200-view data and compare them with those obtained with an analytic-based algorithm that is used currently in practical applications. We also performed reconstructions from 600- and 240-view data. The results show that the ASD-POCS algorithm can reconstruct from 1200- and 600-view data images with quality comparable to, or improved over, what can be obtained currently. In addition, although ASD-POCS reconstructions from 240-view data sets are visibly degraded, it has clear advantage over analytic-based reconstructions in terms low-contrast preservation and noise suppression, and thus may yield images of potential practical utility.**

I. INTRODUCTION

There exists an increased interest in development and evaluation of optimization-based algorithms for image reconstruction in computed tomography (CT), because, when applied to the large amount of data typically collected in current applications, they may yield images with improved quality over that of reconstructions obtained by use of analytic-based algorithms such as FDK-based algorithms, and because they can be more flexible for accommodating imaging conditions of practical significance than analytic-based algorithms. A great deal of results have been reported on image reconstruction by use of optimization-based algorithms from data acquired with non-diagnostic CT. However, applications of optimization-based algorithms to reconstructing images from data collected with advanced diagnostic CT seem to be limited.

Among optimization-based algorithms developed recently, algorithms exploiting image-sparsity properties have attracted considerable attention as they have shown some potential to yield reconstructions of practical utility. The adaptive-steep-descent (ASD)-projection-onto-convex-set (POCS) algorithm is one of such algorithms, and it has been applied to reconstructing images from data collected with an array of scanning configurations largely in non-diagnostic CT systems. Evaluation studies have shown a potential of the ASD-POCS algorithm in yielding quality images from data less than what are needed by an analytic-based algorithm in current imaging applications. Although some of the studies involving the ASD-POCS algorithm used diagnostic CT data, a majority of them was carried out by use of data collected with non-diagnostic CT systems.

In this work, we focus on tailoring the ASD-POCS algorithm to reconstructing images from patient and animal data acquired with a Toshiba 320-slice CT scanner. One goal of the investigation is to study and evaluate, whether the ASD-POCS algorithm can yield images comparable to or better than what the currently used FDK-based algorithm can produce. Another objective of the work is to investigate and evaluate image reconstructions obtained with the ASD-POCS algorithm from sparse-view data extracted from data acquired in typical clinical scans. Although current diagnostic CT scanners generally collect projection data at a large number (e.g., 1200) of views over 2π, they can also readily be used for collecting data at a substantially reduced view number such as $\sim$ 600 by taking every other view or combining views pair-wise. Investigation of these scanning configurations may provide insights into issues such as how the total imaging dose can "optimally" be distributed. Also, even though a data set containing extremely sparse views may be a hypothetic scenario for current diagnostic CT scanners, its study allows an evaluation of image reconstruction from sparse-view data of diagnostic-CT-data quality, thus yielding insightful information for possible design of future diagnostic CT systems with innovative scanning configurations.

The submission is organized as below. Following the introduction in Sec. I, we briefly describe in Sec. II the imaging model, optimization program, and ASD-POCS algorithm for image reconstruction, and in Sec. III real-data acquisition. In Sec. IV, reconstruction results were obtained by use of our FDK-based and ASD-POCS algorithms from patient and swine data acquired with the 320-slice Toshiba CT scanner. Final comments and discussion are given in Sec. V.

Z. Zhang, X. Han, J. Bian, E. Y. Sidky and X. Pan are with the University of Chicago.

D. Shi and A. Zamyatin are with Toshiba Medical Research Institute USA.

P. Rogalla is with UHN Toronto General Hospital, Canada.

II. OPTIMIZATION-BASED RECONSTRUCTIONS

An optimization-based reconstruction generally includes the establishment of an imaging model, an optimization program, and an algorithm that reconstructs the image through solving the optimization program. In this section, we briefly discuss these components involved in the study.

A. Imaging model

In an optimization-based reconstruction, the model data $\mathbf{g}_0$ and image $\mathbf{f}$ are vectors with M pixels and N voxels, respectively, and the imaging model links the two vectors through a discrete-to-discrete (D-D) linear model:

$$\mathbf{g}_0 = \mathcal{H}\mathbf{f}, \tag{1}$$

where $\mathcal{H}$ denotes a system matrix of size $M \times N$. It should be reminded that system matrix $\mathcal{H}$ is determined by not only the selection of data and image vectors but also the way as to how the discrete X-ray transform is calculated. In the work, the system matrix is calculated as, for a given detector bin, the sum of voxel intersections, weighted by the values within the voxels, of a line connecting the source and the center of the detector bin. It should be noted that model data $\mathbf{g}_0$ differ from measured data $\mathbf{g}$ that will be considered below in the optimization formulation.

B. Optimization programs

The inversion of Eq. (1) can be formulated into an optimization problem that can be solved by use of optimization-based algorithms. We first consider an optimization program

$$\mathbf{f}^* = \text{argmin} \parallel \mathbf{f} \parallel_{\text{TV}} \quad \text{s.t.} \quad D(\mathbf{f}) \leq \epsilon, \tag{2}$$

where

$$D(\mathbf{f}) = \mid \mathcal{H}\mathbf{f} - \mathbf{g} \mid \tag{3}$$

denotes the Euclidean-data divergence between measured data $\mathbf{g}$ and imaging model $\mathcal{H}\mathbf{f}$, and ϵ is a pre-selected, positive parameter for accommodating inconsistencies between measured data $\mathbf{g}$ and imaging model $\mathcal{H}\mathbf{f}$. The optimization program in Eq. (2) includes no positivity constraint, because real data used in the study contain negative values as a result of the specific method that corrects for physical factors.

C. Optimization-based algorithm

We use the ASD-POCS algorithm that has been developed previously to solve the optimization program in Eq. (2). The algorithm uses alternatively the ASD to lower the image TV and the POCS to reduce the data divergence in Eq. (3). A necessary convergence condition was obtained for the ASD-POCS algorithm when Eq. (2) contains an additional positivity constraint. In the work, we derive a similar necessary condition on the convergence of the ASD-POCS algorithm as it is applied to solving the optimization program in Eq. (2) in which no positivity constraint is imposed: If the ASD-POCS algorithm converges, parameter $c(\mathbf{f})$ that can be calculated at any given iteration must satisfy

$$c(\mathbf{f}) = -1, \tag{4}$$

where

$$\begin{aligned} c(\mathbf{f}) &= \frac{\mathbf{d}_{\text{TV}} \cdot \mathbf{d}_{\text{D}}}{|\mathbf{d}_{\text{TV}}||\mathbf{d}_{\text{D}}|} \\ \mathbf{d}_{\text{TV}} &= \bigtriangledown_{\mathbf{f}} \parallel \mathbf{f} \parallel_{\text{TV}} . \\ \mathbf{d}_{\text{D}} &= \bigtriangledown_{\mathbf{f}} D^2(\mathbf{f}) \end{aligned} \tag{5}$$

Other methods than the POCS can be used to reduce the value of $c(\mathbf{f})$ to -1. Previous studies suggest that the ASD-POCS reconstructions at iterations with $-1 < c(\mathbf{f}) < -0.5$ show little visual differences.

III. MATERIALS

A. CT imaging system

In the work, we focus on image reconstruction from data collected with a Toshiba 320-slice diagnostic CT scanner from swine and patient. In the scanner, the distance between the X-ray source and the center of rotation is 60 cm; the detector consists of 320 rows of detector bins, each of the 320 rows composes 896 bins and forms a fan angle of $49.2°$, thus yielding a field of view of ~50 cm within a transverse plane. Data are collected at a gantry-rotation speed that can be pre-selected in the range of 0.3 to 0.5 sec/per rotation

B. Data acquisition

We have performed real-data studies in which swine and patient data were collected at 1200 views over 2π by using the Toshiba 320-slice diagnostic scanner. In the swine study, the animal was scanned with X-ray energy of 100 kV and current at 275 mAs, whereas in the patient study, the subject was scanned with X-ray energy of 135 kV and current at 100 mAs. The projection data were corrected for scatter and beam-hardening by use of Toshiba's standard method installed on the scanner. We refer to the 1200-view data as the full data. From each of the full data sets, we also extracted sparse-view data sets at 600 and 240 views uniformly distributed over 2π, and then perform image reconstructions from the extracted sparse-view data sets.

C. Inverse-crime studies

In an attempt to validate the modified ASD-POCS algorithm and its implementation, we first carried out an inverse-crime study in which simulation data were generated by use of a system matrix from a discrete image and images were reconstructed by use of the same system matrix in the ASD-POCS algorithm. In the study, data are completely consistent with the imaging model, and the same system matrix was used for data generation and image reconstruction. Therefore, it provides a validation of the algorithms under ideal conditions. We have used imaging parameters mimicking the Toshiba 320-slice diagnostic CT scanner to generate simulated, full data at 1200 views from discrete images. From the full data, we then extracted sparse-view data at 600 and 240 views uniformly distributed over 2π. We then performed reconstructions from full and sparse-view data generated. Results of the study, which are not included in the abstract, validate that the ASD-POCS algorithm described above can solve the optimization program in Eq. (2), and they will be reported at the conference.

IV. RESULTS

In real-data studies below, images are reconstructed from the acquired full data sets and extracted sparse-view data sets; and the swine images are displayed on a 620×620 array with a pixel size of 0.065 cm, whereas the patient images are displayed on a 500×500 array with a pixel size of 0.064 cm.

A. Reconstruction from 1200-view data (full data)

We first reconstructed a swine image by using our FDK-based algorithm from full data, and display in Fig. 1a the reconstruction within a transverse slice, and refer to the image as the *FDK-reference* image. Two ROIs, enclosed by solid white lines in Fig. 1a, are chosen for zoomed-in examination of subtle, low-contrast details. In Fig. 1b, we show the swine image within the same transverse slice reconstructed by use of the ASD-POCS algorithm from full data. The images within the ROI indicated in Fig. 1a are shown in a zoomed-in view in Fig. 2. Examination of the images suggests that although the overall visual quality of the ASD-POCS reconstruction is comparable to that of the FDK-reference image, the former appears to suggest slightly improved contrast and reduced background noise. Closer inspection of them in the zoomed-in views further reveals that the ASD-POCS reconstructions generally have soft-tissue boundaries better defined, potentially leading to easier delineations of spiculated structures from the background, than the FDK-reference images.

We also carried out ASD-POCS reconstructions from full data of a patient and display them in Fig. 3, along with the corresponding FDK-reference images, within a transverse slice. Again, we select three ROIs, labeled with A, B, and C in Fig. 3a and show three ROIs in a zoomed-in view in Fig. 4. Observations similar to those for swine-data reconstructions can be made. The overall visual appearance of the FDK-reference and ASD-POCS reconstructions are comparable. However, careful inspection of reconstruction details in zoomed-in views reveals that the ASD-POCS algorithm seems to be able to yield images with finer texture and less background noise than the FDK-based algorithm.

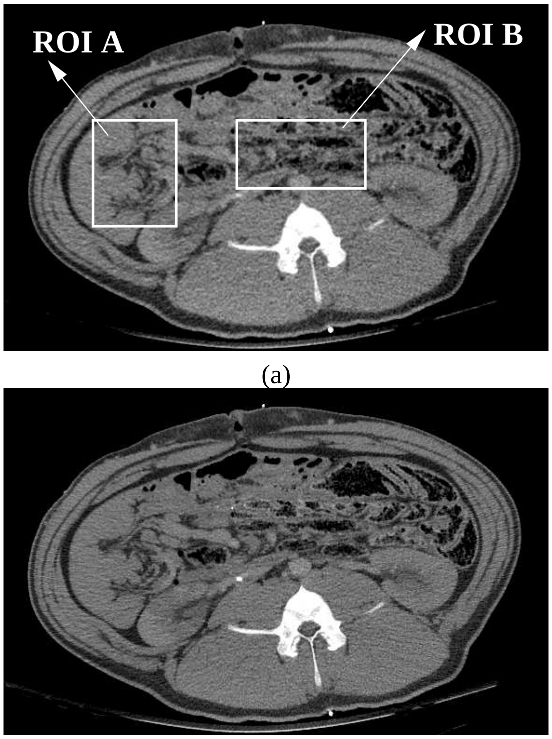

(a)

(b)

Figure 1. Swine images within a transverse slice reconstructed from 1200-view data by use of the FDK-based (a) and ASD-POCS (b) algorithms. A narrow display window [-8.5, 16] is used. ROIs A and B are enclosed in solid white lines.

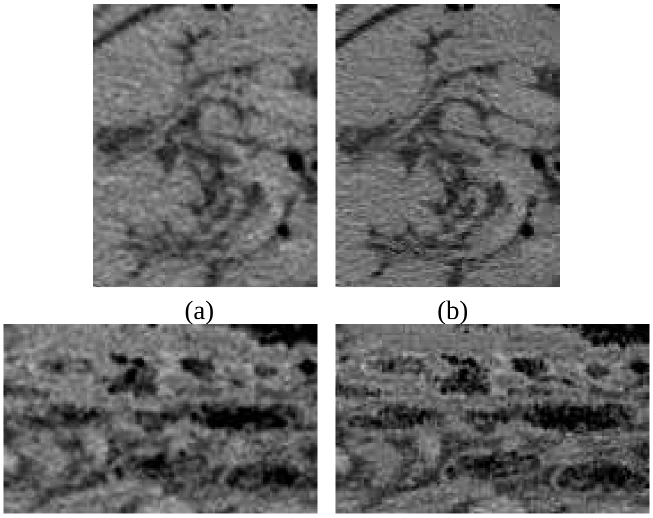

(a) (b)

(c) (d)

Figure 2. Swine images, displayed in a zoomed-in view, in ROI A (upper row) and ROI B (lower row), reconstructed from 1200-view data by use of the FDK-based (left) and ASD-POCS (right) algorithms. A narrow display window [-8.5, 16] is used.

B. Reconstruction from 600-view data

We performed ASD-POCS reconstructions from the 600-view data sets extracted from the respective full data sets of swine and patient. In an attempt to demonstrate the effect of angular undersampling, an image was also reconstructed by

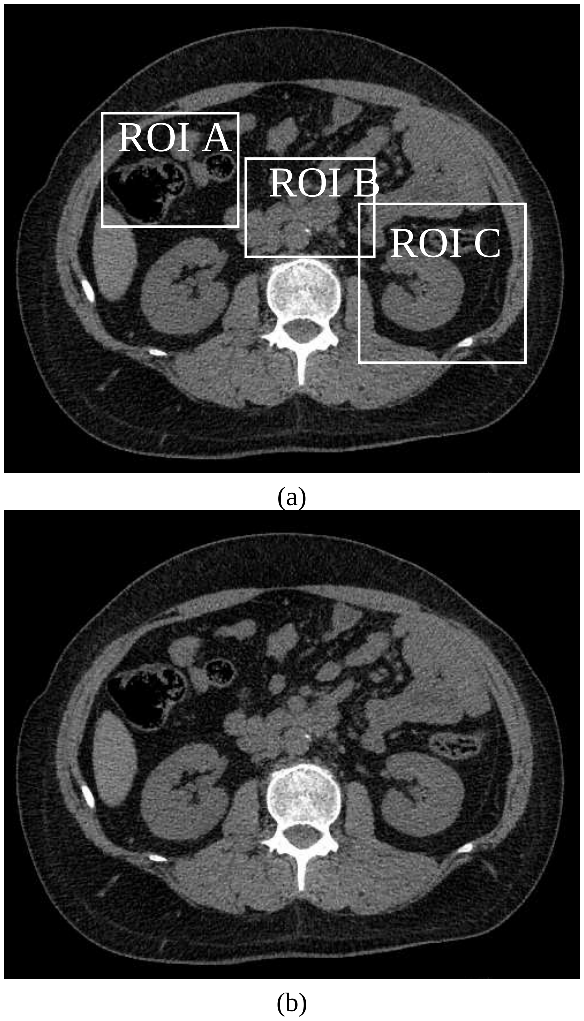

(a)

(b)

Figure 3. Patient images within a transverse slice reconstructed from 1200-view data by use of the FDK-based (a) and ASD-POCS (b) algorithms. A narrow display window [-6, 13] is used. ROIs A, B, and C are enclosed in solid white lines.

use of our FDK-based algorithm. We show reconstructions within a transverse slice and within ROIs in a zoomed-in view, respectively, in Figs. 5 and 6 from swine data and in Figs. 7 and 8 from patient data. Based upon the reconstructions, observations can be made that noise and streak artifact result in visible quality degradation in FDK-based reconstructions. However, the reduction of view numbers from 1200 to 600 appears to have a less noticeable impact on ASD-POCS reconstructions, as low-contrast soft tissues remain better preserved than FDK-based reconstructions. In particular, the high contrast, but small, structure in ROI B in the patient image can visually be somewhat challenging to pinpoint in the FDK-based reconstruction due to ambiguity of the surrounding noisy background; however, they can be identified in the ASD-POCS reconstruction. The overall image quality and recovery of subtle structures in ROIs suggest that the 600-view ASD-POCS reconstruction is comparable to the FDK-reference image.

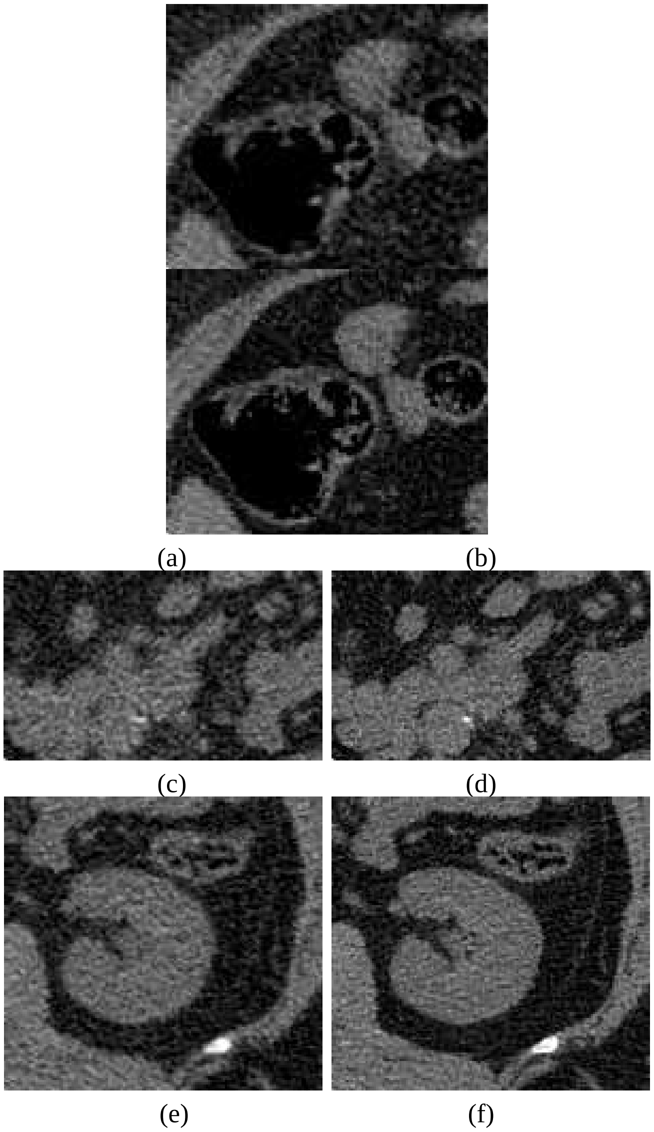

(a) (b)

(c) (d)

(e) (f)

Figure 4. Patient images, displayed in a zoomed-in view, in ROI A (top row) ROI B (middle row), and ROI C (bottom row), reconstructed from 1200-view data by use of the FDK-based (left) and ASD-POCS (right) algorithms. A narrow display window [-6, 13] is used.

C. Reconstruction from 240-view data

Finally, we reconstructed swine and patient images by use of the ASD-POCS algorithm from the 240-view data sets extracted from the corresponding full data sets. Again, for the purpose of demonstrating the impact of angular undersampling, an image was also reconstructed by use of our FDK-based algorithm. We show both ASD-POCS reconstructions within a transverse slice and within ROIs in a zoomed-in view, respectively, in Figs. 9 and 10 from swine data and in Figs. 11 and 12 from patient data. Comparison of the reconstructions in Figs. 9-12 to their corresponding full-data reconstructions in Figs. 1-4 clearly reveals that both FDK-based and ASD-POCS reconstructions are visibly degraded by substantial data reduction. However, an increased difference in reconstruction performance can be observed

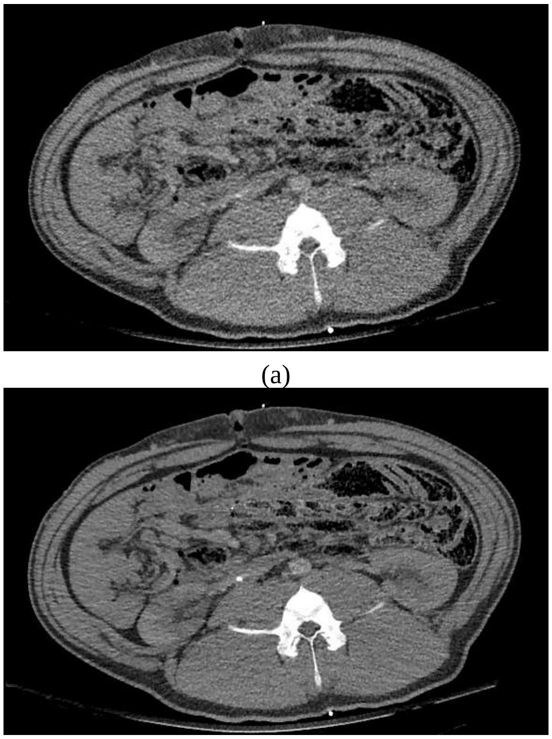
(a)

(b)

Figure 5. Swine images within a transverse slice reconstructed from 600-view data by use of the FDK-based (a) and ASD-POCS (b) algorithms. A narrow display window [-8.5, 16] is used.

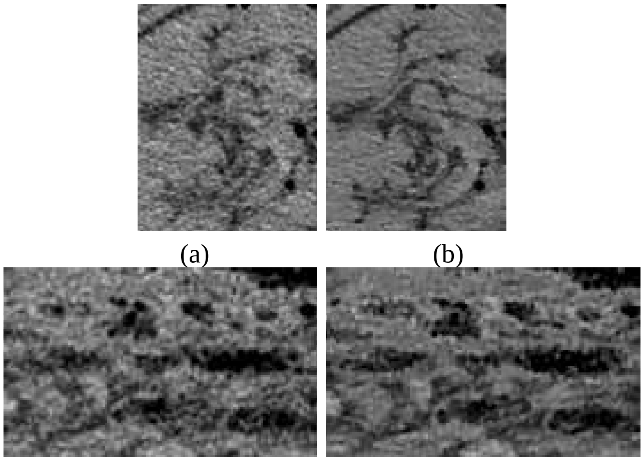
(a) (b)

(c) (d)

Figure 6. Swine images, displayed in a zoomed-in view, in ROI A (upper row) and ROI B (lower row), reconstructed from 600-view data by use of the FDK-based (left) and ASD-POCS (right) algorithms. A narrow display window [-8.5, 16] is used.

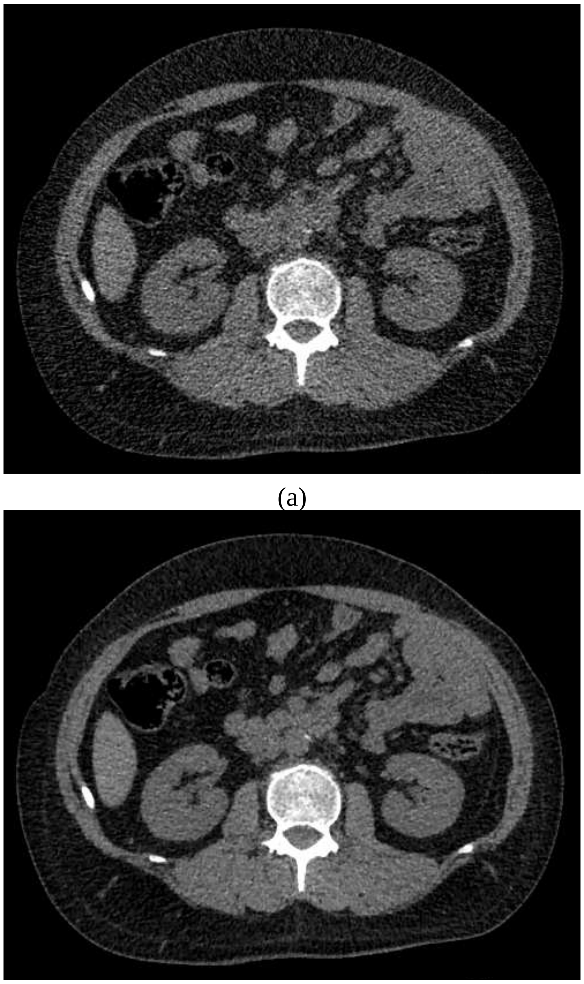
(a)

(b)

Figure 7. Patient images within a transverse slice reconstructed from 600-view data by use of the FDK-based (a) and ASD-POCS (b) algorithms. A soft-tissue display window of [-6, 13] is used.

between the FDK-based and ASD-POCS algorithms: the FDK-based reconstructions suffer from noise and streak artifacts that distort soft tissue structures, whereas the ASD-POCS reconstructions appear to show suppressed noise and mitigated streak artifact. It should be pointed out that it remains unclear whether 240-view ASD-POCS reconstructions would be of some utility in making a clinical diagnosis decision.

V. DISCUSSIONS

In this work, we have investigated the application of the ASD-POCS algorithm to reconstructing images from full- and sparse-view data collected in swine and patient studies with a Toshiba 320-slice CT scanner. We evaluated the ASD-POCS reconstruction from full data as well as sparse-view data sets containing 600 and 240 views and compare them to those obtained with our FDK-based algorithm currently used in practical applications. Results suggest that ASD-POCS reconstructions from 1200 and 600 views are comparable to, or better than, FDK-based reconstructions. The 240-view

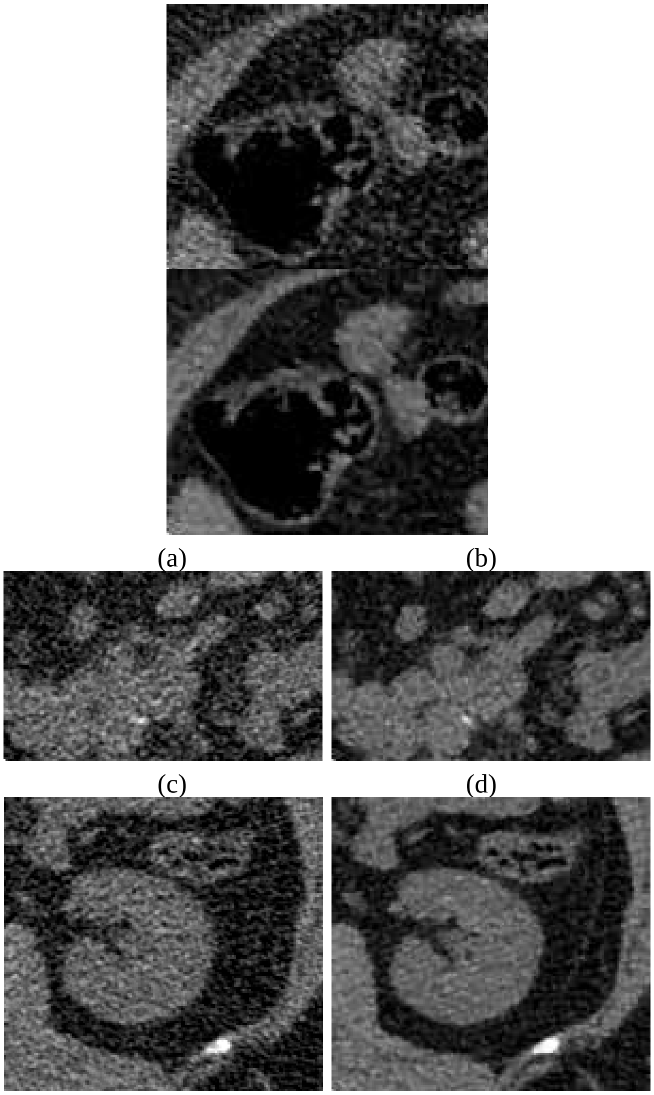
(a) (b)

(c) (d)

(e) (f)

Figure 8. Patient images, displayed in a zoomed-in view, in ROI A (top row), ROI B (middle row), and ROI C (bottom row), reconstructed from 600-view data by use of the FDK-based (left) and ASD-POCS (right) algorithms. A narrow display window [-6, 13] is used.

ASD-POCS reconstructions, while visibly degraded, shows reduced artifacts than observed in the corresponding FDK-based reconstructions. The study suggests that appropriately designed optimization-based algorithms may be used for potentially improving diagnostic image quality. Further research and development of these algorithms may enable and potentially engender novel CT system design and data-acquisition configurations of practical utility.

VI. ACKNOWLEDGMENTS

This work was supported in part by the National Institutes of Health (NIH) under Grants CA120540, EB000225 and CA158446. The work of X. Han was supported in part by the Department of Defense (DoD) Predoctoral training Grants PC094510.

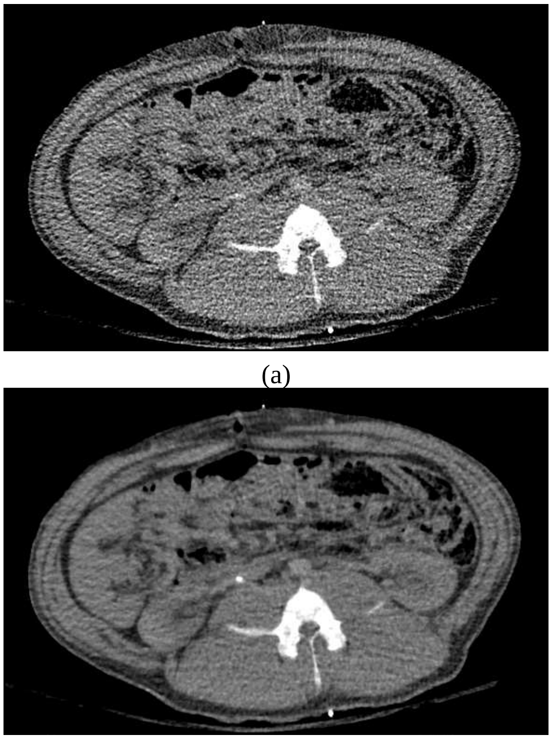
(a)

(b)

Figure 9. Swine images within a transverse slice reconstructed from 240-view data by use of the FDK-based (a) and ASD-POCS (b) algorithms. A narrow display window [-8.5, 16] is used.

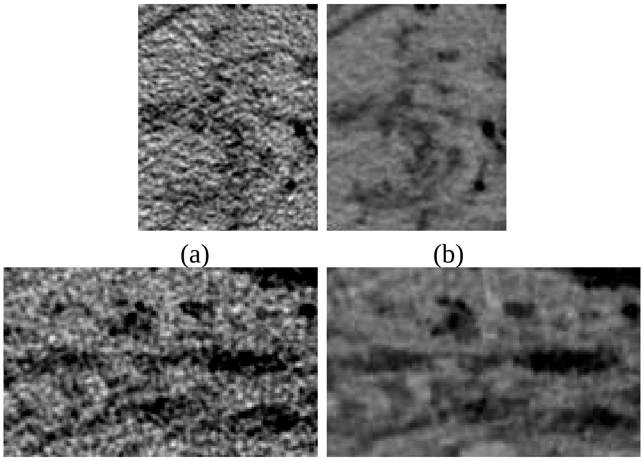
(a) (b)

(c) (d)

Figure 10. Swine images, displayed in a zoomed-in view, in ROI A (upper row) and ROI B (lower row), reconstructed from 240-view data by use of the FDK-based (left) and ASD-POCS (right) algorithms. A narrow display window [-8.5, 16] is used.

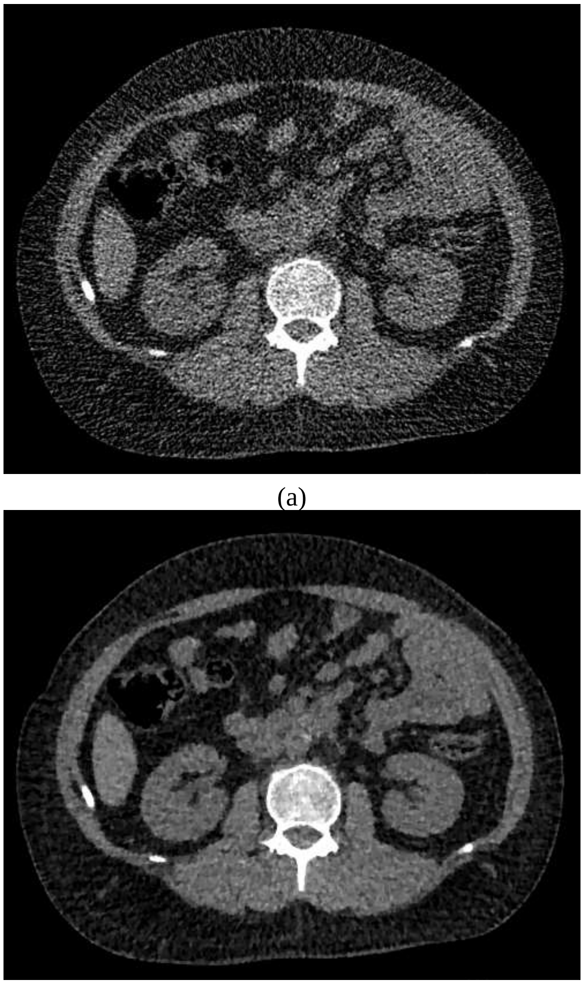
(a)

(b)

Figure 11. Patient images within a transverse slice reconstructed from 240-view data by use of the FDK-based (a) and ASD-POCS (b) algorithms. A narrow display window [-6, 13] is used.

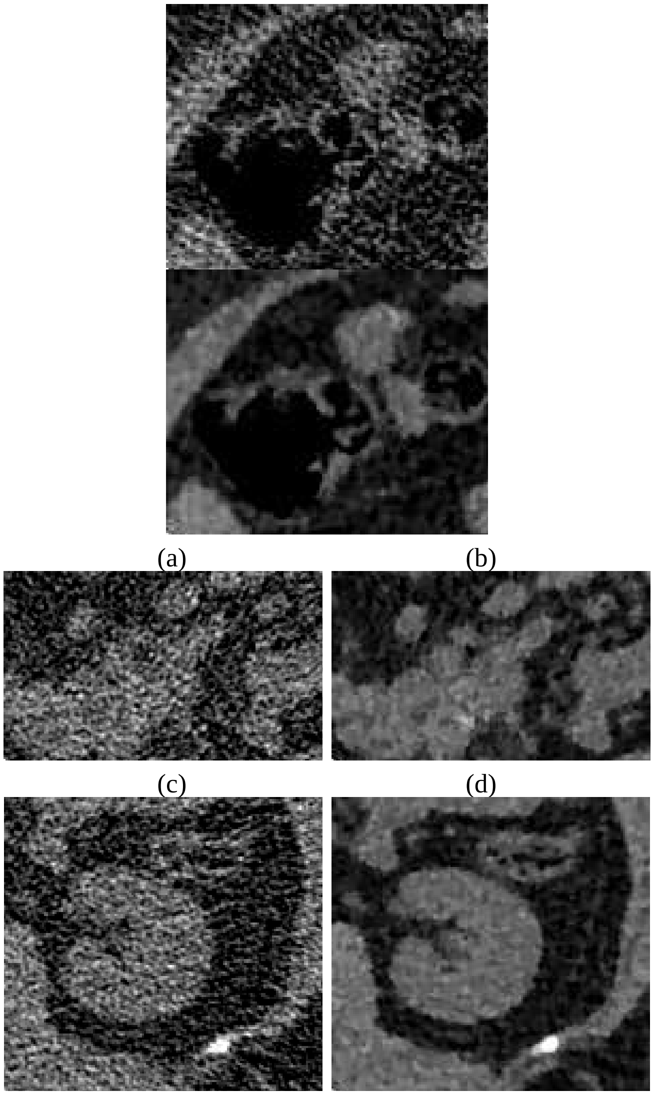
(a) (b)

(c) (d)

(e) (f)

Figure 12. Patient images, displayed in a zoomed-in view, in ROI A (top row), ROI B (middle row), and ROI C (bottom row), reconstructed from 240-view data by use of the FDK-based (left) and ASD-POCS (right) algorithms. A narrow display window [-6, 13] is used.

Total Variation Regularized Weighted Simultaneous Algebraic Reconstruction Technique – A Parallel Scheme

Daxin Shi, Alexander A. Zamyatin and Mihail P. Dinu

Abstract–**In this work, we propose a total variation (TV) regularized weighted simultaneous algebraic reconstruction technique (wSART) for the conventional x-ray CT image reconstruction problem. The proposed approach employs both the weighted property of wSART and the limited view reconstruction capability of TV-regulated algorithm. Compared to the conventional TV minimization reconstruction algorithm where projection on convex sets step and TV minimization step are in sequential, our proposed reconstruction algorithm assumes a parallel structure of these two procedures. As a consequence, the parallel structure of our algorithm enables its convenient implementation in parallel computing devices such as graphics processing units. We validate our approach by using physical phantom data collected from Aquilion ONE^{TM} CT scanner (Toshiba America Medical Systems, Tustin, CA, USA).**

I. INTRODUCTION

ONE of the advantages of the conventional TV regulated iterative reconstruction algorithms [1] [2] proposed for the x-ray CT imaging problem is to reduce the dose delivered to patients by reconstructing clinically useful images from fewer projection views than which are needed by the classic filtered backprojection (FBP) reconstruction algorithms. However, in some imaging cases, both statistical and deterministic weighting information are important to improve image quality and/or mitigate imaging artifacts. It is not yet clearly revealed how to build the statistical and/or deterministic weighting information in the conventional TV minimization iterative reconstruction algorithm. Recently, we proposed a weighted simultaneous algebraic reconstruction technique (wSART) for the conventional x-ray imaging problem [3]. We have demonstrated that wSART can be employed to mitigate the photon starving induced streaking artifacts. We have also demonstrated that the deterministic weighting scheme can be easily built into our wSART algorithm [3]. It is natural to integrate the wSART algorithm into the framework of TV minimization iterative reconstruction algorithm. We will show in this paper that the combination of wSART and TV minimization improves image quality.

The basic structure of the conventional TV regulated algorithms contains two steps [1] [2]. The first step is so-called projection on convex sets (POCS) step. The second step is the TV minimization procedure. These two steps alternate and form the main iterations of the TV minimization algorithm. It is easily seen that these two main steps are in sequential where the POCS step is followed by the TV minimization step. An improved TV-regulated iterative reconstruction algorithm has been proposed in [4] where a linear combination of the POCS image and TV image from the n^{th} iteration was formed to be the seed for the $n+1^{\text{st}}$ iteration. It was demonstrated in [4] that the combination scheme can produce images of better image quality. However, in the improved scheme [4], the basic data flow chart was not changed, i.e., the POCS and TV minimization steps are still in sequential (POCS followed by TV minimization). The sequential structure of the algorithm can potentially hinder the computational speed and impair taking advantages of currently available parallel computing devices, such as GPU's. In this paper, we propose a new scheme which contains a parallel structure of wSART and TV minimization steps. Due to its parallel structure, our proposed algorithm can be easily implemented with parallel computing devices.

II. PARALLEL TOTAL VARIATION REGULATED WEIGHTED SIMULTANEOUS ALGEBREIC RECONSTRUCTION TECHNIQUE

In this section, we propose the TV regulated weighted simultaneous algebraic reconstruction technique with a parallel structure for the conventional x-ray CT imaging problem.

In the conventional x-ray CT imaging problem, an image volume was reconstructed from a set of projection data usually uniformly sampled along the view direction. Unlike the classic analytic reconstruction method such as the FBP algorithm which models the projection procedure as the x-ray transform, iterative reconstruction algorithms in general model the projection procedure as a system of linear equations [5]

$$Ax = p\,, \tag{1}$$

where the system matrix A mimics the x-ray projection procedure whose entries are denoted by $\{a_{i,j}\}$. One of the simplest ways to compute the matrix A might be using Siddon's method [6]. The vector p in Eqn. (1) denotes the projection data arranged in a column vector $\{p_i\}$, where p_i is the readout of the i^{th} detector bin. The quantity x in Eqn. (1) is the unknown image. The imaging task in iterative reconstruction algorithm is to invert Eqn. (1) to produce the desired image volume x. To simplify our description, we consider only the two dimensional (2D) imaging problem hereafter. Also the image x will be denoted by both a column

---

Manuscript received Jan 25, 2012.

A. A. Zamyatin, D. Shi and M. Dinu are with Toshiba Medical Research Institute of USA, Inc., 706 N. Deerpath Dr., Vernon Hills, IL, 60061, USA. (e-mail: {azamyatin, dshi, mdinu}@tmriusa.com).

vector whose elements are represented by {x_i} and a 2D matrix whose elements are represented by {$x_{i,j}$} in different context.

There exist many algorithms to invert Eqn. (1) such as the algebraic reconstruction technique (ART) and SART [5]. To employ statistical information, a weighted ART scheme was proposed in [7] for the PET imaging problem, but its performance on the x-ray CT imaging problem was not evaluated. We had proposed a empirical wSART algorithm in [3] to accommodate the statistical weighting scheme. The wSART algorithm employs the following form,

$$x_j^{(k+1)} = x_j^{(k)} + \lambda^{(k)} \frac{\sum_i a_{i,j} w_i \left(\frac{p_i - \sum_j a_{i,j} x_j^{(k)}}{\sum_j a_{i,j}} \right)}{\sum_i a_{i,j} w_i} \quad , \qquad (2)$$

where the weights w_i was created in a ray by ray manner and the parameter $\lambda^{(k)}$ is the usual relaxation parameter. It should be noted that when the weights w_i are constant, the wSART reduces to the conventional SART. It should be noted also that the wSART algorithm can accommodate both statistic and deterministic weighting schemes. A good example of combining the statistic information and deterministic information to mitigate CT image artifacts can be found in [8].

The TV regulated iterative reconstruction algorithm also tries to solve the following minimization problem,

$$\min \mathrm{U} = \sum_{i,j} \sqrt{\left(x_{i+1,j} - x_{i,j}\right)^2 + \left(x_{i,j+1} - x_{i,j}\right)^2} \qquad (3)$$

where the gradient descent algorithm was simply applied to solve the minimization algorithm. The conventional TV regulated iterative reconstruction algorithm contains a sequential structure in which the TV minimization step follows the POCS method [1] [2]. We could follow the same framework in which our wSART algorithm follow the TV minimization step. In [4], a modified structure was proposed which combines the output of the POCS step and the output of TV minimization to form a final image for one iteration. It was demonstrated that the combination scheme can improve image quality. However, the structure is still in sequential which could potentially impair the parallel computing ability of currently available parallel computing devices. To avoid the disadvantage of the sequential scheme, we propose a parallel reconstruction algorithm which is schematically described in Fig. 1.

In Fig. 1, the image of the *n-1*st iteration, $x^{(n-1)}$, goes through the wSART module and TV minimization module in parallel. The output of wSART module, $x_{SART}^{(n)}$, is linearly combined with $x^{(n-1)}$ to form an intermediate image $x_S^{(n)}$ with the coefficient β. Output of the TV branch, $x_{REG}^{(n)}$, is also combined with the input image $x^{(n-1)}$ with the coefficient α to form another intermediate image $x_R^{(n)}$. The two intermediate images, $x_S^{(n)}$ and $x_R^{(n)}$ are again combined linearly via the coefficient λ to form the final output, $x^{(n)}$ of iteration *n*.

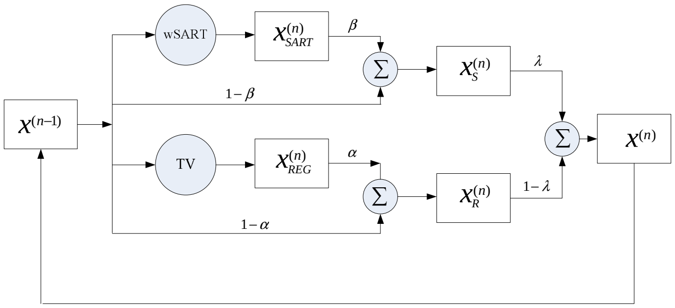

Fig. 1. A schematic description of the proposed parallel TV regulated weighted simultaneous reconstruction technique for the conventional x-ray CT imaging problem. The image in *n-1*st iteration goes through the wSART module and the TV module in parallel. A combination of the output of these two modules forms the final image of one iteration. See the text for detailed description.

In the actual implementation, the wSART module was implemented in an ordered subset version to speed up the convergence of wSART, i.e., the projection data were partitioned into different sets; within each subset the wSART was implemented. The simple gradient descent algorithm was employed to solve the TV minimization problem. In the data flow, we do not form the intermediate images $x_S^{(n)}$ or $x_R^{(n)}$. In fact, the output of the *n*th iteration and the *n-1*st iteration assumes the following relation,

$$\begin{aligned} x^{(n)} = {} & \lambda[(1-\beta)\, x^{(n-1)} + \beta\, x_{SART}^{(n)}] + \\ & (1-\lambda)[\alpha\, x_{REG}^{(n)} + (1-\alpha)\, x^{(n-1)}] \end{aligned} \; . \qquad (4)$$

There is no need to compute the two intermediate images $x_S^{(n)}$ or $x_R^{(n)}$. In Eqn. (4), the parameter λ serves as a noise-resolution trade-off. In general, the larger, the value of λ is, sharper and noisier is the final image. The other two parameters α and β are computed in the fly whose are enforced in [0, 1]. To compute the combination coefficients α and β, we estimate the variances of the images $x^{(n-1)}$, $x_{SART}^{(n)}$ and $x_{REG}^{(n)}$. Let $\mathrm{Var}\{x^{(n-1)}\}$, $\mathrm{Var}\{x_{SART}^{(n)}\}$ and $\mathrm{Var}\{x_{REG}^{(n)}\}$ denote the estimated variance of the images $x^{(n-1)}$, $x_{SART}^{(n)}$ and $x_{REG}^{(n)}$, respectively. We compute the two parameters α and β as follow,

$$\alpha = \frac{\mathrm{Var}\{x^{(n-1)}\}}{\mathrm{Var}\{x^{(n-1)}\} + \mathrm{Var}\{x_{REG}^{(n)}\}} \quad , \qquad (5)$$

$$\beta = \frac{\mathrm{Var}\{x^{(n-1)}\}}{\mathrm{Var}\{x^{(n-1)}\} + \mathrm{Var}\{x_{SART}^{(n)}\}} \quad . \qquad (6)$$

It can be seen from Eqns. (5) and (6) that the values of α and β are confined within the range [0, 1].

III. NUMERICAL RESULTS

The proposed parallel TV regulated wSART algorithm was implemented with a parallel computing device GPU. In this section, we validate our proposed reconstruction scheme by showing examples using physical phantom data collected from a Toshiba Aquilion ONE scanner. We demonstrate that our parallel TV regulated wSART inherits the few view reconstruction ability of the conventional TV minimization algorithm. We also demonstrate that the parallel TV regulated wSART algorithm can improve image quality compared to our previously proposed wSART algorithm due to the TV regularizer.

A. *Reconstructed Images from Few Projection Views*

In this section, we show a set of images were reconstructed from physical phantom data. Images were reconstructed from the full number of views by use of both FBP algorithm and the proposed TV regulated wSART algorithm. Results are shown in Fig. 2 (a) and (b), respectively. The projection data were then uniformly down sampled by a factor of 3 and 5 respectively. The reconstructed images from the down sampled projection data are shown in Fig. 2 (c) and (d), respectively. Our results showed that even only one fifth of the full number of projection views were employed for the reconstruction, an image of reasonably good quality can be produced by use of our proposed algorithm.

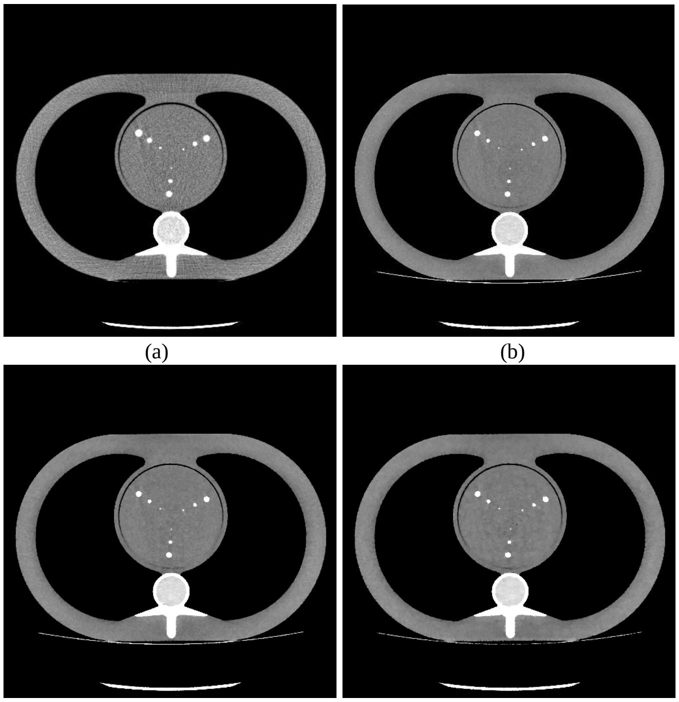

Fig. 2. (a) Image reconstructed by use of the classic FBP algorithm from full number of views. (b) Image reconstructed by use of the proposed reconstruction algorithm from full number of views. (c) Image reconstructed by use of proposed algorithm from one third of the full number of views. (d) Image reconstructed by use of the proposed reconstruction algorithm from one fifth of the full number of views.

B. *Reconstructed Images from Shoulder Data*

It is well known that photon starvation often happens when imaging shoulder. The resulting phenomenon is the streaking artifacts in the reconstructed images. We had demonstrated [3] that the streaking artifacts can be greatly reduced by use of our wSART algorithm. In this section we show that with the TV regularization procedure the image quality can be improved. Fig. 3 (a) shows the reconstructed image by use of the conventional SART algorithm which is contaminated by streaking artifacts as expected due to the photon starvation problem. Fig. 3 (b) shows that the streaking artifacts can be greatly suppressed by use of the wSART algorithm. Fig. 3 (c) shows the image reconstructed by use our proposed parallel TV regulated wSART. One can see that noise in Fig. 3 (c) is improved compared to Fig. 3 (b).

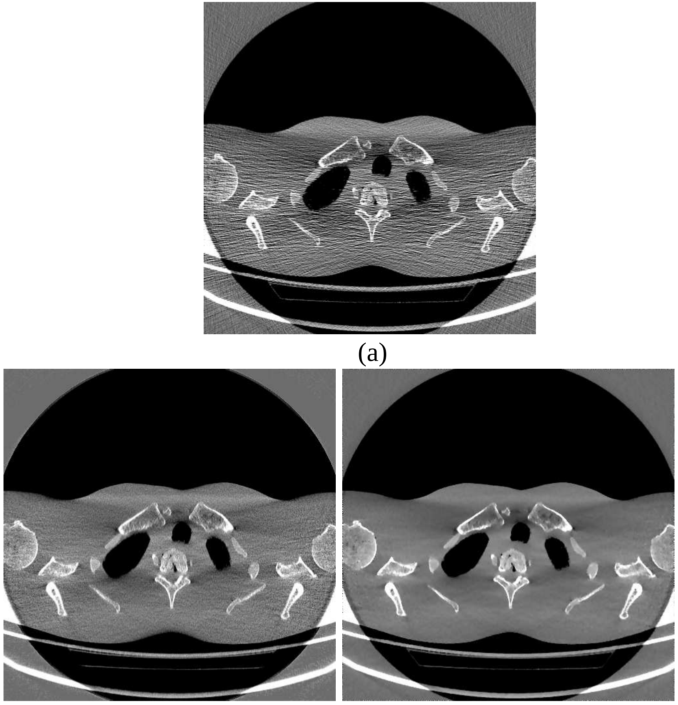

Fig. 3. (a) Image reconstructed by use of the conventional SART. (b) Image reconstructed by use of wSART. (c) Image reconstructed by use of proposed parallel TV regulated wSART algorithm.

Fig. 4 shows the profiles through the central row of Fig. 3 (b) and (c). One can see that the ripples in the wSART image are diminished in Fig. 3 (c) due to the TV regularization procedure.

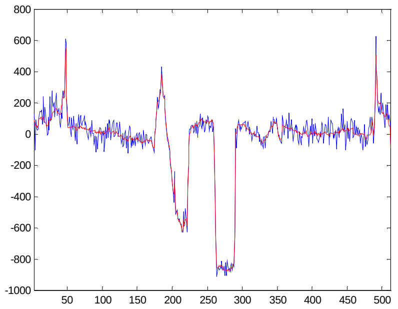

Fig. 4. The profiles through the central row of Fig. 3 (b) and (c). The horizontal axis is the number of pixels and vertical axis is the value of pixels. The blue and red curves are the plots of the wSART and TV regulated wSART images, respectively..

IV. SUMMARY

In this work, we have proposed a parallel TV regulated wSART reconstruction algorithm. The wSART algorithm which accommodates both statistic and deterministic weighting information has been integrated into the TV minimization reconstruction framework. Compared to the conventional TV minimization algorithm, we proposed a parallel structure for the main loop in which the POCS and TV minimization steps are processed in parallel instead of in sequential. This parallel structure facilitates the full utility of currently available parallel computing devices. We demonstrated that our proposed algorithm inherits the few view reconstruction ability of the conventional TV minimization algorithm. We demonstrated also that compared to our previously proposed wSART algorithm, the TV regulated wSART algorithm can improve the image quality induced by photon starvation.

ACKNOWLEDGMENT

The authors thank Mr. S. Nakanishi at TMSC for collecting the real phantom data for this study.

REFERENCES

[1] E. Sidky, C. Kao and X. Pan, “Accurate image reconstruction from few-views and limited-angle data in divergent-beam CT,” *J. X-ray Sci. & Tech.*, vol. 14, pp. 119-139, 2006.
[2] E. Sidy and X. Pan, “Image reconstruction in circular cone-beam computed tomography by constrained, total-variation minimization,” Phys. Med. Biol., vol. 53, pp. 4777-4807, 2008.
[3] D. Shi, Y. Zou and A. Zamyatin, “Weighted Simultaneous Algebraic Reconstruction Technique,” 11th International Meeting on Fully Three-Dimensional Image Reconstruction in Radiology and Nuclear Medicine, pp. 157, 2011.
[4] L. Ritschl, F. Bergner, C. Fleischmann and M. Kachelriess, “Improved total variation-based CT image reconstruction applied to clinical data,” Phys. Med. Biol., vol. 56, pp. 1545-1561, 2011.
[5] A. C. Kak and M. Slaney, “*Principles of Computerized Tomographic Imaging*”, IEEE Press. 1988**.**
[6] R. L. Siddon, “Fast calculation of the exact radiological path for a three-dimensional CT array,” *Med. Phys*., vol. 12 pp. 252-255, 1985.
[7] T. Kohler, R. Proksa and T. Nielsen, “SNR-weighted ART applied to transmission tomography”, *IEEE Nuclear Science Symposium Conference Record*, vol. 4, 2003, pp. 2739–2742.
[8] A. Zamyatin, D. Shi and M. Dinu, “Extension of Axial Coverage and Artifact Reduction in Iterative Reconstruction in Computed Tomography,”, IEEE MIC 2011, MIC21.S-102.

A Low Dose Simulation Tool

Stanislav Žabić[1], Qiu Wang[2], Kevin M. Brown[1]

Abstract—**This paper introduces a new algorithm for simulation of low dose computed tomography (CT) scans, starting from a higher dose scan. We derive and analyze a monochromatic noise addition model based on statistical properties of an X-ray in a CT scan. The model is verified against simulations and compared to the other models found in literature.**

I. INTRODUCTION

Motivation for creating a tool which simulates low dose scans from a high dose scan is at least two-fold. A tool that accurately simulates low dose scans would be useful in clinical research to determine how low a user can go with the dose without loosing the relevant diagnostic information in the volume without multiple scanning. Another application of this tool could be in the research of algorithms that promise image quality in low dose scans equivalent to the higher dose scans. These promises are sometimes made even for ultra low dose scans, which calls for an extremely accurate dose simulation tool. Modern task based image quality metrics require multiple noise realizations. A low dose simulation tool would make such metrics possible also for the clinical data.

II. STATE OF THE ART

In the review of literature, we have identified several different approaches of simulating low dose scans from a high dose scan. Some approaches [1], [2], [3], [4] involve combining the higher current data with Poisson, Gaussian or a combination of Poisson and Gaussian noise either to the measured intensity signal or to the line integrals (negative logarithm of the intensity signal).

The earliest approach of adding more noise to real scans, dates back to 1997 and the paper of Mayo et. al. [2]. The same group of authors published details of this simulation algorithm five years later in a paper from a group headlined by Frush [1]. In their work, Gaussian noise is added to the intensity data, with the removed dark current offset. Another approach was published shortly afterwards, in 2003 by Amir et. al. [3]. In their work, Gaussian noise is realized according to the line integral sinogram. The Gaussian noise is then reconstructed separately and added to the higher current volume in the image space.

A very valuable volume of work when it comes to low dose CT simulation was performed by Bruce Whiting's group. Whiting's papers in 2002 [5] and 2006 [6] provide a detailed characterization of the signal statistics of an X-ray in CT and it is a foundation for a model developed and validated in the 2005-2009 period [7], [8]. Like in Frush's work [1], Whiting's group adds noise to the intensity data with the removed dark current offset, but it also takes the electronic noise in consideration, which Frush's group does not do.

One of the most recent efforts in low dose simulation was in 2010. Benson and De Man [4] add a form of Poisson noise realization to the intensity signal. In addition, like Whiting's group [7], [8], they stress the importance of adding the detector noise into the model which they simulate in the form of a Gaussian noise realization.

Let us also mention several other relevant low dose simulation tools, which will not be considered in this paper for various reasons. For instance, in 2010, Wang and Pelc [9] apply a model very similar to Frush's [1]. The novelty of this algorithm is that it utilizes dual energy data with a goal to simulate data with varous tube voltages, which is out of the scope of our research since our low dose simulations have the same energy as the higher dose inputs. Also, in 2004 Sennst et. al. [10] reported on a noise addition tool as a part of the Siemens' *syngo Explorer* package. Unfortunately, to our knowledge, no theoretical support is provided to explain finer details of the algorithm. Lastly, in 2011 Nakashini [11] et. al. presented another interesting approach in which system noise model is determined through a series of experimental measurements.

All state of the art approaches for the single energy simulation have one thing in common: a low dose scan is simulated using a monochromatic model and synthetic noise is added on to a higher dose scan. Our model is different in that it does not add the noise to a higher dose scan, but it simulates a low dose scan as an entirely new noise realization. In addition, all previously published papers on this topic make certain approximations to the realistic noise models that break down for ultra low dose simulations. We will discuss these approximations and provide evidence for our concerns regarding the ultra low dose scans and show that our model is the most accurate one, especially in those conditions.

III. PROBLEM STATEMENT

Suppose a three dimensional object is scanned by acquiring projections on a CT scanner with energy integrating detectors, using the tube current α and a fixed tube voltage. Let N_α be the number of photons emitted from the tube at current α within a given integration period. We will assume that the tube voltage does not vary throughout this

---

[1] Philips Healthcare, [2] Cornell University

paper. According to the Beer's law, the mean number of detected photons along a ray l_i connecting tube source with a detector element through the scanned object μ is:

$$y^\alpha = N_\alpha e^{-l}, \tag{1}$$

where $l = \int_{l_i} \mu \, dl$ is the line integral of the scanned object along ray l_i.

In practice, the value of the mean y^α is not available and we actually record a value which is corrupted by noise. The X-ray detection is a statistical event which has a Poisson distribution. Thus, if we denote by $\mathcal{P}(m)$ a realization of a Poisson noise variable with mean m, the number of photons that arrives at the detector can be written as

$$\hat{y}^\alpha = \mathcal{P}(N_\alpha e^{-l}). \tag{2}$$

Since $\mathrm{Mean}(\hat{y}^\alpha) = y^\alpha = N_\alpha e^{-l}$, and $\hat{y}^\alpha$ is a Poisson realization, we also have

$$y^\alpha = \mathrm{Var}(\hat{y}^\alpha) = N_\alpha e^{-l}.$$

The signal $\hat{y}^\alpha$ then enters the energy integrating detector where it gets converted into a digital reading. Design of a detector can vary from one type of scanner to another and therefore the process and results of conversion of the photons to a digital reading varies. However, we believe that the common practice is very similar among all manufacturers. The signal is multiplied by a gain, which we denote by A, and a constant electronic bias signal is added, which has a noise realization independent of the X-ray event Poisson noise. Assuming that the mean of this bias signal can be measured and subtracted from the signal, we will denote by $\mathcal{D}(c)$ a zero mean realization of the statistical distribution contributed by the detector electronics. Then we can write the complete monochromatic noise model as:

$$\hat{s}^{\alpha,c} = A\mathcal{P}(N_\alpha e^{-l}) + \mathcal{D}(c). \tag{3}$$

Let us mention that this is essentially the same model as the one used in Massoumzadeh et. al [7] and which is justified in Whiting's 2006 paper [6]. The first term represents the influence of the photon statistics, and the second represents the influence of the detector noise.

Now we can precisely state the goal of the low dose simulation. We wish to find a corresponding signal $s^{\beta,c}$ for lower current β, $\beta < \alpha$. In the next section, we derive a solution to this problem when $\mathcal{D}(c) = 0$ and $A = 1$. One can also find the solution for a more realistic case, $\mathcal{D}(c) \neq 0$ and $A > 0$, but we will leave that for a different occasion.

Associated to measurements $\hat{y}^\alpha$ and $\hat{s}^{\alpha,s}$ are the values

$$l^\alpha = -\ln \frac{\hat{y}^\alpha|_+}{N^\alpha}, \qquad l^{\alpha,c} = -\ln \frac{\hat{s}^{\alpha,c}|_+}{AN^\alpha}, \tag{4}$$

which are used for the reconstruction in filtered backprojection algorithms. The symbol $|_+$ means that we replace all values that are less or equal to 0 by a small positive value.

IV. ALGORITHM DERIVATION

Our approach involves finding a value $\hat{y}^{\alpha\to\beta}$ as a function of $\hat{y}^\alpha$, such that the mean and variance of $\hat{y}^{\alpha\to\beta}$ is equal to $N_\beta e^{-l}$, where N_β is the number of photons emitted from the tube at current β within a given integration period. Then we can think of $\hat{y}^{\alpha\to\beta}$ as a realization of the Poisson noise with mean $N_\beta e^{-l}$ and derive the line integral $l^{\alpha\to\beta}$ as $-\ln(\hat{y}^\beta / N_\beta)$.

Let us denote by $\hat{y}_0^\beta$ a Poisson noise realization with mean $\frac{\beta}{\alpha-\beta}\hat{y}^\alpha$:

$$\hat{y}_0^\beta := \mathcal{P}\left(\frac{\beta}{\alpha-\beta}\hat{y}^\alpha\right). \tag{5}$$

We claim that the noisy variable

$$\hat{y}^{\alpha\to\beta} = \frac{\alpha-\beta}{\alpha}\hat{y}_0^\beta$$

has variance and mean equal to $N_\beta e^{-l}$. The only difficult task in proving this claim lies in finding the variance of the variable $\hat{y}_0^\beta$. There we use the *conditional variance identity* [12] (which is also known in probability theory as the *law of total variance* and *variance decomposition formula*), and it states the follwing in this case:

$$\mathrm{Var}(\hat{y}_0^\beta) = \mathrm{Var}\left(\mathrm{Mean}(\hat{y}_0^\beta|\hat{y}^\alpha)\right) + \mathrm{Mean}\left(\mathrm{Var}(\hat{y}_0^\beta|\hat{y}^\alpha)\right).$$

Once each contribution of the sum is calculated, which is not a difficult task, one can calculate the variance of the signal $\hat{y}_0^\beta$ without any approximation. The equation above completely incorporates the covariance of the signal $\hat{y}^\alpha$ into the signal $\hat{y}_0^\beta$. Other parts of the proof of our claim will be presented in a follw up publication where we will have more room for such details.

Given this claim, we can come up with an algorithm that adds noise to the line integrals l^α in order to simulate signal at current β:

1) Determine N_α using air scans
2) Use the result of the calibrated and corrected sinogram l^α of a scan with tube current α, just before it enters the reconstruction algorithm.
3) Unlog l^α to get $\hat{y}^\alpha$,
4) Use a Poisson noise generator (for example in *Numerical Recipes* [13], page 293) to make $\mathcal{P}\left(\frac{\beta}{\alpha-\beta}\hat{y}^\alpha\right)$,
5) Divide the result of 3) by $\frac{\beta}{\alpha-\beta}N_\alpha$,
6) log the result of 4),
7) Save.

Indeed, since N_α and N_β relate to one another as $N_\beta = \frac{\beta}{\alpha}N_\alpha$, we have

$$\frac{\beta}{\alpha-\beta}N_\alpha = \frac{\alpha}{\alpha-\beta}N_\beta.$$

Obviously, the variable $\hat{y}^{\alpha\to\beta}$ is not a Poisson random since it does not take integer values, but its mean and variance are precisely $N_\beta e^{-l}$, which means that its probability mass function agrees with Poisson on the first two moments. Also, the value of the result of this algorithm is $-\ln \frac{\hat{y}^{\alpha\to\beta}}{N^{\beta}}$.

One obstacle is that for β low enough, the result of the step 4) can be zero. In that case, logarithm will not be defined, and to accommodate this, we adopt a strategy when detector happen to count zero, which we believe is commonly used in practice: if the result of the step 4) is zero, it shall be replaced by a small positive value.

V. COMPARISON TO OTHER METHODS

Other works that promise to simulate low dose scans from higher dose scans report a great match of their low dose simulations when compared to the real scans (clinical or those of phantoms). However, we think that the approximations encountered in these methods are not appropriate for ultra low dose simulations, which are important for the research of low dose scanning strategies, be it optimization of the existing protocols or development of new noise reducing algorithms and reconstructions. We will overview these concerns in this section and compare them to our results.

If we assume that no electronic noise is present in the system, method described in Benson and De Man's work [4] attempts to simulate low current (β) scan as

$$\hat{y}_1^{\alpha\to\beta} = \frac{\beta}{\alpha}\hat{y}^{\alpha} + \mathcal{P}_0\left(\frac{\beta\alpha-\beta^2}{\alpha^2}\hat{y}^{\alpha}\right),$$

where

$$\mathcal{P}_0\left(\frac{\beta\alpha-\beta^2}{\alpha^2}\hat{y}^{\alpha}\right) = \mathcal{P}\left(\frac{\beta\alpha-\beta^2}{\alpha^2}\hat{y}^{\alpha}\right) - \frac{\beta\alpha-\beta^2}{\alpha^2}\hat{y}^{\alpha}.$$

In other words, the noise is added to the signal using the Poisson variable from which the mean of that variable is then subtracted. The authors claim that, by approximating the noisy variable $\hat{y}^{\alpha}$ with its mean y^{α}, the variance of $\hat{y}_1^{\alpha\to\beta}$ is $N_{\beta}e^{-l}$. Unfortunately, in ultra low dose situations, it is not easy to justify $y^{\alpha} \approx \hat{y}^{\alpha}$ unless α is sufficiently high since due to the noise, the two variables can differ by a large percent, which is particualry problematic when converting these values to line integrals.

On the other hand, we also have a strategy developed by Frush et. al. [1]. There, the Poisson noise is replaced with noise added to the data using a Gaussian approximation. A high current signal l^{α} is first "unloged" by finding $p^{\alpha} = e^{-l^{\alpha}}$, and then the low current signal is approximated using the following strategy:

$$p^{\alpha\to\beta} = p^{\alpha} + \left(\frac{\alpha-\beta}{\beta}\right)^{1/2}\mathcal{G}_2, \tag{6}$$

where the variance of the added Gaussian noise $\mathcal{G}_2$ is σ_2^2 and is derived as:

$$\sigma_2^2 = \frac{e^{-l^{\alpha}}}{N_{\alpha}}.$$

Similar to the method of Benson and De Man [4], the derivation of the variance σ_2^2 assumes that the noisy signal $\hat{p}^{\alpha}$ approximates the noiseless mean p^{α}, which as we already discussed, can be problematic for as the current α becomes sufficeiently small.

In the work of Amir et. al. [3], the noise is added to the line integral l^{α} (instead of the intensity) using a Gaussian noise realization $\mathcal{G}_3$, with variance σ_3^2:

$$l^{\alpha\to\beta} = l^{\alpha} + \left(\frac{\alpha-\beta}{\beta}\right)^{1/2}\mathcal{G}_3, \tag{7}$$

where the variance σ_3^2 of the random variable $\mathcal{G}_3$ is derived to be

$$\sigma_3^2 = \frac{e^{l^{\alpha}}}{N_{\alpha}}.$$

Using the additive rule for the filtered backprojection based algorithms, this method involves separate reconstruction of $\mathcal{G}_3$, which is later blended in the image domain with the original image from l^{α}. This is a very good practical solution for the evaluation of filtered backprojection algorithms, since user does not have to perform a separate reconstruction whenever the new β is selected, but it loses its practical value in some other reconstruction strategies, for instance, in statistical iterative reconstruction algorithms. Moreover, derivation of σ_3^2 also assumes that the noisy signal l^{α} can be approximated by the noiseless signal l. Another, more important issue with approximating Poisson noise in the intensity domain with Gaussian noise in line integrals, is that the Poisson noise model inherently introduces bias in the line integrals. Fessler [14] shows using the Jensen's inequality that the following holds:

$$\mathrm{Mean}(l^{\alpha}) \geq l. \tag{8}$$

The inequality (8) says that the line integrals are systematically overestimated on the average. This was previously reported in several papers on transmission tomography [15], [16], [17]. One has to be aware of this bias when developing reconstruction algorithms for very low dose scans or when processing data of large objects – in other words, when the attenuated number of photons becomes very low.

We end this section by illustrating how approximating the signal obtained with the current α with the noiseless signal creates an issue when it comes to the accuracy of the state-of-the-art low dose simulation tools. The phantom used in our analysis consists of the outer ellipse with the long axis of 350mm, short axis of 210mm and HU of 0. The circle at the top has diameter of 70mm and 750HU. Circle at the bottom has diameter of 50mm and HU of 1000. As we see in in Figures 1, 2 and 3, the state-of-the-art methods significantly underestimate or overestimate both mean and the variance of the synthesized line integrals. On the other hand, our approach is the most accurate in that sense.

VI. CONCLUSION

The low dose simulation strategy presented in this paper has an advantage over the state of the art methods in that it makes fewer approximations in the statistical model of the

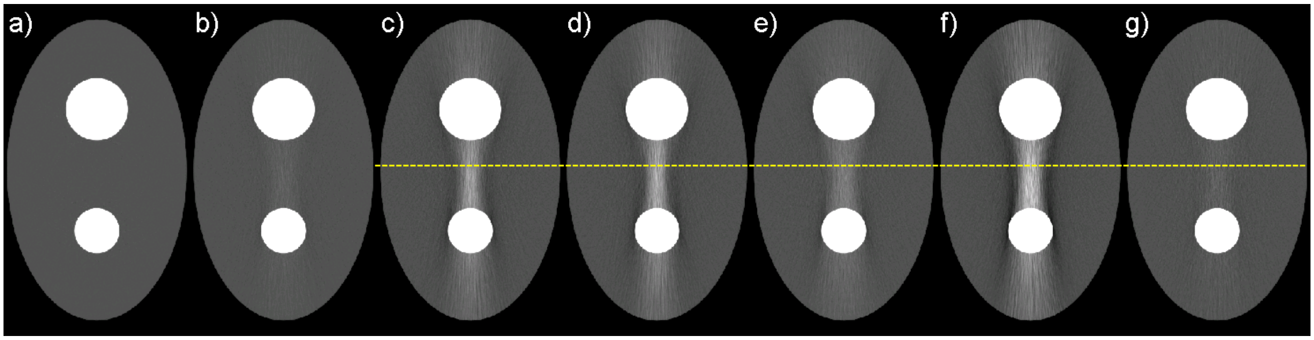

Fig. 1. Figure shows: a) noiseless reconstruction of the phantom described in the text. Figure b) is the average of 1000 direct noise simulations each equivalent to a 150mAs scan. The rest of the figures represent the mean of 1000 Poisson simulations of 50mAs using: c) direct realizations and d) the method from section IV. Figures e)-g) represent three different state of the art methods: Benson's [4], Frush's [1] and Amir's [3] respectively. See Section V for more details on these three methods. We consider image c) to be the ground truth in this experiment, in order to compare low dose simulation tools to a direct Poisson method. We observe that the mean levels are correctly estimated by our method, underestimated by the methods in e) and g), and overestimated by the method in f). A small bias in g) is due to the bias in the 150mAs direct simulation which was used as a source point for the corresponding projections. This state-of-the-art method simply maintained that mean. Biases in e) and f) are due to the errors when approximating Poisson random events. Images are in HU, they are centered at 25 and represented in window of 150. The yellow horizontal line represents the profile level used in Figures 2 and 3.

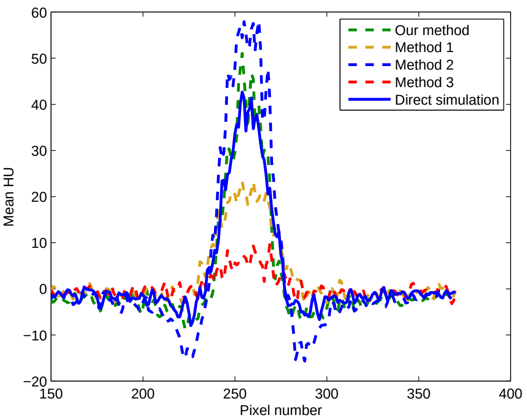

Fig. 2. Figure represents the profile mean of the central row in reconstructed volumes for direct noise simulation (full blue line), method from section IV (dashed green line), Benson's method [4] (dashed gold line), Frush's method (dashed blue line) method [1] and Amir's method [3] (dashed red line). Mean levels are most closely calculated by our method.

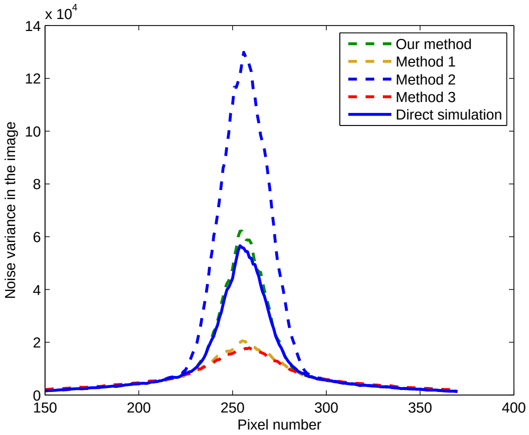

Fig. 3. Like in figure (2) we see five profile lines, all through the middle section of the phantom, but this time we represent the noise variance in that region. Noise levels of images simulated by our method are the closest to the direct simulations when compared to the other methods.

X-ray attenuation. Because the X-ray event portion of our noise simulation tool agrees with the Poisson probability mass function on the first two moments (mean and variance), it has a potential to be used as a very accurate tool in practice, but that requires the electronic detector noise to be incorporated into the complete model (Poisson plus detector noise). The results of the full model, with noise simulations compared to real low dose data will also be presented at the conference. We skipped it in this summary due to the space constraints.

REFERENCES

[1] D. Frush, C. Slack, C. Hollingsworth, G. Bisset, L. Donnelly, J. Hsieh, T. Lavin-Wensell, and J. Mayo, "Computer-simulated radiation dose reduction for abdominal multidetector ct of pediatric patients," *AJR Am J Roentgenol*, vol. 179, no. 5, pp. 1107–13, 2002.

[2] J. R. Mayo, K. P. Whittall, A. N. Leung, T. E. Hartman, C. S. Park, S. L. Primack, G. K. Chambers, M. K. Limkeman, T. L. Toth, and S. H. Fox, "Simulated dose reduction in conventional chest ct: validation study," *Radiology*, vol. 202, no. 2, pp. 453–7, 1997.

[3] O. Amir, D. Braunstein, and A. Altman, "Dose optimization tool," *Medical Imaging 2003: Visualization, Image-Guided Procedures, and Display*, vol. 5029, pp. 815–821, 2003.

[4] T. M. Benson and B. K. B. De Man, "Synthetic ct noise emulation in the raw data domain," *IEEE Medical Imaging Conference Proceedings*, 2010.

[5] B. R. Whiting, "Signal statistics of x-ray computed tomography," *Proc SPIE Physics of Medical Imaging*, pp. 53–60.

[6] B. R. Whiting, P. Massoumzadeh, O. A. Earl, J. A. O'Sullivan, D. L. Snyder, and J. F. Williamson, "Properties of preprocessed sinogram data in x ray computed tomography," *Med Phys*, vol. 33, no. 9, pp. 3290–3304, 2006.

[7] P. Massoumzadeh, S. Don, C. Hildebolt, K. Bae, and B. Whiting,

"Validation of ct dose-reduction simulation," *Med Phys*, vol. 36, no. 1, pp. 174–89, 2009.

[8] P. Massoumzadeh, O. Earl, and B. Whiting, "Signal statistics of x-ray computed tomography," pp. 898–905.

[9] A. Wang and N. Pelc, "Synthetic ct: simulating arbitrary low dose single and dual energy protocols," 2011.

[10] D. Sennst, M. Kachelriess, C. Leidecker, B. Schmidt, O. Watzke, and W. Kalender, "An extensible software-based platform for reconstruction and evaluation of ct images.," *Radiographics*, vol. 24, no. 2, pp. 601–13, 2004.

[11] S. M. D. Nakanishi, Satoru and Z. A. A., "Low dose ct simulation using experimental noise model," 2011.

[12] G. Casella and R. Berger, *Statistical Inference*. Duxbury Resource Center, June 2001.

[13] W. H. Press, S. A. Teukolsky, W. T. Vetterling, and B. P. Flannery, *Numerical recipes in C (2nd ed.): the art of scientific computing*. New York, NY, USA: Cambridge University Press, 1992.

[14] J. Fessler, "Statistical image reconstruction methods," in *SPIE Handbook on Medical Imaging - Volume II: Medical Image Processing and Analysis* (J. M. Fitzpatrick and M. Sonka, eds.), SPIE, 2000.

[15] J. A. Fessler, "Hybrid poisson/polynomial objective functions for tomographic image reconstruction from transmission scans," *IEEE Tr. Im. Proc*, vol. 4, pp. 1439–1450, 1995.

[16] D. S. Lalush and B. M. W. Tsui, "Map-em and wls-map-cg reconstruction methods for transmission imaging in cardiac spect," *Proc. IEEE Nuc. Sci. Symp. Med. Im. Conf.*, vol. 2, pp. 1174–1178, 1993.

[17] J.-B. Thibault, C. A. Bouman, and K. D. Sauer, "A recursive filter for noise reduction in statistical iterative tomographic imaging," *Computational Imaging IV: Proc. of SPIE-IS&T Electronic Imaging*, vol. 6065, 2006.

A Realistic CT/Human-Model Simulation Package

George S.K. Fung, Karl Stierstorfer, Katsuyuki Taguchi, W. Paul Segars,
Thomas G. Flohr, Benjamin M.W. Tsui

Abstract – **The aim of this research is to develop a complete CT/human-model simulation package by integrating (1) a realistic 4D digital model of human anatomy and motion -- the 4D eXtended CArdiac-Torso (XCAT) phantom, and (2) an accurate CT projection data simulation program -- the DRASIM (Siemens Healthcare) simulator. Unlike other CT simulation tools which are based on simple mathematical primitives or voxelized phantoms, this new simulation package has the advantages of utilizing a realistic model of human anatomy and physiological motions without voxelization and with accurate modeling of the characteristics of clinical CT systems. First, we incorporated the 4D XCAT anatomy and motion models into DRASIM by implementing a new library which consists of functions to read-in the NURBS surfaces of anatomical objects, their overlapping order, and material properties of the XCAT phantom. Second, we incorporated an efficient ray-tracing algorithm for line integral calculation in DRASIM by computing the intersection points of the rays cast from the x-ray source to the detector elements through the surfaces of the multiple XCAT anatomical objects along the ray paths. To evaluate the new integrated software package, we simulated a number of sample CT projection data for different body parts using the new integrated simulation package. Image reconstruction was performed by uploading the projection data back to scanner or own reconstruction program followed by beam hardening correction. In our initial results, the package shows its capability in the generation of clinically realistic CT images for different human body parts at different doses, x-ray spectra, and pathological conditions. This unique CT/human-model simulation package has great potential as a tool in the design and optimization of CT scanners, and the development of scanning protocols and image reconstruction methods for improving CT image quality with reduced radiation dose.**

I. INTRODUCTION

Tremendous research activities have been conducted to develop methods and techniques to further improve image quality and minimize the radiation dose to the patient in the field of x-ray Computed Tomography (CT). With the advancement of multi-detector CT (MDCT) or other technologies, CT scanners become exceedingly complex and any optimization becomes a challenge. It is impractical to optimize the large number of parameters of existing imaging protocols and design settings available in modern CT systems for human patients due to the prohibitive high cost and unnecessary radiation concerns. In additional, the heterogeneity in patient size and pathological conditions multiplying with the large number of technical parameters in modern CT systems forbid the optimization studies performed with human subjects. On the other hand, it is equally impractical to do optimization studies by performing experiments on physical test objects that cannot realistically mimic the true clinical scenario. It is due to the prohibitively high cost in fabricating physical phantoms to simulate a range of patient sizes and pathological conditions with a range of physiologic motion. Therefore, the most promising practical approach to these optimization problems is through realistic computer simulation [1] with realistic human-model phantom and accurate CT simulator. The main advantage of using computer generated phantoms in simulation studies is that the exact anatomy and physiological functions of the phantom are known, thus providing a ground truth from which to quantitatively evaluate medical imaging instrumentations, imaging and image processing techniques.

In this research, we develop a complete CT/human-model simulation package by integrating the 4D eXtended CArdiac-Torso (XCAT) phantom, a computer generated Non-Uniform Rational B-Spline (NURBS) surface based phantom that provides a realistic model of human anatomy and respiratory and cardiac motions, and the Deterministic RAdiological SIMulation (DRASIM) (developed by Siemens Healthcare) CT projection data simulation program. Unlike other CT simulation tools which are based on simple mathematical primitives or voxelized phantoms, this new simulation package has the advantages of utilizing a realistic model of human anatomy and physiological motions without voxelization and with accurate modeling of the characteristics of clinical CT systems. We have further enhanced various parts of our initial concept-proving implementation [2], such as program parallelization, projection data format conversion for data upload to CT scanners, and beam hardening correction for polychromatic x-ray CT simulation.

II. METHODS

Essentially, the simulation package consists of multiple components: XCAT phantom, DRASIM simulator, ray-

---

Manuscript received February 1, 2012. This work was partly supported by Siemens-JHU research.

G. S. K. Fung, K. Taguchi, and B. M. W. Tsui are with the Department of Radiology, Johns Hopkins University, Baltimore, MD 21287 USA (e-mail: gfung2@jhmi.edu).

K. Stierstorfer and T. Fholr are with the Siemens Healthcare, Forchheim, Germany.

W. P. Segars is with the Department of Radiology, Duke University, Durham, NC 27710, USA.

tracing algorithm, and image reconstruction. The schema and data flow diagram of the integration is depicted in Figure 1.

A. *Realistic human-model digital phantom*

The 4D XCAT phantom [3] is a whole-body computer model of the human anatomy and physiology based on NURBS surfaces. Unlike other phantoms based on simple mathematical primitives or voxelized phantoms, the 4D XCAT provides an accurate representation of the complex human anatomy and has the advantage that its organ shapes can be changed to realistically model anatomical variations and patient respiratory and cardiac beating motions. The XCAT phantom, as well as its predecessor, the NCAT phantom, have been widely used for medical imaging simulation. The XCAT phantom includes a detailed human anatomy consisting of over 2,000 objects defined by NURBS surfaces. The parameters of the XCAT phantom are adjustable in order to model different patient anatomy, motions and other variations. To make the phantom applicable to CT imaging research, we previously developed a simplified CT projector specific to the XCAT phantom previously [4]. This projector could calculate x-ray projections directly from the NURBS surface definition of the phantom in a very efficient manner. However, this projection algorithm is generic and can only handle simplified CT system geometries and basic scanner specific design parameters. Advanced scanner parameters, such as flying focal spot, detector response, bowtie filter setting, found in commercial CT systems, could not be modeled.

B. *Accurate CT projection simulator*

The DRASIM software package [5], developed by Siemens Healthcare, is a CT projection data simulation program which allows simulation of x-ray transmission data based on a narrow beam assumption. Since DRASIM is developed by the research department of the manufacturer, it has all the necessary parameters that need to accurately reproduce the projection data generated by actual Siemens clinical CT scanners. DRASIM can accurately model a detailed list of CT scanner specific parameters, such as focus size and the detector aperture with oversampling, the motion of the focal spot on the anode plate, and the polychromatic x-ray beam. However, DRASIM only works with simple geometric phantoms composed of multiple simple geometric primitive objects, such as spheres, ellipsoids, and cylinders.

C. *Efficient ray-tracing algorithm for NURBS surfaces*

For the simulation of high spatial resolution x-ray projection data, it is essential to calculate directly from the NURBS surface definition without voxelization of the phantom in order to avoid alias artifact. We need to define the projection rays which are the lines cast from the x-ray source connecting to the detector elements. Without sub-sampling at source and detector element, there is one projection ray that joins the source to each detector element. We previously developed an efficient ray–tracing algorithm for NURBS surfaces as part of the development of the CT projector for the XCAT phantom [4]. The NURBS ray-tracing algorithm calculated the intersection points of each projection ray with the object surfaces defined in the XCAT phantom. It is known that the computation cost for intersection point calculation of projection rays on NURBS surfaces is high. Therefore, an efficient implementation of the ray-tracing algorithm is necessary since large number of projection rays and NURBS surfaces are employed in our application. First, the NURBS objects of the XCAT phantom were converted into cubic Beizier surfaces by inserting multiple knots using accepted methods [6]. Then, a Bezier clipping method was used to recursively subdivide the Bezier surfaces into smaller and smaller sub-surfaces in order to determine the intersections of the surface with the projection ray. A bounding volume hierarchy representation [7] and fast ray-box intersection calculations [8] were implemented to speed up the calculation. Further details of this implementation could be found in [4]. Due to the extremely high spatial resolution of the projection rays, additional work has been performed in fine-tuning the stopping tolerance for the recursive subdivision process in Bezier clipping method in order to achieve highly accurate ray-sum calculation. Additional logic has been designed to keep track the incident and exit sequence of the casting ray through a surface using the surface normal at intersection point in order to achieve highly robust ray-sum calculation.

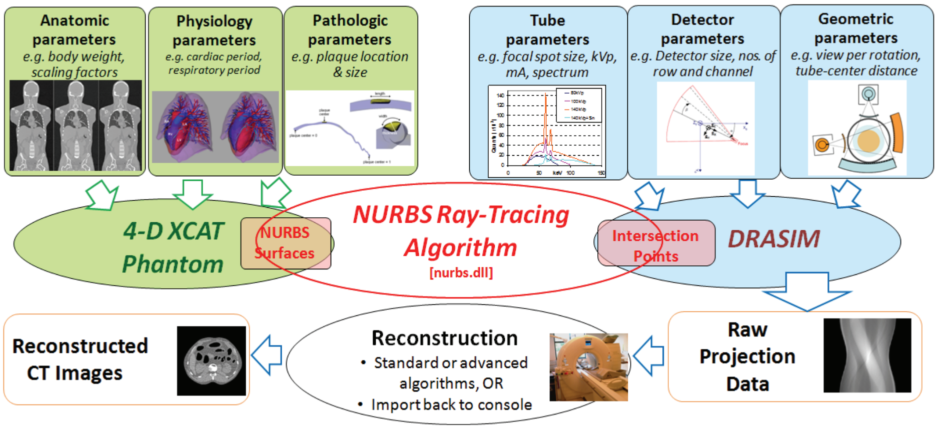
Anatomic parameters
e.g. body weight, scaling factors
Physiology parameters
e.g. cardiac period, respiratory period
Pathologic parameters
e.g. plaque location & size
Tube parameters
e.g. focal spot size, kVp, mA, spectrum
Detector parameters
e.g. Detector size, nos. of row and channel
Geometric parameters
e.g. view per rotation, tube-center distance
4-D XCAT Phantom
NURBS Surfaces
NURBS Ray-Tracing Algorithm
[nurbs.dll]
Intersection Points
DRASIM
Raw Projection Data
Reconstruction
• Standard or advanced algorithms, OR
• Import back to console
Reconstructed CT Images

Figure 1. The schema and dataflow diagram of the XCAT/DRASIM integration

D. Projection data generation and image reconstruction

We employed the dynamic-link library (DLL) approach to integrate the 4D XCAT phantom and the DRASIM software programs. The new NURBS-based DLL is loaded into the DRASIM program when it is called at runtime only. It has two advantages: the performance of the individual DRASIM and XCAT programs are not affected by the integration; and, if the new integration features are not used, the integrated programs work exactly the same as before the integration and the changes are transparent to users.

The simulation involved multiple steps. First, the required anatomic, physiologic, and pathologic parameters were defined in the parameter input files for the XCAT program. Instead of generating a voxelized XCAT phantom as is typically done, we switched the XCAT program to generate NURBS surface files for the objects in XCAT phantom as output. Second, the required source, detector, geometric and other parameters of the CT scanner were defined in the DRASIM script. A new phantom type called "NURBS" was allowed to enable DRASIM to read in the NURBS surfaces from the specified files, the material properties of the objects, and the overlapping order of the XCAT anatomical objects. Third, this process trigger the NURBS ray-tracing algorithm in DLL, as described in section II.C, was used to compute the intersection points of the rays cast from the x-ray source to the detector elements through multiple XCAT objects. The calculated intersection points and the materials of the objects were passed to DRASIM for line integral calculation for each detector element. By concatenating the linear integrals of all the detector elements of different channels, rows, and views, the raw projection data were generated.

The simulated project data can then be processed by standard or advanced reconstruction algorithms, or imported back to the console for image reconstruction. However, there were no direct ways to generate a "virtual" projection file from the XCAT/DRASIM tool directly. We needed to do a test scan using the targeted protocol and export the raw projection data in a proprietary format. Then, through a proprietary program, we replaced the original projection data with our simulated ones. The modified projection data file was uploaded back to scanner console for reconstruction with desired kernel, FOV, and other reconstruction parameters as shown in Figure 2.

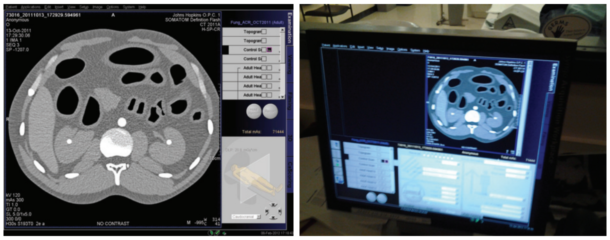
(a) (b)

Figure 2. (a) A screen capture and (b) a photo of a CT image reconstructed from simulation data on a CT console.

E. Sample simulation datasets

The integrated simulation package was tested on a series of simulations of multiple x-ray projections from different views followed by image reconstruction. The scout scans of the torso, and the abdominal, head, coronary, and cardiac scans were simulated. The data acquisition parameter settings of DRASIM were based on the Definition Flash dual-source CT scanner (Siemens Healthcare). The geometry settings, including source to center distance, center to detector distance, number of detector channels, number of views per rotation, fan angle of the detector, filters, and many other were specified. Unless otherwise stated, a polychromatic x-ray source of 120 kVp and tube current setting of 230mAs per rotation were employed for all simulations. Subsampling on focus and detector elements was employed. The CT image reconstruction was performed by the console station of our CT scanner using the uploaded "virtual" projection data file.

III. RESULTS AND DISCUSSIONS

We performed a number of simulations using the new integrated XCAT/DRASIM simulation package followed by a CT scanner control console or standard filtered backprojection reconstruction. These simulations included: (1) anteroposterior and lateral topograms of the torso (Fig 3), (2) abdominal scans at normal and reduced doses (Fig 4), (3) head scans of monochromatic and polychromatic x-ray sources without beam hardening correction (Fig 5), (4) coronary scans without plaques and with calcium and soft plaques (Fig 6), (5) dual-energy abdominal scans with uric acid and calcified stones (Fig 7), and (6) cardiac scan with and without cardiac motion (Fig 8).

In Fig 3, the realistic anatomy of the human torso, including all the major organs, are clearly identified in the x-ray scout views of the torso of the XCAT phantom. As shown in Fig 4, the abdominal images acquired at reduced dose has higher noise magnitude compared to the one at normal dose. In Fig 5(a), no beam hardening artifacts were found when a monochromatic x-ray source was employed, while, in Fig 5(b), beam hardening artifacts are clearly visible (arrows) when a polychromatic x-ray source was employed. In Fig 6, normal coronary and diseased coronary with calcified and soft plaques were simulated with contrast enhanced blood. In the 80kVp image (Fig 7(a)), both bone and contrast-enhanced aorta show higher CT numbers than those in 140kVp with tin filter image (Fig 7(b)). Higher mAs was used for 80kVp scan 140kVp with tin scan in order to achieve similar noise level (~1.85 times). Finally, we showed that our new simulation package can be used to study motion artifacts caused by the beating heart using the 4D XCAT phantom that includes cardiac motion. In Fig 8(a), the motion-free image of the XCAT cardiac phantom is shown. In Fig 8(b), the motion artifacts of the right coronary artery (RCA) and the left circumflex artery (LCX) are clearly shown as compared to phantom image at the corresponding heart phase. These initial simulation results demonstrate the great potential of the CT/human-model simulation package.

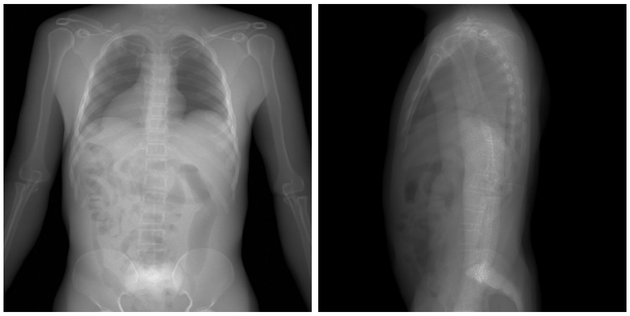

Figure 3. (a) Anteroposterior and (b) lateral simulated topograms of torso.

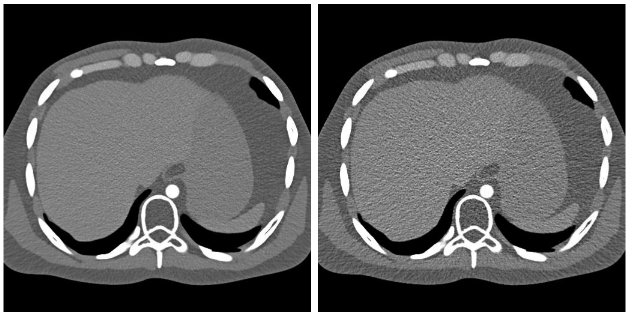

Figure 4. The simulated abdominal images at (a) high radiation dose (460 mAs/rot) and (b) reduced radiation dose (115 mAs/rot).

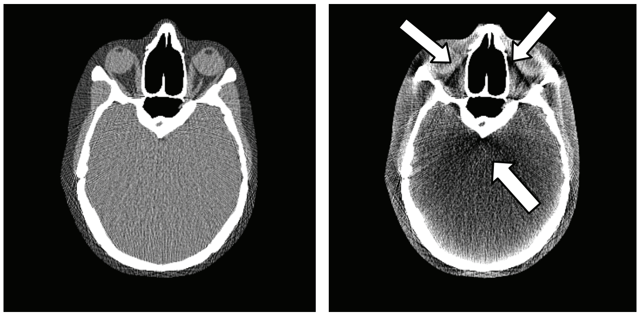

Figure 5. The simulated head images using (a) monochromatic (80keV) and (b) polychromatic (120kVp) x-ray sources.

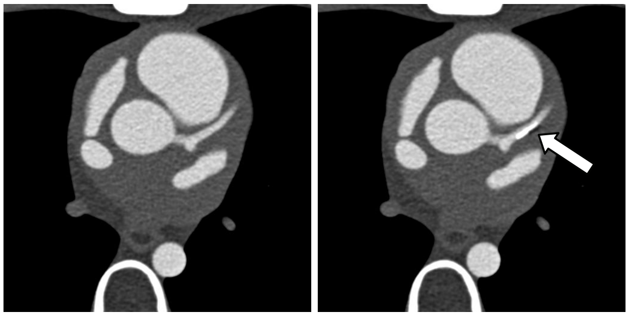

Figure 6. The reconstructed coronary images (a) without plaques and (b) with plaques

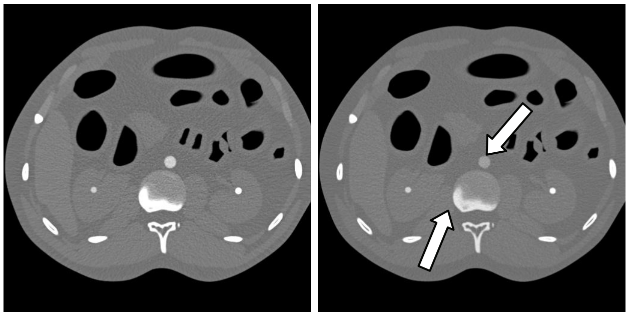

Figure 7. The simulated dual-energy abdominal scans with kidney stones using (a) 80kVp and (b) 140kVp with tin.

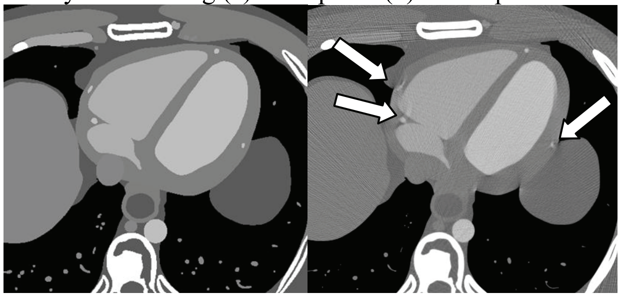

Figure 8. (a) A motion-free sample transaxial slice of the 4D XCAT phantom and (b) the simulated cardiac images of the beating heart (courtesy of Dr. Jochen Cammin).

IV. CONCLUSION

In conclusion, we have developed a unique CT/human-model simulation package that can provide a valuable tool in the design and optimization of CT scanners, and the development of scanning protocols and image reconstruction methods for improving image quality and reducing dose. Quantitative evaluation of the simulated data in comparing with the experimental data using CT scanners and a physical phantom is currently underway.

ACKNOWLEDGEMENT

We thank Dr. E. Fishman, Dr. S. Kawamoto, Ms. B. Mudge, and Mr. V. Blasko for their assistance on performing scans and reconstruction on a CT scanner.

REFERENCES

[1] Segars, W. P. and Tsui, B. M. W., “MCAT to XCAT: The evolution of 4-D computerized phantoms for imaging research,” Proceedings of the IEEE, 97(12), 1954-1968 (2009).

[2] Fung G.S.K., Stierstorfer K., et al., “XCAT/DRASIM: A Realistic CT/Human-Model Simulation Package,” SPIE Medical Imaging (2011).

[3] Segars, W. P., Sturgeon, G., Mendonca, S., Grimes, J., and Tsui, B. M. W., “4D XCAT phantom for multimodality imaging research,” Medical Physics, 37(9), 4902-4915 (2010).

[4] Segars, W. P., Mahesh, M., Beck, T.J., Frey, E. C., and Tsui, B. M. W., “Realistic CT simulation using the 4D XCAT phantom,” Medical Physics, 35(8), 3800-3808 (2008).

[5] Stierstorfer, K., "DRASIM: A CT-simulation tool," Internal Report, Siemens Healthcare.

[6] Cohen, E., et al., “Discrete B-splines and subdivision techniques in computer-aided geometric design and computer graphics,” Comput. Grap. Image Process., 14, 87-111 (1980).

[7] Martin, W. et al., “Practical ray tracing of trimmed NURBS surfaces,” J. Comput. Graphics Tools, 5, 27-52 (2000).

[8] Williams, A., et al., “An efficient and robust ray-box intersection algorithm,” J. Comput. Graph. Tools, 10, 49-54 (2005).

Dedicated Breast CT: Anatomic Power Spectrum

Srinivasan Vedantham[1], Linxi Shi[1], Andrew Karellas[1], Avice M. O'Connell[2], and David Conover[2, 3]

Abstract—**Dedicated breast CT is being actively investigated to overcome the tissue superposition problem present in mammography. Tissue superposition can result in missed cancers due to the masking effect of the anatomic background or can mimic the presence of a lesion resulting in additional imaging and potentially unnecessary biopsies. In this study, the anatomic power spectrum of coronal slices, parallel and adjacent to the chest wall was computed from 75 subjects, all women, who were scheduled to undergo tissue sampling (biopsy). The anatomic power spectrum at low spatial frequencies was observed to follow a power-law dependence of the form k/f^{β}, where the value of the exponent β was found to be 1.581. The standard error in estimate of β was 0.163.**

I. INTRODUCTION

THE success of mammography as a screening tool is well-established in literature [1-3]. Mammography provides a two-dimensional (2-D) image of the three-dimensional (3-D) breast resulting in tissue superposition. This can result in missed cancers due to the masking effect of the anatomic background or can mimic the presence of a lesion resulting in additional imaging and potentially unnecessary biopsies. Chakraborty and Kundel [4] and Burgess et al. [5] independently showed that the anatomic power spectrum in mammography for spatial frequencies less than ~1 cy/mm follows a power law dependence of the form k/f^{β}, where the exponent $\beta \approx 3$. Further, human visual studies conducted by Burgess et al. [5] showed that the lesion detection is impaired by the anatomic power spectrum. Recently, Reiser et al. [6], noted that the anatomic power spectrum in mammography while following a power-law process was non-isotropic.

We and others are actively investigating dedicated breast CT as an imaging tool to overcome the tissue superposition problem present in mammography [7-13]. In addition to the inherent improvement in contrast with tomography, the lack of physical compression of the breast and the ability to display the imaged breast in any desired orientation using multi-planar reconstructions are distinct advantages. In order to understand the effect of background anatomic structure on lesion detection and characterization and for task-specific optimization of dedicated breast CT, it is essential to quantify the anatomic power spectrum. The frame-work for task-specific optimization and the importance of including the anatomic power spectrum have been described in literature [14, 15]. In dedicated breast CT, Metheany et al. [16] theoretically derived an expression relating the exponent of the anatomic power spectrum in the projections to that of the reconstruction. Also, the power spectrum of transverse (coronal) slices from 43 subjects was estimated and the exponent $\beta \approx 1.86$ was observed in the frequency range of 0.07 to 0.45 cy/mm [16]. The exponent of the power-law fit was determined to be 2.32 for mastectomy specimens [17]. In this work, we estimated the anatomic power spectrum of coronal slices, parallel and adjacent to the chest wall from 75 subjects, all women, who were scheduled to undergo tissue sampling (biopsy).

II. METHODS AND MATERIALS

A. Dedicated Breast CT System

A prototype cone-beam dedicated breast CT system was used in this study. The system features an amorphous silicon flat-panel detector with Thalium-doped Cesium Iodide (CsI:Tl) scintillator (PaxScan® 4030CB, Varian Medical Systems, Salt Lake City, UT) and a 4-inch tungsten target rotating anode x-ray tube (RAD 71SP, Varian Medical Systems, Salt Lake City, UT) powered by a high-frequency x-ray generator (Sedecal USA) [18]. Detailed description of the system has been previously published [18]. The clinical acquisition parameters used in this study are summarized in Table 1.

B. Clinical Study

The clinical study was conducted in accordance with a protocol that was approved by the human subjects review board from both institutions. All study participants provided written informed consent. Recruitment, all imaging including the breast CT exam, tissue sampling (biopsy) and histopathology were conducted at the Highland Hospital, University of Rochester Medical Center, while analysis of the image data was performed at the University of Massachusetts Medical School. While the study enrolled 150 subjects, all women, image data from 75 women were included in this analysis. All women included in this analysis were assigned BI-RADS® 4 or 5 as per the American College of Radiology assessment categories [19].

This work was supported in part by the National Institutes of Health (NIH) grants R01 CA128906 and R21 CA134129. The contents are solely the responsibility of the authors and do not represent the official views of the NIH or NCI.

S. Vedantham, L. Shi, and A. Karellas are with the Department of Radiology, University of Massachusetts Medical School, Worcester, MA 01666 USA (corresponding author: S. Vedantham; phone: 508-856-1241; fax: 508-856-6363; e-mail: srinivasan.vedantham@umassmed.edu).

A.M. O'Connell and D. Conover are with the Department of Radiology, University of Rochester Medical Center, Rochester, NY 14642 USA.

D. Conover is also an employee of Koning Corporation, West Henrietta, NY 14586 USA that is developing this technology towards commercialization under agreement with University of Rochester Medical Center.

TABLE I
DEDICATED BREAST CT ACQUISITION PARAMETERS

Description	Value
Applied tube voltage	49 kVp
1st half-value layer of x-ray beam	1.4 mm of Al
X-ray pulse width	8 ms
Number of projections	300
Angular range	360°
Binned pixel pitch	388 µm
Scan time	10 seconds

These categories correspond to either suspicious abnormality or highly suggestive of malignancy. All women included in this analysis had a dedicated CT exam of the breast(s) with the finding(s) that was/were assigned BI-RADS 4 or 5 and prior to biopsy. For this analysis, ramp-filtered FDK [20] reconstructions of the projections were used. The reconstructions provided an isotropic voxel size with dimensions of 155 µm.

C. 2-D Power Spectrum

In order to determine the coronal slice appropriate for estimating the anatomic power spectrum, one author (S.V.) reviewed the reconstructions. The criteria used for selection were that the coronal slice should be as close to the chest wall as possible, should not contain the *pectoralis major* muscle and should not contain visually discernible artifacts. This slice was chosen as it represents a cone angle that is near-zero so that the cone-beam artifacts, if present, are minimized. Thus, from each subject one slice was selected. For each selected slice, a 128 x 128 region of interest (ROI) centered to the reconstructed field of view was obtained and used for estimating the anatomic power spectrum.

The anatomic power spectrum was determined in two ways: one inclusive of any non-stochastic noise that may be present, and one excluding the non-stochastic noise component. The anatomic power spectrum inclusive of non-stochastic noise is represented as $S^I(u,v)$, where u and v represent the spatial frequency coordinates, and was determined as:

$$S^I(u,v) = \frac{1}{N}\sum_{i=1}^{N}\left|\mathbb{F}\left(ROI_i(x,y) - \overline{ROI_i(x,y)}\right)\right|^2 \Delta x\,\Delta y \quad (1)$$

In equation (1), $\overline{ROI_i(x,y)}$ represents the mean value of the *i*-th ROI, $\mathbb{F}$ represents the Fourier transform, Δx and Δy represent the voxel dimensions in the *x* and *y*-directions, respectively, and N the number of regions of interest (ROIs) used in the analysis. In our analysis, $\Delta x = \Delta y = 0.155$ mm and $N = 75$. The anatomic power spectrum excluding the non-stochastic noise component represented as $S^E(u,v)$ was determined as:

$$S^E(u,v) = \frac{1}{N}\sum_{i=1}^{N}\left|\mathbb{F}\left(ROI_i(x,y) - \overline{\overline{ROI(x,y)}}\right)\right|^2 \Delta x\,\Delta y \quad (2)$$

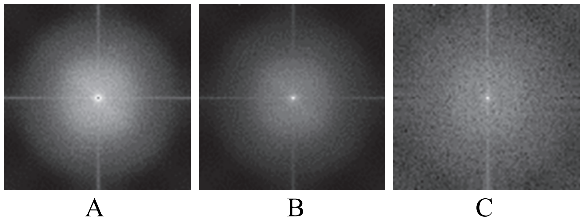

Fig. 1. The two-dimensional anatomic power spectrum inclusive of non-stochastic noise (A) and excluding the non-stochastic noise (B). The non-stochastic noise component (C) was determined by subtracting (B) from (A). For display purposes, all spectra are shown in log-scale with the origin set to spectral mean.

In equation (2), $\overline{\overline{ROI(x,y)}}$ represents the 2-D average ROI obtained by averaging all 75 ROIs.

D. 1-D Power Spectrum

The one-dimensional (1-D) power spectrum was determined by radially averaging the 2-D power spectrum after excluding the axes and the rows/columns immediately adjacent to the axes. The 1-D spatial frequency f, was computed as $f = \sqrt{u^2 + v^2}$. The resulting 1-D estimate was resampled to 64 spatial frequency bins over the range $[0, f_N]$, where f_N is the Nyquist frequency, which in our case is 3.23 cy/mm.

E. Estimation of the power-law exponent

Previous work by Benitez et al. [18], showed that the noise power spectrum (NPS) with a uniform water phantom demonstrated a monotonic increase in amplitude from low to mid-spatial frequencies, followed by a monotonic decrease in amplitude from mid to high-spatial frequencies. They observed that the peak NPS amplitude occurred at ~0.6 cy/mm [18]. Hence, 1-D anatomic power spectra corresponding to spatial frequencies between 0.1 and 0.45 cy/mm were fitted with a power-law equation. This was achieved by linear fitting (OriginPro 8.6.0, OriginLab Corporation, Northampton, MA) after logarithmic transform of the spatial frequency and the anatomic power spectrum.

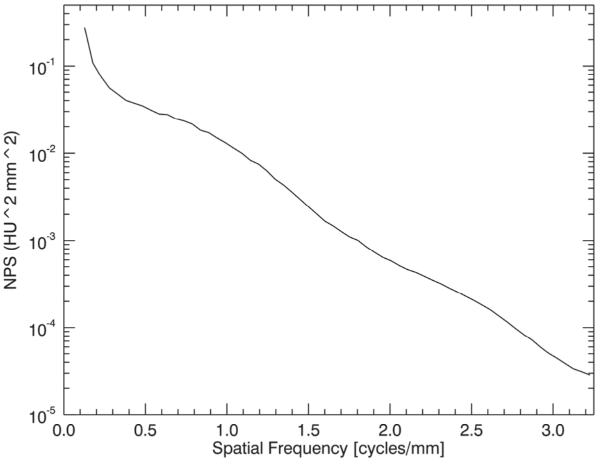

Fig. 2. One-dimensional power spectrum determined by radially averaging $S^E(u,v)$ after excluding the axes and the rows/column immediately adjacent to the axes.

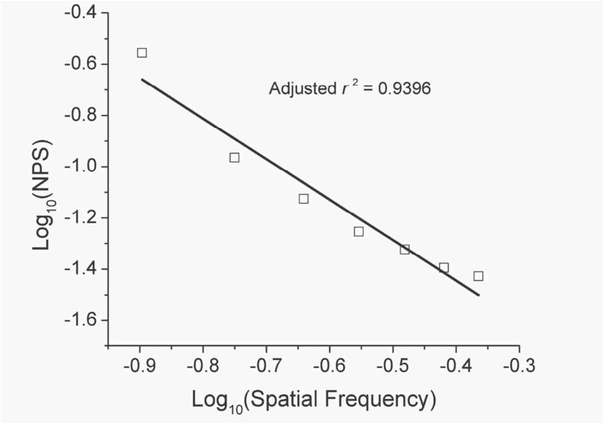

Fig. 3. Linear fit to the logarithmic transform of the spatial frequency and the NPS.

III. RESULTS

Figure 1 shows the two-dimensional anatomic power spectra inclusive of non-stochastic noise (A) and excluding the non-stochastic noise (B). The non-stochastic noise component was determined as $S^I(u,v) - S^E(u,v)$, i.e., by subtracting (B) from (A), and is shown in (C).

Figure 2 shows the one-dimensional anatomic power spectrum determined by radial averaging $S^E(u,v)$ after excluding the axes and the rows/columns immediately adjacent to the axes.

Figure 3 shows the linear fit of the one-dimensional anatomic power spectrum as a function of spatial frequency after logarithmic transform of the spatial frequency and the NPS. The slope of this fit corresponds to the exponent of the power-law, β. The determined value of β was 1.581. The confidence intervals and the standard error are summarized in Table II.

TABLE II
POWER-LAW EXPONENT

Description	Value
Fit estimate	1.581
Standard error in estimate	0.163
Lower confidence level (95 %)	1.162
Upper confidence level (95 %)	1.999
Confidence interval half-width	0.419

IV. DISCUSSION

The presence of non-stochastic noise component was observed in Figure 1. The two-dimensional anatomic power spectrum shown in Figure 1 exhibited good radial symmetry. Hence the use of radial averaging to estimate the 1-D power spectrum is appropriate. Comparing the 1-D anatomic power spectrum shown in Figure 2 to that reported in Figure 13 of Benitez et al. [18], it is apparent that for spatial frequencies less than 0.5 cycles/mm, the anatomic noise is the dominant factor. Hence, NPS corresponding to spatial frequencies between 0.1 and 0.45 cycles/mm were fitted with a linear curve after logarithmic transform. Good correspondence was observed between the empirical values and the linear fit (adjusted r^2=0.94). Considering the 95% confidence intervals of our estimate of the power-law exponent the determined value is in reasonable agreement with that reported by Metheany et al. [16]. Importantly, the exponent with breast CT was substantially lower than that reported for mammography. Following the analysis provided by Burgess et al. [5], the aforementioned observation suggests that the threshold size for lesion detection would be less impaired by the anatomic noise in breast CT than in mammography.

ACKNOWLEDGMENT

The system used in this study was developed at the University of Rochester with support from the National Institutes of Health (Ruola Ning, PhD, principal Investigator). Koning Corporation has licensed several patents from the University of Rochester, and seeks to commercialize medical imaging equipment utilizing the cone beam CT technology. The University of Rochester holds a small equity interest in Koning Corporation. At the time of this report the dedicated cone beam breast CT is an investigational device.

The authors thank Ricardo Betancourt Benitez for discussions pertaining to the noise power spectrum measurements of the dedicated breast CT system with the water phantom. The authors thank Radha Iyer, M.D., for reviewing the cone-beam breast CT images and the corresponding mammograms.

REFERENCES

[1] D. A. Berry, K. A. Cronin, S. K. Plevritis, D. G. Fryback, L. Clarke, M. Zelen, J. S. Mandelblatt, A. Y. Yakovlev, J. D. Habbema, and E. J. Feuer, "Effect of screening and adjuvant therapy on mortality from breast cancer," *N Engl J Med,* vol. 353, pp. 1784-92, Oct 27 2005.

[2] The Swedish Organized Service Screening Evaluation Group, "Reduction in breast cancer mortality from organized service screening with mammography: 1. Further confirmation with extended data," *Cancer Epidemiol Biomarkers Prev,* vol. 15, pp. 45-51, Jan 2006.

[3] The Swedish Organized Service Screening Evaluation Group, "Reduction in breast cancer mortality from the organised service screening with mammography: 2. Validation with alternative analytic methods," *Cancer Epidemiol Biomarkers Prev,* vol. 15, pp. 52-6, Jan 2006.

[4] D. P. Chakraborty and H. L. Kundel, "Anomalous nodule visibility effects in mammography images," *Proc SPIE* 4324, 2001, pp. 68-76.

[5] A. E. Burgess, F. L. Jacobson, and P. F. Judy, "Human observer detection experiments with mammograms and power-law noise," *Med Phys,* vol. 28, pp. 419-437, 2001.

[6] I. Reiser, S. Lee, and R. M. Nishikawa, "On the orientation of mammographic structure," *Med Phys,* vol. 38, pp. 5303-6, Oct 2011.

[7] K. K. Lindfors, J. M. Boone, T. R. Nelson, K. Yang, A. L. Kwan, and D. F. Miller, "Dedicated breast CT: initial clinical experience," *Radiology,* vol. 246, pp. 725-33, Mar 2008.

[8] N. D. Prionas, K. K. Lindfors, S. Ray, S. Y. Huang, L. A. Beckett, W. L. Monsky, and J. M. Boone, "Contrast-enhanced dedicated breast CT: initial clinical experience," *Radiology,* vol. 256, pp. 714-23, Sep 2010.

[9] A. O'Connell, D. L. Conover, Y. Zhang, P. Seifert, W. Logan-Young, C. F. Lin, L. Sahler, and R. Ning, "Cone-beam CT for breast imaging: Radiation dose, breast coverage, and image quality," *AJR. American Journal of Roentgenology,* vol. 195, pp. 496-509, Aug 2010.

[10] S. J. Glick, S. Vedantham, and A. Karellas, "Investigation of optimal kVp settings for CT Mammography using a Flat-panel Imager," presented at the Medical Imaging 2002: Physics of Medical Imaging, 2002.

[11] I. Sechopoulos, S. Vedantham, S. Suryanarayanan, C. J. D'Orsi, and A. Karellas, "Monte Carlo and phantom study of the radiation dose to the body from dedicated CT of the breast," *Radiology,* vol. 247, pp. 98-105, Apr 2008.

[12] W. A. Kalender, M. Beister, J. M. Boone, D. Kolditz, S. V. Vollmar, and M. C. Weigel, "High-resolution spiral CT of the breast at very low dose: concept and feasibility considerations," *Eur Radiol,* vol. 22, pp. 1-8, Jan 2012.

[13] Y. Shen, Y. Yi, Y. Zhong, C. J. Lai, X. Liu, Z. You, S. Ge, T. Wang, and C. C. Shaw, "High resolution dual detector volume-of-interest cone beam breast CT--Demonstration with a bench top system," *Medical Physics,* vol. 38, p. 6429, Dec 2011.

[14] S. J. Glick, S. Thacker, X. Gong, and B. Liu, "Evaluating the impact of x-ray spectral shape on image quality in flat-panel CT breast imaging," *Medical Physics,* vol. 34, pp. 5-24, Jan 2007.

[15] G. J. Gang, D. J. Tward, J. Lee, and J. H. Siewerdsen, "Anatomical background and generalized detectability in tomosynthesis and cone-beam CT," *Medical Physics,* vol. 37, pp. 1948-65, May 2010.

[16] K. G. Metheany, C. K. Abbey, N. Packard, and J. M. Boone, "Characterizing anatomical variability in breast CT images," *Med Phys,* vol. 35, pp. 4685-94, Oct 2008.

[17] J. M. O'Connor, M. Das, C. Didier, M. Mah'd, and S. J. Glick, "Development of an Ensemble of Digital Breast Object Models," *Lect Notes Comput Sci,* vol. 6136, pp. 54-61, 2010.

[18] R. B. Benitez, R. Ning, D. Conover, and S. H. Liu, "NPS characterization and evaluation of a cone beam CT breast imaging system," *Journal of X-Ray Science and Technology,* vol. 17, pp. 17-40, 2009.

[19] ACR, *Breast Imaging Reporting and Data System, Breast Imaging Atlas*, 4th Edition ed. Reston, VA: American College of Radiology (ACR), 2004.

[20] L. A. Feldkamp, L. C. Davis, and J. W. Kress, "Practical Cone-Beam Algorithm," *Journal of the Optical Society of America A-Optics Image Science and Vision,* vol. 1, pp. 612-619, 1984.

Prediction of Human Observer Performance in a Low-contrast Detection Task Using Channelized Hotelling Observer: Impact of Radiation Dose and Reconstruction Algorithms

Lifeng Yu, PhD, Shuai Leng, PhD, Lingyun Chen, PhD,
James M. Kofler, PhD, Cynthia H. McCollough, PhD

Abstract— **Efficient optimization of CT protocols demands a quantitative approach to predicting human observer performance on specific tasks at various scan and reconstruction settings. The goal of this work was to investigate how well a channelized Hotelling observer (CHO) can predict human observer performance on 2-alternative forced choice (2AFC) lesion-detection tasks at various dose levels and two different reconstruction algorithms: a filtered-backprojection (FBP) and an iterative reconstruction (IR) method (SAFIRE, Siemens Heathcare). A stadium-shaped phantom filled with water was used to represent an average-sized patient. Three rods with different diameters were placed in the phantom to simulate low-contrast lesions with different sizes. The phantom was scanned 100 times each at 5 dose levels. Twenty-one 2-alternative forced choice (2AFC) studies were created, including 15 for FBP (5 mAs settings × 3 lesion sizes) and 6 for IR (2 mAs settings x 3 lesion sizes). A CHO with Gabor channels was used to predict the percent correct for each 2AFC task. The performance predicted by the CHO was compared with that obtained by 4 medical physicists. The human and model observers were highly correlated at each dose level for each lesion size for both FBP and IR. The Pearson's product-moment correlation coefficients were 0.985 for both methods. Bland-Altman plots showed excellent agreement for all dose levels and lesions sizes with a mean absolute difference of 1.2%±1.0% for FBP and 2.3%±2.4% for IR). Therefore, the CHO model observer has a potential to accurately predict the human observer performance in CT at different radiation dose levels and reconstruction algorithms.**

Keywords: Computed tomography (CT), model observer, image quality, radiation dose, iterative reconstruction

I. INTRODUCTION

Optimizing scan protocols to achieve adequate diagnostic capability with the lowest reasonable dose is an important task in CT. Clinical evaluation by interpreting physicians is the most commonly used approach to determining the lowest possible radiation dose in CT protocols. However, this approach is very laborious, produces results that cannot be readily generalized to other scanner models and reconstruction algorithms. A more efficient and quantitative method is desired by the CT community in order to meet the ever-growing need for radiation dose and protocol optimization in CT. The key to a quantitative method for dose optimization is to determine image quality metrics that can be accurately measured in phantoms and that are highly correlated with interpreting physicians' performance for a specific diagnostic task.

Currently, many physical metrics, including modulation transfer function (MTF), slice-sensitivity profile (SSP), noise level, and noise power spectrum (NPS) are used to quantify or monitor various aspects of CT image quality. These metrics are not complete descriptors of image quality and do not directly reflect the diagnostic performance for a given task. Improving quality according to each of these metrics will not necessarily increase diagnostic accuracy. In addition, with the wider employment of iterative reconstruction, traditional simple physical metrics may have some difficulty in characterizing image quality. One example showing that MTF is not an ideal metric is the difficulty when it is used in quantifying spatial resolution for iterative reconstruction. Due to the non-linearity of the regularization process in most of the iterative reconstruction algorithms, the spatial resolution varies with the object contrast. Traditional MTF measurement with high-contrast wires would deliver incorrect information about the resolution in low-contrast situation.

Task-based image quality metrics using model observers have been studied extensively over the past 3 decades [1, 2]. Various model observers have been applied to different imaging modality areas to assess or optimize image quality, including nuclear medicine imaging, mammography, x-ray dual-energy imaging, tomosynthesis and flat-panel cone-beam CT, and MRI.

Relatively fewer studies have been done in clinical CT [3-6]. Boedeker et al used a non-prewhitening (NPW) model observer calculated from spatial frequency–based metrics (MTF and NPS) to quantify the influence of reconstruction kernel and radiation dose on the signal-to-noise-ratio (SNR) in a simple detection task [3]. The signal in that study was generated by simulation, whereas NPS was measured from repeated phantom scans. Wunderlich and Noo derived the analytical formula of image covariance in direct fan-beam CT reconstruction and used a channelized Hotelling observer (CHO) for modeling the performance in a simulated lesion detection task [6]. Richard et al investigated the relationship between model observers and human observer performance for detection tasks in multi-slice CT [5]. In their study, the model observers were Fourier-based metrics using NPS and MTF and a computer simulation was employed to generate the lesions in the detection task.

Before a model observer can be applied to clinical CT as an image quality metric to optimize radiation dose and parameter settings of various reconstruction algorithms, it is important to quantify how well the performance of the model observer is correlated with human observers in realistic CT scans. Once a set of model observers is determined to be highly correlated with or be able to predict the human observer performance, they can be used clinically to efficiently and accurately optimize scanning protocols and radiation dose levels in CT. To the best of our knowledge, there has been no such study performed in realistic CT scans without invoking any computer simulation. Furthermore, image-based model observers are required to overcome the difficulty of Fourier-based methods in iterative reconstructions.

The purpose of this work was to investigate how well a channelized Hotelling observer (CHO) can predict human observer performance on 2-alternative forced choice (2AFC) lesion-detection tasks at various radiation dose levels and two different reconstruction algorithms: a filtered-backprojection (FBP) reconstruction and an iterative reconstruction method (Sinogram AFfirmed Iterative Reconstruction or SAFIRE, Siemens Heathcare or SAFIRE, Siemens Heathcare).

II. METHODS AND MATERIALS

A. Data Acquisition and image reconstruction

A 35 × 26 cm stadium-shaped phantom filled with water was used to simulate the abdomen of an average-sized patient. Three rods with different diameters (small: 3 mm; medium: 5 mm; large: 9 mm) were placed in the center region of the water tank. The contrast relative to water background was -15 HU at 120 kV. The phantom was scanned 100 times each at 60, 120, 240, 360, and 480 quality reference mAs on a 128-slice scanner (Definition Flash, Siemens Healthcare). The tube current modulation was on (CAREDose4D, Siemens Healthcare). The corresponding scanner radiation outputs, expressed as CTDIvol, were 2.8, 5.7, 11.4, 17.1, and 22.8 mGy. After removing the 3 rods, the water phantom was again scanned 100 times to provide signal-absent background images. Images were reconstructed using the traditional 3D weighted filtered backprojection algorithm available on the scanner (B40 kernel) with a slice thickness of 5 mm and an interval of 5 mm. Images were also reconstructed with an IR algorithm available from the scanner (SAFIRE) for the two lower mAs levels: 60 mAs and 120 mAs. The kernel of the IR was I40 with a strength setting of 3.

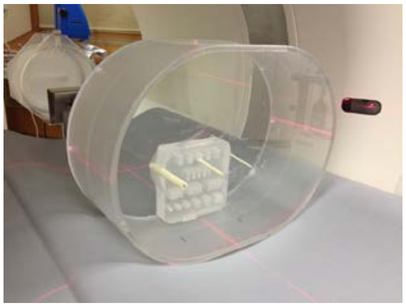

Figure 1. Phantom setup on a 128-slice CT scanner.

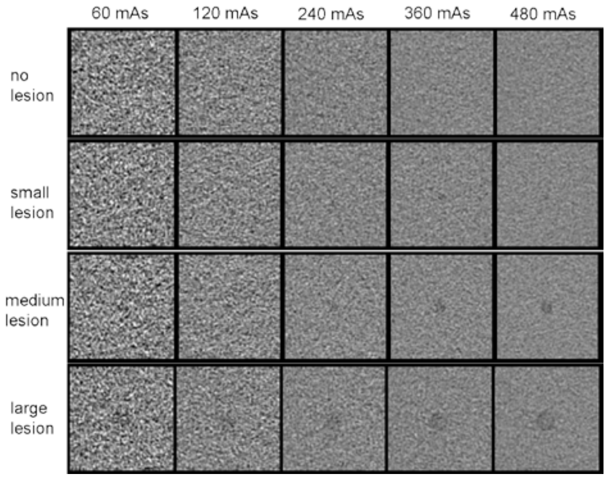

Figure 2. A collage of images with no, small (3 mm), medium (5 mm), or large (9 mm) lesions at different mAs settings.

B. Creation of 2AFC tasks

By extracting regions of interest (ROI) around the 3 rods and on the signal-absent images, we generated 21 2-alternative forced choice (2AFC) studies, including 15 studies for FBP reconstructed images (5 mAs settings x 3 lesion sizes) and 6 studies for IR reconstructed images (2 mAs settings x 3 lesion sizes). The 2 mAs settings (60 mAs and 120 mAs) for IR were intentionally selected to be the two lower dose settings because this can demonstrate if the IR can improve the performance of the 2AFC task.

Each 2AFC study had 100 trials, with each trial consisting of a signal-present image and a signal-absent image side-by-side in randomized order. In total, 2100

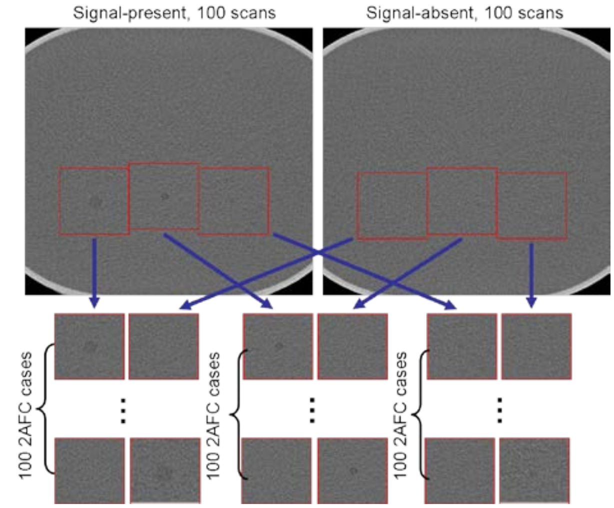

Figure 3. Twenty-one 2AFC studies (FBP: 5 mAs settings × 3 lesion sizes; SAFIRE: 2 mAs settings x 3 lesion sizes) were generated by extracting a small region of interest around the lesion and at the corresponding location on the background image. Each 2AFC study had 100 trials obtained from repeated scans, totaling 2100 trials.

trials were presented to both the model and human observers.

C. Human psychophysical experiments

Four medical physicists acted as human observers. Observers were first trained using the training datasets for each experimental condition so that lesion characteristics (size, shape, contrast, location) were known for observers. They then participate in the formal sessions for each task. Monitors were calibrated according to the DICOM standards. Experiments were conducted in a darkened room with a consistent ambient light. Observers were instructed to view the images binocularly from a distance of approximately 40 cm and have unlimited time to reach a decision. The image review was limited to 2 hours per session to avoid fatigue. Percent correct was calculated for each 2AFC study. The overall performance for each study was averaged over the 4 observers.

D. Channelized Hotelling Observers

The general form of the test statistics for a linear model observer is the inner product between the observer template and the image, which yields a scalar response given by $\lambda = \boldsymbol{\omega}^{\boldsymbol{t}}\boldsymbol{g} = \sum_{n=1}^{N^2} \omega_n g_n$, where the vector $\boldsymbol{g}$ denotes an image and $\boldsymbol{\omega}$ a template, each being an N × N matrix expressed in a column vector format with a dimension of N^2. The template is different when selecting different model observers: An NPW observer's template is the expected signal, filtered by the square of the contrast sensitivity function of the human visual system when an eye filter is incorporated. CHO uses a set of channels to reflect the response of neurons in the primary visual cortex [2]. The template in the CHO observer is given by $\boldsymbol{\omega}_{\boldsymbol{CHO}} = S_c^{-1}\left[\bar{g}_{sc} - \bar{g}_{bc}\right]$, where $S_c = \frac{1}{2}\left[K_{sc} + K_{bc}\right]$ is the intraclass channel scatter matrix (average of the channel output covariance matrix when the signal is present and absent: $K_{sc} = U^T K_s U$, $K_{bc} = U^T K_b U$) and $\bar{g}_{sc}$ and $\bar{g}_{bc}$ are the channel output means of signal plus background and background: $\bar{g}_{sc} = U^T \bar{g}_s$, $\bar{g}_{bc} = U^T \bar{g}_b$.

We used a CHO with Gabor channels, which involves 6 channel passbands: [1/128, 1/64], [1/64, 1/32], [1/32, 1/16], [1/16, 1/8], [1/8, 1/4], and [1/4, 1/2] cycles/pixel. The center frequencies were 3/256, 3/128, 3/64, 3/32, 3/16, and 3/8 cycles/pixel, respectively. Five orientations (0, 2π/5, 4π/5, 6π/5, and 8π/5 radians) and 2 phases (0 and π/2) were also used, leading to a total of 60 channels in the CHO implementation. Figure 4 shows the 30 channels at one phase.

In addition, internal noise is a known component of human inefficiency in perceptual tasks and it is necessary to be included in visual detection models. We added the internal noise to the decision variables by sampling the noise from a normal distribution with zero mean and the standard deviation was proportional to the decision variable's standard deviation caused by external noise.

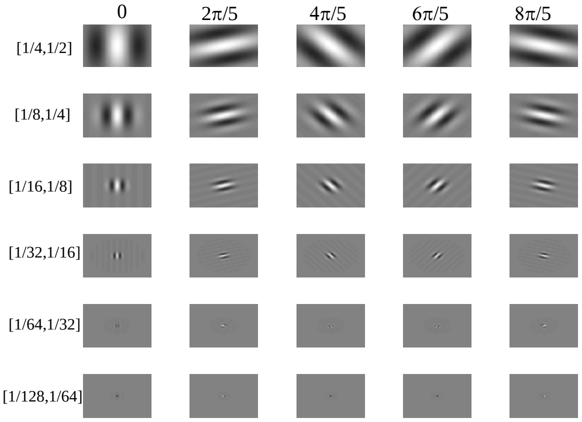

Figure 4. Garbor filters with 6 channel passbands, 5 orientations, and 2 phases. Only the 30 channels when phase equals zero are displayed.

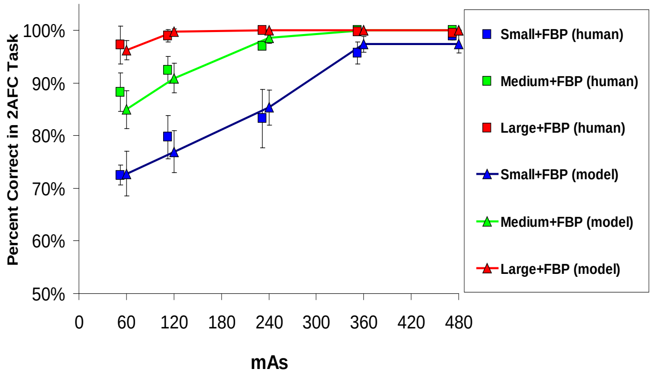

Figure 5. Percent correct in each of the 15 2AFC tasks obtained by human observers (rectangular symbols) and predicted by the CHO model observer (triangular symbols). The 15 2AFC tasks were generated at 5 mAs levels (60, 120, 180, 240, 360, and 480 mAs) and 3 lesion sizes (small, medium, and large).

III. RESULTS

A. Performance correlation between model and human observers for FBP reconstruction at various dose levels

The performance in terms of percent correct predicted by the CHO was compared with that obtained by 4 medical physicists for the 15 2AFC studies involving images reconstructed with the FBP method. The human and model observers were highly correlated at each dose level for each lesion size (Figure 5). The Pearson's product-moment correlation coefficients were 0.983, 0.987, and 0.958 for small, medium, and large lesions, respectively. The overall correlation coefficient was 0.985. Bland-Altman plots showed excellent agreement for all dose levels and lesions sizes with a mean absolute difference of 1.2%±1.0% (Figure 6).

B. *Impact of iterative reconstruction on performance correlation between human and model observers*

Figure 7 compares the performance predicted by the CHO with that obtained by the human observers for the IR reconstructed images at the two lower mAs settings (60 mAs and 120 mAs). As a reference, the performance with the FBP reconstruction was also shown on the same figure.

One can see that, with the use of IR, the percent correct predicted by the model observer is still in excellent agreement with that measured by the human observer with a mean absolute difference of 2.3%±2.4%. The highest discrepancy occurs for small lesion at 120 mAs, where the difference between the two was 7.1%. In this setting, all human observers performed much worse than expected (even worse than a lower dose setting at 60 mAs). The reason is still unclear. Excluding this unexpected exceptions, the mean absolute difference of other five predictions were 1.3%±0.5%.

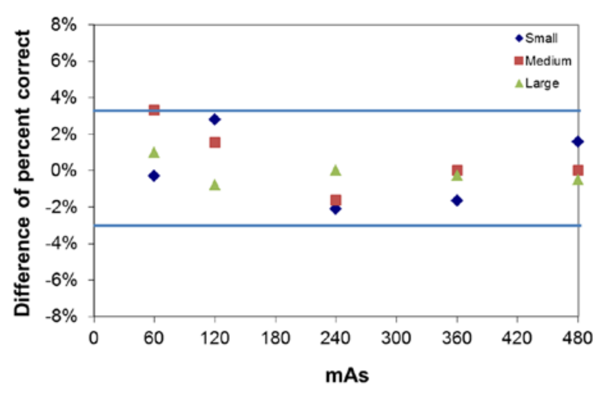

Figure 6. Bland-Altman plot of percent correct difference between human and model observers in the 15 2AFC tasks. The two blue lines (-3% and 3.3%) indicate the average difference ± 2σ, where σ is the standard deviation of the differences.

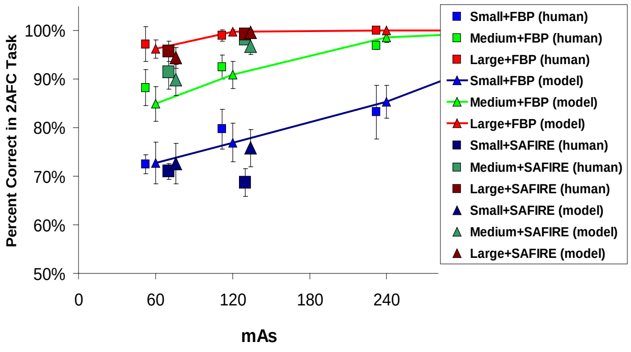

Figure 7. Performance comparison between human observers (rectangular symbols) and model observers (triangular symbols) for the 6 2AFC tasks when IR reconstruction (SAFIRE, Siemens Healthcare) was applied. The 6 2AFC tasks were generated at 2 mAs levels (60 mAs and 120 mAs) and 3 lesion sizes (small, medium, and large). The performance for the 2AFC tasks when FBP reconstruction was used was also displayed as a reference.

C. *Does iterative reconstruction improve performance?*

From Fig. 7, one can see that the performance achieved by human observers and predicted by model observers both did not show a clear sign that IR (SAFIRE, Siemens Healthcare) improves the performance in the 2AFC tasks for every dose and lesion size setting. It is interesting to note that for medium lesion size (5 mm in diameter), there is an improvement by human observers, from 88.3%+/-3.7% to 91.5%+/-3.5% at 60 mAs (p=0.14) and from 92.5%±2.5% to 98.3±0.5% at 120 mAs (p=0.028). The improvement at 120 mAs was significant. Such a trend of improvement was predicted correctly by the model observer. For large lesion size (9 mm), the performance was almost identical for both human and model observers, maybe due to the fact that the percent correct is close to saturation (100%). For small lesion size (3 mm), however, the performance became unexpectedly worse at 120 mAs for human observers when IR was applied (from 79.8%±4.1% to 68.8±2.9%, p=0.021). Model observer predicted a slight drop from 77.0%±4.0% to 75.8%±3.8%, but not as significant as human observers. The prediction by model observers appeared to be more reasonable because 60 mAs did not show significant changes for any observer. The reason for this unexpected substantial drop in human observers remains to be investigated.

IV. CONCLUSIONS AND DISCUSSIONS

We investigated how well a CHO model can predict human observer performance on simple 2AFC lesion-detection tasks using repeated and realistic CT scans. An excellent agreement of performance was achieved between human and model observers at various dose levels for both FBP and an iterative reconstruction method. These results imply that the CHO model has a potential to be employed in clinical CT for optimizing radiation dose and scanning protocols.

In the current study, the 2AFC lesion detection task consists of a uniform water background. How realistic anatomical background affects the agreement of model and human observers remains to be investigated. The model observers may need to be modified in this situation in order to achieve a reasonable agreement. Phantoms representing realistic background need to be constructed to accurately simulate realistic diagnostic tasks. More complicated tasks such as lesion classification and lesion detection with signal known statistically (SKS) in realistic background also remain to be evaluated.

REFERENCES

[1] ICRU Report 54, "Medical Imaging - The Assessment of Image Quality," *International Commission on Radiation Units and Measurements (ICRU)*, 1995.

[2] H. H. Barrett, J. Yao, J. P. Rolland, and K. J. Myers, "Model observers for assessment of image quality," *Proc Natl Acad Sci U S A*, vol. 90, pp. 9758-65, Nov 1 1993.

[3] K. L. Boedeker and M. F. McNitt-Gray, "Application of the noise power spectrum in modern diagnostic MDCT: part II. Noise power spectra and signal to noise," *Phys Med Biol*, vol. 52, pp. 4047-61, Jul 21 2007.

[4] P. F. Judy, R. G. Swensson, and M. Szulc, "Lesion detection and signal-to-noise ratio in CT images," *Med Phys*, vol. 8, pp. 13-23, Jan-Feb 1981.

[5] S. Richard, G. Yadava, X. Li, and E. Samei, "Predictive models for observer performance in CT: Applications in protocol optimization," *Proc SPIE*, vol. 7961, 2011.

[6] A. Wunderlich and F. Noo, "Image covariance and lesion detectability in direct fan-beam x-ray computed tomography," *Phys Med Biol*, vol. 53, pp. 2471-93, May 21 2008.

Noise and Bias Properties of PET images using DECT based Attenuation Correction

Ting Xia, Adam M Alessio, Paul E Kinahan
Imaging Research Laboratory
Department of Radiology
University of Washington

Abstract

The use of dual-energy CT (DECT) for accurate attenuation correction of PET and SPECT data in PET/CT and SPECT scanners has been proposed. Using synthesized monoenergetic images at the appropriate photon energy would allow for accurate attenuation correction where there is both bone and confounding high-Z materials (e.g. contrast or implants) in the CT image. DECT methods, however, are known to increase image noise. **Methods**: We used joint PET and CT simulation studies of the NCAT phantom to evaluate the energy dependent noise and bias properties of monoenergetic attenuation images synthesized from dual-energy CT (DECT) acquisitions. The monoenergetic images were then used to estimate attenuation correction coefficients for the PET emission data. The noise and bias of PET tracer uptake in a variety of lesions (soft tissue, bone) was evaluated as a function of CT technique and CT image noise suppression parameters. **Results**: In general there was a trade off of increased noise but reduced bias when attenuation correction was determined from DECT acquisition when compared to single-kVp CT based attenuation correction. Sinogram smoothing can dramatically reduce noise in the DECT-derived PET attenuation image without increasing PET image bias. Through appropriate selection of tube currents for the high and low kVp scans, DECT delivered roughly the same amount of radiation dose as that of a single kVp CT scan, but could be used for PET attenuation correction with reduced bias in contrast agent regions by a factor of ~2.6 and a reduced RMSE for the total object. **Conclusions**: With careful optimization of DECT techniques, DECT-based attenuation correction for PET can deliver the same radiation dose as that of a single spectra CT, while also leading to reduced bias and RMSE for PET imaging of high-Z materials.

Introduction

Quantitative imaging with positron emission tomography (PET) and single-photon emission computed tomography (SPECT) is receiving increased attention for clinical applications (1,2). In quantitative PET and SPECT, correction for the effect of photon attenuation is of paramount importance. The X-ray Computed Tomography (CT) component in a PET/CT or SPECT/CT system not only provides precise anatomical localization of regions identified on the tracer uptake images, but is also used for attenuation correction of the PET or SPECT emission data (3,4). At the energies of X-ray CT, attenuation is due to Compton scatter and photoelectric absorption, while at SPECT energies, and particularly PET energies, Compton scatter is the dominant process for biological materials.

Table 1. Photon energies of common isotopes used in PET/CT and SPECT/CT Imaging.

Mode	Isotope	Energy (keV)
PET	All (F-18, C-11, etc.)	511
SPECT	Xe-133	80.9
SPECT	Tc-99m	140
SPECT	I-123	160
SPECT	Ga-67	185
SPECT	In-111	171, 245

A list of energies of interest are given in Table 1, and Figure 1 plots the mass attenuation coefficients of common materials over the energy ranges relevant to PET/CT and SPECT/CT imaging.

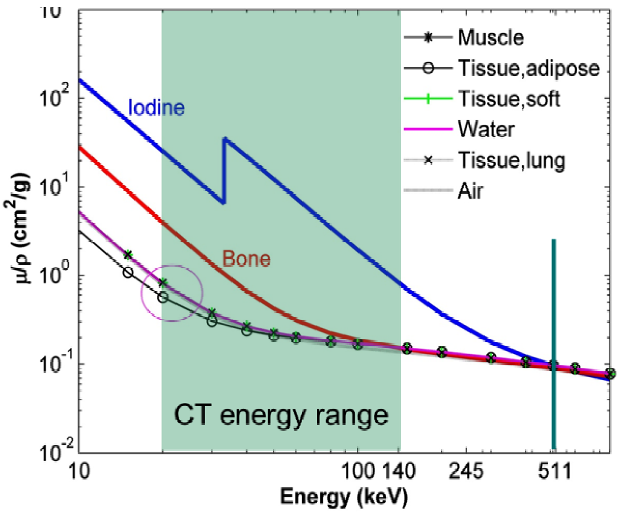

Figure 1. Mass attenuation coefficient as a function of energy for different materials.

The most common method for transforming CT images to SPECT or PET energies is Multilinear/Hybrid Scaling (3.4). In these methods, different scaling factors (for water and air, and for water and bone respectively) are used to calculate the attenuation values for CT numbers H for which -1000 < H < 0, and for H >0. The multilinear scaling method and other hybrid methods have been shown to give reasonable results for low-Z biological materials in practice. However, for high-Z materials such as contrast agents there is possibility for significant bias (4).

Dual energy CT (DECT) (5-7) has been proposed as a method to estimate material properties using either photoelectric and Compton components or physical basis materials such as plastic and aluminum. DECT has been proposed to remove the bias from the CT-based attenuation correction (CTAC) image for SPECT and PET (6.7).

A challenge with the use of DECT is the significant noise amplification due to the poorly conditioned inverse problem of estimating the component sinograms, leading to excessive noise amplification. It has already been shown in the literature that the noise amplification is energy dependent in the diagnostic CT energy range, but the noise and bias at SPECT or PET energies is largely unknown. Another potential drawback of dual energy is the additional patient radiation dose required to acquire two separate energies and to reduce noise.

To address these issues with DECT-based attenuation correction, we evaluated the energy dependent noise properties of synthesized mono-energetic attenuation images in the energy range appropriate for nuclear imaging (140-511 keV). We also evaluated the impact on corresponding PET images.

Methods

CT-based attenuation correction was provided by either single-kVp CT scans (3,4) or dual-kVp (i.e. dual-energy CT (DECT)) CT scans (5-7). We used simulation studies to evaluate the bias and noise of synthesized monoenergetic images of a modified NCAT phantom from 40 to 520 keV, a range suitable for SPECT and PET energies. In addition we evaluated strategies of noise suppression by sinogram smoothing and dose minimization by optimization of tube currents. We compared the impact of DECT-based attenuation correction with similar dose single-kVp based attenuation correction on PET quantitation for an NCAT phantom with hot-spot regions representing tumors in soft tissue, bone, and also with iodine based CT contrast agent enhanced soft tissue. The simulations used the Catsim (8) and ASIM (9) simulation tools for CT and PET. The overall data flow is illustrated in Figure 2.

Results

Both analytic calculations and simulations showed the expected minimum noise value for a synthesized monoenergetic image at an energy between the mean energies of the two spectra. In addition we found that the normalized coefficient of variation in the synthesized attenuation image plateaued near the 160 keV energy of I-123 (i.e. SPECT) and then remained constant with increasing energy up to 511 keV and beyond (i.e. PET). As a check, the linear attenuation coefficients of the synthesized monoenergetic images were within 2.4% of the known true values across the entire energy range. Compared with no sinogram smoothing, sinogram smoothing can dramatically reduce noise in the DECT-derived attenuation image. Through appropriate selection of tube currents for high and low kVp scans, DECT can deliver roughly the same amount of radiation dose as that of a single kVp CT scan, but could be used for PET attenuation correction with reduced bias in contrast agent regions by a factor of ~2.6 and slightly reduced RMSE for the total image.

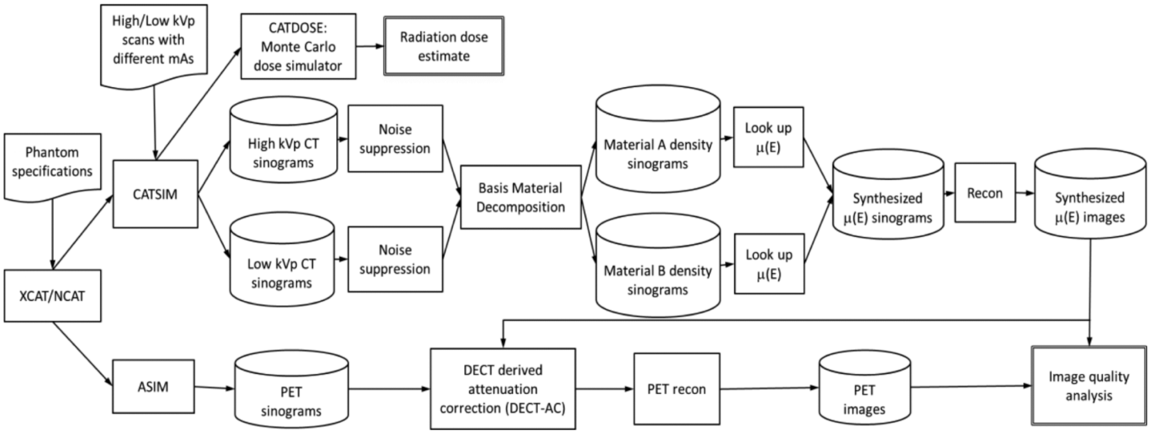
High/Low kVp scans with different mAs
CATDOSE: Monte Carlo dose simulator
Radiation dose estimate
Phantom specifications
CATSIM
High kVp CT sinograms
Noise suppression
Low kVp CT sinograms
Noise suppression
Basis Material Decomposition
Material A density sinograms
Material B density sinograms
Look up μ(E)
Look up μ(E)
Synthesized μ(E) sinograms
Recon
Synthesized μ(E) images
XCAT/NCAT
ASIM
PET sinograms
DECT derived attenuation correction (DECT-AC)
PET recon
PET images
Image quality analysis

Figure 2. Data flow for evaluating use of DECT for PET attenuation correction.

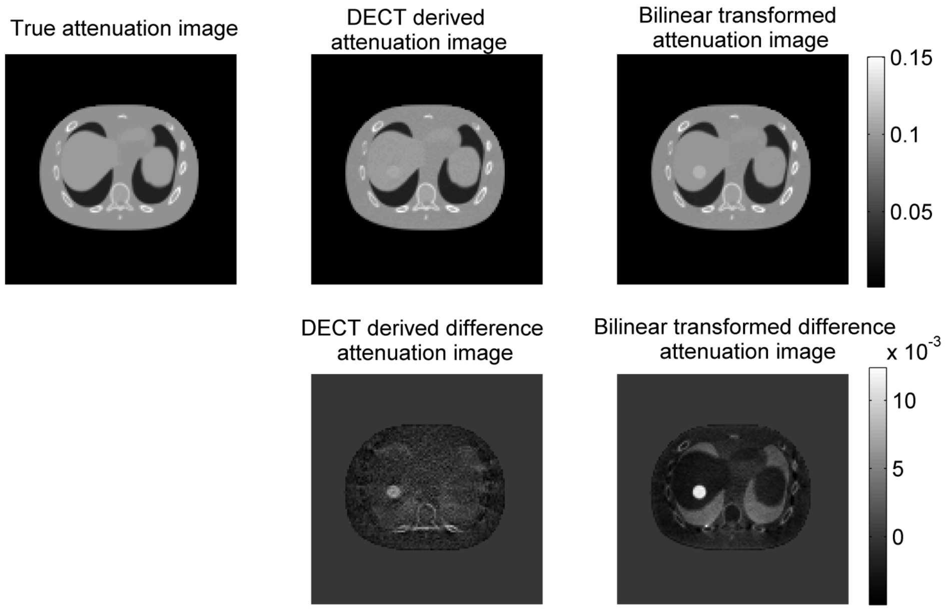
True attenuation image
DECT derived attenuation image
Bilinear transformed attenuation image
0.15
0.1
0.05
DECT derived difference attenuation image
Bilinear transformed difference attenuation image
x 10^{-3}
10
5
0

Figure 3. Comparison of CT-based attenuation images of the modified NCAT phantom at 511 keV.

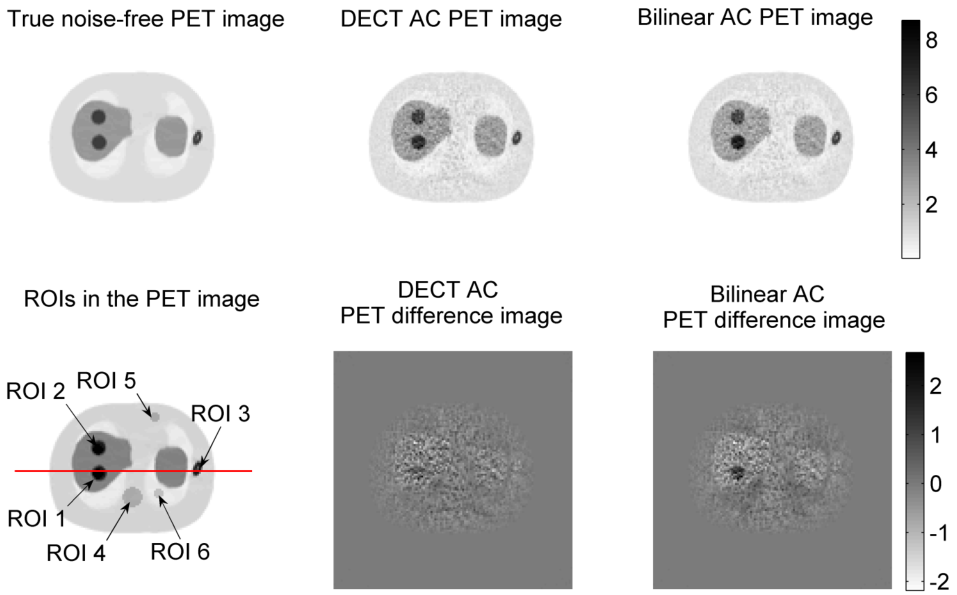
True noise-free PET image
DECT AC PET image
Bilinear AC PET image
8
6
4
2
ROIs in the PET image
ROI 2
ROI 5
ROI 3
ROI 1
ROI 4
ROI 6
DECT AC PET difference image
Bilinear AC PET difference image
2
1
0
-1
-2

Figure 4. Comparison of PET images of the modified NCAT images using the different CT-based attenuation images shown in Figure 3.

Table 2. Bias in noisy PET images with DECT and single CT based attenuation correction for different ROIs in the NCAT phantom as shown in Figure 4.

Methods	ROI 1	ROI 2	ROI 3	ROI 4	ROI 5	ROI 6	Entire object
True PET value	6.0	5.9	5.8	1.0	1.0	0.5	n/a
PET image with DECT-AC	6.9%	-1.2%	-3.3%	0.6%	-1.2%	11.7%	21.0%
PET image with single-kVp CT	17.8%	-5.4%	-1.1%	-16.7%	-4.3%	42.9%	23.3%

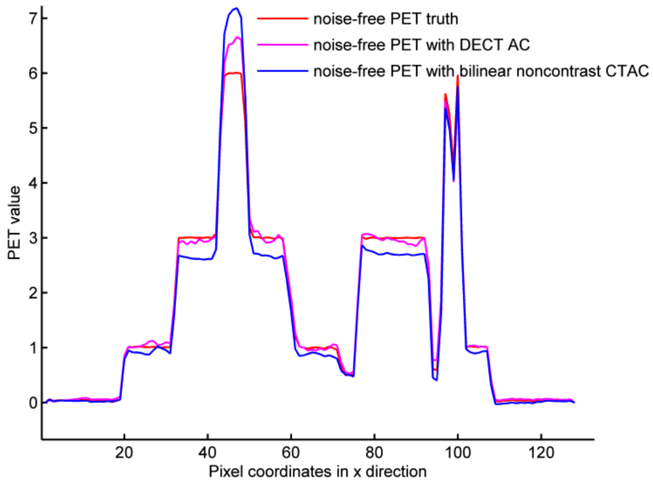

Figure 5. Profiles through the modified NCAT PET images shown in Figure 4.

Conclusions

If DECT is used for attenuation correction of emission tomography, there is a noise amplification that is dependent on the energy of the synthesized mono-energetic image of linear attenuation coefficients. For SPECT and PET imaging the bias and noise levels of DECT based attenuation correction is unlikely to affect image quality. Sinogram smoothing can be used to reduce the noise amplification in DECT-derived attenuation map without undue increase of PET image bias. With careful optimization of DECT techniques, DECT could deliver the same radiation dose as that of a single spectra CT, and lead to reduced bias and RMSE for PET imaging of high-Z materials.

Acknowledgements

We acknowledge the support of GE for the use of CatSim, in particular Drs Jed Pack, Bruno De Mann and Paul Fitzgerald. We also thank Drs Jeffrey Fessler, Bruce Whiting, Patrick La Riviere and William Paul Segars for useful discussions. This work was supported by NIH grant R01-CA115870.

References

1. Weber WA. Assessing tumor response to therapy. J Nucl Med 50 Suppl 1:1S-10S, 2009
2. W. Jentzen, L. Freudenberg and A. Bockisch, "Quantitative imaging of (124)I with PET/ CT in pretherapy lesion dosimetry. Effects impairing image quantification and their corrections," Q J Nucl Med Mol Imaging 55, 21-43 (2011)
3. P. E. Kinahan, B. H. Hasegawa and T. Beyer, "X-ray-based attenuation correction for positron emission tomography/computed tomography scanners," Semin Nucl Med 33, 166-179 (2003)
4. S. C. Blankespoor, X. Wu, K. Kalki, J. K. Brown, H. R. Tang, C. E. Cann and B. H. Hasegawa, "Attenuation correction of SPECT using X-ray CT on an emission-transmission CT system: Myocardial perfusion assessment," Ieee T Nucl Sci 43, 2263-2274 (1996).
5. R. E. Alvarez and A. Macovski, "Energy-Selective Reconstructions in X-Ray Computerized Tomography," Physics in Medicine and Biology 21, 733-744 (1976).
6. B. H. Hasegawa, T. F. Lang, J. K. Brown, E. L. Gingold, S. M. Reilly, S. C. Blankespoor, S. C. Liew, B. M. W. Tsui and C. Ramanathan, "Object-Specific Attenuation Correction of SPECT with Correlated Dual-Energy X-Ray CT," IEEE T Nucl Sci 40, 1242-1252 (1993).
7. P. E. Kinahan, A. M. Alessio and J. A. Fessler, "Dual energy CT attenuation correction methods for quantitative assessment of response to cancer therapy with PET/CT imaging," Technol Cancer Res Treat 5, 319-327 (2006).
8. B. De Man, S. Basu, N. Chandra, B. Dunham, P. Edic, M. Iatrou, S. Mcolash, P. Sainath, C. Shaughnessy, B. Tower and E. Williams, "CATSIM : a new Computer Assisted Tomography SIMulation environment," in Medical Imaging 2007: Physics of Medical Imaging, Vol. 6510, edited by J. Hsieh and J. Flynn (Proc. of SPIE, 2007), pp. 65102G.
9. Comtat C, Kinahan PE, Defrise M, and Michel C, Lartizien C, Townsend DW. Simulating Whole-body PET scanning with rapid analytical methods. Proceedings of: IEEE Nuclear Science Symposium and Medical Imaging Conference, Seattle, WA, October 24-30, Vol.3 Page 1260-1264, 1999.

On the statistical analysis of image quality metrics based on alternative forced choice experiments

Frédéric Noo, Adam Wunderlich, Dominic J Heuscher, Katharina Schmitt, Zhicong Yu

***Abstract*—Task-based image quality assessment is a valuable methodology for development, optimization and evaluation of new image formation processes in CT. Such an assessment can be performed by building a receiver-operating characteristic (ROC) curve, or variants of it, such as the localization ROC (LROC) curve or the free-response ROC (FROC) curve. For comparisons, it is common to reduce the entire curve to a single scalar that is generally chosen as the area under the curve. In this setting, building the entire curve is not necessary: a two alternative forced choice (AFC) experiment can be performed to directly obtain the desired scalar. In this work, we discuss statistical inference for comparisons of image formation processes using multiple AFC studies.**

I. INTRODUCTION

Significant effort is currently spent on the development of statistical iterative reconstruction methods for CT imaging, particularly for the aim of enabling CT exams with a lower dose. To be successful, this effort needs to be accompanied by a careful methodology for assessment of image quality. Such an assessment should be task-based [1], particularly because the algorithms that are under development are non-linear, so that resolution, contrast and anatomical background effects are tangled and thus cannot be analyzed each on their own.

A popular methodology for task-based image quality assessment is the construction of a receiver operating characteristic (ROC) curve [1], [2]. The main idea behind this approach is to evaluate how well an observer (also called a reader) can differentiate images from two separate classes. Typically, these two classes are chosen as sets of images with signal (lesion) either present or absent, but the theory is not limited to such a type of classes. For example, the ROC curve can be used to evaluate the ability of an observer to distinguish lesions with fuzzy boundaries from lesions with sharp boundaries.

Two other popular methodologies for image quality assessment are the localization ROC (LROC) curve, and the free-response ROC (FROC) curve. When the task is defined as that of detecting a signal with unkown location, these two methodologies are often preferred over the classical ROC curve. This preference is due to the fact that, unlike the ROC methodology, the LROC and FROC curves do account for the visual search process. (When the lesion location is not specified, the ROC approach suffers from the fact that an observer may rate an image as containing a lesion and be correct while basing its decision on a reconstruction artifact.) Note that the FROC curve is more powerful than the LROC curve as it does not require telling the observer how many instances of the signal are present in an image.

Whether ROC, LROC or FROC curves are used, it is typical to reduce all information brought by the curve to a single scalar. For ROC and LROC studies, this scalar is generally chosen as the area under the curve. For FROC studies, the area under the curve is not defined, and no single metric has yet been universally accepted.

Interestingly, the area under the ROC or LROC curve has a clear probabilistic meaning: it is the probability of correct decision. In the ROC case, correct decision means correct classification. In the LROC case, correct decision means correct classification together with correct localization [3]. Given this probabilistic meaning, it was noted that the area under the ROC or LROC curve can be estimated without seeking the curve, using the concept of Bernoulli trials. In the context of image quality assessment, this trial is often referred to as a two alternative forced choice (2-AFC) experiment. Whereas the ROC or LROC curve involves only two choices, AFC experiments do not need to be limited to two choices. Multiple AFC experiments (MAFC) can be as easily implemented, and they can be advantageous over a 2-AFC experiment by allowing more stringent testing of image formation processes. However, note that the MAFC experiment does not have an ROC-curve interpretation.

The primary aim of a 2-AFC or MAFC experiment is to evaluate a proportion that serves as an estimate of the probability of correct decision. To achieve this aim, the experimentalist creates a number n of independent trials (cases), present these cases one after the other to an observer and records the number of times when the observer succeed to make a correct decision; this number divided by n is the sought proportion.

As presented above, the probability of correct decision in an MAFC experiment is a quantity that depends on the observer. To reduce this dependence, the mean probability of correct decision over a set of observers is often preferred as a figure-of-merit. Moreover, the proportion obtained for a given observer in an MAFC experiment depends on the selected cases as well as their number. The larger the number of cases, the closer the proportion is to the desired probability of correct decision. However, there are practical limits on the number of trials an observer can be subjected to. Hence, it is important to realize that image quality assessment results based on MAFC experiments include variability due to randomness in cases as well as in the reader pool. An MAFC experiment is inherently a so-called multi-reader multi-case (MRMC) study.

There are four different ways of reporting results from an

The authors are with the Department of Radiology, University of Utah, Salt Lake City, Utah, USA. E-mail: noo@ucair.med.utah.edu

This work was partially supported by NIH grants R01 EB007236 and R21 EB009168.

MRMC study: the cases can either be seen as a fixed or a random effect, and the observers can also either be seen as a fixed or a random effect. Naturally, treating the readers and also the cases as a random rather than a fixed effect enables more general conclusions. However, it is important to realize that generality comes with a cost: error bars are increased. If only 3 or 4 observers are available, there is virtually no hope to make any useful conclusion between image formation processes while treating the readers as a random effect. In this paper, we are interested in the statistical analysis of MRMC results obtained with alternative forced choice experiments under the condition that the readers are seen as a fixed effect, and the cases as a random effect. Our results are primarily relevant for image quality assessment studies related to development and optimization of image formation processes, for which generating a large number of cases is typically easy whereas readers are scarce due to limited availability and high cost.

Technically speaking, the statistical analysis we are interested in amounts to making inferences based on a set of correlated proportions. Proper handling of correlations is where the complexity lies. In practice, correlations can be induced through a number of mechanisms. For example, a study involving two observers that read the exact same cases from one image formation process yields two correlated proportions. Similarly, comparing two image reconstruction algorithms using the exact same data sets with a single observer will yield two correlated proportions. Hypothesis tests have been developed for comparing two [4] or more [5] correlated proportions. Here, we extend on these results in two ways: first, we enable comparisons using confidence intervals rather than hypothesis testing, and second, we enable these comparisons to be performed between linear combinations of proportions, instead of proportions, which is crucially needed to compare reader-averaged proportions.

II. THEORY

The problem we consider is that of drawing statistical inferences from K correlated proportions that are each the result of one MAFC experiment. The difference from one experiment to another may either be a change in the observer, or a change in the image formation process used to define the cases. In this section, we first give a mathematical formulation for this problem. Then, we derive the covariance matrix for the vector of correlated proportions, and we introduce a robust estimator for this matrix. Together with properties of asymptotic normality, this covariance matrix estimator is essentially all that we need to build confidence intervals for any function of the K correlated proportions.

A. Mathematical formulation

Let θ_k with $k = 1, \ldots K$ denote the probability of correct decision associated with the k-th MAFC experiment, and let $\hat{\theta}_k$ be the proportion used as estimate of this probability.

As discussed earlier, each $\hat{\theta}_k$ is obtained from a number n of independent Bernoulli trials. Let X_{ik} be the outcome of the i-th trial in the k-th MAFC experiment. This outcome is equal to one in case of success, and equal to zero otherwise. By definition,

$$\hat{\theta}_k = \frac{1}{n} \sum_{i=1}^{n} X_{ik} \,. \tag{1}$$

Also, the expected value of X_{ik}, denoted as $E(X_{ik})$, is θ_k, and consequently, $E(\hat{\theta}_k) = \theta_k$.

Now, let $\underline{\theta}$ and $\hat{\underline{\theta}}$ be the two vectors in the K-dimensional Cartesian space that have the θ_k and $\hat{\theta}_k$ values as their components, respectively, and let $\underline{u}_i$ be the vector that has the X_{ik} as components for any fixed value of i. Using this vectorial notation, we can write $E(\hat{\underline{\theta}}) = \underline{\theta}$ and

$$\hat{\underline{\theta}} = \frac{1}{n} \sum_{i=1}^{n} \underline{u}_i \,. \tag{2}$$

In our setting, vector $\hat{\underline{\theta}}$ is a multivariate random variable with covariance matrix C. If there were no correlations between the MAFC experiments, C would be a diagonal matrix. However, here, we consider that correlations are present and thus C is not diagonal. In any case, the diagonal elements of C are each given by the variance expression for a proportion based on n Bernoulli trials, i.e.,

$$C(k,k) = \frac{\theta_k\,(1-\theta_k)}{n} \,. \tag{3}$$

B. Covariance matrix

Theorem 1. *Let p_{rs} be the probability of jointly reaching a correct decision in the experiments of indices r and s with $r \neq s$. Then,*

$$C(r,s) = \frac{p_{rs} - \theta_r\,\theta_s}{n} \,. \tag{4}$$

This theorem is proved as follows. First, recall that, by definition

$$\begin{aligned} C(r,s) &= E((\hat{\theta}_r - \theta_r)(\hat{\theta}_s - \theta_s)) \\ &= E(\hat{\theta}_r\,\hat{\theta}_s) - \theta_r\,\theta_s \,. \end{aligned} \tag{5}$$

From (1), we get

$$\begin{aligned} E(\hat{\theta}_r\,\hat{\theta}_s) &= \frac{1}{n^2} \sum_{i=1}^{n} \sum_{l=1}^{n} E(X_{ir}\,X_{ls}) \\ &= \frac{1}{n^2} \sum_{i=1}^{n} \sum_{l \neq i} E(X_{ir}\,X_{ls}) + \frac{1}{n^2} \sum_{i=1}^{n} E(X_{ir}\,X_{is}) \,. \end{aligned} \tag{6}$$

Given that the cases correspond to independent trials, $E(X_{ir}\,X_{ls}) = \theta_r\,\theta_s$ when $l \neq i$. Moreover, from the definition of p_{rs}, we have $E(X_{ir}\,X_{is}) = p_{rs}$ for any value of i. Therefore,

$$\begin{aligned} E(\hat{\theta}_r\,\hat{\theta}_s) &= \frac{n\,(n-1)}{n^2}\,\theta_r\theta_s + \frac{1}{n}\,p_{rs} \\ &= \theta_r\,\theta_s + \frac{1}{n}\,(p_{rs} - \theta_r\,\theta_s) \,. \end{aligned} \tag{7}$$

Direct combination of this last result with (5) yields the announced result.

Note, as expected, that (3) and (4) are fully consistent with each other, since $p_{rs} = \theta_r$ when $r = s$. In addition, when the proportions are independent, $p_{rs} = \theta_r\,\theta_s$ and thus $C(r,s) = 0$.

C. Estimator for the covariance matrix

Theorem 2. *Let*

$$\hat{p}_{rs} = \frac{1}{n} \sum_{i=1}^{n} X_{ir} \, X_{is} \, . \tag{8}$$

Then,

$$\hat{C}(r,s) = \frac{1}{n-1} \left(\hat{p}_{rs} - \hat{\theta}_r \, \hat{\theta}_S \right) \tag{9}$$

is an unbiased and consistent estimator of C. Furthermore, $\hat{C}$ is definite positive with probability one.

The unbiasedness of C is proved as follows. First, we note, from its definition, that $E(\hat{p}_{rs}) = p_{rs}$. Second, we observe that

$$E(\hat{\theta}_r \, \hat{\theta}_s) = C(r,s) + \theta_r \, \theta_s \, . \tag{10}$$

Consequently,

$$\begin{aligned} E(\hat{C}(r,s)) &= \frac{1}{n-1} \, E(\hat{p}_{rs}) - \frac{1}{n-1} \, E(\hat{\theta}_r \, \hat{\theta}_s) \\ &= \frac{1}{n-1} \, p_{rs} - \frac{1}{n-1} \, \left(C(r,s) + \theta_r \, \theta_s\right) \\ &= \frac{1}{n-1} \, \left(p_{rs} - \theta_r \, \theta_s\right) - \frac{1}{n-1} \, C(r,s) \\ &= C(r,s) \end{aligned} \tag{11}$$

where the last equality comes from (4).

To prove consistency, we need to evaluate the behavior of $\hat{C}(r,s)$ as a function n. Given that $\hat{C}(r,s)$ is expressed as the sum of two random variables, we have

$$\begin{aligned} \text{Var}\left(\hat{C}(r,s)\right) &\leq \left(\sqrt{\text{Var}\left(\frac{\hat{p}_{rs}}{n-1}\right)} + \sqrt{\text{Var}\left(\frac{\hat{\theta}_r \hat{\theta}_s}{n-1}\right)} \right)^2 \\ &\leq \frac{1}{(n-1)^2} \left(\sqrt{\text{Var}(\hat{p}_{rs})} + \sqrt{\text{Var}(\hat{\theta}_r \hat{\theta}_s)} \right) \\ &\leq \frac{1}{(n-1)^2} \left(\sqrt{\frac{\hat{p}_{rs}\,(1-\hat{p}_{rs})}{n}} + \sqrt{\text{Var}(\hat{\theta}_r \hat{\theta}_s)} \right) \, . \end{aligned} \tag{12}$$

Also, by the delta method, we know that

$$\text{Var}(\hat{\theta}_r \hat{\theta}_s) \simeq \frac{W}{n} \tag{13}$$

for n large where W is a constant. Therefore, $\text{Var}(\hat{C}(r,s))$ decays at least as $n^{-5/2}$ with n, which proves consistency.

Last, to prove that $\hat{C}$ is definite positive with probability one, we first note that the following equality holds:

$$n \, \hat{C} = \frac{1}{n} \sum_{i=1}^{n} \underline{u}_i \, \underline{u}_i^T - \hat{\underline{\theta}} \, \hat{\underline{\theta}}^T \, . \tag{14}$$

Thus, for any vector $\underline{x}$, we have

$$n \, \underline{x}^T \hat{C} \underline{x} = \frac{1}{n} \sum_{i=1}^{n} (\underline{x}^T \, \underline{u}_i)^2 - (\underline{x}^T \hat{\underline{\theta}})^2 \, . \tag{15}$$

Furthermore, since $\hat{\underline{\theta}} = \frac{1}{n} \sum_{i=1}^{n} \underline{u}_i$, this last equality is equivalent to

$$n^2 \, \underline{x}^T \hat{C} \underline{x} = \sum_{i=1}^{n} (\alpha_i)^2 - \frac{1}{n} \left(\sum_{i=1}^{n} \alpha_i \right)^2 \tag{16}$$

with $\alpha_i = \underline{x}^T \, \underline{u}_i$. However, Cauchy-Schwartz's inequality implies that

$$\left(\sum_{i=1}^{n} \alpha_i \right)^2 \leq n \, \sum_{i=1}^{n} (\alpha_i)^2 \, . \tag{17}$$

Therefore,

$$n^2 \, \underline{x}^T \hat{C} \underline{x} \geq 0 \, , \tag{18}$$

which demonstrates that $\hat{C}$ is semi-definite positive.

Last, we examine the condition under which the equality in (18) can hold. Because the inequality in (18) was found using Cauchy-Schwartz's inequality, the condition is simple: equality only holds only when $\underline{x}^T \, \underline{u}_i$ is equal to a constant for all i. Since this constraint corresponds to a set of measure zero for any given $\underline{x}$, the strict inequality holds with probability one.

D. Asymptotic properties

Theorem 3. *The random vector $\hat{C}^{-1/2}(\hat{\underline{\theta}} - \underline{\theta})$ converges in distribution to a multivariate normal vector with mean zero and identity covariance matrix.*

This theorem is a direct consequence of the following two results. First, $\hat{C}$ converges towards C with probability one, because $\hat{C}$ is a consistent estimator of C with a converging rate of $n^{-5/2}$. Second, equation (2) and the central limit theorem for multivariate random variables imply together that $\hat{C}^{-1/2}(\hat{\underline{\theta}} - \underline{\theta})$ converges in distribution to a multivariate normal vector with mean zero and identity covariance matrix.

E. Summary

Thanks to the asymptotic properties of Theorem 3, the covariance matrix estimator defined by (9) can be used to build confidence intervals (or regions) for any linear combination of components of $\hat{\theta}$. More precisely, let $\hat{\underline{d}} = F \hat{\underline{\theta}}$ where F is a matrix of non-random coefficients, and let $\Omega = FCF^T$ be the covariance matrix of $\hat{\underline{d}}$. Our results imply that $\hat{\Omega} = F\hat{C}F^T$ is a consistent unbiased estimator of Ω and that $\hat{\Omega}^{-1/2}(\hat{\underline{d}} - E(\hat{\underline{d}}))$ is asymptotically distributed as a multivariate normal vector with mean zero and identity covariance matrix.

III. EXAMPLE OF UTILIZATION

In this section, we illustrate how the results of the previous section can be utilized for comparison between image reconstruction algorithms using results from 2-AFC experiments.

A. Reconstruction algorithms

The algorithms selected for our example perform image reconstruction from fan-beam data collected in two dimensions. The first two algorithms, called algorithms A and B, use a full-scan of data, whereas the third algorithm, called algorithm C, only uses a short-scan of 240 degrees. Algorithms A and C are both implementations of the fan-beam filtered-backprojection (FBP) formula with different weighting schemes: algorithm A weights all measurements with a factor of 1/2, whereas algorithm C invokes a Parker weighting so that only data over a short-scan are needed. Algorithm B is an implementation of the parallel-beam FBP formula that is applied after rebinning

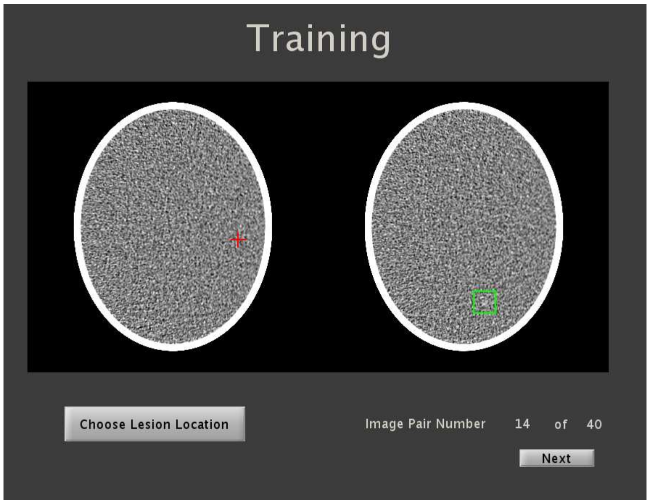

Fig. 1. Image display for a 2-AFC experiment that assesses the area under an LROC curve.

the fan-beam data to the parallel-beam geometry. Like algorithm A, algorithm C assigns a weight of 1/2 to handle all data redundancy.

B. Task description

Image quality was assessed using two-AFC experiments corresponding to LROC analysis. The LROC task was to detect a small lesion within a uniform brain phantom. Both the position of the lesion and the contrast of the lesion were random ($[25, 35]$ HU), whereas the lesion size was fixed (5 mm diameter). The lesion was always within the gray-matter area of the brain, and was not allowed to overlap with the skull.

In our context, the Bernoulli trial corresponded to presenting the observer with a pair of images as shown in Figure 1. One of the images always contained exactly one lesion whereas the other image did not contain any lesion. The observer was asked to insert a mark within one of the two images (see the red cross). A success was recorded when the mark identified the lesion within 10 pixels, otherwise a failure was recorded. In Fig.1, the lesion is indicated with a green square, showing that the mark was inserted at the wrong location.

C. Study design

We decided to assess performance using four observers reading each 250 pair of images (in two sessions of 125 images, with 40 training images before each session). To optimize statistical power, the exact same data sets were used for all three reconstruction algorithms, and different cases were used from one reader to another. Hence, the computed proportions were only correlated between algorithms.

Denote the proportions for algorithms A, B and C and reader j as A_j, B_j and C_j, and let $\hat{C}_j$ be the 3×3 covariance matrix for these three proportions. This matrix was estimated for each reader using (9). Next, define the reader-averaged proportions for the three algorithms as $\overline{A} = (A_1 + A_2 + A_3 + A_4)/4$, $\overline{B} = (B_1 + B_2 + B_3 + B_4)/4$, $\overline{C} = (C_1 + C_2 + C_3 + C_4)/4$. Given that the cases were independent from one reader to another, the covariance matrix for these reader-average proportions was

$$\Omega = \frac{1}{16} \sum_{j=1}^{4} C_j \, . \tag{19}$$

Confidence intervals were estimated for $\overline{A}$, $\overline{A} - \overline{B}$ and $\overline{A} - \overline{C}$; $\overline{A}$ was included to provide a reference value. Let $\underline{\hat{d}} = [\overline{A},\, \overline{A} - \overline{B},\, \overline{A} - \overline{C}]$. The covariance matrix for $\underline{\hat{d}}$ was obtained from Ω and the diagonal elements of this matrix were used to find a 98.33% confidence interval for each entry of $\underline{\hat{d}}$, by relying on asymptotic normality. The confidence intervals found for $\overline{A}$, $\overline{A} - \overline{B}$ and $\overline{A} - \overline{C}$ were $[0.7909, 0.8491]$, $[-0.0199, 0.0359]$ and $[0.1141, 0.1819]$ respectively. By Bonferroni's inequality, the joint probability for the three intervals together is at least 95%. As expected, we observe that Algorithm A significantly performs better than Algorithm C, due in particular to the extra amount of data involved in the reconstruction process. On the other hand, the difference between algorithms A and B is relatively small, and no conclusion can be made in favor of one method versus the other.

IV. CONCLUSION

We have presented a nonparametric methodology to evaluate the statistical variability of image quality assessment results based on MAFC experiments with multiple readers and cases. Our methodology views the readers as a fixed effect and the cases as a random effect. This setting is ideal for development and optimization of image formation processes, where using a large number of readers is impractical. For studies that invoke many readers, we recommend evaluating the variability due to the reader pool as well as that due to the cases, which may be done using the results in [6].

Although not discussed here, it can be shown that our theory also enables simple sample size calculations. The procedure to follow is very similar to that presented in [3] for LROC studies. Moreover, it turns out that there exist interesting links between our covariance matrix estimator, Jack-knifing techniques, and maximum likelihood estimation. These links will be discussed in the future.

REFERENCES

[1] H. H. Barrett and K. J. Myers, *Foundations of Image Science.* Wiley, 2004.
[2] M. S. Pepe, *The Statistical Evaluation of Medical Tests for Classification and Prediction.* Oxford Univ. Press, 2003.
[3] A. Wunderlich and F. Noo, "A nonparametric procedure for comparing the areas under correlated lroc curves," *IEEE Trans. Med. Imaging,* In Press. 2012.
[4] Q. McNemar, "Note on the sampling error of the difference between correlated proportions or percentages," *Psychometrika,* vol. 17, pp. 153–157, 1947.
[5] B. Bennett, "Tests of hypotheses concerning matched samples," *Journal of the Royal Statistical Society. Series B (Methodological),* vol. 29, no. 3, pp. 468–474, 1967.
[6] P. G. Gallas, B.D. and K. Myers, "Multireader multicase variance analysis for binary data," *J. Opt. Soc. Am. A,* vol. 24, no. 12, pp. B70–B80, Dec. 2007.

Temporal Interpolation of Partial Scan Sinograms in Myocardial CT Perfusion

Juan C. Ramirez-Giraldo, John A. Crane, Lifeng Yu, Shuai Leng,
Lilach O. Lerman, Cynthia H. McCollough

Abstract— **Partial scan reconstruction (PSR) is used in cardiac CT imaging to improve temporal resolution. Artifactual CT number variations over time, named PSR artifacts, are observed during myocardial CT perfusion (CTP) due to different angular range of projections used. The purpose of this study was to evaluate a novel noninvasive method to reduce PSR artifacts, which is based on the temporal interpolation of partial scan sinograms (TIPS). The TIPS method estimates the projection data missing to complete a full scan (2π) from each partial scan of a myocardial CTP sequence. The TIPS method was evaluated using a stationary anthropomorphic phantom and data from two *in vivo* myocardial CTP experiments using pigs. Scan protocols used 80 kVp, 350 mAs/rot, and 24 x 1.2 mm collimation using a dual-source CT scanner. PSR artifacts were quantified by measuring the temporal standard deviation of CT numbers in selected regions-of-interest. PSR artifacts were reduced up to 75% in the phantom when the partial scans were processed with TIPS. Likewise, PSR artifacts were reduced on average of 50% for the *in vivo* data, facilitating the analysis of myocardial time-attenuation-curves from which myocardial perfusion estimates can be derived. Further, because images reconstructed from TIPS processed data use more projections, image noise was reduced by about 30%. In conclusion, the TIPS method was effective reducing the PSR artifacts while at the same time reducing image noise. The use of TIPS can promote the clinical utilization of myocardial CTP for appropriately selected patients, by providing more accurate myocardial perfusion estimates, and also by reducing the radiation dose of this examination.**

Index Terms— **Image Artifacts, Myocardial CT perfusion, Partial Scan Reconstruction.**

I. INTRODUCTION

A major technical challenge to myocardial CT Perfusion (CTP) imaging is temporal resolution. Faster rotating gantries, partial (or short) scan reconstruction, and dual source CT are three major approaches to improve temporal resolution in multidetector row CT.

In myocardial CTP several consecutive partial scans are used to follow the transient arrival and washout of intravascular contrast agent through the myocardium. To reduce radiation dose the myocardial CTP technique is performed with prospective ECG triggering, thus x-ray exposure is limited to a predefined cardiac phase which is typically selected in mid diastole (i.e. 70% of the RR interval).

When using prospectively ECG triggered acquisitions in myocardial CTP, it is not possible to guarantee that the angular data range, corresponding to a specific anatomic location and phase in the cardiac cycle, consistently uses the same angular source position. It has been shown that small variations in beam hardening and scatter as a function of source position leads to artifactual temporal variations in CT numbers, since different angular ranges are covered from one partial scan to another [1]. Such fluctuations, different from statistical noise, can compromise the quantitative accuracy of myocardial CTP, and have been characterized as *partial scan reconstruction (PSR) artifacts*.

PSR artifacts are considered to belong to multidetector row CT but not to the electron beam CT (EBCT) technology used earlier on for myocardial CTP. EBCT provided a temporal resolution in the range of 50 to 100 ms by magnetically steering an electron beam around a 210° stationary tungsten target. Hence, by its design, the EBCT ensured that the partial scans always covered a consistent angular range [2].

Existing strategies to reduce PSR artifacts include both invasive and noninvasive approaches. Primak and colleagues demonstrated that guaranteeing consistent angular data ranges (such as in EBCT), PSR artifacts were avoided. In their study, the gantry rotation was synchronized with an animal's heart rate driven by a pacing device. While the technique effectively avoided

Manuscript received February 1, 2012. This work was supported in part by the American Heart Association, predoctoral fellowship 10PRE2560028, NIH Grant No. R01EB07986 from National Institute of Biomedical Imaging and Bioengineering, and by the NIH Opus CT Imaging Resource Construction Grant No. R018898.

J.C. Ramirez-Giraldo, L. Yu, S. Leng, and C. H. McCollough are affiliated with the CT Clinical Innovation Center, Department of Radiology, Mayo Clinic, Rochester MN.

J. Crane and L.O. Lerman are affiliated with the Division of Nephrology and Hypertension, Mayo Clinic, Rochester MN.

E-mail of corresponding author: mccollough.cynthia@mayo.edu.

PSR artifacts, its invasiveness precluded clinical use [1]. Noninvasive approaches to reduce PSR artifacts include the use of an *a priori* full scan dataset to correct subsequent partial scans [3]. Stenner et al. used an approach in which the projection data of several consecutive partial scans are averaged to obtain both an artificial full scan and an artificial partial scan, the later coinciding with the angular range of the actually acquired partial scan [4]. The artificial scans are reconstructed to estimate an artifact image that is substrated from the acquired partial scan. While Stenner's method was very successful in stationary phantoms, disadvantages include that it requires several image reconstruction steps (3 instead of 1), and the required superposition operations are potentially error prone *in vivo* due to the rapid heart motion (i.e. variations in position from one heart beat to another). Recently, another noninvasive method was proposed, which is based on a targeted spatial frequency filter (TSFF) that requires the acquisition of 360^o degrees of projection data (a full scan), from which also a partial scan image can be also reconstructed [5,6]. The TSFF uses the low frequency components of the full scan (with no PSR artifact) and superimpose it with the high frequency components of the partial scan (which has better temporal resolution). The TSFF method effectively reduced PSR artifacts in a stationary phantom. TSFF was also validated *in vivo* using a reference (and invasive) method. Limitations of the TSFF include a small increase in radiation dose needed (~14% if tube current is modulated to 20% to complete a full scan), and the use of the low frequency of the full scan can degrade temporal resolution.

Here, we evaluate a novel noninvasive method to reduce PSR artifacts based on the temporal interpolation of partial scan sinograms (TIPS). The TIPS method relies in the use of consecutive phase-correlated partial scans, as Stenner's method; however, it does not average them. Instead, the TIPS method preserves the partial scan sinogram data acquired in an angular range of (π + fan angle α), and uses an interpolation method to estimate the projections in the (π – α) angular range that is missing to complete a full scan. Here, we demonstrate the method using a stationary phantom and with *in vivo* data.

II. MATERIALS AND METHODS

A. Formulation of TIPS

Consider a sequence of partial scan sinograms $p_\pi(\beta,\theta,\psi, t)$ acquired at a constant position *z* (i.e. cine mode), where β is the detector index, θ the projection angle, ψ the detector row position, and *t* the time of each partial scan in a myocardial CTP scan sequence. For convenience we will not state the dependence of detector index and detector row position. Let's also consider that for each partial scan we record the initial and final angular position $\theta_1(t)$ and $\theta_2(t)$, respectively, where $\theta_i(t) \in [0,2\pi]$ and $|\theta_2(t) - \theta_1(t)| = \pi + \alpha$.

The formula that TIPS uses to estimate corresponding full scans $p_{2\pi}(\theta, t)$ is as follows:

$$p_{2\pi}(\theta,t) = \begin{cases} p_\pi(\theta,t) & \theta_1 \le \theta(t) \le \theta_2 \\ \sum_{i\in I} \omega_i \, p_\pi(\theta,t_i) & otherwise \end{cases} \quad (1)$$

where ω_i is a weighting scheme of phase correlated partial scans $p_\pi(\theta, t_i)$ based on interpolation (i.e. cubic splines) or a suitable weighing scheme. Note that Eq. 1 maintains the originally acquired projection data over angles $\theta_1(t)$ to $\theta_2(t)$, and the remaining angular projections to complete a full scan (π–α) need to be estimated.

The TIPS method relies on the assumption that the angular range covered by each partial scan during a myocardial CTP sequence changes continuously, such that data from all projection angles over 2π can be collected within a few consecutive partial scans. Primak et al. [1] described the following equation to characterize the angular range change $\Delta\theta$ in a sequence of ECG triggered partial scan acquisitions:

$$\Delta\theta = \left[\frac{T_{RR}}{T_{rot}} - floor\left(\frac{T_{RR}}{T_{rot}} \right) \right] \times 360° \quad (2)$$

where T_{RR} is the R-R interval time, T_{rot} is the gantry rotation time, and the function floor(X) rounds X to the nearest integer less than or equal to X. Primak et al demonstrated that to eliminate the PSR artifacts it is necessary to ensure that the source trajectory does not change from one heart cycle to the other $\Delta\theta = 0°$. This is achieved when $T_{RR} = T_{rot} \times N$, where *N* is an integer number. In practice however, exact periodicity of the heart cycle with respect to the gantry rotation, leading to $\Delta\theta = 0°$, is very unlikely. On the contrary, the probability of acquiring projection angles over the whole 360° is very high. And, if the unlikely event of the heart rate naturally synchronizing with the gantry rotation, because $\Delta\theta \sim 0°$, then PSR artifacts will be minimized as was achieved by pacing the heart directly as shown by Primak et al. in the animal model with no PSR artifact correction needed [1].

B. Phantom Experiment

An anthropomorphic thorax phantom (QRM, Möhrendorf, Germany) with the cardiac calcium insert was scanned using a dual-source CT scanner (Somatom Definition, Siemens Healthcare, Forchheim, Germany). The phantom was placed 5-cm off isocenter in the vertical direction with the purpose of increasing anisotropy and hence exacerbating PSR artifacts [1]. The phantom was scanned using two CTP protocols, in a constant position (cine mode), using either full or partial scan acquisitions. The full scan protocol used a 330 ms temporal resolution and 145 mAs/rotation, and the partial scan protocol used 83 ms (using dual source reconstruction) and 350 mAs/rotation. The tube current time settings were chosen such that image noise values of the corresponding reconstructions were approximately the same. All other acquisition parameters were identical (Table 1).

Table 1. CT scan protocol.

Parameter	Value
Tube potential [kVp]	80
Collimation [mm]	24 x 1.2
Automatic Exposure Control	Off
Scan frequency [s]	0.75
Scan duration [s]	40
Rotation time [ms]	330

C. *Image reconstruction and TIPS*

Data corresponding to the four inner collimated detector rows were used for reconstruction to avoid potentially confounding cone-beam artifacts. Image slice thickness was 4.8 mm. Fan-beam filtered backprojection was employed. Partial scans were also processed with the TIPS method using cubic spline interpolation resulting in three datasets of images: full scans, partial scans, and partial scans corrected with the TIPS method. All algorithm code and data processing was performed using Matlab 7.11®.

D. *Animal Data*

Data from two myocardial CTP acquisitions using female pigs were used. Animals were scanned under anesthesia and mechanically ventilated. Before each perfusion scan, the animal was hyperventilated. Ventilation was suspended for 30 to 40 seconds during scanning to minimize spontaneous respiratory thoracic motion. The myocardial CTP scan parameters were similar to the scans performed with the phantom (Table 1), with the exception of scan frequency that depends on the animal heart rate (one scan per heart beat).

III. RESULTS

A. *Phantoms*

The use of TIPS method resulted in decreased PSR artifacts by about fourfold, as quantified by the temporal standard deviation of CT numbers in a selected ROI (Figure 1 and Table 2). The use of TIPS method also decreased image noise values from 20.1 HU to 14.3 HU (Table 2). The noise reduction with the TIPS algorithm is achieved because it uses more projection data for image reconstruction (i.e. full scan reconstruction instead of partial scan reconstruction). Image noise values for the full scans were 19.8 HU, but as previously indicated the tube current was adjusted with respect to the partial scans to match image noise.

B. *Animal data*

PSR artifacts were reduced when using TIPS leading to a smoother myocardium tissue TAC (Figure 2), which facilitates dual gamma-variate curve fitting for perfusion estimations. The TIPS method reduced the temporal standard deviation of CT numbers in selected ROIs under the animal skin from 3.8 HU to 2.1 HU. The TIPS method also reduced image noise from 24 HU to 18 HU in the selected ROI within the myocardium (Figures 2 and 3).

Table 2. Quantitative assessment of temporal CT number variations in the phantom study before and after the use of the temporal interpolation of partial scan sinograms (TIPS) method.

Location	Standard deviation of PSR artifacts [HU]			Image Noise [HU]		
	Full Scan	Partial Scan	Partial Scan +TIPS	Full Scan	Partial Scan	Partial Scan +TIPS
Selected ROI	1.8	4.0	0.9	19.8	20.1	14.3

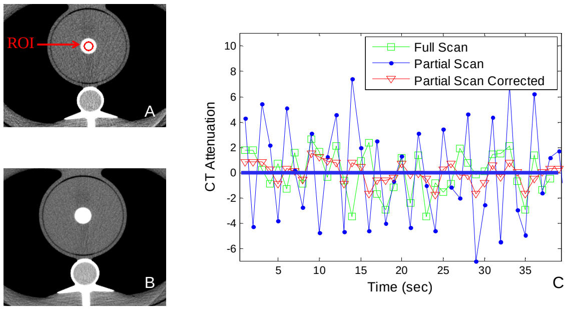

Figure 1. Phantom evaluation of the temporal interpolation of partial scan sinograms (TIPS). Partial scan image (A) before and (B) after TIPS correction, and (C) corresponding temporal CT number variations in identical regions-of-interest (ROI) as noted in figure (A).

IV. DISCUSSION

The main advantages of the TIPS method are: (1) PSR artifacts are decreased by using the TIPS-estimated full scans. (2) No additional radiation dose is required. (3) The scanner's best temporal resolution (in either single or dual source CT) is used. (4) Image noise in reconstructed images is decreased because each reconstruction uses a larger number of projections, potentially offering an alternative for dose reduction. (5) While the TIPS method uses several consecutive partial scans (similar to Stenner's method), only one set of sinograms (rather than 3) need to be reconstructed.

Temporal interpolation of sinogram data was previously proposed by Montes and Lauritsch with the purposes of dose reduction and improving temporal resolution in slowly acquired CTP data [7]. They later studied its utility for brain CTP [8]. Hsieh and colleagues also proposed a method in which only a fraction of the projection data is acquired in each acquisition during a brain CTP sequence, with full scan data estimated by linear interpolation of the sinograms with the major purpose of reducing dose [9]. Neither of the aforementioned approaches however was considered for reducing PSR artifacts and nor to reduce dose in myocardial CTP.

In conclusion, the TIPS method was effective reducing the PSR artifacts while at the same time reducing image noise. The use of TIPS can promote the clinical utilization of myocardial CTP for appropriately selected patients, by providing more accurate myocardial perfusion estimates, and also by reducing the radiation dose of this examination.

REFERENCES

[1] A. N. Primak, *et al.*, "A technical solution to avoid partial scan artifacts in cardiac MDCT," *Med Phys,* vol. 34, pp. 4726-37, Dec 2007.

[2] C. H. McCollough and R. L. Morin, "The technical design and performance of ultrafast computed tomography," *Radiol Clin North Am,* vol. 32, pp. 521-36, May 1994.

[3] J. A. Meinel, *et al.*, "Reduction of Half-Scan Shading Artifact Based on Full-Scan Correction1," *Academic Radiology,* vol. 13, pp. 55-62, 2006.

[4] P. Stenner, *et al.*, "Partial scan artifact reduction (PSAR) for the assessment of cardiac perfusion in dynamic phase-correlated CT," *Medical Physics,* vol. 36, pp. 5683-5694, 2009.

[5] J. C. Ramirez-Giraldo, *et al.*, "A strategy to decrease partial scan reconstruction artifacts in myocardial perfusion CT: Phantom and in vivo evaluation," *Medical Physics,* vol. 39, pp. 214-223, 2012.

[6] R. Raupach, *et al.*, "A novel spatiotemporal filter for artifact and noise reduction in CT," in *European Congress of Radiology*, Vienna, Austria, 2009.

[7] P. Montes and G. Lauritsch, "A temporal interpolation approach for dynamic reconstruction in perfusion CT," *Medical Physics,* vol. 34, pp. 3077-3092, 2007.

[8] P. Montes, *et al.*, "Low-Noise Dynamic Reconstruction for X-Ray Tomographic Perfusion Studies Using Low Sampling Rates," *International Journal of Biomedical Imaging,* vol. 2009, 2009.

[9] J. Hsieh, *et al.*, "Fractional scan algorithms for low-dose perfusion CT," *Med Phys,* vol. 31, pp. 1254-7, May 2004.

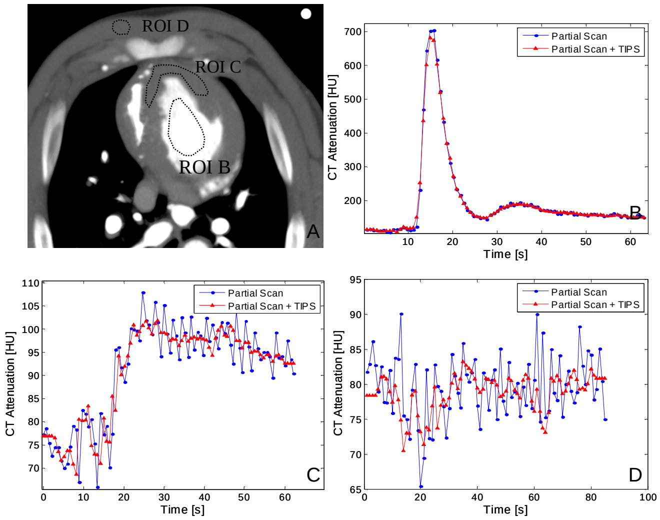

Figure 2. Effect of TIPS method in time attenuation curves (TACs) (A) Sample regions-of-interest (ROI) location at the left ventricle (ROI B), the myocardium (ROI C) and a reference region with minimal enhancement (ROI D). Corresponding time attenuation curves with and without TIPS method processing in (B) ROI B, (C) ROI C, and (D) ROI D.

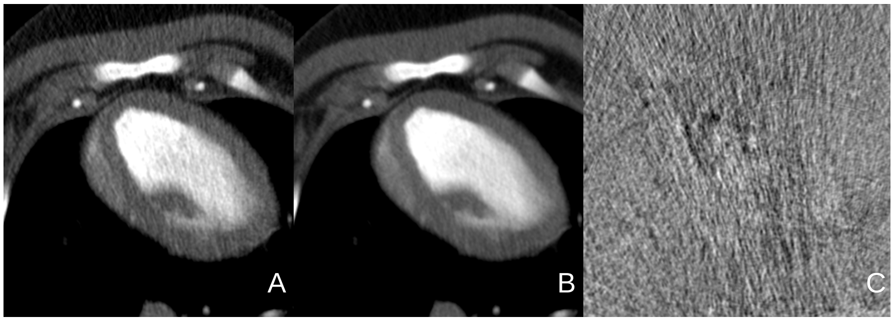

Figure 3. TIPS method effect on image noise. Partial scan image (A) before and (B) after TIPS processing. (C) Difference image A-B with window level [-100 100].

A New Registration Algorithm for Motion–Compensated Computed Tomography for Image–Guided Radiation Therapy

Marcus Brehm, Pascal Paysan, Markus Oehlhafen, Patrik Kunz, and Marc Kachelrieß,

***Abstract*—In image–guided radiation therapy (IGRT) beside the linear particle accelerator an additional kV system provides information for an accurate patient positioning. However, the acquisition time of the system is much longer than the patient's breathing cycle due to the low gantry rotation speed. Severe artifacts like blurring or streaks are the consequence.**

A novel method is proposed for the motion–compensated reconstruction of high quality respiratory–correlated 4D volumes from flat panel detector cone–beam CT (CBCT) scans with slowly rotating gantry. The reconstruction is done without the application of knowledge of a planning CT with the intent to reduce the influences of intra– and inter–fractional variations in patient motion and tissue. Instead a strategy how to apply a deformable registration method is developed based on the small motion assumption widely used inside registration algorithms. Within this strategy temporal restrictions like the cyclic motion patterns of respiration are incorporated. Thus, a common spatial registration algorithm is enhanced to be spatiotemporal.

The proposed method is verified applying simulated rawdata obtained by deforming a clinical patient dataset using realistic deformation vector fields. Furthermore, we successfully processed patient data and the results will be presented at the meeting. The method outperforms the phase–correlated Feldkamp reconstruction regarding undersampling artifacts with a temporal resolution only slightly lower at the same time. In addition, the results show noise levels comparable to 3D standard reconstructions.

***Index Terms*—IGRT, cone–beam CT, motion compensation, deformable registration**

I. INTRODUCTION

In radiation therapy accurate patient positioning is of great importance to assure success of treatments with small irradiation margins. Due to motion and tissue variation between planning and treatment session on–line or off–line corrections are required. In image–guided radiation therapy (IGRT) adjustment information is provided by an on–board kV flat panel cone–beam computed tomography (CBCT) unit which is mounted orthogonal to the MV linear accelerator (LINAC). By design the LINACs are rotating slowly in comparison to clinical CT scanners. For this very reason on–board CBCT–imaging in the thoracic region is handicapped by the respiratory motion in particular and suffers from motion artifacts.

To deal with motion–contaminated projections the respiratory motion is assumed to be cyclic. This respiratory cycle $C = [0\%, 100\%]$ is separated into small subsets with size Δc by amplitude or by phase gating. Consequently a standard reconstruction like the filtered backprojection is applied not on the entire dataset but for each subset on the associated projections. But the classification into subsets results in an enlarged angular spacing of the projection bins. Due to the Nyquist–Shannon theorem the enlarged angular spacing leads to prominent streak artifacts.

Compensating for motion is an interesting option. Here, the entire data set with all projections is used at any time and the motion is compensated by the additional information from motion vector fields (MVF). In references [1], [2] the MVFs are estimated from the 4D planning CT under the assumption that motion over all respiratory cycles is identical both in CBCT and planning CT. To allow for inter–fractional motion and tissue variation, the registration has to be performed on the phase–correlated Feldkamp reconstructions. But a high number of projections is needed. Otherwise the undersampling artifacts make a precise registration impossible for the applied registration approaches.

The purpose of this work is a motion–compensated reconstruction of low sampled on–board CBCT scans. The motion vector fields are extracted via deformable registration. In this case, no a priori knowledge is used from prior acquisitions like planning CTs. Instead a registration strategy is developed based on the small motion assumption. With this strategy a spatial registration is enhanced to act as a spatiotemporal registration by taking temporal restrictions into account.

II. MATERIALS AND METHODS

A. Phase–Correlated Feldkamp (PCF) Reconstruction

As our standard reconstruction algorithm we use the well–known Feldkamp–Davis–Kress (FDK) filtered backprojection [3]. But patient motion during the acquisition is not considered by FDK. In this work the projections were associated to the respiratory cycle by a retrospective phase gating. A phase–correlated Feldkamp (PCF) reconstruction considers the relation between projection and respiratory phase by an FDK reconstruction just using the projections associated to one subset and discarding all the others. The operator is denoted as $\mathsf{X}_{\mathrm{PCF}}^{-1}$ such that the PCF image f_{PCF} is given by

$$f_{\mathrm{PCF}} = \mathsf{X}_{\mathrm{PCF}}^{-1} p.$$

Here p are the projection data.

Marcus Brehm, Prof. Dr. Marc Kachelrieß: Institute of Medical Physics, University of Erlangen–Nürnberg, Henkestr. 91, D–91052 Erlangen, Germany.

Prof. Dr. Marc Kachelrieß: Medical Physics in Radiology, German Cancer Research Center (DKFZ), Im Neuenheimer Feld 280, D–69120 Heidelberg, Germany.

Dr. Pascal Paysan, Dr. Markus Oelhafen, Dr. Patrik Kunz: Varian Medical Systems, Täfernstr. 7, CH–5405 Baden–Dättwil, Switzerland.

Corresponding author: marcus.brehm@imp.uni–erlangen.de

B. Motion–Compensated Reconstruction Algorithm

Under the assumption that the patient's appearance is the same for each single respiratory phase, a gating is performed to resort the acquisition into the respiratory cycle. This cycle is divided up into N_{Phases} subsets. Motion between two phases can be represented by a transformation

$$\mathrm{T} : (x, y, z) \rightarrow (x, y, z) + \boldsymbol{u}(x, y, z)$$

which consists of the identity mapping and a displacement field $\boldsymbol{u}$. Hence, the motion between two phases can be compensated by a transformation according to the corresponding MVF. We assume that the transformations $\mathrm{T}_{i,j}$ and $\mathrm{T}_{j,i}$ for each phase pair (i, j) are known, with $i, j \in [1, N_{\text{Phases}}]$. The way how to find the displacement fields by deformable registration will be discussed later on. Our motion–compensated reconstruction $f_{\mathrm{MC}(i)}$ at a respiratory phase i is given by

$$f_{\mathrm{MC}(i)} = \sum_{j=1}^{N_{\text{Phases}}} \left(\mathsf{X}_{\mathrm{PCF}(j)}^{-1}\, p \right) \circ \mathrm{T}_{i,j}.$$

C. Spatial Registration

We apply the so–called demons algorithm to obtain the MVFs between respiratory phases [4]. As an iterative approach the demons algorithm is working under the assumptions of intensity conservation and small motion. For a single iteration step, the displacement of a voxel $\boldsymbol{r} := (x, y, z)$ in the model image m is thus given by intensity matching on the linear approximation of the scene image s in $\boldsymbol{r}$. The displacement shift $\boldsymbol{u}(\boldsymbol{r})$ is accordingly described by

$$\boldsymbol{u}(\boldsymbol{r}) := \frac{m(\boldsymbol{r}) - s(\boldsymbol{r})}{\left\| \boldsymbol{\nabla} s(\boldsymbol{r}) \right\|^2} \boldsymbol{\nabla} s(\boldsymbol{r})$$

with $\boldsymbol{\nabla} s$ being the gradient image of s. The formula can additionally be enhanced by step width control [5] and symmetric forces [6]. This results in the finally used equation including transfer to iterative context, written as

$$\boldsymbol{u} = \frac{\frac{1}{2} \left(m \circ \mathrm{T} - s \right) \left(\boldsymbol{\nabla} s + \boldsymbol{\nabla} \left(m \circ \mathrm{T} \right) \right)}{\left\| \frac{1}{2} \left(\boldsymbol{\nabla} s + \boldsymbol{\nabla} \left(m \circ \mathrm{T} \right) \right) \right\|^2 + \alpha^2 \left(m \circ \mathrm{T} - s \right)^2}$$

with maximum step width $1/\alpha$, current vector field T and its displacement update $\boldsymbol{u}$. By starting with T as identity mapping or a prior estimation, the update of T is given by composition with its displacement update $\boldsymbol{u}$

$$\mathrm{T} \leftarrow G_{\text{post}} * \left(\mathrm{T} \circ \exp \left(G_{\text{prior}} * \boldsymbol{u} \right) \right)$$

with G_{post} and G_{prior} being Gaussian convolution kernels [7]. To speed up the registration and to meet the small motion assumption the registration is applied hierarchical. More details on the multi–resolution approach will be given at the meeting.

D. Spatiotemporal Registration

Motion–compensated reconstruction of a specific phase $n \in [1, N_{\text{Phases}}]$ requires the MVFs of the phase n to be reconstructed, and all other phases. These vector fields can be directly estimated by a deformable registration of the predetermined images of each phase to the one of phase n. But instead we propose to identify the MVFs between adjacent phases first, like illustrated in figure 1. For predetermined phase images I and the sought–after vector fields T the relation is given by

$$I_{j+1} \leftarrow I_j \circ \mathrm{T}_j$$

with $j \in [1, N_{\text{Phases}} - 1]$. The ring is closed by the last remaining adjacent phase pair and its vector field

$$I_1 \leftarrow I_{N_{\text{Phases}}} \circ \mathrm{T}_{N_{\text{Phases}}}.$$

In the following we consider the ring property to simplify the notation. Thus gives us that index $N_{\text{Phases}} + j$ is synonymous with index j, i.e. $I_{N_{\text{Phases}}+j}$ is equivalent to I_j. Furthermore, we denote by $\prod$ the noncommutative concatenation of several vector fields, i.e. $\prod_{n=1}^{N_{\text{Phases}}} := \mathrm{T}_1 \circ \mathrm{T}_2 \circ \ldots \circ \mathrm{T}_{N_{\text{Phases}}}$.

One benefit is the direct applicability of additional knowledge like temporal restrictions. With the estimated MVFs between adjacent phases and the resulting ring closure it is possible to draw conclusions on errors of single vector fields.

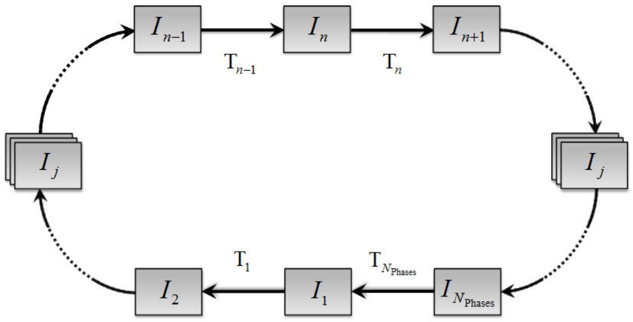

Fig. 1. Illustration of the ring–registration: I_j denotes the predetermined phase images with $j \in [1, N_{\text{Phases}}]$. The motion vector fields T_j describe the corresponding motion in–between two adjacent phases. The ring is closed with the motion vector field between phase 1 and N_{Phases} denoted by $\mathrm{T}_{N_{\text{Phases}}}$. The approach can also be applied in reverse order.

An example for prior knowledge is the assumption of periodical breathing motion. Hence, the concatenation of all vector fields in an appropriate order is expected to result in the identity mapping. To obtain vector fields appropriate for motion compensation the registration algorithm has to keep the error from the concatenations

$$E := \sum_{k=1}^{N_{\text{Phases}}} \left\| \mathrm{E}_k \right\|^2 := \sum_{k=1}^{N_{\text{Phases}}} \left\| \prod_{n=k+1}^{N_{\text{Phases}}+k} \mathrm{T}_n - \mathrm{Id} \right\|^2$$

sufficiently small. The differences E_k, in the following called concatenation error vector fields, can be determined directly from the estimated vector fields T_n itself.

To remove an error E we propose a temporal correction step to correct each single approximated vector field T_n by the concatenation error vector fields E_k. The vector fields T_n as well as E_k are given for different images and thus on different grids. For applying the error field information both have to be defined on the same grid. In our following approach the required inverse of the MVFs are not calculated directly via an additional registration but are estimated from the already approximated T_j. For this in a first step we assume the error E to be small, i.e.

$$\mathrm{Id} \approx \prod_{n=k+1}^{N_{\text{Phases}}+k} \mathrm{T}_n$$

for all $k \in [1, N_{\text{Phases}}]$. From the assumption above we directly yield an appropriate approximation of the inverse vector fields and their concatenations

$$\left(\prod_{n=j+1}^{N_{\text{Phases}}+k} \mathrm{T}_n \right)^{-1} \approx \prod_{n=k+1}^{j} \mathrm{T}_n$$

for all $j \in [k+1, N_{\text{Phases}}+k-1]$. Hence, each E_k can be transformed to be defined on the same grid as an arbitrary vector field T_j with $j, k \in [1, N_{\text{Phases}}]$ and $j \neq k$. In case of $j = k$ the grid is already the same and a transformation becomes thus obsolete. The continuity of breathing motion and scanner rotation as well as the equidistant phase windows allow us to divide each E_k between all single motion vector fields of adjacent phases in equal parts. With the aid of the inverse approximation and the uniform error distribution the temporal correction step is given by

$$\begin{aligned}
j = k: &\quad \mathrm{T}_j \quad \leftarrow \quad \mathrm{T}_j - \frac{E_k}{N_{\text{Phases}}} \\
j < k: &\quad \mathrm{T}_j \quad \leftarrow \quad \mathrm{T}_j - \frac{E_k \circ \prod_{n=k+1}^{N_{\text{Phases}}+j} \mathrm{T}_n}{N_{\text{Phases}}} \\
j > k: &\quad \mathrm{T}_j \quad \leftarrow \quad \mathrm{T}_j - \frac{E_k \circ \prod_{n=k+1}^{j} \mathrm{T}_n}{N_{\text{Phases}}}.
\end{aligned}$$

However, the correction of all the T_j is done for just one E_k at a time. Rather the optimization is done step by step and the next E_k is determined by incorporating the resulting T_j of previous correction steps. The correction in parts requires the vector fields to be smooth. This assumption is ensured by the regularization term of the registration algorithm and its smoothing behavior.

Nevertheless motion compensation requires also vector fields for non–adjacent phases. Theoretically, they are given by concatenation of vector fields from adjacent phases forming a path from the start phase to the end phase, i.e.

$$I_i \leftarrow I_j \circ \prod_{n=j}^{i-1} \mathrm{T}_n$$

with $j \in [1, N_{\text{Phases}}]$ and $i \in [j+1, N_{\text{Phases}}+j-1]$. In the following the vector fields of adjacent phases are denoted by $\mathrm{T}_j^1 := \mathrm{T}_j$ and for non–adjacent phases by T_j^m with $I_{j+m} \leftarrow I_j \circ \mathrm{T}_j^m$, $j \in [1, N_{\text{Phases}}]$ and $m \in [2, N_{\text{Phases}} - 1]$. Despite small motion left in–between adjacent phases the deformable registration yields only an approximation of the true vector fields with some minor errors left. For a single vector field these errors are insignificant. But that may not be true in the case of a more sophisticated MVF yielded by concatenation.

To consider the error propagation of the concatenation, we apply a further registration for each non–adjacent phase pair. While the registration for adjacent phases starts with the identity mapping, this re–registration is initialized by the concatenation of the already determined vector fields. Instead of using longer concatenations of several vector fields, the results from former re–registrations, performed on lower levels (smaller m), are incorporated to reduce the propagation error (c.f. figure 2). Hence, the re–registrations are done with $\mathrm{T}_j^1 \circ \mathrm{T}_{j+1}^{m-1}$ as starting vector fields.

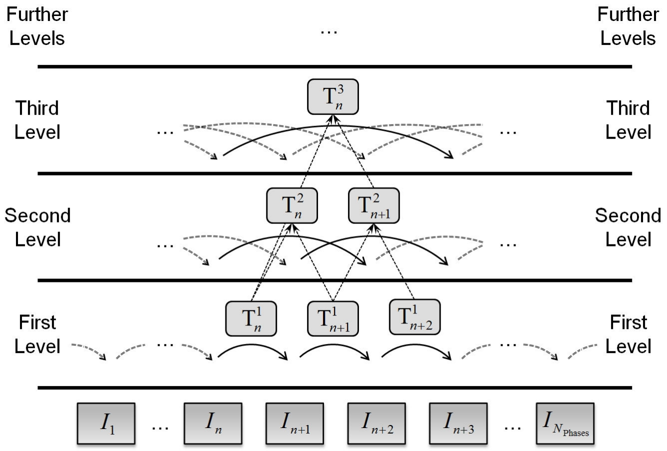

Fig. 2. Illustration of the re–registration: First a registration between adjacent phases with no prior information, i.e. starting with the identity mapping, is performed to determine T_j^1. On the second level vector fields of phases with one phase in–between are determined with the concatenation of results from level one as prior. One vector field from the second and one from the first level are used next to yield a prior via concatenation with minimum propagation error for calculations on the third level. The procedure is continued with further levels up to a given level $M < N_{\text{Phases}}$. In cases of $M < m < N_{\text{Phases}}$ all T_j^m are given by the concatenation of results from lower levels without an additional re–registration step.

The re–registration approach can also be stopped at a previous level $M < N_{\text{Phases}} - 1$ or some levels can be skipped, if the remaining propagation error is sufficient small. In this case all T_j^m with $M < m < N_{\text{Phases}}$ are obtained by the starting vector fields for a possible re–registration itself, i.e. $\mathrm{T}_j^m := \mathrm{T}_j^1 \circ \mathrm{T}_{j+1}^{m-1}$.

E. Simulations

For evaluation we carried out simulations. The geometry of the On–Board Imager's® and TrueBeam's™ integrated kV imaging unit (Varian Medical Systems, Palo Alto, CA) forms the basis of the scan configuration. To simulate projection data we used a clinical CT reconstruction of a patient thorax as a phantom. We created realistic motion vector fields to simulate respiration. The deformation intensity is direction sensitive with a maximum of 11 mm in posterior–anterior and 20 mm in superior–inferior direction. The deformation is directly coupled to the RPM signal, which was set to be continuous with a rate of 29 respirations per minute. The detector was laterally shifted by 160 mm. The rotation speed was limited to 6° per second, i.e. about 60 s per rotation. Quantum noise was added to the simulated projections to obtain an image noise level of 70 HU in the FDK images.

III. RESULTS

Phase–correlated and motion–compensated reconstructions were conducted for 20 overlapping subsets with size $\Delta c = 0.1$. This classification results in the fact that only every tenth projection account for each PCF reconstruction.

For evaluation two motion–compensated reconstructions were performed. Each estimates the required MVFs in a different way from the phase images, which are the PCF reconstructions in our case. A standard motion compensation was applied on the one hand, where the MVFs are obtained directly from their corresponding phase pair images via spatial registration. On the other hand there is the proposed motion compensation, where the MVFs are extracted by the registration approach in section II-D. In both cases the demons algorithm from section II-C was used for the spatial registration. The motion compensation results of the simulation study are shown for end–exhale as well as end–inhale (figure 3). The results for patient data will be presented at the meeting.

The results of the standard method are strongly deteriorated by streaks and suffer partially from a low temporal resolution. This arise from the fact that the PCF reconstructions are also strongly influenced by streak artifacts. In consequence there is an additional contribution to the vector field not originating from the patient's breathing in case of the standard motion compensation. The fact is taken into account by the proposed method and its temporal correction step. Thus, the rotating but not cyclic motion of streak artifacts inside the PCF images is successfully corrected, and streak-free images with high temporal resolution are achieved by the proposed method.

IV. CONCLUSION AND DISCUSSION

A new algorithm is proposed to compensate for motion in case of on–board kV imaging units in radiation therapy. It was proven by simulation that the method is capable of compensating the motion on basis of the PCF reconstructions. In this case, no a priori knowledge is used from prior acquisitions like planning CTs. The influences of intra– and inter–fractional variations in patient motion and tissue are consequently reduced. The proposed algorithm shows significantly improved image quality in comparison to a standard motion compensation in case of a MVF estimation based on the PCF images.

ACKNOWLEDGMENTS

This work was supported by a research grant from Varian Medical Systems, Palo Alto, CA. Parts of the reconstruction software were provided by RayConStruct® GmbH, Nürnberg, Germany.

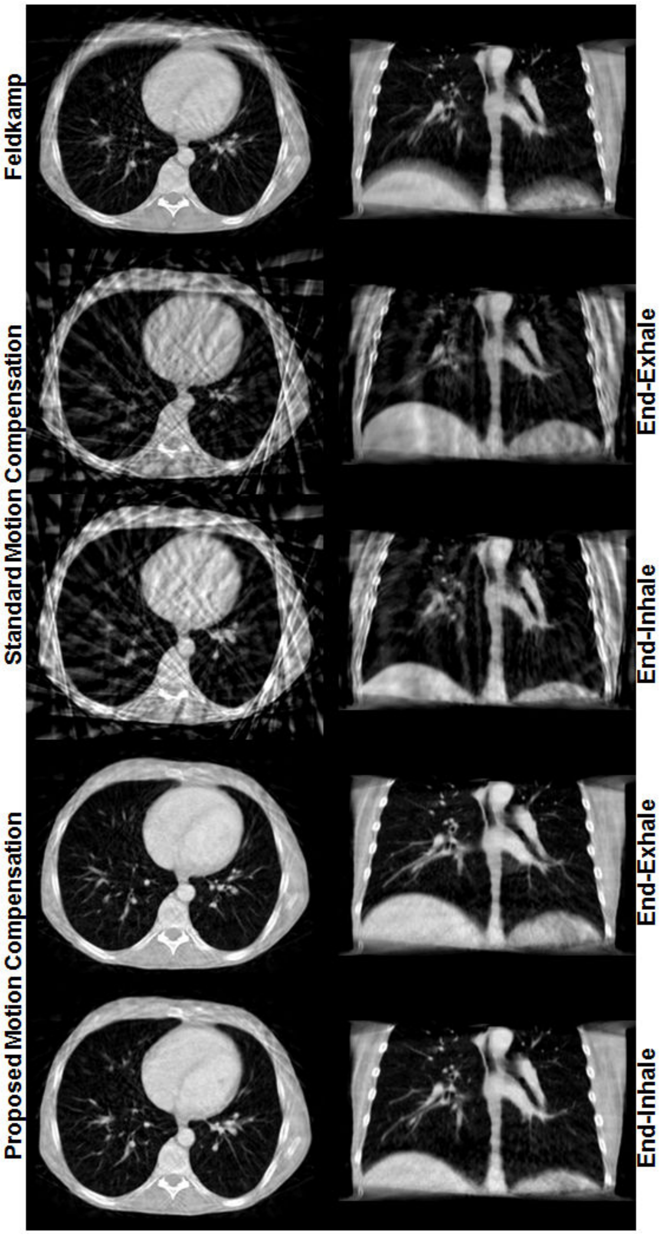

Fig. 3. Motion compensation of the simulated patient: Identical slices are shown from top to down for a Feldkamp reconstruction, a standard motion compensation in end–exhale and end–inhale as well as the proposed motion compensation in end–exhale and end–inhale. All images are shown at the same grayscale window of $C = -200$ HU, $W = 1400$ HU.

REFERENCES

[1] T. Li, E. Schreibmann, Y. Yang, and L. Xing, "Motion correction for improved target localization with on–board cone–beam computed tomography," *Phys. Med. Biol.*, vol. 51, no. 2, pp. 253–267, Feb. 2006.

[2] S. Rit, D. Sarrut, and L. Desbat, "On–the–fly motion–compensated cone–beam CT using an a priori model of the respiratory motion," *Med. Phys.*, vol. 36, no. 6, pp. 2283–2296, Jun. 2009.

[3] L. Feldkamp, L. Davis, and J. Kress, "Practical cone–beam algorithm," *Journal of the Optical Society of America*, vol. 1, no. 6, pp. 612–619, Jun. 1984.

[4] J.-P. Thirion, "Image matching as a diffusion process: An analogy with Maxwell's demons," *Medical Image Analysis*, vol. 2, no. 3, pp. 243–260, Sep. 1998.

[5] P. Cachier, X. Pennec, and N. Ayache, "Fast non rigid matching by gradient descent: Study and improvements of the "demons" algorithm," Institut national de recherche en informatique et en automatique, Tech. Rep. 3706, Jun 1999.

[6] H. Wang, L. Dong, J. O'Daniel, R. Mohan, A. S. Garden, K. K. Ang, D. A. Kuban, M. Bonnen, J. Y. Chang, and R. Cheung, "Validation of an accelerated 'demons' algorithm for deformable image registration in radiation therapy," *Phys. Med. Biol.*, vol. 50, no. 12, pp. 2887–2905, Jun. 2005.

[7] T. Vercauteren, X. Pennec, A. Perchant, and N. Ayache, "Diffeomorphic demons: Efficient non–parametric image registration," *NeuroImage*, vol. 45, no. 1, pp. 61–72, Mar. 2009.

Cardiac function analysis with four dimensional CT image

Qiulin Tang, Tatsuya Kigure, Takahiro Higuchi, George S. K. Fung,
Elliot K. Fishman and Katsuyuki Taguchi

Abstract—**Multidetector-row CT has been developed and widely used in cardiac imaging, recently. Comparing with traditional cardiac imaging modalities, such as single photon emission computed tomography (SPECT) and Magnetic resonance imaging, multi-detector CT imaging can provide rapid noninvasive diagnostic and prognostic evaluation of patients with acute myocardial infarction (MI). In this work, we develop a method for cardiac CT to provide comprehensive assessments of regional wall motion (RWM), ventricular function, and dys-synchronization of wall motion. The proposed motion estimation and motion analysis method has two steps: First, four-dimensional (4D) cardiac motion is obtained by performing non-rigid image registration on 4D Electrocardiogram (ECG)-gated cardiac CT reconstructions; then, the obtained 4D cardiac motion was analyzed to produce diagnostic assessments.**

***Index Terms*—MI, ME**

I. PURPOSES

CARDIAC diseases such as myocardial ischemia, infarction and stroke are one of the leading causes of death in the United States. Early detections of abnormalities in cardiac anatomy, global and regional left ventricle function, and PDs are crucial for clinical diagnosis and treatment, and a rapid noninvasive diagnostic and prognostic evaluation for acute MI is required [1].

Currently, cardiac imaging modalities are including transthoracic echocardiography (TTE), MRI, SPECT, PET, and invasive coronary angiography [2-5]. These traditional modalities have several disadvantages. First, each of them cannot provide both static and dynamic diagnostic information. SPECT, PET, MRI can only provide information of PDs, coronary angiography shows the anatomical abnormalities, and TTE can be used to diagnose motion defects but not PDs. To perform comprehensive clinical evaluation, results from two or even more modalities need to be integrated. Second, high spatial and temporal resolutions cannot be achieved. The spatial resolution of SPECT and PET is about 1 cm, and data acquisition time is about 15 minutes; MRI has a good spatial resolution, but the scanning time is around 40 minutes; TTE is real time imaging, but the spatial resolution is worse. Finally, SPECT and PET give a relatively large radiation dose to patient.

Recently, ECG-gated cardiac CT imaging has been developed for evaluation of MI [5]. It can provide both static and dynamic diagnostic information, which cannot be achieved by traditional cardiac imaging modalities. Due to its fast scanning speed (around 300 ms per rotation), 3D image of interested cardiac phase or 4D cardiac image can be obtained with ECG-gated reconstruction in several seconds. After administrating contrast agent, the myocardial PDs can be detected with reconstructed images. By comparing the end-diastolic and end-systolic volume image, the global left ventricular functions and ejection function can be measured. Also, RWM assessment is performed by evaluating the 4D image. Finally, the treatment plan of acute PD is determined based on the results from all these evaluations. Therefore, cardiac CT imaging is an excellent rapid one-stop shopping technique [5].

The ejection fraction and RWM calculated from pixel values may not reflect the true heart motion. In this study, we improve a method that provides comprehensive cardiac function/motion analysis for cardiac CT. The proposed method has two steps: First, 4D cardiac motion vector field (MVF) is obtained by performing non-rigid image registration on 4D ECG-gated cardiac CT reconstructions [6]; then, cooperating with myocardial segmentation analysis; cardiac motion is assessed with the 4D MVF.

II. METHOD

In this section, we outline three main tasks for the proposed method: to obtain 4D cardiac image; to obtain 4D MVF; and to analyze cardiac motion with 4D MVF. In this work, the 4D cardiac image is acquired by ECG-gated reconstruction; 4D MVF is obtained by performing non-rigid image registration on the 4D cardiac image; and cardiac motion is evaluated with MVF in the way of bullseye map of myocardium.

A. *4D cardiac image*

Currently, ECG-gated cardiac CT imaging reconstructs

This work was supported in part by NIH Grant Nos. R01 HL087918 and R01 HL087918A2S1, and AHA grant 0865315E.

Q. Tang, G. S. K. Fung, E. K. Fishman and K. Taguchi are with The Russell H. Morgan Department of Radiology and Radiological Science, Johns Hopkins University School of Medicine, Baltimore MD. 21287. USA. (e-mail: qtang7@jhmi.edu)

T. Kigure is with Department of Mechanical and Environmental Informatics, Tokyo Institute of Technology (Tokyo, Japan)

T. Higuchi is with University of Würzburg (Würzburg, Germany)

volume image of quite cardiac phase using only the corresponding part of the acquired data and throws away the rest of “off-phase” data. In this work, images of all cardiac phases are reconstructed with all the acquired data. First, the whole cardiac cycle is divided into different cardiac phases using ECG signal, which is recorded synchronously with the acquisition of projection data; second, projection data of each cardiac phase were selected by a given gating window; finally, the image of each phase is reconstruct from the corresponding projection data.

B. 4D MVF

We perform non-rigid image registration on 4D cardiac image to obtain 4D MVF. The ME algorithm was developed in our previous work [6], which is briefly described in convenience.

Deformation model: A volume at the least motion phase is chosen as the reference, $f_r(\vec{x})$, and we assume that moving volumes are all deformations of the reference volume as follows:

$$f(\vec{x},t) = f(\vec{x}+\vec{V}(\vec{x},t),t_r). \tag{1}$$

The deformation $\vec{V}(\vec{x},t)$ can be modeled by a finite number of knots using cubic B-splines as

$$\vec{V}(\vec{x},t) = \sum_{\tau=1}^{K}\sum_{\vec{\imath}}\theta_{\vec{\imath},\tau}b\left(\frac{t}{\Delta t}-\tau\right)\beta\left(\frac{\vec{x}}{|\Delta\vec{x}|}-\vec{\imath}\right), \tag{2}$$

where $|\Delta\vec{x}|$ and Δt are the knot spacing in the spatial domain and the temporal domain, respectively; $\vec{\imath}$ and τ are discrete sampling indices in the spatial and temporal domains, respectively; $\theta_{\vec{\imath},\tau}$ is the cubic B-spline coefficients at knot positions; K is the number of knots in time; b is a 1D cubic B-spline, and β is a 3D tensor product of cubic B-splines.

Cost function: We estimate the deformation parameters $\theta_{\vec{\imath},\tau}$ by minimizing a regularized sum of squared weighted difference $\emptyset(\theta_{\vec{\imath},\tau})$ between the warped reference volume and the target volumes:

$$\hat{\theta}_{\vec{\imath},\tau} = \arg\min_{\theta_{\vec{\imath},\tau}}\Phi(\theta_{\vec{\imath},\tau}), \tag{3}$$

$$\Phi(\theta_{\vec{\imath},\tau}) = L_\omega(\theta_{\vec{\imath},\tau}) + R(\theta_{\vec{\imath},\tau}), \tag{4}$$

where $L_\omega(\theta_{\vec{\imath},\tau})$ denote a similarity metric

$$L_\omega = \frac{1}{2MN}\sum_{m=1,\dots,M}\|\omega(\vec{x},t_m)(f(\vec{x},t_m)-(\vec{x},t_m))\|^2, \tag{5}$$

and $R(\theta_{\vec{\imath},\tau})$ denote a quadratic penalty term [12]

$$R(\theta_{\vec{\imath},\tau}) = \frac{1}{2S}\alpha_x\sum_{\vec{\imath}}\sum_{\tau}\left|C_x\,\theta_{\vec{\imath},\tau}\right|^2 + \frac{1}{2S}\alpha_t\sum_{\vec{\imath}}\sum_{\tau}\left|C_t\,\theta_{\vec{\imath},\tau}\right|^2. \tag{6}$$

In Eq. (5), N is the number of voxels in a 3D image, m is a phase index, and M is the number of discrete phase points in one heart beat, and $\omega(\vec{x},t_m)$ is a weighting function; In Eq. (6), S is the number of 4D knots, α_x and α_t are the weighting factors for the spatial and temporal smoothness terms, and C_x and C_t are differencing matrixes in the spatial and temporal domains, respectively.

Optimization: An iterative nested conjugate gradient (CG) method is used to minimize the cost function; in the inner loop, MVF between a pair of volumes, one at the reference time, t_r, and the other at one of the other phases, t_m’s, $m = 1, \dots, K$, was updated one and only one time. Note that the knots number in time is chosen to be the same as the number of discrete phase points in this study, that is, $K = M$. We choose conjugate gradient because it often provides fast convergence and does not require an inversion of the Hessian matrix. From the current estimation $\theta_{\vec{\imath},\tau}^{k}$, the next estimation $\theta_{\vec{\imath},\tau}^{k+1}$can be obtained by a conjugate vector (searching direction) d^k as

$$\theta_{\vec{\imath},\tau}^{k+1} = \theta_{\vec{\imath},\tau}^{k} + \lambda^k d^k, \tag{7}$$

where

$$\lambda^k = -\frac{(B^k)^T d^k}{(d^k)^T A^k d^k}, \tag{8A}$$

$$d^k = -B^k + \sum_{j=0}^{k-1}\eta^j d^j, \tag{8B}$$

$$\eta^k = \frac{(B^k)^T A^k d^k}{(d^k)^T A^k d^k}. \tag{8C}$$

Here, T is the transpose operator, k is the iteration number, B^k is $-\frac{\partial\emptyset}{\partial\theta_{\vec{\imath},\tau}}$ evaluated at $\theta_{\vec{\imath},\tau}^{k}$, and A^k is $\frac{\partial\emptyset}{\partial\theta_{\vec{\imath},\tau}\partial\theta_{\vec{\imath}',\tau'}}$ evaluated at $\theta_{\vec{\imath},\tau}^{k}$, which is similar to Zeng and Fessler’s method [7].

C. Cardiac motion analysis

In this step, cardiac motion/function is comprehensively investigated with MVF in the way of bullseye map, which is often used in nuclear imaging. Three main procedures are involved: to obtain the long and short-axis images; to segment the myocardium; and to generate polar map.

As the heart tilts in the chest, long and short-axis images are not acquired directly by CT imaging. Therefore, the long and short axes (principle axes) of heart are first obtained from the volume image. Then, the volume images and vectors of MVF are rotated according to the long and short axes (rotated coordinates). And, a new (cylindrical) coordinate system, which consists of radial, tangential and longitudinal axes, is defined. The radial and tangential axes are in short axis image, and longitudinal axis is perpendicular to the short axis image.

The rotated 4D MVF are then analyzed by calculating the following three indices: (1) The magnitude and three directional motion; (2) the peak (maximum) velocity; (3) time-to-peak or phase-to-peak velocity; (4) timing-to-initiate systole; and (5) timing-to-initiate diastole. The last three indices may reflect mechanical cardiac function related to electro-physiology much better than simple indices such as ejection fraction or RWM.

Once the apex and base of left ventricle are determined, the myocardium of left ventricle is segmented by tracing epicardial and endocardial contours in the stack of short-axis images. Myocardium mass and ventricular volumes at different phases are then measured. Rotated MVF related to the myocardium is then segmented as well as the three components: radial, circumferential, and longitudinal motions.

Polar maps of the segmented volume image and MVF are finally obtained. The segmented ring of short-axis image is averaged along radial direction, then each short axis image is corresponding to one circle of the polar map. The apex of left ventricle corresponds to the origin of the polar map, and the base of left ventricles to outer most circle of the polar map. Based on all these polar maps, the cardiac motion is assessed.

III. EVALUATIONS

A. *Data acquisition*

Patient data were obtained by a 64-slice CT scanner (Sensation 64; Siemens Healthcare; Forchheim, Germany) with the following standard cardiac protocol was used: detector collimation of 2 × 32 × 0.6 mm with z-flying focal spot technique, helical pitch of 0.29/rot., gantry rotation speed of 330 msec/rot, and 1160 projections/rot. ECG signals were also acquired during the scan. The average heart rate during the scan was 52.2 beats-per-minute. Results from only one patient are shown in following because of space limitation.

We used 20 phases with a 5 % R-R interval in this experiment; the volume size at one phase was 512×512×321. The quiescent cardiac phases with least motion were determined manually as 5% of the R-R interval (end-diastole), 40% (end-systole), and 75% (mid-diastole), and they are chosen as reference phases for this patient.

In our study, there are 16 × 16 × 11 knots in *x*, *y*, and *z*-axes and 20 knots in temporal axis, respectively. The knots spacing are $\Delta_x = 14.6$ mm, $\Delta_y = 14.6$ mm, $\Delta_z = 16$ mm, and $\Delta_t = 5\%$ of one cardiac cycle (or R-R interval).

B. *Results*

Figure 1 shows the results of motion estimation. The three short and long-axis images are of mid-diastole. The arrows show the estimated MVFs from mid-diastole to end-systole. It can be seen that the magnitudes and directions of the estimated MVFs physiologically sounded and agreed with subjective findings. Expansion and contraction of ventricles were estimated well, and so were those of atria, which were off-synchronized from ventricles.

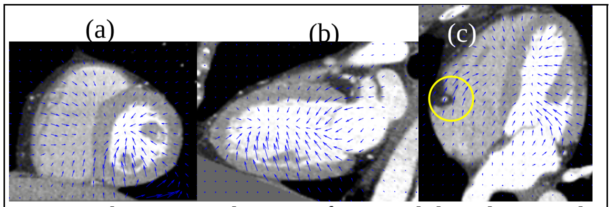

Fig. 1 The estimated MVFs from mid-diastole to end-systole superimposed on (a) short-, (b) vertical-long-, (c) and horizontal-long-axis images at mid-diastole.

Figure 2 shows the segmentation of myocardium of left ventricle. It shows that the segmentation of myocardium was accurate.

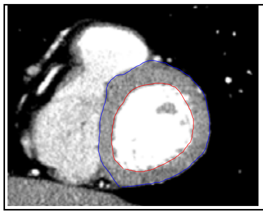

Fig. 2 The segmentation of myocardium in short-axis image. The red and blue lines are the epicardial and endocardial contours, respectively.

Figure 3 shows the polar maps of the estimated MVF from MD to ES after the global heart translation are corrected, and (a), (b), (c), (d) are the norm of vectors, circumferential, radial, and longitudinal components of vectors. It shows that, during the systole, this heart had a large circumferential motion in the ventricular septa, a large radial contraction in inferior wall, and a symmetric contraction between apex and base.

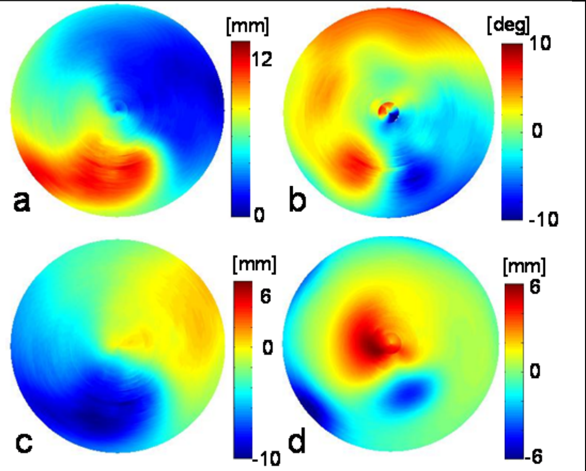

Fig. 3 Polar maps of the estimated MVF from MD to ES after the global heart translation are corrected. (a) The magnitude of deformation (the norm of vectors); (b) circumferential, (c) radial, and (d) longitudinal components of vectors.

Figure 4 shows the polar maps of time-to-peak velocities during systole (a) and diastole (b) with time measured from a global reference time. It indicates that during systole, this heart had a moderate delay laterally between the ventricular septa and the lateral wall, and a significant delay from the anterior wall to the inferior wall. The motion during diastole was synchronized. Figure 4(c) and 4(d) are the polar maps of timing-to-initiate systole and timing-to-initiate diastole, respectively. It shows that systolic motion of the ventricular septa and lateral wall started later than that of anterior and inferior walls.

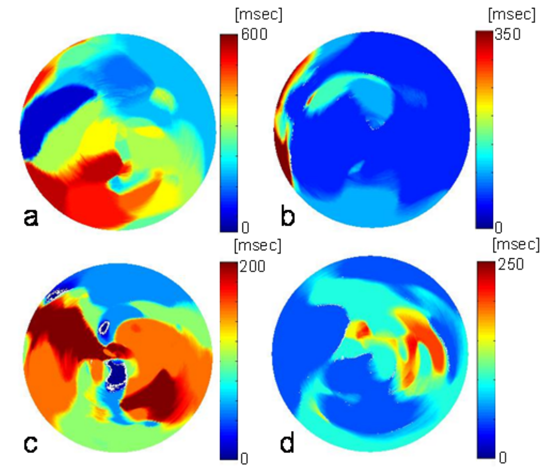

Fig. 4 (a, b) Polar maps of time-to-peak velocities during systole (a) and diastole (b) with time measured from a global reference time; (c) and (d) are polar maps of timing-to-initiate systole and timing-to-initiate diastole, respectively.

IV. CONCLUSIONS

In this work, we develop a two-step method for cardiac CT to provide comprehensive assessments of cardiac motion/function. The first step is using previous developed motion estimation method to estimate cardiac motion; the second step is analyzing cardiac motion with the estimated MVFs. The method was verified by patient data. The results show that MVFs estimated by our method are physiologically agreed with subjective findings. Expansion and contraction of ventricles were estimated as expected, and so were those of atria, which were off-synchronized from ventricles. The polar maps of the circumferential, radial and (d) longitudinal components of MVFs from MD to ES also show the accuracy of the estimated MVFs. They also show the relative motion between each part of the left ventricle, which is also agree with the physiological and clinical understandings. Finally, the polar maps of dynamic index of cardiac motion, such as time-to-peak velocities, initial-time-of-systole and initial-time-of-diastole, are obtained. They show the important synchronization information of cardiac motion, which are very helpful for diagnosis the myocardial infarction. In all, a cardiac motion estimation and motion analysis method was developed and its feasibility and contribution to clinical evaluation was verified by study with patient data.

ACKNOWLEDGEMENT

We thank Thomas G. Flohr, Ph.D. of Siemens Healthcare, Bernhard Schmidt, Ph.D. of Siemens Healthcare, and Hiroshi Ashikaga, M.D., Ph.D. for their helpful discussion. We appreciate Meiyappan Solaiyappan, Ph.D., Arkadiusz Sitek, Ph.D., and Martin Stumpf, M.Sc. for their help with GPU implementation, and Danny Ruijters for his CUDA Cubic B-Spline interpolation library.

REFERENCES

[1] E. M. Antman, D. T. Anbe, P. W. Armstrong, et al, “ACC/AHA guidelines for the management of patients with ST-elevation myocardial infarction: executive summary—a report of the ACC/AHA Task Force on Practice Guidelines,” Circulation **110**(5), 588– 636 (2004).

[2] T. Arita, G. P. Sorescu, B. T. Schuler, L. S. Schmarkey, J. D Merlino, J. Vinten-Johansen, A. R. Leon, R. P. Martin and D Sorescu, “Speckle-tracking strain echocardiography for detecting cardiac dyssynchrony in a canine model of dyssynchrony and heart failure,” American Journal of Physiology - Heart and Circulatory Physiology **293,** H735-H742 (2007).

[3] T. Kukulski, F. Jamal, J. D'Hooge, B. Bijnens, I. De Scheerder and G. R. Sutherland, “Acute changes in systolic and diastolic events during clinical coronary angioplasty: A comparison of regional velocity, strain rate, and strain measurement,” Journal of American Society of Echocardiography. **15**, 1-12 (2002).

[4] B. H. Amundsen, T. Helle-Valle, T. Edvardsen, H. Torp, J. Crosby, E. Lyseggen, A. r. Støylen, H. Ihlen, J. o. A. C. Lima, O. A. Smiseth and S. A. Slørdahl, “Noninvasive Myocardial Strain Measurement by Speckle Tracking Echocardiography: Validation Against Sonomicrometry and Tagged Magnetic Resonance Imaging,” Journal of the American College of Cardiology **47**, 789-793 (2006).

[5] R. C. Cury, K. Nieman, M. D. Shapiro, J. Butler, C. H. Nomura, M. Ferencik, U. Hoffmann, S. Abbara, D. S. Jassal, T. Yasuda, H. K. Gold, I. K. Jang, T. J. Brady, “Comprehensive Assessment of Myocardial Perfusion Defects, Regional Wall Motion, and Left Ventricular Function by Using 64-Section Multidetector CT,” Radiology **248**, 466-475 (2008).

[6] Q. Tang, J. Cammin, S. Srivastava and K. Taguchi, “Four-dimensional non-rigid cardiac motion estimation,” Submitted to Medical Physics (under review).

[7] R. Zeng, J. A. Fessler and J. M. Balter, “Respiratory motion estimation from slowly rotating x-ray projections: theory and simulation,” Medical physics **32**, 984-991 (2005).

High-speed Dynamic Imaging with a Real Time Tomography System

William M. Thompson[1], William R. B. Lionheart[1] and Edward J. Morton[2]

***Abstract*—The Real Time Tomography (RTT) system is a new type of fast cone beam CT scanner, using fixed rings of multiple sources and detectors in an offset geometry. We demonstrate the potential of this system for use in the imaging of high speed dynamic processes, such as moving fluid flows. Through the use of a simple temporal regularisation term, we show that temporal resolution can be further increased, at the expense of a slight loss in spatial resolution.**

***Index Terms*—Cone beam CT, dynamic imaging, real-time tomography**

I. INTRODUCTION

Conventionally, X-ray tomographic imaging systems have used a single X-ray source and an array of detectors which together rotate around the object of interest to form a set of X-ray projections through the object. These projections can be reconstructed to form an image of the object in 2D or 3D, depending on whether the detector configuration is single row fan beam or multi-row cone beam.

Due to the mechanical motion involved in this scanning process, scan rates are restricted to only a few source revolutions per second. The latest dual source medical CT scanners are able to perform just over 3 per second [1]; this gives a reconstructed image frame rate of less than 10 per second. In some applications, such frame rates are too slow to provide the required temporal resolution; for example in the visualisation of the flow of liquids in pipes.

The main factor limiting the speed of conventional rotating gantry cone beam CT scanners is the physical rotation of the source [2]. To address this problem, it is necessary to eliminate the mechanical scanning motion, replacing this with an electronic equivalent comprising a circular array of X-ray sources which can be selected individually under computer control. Through the choice of a suitable source scanning sequence, the impression of movement can be generated without physical motion of any component of the system.

A Real-Time Tomography (RTT) system has been developed to solve this technological problem ([3], [4]), in which an approximately circular array of X-ray sources over an angular distribution of 180 degrees plus fan angle is matched with a corresponding array of X-ray detectors to provide a no-moving-parts X-ray tomographic scanning system. The plane containing the X-ray sources is offset from the plane containing the X-ray detectors to avoid attenuation of the primary beam before it is transmitted through the object under inspection.

The X-ray sources comprise an array of electron guns, each of which is controlled by an independent electronic switching circuit. These switching circuits can be pulsed in microsecond timescales. The electron beam from a given source is accelerated through a high potential difference to a tungsten coated anode to produce X-rays. A single distributed anode is arranged in a circular configuration such that each electron gun irradiates a different region of the anode around the circumference of a circle or polygon, resulting in an effective X-ray focus when viewed from the detectors of typically 1mm^2. The electron gun control electronics can be programmed to irradiate the electron guns in any given sequence. Therefore, this is a flexible data acquisition platform and is capable of generating tomographic scan data at theoretical source rotation rates of up to 480 frames per second.

II. THE RTT20 SYSTEM

RTT20 is a small-scale prototype RTT system which has been acquired by the University of Manchester. A two-dimensional cross-section of the RTT20 geometry is shown in figure 1; the sources are arranged in 8 blocks of 32, with two ‘missing’ blocks of sources at the bottom, creating an incomplete source ring. The incomplete ring is part of the original design to enable a small scanner to be easily fixed onto pipes for imaging flowing fluids. The two blocks adjacent to the gap also do not use their outermost 4 sources, giving a total of 248 sources. There is one full ring of detectors arranged in 21 blocks of 16, giving 336 detectors in total; this is offset from the source plane by 5.48mm in the z direction. The tunnel diameter is 20cm (hence RTT20) giving the reconstruction region of interest (ROI) as a circle of diameter 200mm.

The machine is capable of acquiring a complete set of projections from all 248 sources 60 times per second, enabling imaging of very fast moving processes. Sources may be fired in almost any order we desire; for a general RTT system with N sources, this is defined by a bijective function

$$\phi : [1, N] \longrightarrow [1, N], \tag{1}$$

known as a *firing order*. The firing order used for collection of the RTT20 experimental data is defined for 256 sources by the function

$$\phi(i) = \Big[\big(32(i-1) + \lfloor (i-1)/8 \rfloor\big) \bmod 256\Big] + 1. \tag{2}$$

The first and last 4 sources in the sequence are simply removed to reduce this to 248 sources.

---

1. Henry Moseley X-ray Imaging Facility and School of Mathematics, University of Manchester.

2. Rapiscan Systems.

Corresponding author: William R. B. Lionheart, E-mail: bill.lionheart@manchester.ac.uk.

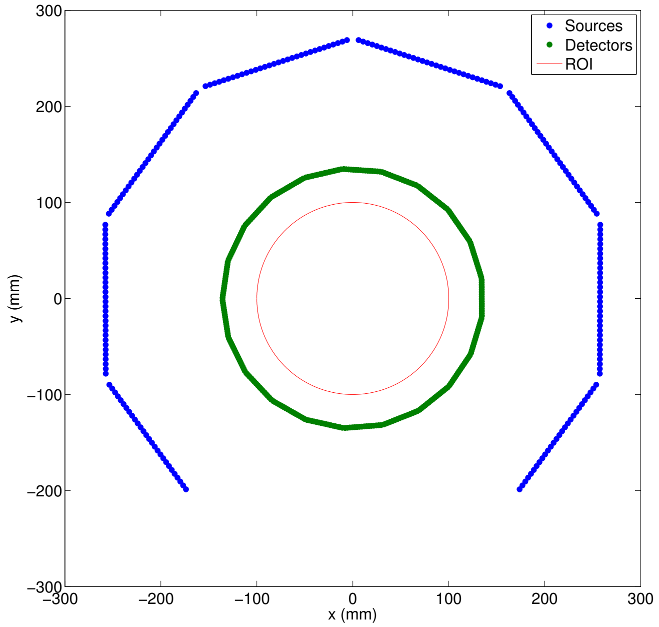

Fig. 1: The RTT20 geometry

III. The Reconstruction Process

The reconstruction of an RTT20 dynamic data set forms a sequence of images, each of which is referred to as a *frame*. The simplest method of reconstruction is to regard each complete set of 248 projections as representing a frame and reconstruct each one of these independently. For applications where the motion of the object is slow compared to the data collection rate this should be adequate. However, if the firing order is chosen appropriately, so that the distribution of projection angles is even for smaller subsets of projections, then we may divide each full set of projections to represent multiple frames. This effectively trades spatial for temporal resolution. The firing order described by equation (2), whilst not optimal, satisfies this condition to a reasonable extent.

The process of reconstructing each two-dimensional frame is simple and well-understood; however, the construction of RTT20 presents some problems. Firstly, the polygonal nature of the source and detector rings means that the distribution of projection angles, and the angles of rays within each projection, are highly uneven. This, combined with the incomplete source ring, causes an uneven sampling of the two-dimensional Radon transform; this is shown in figure 2. Secondly, the offset detector means that we do not really measure rays in a plane through the object. However, compared to the x-y resolution of the system, the effect of the offset is considered small enough to ignore within the reconstruction region of interest.

IV. Reconstruction Algorithms

A. Analytical Algorithms

Analytical reconstruction algorithms based on filtered back projection (FBP) for the 2D fan beam geometry are well-known [5]. However, these assume an equal spacing of the projection angles, and either an equiangular or equally spaced linear sampling scheme for the rays within each projection.

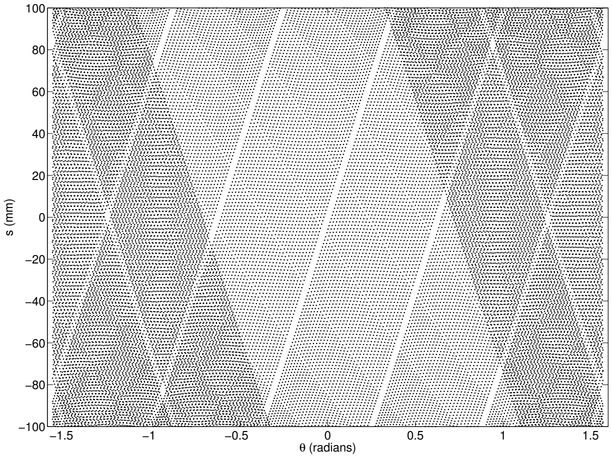

Fig. 2: Distribution of sampling points in the 2D Radon transform domain

Due to the construction of RTT20, with its polygonal source and detector rings, neither of these conditions are satisfied. For applications where low reconstruction time is important, such as real time observation of flow through an oil pipe for example, taking all 248 projections per frame and using a simple interpolation to the parallel beam geometry gives adequate results. However, for fast moving objects, motion artefacts will be observed.

B. Algebraic Reconstruction

For applications where the data acquisition and image analysis processes are separate, such as the scientific applications the machine will be used for at the university, the problem is small enough to enable solution by algebraic methods in a reasonable amount of time. Algebraic methods make no assumptions at all about the system geometry, so in theory should be capable of better reconstructed image quality. Performance of algebraic algorithms with reduced numbers of projections is also better, which should allow fewer projections per frame, resulting in better temporal resolution.

We let the matrix A represent the projection process for each complete set of 248 projections; this may represent more than one frame, and is simply re-used for each projection set. Elements of A are calculated using the ray tracing algorithm of Jacobs et al. [6], which is itself a development of Siddon's algorithm [7]. In order to take the offset geometry into account, ray tracing is performed in 3D; to ensure only a single slice is considered, the voxels are simply defined to be long in the z direction. This has been implemented in MATLAB as a C `.mex` routine, with output in the MATLAB double precision sparse matrix format. Using 1×1mm pixels and covering the entire circular ROI, storage requirements for A are approximately 100MB.

For each complete set of projections, the system of equations $A\mathbf{x} = \mathbf{b}$ is solved using the conjugate gradient least squares (CGLS) algorithm. We use the MATLAB implementation of CGLS provided in Hansen's Regularisation Tools package [8].

C. Regularisation

Although with CGLS, the number of iterations plays the role of a regularisation parameter, it is unclear how many iterations should be performed in order to provide the correct degree of regularisation. We may therefore apply additional systematic regularisation by solving the augmented system

$$\begin{bmatrix} A \\ \alpha L \end{bmatrix} \mathbf{x} = \begin{bmatrix} \mathbf{b} \\ \mathbf{0} \end{bmatrix}, \tag{3}$$

in the least squares sense, where α is a regularisation parameter, L is some finite difference approximation to a differential operator, for example the Laplacian, and $\mathbf{0}$ is the zero vector of length equal to the total number of image pixels. This gives the least squares solution

$$\arg\min_{\mathbf{x}} \{ \|A\mathbf{x} - \mathbf{b}\|_2^2 + \alpha^2 \|L\mathbf{x}\|_2^2 \}. \tag{4}$$

D. Temporal Regularisation

By considering the data set as a whole, rather than as a set of discrete independent frames, we can also add regularisation in the temporal dimension. The matrix A_{total}, representing the whole system, is formed from A by a Kronecker product with the identity matrix of size equal to the number of complete projection sets. We can then solve an augmented system of equations as in (3). This is a simple process and can be implemented efficiently.

Regularisation has been performed by taking L to be the three-dimensional discrete Laplacian. By incorporating the regularisation parameter into the matrix L, it is possible to choose differing amounts of regularisation in the spatial and temporal dimensions. Letting m and n be the number of image pixels in the x and y directions respectively, and letting p be the number of frames, L has the following Kronecker product decomposition:

$$L = \alpha_s I_p \otimes I_n \otimes D_m + \alpha_s I_p \otimes D_n \otimes I_m + \alpha_t D_p \otimes I_n \otimes I_m, \tag{5}$$

where I_m is the $m \times m$ identity matrix, D_m is the one-dimensional discrete Laplacian on m points and α_s and α_t are respectively the spatial and temporal regularisation parameters.

V. RESULTS

A. Simulated Data

Simulated data were generated for a ball of radius 10mm, moving horizontally along a line through the centre of the scanner in a sinusoidal motion of frequency 0.5Hz and amplitude 80mm. Ray integrals were calculated analytically, with the object position being re-calculated for each projection. The simulation was performed at the scanner's standard speed of 60 full sets of 248 projections per second, and using the firing order described by equation (2). 1% Gaussian noise was added to the calculated data.

Figure 3 shows a frame from reconstructions of the simulated data using differing values of the temporal regularisation parameter, comparing a full set of projection data per frame with 31 projections per frame (8 frames per full projection set). In all cases, the spatial regularisation parameter was chosen empirically as $\alpha_s = 5$. Figures 4 and 5 show respectively the 2-norms of the data error, and the error from the reference image at each iteration.

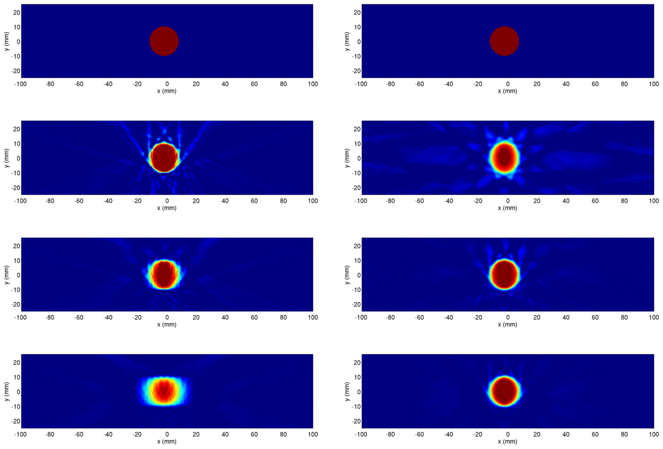

Fig. 3: Reconstructed images of a single frame from the simulated data (left, 248 projections; right, 31 projections; top–bottom, reference image, $\alpha_t = 0$, $\alpha_t = 5$, $\alpha_t = 25$)

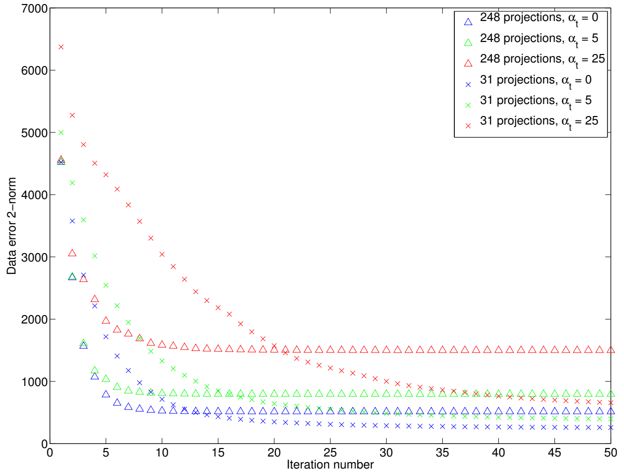

Fig. 4: Data error for the simulated data reconstructions

We see that by reducing the number of projections per frame, the motion between subsequent frames is reduced so that it makes sense to smooth in the temporal dimension. By doing this, streak artefacts are reduced and temporal resolution has increased by a factor of 8.

B. Real Data

Real experimental data were available for a mixture of oil, water and air moving in a bottle. The data set consists of 61 full projection sets representing 1 second of the motion, and was collected during the machine's initial testing process. The scanner settings used were a voltage of 120keV, and current of 10mA. Three of the sources in the prototype scanner were defective, resulting in a total of 245 sources.

Figure 6 shows a frame from reconstructions of the data, again using differing values of the temporal regularisation parameter, comparing a full set of projection data per frame with 49 projections per frame (5 frames per full projection set). Again, in all cases, the spatial regularisation parameter

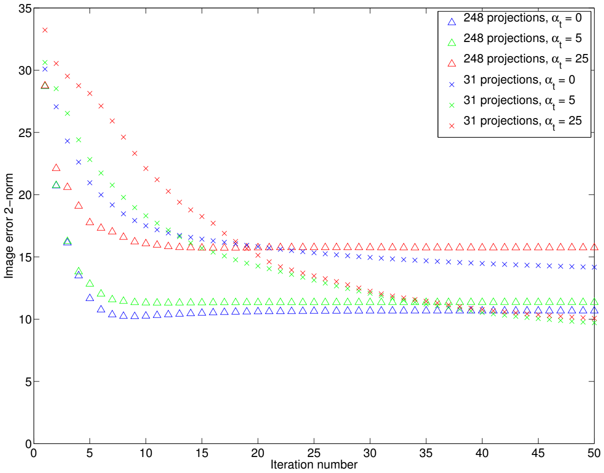

Fig. 5: Image error for the simulated data reconstructions

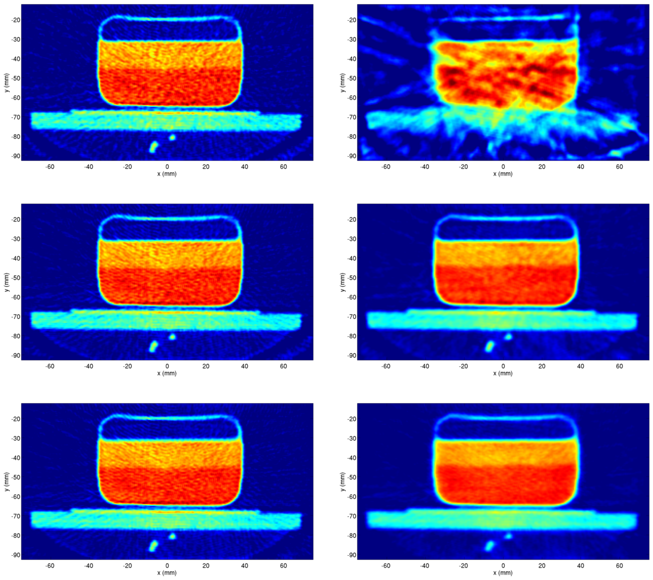

Fig. 6: Reconstructed images of a single frame from the oil and water data (left, 245 projections; right, 49 projections; top–bottom, $\alpha_t = 0$, $\alpha_t = 5$, $\alpha_t = 25$)

was chosen empirically as $\alpha_s = 5$. Figure 7 shows the 2-norm of the data error at each iteration.

The motion in this case is not as fast as the simulated data, and reasonable results are obtained by simply using all 245 projections per frame. However, by using only 49 projections per frame and applying temporal regularisation, temporal resolution has increased by a factor of 5; this improvement is very noticeable when viewing the full dynamic reconstruction as a movie. Although the 49 projection temporally regularised images are noticeably softer than those using the full set of projections per frame, they compare well, and in certain applications the gain in temporal resolution may be more important.

VI. CONCLUSIONS

The RTT system has the potential to produce some novel visualisations of rapidly moving processes such as fluid and granular flows. Problems caused by the highly uneven sampling generated by the RTT20 geometry have been solved by using algebraic reconstruction and regularisation, rather than the more widely used filtered back projection based algorithms. By implementing a simple temporal regularisation process, we have shown that temporal resolution can be increased in real world applications by at least a factor of 5, with only minor impact on reconstructed image quality.

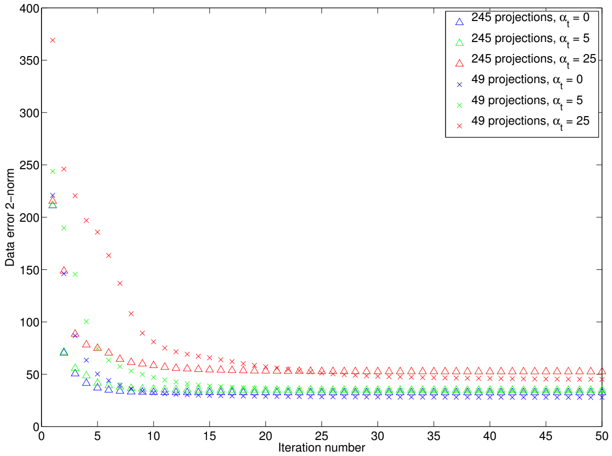

Fig. 7: Data error for the oil and water data reconstructions

ACKNOWLEDGMENTS

The authors would like to thank Rapiscan Systems Ltd. and EPSRC (grant EP/E010997/1) for supporting this work. We would particularly like to thank the RTT development team for providing us with access to technical details of the system and experimental data.

REFERENCES

[1] B. Krauss, B. Schmidt, and T. G. Flohr, “Dual source CT,” in *Dual Energy CT in Clinical Practice*, ser. Medical Radiology, T. Johnson, C. Fink, S. O. Schönberg, and M. F. Reiser, Eds. Springer Berlin Heidelberg, 2011, pp. 11–20.
[2] W. A. Kalender, “X-ray computed tomography,” *Physics in Medicine and Biology*, vol. 51, no. 13, p. R29, 2006.
[3] E. J. Morton, R. D. Luggar, M. J. Key, A. Kundu, L. M. N. Tavora, and W. B. Gilboy, “Development of a high speed x-ray tomography system for multiphase flow imaging,” *IEEE Trans. Nucl. Sci.*, vol. 46 III(1), pp. 380–384, 1999.
[4] E. J. Morton, “X-ray monitoring,” US patent application US2006023961(A1), 2006.
[5] A. Kak and M. Slaney, *Principles of Computerized Tomographic Imaging*. IEEE Service Center,Piscataway, NJ, 1988.
[6] F. Jacobs, E. Sundermann, B. D. Sutter, and I. Lemahieu, “A fast algorithm to calculate the exact radiological path through a pixel or voxel space,” *J. Comput. Inform. Technol.*, vol. 6, pp. 89–94, 1998.
[7] R. L. Siddon, “Fast calculation of the exact radiological path for a 3-dimensional CT array,” *Medical Physics*, vol. 12, no. 2, pp. 252–255, 1985.
[8] P. C. Hansen, “Regularization tools - a MATLAB package for analysis and solution of discrete ill-posed problems - version 3.0 for matlab 5.2,” *Numer. Algorithms*, vol. 6, pp. 1–35, 1998.

View-Based Noise Modeling in the Filtered Backprojection MAP Algorithm

Gengsheng “Larry” Zeng

***Abstract*—The goal of this paper is to extend our recently developed FBP (filtered backprojection) algorithm, which has the same characteristics of an iterative Landweber algorithm, to an FBP algorithm with the same characteristics of an iterative MAP (maximum *a posteriori*) algorithm. The newly developed FBP algorithm also works when the angular sampling interval is not uniform. The projection noise variance can be modeled using a view-based weighting scheme. The new FBP algorithm with view-based noise modeling has the same computation time as the conventional FBP algorithm.**

I. INTRODUCTION

The filtered backprojection (FBP) algorithm is simple and fast, and can be used to reconstruct images in Nuclear Medicine, X-ray CT [1]. Compared with iterative reconstruction algorithms, the FBP algorithm generally produces noisier images, even when the iterative algorithm (e.g., the iterative Landweber algorithm) does not model the projection noise or does not model the projection noise correctly [2][3]. As a result, the FBP algorithm has gradually been replaced by iterative image reconstruction algorithms. Recently, we have developed a windowed FBP algorithm that is able to produce similar images to those reconstructed by the iterative Landweber algorithm [4]. One goal of this paper is to modify this windowed FBP algorithm so that it can produce similar images to those reconstructed by the iterative Landweber MAP algorithm. Another goal of this paper is to extend the windowed FBP algorithm to model the projection data noise.

Iterative MAP algorithms can produce noise/resolution balanced images and have wide applications [5]-[8]. Due to their huge projection operator matrix size, MAP algorithms use iterative methods to optimize the objective function. Recently Cao *et al* proposed a special representation of the huge sparse projection matrix so that the condensed projection matrix can be stored in a computer and a non-iterative reconstruction becomes possible [9]. However, this sparse-matrix transformation approach is not easy to implement. Three new methods of the FBP algorithms are presented in the next section. The new methods are practical and can include some noise information and image prior information in the FBP reconstruction.

II. METHODS

A. A new FBP algorithm that emulates an iterative MAP algorithm

A typical MAP (maximum *a posteriori*) algorithm is to optimize the Bayesian estimation as

$$\hat{X} = \arg\min_{X}\{\|P - AX\|^2 + \beta X^T R X\}\,. \tag{1}$$

In the context of tomography, A in (1) is the projection matrix, X is the image array written as a column vector, P is the projection array written as a column vector, and β is a relative weighting factor that adjusts the importance of the Bayesian term X^TRX relative to the fidelity term $\|P\text{-}AX\|^2$. The square matrix R in (1) can be understood in such a way that X is modeled by a Gaussian random field with a covariance matrix R^{-1}. In practice, X is not random, the matrix R is used to enforce some smoothness of the image so that the reconstruction is not too sensitive to noise. One way to promote the smoothness is to suppress the difference between the central pixel value and its neighbors.

The problem (1) has a quadratic objective function, so the solution can be obtained by the Landweber algorithm:

$$X^{(k+1)} = X^{(k)} + \alpha[A^T(P - AX^{(k)}) - \beta R X^{(k)}]\,, \tag{2}$$

where A^T is the backprojection matrix, $X^{(k)}$ is the estimated image at the kth iteration, and $\alpha > 0$ is the step size. This relation can be re-written as a non-recursive expression as

$$\begin{aligned} X^{(k+1)} &= X^{(k)} + \alpha[A^T(P - AX^{(k)}) - \beta R X^{(k)}] \\ &= [\sum_{n=0}^{k}(I - \alpha A^T A - \alpha R)^n]\alpha A^T P + (I - \alpha A^T A - \alpha R)^{k+1} X^{(0)}\,. \end{aligned} \tag{3}$$

If the initial image $X^{(0)}$ is set to zero, the result from k iterations of the Landweber algorithm is

$$X^{(k)} = \alpha[\sum_{n=0}^{k-1}(I - \alpha A^T A - \alpha\beta R)^n]A^T P\,. \tag{4}$$

This non-iterative expression of the Landweber algorithm resembles a “backproject first, then filter” algorithm, in the sense that the projection data P are first backprojected by the operator A^T and then filtered by $\alpha[\sum_{n=0}^{k-1}(I - \alpha A^T A - \alpha\beta R)^n]$.

When the step size α is small enough, the Landweber algorithm will converge and we have

$$\alpha[\sum_{n=0}^{k-1}(I - \alpha A^T A - \alpha\beta R)^n] \to (A^T A + \beta R)^{-1} \text{ as } k \to \infty\,, \tag{5}$$

if $(A^T A + \beta R)^{-1}$ exists, otherwise $(A^T A + \beta R)^{-1}$ is replaced by a generalized inverse. For a finite k, we have

---

Gengsheng Zeng is with the Utah Center for Advanced Imaging Research, Department of Radiology, University of Utah, Salt Lake City, UT 84108, USA, Phone: (801) 581-3918, E-mail: larry@ucair.med.utah.edu

$$\alpha[\sum_{n=0}^{k-1}(I-\alpha A^T A-\alpha\beta R)^n] \\ =(A^T A+\beta R)^{-1}[I-(I-\alpha A^T A-\alpha\beta R)^k] \quad . \quad (6)$$

The proofs of the above equations are available in a review paper by Schafer *et al*[10].

If the projection operator A is the line-integral in 2D space and A^T is the the backprojection transform, the combined operator of $A^T A$ is the 2D convolution of the original image with a 2D kernel $1/r$, where $r=\sqrt{x^2+y^2}$ in the *x*-*y* Cartesian coordinates [11]. The 2D ramp filter is able to cancel the $1/r$ blurring effect [10]. In this ideal situation, the $(A^T A)$ operation is a $1/r$ convolution, the $(A^T A)^{-1}$ operation is 2D ramp filtering, and $[I-(I-\alpha A^T A-\alpha\beta R)^k]$ in (6) can be treated as a window function in the frequency domain:

$$W_k(\nu_x,\nu_y)=1-(1-\alpha(\frac{1}{\|\vec{\nu}\|}+\beta h(\|\vec{\nu}\|)))^k \,,\ \|\vec{\nu}\|=\sqrt{\nu_x^2+\nu_y^2} \quad (7)$$

where ν_x and ν_y are the frequencies with respect to *x* and *y*, respectively, $\vec{\nu}=(\nu_x,\nu_y)$ is the 2D frequency vector, and h is the Fourier transform of R when R is expressed as a convolution kernel. Thus, the conceptual shift-invariant Landweber algorithm is equivalent to: first, backprojecting the data into the image domain; second, filtering the backprojected image with a 2D windowed ramp-filter defined in (7).

B. *Implementation*

In fact, a "backproject first, then filter" algorithm is equivalent to an FBP algorithm, which filters the projections first, then backprojects[4][11]. The 1D frequency-domain filter in the FBP algorithm is the 1D profile of the 2D filter in the "backproject first, then filter" algorithm [4][11]. Therefore, an iterative-Landweber-MAP-equivalent FBP-MAP algorithm can be obtained, and the implementation steps are: Step 1: Perform the 1D Fourier transform of the projection at each view. Step 2: Filter the frequency domain data with a 1D windowed ramp-filter

$$H_k(\nu_t)=[1-(1-\alpha(\frac{1}{|\nu_t|}+\beta h(|\nu_t|)))^k]/\left|\frac{1}{|\nu_t|}+\beta h(|\nu_t|)\right| \,, \quad (8)$$

where ν_t is the frequency with respect to the linear variable on the 1D detector. Step 3: Perform a 1D inverse Fourier transform of the filtered data. Step 4: Perform the backprojection. When $k=\infty$ and $\beta=0$, (8) is the ramp filter in the conventional FBP algorithm.

C. *Noise variance weighted FBP algorithm*

In order to make the derivation more clearly, we turn off the Bayesian term in the objective function by setting $\beta=0$. When noise is modeled, (1) becomes

$$\hat{X}=\arg\min_X\{(P-AX)^T W(P-AX)\} \,, \quad (9)$$

where W is a diagonal square matrix with weighting factors as the diagonal elements. In principle, a larger weighting factor is assigned to a less noisy measurement and a smaller factor for a noisier measurement. For example, the weighting factors can be chosen as a function of the noise variance of the corresponding projection. Since an FBP algorithm has a shift-invariance PRF, we require that the weighting factor has the same value for all projections in each view. In x-ray CT imaging, this weighting factor assignment strategy is reasonable. When the x-rays travel in the direction from shoulder to shoulder, the projections are noisier than when the x-rays travel in the direction from the front to the back of the torso. If an iterative Landweber algorithm is used to solve (9), following the similar derivation as in Part A and replacing $A^T A$ by $A^T WA$ everywhere, the result of the *k*th iteration is given as

$$X^{(k)}=\alpha[\sum_{n=0}^{k-1}(I-\alpha A^T WA)^n]A^T WP \\ =[I-(I-\alpha A^T WA)^k](A^T WA)^{-1}A^T WP \quad . \quad (10)$$

In this symbolic derivation, we assume that $(A^T WA)^{-1}=A^{-1}W^{-1}(A^T)^{-1}$ exists. Thus, (10) is simplified as

$$X^{(k)}=[I-(I-\alpha A^T WA)^k]A^{-1}P \,. \quad (11)$$

Following the same steps as in Part B, (11) can be turned into an FBP algorithm and the windowed ramp filter is given as

$$H_k(\nu_t)=[1-(1-\alpha(\frac{w_{view}}{|\nu_t|}))^k]\cdot|\nu_t| \text{ and } H_k(0)=0 \quad (12)$$

where w_{view} is the weighting factor for the projection at a particular view.

III. COMPUTER SIMULATION RESULTS

A. *FBP-MAP*

The Shepp-Logan phantom [1] was used in computer simulation studies. A 1D parallel-hole detector was rotated over 180° with 120 views and 128 detector bins on the detector. The images were reconstructed in a 256x256 array and the central 128x128 array was used for display and image comparison studies.

In all computer simulations, both the iterative MAP algorithm and the new FBP-MAP algorithm used the same step-size α=0.5, the same parameter β (=0.3) and the same iteration indices k = 2, 20, and 200, respectively. The requirement of choosing parameter α is that $\alpha/|\nu_t|\le 1$ in the newly developed FBP-MAP algorithm and $\alpha\cdot w_{view}/|\nu_t|\le 1$ in the newly developed noise variance weighted FBP algorithm, where w_{view} is a noise weighting factor. In order to use the same parameter α=0.5, we scaled the iterative algorithm's projection/backprojection operator $A^T A$ by 0.00005, that is,

$$X^{(k+1)}=X^{(k)}+\alpha[0.00005\cdot A^T(P-AX^{(k)})-\beta RX^{(k)}] \,. (13)$$

This value of 0.00005 and the parameter α were selected by trial-and-error. If the step-size α was chosen to be too large, the iterative algorithm would diverge and the FBP algorithm would produce unreasonable images. The Bayesian operator R was a Laplacian, whose convolution kernel is {-0.5, 1, -0.5}. The discrete Fourier transform of this kernel is $h(n)$.

Images in Table 1 used noiseless projections, and they are used to illustrate the resolution improvement as the index *k* gets larger. The profiles are drawn horizontally at the center of the images. The images almost converge when $k = 200$.

B. *Noise weighted FBP*

In Figure 1, results of an actual low-dose x-ray CT cadaver study are presented (Raw data courtesy of Leiden University Medical Center). One non-central transverse slice is shown. The image size of this slice is 512x512. The noise weighted FBP algorithm effectively removes the streaking artifacts in the normal FBP (Feldkamp [12]) reconstruction. No pre- or post filtering was performed.

IV. Conclusions

This paper derived an FBP-MAP algorithm that has a window function with an index k that can emulate the iterative Landweber MAP algorithm of the kth iteration. Computer simulations show that the FBP-MAP algorithm and the iterative MAP algorithm give very similar images and noise texture if they have the same index k, same parameter α, and same parameter β. The most significant advantage of the FBP-MAP algorithm is its fast computation time; the iterative MAP algorithm is $2k$ times slower.

This paper first incorporates view-based noise model in the FBP algorithm. This noise weighted FBP algorithm has the same computation time as the conventional FBP algorithm, and may find applications in low-dose x-ray CT applications and in nuclear medicine imaging applications.

References

[1] L. A. Shepp and B. F. Logan, "The Fourier reconstruction of a head section," *IEEE Trans. Nucl. Sci*., **NS-21**, 21-43 (1974).

[2] X.-L. Xu, J.-S. Liow, and S. C. Strother, "Iterative algebraic reconstruction algorithms for emission computed tomography: A unified framework and its application to positron emission tomography," *Med. Phys*., **20**, 1675-1684 (1993)

[3] O. N. Strand, "Theory and methods related to the singular-function expansion and Landweber's iteration for integral equations of the first kind," *SIAM J. Numer. Anal*., **11**, 798-825 (1974)

[4] G. L. Zeng, "A filtered backprojection algorithm with characteristics of the iterative Landweber algorithm," *Med. Phys*., **39**, 603-607(2012)

[5] C. X. Wang, W. E. Snyder, G. Bilbro, and P. Santago, "Performance evaluation of filtered backprojection reconstruction and iterative reconstruction methods for PET images," *Computers in Biology and Medicine*, **28**, 13-25 (1998)

[6] S. Geman and D. E. McClure D E, "Statistical methods for tomographic image reconstruction," *Bull. Int. Statist. Inst.,* **LII-4,** 5-21 (1987)

[7] E. Levitan and G. T. Herman, "A maximum a posteriori probability expectation maximization algorithm for image reconstruction in emission tomography," *IEEE Trans. Med. Imag*., **6,** 185-192 (1987)

[8] P. J. Green P J, "Bayesian reconstruction from emission tomography data using a modified EM algorithm," *IEEE Trans Med. Imag*., **9,** 84-93 (1990)

[9] G. Cao, C. A. Bouman C A, and K. J. Webb, "Noniterative MAP reconstruction using sparse matrix representations," *IEEE Trans Imag. Proc*., **18,** 2085-2099 (2009)

[10] R. W. Schafer, R. M. Mersereau, and M. A. Richards, "Constrained iterative restoration algorithms," *Proc. IEEE,* **69**, 432-450 (1981)

[11] G. L. Zeng, *Medical Image Reconstruction, A Conceptual Tutorial* (Springer, Beijing, 2010)

[12] L. A. Feldkamp, L. C. Davis, and J. W. Kress, "Practical cone beam algorithm," *J. Opt. Soc. Am. A*, **1**, 612-619 (1984)

Table 1. Iterative MAP vs. FBP-MAP with $\beta = 0.3$ using noiseless data

	Iteration index $k = 2$	$k = 20$	$k = 200$
Iterative result	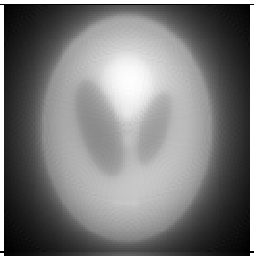	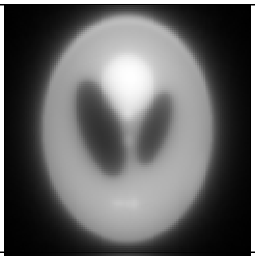	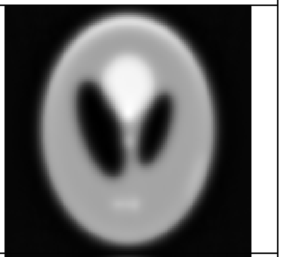
FBP result	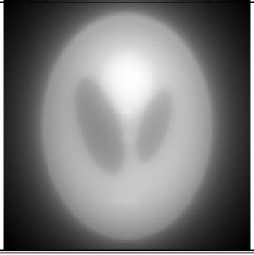	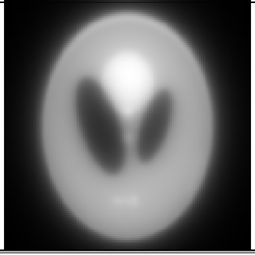	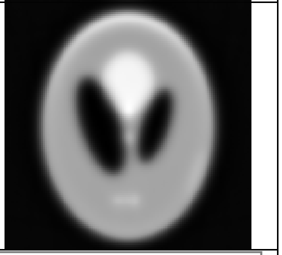
Central horizontal profiles	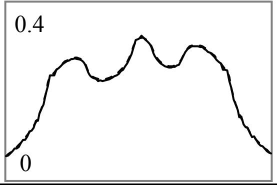	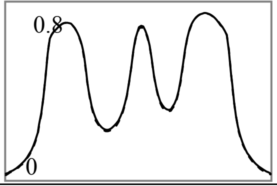	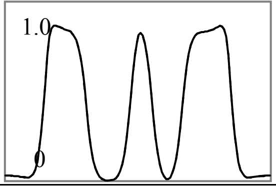

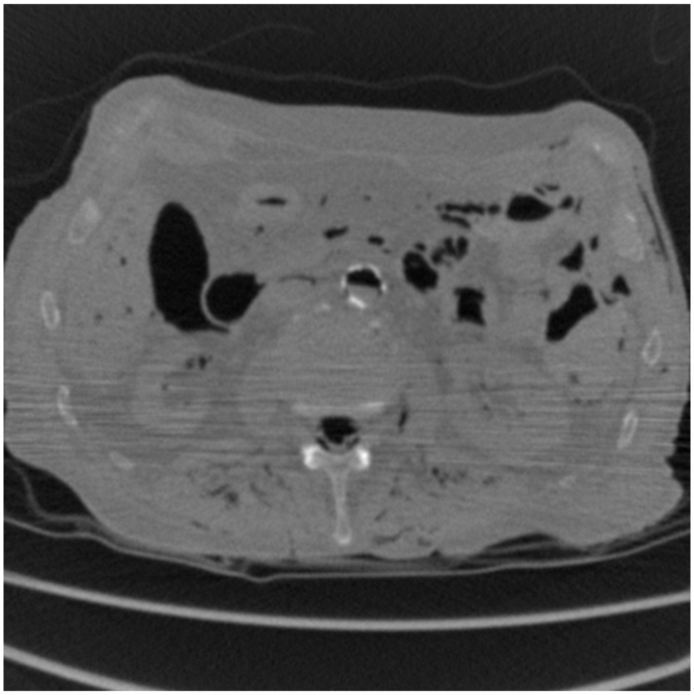

Reconstruction by conventional FBP

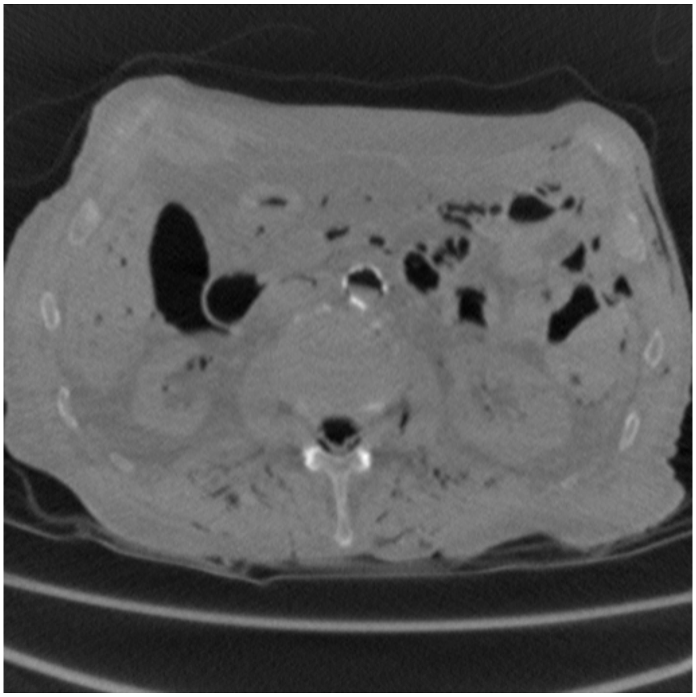

Reconstruction by proposed FBP with noise weighting

Figure 1: Cone-beam reconstruction of a low-dose cadaver torso X-ray CT study (Raw data courtesy of Leiden University Medical Center). One non-central transverse slice is shown. The upper image is reconstructed with the normal FBP (Feldkamp) algorithm. Severe streaking artifacts can be observed horizontally across the torso. The lower image is reconstructed with the proposed FBP (Feldkamp) algorithm with view-based noise weighting. At each view, the noise variance is determined by the largest line-integral in this view. It is clear that the severe streaking artifacts have been successfully suppressed or removed while the resolution is maintained.

Bi-modal CT Reconstruction (BMR)

Herbert Bruder, Rainer Raupach, Martin Petersilka, Johan Sunnegårdh, Karl Stierstorfer

Abstract— In CT imaging, a variety of applications exist where reconstructions are SNR and/or resolution limited. However, in some cases the measured data provide additional information capable of creating composite image volumes with high SNR. These composite image volumes might be a mixture with respect to spectral information and/or spatial resolution and/or temporal resolution.

Examples: in Dual Energy CT, the resolution has to be compromised to provide good SNR for material decomposition. Perfusion CT is a high dose application, and dose reduction is highly desirable. However, if the time frames are too noisy, a meaningful evaluation of perfusion parameters might not be possible. On the other hand the SNR in the composite of all time frames is extremely high.

These observations bring us to the idea of transferring high SNR of the composite image volume to low SNR (but high resolution) 'source' image volumes. It has been shown that the noise characteristics of CT data can be improved by iterative reconstruction. In case of data dependent Gaussian noise they can - in a mathematically equivalent manner - be modeled with image-based iterative reconstruction [1].

We present a generalized update equation in image space, consisting of a linear combination of the previous update, a correction term which is constrained by the source image data and the composite data, and a regularization prior, which is initialized by the composite image volume.

For different CT applications, we show that - at constant patient dose - SNR can efficiently be transferred from the composite image to the source image data, while maintaining resolution properties of source data.

Index-Terms: Regularization, regularization prior, dual source CT (DSCT), dual energy CT, cardiac CT, perfusion CT, Ultra-high resolution CT.

I. INTRODUCTION

In the past few years, iterative reconstruction methods have received increased attention in the CT reconstruction community. The advantage of iterative methods is that they allow for an easy modeling of system optics. Another successful application is the suppression of artifacts caused by approximations in direct reconstruction methods [2].

A general approach to iterative reconstruction methods is statistical iterative reconstruction. While traditional reconstruction methods assume Gaussian noise with data independent variance, statistical reconstruction methods employ the more realistic Poisson noise model or the Penalized Weighted Least Squares (PWLS) objective function, corresponding to a simplified Gaussian noise model with data dependent variance. PWLS methods have been shown to improve image quality in terms of contrast to noise ratio [3].

The fundamental limiting factor for practical use of statistical reconstruction methods and most iterative reconstruction methods, is the computational effort they require. Therefore, it was of great interest to find new equivalent, or approximately equivalent, update steps that are computationally less expensive than currently existing ones. It was been shown [4] that statistical data weighting and regularization can be transferred to non-linear image processing if the noise model is known. Due to the image-based nature of this type of Iterative Reconstruction, the algorithm is computationally much less expensive as raw data based Iterative Reconstruction.

In this paper we present a generalized image-based update equation, which supports a variety of clinical applications (section II). It is termed: "Bi-modal CT Reconstruction (BMR)".

In CT imaging, a variety of clinical applications exist, where image data are SNR and/or resolution limited. Here, we denote them as 'source' image data. In some situations additional measurement data are available which do not suffer from these limitations. Also, different reconstruction modes might provide 'composite' image data with beneficial characteristics regarding SNR and/or resolution. The question is: how can we transfer the beneficial characteristics of composite image data into the source image data, while maintaining the beneficial characteristics of the source image data?

In section III a variety of potential CT applications is discussed, which can profit from the novel reconstruction

---

All authors are with SIEMENS, Healthcare Division,
Siemenstr. 1, 91301 Forchheim, Germany,
Phone: +49-9191-188793
Fax: +49-9191-189996
e-mail: herbert.bruder@siemens.com

technique. We conclude with a final discussion in chapter IV.

II. METHOD

A. *Regularization based Iterative CT - Reconstruction*

In [1] an image based Iterative Reconstruction scheme was derived approximating under certain, very general conditions Statistical Iterative CT – Reconstruction to a high degree of accuracy. The update equation is given by

$$f_{k+1} = f_k - \gamma \cdot \nabla R(f_k) \tag{1}$$

with the regularization prior

$$\nabla R(f_k(i)) = \sum_{j \in \Omega_i} d_{ij} \cdot \Delta_{ij} \cdot \mu(\theta_j)(i) \cdot H\left(\frac{\Delta_{ij}}{\sigma(i) \cdot \mu(\theta_j)(i)}\right) \tag{2}$$

Here, *f* represents the vector of image grey values at the 3D voxel grid. Eq. (1) introduces prior knowledge about correlation of voxels in the immediate neighborhood of central voxel *i* with adjacent nodes $j \in \Omega_i$. *N* counts the total number of voxels. The domain filter d_{ij} denotes a high pass filter and may be chosen as the inverse distance of node vertices *j* to central voxel *i*. Adjacent grey values are weighted using the influence function *H*. $\sigma(i)$ denotes the local background noise at voxel *i*. It can be estimated by computing the variances in direction of the neighborhood voxels, e.g. taking the minimum value. The influence function *H* is conveniently defined as a function of local contrast-to-noise ratio $\frac{\Delta_{i,j}}{\sigma_i}$ in the image domain. Hence, we have an instrument to establish contrast dependent sharpness by correlating adjacent image voxels using the *H*-weight. The anisotropy factor $\mu(\theta_j) = \frac{\sigma_j^2}{\sigma_0^2} = \frac{\exp(-p_0)}{\exp(-p(\theta_j))}$ accounting for anisotropic image noise, is estimated from projecting the image data in angular direction θ_j to data space in parallel geometry. Further, p_0 denotes a normalization signal, e.g. the attenuation in 30cm water disk with the corresponding noise variance σ_0^2.

B. *Bi-modal CT-Imaging*

Bi-modal CT reconstruction uses a generalized version of update eq. (1) by additionally introducing a correction term:

$$\begin{aligned} f_{k+1} = {} & f_k + \alpha_{1.} \cdot \Lambda \otimes (f_{Source} - f_k) + \\ & \alpha_2 \cdot (1 - \Lambda) \otimes (f_{Composite} - f_k) - \gamma \cdot \nabla R(f_k) \end{aligned} \tag{3}$$

The initial loop is started with the regularization ∇R operating on the composite image volume $f_{Composite}$. α_1, α_2, and γ are scalar constants that individually control the contribution of different terms in the update equation (3) and thus determine the characteristics of the final image ($k \rightarrow \infty$). The operator Λ describes a complementary split of the frequency contents of image data. Λ denotes the low pass part of this weighting in frequency space. For most applications the cutoff frequency of Λ should be identical to the cutoff frequency of the convolution kernel used for reconstruction of source data.

III. EVALUATION

In this section we discuss a variety of CT applications (sections III A-D), which might benefit from Bi-modal CT reconstruction.

A. *Spectral CT imaging*

In Dual Energy CT (DE) imaging, the quality of material decomposition is largely influenced by image noise. In addition: the decomposition is obtained by matrix inversion, which for some materials might have eigenvalues on a different scale. In turn, this further increases image noise of reconstructed image volumes. Currently, the problem is combated by improving SNR of spectral images using smooth CT convolution kernels. At the same time, however, the spatial resolution is affected.

In Bi-modal reconstruction of spectral CT data the spectral images are used as source images. Composite images are calculated as a weighted sum of the spectral images, with weights that optimize SNR.

We expect the bi-modal image data f_∞ to preserve the spatial resolution and the spectral contrast at a significantly higher SNR. This is well-demonstrated in Fig. 1. The spectral images of bi-modal reconstruction show a significantly improved SNR with 70% noise reduction compared to the source images. The spatial resolution is well preserved. Also the spectral information is largely preserved which is well demonstrated evaluating the iodine filled region (red circle).

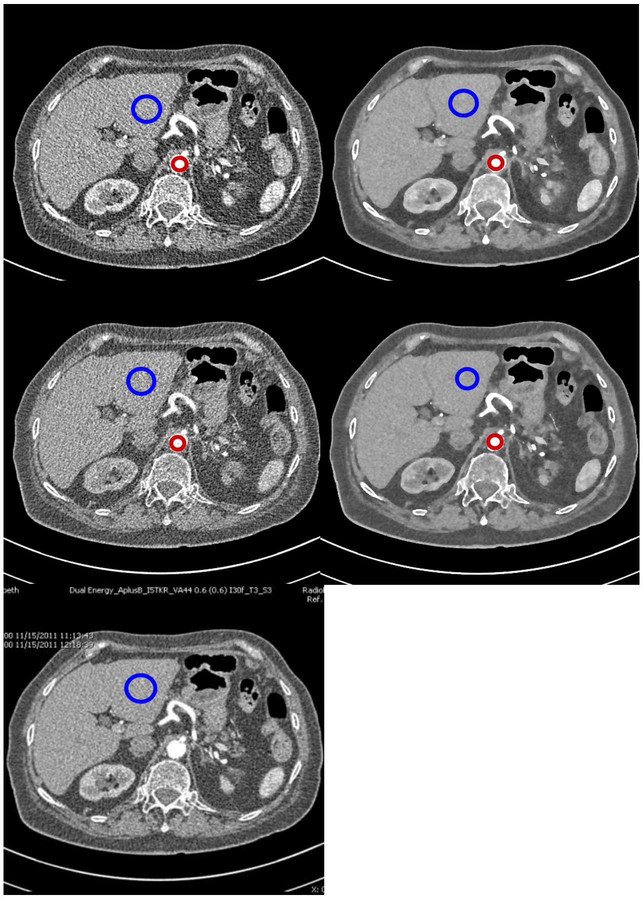

Fig. 1: FBP reconstructions of clinical DE image data measured with a SIEMENS Definition FLASH scanner (top left) 100kV image with 100% image noise. The average grey value of iodine in the red circle area is 555HU (middle left) 140kV image with 100% image noise. Average grey value of iodine in red circle area 280HU (bottom left) Composite image as average of 100kV and 140kV image data with 71% image noise. (top right) BMR of 100 kV data with 31.8% image noise. Average grey value of iodine in red circle area 550 HU (middle right) BMR of 140 kV data with image noise of 32.2% Average grey value of iodine in red circle area 289HU. Image window (C = 0, W = 500 HU)

B. *CT Perfusion imaging*

CT Perfusion imaging is a high dose CT application. Dose reduction is highly desirable. However, the acquired time frames (source images) need high SNR to derive meaningful perfusion parameters. Low noise composite data can be obtained by averaging all time frames. It will be shown that the high SNR of the composite image can be transferred to the time frames while preserving the spatial and temporal resolution of each specific time frame. This gives us control of the applied radiation exposure. We will demonstrate dose reduction potential down to 15% of typical reference mAs

C. *Cardiac CT*

In cardiac CT imaging the temporal resolution is improved by decreasing the range of projection data used for image reconstruction down to the limit of a half rotation dataset (after parallel resorting of fan-beam data). Optimization of best cardiac phase of retrospective image reconstruction requires redundant data acquisition. In addition, the temporal range of high radiation exposure has to be flexible controlled to account for heart rate variability. Full dose utilization in the retrospectively, phase-correlated reconstructions (source images) is highly desirable. Composite images can be provided by extending the reconstruction range to the entire range of high radiation exposure. It will be demonstrated, that significant SNR improvement of the source images is possible, while preserving the high temporal resolution of the time frames.

D. *Ultra- high resolution Imaging (UHR)*

Ultra high resolution acquisition data are measured using a comb grid placed over on the detector elements. Thus the aperture of each detector element is smaller, which increases sharpness while reducing noise equivalent quanta (NEQ). In Dual Source CT [5] a second X-ray source – detector system mounted on the CT-gantry with a 90 deg offset provides additional data measured with a wider aperture. We denote the reconstructions of these data as $f_{Composite}$, whereas the reconstructions of low aperture data as f_{Source}. Applying eq. (3) final image volumes f_{∞} with high spatial resolution and increased SNR compared to the source image volume, are obtained (Fig. 21). However, in this study a detailed analysis of the NoisePowerSpectrum (NPS) is needed to correctly design the frequency split function Λ.

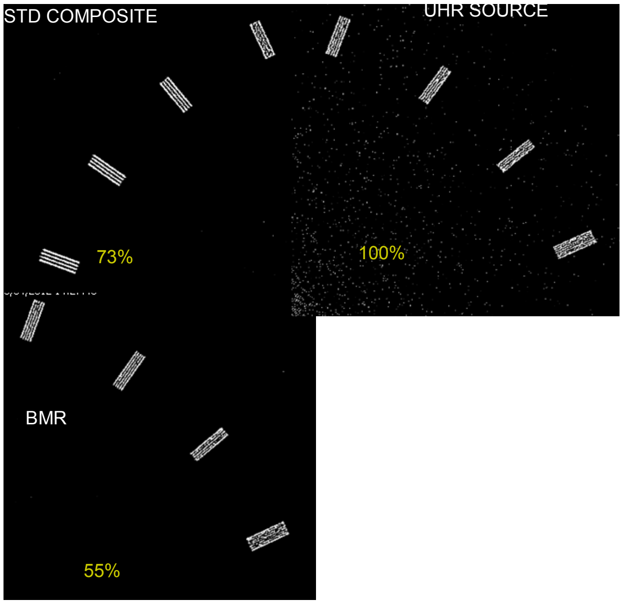

Fig. 2: FBP reconstructions of the high resolution CATPHAN phantom (top left) STD Composite image with 71% image noise.

The normalized detector pitch was 1. 18lp/cm are visible (top right) Ultra High Resolution source image with 100% image noise. The normalized detector pitch was 0.5, hence the NEQ were reduced by the factor 2. 23 lp/cm are visible (bottom left) Bi-modal reconstruction with 55% image noise. Notice, the spatial resolution is preserved (23 lp/cm are visible). Image window (C = 1200, W = 200 HU)

E. ROC analysis

An ROC analysis was employed (Fig 3), to demonstrate the improved noise statistics in BMR reconstructions. Based on the observer task: signal known exactly (SKE) and background known exactly (BKE) a channelized Hotelling Observer study using 4 channel Gauss-Laguerre polynomials was performed. This study uniquely supports the assumption that in BMR SNR can efficiently be transferred to low SNR source data

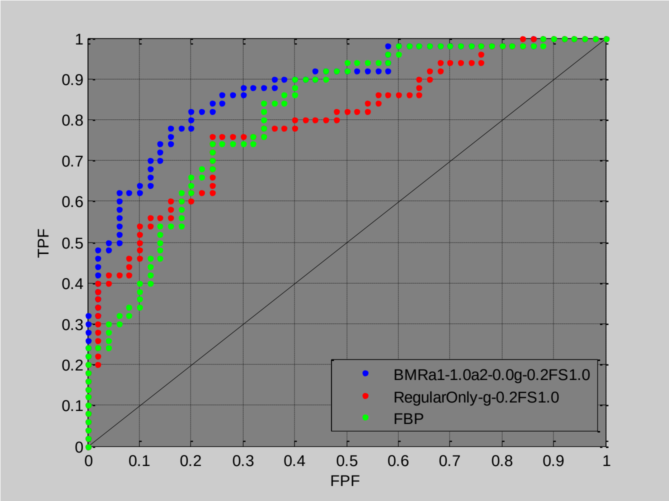

Fig.3: ROC analysis of BMR reconstruction.100 noise samples of SKE / BKE observer task (for details see text) have been evaluated using a Hotelling observer study with 4 channel Gauss-Laguerre polynomials. (green curve) FBP reconstruction (blue curve) BMR reconstruction (red curve) Regularization on source data ($\alpha_1 = 0$, $\alpha_2 = 0$).

IV. Conclusion

We presented a novel image based Iterative Reconstruction scheme, the Bi-modal CT Reconstruction. It is governed by an update equation, containing a linear combination of the previous update and specific low pass and high pass terms. Depending on the set of coefficients of this linear combination, the iteration loop converges to different fixed points. Future work has to focus on properly adjusting this set of coefficients for different CT applications.

The Bi-modal Reconstruction can be utilized to transfer beneficial characteristics of high SNR/low resolution composite images to low SNR/high resolution source images. Several applications have been investigated regarding the efficiency of the method. The current implementation seeks to preserve the low frequency content of the source images and transfers high pass signals from the composite image and the regularization filter.

In cardiac case, however, the benefit might be limited due to motion artifacts showing up in the composite images. Unfortunately, the spectrum of motion artifacts is not localized. Therefore, low frequency signals of motion artifacts might remain in the final image. From this, major benefits of BMR in the cardiac field can only be expected in cardiac Dual Source imaging. In this case composite data also have sufficient temporal resolution. A variety of further CT applications like multi-phase liver, neuro DSA etc. are thinkable, which can also benefit from the novel reconstruction scheme.

V. References

1. Bruder, H., Raupach, R. Sunnegårdh, J., Stierstorfer, K., Flohr, T., 'Adaptive Iterative Reconstruction', Proceedings of the SPIE conference, Physics in Medical Imaging, 2011
2. Sunnegårdh, J.; Danielsson, P.-E. (2008), 'Regularized iterative weighted filtered backprojection for helical cone-beam CT', Medical Physics **35**(9), 4173-4185.
3. Thibault, J.-B., Sauer, K.; Bouman, C.; Hsieh, J, 'A three-dimensional statistical approach to improved image quality for multislice helical CT, Med. Phys. **34**, 4526 (2007)
4. Bruder, H., Raupach, R. Sunnegårdh, J., Stierstorfer, K., Flohr, T., 'Adaptive Iterative Reconstruction', Proceedings of the SPIE conference, Physics in Medical Imaging, 2011
5. Flohr T., Bruder, H., et al., 'Image reconstruction and image quality evaluation for a dual source CT scanner', Med. Phys. **35** 5882 (2008)

Database-Assisted Low-Dose CT Image Restoration

Wei Xu, Sungsoo Ha and Klaus Mueller, *Senior Member, IEEE*

Abstract– **The image quality of low-dose CT scans typically suffers greatly from the limited utilization of X-ray radiation. Although the harmful effects to patient health are reduced, the low quality of the reconstructions makes diagnostics difficult. In previous work, we have demonstrated a method that can restore a low-dose image by ways of a database of reference images. This database stored a set of pre-aligned non- and pre-corrupted reference CT images to support a matched-reference non-local means (MR-NLM) filtering approach. While effective, the need to store images with many different types of corruptions and alignments greatly impeded system scalability. In this current work, we have significantly simplified the database which now is comprised of just a set of regular-dose patient scans. Our present scheme performs both alignment and artifact generation on the fly and uses a sophisticated image and feature matching scheme to find good candidates to support our MR-NLM filtering scheme.**

I. INTRODUCTION

In recent years a growing amount of research has been dedicated to low-dose CT, motivated by the need to minimize the radiation exposed to patients while maximizing the clarity of the reconstructed images to facilitate accurate diagnoses. The adverse low-dose conditions greatly challenge conventional CT reconstruction algorithms, both analytical and iterative. They usually result in images with severe noise artifacts and reduced feature detail. To solve this conundrum, one type of approach enforces better image quality directly in the reconstruction process [6][12][17], while another improves the image quality in a post-processing de-noising step [7]. Our paper belongs to the second category.

Neighborhood filters, in particular non-local means (NLM) [1] have shown great promise for the restoration of noisy low-dose CT imagery [17]. To filter a pixel p_i with NLM, its updated value is determined by the values of pixels p_j inside a local neighborhood around p_i, called *search window*. Here, the contribution of a p_j to p_i depends on the similarity between small regions around them, called *patches*. Recently, to extend the search space beyond the current image, some medical imaging researchers have devised schemes that utilize prior scans of the same patient to search for high-quality updates [7][15][16]. We extended these ideas in [18], proposing an approach that utilized an image database of *different* patients which eliminated the need for a prior patient scan. The scheme achieved good artifact mitigation for low-dose scans acquired from only 45 noise-free projections or 60 noisy projections with SNR=10. The database itself contained pairs of artifact-free and artifact-matched reference images. We found that much better filtering results could be achieved by using the latter to find good NLM matches for a contaminated target pixel, but then replacing the noisy target pixel by the corresponding value from the artifact-free counterpart. We therefore called this method *Matched Reference-Based Non-Local Means* (*MR-NLM*). A shortcoming of this implementation was that the database could grow rather large since all images needed to be pre-aligned to the target image and also had to contain all possible types of artifacts for matching. In the current paper, we have aimed to reduce these problems and establish a more general framework.

Our present framework embodies a database of regular-dose patient CT scans with no pre-alignment and prior artifact simulation needed. Such scans are commonly available in clinical practice. For image restoration the only assumption we make is that the low-dose CT condition is known. This is reasonable since CT scans are typically obtained following a known reconstruction routine under some geometry configuration with a specific number of projections and mA/kV setting. In the current work we use fan-beam filtered backprojection (FBP) with a limited number of projections with Gaussian noise to simulate the low-dose conditions, but in practice any reconstruction setting can be supported. Our new method still applies the effective MR-NLM scheme, only now we perform alignment and artifact generation on the fly, assisted by a much more sophisticated image and feature matching scheme. We therefore call our framework simply *Database-Assisted CT Image Restoration (DA-CTIR).*

The overall workflow of our method is illustrated in Fig. 1. It consists of three major components:

- **Offline database construction**: given an image database, we create the global image feature descriptor *G* for each image and build up the global feature database. A visual vocabulary *V* is also learned.
- **Online prior search**: for the input image *I*, generate *G(I)* with *V* and use it to query the global feature database to find the *M* nearest neighbors (NN) as regular-dose *priors*. The priors have the most similar artifact-free content to *I*.
- **Online de-noising**: align the regular-dose priors to the input image as registered priors (*CRP*) and corrupt them with the low-dose condition (*DRP*) to form the prior pairs <CRP_i, DRP_i>. Finally a refined MR-NLM is performed.

The organization of the paper is as follows. In section II, we describe the methodology including all technical details. Experimental results are presented in section III, followed by conclusions and future work in section IV.

II. METHODOLOGY

A. Local Image Feature Descriptor

Image matching is a fundamental operation in computer vision and image processing and is often used for scene matching and object recognition. An image is usually represented as a high dimensional vector to describe the distinct salient properties of the image. In other words, an image feature

---

Wei Xu, Sungsoo Ha and Klaus Mueller are with the Visual Analytics and Imaging (VAI) Lab, Computer Science Department, Stony Brook University, NY 11794 USA. (e-mail: {wxu, sunha, mueller}@cs.sunysb.edu).

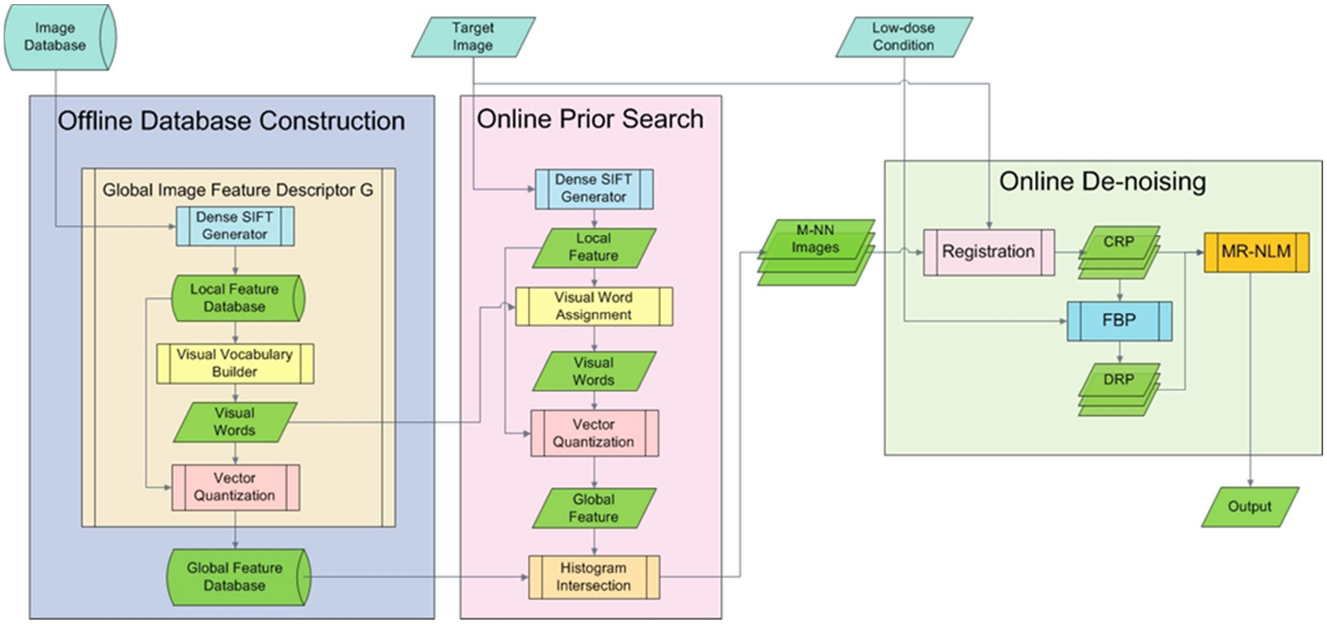
Image Database
Target Image
Low-dose Condition
Offline Database Construction
Global Image Feature Descriptor G
Dense SIFT Generator
Local Feature Database
Visual Vocabulary Builder
Visual Words
Vector Quantization
Global Feature Database
Online Prior Search
Dense SIFT Generator
Local Feature
Visual Word Assignment
Visual Words
Vector Quantization
Global Feature
Histogram Intersection
M-NN Images
Online De-noising
Registration
CRP
MR-NLM
FBP
DRP
Output

Figure 1: Workflow of the framework: offline database construction, online prior search and online de-noising.

descriptor is employed to map one image from 2D image space to high-D image feature space where image matching is performed. For instance, the GIST descriptor [11] is an aggregated multi-scale oriented edge histogram of the image in a coarse spatial resolution. The Haralick texture features [5] describe the global image statistics based on co-occurrence matrices with different pixel distance values. Although these methods have been shown to work effectively in many applications, they are sensitive to image rotation, distortion and appearance of noise which usually occur in our case.

The scale-invariant feature transform (SIFT) feature descriptor [9], on the contrary, solves these concerns. It captures the histogram of edges in a local neighborhood at multiple levels of scale, characterizes salient local and transform-invariant image structures and encodes contextual information. A SIFT feature descriptor is usually a 128-D vector encoding 8-orientation histograms of edges over 4×4 blocks with each block of size 4×4, serving as a local descriptor of the image. In its original definition, only keypoint locations are selected. However, it was shown that dense SIFT vectors on a regular spaced grid work better and are more robust [8][10]. Here we also exploit this dense feature scheme so that each image is represented by a fixed number of SIFT vectors.

In this work, we chose a grid spacing of 8 pixels. So for image size 256^2, 32×32 SIFT vectors are generated while for image size 512^2 there are 64×64 SIFT vectors.

B. Spatial Pyramid Based Global Image Feature Descriptor

To form a global image feature descriptor, traditional dense SIFT algorithms follow the bag-of-feature method [3]. It includes the following steps to combine the local feature vectors into a single one:

- **Extract the local feature descriptors.** Generate a set of SIFT local feature descriptors $\{S_0, S_1, .., S_{N-1}\}$ to represent each image.
- **Build the visual vocabulary.** Randomly select the local feature descriptors of all images in the database and perform k-means clustering to learn K cluster centers as visual words $\{V_0, V_1, \ldots, V_{K-1}\}$ and so form the visual vocabulary V of the database.
- **Label the local feature descriptors to the visual words.** For each image, its local feature descriptors are assigned to their corresponding closest visual words.
- **Perform vector quantization to generate a global feature descriptor.** Quantize each image's visual words to form histogram series $\{H_0, H_1, .., H_{K-1}\}$ of that image. By concatenating the weighted histogram series, a global descriptor is formed.

One drawback of this method is that the feature's location information in the original 2D image space is discarded. To make use of the spatial information and keep track of it in multi-resolution, we exploit a spatial pyramid scheme [8] to implement a "stronger" feature description. The multi-resolution layers are formed by recursively subdividing the image space into $a \times a$ blocks. In a layer L, for each block, only the feature vector extracted from that block is aggregated to the histogram of its specific visual word. In this way, the clustering is still performed in the feature space while the histogram pyramid is built in 2D image space. The weight to each histogram is inversely proportional to its block width.

In this work, for clustering we tried several k values and empirically chose k=50 for all databases. This number is relatively small compared to other papers (where k=200) which is due to the fact that CT scans are not as complicated as natural images. We set L=1 (two layers) and a=5 to prevent the splitting of significant body structures [4]. Therefore, for image size 256^2 its global vector dimension is 1,300 while for image size 512^2 it is 2,600.

C. Histogram Intersection and Multiple kd-Trees Based Vector Matching

In the *online prior search*, given the learned visual vocabulary V and the computed local features of the target scan, the task of the *visual word assignment* is to find the nearest visual word V_j for each local feature S_i in SIFT vector space (128-D). When processing a set of query images with a large number of dense SIFT vectors, this process could be time consuming. To speed up, we exploit the commonly used *kd*-tree as the nearest neighbor searching data structure. A *kd*-tree is a binary tree that recursively partitions and stores the nodes in *k*-dimensional space. Counting the number of visited tree nodes is used to measure the complexity of querying the tree.

To handle the query for high-D nodes such as a SIFT vector and reduce backtracking, we employ a multiple principal component *kd*-trees method denoted PKD-trees to perform fast approximate search [13]. In essence, data is first projected onto a PCA-reduced sub-space and arbitrary rotations to data are applied to create multiple trees with different structures. The search order among trees is organized by multithreading. The maximum number of visited nodes is pre-set. We use a Householder matrix as the transformation matrix to speedup arbitrary rotations, and 6 trees are built to accommodate data reduced to 30 dimensions for SIFT vectors.

In the same part, after generating a global feature vector for the target scan, vector matching is performed to search for similar priors in the database that anatomically characterize the same content as the target scan but may contain scale, rotation, and deformation variance. We found that histogram intersection performs better than a Euclidean distance measure. Therefore we implemented the matching with spatial pyramid based histogram intersection which is counted block-wise and visual word-wise and summed up to form a single value [8].

D. Online Denoising

Once the regular-dose prior (or reference) scans have been found, the online de-noising process can be executed. We first register the prior scans with the target scan using the SIFT-flow registration algorithm [10] to make sure the neighborhoods of any pixel position are roughly aligned. Then we reconstruct the artifact matched prior images using the same low-dose condition.

The MR-NLM follows the standard NLM filtering scheme but using a pair of artifact-free and artifact-matched registered prior images <*CRP*, *DRP*> [18]. More specifically, the weight generation is conducted by comparing patches from the target image and artifact-matched prior images, while the pixel value summation is performed in the corresponding locations in the artifact-free reference images using the weights. The equation of MR-NLM is as follows:

$$p'_x = \frac{\sum_{y\in W_x} \exp\left(-\sum_{t\in P} G_a(t)\left|p_{x+t} - p^{drp}_{y+t}\right|^2 / h^2\right)\cdot p^{crp}_y}{\sum_{y\in W_x} \exp\left(-\sum_{t\in P} G_a(t)\left|p_{x+t} - p^{drp}_{y+t}\right|^2 / h^2\right)} \qquad (1)$$

Here x is the location of the target pixel and y are the locations of the candidate pixels with values p_y. W_x is the search window around x, and P is the patch size of each pixel. The patch similarity is measured by the Gaussian weighted L_2 distance between two patch vectors with t representing the index within a patch and G_a being a Gaussian kernel with standard deviation a. h controls the overall smoothness of the filtering. The superscript *crp* indicates that the pixels originate from the artifact-free registered prior *CRP*, while *drp* denotes the degraded artifact matched registered prior *DRP*.

In order to further improve de-noising accuracy and enable more efficient computations, we use three refinement strategies. The first two are redundancy control methods designed originally for traditional NLM: (1) reduce patch redundancy by applying PCA to high-D patch space and project patches to a lower dimensional sub-space accordingly [14], (2) reduce search window redundancy by discarding unrelated pixels whose mean and variance values are different enough from the central pixel of the search window in the target image [2], and (3) consider multiple pairs (3 in the experiments) of reference images to broaden the search range.

In this paper, both search and patch windows are of size 7×7. For the Gaussian kernel, its standard deviation $a = 1$ and the smoothing parameter h is chosen to bring best results.

III. RESULTS

We constructed two databases: a head database (48 256^2 images) by mixing the NIH Visible Human Head (15 images) with a CT cadaver head (33 images) and a human lung database of two patients (150 512^2 images). The images were not pre-aligned. Their original reconstructions were utilized in three different ways. (1) They served as the basis for a high-quality projection simulation in fan-beam geometry (fan angle = 20°). We then picked a subset of these projections with Gaussian random noise propagated and reconstructed them under the current low-dose condition. (2) We used them to generate an experimental target scan subject to restoration. To create a new scan different from any image in the database, the selected scan was first deformed or rotated (to mimic a real clinical situation), projected, and then reconstructed with the studied low-dose condition. (3) We used the deformed uncorrupted scan to represent the gold standard for evaluation.

A. Performance of the Global Image Feature Descriptor

This experiment was conducted to test the performance of the global image feature descriptor under low-dose conditions. In Fig. 2, both a head scan and a human lung scan were simulated (neither was in the database). I(b) was created by reconstructing a CT head scan after a twirl-like deformation (see I(a)) with 45 projections of SNR 15, and II(b) was created by reconstructing a human lung scan after rotation 5° ccw (see II(a)) with 60 projections of SNR 20. Ideally, the adjacent slices in the same dataset should be found as reference images. The three matched prior images for the head scan are shown as Fig. 2 (c), (d) and (e) and are consistent with our expectations. The case for the lung scan is similar. It confirms that moderate deformations and low-dose artifacts (both streak and noise) do not affect the global feature descriptor to express the underlying anatomical content of the CT images.

B. Performance of PKD-trees Data Structure

For the visual words learned in the first experiment, 6-PKD-tree data structures were created for matching dense SIFT vectors to the visual words. Two configurations for reducing the dimension of the vectors were set: full 128 and 30. By generating a head scan with various changes such as rotation, resizing, Gaussian noise and affine transform, we extracted 100,000 SIFT vectors from it. As an approximated search, the error rate versus the maximum number of visited nodes *M* was tested for both dimension settings and is plotted in Fig. 3. When *M* is above 200, the error rate is lower than 10%. We also observe that dimension reduction of the data does not affect the querying accuracy when the vector is sparse.

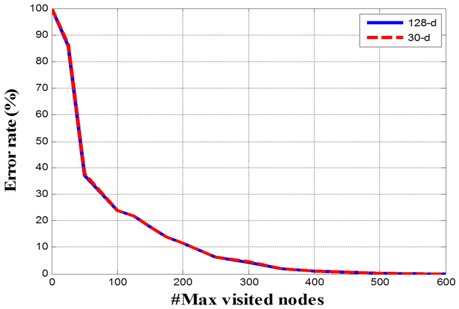

Figure 3: 6-PKD-tree error rate.

C. *Performance of Refined MR-NLM*

We tested the de-noising effect for both a head image and a human lung scan. In Fig. 2, I(f) and I(g) are the de-noised head image without and with refinement. The lung results are shown as II(c) and II(d) for without and with refinement respectively. For both cases, the basic method restored fine details well. The refined result keeps the same (sometimes better as the area labeled in the box) quality level but reduces the computational complexity greatly.

IV. CONCLUSIONS AND FUTURE WORKS

In this paper, we proposed a general framework for high quality restoration of low-dose CT scans with a general CT image database. A spatial pyramid based global image feature descriptor, a local feature matching PKD-trees and a refined MR-NLM scheme were presented. As future work, PKD-trees used for global feature vector, GPU acceleration for faster execution and a more complete database will be tested.

REFERENCES

[1] A. Buades, B. Coll, and J. M. Morel, “A review of image denoising algorithms, with a new one,” Multiscale Model. Simul., vol. 4, no. 2, 490-530, 2005.
[2] P. Coupe, P. Yger, and S. Prima et al., “An optimized blockwise non local means denoising filter for 3D magnetic resonance images,” Trans. on Med. Imag., vol. 27, 425–441, 2008.
[3] G. Csurka, C. Bray, and L. Fan et al., “Visual categorization with bags of keypoints,” In ECCV Workshop on Stat. Learn. in Comp. Vis. 2004.
[4] T. Emrich, F. Graf, and H.-P. Kriegel et al., “CT Slice Localization via Instance-Based Regression,” Proc. SPIE, vol. 7623, 76232O, 2010.
[5] R. M. Haralick, K. Shanmugam, and I. Dinstein, “Textural features for image classification," IEEE TSAP, vol. 3, no. 6, 613-623, 1973.
[6] X. Jia, Y. Lou, R. Li, W. Song, S. Jiang, “GPU-based fast cone beam CT reconstruction from undersampled and noisy projection data via total variation,” Medical Physics, vol. 37, pp. 3441-3447, 2010.
[7] Z. Kelm, D. Blezek, B. Bartholmai, B. Erickson, “Optimizing non-local means for denoising low-dose CT,” IEEE Symp. on Biomedical Imaging (ISBI), pp. 662-665, 2009.
[8] S. Lazebnik, C. Schmid, and J. Ponce, “Beyond bags of features: Spatial pyramid matching for recognizing natural scene categories,” Proc. CVPR, vol. 2, 2169–78, 2006.
[9] D. Lowe, “Object recognition from local scale-invariant features,” Inter. Conf. on Computer Vision, pp. 1150-1157, 1999.
[10] C. Liu, J. Yuen, A. Torralba, “SIFT flow: dense correspondence across scenes and its applications,” IEEE Trans. Pattern Anal. Mach. Intell., vol. 33, no. 5, pp. 978-994, 2011.
[11] A. Oliva and A. Torralba, “Building the gist of a scene: The role of global image features in recognition,” Visual Perception, Progress in Brain Research, vol. 155, 2006.
[12] E. Sidky, X. Pan, “Image reconstruction in circular cone-beam computed tomography by constrained, total-variation minimization,” Phys. Med. Biol, vol. 53, no. 17, pp. 4777-4807, 2008.
[13] C. Silpa-Anan, R. Hartley, “Optimised KD-trees for fast image descriptor matching,” Proc. CVPR, pp. 1-8, 2008.
[14] T. Tasdizen, “Principal neighborhood dictionaries for Non-local Means image denoising,” Trans. Imag. Proc., vol. 18, no. 12, pp. 2649-60, 2009.
[15] H. Yu, S. Zhao, E. Hoffman and G. Wang, “Ultra-low dose lung CT perfusion regularized by a previous scan,” Academic Radiology, vol. 16, pp. 363-373, 2009.
[16] Q. Xu, H. Yu and G. Wang et al., “Dictionary learning based low-dose X-ray CT reconstruction,” Proc. Fully3D, pp. 258-261, Germany, 2011.
[17] W. Xu, K. Mueller, "Evaluating popular non-linear image processing filters for their use in regularized iterative CT," IEEE Medical Imaging Conference, Knoxville, TN, October, 2010.
[18] W. Xu, K. Mueller, "A reference image database approach for NLM filter-regularized CT reconstruction," Proc. Fully3D, pp. 116-119, 2011.
[19] Boost C++ libraries, www.boost.org.

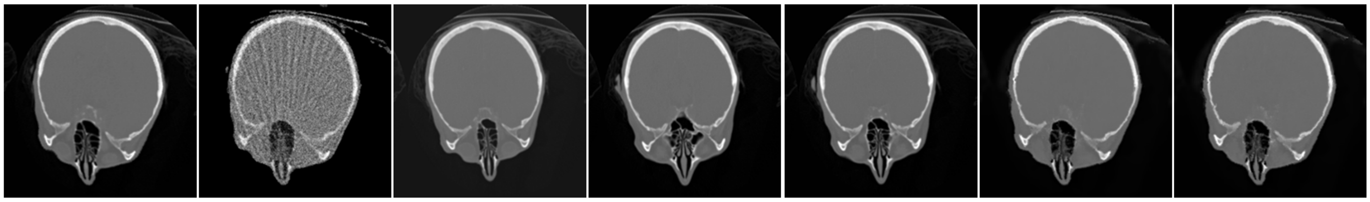

I: (a) ideal (b) input (c) prior 1 (d) prior 2 (e) prior 3 (f) basic DA-CTIR (g) refined

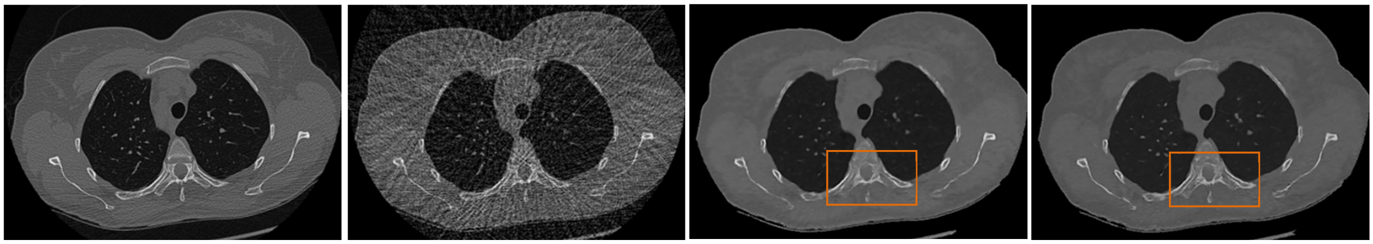

II: (a) ideal human lung (b) input scan (c) basic DA-CTIR (d) refined DA-CTIR

Figure 2: Results with (I) a CT head database and (II) a human lung database.

CT Dose Reduction Using Dynamic Collimation

Dominic J. Heuscher, Ph.D., Frederic Noo, Ph.D.
UCAIR, University of Utah, Salt Lake City, Utah

Abstract– **This paper demonstrates how a transverse dynamic collimator can significantly reduce dose in CT scans and briefly reviews our earlier results on motion analysis of dynamic collimators. Today, helical scans already use the axial collimator. A separate transverse dynamic collimator is proposed that would be used for both helical and axial scans. The leaves of both the helical and transverse collimators move such that only those x-rays that intersect a predefined VOI are exposed to the patient. Our earlier work has already demonstrated the feasibility of implementing a transverse dynamic collimator. By moving the collimator close to the source and upgrading the collimator motor controller to handle leaf velocities up to 90 cm/sec (less than 4 times the leaf velocity of a helical collimator), a 12 cm ROI can be targeted up to 18 cm from scan center. Elliptical models were utilized to calculate the skin exposure for heart and kidney scans, with and without transverse dynamic collimation. The results translate to a significant skin dose reduction in both cases: A 3.7:1 reduction in skin exposure is calculated for the whole-heart scan. A 1.6:1 to 2.1:1 reduction in skin exposure is calculated for a kidney scan and a 3.6:1 reduction for a whole organ kidney scan, even when both kidneys are included in the target ROI.**

I. INTRODUCTION

X-ray dose to the patient can be greatly reduced not only in the axial direction using a dynamic helical collimator [1], [2], but also in the transverse direction using a dynamic collimator shown in Fig. 1. The first limits exposure to only the ends of a cylindrical volume of interest (VOI) scanned during a cone-beam helical CT scan. The second limits exposure to an arbitrary volume of interest within the cylindrical VOI. An example of this is shown in Fig. 2 for a VOI defined by the outline of the heart. The leaves of the transverse collimator move in and out independently such that x-rays are limited to the region defined by the outline of the heart, which is typically located well off-center of the scan isocenter. How fast the leaves need to move depend on how far off-center a given cross-sectional region of interest (ROI) is located from scan center.

We have already presented [4] an analysis of the velocity requirements of the transverse collimator for off-center ROIs within the field of view (FOV) and compared this with the known velocity requirements of today's helical collimators. This analysis concluded that a transverse collimator can handle a 12 cm ROI up to 18 cm off-center, provided the collimator is positioned 12 cm from the source and the collimator motor controller is upgraded to handle leaf velocities approximately 4 times that of the helical collimator (less than 90 cm/sec).

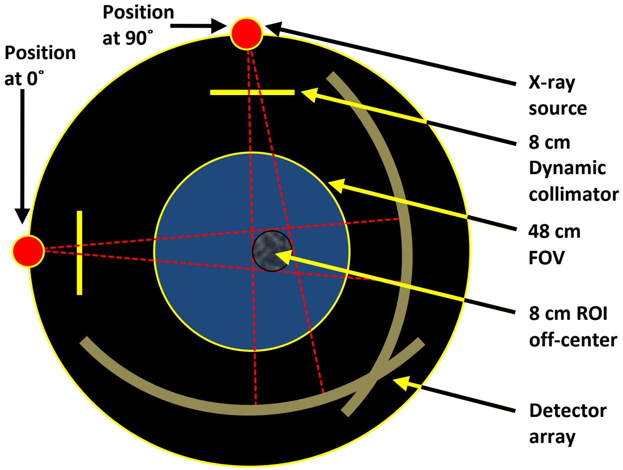

Fig. 1. Dynamic collimator positioned at 0 and 90 degrees for an 8 cm off-center ROI.

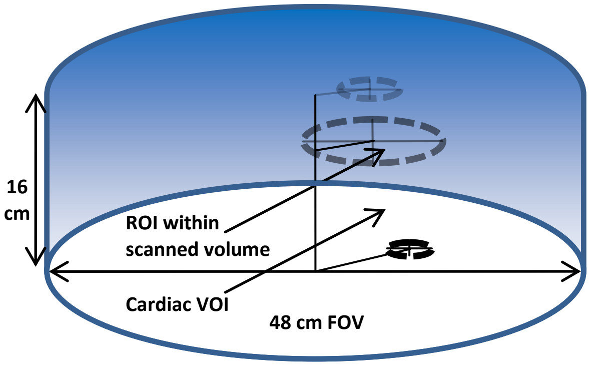

Fig. 2. Cardiac VOI defined by both the dynamic transverse and helical collimators.

II. METHODOLOGY

To demonstrate the reduction in skin exposure that can be achieved using a transverse dynamic collimator, both heart and kidney scans were analyzed. We believe the corresponding clinical applications, namely coronary CT angiography and kidney perfusion, would greatly benefit from a reduction in dose.

For the heart, the dynamic collimation follows the outline of the heart defined by an ellipse representing the target ROI (shown in the following 3 out of 5 sequence of images in Fig. 3). The body outline was approximated also with an ellipse, from which the skin exposure values were calculated. The five sections of the heart are equally spaced. In the un-collimated case, all sections are fully exposed, while in the collimated case, the exposure is limited to the target VOI, with the first and last sections fully collimated down to a 0 cm diameter circle. Reference lines are shown that intersect scan center, the body ellipse, and target ROI.

Manuscript received February 1, 2012. This work was partially supported by a Benning Foundation grant from the University of Utah and partially funded by NIH grants R01 EB007168 and R21 EB007236. Its contents are solely the responsibility of the authors.

Authors are with the Utah Center for Advanced Imaging Research, Radiology Department at University of Utah, Salt Lake City, UT 84108 USA(telephone: 801-581-4418, e-mail: dheuscher@ucair.med.utah.).

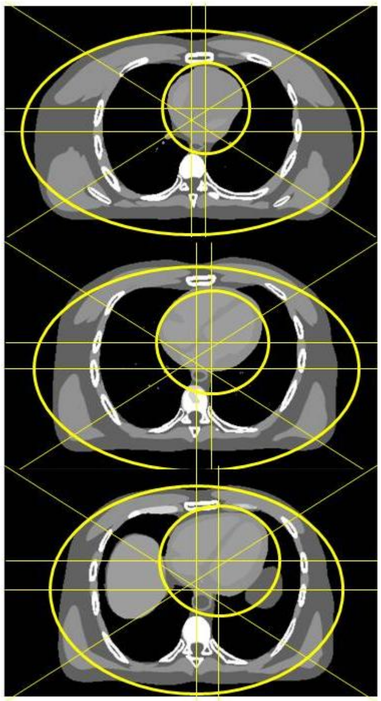

Fig. 3. Middle three out of five heart cross-sections showing body outlines and target ROIs approximated by ellipses with reference lines.

The average un-collimated skin exposure relative to the average exposure at the center of the target ROIs is compared to the average collimated skin exposure over the five slices again relative to the average exposure at the center of the target ROI.

For the exposure analysis of the heart, reconstructions of an XCAT phantom [6] were used with an X-ray source radius S of 57 cm. A compensator in front of the X-ray source, generally used in most CT scans today, provides a more uniform signal to the detector and reduces the overall dose to the patient. We therefore modeled a compensator that perfectly compensates for a disc with a radius *rc* of 24 cm and an attenuation coefficient equal to water (.183/cm at 80 KeV, approximately the average energy for a typical CT system performing 120 KeV scans).

As an initial approximation, the water attenuation value of .183/cm was also assumed for all path lengths throughout the body. The exposure for each of 100 points equally spaced in angle β on the surface of the body ellipse was calculated for 1000 angular views, θ, of the source covering 360 degrees. Rays emanating from the source pass either just through the compensator (Fig. 4), or both through the compensator and the body (Fig. 5). These exposure values were then averaged over the 1000 views. Likewise, the exposure at the center of the target ROI (Fig. 6), was averaged over 1000 views. This provided a reference for the skin exposure values. Thus all skin exposure values are measured as a ratio with respect to the exposure at the center of the target ROI.

For the scans utilizing a dynamic collimator, the fan angles for which the collimated x-rays intersect tangentially to the target ROI are calculated for each x-ray source position and used to exclude all exposure from the x-ray source that falls outside the corresponding angular range. Again, all skin exposure values are averaged over 1000 views.

In the case of the heart, 5 equally-spaced sections of the heart were used to define the cardiac VOI, with the first and last sections fully collimated. The relative skin dose for the center section was compared with and without dynamic collimation. The final skin exposure values were then averaged over the five sections, both with or without dynamic collimation.

The boundaries of the ellipses are defined by specifying 6 user-defined points around the periphery of both the body outline and target ROI. A least-squares solution to the parameters of each ellipse, *(a, b, r0, t0, tr) = (major axis, minor axis, polar radius of the origin of the ellipse, polar angle of the origin, and angular orientation of the ellipse)*, is then obtained given the *(R,T)* polar coordinates of these 6 points along with the following constraints:

$$\frac{X^2}{a} + \frac{Y^2}{b} = 1 \ \ and \ \ |tr - \frac{\pi}{2}| < \frac{\pi}{2}$$

where:

$$X = R \cdot cos(T - tr) - r0 \cdot cos(t0 - tr)$$
$$Y = R \cdot sin(T - tr) - r0 \cdot sin(t0 - tr)$$

(R,T) correspond to the polar coordinates of the 6 points

and the following initial values are provided:

(a, b, r0, t0, tr) = (TOL, TOL, com(R,T), mean(T), TOL)

where:

$$com(R,T) = \sqrt{mean(R \cdot cos(T))^2 + mean(R \cdot sin(T))^2}$$

$$TOL = tolerance\ value = .00001$$

Given both the body and target ellipses along with the compensator attenuation as a function of the fan angle, the skin exposures could then be calculated. For all ray angles up to the tangent to the body ellipse, the exposure is simply the attenuated exposure through the compensator[*] (Fig. 4). For all other angles for which the rays pass through the body to the selected point on the ellipse, the x-ray exposure is further attenuated by the path length through the body. Given the source radius, source angle, and point on the body ellipse, the path length p relative to the distance p0 (Fig. 5) can be calculated as a solution to a quadratic equation resulting from the condition that the entrance point of the ray also satisfies the equation for the body ellipse [5].

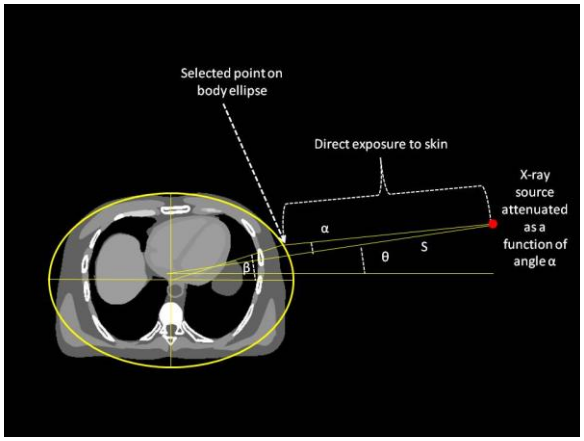
Selected point on body ellipse
Direct exposure to skin
X-ray source attenuated as a function of angle α
α
S
θ
β

Fig. 4. Geometry for a ray at angle α directly exposing the skin, emanating from the x-ray source located at angle θ. The ray is only attenuated by the compensator as a function of angle α.

---

[*] Note: A point on the skin is treated like any other point within the body ellipse. In the case of a point on the boundary of the ellipse directly exposed by the x-ray source, the path lengths through the body converge to zero at all angles up to those angles tangent to ellipse.

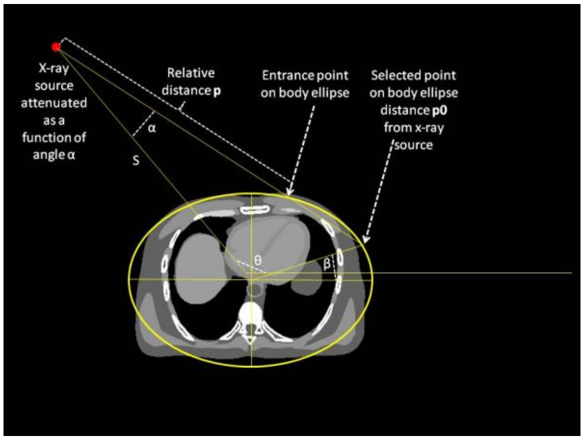
X-ray source attenuated as a function of angle α
Relative distance p
Entrance point on body ellipse
Selected point on body ellipse distance p0 from x-ray source
α
S
θ
β

Fig. 5. Geometry for a ray at angle α indirectly exposing the skin, emanating from the x-ray source located at angle θ. The ray is further attenuated by the body path length (1-p)□p0

The resulting skin exposure is then calculated as an average value over 360 degrees of the angular position (θ) of the x-ray source:

$$Exposure(\beta) = .001 \cdot \sum_{i=1}^{1000} intensity(\alpha(\beta,\theta_i)) \cdot att(\beta,\theta_i)$$

where:

β = the angle of the point on the body ellipse
θ = the source angle
α = fan angle of the ray intersecting the point on the body ellipse
$intensity(\alpha) = e^{2\cdot .183\cdot\left(\sqrt{rc^2-(S\cdot\sin\alpha)^2}-rc\right)}$
$att(\beta,\theta) = e^{-.183\cdot(1-p(\beta,\theta))\cdot p0(\beta,\theta)}$
p is the path length to the entrance point on the body ellipse relative to p0
p0 is the path length to the selected point on the body ellipse

The average skin exposure is then the average of the exposure for all points around the body ellipse. For the average collimated exposure, the same exposure equation is used, but with the intensity set to zero for all ray angles whose fan angle exceeds that of the range of angles spanned by the two rays that intersect the tangents to the target ellipse, i.e.:

$$intensity(\alpha(\beta,\theta)) = 0 \; if \; \alpha > AC(\theta) \; or \; \alpha < ACC(\theta)$$

AC is the clockwise angular position of the collimator leaf for source angle θ
ACC is the counter-clockwise angular position of the collimator leaf

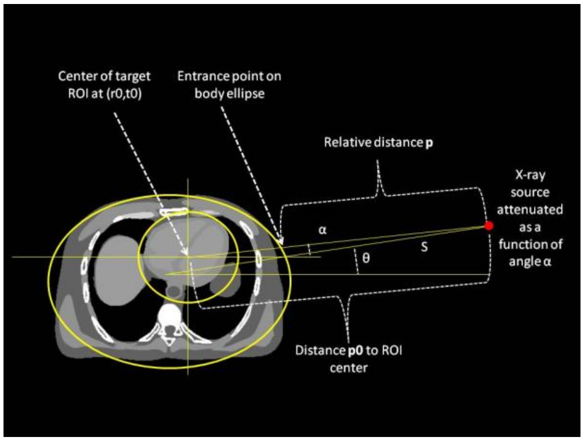
Center of target ROI at (r0,t0)
Entrance point on body ellipse
Relative distance p
X-ray source attenuated as a function of angle α
α
S
θ
Distance p0 to ROI center

Fig. 6. Geometry for a ray at angle α exposing the center of the target ROI. The ray is further attenuated by the body path length (1-p)□p0

Finally, the exposure at the center of the target ROI is calculated as a reference for the skin exposure values. In this case, p0 corresponds to the path length to the point at the center of the target ellipse and p is calculated as the relative path length to the point on the body ellipse (Fig. 6). As this is the center of the target ellipse, the same value applies whether or not dynamic collimation is used.

For the kidneys, ellipses were again used to outline the target ROI and body of the patient. A single multi-slice scan was used to acquire the kidney perfusion images with the central image shown in Fig. 7. The average relative (un-collimated) skin dose was compared to the average relative (collimated) skin dose.

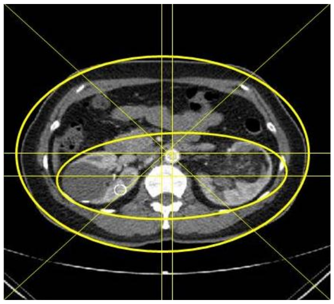

Fig. 7. Kidney study I: Central kidney cross-section showing ellipses defining the outline of the body and target ROI including both kidneys with reference lines.

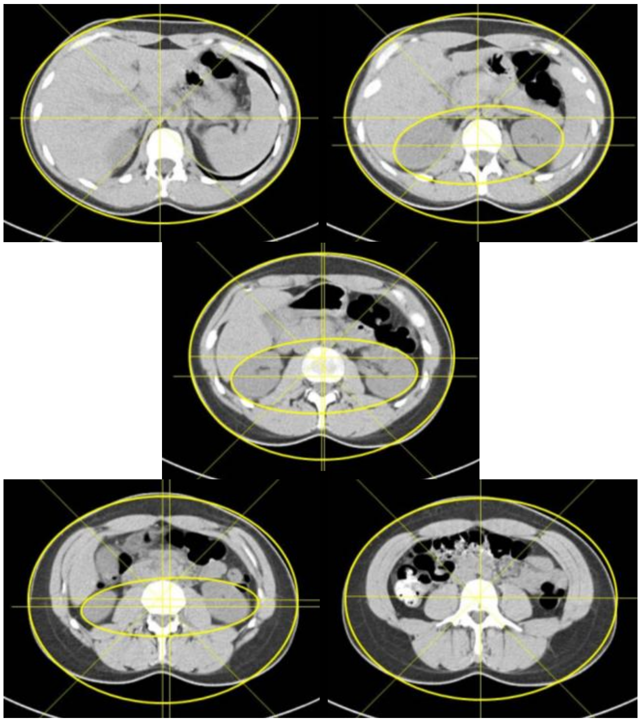

Fig. 8. Kidney study II: Five equally-spaced kidney cross-sections showing body outlines and target ROIs including both kidneys with reference lines.

A second kidney study was used to not only corroborate the results of the first study, but to demonstrate the additional dose savings that would be achieved for a whole-organ kidney study. Five equally-spaced sections (Fig. 8) were selected spanning the entire kidney with the first and last sections fully collimated when utilizing dynamic collimation. The central section was used to compare with the central section of the previous study and the overall whole-organ un-collimated (relative) kidney dose was compared with the overall dynamically collimated (relative) kidney dose.

III. RESULTS

The reduction in skin exposure that can be achieved using transverse dynamic collimation of heart and kidney scans was calculated using the above-described elliptical models.

The results are summarized in Table I below:

	Un-collimated Exposure	Collimated Exposure	Exposure Reduction
Heart	2.61	1.2	2.1:1
Whole Organ	2.605	.704	3.7:1
Kidney Study I	2.545	1.58	1.61:1
Kidney Study II	2.1	1.0	2.1:1
Whole Organ II	2.1	.584	3.6:1

Table I. Collimated and un-collimated exposure values relative to the average exposure calculated at the center of the target ROI.

IV. DISCUSSION

The reduced skin exposure calculated for heart and kidney scans demonstrates the significance of providing transverse dynamic collimation, especially if whole organ studies are performed. Skin exposure values are 2.1 to 2.6 times higher than the exposure at the center of the target ROI, even with an x-ray compensator. This demonstrates how important it is to keep skin exposure values as low as possible.

With regards to defining the VOI encompassed by the dynamic collimators, either a previously-acquired very low dose scan of the same region or two orthogonal localizer scans could be used. In either case, the operator can outline the VOI both in terms of the extent of the scan as well as the width and location of each ROI along the axial direction. This is similar to what is already done in defining a helical scan, except that instead of specifying a single zoomed ROI, an outline of the entire VOI is drawn from two orthogonal views, e.g. sagittal and coronal views.

As in the case of the helical collimator, the couch position determines the position of the collimator leaves. However, in the case of the dynamic transverse collimator, as the couch moves in the axial direction, the rotation angle must also be used to determine where the current ROI is situated with respect to the source. Therefore, given both the couch position and rotation angle, the leaves continuously follow the outline of the overall VOI. For example, in the case of the cardiac scan shown in Fig. 2, the collimator leaves follow the illustrated ROI located along the cardiac volume based on the couch location of the ROI as well as the rotation angle of the x-ray source.

In the case of a sequence of axial or circular scans, one ROI would be determined for each scan in the sequence. For each scan, only the rotation angle would be used to determine the motion of the collimator leaves, adjusting for an off-center and/or non-circular ROI.

With regards to the local reconstruction, attenuation information for the material outside the collimated VOI needs to be acquired. This can be accomplished in two recommended ways: 1) Use the previously-acquired very low dose scan mentioned above, using image registration if necessary to accurately measure the attenuation outside the VOI. 2) Use heavily-attenuated rays [3] through the outer portions of the collimator. This provides an estimate of the attenuation outside the VOI, provided the collimator attenuation is previously calibrated.

V. CONCLUSION

Dynamic collimation to target the VOI can greatly reduce patient dose (up to 4:1 reduction in skin exposure for whole organ cardiac and kidney scans). This reduction in dose may enable coronary CT angiography to be used on a much more routine basis. Likewise, significantly reducing the dose for CT perfusion scans and whole organ kidney scans will greatly benefit the clinical use of such scans. Our future efforts will be directed towards demonstrating how dynamic collimation can greatly reduce dose for other clinical applications as well. Also, similar to the measurements previously made to validate the dose savings achieved using interior computed tomography [7], we plan to validate our analysis with actual CT dose measurements performed on phantoms.

ACKNOWLEDGMENT

This work is part of the low dose CT imaging project supported by a Benning Foundation grant from the University of Utah, with additional support from NIH grants R01 EB007168 and R21 EB007236.

REFERENCES

[1] J. A. Christner, V. A. Zavaletta, C. D. Eusemann, A. I. Walz-Flannigan, C. H. McCollough, "Dose Reduction in Helical CT: Dynamically Adjustable z-Axis X-Ray Beam Collimation" AJR:194, January 2010.

[2] Heuscher, "Dynamic Collimation in Cone Beam Computed Tomography to Reduce Patient Exposure", US Patent Application 20100246752, 2010.

[3] Nalcioglu et al, "Limited Field of View Reconstruction in Computerized Tomography", IEEE Transactions on Nuclear Science, vol. NS-26, No. 1, Feb. 1979.

[4] D. Heuscher, F. Noo, "CT Dose Reduction Using Dynamic Collimation", MIC 23-29 October 2011, Conference Record.

[5] Y. Zhicong, F. Noo, F. Dennerlein, A. Wunderlich, G. Lauritsch, and J. Hornegger, "Simulation tools for two-dimensional experiments in x-ray computed tomography using the FORBILD head phantom", 2012, Appendix I, (preprint: contact the first author at the Department of Radiology, University of Utah, Salt Lake City, UT, USA)

[6] W.P. Segars, M. Mahesh, T.J. Beck, E.C. Frey, B. M. Tsui, "Realistic CT simulation using the 4D XCAT phantom", Medical Physics, 2008 August, 35(8), pp. 3800-3808.

[7] D. Bharkhada, H. Yu, R. Dixon, Y. Wei, J. J. Carr, J. D. Bourland, R. Best, R. Hogan, G. Wang, "Demonstration of dose and scatter reductions in interior computed tomography", Journal of Computer Assisted Tomography, Nov/Dec 2009, Vol. 33, No. 6, pp. 967-972

Fluence Field Modulated Computed Tomography

Steven Bartolac and David Jaffray

Abstract ---- **Dose management in CT is an increasingly important issue as the number of CT scans per capita continues to rise. One proposed approach towards optimal dose management is to allow the pattern of X-ray fluence delivered to the patient to change spatially across the incident field, and independently for each projection angle. This approach is referred to as fluence field modulated CT (FFMCT). In this work, dose and image quality benefits of FFMCT are evaluated using an experimental CT system and a small cylindrical phantom comprised of acrylic spheres, water and teflon rods. Modulated fluence profiles are synthesized from projection sets taken at various tube current settings. SNR patterns and predicted dose outcomes are compared against that of a bowtie filter. FFMCT resulted in improved SNR outcomes with integral dose reduction on the order of 30%. The results of this study suggest that given a suitable collimator approach, fluence field modulated computed tomography could reap significant benefits in terms of reducing dose and optimizing image quality.**

I. INTRODUCTION

Advancements in computed tomography (CT) continue to grow in terms of increased speed, resolution, image quality and volume coverage capabilities. These advancements have been met with a corresponding rise in the number of CT scans per capita and have led to concern regarding the increased radiation risk to the population [1]. A key factor in minimizing the risk to patients is the appropriate management of radiation dose depending on the task and patient.

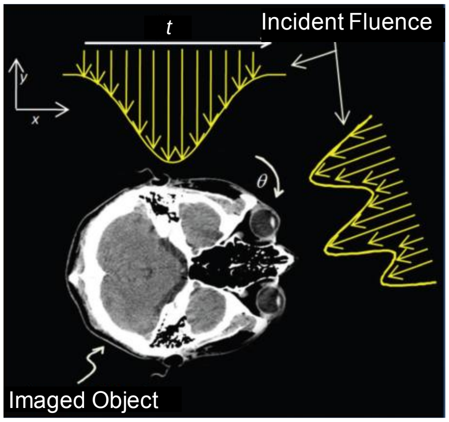

FIGURE 1: Schematic of FFMCT illustrating that the incident pattern of fluence can change both across the field of view and between projections.

Various ways for decreasing dose to the patient while maintaining or bettering image quality have been explored by means of modulating the incident X-ray beam. Some approaches, including automatic exposure control [2] and the addition of bow-tie filters [3-5], have made great strides towards more efficient management of the X-ray fluence. However, the ideal allocation of X-ray fluence would take into account both patient-specific anatomy as well as the imaging task. Previous work [6-8] has shown that optimizing the incident X-ray fluence, allowing its pattern to change spatially across the X-ray beam, and independently for each projection, has the potential to improve or maintain image quality where it is required, and allow for poorer image quality elsewhere. An illustration of this technique is shown in Figure 1. Such an approach could potentially yield great dose sparing to the patient without cost in the utility of the images, reaping benefits that would extend across both diagnostic and image-guided techniques. The methodology shares parallels with fluence planning and delivery used in intensity modulated radiation therapy (IMRT), and so was previously referred to as intensity modulated CT (IMCT). However, to avoid confusion with other tube current modulation techniques and to emphasize that changes can occur over the entire incident fluence field, the authors prefer to call this approach fluence field modulated CT (FFMCT).

While previous work in FFMCT showed large potential dose benefits could be possible, these evaluations were restricted to simulated data sets. The purpose of this study is to evaluate dosimetric and image quality benefits of FFMCT using real data from an experimental CT system.

II. THEORY AND METHODS

Implementation of FFMCT proceeds initially by specifying target image quality objectives and/or dose constraints for the patient. The incident fluence pattern is then optimized as a function of angle and detector position using a chosen optimization algorithm. Implicit to this method is that some *a priori* information of the object is available, either from a previous scan or a patient population model.

Steven Bartolac is with the Department of Medical Biophysics, University of Toronto, 610 University Ave., Toronto, Ontario M5G 2M9 CANADA. (Tel: (416) 946-4501. Email: steve.bartolac@rmp.uhn.on.ca)

David Jaffray is with the Radiation Medicine Program, Princess Margaret Hospital/Ontario Cancer Insitute, 610 University Ave., Toronto, Ontario, M5G 2M9 CANADA. (Email: david.jaffray@rmp.uhn.on.ca)

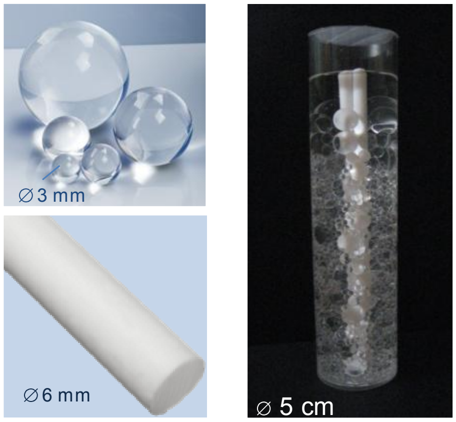

FIGURE 2: Image of phantom used in the study with enlargement of spheres and teflon rod constituents, and with relative dimaters indicated.

Experiments to evaluate the dose and image quality benefits of FFMCT were performed using a cone-beam CT benchtop in circular geometry, collimated to 64 detector rows about the central plane for simulation of a single slice CT acquisition. In this setup, an amorphous silicon flat panel detector (Paxscan 4030A, Varian, Palo Alto) with 194 µm pixel pitch, and a 600 kHU x-ray tube (Rad-94, Varian, Palo Alto) were fixed in position, with the phantom mounted on a precision rotation stage. A cylindrical water phantom (5 cm diameter) was constructed containing acrylic spheres and teflon rods, and is illustrated in Figure 2. Acrylic spheres were chosen because of their low contrast with respect to water simulating soft tissue lesions, while teflon simulates high contrast material such as bony anatomy. The phantom size was kept small relative to the full field of view in order to avoid scatter artifacts from the object; the small size of the object also allowed the use of a simplified parallel ray assumption in the optimization script for noise propagation (described below).

In order to generate a projection with a modulated fluence pattern, multiple scans of the object were taken of the phantom at different mAs settings (from 0.4 – 4 mAs per projection). A set of synthesized modulated projections were then constructed from the available projection sets. The noise in the projection data is modelled in the optimization routine as having two primary components: Poisson noise (based on photon counting statistics) and electronic noise. The noise model was taken from Kak and Slaney's derivation, which assumes a parallel ray model and a filtered backprojection reconstruction algorithm [9].

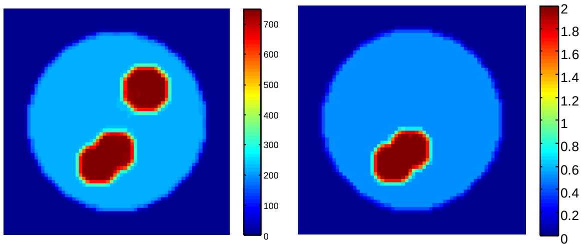

FIGURE 3: (a) prescribed SNR patter within water phantom (b) priority weighting applied to the specified SNR values within the optimization script. Warm colours correspond to higher values.

Optimization was performed utilizing a simulated annealing algorithm which searches for a solution to the target image quality objective in an iterative way. This approach has been used previously in simulation studies of FFMCT and is discussed in detail elsewhere[6]. The main objective is to minimize a cost function, here defined as:

$$C_n = \frac{\left(\sum_{x,y} W_{S_{x,y}} \left(S\dot{N}R_{x,y} - SNR_{\mathbf{m}_n,x,y}\right)^2\right)}{\left(\sum_{x,y} W_{S_{x,y}} \left(S\dot{N}R_{x,y} - SNR_{\mathbf{m}_0,x,y}\right)^2\right)} + \frac{\sum_{x,y} W_{D_{x,y}} D_{\mathbf{m}_n,x,y}^{2}}{\sum_{x,y} W_{D_{x,y}} D_{\mathbf{m}_0,x,y}^{2}} , \qquad (1)$$

where W_S and W_D are regionally varying weights on the desired signal to noise ratio, $S\dot{N}R$, and dose, D, respectively, subscript **m** denotes dependence on the selected modulation profile, subscripts *0* and *n* denote the initial and current iteration number respectively, and subscripts *x,y* denote the dependence of the variables on the spatial coordinates in the *z*=0, *x,y* plane. The weighting terms can be set depending on task-specific priorities. In this study, W_D was set to unity, and the weights in W_s were chosen to boost the priority of a selected high SNR region. The target $S\dot{N}R$ values and corresponding priority weighting is shown in Figure 3. Note that the first term in (2) requires updating the SNR values at each iteration of the optimization algorithm, which can be achieved by application of (1) using an *a priori* model of the object. Here, the input model was derived from a reconstruction of the object using a 1 mAs/projection protocol.

The optimization was constrained such that modulation of the incident fluence was restricted to 64 detector bins (where each bin represents 8 pixels in a row), and was further constrained to allow only one of 11 modulation factors. The first constraint aids in reducing optimization time while maintaining sufficient resolution for achieving desired SNR patterns. Although not meant to represent a particular collimator design, the number of bins also coincidentally corresponds to the number of intervals currently applied in tomotherapy where fluence profiles are similarly modulated for radiation therapy delivery. The second constraint was due to the limited number of mAs settings permitted using pulsed radiographic mode on the control console.

SNR and dose outcomes predicted from the optimization algorithm were compared to that of a bowtie filter that would produce on average the same SNR values in the priority weighted SNR region of interest. The shape of the bowtie filter was designed to match that of the small cylinder rather than a standard bowtie filter that might be used for patients. The optimized fluence modulation profile was then used to dictate the generation of the FFMCT projection sets (as indicated above). FFMCT reconstructions of the phantom were created using a 120 μm voxel size and compared to a reconstruction of the same slice reconstructed using a non-modulated, 1 mAs/projection tube current setting.

III. RESULTS AND DISCUSSION

The optimized fluence modulation profile is shown in Figure 4 as a function of projection angle and detector bin. The resulting SNR map for the FFMCT case is also compared to the case of a bowtie filter in Figure 5. Of the two regions specified for high SNR in the FFMCT case, the prioritized region achieved much better agreement with the objective than the low priority region. However, increased SNR with respect to the surroundings is also evident to a more limited extent for the low priority region. Another observation is made that the contour changes in the high SNR target region were smoother than those specified in the target SNR prescription. This result suggests a limitation in the target delineation capabilities of the system when attempting to meet prescribed SNR targets, particularly when there are ‘kinks’or sharp changes in the plan, although reducing the constraints on the system could possibly achieve better results. Compared to the case of the bowtie filter, FFMCT achieved results much closer to the target distribution, such that the region of high SNR was well localized to the priority region of interest.

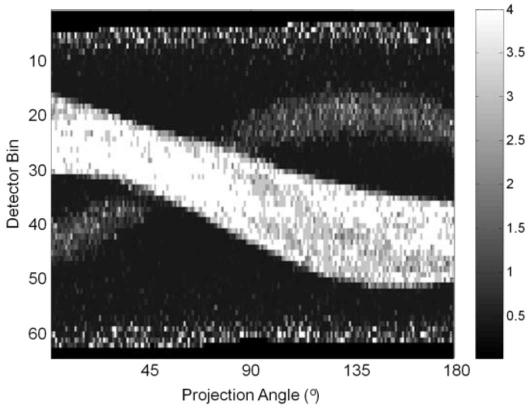

FIGURE 4: Ratio of dose map produced using FFMCT to that of the bowtie filter. Dose is decreased for the majority of the object using FFMCT except near the prescribed high SNR region.

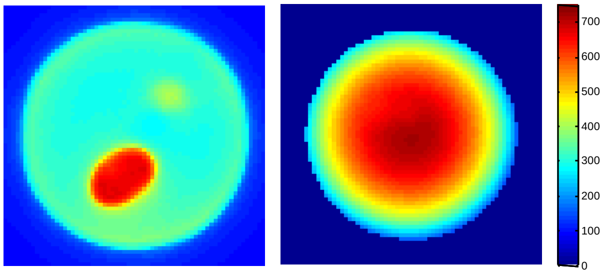

FIGURE 5: Comparison of SNR maps predicted using FFMCT (left) versus that of the bowtie filter (right). FFMCT is superior in approaching the desired SNR distribution (see Figure 3).

Figure 6 shows a ratio of the dose map using FFMCT to that of the bowtie filter. Local dose decreases reached as high as 60%, although some regions close to or within the region of the priority high SNR region experienced increases as much as 20% relative to the bowtie filter. Overall, a decrease in the integral dose was on the order of 30% for this object. Figure 7 shows a comparison of the reconstructions of the cylinder using synthesized FFMCT projections versus a reconstruction using an unmodulated beam. The comparison shows better image quality within the localized region of interest for the FFMCT case, with reduced quality elsewhere.

Advantages of the approach used for creating modulated projections in this study are that it allows for testing a modulation approach prior to construction of the modulator, and secondly that it allows for testing under idealized circumstances which can be treated as a benchmark for future studies; note that since no collimator was used, no correction was required for either beam hardening nor scatter contributions from the collimator which could be modelled separately.

Limitations of this study were principally with inaccuracies with respect to the scatter effects from the object itself since

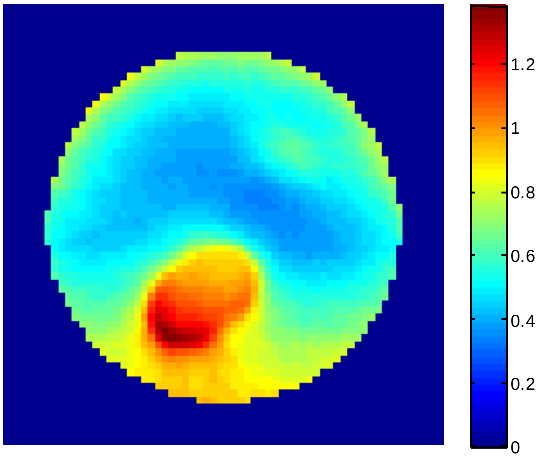

FIGURE 6: Ratio of dose map produced using FFMCT to that of the bowtie filter. Dose is decreased for the majority of the object using FFMCT except near the prescribed high SNR region.

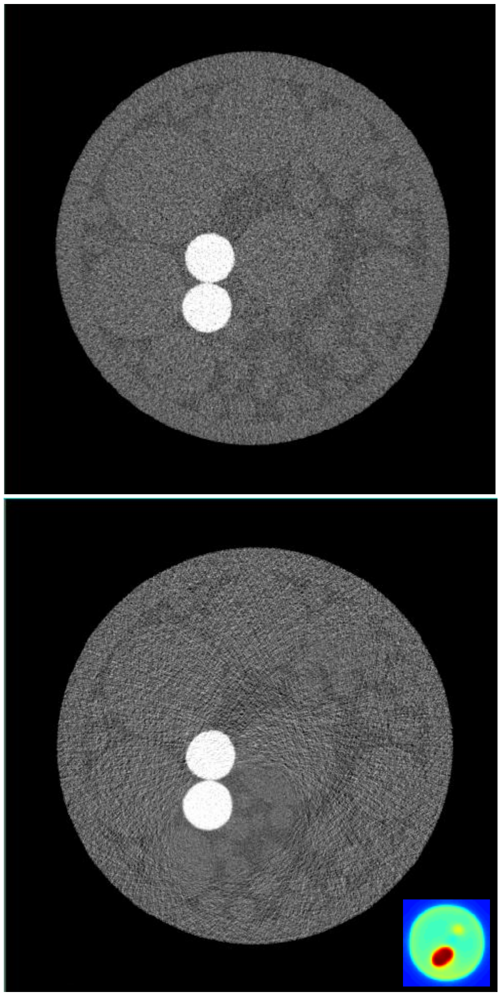

FIGURE 7: (a) Reconstruction of cylindrical phantom at setting of 1 mAs/projection. (b) Reconstruction using modulated projections ranging from 0.4 – 4 mAs. The prescribed SNR distribution is shown in colour in the bottom right corner for comparison.

the modulated projections were synthesized from a series of individual projections rather than using an actual modulator. Typically, one would expect that reduction of fluence outside some region of interest would reduce the scatter-to-primary ratio within that region, which could not be observed when synthesizing FFMCT projections in the manner indicated. However, this issue was circumvented by utilizing a small cylinder, and collimating to the central plane, which is expected to have greatly reduce scatter contribution. Potential artifacts due to abrupt scatter to primary ratio changes in the field of view [10] were also avoided using this technique. The small cylinder also permitted the simplification of using a parallel beam model for noise propagation. Larger objects would require a more accurate fan-beam noise propagation model, such as the one derived by Zhu et al.[11] for modeling variance maps in the optimization routine.

IV. CONCLUSION

The outcomes of this study suggest that FFMCT could potentially be applied with success in real clinical CT systems, provided that a suitable method for modulation be found. Dose outcomes show superior management of dose for achieving local high SNR performance in the presence of both high and low contrast materials.

REFERENCES

[1] D. J. Brenner and E. J. Hall, "Computed tomography--an increasing source of radiation exposure," *N Engl J Med,* vol. 357, pp. 2277-84, Nov 29 2007.

[2] M. Kachelriess, *et al.*, "Strategies for Dose Reduction and Improved Image Quality in MSCT," in *Multidetector-Row CT of the Thorax,* U. Joseph Schoepf, Ed., Berlin: Springer, 2006, pp. 35-45.

[3] S. A. Graham, *et al.*, "Compensators for dose and scatter management in cone-beam computed tomography," *Med Phys,* vol. 34, pp. 2691-703, Jul 2007.

[4] N. Mail, *et al.*, "The influence of bowtie filtration on cone-beam CT image quality," *Med Phys,* vol. 36, pp. 22-32, Jan 2009.

[5] A. Wunderlich and F. Noo, "Achieving uniform noise in direct fan-beam CT reconstruction through bowtie filter design," in *Nuclear Science Symposium Conference Record, 2007. NSS '07. IEEE,* 2007, pp. 4379-4382.

[6] S. Bartolac, *et al.*, "Fluence field optimization for noise and dose objectives in CT," *Med Phys,* vol. 38 Suppl 1, p. S2, May 2011.

[7] S. A. Graham, "Intensity Modulated Cone-Beam CT," M.Sc. M.Sc. Thesis, Medical Biophysics, University of Toronto, Toronto, 2006.

[8] J. Sperl, *et al.*, "Computer-assisted scan protocol and reconstruction (CASPAR)-reduction of image noise and patient dose," *IEEE Trans Med Imaging,* vol. 29, pp. 724-32, Mar 2010.

[9] A. C. Kak and M. Slaney, *Principles of computerized tomographic imaging.* New York: IEEE Press, 1988.

[10] T. P. Szczykutowicz and C. Mistretta, "Practical considerations for intensity modulated CT," San Diego, California, USA, 2012, pp. 83134E-11.

[11] L. Zhu and J. StarLack, "A practical reconstruction algorithm for CT noise variance maps using FBP reconstruction," San Diego, CA, USA, 2007, pp. 651023-8.

Evaluation of a Tight Frame Reconstruction Algorithm for Perfusion C-arm CT Using a Realistic Dynamic Brain Phantom

Michael Manhart*†, Andreas Fieselmann*† and Yu Deuerling-Zheng†

***Abstract*—This work introduces and evaluates an iterative, compressed sensing (CS) reconstruction algorithm based on tight frame regularization for perfusion C-arm CT with a high C-arm rotation speed acquisition protocol. To allow a realistic evaluation, a digital 4D brain phantom was created by extending a recently published phantom emulating time attenuation curves (TACs) inside a virtual brain segmented from clinical MR data. We additionally incorporated MR data to vary perfusion parameters all over the brain to avoid unrealistic homogeneous structures favoring CS algorithms. The iterative algorithm is compared to the Feldkamp algorithm by evaluating the root mean square error of the reconstructed TACs and Pearson correlation of the reconstructed perfusion maps to the ground truth. The results indicate that the tight frame algorithm qualitatively and quantitatively improves reconstructed perfusion maps compared to the Feldkamp algorithm.**

I. INTRODUCTION

Perfusion CT (PCT) is an important imaging modality for diagnosis in case of an ischemic stroke event. Time attenuation curves (TACs) in tissue and vessels are extracted from a time series of brain volumes acquired after a contrast bolus injection. Perfusion parameter maps calculated from TACs, such as cerebral blood flow (CBF), cerebral blood volume (CBV), and mean transit time (MTT), provide information about the extent of the affected tissue. They can be used to identify potentially salvageable ischemic tissue that could be reperfused by catheter-guided stroke therapy procedures such as intra-arterial thrombolysis. For this purpose the patient is transported to an interventional suite with C-arm angiography systems, where perfusion measurement is not yet available. Perfusion measurement using C-arm systems would allow assessing the perfusion parameters directly before and during the interventional procedure and help to determine the treatment success and endpoint. Yet the low rotation speed of common C-arm systems, which typically need ~ 5 s to acquire one volume, makes perfusion C-arm CT (PCCT) challenging. Future C-arm systems with an increased rotation speed of up to 100°/s (Artis zeego, Siemens AG, Forchheim, Germany) will enable protocols with reduced acquisition time. In this study a potential protocol with fast C-arm rotation speed is simulated. The protocol consists of two acquisition sequences: the first sequence acquires one sweep in forward and one in backward rotation direction before bolus injection to reconstruct baseline volumes with static anatomical structures. The second sequence acquires seven consecutive sweeps with alternating forward and backward rotation direction after bolus injection. Each sweep acquires 133 projections in a 200° angular range and requires $T_\mathrm{r} = 2.8$ s for data acquisition with a pause of $T_\mathrm{w} = 1.2$ s between sweeps. Thus TACs can be sampled with a temporal resolution of $T_\mathrm{s} = T_\mathrm{r} + T_\mathrm{w} = 4$ s. However, using the well-known FDK algorithm [1] for reconstruction of the acquired volumes, the limited number of 133 projections leads to streak artifacts. Furthermore, the peaks of the tissue TACs typically lie in a range of $\sim$ 5 – 10 HU, thus perfusion imaging is very sensitive to noise. An important challenge is to find algorithms capable of reliably reconstructing tissue TACs at a higher noise level to limit the radiation exposure to the patient. Recently, new iterative reconstruction techniques have been proposed with a promising application to these challenges: exploiting the idea of CS that the volumes have a sparse representation under a certain transformation. A well-known example for such a transformation is the total variation (TV) norm which is applied by the ASD-POCS [2] and iTV [3] algorithms. In the context of perfusion imaging the TV norm was proposed in combination with a prior image in the PICCS [4], and additionally with a non-convex extension of the TV norm in the NCPICCS algorithm [5]. Another example for a transformation is the tight frame (TF) wavelet based approach presented in [6]. Also special model-based iterative [7] and analytical [8] algorithms have been proposed for reconstruction of dynamic projection data from slowly rotating acquisition systems by using temporal basis functions to approximate the TACs. The scope of this work is the realistic evaluation of an iterative algorithm using a modified version of the TF regularization suggested by Jia et al. [6] with an extension of the realistic digital brain perfusion phantom by Riordan et al. [9]. As discussed in [6] the TF approach has been found to have higher computational efficiency and maintains image contrast better than TV minimization, which are important features in interventional perfusion imaging. The brain phantom data and tools are published online to improve the reproducibility of this and future studies [10].

II. MATERIALS AND METHODS

A. Reconstruction Algorithms

1) TF Shrink: The iterative CS algorithm applies the GPU-based Algebraic Reconstruction Technique with Ordered Subsets (OS-ART) presented in [11] to ensure data consistency

---

*Pattern Recognition Lab, FAU Erlangen-Nürnberg, Germany

†Siemens AG, Angiography & Interventional X-Ray Systems, Forchheim, Germany

Email: michael.manhart@cs.fau.de

between the measured projection data p and the reconstructed volume $f(\mathbf{x}) : \mathbb{N}^3 \rightarrow \mathbb{R}$ with respect to the acquisition system matrix A. The projections are partitioned into 10 disjoint sets, the relaxation factor is initialized with $\beta = 0.8$ and reduced by multiplication with $\beta_r = 0.95$ after each iteration. After processing one subset of projections, all negative values in f are set to zero to obtain a physically correct solution. To reduce noise the wavelet based tight frame regularization proposed by Jia et al. [6] is used. The volume f is decomposed into 27 wavelet coefficients $\alpha_i(\mathbf{x}) = \Psi_i(\mathbf{x}) \otimes f(\mathbf{x}), i = 0...26$ by convolving the volume with the discrete version of a redundant, piecewise linear 3D TF basis [12] consisting of a low-pass filter $\Psi_0(\mathbf{x})$ and high-pass filters $\Psi_i(\mathbf{x}), i = 1...26$. For simplifying notation, we denote this decomposition by $\alpha(\mathbf{x}) = Df(\mathbf{x})$. Then a vector-shrinkage operation is applied to the coefficients, where the l_2 norm of the high-pass coefficients $\tau_h(\mathbf{x}) = \sqrt{\sum_{i=1}^{26} \alpha_i(\mathbf{x})^2}$ determines whether the high-pass coefficients are kept or discarded. The shrinkage parameter μ controls the level of suppressing the high-pass coefficients. In practice the regularization has shown to smoothen out the high contrast vessels, which can lead to underestimation of the contrast attenuation inside the vessels and blurring of the vessel into the encircling tissue. Thus, the shrinkage step is modified by excluding voxels containing vessel structures from the regularization. A vessel mask $V(\mathbf{x}) : \mathbb{N}^3 \rightarrow \{0, 1\}$ was created by simple thresholding a baseline subtracted FDK reconstruction of a sweep with high contrast attenuation. The vector-shrinkage operator $\mathcal{T}_\mu^V$ is then defined as:

$$\mathcal{T}_\mu^V \alpha_i(\mathbf{x}) = \begin{cases} \alpha_i(\mathbf{x}) & i = 0 \text{ or } V(\mathbf{x}) = 1, \\ \alpha_i(\mathbf{x}) \max\left[\frac{\tau_h(\mathbf{x}) - \mu}{\tau_h(\mathbf{x})}, 0\right] & \text{otherwise.} \end{cases} \tag{1}$$

After the shrinkage step the volume is recomposed from the new coefficients $f(\mathbf{x}) = \sum_{i=0}^{26} \Psi_i(-\mathbf{x}) \alpha_i(\mathbf{x})$, for simplicity denoted by $f(\mathbf{x}) = D^T \alpha(\mathbf{x})$. The iterations stop when data consistency has not improved after one full iteration.

Algorithm 1 TF Shrink

```
Initialize: $f^0 = 0$, $\epsilon^0 = ||Af^0 - p||_2$, $k = 0$
Do
    $f^{output} = f^k$, $k = k + 1$
    $f^k =$ OS-ART($f^{k-1}$) (3 Iterations)
    Shrinkage: $f^k = D^T \mathcal{T}_\mu^V D f^k$
    $\epsilon^k = ||Af^k - p||_2$
While ($\epsilon^k < \epsilon^{k-1}$)
```

2) FDK: The iterative algorithm is compared to standard FDK reconstruction with Parker short-scan weights [13]. The filtering step uses a Shepp-Logan filter kernel multiplied with a Gaussian of variance σ^2 controlling smoothness and noise level in the reconstructed volumes.

B. Realistic Dynamic Brain Phantom

Classical digital CT phantoms usually consist of homogeneous structures and have a very sparse representation in TV or wavelet transformation. This highly favors CS reconstruction algorithms, which exploit sparse representations. Thus, simple extensions to 4D dynamic phantoms do not allow for an authentic evaluation. We adopted the dynamic head phantom from [9], which was originally used for evaluation of perfusion parameter calculation methods, to create an appropriate phantom for evaluating the reconstruction algorithms. Similarly to what is proposed in [9], we segmented brain MRI scans from a human volunteer into white and gray matter, cerebrospinal fluid (CSF), and arteries. White/gray matter and CSF segmentation was done from T1 weighted MRI data using the Freesurfer software [14]. Arteries were segmented from a time-of-flight acquisition by thresholding and manual post-processing. The segmentations were combined into a volume consisting of 150 slices with 256x256 voxels of isotropic size 1 mm^3. Inside the volume two different tissue classes were annotated using ellipsoid ROIs: tissue with reduced CBF (2 ROIs, altogether 13197 mm^3) and tissue with severely reduced CBF and CBV (2 ROIs, altogether 5761 mm^3). Furthermore, a ROI of healthy tissue (87949 mm^3) around the stroke affected areas was annotated for evaluation purposes. Figure 1a shows an example of an annotated brain slice. Tissue that was not annotated was simulated like healthy tissue. Different perfusion parameters were assigned to the annotated ROIs as shown in Table I. To further reduce the sparsity of the brain phantom, the MR data was used to vary the perfusion parameters. The parameters were varied according to the intervals shown in Table I. Details of this variation are provided at the phantom web page [10]. The tissue TACs were created as described in [9] by convolution of a real measured arterial input function (AIF) from clinical PCT with a residual function with exponential decay. For vessel structures the TACs were simulated by the real measured AIF. To incorporate the anatomic tissue structures into the phantom, appropriate constant HU values were added to the TACs like in [9]. Also, the HU values of the anatomic structures were varied using the MR data to reduce sparsity. Finally the dynamic C-arm projection data was created by forward projecting the 4D phantom according to the high C-arm rotation speed acquisition protocol. Poisson-distributed noise was added to the projections assuming an emitted X-ray density of $2.1 \cdot 10^6$ photons per mm^2 at the source-to-detector distance as in [7].

C. Perfusion Parameter Calculation and Comparison

To compute perfusion parameters from the reconstructed data, the baseline volumes were subtracted from the dynamic volumes to extract the contrast attenuation. Then the TACs were created from the subtracted volumes. Each volume represents TAC samples at the mid time point of its acquisition. By linear interpolation the TACs were resampled to 1 s temporal resolution. A TAC inside the internal carotid artery was selected as AIF and the perfusion parameters were calculated using a deconvolution approach based on indicator-dilution theory [15]. For quantitative comparison of the reconstruction algorithms the root mean square error (RMSE) over time between the reconstructed and the ground truth time curves of the AIF and inside the annotated tissue was computed. To compare the resulting perfusion maps the Pearson correlation (PC) between maps created from the reconstructed TACs and maps created from the ground truth TACs was computed. Two types of PC have been calculated: the first PC value takes only the annotated tissue into account. It is focused on the regions inside and close to the stroke affected tissue, stating how well it is separated from the healthy tissue. The second value represents all values of the stroke affected slices. This PC value incorporates the higher blurring of vessels in the perfusion maps of smoother reconstructions.

III. RESULTS

Figure 1 shows the resulting CBF, CBV, and MTT perfusion maps from FDK reconstruction with $\sigma = 1.25$ mm, TF Shrink reconstruction with $\mu = 0.0001$, and the reference images for comparison. Table II shows the quantitative results for different parameters, where the best result for each measure is shown in bold. The reconstructions were performed on a laptop computer with an Intel i7 M 620 2 x 2.7 GHz CPU, 8 GB RAM and an Nvidia Quadro FX 880M graphic chipset. The GPU-based implementation required ~ 50 s for one complete TF Shrink iteration, the complete reconstruction of 9 volumes of size 256x256x180 varied between $\sim$ 30 – 75 min depending on the shrinkage parameter μ. Complete reconstruction with FDK took ~ 1.5 min.

IV. DISCUSSION

The perfusion maps in Figure 1 show that the maps created from the TF Shrink reconstructions have a qualitatively good correspondence with the reference maps for CBF and CBV. Stroke affected areas are well separated from the healthy regions. In the TF Shrink MTT map the areas with reduced CBF are well visible. However, the areas with severely reduced CBF/CBV are not visible. Since MTT $= \frac{\text{CBV}}{\text{CBF}}$ and both CBV and CBF values are very low in these regions, it is very challenging to estimate under noisy conditions. In the maps generated from the FDK reconstructions the affected regions are still visible in the CBF and CBV map but not as well separated from the healthy tissue as in the TF Shrink maps. The FDK MTT map does not allow for a reliable location of the stroke affected areas. This corresponds to the quantitative results in Table II. The TF Shrink algorithm has the best PC for most maps with $\mu = 10^{-4}$, e.g. the PC of the CBF map can be increased from 0.79 for the best FDK reconstruction to 0.86. The results also show the advantage of excluding the vessels from regularization, which reduces blurring of vessels and underestimation of contrast attenuation values in vessels. The RMSE of the AIF estimation is improved from 155 HU to 86 HU for $\mu = 5 \cdot 10^{-4}$.

V. CONCLUSIONS

This work shows that iterative reconstruction with tight frame regularization has significant potential to improve perfusion C-arm CT with a fast acquisition protocol. Qualitative and quantitative comparisons of the reconstructed perfusion maps were done using a realistic brain phantom that avoids the sparse structure of classical CT phantoms. Visual impression and correlation of the reconstructed maps to the ground truth is significantly improved compared to the FDK reconstruction results. However, computation time is increased compared to FDK reconstruction, which is critical in interventional applications. Nevertheless, further code optimization and the rapid development of hardware will likely make this approach clinically applicable in the foreseeable future.

ACKNOWLEDGMENT

The authors thank Robert Grimm and Jana Hutter for help with the MR acquisitions for the brain phantom.

REFERENCES

[1] L. Feldkamp, L. Davis, and J. Kress, “Practical cone-beam algorithm,” *Journal of the Optical Society of America A*, vol. 1, no. 6, pp. 612–619, 1984.

[2] E. Y. Sidky and X. Pan, “Image reconstruction in circular cone-beam computed tomography by constrained, total-variation minimization,” *Physics in Medicine and Biology*, vol. 53, no. 17, pp. 4777–4807, 2008.

[3] L. Ritschl, F. Bergner, C. Fleischmann, and M. Kachelrieß, “Improved total variation-based CT image reconstruction applied to clinical data,” *Physics in Medicine and Biology*, vol. 56, no. 6, pp. 1545–1561, 2011.

[4] B. E. Nett, R. Brauweiler, W. Kalender, H. Rowley, and G.-H. Chen, “Perfusion measurements by micro-CT using Prior Image Constrained Compressed Sensing (PICCS): Initial Phantom Results,” *Physics in Medicine and Biology*, vol. 55, no. 8, pp. 2333–2350, 2010.

[5] J. C. Ramirez-Giraldo, J. Trzasko, S. Leng, L. Yu, A. Manduca, and C. McCollougha, “Nonconvex prior image constrained compressed sensing (NCPICCS):Theory and simulations on perfusion CT,” *Medical Physics*, vol. 38, no. 4, pp. 2157–2167, 2011.

[6] X. Jia, B. Dong, Y. Lou, and S. B. Jiang, “GPU-based iterative cone-beam CT reconstruction using tight frame regularization,” *Physics in Medicine and Biology*, vol. 56, no. 13, pp. 3787–3807, 2011.

[7] C. Neukirchen, M. Giordano, and S. Wiesner, “An iterative method for tomographic x-ray perfusion estimation in a decomposition model-based approach,” *Medical Physics*, vol. 37, no. 12, pp. 6125–6141, 2010.

[8] C. Neukirchen, “An extended temporal interpolation approach for dynamic object reconstruction,” in *Proceedings 11th Fully 3D*, 2011, pp. 379–382.

[9] A. J. Riordan, M. Prokop, M. A. Viergever, J. W. Dankbaar, E. J. Smit, and H. W. A. M. de Jong, “Validation of CT brain perfusion methods using a realistic dynamic head phantom,” *Medical Physics*, vol. 38, no. 6, pp. 3212–3221, 2011.

[10] Digital Brain Perfusion Phantom. http://www5.cs.fau.de/data/.

[11] B. Keck, H. Hofmann, H. Scherl, M. Kowarschik, and J. Hornegger, “GPU-Accelerated SART Reconstruction Using the CUDA Programming Environment,” in *Proc. SPIE*, 2009.

[12] B. Dong and Z. Shen, “MRA-based wavelet frames and applications,” IAS Lecture Notes Series, Summer Program on "The Mathematics of Image Processing", Tech. Rep., 2010.

[13] D. L. Parker, “Optimal short scan convolution reconstruction for fan beam CT,” *Medical Physics*, vol. 9, no. 2, pp. 254–257, 1982.

[14] Freesurfer image analysis suite. http://surfer.nmr.mgh.harvard.edu/.

[15] A. Fieselmann, M. Kowarschik, A. Ganguly, J. Hornegger, and R. Fahrig, “Deconvolution-Based CT and MR Brain Perfusion Measurement: Theoretical Model Revisited and Practical Implementation Details,” International Journal of Biomedical Imaging, 2011, article ID 467563.

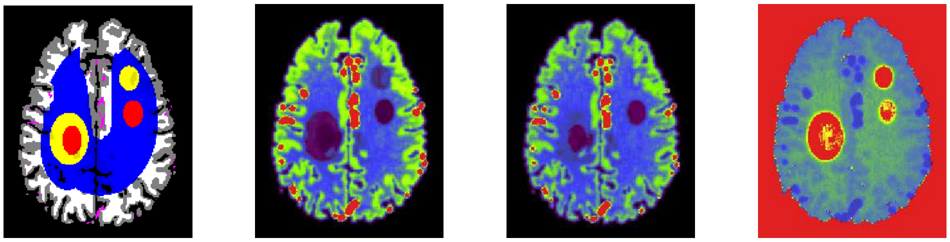

(a) Annotation (b) Reference CBF (c) Reference CBV (d) Reference MTT

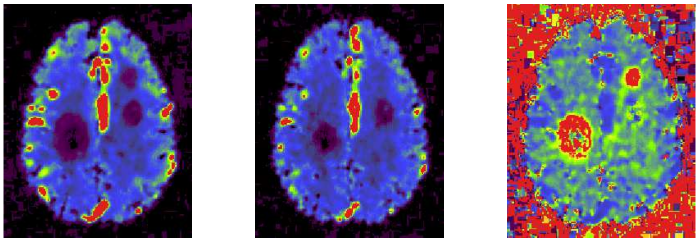

(e) TF Shrink CBF (f) TF Shrink CBV (g) TF Shrink MTT

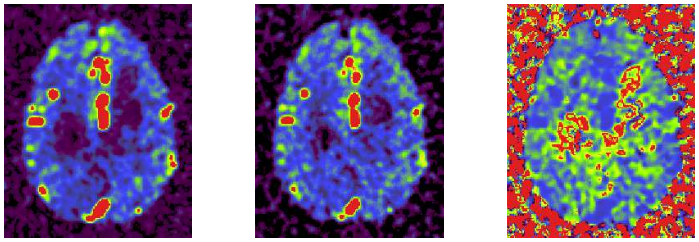

(h) FDK CBF (i) FDK CBV (j) FDK MTT

Fig. 1. Perfusion maps (Annotation legend: yellow: reduced CBF area, red: reduced CBF/CBV area, blue: healthy tissue area used for evaluation).

	Healthy		Reduced CBF		Reduced CBF/CBV	
	WM	GM	WM	GM	WM	GM
CBF [ml/100 ml/min]	25 ± 14	53 ± 14	7.5 ± 4.25	16 ± 4.25	2.5 ± 1.4	5.3 ± 1.4
CBV [ml/100 ml]	1.9 ± 0.9	3.3 ± 0.4	1.7 ± 0.9	3 ± 0.7	0.42 ± 0.2	0.71 ± 0.12
MTT [s]	4.6 ± 0.7	3.7 ± 0.7	14 ± 0.75	11 ± 0.75	10 ± 1	8 ± 1

TABLE I
PERFUSION PARAMETERS (WM = WHITE MATTER, GM = GRAY MATTER).

Algorithm	FDK					Tight Frame Regularization			w.o. vessel mask
Parameter	$\sigma = 0.5$	0.75	1.0	1.25	1.5	$\mu = 5 \cdot 10^{-5}$	$1 \cdot 10^{-4}$	$5 \cdot 10^{-4}$	$5 \cdot 10^{-4}$
RMSE Tissue [HU]	7.26	4.27	3.08	2.54	2.29	2.52	2.21	**2.15**	2.20
RMSE AIF [HU]	78	119	156	184	204	**53**	58	86	155
PC CBF (annotated tissue)	0.68	0.75	0.78	0.79	0.78	0.84	**0.86**	0.84	0.80
PC CBV (annotated tissue)	0.54	0.62	0.68	0.71	0.72	0.77	**0.79**	0.77	0.76
PC MTT (annotated tissue)	0.35	0.47	0.58	0.66	0.73	**0.81**	**0.81**	0.80	0.80
PC CBF (complete tissue)	0.65	0.69	0.68	0.64	0.61	0.73	**0.76**	0.71	0.64
PC CBV (complete tissue)	0.52	0.59	0.62	0.61	0.59	0.67	**0.72**	0.69	0.64
PC MTT (complete tissue)	0.32	0.43	0.55	0.64	0.71	0.70	0.75	**0.78**	**0.78**
Iterations/Volume	N/A	N/A	N/A	N/A	N/A	4	6	10	4

TABLE II
QUANTITATIVE RESULTS.

Phase–Correlated Perfusion Imaging of Free–Breathing Rodents

Stefan Sawall, Jan Kuntz, Michaela Socher, Sönke Bartling, Michael Knaup, and Marc Kachelrieß

Abstract—**Mouse models of cardiac diseases have proven to be a valuable tool in preclinical research. The high cardiac and respiratory rates of free breathing mice prohibit conventional in–vivo cardiac perfusion studies even if gating methods are applied. This makes a sacrification of the animals unavoidable and only allows for the application of ex vivo methods. To overcome this issue we propose a low dose scan protocol and an associated reconstruction algorithm that allows for in vivo imaging of cardiac perfusion and associated processes that are retrospectively synchronized to the respiratory and cardiac motion of the animal. The scan protocol encompasses a repetitive injection of contrast media within several consecutive scans while the ECG, respiratory motion and timestamp of contrast injection are recorded and synchronized to the acquired projections. The iterative reconstruction algorithm employs a six-dimensional edge-preserving filter to provide motion artifact-free images with low noise of the animal examined using our low dose scan protocol. The reconstructions obtained show that the complete temporal bolus evolution can be visualized and quantified in any desired combination of cardiac and respiratory phase including reperfusion phases. The proposed reconstruction method thereby keeps the administered radiation dose at a minimum and thus reduces metabolic inference to the animal allowing for longitudinal studies. Our low dose scan protocol and our phase-correlated dynamic reconstruction algorithm allows for an easy hence effective way to visualize phase-correlated perfusion processes in free-breathing mice and in the laboratory routine.**

I. INTRODUCTION

CEREBRAL and cardiac perfusion studies are a common tool in clinical practice. In case of small rodents, however, and in preclinical research in general perfusion imaging is difficult due to the rapid heart rates (up to 600 beats per minute) and respiratory rates (up to 300 respirations per minute) as well as the consequent technical requirements, e.g. the required detector framerate. By now, no phase–correlated perfusion imaging of rodents is possible as this requires a triple–phase correlation to visualize the flow of contrast media in desired positions within the cardiac and respiratory cycle. Any reconstruction would have to be correlated to three temporal signals: respiratory, cardiac and perfusion. Unless not acquired with very high dose the reconstructed phase–correlated images show severe streak artifacts, image noise is very high and anatomical details vanish in the noise [1]. Several methods have been proposed in the literature to provide perfusion data of mice that are either not compatible with the Animal Use and Care Protocols in several countries (e.g. due to the amount of contrast media adminstered [2]) or are not able to provide phase–correlated volumes [3], [4]. However to keep dose at a reasonable level we propose a scan protocol including a novel injection technique and a reconstruction method that allows us to perform triple–phase correlated perfusion studies of free breathing small animals and to significantly improve image quality of the reconstructed volumes compared to standard phase–correlated reconstructions.

II. MATERIALS AND METHODS

A. Animal Handling and Extrinsic Gating

The wildtype mice used in our studies are subcutaneously administered with an analgetic (Metamizol, 200 mg/kg) prior to all examinations. The animals are placed in a box of plexiglas and anesthesia is delivered via inhalation of Isoflurane (2 %+O_2). As soon as the required depth of anesthesia is reached the mice are placed on the acquisition table where a constant delivery of Isoflurane is ensured using a breathing mask. Contrast media is conventionally delivered via the tail vein. Previous studies however revealed that the injection of highly viscous, iodinated contrast media results in a retrograde blood flow from the inferior caval vein to the liver veins near the diaphragm and thus the delivery to the heart is not sufficient for imaging [5]. To overcome this issue we use a retro–bulbar injection technique. A needle is placed in retro–bulbar position to deliver the contrast agent (Ultravist 300, Bayer Schering Pharma, Berlin, Germany). Contrast media injected to the retro–bulbar sinus is delivered to the heart from the superficial temporal vein, the inferior palpebral vein and the ocular angle vein to the external jugular vein merging to the subclavian vein and superior caval vein [6]. Note that also other possible injection routes exist in rodents, e.g. by direct injection into the jugular vein. However, we did not make use of these alternatives. The needle is connected to a custom–made, high–precision injector that is controlled using MatLab (Mathworks, Natick, USA). To lower the viscosity of the contrast media from 8.7 mPa·s to 4.6 mPa·s, to prevent thermal shock and to ease injection the syringe is heated in a water bath to the body temperature of the mouse (about 37°C). Note that all animal studies were approved by the ethical committee at the German Cancer Research Center (DKFZ), Heidelberg, Germany.

The extrinsic respiratory signal is derived using a pressure sensor beneath the mouse and the ECG is derived using small

Stefan Sawall, and Dr. Michael Knaup: Institute of Medical Physics, Friedrich–Alexander–University (FAU) Erlangen-Nürnberg, Henkestr. 91, 91052 Erlangen, Germany.

Jan Kuntz, Dr. Michaela Socher, and Dr. Sönke Bartling: German Cancer Research Center (DKFZ), Im Neuenheimer Feld 280, Heidelberg, Germany.

Prof. Dr. Marc Kachelrieß: Institute of Medical Physics, Friedrich–Alexander–University (FAU) Erlangen–Nürnberg, Henkestr. 91, 91052 Erlangen, Germany and German Cancer Research Center (DKFZ), Im Neuenheimer Feld 280, Heidelberg, Germany.

Corresponding author: stefan.sawall@imp.uni-erlangen.de

animal electrodes attached to the paws. These signals are recorded using a dedicated small animal monitoring system (Small Animal Instruments, Stony Brook, USA). Furthermore the timepoint of contrast media injection is recorded. This allows for a retrospective synchronization of all three gating signals with the acquired projection images. To acquire all data necessary for image reconstruction ten consecutive scans and hence ten consecutive injections of boli with a size of about 25 µL are performed similar to reference [3].

B. Measurements

Several perfusion imaging studies have been performed at the DKFZ. The results of one mouse shall be presented in more detail here. The datasets were acquired using a volume CT (VCT) prototype (Siemens Healthcare, Forchheim, Germany) consisting of a standard slip–ring CT gantry equipped with a flat detector. This flat detector with its CsI scintillator provides a matrix of 2048×1536 pixels, each of size 0.388 µm allowing for a theoretical spatial resolution in the center of rotation of 238 µm. To increase the detector frame rate from 20 to 100 projections per second only an area fraction of 1024×192 pixels in the detector center is read out. The x–ray source providing a focal spot size of about 570 µm is mounted at a distance of 570 mm from the isocenter and the flat–panel is mounted at a distance of 360 mm from the isocenter. The scans were conducted with a tube voltage of 80 kV and a tube current of 50 mA. Each scan consists of 2000 projection images acquired in a single gantry rotation over 20 s thus the scanner rotates with a speed of 18 °/s.

The mean respiratory rate of the mouse was 190 rpm (respirations per minute) and the mean heart rate was 350 bpm (beats per minute). Using an integration time of 10 ms per projection implies that about 16 projection images where acquired during one cardiac cycle and similarily about 33 projections were acquired within a single respiratory cycle. This implies that the cardiac–temporal resolution is limited to about 7 % of the cardiac cycle and the respiratory–temporal resolution is limited to about 3 % of the respiratory cycle. However recent works show that a cardiac window of $\triangle c = 20\,\%$ and a respiratory window of $\triangle r = 20\,\%$ are sufficient to reconstruct volumes without noticeable motion artifacts. The usage of this phase window configuration with a perfusion window width of $\triangle p = 5\,\%$, assuming 10 scans with 2000 projections each, in turn implies that only about 40 projection images are available for the reconstruction of a volume in a desired cardiac, respiratory and perfusion phase.

C. Image Reconstruction

Our standard image reconstruction is the Feldkamp algorithm which we denote with $\mathsf{X}_{\mathrm{Std}}^{-1}$ and which results in the standard image $f_{\mathrm{Std}} = \mathsf{X}_{\mathrm{Std}}^{-1} q$ based on the measured rawdata q [7]. The standard Feldkamp algorithm is not phase–correlated. We make use of it below to define the McKinnon–Bates algorithm.

To perform phase–correlated image reconstruction we use a phase–correlated Feldkamp algorithm $\mathsf{X}_{\mathrm{PC}}^{-1}$ that filters and backprojects only those projections that lie in the desired temporal window. The temporal window itself is defined by specifying the respiratory phase r, the cardiac phase c and the perfusion phase p. All of these values are between 0 and 1 and count relative to one motion period in case of cardiac and respiratory motion and relative to one scan in case of perfusion, respectively, and by specifying the widths $\triangle r$, $\triangle c$ and $\triangle p$ of these temporal windows. The respiratory, cardiac and perfusion phase–correlated image is denoted as $f_{\mathrm{PC}} = \mathsf{X}_{\mathrm{PC}}^{-1} q$.

Since only few projections fall into the desired temporal window, streak artifacts may occur unless a very large number of projections at very fine angular increments is acquired. The McKinnon–Bates (MKB) algorithm can be used to address this issue [8], [9]. It works as follows. First, a standard reconstruction is performed to obtain a prior image. This prior image is blurry in those regions where motion is present, and it is of high image quality elsewhere. Then, a forward projection of the prior image is performed and subtracted from the measured rawdata. These subtracted data are then used for a phase–correlated reconstruction which is added to the prior image. Mathematically:

$$f_{\mathrm{MKB}} = f_{\mathrm{Std}} + \mathsf{X}_{\mathrm{PC}}^{-1}(\hat{q} - \mathsf{X} f_{\mathrm{Std}}) \tag{1}$$

Due to the several injections contrast media is accumulated in the participating tissue and thus the rawdata are not consistent between different scans. To compensate for the contrast media take–off we preprocess the rawdata q as follows to obtain $\hat{q}$:

$$\hat{q} = q - \mathsf{X}\left(\mathsf{B}\overline{\mathsf{X}}_{\mathrm{PC}}^{-1} q_0 - \mathsf{B}\overline{\mathsf{X}}_{\mathrm{PC}}^{-1} q_n\right) \tag{2}$$

Therein q_0 are the rawdata obtained from the first scan and q_n are the rawdata obtained in scan n. $\overline{\mathsf{X}}_{PC}^{-1}$ denotes a phase–correlated reconstruction that neglects the perfusion phase and only recognizes the cardiac and respiratory phases. B is a bilateral filter operator used to reduce noise and to suppress streak artifacts [10]. In case of the preprocessing step the filter is applied in five dimensions (three spatial dimensions, two temporal dimensions: cardiac and respiratory). In case of the final MKB images the filter is applied in six dimensions (three spatial dimensions, three temporal dimensions: cardiac, respiratory and perfusion). To define the bilateral filter let us restrict to one dimension, for convenience. The filtering of a function $f(x)$ is then defined as

$$\mathsf{B}f(x) = \frac{\int dt D(x,t) R(x,t) f(t)}{\int dt D(x,t) R(x,t)} \tag{3}$$

with

$$D(x,t) = \exp\left(-\left(\frac{x-t}{\sigma_x}\right)^2\right) \tag{4}$$

$$R(x,t) = \exp\left(-\left(\frac{f(x)-f(t)}{\sigma_f}\right)^2\right) \tag{5}$$

being the domain and the range filter, respectively. The parameters σ_x and σ_f are the widths of the Gaussian domain and range filters, respectively. Note that other shapes of range

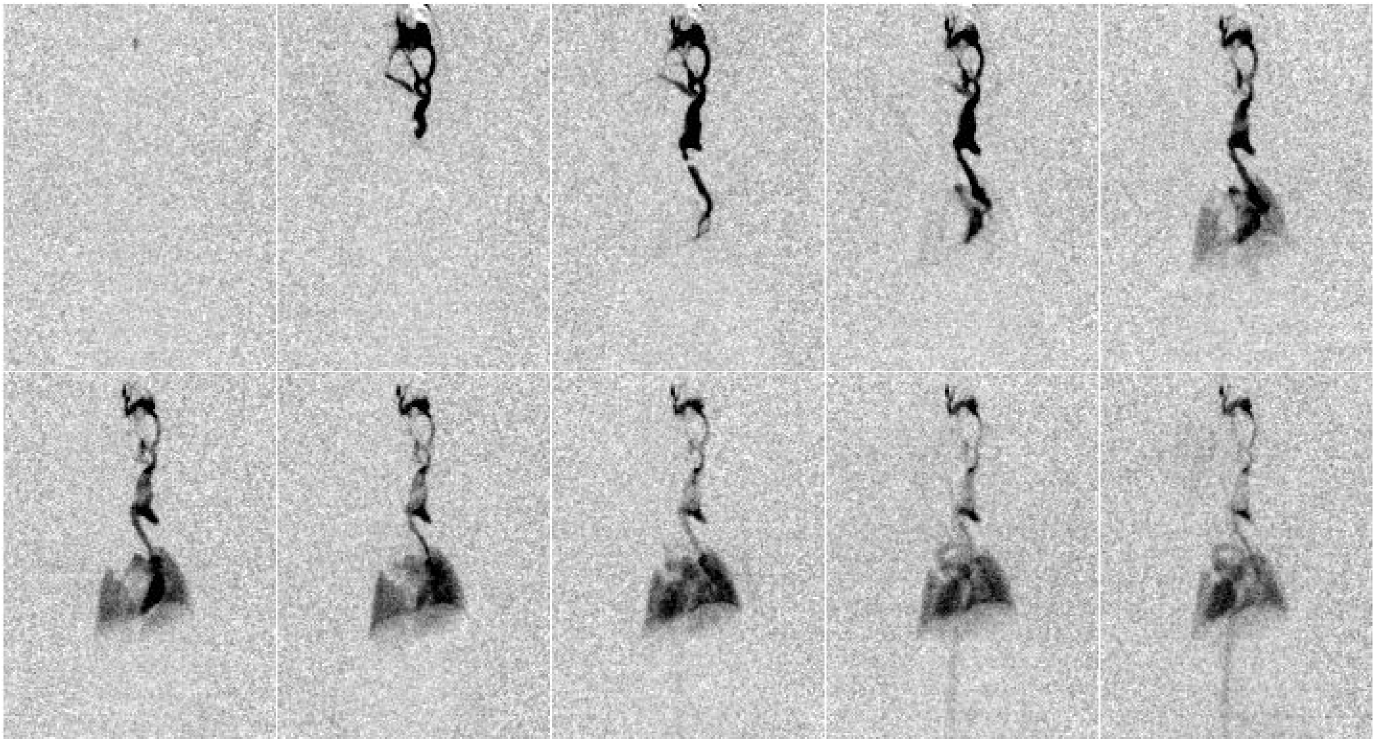

Fig. 1. Phase–correlated digital subtraction angiography.

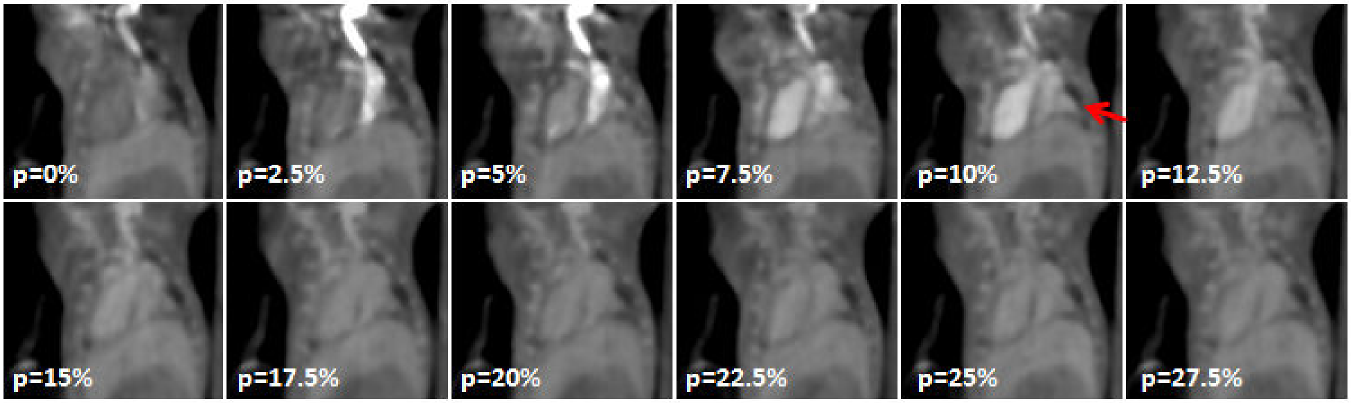

Fig. 2. Coronal slices of a mouse perfusion series. $c = 0\,\%$, $\triangle c = 20\,\%$, $r = 0\,\%$, $\triangle r = 20\,\%$, $\triangle p = 5\,\%$ and step size $\delta p = 2.5\,\%$ in perfusion direction. The red arrow marks a part of the lung that is contrast–enhanced once the contrast agent passes the pulmonary circulation. (C/W=1300/1200 HU)

and domain filters may be used as well. In this study, however, we restricted ourselves to considering Gaussian–shaped filters. Since respiratory, cardiac and perfusion gating yields six–dimensional volumes $f(x, y, z, r, c, p)$ we can apply bilateral filtering in up to six dimensions. The corresponding domain filter parameters are denoted as σ_x, σ_y, σ_z, σ_r, σ_c and σ_p, respectively.

III. RESULTS

A. Digital Subtraction Angiography

Before any tomographic projections are acquired a phase–correlated digital subtraction angiography in anterior–posterior direction is performed to validate the correct placement of the needle. Similar to the tomographic scans ECG and respiratory signals are recorded during image acquisition. The DSA scan comprises 2000 projections within 20 s at a tube voltage of 80 kV and a tube current of 50 mA. The contrast bolus injection is started 10 s after the scan start ensuring that a sufficient amount of cardiac and respiratory phases have been acquired for a phase–correlated subtraction. The DSA images are obtained by subtracting a projection image acquired post injection from an appropriate projection image acquired before contrast injection within the same cardiac and respiratory phase. Such a digital subtraction angiography is shown in figure 1. The contrast agent in form of a bolus with a volume of about 25 µL is injected into the retro–bulbar sinus and arrives

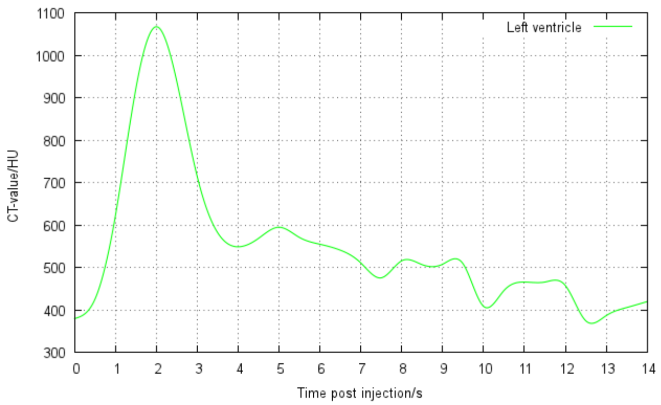

Fig. 3. Time–density curve in the left ventricle over 14 s.

in the right ventricle after about 1 s. The contrast media is further transported into the pulmonary circulation resulting in a contrast enhancement of the lung. The arrival of the contrast media in the left ventricle can be noted about 2 s post injection. After 3 s a contrast enhancement of the aortic arc and the aorta is clearly visible.

B. Reconstructions

Figure 2 shows coronal slices of a reconstructed perfusion scan using a cardiac window of $\triangle c = 20\,\%$, a respiratory window of $\triangle r = 20\,\%$ and a perfusion window of $\triangle p = 5\,\%$. Volumes were reconstructed in all temporal directions using step sizes of $\triangle c/2$, $\triangle r/2$ and $\triangle p/2$, respectively, to further limit the influence of the finite temporal resolution. The figure shows a perfusion series starting at $p = 0\,\%$, ending at $p = 27.5\,\%$. The flow of the contrast agent is clearly visible from the figure. The contrast media arrives in the right ventricle, is transported to the respiratory circulation (note the enhancement of lung tissue during this process – red arrow) and arrives in the left ventricle.

Image noise was measured in the difference images between to adjacent slices in z–direction to provide a fair comparison and to limit the influcence of artifacts. The noise evaluation showed that image noise is no greater than 70 HU in any of the reconstructed volumes.

Figure 3 shows the grey values in an ROI placed in the left ventricle. The first pass enhancement due to the contrast agent bolus appears after about 2 seconds and provides an enhancement of about 700 HU. Further reperfusion peaks can be found after 5 s, 8 s and 11 s.

IV. CONCLUSION AND DISCUSSION

The proposed scan and injection protocol in combination with the proposed reconstruction method allows for the reconstruction of phase–correlated volumes in any desired cardiac, respiratory and perfusion phase. The resulting images show no obvious streaking artifacts and image noise is at a reasonable level to easily allow for the identification of anatomical structures. The used contrast media administration technique is further minimal invasive allowing for a full recovery of the animals under examination and thus for longitudinbal studies. This boosts preclinical research as for the first time an easy and practical way of performing perfusion studies using small rodents was proposed.

ACKNOWLEDGEMENTS

This work was supported by the Deutsche Forschungsgemeinschaft (DFG) under grant FOR 661. The high–speed image reconstruction software RayConStruct–IR was provided by RayConStruct® GmbH, Nürnberg, Germany. The authors thank the Intel Corporation and Fujitsu Technology Solutions GmbH for providing their latest multicore hardware. The high–precision pump was assembled by Klaus Schewiola and Steffen Seeber at the DKFZ.

REFERENCES

[1] S. Sawall, F. Bergner, R. Lapp, M. Mronz, M. Karolczak, A. Hess, and M. Kachelrieß, “Low-dose cardio-respiratory phase-correlated cone-beam micro-CT of small animals,” *Medical Physics*, vol. 38, no. 3, pp. 1416–1424, 2011.

[2] M. Nahrendorf, C. Badea, K. W. Hedlund, J.-L. Figueiredo, D. E. Sosnovik, G. A. Johnson, and R. Weissleder, “High-resolution imaging of murine myocardial infarction with delayed-enhancement cine micro–CT,” *American Journal of Physiology–Heart*, vol. 292, no. 6, pp. 3171–3178, 2007.

[3] C. T. Badea, L. W. Hedlund, M. D. Lin, J. S. B. Mackel, E. Samei, and G. A. Johnson, “Tomographic digital subtraction angiography for lung perfusion estimation in rodents,” *Medical Physics*, vol. 34, no. 5, pp. 1546–1555, 2007.

[4] C. T. Badea, S. M. Johnston, E. Subashi, Y. Qi, L. W. Hedlund, and G. A. Johnson, “Lung perfusion imaging in small animals using 4D micro-CT at heartbeat temporal resolution,” *Medical Physics*, vol. 37, no. 1, pp. 54–62, 2010.

[5] C. Steel, A. Stephens, S. Hahto, S. Singletary, and R. Ciavarra, “Comparison of the lateral tail vein and the retro-orbital venous sinus as routes of intravenous drug delivery in a transgenic mouse model,” *Lab Anim*, vol. 37, no. 1, pp. 26–32, 2008.

[6] T. Yardeni, M. Eckhaus, H. D. Morris, M. Huizing, and S. Hoogstraten-Miller, “Retro–orbital injections in mice,” *Lab Anim*, vol. 40, no. 5, pp. 155–160, 2011.

[7] L. Feldkamp, L. Davis, and J. Kress, “Practical cone–beam algorithm,” *Journal of the Optical Society of America*, vol. 1, no. 6, pp. 612–619, Jun. 1984.

[8] G. C. McKinnon and R. Bates, “Towards imaging the beating heart usefully with a conventional CT scanner,” *IEEE Transactions on Biomedical Engineering*, vol. BME-28, no. 2, pp. 123–127, Feb. 1981.

[9] K. L. Garden and R. A. Robb, “3-D reconstruction of the heart from few projections: A practical implementation of the McKinnon–Bates algorithm,” *IEEE Transactions on Medical Imaging*, vol. MI-5, no. 4, pp. 233–239, Dec. 1986.

[10] C. Tomasi and R. Manduchi, “Bilateral filtering for gray and color images,” *Proc. 6th Int. Conf. Computer Vision*, pp. 839–846, 1998.

Improving Motion Accuracy for the McKinnon-Bates 4D-CBCT Reconstruction Algorithm

Mingshan Sun, Markus Oelhafen, Luis Carvalho, John Pavkovich, Timo Berkus, Josh Star-Lack

***Abstract*—On-board 4D cone-beam computed tomography (CBCT) is being actively pursued to help guide radiotherapy treatments of lung tumors. Among the existing 4D-CBCT methods, the McKinnon-Bates (MKB) reconstruction algorithm has the advantage of being computationally efficient and not requiring additional scan time much beyond a typical 1 minute 3D acquisition. The resulting images, however, can suffer from temporal hysteresis and ghosting artifacts that hinder tumor delineation and determination of motion trajectories. This work describes how the MKB algorithm can be improved by destreaking the prior image thus reducing ghosting artifacts and improving lung tumor conspicuity.**

***Index Terms*—Computed tomography, Cone-beam, Dynamic imaging, Reconstruction algorithms**

I. INTRODUCTION

As the precision of delivering a high intensity radiotherapy dose to a local target increases, the need for "on-board" imaging techniques to accurately localize the target also increases. This particularly applies to cases where intra- and inter-faction motion is significant, as for thoracic treatments.

On-board 4D-CBCT has the potential to appreciably improve motion management during radiotherapy treatment of lung tumors. 4D-CBCT can be used to determine a tumor's "trajectory-of-the-day" that, when correlated with an external surrogate, enables real time beam gating or multi-leaf collimator (MLC) tracking to be performed. This may allow for a reduction of treatment margins thus reducing normal tissue toxicities.

CBCT acquisition times in a radiotherapy environment are typically on the order of 1 minute due to slow gantry rotation times and flat panel detector readout limitations. This creates a challenge for lung tumor imaging where sub-second temporal resolution is required to resolve respiratory-induced motion.

A workaround is to assume that respiratory-related motion is periodic, and to sort and group the projections according to their respective phases in the respiratory cycle. Each projection group is reconstructed separately and the resulting images are combined to form a 4-D image. However, since only a limited number of breathing cycles occur in a typical acquisition, sparse angular sampling patterns are created, which cause severe streaking artifacts in the final reconstructions. One means of reducing these view aliasing artifacts is to further decrease the gantry rotation speed thereby increasing the total number of breathing cycles in a scan [1] which, unfortunately, increases scan times and radiation dose. Recently, it has been shown [2, 3] that the computationally efficient McKinnon-Bates algorithm (MKB) [4] has the potential to significantly reduce view aliasing artifacts for 1-minute acquisition times, but that temporal resolution can be compromised. In this work, an inherent shortcoming in the original MKB algorithm is identified and a solution to overcome this limitation and restore temporal resolution is proposed.

II. METHOD

The original MKB algorithm is outlined in Figure 1. A time-averaged **prior image** is first reconstructed, from which reprojections are computed at the same angles as the original projections. Differences are taken between the original projections and the reprojections, and a **difference image** is reconstructed for each motion phase bin. Each difference image is then added to the time-averaged prior image to create each **phase image**.

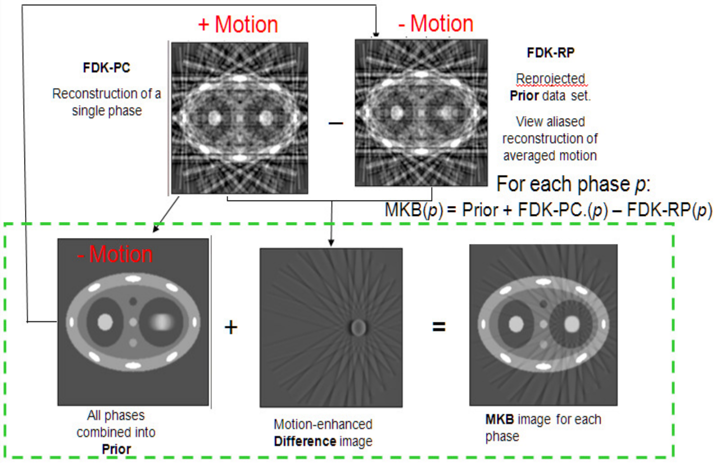
+ Motion
- Motion
FDK-PC
Reconstruction of a single phase
–
FDK-RP
Reprojected Prior data set.
View aliased reconstruction of averaged motion
For each phase p:
MKB(p) = Prior + FDK-PC.(p) – FDK-RP(p)
- Motion
+
=
All phases combined into Prior
Motion-enhanced Difference image
MKB image for each phase

Fig 1. The Mckinnon-Bates (MKB) 4D reconstruction algorithm. A motion-blurred **prior** image is reconstructed with the FDK algorithm using all projections belonging to all respiratory phases. The prior is then forward-projected and the resulting projections are subtracted from the original projections to create motion-enhanced difference projections. These projections are convolved and backprojected to create **difference** images (one for each respiratory phase), which are then added to the prior image to create the final streak-reduced phase-correlated images.

J. Star-Lack (phone: 650-251-5544; fax: 650-251-5501; e-mail: josh.star-lack@ varian.com), J. Pavkovich and M. Sun are with Varian Medical Systems, Ginzton Technology Center, Palo Alto, CA 94304 USA.

Markus Oelhafen, Luis Carvalho and Timo Berkus are with Varian Medical Systems, Imaging Laboratory, Baden-Daettwil, Switzerland.

Figure 2 shows simulation results from a digital lung phantom [2] containing an object moving horizontally. As shown in Fig. 2c, a single-phase image reconstructed by the original MKB algorithm exhibits ghosting near the moving object. This ghosting results because a key assumption in the algorithm is not fulfilled, which is that the prior image is a time-averaged representation of all phases. As shown in Fig 2b, the FDK-reconstructed prior contains streaks caused by motion-induced inconsistencies. These streaks, which after being forward-projected, encode unwanted motion-related information into the re-projections are the cause of the undesired ghosting artifacts. When a streak-free prior (Fig 2d) is used, ghosting is eliminated and the moving object is well defined (Fig 2e).

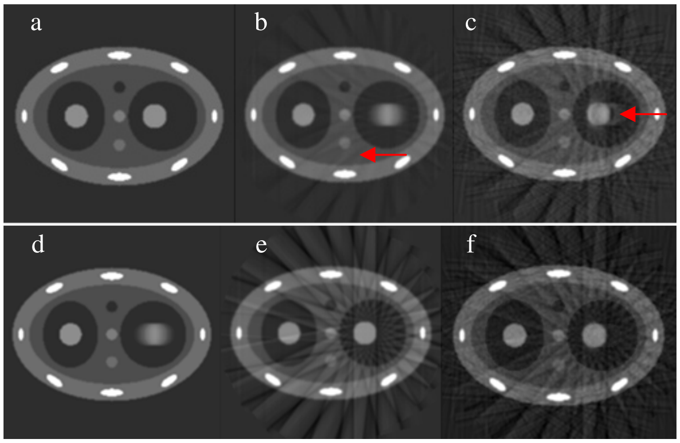

Fig. 2. a) Digital motion phantom. b) Reconstructed prior showing streaks emanating from the moving object (an example is shown by the arrow). c) A single phase of the MKB reconstruction showing ghosting (indicated by the arrow). d) Ideal time-averaged prior with no motion streaks. e) MKB reconstruction of a single-phase image based on the streak-free ideal prior showing no ghosting. f) MKB single-phase image based on the destreaked prior using the proposed algorithm.

These results suggest that the key to improving the MKB algorithm is to remove motion-induced streaks from the prior image. Our proposed prior destreaking method is based on a combination of segmentation and boundary erosion operations, and is designed to make the prior more uniform while minimizing discontinuities.

A. *Prior image de-streaking*

The destreaking method we propose, named *threshold erosion*, is outlined below:

1) Select a set of CT number (HU) thresholds that best separate key target segments - air, lung, soft tissue, and bone.
2) Apply the thresholds and segment the corresponding structures accordingly.
3) For each structure, erode its boundary by and amount ranging from 2-5 mm.
4) Replace the un-eroded pixels in each structure with the mean HU value of the structure. This fills the inner region of each segment with a constant value, thus removing the streaks. The erosion and replacement operation creates a transition zone between neighboring segments. By preserving the original intensity values at these tissue boundaries, discontinuities that introduce streaking in the difference images are prevented.

The threshold plus erosion process is graphically illustrated in Fig. 3.

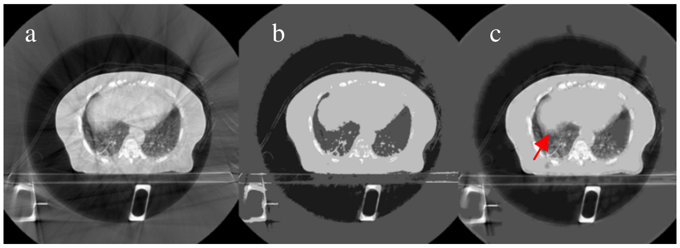

Fig. 3. Destreaking method. a) original prior; b) segmentation into bone, air, lung tissue, muscle/fat; c) boundary erosion (example shown by arrow).

We choose HU-based thresholds to segment key tissue types since the mean intensities of air, lung, soft tissue, and bone differ significantly. For a well calibrated system with stable performance, air has an intensity of -1000 HU, lung values are in the range of -750 to -650 HU, other soft tissue values (fat, muscle etc) range between -150 to 100HU, and bone values are generally above 700 HU. Thresholds could thus be simply set to -800 HU, -300 HU and 300 HU, for example, to safely separate one tissue type from another. However, due to the existence of image artifacts from motion and other sources, as well as patient-to-patient variations in anatomy, we have found it impractical to use the same thresholds for all cases. It is thus desired to determine optimal thresholds for the 3D prior image in a robust fashion. Here we describe an efficient automatic thresholding algorithm.

B. *Adaptive thresholding*

One of the methods commonly used for automatic thresholding is the k-means algorithm [5], which is well suited to problems that have a fixed number of segments or classes. In our case, there are four segments - air, lung, soft tissue, and bone, and three thresholds separating these four classes.

The k-means algorithm makes an initial guess as to the thresholds and evolves them iteratively until convergence is reached:

k-means algorithm:

1) Initialize thresholds to default values
2) Segment the image.
3) Calculate the mean of each segment.
4) Set the new thresholds so that they are halfway between the mean values of adjacent classes.
5) Check for convergence.
6) If convergence has not been achieved, then repeat steps 2-5.

There are several important considerations in the segmentation process that are unique to thoracic CBCT applications. First, of the four segments, bone occupies only a small fraction of the total voxels in typical lung scan. Thus, its presence in the intensity histogram may be too small to provide an accurate measure of its mean value. As a result, we set the soft tissue-to-bone threshold to be a fixed offset relative to the mean soft-tissue intensity.

We have also observed that the air-lung threshold should be set closer to the air intensity value than the lung intensity value to ensure that, after thresholding, the lung voxels do not contain abnormal amounts of "air" (-1000HU). In this way, the destreaked lung is more uniform, reducing noise in the individual phase images.

For computational efficiency and for purposes of simplicity, we apply the algorithm only to the central slice of the volume. In addition, because the prior image can be larger than the scanned field-of-view, particularly after de-truncation operations are performed, only the central region of the central slice is used.

Considering all the above points, the entire auto-thresholding procedure is described as follows:

1) Extract the central slice of the prior image volume
2) Mark a central ROI with a diameter of 44 cm. Mask out everything outside the ROI.
3) Apply the modified k-means algorithm with k=4 to the data in the ROI as follows:
    a. Initialize the thresholds based on standard tissue intensity values.
    b. Calculate the means for air, lung, soft-tissue, and bone.
    c. Set the new thresholds midway between each of the adjacent mean pairs.
    d. Adjust the soft tissue-to-bone threshold to be equal to the soft tissue mean + 300 HU.
    e. Check for convergence. If the difference between the thresholds from this and the previous iteration is within 1 HU, assume that convergence is reached. If not, go to step b.
4) Reset the air-to-lung threshold so that it is not halfway between the lung and air values, but 3 times further from the lung mean than the air mean, i.e. to a value equal to 0.75 mean(air) + 0.25 mean(lung)

Note the algorithm can be applied to more than one slice or a significant portion of the volume.

C. *Experimental study*

The prior destreaking method was tested on simulated data and *in vivo* data sets from lung tumor patients imaged with either the Varian OBI or Varian TrueBeam systems. The *in vivo* scans were acquired using the offset-detector geometry where the detector is laterally offset by 16cm to increase the FOV. Approximately 660 projections were taken over 360 degrees with a 1-minute rotation time. After reconstruction, assessments of the sharpness of the moving objects and accuracy of motion were made, and comparisons were performed between the original MKB algorithm, the improved MKB algorithm, and the standard phase-correlated (PC) reconstruction approach.

III. RESULTS

Application of prior destreaking produced substantially improved images compared with those from the original MKB algorithm and from the traditional phase-correlated algorithm. The digital phantom results in Fig. 2 show that ghosting from the moving sphere is removed after application of the proposed modification (Fig 2f).

Typical results from a patient scan are shown in Figure 4. Without prior destreaking, there is almost no change in diaphragm position between the inhale and exhale phases (Fig 4a). With prior destreaking, diaphragm motion is well resolved and measured at +/-7mm and +/-6mm for the left and right sides respectively (Fig 4b). These displacement values match those seen in the standard phase-correlated (PC) reconstructions (Fig 4c). However, unlike in the PC reconstruction, the improved MKB reconstruction has sufficient SNR to visualize the tumors (arrows).

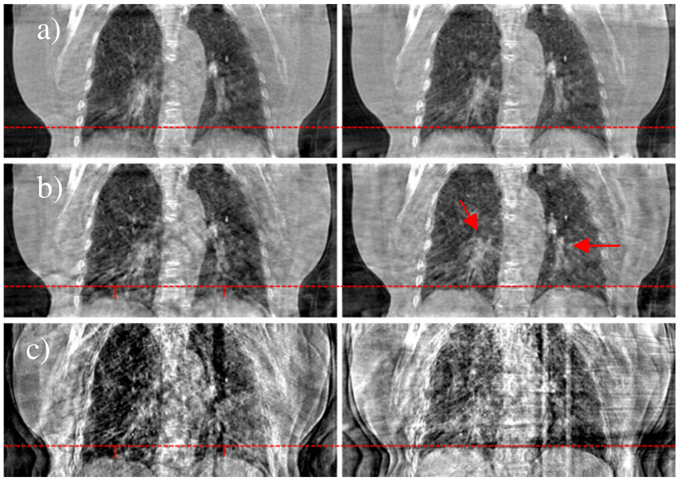

Fig. 4. a) Traditional MKB reconstruction without prior destreaking shows little difference in the diaphragm position between the inhale (left column) and exhale phases (right column) b) After prior destreaking, diaphragm motion is evident. Motion is measured at +/-7mm and +/-6mm for the left and right sides, respectively. c) Standard phase-correlated (PC) reconstruction verifies the diaphragm motion amplitudes measured in b), but are too noisy to visualize the tumors (arrows).

The ability to adaptively adjust the thresholds for a given data set makes the destreaking technique more robust to HU inconsistencies which can result from, for example, data truncation, object scatter, or system miscalibration. To investigate the robustness of the algorithm, we applied a 20% HU scaling error and a 500 HU offset to one of the *in vivo* data sets. As shown in Figure 5, the auto-thresholding algorithm yields virtually the same destreaked image quality in the miscalibrated images as in the calibrated images, demonstrating that, although the algorithm is based on a global thresholding approach, HU inaccuracies and errors in the prior image are well-tolerated.

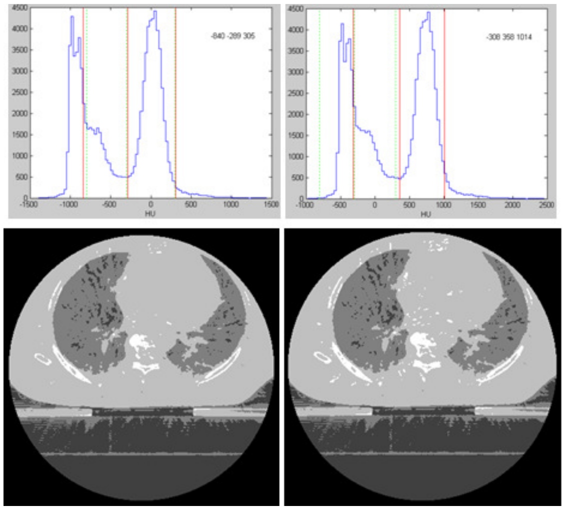

Fig 5. The autothresholding algorithm is robust to HU scaling and offset errors. The left column contains the auto-thresholding result when starting with accurate HU values. The right column shows results after a 20% HU scaling error and 500 HU offset were first applied to the images. The top row shows the respective histograms (threshold boundaries are in red) while the bottom row shows the respective slices. The two destreaked slices are of equivalent quality.

As shown in Figure 6, the automatic thresholding algorithm is also robust to metal artifacts. We surmise that this is because the algorithm uses the soft tissue intensities to infer the soft tissue-to-bone threshold rather than segmenting the bone itself, a process that could be confused by the presence of metal.

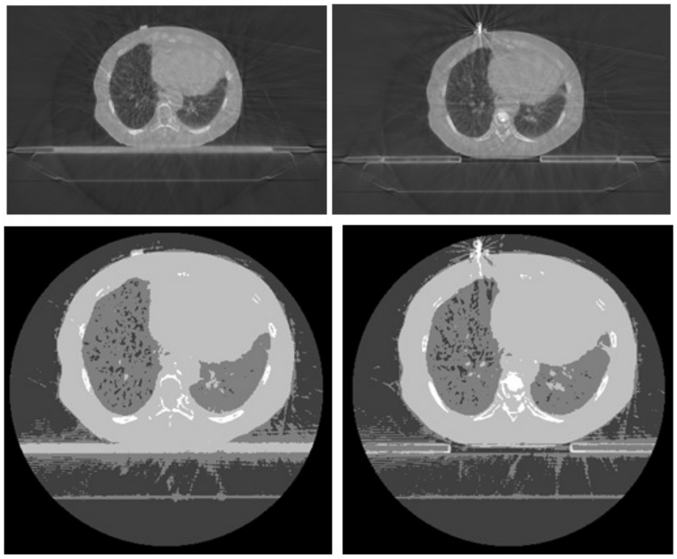

Fig 6.. Autothresholding is robust to metal artifacts. The top row contains images before destreaking is applied while the bottom row contains images that have been destreaked. Metal is present in the images in the right column.

IV. CONCLUSIONS

The MKB algorithm is enhanced by destreaking the prior image before reprojection, resulting in increased motion conspicuity and elimination of ghosting in the final 4-D images. The proposed destreaking technique is shown to be efficient and robust to anatomy variations , metal artifacts, and systemic HU errors.

Of note is that, while the destreaking operation improves the image quality of moving objects, it also can increase noise in the final images when compared to images produced by the traditional MKB algorithm. The increased noise can be addressed by applying a 4-D bilateral nonlinear filter to the final phase images [6]. When implemented on a GPU, the computation time required is minimal.

In summary, we describe an important enhancement to the McKinnon-Bates algorithm that improves spatial and temporal resolution for 4-D CBCT. The approach allows for images to be acquired and reconstructed in a sufficiently short period of time to enable essential image-guided radiotherapy applications such as patient set-up.

ACKNOWLEDGMENTS

The authors thank Drs. Peter Munro and Patrik Kunz for helpful discussions.

REFERENCES

[1] J. J. Sonke, L. Zijp, P. Remeijer and M. van Herk, "Respiratory correlated cone beam CT," Med Phys 32, 1176-1186 (2005).

[2] S. Leng, J. Zambelli, R. Tolakanahalli, B. Nett, P. Munro, J. Star-Lack, B. Paliwal and G. H. Chen, "Streaking artifacts reduction in four-dimensional cone-beam computed tomography," Med Phys 35, 4649-4659 (2008).

[3] F. Bergner, T. Berkus, M. Oelhafen, P. Kunz, T. Pan, R. Grimmer, L. Ritschl and M. Kachelriess, "An investigation of 4D cone-beam CT algorithms for slowly rotating scanners," Medical Physics 37, 5044-5053 (2010).

[4] G. C. McKinnon and R. H. T. Bates, "Towards imaging the beating heart usefully with a conventional CT scanner," IEEE Trans Biomed Eng 28, 123-127 (1981).

[5] J. B. MacQueen, "Some Methods for classification and Analysis of Multivariate Observations", Proceedings of 5-th Berkeley Symposium on Mathematical Statistics and Probability, Berkeley, University of California Press, 1:281-297 (1967)

[6] Z. Zheng, M. Sun. J. Pavkovich, J. Star-Lack. "Fast 4D Cone-Beam CT Reconstruction using the McKinnon-Bates algorithm with truncation correction and nonlinear filtering". Proc. SPIE Medical Imaging, 7961 2011

Temporal Resolution and Motion Artifacts in Dual-Source Cardiac CT and Single-Source CT with Iterative Reconstruction

Harald Schöndube, Thomas Allmendinger, Steffen Kappler, Herbert Bruder and Karl Stierstorfer

I. INTRODUCTION

The temporal resolution (TR) of an image has become an important property in computed tomography (CT) when examining organs whose motion can not be stopped for the duration of the CT scan, such as in cardiac CT. In this context, "higher TR" conventionally means that the raw data from which a given image was reconstructed was measured within a shorter time interval than the raw data of a similar image with a lower TR value. Since object motion during data acquisition will inevitably lead to artifacts in the reconstructed image, and "more motion" usually also means "more artifacts", there are typically less motion artifacts visible in a high TR image of a moving object than in an image with lower TR of the same object. One essential property of TR is that it is not necessarily constant within a given image. The stated quantity therefore usually refers to the value in the isocenter (i.e., at the intersection point of the image plane with the rotation axis of the CT system) [1], [2].

For single-source CT (SSCT) and conventional filtered backprojection (FBP) reconstruction, the topic of TR in CT images has been extensively studied (see, e.g., [1], [2] and references therein). For the case of dual-source CT (DSCT) some practical experiments exploring the TR of reconstructed images either in the isocenter or in the full field-of-view (FOV) have been published [3], [4], but to our knowledge a theoretical analysis of raw data usage within the FOV and its implications on the resulting TR has never been performed so far. Another important point that has so far not been studied is the question if "same TR" also necessarily implies "same amount of motion artifacts in the reconstructed images" in the context of SSCT and DSCT. The same question can be raised in the context of iterative reconstruction methods with enhanced TR such as TRI-PICCS [5] and TRIM [6]. The purpose of this paper is to address these topics. We will begin our considerations with an introduction into cardiac CT and a comprehensive review of the TR properties in conventional SSCT. From there, we will discuss the extension of these properties to iterative reconstruction methods. Finally, we will explore the application of our results to DSCT. For brevity and simplicity, our discussions will be limited to two-dimensional data acquisition and reconstruction. However, all our results presented in this paper are also directly applicable to both circular and helical cone-beam CT.

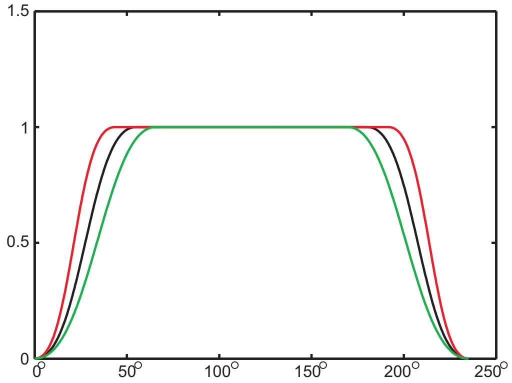

Fig. 1. Relative projection weights that each fan-beam projection receives in a short-scan FBP with Parker weighting at different pixel locations: isocenter (black), at the edge of the FOV located away from the short-scan segment (red) and at the edge of the FOV located closest to the short-scan segment (green)

II. TEMPORAL RESOLUTION AND MOTION ARTIFACTS IN SINGLE-SOURCE CT

The goal in cardiac CT is to maximize the TR of the reconstructed image. In conventional SSCT this amounts to using just as much raw data as necessary for a stable (approximate or theoretically-exact) image reconstruction. Since for each image pixel a relative data angular coverage of at least 180° as viewed from the location of the pixel is necessary to achieve this goal [7], two approaches are commonly used: either a direct short-scan fan-beam FBP reconstruction using the Parker weighting scheme [1] or an algorithm employing a rebinning step to parallel beam geometry followed by a 180° parallel-beam FBP reconstruction.[1] In this section, these two approaches and their respective TR distributions will be reviewed and compared.

A. Fan-beam FBP with Parker weighting

As mentioned above, for each image pixel an angular coverage of at least 180° as viewed from the location of the

Manuscript received February 1st, 2012.

All authors are with Siemens AG, Healthcare Sector, Imaging & Therapy Division, Computed Tomography & Radiation Oncology, Forchheim, Germany. Contact: harald.schoendube@siemens.com

---

[1] In the past the so-called multi-segment reconstruction, in which raw data segments from several consecutive heart beats are combined, has also been used extensively to maximize TR [1], [2]. In the optimal case, its properties with respect to TR are similar to the case of DSCT discussed below. A further analysis of this topic is, however, beyond the scope of this paper.

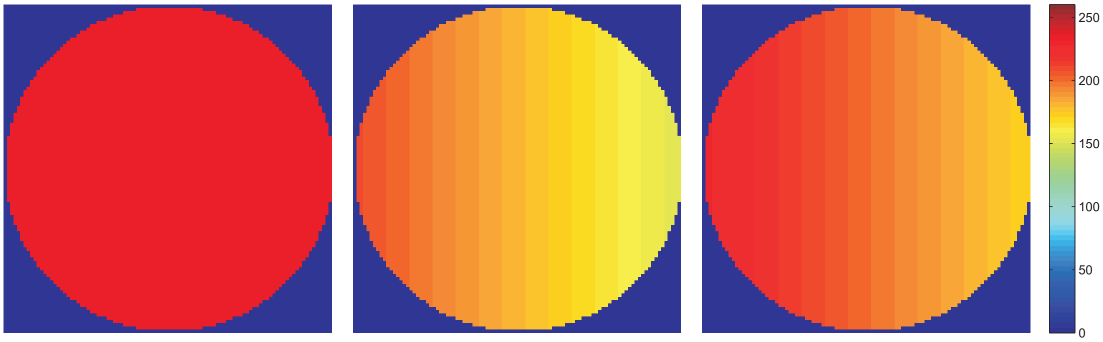

Fig. 2. Total TR of fan-beam FBP with Parker weighting (left), FWHM-TR of both fan-beam and rebinned FBP (center), total TR of rebinned FBP with 20° of transition weight (right).

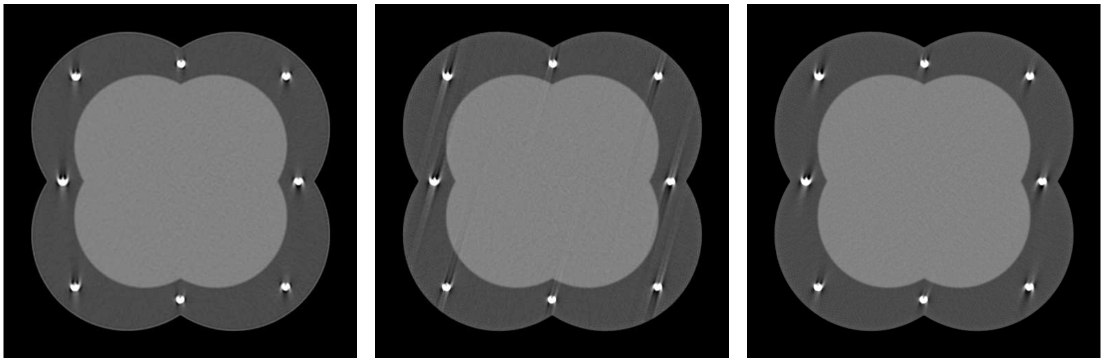

Fig. 3. Images reconstructed from SSCT data using a direct fan-beam FBP with Parker weighting (left) and a parallel-beam rebinning FBP with no transition weight (center) and 30° transition weight (right).

pixel is required to ensure a stable image reconstruction. To cover the complete FOV, a data range of $180° + 2 \cdot \gamma_{\max}$, where $\gamma_{\max}$ denotes the maximum fan angle, is therefore necessary. However, for all pixels in the FOV besides the one at maximum distance from the short-scan source trajectory this means that a certain degree of redundancy in the data has to be taken into account. For this task, the Parker weighting scheme [7], [8] is commonly employed. The resulting relative weights that each projection receives for the reconstruction of a given image pixel are displayed in fig. 1 for three different representative pixel locations [1].

At this point, we need to refine the term "temporal resolution". Relative to the weight that each projection receives during backprojection, two definitions are commonly adapted: either, the total time interval from the first to the last projection that contribute to a given pixel is considered, or only the full width at half maximum (FWHM) of the weight function is used as TR measure. As can be clearly seen in fig. 1, the two quantities can potentially differ significantly. For clarity we will use the terms "total TR" and "FWHM-TR" in the remainder of this paper. Both quantities will be stated in terms of the angular range of fan-beam FBP projection data required to achieve a stable reconstruction at a given location to enable a representation that is independent of gantry rotation times.

In the case of a fan-beam FBP with Parker weighting, total TR is constant within the full FOV and corresponds to an angular range of $180° + 2 \cdot \gamma_{\max}$ of fan-beam data. In contrast, FWHM-TR is location-dependent, with the value in the isocenter corresponding to 180° of fan-beam data. The distributions of the TRs for $\gamma_{\max} = 27.5°$ within a typical cardiac FOV of about 25cm diameter are displayed in fig. 2 (left and center). Note that in these as well as all other plots of this kind in this paper, the center of the short-scan vertex path was assumed to be located at the three o'clock position relative to the image. An example reconstruction of a simulated object which features a continuous linear motion of the high contrast "vessels" away from the image center is shown in fig. 3 on the left, with the center of the short-scan again being located at the three o'clock position relative to the image.

B. Rebinning to parallel-beam geometry

A different approach for cardiac CT reconstruction is to rebin the data into the parallel-beam geometry first and then to perform a parallel-beam FBP reconstruction over a data range of 180° of rebinned data. Due to the properties of the rebinning operation, this procedure ensures that only the amount of the original fan-beam data that is minimally necessary for a stable reconstruction is used at each pixel location. The relative weight that each of the *original fan-beam projections* receives for the same three representative pixel locations as above is plotted in fig. 4. From the plot, it is intuitively clear that both total TR and FWHM-TR are identical in this case. Interestingly, both are also identical to the FWHM-TR of images reconstructed using a fan-beam FBP with Parker weighting (cf. fig. 2, center).

However, when looking at the example reconstruction shown in fig. 3 in the center, the result is disappointing:

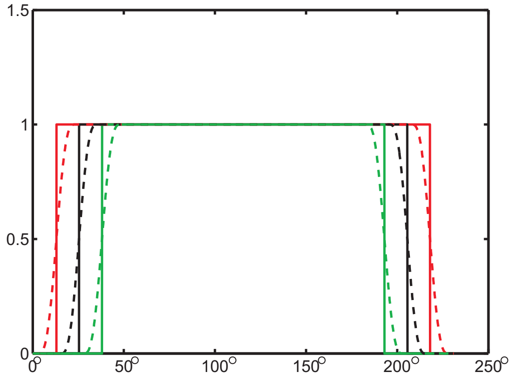

Fig. 4. Relative projection weights that each fan-beam projection receives in a parallel-beam rebinned FBP with no transition weight (solid lines) or with a transition weight equivalent of 20° (dashed lines) at different pixel locations: isocenter (black), at the edge of the FOV located away from the short-scan segment (red) and at the edge of the FOV located closest to the short-scan segment (green).

even though the motion artifacts compared with the case of direct fan-beam FBP are slightly reduced (cf. fig. 3, left), new, so-called "quickscan" artifacts stretching over large distances are visible in the image. These artifacts result from the fact that due to the object motion opposing parallel projections do not match. To remove these artifacts, the transition at the beginning and the end of the reconstruction range needs to be softened by extending the reconstruction data range by a certain amount (e.g., 30°) and employing transition weights to account for the newly added redundancy. For the case of a transition range of 30°, the relative weight that each of the original fan-beam projections receives is plotted in fig. 4. As can be discerned by comparing the plots with and without transition weight, the FWHM-TR does not change by employing the transition weight while the total TR is reduced proportional to the amount of redundant data added. The resulting distribution of the total TR is displayed in fig. 2 on the right, an example image is shown in fig. 3 on the right.

In conclusion, images both from fan-beam FBP with Parker weighting and from parallel-beam rebinned FBP share the same distribution of FWHM-TR. Total TR, however, is better when employing the parallel-beam rebinning, even when adding a moderate transition range to remove quickscan artifacts.

III. ITERATIVE RECONSTRUCTION METHODS

One way to further improve the TR of a fan-beam FBP image with Parker weighting is to apply an algebraic iterative algorithm such as SART or SIRT: One can use the fan-beam FBP image as start image and then perform the iteration using only the first or the second half of the fan-beam data. The resulting image looks very similar to the image reconstructed with parallel-beam FBP from 180° of rebinned data with no transition weight (see fig 5, center-left, reference image in the same figure on the left). This effect can be explained by visualizing the iterative process in the case of redundant data: For projection directions where redundant projections are used to reconstruct the image the forward projected data will be a weighted average between the two projections. This forward projected data will then be compared to only one of the input projections and the difference is used to update the image. Since only part of the original input data (and therefore no redundant data) is used for the iteration, all redundancy is removed from the image after some iterations.

An interesting observation can be made when comparing this result to the TRI-PICCS algorithm proposed by Chen et. al. [5]. In TRI-PICCS, the SART iteration as described in the previous paragraph is complemented by an additional iterative step which aims to minimize a linear combination of the TV norm of the target image and the TV norm of the difference between the target image and the Parker-weighted input image. TRI-PICCS uses exactly the same iteration range as the linear SART approach above, but due to the additional TV step constitutes a non-linear iterative algorithm. In the resulting image (cf. fig. 5, center-right), the level of motion artifacts is about the same as when employing the linear iteration approach or the parallel-rebinned FBP. In contrast to the latter two, however, there are somewhat less quickscan artifacts visible in the TRI-PICCS image. An even better result can be reached when employing the (also non-linear) TRIM algorithm [6] (cf. fig. 5, right). It is interesting to note that although all three iterative approaches are using the same iteration data range the output image differs significantly. This confirms an observation earlier made by Maass et. al. [4] that in the context of iterative reconstruction the data input range alone does not allow definite conclusions about the TR or the motion artifact level of the resulting images.

IV. DUAL-SOURCE CT

In DSCT a parallel-rebinned FBP is commonly used for reconstruction; due to space constraints we will only discuss this case. The two source-detector systems are mounted such that the angle between them is 90°. The minimum range for a stable FBP reconstruction is thus two times 90 ° of rebinned data. Due to the linearity of the FBP, the DSCT reconstruction can be imagined as first reconstructing a sub-image by applying a FBP over 90° of rebinned data from each of the source-detector systems and then adding the two sub-images to obtain the final reconstruction. The DSCT FWHM-TR can thus be computed at each pixel location as the average of the individual FWHM-TR of the two sub-images, whereas for the total TR the maximum value of the total TR of the sub-images must be taken. The resulting distributions of the FWHM-TR and the total TR are displayed in fig. 6 both for the case with no transition weight and for a transition weight of 20°. Note that at each pixel location the value of FWHM-TR is exactly half the one of SSCT with a parallel-rebinned FBP (cf. fig 2).

The better TR of DSCT is also reflected in the reconstructed images. Fig. 7 shows an image reconstructed from SSCT data on the left and a DSCT image at the center. Both data sets were simulated with the same gantry rotation time, yet the motion artifacts in the DSCT case are significantly smaller. An unexpected observation can be made, however, when examining the image in the same figure on the right, which was reconstructed using *two times 180° of rebinned*

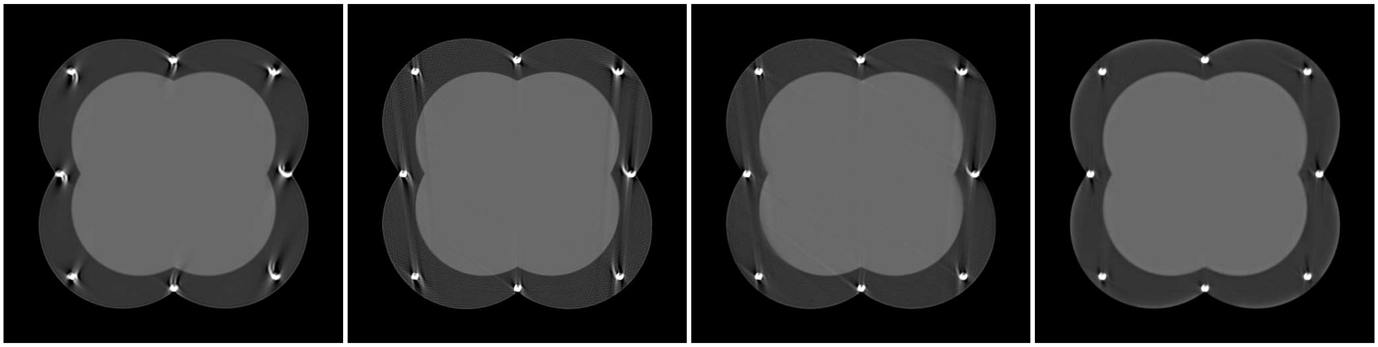

Fig. 5. Images reconstructed from simulated data: using a fan-beam FBP with Parker weighting (left), using fan-beam FBP with an SART approach to improve the TR (center-left), using TRI-PICCS (center-right) and using TRIM (right).

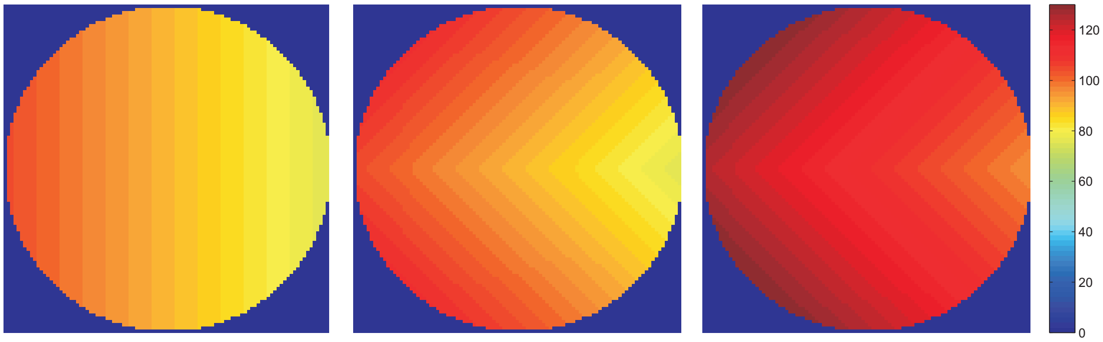

Fig. 6. FWHM-TR (left), total TR with no transition weight (center) and total TR with 20° transition weight (right) for DSCT.

DSCT data instead of the usual two times 90°. One would naïvely expect the TR being equivalent to the SSCT case, with a deeper analysis confirming that the distribution is indeed very similar[2]. However, the motion artifact level is much lower than in the SSCT case. Apparently, seeing the same motion from two different angles and therefore adding a certain degree of redundancy can help suppressing motion artifacts. It is therefore important to note that when comparing SSCT and DSCT, "same TR" does not necessarily imply "identical level of motion artifacts".

V. CONCLUSION

In this paper, we have examined the distribution of the TR in DSCT and compared it to the SSCT case. Our results show that in terms of its FWHM, DSCT exactly doubles the TR compared to SSCT at each pixel location. However, our experiments also show that one needs to be very careful when assessing TR, as even for the same theoretical TR the motion artifact level can differ significantly. The same holds true for approaches aiming to enhance TR via iterative methods: even when using the same input data, the resulting images show significant differences in terms of motion or quick-scan artifacts. Consequently, metrics which do not only simply measure the TR but also take the motion artifact level into account appear to be necessary for a qualified comparison of cardiac CT reconstruction algorithms (cf. [4]).

REFERENCES

[1] J. Hsieh, *Computed Tomography - Principles, Design, Artifacts and Recent Advances*, ser. SPIE Press monograph. Bellingham, WA: SPIE Press, 2003.

[2] B. M. Ohnesorge, T. G. Flohr, C. R. Becker, A. Knez, and M. F. Reiser, *Multi-slice and Dual-source CT in Cardiac Imaging*, 2nd ed. Berlin: Springer Verlag, 2007.

[3] C. H. McCollough, B. Schmidt, L. Yu, A. Primak, S. Ulzheimer, H. Bruder, and T. G. Flohr, "Measurement of temporal resolution in dual source CT," *Medical Physics*, vol. 35, no. 2, pp. 764–768, 2008. [Online]. Available: http://link.aip.org/link/?MPH/35/764/1

[4] C. Maaß and M. Kachelrieß, "Quantification of temporal resolution and its reliability in the context of TRI-PICCS and dual source CT," in *Medical Imaging: Physics of Medical Imaging*, N. J. Pelc, E. Samei, and R. M. Nishikawa, Eds., vol. 7961, no. 1. SPIE, 2011, p. 79611M. [Online]. Available: http://link.aip.org/link/?PSI/7961/79611M/1

[5] G.-H. Chen, J. Tang, and J. Hsieh, "Temporal resolution improvement using PICCS in MDCT cardiac imaging," *Medical Physics*, vol. 36, no. 6, pp. 2130–2135, 2009. [Online]. Available: http://link.aip.org/link/?MPH/36/2130/1

[6] H. Schöndube, H. Kunze, H. Bruder, and K. Stierstorfer, "Using the positivity constraint to enhance temporal resolution in CT," in *Proceedings of the first international Conference in X-ray Computed Tomography (Salt Lake City, USA)*, June 2010, pp. 189–193.

[7] A. C. Kak and M. Slaney, *Principles of Computerized Tomographic Imaging*. IEEE Press, 1998, available online at http://www.slaney.org/pct/pct-toc.html.

[8] D. L. Parker, "Optimal short scan convolution reconstruction for fan beam ct," *Medical Physics*, vol. 9, no. 2, pp. 254–257, 1982. [Online]. Available: http://link.aip.org/link/?MPH/9/254/1

---

[2] Further details are omitted here due to space constraints

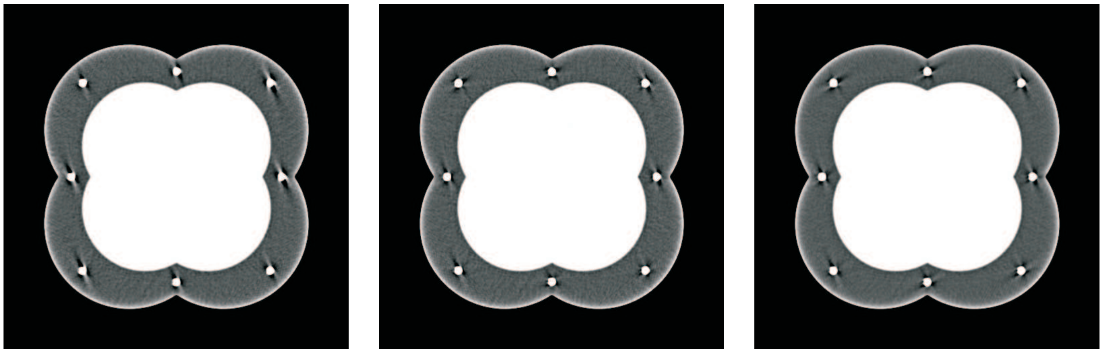

Fig. 7. Images reconstructed from 180° SSCT data (left), 2×90° DSCT data (center) and 2×180° DSCT data (right).

Evaluation of Low Dose CT Perfusion Using a Reproducible Biological Phantom

Juan C. Ramirez-Giraldo, Scott Thompson, Bruce Knudsen, Lifeng Yu, David A. Woodrum
Mathew R.. Callstrom, Cynthia H. McCollough

***Abstract*—The purpose of this study was to evaluate the feasibility of using a fixed *ex vivo* porcine liver to systematically evaluate dose reduction strategies in computed tomography perfusion (CTP). A biological phantom was created with a fixated liver and connected to a continuous flow pump. The liver was submerged in a body-shaped acrylic phantom of 32 cm diameter, and filled with water. Four cine-mode CTP scans were performed using 80 kVp and 400, 400, 100 and 20 mAs. Frequency was 1 scan per second, and total scan time was 50 s. Two seconds after each CTP scan, 4 cc of iodine contrast agent (300 mg/ml) were injected at 1 cc/s. Images were processed with commercially available software to estimate perfusion parameters such as blood flow (BF), blood volume (BV) and mean transit time (MTT). Selected regions-of-interest (ROIs) were traced to assess the agreement of time-attenuation-curves and to compare the perfusion parameters estimates. The percent RMS error in the time-attenuation-curves between the first 400 mAs scan and subsequent scans at 400, 100 and 20 mAs were 1.0%, 2.9% and 4.3% (input function) and 2.8%, 8.4%, 15.5% (tissue ROIs), respectively. The average error across three tissue ROIs were 12.1%, 25.5%, 85.5% for BF, 6.45%, 7.1%, 68.2% for BV, and 10.5%, 36.9%, 31.4% for MTT, for the 400, 100 and 20 mAs acquisitions respectively. It was found that the biological phantom was highly reproducible as demonstrated by the small differences in time-attenuation-curves. Quantitative perfusion estimates of BF, BV and MTT agreed within 12% for identical CTP acquisitions. Low dose acquisitions revealed lower perfusion parameter accuracy. The developed biological phantom can be used to determine the lowest dose CTP scan protocols that provide accurate perfusion estimates.**

***Index Terms*— CT perfusion, Phantom, Radiation dose reduction.**

I. INTRODUCTION

THE use of CT perfusion (CTP), provides an opportunity for functional assessment of vascular and oncologic diseases [1, 2]. A primary concern however with CTP that precludes its widespread use in clinical practice is the radiation dose. Higher radiation dose is expected in CTP because multiple time-resolved images of the same anatomic section are required to track the transient arrival and washout of contrast media. The signal is then used to fit a model to ultimately estimate perfusion.

Several strategies exist that can help in decreasing radiation exposure in CTP examinations. First, it is advantageous to use a lower tube potential of 80 or 100 kVp, instead of the typical 120 kV employed commonly in routine anatomical CT scanning, given the appropriate body habitus [3, 4]. Likewise, it is possible to reduce the tube current time product, since the functional task is different from the one required for anatomical CT scanning [5]. A challenge that results from reducing both the tube current and tube potential is the increase of image noise in the data and potential increase of susceptibility to artifacts. Several strategies have emerged to address the excessive noise of low dose acquisitions including iterative reconstruction methods [6], as well as processing of either the x-ray projections [7] or the image datasets [8]. Dedicated algorithms to reduce image noise in time-resolved CT sequences have also been developed [9, 10].

Another approach to spare radiation dose pertains to the reduction of the scan frequency and total acquisition time [11, 12]. The advantage of this approach is that the image quality is preserved in each individual image. However, a potential shortcoming of this approach is that insufficient temporal sampling might lead to inaccurate perfusion estimates. A further complication is the existence of various perfusion models such as deconvolution [13] and the maximum slope [14], without consensus on which one to use [15, 16].

With the exception of brain CTP [17], there exists no consensus or explicit guidelines on acquisition parameters (tube potential, tube current), scan frequency, total scan time or perfusion model. Further, this task will probably be application dependent (i.e.

Manuscript received February 1, 2012. This work was supported in part by the American Heart Association, predoctoral fellowship 10PRE2560028, NIH Grant No. R01EB07986 from National Institute of Biomedical Imaging and Bioengineering, and by the NIH Opus CT Imaging Resource Construction Grant No. R018898.

J.C. Ramirez-Giraldo, L. Yu, and C. H. McCollough are affiliated with the CT Clinical Innovation Center, Department of Radiology, Mayo Clinic, Rochester MN.

S. Thompson is affiliated with the Center for Traslational Science, Mayo Clinic, Rochester MN.

D. A. Woodrum and M.R. Callstrom are affiliated with the vascular interventional radiology department, Mayo Clinic, Rochester MN.

E-mail of corresponding author: mccollough.cynthia@mayo.edu.

organ and disease of interest) as well as patient dependent (i.e. body habitus, age, disease). Hence, working under the ALARA (As Low As Reasonable Achievable) principle, there exists a critical need of methodologies to systematically establish CTP protocols that use the lowest dose possible while at the same time confidently providing perfusion parameter estimations. Unfortunately, due to the potential higher doses of CTP, repetitive patient scans are undesirable. Animal experimentation is a good alternative but expensive.

In the literature there are reports of physical and engineered phantoms that have been used for perfusion imaging [18, 19]. The main strength of this approach is reproducibility. But, physical phantoms are mostly limited blood flow of larger vasculature rather than perfusion (microvasculature level blood flow). Recently, biological phantoms that consist of organs extracted from animals and then fixated for preservation have been proposed [20, 21]. Thompson et al. used a porcine liver that showed homogenous perfusion in all lobes. Further, microvasculature was exquisitely preserved as confirmed by histological analysis [21].

This work used a liver phantom as in [21]. The purpose of this study was to demonstrate a methodology for systematic comparison of radiation dose reduction approaches in CTP.

II. MATERIALS AND METHODS

A. *Preparation of the ex-vivo liver phantom*

A fresh porcine liver was perfused with formalin to preserve the specimen and ensure patency of the vascular structures [21]. The portal vein was connected to a continuous flow pump (Bio-Medicus® 560, Medtronic Inc., Minneapolis, MN), allowing control of input pressure and flow. Flow rate was adjusted and fixed at 250 ml/min for all experiments. Only single input perfusion was pursued using the portal vein.

B. *Scan protocols*

Scanning was performed using a 64-slice CT scanner (Somatom Definition, Siemens Healthcare, Forcheim, Germany), using 80 kVp and 24 x 1.2 mm collimation, hence expanding 28.8 mm range. The scans were repeated four times using 400, 400, 100 and 20 mAs. Frequency was 1 scan/s, with a total scan time of 50 s. Images were reconstructed using 5 mm slice thickness and a medium-soft kernel (B30). A total of 4 cc of iodinated contrast (300 mg/ml), was injected at 1 cc/s for each scan. All scans were performed consecutively, with at least 10 minutes in between scans with continuous flow of saline, to allow for clearance of contrast media from the vasculature.

C. *Analysis*

Perfusion image data was analyzed in two steps. First, we selected regions of interest (ROI) within the phantom, from which time attenuation curves (TACs) were obtained by taking the mean CT numbers. The procedure was repeated for the four scanning conditions. Taking the first CTP acquisition (400 mAs) as reference, percent root mean square (RMS) error between TACs was calculated with respect to maximum CT attenuation minus the background. Second, image data was processed using commercially available perfusion software (syngo volume perfusion CT Body, Siemens, Forchheim). Using a maximum slope method, we calculated voxel by voxel perfusion maps, corresponding to parameters such as blood flow (BF), blood volume (BV) and mean transit time (MTT). Parameters were averaged in selected ROIs, and resulting values were compared with estimations from the first performed CTP scan (400 mAs).

III. RESULTS

A. Vasculature preservation in the phantom

Portal venous CT angiograms, performed prior to the CTP scans, demonstrated homogeneous enhancement through several vascular branches down to the periphery of all the lobes in the liver (Figure 1).

B. Image noise

The image noise values, measured as the standard deviation of CT numbers within uniform regions-of-interest, were 17.3, 16.5, 26.0 and 70.8 HU, for the 400, 400, 100 and 20 mAs acquisitions, respectively. The image noise values were severely affected by the tube current employed, as expected (Figure 2).

C. Time attenuation curves (TACs)

The TACs showed excellent agreement at all mAs levels (Figure 3). Correspondingly, the percent RMS error in TACs between the first 400 mAs scan and subsequent scans at 400, 100 and 20 mAs were 1.0%, 2.9% and 4.3% for the input function, and 2.8%, 8.4%, 15.5% for the tissue ROI, respectively.

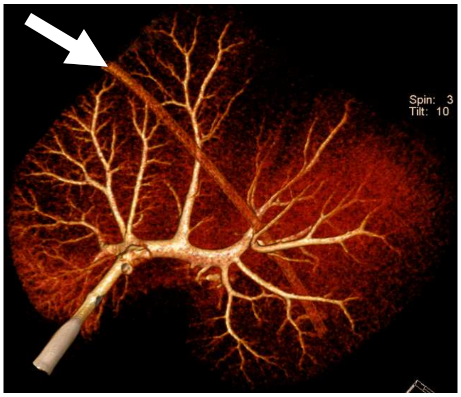

Figure 1. CT angiogram depicting enhancement of the portal vein branching and vasculature across all the lobes. Arrow points to a piece of tubing, that does not belong to the liver phantom, but that was used to hold the liver static within the water phantom.

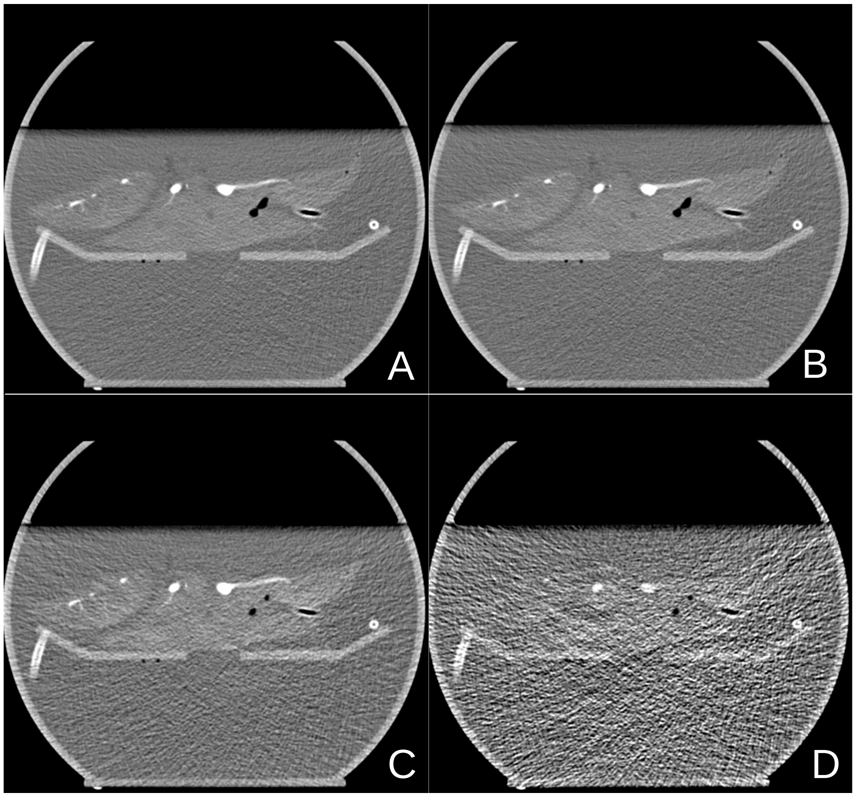

Figure 2. Sample images corresponding to CTP acquisitions using (A) 400 mAs, (B) 400 mAs, (C) 100 mAs, and (D) 20 mAs.

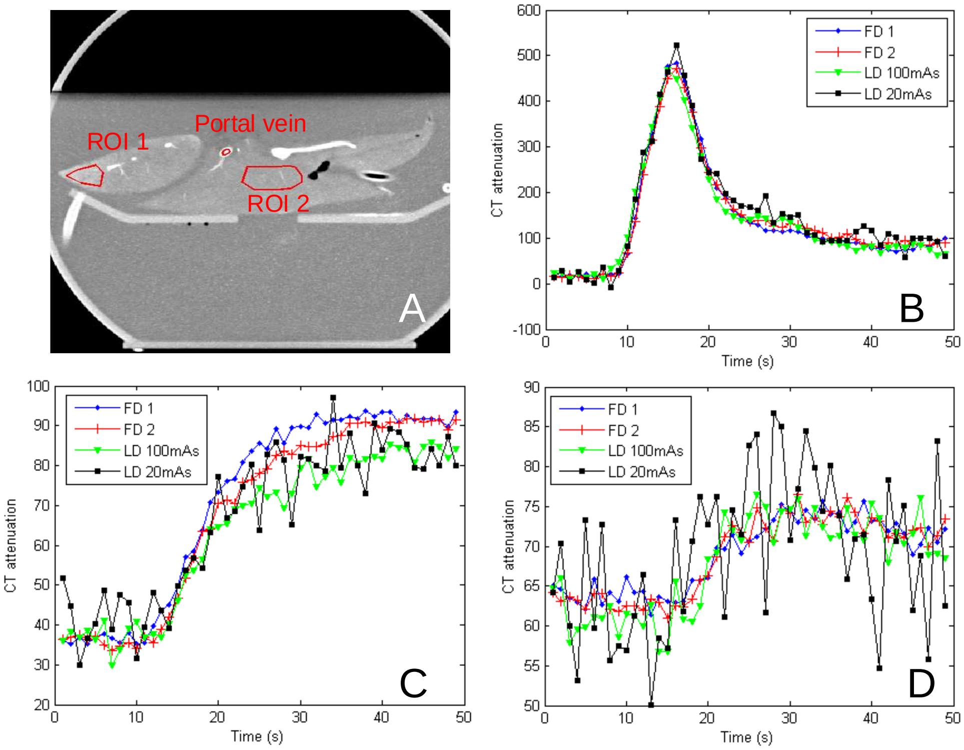

Figure 3. Reproducibility of the biological phantom as reflected with the remarkable agreement of TACs (A) ROI locations (B) TACs of input functiona at portal vein, (C) TACs of tissue perfusion at ROI 1, (D) TACs of tissue perfusion at ROI 2. FD = Full dose (400 mAs), LD = Low dose (100 and 20 mAs).

Table 1. Measurements of perfusion parameters at selected regions of interest (ROI). BF = blood flow in [ml/100g/min], BV = blood volume in [ml/100g], and MTT = mean transit time in [sec].

Condition	ROI 1			ROI 2			ROI 3			Average Difference (%)		
	BF	BV	MTT	BF	BV	MTT	BF	BV	MTT	BF	BV	MTT
400 mAs	31.8	7.8	19.4	49.8	7.9	13.2	37.1	2.7	24.3	0.0	0.0	0.0
400 mAs	30.6	7.7	21.1	39.0	7.8	13.3	33.1	2.3	19.1	12.1	6.4	10.5
100 mAs	27.7	6.6	29.3	28.4	7.9	10.3	29.4	2.5	33.4	25.6	7.1	36.9
20 mAs	6.8	1.6	28.5	0.8	2.1	8.8	7.6	4.1	27.7	85.5	68.2	31.4

D. Perfusion parameter accuracy

The average difference of perfusion estimates increased with lower mAs acquisitions (Table 1). The average difference between the two identical 400 mAs acquisitions was 12.1%, 6.4% and 10.5%, for BF, BV and MTT, respectively. At 100 mAs, the average difference of perfusion estimates was up to 36.9%, while at 20 mAs they were as large as 85.5 %.

IV. DISCUSSION

Under identical CTP scanning conditions, the calculated percent RMS errors were below 3% for the evaluated TACs, while quantitative perfusion estimations of BF, BV and MTT agreed within 12%, demonstrating a high degree of reproducibility of the phantom when scanned under identical conditions. The TACs corresponding to low dose acquisitions (100 and 20 mAs) had a good correspondence with the reference acquisition (400 mAs), showing moderate RMS error, however, the accuracy of perfusion estimates was compromised.

REFERENCES

[1] K. A. Miles, et al., "Functional images of hepatic perfusion obtained with dynamic CT," Radiology, vol. 188, pp. 405-411, August 1, 1993 1993.

[2] M. Bellomi, et al., "CT Perfusion for the Monitoring of Neoadjuvant Chemotherapy and Radiation Therapy in Rectal Carcinoma: Initial Experience1," Radiology, vol. 244, pp. 486-493, August 2007 2007.

[3] M. Wintermark, et al., "Using 80 kVp versus 120 kVp in perfusion CT measurement of regional cerebral blood flow," AJNR Am J Neuroradiol, vol. 21, pp. 1881-4, Nov-Dec 2000.

[4] L. Yu, et al., "Automatic selection of tube potential for radiation dose reduction in CT: A general strategy," Med Phys, vol. 37, pp. 234-43, Jan 2010.

[5] A. B. Smith, et al., "Radiation dose reduction strategy for CT protocols: successful implementation in neuroradiology section," Radiology, vol. 247, pp. 499-506, May 2008.

[6] J. B. Thibault, et al., "A three-dimensional statistical approach to improved image quality for multislice helical CT," Med Phys, vol. 34, pp. 4526-44, Nov 2007.

[7] A. Manduca, et al., "Projection space denoising with bilateral filtering and CT noise modeling for dose reduction in CT," Med Phys, vol. 36, pp. 4911-4919, 2009.

[8] M. S. May, et al., "Dose Reduction in Abdominal Computed Tomography: Intraindividual Comparison of Image Quality of Full-Dose Standard and Half-Dose Iterative Reconstructions With Dual-Source Computed Tomography," Investigative Radiology, vol. 46, pp. 465-470, 2011.

[9] X. Liu, et al., "Renal Perfusion and Hemodynamics: Accurate in Vivo Determination at CT with a 10-Fold Decrease in Radiation Dose and HYPR Noise Reduction," Radiology, vol. 253, pp. 98-105, October 2009 2009.

[10] G. H. Chen, et al., "Prior image constrained compressed sensing (PICCS): a method to accurately reconstruct dynamic CT images from highly undersampled projection data sets," Med Phys, vol. 35, pp. 660-3, Feb 2008.

[11] M. Wiesmann, et al., "Dose reduction in dynamic perfusion CT of the brain: effects of the scan frequency on measurements of cerebral blood flow, cerebral blood volume, and mean transit time," Eur Radiol, vol. 18, pp. 2967-74, Dec 2008.

[12] S. M. Kim, et al., A method for patient dose reduction in dynamic contrast enhanced CT study vol. 38: AAPM, 2011.

[13] K. Kudo, et al., "Difference in Tracer Delay–induced Effect among Deconvolution Algorithms in CT Perfusion Analysis: Quantitative Evaluation with Digital Phantoms1," Radiology, vol. 251, pp. 241-249, April 2009 2009.

[14] K. A. Miles, "Measurement of tissue perfusion by dynamic computed tomography," The British journal of radiology, vol. 64, pp. 409-412, May 1, 1991 1991.

[15] K. Kudo, et al., "Differences in CT perfusion maps generated by different commercial software: quantitative analysis by using identical source data of acute stroke patients," Radiology, vol. 254, pp. 200-9, Jan 2010.

[16] B. Abels, et al., "Perfusion CT in Acute Ischemic Stroke: A Qualitative and Quantitative Comparison of Deconvolution and Maximum Slope Approach," American Journal of Neuroradiology, vol. 31, pp. 1690-1698, October 1, 2010 2010.

[17] R. E. Latchaw, et al., "Recommendations for imaging of acute ischemic stroke: a scientific statement from the American Heart Association," Stroke, vol. 40, pp. 3646-78, Nov 2009.

[18] B. Ebrahimi, et al., "A Microfabricated Phantom for Quantitative MR Perfusion Measurements: Validation of Singular Value Decomposition Deconvolution Method," Biomedical Engineering, IEEE Transactions on, vol. 57, pp. 2730-2736, 2010.

[19] B. Driscoll, et al., Development of a dynamic flow imaging phantom for dynamic contrast-enhanced CT vol. 38: AAPM, 2011.

[20] U. Haberland, et al., "A Biological Phantom for Contrast-Media-Based Perfusion Studies With CT," Investigative Radiology, vol. 44, pp. 676-682 2009.

[21] S. M. Thompson, et al., "Porcine Ex Vivo Liver Phantom for Dynamic Contrast-Enhanced Computed Tomography: Development and Initial Results," Investigative Radiology, vol. 46, pp. 586-593, 2011.

Guiding decisions in CT image reconstruction algorithm design via the Hotelling template

Adrian A Sanchez[1], Emil Y Sidky[1], and Xiaochuan Pan[1,2]

Abstract—**In this work, ideal observer performance is computed on a single detection task. The modeled signal for detection is taken to be very small – size on the order of a detector bin – and inspection of the accompanying Hotelling template is suggested. We hypothesize that improved detection on small signals may be sensitive to the reconstruction algorithm. Further, we hypothesize that structurally simple Hotelling templates may correlate with high human observer performance.**

Description of purpose

The main goal of this work is to adapt model observer technology for use as a tool to aid in image reconstruction algorithm design. In particular, we investigate the Hotelling template (see chapters 13 and 14 in [**?**]). For the present case, the Hotelling observer is equivalent to the ideal observer, and the Hotelling template is the image with which the observer masks the reconstructed image in order to make the optimal decision between signal-absent and signal-present. Therefore, by inspecting the Hotelling templates that correspond to different implementations of the reconstruction algorithm, we expect to be able to draw conclusions about human observer performance based on the structure of the Hotelling template and its apparent similarity (or lack thereof) to the signal in question. Specifically, we hypothisize that a Hotelling template that is structurally simple and similar to the signal will result in better human observer performance on the detection task. A Hotelling observer model for detection is designed, and the Hotelling templates computed for the case of circular cone-beam CT image reconstruction. The method is demonstrated on alternative derivative filter designs.

Methods

a) Synopsis of relevant image reconstruction algorithm theory: : The particular image reconstruction algorithm used is the back-projection filtration (BPF) image reconstruction algorithm developed by our group [**?**]. In this algorithm, the imaging volume is decomposed into individual chords of the scanning trajectory, along which the reconstruction takes place. Although this algorithm is developed based on a continuous-to- continuous model, in practice the reconstruction is performed using discretized versions of the various continuous inversion operations that comprise the algorithm. In general terms, we consider a linear image reconstruction algorithm A that takes a discrete set of data $\vec{g}$ and produces a discrete representation of an image in the form of voxel coefficients $\vec{f}$:

$$\vec{f} = A\vec{g}. \tag{1}$$

As the BPF algorithm consists of many linear processing steps, it is useful to consider A as the product of matrices representing each processing step:

$$A = \prod_i A_i. \tag{2}$$

The BPF algorithm can be said to consist of eight distinct processing steps as follows:

(1) Derivative filtration of the projection data
(2) Back-projection onto the chords comprising the image volume
(3) Computation of boundary terms for back-projection
(4) Weighting of chord profiles
(5) Inverse Hilbert transform of chord profiles
(6) Evaluation and addition of constant offset to chord profiles
(7) Inverse weighting of chord profiles
(8) Interpolation onto 3D Cartesian grid.

In our case, the final step is trivial, as we consider reconstruction onto a set of chords defined on a Cartesian grid, but it is included here for completeness.

In particular, for this work, we focus on A_{deriv} which is the discrete implementation of the directional derivative of projection data $P(u,v)$ measured at the detector:

$$P_{\hat{t}}(u,v) \equiv \hat{t} \cdot \left(\frac{\partial P(u,v)}{\partial u}, \frac{\partial P(u,v)}{\partial v} \right). \tag{3}$$

We consider A_{deriv} such that

$$\begin{aligned} \frac{\partial P(u,v)}{\partial u} &= \mathscr{F}^{-1}\{K_u \cdot \mathscr{F}\{P(u,v)\}\} \text{ and} \\ \frac{\partial P(u,v)}{\partial v} &= \mathscr{F}^{-1}\{K_v \cdot \mathscr{F}\{P(u,v)\}\}, \end{aligned}$$

where $\mathscr{F}$ represents the discrete Fourier transform, and K_u and K_v are the discrete Fourier transforms of the convolution kernels representing derivatives in the u and v directions, respectively. For example, K corresponding to forward differencing would be given by $K = \mathscr{F}\{[1,-1]\}$. In this formulation, it is helpful to consider the various implementation options for K_u and K_v as being analogous to filters employed in conventional filtered backprojection algorithms. For instance, the imaginary component of the filter corresponding to forward differencing will be a sine wave in the Fourier domain, since the discrete Fourier transform of an antisymmetric impulse pair is an imaginary sine wave. In this work, we consider this implementation of the forward differencing filter, and a similar implementation of a symmetric differencing filter, where the derivative by symmetric differencing is, for example, given by

---

[1] The University of Chicago, Department of Radiology, Chicago, IL 60637

[2] The University of Chicago, Department of Radiation and Cellular Oncology, Chicago IL 60637

$$f_i' = \frac{f_{i+1} - f_{i-1}}{2\Delta} \tag{4}$$

We then consider a linear filter, since in the continuous limit we have $\mathscr{F}\{\delta'(x)\} = \nu_x$, where $\delta'(x)$ is the derivative of the Dirac delta function and ν_x is the spatial frequency variable corresponding to x. This linear filter can be seen as being analogous to the ramp filter in conventional filtered backprojection. Finally, we consider a linear filter modulated by Hanning apodization windows of various cutoff frequencies. These four filters are shown in Fig. **??**. Note that only the finite differencing filter has non-trivial real and imaginary parts, while the other filters are purely imaginary.

b) Synopsis of relevant model observer theory and strategy: : We seek a metric for image quality that is easy to compute, is sensitive to the image reconstruction algorithm, and may have some generality by being correlated with a range of imaging tasks. We have previously investigated the use of the Hotelling observer for a signal-known-exactly/background-known-exactly (SKE/BKE) detection task [**?**]. The idea of using the Hotelling observer, which will be equivalent to the ideal observer for the present data model, is that we seek the image reconstruction algorithm that best preserves in the reconstructed image, the detectability of a signal inherent in the sinogram data. In previous studies, we have found the efficiency of the reconstruction algorithm, the square of the ratio of the SNR for detection before and after reconstruction, a useful metric [**?**]. We have employed this metric to find optimal combinations of circular, cone-beam CT images obtained through different algorithm implementations. This efficiency, however, has potential shortcomings in terms of artifact removal, because the detection task for a given signal and noise model may be insensitive to commonly occurring artifacts in CT.

In this work, we propose to employ as an evaluation tool the Hotelling template, the image with which the ideal observer masks the reconstructed image in order to make the optimal decision between signal-present and signal-absent. The detection task is performed on a small object, a uniform disk of width 2 Δ, and the noise model in the data is taken to be independent, Gaussian-distributed noise. This noise model closely approximates the actual CT application and preserves the equivalence between the Hotelling and ideal observers. The use of a small signal for the detection task is important because of: sensitivity, the image reconstruction algorithm can have a big impact on this task performance; and generality, we speculate that better performance on small signal detection will improve the performance of the CT image reconstruction algorithm on many other tasks. We believe the latter, because many CT classification tasks do rely on detection of components of the image, e.g. small spiculations of a tumor. We speculate further that examining the Hotelling template will provide an even more

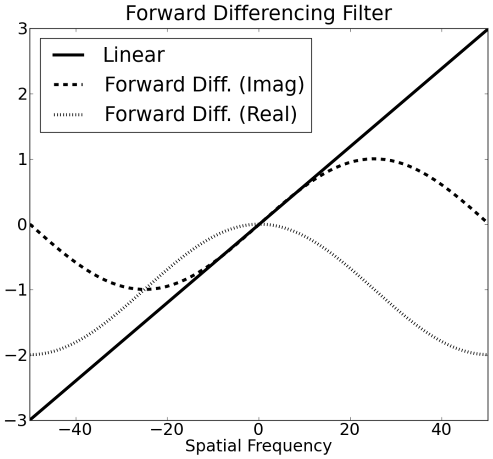

(a) A linear filter corresponding to $\mathscr{F}\{\delta'(x)\}$ and a sinusoidal filter corresponding to the forward differencing algorithm

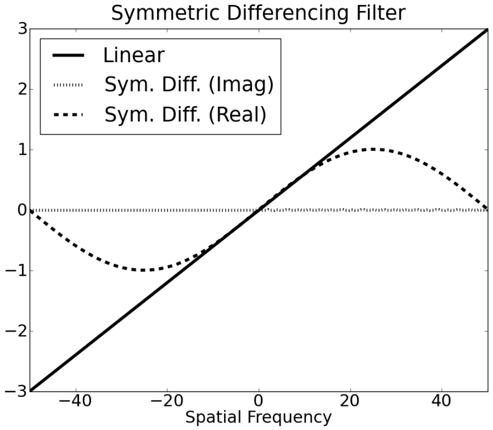

(b) A linear filter corresponding to $\mathscr{F}\{\delta'(x)\}$ and a sinusoidal filter corresponding to the symmetric differencing algorithm

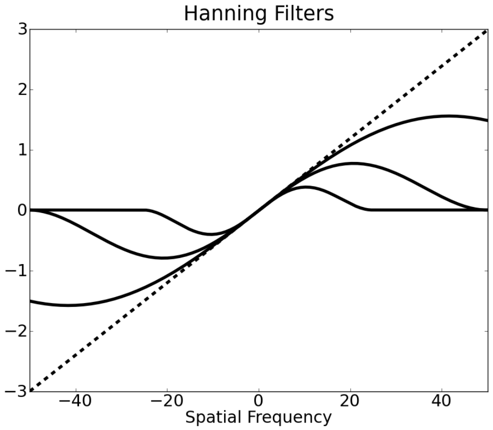

(c) A linear filter along with Hanning filters of cutoff frequencies $\frac{1}{2\Delta x}$, $\frac{1}{\Delta x}$, and $\frac{2}{\Delta x}$

Fig. 1. The four derivative filters considered in this work. Note that the above plots correspond to the imaginary component of each filter unless otherwise stated.

sensitive tool for algorithm design. The reasoning is that if the Hotelling template for this simple signal is also simple and resembles the signal, it may be that human performance will be closer to that of the ideal observer.

In order to illustrate the computation of the Hotelling template performed in this work, we begin by inspecting the CT data model, the noise properties of which are essential to the Hotelling observer model. The CT data model relates the object function $f(\vec{r})$ to the data vector g_i via a line integral over $f(\vec{r})$ along the ith ray, defined by the source position s_i and the ray direction $\hat{\theta}_i$:

$$g_i = \int_{-\infty}^{\infty} f\left(s_i + l\hat{\theta}_i\right) dl + n_i, \text{ where } i \in [1, N] \quad (5)$$

where n_i represents data noise and g_i and n_i are random variables. The data noise is taken to be independent and Gaussian-distributed. This implies that the data covariance vector K_g is diagonal such that

$$(K_g)_{i,j} = \begin{cases} \alpha & : i = j \\ 0 & : i \neq j \end{cases} \quad (6)$$

where we take α to be a constant for our purposes.

Given Eqn.**??**, it is clear that the reconstructed image covariance matrix will be given by

$$K_y = AK_gA^T = \alpha AA^T. \quad (7)$$

Hence knowledge of the transpose of the reconstruction matrix implies knowledge of the reconstructed image covariance. Now utilizing the fact that

$$K_y w_y^{(Hot)} = \Delta y \quad (8)$$

where $\Delta y = A\Delta g$ is the reconstructed signal, we can solve for the Hotelling template in reconstructed image space. However, while the corresponding equation in data space is easily solvable given that K_g is diagonal, various steps in the reconstruction and its transpose (e.g. back-projection) lead to K_y being non-diagonal. Further, K_y can be very large (e.g. $10^9 \times 10^9$). Fortunately, as long as Δy is in the range of K_y, Eqn.**??** satisfies the necessary conditions to be solved iteratively via conjugate gradients.

c) Synopsis of imaging and reconstruction configurations and geometries: : The CT geometry used to generate the noise-free simulation data in our study is circular cone-beam. Fig. **??** illustrates this geometry, in which the x-ray source and flat-panel detector follow a circular orbit. 512 views were acquired over a full 2π trajectory. The (unitless) relative dimensions of the acquisition were a 6x2 detector, a trajectory radius of 5, and a source-to-detector distance of 8. The chords upon which the reconstruction is performed are parallel to one another so that the reconstruction mimics that of conventional FDK reconstruction onto a Cartesian grid.

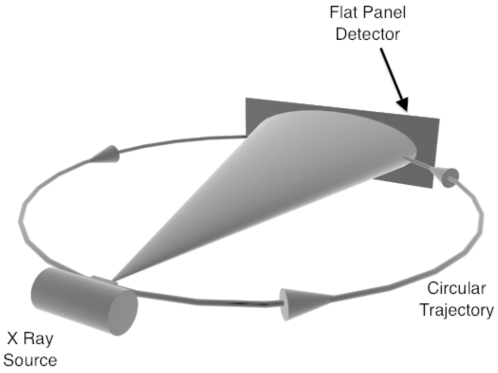

Fig. 2. The circular cone-beam geometry used to generate the noise-free simulated data used in this study. This acquisition configuration was chosen for its ubiquity in clinical settings.

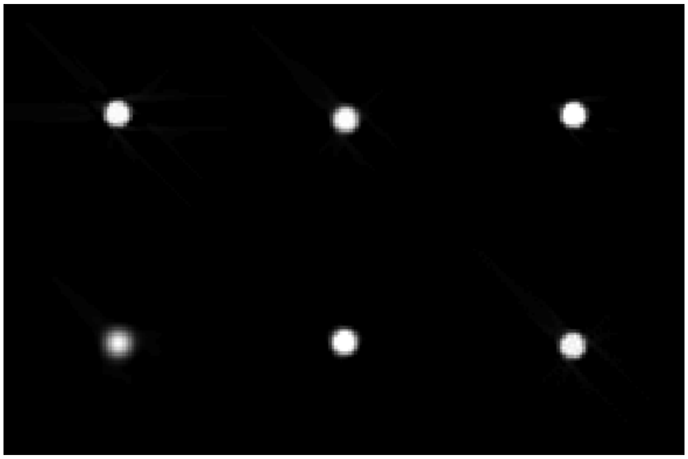

Fig. 3. Midplane reconstructions corresponding to various implementations of the directional derivative filter. The associated derivative filters are as follows: top row (from left to right): forward differencing, symmetric differencing, and linear (analogous to ramp filter); bottom row (from left to right): Hanning window of cutoff $\frac{1}{2\Delta x}$, Hanning window of cutoff $\frac{1}{\Delta x}$, and Hanning window of cutoff $\frac{2}{\Delta x}$. Note that the only obvious difference among any of the implementations is the blurring achieved by the low frequency cutoff Hanning filter.

Results

We have obtained the Hotelling template for detection of a small signal in images reconstructed from circular, cone-beam CT data onto a Cartesian chord grid with six different implementations of the projection data derivative. Shown in Fig. **??**, are the reconstructed signals from the linear, Hanning, symmetric differencing and forward differencing kernels. The corresponding Hotelling templates are shown in Fig. **??**. The fact that the various reconstructed images do not appear substantially different gives a sense as to how small a difference there is between the three image reconstruction algorithm implementations. On the other hand, the Hotelling templates are noticeably different. The implementations using finite differencing and the low-frequency cutoff Hanning filters show considerably more structure than the linear filter

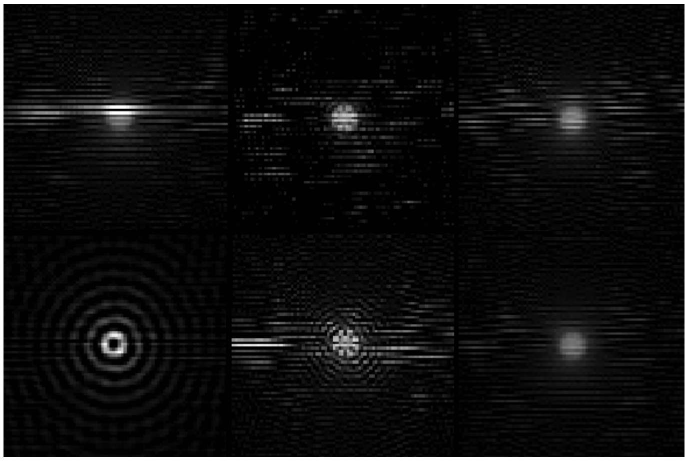

Fig. 4. Midplane Hotelling templates corresponding to various implementations of the directional derivative filter. The associated derivative filters are as follows: top row (from left to right): forward differencing, symmetric differencing, and linear (analogous to ramp filter); bottom row (from left to right): Hanning window of cutoff $\frac{1}{2\Delta x}$, Hanning window of cutoff $\frac{1}{\Delta x}$, and Hanning window of cutoff $\frac{2}{\Delta x}$. Again, we see little perceptible change in the reconstructed images, while the Hotelling templates are quite different. In this case, the templates corresponding to the linear kernel and to the widest of the three Hanning windows appear to have a structure most closely resembling the signal. We therefore hypothesize improved human observer performance for these implementation of the derivative filter, relative to the finite differencing filters, or Hanning filters with lower cutoffs.

and the Hanning filter with cutoff $\frac{2}{\Delta x}$. We hypothesize that the simplest Hotelling template will result in better detection performance for human observers, and may result in improvement on other imaging tasks.

Conclusions

The Hotelling template may prove as a useful tool for linear image reconstruction algorithm design. Our results show that these templates can be quite sensitive to algorithm implementation. Future work will investigate the conjecture that a simple Hotelling template for simple signals implies better human observer performance. If there is such a correlation, the use of the Hotelling template will be developed into a summary metric. In sum, inspection of the template is potentially useful for discrete implementation decisions, i.e. which particular implementation of the discrete directional derivative to use.

ACKNOWLEDGEMENTS

This work was supported in part by NIH R01 Grant Nos. CA120540 and EB000225 and NIH T32 Grant No. EB002103-22. The contents of this article are solely the responsibility of the authors and do not necessarily represent the official views of the National Institutes of Health.

REFERENCES

[1] H. H. Barrett and K. J. Myers, *Foundations of Image Science*, John Wiley & Sons, Inc., Hoboken, New Jersey, 2004.

[2] Y. Zou, X. C. Pan, and E. Y. Sidky, “Theory and algorithms for image reconstruction on chords and within regions of interest,” *J. Opt. Soc. Am. A* **22**, pp. 2372–2384, 2005.

[3] E. Y. Sidky, S. J. LaRoque, and X. Pan, “Accurate computation of the hotelling template for SKE/BKE detection tasks,” in *Medical Imaging: Image Perception, Observer Performance, and Technology Assessment*, B. Sahiner and D. J. Manning, eds., *Proc. SPIE* **6917**, pp. 69170W–69170W–5, 2008.

[4] E. Y. Sidky and X. Pan, “In-depth analysis of cone-beam ct image reconstruction by ideal observer performance on a detection task,” in *IEEE Med. Imaging Conf. Record*, pp. 5161–5165, 2008.

[5] S. J. LaRoque, E. Y. Sidky, D. C. Edwards, and X. Pan, “Evaluation of the channelized hotelling observer for signal detection in 2d tomographic imaging,” in *Medical Imaging: Image Perception, Observer Performance, and Technology Assessment*, Y. Jiang and B. Sahiner, eds., *Proc. SPIE* **6515**, p. 651514, 2007.

CT image assessment by low contrast signal detectability evaluation with unknown signal location

Lucretiu M. Popescu and Kyle J. Myers

Abstract— **In this paper we investigate new methodologies for CT image quality evaluation based on measuring the detectability of small, low contrast signals at locations unknown to the observer. We propose a phantom design that facilitates human observer studies in the condition of unknown signal locations. The setup allows for the random selection of regions of interest (ROI) around each signal, so that the relative signal location is unknown if the ROIs are shown separately. With such setup one can perform signal detectability measurements with a variety of image reading arrangements and data analysis methods. In this work we test the use of the localization relative operating characteristic (LROC) method. The design allows also for efficient image evaluation, utilizing an automatic signal search technique and a recently developed nonparametric data analysis method using the exponential transformation of the free response characteristic curve (EFROC). Here we present the application of these methods by performing a comparison between the filtered back projection algorithm and a polychromatic iterative image reconstruction algorithm. The results demonstrate the ability of these methods to determine signal detectability indices with good accuracy with only a small number, of the order of few tens, of image samples. The expected improved performance of the iterative reconstruction technique is confirmed.**

I. INTRODUCTION

Iterative image reconstruction techniques are increasingly gaining acceptance in X-ray computer tomography (CT) applications. The nonlinear nature of the image reconstruction, with markedly different noise patterns, challenges the way image quality is traditionally evaluated in CT, and makes it difficult to appreciate the improvements of this type of algorithms compared to the more traditional analytical reconstruction methods. The aggregation of signal to noise ratio (SNR) metrics from modulation transfer function (MTF) and noise power spectrum (NPS) measurements relies strongly on the assumption of system linearity. This state of affairs points us to the need to evaluate the images by using task-based methods. One such type of task is the detection of a small low-contrast signal. In this category we can distinguish the detection of a signal at a known location [1]. However, it can be argued that the metrics based on the known-signal-location approach do not fully capture the noise properties of the image, since they do not account for the extreme, random occurrences of noise clumps in images, more likely to be mistaken for true signals. For these reasons, the more general problem of detection of a signal at an unknown location has received increased attention in the recent years [2]–[4].

In this work we propose to address one of the practical difficulties of carrying out such studies with human observers. The commonly used CT image quality phantoms, such as ACR or Catphan, present a closely packed pattern of signals of different sizes and contrast values. This setup is very efficient for a subjective evaluation of image quality. A medical physicist just has to identify the size and contrast below which the phantom features become harder to recognize. However, this compact phantom setup makes it difficult to perform an objective evaluation of signal detectability, because the signal pattern is well known to the human readers. Therefore, we propose a phantom arrangement in which the signals are separated by large enough distances so that a region of interest (ROI), significantly larger than a signal, can be randomly delimited around each signal without overlap. With the ROIs shown separately, this approach hides from the readers the signal arrangement pattern, and allows for easy generation of multiple ROI samples, thus enabling an objective quantitative evaluation of signal detectability.

We will study the feasibility of this image quality evaluation setup by using an automatic signal searching technique and simulating the reading arrangement of a localization relative operating characteristic (LROC) study [5], [6]. In addition we will analyze the data using a recently developed nonparametric method based on the exponential transformation of the free response operating characteristic (EFROC) [7]. We will apply these techniques for comparing images obtained with the filtered back projection (FBP) algorithm and an iterative polychromatic transmission reconstruction algorithm.

II. METHODS

A. Phantom design

The phantom design we propose is illustrated in Fig. 1. It has a diameter of 15 cm and 5 signal locations equally spaced at 4.5 cm from the center. The ROIs should be selected so that the signal could be found at any position within an ROI. The signals can be arranged in modules, each module containing a slice with signals of the same size and contrast. A background-only module should be available in order to obtain signal-absent images. The size and the contrast of the signals should be chosen so that they are moderately difficult to identify for

---

Food and Drug Administration, Center for Devices and Radiological Health, Office of Science and Engineering Laboratories, Division of Imaging and Applied Mathematics, 10903 New Hampshire Ave., Silver Spring, MD 20993, E-mail: lucretiu.popescu@fda.hhs.gov

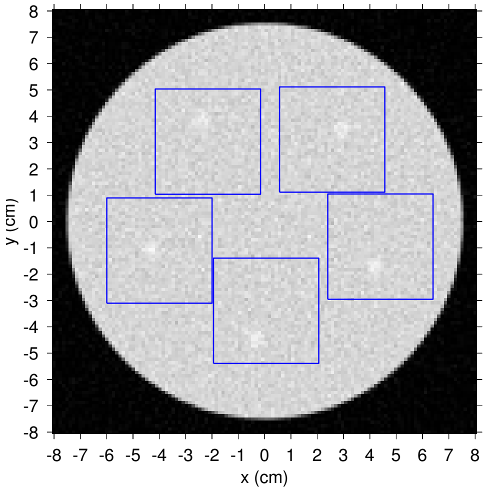

Fig. 1. Example of signal placement and random selection of $4 \times 4\,\mathrm{cm}^2$ ROIs on a simulated image reconstruction using a 15 cm diameter phantom.

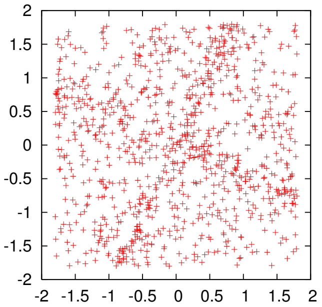

Fig. 2. Spatial distribution of the random signal location within the ROI. Results obtained from 200 image samples based on the setup shown in Fig. 1.

the devices, the doses, and the image reconstruction algorithms studied.

The phantom is imaged multiple times, each time the phantom is randomly rotated so that the pentagonal formation of signals is in a different position relative to the horizontal axis. For each image realization a different random selection of the ROIs is used. As shown in Fig. 2 this procedure assures a fairly uniform distribution of the signal position within the selected ROIs. With such an imaging setup one can perform signal detectability studies using a variety of image reading arrangements and data analysis methods.

B. Simulation setup

For our study we simulated the phantom design presented in Fig. 1. Around it we placed an exterior shell so the total phantom diameter is 24 cm. For the background we used a water equivalent composition. The results presented in this summary paper are based on cylindrical shaped signals of 4 mm diameter and contrast of 1%. For the generation of images we considered a two-dimensional parallel ray scanner with a polychromatic X-ray source and an energy integrating detector. Different noise levels were obtained by considering a Poisson process for the number of photons incident on the detector, with the average depending on the source intensity. An additional intra-detector energy deposition fluctuation modeled using a Gaussian with a 3% standard deviation was considered. The images were reconstructed using FBP and an iterative image reconstruction algorithm that will be described in more detail elsewhere [8]. The doses (or the tube current intensities) emulated were chosen so that they span the full performance range for both algorithms, from very poor signal detectability to virtually certain signal detectability.

C. The image scanning procedure

The signal detection was done using a signal search (or image scanning) algorithm, following a similar scheme as the one described in [3]. The procedure comprises two main steps. The first step is analogous to a filtering procedure. For each image point, $\mathbf{x}_i$, a measure of the match between the pixels around that location and the signal is computed according to a given signal template,

$$z_i = \sum_{||\mathbf{x}_{i+k} - \mathbf{x}_i|| < R_t} w_k f^*_{i+k} \,, \tag{1}$$

where $\{f^*_j\}$ are the image values corrected for the slowly varying background inhomogeneities (such as the cupping artifact due to beam hardening in FBP case). If the weights $\{w_k\}$ are uniform, the procedure simply determines the local contrast of the disk of radius R_t centered at the point $\mathbf{x}_i$. The output of this step is the auxiliary scan image $\{z_i\}$. In the second step we start by determining the maximum point of the scan image. Once this point is found, the value is entered in a list and the pixels in the disk of radius double the signal radius around that position are masked. The procedure continues with the rest of the unmasked image pixels as long as the local maximum found exceeds a given stopping limit z_0. In this manner a list with non-overlapping signal-sized local maxima is obtained in the decreasing order of their score values.

For both algorithms studied we used images represented by pixels of 0.5 mm size. In order to assure a more fine positioning of the scanning window and to better account for the signal shape in the scanning procedure, we have oversampled the images up to a pixel size of 0.3 mm, by interpolating. Also because of the small signal size we employed a simple local-contrast evaluation template. The combination of oversampling and uniform signal template has a similar effect as using a template on the original image with weights that account for the partial volume effect. Several signal template sizes, R_t, were tested in order to study the stability of the results. Examples of image-scan results (with $R_t = 0.24\,\mathrm{cm}$) are shown in Fig. 3.

D. Free-response data analysis

The results returned by the image scanning procedure described above correspond to a free-response image reading methodology in which the image observer is allowed to mark

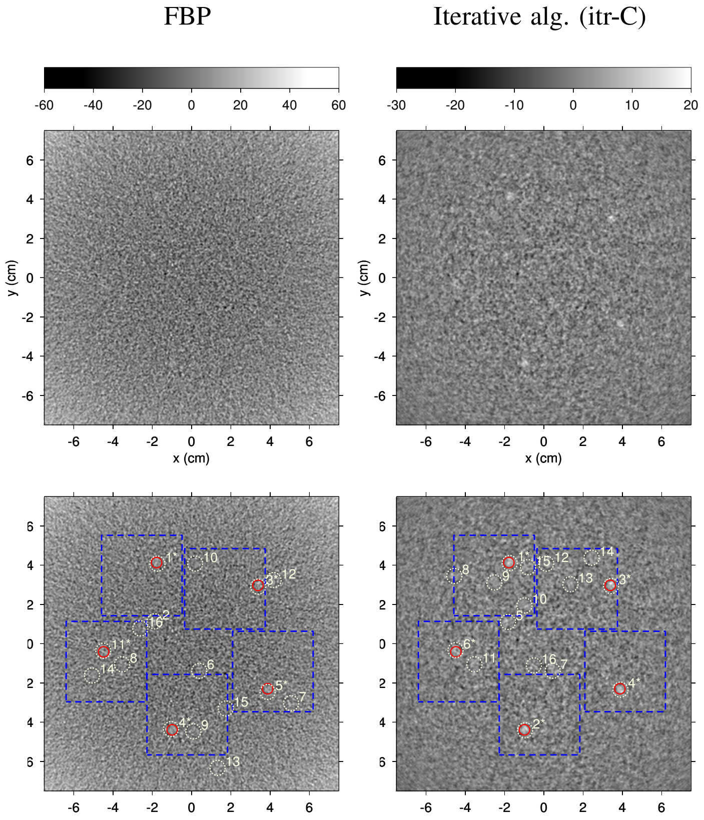

n	x	y	score	status
1	-1.74	4.08	9.25	true
2	-1.89	1.14	7.91	
3	3.39	2.91	7.83	true
4	-1.05	-4.35	6.89	true
5	3.87	-2.46	6.72	true
6	0.39	-1.38	6.35	
7	5.07	-3.03	5.98	
8	-3.54	-1.05	5.82	
9	0.09	-4.47	5.80	
10	0.18	4.08	5.76	
11	-4.50	-0.36	5.76	true
12	4.17	3.24	5.63	
13	1.32	-6.33	5.56	
14	-5.07	-1.62	5.51	
15	1.74	-3.30	5.48	
16	-2.61	0.78	5.29	

n	x	y	score	status
1	-1.74	4.11	7.48	true
2	-0.96	-4.41	6.67	true
3	3.42	2.94	5.91	true
4	3.90	-2.34	5.61	true
5	-1.83	1.11	4.56	
6	-4.50	-0.33	4.37	true
7	0.45	-1.38	4.36	
8	-4.56	3.45	3.91	
9	-2.52	3.12	3.67	
10	-0.99	1.95	3.56	
11	-3.54	-1.05	3.56	
12	0.12	4.08	3.56	
13	1.35	3.03	3.37	
14	2.43	4.38	3.27	
15	-0.81	3.90	3.12	
16	-0.51	-1.11	3.09	

Fig. 3. Example of scan results for images obtained from the same data set, dose point $I = 300$, with FBP and the iterative algorithm (itr-C). The second row of images shows the suspicious signal locations, the true signals (marked with small red circles), and the ROIs randomly selected for LROC analysis.

and score all potentially suspicious locations. Such results can be conveniently analyzed using the an exponential transformation of the free-response characteristic (EFROC) method [7]. This transformation addresses the main drawback of the regular FROC, which is the lack of a well-defined right-side limit. The area under the transformed curve, called EFROC, is well defined, and represents an overall signal detectability performance index.

For a given set of image samples the scanning procedure returns the results $\{x_i\}$, the scores of all I true signals present, and $\{y_j\}$, the scores of a total J of false marks retrieved from N signal-absent images. From these data the area under the EFROC can be estimated in a nonparametric fashion using the formula

$$\hat{A}_{\mathrm{FE}} = \frac{1}{I} \sum_{i=1}^{I} \mathrm{e}^{-\frac{1}{N} \sum_{j=1}^{J} H(y_j - x_i)}, \tag{2}$$

where $H(z) = \begin{cases} 1 & ; z > 0 \\ \frac{1}{2} & ; z = 0 \\ 0 & ; z < 0 \end{cases}$.

The properties of this estimator are studied in [7], where the equations for the variance calculation are provided.

A very useful property of the EFROC estimator is its scalability with the search area size. For homogeneous regions we can express the results relative to a given reference image size Ω by taking $N = \Omega_T/\Omega$, where Ω_T is the total searched area for false signals. This rescaling property is particularly advantageous for phantom experiments containing large background volumes that can be scanned for false signals, enabling the retrieval of statistically relevant data with only a few image samples, as is the case with the phantom design proposed here.

E. ROI reading and LROC data analysis

With human readers we cannot perform a full free-response reading of the images, as above, because the presence of the signals in a well-known pattern would easily betray their presence. Therefore we hide the signal locations by randomly selecting ROIs around each signal, so that the signal position can be anywhere inside the ROI, and show the ROIs separately for reading. In an LROC experiment the reader is asked to score the ROI shown and mark only one (the most) suspicious signal location.

We emulate this reading arrangement by selecting form each ROI (as shown in Fig. 3) the maximum suspicious location. If no scan value is above the threshold, the ROI is assigned the minimum score available in the rating scale. Thus from M signal-present ROIs we obtain the maximum-scan scores $\{X_m\}$, as well as the localization success values $\{q_m\}$; 1 if the maximum scan value corresponds to a true signal, 0 if not. From the N signal absent ROIs we obtain the maximum-scan scores $\{Y_n\}$. With these notations we have the following performance index estimator

$$\hat{A}_{\mathrm{L}} = \frac{1}{MN} \sum_{m=1}^{M} \sum_{n=1}^{N} q_m H(X_m - Y_n) \tag{3}$$

corresponding to the area under the LROC curve [6].

The relations between EFROC and LROC, as well as other metrics, are discussed in [7], in conditions that are fairly well satisfied in this type of phantom experiment. The LROC index, A_{L}, ideally should be equivalent to the EFROC metric, A_{FE}, expressed for a search area size twice the size of the ROI area. The departures from the ideal case are mainly introduced by the finite size of the signal and the search area size. For the comparisons of the two methods we will report A_{FE} values scaled for a search area of size $\Omega = 32\,\mathrm{cm}^2$, given the fact that we used $4 \times 4\,\mathrm{cm}^2$ ROIs.

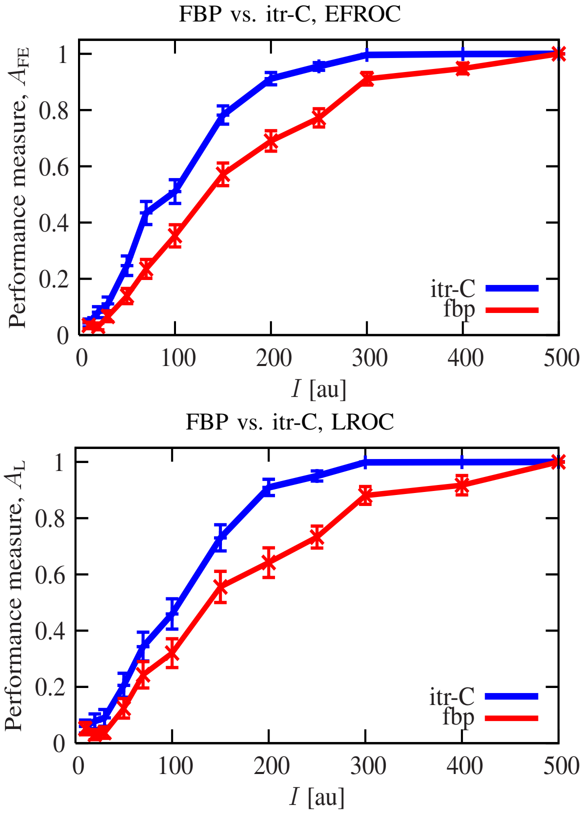

Fig. 4. Comparison between the FBP and the iterative algorithm (itr-C) signal detectability as function of dose, as measured by the EFROC and LROC indices. The results were obtained from 20 signal-present and 20 signal-absent image samples. The error bars correspond to one standard deviation.

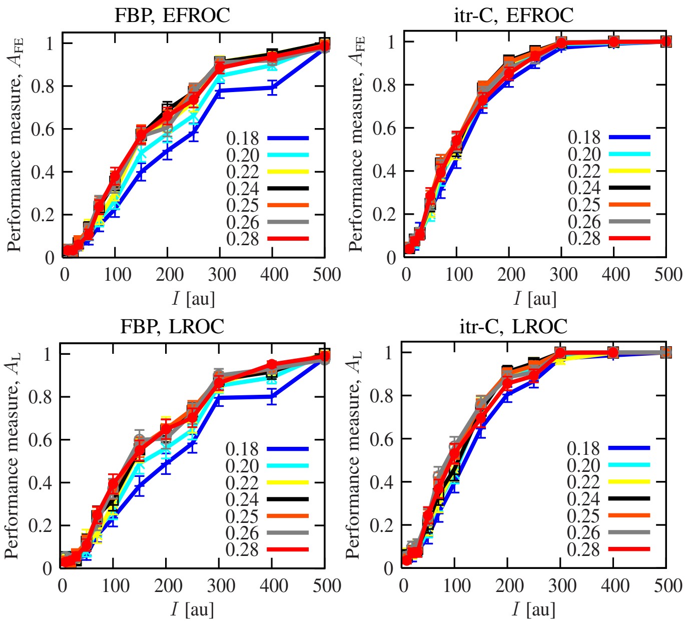

Fig. 5. EFROC and LROC results variation with the size of the scanning template radius, R_t.

III. Results

In Fig. 4 we compare the signal detectability performance of the FBP and the iterative algorithm (itr-C) as functions of dose, as measured by the EFROC and LROC indices. The results were obtained using only 20 signal-present and 20 signal-absent image samples. The LROC results show greater uncertainty compared to the EFROC results, however the error bars are small enough to clearly differentiate the performance of the two algorithms around the 80% signal detectability index point. Because the images obtained with the two image reconstruction algorithms originate from the same data sets, the performance values are correlated; therefore the standard deviations of the differences between the two reconstruction methods should be even smaller than the error bars indicate.

The difference in precision between EFROC and LROC is chiefly due to the difference in the size of signal-search area the two methods are using. The EFROC method takes advantage of the full scanned area, the interior disk of radius 7.3 cm of area 167 cm^2, while the LROC uses only the five ROIs with a total of 80 cm^2.

In Fig. 5 we study the stability of the results with the variation of the scanning template radius, R_t. We find very good stability, for both algorithms and evaluation methods, once the scanning template size exceeds the signal size, but not much more more than a full pixel size, $R_t \in [0.22, 0.26]$. Poorer performances are obtained for small scanning templates, as result of the increased probability for the appearance of smaller noise clumps in the background that are not smoothed out in a small template.

IV. Conclusions

In this work we have tested via simulations a phantom design that allows for signal detectability evaluation studies for the signal at unknown location problem, both in an automated reading setting, and with human observers. We have demonstrated the application of an automatic signal searching method in conjunction with the EFROC data analysis method. Also we have tested a reading arrangement using regions of interest randomly delimited so that the signal location will be unknown to the human observers, in a LROC setting.

The results show that the EFROC method is more precise and versatile than the ROI arrangement used for LROC. However, both methods provide good discrimination ability with only a few tens of image samples. This result is encouraging and allows us to move towards the next phase of this project using human readers. Both evaluation methods unambiguously confirm the better performance of the iterative reconstruction algorithm compared to FBP.

References

[1] H. H. Barrett, J. Yao, J. P. Rolland, and K. J. Myers, “Model observers for assessment of image quality,” *Proc. Nat. Acad. Sci. USA*, vol. 90, no. 21, pp. 9758–9765, 1993.

[2] H. C. Gifford, M. A. King, P. H. Pretorius, and R. G. Wells, “A comparison of human and model observers in multislice LROC studies,” *IEEE Trans. Med. Imag.*, vol. 24, no. 2, pp. 160–169, 2005.

[3] L. M. Popescu and R. M. Lewitt, “Small nodule detectability evaluation using a generalized scan statistic model,” *Phys. Med. Biol.*, vol. 51, no. 23, pp. 6225–6244, 2006.

[4] D. J. Kadrmas, M. E. Casey, M. Conti, B. W. Jakoby, C. Lois, and D. W. Townsend, “Impact of time-of-flight on PET tumor detection,” *J. Nucl. Med.*, vol. 50, no. 8, pp. 1315–1323, 2009.

[5] R. G. Swensson, “Unified measurement of observer performance in detecting and localizing target objects on images,” *Med. Phys.*, vol. 23, no. 10, pp. 1709–1725, 1996.

[6] L. M. Popescu, “Nonparametric ROC and LROC analysis,” *Med. Phys.*, vol. 34, no. 5, pp. 1556–1564, 2007.

[7] L. M. Popescu, “Nonparametric signal detectability evaluation using an exponential transformation of FROC curve,” *Med. Phys.*, vol. 38, no. 10, pp. 5690–5702, 2011.

[8] L. M. Popescu, “Iterative multiplicative algorithms for polychromatic transmission image reconstruction.” In preparation., 2012.

New Results for Efficient Estimation of CHO Performance

Adam Wunderlich, Frédéric Noo and Marta Heilbrun

Abstract—**Task-based assessments of image quality constitute a rigorous, principled approach to the evaluation of imaging system performance. To conduct such assessments, it has been recognized that mathematical model observers are very useful, particularly for purposes of imaging system development and optimization. One type of model observer that has been widely applied in the medical imaging community is the channelized Hotelling observer (CHO). Since estimates of CHO performance typically include statistical variability, it is important to control and limit this variability to maximize the statistical power of image quality studies. Previously, we demonstrated that by including prior knowledge of the image class means, a large decrease in the bias and variance of CHO performance estimates can be realized. Here, we present refinements and extensions of this estimation theory, which was limited to point estimation with equal numbers of images from each class. Specifically, we present minimum-variance unbiased point estimators for observer SNR that allow for unequal numbers of lesion-absent and lesion-present images. Also, we develop both exact and approximate confidence intervals for commonly-used CHO performance measures.**

I. INTRODUCTION

Because they can be implemented efficiently using computers, mathematical model observers are a valuable tool for task-based image quality assessments, particularly for imaging system development and optimization [1], [2]. One type of model observer that has been widely utilized in the medical imaging community is the channelized Hotelling observer (CHO) [1]. Due to nice optimality properties and flexibility afforded through the selection of channels, CHOs have been shown to track both human and ideal observer performance [1]. Consequently, CHO methodology has been applied in many areas of medical imaging research.

Although CHO performance can be calculated accurately from analytical models in some cases [3], [4], this is not usually feasible due to complexities in the image formation process. Instead, most practical evaluations must be carried out by estimating CHO performance from a finite set of images, and the results necessarily suffer from statistical variability.

One way to reduce variability in CHO performance estimates is by utilizing prior knowledge of the channel output means for each class of images, which can be obtained from the image means. Fortunately, the image means turn out to be available in many practical situations. Specifically, when evaluations are performed with simulated tomographic data, the image means can often be accurately estimated by reconstructing the data means. This is clearly true for linear reconstruction algorithms, and it is often a very good approximation for nonlinear iterative reconstruction algorithms [5]–[7]. In addition to simulated-data evaluations, accurate estimates of the difference of image class means can also be produced for some types of real-data experiments [2], [8].

In [9], we proposed and characterized point estimators for CHO performance when either the image class means, or their difference, is known. Our evaluation demonstrated that a very large statistical advantage can be realized by utilizing prior knowledge of the class means. The estimators in [9] were based on three assumptions: (i) the class means of the channel outputs, or their difference, is known, (ii) the channel outputs follow a multivariate normal distribution for each image class, and (iii) the covariance matrices for the channel outputs are the same for each class. These assumptions are generally satisfied for a CHO applied to the detection of small, low-contrast lesions at a known location.

Here, we present refinements and extensions of the theory in [9] in four useful ways. First, we develop minimum-variance, unbiased estimators of SNR, improving on [9], which was limited to unbiased estimation of SNR^2. Second, while the estimators in [9] require equal numbers of images from each class, the theory presented in this work allows for unequal numbers of lesion-absent and lesion-present images, with the practically convenient option of zero images from one class. Third, we propose and characterize exact confidence intervals for commonly used CHO performance measures. Fourth, we present robust, approximate confidence intervals that can be used as simple alternatives to the exact confidence intervals. For conciseness, the proofs of our results are omitted.

II. CHO PERFORMANCE MEASURES

The present work concerns estimation of CHO [1] performance for any binary discrimination task at a fixed image location. Consider a binary discrimination task in which an observer attempts to classify each image as belonging to one of two classes, denoted as class 1 and class 2. A CHO generates a rating statistic, t, for each image, and classifies the image by comparing t to a threshold, c. If $t > c$, then the image is classified as belonging to class 2, otherwise, the image is classified as belonging to class 1.

Before generating the rating statistic for an image, a CHO applies channel weights to reduce the image to a $p \times 1$ channel output vector, denoted $\mathbf{v}$. Let the means of $\mathbf{v}$ for classes 1 and 2 be $\boldsymbol{\mu}_1$ and $\boldsymbol{\mu}_2$, respectively, and let their difference be $\Delta\boldsymbol{\mu} = \boldsymbol{\mu}_2 - \boldsymbol{\mu}_1$. Also, denote the covariance matrices of $\mathbf{v}$ for class 1 and class 2 as Σ_1 and Σ_2, respectively, and their average as $\overline{\Sigma} = (\Sigma_1 + \Sigma_2)/2$. Once the channel outputs for an image are obtained, a CHO computes the rating statistic as $t = \mathbf{w}^T\mathbf{v}$, where $\mathbf{w} = \overline{\Sigma}^{-1}\Delta\boldsymbol{\mu}$ is the $p \times 1$ CHO template.

Let the channel outputs for classes 1 and 2 be denoted as $\mathbf{v}^{(1)}$ and $\mathbf{v}^{(2)}$, respectively. Throughout this work, we assume that $\mathbf{v}^{(1)} \sim \mathcal{N}_p(\boldsymbol{\mu}_1, \Sigma)$ and $\mathbf{v}^{(2)} \sim \mathcal{N}_p(\boldsymbol{\mu}_2, \Sigma)$, i.e., $\mathbf{v}^{(1)}$ and $\mathbf{v}^{(2)}$ are multivariate normal vectors with the same covariance

---

The authors are with the Department of Radiology, University of Utah, Salt Lake City, Utah, USA. E-mail: awunder@ucair.med.utah.edu

This work was partially supported by NIH grants R01 EB007236, R21 EB009168 and by a grant from the Ben B. and Iris M. Margolis Foundation.

matrix. In this setting, the CHO template is $\mathbf{w} = \Sigma^{-1}\Delta\boldsymbol{\mu}$, and the CHO is optimal among all observers that act on the channelized images [1].

The performance of an observer on a binary classification task is fully characterized by the observer's receiver operating characteristic (ROC) curve [1]. Under the aforementioned distributional assumptions for the channel outputs, the area under the ROC curve is $\mathrm{AUC} = \Phi(\mathrm{SNR}/\sqrt{2})$, where $\Phi(x)$ is the cumulative distribution function for the standard normal distribution and $\mathrm{SNR} = \sqrt{\Delta\boldsymbol{\mu}^T\Sigma^{-1}\Delta\boldsymbol{\mu}}$ is the CHO signal-to-noise ratio [1]. In the present setting, both SNR and AUC are suitable figures-of-merit for CHO performance [1].

III. SNR POINT ESTIMATION

Here, we introduce our unbiased SNR point estimator. To allow for zero images from one class, we use the notational convention that a summation is zero if its upper limit is zero. Throughout, we assume that we have m independent, identically distributed (iid) measurements of the class-1 channel outputs, denoted as $\mathbf{v}_1^{(1)}, \mathbf{v}_2^{(1)}, \ldots, \mathbf{v}_m^{(1)}$, and n iid measurements of the class-2 channel outputs, denoted as $\mathbf{v}_1^{(2)}, \mathbf{v}_2^{(2)}, \ldots, \mathbf{v}_n^{(2)}$.

A. Estimator Definition

Two scenarios can be considered: (1) known $\boldsymbol{\mu}_1$ and $\boldsymbol{\mu}_2$ with unknown Σ and (2) known $\Delta\boldsymbol{\mu}$ with unknown $\boldsymbol{\mu}_1$, $\boldsymbol{\mu}_2$, and Σ. We have extended the results in [9] for both scenarios. However, for brevity, we only present the results for scenario 2, which is less constraining and thus more practical.

To build our SNR estimator for scenario 2, we first define a sample covariance matrix estimator that incorporates $\Delta\boldsymbol{\mu}$ as

$$\widetilde{S} = \frac{1}{m+n-1}\Big[\sum_{i=1}^{m}(\mathbf{v}_i^{(1)} - \widetilde{\mathbf{v}}_1)(\mathbf{v}_i^{(1)} - \widetilde{\mathbf{v}}_1)^T + \sum_{j=1}^{n}(\mathbf{v}_j^{(2)} - \widetilde{\mathbf{v}}_2)(\mathbf{v}_j^{(2)} - \widetilde{\mathbf{v}}_2)^T\Big] \quad (1)$$

where $\widetilde{\mathbf{v}}_1$ and $\widetilde{\mathbf{v}}_2$ are the unbiased sample mean estimates

$$\widetilde{\mathbf{v}}_1 = \Big[\sum_{i=1}^{m}\mathbf{v}_i^{(1)} + \sum_{j=1}^{n}\mathbf{v}_j^{(2)} - n\Delta\boldsymbol{\mu}\Big]/(m+n)\,, \quad (2)$$

$$\widetilde{\mathbf{v}}_2 = \Big[\sum_{i=1}^{m}\mathbf{v}_i^{(1)} + \sum_{j=1}^{n}\mathbf{v}_j^{(2)} + m\Delta\boldsymbol{\mu}\Big]/(m+n). \quad (3)$$

The SNR point estimator for scenario 2 is then defined as

$$\widehat{\mathrm{SNR}}_2 = \gamma_2\sqrt{\Delta\boldsymbol{\mu}^T\widetilde{S}^{-1}\Delta\boldsymbol{\mu}}, \quad (4)$$

where $\gamma_2 = \sqrt{2\pi/(m+n-1)}/B((m+n-p-1)/2, 1/2)$ and $B(x,y)$ is the Euler Beta function.

B. Sampling Distribution and Optimality

It turns out that the sampling distribution of our SNR estimator is closely related to the inverted gamma distribution. If a random variable, X, follows an inverted gamma distribution with parameters α and β, we will write $X \sim IG(\alpha,\beta)$. The following theorem characterizes $\widehat{\mathrm{SNR}}_2$.

Theorem 1. *Under our assumptions, if* $m+n-p > 2$, *then*

(i) $(\widehat{\mathrm{SNR}}_2)^2 \sim IG(\alpha,\beta)$ *with* $\alpha = (m+n-p)/2$ *and* $\beta = \eta_2\,\mathrm{SNR}^2$ *where* $\eta_2 = (m+n-1)\gamma_2^2/2$

(ii) $\widehat{\mathrm{SNR}}_2$ *is the UMVU (uniformly minimum variance unbiased) estimator for* SNR

(iii) $\sqrt{\mathrm{Var}[\widehat{\mathrm{SNR}}_2]} = \tau_2\,\mathrm{SNR}$ *with* $\tau_2 = \sqrt{\frac{2\eta_2}{(m+n-p-2)} - 1}$.

From the above theorem, we can make several observations. First, the distribution of $\widehat{\mathrm{SNR}}_2$ only depends on two independent parameters: $m+n-p$ and SNR. We will rely on this fact later in our confidence interval evaluations. Second, our SNR estimator is optimal in that it is the minimum variance estimator among all unbiased estimators of SNR under scenario 2. Last, the ratio of the mean of $\widehat{\mathrm{SNR}}_2$ to its standard deviation only depends on $m+n-p$. This property enables quick sample-size estimates when setting up a study. Later, in Section V, we will see that part (iii) can also be used to construct useful approximate confidence intervals.

IV. EXACT CONFIDENCE INTERVALS

Remarkably, $\widehat{\mathrm{SNR}}_2$ can be used to construct confidence intervals for SNR and AUC with exactly-known coverage probabilities. This original result is stated in the next theorem.

Theorem 2. *Let* $X = (\widehat{\mathrm{SNR}}_2)^2$ *and let* $\omega_1, \omega_2 \in (0,1)$ *with* $\omega_1 + \omega_2 = \omega \in (0,1)$. *Then, under our assumptions,*

(i) *For each observation* x *of* X, *there exist unique values* $\beta_L(x)$ *and* $\beta_U(x)$ *in* $(0,\infty)$ *satisfying* $F_X(x\,;\alpha,\beta_L(x)) = 1-\omega_1$ *and* $F_X(x\,;\alpha,\beta_U(x)) = \omega_2$, *where* $F_X(x\,;\alpha,\beta)$ *is the cdf of the inverted gamma distribution with* $\alpha = (m+n-p)/2$.

(ii) *Let* $\eta_2 = (m+n-1)\gamma_2^2/2$, *then*

$$\Big[\sqrt{\beta_L(X)/\eta_2},\ \sqrt{\beta_U(X)/\eta_2}\,\Big] \quad \textit{and}$$

$$\Big[\Phi(\sqrt{\beta_L(X)/2\eta_2}\,),\ \Phi(\sqrt{\beta_U(X)/2\eta_2}\,)\Big]$$

are exact $1-\omega$ *confidence intervals for* SNR *and* AUC.

Thus, we can calculate confidence intervals with a coverage probability of $1-\omega$ for both SNR and AUC from a realization of $\widehat{\mathrm{SNR}}_2$, by numerically solving the equations in Theorem 2(i) for β_L and β_U and then inserting these values into the relations of Theorem 2(ii). Plots of mean confidence interval length (MCIL) for the exact AUC confidence intervals of Theorem 2 are shown in Fig. 1. For these plots, MCIL was computed with an accuracy of 10^{-6} using numerical integration and our knowledge of the distribution for $(\widehat{\mathrm{SNR}}_2)^2$.

V. APPROXIMATE CONFIDENCE INTERVALS

While being exact, the confidence intervals introduced in the previous section require sophisticated numerical machinery for their computation. In this section, we introduce simpler, but approximate, confidence intervals that are robust and straightforward to compute. These confidence intervals are constructed by using part (iii) of Theorem 1 together with assumptions of asymptotic normality, as described next.

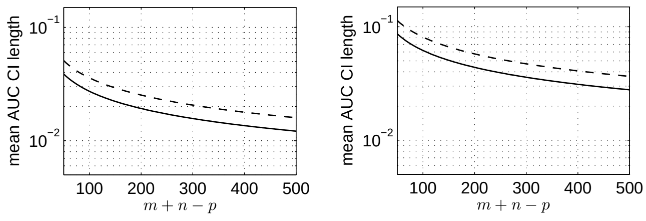

Fig. 1. Mean confidence interval length (MCIL) plotted versus $m+n-p$ for the AUC confidence intervals of Theorem 2. The solid curves are for 95% intervals with $\omega_1=\omega_2=0.025$, and the dashed curves for 99% intervals with $\omega_1=\omega_2=0.005$. Left: AUC value of 0.6. Right: AUC value of 0.9.

Assuming that $(\widehat{\mathrm{SNR}}_2-\mathrm{SNR})/(\tau_2\widehat{\mathrm{SNR}})$ approximately follows a standard normal distribution, the usual Wald-style $1-\omega$ confidence interval is found to be

$$\left[\widehat{\mathrm{SNR}}_2\left(1-\tau_2 z_{\omega/2}\right),\ \widehat{\mathrm{SNR}}_2\left(1+\tau_2 z_{\omega/2}\right)\right], \qquad (5)$$

where $z_{\omega/2}=\Phi^{-1}(1-\omega/2)$ is a standard normal quantile. Alternatively, the explicit dependence of the variance of $\widehat{\mathrm{SNR}}_2$ on SNR enables construction of a Wilson-style confidence interval [10]. Namely, supposing that $(\widehat{\mathrm{SNR}}_2-\mathrm{SNR})/(\tau_2\mathrm{SNR})$ approximately follows a standard normal distribution, we obtain the Wilson-style $1-\omega$ confidence interval

$$\left[(\widehat{\mathrm{SNR}}_2)/(1+\tau_2 z_{\omega/2}),(\widehat{\mathrm{SNR}}_2)/(1-\tau_2 z_{\omega/2})\right], \qquad (6)$$

where we assumed that $1-\tau_2 z_{\omega/2}>0$.

Note from (5) and (6) that the endpoints for the Wald and Wilson style intervals for SNR are both strictly positive and well-defined if $1-\tau_2 z_{\omega/2}>0$. For 95% and 99% confidence intervals, this condition is satisfied if $m+n-p$ is at least 5 and 6, respectively.

Since AUC is related to SNR through a strictly increasing transformation, we can obtain approximate $1-\omega$ intervals for AUC from the above Wald and Wilson intervals by transforming them accordingly. Moreover, the coverage probabilities of these AUC intervals are exactly the same as the SNR intervals.

Because we know the sampling distribution for $\widehat{\mathrm{SNR}}_2$, we can analytically calculate the coverage probabilities for the approximate Wald and Wilson-style intervals; we omit the details here for brevity. It turns out that the coverage probabilities for the Wald and Wilson intervals have the unique property of being independent of SNR, which enables easy evaluations. The coverage probabilities for the approximate 95% and 99% Wald and Wilson-style confidence intervals are plotted in Fig. 2. They indicate that both types of confidence intervals are highly accurate and quickly approach the desired coverage probability. They also show that the Wald-style intervals generally have more accurate coverage probabilities. The same conclusion applies to AUC confidence intervals obtained as strictly increasing transformations of the Wald and Wilson SNR intervals.

The plots in Fig. 3 compare the relative differences in MCIL of the Wald and Wilson AUC intervals to the exact AUC confidence intervals introduced in Section IV with $\omega_1=\omega_2$. We have observed that the 95% and 99% Wald intervals are always slightly larger than the exact AUC confidence intervals, with the discrepancy increasing with AUC value. For the

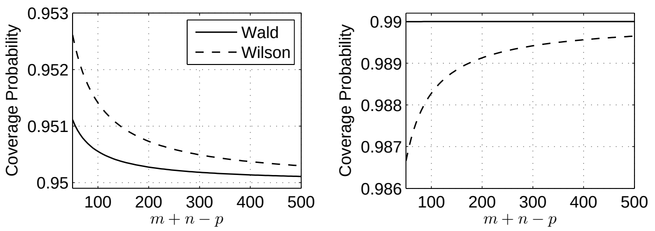

Fig. 2. Coverage probabilities of approximate 95% (Left) and 99% (Right) Wald and Wilson confidence intervals for SNR.

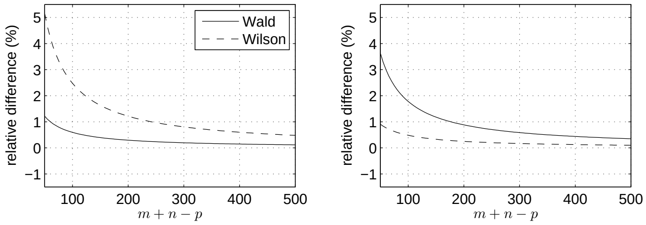

Fig. 3. Relative difference in mean confidence interval length for 95% AUC confidence intervals. Left: AUC value of 0.6. Right: AUC value of 0.9.

Wilson intervals, the situation is more complex. Specifically, the Wilson intervals are larger than the Wald intervals for small AUC values, with the difference shrinking until the Wilson intervals become smaller for AUC values greater than 0.8.

The approximate Wald and Wilson AUC confidence intervals are both simple alternatives to the exact AUC intervals of Section IV. From our evaluations, it appears that the Wald intervals are slightly more attractive than the Wilson intervals when AUC is smaller than 0.8. Whereas the Wilson intervals may be preferred when AUC is larger than 0.8.

VI. EXAMPLE

To illustrate our theory, we now present an image quality comparison of three fan-beam CT image reconstruction methods. This example involves a known-location, background-variable classification task in which a CHO is applied to discriminate between two types of kidney stones.

According to Kambadakone at al. [11], knowledge of kidney stone composition is an important factor influencing patient management. In particular, CT attenuation measurements have been found to be valuable for differentiation of uric acid stones from other stone types [11]. Motivated by this knowledge, we selected the task to consist of discriminating between a uric acid stone (450 HU) and a struvite stone (600 HU) at a fixed location in the left kidney (recall that the left kidney is commonly displayed on the right side of transverse-plane CT images). For our observer, we used a CHO with three symmetric difference of Gaussian (DOG) channels [12] centered on the kidney stone.

To generate kidney images, we used the XCAT phantom slice shown in Fig. 4. All images were reconstructed for a 96×96 region of interest (ROI) centered on the left kidney, with a pixel size of 1 mm by 1 mm. Since the XCAT phantom kidneys are relatively simple, we added additional realism to the left kidney as follows. First, a circular disk of fat with a random radius between 5 mm and 10 mm was added to the kidney, near the ureter. Second, a random background was added to the kidney to simulate texture. This variable background was modeled as colored Gaussian noise following a power law model with an exponent of two, as described in [13], with an amplitude of ±6 HU. Last, a kidney stone of diameter 4 mm was added at a fixed location, with attenuation values of 450 HU for class 1 and 600 HU for class 2; see Fig. 4. Once a realization of the phantom was defined, fan-beam sinograms were computed as in [4]. Poisson noise with a photon level of 20,000 was added to the data with additional models for tube current modulation and a bowtie filter [4].

We compared three fan-beam filtered backprojection (FBP) image reconstruction algorithms: **A:** Noo et al. [14] for full-scan data, **B:** Dennerlein et al. [15] for full-scan data, and **C:** Noo et al. [14] for short-scan data (240°). All algorithms were implemented so that resolution was matched near the field of view center. Algorithms A and B were expected to yield comparable CHO performance, whereas algorithm C was anticipated to be worse since it uses less CT data.

To carry out the evaluation, 150 class-1 sinograms and 100 class-2 sinograms were generated. Every sinogram was reconstructed with the three algorithms to yield three sets of 250 images, i.e., one set for each reconstruction method. In addition, the difference of image class means was calculated for each reconstruction algorithm by reconstructing the two types of kidney stones without noise and then taking their difference. Finally, AUC confidence intervals describing CHO performance were estimated for each reconstruction algorithm.

Multivariate normality of the channel outputs was validated at the 10% significance level with the Henze-Zirkler normality test [16]. To account for correlations, the coverage probability for each confidence interval was selected to be 98.33% so that the joint coverage probability for the three intervals was at least 95% by the Bonferroni inequality. Since the AUC values were all above 0.8, the Wilson-style AUC confidence intervals were used. The results, given in Table 1, indicate that algorithms A and B were both better than algorithm C with statistical significance. However, there was no statistically significant difference between algorithms A and B. These observations are consistent with our expectations.

VII. Discussion and Conclusions

We have presented refinements and extensions of the results in [9] that make CHO performance estimation with known-$\Delta\mu$ more attractive. In particular, we have developed an unbiased SNR point estimator, extended our theory to unequal numbers of images from each class, and proposed both exact and approximate confidence intervals. Naturally, the results presented here retain the statistical advantage that was observed in [9], since our theory is based on an SNR point estimator that is closely related to an SNR^2 estimator in [9]. The practical use of our theoretical results was demonstrated with a task-based image quality evaluation of three fan-beam CT image reconstruction algorithms.

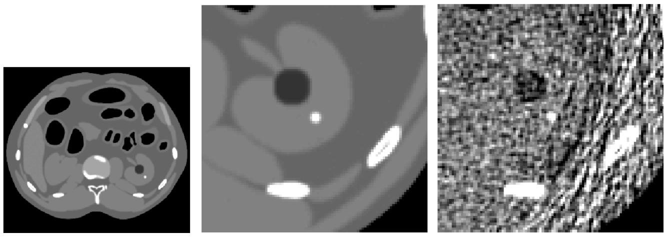

Fig. 4. (Left) Slice of the XCAT phantom. (Middle) ROI centered on left kidney. (Right) A noisy reconstruction. Grayscale: [-150, 250] HU

A:	[0.915,	0.956]
B:	[0.912,	0.953]
C:	[0.817,	0.869]

TABLE I
Wilson-style 98.33% AUC confidence intervals for the three reconstruction methods.

References

[1] H. H. Barrett and K. J. Myers, *Foundations of Image Science*. Wiley, 2004.

[2] S. Park, R. Jennings, H. Liu, A. Badano, and K. Myers, "A statistical, task-based evaluation method for three-dimensional x-ray breast imaging systems using variable-background phantoms," *Med. Phys.*, vol. 37, pp. 6253–6270, 2010.

[3] P. Bonetto, J. Qi, and R. Leahy, "Covariance approximation for fast and accurate computation of channelized Hotelling observer statistics," *IEEE Trans. Nucl. Sci.*, vol. 47, no. 4, pp. 1567–1572, Aug. 2000.

[4] A. Wunderlich and F. Noo, "Image covariance and lesion detectability in direct fan-beam x-ray computed tomography," *Phys. Med. Biol.*, vol. 53, no. 10, pp. 2471–2493, May 2008.

[5] H. H. Barrett, D. W. Wilson, and B. M. W. Tsui, "Noise properties of the EM algorithm: I. Theory," *Phys. Med. Biol.*, vol. 39, pp. 833–846, 1994.

[6] D. W. Wilson, B. M. W. Tsui, and H. H. Barrett, "Noise properties of the EM algorithm: II. Monte Carlo simulations," *Phys. Med. Biol.*, vol. 39, pp. 847–871, 1994.

[7] J. A. Fessler, "Mean and variance of implicitly defined biased estimators (such as penalized maximum likelihood): applications to tomography," *IEEE Trans. Image Processing*, vol. 5, no. 3, pp. 493–506, March 1996.

[8] A. Wunderlich and F. Noo, "Practical estimation of detectability maps for assessment of CT scanner performance," in *IEEE Nucl. Sci. Symp. Conf. Record*, November 2010, pp. 2801–2804.

[9] A. Wunderlich and F. Noo, "Estimation of channelized Hotelling observer performance with known class means or known difference of class means," *IEEE Trans. Med. Imaging*, vol. 28, no. 8, pp. 1198–1207, Aug. 2009.

[10] E. B. Wilson, "Probable inference, the law of succession, and statistical inference," *J. Am. Stat. Assoc.*, vol. 22, no. 158, pp. 209–212, June 1927.

[11] A. Kambadakone, B. Eisner, O. Catalano, and D. Sahani, "New and evolving concepts in the imaging and management of urolithiasis: Urologists perspective," *Radiographics*, vol. 30, no. 3, pp. 603–623, 2010.

[12] C. Abbey and H. Barrett, "Human-and model-observer performance in ramp-spectrum noise: effects of regularization and object variability," *J. Opt. Soc. A. A*, vol. 18, no. 3, pp. 473–488, 2001.

[13] K. Metheany, C. Abbey, N. Packard, and J. Boone, "Characterizing anatomical variability in breast CT images," *Med. Phys.*, vol. 35, no. 10, pp. 4685–4694, Oct. 2008.

[14] F. Noo, M. Defrise, R. Clackdoyle, and H. Kudo, "Image reconstruction from fan-beam projections on less than a short scan," *Phys. Med. Biol.*, vol. 47, no. 14, pp. 2525–2546, 2002.

[15] F. Dennerlein, F. Noo, J. Hornegger, and G. Lauritsch, "Fan-beam filtered-backprojection reconstruction without backprojection weight," *Phys. Med. Biol.*, vol. 52, no. 11, pp. 3227–3240, 2007.

[16] N. Henze and B. Zirkler, "A class of invariant consistent tests for multivariate normality," *Commun. Stat. Theory*, vol. 19, no. 10, pp. 3595–3617, 1990.

A B-spline based and computationally performant projector for iterative reconstruction in tomography
Application to dynamic X-ray gated CT

Fabien Momey, Loïc Denis, Catherine Mennessier, Éric Thiébaut, Jean-Marie Becker, Laurent Desbat

I. INTRODUCTION

ITERATIVE reconstruction methods for tomography have long proven their potential to enhance reconstruction quality, compared to the filtered backprojection (FBP) [2]. The drawback of iterative methods is their expensive computation time. However ongoing researches on algorithms and recent enhancements in computational power, call for a re-evaluation of the potential of iterative reconstruction in this domain.

Such methods require an accurate numerical modelization of the data acquisition process: the so-called *projector*. The representation of the object of interest (image) is the starting point of the projector. It is assimilated to a continuous function decomposed on a discrete basis of functions. The choice of this basis is essential for an accurate representation of the true function. Standard models such as *voxel driven* or *ray driven* [5] are based on raw samples, yielding modelization errors and artifacts on the reconstructed image. More advanced models, such as the recent *distance driven* [1] projector, define the function at any point considering staircase voxels, and thus make a better modelization. However such a basis of functions provides a coarse representation of the image because of its anisotropic behaviour, causing large modelization errors. Such issues can be dealt with the spherically symmetric volume elements, mostly known as blobs [7] [8] [9] [10] [11], but at the cost of increased complexity. Finally, for implementation purposes, the projection of the staircase voxel, in the *distance driven* model, is approximated, increasing its modelization errors.

We propose the use of B-splines as an alternative to both staircase voxel and blob approaches. B-splines are well known piecewise polynomial functions, and are characterized by the degree of their constituting polynomials. Recent works in sampling theory [18] [19] [15] have shown their efficiency in representing a continuous signal, with a good recovering accuracy. Increasing their degree makes them more and more similar to the 3D Gaussian functions, with a quasi-isotropic behaviour, while keeping local influence and separability property.

This gives us clues to develop a new efficient numerical projector for iterative reconstruction. One of the most important improvements we get is the reduction of the angular sampling of projections without any loss of quality.

Such an improvement is particularly of interest in the case of dynamic gated X-ray CT, which can be considered as a tomographic reconstruction problem with very few projection data, and for which we show some preliminary results.

II. MATERIALS AND METHODS

A. *Use of B-splines for image representation*

Let $f : \boldsymbol{x} \mapsto f(\boldsymbol{x})$, with $\boldsymbol{x} = (x_1, x_2, \ldots, x_n) \in \mathbb{R}^n$, be the n-dimensional continuous function modelizing the true image to be reconstructed. Its decomposition on a discrete basis of functions gives:

$$f(\boldsymbol{x}) = \sum_{\boldsymbol{k} \in \mathbb{Z}^n} \mathrm{c}_{\boldsymbol{k}} \varphi_{\boldsymbol{k}}(\boldsymbol{x}) = \sum_{\boldsymbol{k} \in \mathbb{Z}^n} \mathrm{c}_{\boldsymbol{k}} \varphi(\boldsymbol{x} - \boldsymbol{x}_{\boldsymbol{k}}) \tag{1}$$

where this discrete shift-invariant basis is assumed to be composed of the compact atom function $\varphi(\boldsymbol{x})$, regularly spaced on a n-dimensional grid of N samples. $\boldsymbol{k} = (k_1, k_2, \ldots, k_n)^{\mathrm{T}} \in \mathbb{Z}^n$ corresponds to indexes of the N samples of the discrete grid in the n-dimensional space, $\boldsymbol{x}_{\boldsymbol{k}} = (x_{k_1}, x_{k_2}, \ldots, x_{k_n})^{\mathrm{T}} \in \mathbb{R}^n$ are the coordinates of this discrete grid.

For numerical purposes, f is described as a vector of its N coefficients:

$$\mathbf{c} = (\mathrm{c}_{\mathbf{1}}, \mathrm{c}_{\mathbf{2}}, \ldots, \mathrm{c}_{\boldsymbol{N}})^{\mathrm{T}} \in \mathbb{R}^n \tag{2}$$

The choice of the atom function φ of the basis is essential for warranting consistency with the image intrinsic continuity. It will be a key point for the design of the projector which has to modelize accurately the data.

B-splines are piecewise polynomial functions with degree d, continuously differentiable up to order $d-1$ [18]. Let $\beta^0(x)$ be the rectangular pulse. Thus β^d is a B-spline of degree d, constructed by d convolutions of β^0.

$$\beta^d(x) = \underbrace{\beta^0 * \cdots * \beta^0}_{d+1 \ \text{terms}}(x) \tag{3}$$

This work was supported by the MiTiV project (Méthodes Inverses pour le Traitement en Imagerie du Vivant), funded by the French ANR (N° ANR-09-EMER-008).

Fabien Momey is with the Centre de Recherche Astrophysique de Lyon - Observatoire de Lyon, Lyon, France, and with the Laboratoire Hubert Curien, Université Jean Monnet, Saint-Étienne, France (telephone: +33 478 868 546, e-mail: author fabien.momey@univ-lyon1.fr).

Loïc Denis is with the Laboratoire Hubert Curien.

Catherine Mennessier is with the Laboratoire Hubert Curien, and with the engineer school CPE, Lyon, France.

Éric Thiébaut is with the Centre de Recherche Astrophysique de Lyon - Observatoire de Lyon.

Jean-Marie Becker is with the Laboratoire Hubert Curien, and with CPE Lyon.

Laurent Desbat is with the TIMC-IMAG, Grenoble, France.

Hence going back to the formulation of the image representation in (1), we choose B-splines as our basis of functions φ, leading to:

$$f(\boldsymbol{x}) = \sum_{\boldsymbol{k}\in\mathbb{Z}^n} \mathrm{c}_{\boldsymbol{k}} \boldsymbol{\beta}^d_{\boldsymbol{k}}(\boldsymbol{x}) = \sum_{\boldsymbol{k}\in\mathbb{Z}^n} \mathrm{c}_{\boldsymbol{k}} \boldsymbol{\beta}^d(\boldsymbol{x} - \boldsymbol{x}_{\boldsymbol{k}}) \tag{4}$$

Classical basis functions used by some existing projectors are the simple staircase voxels. This is the case for the *distance driven* projector [1]. These functions are advantageous for being the most compact B-splines (of degree 0), easy to manipulate. However, staircase voxels suffer from a high anisotropic behaviour. They constitute a too coarse basis of representation of a continuous object, leading to large modelization errors. A finer sampling rate lowers these errors, but at the cost of an increased computational burden.

The accuracy of the model can be improved using B-splines of higher degree. Indeed B-splines are close to a Gaussian function when their degree d is large. Thus they tend to spherically symmetric function, while preserving a local support. As a result we can deal with quasi-isotropic functions. We also get a better approximation order in the modelization of $f(\boldsymbol{x})$. These two properties are related by the fact that B-splines are the shortest and smoothest scaling functions for a given order of approximation [19].

B. Projector

We consider a general tridimensional system with coordinates $\boldsymbol{x} = (x, y, z)$ linked to the object of interest. The regular sampling grid is therefore identified by the samples positions $\boldsymbol{x}_{\boldsymbol{k}}$, corresponding also to the center of each basis function $\boldsymbol{\beta}^d_{\boldsymbol{k}}$. Then we consider a flat detector, with coordinates $\boldsymbol{u} = (u, v)$. The detector acquires the projection with a given orientation denoted θ. Let $\mathbf{c}$ be the vector of coefficients of the image, defined in (2). The numerical data modelization at orientation θ is:

$$\mathbf{g}^\theta = \mathbf{R}^\theta \cdot \mathbf{c} \;, \quad \mathrm{g}^\theta_q = \sum_{k\in\Omega^\theta_q} \mathbf{R}^\theta_{qk} \cdot \mathrm{c}_k \tag{5}$$

where $\mathbf{R}^\theta$ is the projector and $\mathbf{g}^\theta$ is the resulting data vector, the elements of which are noted g^θ_q. The coefficient $\mathbf{R}^\theta_{qk}$ of the matrix $\mathbf{R}^\theta$ is the contribution of the voxel function k on the q^{th} data element. Ω^θ_q is the set of voxels k impinging the θ-oriented detector pixel q. Let $P_q : \boldsymbol{u} \mapsto P_q(\boldsymbol{u}) = \boldsymbol{\beta}^0(\boldsymbol{u} - \boldsymbol{u}_q)$ be the q^{th} detector pixel response, assumed to be a 2D rectangular pulse, centered at position $\boldsymbol{u}_q$. This response is shift-invariant over each detector pixel. Thus:

$$\mathbf{R}^\theta_{qk} = \int\!\!\int F^\theta_{\boldsymbol{k}}(\boldsymbol{u}) \cdot P_q(\boldsymbol{u}) \; d\boldsymbol{u} \tag{6}$$

$F^\theta_{\boldsymbol{k}}$ is the footprint of the basis function $\boldsymbol{\beta}^d_{\boldsymbol{k}}$. It is nothing else than the X-ray transform of this function on the θ-oriented detector, along each ray trajectory $\{S(\theta), \vec{r}(\theta, \boldsymbol{u})\}$ crossing it, and impinging the detector plane at the position $\boldsymbol{u}$.

$$F^\theta_{\boldsymbol{k}}(\boldsymbol{u}) = \int_{\boldsymbol{x}\in\{S(\theta),\vec{r}(\theta,\boldsymbol{u})\}} \boldsymbol{\beta}^d_{\boldsymbol{k}}(\boldsymbol{x}) \; d\boldsymbol{x} \tag{7}$$

A given projector $\mathbf{R}^\theta$ determines the expression of this footprint $F^\theta_{\boldsymbol{k}}$. Obviously, $F^\theta_{\boldsymbol{k}}$ depends on the chosen basis of functions. Moreover some approximations are often made in the calculation of this footprint and its contribution to detector pixels, in order to lower the computation cost.

Our approach uses the quasi-isotropy property of B-splines of higher degree, stated in section II-A, to suppose that the footprint is identical whatever the orientation θ. As a result, we first state that the footprint of $\boldsymbol{\beta}^d_{\boldsymbol{k}}$, in parallel beam geometry, is a $n-1$-dimensional B-spline of degree d, separable over the detector axis. For the 3D case, this gives:

$$F^\theta_{\boldsymbol{k}}(\boldsymbol{u}) = \beta^d(u - u_k) \cdot \beta^d(v - v_k) \tag{8}$$

where $(u_k, v_k) = \boldsymbol{u}_{\boldsymbol{k}}$ is the position, on the detector, of the projection of the center $\boldsymbol{x}_{\boldsymbol{k}}$ of $\boldsymbol{\beta}^d_{\boldsymbol{k}}$.

In the case of cone beam geometry, the magnification effect has to be taken into account, as well as the distorsion effect depending on the position of the voxel in the field of view. For the 3D case, this gives:

$$F^\theta_{\boldsymbol{k}}(\boldsymbol{u}) = \beta^d\left(\frac{u}{\Gamma^\theta_S \cdot \delta_{u_{\boldsymbol{k}}}} - u_{\boldsymbol{k}}\right) \cdot \beta^d\left(\frac{v}{\Gamma^\theta_S \cdot \delta_{v_{\boldsymbol{k}}}} - v_{\boldsymbol{k}}\right) \tag{9}$$

Γ^θ_S is the magnification factor; δ_{u_k} et δ_{v_k} are the distorsion factors.

A study of modelization and approximation errors of our model, compared with the *distance driven* model, has been done previously in [12], and has proven its better accuracy. We have shown that the use of cubic B-splines (degree 3) already reaches almost the best accuracy. However such a gain is at the cost of an increase of the required number of operations, due to the larger footprint of a given voxel as a function of the B-spline degree, as shown in Fig.1. But at the degree 3, it is only about 6 times larger, which remains is the same range of computational burden. Moreover our projection scheme, as well as the staircase voxel based approaches, is highly parallelizable, making possible to optimize the implementation for speeding up the calculation.

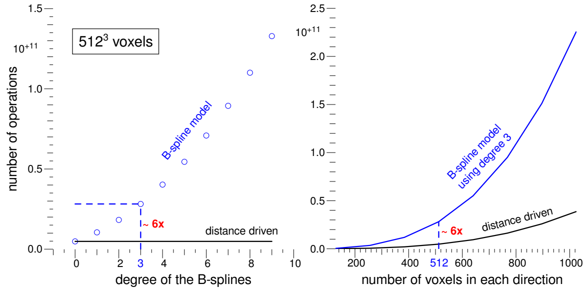

Fig. 1. Number of operations involved in the calculation of the 3D B-spline based projector, as a function of the B-spline degree and the number of voxels in each direction, compared with the *distance driven* projector.

III. RESULTS ON 2D FAN BEAM RECONSTRUCTIONS

A linear detector, linked to the fan beam source, is considered. The set source-detector rotates around the 2-dimensional object of interest. The B-spline coefficients of the image $\mathbf{c}$, are reconstructed from the set of projections $\mathbf{g} = \{\mathbf{g}^\theta | \theta \in \Theta\}$, where Θ is the set of projection angles, by minimization of:

$$\mathbf{c} = \underset{\hat{\mathbf{c}}}{argmin} \underbrace{\sum_{\theta\in\Theta} ||\mathbf{g}^\theta - \mathbf{R}^\theta \cdot \hat{\mathbf{c}}||^2_{\mathbf{W}}}_{\text{data residuals}} + \underbrace{\mu \cdot \Psi(\mathbf{\Phi} \cdot \hat{\mathbf{c}})}_{\text{regularization term}} \qquad (10)$$

where $|| \cdot ||^2_{\mathbf{W}}$ corresponds to the weighted least squares term. The weighting matrix $\mathbf{W}$ is the inverse of the noise covariance. $\Psi : \mathbf{f} \mapsto \Psi(\mathbf{f})$ is a regularization operator applied to the image in the samples space. The interpolation operator $\mathbf{\Phi}$, which transforms the B-spline coefficients in samples values, can be applied using fast digital filtering operations [16] [17] [18], as well as its inverse. Thus the additional computational burden is negligible. The regularization we use is a relaxed total variation prior [14]. The minimization of (10) is performed with a quasi-Newton optimization algorithm: the L-BFGS method [13].

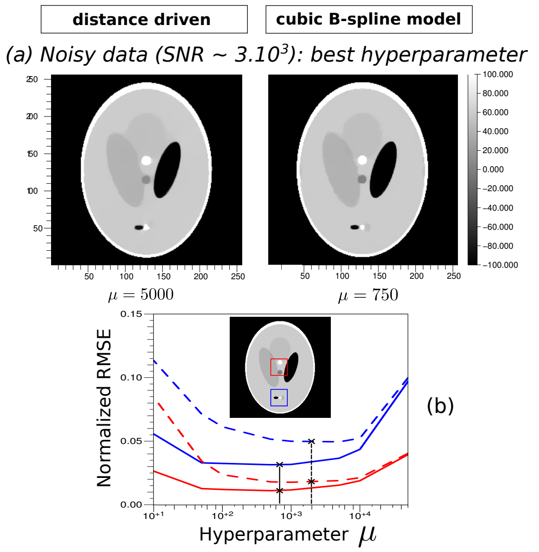

Fig. 2. (a) Reconstructions of a Shepp-Logan phantom 256×256, from a set of 60 projections with 512 detector pixels, with both the B-spline projector using cubic B-splines and the *distance driven* projector. Visualization in Hounsfield units. Reconstructions from noisy data (additional non-stationary Gaussian noise with a signal to noise ratio of about 3000), obtained with the value of μ giving the best visual image quality. (b) Normalized root mean square error in 2 regions of interest (ROI) of the reconstructed image, for various values of the hyperparameter μ (logarithmic scale). The ROIs are indicated on the image, with the corresponding color on the graphs. Solid curves : reconstructions with the B-spline projector. Dashed curves : reconstructions with the *distance driven* projector.

Fig.2 shows some of the previous results obtained in [12]. We had reconstructed a 256×256 Shepp-Logan phantom, from a set of 60 projections with 512 detector pixels, calculated analytically. The sampling rate was the same for both voxels and detector pixels. The reconstructions were performed with both our B-spline based projector, using cubic B-splines, and the *distance driven* projector, for comparison. The data were corrupted by a non-stationary Gaussian noise, with a signal to noise ratio approximately 3000.

Fig.2(a) displays some reconstructed images, obtained in [12]. The best value of the hyperparameter μ is found, which gives the best qualitative visual quality of the reconstructed image. Our B-spline based projector leads to a better image quality than *distance driven*, without regularizing a lot. Fig.2(b) shows curves of the normalized root mean square error (RMSE), calculated on 2 regions of interest (ROI) taken on the image, as a function of the hyperparameter μ, using both the B-spline based projector using cubic B-splines (solid curves) and the *distance driven* projector (dashed curves). The curves show that, for each ROI, the B-spline based projector's RMSE is always lower than the *distance driven* projector's RMSE. Thus for this given evaluation metric, our projector shows again the best performances.

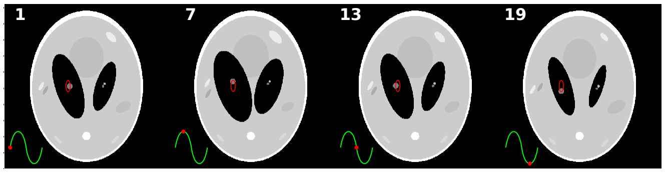

Fig. 3. Dynamic Shepp-Logan phantom 512×512. A 5 seconds period of motion is chosen and 25 frames are extracted. The frames 1, 7, 13 and 19 are represented. The position of each frame's date in the temporal sinusoidal signal is indicated. The red ellipse corresponds to the trajectory of the small circular insert in the left big ellipse distorted over time.

IV. APPLICATION ON SIMULATED 2D DYNAMIC X-RAY GATED CT

We experiment our projector in the context of dynamic X-ray tomography. More precisely we simulate a 2D case of gated iterative reconstruction of a Shepp-Logan phantom, some ellipses of which see its parameters periodically moving over time (semi-minor or major axis, center's position). Hence the motion of the phantom's ellipses can be either translations or distorsions. The temporal signal associated to the periodic variation of the parameters is a sinus function, that is to say that the speed of motion is not constant over a period. Fig.3 shows frames of the simulated object. Each frame's size is 512×512. The speed of the motion is almost the fastest for frames 1 and 13, and almost the slowest for frames 7 and 19. For instance the trajectory of motion of the small circular insert in the left big ellipse is indicated on Fig.3 for illustration. The position of the frame's date in the temporal sinusoidal signal is also indicated.

The geometry of the acquisition system is the same as in III, but now a period is defined for a whole rotation of the detector around the object. We choose this acquisition time to be equal to 120 seconds. During this period, 600 projections, regularly spaced in time, and on 360°, are simulated analytically from the state of the object at the corresponding date. The period of motion lasts 5 seconds. As a result 24 periods of motion occur during the acquisition. We want to be in gated mode, so we reconstruct 25 frames of a period of motion of the object, such that a given projection is exactly registered to a given frame. Hence we have 25 frames, each one repeated 24 times during the acquisition, thus associated with 24 projections regularly spaced on 360°. It is very important to notice that this problem results in reconstructing each frame from very angularly undersampled data.

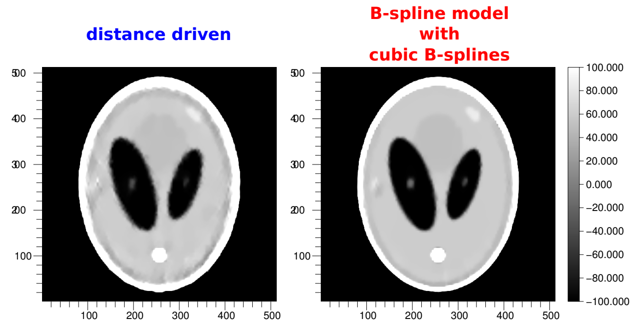

Fig. 4. Frame 13 of the reconstructed gated 128 × 128 Shepp-Logan sequence, with both the B-spline projector using cubic B-splines (right) and the *distance driven* projector (left). The reconstructed images are re-interpolated on a finer 512 × 512 grid, using cubic B-spline interpolator.

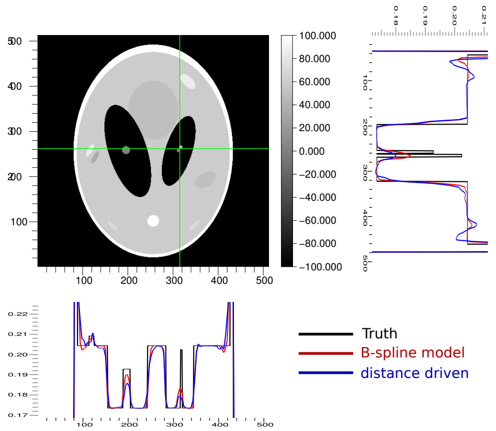

Fig. 5. Horizontal and vertical profiles taken on frame 13 of the reconstructed gated 128 × 128 Shepp-Logan sequence, with both the B-spline projector using cubic B-splines (right) and the *distance driven* projector (left). The reconstructed images are re-interpolated on a finer 512 × 512 grid, using cubic B-spline interpolator.

From this set of projections, we perform gated reconstructions of the 25 frames. The reconstruction of this sequence is performed globally, each frame reconstruction following the same optimization scheme as in Eq.10, for the data residuals' part. A global spatio-temporal regularization is performed on the "2D + time" sequence, which consists in the same regularizer used in III, but extended to 3 dimensions to take into account the temporal correlation between frames.

Fig.4 shows preliminary results of reconstructions, with both our B-spline based projector, using cubic B-splines, and the *distance driven* projector, for comparison. We focus our visualization on a single frame, the 13^{th}, at which the speed of the motion is faster. The reconstructed 128 × 128 images are re-interpolated on a finer 512 × 512 grid, using a cubic B-spline interpolator, for a better image quality. We can see the better visual quality of the frame reconstructed with our B-spline projector.

Fig.5 shows profiles of the reconstructions shown in Fig.4, for a more precise evaluation. Again the superior ability of our projector to recover finer details is visible.

V. CONCLUSION AND FURTHER WORKS

We have presented a new type of numerical projector for iterative reconstruction in tomography. It is based on the use of a basis of separable 3D B-splines, which is much more adapted for data modelization than the staircase voxels.

We have demonstrated the better accuracy of our projector based on cubic B-splines, on 2-dimensional regularized iterative reconstructions, from simulated data, using a small number of projections, compared with the *distance driven* projector.

We also have studied its behaviour in the context of dynamic gated X-ray tomography. The fact that the temporal dimension has to be included in the reconstructed image, i.e. it becomes a "2D + time" image, reduces drastically the number of projections available for a given temporal frame. Preliminary results have again shown that the accuracy of the projector is a key point to deal with this lack of data in the reconstruction process, and to make the best use of available information.

REFERENCES

[1] B. DeMan and S. Basu. *Distance driven projection and backprojection in three dimensions*. Physics in Medicine and Biology, 2004, 49, p2463-2475.
[2] J.A. Fessler. *Iterative methods for image reconstruction*. IEEE International Symposium on Biomedical Imaging Tutorial, Arlington Virginia, 2006.
[3] Y. Long, J.A. Fessler and J.M. Balter. *3D Forward and Back-Projection for X-Ray CT Using Separable Footprints*. IEEE Transactions on Medical Imaging, 2010, 29, p1839-1850.
[4] S. Horbelt, M. Liebling and M. Unser. *Discretization of the Radon transform and of its inverse by spline convolutions*. IEEE Transactions on medical imaging, 2002, 21, p363-376.
[5] P.M. Joseph. *An improved algorithm for reprojecting rays through pixel images*. IEEE Transactions on Medical Imaging, 1982, 1, p192-196.
[6] M. Slaney and A. Kak. *Principles of computerized tomographic imaging*. SIAM, Philadelphia, 1988.
[7] R.M. Lewitt. *Multidimensional digital image representations using generalized Kaiser-Bessel window functions*. JOSA A, 1990, 7, p1834-1846.
[8] R.M. Lewitt. *Alternatives to voxels for image representation in iterative reconstruction algorithms*. Physics in Medicine and Biology, 1992, 37, p705-716.
[9] S. Matej and R.M. Lewitt. *Image representation and tomographic reconstruction using spherically symmetric volume elements*. IEEE Medical Imaging Conference Record, 1992, p1191-1193.
[10] S. Matej and R.M. Lewitt. *Efficient 3D grids for image reconstruction using spherically-symmetric volume elements*. IEEE Transactions on Medical Imaging, 1995, 42, p1361-1370.
[11] S. Matej and R.M. Lewitt. *Practical considerations for 3D image reconstruction using spherically symmetric volume elements*. IEEE Transactions on Medical Imaging, 1996, 15, p68-78.
[12] F. Momey, L. Denis, C. Mennessier, É. Thiébaut, J.M. Becker and L. Desbat. *A new representation and projection model for tomography, based on separable B-splines*. IEEE Medical Imaging Conference Record, 2011, p2602-2609.
[13] J. Nocedal. *Updating quasi-Newton matrices with limited storage*. Mathematics of computation, 1980, 35, p773-782.
[14] L.I. Rudin, S. Osher and E. Fatemi. *Nonlinear total variation based noise removal algorithms*. Physica D: Nonlinear Phenomena, 1992, 60, p259-268.
[15] P. Thévenaz, T. Blu and M. Unser. *Interpolation Revisited*. IEEE Transactions on Medical Imaging, 2000, 19, p739-758.
[16] M. Unser., A. Aldroubi and M. Eden. *B-spline signal processing: Part I-Theory*. IEEE Transactions on Signal Processing, 1993, 41, p821-833.
[17] M. Unser., A. Aldroubi and M. Eden. *B-spline signal processing: Part II-Efficient design and applications*. IEEE Transactions on Signal Processing, 1993, 41, p834-848.
[18] M. Unser. *Splines: A perfect fit for signal and image processing*. IEEE Signal Processing Mag., 1999, 16, p22-38.
[19] M. Unser. *Sampling-50 years after Shannon*. Proceedings of the IEEE, 2000, 88, p569-587.

Toward quantifying admissible undersampling of sparsity-exploiting iterative image reconstruction for X-ray CT

Jakob H. Jørgensen, Emil Y. Sidky, and Xiaochuan Pan

***Abstract*—For the discrete-to-discrete X-ray CT imaging model we propose a sufficient sampling condition (SSC) in order to establish existence of a unique and stable solution. We demonstrate in a numerical simulation modeling breast CT how the SSC can be used to quantify the undersampling admitted by TV-minimization. Our results indicate a direct connection between the sparsity of the image and the admitted undersampling. Also, the SSC reveals an asymmetry between view- and detector bin-undersampling, which explains differences in obtainable reconstruction quality.**

***Index Terms*—Compressed sensing, total-variation, sampling conditions, undersampling, iterative image reconstruction**

I. INTRODUCTION

In recent years, the field of compressed sensing (CS) [1], [2] has motivated much development in sparsity-exploiting iterative image reconstruction (IIR) for X-ray computed tomography (CT). CS promises accurate reconstruction from less data than is required by standard IIR methods, such as the algebraic reconstruction technique (ART). This is made possible by exploiting sparsity, i.e., few non-zeros in the image or of some transform applied to the image. What is seldom discussed, however, is that the theoretical results from CS do *not* extend to the CT setting. CS only provides theoretical guarantees of accurate undersampled recovery in case of random or certain special measurement matrices, not deterministic matrices such as CT system matrices. Nevertheless, sparsity-exploiting methods, such as total-variation (TV) minimization and the use of wavelet-expansions, have been shown empirically to allow accurate reconstruction, both from simulated ideal data, as well as clinical scanner data [3], [4].

One fundamental problem in uncritically applying sparsity-exploiting methods to CT is that there is no quantitative notion of full sampling: While results exist for analytic inversion methods based on the continuous-to-continuous (CC) imaging model [5], no similar results exist for the discrete-to-discrete (DD) model, which is the one employed in most IIR, including sparsity-exploiting methods. As is well-known, and as we will demonstrate, it is not sufficient to have a square system matrix for ensuring that there is a unique well-defined solution image. Furthermore, CT-matrices can be numerically ill-conditioned, which makes the solution unstable w.r.t. noisy measurements.

The present paper proposes a sufficient sampling condition (SSC), which is to serve as a reference for quantifying the undersampling sparsity-exploiting reconstruction methods allow for, here TV-minimization. The SSC is based on the condition number of the CT system matrix. The use of the SSC is demonstrated in a numerical simulation modeling breast CT, and leads to a possible explanation of the potential in few-view reconstruction using TV-minimization.

In Sec. II we define the DD imaging model, in Sec. we present our SSC, and in Sec. IV we demonstrate the application in a breast CT simulation study.

II. DISCRETE-TO-DISCRETE IMAGING MODEL FOR CIRCULAR FAN-BEAM GEOMETRY

A. Continuous-to-continuous and discrete-to-discrete models

Analytic reconstruction algorithms, e.g., filtered-back projection (FBP), rely on inversion formulas for the continuous-to-continuous (CC) cone-beam or X-ray transform model

$$g[\vec{s}, \vec{\theta}] = \int_0^\infty dt f(\vec{s} + t\vec{\theta}), \tag{1}$$

where g, the line integral over the object function f from source location $\vec{s}$ in the direction $\vec{\theta}$, is considered data.

For IIR algorithms, the CC imaging model is discretized by expanding the object function in a finite expansion set, e.g., in pixels/voxels. The digital sampling of the CT device is accounted for by directly using the sampled data without interpolation. The discrete-to-discrete (DD) imaging model

$$\vec{g} = X\vec{f}, \tag{2}$$

is hereby obtained. $\vec{g}$ is a finite set of ray-integration samples, $\vec{f}$ the object expansion coefficients, and X the system matrix modeling the ray integration. (2) is solved by an IIR method, such as ART, expectation-maximization (EM) or variants.

B. Circular fan-beam geometry

As an example, we use the most common setup: circular fan-beam CT with equi-angular projection spacing. In the CC model, we have the source location specified by the scalar (angular) parameter λ, $\vec{s}(\lambda) = R_0(\cos\lambda, \sin\lambda)$, where R_0 is the distance from the center-of-rotation to the X-ray source. The detector bin locations are given by

$$\vec{b}(\lambda, u) = (R_0 - D)(\cos\lambda, \sin\lambda) + u(-\sin\lambda, \cos\lambda),$$

Jakob H. Jørgensen is with the Department of Informatics and Mathematical Modeling, Technical University of Denmark, Richard Petersens Plads, Building 321, 2800 Kgs. Lyngby, Denmark. Corresponding author: Jakob H. Jørgensen, E-mail: jakj@imm.dtu.dk.

Emil Y. Sidky and Xiaochuan Pan are with the Department of Radiology, The University of Chicago, 5841 S. Maryland Avenue, Chicago, IL 60637, USA.

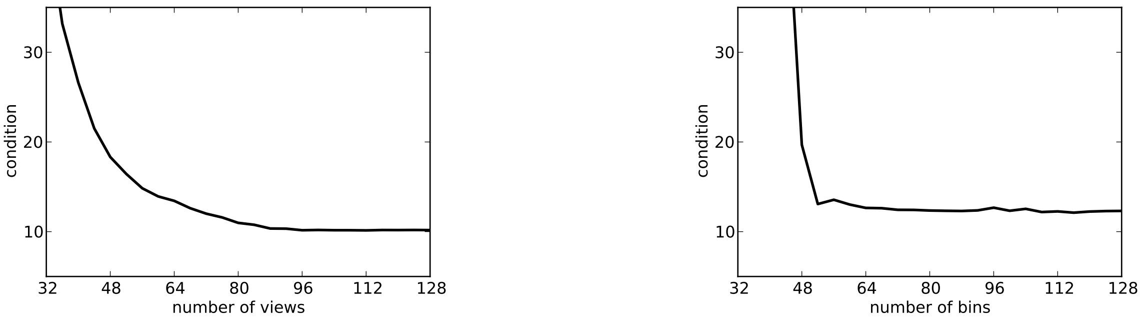

Fig. 1. Condition numbers for system matrices (line intersection) modeling circular fan-beam projection data from the 812 pixels circular FOV contained within a 32×32 pixel square. Left: number of bins is fixed at 64. Right: the number of views is fixed at 64.

where D is the source-to-detector-center distance, and u specifies a position on the detector. We divide the 2π arc into N_{views} arranged at equally spaced angular intervals, so that the source parameters follow $\lambda_i = i2\pi/N_{\text{views}}$, and $i \in [0, N_{\text{views}} - 1]$. The detector is subdivided into N_{bins}, $u_j = u_{\text{min}} + (j + 0.5)\Delta u$, where D_L is the detector length, $u_{\text{min}} = -D_L/2$, $\Delta u = D_L/N_{\text{bins}}$, and $j \in [0, N_{\text{bins}} - 1]$. The detector length is determined by requiring it to detect all rays passing through the largest circle inscribed within the square $N \times N$ image array. Only this central circle is visible from all views and only pixels within are considered variable. The resulting number of unknown pixel values N_{pix} is $N_{\text{pix}} \approx (\pi/4)N^2$. The dimensions of the projector X are $M = N_{\text{views}} \times N_{\text{bins}}$ rows (number of ray integrations) and N_{pix} columns (number of variable pixels). The elements of X are computed by the line-intersection method, where $X_{m,n}$ is the intersection length of the mth ray with the nth pixel.

III. SUFFICIENT SAMPLING CONDITIONS

The basic sufficient sampling condition (SSC) is that the null space of X is empty, because if it is not, then multiple images yield the same data. For the matrices typically used in CS, such as random matrices or partial discrete Fourier transform matrices, an empty null space is obtained when the number of rows in X equals the number of columns. For CT, however, this is not necessarily true, as we will demonstrate, and hence, more samples are needed. This means that we can not directly use $M = N_{\text{pix}}$ as SSC. Even if X has an empty null space, it might be numerically ill-conditioned leading to an unstable solution in presence of noise. The condition number $\kappa(X) = \sigma_{\max}/\sigma_{\min}$, i.e., the ratio of the max. and min. singular values of X, reveals both a non-empty null space, by $\kappa(X)$ being ∞, and ill-conditioning, by $\kappa(x) \gg 1$.

To gain intuition on the dependence $\kappa(X)$ on the number of views and detector bins for a fixed image representation, we carry out the following experiment: We set up a small $N = 32$ image array, with a total of $N_{\text{pix}} = 812$ pixels, and generate system matrices X for different numbers of views and detector bin sampling: $N_{\text{views}} \in [8, 128]$ and $N_{\text{bins}} \in [8, 128]$. Our first observation is that at $N_{\text{views}} = 64$ and $N_{\text{bins}} = 13$, we have $M = 832 > 812 = N_{\text{pix}}$, but $\kappa(X)$ is infinite. This confirms that it is not enough for SSC to have more rows than columns in X. In Fig. 1, we have mapped out $\kappa(X)$ for fixed $N_{\text{bins}} = 64$ and $N_{\text{views}} \in [32, 128]$ as well as for fixed $N_{\text{views}} = 64$ and $N_{\text{bins}} \in [32, 128]$. Each sampling configuration in the shown range leads to a well-posed linear system (2), but it is clear that the more sparsely sampled end of the study has relatively large condition number. Going to more samples, the condition number decreases, however, the decrease is asymmetric in N_{views} and N_{bins}. The decay with N_{views} is quite gradual while that of N_{bins} is step-like at $N_{\text{bins}} = 48$. It would be mathematically tidy to define SSC as simply the values of N_{bins} and N_{views} where κ no longer decreases, but we must take into account the practical issue that adding views to the data scan is expensive. Based on Fig. 1, we therefore select the sampling condition

$$N_{\text{views}} = 2N \quad \text{and} \quad N_{\text{bins}} = 2N, \tag{3}$$

as values that provide a reasonable balance between sampling and condition number. While the presented results are for $N = 32$, we found a similar behavior of $\kappa(X)$ for larger N, and hence we can use $N_{\text{views}} = 2N$, $N_{\text{bins}} = 2N$ as a simple, yet useful, definition of sufficient sampling.

In the remaining part of the paper, we carry out a numerical simulation for evaluating the proposed SSC. While the example is breast CT, the approach is not limited to this application.

IV. NUMERICAL SIMULATIONS

A. Breast CT background

Breast CT is considered a possible screening or diagnostic tool for breast cancer. System requirements are challenging as total exposure must be similar to the two full-field digital mammograms used in screening exams. Breast CT acquires on the order of 500 X-ray projections, i.e., 250 times more projections sharing the same exposure. Sparsity-exploiting IIR algorithms can potentially reconstruct from fewer views and hence allow for an increased exposure per view.

We employ the breast phantom displayed in Fig. 3 (left), which consists of $N_{\text{pix}} = 51468$ pixels within the circular image region, contained in a 256×256 array. A small region of interest (ROI) contains 5 tiny ellipses modeling microcalcifications. The gray values are in units of the attenuation of water: 1.00 (fat), 1.10 (fibroglandular tissue), 1.15 (skin) and $1.9-2.3$ (microcalcifications). The sparsity, i.e. the number of non-zeros, in the gradient magnitude image is approx. 10,000, or roughly one fifth of N_{pix}.

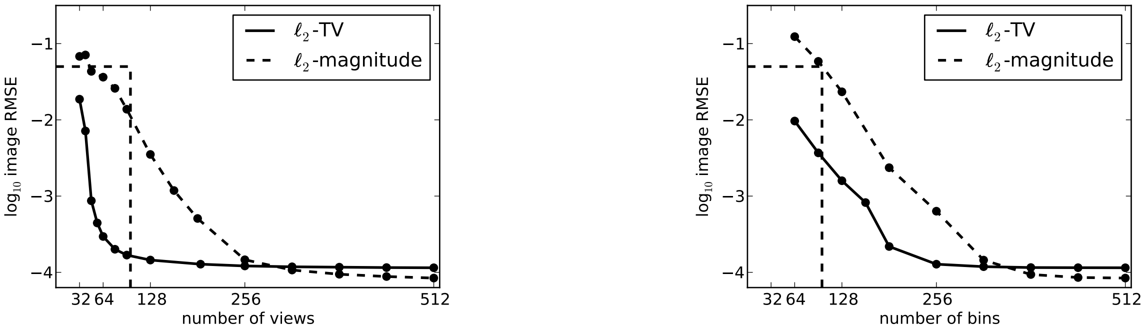

Fig. 2. Image RMSE for ℓ_2-TV and ℓ_2-magnitude reconstructions with $\epsilon = 10^{-5}$. Left: Fixed $N_{\text{bins}} = 2N = 512$, and $N_{\text{views}} \in [32, 512]$. Right: Fixed $N_{\text{views}} = 2N = 512$, and $N_{\text{bins}} \in [32, 512]$.

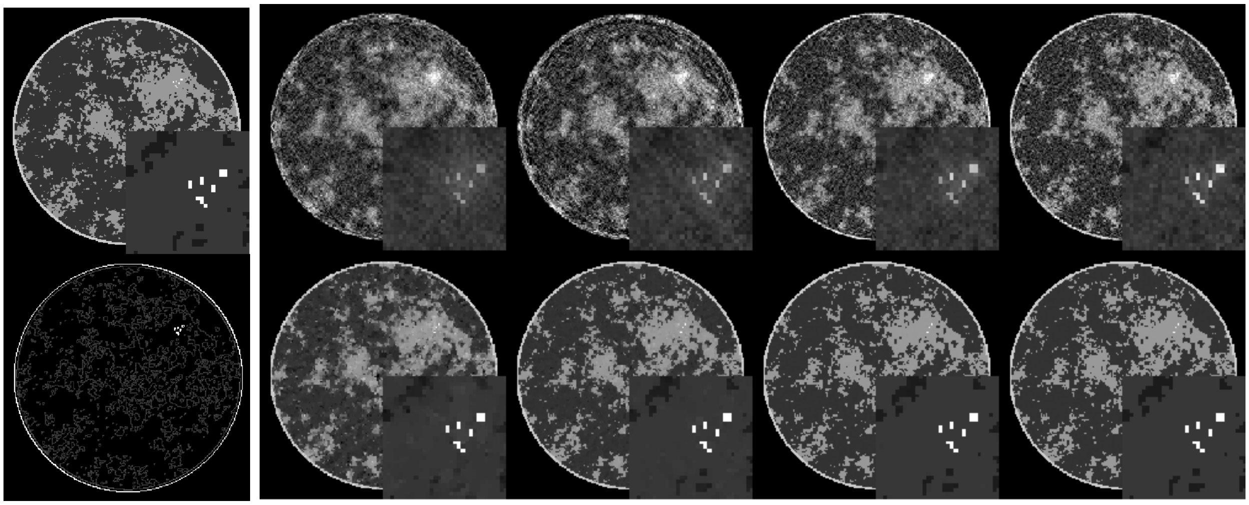

Fig. 3. Left, upper: 256×256 pixelized breast CT phantom. Microcalcifications are seen in the upper right quarter and magnified in the ROI inset. Left, lower: the gradient magnitude image, which has a sparsity of approx. 10,000 non-zero pixel values. Right, top and bottom: ℓ_2-magnitude and ℓ_2-TV with $\epsilon = 10^{-5}$ reconstructions, respectively. From left to right 32, 40, 48, 64 view data, with the number of detector bins fixed at 512. The gray scale window for the complete image is [0.95, 1.20], and for the ROI insets [0.9, 1.8].

B. Simulation setup

A common sparsity-exploiting IIR is total-variation (TV) minimization, which exploits that typical CT-images consist of fairly well-separated regions of constant gray-level, i.e., are sparse in the image gradient magnitude. We consider here TV-minimization subject to the constraint

$$\frac{1}{N_{\text{views}} N_{\text{bins}}} \|X\vec{f} - \vec{g}\|_2^2 \leq \epsilon^2, \tag{4}$$

i.e., the data residual norm (normalized to facilitate comparison of different sampling levels) is to be smaller than a parameter ϵ. For a non-sparsity-exploiting reference method, we employ Tikhonov regularization, here in the equivalent constrained formulation:

$$\ell_2\text{-TV:} \quad \vec{f}^* = \underset{\vec{f}}{\operatorname{argmin}} \|\vec{f}\|_{\text{TV}} \quad \text{s.t.} \quad (4), \tag{5}$$

$$\ell_2\text{-magnitude:} \quad \vec{f}^* = \underset{\vec{f}}{\operatorname{argmin}} \|\vec{f}\|_2^2 \quad \text{s.t.} \quad (4). \tag{6}$$

Here, $\|\vec{f}\|_{\text{TV}}$ is the discrete TV of $\vec{f}$,

$$\|\vec{f}\|_{\text{TV}} = \sum_{j=1}^{N_{\text{pix}}} \|D_j \vec{f}\|_2, \tag{7}$$

where N_{pix} is the number of pixels and D_j is the forward difference approximation to the gradient at voxel j.

Both problems are solved by converting to the equivalent Lagrangian formulation and applying an optimal gradient-based optimization algorithm described in [6].

C. Simulation results

We fix $N_{\text{bins}} = 512$ and vary the number of views $N_{\text{views}} \in [32, 512]$, evenly distributed over a 2π scanning. Similarly, we fix $N_{\text{views}} = 512$ and vary N_{bins} in the same range. Ideal data is generated from forward projection of the discrete phantom. No noise is added. While ideal data would call for ϵ equal to zero, we use $\epsilon = 10^{-5}$ since we are interested in the ideal case behavior of an optimization problem that allows for reconstruction from noisy data. The root mean square error (RMSE) of the reconstructed images relative to the original discrete phantom are shown in Fig. 2, and selected images are shown in Fig. 3. To help in the interpretation of the results, two reference lines are drawn in the graphs. The vertical line indicates the smallest number of views, $N_{\text{views}} = 101$, for which the number of samples $N_{\text{views}} \times 512$ is larger than N_{pix}. For fewer N_{views} the null space is non-empty; for ensuring emptiness, we typically need slightly more samples, due to possible linear dependence, as we saw earlier. The horizontal line shows the minimum gray level contrast, 0.05, in the phantom and provides a reference for the RMSE. A much smaller RMSE indicates visual closeness of the reconstructed image to the original phantom.

For varying N_{views}, the ℓ_2-magnitude RMSE decays gradually w.r.t. N_{views} until becoming nearly flat at our proposed SSC, $N_{\text{views}} = 2N = 512$. It seems reasonable to have SSC be at a point where no further improvement is obtained. ℓ_2-TV shows a much faster transition to low RMSE images already at $N_{\text{views}} \geq 50$, much lower than ℓ_2-magnitude, and, in fact, also than the vertical reference line. For fewer views, quality quickly deteriorates, and the RMSE approaches that of the ℓ_2-magnitude at $N_{\text{views}} = 32$. The step-like shape for ℓ_2-TV at $N_{\text{views}} \approx 50$ indicates that this number of views is sufficient for accurate ℓ_2-TV reconstruction for the present phantom image.

For varying N_{bins}, both ℓ_2-magnitude and ℓ_2-TV need a larger number of samples before no more improvement can be obtained. Moreover, and somewhat surprisingly, the ℓ_2-TV behavior is quite different, in that the transition is much more gradual and the flat portion does not extend to nearly as low a sampling rate. This demonstrates an asymmetry in sampling of the two parameters of X. A possible explanation is found in the condition number dependence on N_{views} and N_{bins} from Fig. 1, where a similar asymmetry was seen. It seems that if we decrease N_{bins} below $2N$ the condition number increases quickly leading to the reduced reconstruction quality. For reducing N_{views}, where the condition number increases more gradually, there is a more limited loss in reduction. Clearly, we need to make the distinction between view undersampling and bin undersampling.

From Fig. 3, it may be argued that 32 views would suffice if we are solely interested in the microcalcifications and disregard the prominent artifacts of the background. For visually accurate ℓ_2-TV reconstruction $N_{\text{views}} \approx 50$ suffices, while at this point ℓ_2-magnitude still shows clear artifacts.

D. Connection between undersampling and sparsity

Using the SSC of $N_{\text{views}} = N_{\text{bins}} = 512$ as a reference, we can now quantify that ℓ_2-TV admits a view undersampling of $50/512 \approx 0.1$. Central to CS is connecting the number of samples and the sparsity, here, of the gradient magnitude image. $N_{\text{views}} = 50$ corresponds to approx. 25,000 samples or roughly 2.5 times the gradient magnitude sparsity.

We repeat the study for a phantom of same dimensions but with a gradient magnitude sparsity of approx. 2,500, i.e, 4 times lower than the breast phantom. The ℓ_2-magnitude RMSE decay is almost identical, and for ℓ_2-TV, we see again the step-like decay, however, already at $N_{\text{views}} = 12$, i.e. an undersampling of $12/512 \approx 0.025$. This is the same factor of 4 lower as was the case for the sparsity. There appears to be a direct connection between the sparsity of the image and the sufficient number of views for accurate ℓ_2-TV reconstruction.

We conclude that while undersampled reconstruction is indeed possible with ℓ_2-TV, the actual admissible undersampling depends on the sparsity of the phantom. To avoid an over-optimistic estimate of the sufficient number of views, it is essential to consider phantoms with similar sparsity to what might be encountered in a given application.

V. DISCUSSION AND CONCLUSION

We have argued that a quantitative notion of a sufficient sampling condition (SSC) for X-ray CT using the DD model is necessary in order to evaluate potential of sparsity-exploiting methods. We proposed an SSC at $N_{\text{views}} = N_{\text{bins}} = 2N$ for the circular, fan-beam, full angular range geometry as a compromise between ensuring a unique and stable solution and the impracticality of an infinite number of views and detector bins. The SSC allows quantification of admissible undersampling, i.e., for the breast CT example we saw accurate ℓ_2-TV reconstruction at an undersampling of 0.1. With an SSC, such as the proposed, we can then compare undersampling admitted by other sparsity-exploiting reconstruction methods, such as wavelet-based, as well as explore the connection between sparsity and undersampling. Also, the effect of using other discretizations for the system matrix, such as ray-tracing, as well as the influence of the problem size N can be studied. The SSC also allows us to distinguish between view undersampling and bin undersampling. For the considered model, we saw an asymmetry in condition number decay with number of views and number of detector bins, which can possibly explain the more promising reconstruction results seen for view undersampling compared to bin undersampling.

It should be emphasized that the presented results are only for the circular fan-beam 2π scan arc geometry, and for ideal simulated data. As such, the results serve as a best-case bound for the undersampling level at which similar sparsity images can be reconstructed accurately by TV-minimization. However, the same methodology can be applied to other geometries and other variants of sparsity-exploiting IIR.

ACKNOWLEDGMENT

This work is part of the project CSI: Computational Science in Imaging, supported by grant 274-07-0065 from the Danish Research Council for Technology and Production Sciences. This work was supported in part by NIH R01 grants CA120540 and EB000225. The contents of this article are solely the responsibility of the authors and do not necessarily represent the official views of the National Institutes of Health.

REFERENCES

[1] D. Donoho, “Compressed sensing,” *IEEE Transactions on Information Theory*, vol. 52, pp. 1289–1306, 2006.

[2] E. Candès, J. Romberg, and T. Tao, “Robust uncertainty principles: Exact signal reconstruction from highly incomplete frequency information,” *IEEE Transactions on Information Theory*, vol. 52, pp. 489–509, 2006.

[3] J. Bian, J. H. Siewerdsen, X. Han, E. Y. Sidky, J. L. Prince, C. A. Pelizzari, and X. Pan, “Evaluation of sparse-view reconstruction from flat-panel-detector cone-beam CT,” *Physics in Medicine and Biology*, vol. 55, pp. 6575–99, 2010.

[4] E. Y. Sidky, M. A. Anastasio, and X. Pan, “Image reconstruction exploiting object sparsity in boundary-enhanced X-ray phase-contrast tomography,” *Optics Express*, vol. 18, pp. 10 404–10 422, 2010.

[5] H. H. Barrett and K. J. Myers, *Foundations of Image Science*. Hoboken, NJ: John Wiley & Sons, 2004.

[6] T. L. Jensen, J. H. Jørgensen, P. C. Hansen, and S. H. Jensen, “Implementation of an optimal first-order method for strongly convex total variation regularization,” *BIT Numerical Mathematics*, 2011. [Online]. Available: http://www.springerlink.com/index/10.1007/s10543-011-0359-8

A Preliminary Study of Optimization-based Image Reconstruction from Offset-Detector CBCT

Junguo Bian, Jiong Wang, Xiao Han, Emil Y. Sidky, Lingxiong Shao, and Xiaochuan Pan

***Abstract*—In this work, we have performed a preliminary study on image reconstruction by using optimization-based algorithms from data containing partial redundancy collected with an offset-detector CBCT. We have modified ASD-POCS algorithm to accommodate the partially redundant data and studied the effect of weighting functions that are used for normalization of the data redundancy. The results suggest that, when data contain components inconsistent with the imaging model, smooth weighting functions can be designed for reducing the artifacts.**

I. INTRODUCTION

In advanced single-photon emission computed tomography (SPECT), cone-beam computed tomography (CBCT) is added for acquisition of anatomic information of the imaged subject. For example, a CBCT with a flat-panel detector has been developed for isotropic volume CT imaging in a SPECT/CT unit (XCT system) [1]–[6]. Due to cost and geometric considerations, the size of the flat-panel detector used in added CBCT is often smaller than the cross section of imaged patient, and, when used in a conventional geometric configuration, it yields a field of view (FOV) smaller than the cross section of the patient, resulting in data truncations and image artifacts. In an attempt to increase the FOV, an approach has been developed [7] in which the detector is offset by some amount along an appropriate direction. It can be shown that, as long as the detector offset is less than a half of the detector size, although truncations occur at each projection view, data collected over an angular range of 2π contain information sufficient for reconstruction of CT images without suffering truncation artifacts.

The CBCT unit promises added values for SPECT-based studies through providing information about patient anatomy and attenuation correction. However, radiation dose involved in CBCT scans constitutes a health concern to the imaged patient. One potential approach to reducing CBCT imaging dose in SPECT/CT is to reduce the number of projections acquired. It has been demonstrated recently in both simulated and real-data studies [8]–[11] that optimization-based reconstruction approaches have the potential to reconstruct images from projections collected at views fewer than what are used currently as required by conventional analytic-based algorithms such as the FDK algorithm [12].

In this work, we carry out a preliminary study on the development and application of optimization-based algorithms for image reconstruction from data collected in CBCT with an offset-detector. In particular, as data collected contain certain amount of "redundant" information, we investigate the exploitation of such data redundancy in optimization-based approaches to minimize artifacts in images reconstructed from simulated- and real-data.

II. OFFSET-DETECTOR CONFIGURATION

As shown in reference [7], the FOV of CBCT can be enlarged by use of an offset-detector configuration. Under continuous condition, it can be shown that, as long as the offset is less than a half of the detector size, data collected over an angular range of 2π contain information sufficient for accurate image reconstruction. Moreover, redundant information can be identified in the data, and it has to be normalized adequately in analytic-based reconstruction and can be exploited for controlling reconstruction quality in the presence of discrete error and noise.

The CBCT unit of the XCT system under consideration composes an X-ray source and a flat-panel detector. The distances of the X-ray source to detector and to the center-of-rotation are 133.2 cm and 88.1 cm, and the detector panel consists of 1024×386 detection elements of sizes 0.388×0.776 mm^2 under a 2×4 binning mode. The detector panel has an offset of $L = 17.7$ cm.

Using this system, we collected cone-beam data at 720 projection views evenly distributed over 2π with a circular trajectory from a physical pelvis phantom. Data were corrected for scatter and other physical factors. From the 720-view data set, we subsequently extracted a data set consisting of projections acquired only at 360 views uniformly distributed over 2π. From this data set, we reconstructed images and compared them with a reference image reconstructed from the 720-view data set.

III. DISCRETE IMAGING MODEL AND OPTIMIZATION-BASED ALGORITHMS

A. Continuous imaging model and analytic-based algorithms

As mentioned above, data collected with an offset-detector geometry contain redundant information. Analytic-based algorithms such as FDK have been developed based upon a continuous-to-continuous (C-C) imaging model in which data is an integration of the object function along a

---

J. Bian, X. Han and E. Y. Sidky are with Department of Radiology, the University of Chicago.

J. Wang and L. Shao are with Philips Healthcare.

X. Pan is with Departments of Radiology & Cellular Oncology, the University of Chicago.

line. However, these algorithms cannot be applied directly to data containing only partial redundancy collected with, e.g., an offset-detector geometry, and appropriate weighting functions have to be used for normalizing data redundancy before the algorithms can be applied. Different weighting [13], [14] have been investigated based upon the C-C model.

B. Discrete imaging model

In offset-detector CBCT, the imaging process can also be modeled as a discrete linear system, which we refer to as a discrete-to-discrete (D-D) model,

$$\mathbf{g_0} = \mathcal{H}\mathbf{f}, \tag{1}$$

where $\mathcal{H}$ is a system matrix modeling the cone-beam X-ray transform, and vectors $\mathbf{g_0}$ and $\mathbf{f}$ indicate the model data and image to be reconstructed. An element of $\mathbf{g_0}$ or $\mathbf{f}$ denotes the value on a detector bin or an image voxel. It should be noted that $\mathbf{g_0}$ differs from the actual measured data $\mathbf{g}$. In practical CBCT applications, it is only possible to solve the linear system in Eq. (1) by use of optimization-based approaches, which include the design of an optimization program and development of algorithms for reconstructing images through solving the optimization program.

C. Optimization program

In this work, we consider an optimization program that has been discussed previously [8]–[11], [15]:

$$\mathbf{f}^* = \mathrm{argmin}||\mathbf{f}||_{\mathrm{TV}} \quad \text{s.t.} \quad D_W(\mathbf{f}) \leq \epsilon \ \text{ and } \ f_n \geq 0, \tag{2}$$

where $||\mathbf{f}||_{\mathrm{TV}}$ denotes the total variation (TV) of image $\mathbf{f}$, f_n the image value on voxel n, $D_W(\mathbf{f})$ a weighted Euclidean data divergence between measured data and the imaging model, W a diagonal matrix in which each diagonal element represents a weighting factor for each measurement ray that can be selected to control image reconstruction, and $\epsilon > 0$ a given parameter for accommodating inconsistency between measured data and imaging model. The data divergence can be zero only in a simulation study in which data are generated by use of the same imaging model for describing the imaging process. A focus of the study is to demonstrate the selection of W and its implication for image reconstruction. When W is an identity matrix, the optimization program in Eq. (2) becomes the one for a conventional CBCT configuration with no detector offset that has been studied previously [9]. A necessary convergence condition similar to that in reference [9] has been derived for the optimization program specified by Eq. (2).

D. Optimization-based algorithm

We develop an algorithm to reconstruct image $\mathbf{f}$ by solving the optimization problem in Eq. (2). Specifically, the algorithm is a modification of the adaptive steepest descent-projection onto convex sets (ASD-POCS) algorithm that solves the optimization program in Eq. (2) when W is an identity matrix [9]. The key modification to the ASD-POCS algorithm is the introduction of the weighting factor, which is the diagonal element of W, in the POCS step so that the partially redundant information can be appropriately normalized. In the work, we refer to the weighted POCS algorithm as the W-POCS algorithm. The W-POCS algorithm is used to lower the data divergence until reaching ϵ. For achieving a necessary convergence condition, one can use other algorithms such as gradient descent for further calculation of the weighted data divergence. We have also modified other iterative algorithms such as the expectation maximization (EM) [16]–[18] and simultaneous algebraic reconstruction technique (SART) [19] so that they can be applied to offset-detector data containing only partial redundancy .

IV. SELECTION OF WEIGHTING FUNCTION

For the C-C imaging model, partial-data redundancy has to be normalized so that the analytic-based algorithms can be applied. However, it has been shown that multiple weighting functions can satisfy the normalization condition. Under ideal imaging condition, different weighting functions yield identical reconstructions. However, in the presence of inconsistencies between imaging model and measured data, reconstructions with different weighting functions can yield different reconstructions. On the other hand, for a D-D imaging model, even if data contain "redundant" information, the optimization-based algorithms can reconstruct images from data with or without normalization of such data redundancy. However, as shown below, in the presence of data inconsistencies, artifacts in images obtained with optimization-based algorithms can be minimized by use of an appropriately selected weighting functions. Therefore, we investigate the impact of different weighting functions on image reconstructions for both analytic- and optimization-based algorithms.

We first consider reconstructions directly from data without applying weighting (or, equivalently, with an identity weighting matrix.) In this study, the optimization-based algorithms can reconstruct images accurately from data containing no inconsistencies, whereas the analytic-based FDK algorithm cannot. In the second study, we investigate several weighting functions satisfying a normalization condition with "continuous" and "discontinuous" properties. Specifically, we consider a continuous weighting function

$$W_1(u,\lambda) = \begin{cases} \cos^2\Big(\frac{\pi}{4}(\frac{\gamma}{\gamma_{\mathrm{m1}}} - 1)\Big) & -u_{m1} \leq u \leq u_{m1} \\ 1 & u_{m1} < u \leq u_{m2} \end{cases} \tag{3}$$

where $\gamma = \mathrm{atan}\frac{\mathrm{u}}{\mathrm{S}}$, $\gamma_{m1} = \mathrm{atan}\frac{\mathrm{u_{m1}}}{\mathrm{S}}$, and S is the source-to-detector distance. We assume that the origin of the detector is the intersection of detector and the line connecting source and iso-center. The two detector edges are at $-u_{m1}$ and u_{m2}, and $u_{m1} < u_{m2}$. It can be observed that the weighting function is continuous in u. This weighting function has been widely used.

We also consider two discontinuous weighting functions

$$W_2(u,\lambda) = \begin{cases} \frac{1}{2} & -u_{m1} \leq u \leq u_{m1} \\ 1 & u_{m1} < u \leq u_{m2} \end{cases} \tag{4}$$

and

$$W_3(u,\lambda) = \begin{cases} \frac{1}{4} & -u_{m1} \leq u \leq 0 \\ \frac{3}{4} & 0 < u \leq u_{m1} \\ 1 & u_{m1} < u \leq u_{m2} \end{cases} \tag{5}$$

The weighting functions above are in continuous form and need to be discretized so that they can be applied to discrete data. However, once the weighting functions are discretized, the normalization conditions are only approximately satisfied.

V. NUMERICAL STUDIES USING SIMULATED DATA

For the case involving the C-C model and analytic-based algorithms, mathematically exact reconstruction can be achieved only by applying the analytic-based algorithms to data generated with the same imaging model. We refer to such a study as an inverse-crime study [20]–[22] based upon a C-C imaging model, which has been carried out previously.

In the study below, instead, we consider an inverse-crime study based upon a D-D imaging model by demonstrating (numerically accurate) image reconstruction from data that are completely consistent with a D-D imaging model. For such an inverse-crime study, discrete data can be generated by applying the imaging matrix $\mathcal{H}$ to a discrete image, and the optimization algorithm uses the same matrix $\mathcal{H}$ to reconstruct a discrete image from the discrete data. The value of inverse-crime studies lies in the fact that they can evaluate whether the optimization-based algorithm can achieve the reconstruction specified by the optimization program in Eq. (2) within the computer numerical precision and that they can verify how close the achieved reconstruction is relative to the image that is used to generate the discrete projection data.

A. *Simulation-data generation*

We have generated simulation data with a geometry identical to that of the XCT system. A discrete image of the physical phantom that is reconstructed on an image array with a pixel size of 0.3 cm by use of the FDK algorithms from real data is used as the “truth” image. In the panel specified by row 1 and column 1 of Fig. 1, we display a region of interest (ROI) within the discrete truth image. From the discrete truth image, we generated projection data at 720 views uniformly distributed over 2π, with a detector consisting 256 bins each of which has a size of 0.1552 cm. From the 720-view data, we extracted a data set with 360 views uniformly distributed over 2π. Because these data sets are generated by use of matrix $\mathcal{H}$ from the discrete truth image, and because the same matrix $\mathcal{H}$ is used in the optimization-based algorithm, image reconstruction from these data sets constitutes an inverse-crime study. We reconstruct images on the same image array of the discrete truth image and show below reconstruction details within the ROI obtained with different weighting functions.

B. *Reconstructions from simulation data*

We first performed an inverse-crime study without weighing from the 360-view data set. The algorithm was shown to converge in terms of the necessary condition derived, thus suggesting that the algorithm can achieve the designed solution. Also, the data divergence approaches 0, and differences between reconstructions and the discrete truth image decreases to 0, as the iteration number increases, thus indicating that the designed solution in the optimization program in Eq. (2) approaches the discrete truth image. In Fig. 1, we display intermediate and final reconstructions and their differences relative to the discrete truth image.

We also performed studies in which data are normalized with the weighting functions in Eqs. (3), (4), and (5). As the results in Fig. 1 show, observation similar to that for the study without weighting can be obtained. Specifically, the algorithm was shown to converge in terms of the necessary condition derived, thus suggesting that the algorithm can achieve the designed solution. Also, the data divergence approaches 0, and differences between reconstructions and the discrete truth image decreases toward 0, as the iteration number increases, thus indicating that the designed solution in the optimization program in Eq. (2) approaches the discrete truth image. In Fig. 1, we display intermediate and final reconstructions and their differences relative to the discrete truth image. It can be observed that different weightings, representing different optimization paths, impact only on the intermediate, but not final, reconstructions.

The inverse-crime studies above show that, unlike analytic-based algorithms, the optimization-based algorithm can reconstruct accurate images directly from discrete data in which “redundant” information is not normalized. They also demonstrates that, like analytic-based algorithms, the optimization-based algorithm can reconstruct accurate images from discrete data in which “redundant” information is normalized.

VI. NUMERICAL STUDIES USING REAL DATA

Following the simulation studies above that evaluate the algorithm properties in terms of its convergence to the designed reconstruction and its difference relative the discrete truth image, we also conducted studies on the algorithm’s reconstruction from data of a physical pelvis phantom collected at 360 views over 2π. Unlike the simulation data that are consistent with the imaging model in the inverse-crime studies above, the real data collected contain various physical factors such as scatter that are inconsistent with the imaging model used in the algorithm. In this case, we expect that the selection of different weighting functions can lead to reconstructions with different artifacts. Again, we studied image reconstruction from data without weighting and from

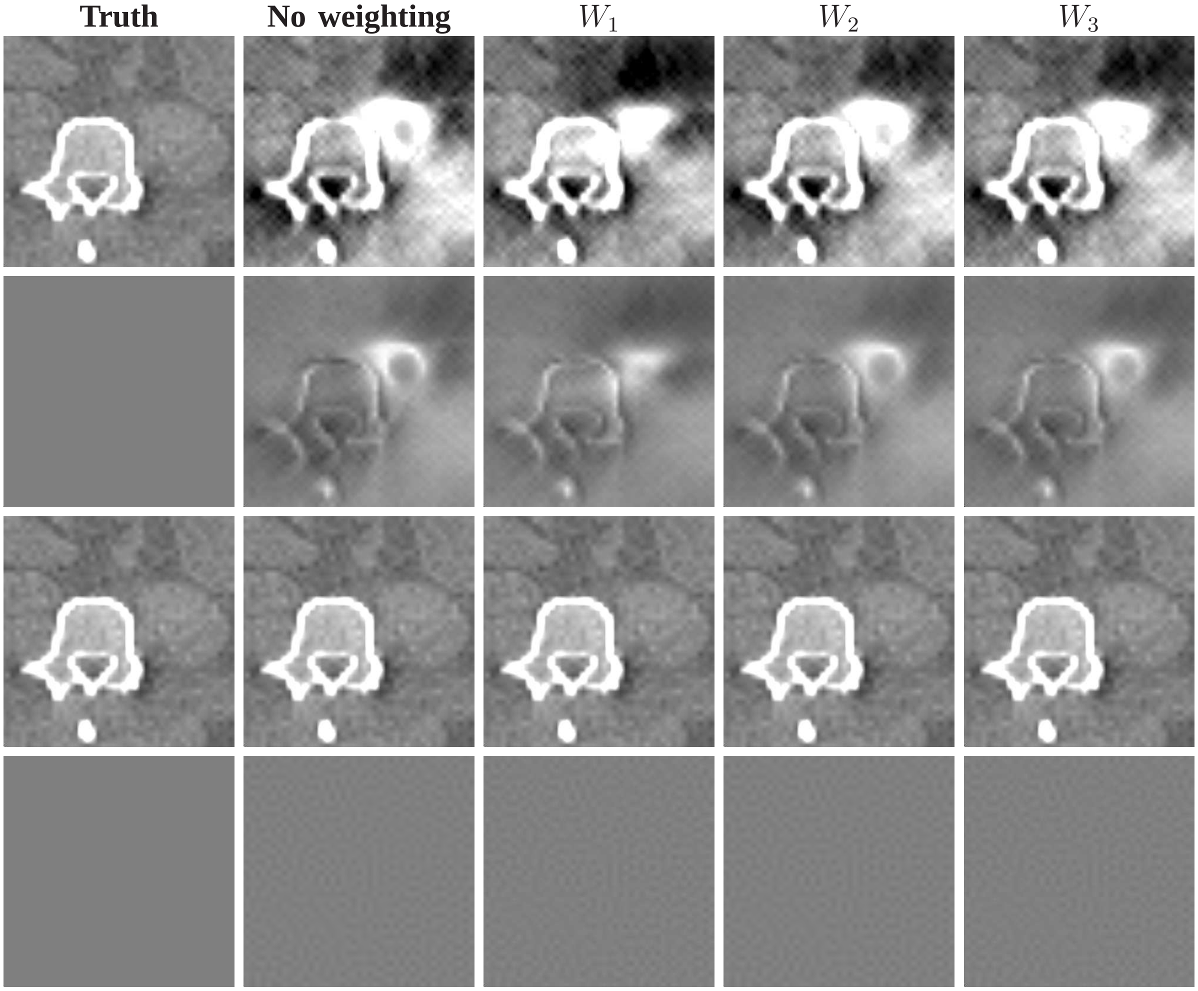

Figure 1. Truth ROI image (column 1) and ROI images (columns 2-5) at iteration 5 (row 1), and their differences from the truth ROI image (row 2); and final ROI image (row 3) and their differences from the truth ROI image (row 4) reconstructed from 360-view data normalized with different weighting functions by use of the modified ASD-POCS algorithm: no weighting (column 2), W_1 (column 3), W_2 (column 4), and W_3 (column 5). The grayscale window for rows 1 and 3 is $[0.1, 0.25]$ cm^{-1}, whereas grayscale windows for rows 2 and 4 are $[-0.2, 0.2]$ cm^{-1} and $[-0.00001, 0.00001]$ cm^{-1}.

data with each of the three weighting functions in Eqs. (3), (4), and (5). In Fig. 2, we display the ROI images within the reconstructions without and with different weighting functions. For cases without weighting and with W_2 and W_3 weighting functions, ring artifacts can be observed in the reconstructions. This is because the discontinuity in data without weighting or in data normalized by W_2 and W_3, which are discontinuous functions of u.

Because there is no truth available for this real data study, we use the FDK reconstruction from the 720-view data, normalized with W_1, as a surrogate truth image. In the second row of Fig. 2, we show ROI images difference between reconstructions and the surrogate truth image. It can be observed that reconstruction with the weighting W_1 contains much reduced artifacts than reconstructions with other weightings, as W_1 is a smooth weighting function that can reduce the artifacts resulted from data discontinuity in u. This observation is also consistent with that in analytic-based algorithm studies in which W_1-type smooth weighting functions are used. Similar results can be obtained for other iterative algorithms such as SART and EM algorithm designed for offset-detector configuration.

VII. DISCUSSION

In this work, we have performed a preliminary study on image reconstruction by using optimization-based algorithms from data containing partial redundancy collected with an offset-detector configuration in CBCT. In particular, the ASD-POCS algorithm has been modified to accommodate partially redundant data for achieving accurate image reconstruction; and the effect of weighting functions that are used for normalization of the data redundancy has been studied. The results suggest that, when data contain components inconsistent with the imaging model, different weighting functions can result in reconstructions with different artifacts and that smooth weighting functions can be designed for reducing the artifacts.

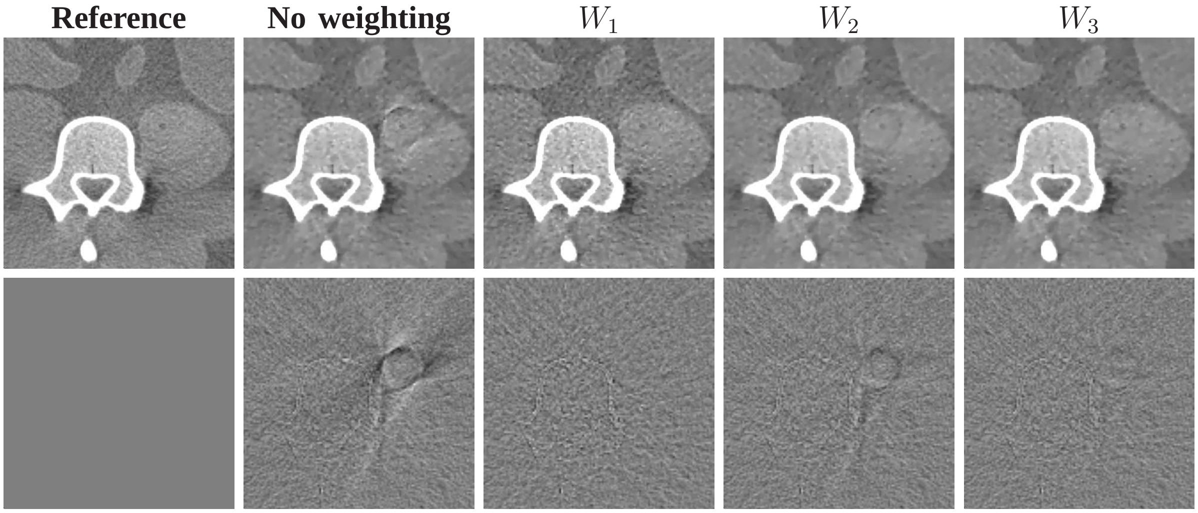

Figure 2. Row 1: The surrogate truth ROI image (column 1), and ROI images reconstructed by use of the ASD-POCS algorithms from 360-view data of the physical pelvis phantom normalized by different weighting functions: No weighting (column 2), W_1 (column 3), W_2 (column 4), and W_3 (column 5). Row 2: differences of ROI images in row 1 from the surrogate truth ROI image. The grayscale window for row 1 is $[0.1, 0.25]$ cm^{-1}, whereas the grayscale window for row 2 is $[-0.05, 0.05]$ cm^{-1}.

VIII. ACKNOWLEDGMENTS

The authors would like to thank Dr. Dan Xia and Professor Chien-Min Kao for helpful discussions. This work was supported in part by the National Institutes of Health (NIH) under Grants CA120540, CA158446 and EB000225. The work of X. Han was supported in part by the Department of Defense (DoD) Predoctoral training Grants PC094510. Some computation in the work was performed on a cluster partially funded by the University of Chicago for Comprehensive Cancer Center.

REFERENCES

[1] B. H. Hasegawa, E. L. Gingold, S. M. Reilly, S. C. Liew, and C. E. Cann, “Description of a simultaneous emission-transmission CT system,” in *Proc. SPIE*, vol. 1231, 1990, p. 50.

[2] T. F. Lang, B. H. Hasegawa, S. C. Liew, K. J. Brown, S. C. Blankespoor, S. M. Reilly, E. L. Gingold, and C. E. Cann, “Description of a prototype emission transmission computed tomography imaging,” *J. Nucl. Med.*, vol. 33, pp. 1881–1887, 1992.

[3] M. Bocher, A. Balan, Y. Krausz, Y. Shrem, A. Lonn, M. Wilk, and R. Chisin, “Gamma camera-mounted anatomical X-ray tomography: technology, system characteristics and first images,” *Eur. J. Nucl. Med. Mol. Imaging*, vol. 27, pp. 619–627, 2000.

[4] J. A. Patton, D. Delbeke, and M. P. Sandier, “Image fusion using an integrated, dual-head coincidence camera with X-ray tube-based attenuation maps,” *J. Nucl. Med.*, vol. 41, pp. 1364–1368, 2000.

[5] B. Hasegawa, K. Wong, K. Iwata, W. Barber, A. Hwang, A. Sakdinawat, M. Ramaswamy, D. Price, and R. Hawkins, “Dual-modality imaging of cancer with SPECT/CT,” *Techno. Cancer Res. Treat.*, vol. 1, pp. 449–458, 2002.

[6] D. Sowards-Emmerd, J. Vesel, L. Shao, J. Timmer, M. Bertram, J. Ye, and H. Hines, “Flat Panel X-ray Detector Based Volume Imaging SPECT/CT,” in *Seminars in Nuclear Medicine*. Elsevier, 2009.

[7] W. Chang, S. Loncaric, G. Huang, and P. Sanpitak, “Asymmetric fan transmission CT on SPECT systems,” *Phys. Med. Biol.*, vol. 40, pp. 913–928, 1995.

[8] E. Y. Sidky, K.-M. Kao, and X. Pan, “Accurate image reconstruction from few-views and limited-angle data in divergent-beam CT,” *J. X-Ray Sci. and Technol.*, vol. 14, pp. 119–139, 2006.

[9] E. Y. Sidky and X. Pan, “Image reconstruction in circular cone-beam computed tomography by constrained, total-variation minimization,” *Phys. Med. Biol.*, vol. 53, pp. 4777–4807, 2008.

[10] J. Bian, J. H. Siewerdsen, X. Han, E. Y. Sidky, J. L. Prince, C. A. Pelizzari, and X. Pan, “Evaluation of sparse-view reconstruction from flat-panel-detector cone-beam CT ,” *Phys. Med. Biol.*, vol. 55, pp. 6575–6599, 2010.

[11] X. Han, J. Bian, D. R. Eaker, T. L. Kline, E. Y. Sidky, E. L. Ritman, and X. Pan, “Algorithm-enabled low-dose micro-CT imaging,” *IEEE Trans. Med. Imag.*, vol. 30, pp. 606–620, 2011.

[12] L. A. Feldkamp, L. C. Davis, and J. W. Kress, “Practical cone-beam algorithm,” *J. Opt. Soc. Am. A*, vol. 1, pp. 612–619, 1984.

[13] D. L. Parker, “Optimal short scan convolution reconstruction for fan beam CT,” *Med. Phys.*, vol. 9, pp. 254–257, 1982.

[14] P. S. Cho, R. H. Johnson, and T. W. Griffint, “Cone-beam CT for radiotherapy applications,” *Phys. Med. Biol.*, vol. 40, pp. 1863–1883, 1995.

[15] X. Pan, E. Y. Sidky, and M. Vannier, “Why do commercial CT scanners still employ traditional, filtered back-projection for image reconstruction?” *Inverse Probl.*, vol. 25, p. 123009, 2009.

[16] A. P. Dempster, N. M. Laird, and D. B. Rubin, “Maximum likelihood from incomplete data via the EM algorithm,” *J. R. Stat. Soc. Series B Stat. Methodol.*, vol. 39, pp. 1–38, 1977.

[17] L. A. Shepp and Y. Vardi, “Maximum likelihood reconstruction for emission tomography,” *IEEE Trans. Med. Imag.*, vol. 1, pp. 113–122, 1982.

[18] H. H. Barrett and K. J. Myers, *Foundations of Image Science*. John Wiley Sons, Inc., 2003.

[19] A. H. Andersen and A. C. Kak, “Simultaneous algebraic reconstruction technique (SART): a superior implementation of the ART algorithm,” *Ultrason. Imaging*, vol. 6, pp. 81–94, 1984.

[20] D. L. Colton and R. Kress, *Inverse acoustic and electromagnetic scattering theory*. Springer-Verlag, Berlin, 1992.

[21] A. Wirgin, “The inverse crime,” *arXiv:math-ph/0401050v1*, 2004.

[22] J. Kaipioa and E. Somersalob, “Statistical inverse problems: discretization, model reduction and inverse crimes,” *J. Comput. Appl. Math.*, vol. 198, pp. 493–504, 2007.

Spatial Variations in Reconstruction Methods for CT

Linda Plantagie,
Willem Jan Palenstijn, Jan Sijbers, and Kees Joost Batenburg

***Abstract*—In both Filtered Backprojection and algebraic reconstruction algorithms for tomography, the reconstruction of an object can depend on the position of the object within the discretized region, even if the object is aligned perfectly with pixel boundaries. In this paper, we investigate this effect and report on a simulation study concerning *spatial dependencies* in these reconstruction methods. We demonstrate that for algebraic methods, these dependencies are influenced not only by the discretization within the reconstruction region, but also by the *shape* of the reconstruction region itself.**

***Index Terms*—algebraic reconstruction, reconstruction region, artefacts.**

I. INTRODUCTION

Most reconstruction algorithms for CT can be assigned to either the class of analytical reconstruction methods, which are based on analytical inversion formulas of the Radon transform, or to the class of algebraic reconstruction methods, which start with a discretized inverse problem and then apply a numerical solver [1]–[3].

One of the fundamental differences between these two classes relates to the spatial locality of the reconstruction properties. Analytical inversion formulas are usually spatially invariant, in the sense that the value of a particular point in the reconstruction only depends on the measured values relative to the position of that point. If this dependency is known for a single point, it can be applied to all image points (e.g., pixel centers) to obtain a full reconstruction. Also, there is no pre-defined window outside which the reconstruction must be zero. The well-known Filtered Backprojection (FBP) algorithm is obtained by discretizing an analytical inversion formula of the Radon transform, and can therefore be expected to have approximately similar properties.

For *algebraic methods* on the other hand, there is no intrinsic reason why the reconstruction should be spatially invariant, and the reconstruction is constrained a priori to a *reconstruction region*, which is discretized and represented by a collection of basis functions. Outside this region, the reconstruction is automatically set to zero, as the exterior region is not covered by the support of the basis functions.

For both FBP and algebraic methods, there may be differences in the way projection values are sampled to determine the value of an image pixel, depending on the position of that pixel, due to discretization and interpolation effects within the projection model. As a consequence, reconstructing an object centered at one position within the reconstruction region may yield a different result from reconstructing this same object centered at another position. We refer to these variations as *discretization-effects*.

For algebraic methods, the *shape* and position of the reconstruction region with respect to the object can also influence its reconstruction. For example, if a line intersects the reconstruction region as a short segment in a corner, noise that is present in the projection for that line can have a strong impact on the values of the pixels on the small segment. For a line segment that has a longer intersection with the reconstruction region, the noise can be distributed among many pixels on that segment. We refer to these local reconstruction variations, which depend on the shape of the reconstruction grid, as *shape-effects*.

In this paper, we report on a case study that was carried out to investigate both discretization-effects and shape-effects for the FBP method and the Simultaneous Iterative Reconstruction Technique (SIRT), respectively. By moving an object across the reconstruction region and observing how its reconstruction changes with position, we keep track of both effects and obtain error maps that can be interpreted visually and analyzed quantitatively.

This paper is structured as follows: In Section II, we briefly review the discretization approach followed for FBP and SIRT, respectively. Section III describes the simulation experiments performed. The results of these experiments are presented in Section IV, mainly by providing a sequence of images that represent two different error measures, as a function of the position within the reconstruction region. In Section V, the observations are discussed and future work in this direction is briefly outlined.

II. METHOD

The Filtered Backprojection (FBP) algorithm is obtained by discretizing the following inversion formula of the Radon

---

This work was financially supported by the NWO (the Netherlands Organisation for Scientific Research - The Netherlands), project number 639.072.005, and by the FWO (The Research Foundation - Flanders, Belgium).

Linda Plantagie and Kees Joost Batenburg are with the Centrum Wiskunde & Informatica (CWI), Science Park 123, 1098 XG Amsterdam, The Netherlands.

Kees Joost Batenburg, Willem Jan Palenstijn, and Jan Sijbers are with the IBBT-Vision Lab, University of Antwerp, Universiteitsplein 1, 2610 Wilrijk, Belgium.

Corresponding author: Linda Plantagie, E-mail: linda.plantagie@cwi.nl.

transform (see Section 3.3.2 of [1] for details):

$$f(x,y)=\int_{\theta=0}^{\pi}\int_{\tau=-\infty}^{\infty}p(\theta,\tau-x\cos\theta-y\sin\theta)g(\tau)\,\mathrm{d}\tau\,\mathrm{d}\theta, \tag{1}$$

where $f:\mathbb{R}^2\rightarrow\mathbb{R}$ denotes the unknown image, $p(\theta,\tau)$ denotes the measured line projection at angle θ and detector coordinate τ, and g denotes a *filter*, which determines how the detector values are weighted before backprojection to form the value at position (x,y). If we assume that p corresponds to the Radon transform of a certain original object, it is easy to see that translating this object over $(\Delta x,\Delta y)$ leads to a corresponding translation in the reconstruction over $(\Delta x,\Delta y)$. As a consequence of the discretization step in FBP, interpolation steps are required to compute an approximation of Eq. (1), leading to violations in this translational property, which we refer to as *discretization-effects*.

In *algebraic* reconstruction methods, the image is represented as a finite weighted sum of *basis functions* (see, e.g., Chapter 7 of [1] or Section 6.3 of [2]). For this paper, we limited ourselves to the reconstruction of 2-dimensional (2D) slices from 1D parallel beam projections using a standard pixel basis, yet the general methodology can be applied to 3D volume reconstruction using various types of basis functions, and various acquisition geometries.

When setting up an algebraic method, it is assumed that a certain *reconstruction region* is known, which completely contains the scanned object. Typically, this region is chosen to be either square or rectangular, while sometimes it is modelled as a disk. This region is then discretized along with the projection operator, leading to the following relation between the unknown image $\boldsymbol{x}$ and the measured projection data $\boldsymbol{p}$:

$$\boldsymbol{W}\boldsymbol{x}=\boldsymbol{p}, \tag{2}$$

where $\boldsymbol{W}=(w_{ij})\in\mathbb{R}^{m\times n}$ denotes the *projection matrix*, $\boldsymbol{x}=(x_j)\in\mathbb{R}^n$ is a vector representation of the pixel values in the unknown image, and $\boldsymbol{p}=(p_i)\in\mathbb{R}^m$ represents the full set of measured detector values in all projections.

The exact projection matrix $\boldsymbol{W}$ depends on the selection of the reconstruction region, the choice and distribution of basis functions to represent the image within this region, and the model used for the projection operator.

The system in Eq. (2) is typically solved using iterative numerical solvers, as it is both very large and sparse. In this article, we consider one such iterative method called SIRT [4], [5], which converges to a weighted least-squares solution of the equation system.

Note that not all individual linear equations in Eq. (2) have the same algebraic structure. Each equation corresponds to a projected line. Depending on the intersection properties of that line with the discretized reconstruction region, the number of unknown pixel values that occur in the equation can vary, as well as their coefficients. As a consequence, the shape of the reconstruction region can influence the reconstruction of an object, depending on its location within that region, referred to as *shape-effects* of the reconstruction region.

III. Experiments

To investigate discretization-effects and shape-effects for both FBP and SIRT, we performed a simulation study on the reconstruction of a small object that is placed at varying positions within the reconstruction region. All experiments were carried out using two different choices for the reconstruction region: (a) a square region of size 63×63 square pixels of unit size; (b) a pixelated circular region that is circumscribed around the square region of (a).

We compare the results for Filtered Backprojection (FBP) using the ramp-filter, which exhibits only discretization-effects, with the Simultaneous Iterative Reconstruction Technique (SIRT), which is expected to show both discretization-effects and shape-effects. For SIRT, 200 iterations are performed with a relaxation factor of 1. This iteration number ensures that convergence has been reached.

Projection data were simulated for a parallel detector geometry, using a detector consisting of 91 bins of unit size, thereby ensuring that the full reconstruction region is covered by the detector. The simulation was performed using a ray-driven projector based on the Joseph kernel to determine the contribution of an image pixel to each ray [6], implemented as a parallel operation on the GPU [7]. The projection angles of the parallel beam projections are regularly distributed between 0 and 180 degrees. The number of projection angles is kept fixed at 64. For the SIRT reconstruction, a forward projector based on the Joseph kernel was used.

As test objects, the square and cross images in Fig. 1a were used. The reconstructions of these objects, when placed in the center of a square reconstruction region, are shown in Fig. 1b and 1c.

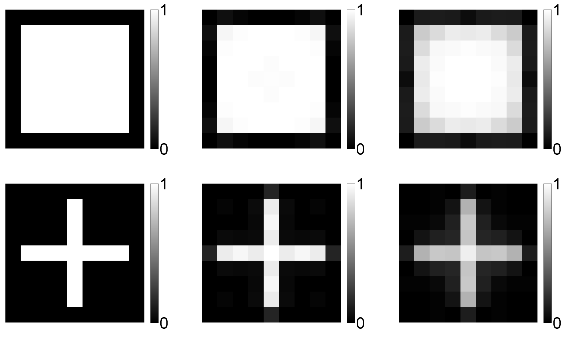

(a) (b) (c)

Fig. 1. Test objects and their reconstructions when placed in the center of the reconstruction region; (a) original, (b) SIRT, (c) FBP.

A. Experiments without noise

In the first experiment, based on noiseless projection data, the test objects were moved across the reconstruction area. For each position of the object, its forward projection was computed and the object was reconstructed. The reconstruction within a small window around the object (a surrounding square, containing a boundary layer of one pixel thickness) was then shifted, placing the reconstructed object in the center of the reconstruction region. A comparison was made with the reconstruction for which the object was placed in the center, using the following two error measures: (a) the root mean square error (RMSE) for all pixels in the window; (b) the absolute value of the difference in average intensity within the object (AIE).

B. Experiments that include noise

In the second experiment, the test objects were again moved across the reconstruction area. Poisson distributed noise was applied to the projection data based on a flatfield photon count of 10^6 per detector pixel. As the exact noise realization depends on the simulated photon counts, which in turn are affected by discretization issues, we chose to compare the reconstructions to the actual test object, instead of comparing to its reconstruction in the center. The reconstruction within a window around the object (a surrounding square, containing a boundary layer of five pixels thickness) was compared with the original object, using the following two error measures: (a) the root mean square error (RMSE) for all pixels in the window; (b) the absolute value of the difference in average intensity within the object (AIE).

IV. RESULTS

In this section, we examine the discretization and shape effects of SIRT and FBP for two test objects and two different shapes of the reconstruction grid.

A. Noiseless projection data

In the first series of experiments, the reconstructions of the noiseless projection data of a shifted object are compared with the reconstructions of the same object placed in the center of the reconstruction region. Reconstructions of the phantoms contain a variety of intensity levels within the reconstructed object. These intensity levels can be visualized by an intensity profile along a horizontal line through the center of the reconstructed object. In Fig. 2, the intensity profiles are shown for SIRT reconstructions of the test objects placed in the center of the reconstruction region and placed near the left boundary of the reconstruction region.

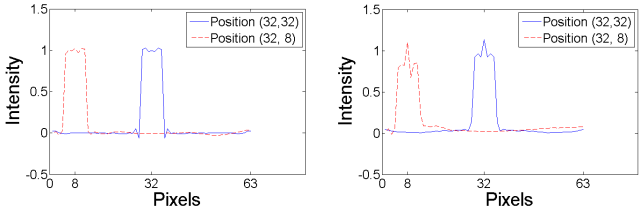

(a) (b)

Fig. 2. Intensity profile of an object at the center (blue line) and centered at pixel $(32, 8)$ (dashed red line); (a) square object, (b) plus object.

The reconstructions of the test objects clearly depend on their position in the reconstruction grid. The root mean square error for all pixels in the window is used to examine these spatial variations. In Fig. 3 the RMSE are shown for SIRT and FBP reconstructions of both test objects in a square reconstruction grid. The results are similar for the circular grid. Since the discretization-effects of SIRT and FBP appear to be very similar, we subtract the RMSE of FBP from that of SIRT to obtain an approximation of the shape-effects for SIRT. The absolute value of this difference is shown in Fig. 4. Note that some scaling was required to enhance the visibility.

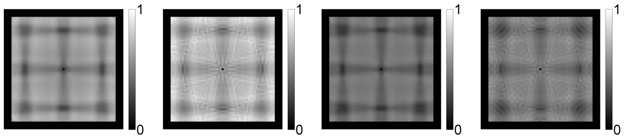

(a) (b) (c) (d)

Fig. 3. RMSE of reconstruction of the test objects using a square reconstruction grid without noise; (a) SIRT, square object, (b) SIRT, plus object, (c) FBP, square object, (d) FBP, plus object.

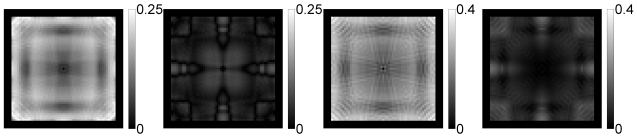

(a) (b) (c) (d)

Fig. 4. Absolute value of the difference of RMSE between SIRT and FBP of the reconstruction of the test object; (a) square phantom, square grid, (b) square phantom, circular grid, (c) plus phantom, square grid, (d) plus phantom, circular grid.

For square reconstruction grids, reconstructions of an object near the edge can differ substantially from a reconstruction of the same object placed in the center of the reconstruction grid. Fig. 4 shows that, at least in some cases, these shape-effects can be reduced by choosing a different, for example circular, reconstruction grid. These results are also supported by the second error measure (AIE), as is shown in Fig. 5 and 6.

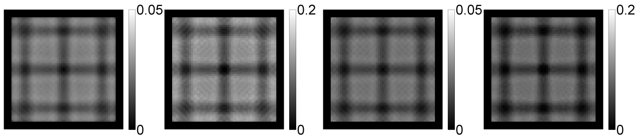

(a) (b) (c) (d)

Fig. 5. AIE of reconstruction of the test objects using a square reconstruction grid without noise; (a) SIRT, square object, (b) SIRT, plus object, (c) FBP, square object, (d) FBP, plus object.

B. Noisy projection data

In the second series of experiments, Poisson noise is applied to the projection data of the shifted object. An

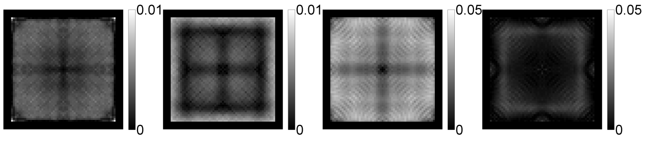

(a) (b) (c) (d)

Fig. 6. Absolute value of the difference of AIE between SIRT and FBP of the reconstruction of the test phantom; (a) square phantom, square grid, (b) square phantom, circular grid, (c) plus phantom, square grid, (d) plus phantom, circular grid.

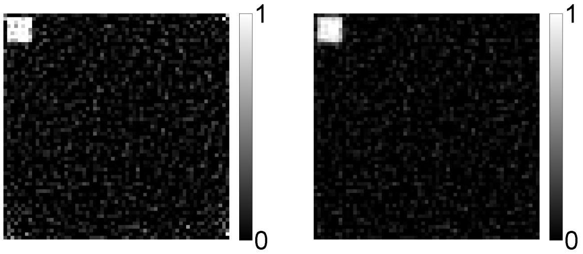

(a) (b)

Fig. 7. Reconstruction of the shifted square test object with Poisson noise applied to the projection data; (a) SIRT, (b) FBP.

example of a SIRT and FBP reconstruction of the shifted square test object is shown in Fig. 7.

As mentioned in section III the reconstructions are compared to the original shifted image instead of the reconstruction of the object placed at the center of the reconstruction region. The spatial variations of SIRT due to shape-effects are again visualized by comparing both the RMSE and AIE measures of SIRT and FBP; see Fig. 8 and 9 for the RMSE and AIE measure, respectively.

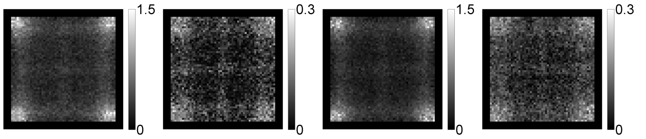

(a) (b) (c) (d)

Fig. 8. Absolute value of the difference of RMSE between SIRT and FBP of the reconstruction of the test object with Poisson noise; (a) square phantom, square grid, (b) square phantom, circular grid, (c) plus phantom, square grid, (d) plus phantom, circular grid.

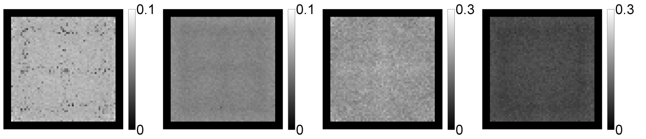

(a) (b) (c) (d)

Fig. 9. Absolute value of the difference of AIE between SIRT and FBP of the reconstruction of the test object with Poisson noise; (a) square phantom, square grid, (b) square phantom, circular grid, (c) plus phantom, square grid, (d) plus phantom, circular grid.

Apparently, as suggested by Fig. 9, the total intensity within the object is invariant under the position of the test object. Fig. 8 shows that, also in the case of noisy projection data, SIRT reconstructions of an object depend on the position of the object in the reconstruction region. These spatial variations are influenced by the shape of the reconstruction region.

V. DISCUSSION AND CONCLUSIONS

The results of our case study demonstrate that significant discretization-effects can be observed in both FBP and SIRT reconstructions. Moreover, this effect is highly similar for both algorithms. For SIRT, the shape-effects also comes into play, yet mainly near the corners of a square reconstruction region. It appears that this effect can be mitigated by using a disk-shaped reconstruction region. The magnitude of shape-effects is increased by the influence of noise in the projection data, which can cause serious artefacts near the corners of the reconstruction region.

The actual position dependency may well depend strongly on the particular projection model used for the reconstruction. Here, we only considered the Joseph's method, which is broadly used in tomographic algorithms. In ongoing and future research, we are now focusing on the influence of different types of discretizations (e.g., blobs, wavelets) on the spatial dependencies, along with various projection models (e.g., lines, strips).

REFERENCES

[1] A. C. Kak and M. Slaney, *Principles of Computerized Tomographic Imaging*. SIAM, 2001.
[2] G. T. Herman, *Fundamentals of Computerized Tomography: Image Reconstruction from Projections, 2nd edition*. Springer, 2009.
[3] X. Pan, E. Y. Sidky, and M. Vannier, "Why do commercial CT scanners still employ traditional, filtered back-projection for image reconstruction?" *Inv. Problems*, vol. 25, p. 123009, 2009.
[4] P. Gilbert, "Iterative methods for the 3d reconstruction of an object from projections," *J. Theoretical Biology*, vol. 36, no. 1, pp. 105–117, 1972.
[5] J. Gregor and T. Benson, "Computational analysis and improvement of SIRT," *IEEE Trans. Med. Imaging*, vol. 27, no. 7, pp. 918–924, 2008.
[6] P. M. Joseph, "An improved algorithm for reprojecting rays through pixel images," *IEEE Trans. Med. Imaging*, vol. 1, no. 3, pp. 192–196, 1982.
[7] W. J. Palenstijn, K. J. Batenburg, and J. Sijbers, "Performance improvements for iterative electron tomography reconstruction using graphics processing units (GPUs)," *J. Structural Biology*, vol. 176, no. 2, pp. 250–253, 2011.

Effective CT Scattering Simulation with Bi-directional Ray Tracing on GPU

Jaewoo Pi, Sungsoo Ha, and Klaus Mueller, *Senior Member, IEEE*

***Abstract*—In Computed Tomography, scatter effect of X-ray photons imposes artifacts which affect quality of images significantly. Many of studies have done to model the scattering nature to reduce the artifacts. Widely used methods, however, demand trade-off between speed and accuracy. We present effective single scattering algorithm, based on bi-directional path tracing. We implemented the code optimized for a general-purpose GPU (GPGPU) and the result is showing effective mark on the demonstration.**

Keywords- CT Scattering; Bi-directional ray-tracing; GPU; Parallel Processing

I. INTRODUCTION

In Computed Tomography (CT), scatter effect of X-ray photons significantly impact to quality of output images, such as CT number inaccuracy, contrast difference, and artifacts. To minimize scatter effect, many researches have been done in an effort to model and simulate the characteristic of scattering X-ray photons.

Simulating scatter effect at all portion of a target object involves extremely heavy computation. So far, to achieve fast computation time, one must reduce the number of samples that contribute to scatter effect. Generally two methods are widely used; these are, deterministic and Monte Carlo. Deterministic method uses down-sampling with interpolation algorithm, and Monte Carlo method relies on repeated random sampling [1], [2]. There is also hybrid approach combining two methods to compensate drawbacks of each method [3]. In consequence, all methods have to confront speed-accuracy trade-off.

In advance of general-purpose GPU, we can take advantage of high performance parallel processing with relatively low cost. While implementations of classical scatter simulation method on a GPU can achieve some speed-ups, compromise between speed and accuracy is still unavoidable.

We present an effective model for simulating single scatter effect of X-ray beams. Our method is based on bi-directional path tracing, a novel approach of evaluating scatter effect of photons. Our implementation of the algorithm is especially optimized to multi-processors on a GPU. Simulation is showing effective mark, even with the large-scale resolution images.

The remainder of the paper is organized as follows: section II, we depict background of algorithm, and section III, we describe methodology used to simulate the scattering. In section IV, experiment result of the GPU code is shown with time and memory performance evaluations.

II. BACKGROUND

A. Characteristics of X-Ray Photon

When X-ray photons travel from beam source through the matter, the energy of photos is attenuated exponentially. The simple model of this property is modeled

$$I_d = I_0 \exp(-\int \mu(\hat{t}) d\hat{t}), \tag{1}$$

where I_d is energy intensity at the detector, $I_0$is intensity at the source, $\hat{t}$ is ray path vector from source to detector. Attenuation function μ is probability function determining amount of energy attenuated by absorbance of the matter.

Portions of a scanned matter undergo Compton scattering. Compton scattering is scattering of X-rays and gamma rays. Photon collision in matter results in decreased energy and increased wavelength.

$$\lambda - \lambda' = \frac{h}{m_e c}(1 - cos\theta), \tag{2}$$

where λ is initial wavelength, $\lambda'$is wavelength after scattering, $h/m_e c$ is Compton wavelength of the electron.

B. Bi-directional Path Tracing

In Computer Graphics, Ray tracing is technique that used to simulate the effects of light encountering with objects. Classical ray tracing method has, however, difficulty to model reflected or refracted ray.

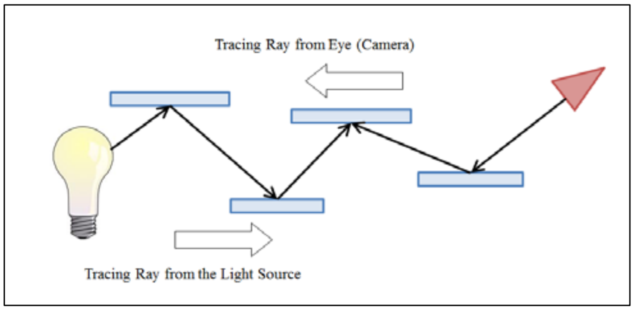
Tracing Ray from Eye (Camera)
Tracing Ray from the Light Source

Figure 1. Bi-directional Path Tracing Technique – it traces rays from the light source as well as from the eye.

Jaewoo Pi, Sungsoo Ha, and Klaus Mueller are with the Center for Visual Computing, Computer Science Department, Stony Brook University, NY 11794 USA (e-mail: { jpi, sunha, mueller}@cs.sunysb.edu).

In order to overcome the problem, bi-directional path tracing was developed [5]. Bi-directional method traces two rays from different directions. To sample each transport path, we generate one sub-path starting from a light source, and another sub-path starting from eye, and join them together. As a result, the method applies more than one importance sampling. Using this property, bi-directional path tracing technique is also applicable to model and simulate scatter of X-ray photons.

C. Parallel Processing on GPU

High-performance modern GPUs, which are equipped with a lot of small processors (threads), have enabled parallel processing for graphical purpose. NVIDIA CUDA is C-like API, and has been available to make parallel processing on a GPU easier. GPU is an external device in CPU(host)'s view, thus GPU cannot access main memory directly. Memory transfer operation between device and host machine is expensive. Optimization is mainly focused on memory operation bottleneck.

III. METHODOLOGY

The implementation consists of two phases. In first phase, the simulator build attenuation layer, by method of a source to pixel ray casting. In the next step, for every bin of detector, add up all computed scattered energy from pixel in the region of interest (RoI).

A. Variables and Symbols

We set simple 2-D cone-beam CT model and its variable. Beam source has beam angle θ. To cover entire region of the object, the position of source (Src_x, Src_y) is set according to beam angle, i.e. for narrower beam angle, source position is farther from the object. (Ray_x, Ray_y) indices sampling position as ray marching through object. Scatter angle φ is difference between source-to-pixel angle and pixel-to-detector angle, and being used to index scatter coefficient at phase function. Each bin has its region of interest, or RoI_j, a Boolean filter determines pixels that contribute to scatter.

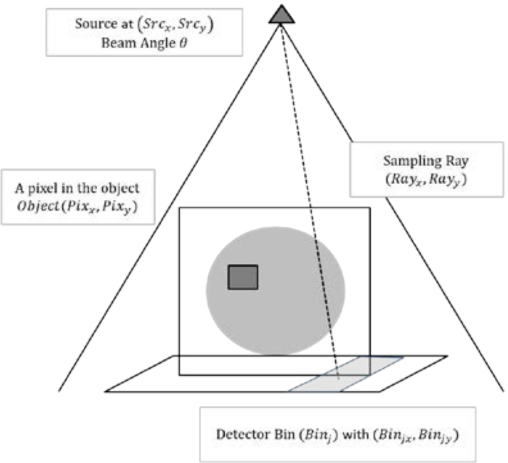

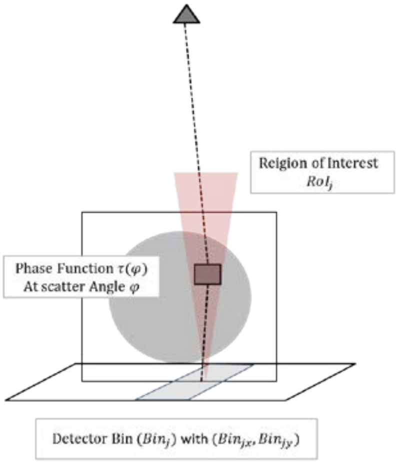
Region of Interest
RoI_j
Phase Function $\tau(\varphi)$
At scatter Angle φ
Detector Bin (Bin_j) with (Bin_{jx}, Bin_{jy})

Figure 2. Simple 2-D CT Model and Variables

B. Attenuation Layer of Source-to-Pixel

We assume that all pixels in the object potentially contribute to scattering and assume that we have only one beam source. Pre-computation of attenuation from X-ray source to all pixels is more advantageous, in terms of computational efficiency at GPU threads.

```
For each $(Thread_x, Thread_y)$
    $(Pix_x, Pix_y) = (Thread_x, Thread_y)$
    $Attn = 1.0$
    For $(Ray_x, Ray_y) = (Src_x, Src_y)$ to $(Pix_x, Pix_y)$
        $Attn = Attn * Object(Ray_x, Ray_y) * \mu(Ray_x, Ray_y)$
    End
    $AttenLayer(Thread_x, Thread_y) = Attn$
End
```

Figure 3. GPU Pseudo Code of Generating Layer of Cross Section

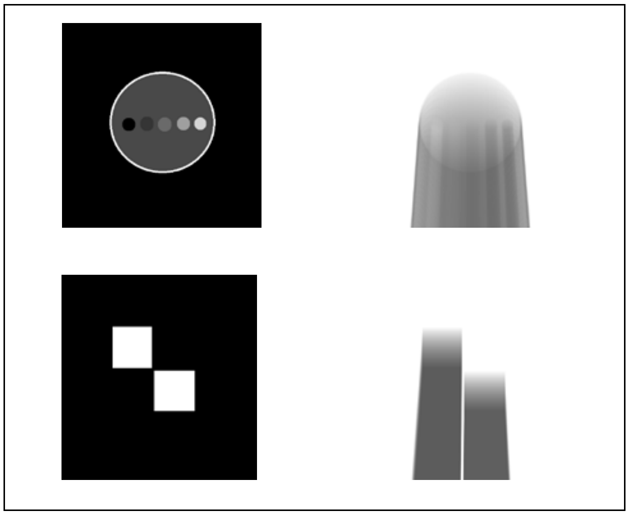

Figure 4. Examples of Cross Section Layer

C. *Computing Scattering from Contributor Pixels*

Computing Scattering consists of three steps. For the first step, a thread in the RoI takes one pixel and compute attenuation from the pixel to detector bin. In the next step, combine two attenuation (source to pixel and detector to pixel), and phase function τ(φ). Finally, to extract a final value of Bin_j, sum up all values in RoI.

```
For each $Bin_j$
  For each $(Thread_x, Thread_y)$ in ROI
    $(Pix_x, Pix_y) = (Thread_x + Offset_x, Thread_y + Offset_y)$
    $Attn = 1.0$
    For $(Lay_x, Lay_y) = (Pix_x, Pix_y)$ to $(Bin_{jx}, Bin_{jy})$
      $Attn = Attn * Object(Lay_x, Lay_y) * \mu(Lay_x, Lay_y)$
    End
    $Roi_j(Pix_x, Pix_y) = Attn * AttenLayer(Pix_x, Pix_y) * \tau(\varphi)$
  End
  $Bin_j = sum(Roi_j)$
End
```

Figure 5. GPU Pseudo Code of Computing Scatter at All Pixels

IV. EXPERIMENT AND RESULTS

For the implementation, we have used Intel Core i7-2640M CPU with 8GB of RAM, and NVIDIA GT 525M GPU, has 96 CUDA Cores and 2GB of video memory. We set phase function $\tau(\varphi)$ and attenuation coefficient $\mu(t)$ equally for all pixels. In this way, we can take the simulation to full throttle to acquire upper limit of time complexity.

Phase function of each pixel decides how much energy is scatter to certain direction. In practice, it is decided by types of matter and energy spectra of X-ray beam. We chose simple probability function, as shown in Figure 6, for simplicity.

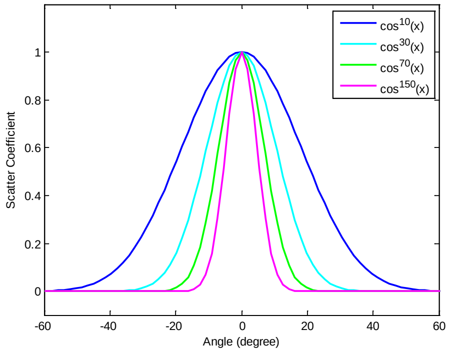

Figure 6. Phase Functions for Experiments

We simulated with two modes of operation: (i) iteration and (ii) 3-D grid. In iteration mode, scatter is computed in 2-D GPU kernel at Bin_j one by one. This mode requires less memory and computation time is increased significantly as image size larger. In 3-D grid mode, on the other hand, number of threads in GPU kernel is increased by N_{Bin} times, where N_{Bin} is number of bins in the detector. All threads in the kernel have to write outputs at different address of memory to prevent race condition of parallel processing. As a result more GPU memory consumption is unavoidable. For high-resolution images we can use hybrid approach; iterating a smaller 3-D multiple times.

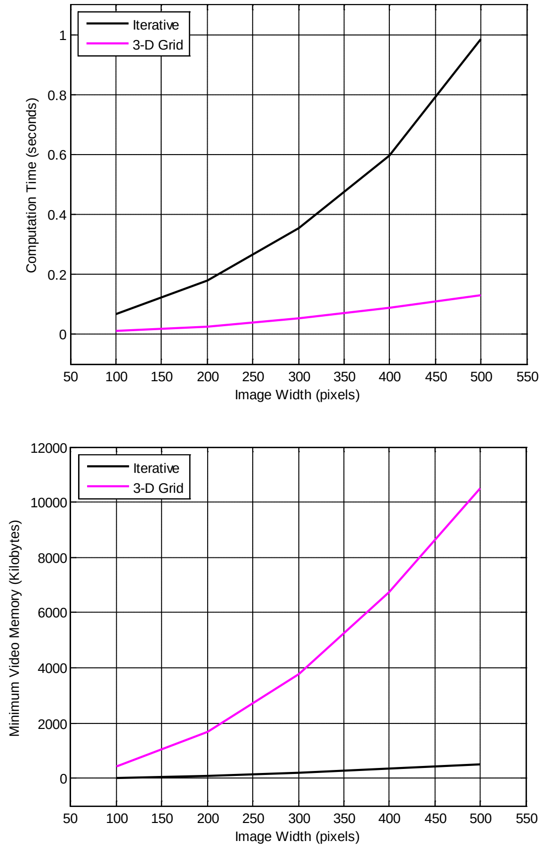

Figure 7. Scattering computation time average versus object resolution (upper) and minimum required memory vs. object image resolution (lower).

The result of scatter is shown in Figure 7, showing original image (300x300 pixels), projection without scattering, and two different types of phase functions: $cos^{30}(x)$, and $cos^{150}(x)$, respectively. Source angle is 20° with 500 bins of detector. Note that former phase function represents much higher reflective material, and later one represents absolving material. In phase function τ(φ), scatter coefficient is higher as angle smaller. Due to cone-beam source CT has one point source at the top-middle, bins at the middle of detector have higher value and bins at each side have relatively lower value. We can tune the RoI at each detector bin to reduce under-estimate or over-estimate of scatter effect.

V. CONCLUSION AND FURTHER WORK

In this study, we modeled an algorithm and implemented code for simulating effective X-ray photon scattering. While Monte Carlo technique is widely used to estimate photon scattering, it has to confront speed-accuracy trade-off.

To overcome the problem, we exploited bi-directional path tracing method, a novel algorithm to model one or more scatter (or reflect). We implemented and optimized code for general purpose GPU, which supports parallel processing with multiple threads. We have achieved satisfactory computation time that linear to slice (2-d) image size. Our further research will focus on finding accurate photoelectric and Compton scattering coefficient determined by materials and other factors for more sophisticated simulation, which will later be used for minimizing artifacts in CT images.

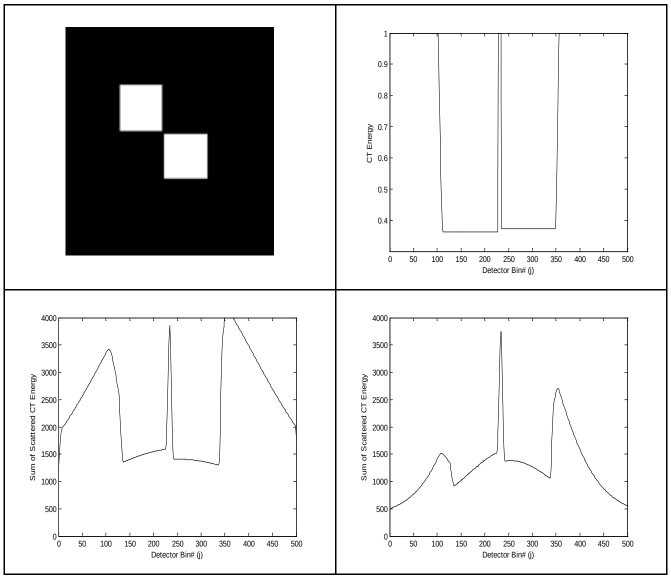

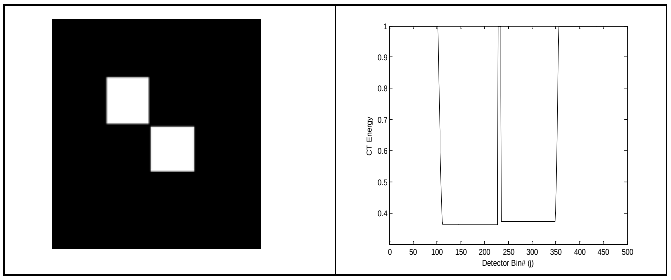

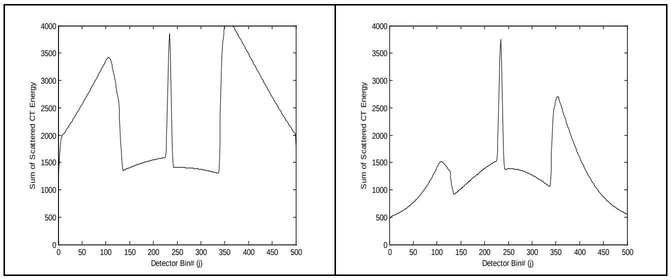

Figure 8. Scatter Result. Original Data (top left), Projection without Scatter (top right), Scatter at high-reflective material ($cos^{30}(x)$) (bottom left), Scatter at less reflective material ($cos^{150}(x)$) (bottom right).

REFERENCES

[1] G. Poludniowski, P. M. Evans, V. N. Hansen and S. Webb “An efficient Monte Carlo-based algorithm for scatter correction in keV cone-beam CT”, Phys. Med. Biol. vol. 54 issue 18, June 2009.

[2] W. Zbijewski, and F.J. Beekman, “Efficient Monte Carlo based scatter artifact reduction in cone-beam micro-CT,” IEEE Transactions on Medical Imaging, vol. 25 issue 7 pp. 817-827, Jul. 2006.

[3] Yiannis Kyriakou, Thomas Riedel and Willi A. Kalender, “Combining deterministic and Monte Carlo calculations for fast estimation of scatter intensities in CT,” Phys. Med. Biol. vol. 51 issue 18, Aug. 2006.

[4] Siewerdsen JH, Daly MJ, Bakhtiar B, Moseley DJ, Richard S, Keller H, Jaffray DA, “A simple, direct method for x-ray scatter estimation and correction in digital radiography and cone-beam CT,” Med Phys 33(1) pp.187-197, Jan. 2006

[5] J. Giersch, A. Weidemann, and G. Anton, “ROSI—an object-oriented and parallel-computing Monte-Carlo simulation for x-ray imaging,” *Nucl. Instrum. Methods Phys. Res*. A, 509:151-156, 2003.

[6] E. Lafortune and Y. Willems, “Bi-directional path tracing,” in CompuGraphics, pp. 145–153, Dec. 1993

[7] Eric Veach and Leonidas Guibas, "Bidirectional Estimators for Light Transport", Eurographics Workshop on Rendering, pp. 147-162, Jun. 1992.

[8] J. Logan, H. J. Bernstein, “A Monte Carlo Simulation of Compton Scattering in Positron Emission Tomography,” Journal of Computer Assisted Tomography, vol. 7 issue 2, pp. 316-320, Apr. 1983.

[9] Anthony Pajot, Loïc Barthe, Mathias Paulin, Pierre Poulin, “Combinatorial Bidirectional Path-Tracing for Efficient Hybrid CPU/GPU Rendering,” Computer Graphics Forum, vol. 30 issue 2 pp. 315-324, Apr 2011.

GPU-Accelerated First-Order Scattering Simulation for X-Ray CT Image Reconstruction

Sungsoo Ha, Jaewoo Pi, and Klaus Mueller, *Senior Member, IEEE*

Abstract— **In recent years the GPU has become an increasingly popular tool in various fields. In this paper, we will introduce our preliminary work on first-order scatter simulation in X-ray imaging accelerated by GPU. As this is preliminary work, we explore the GPU accelerated scattering simulation in 2D space and test it with physics-based simulated data. The results are promising.**

I. INTRODUCTION

There has been much research on investigating the fast simulation of scattering effects in various fields. It is now well established that restricting efforts to single scatter and simulating it based on ray tracing techniques make it possible for the simulation to be done in a short time [1][2]. Several research groups have proposed hybrid approaches by adding stochastic properties into the deterministic approaches to achieve physical accuracy [3][4]. Furthermore, some have also introduced parallel implementations of scattering simulations to overcome the tremendous amount of computations in the simulation [5][6]. We have pursued the latter where we seek to overcome the challenge by GPU-acceleration [7][8], using their massively parallel computations to meet this challenge.

In general, mapping a CPU-based algorithm to the GPU and achieving 1-2 orders of speedup is not straightforward. It requires a deep understanding of the GPU architecture and its programming model. Furthermore, the CPU-based algorithm often needs to be reordered or decomposed to fit into the GPU. In our case, the ray-tracing based deterministic scattering algorithm [4] is divided into two blocks of separate stages and executed as follows. We first compute the attenuation from the x-ray source to object layers and then use the result in the second stage to perform the scattering simulation. This avoids a lot of redundant attenuation computations that occur when similar rays scatter at different locations in the object.

The outline of this paper is as follows. In section 2, we present a brief background on x-ray interaction as well as GPU. In section 3, we provide a detailed explanation of our methods for the first-order scattering simulation on GPUs. The test results are presented in section 4 and section 5 concludes our paper and points to future work.

II. BACKGROUND

A. X-ray Interaction with Matter

The number of x-ray photons, $N(E)$, is attenuated as it passes through matter in an exponential fashion:

$$N(E) = N_o(E)\exp\left[\sum_i -\mu_i(E)x_i\right] \tag{1}$$

Here, $N_o(E)$ refers to the number of photons emitted from the x-ray source, $\mu_i(E)$ is the linear attenuation coefficient associated with the material i at energy E, and x_i is the total path length through the material i. The linear attenuation coefficient can be re-written as the sum of three individual interaction mechanisms: $\mu(E) = \tau(E) + \sigma_R(E) + \sigma_C(E)$ which are the probabilities of *photoelectric absorption (τ)*, *Rayleigh scattering (σ_R)*, and *Compton scattering (σ_C)*. In photoelectric absorption, the incident x-ray photon transfers its energy to an inner shell electron in the absorbing atom that has a binding energy similar to but less than the energy of the incident photon. In Rayleigh scattering, an incident x-ray photon interacts with an electron and is scattered with a small angle but without loss in energy. Finally, in *Compton scattering* the scattered photon travels in any direction, but with loss of energy. More information on the three interactions can be found in [9]. The form-factor (FF) approximation and the incoherent scattering function (ISF) approximation is the model of Rayleigh- and Compton-scattering, respectively, and most widely used in photon transport simulation [4].

B. NVIDIA GPU and CUDA

We have accelerated the first-order scattering simulation on a NVIDIA 480 GTX GPU with 1.5GB off-chip memory. This GPU has 480 CUDA cores organized into 15 streaming multiprocessors (SM) of 32 processors each. Its theoretical computing power is about 1.3 TFLOPS. This GPU, like all modern GPUs, has off-chip memory and on-chip caching mechanisms. Off-chip memory includes global, texture and constant memory and incurs hundreds of cycles of memory latency. It is often the bottleneck of a GPU application. However, texture and constant memory can be cached, replacing the hundreds of cycles of latency with only a few cycles for on-chip cache access. The GTX 480 has a peak memory bandwidth of 177.4 GB/s for its 1.5 GB DDR5 device memory.

The CUDA (Computer Unified Device Architecture) is a C-like API used to program the NVIDIA GPUs. Execution

Sungsoo Ha, Jaewoo Pi, and Klaus Mueller are with the Center for Visual Computing, Computer Science Department, Stony Brook University, NY 11794 USA (e-mail: {sunha, jpi, mueller}@cs.sunysb.edu).

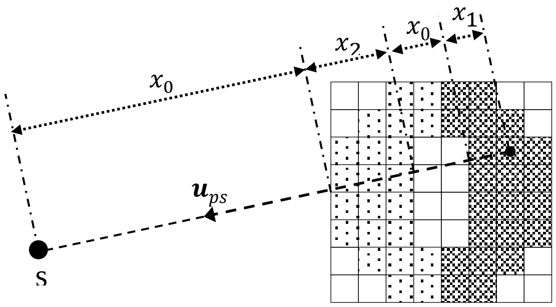

< 1st stage of scattering simulation >

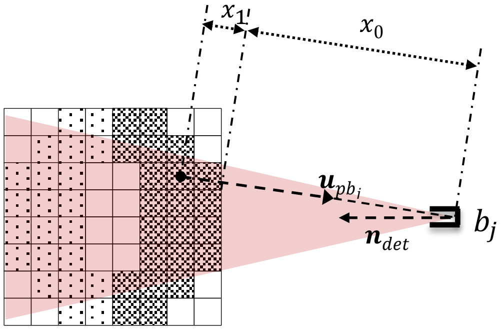

< 2nd stage of scattering simulation >

s: point source
x_i: ray path length in material i
b_j: j-th bin of 1D virtual detector

$\boldsymbol{u}_{ps}$: unit vector from a pixel to point source
$\boldsymbol{u}_{pb_j}$: unit vector from a pixel to j-th bin
$\boldsymbol{n}_{det}$: normal vector of 1D virtual detector

☐ ▨ ▩ : material i

▶ : a region of interest for a j-th bin

Fig. 1. The first-order scattering simulation method consists of two stages. The first stage computes the attenuation from source to pixels (top). The second stage scatters photons into bins in a 1D virtual detector (bottom). For convenience x_i only reflects the path length in different materials not the actual length.

of a task by a CUDA kernel is organized into thread blocks. Thread blocks are organized into a grid. The GTX 480 can have a maximum of 1,024 threads per thread block. Once a thread block is assigned to a streaming multi-processor, it is further divided into 32-thread units called warps and each warp is following same instruction (SIMT: Single Instruction Multiple Thread).

III. METHODOLOGY

Our current implementation serializes the computations for the different energy windows, but it parallelizes the computations for the detector bins by assigning each bin a different set of CUDA blocks. The following description refers to one bin and one energy window. To simulate the first-order scattering in a 2D macroscopic object, the object is divided into small pixels. The simulation is comprised of two major stages: (1) the pre-attenuation from the x-ray source to each pixel is computed and stored in memory, and (2) the post-attenuation from each pixel to each bin is computed and combined with the pre-attenuation to obtain the number of Rayleigh- and Compton-scattered photons for the detector bin (Fig. 1). We now describe how the scattering simulation is parallelized.

A. *Early termination in 1st and 2nd stages*

All x-rays from source to pixels (or pixels to a bin) are parallelized. To reduce the amount of computation in the ray traveling, we terminate the sampling of a ray when the current sampling point is outside of the object. The attenuation from the rest of the x-ray is computed based on pre-defined background material and the remained length.

From the view of CUDA programming, the CUDA kernel has 256 (16x16) threads per a thread block. A grid contains $O((width\ of\ the\ object/16) \times (height\ of\ the\ object/16))$ of thread blocks. The configuration is found by considering the tradeoff between processing speed and code scalability. Each pixel in the object has a pre-defined unique object ID such as air (0) and iron (5), and is stored in a 2D texture which is specifically designed to allow fast 2D memory access and hardware accelerated linear interpolation. The texture memory is also used to store material attenuation coefficients, FFs, and ISFs. This helps to get the data values at a specific energy efficiently. The attenuation coefficient data are obtained from [10] and the FFs and ISFs are from EPDL97 [11]. Before binding these data to texture memory, they are uniformly sampled over a 1keV~1MeV energy range by means of logarithmic interpolation. The constant memory is used to store (effective) atom number and density.

B. *Sum reduction in 2nd stage*

After each thread has computed the number of scattered photons from a pixel to the bin, it stores this number in shared memory. This allows communication of the results among all threads in a thread block. Next we need to combine these pixel photons to obtain the total number of photons arriving in the bin. We use a two-staged approach. First, we use parallelizable sum reduction for computing the

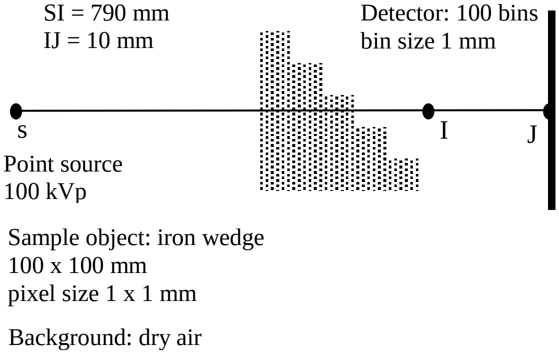

Fig. 2. Simulation of first-order scattering. A 1D virtual detector is placed behind the sample object. The schematic view of the test setup is not to scale.

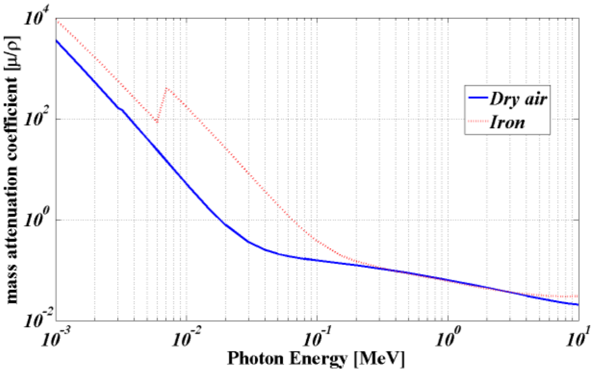

Fig. 4. The mass attenuation coefficient for dry air and iron

total number of scattered photons for each thread block. Then we transfer each block result to the CPU and combine them into the total number of bin photons. This turned out to be faster than a GPU-based block-summation.

C. Region of interest for a bin at 2nd stage

To save overall computation at the second stage, we restrict a region of interest (ROI) of the object for a bin (Fig. 1). This can be regarded as a virtual collimator in the detector. Assuming that bins are uniformly distributed over the detector and have the same acceptance angle (between $\boldsymbol{n}_{det}$ and $\boldsymbol{u}_{pb}$, Fig. 1), only a single ROI needs to be computed at the center of the detector. The ROI is repeatedly re-used for all bins with proper translation. The typical time for computing the ROI takes about 1ms, which is considerably less than the time consumed in the two major stages (Table. I). The total number of thread blocks used in the second stage is reduced to $O(size\ of\ the\ ROI/256)$, where the size of the ROI refers to the number of pixels within the ROI and it is typically much less than the total number of pixels of an object.

D. Parallelizing all bins at 2nd stage

As the final optimization, the computations for all bins are parallelized so that the first-order scattering simulation with a given x-ray energy window can be done in one GPU kernel invocation. To enable this parallelization, the number of thread blocks is increased. A thread block computes a portion of the number of scattered photons for a bin. This allows to reduce memory transfer from GPU to CPU to the order of $(the\ total\ number\ of\ bins)$.

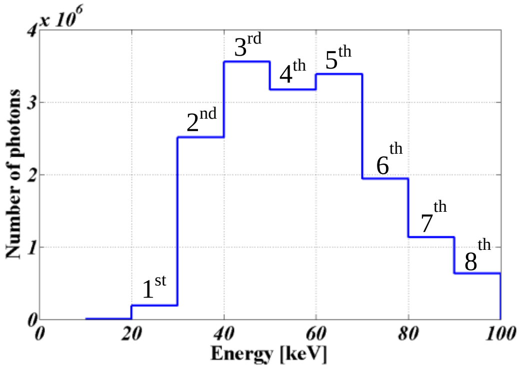

Fig. 3. Discrete x-ray spectrum generated by SpekCalc (100 kVp with 10 keV bin size)

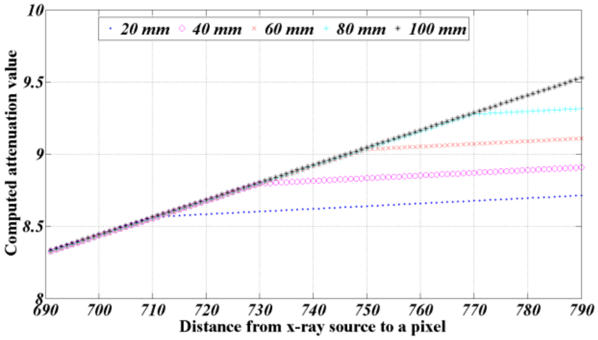

Fig. 5. Profile of pre-attenuation values from 1st stage of the first-order scattering simulation with the test setting at 60~70 keV intervals of x-ray source. Each curve is the profile at the center of a stair of the iron wedge.

IV. EXPERIMENT AND RESULTS

A. X-ray source

To generate a discrete x-ray source, we used the SpekCalc x-ray spectrum generator program [12]. In this study, we only adjust the peak energy (kVp) and the energy bin size (keV) of the x-ray spectrum. The other parameters of the software are kept as default settings. There are 8 energy windows between 20 and 100 keV (Fig. 3) and the total number of scattered photons is computed as the sum of the photons from all windows. The total time for the simulation is computed as the sum of the time spent in all windows in x-ray spectrum.

B. Test configuration

The x-ray source is located at the origin of the 2D space and the sample object stands 790 mm apart from the source. The detector is placed behind the sample object with 10 mm distance. An iron step wedge is selected as the test sample object. The dimensions of the wedge are 100 x 100 mm. The step width is varying from 20 mm to 100 mm with 20 mm intervals. Dry air is selected as the background material. The detail of this test configuration is illustrated in Fig. 2.

TABLE I. TIME PERFORMANCE [SEC]

	Value	ROI	Avg. stage 1[4]	Avg. stage 2[4]	Total[5]
Angle[1]	1	0.001	0.003	0.015	0.149
	3	0.001	0.003	0.039	0.349
	5	0.001	0.003	0.064	0.542
Pixel Size[2]	1x1	0.001	0.003	0.082	0.687
	0.5x0.5	0.001	0.007	0.294	2.425
	0.1x0.1	0.015	0.131	5.578	45.766
Bin Size[3]	1	0.001	0.003	0.082	0.687
	0.5	0.001	0.003	0.161	1.322
	0.1	0.001	0.003	0.799	6.429

1. Unit of degree, and fixed 1 x 1mm pixel and 1mm bin
2. Unit of millimeter, and fixed 7 degree angle and 1mm bin
3. Unit of millimeter, and fixed 7 degree angle and 1x1 mm pixel
4. Average time to complete a given task
5. Time to finish scattering simulation with x-ray spectrum (8 windows)

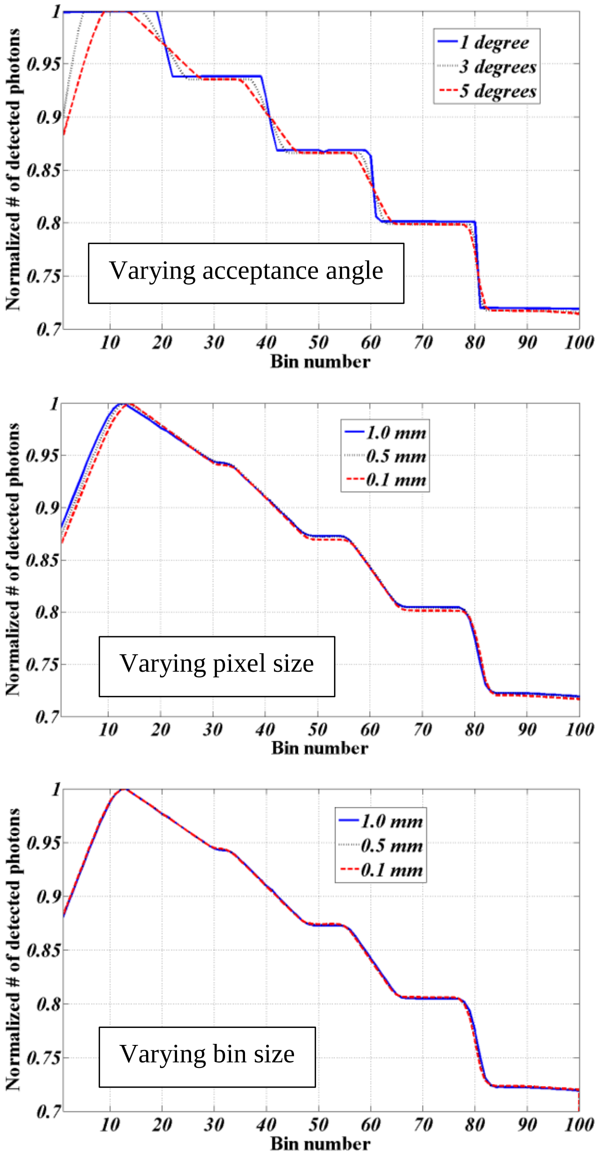

Fig. 6. The number of detected photons with different acceptance angles (top), pixel size (middle) and bins size (bottom). The number is normalized with maximum value at each simulation result for comparison purpose.

C. *Test results*

Fig. 5 shows the pre-attenuation values obtained from the 1st stage of the first-order scattering simulation. The value at each pixel indicates the sum of attenuation values along a ray path from the pixel to x-ray source. As a ray travels further and passes through a wider step, the value is increasing. We can also observe that the attenuation value increase more rapidly as the path travels in iron than in air; this is what we can expect in this experiment from Fig. 4.

There are three factors which can affect the time performance and the simulation result: the acceptance angle, pixel size, and bin size. We measure the time performance and the result by varying those parameters. The time performance is shown in Table I. Fig 6 provides comparisons of the total number of detected photons at the detector with different parameter values as shown in Table I. When increasing the acceptance angles, the contrast at the detector decreases which is symptomatic of the scattering effect (Fig. 6 top); while increasing resolution for the detector or the object, does not yield an improved quality of the scattering simulation result (Fig. 6 center and bottom). It is worth noting that in order to compare different numbers of bins, the number of photons in the bins within the coarsest level size is summed.

V. CONCLUSION AND FUTURE WORKS

In this study we implemented and simulated first-order scattering in 2D space using the GPU. We tested our code with different acceptance angles and different pixel- and bin-sizes. Increasing the acceptance angle to 5 ° gave better scattering effects, while decreasing either pixel or bin size beyond 1.0 was less influential. Using these settings, the measured time performance was about 0.067 seconds for one specific x-ray energy window. For future work, we plan to extend our framework to 3D space and we also plan to verify our results with a well proven scattering simulator and also with directly measured data from real x-ray scanners.

REFERENCES

[1] D. Lazos, Z. Kolitsi, and N. Pallikarakis, “A software data generator for radiographic imaging investigations,” *IEEE Trans. Inf. Technol. Biomed.*, vol. 4, no. 1, pp. 76-79, 2000.

[2] P. Duvauchelle, N. Freud, V. Kaftandjian, and D. Babot, “A computer code to simulate x-ray imaging techniques,” *Nucl. Instrum. Methods Phys. Res. B*, no. 170, pp. 245-258, 2000.

[3] F. Inanc and J. N. Gray, “Scattering simulations in radiography,” *Appl, Radiat. Isot.*, vol. 48, no. 10-12, pp. 1299-1305, 1997.

[4] N. Freud, P. Duvauchelle, S. A. Pistrui-Maximean, J.-M. Letang, D. Babot, “Deterministic simulation of first-order scattering in virtual x-ray imaging,” *Nucl. Instrum. Methods Phys. Res. B*, 222:285-300, 2004.

[5] J. Giersch, A. Weidemann, and G. Anton, “ROSI—an object-oriented and parallel-computing Monte-Carlo simulation for x-ray imaging,” *Nucl. Instrum. Methods Phys. Res*. A, 509:151-156, 2003.

[6] F. Inanc, B. Vasiliu, and D. Turner, “Parallel implementation of the integral transport equation-based radiography simulation code,” *Nucl. Sci. Eng.*, 137:173-182, 2001.

[7] F. Xu, K. Mueller, “Accelerating popular tomographic reconstruction algorithms on commodity PC graphics hardware.” *IEEE Trans. On Nuclear Science*, 52(3):654-663, 2005.

[8] F. Xu, K. Mueller, “Real-Time 3D Computed Tomographic Reconstruction Using Commodity Graphics Hardware,” *Physics in Medicine and Biology*, 52:3405-3419, 2007.

[9] J. A. Seibert, J. M. Boone, “X-Ray Imaging Physics for Nuclear Medicine Technologists. Part 2: X-Ray Interactions and Image Formation,” *J Nucl Med Technol*. 32:139-147, 2004.

[10] J. H. Hubbel, “Photon mass attenuation and energy absorption coefficients from 1 keV to 20 MeV,” *Int. J. Appl. Radiat. Isotopes*, 33:1269, 1982.

[11] D. E. Cullen, J. H. Hubbel, L. Kissel, “EPDL97: The Evaluated Data Library, ’97 Version,” UCRL-ID-50400, 6(5), 1997.

[12] G. Poludniowski, G. Landry, F. DeBlois, P. M. Evans, F. Verhaegen, “SpekCalc: a program to calculate photon spectra from tungsten anode X-ray tubes,” *Phys Med Biol* 54(19):N433-N438, 2009.

Searching Effective Parameters for Low-Dose CT Reconstruction by Ant Colony Optimization

Ziyi Zheng, Eric Papenhausen and Klaus Mueller

***Abstract*— Low-dose Computed Tomography (CT) has been gaining substantial interest, due to the growing concerns with regards to the X-ray dose delivered to the patient. To cope with the limited data collected at 30% of standard radiation, low-dose CT reconstruction algorithms generally involve several iterations of forward projection, back-projection and regularization, requiring many parameters to achieve desirable quality and speed. The interactions among these parameters can be complex, and thus effective combinations can be difficult to identify for a given scanning scenario. Non-optimized parameters can result in increased reconstruction time or reduced image quality. As a result, the parameter choice is often left to a highly-experienced expert. In this work we focus on an automatic parameter optimization framework. In the pre-computation step of our parameter learning framework, effective parameters are learned with the access of a known gold-standard. As these domain-specific and algorithm-dependent parameters are obtained, they are applied in the similar incoming data. In addition, an edge-enhancement component is introduced and automatically tuned to increase the sharpness in iterative reconstruction. The preliminary results with the non-local mean filter indicate that our parameter optimization scheme can identify effective parameters resulting in sharper results than those results generated by popular iterative reconstructions algorithms.**

Index Terms*—*Iterative reconstruction, low-dose CT, ant colony optimization, non-local mean filter

I. INTRODUCTION

Cone-beam CT has become to be a major imaging technique thanks to its image-fidelity and scan time. The traditional cone-beam CT reconstruction method is the FDK [1] algorithm, which provides high resolution results but requires several hundreds of X-ray projections. With the growing concern about the potential risk of X-ray radiation exposure to the human body, low-dose CT has become a significant research topic. Dose reduction usually involves lowering the X-ray energy per projection and/or reducing the total number of projections. Both methods typically suffer from low signal-to-noise ratio (SNR) in the reconstructions. Iterative reconstruction schemes, matched with suitable regularization methods have been shown to cope well with these few-view or high-noise scenarios.

Iterative methods typically offer a diverse set of parameters that allow control over quality and computation speed, often requiring trade-offs. These expert-picked parameters need to be learned from many experiments which are both domain-specific and algorithm-dependent. Thus the hand-tuning of the parameters in iterative algorithm could be very time-consuming. Researchers have proposed methods to set the parameters by monitoring the convergence and updating reconstruction parameters on the fly [2]. In this work we focus on automatic parameter optimization by pre-computation. We propose a two-step method. The first step is the parameter learning step; which uses the known gold-standard. After parameters are trained, they are re-used in similar data with similar scanner settings. Furthermore, our framework can incorporate an interleaved un-sharp mask to avoid over-smoothing on the reconstruction results. We compared our results with those obtained by automatic controlled iterative reconstructions algorithms and results indicate that our optimized parameters can resolve fine structures as good as or better than previous methods.

Our paper is organized as follows. Section 2 discusses related work. Section 3 describes our framework. Section 4 presents some initial results, and Section 5 concludes the paper.

II. RELATED WORKS

Recent research in iterative reconstruction demonstrates a trend of combining forward and back-projection with various regularization methods. The regularization algorithm usually employed is Total Variation Minimization (TVM) as used in the Adaptive-Steepest-Descent-Projection-Onto-Convex-Sets (ASD-POCS) algorithm [2]. On the other hand, de-noising filters, such as the bilateral filter [3] and the non-local means (NLM) filter [4], can also be used in regularization [5][6][7]. Compared to the ASD-POCS algorithm which can determine the TVM parameters on the fly, de-noising filters based reconstruction methods need a special control unit to guide regularization parameter during the convergence. Our framework fulfills this need and provides optimized parameters which can be directly applied on de-noising filter based regularization algorithm.

This work serves as an extension of previous research focused on optimizing bilateral filter-based iterative reconstruction, using genetic algorithms [8]. The ant colony optimization (ACO) [9] algorithm is inherently a path searching engine driven by a large number of artificial ants and is widely applied to solve many optimization problems. In this paper, we utilize the ACO algorithm to find optimal parameters in NLM-based iterative reconstruction. In addition, we improve the current existing regularization pipeline by adding an edge-boosting stage with optimized parameters.

Ziyi Zheng, Eric Papenhausen and Klaus Mueller are with the Computer Science Department, Stony brook University, Stony Brook, NY 11777 USA. (E-mail: { zizhen, epapenhausen, mueller}@cs.sunysb.edu).

III. APPROACH

A. Iterative Reconstruction with Regularization

We use the OS-SIRT algorithm with GPU-accelerated forward projection and back-projection [8]. The forward projection operator simulates X-ray images at a certain viewing angle φ. The result of this projection is then compared to the acquired image obtained at the same viewing angle. Here, the weight factor w_{il} determines the contribution of v_l to r_i and is given by the interpolation kernel used for sampling the volume. The forward projection is:

$$r_i = \sum_{l=1}^{N} w_{il} \cdot v_l \qquad i = 1,2,\ldots,M \tag{1}$$

where M and N are the number of rays and voxels, respectively. The correction update is computed as:

$$v_j^{(k+1)} = v_j^{(k)} + \lambda \frac{\sum_{p_i \in OS_s} \frac{p_i - r_i}{\sum_{l=1}^{N} w_{il}} w_{ij}}{\sum_{i=1}^{N} w_{ij}} \tag{2}$$

$$r_i = \sum_{l=1}^{N} w_{il} \cdot v_l^{(k)} \tag{3}$$

Here, p_i represents the pixels in the M/S acquired images that form a specific (ordered) subset OS_S where $1 \leq s \leq S$ and S is the number of subsets. The factor λ is the relaxation factor that scales the corrective update to each voxel. This factor is important in balancing quality and speed and will be optimized by our framework. The factor k is the iteration counter. It will be incremented when all M projections have been processed. In the GPU implementation, only the forward projection uses a ray-driven approach, where each ray is a parallel thread and interpolates the voxels on its path. Conversely, the back-projection uses a voxel-driven approach, where each voxel is a parallel thread and interpolates the 2D correction projections. Thus, the weights used in the projection and the back-projection are slightly different but it has minimum effect on the reconstruction quality [5][8].

We use a 2D NLM filter [4] for regularization. The NLM filter is a non-linear filter that replaces the pixel located at x with the mean of the pixels whose Gaussian neighborhood looks similar to the neighborhood of x:

$$NLM(x) = \frac{\sum_{y \in W} e^{-\frac{\sum_{t \in N} G_a(t) \left| f(x+t) - f(y+t) \right|^2}{h^2}} f(y)}{\sum_{y \in W} e^{-\frac{\sum_{t \in N} G_a(t) \left| f(x+t) - f(y+t) \right|^2}{h^2}}} \tag{4}$$

Here, x, y and t are 2D spatial variables. W is the window centered at x. N is the 2D neighborhood centered at x or y. G_a is a 2D Gaussian kernel with a standard deviation a. The variable h acts as a parameter to control smoothing. Thus, the NLM filter contains several parameters to achieve best quality. For the performance, one observation of NLM filtering is that the computational time spend on NLM does not change as like it does in TVM regularization.

At the last stage of our regularization scheme, the un-sharp masking is used to avoid over-smoothness in iterative reconstruction. The control factor of sharpness is given by later optimizations.

B. Ant Colony Optimization (ACO)

The ant colony optimization (ACO) algorithm is a swarm intelligence method to search for good paths in discrete graphs. Intuitively, it launches a large number of artificial ants searching for best score. Each artificial ant independently moves in the graph and reports the scores it gets. The probability for an ant to choose an edge connecting two nodes is affected by the moving trend of all ants. More specifically, the probability for choosing one choice will increase if a large number of high score-ants choose it.

Iterative CT reconstruction can be modeled as a classic path searching problem. In this discrete graph of nodes and edges, each node represents a unique state of the volume being reconstructed, after a certain number of iterations and tagged with a score that encodes a quality metric. Each edge represents the computation of a correction pass and a regularization pass. The weight on an edge represents the time cost, which in our case is treated uniformly as one. The overall goal is to find the node having the highest score within a given cost. Since we have a uniform cost for NLM filtering, the problem is reduced to find the best score after a fixed number of steps.

We attempt to optimize six parameters including the relaxation factor λ in Equation (2), the h factor, Gaussian blur factor, window size and block size for the NLM filter in equation (4) and the un-sharp masking factor. These parameters can be different per iteration, resulting in an astronomical search space. For example, assuming we allow 100 discretized values for each parameter and allow 10 iterations, the search space will be 10^{120}. This search space is so huge that simple exhaustive search algorithm will fail to find the optimal solution in a reasonable amount of time.

We adopt a greedy heuristic to prune the search tree. This heuristic guides ants with a "best guess" for the path on which the solution lies. The greedy ant system only searches the best parameter setting for a single iteration, then adopts the best setting and moves on to the next iteration. The solution space can then be reduced from 10^{120} to 10^{13}. Assuming the optimal parameters would be similar or slightly adjusted for adjacent iterations, we can improve the search efficiency through pheromone control. The pheromone for the current iteration is re-used in the next iteration, making ants more likely to choose parameters similar to previous best parameters.

In the following, we describe our version of the ant system in detail. The probability for an ant to choose a discretized value j for ith parameter is:

$$P(i,j) = \frac{\tau_{ij}}{\sum_{q=0}^{R_i} \tau_{iq}} \tag{5}$$

where τ_{ij} is the pheromone on value j for ith parameter and R_i is the discrete resolution of the ith parameter. The value of τ_{ij} is initially set to one; this will allow ants to make purely random decisions. After a small group of ants (in our case it is 10) finishes their moves for all 6 parameters, the pheromone is updated as:

$$\tau_{ij} \leftarrow (1-\rho)\tau_{ij} + \textstyle\sum_{k=1}^{10} s_k/10 \qquad \forall j \in J \qquad (6)$$

where s_k is the normalized score (with $0 < s_k < 1$) of the kth ant, as the amount of new pheromone put on ρ is the pheromone evaporation factor (with $0 < \rho < 1$). The range of pheromone is clamped within $[0, 1]$. The equation (6) updates the pheromone such that later ants will be more likely to follow the path of previous high-score ants. If in the current iteration no ants report better scores than in the previous iteration, we launch another group of ants until better scores are found or the maximum number of ants for one iteration is reached. In the absence of a human observer, s_k is generated by a computer based on a quality metric. In this paper, we use the correlation coefficient (CC) to determine s_k.

IV. RESULTS

In our experiments, we collected two sets of data from a cone-beam CT scanner (Medtronic O-arm system). We perform the reconstruction algorithms on the central slice only. The detector 1D resolution was 1,024 pixels with pixel-size 0.388mm. The low-dose case was set as 60 evenly-distributed projections and the gold-standard was generated by the FDK algorithm with 360 projections. In the OS-SIRT scheme, we made 40 subsets which contain 1-2 projections. Head phantoms were used to test the parameter optimization algorithm and the training results are shown in Figure 1. The result from 60 iterations of the OS-SIRT algorithm with a constant λ=1 is in panel (a) and the gold-standard is in panel (b). 60 iterations of the ASD-POCS result is displayed in panel (c). We use SART instead of ART in this ASD-POCS implementation to make a fair comparison. The ASD-POCS result is smooth but has some typical cartoon-like structures due to the TVM scheme. On the other hand, our trained results (d) are the more similar to the gold standard (b) and can preserve sharper details than ASD-POCS can (c).

Figure 2 shows the plot of trained parameters through 60 iterations with CC scores. We can see that the CC score stops improving after 25 iterations. Figure 3 shows the plot of relaxation-correction factor λ in equation (2). The optimized parameter suggests starting with a bigger value around 2.0 and gradually decreasing to 0.0. Note the overall decreasing trend contains a certain amount of perturbation and there was very little correction after 40 iterations.

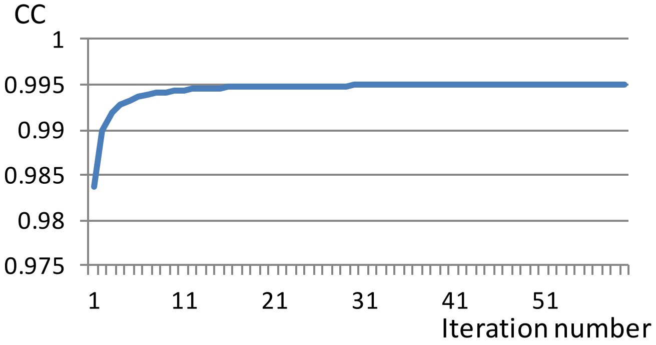

Figure 2. The correlation-coefficient CC through 60 iterations

We tested the learned parameter setting on another similar head phantom. Now the central slice was shifted to another autonomy region in the head phantom. Figure 4 documents the

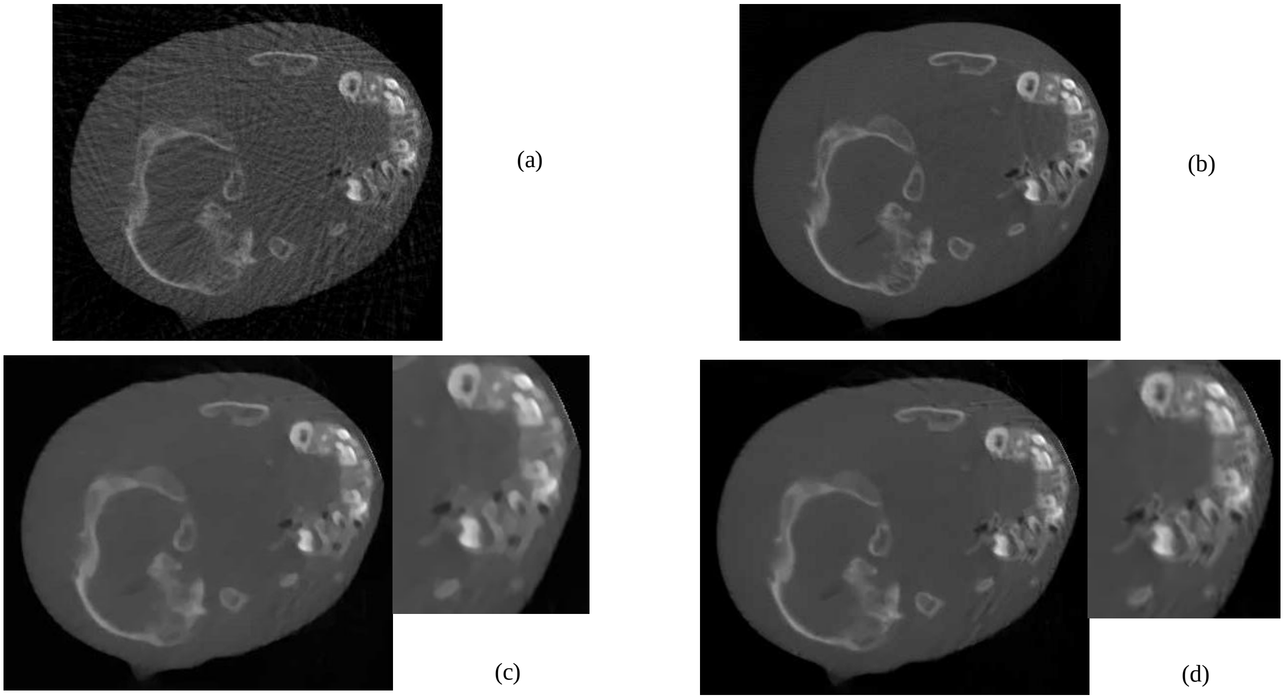

Figure 1. A central slice of a reconstruction for a training dataset. (a) low-dose OS-SIRT. (b) gold-standard FDK by 360 projections. (c) low-dose ASD-POCS and (d) optimized low-dose. (a), (c) and (d) use 60 projections and 60 iterations.

image quality of the new dataset with (a) 60 iterations of OS-SIRT with a constant λ=1, (b) 360 projection FDK, (c) 60 iterations of ASD-POCS and (d) 60 iterations of optimized parameters. We observed that even in another scan, the parameters can guide the reconstruction to achieve better visual quality than ASD-POCS.

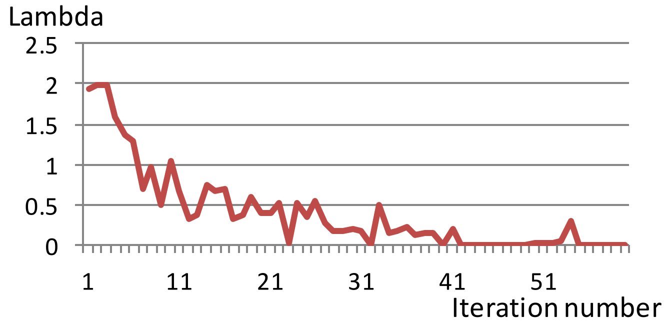

Figure 3. The λ in Equation (2) through 60 iterations

All of our experiments were conducted on an NVIDIA GTX 480 GPU, programmed with CUDA 3.2 runtime API and with an Intel Core 2 Duo CPU @ 2.66GHz. We display the reconstruction results simultaneously during the optimization. In the implementation, we use shared-memory in the GPU to perform prefetching, which enables 4× speedups [6]. Table I shows the configurations and performance of our framework. The iteration versus time does not scale linearly since later iterations will need to launch more ants to improve the score, especially in the case when the scores do not increase after a large number of iterations. We try to avoid over-fitting by detecting whether λ becomes close to zero ($\lambda < 0.05$).

TABLE I
PERFORMANCE OF ANT COLONY OPTIMIZATION

Maximum # of Ants	Iterations	Time(s)
1000	10	92
1000	30	265
1000	50	1.44k

V. CONCLUSIONS

We have devised an efficient framework to optimize various parameters for iterative CT reconstruction using an ant colony optimization algorithm. Our preliminary results show that the learned parameters can be readily applied to similar scans with promising results.

In future work, we would like to employ other perceptual quality metrics. We are also planning to extend the current framework to 3D reconstruction and study parameter optimization in different scanning scenarios, for example, patient size, X-ray tube's voltage and current.

ACKNOWLEDGMENT

We thank Medtronic for providing access to their O-arm scanner and head phantoms.

REFERENCES

[1] L. A. Feldkamp, L. C. Davis, and J. W. Kress, "Practical cone-beam algorithm," J. Opt. Soc. Am. Vol 1, No. A6, 612–619 , 1984.

[2] E. Y. Sidky and X. Pan, "Image reconstruction in circular cone-beam computed tomography by constrained, total-variation minimization," Physics in Medicine and Biology, vol. 53, pp. 4777-4807, 2008.

[3] C. Tomasi, and R. Manduchi, "Bilateral filtering for gray and color images," IEEE International Conference on Computer Vision, pp. 839-846, 1998.

[4] A. Buades, B. Coll, and J. M. Morel, "A non-local algorithm for image denoising," Computer Vision and Pattern Recognition, pp. 60-65, 2005.

[5] W. Xu and K. Mueller, "A performance-driven study of regularization methods for GPU-accelerated iterative CT," In *Workshop on High Performance Image Reconstruction*, 2009.

[6] Z. Zheng, W. Xu, and K. Mueller, "Performance tuning for CUDA-accelerated neighborhood denoising filters," In *Workshop on High Performance Image Reconstruction*, 2011.

[7] J. Huang, J. Ma, N. Liu, H. Zhang, Z. Bian, Y. Feng, Q. Feng, and W. Chen, "Sparse angular CT reconstruction using non-local means based iterative-correction POCS," *Computers in Biology and Medicine*, 41(4):195-205, 2011.

[8] W. Xu and K. Mueller, "Using GPUs to learn effective parameter settings for GPU-accelerated iterative CT reconstruction algorithms", GPU Computing Gems Emerald Edition, Chapter 43, January 26, 2011

[9] M. Dorigo, G. DiCaro, and L. M. Gambardella, "Ant algorithms for discrete optimization," *Artificial Life*, 5(2):137–172,1999.

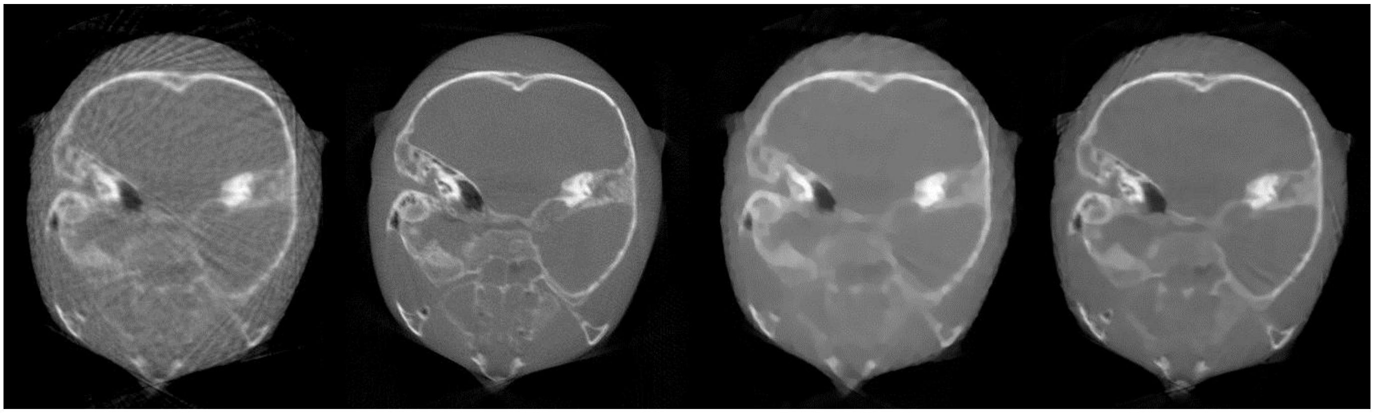

(a) (b) (c) (d)

Figure 4. A central slice of a reconstruction for a new dataset. (a) low-dose OS-SIRT. (b) gold-standard FDK by 360 projections. (c) low-dose ASD-POCS and (d) optimized low-dose. (a), (c) and (d) use 60 projections and 60 iterations.

Spectral Response Compensation for Photon Counting Clinical X-ray CT and Application to Coronary Vulnerable Plaque Detection

J. Cammin*, S. Srivastava, G.S.K. Fung, and K. Taguchi

Abstract—**Computed tomography with photon-counting detectors (PCD-CT) is an emerging technology that will decrease noise, increase contrast, and enable quantitative and molecular CT imaging. Several spectral response effects (SRE) distort the energy spectrum recorded by PCDs: finite energy resolution, Compton scatter, charge-sharing, K-escape, etc. They lead to severe artifacts if left uncorrected. We propose a new SRE compensation scheme for PCD-CT that restores the projection data and allows for quantitative imaging using material decomposition. The performance was evaluated against conventional energy-integrating detectors (EID) and applied to the clinical task of detecting coronary plaques, in particular soft plaque prone to rupture. Simulations using the 4D XCAT computer phantom indicate that a contrast-to-noise ratio (CNR) enhancement for certain plaques up to a factor of 8 compared to EID-CT may be possible, resulting in dose reduction well over 90%. ROC curves were obtained for the detectability of soft plaque with and without a novel Bismuth-nanoparticle contrast agent. The area under the ROC curves (AUC) was used as a performance index for the various systems and compensation methods. In all cases the PCD-CT with the proposed SRE compensation scheme outperforms EID-CT by a large margin (e.g., for soft plaque vs. tissue: AUC=0.99 for PCD-CT and AUC=0.63 for EID-CT).**

Index Terms—**spectral CT, photon-counting detectors, material decomposition, XCAT computer phantom, coronary plaque detection, atherosclerosis, ROC curve.**

I. INTRODUCTION

Computed tomography (CT) has been a valuable diagnostic imaging modality since its development by Hounsfield in the 1970s. Recent developments in this field aim at exploring not only the intensity but also the energy information of the transmitted x-ray spectrum. Together with contrast agents and K-edge imaging the additional information leads to increased contrast, more quantitative data, and opens the field of functional and molecular imaging to x-ray CT.

These new imaging opportunities, however, require a paradigm shift in detector technology. Conventional CT systems with energy integrating detectors (EIDs) have the following limitations: 1) the contrast between tissue types is not sufficient for many diagnostic purposes; 2) images are not tissue-specific; 3) some exams require relatively high-dose protocols. These limitations can be overcome with photon-counting detectors (PCDs) which are capable of counting individual photons and their energies, thus providing both intensity and spectral information.

In the following two subsections we describe PCDs in more detail and then discuss a specific application of high significance (coronary plaque detection) that will become accessible to CT imaging with the compensation scheme for PCDs proposed in this paper.

A. *Computed tomography with photon-counting detectors*

PCDs consist of crystal sensors such as Cadmium Telluride (CdTe) to convert x-ray photons into electrical signals. Electronic circuits attached to the sensor amplify and shape the signal pulse for each photon. Comparators measure the signal height which is a measure for the incident photon energy and count the photon if the signal is above a given threshold. Current PCDs intended for x-ray and CT imaging have between two and six separate counters for different energy windows and can register up to 150 million photons per second per square-millimeter (Mcps/mm^2). Some CdTe-based PCDs are described in [1-7].

Despite significant advancements in detector technology PCD data are affected by several inherent degradation factors. If these are not accounted for, the resulting CT images will be of little value for diagnostic purposes. Count-rate independent effects that alter the measured photon energy (spectral response effects, SREs) include charge sharing, K-escape x-rays, and Compton scattering. Count-rate dependent effects (pulse-pileup effect, PPE) originate from the limited count rate of current PCDs: when the x-ray flux is very high, the detector response time is insufficient to resolve individual photons, which are then counted as one photon with added energies. This leads to a loss of count and wrong energy information.

In this paper we address the spectral response effects and propose a compensation scheme that restores the spectral information in the projection data domain. The PPE has been addressed by the authors previously [8, 9].

B. *Coronary plaque*

Cardiovascular diseases remain the leading cause of death in the western world with ever-increasing costs on health services. Cardiac catheterization to determine a possible

This work was supported in part by NIH grants R44 EB008612, R01 HL087918 and AHA grant BGIA 0865315E.

J.C., S.S., G.F, and K.T. are with the Russell H. Morgan Department of Radiology and Radiological Science, The Johns Hopkins School of Medicine, Baltimore, MD 21287, USA (phone: 410-502-3773; fax: 410-614-1060; e-mail: jcammin1@jhmi.edu).

stenosis due to plaque deposits is expensive, invasive, and connected to certain risks for the patient. A promising non-invasive alternative is ECG-gated CT [10]. However, the limitations of current EIDs described before make it challenging to accurately detect and characterize plaques. It is especially important to detect soft plaque (atherosclerosis) that is prone to rupture and form blood clots (vulnerable plaque, high-risk atherosclerosis).

Spectral CT with PCDs will be able to solve this problem due to decreased noise, increased contrast, and the ability to reconstruct material specific images for certain tissue types and contrast agents. Recently developed nanoparticles that can carry high-Z contrast agents such as bismuth or gold and that specifically attach to soft plaques will allow to image high risk atherosclerosis and help to distinguish different plaque types.

In this paper we apply the SRE compensation algorithm to simulated coronary plaques and study the detectability of atherosclerosis using spectral PCD-CT.

II. MATERIALS AND METHODS

A. *Spectral response effect compensation for PCD-CT*

A new SRE compensation algorithm was developed with an efficient conjugate gradient method in which the first and second derivatives are calculated analytically. The SRE compensation integrates a sinogram restoration approach, applies the SRE in the forward projection model, and then compensates for the SRE by maximizing a penalized log-likelihood function. The following subsections describe the algorithm in more details:

1) *Forward imaging model*

The forward model can be outlined as follows: a polychromatic x-ray spectrum exiting from a bowtie filter is modeled by the number of photons in multiple energy bins. The attenuation of the photons by the object is modeled using a material decomposition approach [11]. The x-ray photons are then incident on a PCD pixel, where the x-ray spectrum is distorted as described by a parameterized spectral response function (SRF). The output of an energy bin is the number of counts within the corresponding energy range of the distorted spectrum.

a) *Object model based on material decomposition*

The object being imaged is a spatial distribution of the energy-dependent x-ray attenuation coefficient: $f(\underline{x}, E)$, where $\underline{x}$ is a location and E is an energy. Using the concept of material decomposition, $f(\underline{x}, E)$ can be modeled accurately by a sum of L basis materials,

$$f(\underline{x}, E) = \Sigma_{k=1}^{L} a_k(\underline{x}) \rho_k \mu_k^{(\rho)}(E),$$

where ρ_k is the density, $\mu_k^{(\rho)}(E)$ is the mass attenuation coefficient, and $a_k(\underline{x})$ is the coefficient of the kth basis.

b) *Spectral response function (SRF)*

The SRF for monochromatic incident x-rays was measured for several input energies, E_0, using radioisotopes at a very low count rate. The recorded spectrum was normalized to obtain the SRF. The SRFs varied gradually depending on the input energy E_0. The mathematical equation for the SRF, $D_{SRF}(E; E_0)$, is defined to model the measurements with only a few parameters. The SRF for E_0 is a weighted summation of two normalized functions for the photopeak (D_G) and a long tail (D_T). The photopeak is modeled by a Gaussian curve with a parameter $\sigma(E_0)$ centered at E_0. The tail is a constant that extends from E_0 down to E_{min}. The SRF can then be described as

$$D_{SRF}(E; E_0) = w D_G(E; E_0) + (1-w) D_T(E; E_0),$$

$$D_G(E; E_0) = \frac{1}{\sqrt{2\pi}\sigma(E_0)} \exp(-\frac{(E-E_0)^2}{2\sigma^2(E_0)}),$$

$$\sigma(E_0) = k\sqrt{E_0} \quad (E_0 \; in \; keV),$$

$$D_T(E; E_0) = \begin{cases} 1/(E_0 - E_{\min}), & E_{\min} \le E \le E_0, \\ 0, & otherwise. \end{cases}$$

There are three parameters that change the SRF: k for the width of the photopeak; w for a balance between the photopeak and the tail; and E_{min} for the minimum tail energy or noise floor (E_{min} is fixed in this study).

2) *Spectral response compensation*

The compensation scheme comprises the following elements: (a) a cost function computed for each ray, including a regularization term; (b) an optimization algorithm that estimates line integrals by minimizing the cost function; (c) reconstruction of basis materials from the estimated line inetgrals using filtered backprojection. A monoenergetic CT image at a desirable energy E_r, can then be synthesized from the density images of the basis materials.

a) *Cost function*

The penalized log-likelihood function is given by

$$\Phi(\underline{l}) = -L(\underline{y}; \underline{\bar{y}}(\underline{l})) + \beta R(\underline{l}),$$

$$-L(\underline{y}; \underline{\bar{y}}(\underline{l})) = \sum_{l=1}^{N_i} \sum_{n=1}^{N_{bin}} \bar{y}_{n,i}(\underline{l}_i) - y_{n,i} \log \bar{y}_{n,i}(\underline{l}_i),$$

$$\underline{l}_i \equiv [l_{i,1}, \ldots l_{i,L}],$$

$$R(\underline{l}) = \frac{1}{2} \sum_{k=1}^{L} \sum_{i=1}^{N_i} \sum_{j \in Neighborhood(i)} (l_{i,k} - l_{j,k})^2,$$

where $-L(\underline{y}; \underline{\bar{y}}(\underline{l}))$ is the Poisson log-likelihood function, $\underline{l}$ is a vector over $l_{i,k}$ ($l_{i,k}$ is the line integral of the kth basis material along the ith ray), β is the regularization parameter, $y_{n,i}$ are the counts in the nth energy bin along the ith ray, $\bar{y}_{n,i}(\underline{l}_i)$ are the mean detector counts based on the forward imaging model, and $R(\underline{l})$ is a quadratic regularization function in the sinogram domain [12].

b) *Conjugate gradient optimization method*

The optimization method is described in this section. The direction of the line search is computed using the conjugate gradient (CG) method. Each line search is performed by a quasi-Newton method. The gradient ($\nabla\Phi$) and Hessian ($\nabla^2\Phi$) used by the conjugate gradient and quasi-Newton methods, respectively, are computed analytically using the chain rule.

The pseudo code of the algorithm is given below:

```
* Compute initial guess of $\underline{l}$
* For iteration $m=1,\ldots,N_{iter}$ Do
  * For ray $i=1,\ldots,N_i$ Do
      * Do
          * Compute gradient, $\underline{g} = \nabla\Phi$, using the chain rule
          * Compute search direction, $\underline{d}$, using CG
          * Do
              * Update $\underline{l}$ using quasi-Newton method applied along d
          * While (Wolfe conditions are not satisfied)
      * While (Gradient, $\underline{g}$, is large)
  * EndFor
* EndFor
```

B. Nanoparticles for contrast enhancement of vulnerable plaque

Recently, novel nanoparticle contrast agents have been developed [13] which combine with fibrins or macrophages of the vulnerable plaque. These nanoparticles can carry atoms with high atomic numbers like bismuth, yttrium, barium, or gold. PCD-CT is especially suited to image these elements contained in the nanoparticles using K-edge imaging.

C. XCAT computer phantom with coronary plaque

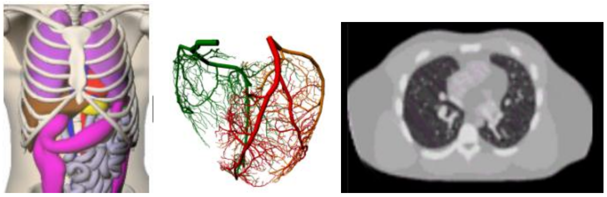

Fig. 1: (left) and (middle): The 4D XCAT male anatomy and coronary trees. (right): Reconstructed CT image from simulation data with pulmonary vessels and bronchi.

The 4D XCAT phantom (Fig. 1) that was developed in our division [14] is a realistic computer model of the human anatomy, physiology, and heartbeat motion. The orientation, size, and shape of the chest and heart are parameterized, and it is possible to simulate various populations of patients. Recently, realistic plaque and perfusion defects [15] and integration with an accurate CT projection data simulator [16] were added. To simulate coronary plaque, we added calcium deposits and atherosclerosis with and without a layer of Bismuth nanoparticle contrast agent to a coronary vessel as shown in Fig. 2.

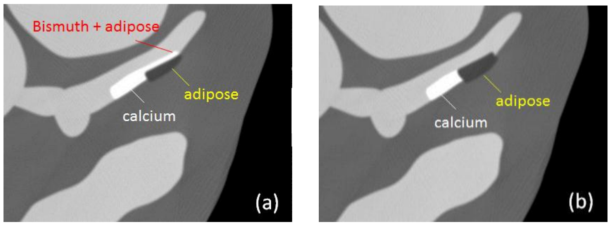

Fig. 2: The XCAT phantom with coronary plaque. (a) With calcified plaque, adipose with Bismuth contrast agent, and adipose (b) as in (a) but without the Bismuth contrast agent.

D. Plaque Detection

The performance of the PCD-CT compensation algorithm for detection of vulnerable plaque was evaluated using simulation studies with the XCAT phantom as described in section II.C. Two detection tests were performed:

#1: Test for atherosclerosis (soft plaque)

#2: Test for high-risk atherosclerosis (vulnerable plaque)

The detection tests were performed by choosing ROIs in various tissues and comparing both the average pixel values in the ROIs and also the distribution of pixel values.

For test #1 the detection test was positive (plaque present) if the average pixel value in the ROI is lower than a chosen threshold and negative if not (plaque absent). To compare the performance between different CT systems and PCD-CT compensation schemes, the decision was repeated by sweeping the threshold value. In this way a *receiver operating characteristics* (ROC) curve was obtained that expresses the true positive rate against the false positive rate. The area under the ROC curve, AUC, is a performance index for how well the system or compensation scheme could separate the signal from the background. Larger AUC values indicate better performance and capability to separate two tissue types.

For test #2 a similar approach was taken but instead of the reconstructed CT image, the difference of one image above the K-edge of bismuth and one image below the bismuth K-edge was used instead. A pixel value larger than a given threshold indicated the presence of Bismuth nanoparticles.

The plaque detectability was compared for PCD-CT without energy binning [method (1)], PCD-CT without SRE compensation [method (2)], PCD-CT with SRE compensation [method (3)], and for EID-CT.

III. RESULTS

A. PCD-CT compensation for spectral response effects

The performance of the SRE compensation scheme was evaluated using a simulation of a water cylinder containing inserts of I and Gd in various concentrations. An arc detector with 768 pixels of size 1mm × 1 mm and six energy bins was simulated and the simulated phantom was scanned at 120 kVp with a 5 mm flat Al filter, 216 mAs dose and 1000 views over one rotation. The count rate incident on the detector was 2.1 Mcps/mm^2. Images were reconstructed using FBP without SRE and with SRE compensation (Fig. 3). Without SRE compensation the image is subject to severe cupping artifacts and biased pixel values. Accurate material decomposition is only possible when SRE compensation is applied (Fig. 4).

B. Evaluation of Plaque Detection

The contrast-to-noise ratio (CNR) for the three PCD-CT methods normalized to the CNR of EID-CT are shown in Tab. 1. The CNR is enhanced for all detection tasks using PCD-CT with the proposed SRE compensation yielding the best improvements up to a factor of 8. This increase in CNR can be translated into a possible reduction of the patient dose and is also shown in Tab. 1.

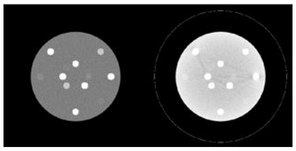

Fig. 3: CT images with (left) and without (right) SRE compensation.

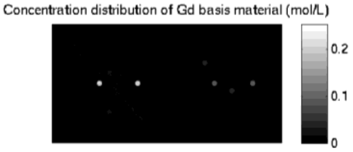

Fig. 4: Basis material images for gadolinium with (left) and without (right) SRE compensation.

Tab. 1: CNR of the three PCD-CT methods (1)-(3) normalized to EID-CT with the same radiation dose and possible radiation dose reduction in percent to achieve the CNR comparable to EID-CT.

		Normalized CNR			Dose reduction (%)		
Apps.	Tasks	(1)	(2)	(3)	(1)	(2)	(3)
(A)	Plaque-tissue	3.4	3.3	8.0	91	91	98
	Plaque-lumen	3.0	3.1	5.6	89	90	97
(B)	Bi-tissue	2.5	2.3	3.4	85	80	92
	Bi-lumen	0.9	0.8	2.2	-35	-60	79

The ROC curves for detection task #1 (general atherosclerosis) are shown in Fig. 5 for PCD-CT with SRE compensation, PCD-CT without SRE compensation, and for EID-PCT. The proposed PCD-CT scheme outperforms EID-CT by a large margin: the AUC values for the three cases are (1) 0.986, (2) 0.833, (3) 0.628.

The reconstructed images for detection task #2 (including Bismuth contrast agent at the vulnerable plaque) are shown in Fig. 6. In the PCD-CT image material decomposition allowed to separately reconstruct an image for the contrast material which is overlaid in color over the CT image. In contrast, the EID-CT image is much nosier, does not allow for material decomposition, and the enhancement due to Bismuth is almost undetectable. The AUC values for detection task #2 are (1) 0.996, (2) 0.980, (3) 0.541. The EID-CT value is close to 0.5 (no separation) which confirms the visual impression.

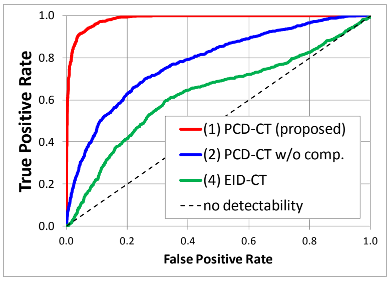

Fig. 5: ROC curve for detection test on rupturing atherosclerosis.

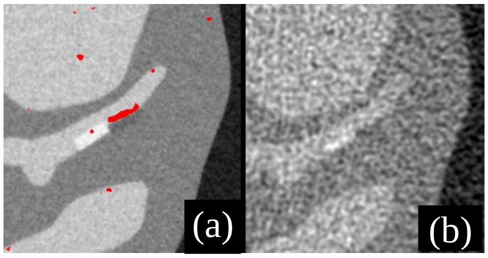

Fig. 6: Reconstructed images of the phantom with Bismuth contrast agent (a) PCD-CT with regularized compensation and (b) with EID-CT. The bismuth densities are shown in red (only for PCD-CT).

IV. CONCLUSION

We developed a novel sinogram restoration algorithm for CT with photon-counting detectors that compensates for spectral distortions due to count-rate independent physical effects. The algorithm allows to reconstruct quantitative and accurate CT images.

We applied the algorithm to a specific clinical task (detection of vulnerable plaque) and evaluated it using computer simulations. In contrast to CT with energy-integration detectors, PCD-CT with our compensation scheme allowed to detect coronary soft plaques. Using bismuth nanoparticles it was also possible to detect vulnerable plaque that may be prone to rupture.

V. REFERENCES

[1] J. P. Schlomka, E. Roessl, R. Dorscheid, S. Dill, G. Martens, T. Istel, C. Baumer, C. Herrmann, R. Steadman, G. Zeitler, A. Livne and R. Proksa, "Experimental feasibility of multi-energy photon-counting K-edge imaging in pre-clinical computed tomography," Physics in Medicine and Biology **53**, 4031-4047 (2008).

[2] P. M. Shikhaliev, "Energy-resolved computed tomography: first experimental results," Physics in Medicine and Biology **53**, 5595-5613 (2008).

[3] J. S. Iwanczyk, E. Nygard, O. Meirav, J. Arenson, W. C. Barber, N. E. Hartsough, N. Malakhov and W. J. C., "Photon counting energy disparsive detector arrays for x-ray imaging," in *IEEE Nuclear Science Symposium and Medical Imaging Conference*, *Vol. M09-04,* (IEEE, Honolulu, HI, 2007), pp. 2741-2748.

[4] W. C. Barber, E. Nygard, J. S. Iwanczyk, M. Zhang, E. C. Frey, B. M. W. Tsui, J. C. Wessel, N. Malakhov, G. Wawrzyniak, N. E. Hartsough, T. Gandhi and K. Taguchi, "Characterization of a novel photon counting detector for clinical CT: count rate, energy resolution, and noise performance," in *SPIE Medical Imaging 2009: Physics of Medical Imaging*, *Vol. 7258,* (SPIE, Lake Buena Vista, FL, USA, 2009), pp. 725824-725829.

[5] S. Feuerlein, E. Roessl, R. Proksa, G. Martens, O. Klass, M. Jeltsch, V. Rasche, H.-J. Brambs, M. H. K. Hoffmann and J.-P. Schlomka, "Multienergy Photon-counting K-edge Imaging: Potential for Improved Luminal Depiction in Vascular Imaging," Radiology **249**, 1010-1016 (2008).

[6] Y. Tomita, Y. Shirayanagi, S. Matsui, T. Aoki and Y. Hatanaka, "X-ray color scanner with multiple energy discrimination capability," in *Medical Imaging 2005: Physics of Medical Imaging*, *Vol. 5922,* (SPIE, San Diego, CA, USA, 2005), pp. 59220A.

[7] Y. Tomita, Y. Shirayanagi, S. Matsui, M. Misawa, H. Takahashi, T. Aoki and Y. Hatanaka, "X-ray color scanner with multiple energy differentiate capability," in *IEEE Nuclear Science Symposium and Medical Imaging Conference*, *Vol. 0-7803-8701-5/04,* (IEEE, Roma, Italy, 2004).

[8] K. Taguchi, E. C. Frey, X. Wang, J. S. Iwanczyk and W. C. Barber, "An analytical model of the effects of pulse pileup on the energy spectrum recorded by energy resolved photon counting x-ray detectors," Medical Physics **37**, 3957-3969 (2010).

[9] S. Srivastava, J. Cammin, Q. Tang, G. S. K. Fung, B. M. W. Tsui and K. Taguchi, "Spectral response compensation for photon-counting clinical x-ray CT using sinogram restoration," in *SPIE Medical Imaging 2012: Physics of Medical Imaging*, *Vol. 8315,* (SPIE, San Diego, CA, USA, 2012), pp. 8315-8337.

[10] M. Gilard, J.-C. Cornily, P.-Y. Pennec, C. Joret, G. Le Gal, J. Mansourati, J.-J. Blanc and J. Boschat, "Accuracy of Multislice Computed Tomography in the Preoperative Assessment of Coronary Disease in Patients With Aortic Valve Stenosis," Journal of the American College of Cardiology **47**, 2020-2024 (2006).

[11] R. E. Alvarez and A. Macovski, “Energy-selective reconstructions in x-ray computerised tomography”, Phys. Med. Biol., Vol 21 (1976), pp 733-44.

[12] P.J. La Reviere, “Penalized-likelihood sinogram smoothing for low-dose CT”, Med. Phys. 32, 1676 (2005); doi:10.1118/1.1915015

[13] D. Pan, E. Roessl, J.-P. Schlomka, S. D. Caruthers, A. Senpan, M. J. Scott, J. S. Allen, H. Zhang, G. Hu, P. J. Gaffney, E. T. Choi, V. Rasche, S. A. Wickline, R. Proksa and G. M. Lanza, "Computed Tomography in Color: NanoK-Enhanced Spectral CT Molecular Imaging," Angewandte Chemie International Edition **49**, 9635-9639 (2010).

[14] W.P. Segars, G.Sturgeon, S. Mendonca, J. Grimes, B.M.W. Tsui, “4D XCAT phantom for multimodality imaging research,” Med. Phys., 37(9), pp. 4902-4915 (2010).

[15] G. S. K. Fung, W. P. Segars, T.-S. Lee, T. Higuchi, A. I. Veress, G. T. Gullberg and B. M. W. Tsui, "Realistic simulation of regional myocardial perfusion defects for cardiac SPECT studies," in *IEEE Nuclear Science Symposium and Medical Imaging Conference,* (IEEE, Nashville, TN, 2010), pp. 3061-3064.

[16] G. S. K. Fung, K. Stierstorfer, W. P. Segars, K. Taguchi, T. G. Flohr and B. M. W. Tsui, "XCAT/DRASIM: a realistic CT/human-model simulation package," in *Medical 8Imaging 2011: Physics of Medical Imaging, Vol. 7961,* (SPIE, Lake Buena Vista, Florida, USA, 2011), pp. 79613D-79616.

Noise Reduction using Coupled Projections in Helical Computed Tomography

Yi Fan, Jianhua Ma, Yan Liu, Hongbing Lu and Zhengrong Liang

***Abstract* –Helical computed tomography (HCT) has demonstrated the effectiveness in virtual colonoscopy (VC) or CT-colonography (CTC). One major concern with this clinical application is associated with the risk of high radiation exposure, especially for its use for screening purpose at a large population. In this work, we presented an improved Karhunen-Loeve (KL) domain penalized re-weighted least-squares (PWLS) strategy which considers the data correlations among the projection rays mainly due to partially overlap when system rotates. Two one-dimensional (1D) projections, which are called coupled projections (CPs), are composed according to the geometry. Each element of the 1D projection is carefully selected for a specific point within 2π angular range, along which the system rotates, and thus a highly correlation can be observed between any specific projection and the CPs. These highly correlated projections can be treated by an adaptive KL-PWLS strategy for accurate noise reduction. This method has been implemented and tested on computer simulated sinograms which mimic low-dose CT scans. The reconstructed images by the presented strategy demonstrated the potential for ultra low-dose CT applications.**

***Index Terms*—Low-dose computed tomography, noise simulation**

I. INTRODUCTION

Compared to the conventional computerized axial tomography scan (CAT scan or CT scan), a helical or spiral CT (HCT), can provide greater visualization of blood vessels and internal tissues, such as those within the chest and abdominal cavities. This type of scanning is very helpful in the rapid evaluation of severe trauma injuries, such as those sustained in automobile accidents. However, the patient will be subject to the risks of being exposed to the excessive X-ray radiation during CT scanning, which is considered as a reason to cause cancer according to the related reports. One of the solutions to minimize the risk can be achieved by reducing the mAs or kVP settings applied to the X-ray tube for the CT scanning. However, the CT image quality will be degraded by the excessive noise due to the reduced X-ray photons with low-mAs or kVp protocols. Research efforts have been devoted to both hardware optimization and post-processing techniques on the acquired data and noticeable progress has been made.

In our previous studies, we investigated a Karhunen-Loeve (KL) domain penalized re-weighted least-squares (PWLS) strategy to restore the sinogram data at low mAs levels[1,2]. In that work, three neighboring projections with each of them being a two-dimensional (2D) image acquired along the spiral trajectory are considered by the KL-PWLS strategy. Promising results have been observed over simulation data acquired at low-dose and ultra low-dose levels[3]. However, due to the traverse movements of object in HCT, the blurs will be introduced in the reconstructed images, which are not desired in clinic applications.

In this work, we extended our previous works by using the correlated information of each projection ray other than considering all the projection rays at a specific view angle together. Specifically, for any fixed single X-ray, $\boldsymbol{l}$, a pair of X-rays, $\boldsymbol{l}_+$, $\boldsymbol{l}_-$, which pass through the same route as $\boldsymbol{l}$ but in opposite directions and differ from each other in their positions along the path as the gantry rotates by a full circle, are firstly selected. Considering the continuous distribution of image density of human body and partially overlap between the line integrals ($\boldsymbol{l}$, $\boldsymbol{l}_+$) and ($\boldsymbol{l}$, $\boldsymbol{l}_-$), which are usually the case in most of the clinical applications, a high correlation can be expected between the $\boldsymbol{l}$, $\boldsymbol{l}_+$ and $\boldsymbol{l}_-$. Running over all the X-rays at a specific angle and then two vectors can be composed. Let $\boldsymbol{p}$ be the 1D projection, then the composed $\boldsymbol{p}_+$, $\boldsymbol{p}_-$, are the coupled projections (CPs) of $\boldsymbol{p}$. Based on our previous works, the correlations between $\boldsymbol{p}$, $\boldsymbol{p}_+$ and $\boldsymbol{p}_-$ can be fully addressed by using a KL-PWLS strategy for noise reduction.

.

II. METHODS

A. *Coupled-projections in HCT*

This section describes our method for selecting the coupled projections, as illustrated in Fig. 1. $\boldsymbol{S}$ indicates the current position of the X-ray source at view angle $\boldsymbol{\beta}$ in the circular trajectory. $\boldsymbol{t}_1$ and $\boldsymbol{t}_2$ are the X-rays emitted from $\boldsymbol{S}$ which compose the field-of-view (FOV). The angle between $\boldsymbol{t}_1$ and $\boldsymbol{t}_2$ is $\boldsymbol{\alpha}$. For any single X-ray $\boldsymbol{l}$ acquired at this

---

Yi Fan, Jianhua Ma, and Yan Liu and Zhengrong Liang are with the department of Radiology, State University of New York, Stony Brook, NY 11794(e-mail: yifan@live.com).

Hongbing Lu is with the department of Biomedical Engineering, Fourth Military Medical University, Xi'an , Shaanxi, China, 710072 (email: luhb@fmmu.edu)

Zhengrong Liang is with the department of Radiology, State University of New York, Stony Brook, NY 11794 (e-mail: : jerome.liang@sunysb.edu).

position, it can be expressed by $S(\boldsymbol{\beta},\boldsymbol{\varphi})$, where $\boldsymbol{\varphi}$ is the angle composed by $(\boldsymbol{l},\boldsymbol{t}_1)$. According to the geometry, one specific X-ray which passes through the same route as $\boldsymbol{l}$ but in the opposite direction, $\boldsymbol{l'}$, can be found according to Eqs. (1) and (2) below.

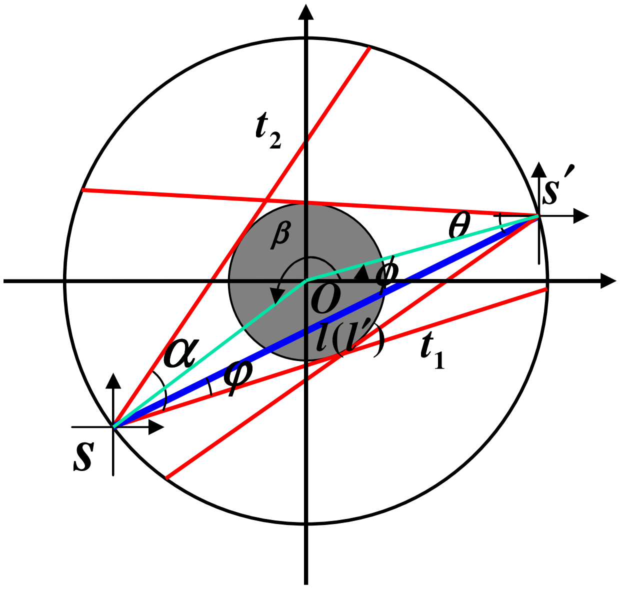

Figure 1: Illustration of calculating pared X-rays for selection of coupled rays.

The position of X-ray source where $\boldsymbol{l'}$ originated can be expressed by $\boldsymbol{S'}(\boldsymbol{\phi},\boldsymbol{\theta})$. According to the geometry, the relationship between $(\boldsymbol{\beta},\boldsymbol{\varphi})$ and $(\boldsymbol{\phi},\boldsymbol{\theta})$ can be expressed by:

$$\boldsymbol{\phi} = \boldsymbol{\beta} - \boldsymbol{\alpha} + 2\boldsymbol{\varphi} + 180^o \qquad (1)$$

$$\boldsymbol{\theta} = \boldsymbol{\alpha} - \boldsymbol{\varphi} \qquad (2)$$

When considering the helical modality, $\boldsymbol{l'}$ will be replaced by $\boldsymbol{l}_+$ and $\boldsymbol{l}$-, which are also originated from $\boldsymbol{S'}$ in the circular plane but differ from each other by 360° along the direction of system rotation. Then equation (1) can be modified as:

$$\boldsymbol{\phi}_{1,2} = \boldsymbol{\beta} - \boldsymbol{\alpha} + 2\boldsymbol{\varphi} \pm 180^o \qquad (3)$$

For all the X-rays originated from $S(l_1,l_2,\cdots,l_n)$, two 1D vectors, $S_+(l_{1+},l_{2+},\cdots,l_{n+})$ and $S_-(l_{1-},l_{2-},\cdots,l_{n-})$, can be obtained according to Eq. (3) and which are the CPs of $\boldsymbol{S}$.

B. Penalized-weighted Least-square(PWLS) restoration in KL domain

Based on our previous studies, there are strong signal correlations between the nearby projections in HCT. Motivated by the observation, in this work we use the KL transform to consider the signal correlations between $\boldsymbol{S}$ and it's CPs. The KL transform of the correlated projections can be expressed by:

$$\tilde{y} = Ay \qquad (4)$$

where $\boldsymbol{y} = [\boldsymbol{S}_+^T \boldsymbol{S}^T \boldsymbol{S}_-^T]^T$ is a $\boldsymbol{3 \times N}$ matrix with each row being the 1D projection, $\boldsymbol{N}$ is the number of detector bins and $\boldsymbol{T}$ is the transpose operation. $\boldsymbol{A}$ is a $\boldsymbol{3 \times 3}$ transform matrix which can be computed with the give data. $\tilde{\boldsymbol{y}}$ is the KL transformed components.

In the KL domain, the PWLS criterion is used to restore the sinogram by minimizing the following objective function:

$$\Phi_l(\tilde{\lambda}_l) = (\tilde{y}_l - \tilde{\lambda}_l)'\tilde{\Sigma}_l^{-1}(\tilde{y}_l - \tilde{\lambda}_l) + (\frac{\gamma}{d_l})R(\tilde{\lambda}_l) \qquad (5)$$

where the first term in function (5) denotes the WLS measure, $\tilde{y}_l$ is the $N \times 1$ dimensional vector which denotes the l-th component of the KL transformed sinogram and $\tilde{\lambda}_l$ is the $N \times 1$ dimensional noise-free data to be estimated. $\tilde{\Sigma}_l$ is the $N \times N$ dimensional diagonal variance matrix with each element being the variance of projection at each detector bins[1,2]. Since the variance depends on the ideal date $\tilde{\lambda}_l$ to be estimated, which is different from the previous WLS definition where the variance is independent from the estimate, so the WLS is called re-weighted least squares.

In the second term of function (5), d_l is the l-th eigenvalue defined in Eq. (4) and γ is the parameter which controls the penalty R. The penalty takes the quadratic form as used in our previous reports[1,2].

Minimizing the PWLS objective function (5) for estimating $\tilde{\lambda}_l$ from $\tilde{y}_l$ in the KL domain could be performed by many numerical means[4]. In this work, we use the GS iterative update algorithm[5].

C. Algorithm summary

The implementation of the presented method for low-dose helical CT sinogram is summarized as following:

1. For any 1D projection $\boldsymbol{S}$ acquired at a given angle along the direction of gantry rotation, compose the coupled projections, $\boldsymbol{S}_+$ and $\boldsymbol{S}_-$, each element in $\boldsymbol{S}_+$ and $\boldsymbol{S}_-$ is selected based on the geometrics described in Section $\boldsymbol{A}$;

2. Apply the KL transform to $\boldsymbol{S}$, $\boldsymbol{S}_+$ and $\boldsymbol{S}_-$;

3. In the KL domain, apply the PWLS criteria to restore all the projections, followed by the inverse KL transform to obtain the restored projection of $\boldsymbol{S}$;

4. Run over all the 1D sinogram data and obtain the reconstructions by FBP in 2D case.

III. RESULTS

We tested the proposed method by phantom studies on an array of $512\times512\times413$ cubic voxels. Projections were simulated in helical geometry, where each projection or line integral value along a ray through the phantom was computed based on the known densities. A total 1,200 projections, each projection contains 1024 detector bins, over 2π angular range were sampled with pitch equal to 1. For comparison purpose, we included the results of using our previous work, which considers the 2D neighboring projections to utilize the signal correlations. Figure 2 shows the calculated correlation coefficients for: (1) the 1D projections with the CPs over 50^o angular interval, and (2) the 2D projections with the nearest 2D views along the direction of gantry rotation. It can be observed that the correlation between the 1D projections and CPs is higher than that in the 2D projections, which indicates the higher signal correlation can be utilized by the proposed noise reduction strategy.

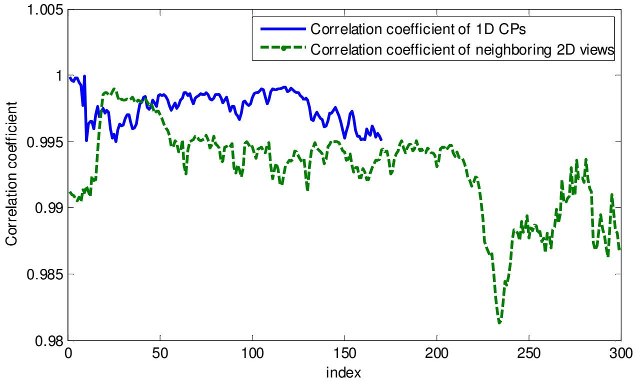

Figure 2: Correlation coefficients of using the presented 1D CPs-based approach and our previous 2D neighboring views approach.

The restored sinogram data can be processed by the inverse KL transform and FBP algorithm to obtain the reconstructions. Figure (3) shows a reconstructed image by using our previous 2D view-by-view KL-PLWS strategy and the proposed 1D CPs-based method. We also calculated the standard deviation (STD) in selected regions of interest (ROIs). There are 17 out of 20 calculations indicating better noise reduction by using the proposed method than our precious algorithm.

IV. DISCUSSION AND CONCLUSION

In the above presented method, the CPs for each 1D projection is composed. The coupled projections are partially overlapped with the processed 1D projection in the HCT geometry and thus the signal correlations are further enhanced compared with the use of the neighboring projections in our previous work. The signal correlations within HCT sinograms can be fully considered by using the KL transform. In the KL domain, the correlations are utilized by the adaptive PWLS criteria. Numerical tests on the presented method show significant suppression of the noise for low-dose CT image reconstruction. Improvement for the anisotropic properties in the reconstructions is also observed in these preliminary results. More simulation studies and quantitative evaluations on the method are under investigation.

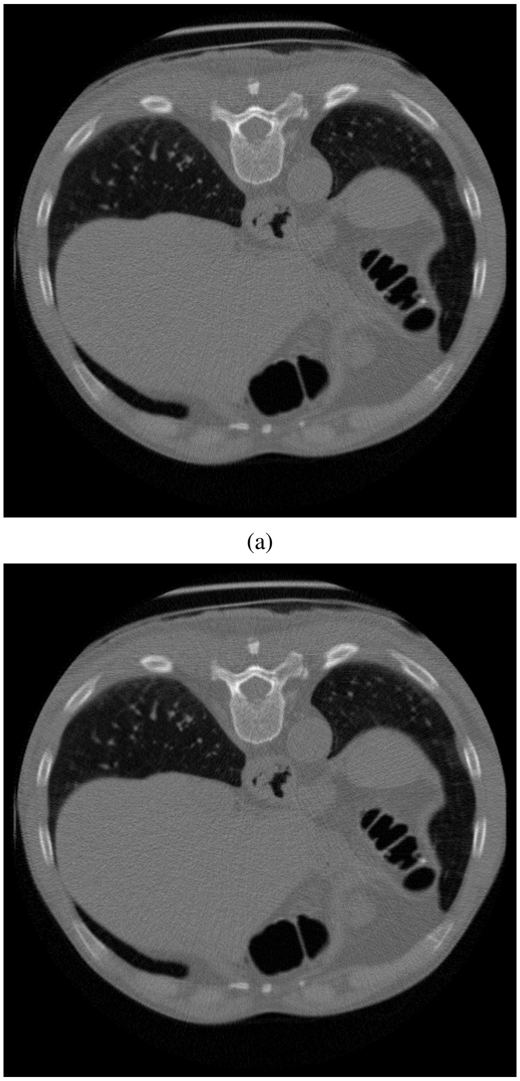
(a)

(b)

Figure 3: Selected slice of FBP reconstructed image by (a) using 2D KL-PWLS method; and (b) using proposed coupled projection-based method.

REFERENCES

[1] J. Wang, T. Li, H. Lu, and Z. Liang, “Noise reduction for low-dose single-slice helical CT sinograms”, *IEEE Trans. Nuclear Science*, vol. 535, pp. 1230-1237, 2006.

[2] Y. Fan, J. Wang, H. Lu, and Z. Liang, “Implementation of an effective KL domain penalized weighted least-squares sinogram restoration for low-dose CT colonography”, *SPIE Medical Imaging*, vol. 7258, 2009.

[3] J. Wang, S. Wang, L. Li, Y. Fan, H. Lu, and Z. Liang, “Virtual colonoscopy screening with ultra low-dose CT and less-stressful bowel preparation: A computer simulation study”, *IEEE Trans. Nuclear Science*, vol. 55, pp. 2566-2575, 2008.

[4] P. La Rivière, “Penalized-likelihood sinogram smoothing for low-dose CT”, *Medical Physics*, vol. 32, pp. 1676-1683, 2005.

[5] K. Sauer and C. Bouman, “A local update strategy for iterative reconstruction form projections”, *IEEE Trans. Signal Process*, vol. 41, pp. 534-548, 1993.

PERTURBATION-BASED ERROR ANALYSIS OF ITERATIVE IMAGE RECONSTRUCTION ALGORITHM FOR X-RAY COMPUTED TOMOGRAPHY

Jung Kuk Kim, Jeffrey A. Fessler, Zhengya Zhang

EECS Department, University of Michigan, Ann Arbor, MI 48109-2122, USA

ABSTRACT

Statistical iterative image reconstruction methods are compute intensive. Fixed-point calculations can substantially reduce the computational load, but also increase quantization error. To investigate the effect of fixed-point quantization, we analyze the error propagation after introducing perturbation in a diagonally preconditioned gradient descent algorithm for X-ray computed tomography. The effects of the quantization error in forward-projection, back-projection, and image update are calculated using the open loop and loop gain of the iterative algorithm. We derive an analytical upper bound on the quantization error variance of the reconstructed image and show that the quantization step size can be chosen to meet a given upper bound. The analytical results are confirmed by numerical simulations.

I. INTRODUCTION

Statistical iterative image reconstruction methods for X-ray computed tomography (CT) have been proposed to improve image quality and reduce dose [1]. These methods are based on accurate projection models and measurement statistics, and formulated as maximum likelihood (ML) estimation [2]. Iterative algorithms have been designed to estimate the image by minimizing a cost function [3]–[5].

CT image reconstruction algorithms are usually implemented in 32-bit single-precision floating-point quantization to provide high image quality. Fixed-point (integer) arithmetic uses much less hardware resources than floating-point and can shorten the latency [6], but it introduces quantization errors and potentially degrades the image quality. Therefore it is desirable to analyze the quantization effects to assess the feasibility of a fixed-point conversion.

In this paper, we model the effect of fixed-point quantization as a perturbation of floating-point arithmetic by injecting uniform white noise after the arithmetic [7]. For simplicity of the analysis, we choose a diagonally preconditioned gradient descent algorithm with a quadratic regularizer [8], and inject noise in the three steps of an iterative image reconstruction: forward-projection, back-projection, and image update. We derive an upper bound on the quantization error variance of the image update in every iteration and the results are verified by numerical simulations based on a 40×40×4 test object over 90 projection views.

II. BACKGROUND

A CT system captures a large series of projections at different view angles, recorded as sinogram. Mathematically, sinogram y can be modeled as $y = Af + \epsilon$, where f represents the volume being imaged and A is the system matrix, or the forward-projection model, and ϵ denotes measurement noise. The goal of image reconstruction is to estimate the 3D image f from the measured sinogram y. A statistical image reconstruction method estimates f, or $\hat{f}$, based on measurement statistics, which can be formulated as a weighted least square (WLS) problem [2].

$$\hat{f} = \arg\min_{f} \frac{1}{2}\|y - Af\|_W^2, \tag{1}$$

where W is a diagonal matrix with entries based on photon measurement statistics [2]. To control undesired noise in $\hat{f}$ of (1), a penalty term is added to form a penalized weighted least square (PWLS) [2], [8] cost function:

$$\hat{f} = \arg\min_{f} \Psi(f) = \arg\min_{f} \frac{1}{2}\|y - Af\|_W^2 + \beta R(f), \tag{2}$$

where $R(f)$ is known as the regularizer and β is a regularization parameter. For simplicity of analysis, we choose a quadratic regularizer that adds to the cost function the square of differences among neighboring pixels, or $R(f) = \|Cf\|^2/2$, where C is the difference matrix.

Using a quadratic regularizer and assuming that $(A'WA + \beta C'C)$ is invertible, the solution to (2) is given by $\hat{f} = (A'WA + \beta C'C)^{-1}A'Wy$. However, the practical size of matrix A for a commercial axial CT scanner is 10 million by 10 million [2], thus evaluating the inverse of $A'WA + \beta C'C$ is inefficient, if not infeasible. Alternatively, iterative methods have been proposed [3]–[5]. In this paper we consider a diagonally preconditioned gradient descent method to solve (2) [5], [8]:

$$\begin{aligned}\hat{f}^{(i+1)} &= \hat{f}^{(i)} - D\nabla\Psi(\hat{f}^{(i)}) \\ &= \hat{f}^{(i)} + D\left[A'W(y - A\hat{f}^{(i)}) - \beta C'C\hat{f}^{(i)}\right].\end{aligned} \tag{3}$$

This work was supported in part by a Korea Foundation for Advanced Studies (KFAS) Scholarship and the University of Michigan. J. A. Fessler's effort is supported by NIH grant R01-HL-098686.

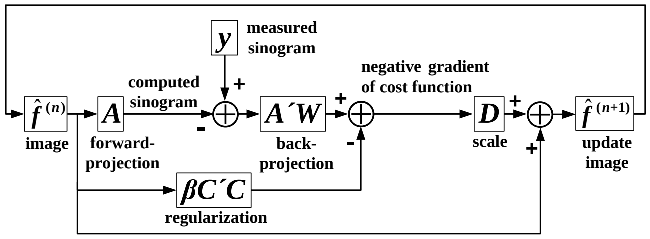

Fig. 1. Block diagram of iterative image reconstruction.

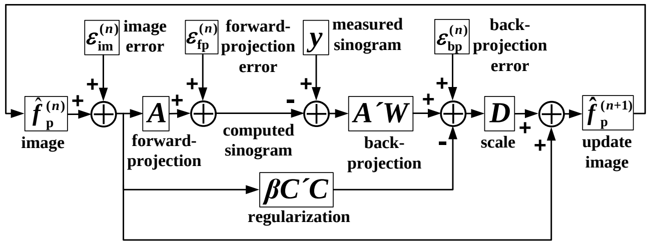

Fig. 2. Iterative image reconstruction with perturbed forward-projection, back-projection and image update.

Fig. 1 shows a block diagram of this iterative image reconstruction method. Typically a FBP reconstructed image is used as the initial image, $\hat f^{(0)}$. In each iteration, a new 3D image estimate $\hat f^{(i+1)}$ is obtained by updating the previous image $\hat f^{(i)}$ with a step of the negative gradient of the cost function $\Psi(\hat f)$ scaled by a diagonal matrix D. This algorithm is guaranteed to converge to the unique minimizer of Ψ when D is chosen properly [5]. This is a one subset version of the ordered subsets (OS) algorithm given in [5].

III. PERTURBATION-BASED ERROR ANALYSIS

We analyze the effect of perturbation in iterative image reconstruction and show that both the maximum and the mean error variance in an image update are bounded for a given level of uniform white noise. Hereafter, we define $\hat f_{\mathrm{p}}^{(n)}$ as the n^{th} image update of the perturbed iterative algorithm, and $e^{(n)}$ as the corresponding image error relative to the unperturbed version $\hat f^{(n)}$, i.e., $e^{(n)} = \hat f^{(n)} - \hat f_{\mathrm{p}}^{(n)}$.

III-A. Perturbation of forward-projection

We proceed by first perturbing the forward-projection to model the effect of fixed-point quantization [7]. We add a random error vector, $\varepsilon_{\mathrm{fp}}^{(n)}$, to the ideal forward-projection, as illustrated in Fig. 2. We further assume that the error samples are uncorrelated. Specifically, we assume

$$\varepsilon_{\mathrm{fp}}^{(n)} \sim U\left[-\frac{\Delta_{\mathrm{fp}}}{2}, \frac{\Delta_{\mathrm{fp}}}{2}\right], \quad \mathrm{cov}(\varepsilon_{\mathrm{fp}}^{(i)}, \varepsilon_{\mathrm{fp}}^{(i)}) = \frac{\Delta_{\mathrm{fp}}^2}{12} I,$$
$$\mathrm{cov}\left(\varepsilon_{\mathrm{fp}}^{(i)}, \varepsilon_{\mathrm{fp}}^{(j)}\right) = 0 \qquad \forall i,\ \forall j,\ i \neq j, \tag{4}$$

where Δ_{fp} denotes the quantization step size.

From (3), the first image update of the perturbed algorithm can be written as

$$\begin{aligned}\hat f_{\mathrm{p}}^{(1)} &= \hat f^{(0)} + D\left[A'W\left(y - \left(A\hat f^{(0)} + \varepsilon_{\mathrm{fp}}^{(0)}\right)\right) - \beta C'C\hat f^{(0)}\right] \\ &= \hat f^{(1)} + K_{\mathrm{fp}}\varepsilon_{\mathrm{fp}}^{(0)},\end{aligned} \tag{5}$$

where $K_{\mathrm{fp}} \triangleq -DA'W$ is the open loop gain of the error due to perturbation in forward-projection. Similarly, we have the second image update as

$$\hat f_{\mathrm{p}}^{(2)} = \hat f_{\mathrm{p}}^{(1)} + D\left[A'W\left(y - \left(A\hat f_{\mathrm{p}}^{(1)} + \varepsilon_{\mathrm{fp}}^{(1)}\right)\right) - \beta C'C\hat f_{\mathrm{p}}^{(1)}\right]. \tag{6}$$

Substituting (5) into (6) and simplification yields

$$\hat f_{\mathrm{p}}^{(2)} = \hat f^{(2)} + MK_{\mathrm{fp}}\varepsilon_{\mathrm{fp}}^{(0)} + K_{\mathrm{fp}}\varepsilon_{\mathrm{fp}}^{(1)},$$

where $M \triangleq I - D(A'WA + \beta C'C)$ is the loop gain of the error in this iterative method. (Note that M is related to the Hessian of the cost function [8], which is given by $H = A'WA + \beta C'C$). By induction, the image update of the n^{th} iteration and the image update error are given by

$$\begin{aligned}\hat f_{\mathrm{p}}^{(n)} &= \hat f^{(n)} + e^{(n)} \\ e^{(n)} &= \sum_{k=0}^{n-1} M^k K_{\mathrm{fp}}\varepsilon_{\mathrm{fp}}^{(n-1-k)}.\end{aligned}$$

Using (4), the mean of $e^{(n)}$ is zero, and the covariance is

$$\mathrm{cov}\left(e^{(n)}, e^{(n)}\right) = \frac{\Delta_{\mathrm{fp}}^2}{12}\sum_{k=0}^{n-1} M^k K_{\mathrm{fp}}K_{\mathrm{fp}}'\left(M^k\right)'. \tag{7}$$

Note that a covariance matrix is positive semidefinite [9], and its eigenvalues are nonnegative [10]. Thus, an upper bound on the error variance is the maximum eigenvalue, i.e., spectral radius, of the covariance matrix of $e^{(n)}$. Evaluating the spectral radius is nontrivial due to the term M^k. Since matrix D is a real diagonal matrix with positive diagonal entries, we can decompose M as

$$M = I - DH = D^{\frac{1}{2}}\left(I - D^{\frac{1}{2}}HD^{\frac{1}{2}}\right)D^{-\frac{1}{2}}.$$

The Hessian matrix H is a nonnegative definite and so is $I - D^{\frac{1}{2}}HD^{\frac{1}{2}}$, by the design of D. Thus by the spectral theorem [11], there exists a unitary matrix U and a diagonal matrix Σ such that $I - D^{\frac{1}{2}}HD^{\frac{1}{2}} = U\Sigma U'$. Then M becomes

$$M = D^{\frac{1}{2}}U\Sigma U'D^{-\frac{1}{2}}. \tag{8}$$

Similarly, $(A'W)(A'W)'$ is also nonnegative definite and can be decomposed using a unitary matrix V and a nonnegative diagonal matrix F [11]. It follows that

$$K_{\mathrm{fp}}K_{\mathrm{fp}}' = (-DA'W)(-DA'W)' = D(VFV')D. \tag{9}$$

Substituting (8) and (9) into (7), we have

$$\begin{aligned}&\operatorname{cov}\left(e^{(n)}, e^{(n)}\right)\\ &= \frac{\Delta_{\mathrm{fp}}^2}{12}\sum_{k=0}^{n-1} D^{\frac{1}{2}}U\Sigma^k U' D^{\frac{1}{2}}\left(VFV'\right)D^{\frac{1}{2}}U\Sigma^k U' D^{\frac{1}{2}}.\end{aligned}$$

Thus the spectral radius equals the 2-norm and its upper bound can be derived using the matrix norm property that $\parallel AB \parallel \leq \parallel A \parallel \parallel B \parallel$ [12]. After considerable simplification, we have

$$\begin{aligned}&\rho\left(\operatorname{cov}\left(e^{(n)}, e^{(n)}\right)\right)\\ &= \max_{x:\|x\|=1}\left(x'\operatorname{cov}\left(e^{(n)}, e^{(n)}\right)x\right)\\ &= \frac{\Delta_{\mathrm{fp}}^2}{12}\max_{x:\|x\|=1}\left(\sum_{k=0}^{n-1}\parallel F^{\frac{1}{2}}V'D^{\frac{1}{2}}U\Sigma^kU'D^{\frac{1}{2}}x\parallel^2\right)\\ &\leq \frac{\Delta_{\mathrm{fp}}^2}{12}\rho(F)\rho(D^2)\frac{1-\rho(\Sigma^2)^n}{1-\rho(\Sigma^2)}. \qquad (10)\end{aligned}$$

The spectral radius of the covariance matrix measures the maximum error variance in the n^{th} iteration. i.e., $\sigma^2_{(n)\max} \triangleq \rho\left(\operatorname{cov}\left(e^{(n)}, e^{(n)}\right)\right)$. Next, we analyze the mean error variance in an image update, which is related to the trace, or sum of diagonal entries, of the covariance matrix, i.e., $\sigma^2_{(n)\mathrm{mean}} \triangleq \operatorname{tr}\left(\operatorname{cov}\left(e^{(n)}, e^{(n)}\right)\right)/n_{\mathrm{v}}$, where n_{v} is the number of diagonal entries in the covariance matrix. Using the property that $\operatorname{tr}(AB) \leq \rho(B)\operatorname{tr}(A)$ [11], we have

$$\begin{aligned}&\operatorname{tr}\left(\operatorname{cov}\left(e^{(n)}, e^{(n)}\right)\right)\\ &= \frac{\Delta_{\mathrm{fp}}^2}{12}\operatorname{tr}\left(\sum_{k=0}^{n-1} D^{\frac{1}{2}}U\Sigma^kU'D^{\frac{1}{2}}\left(VFV'\right)D^{\frac{1}{2}}U\Sigma^kU'D^{\frac{1}{2}}\right)\\ &\leq \frac{\Delta_{\mathrm{fp}}^2}{12}\sum_{k=0}^{n-1}\rho\left(\Sigma^k\right)\operatorname{tr}\left(D^{\frac{1}{2}}\left(VFV'\right)D^{\frac{1}{2}}U\Sigma^kU'D\right)\\ &\leq \frac{\Delta_{\mathrm{fp}}^2}{12}\operatorname{tr}(D\left(VFV'\right)D)\frac{1-\rho(\Sigma^2)^n}{1-\rho(\Sigma^2)}. \qquad (11)\end{aligned}$$

To guarantee the convergence of iterative reconstruction algorithm, the matrix D is always selected such that $D^{-1} \succ H$, i.e., $D^{-1} - H$ is positive definite, which implies $\rho(I - DH) < 1$, where H is the Hessian of the cost function [8]. It follows that

$$\begin{aligned}\rho(\Sigma) &= \rho(U'(I - D^{\frac{1}{2}}HD^{\frac{1}{2}})U) = \rho(I - D^{\frac{1}{2}}HD^{\frac{1}{2}})\\ &= \rho(D^{-\frac{1}{2}}(I-DH)D^{\frac{1}{2}}) = \rho(I - DH) < 1.\end{aligned}$$

In steady state as $n \to \infty$, the upper bounds of (10) and (11) become

$$\sigma^2_{(n)\max} \leq \rho(\operatorname{cov}(e^{(\infty)}, e^{(\infty)})) \leq \frac{\Delta_{\mathrm{fp}}^2}{12}\frac{\rho(D^2)\rho(F)}{1-\rho(\Sigma^2)},$$

$$\sigma^2_{(n)\mathrm{mean}}n_{\mathrm{v}} \leq \operatorname{tr}(\operatorname{cov}(e^{(\infty)}, e^{(\infty)})) \leq \frac{\Delta_{\mathrm{fp}}^2}{12}\frac{\operatorname{tr}(D(VFV')D)}{1-\rho(\Sigma^2)}.$$

Therefore, both the maximum and the mean error variance of an image update are bounded. For example, given $\epsilon > 0$, if we choose Δ_{fp} such that

$$\Delta_{\mathrm{fp}} < \sqrt{\frac{12\left(1-\rho(\Sigma)^2\right)}{\rho(D^2)}}\sqrt{\frac{1}{\rho(F)}}\sqrt{\epsilon},$$

then

$$\sigma^2_{(\infty)\max} < \epsilon, \qquad \sigma^2_{(\infty)\mathrm{mean}} < \epsilon.$$

The result implies that we can make the error due to perturbation in forward-projection arbitrarily small for this algorithm by choosing an appropriate quantization step size, provided quantization noise can be modeled as in (4).

III-B. Perturbation of forward-projection, back-projection, and image update

Following the derivation from the previous section, we can also model the effect of fixed-point quantization in the back-projection and image update by injecting uniform white noises $\varepsilon_{\mathrm{bp}}^{(n)}$ and $\varepsilon_{\mathrm{im}}^{(n)}$, as indicated in Fig. 2. Similar to (4), we make the following assumptions:

$$\varepsilon_{\mathrm{bp}}^{(n)} \sim U\left[-\frac{\Delta_{\mathrm{bp}}}{2}, \frac{\Delta_{\mathrm{bp}}}{2}\right],\ \varepsilon_{\mathrm{im}}^{(n)} \sim U\left[-\frac{\Delta_{\mathrm{im}}}{2}, \frac{\Delta_{\mathrm{im}}}{2}\right], \quad (12)$$

where Δ_{bp} and Δ_{im} denote the quantization step sizes of back-projection and image update respectively.

Similar to (5), we can express the perturbed image update of the first iteration as

$$\begin{aligned}\hat{f}_{\mathrm{p}}^{(1)} =&(\hat{f}^{(0)} + \varepsilon_{\mathrm{im}}^{(0)}) + D[A'W(y - (A(\hat{f}^{(0)} + \varepsilon_{\mathrm{im}}^{(0)}) + \varepsilon_{\mathrm{fp}}^{(0)}))\\ &+ \varepsilon_{\mathrm{bp}}^{(0)} - \beta C'C(\hat{f}^{(0)} + \varepsilon_{\mathrm{im}}^{(0)})]\\ =&\hat{f}^{(1)} + K_{\mathrm{fp}}\varepsilon_{\mathrm{fp}}^{(0)} + K_{\mathrm{bp}}\varepsilon_{\mathrm{bp}}^{(0)} + M\varepsilon_{\mathrm{im}}^{(0)},\end{aligned}$$

where $K_{\mathrm{bp}} \triangleq D$ is the open loop gain of the error due to perturbation in back-projection. It follows that the image update error in the n^{th} iteration is

$$e^{(n)} = \sum_{k=0}^{n-1}(M^k(K_{\mathrm{fp}}\varepsilon_{\mathrm{fp}}^{(n-1-k)} + K_{\mathrm{bp}}\varepsilon_{\mathrm{bp}}^{(n-1-k)} + M\varepsilon_{\mathrm{im}}^{(n-1-k)})).$$

We assume independence of the three noise vectors. Using (4), (8), (9), and (12), the mean of $e^{(n)}$ is zero, and the covariance can be written as

$$\begin{aligned}&\operatorname{cov}\left(e^{(n)}, e^{(n)}\right) = \frac{\Delta_{\mathrm{fp}}^2}{12}\sum_{k=0}^{n-1}(M^kK_{\mathrm{fp}}K_{\mathrm{fp}}'(M^k)') +\\ &\frac{\Delta_{\mathrm{bp}}^2}{12}\sum_{k=0}^{n-1}(M^kK_{\mathrm{bp}}K_{\mathrm{bp}}'(M^k)') + \frac{\Delta_{\mathrm{fp}}^2}{12}\sum_{k=0}^{n-1}(M^{k+1}(M^{k+1})').\end{aligned}$$

Following a similar approach as in the previous section, we can derive the upper bounds on the spectral radius and

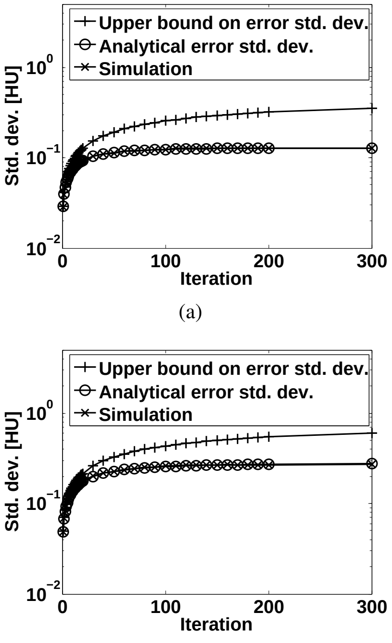

(a)

(b)

Fig. 3. Theoretical bound and numerical simulation of standard deviation of the image updates : (a) forward-projection with the quantization step size of $\Delta_{\mathrm{fp}} = 2^7$[HU×mm] (b) forward-projection, back-projection, and image update with $\Delta_{\mathrm{fp}} = 2^7$[HU×mm], $\Delta_{\mathrm{bp}} = 2^{15}$[mm], $\Delta_{\mathrm{im}} = 2^{-3}$[HU].

the trace of the covariance matrix.

$$\begin{aligned}\rho(\mathrm{cov}(e^{(\infty)}, e^{(\infty)})) \leq & \frac{\Delta_{\mathrm{fp}}^2}{12} \frac{\rho(D^2)\rho(F)}{1-\rho(\Sigma^2)} + \frac{\Delta_{\mathrm{bp}}^2}{12} \frac{\rho(D^2)}{1-\rho(\Sigma^2)} \\ & + \frac{\Delta_{\mathrm{im}}^2}{12} \frac{\rho(\Sigma^2)\rho(D)\rho(D^{-1})}{1-\rho(\Sigma^2)}, \\ \mathrm{tr}(\mathrm{cov}(e^{(\infty)}, e^{(\infty)})) \leq & \frac{\Delta_{\mathrm{fp}}^2}{12} \frac{\mathrm{tr}(VFV'D^2)}{1-\rho(\Sigma^2)} + \frac{\Delta_{\mathrm{bp}}^2}{12} \frac{\mathrm{tr}(D^2)}{1-\rho(\Sigma^2)} \\ & + \frac{\Delta_{\mathrm{im}}^2}{12} \frac{\rho(\Sigma^2)\mathrm{tr}(I)}{1-\rho(\Sigma^2)}.\end{aligned}$$

Therefore, both the maximum and the mean error variance of the reconstructed image are bounded after considering perturbation in forward-projection, back-projection, and image update. The error can be made arbitrarily small for this algorithm by choosing an appropriate quantization step size.

IV. RESULTS AND CONCLUSION

To verify the analysis, we performed numerical simulations of an iterative reconstruction of a 40×40×4 test object in an axial cone-beam arc-detector X-ray CT system with a detector size of 170×10 over 90 projection views. The PWLS diagonally preconditioned gradient descent algorithm (3) was simulated with a quadratic roughness regularizer. We evaluated analytical quantization error variance and its upper bound in each iteration, which are compared to measured quantization error variance from simulations by injecting uniformly distributed error vectors that correspond to quantization step sizes of $\Delta_{\mathrm{fp}} = 2^7$[HU×mm], $\Delta_{\mathrm{bp}} = 2^{15}$[mm], and $\Delta_{\mathrm{im}} = 2^{-3}$[HU]. Fig. 3 shows the standard deviation of the image update error due to (a) perturbation in forward-projection alone and (b) perturbation in forward-projection, back-projection, and image update. The measured standard deviation matches the analytical standard deviation and stays below the upper bound. Due to limited space, we only show one set of quantization step size, but alternative choices could be equally used. Both the analytical and simulation results in Fig. 3 point to the conclusion that the error variance of image updates converges to a fixed level after a sufficient number of iterations. Note that evaluating the analytical error variance is not feasible for large object sizes. Quantizing iterative methods to confirm our perturbation model and tightening the upper bound remain our future work.

V. REFERENCES

[1] J. A. Fessler, "Statistical image reconstruction methods for transmission tomography," *Handbook of Medical Imaging, Volume 2. Medical Image Processing and Analysis*, pp. 1–70, 2000.
[2] T. M. Buzug, *Computed tomography from photon statistics to modern cone-beam CT*. New York: Springer-Verlag, 2009.
[3] S. Kawata and O. Nalcioglu, "Constrained iterative reconstruction by the Conjugate Gradient method," *IEEE Trans. Med. Imag.*, vol. 4, pp. 65–71, 1985.
[4] Z. Q. Luo and P. Tseng, "On the convergence of the coordinate descent method for convex differentiable minimization," *j. Optim. Theory Appl.*, vol. 72, no. 1, pp. 7–35, 1992.
[5] H. Erdogen and J. A. Fessler, "Ordered subsets algorithms for transmission tomography," *Phys. Med. Biol.*, vol. 44, pp. 2835–51, 1999.
[6] J. Kim, Z. Zhang, and J. A. Fessler, "Hardware acceleration of iterative image reconstruction for X-ray computed tomography," in *IEEE Conf. Acoust. Speech Sig. Proc.*, May 2011, pp. 1697–1700.
[7] A. V. Oppenheim, R. W. Schafer, and J. R. Buck, *Discrete-time signal processing*. New Jersey: Prentice Hall, 1997.
[8] J. A. Fessler, *Image reconstruction: Algorithms and analysis*. Book in preparation.
[9] J. A. Gubner, *Probability and random processes for electrical and computer engineers*. Cambridge University Press, 2006.
[10] D. C. Lay, *Linear algebra and its applications*. Pearson Education, Inc, 2003.
[11] K. Hoffman and R. Kunze, *Linear Algebra*. New Jersey: Prentice Hall, 2003.
[12] L. N. Trefethen and D. Bau, *Numerical linear algebra*. SIAM, 1997.

One-Dimensional Study of Methods for Improving Resolution in CT Model-Based Iterative Reconstruction

Kerkil Choi, Lin Fu, Kai Zeng, Xue Rui, and Bruno De Man

***Abstract*— We study iterative reconstruction of a CT image from a data set generated with focal spot wobbles for improving resolution of a reconstructed image. We present preliminary results for four selected methods with one-dimensional simulations and reconstructions. These methods include the finite beamwidth modeling, data interlacing, frequency boosting of the interlaced data, and model-based deconvolution of the interlaced measurements. The reconstructions produced by these methods are compared in terms of MTF numbers and artifacts. Among these methods, we found that the method that incorporates the finite-beamwidth modeling produces the largest MTF improvement while maintaining acceptable image quality. Although the interlacing method combined with frequency boosting can produce higher MTF numbers, it is observed that the reconstructions produced by this method are prone to severe artifacts.**

***Index Terms*— computed tomography, model based iterative reconstruction, MBIR, resolution enhancement, finite beamwidth modeling, interlacing, sinogram deconvolution.**

I. INTRODUCTION

High spatial resolution in CT images is paramount in several clinical applications. Detecting and visualizing small airways is a good example that requires improved resolution. Achieving high resolution while maintaining low noise is desirable. Model-based iterative reconstruction (MBIR) has been demonstrated to meet these requirements [1]. This paper presents a preliminary investigation of selected methods for improving resolution of CT images produced by MBIR methods.

In this paper, we focus on the case where two data sets are produced by *wobbling* a focal spot to two different positions for a fixed detector position. However, some of our methods may also benefit MBIR without using the wobble data set.

Several approaches have tackled the problem of improving resolution in CT MBIR. Our group recently proposed the concept of enlarged voxel footprints for improving MBIR resolution [2]. Although the method produces higher MTF numbers, the reconstructed images are prone to overshoot artifacts, which the authors addressed by a post-processing filter.

Finite beamwidth modeling refers to the modeling of the finite nature of X-ray beams caused by a finite focal spot size, whereas a focal spot is often modeled by a point source [3]. Browne *et. al.* proposed finite beamwidth modeling for CT resolution improvement in 2D reconstructions [4] and presented preliminary results. We consider a similar concept as a candidate for enhancing resolution in our MBIR method by modifying the acquisition physics model.

In filtered back-projection, the two data sets from two wobbling positions are typically interlaced before a reconstruction kernel is applied. The reconstruction kernel is often designed such that the resolution in the reconstructed images is boosted. Motivated by this, we also study a method of interlacing the data, which is discussed in Sec. II in details. In addition, we investigate the performance of the interlacing method combined with high-frequency boosting methods using either a boosting kernel (filter) or a (model-based) deconvolution method.

These methods are compared in terms of reconstruction quality and MTF numbers by using a simplified 1D simulation. The objective of the current 1D study is to select the most promising method for enhancing resolution for CT MBIR.

II. METHODS

A. Simulation model

To simulate a continuous signal, we created a signal with many samples with a sufficiently small sample spacing; we call it a *true* signal. The true signal is then blurred by a rectangle point spread function (PSF) to model the finite beamwidth effect. Figure 1 shows the simulated "continuous" 1D signal of two data sets generated with and without a focal spot wobble. The focal spot wobble may be effectively modeled by a detector shift for a fixed focal spot position as shown in the figure. As illustrated by the arrays of rectangles in the two diagrams on the top row, the wobble data set is obtained by translating the detector by a half of a detector pixel size.

B. Baseline: PWLS

Let the forward models generating the wobble and no-wobble data sets be represented by $y_1 = A_1 x$ and $y_2 = A_2 x$, respectively. y_1 and y_2 signify wobble and no-wobble data, and x represents a signal we desire to reconstruct. A_1 and A_2 are matrices representing distance-driven (DD) (re-)projectors for the parallel-beam geometry [3] while DD back-projectors represent their transposes. Combining the two systems, we construct $y = Ax$, where $y = [y_1; y_2]$ and $A = [A_1; A_2]$ with the semicolon denoting vertical concatenation of the two vectors and matrices. Note that the data are assumed to be

---

The project described was supported by Grant Number 1-R01-HL-098686 from NIH. Its contents are solely the responsibility of the authors and do not necessarily represent the official views of NIH.

The authors are with CT Systems and Applications Laboratory, GE Global Research, Niskayuna, NY 12309 USA.

prepped, meaning that a negative logarithm was taken for the original measurements to create y_1 and y_2; this convention is used throughout this manuscript, unless otherwise stated. With this notation, a baseline reconstruction is obtained by solving a penalized weighted least square (PWLS) problem [1] defined by

$$\hat{x} = \underset{x \geq 0}{\arg\min} \frac{1}{2}(y - Ax)^T W (y - Ax) + \beta R(x), \tag{1}$$

where W denotes a diagonal matrix whose diagonal consists of statistical weights, and the regularization term R is defined as the q-GGMRF with $p = 2$, $q = 1.2$, and $c = 10\text{HU}$ discussed in [5]:

$$R(x) = \sum_{j,k} w_{j,k} \rho(x_j - x_k),$$
$$\rho(\Delta) = \frac{|\Delta|^p}{1 + \left|\frac{\Delta}{c}\right|^{p-q}}. \tag{2}$$

The minimization was performed by adapting the separable quadratic surrogate technique [6].

C. Method 1: PWLS with finite beamwidth modeling

In 1D, we model the finite beamwidth effect with a signal blurred by a kernel representing a focal-spot PSF. This blurring may be expressed in terms of convolution and can be written in matrix form as

$$y = Ax = ABu, \tag{3}$$

where B denotes a circulant matrix representing the blurring convolution operation, and u denotes the signal to be reconstructed that has a higher resolution than x. Note that in 2D or 3D with a more complicated scanning geometry, B would not be a matrix representing a convolution, but rather a more general blurring operation.

The reconstruction is found by solving

$$\hat{u} = \underset{u \geq 0}{\arg\min} \frac{1}{2}(y - ABu)^T W (y - ABu) + \beta R(u). \tag{4}$$

Again, the separable quadratic surrogate method was adapted to solve this minimization problem.

D. Method 2: PWLS with interlaced measurements

The measurement interlacing is conducted by placing the wobble and no-wobble data samples in an alternating manner as described in Fig. 1 on the third row. Let this new measurement be denoted by y_{int}. By interlacing, the method treats the data as if the detector pixel size was half of the actual pixel size. Thus, the system matrix A also needs to be modified accordingly. Let A_{int} represent the new matrix for interlacing. A_{int} is then simply a DD reprojector contructed by setting the detector pixel size as a half of the original size. An illustration of this construction is shown on the bottom row of Fig. 1. With y_{int} and A_{int}, a new minimization problem can be built by replacing y by y_{int} and A by A_{int} in Eq. (1). The corresponding reconstruction can then be produced by solving the new problem involving y_{int} and A_{int}.

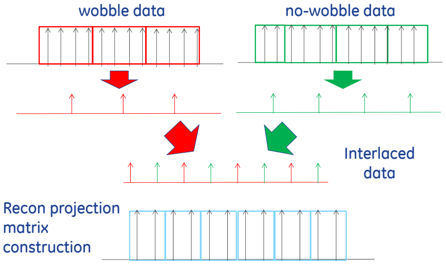

Fig. 1: An illustration of the process of interlacing wobble and no-wobble data sets

E. Method 3: PWLS with frequency boosted interlaced measurements

Inspired by a high-frequency enhancing filter routinely used in FBP [7], we apply a high-frequency "boosting" filter to the interlaced measurements described in Sec. II-D. The high-frequency boosting filter is defined in the frequency domain [8] and has the form of

$$H_b(f) = 2(\alpha - 1)\left|\frac{f}{f_c}\right| \text{rect}\left(\frac{f}{2fc}\right) \left(0.5 - 0.5\cos\left(2\pi\frac{f}{f_c}\right)\right), \tag{5}$$

where f_c is a user-defined cutoff frequency and $rect(x) = 1$ if $|x| \leq 0.5$ and zero otherwise. This step is applied to y_{int} as pre-processing before the data is fed into the optimization problem solved for Method 2. A smoothing filter may be combined with the boosting filter to suppress noise or artifacts. For example, a smoothing filter may be constructed by modifying the Hanning window:

$$H_h(f) = \text{rect}\left(\frac{f}{2f_c}\right)\left(0.5 + 0.5\cos\left(2\pi\frac{f}{2fc}\right)\right). \tag{6}$$

F. Method 4: PWLS with model based sinogram deconvolution

The high-frequency boosting filter used in Method 3 may be considered as an *ad-hoc* deconvolution filter. Instead, we may apply a model-based "sinogram" deconvolution (MBSD) to enhance the high-frequency contents in y_{int}. The model can be constructed by considering the scanning and interlacing geometries, as depicted in Fig. 2. The samples denoted by y_{1*} and y_{2*} represent the no-wobble and the wobble measurement samples, respectively. The deconvolved samples are denoted by $z_1, z_2, \ldots$ and assumed to be measured with smaller non-overlapping pixels. Then, y_{11} may be expressed as $y_{11} = z_1 + z_2$, $y_{21} = z_2 + z_3$, $y_{12} = z_3 + z_4$, and so on. If we consider proper scaling of the samples, the matrix C that maps z samples to y samples can be written as specified in Fig. 2.

Considering this, the MBSD part of Method 4 first finds z by solving the following optimization problem:

$$\hat{z} = \underset{z \geq 0}{\arg\min} \|y_{int} - Cz\|^2 + \gamma \|z\|^2, \tag{7}$$

where z signifies the deconvolved sinogram. This optimization can be performed by adapting a gradient-projection algorithm

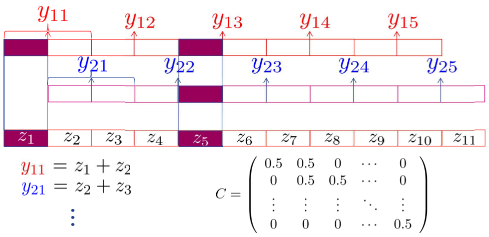
y_{11} y_{12} y_{13} y_{14} y_{15}
y_{21} y_{22} y_{23} y_{24} y_{25}
z_1 z_2 z_3 z_4 z_5 z_6 z_7 z_8 z_9 z_{10} z_{11}
$y_{11} = z_1 + z_2$
$y_{21} = z_2 + z_3$
$\vdots$
$C = \begin{pmatrix} 0.5 & 0.5 & 0 & \cdots & 0 \\ 0 & 0.5 & 0.5 & \cdots & 0 \\ \vdots & \vdots & \vdots & \ddots & \vdots \\ 0 & 0 & 0 & \cdots & 0.5 \end{pmatrix}$

Fig. 2: An illustration of the MBSD approach and its associated matrix construction

[9]. After $\hat{z}$ is found, the following optimization problem can be solved to find a reconstructed image:

$$\hat{x} = \arg\min_{x \geq 0} \frac{1}{2}(\hat{z} - A_{int}x)^T W(\hat{z} - A_{int}x) + \beta R(x), \qquad (8)$$

where the projector A_{int} incorporates the measurement interlacing as discussed in Method 2.

III. RESULTS

This paragraph summarizes the simulation strategy and parameters. Fig. 3a shows a true signal whose sample spacing is 0.0156 mm, and its field of view ranges over [-80 80] cm. The number of signal pixels is 10240. Note that the range beyond 60 cm that contains an impulse of a large magnitude is clipped off for displaying purposes. The size of each detector pixel is 0.625 mm such that each detector pixel contains exactly 40 true signal pixels. Thus, the number of detector pixels is 256. The size of a reconstruction pixel is 0.156 cm, and the number of reconstruction image pixels is 1024. The focal spot "size" is assumed to be 1 mm. A 1 mm-wide rectangle whose area is 1 models the focal spot PSF. The interlaced measurements corrupted by Poisson noise are shown in Fig. 3b. Recall that the measurements are presented in a prepped form: $y_i = -\log(\lambda_i/b_i)$, where $\lambda_i = b_i \exp(-y_i)$ is a detector raw measurement, and b_i is an air scan measurement. The measurement geometry was a parallel-beam geometry. The reprojection and backprojection were performed by the DD projector and backprojector described in [3]. The iteration stopped when the total relative reconstruction error becomes less than 10^{-6}.

Sample reconstructions of the methods for various β values are shown in Fig. 4. The numbers in the legends represent selected β values. The images in the figure correspond to the reconstructions of the features in the ranges marked by a small (red) rectangle. The features are magnified in Fig. 4a.

Baseline reconstructions are shown in Fig. 4b. Interestingly, for $\beta = 0$ and 1, the reconstructions present blocky artifacts which has the lowest data fit term error if there were no prior. As β increase, the artifacts are more suppressed. MTF numbers for reconstructions produced with $\beta = 1000$ are presented in the corresponding table in Fig. 5. For example, MTF50 for the Baseline method was 6.8 lp/cm. The labels on the top rows in each table designate the MTF numbers of which method are summarized in the table. In each table, the indicators "No", "Low", and "High" mean noiseless, low-noise level, and high-noise level, respectively. For conciseness, we denote the noiseless, low-level noise, and high-level noise cases by NN, LN, and HN, respectively.

Method 1 reconstructions are shown in Fig. 4c. Oscillation artifacts are observed for low β reconstructions. However, the reconstruction for β larger than 10000, the artifacts are significantly suppressed while high frequency contents are recovered remarkably better. For example, Method 1 improves the reconstruction of the deep valley near the right end of the range on Baseline. The MTF numbers are improved upon Baseline by 20 %. Note that the HN MTF numbers are significantly different from those for NN and LN. This difference may result from the statistical weighting W in Eq. (1). As discussed in [1], the diagonal elements of W are inversely proportional to estimates of measurement variances, and thus for those HN measurements with large variances, the regularization becomes stronger, resulting in lower MTF numbers. Also, note that HN MTF numbers show much smaller or no improvements compared to the improvements presented in NN and LN. For example, MTF50 of the Baseline method is 4.6 lp/cm; it improves to 5.6 for the LN in Method 1. In contrast, the MTF50 number remains as 3.4 for the HN. We conjecture that for selected β and reconstructions, the regularization becomes strong enough to be a deciding factor for the resolution.

Method 2 reconstructions are presented in Fig. 4d. Recall that the size of a detector pixel for DD re- and back-projector is set to 0.3125 mm. Method 2 reconstructions are comparable to Baseline in terms of high-freuqncy contents, and MTF numbers show no or marginal improvements. This implies that a mere interlacing of the data generally would not improve resolution unless it is combined with a high-frequency boosting or a measurement deconvolution.

Method 3 reconstructions are given in Fig. 4e. The boosting filter parameter α in Eq. (5) was determined such that the filter maximum is 10. Note that because of the large boosting magnitude, the reconstructions are prone to strong artifacts. Furthermore, the density values in the reconstructions do not fall within the original density range shown in Fig. 4a. Although the MTF numbers show more than 30 %improvements in some cases, the reconstructions suffer from overshoot artifacts. However, there might exist efficient boosting filters that can achieve higher-resolution reconstructions while maintaining acceptable image quality, but designing such a filter would be an assiduous task and is out of scope of this paper.

Method 4 reconstructions are shown in Fig. 4f. For MBSD, γ was set to 0.1 for the presented reconstructions. Note that γ modifies measurements and thus changes the reconstructed values as well. Hence, the density range was modified to better show the related features. With small γ (e.g., 0.01), Method 4 could produce MTF numbers slightly worse than those of Method 1. However, in those cases, the artifacts are stronger compared to Method 1. We may reduce the artifacts by increasing the regularization strength γ. However, as expected, it will degrade the MTF numbers as substantiated by the MTF numbers shown in the table for Method 4.

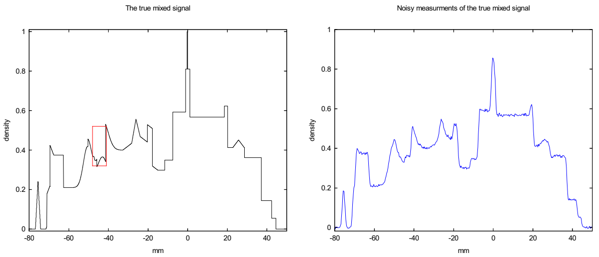

(a) (b)

Fig. 3: Simulation: (a) a true signal and (c) interlaced measurements corrupted by Poisson noise with $b_i = 10^5$.

IV. CONCLUSION

Four methods for improving resolution of CT MBIR images were investigated. A 1D simulated signal containing various high-frequency features and a large impulse was reconstructed. Method 1 with finite beamwidth modeling was shown to be the most powerful method that produces about 20% improvements in MTF20 and MTF50 numbers, while Method 2 produced marginal improvements. Methods 3 and 4 produced comparable or even better improvements in some cases. Nevertheless, the reconstructions with higher MTF numbers suffer from overshoot artifacts. Thus, considering both the MTF numbers and artifacts, we conclude that Method 1 would be the most promising method for improving resolution of MBIR images.

A natural next step is to extend the most promising method based on the study presented here to 2D and 3D CT MBIR. A more thorough evaluation of MTF quality and image quality using clinical and simulated data should be conducted to reach a more pragmatic conclusion on the resolution improvement performance of the extended approach.

REFERENCES

[1] Jean-Baptiste Thibault, Ken D. Sauer, Charles A. Bouman, and Jiang Hsieh, "A three-dimensional statistical approach to improved image quality for multislice helical ct," *Medical Physics*, vol. 34, no. 11, pp. 4526–4544, 2007.

[2] Kai Zeng, B. De Man, J.-B. Thibault, Zhou Yu, C. Bouman, and K. Sauer, "Spatial resolution enhancement in ct iterative reconstruction," in *Nuclear Science Symposium Conference Record (NSS/MIC), 2009 IEEE*, 24 2009-nov. 1 2009, pp. 3748 –3751.

[3] B. De Man and S. Basu, "Distance-driven projection and backprojection," in *Nuclear Science Symposium Conference Record, 2002 IEEE*, nov. 2002, vol. 3, pp. 1477 – 1480 vol.3.

[4] Jolyon A. Browne, John M. Boone, and Timothy J. Holmes, "Maximum-likelihood x-ray computed-tomography finite-beamwidth considerations," *Appl. Opt.*, vol. 34, no. 23, pp. 5199–5209, Aug 1995.

[5] Zhou Yu, J. Thibault, C.A. Bouman, K.D. Sauer, and J. Hsieh, "Fast model-based x-ray ct reconstruction using spatially nonhomogeneous icd optimization," *Image Processing, IEEE Transactions on*, vol. 20, no. 1, pp. 161 –175, jan. 2011.

[6] H Erdogan and J A Fessler, "Ordered subsets algorithms for transmission tomography," *Physics in Medicine and Biology*, vol. 44, no. 11, pp. 2835, 1999.

[7] Jiang Hsieh, *Computed Tomography*, SPIE Publications, 2009.

[8] Thorsten M. Buzug, *Computed Tomography: From Photon Statistics to Modern Cone-Beam CT*, Springer, 2008.

[9] Dimitri P. Bertsekas, *Nonlinear Programming: 2nd Edition*, Athena Scientific, 1999.

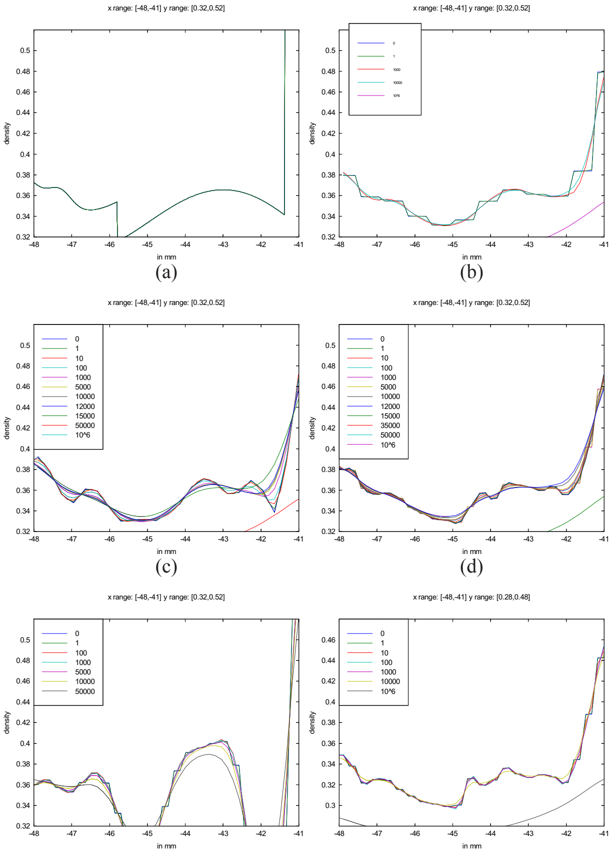

(a) (b) (c) (d) (e) (f)

Fig. 4: A selected feature of (a) the true signal and of (b) Baseline, (c) Method 1, (d) Method 2, (e) Method 3, and (f) Method 4 reconstructions with some selected regularization strengths (β).

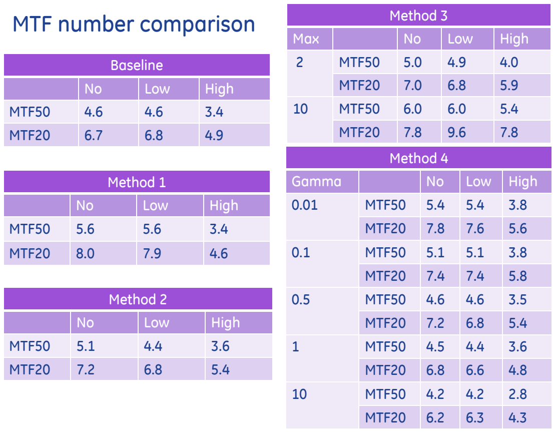

MTF number comparison

Baseline

	No	Low	High
MTF50	4.6	4.6	3.4
MTF20	6.7	6.8	4.9

Method 1

	No	Low	High
MTF50	5.6	5.6	3.4
MTF20	8.0	7.9	4.6

Method 2

	No	Low	High
MTF50	5.1	4.4	3.6
MTF20	7.2	6.8	5.4

Method 3

Max		No	Low	High
2	MTF50	5.0	4.9	4.0
	MTF20	7.0	6.8	5.9
10	MTF50	6.0	6.0	5.4
	MTF20	7.8	9.6	7.8

Method 4

Gamma		No	Low	High
0.01	MTF50	5.4	5.4	3.8
	MTF20	7.8	7.6	5.6
0.1	MTF50	5.1	5.1	3.8
	MTF20	7.4	7.4	5.8
0.5	MTF50	4.6	4.6	3.5
	MTF20	7.2	6.8	5.4
1	MTF50	4.5	4.4	3.6
	MTF20	6.8	6.6	4.8
10	MTF50	4.2	4.2	2.8
	MTF20	6.2	6.3	4.3

Fig. 5: MTF number comparison

Estimating X-ray Spectrum of a Clinic CT Scanner from Transmission Measurements

Xinhui Duan, Jia Wang, Lifeng Yu and Cynthia. H. McCollough[1]

Abstract -

Purpose: In diagnostic CT imaging, multiple important applications depend on knowledge of the x-ray spectrum, including Monte Carlo dose calculations and dual-energy material decomposition analysis. Due to the high photon flux involved, it is difficult to directly measure spectra from the x-ray tube of a CT scanner. One potential method for indirect measurement involves estimating the spectrum from transmission measurements. The expectation maximization (EM) method is an accurate and robust method to solve this problem. In this paper, this method was evaluated in a commercial CT scanner.

Methods: Two step-wedges (polycarbonate and aluminum) were used to produce different attenuation levels. Transmission measurements were performed on the scanner, and the measured data from the scanner were exported to an external computer to calculate the spectra. The EM method was applied to solve the equations that represent the attenuation processes of polychromatic x-ray photons. Estimated spectra were compared with the spectra simulated using software provided by the manufacturer of the scanner. To test the accuracy of the spectra, a verification experiment was performed using a phantom containing different depths of water. The measured transmission data were compared with the transmission values calculated using the estimated spectra.

Results: 80, 100, 120 and 140 kVp spectra from a dual-source CT scanner were estimated. The estimated and simulated spectra were well matched. The differences of mean energies were less than 1 keV. In the verification experiment, the measured and calculated transmission values were in excellent agreement.

Conclusions: Spectrum estimation using transmission data and the EM method is a quantitatively accurate and robust technique to estimate the spectrum of a CT system. This method could benefit studies relying on accurate knowledge of the x-ray spectra from CT scanners.

***Key words*— x-ray spectrum, transmission measurements, CT scanner**

1. PURPOSE

In diagnostic CT imaging, multiple important applications depend on the knowledge of spectrum, including Monte Carlo dose calculation, beam-hardening correction and dual-energy CT imaging. Due to high photon flux, it is very difficult to directly measure spectra from an X-ray tube of a CT scanner with a spectrometer. Therefore, various methods have been developed to estimate the spectra, among which estimating a spectrum from transmission measurements is one of the promising methods. The expectation maximization (EM) method introduced by Sidky et al.[1] is an accurate and robust method to solve this problem. The purpose of this paper is to implement the EM method to measure the spectra of both X-ray tubes in a dual-source CT scanner, which is important for many currently used dual-energy applications.

2. METHODS

A. *Mathematic models*

The transmission measurements of polychromatic X-rays can be expressed as

$$\begin{aligned} p = \frac{I}{I_0} &= \int_E D(E)s(E)e^{-\int_L \mu(E,\mathbf{r})dl} dE \\ &= \int_E W(E)e^{-\int_L \mu(E,\mathbf{r})dl} dE \end{aligned} \qquad (1)$$

where p represents the line integral of linear attenuation $\mu(E,\mathbf{r})$ and path length L, I_0 and I denotes incident and transmitted photon intensity, $s(E)$ is the X-ray spectrum and $D(E)$ is the detector response. E is the photon energy. We use $W(E)$ to represent a system overall spectrum which combines the knowledge of X-ray source and the detector ($W(E)$ may also include all the filters in the system).

After discretization, Eq. 1 is converted to a linear system

$$\begin{aligned} p_j &= \sum_{i=1}^{N} A_{i,j} w_i, \; j = 1,\ldots, M \\ A_{i,j} &= \exp\left(-\int_L \mu_j(E_i,\mathbf{r})dl\right) \end{aligned} \qquad (2)$$

where M is the total number of measurements, N is the number of samplings for the spectrum and A is the measurement matrix calculated from the phantom parameters.

The EM method was applied to solve the linear system1 (Eq.2). Based on statistical models, the EM method is robust to noise and it has inherent positivity which results from a multiplicative update form,

$$w_j^{(k+1)} = \frac{w_j^{(k)}}{\sum_i A_{i,j}} \sum_i \frac{A_{i,j}\, p_i}{\sum_s A_{i,s}\, w_s^{(k)}} \qquad (3)$$

where the index k represents the iteration number.

B. *Phantoms and scanner*

Two step wedge phantoms made of aluminum (Al) and polycarbonate ($C_{16}H_{14}O_3$) were used to represent different attenuation levels. The parameters of the phantoms are shown in Table 1. The aluminum phantom was a standard step-wedge phantom which was originally used for quality control of radiography. The polycarbonate phantom consisted of pieces of plates and each step had three plates. General principles for choosing phantoms include known composition, regular geometry, convenience to measure dimensions and align, etc. Because there are two major mechanisms of X-ray interacting with matters in diagnostic energy range: photoelectric effect and Compton scattering, using two materials with sufficient difference in atomic number (e.g., plastics and metal) gains an

---

[1] CT Clinical Innovation Center, Radiology,
Mayo Clinic, Rochester MN 55905
Mccollough.cynthia@mayo.edu

Table 1. Parameters of the phantoms used in the experiment

Phantom material	Chemical formula	Mass density (g/cm^3)	Number of steps	Min/max thickness (cm)
Aluminum	Al	2.7	16	0.136/2.54
Polycarbonate	$C_{16}H_{14}O_3$	1.21	12	0.876/10.0

improvement of equation stability compared with only one material.

Spectrum measurement was performed on a dual-source scanner (SOMATOM Definition Flash, Siemens Healthcare, Germany). To position the phantoms stably and accurately, the phantoms were directly laid on the gantry to align them with laser beams as shown in Fig.1. In each measurement, only one step of the phantom was exposed in the X-ray beam. The tube current in the experiment was 300 mA and exposure time was 1 s. A small collimation (12 × 1.2 mm) was used for precise alignment and reducing scattering. Three spectra from two tubes (A and B) were measured, including 80 kVp and 140 kVp at Tube A, and 140 kVp with a built-in tin filter at Tube B. These three spectra were used in dual-energy routine protocols. In the experiment, the scanner was operated in service mode and the measured tube was fixed on the bottom of the gantry (6 o'clock position). All the raw projection data were exported from the scanner to an external computer to calculate the spectra.

The experiment was performed in two steps: 1) after transmission measurement all the spectra were reconstructed using the EM method; 2) the estimated spectra were validated by comparing calculated and measured transmission data through different depth of water.

As mentioned in Sidky et al.'s work, the EM method cannot recover the details of the spectrum such as a characteristic peak if the initial guess does not contain a peak at the same energy. Therefore, the initial guess spectrum for the EM method was constructed by multiplying Boone's spectrum[2] by the detector response function (Gd_2O_2S, area mass density 1.05 g/cm^2), so the spectra contained both the peaks from X-ray tubes and the K-edges from the detector. If an estimated spectrum does not need to be exactly the same as the true one, i.e., the estimated spectrum only needs to match the transmission data, a generic initial guess should work well[1].

3. RESULTS

The estimated spectra are shown in Fig. 2 (a)-(c). The total photon counts were normalized to unity and energy interval was 1 keV. In each figure, three spectra are compared: the initial guess for the EM algorithm, the estimated spectrum and the spectrum from simulation (DRASIM, Siemens Healthcare, Germany). As shown in the figure, the estimated and simulated spectra are very close to each other and the differences of the mean energy are 0.23 keV for 80 kVp, 0.27 keV for 140 kVp and 0.81 keV for 140 kVp with a tin filter. The initial guesses are significantly softer than the other two spectra because additional filters installed in the scanner were not counted in. In Fig. 2 (c) there are two downward peaks at around 130 keV, which were introduced by the initial guess. The overall shape of the spectrum will gradually approach the correct one as the iteration continues, but the locations of spectrum details (peaks and edges) will be preserved in the results, even for tiny ones.

Fig. 2 (d) shows the convergence curve of the EM iteration. The smooth curves indicate the stability of the EM method. The error is defined as

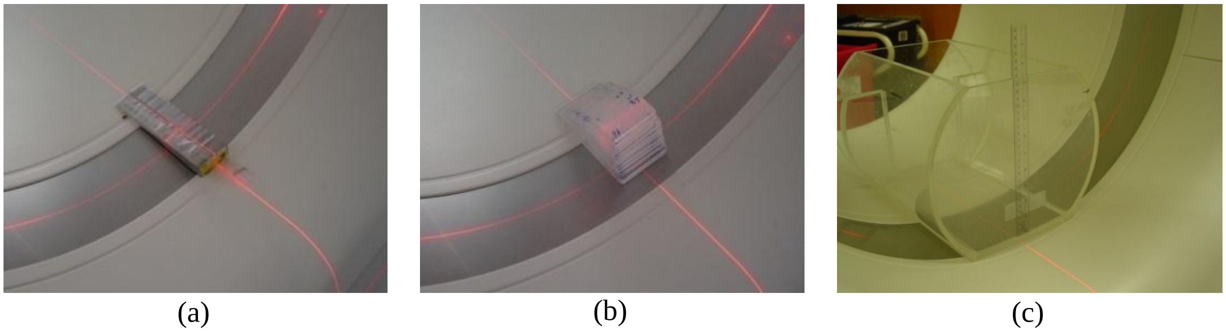
(a) (b) (c)

Fig. 1 Illustrations of experimental setup. The phantoms were directly placed on the gantry cover and aligned with laser beams. (a) Aluminum phantom. (b) Plastic phantom. (c) Water tank for spectrum verification test.

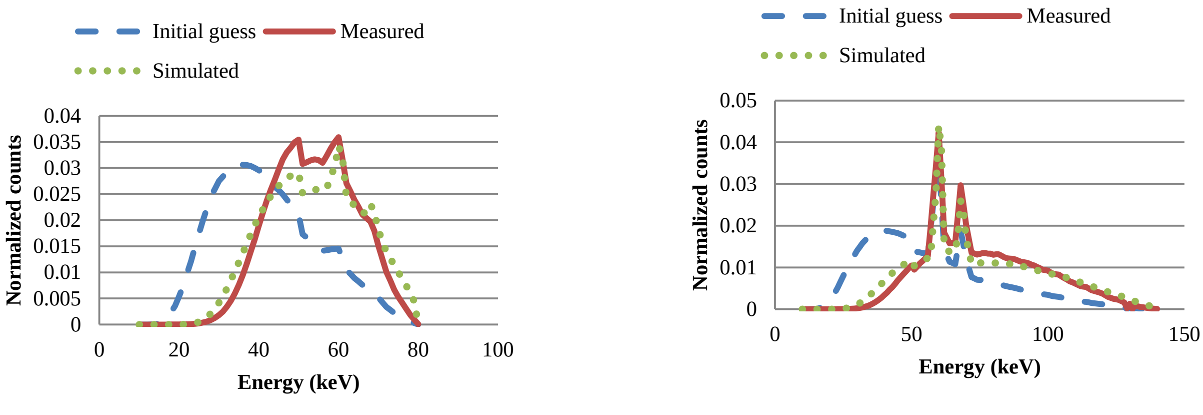

(a) 80 kVp

(b) 140 kVp

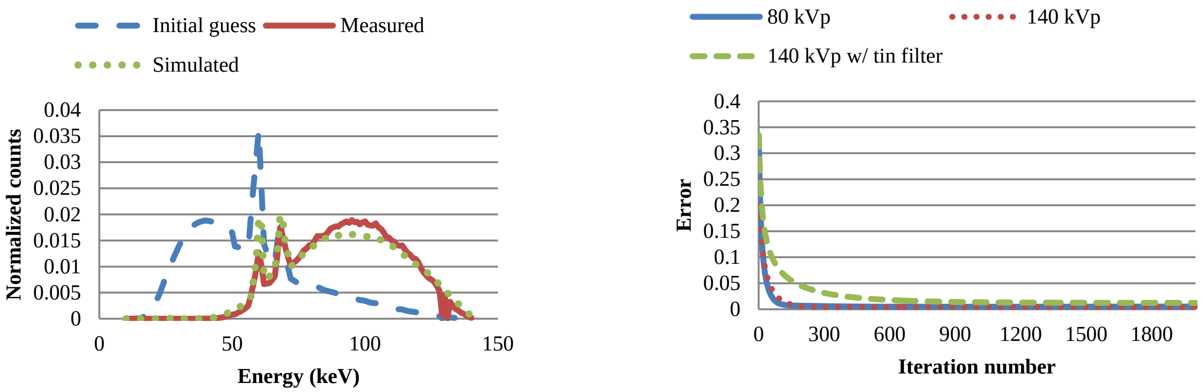

(d) Convergence curve

(c) 140 kVp w/ tin filter

Fig. 2 (a)-(c) X-ray spectra estimated from the transmission data of the step-wedge phantoms using the EM method. The estimated spectra are compared with the initial guess and the simulated one. (d) The convergence curve of the EM iteration.

$$e = \frac{1}{M}\sum_{i=1}^{M}\frac{\left|p_i - p_{mi}\right|}{p_{mi}},$$

where p_i is the calculated transmission data from Eq. 2 and p_{mi} is the measured data. Because of the existing inconsistence in the data, the error curve actually does not monotonically decreases in the flat region. The final spectra were chosen with the least error in a maximum iteration number (5000 in the experiment). The curve of 140 kVp with tin filtration has relatively slower convergence. One possible reason is that the data set has relatively larger inconsistence because of the restriction on Tube B in service mode. The data inconsistence may also cause oscillation in the spectrum, e.g., the spectrum around 100 keV in Fig. 2 (c). The EM method is robust to noise, but the inconsistence of the system such as systematic error and scattering may still cause computation difficulty, e.g., oscillation in spectrum curves or slow convergence.

A water tank filled with different depths of water was used to validate the measured spectra as shown in Fig.1 (c). Transmission were measured for different thickness of water (10 thickness, 2.25~20.25 cm). The measured data were compared with the calculated transmission data from the estimated spectrum. The results are shown in Fig. 3. The transmission data from measurement and calculation are well matched (the dots and the lines). The average difference between the two is 2.36% (standard deviation 16.63%) for 30 logarithm date point (three spectra, 10 thickness for each).

4. DISCUSSION AND CONCLUSIONS

Spectrum estimation using transmission data and the EM method is an accurate and robust technique to acquire spectrum information. It is also easy to implement in practice. In our experiment only two step-wedge phantoms were used and no additional instrument was involved.

For a clinic CT scanner, transmission measurement has to be performed in service mode. In our experiment, the measurement was implemented in static mode, i.e., neither the gantry nor the bed moved. If the mode is not accessible, an alternative way is to use the localization features of a scanner, e.g. “Scout,” “Pilot,” “Topogram,” or “Preview”.

In conclusion, spectrum estimation using transmission data and the EM method is a promising method, which allows user assessment of X-ray spectrum for commercial CT systems.

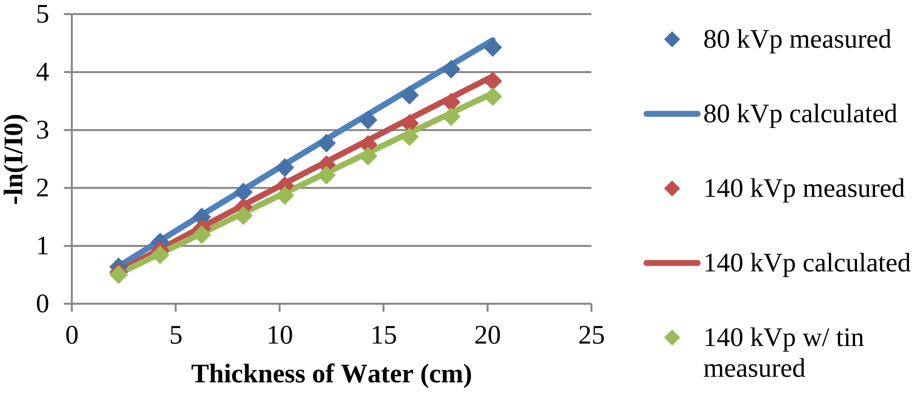

Fig. 3 Comparison of calculated and measured transmission data of the water tank phantom. The dots are measured data and the lines are calculated data.

REFERENCES

1. E. Y. Sidky, L. Yu, X. Pan, Y. Zou and M. Vannier, "A robust method of x-ray source spectrum estimation from transmission measurements: Demonstrated on computer simulated, scatter-free transmission data," Journal of Applied Physics **97**, 124701 (2005).
2. J. M. Boone and J. A. Seibert, "An accurate method for computer-generating tungsten anode x-ray spectra from 30 to 140 kV," Medical Physics **24**, 1661 (1997).
3. L. C. Baird, "X-ray spectra vs attenuation data: a theoretical analysis," Med Phys **8**, 319-323 (1981).

4D-CT Reconstrucion Using Sparsity Level Constrained Compressed Sensing

Haibo Wu, Andreas Maier, Hannes Hofmann, Rebecca Fahrig and Joachim Hornegger

***Abstract*—4D-CT is an important tool for treatment simulation and treatment planning in radiotherapy. In order to capture the tumor and tissue movement over time, 4D-CT has to acquire more projection images compared to 3D-CT. This leads to more radiation dose, which is the main concern of the application. Using fewer projections can reduce the radiation dose. However, lack of projections degrades the reconstructed image quality for traditional methods. In this paper, we propose a novel method based on iterative hard thresholding and compressed sensing. We combine the prior knowledge from both methods in our reconstruction problem formulation. In the experiments, we validate our method with XCAT phantom data. The Euclidean norm of the reconstructed images and the ground truth are calculated for evaluation. The results show that our method outperforms the traditional reconstruction method.**

I. INTRODUCTION

Four dimensional computed tomography (4D-CT) plays an important role in radiation oncology. Besides the 3D information, 4D-CT also captures the movement of the body's organs over time. With the motion information, the target volume definition is improved and accuracy during treatment delivery for patients with tumors in the abdomen or thorax area is enhanced. [1][2].

In 4D-CT, the projection images are continuously acquired. An additional respiratory signal is recorded at the same time. The projection images are then grouped to different phases according to the amplitude or phase-angle sorting [3-5]. However, to achieve clinically usable image quality, hundreds of projections are needed to reconstruct images of each respiratory phase [6]. Therefore the radiation dose is of great concern for 4D-CT. In order to reduce the radiation dose, the number of projections should be reduced. However, the image quality would be degraded for traditional reconstruction methods. Therefore, prior knowledge is introduced to the reconstruction process. The group of Pan developed the reconstruction method based on compressed sensing [7]. They assume the reconstruction result is smooth and use total variation to promote the smooth solution. Blumensath proposes the iterative hard thresholding method [8]. He uses the sparsity level as the prior knowledge. Both methods can reconstruct the image with much better quality compared to the traditional method ART [9] using only a limited number of projections.

In this paper, we propose a 4D-CT reconstruction method based on these two methods. We use the prior knowledge from both methods in our formulation. The details of our method can be found in section 2. The experiments and results are in section 3. Conclusion and outlook in last section.

II. PROPOSED METHOD

A. Formulation of our method

The 4D object can be described by a sequence of 3D spatial images [10]:

$$\vec{X} = \{\vec{x}_j, 1 \leq j \leq n_t\}, \tag{1}$$

where $\vec{X}$ is the 4D object and $\vec{x}_j$ is the image at j-th respiratory phase. n_t is the total number of reconstructed respiratory phases. Thus, the 4D-CT data acquisition process can be viewed as:

$$\vec{Y} = \{\vec{y}_j = A_j\vec{x}_j, 1 \leq j \leq n_t\}, \tag{2}$$

where $\vec{y}_j$ and A_j are the projection image and system matrix. $\vec{Y}$ stands for projection images. Due to the respiratory motion, we use only the projection images of j-th phase ($\vec{y}_j$) to reconstruct the j-th image ($\vec{x}_j$). Therefore, the reconstruction process can be viewed as solving the linear system:

$$\vec{y}_j = A_j\vec{x}_j + \vec{\gamma}. \tag{3}$$

Here $\vec{\gamma}$ stands for the noise of the measurements. The linear system is ill-posed. There exist infinite solutions. The traditional method formulates the reconstruction problem as:

$$\min_{\vec{x}_j} ||\vec{y}_j - A_j\vec{x}_j||_2. \tag{4}$$

The method finds the solutions which fit the measurements best. Although the minimization problem is convex, there could still be infinite solutions. For example in Fig. 1, the objective function is convex and there is only one global minimum, still the number of minimizers are infinite. To further improve the reconstruction quality, compressed sensing uses sparsity as prior knowledge to choose the best solution in the solution set of (4). It formulates the reconstruction problem as:

$$\min_{\vec{x}_j} ||\Phi\vec{x}_j||_1 \quad s.t. \quad ||\vec{y}_j - A\vec{x}_j||_2 < \lambda. \tag{5}$$

Here, Φ is the sparsifying transform (for example total variation or wavelet transform) and $|| \bullet ||_1$ stands for L1 norm which calculates the sum of the absolute value of all entries. λ describes the energy of the noise. Compressed sensing assumes that medical images can be expressed sparsely by a certain sparsifying transform. For example, most wavelet

---

H. Wu, A. Maier, H. Hofmann and J. Hornegger are with Pattern Recognition Lab (LME) of Friedrich-Alexander-University Erlangen-Nuremberg. H. Wu and J. Hornegger are also with Graduate School in Advanced Optical Technologies (SAOT) of Friedrich-Alexander-University Erlangen-Nuremberg. R. Fahrig is with Department of Radiology of Stanford University.

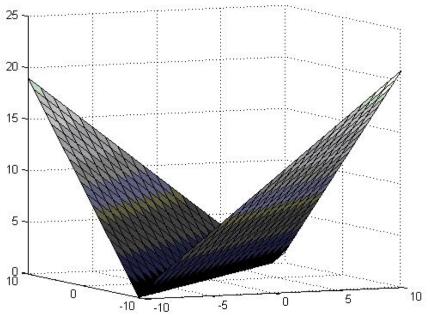

Fig. 1. Example of convex function with non-unique solution

coefficients of a medical image are zero. Minimizing L1 norm of the coefficients promotes the sparse expression of the image under the corresponding sparsifying transform. Total variation and wavelet are used as sparsifying transforms in compressed sensing based reconstruction methods [7] [11] [12]. Both of them improve the reconstruction quality compared to the traditional reconstruction method, when only limited number of projection images can be used.

Similar as compressed sensing, Blumensath proposes another idea to select the best solution from the solution set of (4). The method is called iterative hard thresholding. The formulation is

$$\min_{\vec{x}_j} ||\vec{y}_j - A\vec{x}_j||_2 \quad s.t. \quad ||\Phi\vec{x}_j||_0 < \alpha, \tag{6}$$

where Φ is again a sparsifying transform and $|| \bullet ||_0$ is the L0 norm which counts the nonzero entries. For simplicity, we call $||\Phi\vec{x}_j||_0$ sparsity level. α is a scalar describing the actual sparsity level which can be estimated by prior knowledge. In the context of 4D-CT, a prior image can be reconstructed using all projections. Then α can be estimated from this prior image.

The two methods mentioned above use different prior knowledge to improve the reconstruction quality. We propose to combine the prior knowledge in the reconstruction problem formulation. Therefore, we formulate the reconstruction problem as:

$$\min_{\vec{x}_j} ||\Phi_1\vec{x}_j||_1 \quad s.t. \quad ||\vec{y}_j - A\vec{x}_j||_2 < \lambda \quad ||\Phi_2\vec{x}_j||_0 < \alpha. \tag{7}$$

Here, Φ_1 and Φ_2 are two sparsifying transforms. In practice, the noise energy (λ) is not known. The related constraint can be moved to the objective function to make the optimization problem easier. Thus Equation (7) can be rewritten as :

$$\min_{\vec{x}_j} ||\Phi_1\vec{x}_j||_1 + \beta||\vec{y}_j - A_j\vec{x}_j||_2 \quad s.t. \quad |||\Phi_2\vec{x}_j||_0 < \alpha. \tag{8}$$

β is a weighting factor balancing the data fidelity and sparseness. We use total variation as Φ_1 and haar wavelet as Φ_2 in the experiments. Our method promotes a smooth solution which also obeys the sparsity level constraint.

B. Optimization method

It is challenging to solve the optimization problem (8). First of all, as shown in Equation (6), it is a nonconvex optimization problem. Second, in the context of 4D-CT reconstruction, the dimension of the problem is very high. Blumensath proposed a fast and accurate method to solve Equation (6) [8]. The method is proven to converge to a certain local minimum and the accuracy of the solution is guaranteed to be better than the solution of the traditional method. The method deals with the objective function and the constraint separately. It can be summarized:

- Step 1) One gradient descent step to minimize the objective function which is $||\vec{y}_j - A_j\vec{x}_j||_2$ in Equation (6).
- Step 2) Apply the constraint which is $||\Phi\vec{x}_j||_0 < \alpha$ in (6).
- Step 3) Repeat 1 and 2 until the Euclidean norm of two subsquent image estimates is below a threshold.

Blumensath et al. used haar wavelet as Φ. In step 2, they first transform the image estimate to the wavelet domain. Then they keep the α largest wavelet coefficients and set the other wavelet coefficients to zero. Finally they apply the inverse wavelet transform. Similarly, we develop our optimization algorithm as:

- Step 1) One gradient descent step to minimize the objective function which is $||\Phi_1\vec{x}_j||_1 + \beta||\vec{y}_j - A_j\vec{x}_j||_2$ in Equation (8).
- Step 2) Apply the constraint which is $||\Phi_2\vec{x}_j||_0 < \alpha$ in Equation (8).
- Step 3) Repeat 1 and 2 until the Euclidean norm of two subsquent image estimates is below a threshold.

Due to the high dimension, step 1 would be very time consuming if we applied directly one gradient descent step. Pan proposed an efficient method to minimize $||\Phi_1\vec{x}_j||_1 + \beta||\vec{y}_j - A_j\vec{x}_j||_2$ [7]. They split the objective function into two parts which are $||\Phi_1\vec{x}_j||_1$ and $||\vec{y}_j - A_j\vec{x}_j||_2$ and minimize these two parts separately. We use their idea to further speed up the optimization process and our algorithm can be written as:

- Step 1) One step of ART to minimize $||\vec{y}_j - A_j\vec{x}_j||_2$.
- Step 2) Take the result from step 1 as initial, apply k steps of gradient descent to minimize $||\Phi_1\vec{x}_j||_1$.
- Step 3) Apply the constraint which is $||\Phi_2\vec{x}_j||_0 < \alpha$ in Equation (8).
- Step 4) Repeat 1 and 3 until the Euclidean norm of two subsquent image estimates is below a threshold.

III. EXPERIMENTS AND RESUTLS

We used the digital phantom XCAT [13] to validate our method and compare against the state-of-the-art reconstruction method, namely, ART, total variation regularization method (TVR) [7], wavelet regularization method (WR) [11] and iterative hard thresholding method (IHT) [8]. TVR and WR are in fact compressed sensing based reconstruction methods using total variation and wavelets as sparsifying transforms. We generated 360 projection images in fan beam geometry, equally spaced over an entire 360 degree rotation. They are binned into 15 respiratory phases. Only 24 projeciton images are used for the reconstruction of each phase. The reconstructed image size is 256 x 256 The parameter settings for all methods are chosen to have the best performance. We

TABLE I
RECONSTRUCTION ERROR OF DIFFERENT METHODS AT ALL PHASES. LOWER VALUES INDICATE A SMALLER ERROR.

	ART	TVR	WR	IHT	Our method
Phase 0	954.129	528.115	491.619	502.797	380.308
Phase 1	955.064	530.937	493.409	504.610	383.991
Phase 2	952.191	519.982	489.499	497.777	380.522
Phase 3	924.856	514.082	464.587	475.610	364.402
Phase 4	909.119	509.091	455.989	468.648	353.299
Phase 5	906.057	507.531	453.293	463.976	348.600
Phase 6	899.210	537.518	448.592	460.021	349.38
Phase 7	891.567	501.844	443.407	454.459	341.703
Phase 8	896.414	496.971	447.953	459.659	347.126
Phase 9	892.580	493.052	435.819	447.010	336.634
Phase 10	903.200	520.333	450.953	461.388	354.010
Phase 11	921.861	518.745	461.159	470.909	354.971
Phase 12	940.355	528.281	473.379	483.011	362.820
Phase 13	944.477	527.099	475.758	487.505	364.099
Phase 14	952.982	527.087	488.380	498.830	376.406
Mean	922.938	517.378	464.920	475.747	359.885

use 5 gradient descent steps in step 2. Since we do not know the energy of the noise, TVR and WR are formulated as Equation (8) without the sparsity level constraint. The β are set to 0.1 and 0.001 for TVR and WR, respectively.

The reconstruction results of the different methods are shown in Fig. 2. In the first row, there are ground truth, reconstruction results from ART and TVR. In the second row, there are the reconstruction results from WR, IHT and our method, respectively. The result from ART contains severe streak artifacts due to the lack of projections. The streak artifacts are reduced dramatically in the result from TVR but the edges are blurred. The results from WR and IHT keep the edges, but there are still a lot of streak artifacts. Our result is smooth but preserves sharp edges. To quantitatively evaluate the result, we calculate the reconstruction error for each method. The error is calculated as:

$$Error = ||\vec{x} - \vec{x}_{true}||_2 \tag{9}$$

It is in fact the Euclidean norm of the reconstruction result and the ground truth. The evaluation results can be found in Table 1. The smaller number indicates better image quality. TVR, WR and IHT all improve the image quality significantly compared to the traditional method ART. Our method outperforms all the other methods. The reconstruction error of our method is less than 50% of the reconstruction error from ART.

The convergence maps of TVR, IHT, WR and our methods can be found in Fig. 3. The graph shows that our method converges faster than the others and the accuracy of our reconstructed result is the best.

Our method adopts the prior knowledge from TVR and IHT. Therefore, it keeps the advantages of these two methods. TVR uses total variation as the sparsifying transform and minimizes the total variation of the solution. TVR favors a piecewise constant solution. We also use the total variation in our formulation. Therefore, our method reduces the streak artifacts dramatically and reconstructs a piecewise constant image. IHT uses the sparsity level constraint. IHT assumes that the energy of the real signal should concentrate in the large wavelet coefficients and the energy of noise should concentrate in small wavelet coefficients. Thus, at every iteration step, IHT keeps the α largest wavelet coefficients and sets the others to zero, which keeps the sharp edges and removes the small changes. Our method also uses the sparsity level constraint. Therefore, our method preserves the sharp edges in the reconstruction results.

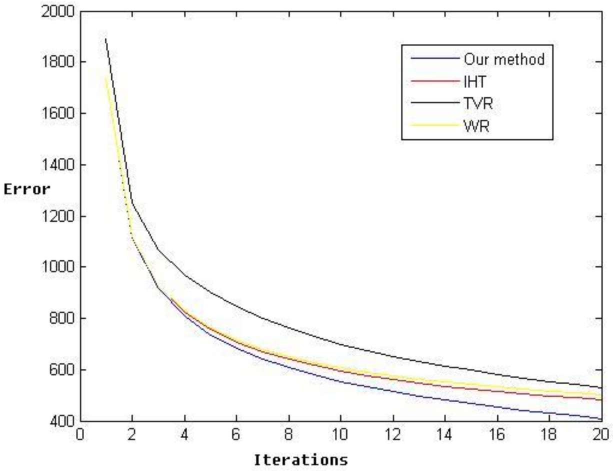

Fig. 3. Convergence maps.

IV. CONCLUSION AND OUTLOOK

In this paper, we have presented a 4D-CT reconstruction method based on compressed sensing and iterative hard thresholding. The experiments indicate that our method can reconstruct images of improved quality compared to ART when only a small number of projections can be used. However, we only consider prior knowledge in spatial domain in this paper. Using the sparsity in the temporal domain can also improve the reconstructed image quality[14][15]. In the future, we will investigate combining the prior knowledge both in the spatial and temporal domains.

V. ACKNOWLEDGEMENT

The first and last authors gratefully acknowledge funding of the Erlangen Graduate School in Advanced Optical Technologies (SAOT) by the German Research Foundation (DFG) in the framework of the German excellence initiative. The first author thanks the financial support from Chinese Scholarship Council (CSC). The authors thank the financial support from NIH grant R01 HL087917.

REFERENCES

[1] E. Ford, G. Mageras, E. Yorke and C. Ling, ”Respiration-correlated spiral CT: A method of measuring respiratory-induced anatomic motion for radiation treatment planning,” *Med. Phys.*, vol. 30, 2003, pp. 88-97.
[2] P. Keall, G. Starkschall, H. Shukla, K. Forster, V. Prtiz, C. Stevens, S. Vedam, R. George, T. Guerrerp and R. Mohan,” Acquiring 4D thoracic CT scans using a multislice helical method,” *Phys. Med. Biol.*, 2004, vol. 49, 2004, pp. 2053-2067.

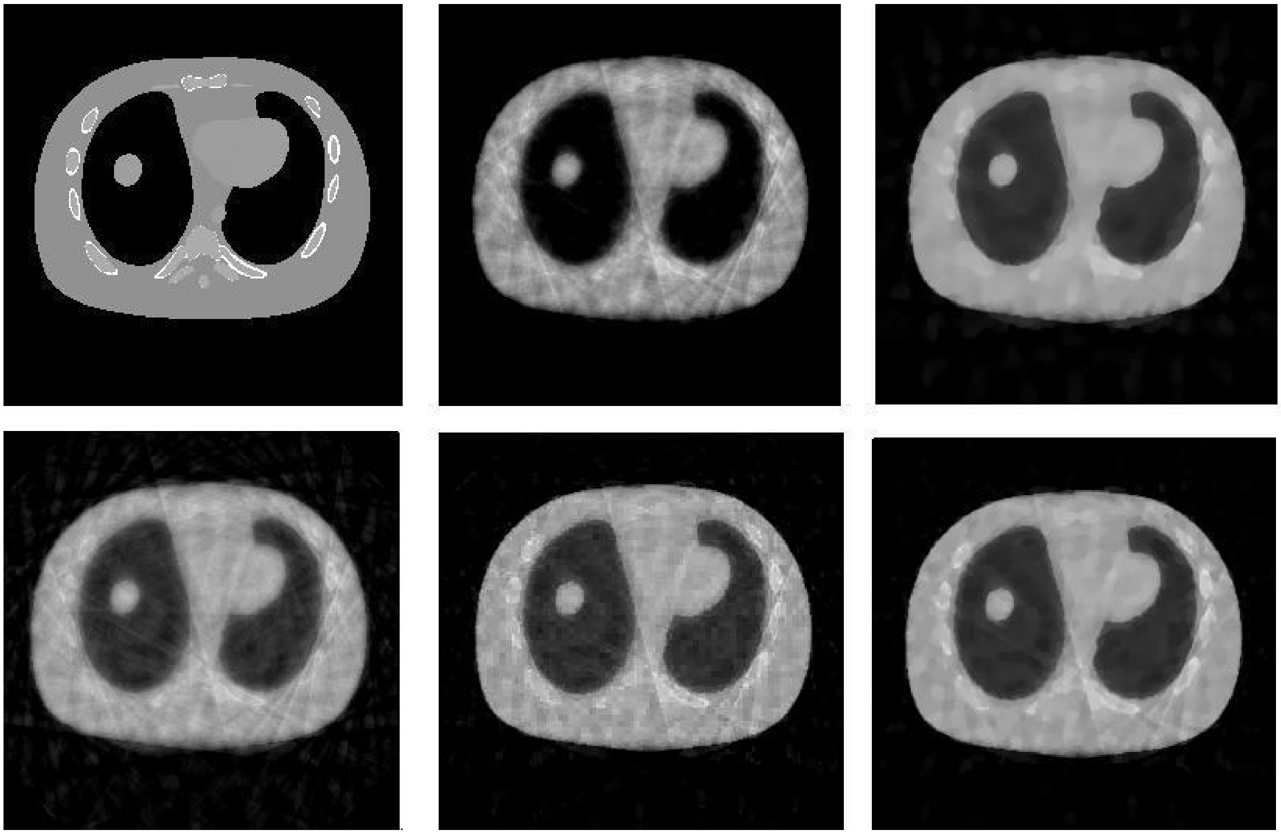

Fig. 2. Reconstruction results of phase 0. All images are set with the same window width and window level. At first row from left to right, they are ground truth, reconstructed images from ART and TVR. At second row from left to right, they are reconstructed images from WR, IHT and our method. The result from ART contains severe streak artifacts due to the lack of projections. The streak artifacts are removed dramatically in the result from TVR but the edges are blurred. The results from WR and IHT keep edges, but there are still a lot of streak artifacts. Our result removes most streak artifacts but keeps sharp edges.

[3] D. Low, M. Nystrom, E. Kalinin, P.parikh, J. Dempsey, J. Bradley, S. Mutic, S. Wahab, T. Islam and G. Christensen," A method for reconstruction of four-dimensional synchronized CT scans acquired during free breathing,"*Med. Phys.*, vol. 30, 2004, pp. 1254-1263.

[4] E. Rietzel, T. Pan and G. Chen, "Four-dimensional computed tomography: Image formation and clinical protocol, "*Med. Phys.*, vol. 32, 2004, pp. 333-340.

[5] S.Vedam, P.Keall, V.Kini, H. Mostafavi, H. Shukla and R. Mohan, "Acquiring a four-dimensional computed tomography dataset using an external respiratory signal," *Phys. Med. Biol.*, vol. 48, 2003, pp. 45-62.

[6] D. Ertel, Y. Kyriakou, R. Lapp and W. Kalender," Respiratory phase-correlated micro-CT imaging of free-breathing rodents," *Phys. Med. Biol.*, vol. 54, 2009, pp. 3837-3845.

[7] E. Y. Sidky and X. Pan, "Image Reconstruction in Circular Cone-beam Computed Tomography by Constrained Total-variation Minimization," *Phys. Med. Bio.*, vol. 53, 2008, pp. 4777-4807.

[8] T. Blumensath and M. Davies, "Iterative hard thresholding for compressed sensing," *Applied and Computational Harmonic Analysis*, vol. 27, pp. 265-274, 2009.

[9] G. L. Zeng, Medical Image Reconstruction, *High Education Press*, China, 2009, pp. 145-146.

[10] H. Gao, J. Cai, Z. shen and H. Zhao "Robust principle component analysis based four-dimensional computed tomography," *Phys Med Biol*, vol. 56, 2011, pp. 3181- 3198.

[11] G. Wang and H. Yu, "SART-type image reconstruction from a limited number of projections with the sparsity constraint," *Int. J. Biomedical Imaging 2010*. vol. 2010, 2010, pp. 541-550

[12] H. Wu, C. Rohkohl, and J. Hornegger, "Total variation regularization method for 3-D rotational coronary angiography,"' *Bildverarbeitung fuer die Medizin*, pp. 434-438, 2011.

[13] W. P. Segars, "A realistic spline-based dynamic heart phantom," *IEEE Trans. Nucl. Sci.*, vol. 46, pp.503–506, 2011.

[14] H. Wu, A. Maier, R. Fahrig and J. Hornegger, "Spatial-temporal Total Variation Regularization (STTVR) for 4D-CT Reconstruction," *SPIE*, San Diego, 2012, accepted.

[15] Z. Tian, X. Jia, B. Dong, Y. Lou, and S. B. Jiang, "Low-dose 4dct reconstruction via temporal nonlocal means,," *Med. Phys.*, vol. 38, pp. 1359-1365, 2008.

An Open Database of Metal Artifact Cases for Clinical CT Imaging

Jan Mueller, Frederik Kaiser, Yulia M. Levakhina, Maik Stille, Imke Weyers, Thorsten M. Buzug

***Abstract*—Metal artifacts are a big problem in (medical) Computed Tomography because they severely degrade the diagnostic value of clinical CT images. During the last decades a large number of different approaches have been presented in literature. Unfortunately, until now it was impossible to compare different results from literature since each research group uses a different set of projection data and reconstruction methods. Therefore, a project has been started towards an open standard database of clinical metal artifact cases from body donors. It will include a large variety of different metallic implant cases and allows for evaluating the performance of metal artifact reduction methods in different situations. To fill the database, each implant is scanned several times with different scan settings in order to determine the influence of scan parameters on metal artifacts. To make the evaluation and comparison as easy as possible, a free and open source reconstruction software will provided in course of the project as well. This will enable researches from fields not directly related to tomography to try ideas on real CT data.**

I. INTRODUCTION

Since Computed Tomography (CT) has been transformed from a brain-only imaging modality into a full body procedure, metal artifacts in the reconstructed images became a severe problem in medical applications. Depending on the scanner, the specific scan protocol and the size and location of a metallic object inside the patient, important morphological features are hidden behind metal artifacts. As it can be seen throughout this publication, these artifacts appear in different forms and shapes. In almost all cases, fine streak artifacts originate at the location of the metal and cover large parts of the image. In addition, bright and dark shadow-like structures appear around the implant. If more than one metallic object or some other dense material is present, these objects are often connected by dark bands.

The main reasons for metal artifacts are i) excessive noise in the measured intensity data due the high absorption of the metal, and sinogram inconsistencies resulting from ii) scattered radiation and iii) beam hardening. While the excessive noise is the main reason for the streak artifacts (see Figure 1 and 2), both sinogram inconsistencies result in shadow-like structures around and between the objects. In the worst case scenario, a metallic object so thick such that no photons arrive at the detector. This means that all the information from these beams is lost and therefore cannot be used for reconstruction. This results in even stronger artifacts. The exact amount of influence each error has on the image artifacts depends on the type of metal, its thickness and form, the spectrum of the incoming X-rays, the detector geometry, the presence of anti-scatter grids and other factors.

Based on this reasons, metal artifacts can be reduced in theory by increasing the dose, by implementing anti-scatter grids, and by narrowing the spectrum of the X-ray tube by strong pre-filtration. Unfortunately, in most situations these measures cannot be fully applied because of dose concerns for the patient or for technical reasons.

In combination with the fact that nowadays a large variety of metal implants like dental fillings, pacemaker, bone screws and plates, stents, aneurysm coils and artificial joints are likely to be present in a patient, other ways of metal artifact reduction have to be found.

One of the first approaches to MAR was introduced by Kalender et al. in 1987 [1]. It is based on the idea that all beams intersecting with a metallic object are considered invalid. The values of these invalid beams are replaced by new values derived from valid beams in the immediate neighborhood by linear interpolation. Although this removes typical metal artifacts, it often introduces a large number of new artifacts. Especially regions far away from the metal where no artifacts were present in the reconstruction with metal artifacts are now degraded by those new artifacts.

In order to improve these results, a lot of different methods of metal artifact reduction have been developed during the last decades. Some of these methods are direct extensions of the sinogram repair method. Instead of using linear interpolation, the missing data is derived via more advanced interpolation schemes. Some examples are: Wavelets [2], NFFT [3], and sinogram inpainting [4]. Other approaches extend the sinogram repair approach even further by introducing a normalization step [5], [6] which simplifies the interpolation.

In addition to the sinogram repair approach, a lot of conceptually different methods have been developed. Some examples are: the combination of the original and repaired images [7], tissue classification [8], and adapted iterative reconstruction algorithms [9], [10].

Most of these metal artifact reduction methods seem to be able to reduce the amount of metal artifacts. Unfortunately, until now it was impossible to compare the results from different publications because each research group uses different datasets, different resolutions, different level/window settings, and different reconstruction methods and kernels to demonstrate their results.

Therefore, the initial stages of an open database of medical

J. Mueller and T. M. Buzug are with the Institute of Medical Engineering, University of Luebeck, Luebeck, Germany (e-mail: buzug, mueller@imt.uni-luebeck.de)

M. Stille and Y. M. Levakhina are with the Graduate School for Computing in Medicine and Life Sciences and Institute of Medical Engineering, University of Luebeck, Luebeck, Germany

I. Weyers is with the Institute of Anatomy, University of Luebeck, Germany

CT scans is presented which can be used in future studies as a simple way to compare the performance of existing and new MAR methods in clinical CT applications.

To make this comparison as easy as possible, a free and cross-platform reconstruction program will provided in addition to the measured data. It can be used to reconstruct 2D CT data for all three standard geometries (parallel beam, fan-beam with curved and flat detector) with different standard reconstruction methods (FBP, ART, SPS, ...). The reconstruction software is based on a more general 2D CT reconstruction framework called *libct2d* which will be available as well.

The paper is organized as follows. The database and the reconstruction software are described in section 2 and 3. Some example cases from the database are shown in section 4. The work is then concluded by an outlook on future developments.

II. THE DATABASE

In its current state, the database consists of a large number of projection data acquired with a Siemens Somatom Definition AS. To provide as realistic data as possible, currently the bodies of 5 body donors have been scanned. In addition, a custom abdomens phantom[1] was scanned with and without different steel rod inserts in different configurations.

The projection data is available in its original fan-beam geometry, but it can be rebinned into other geometries with the help of a command line tool. This will be helpful in situations in which custom reconstruction algorithms should be tested.

The data is stored in .mat MATLAB files which allows easy access from the most popular scientific programming languages (MATLAB/Octave/Freemat, Python in combination with NumPy/SciPy, and C/C++ with the matio library). For those languages which do not support .mat files, the data can also be converted into a well-documented binary format.

A. Body Donor Scans

Currently, the database consists of a large number of scans done with 5 body donors. Each metallic implant was completely scanned under different scan settings. All scans have been acquired with a Siemens Somatom AS scanner. The cases and the respective scanner settings are described in Table I. Some legal details on the work with body donors in Germany can be found at the end of the paper.

B. Abdomen Phantom Scans

The abdomen phantom has a width of 30 cm and a height of 20 cm. It consists mainly of water equivalent plastic. Two low-contrast regions simulate organs. In addition an optional insert simulates a spine. Rods made of stainless steel (5, 7, 10, and 13 mm diameter) can be inserted into 9 different locations.

This relatively simple phantom has several advantages over real patient data. Most important, a phantom made out of plastic is the only viable mean to scan an object with and without metal without deformation between the scans. Therefore, the scan without metal can be used as the ground truth during an evaluation. In addition, the simple structure of the phantom makes the task of metal artifact reduction less demanding than it is for real data. Therefore, this data can be used as a first step to try new ideas. In addition, the simple structure makes it easier to find the source of new artifacts, which a metal artifact algorithm might introduce into the image.

Table I: An overview of all available datasets.

Case	Metal	Scan Settings
1	Dental implants	120 kV, 200 and 550 mAs
2	Pacemaker	120 kV, 200 and 550 mAs
	Dental implants	120 kV, 200 and 550 mAs
3	Artificial knee joint	80 - 140 kV kV, 100 - 400 mAs
	Artificial hip joints	80 - 140 kV kV, 100 - 400 mAs
4	Pacemaker	80 - 140 kV kV, 150 - 400 mAs
	Metal wire in chest	80 - 140 kV kV, 150 - 400 mAs
	Artificial hip joints	80 - 140 kV kV, 220 - 550 mAs
5	Artificial knee joints	80 - 120 kV, 100 - 350 mAs
	Artificial hip joint	80 - 140 kV, 100 - 400 mAs

The provided phantom data consists of two parts. In the first part, different configurations of metal rods have been scanned with four typical scan settings in order to simulate small and big metal artifacts. In addition, one configuration was scanned with a large number of combinations for tube voltage and tube current. This allows the study of the properties of metal artifacts under different settings.

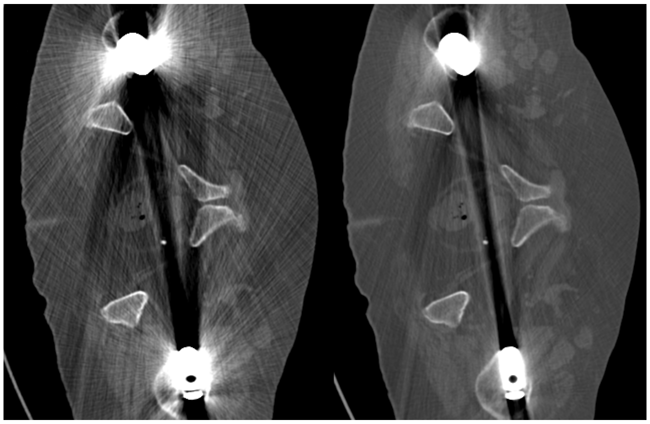

Figure 1: Two scans of the same hip implants with different scan settings. Left image: 80 kV, 550 mAs, right image: 140 kV, 200 mAs. The level/window setting is 300/1500 HU.

III. THE RECONSTRUCTION SOFTWARE

To enable simple reconstruction of the provided data, the database will include a 2D CT reconstruction software package. It is based on a new software framework for 2D CT reconstruction called *libct2d*.

The main goal of this software project is to provide an easy to understand basis for the development of new 2D CT algorithms (for example: reconstruction algorithms, metal artifact reduction, sinogram and image denoising, ...). This allows researchers from fields outside the topic of CT to test their image processing methods (image inpainting, image denoising, ...) on real CT data.

---

[1] Made by QRM - www.qrm.de.

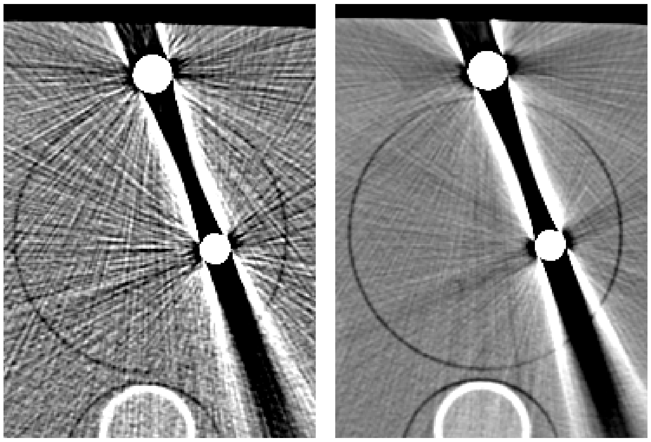

Figure 2: Two scans of the same phantom with different dose. Left: 50 mAs, right: 550 mAs. The level/window setting is 50/300 HU.

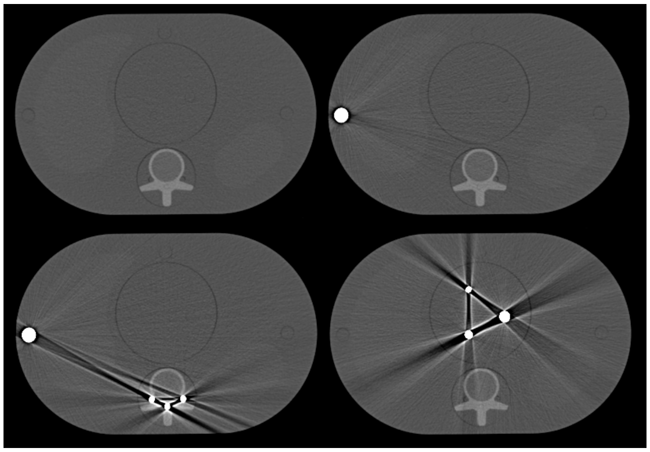

Figure 3: Some example for different rod configuration of the abdomen phantom. The level/window setting is 300/1500 HU.

The main key features of the library and the reconstruction software are:

- All software will be provided for free and it will run on all three major operating systems (Microsoft Windows, Linux and Mac OS X)
- The entire framework is designed with simplicity in mind. The source code is easy to understand and well documented. This will make it easy to start developing.
- It is designed as a standalone library so no external dependencies have to be installed and configured.
- The library includes the three major 2D geometries: parallel beam and fan-beam with curved and flat detector and can be adapted to other geometries.
- It also includes all the standard reconstruction methods: FBP, ART, and several iterative statistical algorithms.
- For iterative reconstruction it provides the most common forward- and backprojection operators (pixel-driven, line-driven, ray-casting, distance-driven, ...).

To reach these goals, the core library and the reconstruction programs are written in pure C++. To enable cross-platform support, the software is built with the CMake[2] system which simplifies development on all three major platforms by supporting a lot of different popular compiler and development environments (gcc/make, Microsoft Visual Studio, XCode, Eclipse, ...). In addition to the C++ version, wrapper libraries for Python and MATLAB are in development. This will give users the best of two worlds: all fast forward-/backprojection and reconstruction methods written in C++ can be combined with easy development and rapid development in both scripting languages.

In order to simplify the development process and to encourage external contributions, the complete software development is hosted on GitHub[3]. GitHub is a platform for collaborative develoment and is built around the version control software git[4]. It is used by a large number of well known open-source software projects.

IV. Results and Discussion

A. Body donor scans

Since the final configuration of the first public version of the database is not completed yet, only a few example cases are shown here. In Figure 1, the same hip implants are scanned in exactly the same location with two different settings. As it can be seen, there are more streak artifacts in the 80 kV, 550 mAs image. In addition, the shadow like structures around the objects are reduced in the 140 kV, 200 mAs scan.

B. Abdomen phantom

In Figure 2 and 3 some example scans of the abdomen phantom are shown. As it can be seen in the first image, the streak artifacts can be reduced by increasing the dose. In addition it can also be seen, that the dark band between the steel rods objects are not influenced by the amount of dose at all.

V. Conclusions and Outlook

In this work, a short overview over a project for developing a free and open database for clinical metal artifact cases was given. Its main goal is to provide a free set of reference cases for metal artifact reduction to allow a more methodically comparison between approaches of different research groups. Because of the open nature of the project it can be used as a base for new algorithms and it also allows scientists from completely unrelated areas to apply their image processing methods on real CT data.

One of the main goals for the future is to provide even more test and to enlarge the focus into non-medical applications. Since most non-medical applications are based on 3D cone beam acquisition the presented software has to be extended into the third dimension.

---

[2] www.cmake.org

[3] www.github.com

[4] www.git-scm.com

NOTE

The human cadavers - respectively bodies/heads/arms/legs feet etc. as parts of cadavers - were used and dissected in this examination under permission of the ”Gesetz ber das Leichen-, Bestattungs- und Friedhofswesen (Bestattungsgesetz) des Landes Schleswig-Holstein vom 04.02.2005, Abschnitt II, 9 (Leichenoeffnung, anatomisch)”. In this case it is allowed to dissect the bodies of the donators (Koerperspender/in) for scientific an/or educational purposes.

REFERENCES

[1] W. Kalender, R. Hebel, and J. Ebersberger, “Reduction of ct artifacts caused by metallic implants.” *Radiology*, vol. 164, no. 2, pp. 576–577, 1987.

[2] S. Zhao, D. Robeltson, G. Wang, B. Whiting, and K. Bae, “X-ray ct metal artifact reduction using wavelets: an application for imaging total hip prostheses,” *Medical Imaging, IEEE Transactions on*, vol. 19, no. 12, pp. 1238–1247, 2000.

[3] B. Kratz, S. Ens, J. Müller, and T. Buzug, “Reference-free ground truth metric for metal artifact evaluation in ct images,” *Medical Physics*, vol. 38, p. 4321, 2011.

[4] X. Duan, L. Zhang, Y. Xiao, J. Cheng, Z. Chen, and Y. Xing, “Metal artifact reduction in ct images by sinogram tv inpainting,” in *Nuclear Science Symposium Conference Record, 2008. NSS’08. IEEE.* IEEE, 2008, pp. 4175–4177.

[5] J. Müller and T. Buzug, “Spurious structures created by interpolation-based ct metal artifact reduction,” in *Proceedings of SPIE*, vol. 7258, 2009, p. 72581Y.

[6] E. Meyer, R. Raupach, M. Lell, B. Schmidt, and M. Kachelrieß, “Normalized metal artifact reduction (nmar) in computed tomography,” *Medical physics*, vol. 37, p. 5482, 2010.

[7] O. Watzke and W. Kalender, “A pragmatic approach to metal artifact reduction in ct: merging of metal artifact reduced images,” *European radiology*, vol. 14, no. 5, pp. 849–856, 2004.

[8] M. Bal and L. Spies, “Metal artifact reduction in ct using tissue-class modeling and adaptive prefiltering,” *Medical physics*, vol. 33, p. 2852, 2006.

[9] G. Wang, D. Snyder, J. O’Sullivan, and M. Vannier, “Iterative deblurring for ct metal artifact reduction,” *Medical Imaging, IEEE Transactions on*, vol. 15, no. 5, pp. 657–664, 1996.

[10] M. Oehler and T. M. Buzug, “Statistical image reconstruction for inconsistent ct projection data,” *Journal of Methods of Information in Medicine*, vol. 3, pp. 261–269, 2007.

Low–Contrast Visibility in Flat Detector CT: A Simulation Study

Michael Knaup, Ludwig Ritschl, and Marc Kachelrieß

Abstract—**Flat detector CT suffers from a limited visibility of low–contrast objects. On the one hand this is due to increased image noise and x–ray scatter, on the other hand this can be attributed to a limited dynamic range of current flat detectors. Compared to clinical CT detectors with their energy absorption efficiency of 90% or more and their dynamic range of 20 bits or more, flat detectors with their energy absorption efficiency around 50 or 60% and their dynamic range of 10 to 12 bits above the noise floor are significantly inferior. Further on, often intended or unintended over– or underexposure occurs in flat detector CT systems, resulting in undesired effects on image quality. To explore the situation we conduct a simulation study that systematically analyzes the effects of limited dynamic range and of over– or underexposure on CT image quality in general and on low–contrast visibility in particular.**

I. INTRODUCTION

Low–contrast objects, like cerebral hemorrhages for example, often are difficult to reveal with flat detector CT systems. While clinical CT systems clearly show objects with very low contrast, say 3 HU, the detectability in flat detector systems is significantly limited and only medium–contrast details (30 HU or more) can be seen. There are several reasons of why this is the case. Scattered radiation in flat detector CT is more dominant than in clinical CT. The absorption of photons in flat detectors is much lower than the absorption efficiency of clinical CT detectors. Both facts yield a decreased contrast combined with increased image noise (given the same patient dose as in clinical CT). Furthermore, the dynamic range of the flat detectors is limited by the capacity of the pixel's photodiode or by the capacity of the read–out capacitors [1], [2]. Under good conditions such detetectors deliver about 10 to 12 effective bits (above the noise floor). Over– or underexposure often occurs in such systems, with undesired effects on CT image quality.

For CT systems which are dominated by quantum noise, it can be shown that an analog square root amplifier results in an optimal detector sampling [3], [4]. However, in this study we will concentrate on electronic noise and the detector dynamic range and therefore assume that quantum noise plays a subordinate role.

II. SIMULATION

To simulate the effects of limited detector dynamics we assume a monochromatic 70 keV x–ray spectrum and perform the simulations and reconstructions in 2D parallel geometry with 512 projection angles and 512 rays per projection. Each ray in parallel geometry is parametrized by the two parameters ϑ and ξ such that $x\cos\vartheta + y\sin\vartheta = \xi$ is the line of integration in the x–y–plane.

Our simulation uses two rawdata sets. One generated by analytical forward projection of a modified Forbild head phantom, and one generated by forward projection of a clinical CT image. Compared to the original Forbild head phantom [5] we added eight additional 5 mm low–contrast spheres with positive and negative contrasts relative to the 50 HU brain matter background. Close to the ±2.5 HU low–contrast inserts in the posterior brain region of the original phantom these eight additional spheres of the modified phantom have contrasts of ±5.0 HU, ±10 HU, ±15 HU and ±20 HU. This extended range of low–contrast objects allows us to easily visualize and quanitfy the low–contrast detectability.

The line integrals obtained from these simulations are denoted as $p(\vartheta, \xi)$. These rawdata are considered to be ideal rawdata. In subsequent steps we will deteriorate the data by adding noise and simulating overexposure and discretization of AD converters, as explained in the following subsections.

A. Relative Intensities

The simulated line integrals $p(\vartheta, \xi)$ are converted into relative intensities as

$$q_0(\vartheta, \xi) = e^{-p(\vartheta, \xi)}\,.$$

Since these and all following manipulations are done detector pixel–wise we will drop the dependency on ϑ and ξ in the following,

B. Scaling

It is interesting to study how the low–contrast visibility changes as a function of object size. To do so, we introduce a scale factor $s > 0$ and use s to convert the relative intensities as

$$q_1 = q_0^s.$$

This scaling operation can also be regarded as applying some kind of gamma function to the relative intensities and therefore may have significant impact on AD conversion (which is typically done in intensity domain).

We will below use scaling to convert the data from patient imaging ($s = 1$) to small animal imaging ($s = 0.2$).

Dr. Michael Knaup, Ludwig Ritschl: Institute of Medical Physics, University of Erlangen–Nürnberg, Henkestr. 91, 91052 Erlangen, Germany.

Prof. Dr. Marc Kachelrieß: Medical Physics in Radiology, German Cancer Research Center (DKFZ), Im Neuenheimer Feld 280, 69120 Heidelberg, Germany.

Corresponding author: michael.knaup@imp.uni-erlangen.de

C. Quantum Noise

We now add quantum noise as follows:

$$q_2 = q_1 + N()\sqrt{q_1/I_0}.$$

Here, $N()$ is a normal–distributed random number with mean 0 and standard deviation 1. I_0 is the number of detected quanta if no object was in the x–ray path and if the detector had no saturation limit. For this study, we chose a fixed $I_0 = 2.7 \times 10^7$ for all simulations. With this I_0, we obtain an image noise of 5 HU in the soft tissue region of the reconstructed head phantom in its original size (scale $s = 1$).

D. Gain Factor

The detector gain factor describes how the signal is amplified before it is being converted to digital values. A gain chosen too high results in detector regions that are saturated due to overexposure. A gain chosen too low implies that the dynamic range provided by the detector is not fully used.

Here we define the gain factor $g > 0$ as follows: Let I_S be the number of x–ray quanta required to bring the detector into saturation. Then we define $g = I_0/I_\mathrm{S}$. With this definition, for $g = 1$ the x–ray exposure and the detector properties are well matched: no saturation occurs and the full dynamic range of the detector is utilized. Typically, one would choose this optimal case of $g = 1$. However, we will see below that an intended overexposure with $g > 1$ may help to visualize low–contrast details.

The gain is simulated by multiplying the noisy intensity data q_2 with the gain factor g.

$$q_3 = g\,q_2.$$

E. AD Conversion and Saturation

Up to now, we performed all calculations in double precision which can be considered as an infinite precision compared to the actual detector resolution. In this step, we assume that the detector has a limited precision of b significant bits, i.e. it can deliver only 2^b distinct values. We simulate discretization and saturation by the following formulae:

$$\begin{aligned} q_4 &= q_3 + U()\,2^{-b}, \\ q_5 &= \varepsilon \vee \frac{\lfloor q_4(2^b-1) + \frac{1}{2} \rfloor}{2^b - 1} \wedge 1. \end{aligned}$$

Here, $U()$ is a uniformly distributed random number in the interval $[-\frac{1}{2}, \frac{1}{2}]$ which simulates noise in the least significant bit of the AD converter. The maximum function clips to the small positive ε to avoid q_5 gets zero (which would make trouble when taking the log in the next step). The minimum function clips the digitized value to the maximum relative intensity 1 which corresponds to a saturation at $I_\mathrm{S} = I_0/g$ quanta. The discretization scheme is illustrated in figure 1.

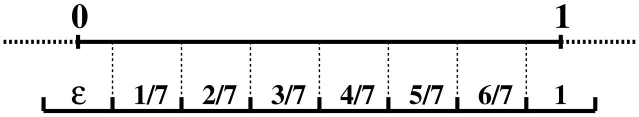

Fig. 1. Analog to digital conversion for the example $b = 3$. Upper line: Analog signal q_4. Lower line: Digital signal q_5.

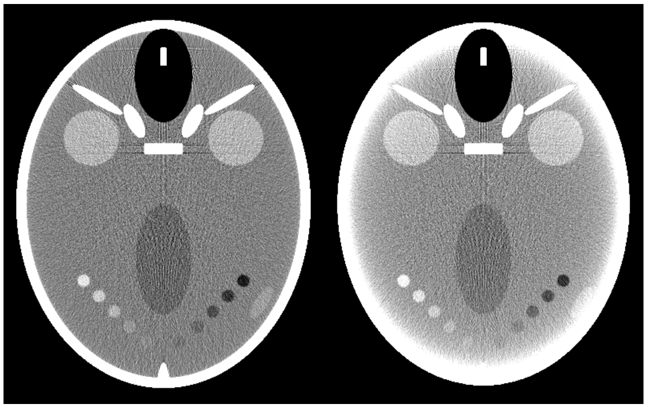

Fig. 2. Left: Standard image with gain factor $g = 1$. Right: Overexposed image with gain factor $g = 4$ as it would look without detruncation. (C/W) = (50/50).

F. Logarithm

Finally, the logrithm will be taken to convert from intensity values to line integrals which are needed for filtered backprojection. Here, one must not forget to account for the gain factor. In addition, overexposure is detected and overexposed values are set to zero. This yields

$$p_6 = \begin{cases} 0 & \text{if } q_5 = 1 \\ \ln g - \ln q_5 & \text{if } q_5 < 1. \end{cases} \tag{1}$$

G. Detruncation

For a gain factor $g > 1$, detruncation should be performed, since line integrals p_6 will be set to zero if the intensity q_2 is greater than $1/g$. This effect occurs mainly at the borders of the object where attenuation is small. It is similar to a truncation effect where the detector is too small to cover the whole object and attenuation outside the detector is assumed to be zero (see figure 2).

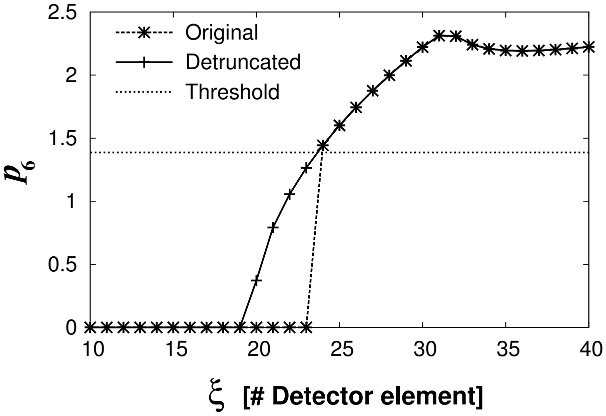

Fig. 3. Detruncation for the case of a gain factor $g = 4$. The detruncation must be performed since all attenuation values below a threshold of $\ln g$ will be set to zero in equation (1).

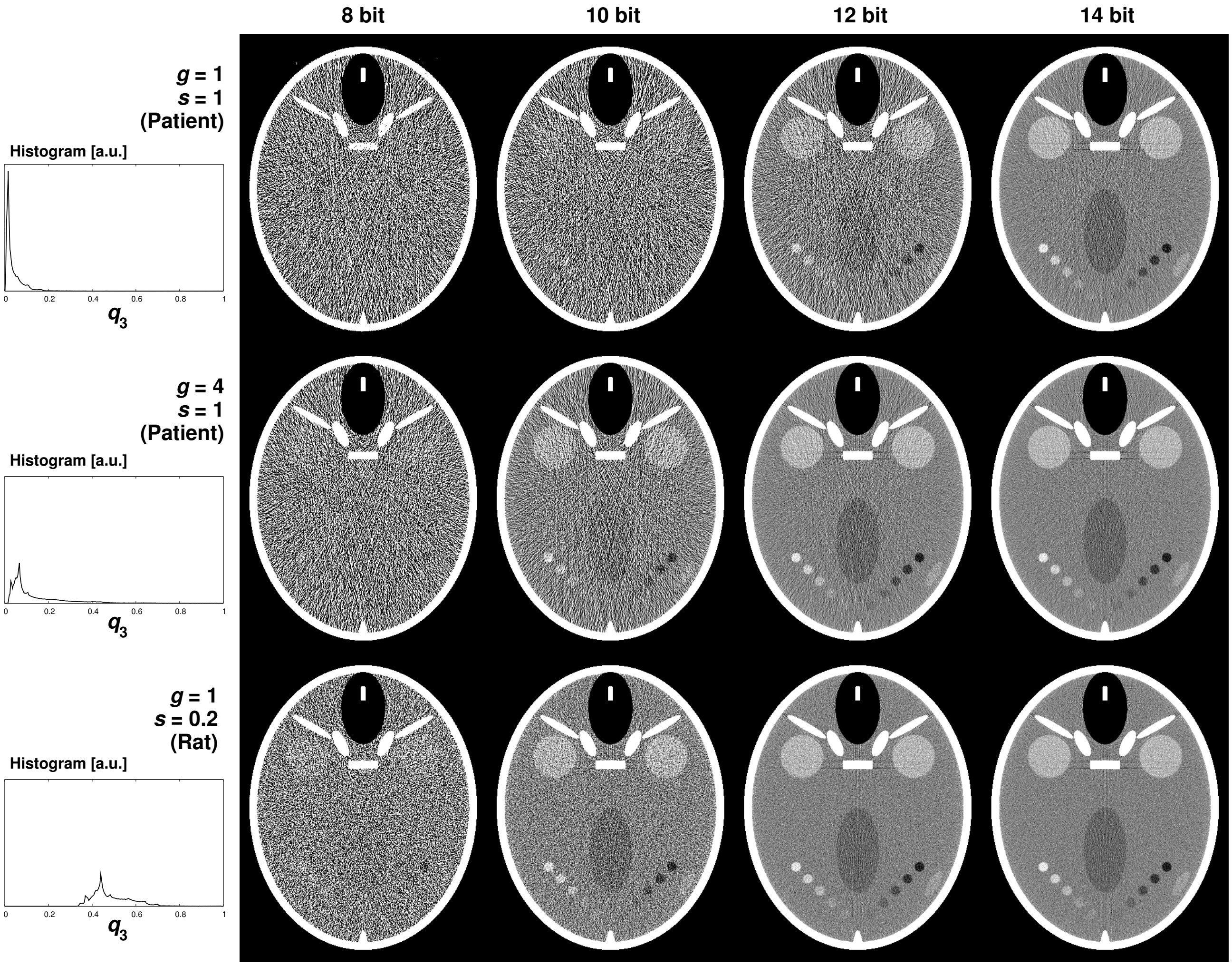

Fig. 4. Modified Forbild head phantom. Top row: Gain $g = 1$, scale $s = 1$ (standard exposure, patient imaging). Middle row: $g = 4$, $s = 1$ (intended overexposure, patient imaging). Bottom row: $g = 1$, $s = 0.2$ (standard exposure, small animal imaging). From left to right: Histogram of analog signal q_3, $b = 8$ bits, 10 bits, 12 bits, 14 bits. (C/W) = (50/50).

For this study, we applied a detruncation algorithm [6] detector row–wise (figure 3). In case of hollow projections, i.e. gaps due to overexposure close to the center of a projection, we propose to bridge these gaps by linear interpolation. In our simulations, however, hollow projections did not appear.

H. Reconstruction

The final rawdata were reconstructed using parallel beam filtered backprojection with a RamLak kernel.

III. RESULTS

Figure 4 shows the results for the simulated modified Forbild head phantom. It compares the situations $g = 1$, $s = 1$ (standard exposure, patient imaging), $g = 4$, $s = 1$ (intended overexposure, patient imaging) and $g = 1$, $s = 0.2$ (standard exposure, small animal imaging) for various values of b.

It is interesting, but not surprising, that the images that are overexposed by a factor of $g = 4$ taken with b true bits are comparable to the images without overexposure taken at $b + 2$ bits. Obviously, given a certain detector low–contrast detectability can be improved in certain situations by overexposing the detector.

It is also interesting to see, that the change in scale by a factor of five results in significantly different images. While the large patient data require a higher detector dynamic range, the small animal size data can do with less bits. Hence, one may apply an optimal analog gamma function to the data prior to doing the AD conversion in order to improve image quality.

Figure 5 shows similar results for patient images. Since detruncation by detector extrapolation works better for the mathematical phantom, the preprocessing with gain factor $g = 4$ suffers evidently from the truncation effect. On the other hand, low–contrast visibility is improved again by applying the overexposure. Again, the small animal size data require less detector dynamic range.

IV. SUMMARY AND CONCLUSIONS

We analyzed and demonstrated the influence of detector quantization and of overexposure on low–contrast detectability. An analog gain factor will improve low–contrast visibility at the price of truncation artifacts which must be corrected.

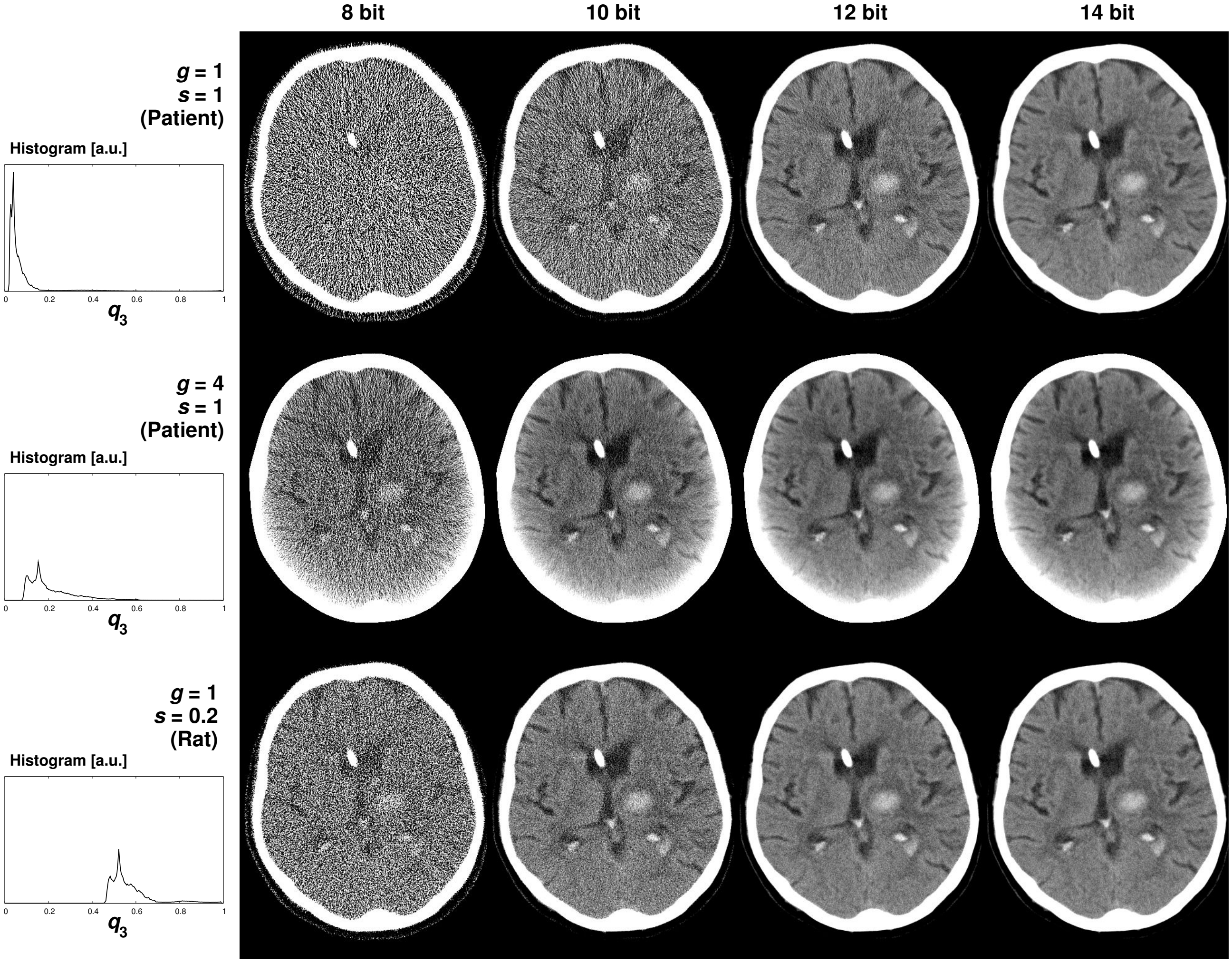

Fig. 5. Patient images of a cerebral hemorrhage with contrast agent. Same layout as figure 4. (C/W) = (40/100).

Imaging on the scale of small animals requires a lower dynamic detector range than imaging on the larger scale of a patient. This might be utilized by applying an analog gamma amplifier prior to digitalization for patient imaging.

ACKNOWLEDGMENT

This work was supported by the Deutsche Forschungsgemeinschaft under grant FOR 661. The reconstruction software was provided by RayConStruct® GmbH, Nürnberg, Germany. The patient images were provided by Prof. Dr. med. Arnd Dörfler, Friedrich-Alexander-University, Erlangen, Germany.

REFERENCES

[1] P. G. Roos, R. E. Colbeth, I. Mollov, P. Munro, J. Pavkovich, E. J. Seppi, E. G. Shapiro, C. A. Tognina, G. F. Virshup, J. M. Yu, G. Zentai, W. Kaissl, E. Matsinos, J. Richters, and H. Riem, “Multiple gain ranging readout method to extend the dynamic range of amorphous silicon flat panel imagers,” *SPIE Medical Imaging Proc.*, vol. 5368, pp. 139–149, 2004.

[2] M. Mase, S. Kawahito, M. Sasaki, Y. Wakamori, and M. Furuta, “A wide dynamic range cmos image sensor with multiple exposure-time signal outputs and 12-bit column-parallel cyclic a/d converters,” *IEEE Journal of Solid–State Circuits*, vol. 40, no. 12, pp. 2787–2795, Dec. 2005.

[3] P. J. Bjorkholm, “Use of a square root amplifier for statistics limited data,” 1984, uS Patent Application 4482957.

[4] M. Bieniosek, “A square root analog to digital converter to optimally convert photonic signals for computed tomography,” Master Thesis, Massachusetts Institute of Technology, 2010.

[5] www.imp.uni erlangen.de/phantoms/head/head.html.

[6] K. Sourbelle, M. Kachelrieß, and W. A. Kalender, “Reconstruction from truncated projections in CT using adaptive detruncation,” *European Radiology*, vol. 15, no. 5, pp. 1008–1014, May 2005.

Optimizing the Antiderivative of X–Ray Differential Phase Contrast Data for Tomographic Reconstruction.

Ludwig Ritschl, Stefan Sawall, Sören Schüller, Andre Ritter, Florian Bayer, Thomas Weber, Georg Pelzer, Lukas Wucherer, Jens Rieger, Karl Gödel, Jürgen Durst, Thilo Michel, Gisela Anton, Wilhelm Haas, Tobias Bäuerle and Marc Kachelrieß

Abstract— **Grating–based differential phase contrast (DPC) imaging is a promising imaging modality which emerged in the last years. The acquisition of projection samples of an object from different view angles allows for tomographic reconstruction. Due to the fact, that the measured projection values represent the derivative of the phase signal, usually an integration of the data is performed before reconstruction. In this paper we present a new approach to do this. Instead of performing an analytic integration we iteratively solve a constrained cost function. This enables to include some *a priori* knowledge into this process, which makes the result less sensitive to non–idealities in the projection data. Especially larger areas of low visibility lead to an ill-posed problem for tomographic reconstruction. The method proposed compensates for these missing data by using redundancies between the absorption images and the integrated phase images. The reconstructed volumes of the phase distribution show strong improvements in terms of streak artifacts, which are caused by erroneous phase values in the projection data. The algorithm is evaluated using experimental tomographic grating–based DPC data.**

I. INTRODUCTION

The refractive index of any material can be expressed by the complex value $n = 1 - \delta + i\beta$. Absorption–based x–ray imaging only yields information about the imaginary part β. Grating–based differential phase contrast imaging (DPC) [1] is a promising way to measure information about the real part δ of the refractive index of an object. Compared to other approaches [2–4] grating–based DPC imaging using a Talbot–Lau interferometer also works with conventional x–ray tubes [1] and in compact setups [5, 6]. The use of grating–based DPC data as input data for computed tomography (CT) was shown in different publications in the last years [7, 8].

To reconstruct a distribution which represents the real part δ of an object, the phase information of the attenuated radiation has to be extracted from the measured intensity data. This procedure is called phase retrieval. In the grating–based setup this information can be gained by the so called phase stepping procedure [1], which yields the first derivative of the phase φ, the transmitted intensity I, which represents absorption effects, and the so called visibility V, which relates to the dark field. For tomographic reconstruction of δ integration of the phase derivative has to be performed.

Under ideal conditions this integration of differential phase data can be directly combined with the reconstruction using a modified filtered backprojection (FBP). Here the filter kernel $k(u) = \mathrm{sgn}(u)/2\pi i$ accounts for the differential nature of the measured phase signal. An equivalent way to reconstruct these data is performing an analytical integration followed by a standard FBP as in absorption CT.

There are different effects which make this integration unstable and create artifacts in the reconstructed CT volume: In case of truncated projection data the boundary conditions of the integration are not well defined. Quantum noise in the projection data [9] also leads to unknown boundary conditions, even

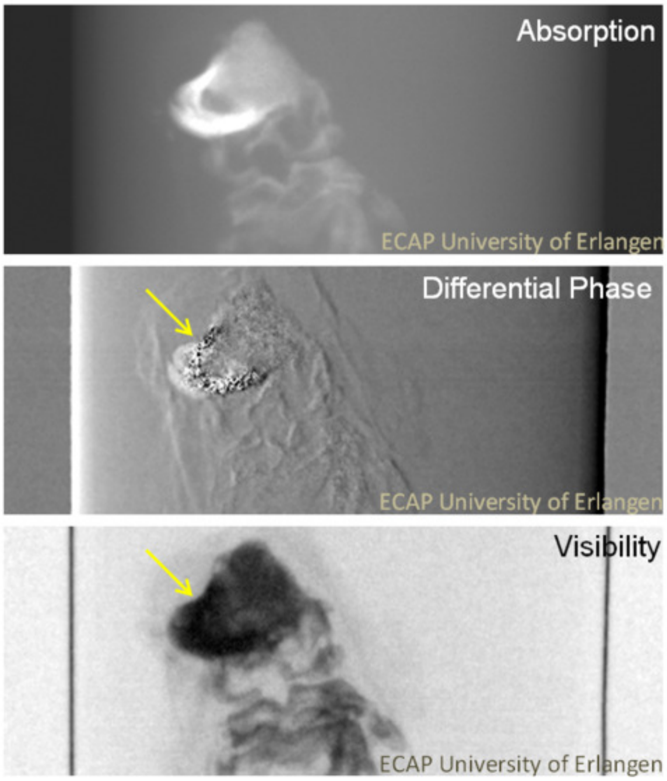
Absorption
ECAP University of Erlangen
Differential Phase
ECAP University of Erlangen
Visibility
ECAP University of Erlangen

Fig. 1. This figure shows the three different images acquired with a grating interferometer. The arrows mark areas of low visibility. In this area the differential phase image φ contains only random values.

Ludwig Ritschl, Stefan Sawall, Sören Schüller: Institute of Medical Physics (IMP), University of Erlangen–Nürnberg, Henkestr. 91, 91052 Erlangen.

Andre Ritter, Florian Bayer, Thomas Weber, Georg Pelzer, Lukas Wucherer, Jens Rieger, Karl Gödel, Jürgen Durst, Thilo Michel, Gisela Anton: Radiation Physics Group at the Erlangen Centre for Astroparticle Physics (ECAP), University of Erlangen-Nürnberg, Erwin-Rommel-Str. 1, 91058 Erlangen, Germany.

Wilhelm Haas: Pattern Recognition Lab, University of Erlangen-Nürnberg, Martensstr. 3, 91058 Erlangen, Germany.

Tobias Bäuerle and Marc Kachelrieß: Medical Physics in Radiology, German Cancer Research Center (DKFZ), Im Neuenheimer Feld 280, 69120 Heidelberg, Germany.

Corresponding author: Ludwig Ritschl, E–mail: ludwig.ritschl@imp.uni–erlangen.de

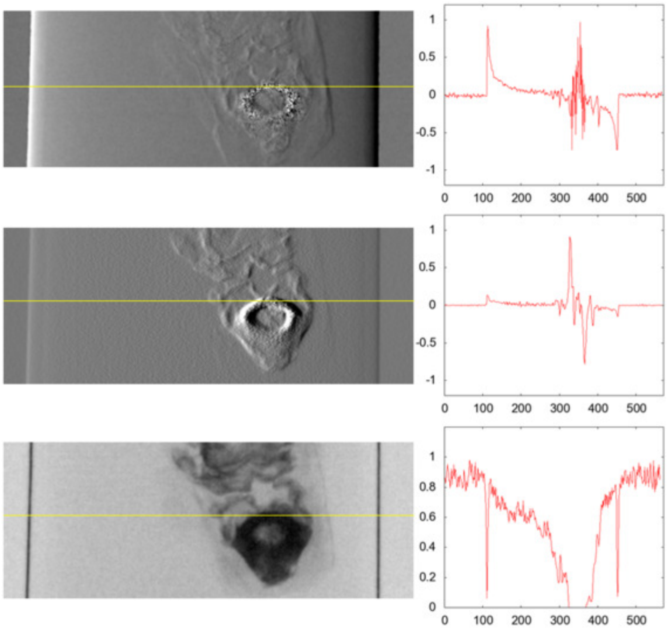

Fig. 2. Here the differential phase image φ (upper row), the first derivative of the absorption image $\partial_u q_A$ (middle row) and the visibility V (bottom) are shown. The greyscales of the upper two images are linear scaled to the interval $[-1,1]$ according to the maximum and minimum values in the corresponding images. The visibility image is normalized with respect to the V_0 image. The plots show the pixel position (x–axis) and the grey values (y–axis) across the yellow line. Note the high noise in the differential phase image in the areas of low visibility V.

in the case of non–truncated data. After integration the noise behaviour in integration direction is of a different characteristic than in other directions. This leads to streak artifacts in the integrated image which can also be present in the reconstructed CT volume, depending on the dose exposure. An exact description of this noise behaviour can be found in reference [10]. Not only noise but also the fact that the phase is a cyclic variable can lead to a wrong phase determination and inconsistent CT data. A method to correct for this artifact has been presented in [11].

Another aspect is the quality of the phase signal which can be measured by the visibility V. If V is small, the extracted phase signal is just a random variable and does not contain any physical information. This can be explained by a decrease of beam coherence by scattered radiation. That means, that pixels with a low visibility do not provide any meaningful information for the integration process. This effect can be seen in Figure 1 and 2. To show the influence of low visiblity on the differential phase signal φ, we compared φ with the first derivative of the absorption image (Figure 2). Here it can be seen, that reduced visibility leads to a higher noise level in the estimated phase values. If these high frequency fluctuations were caused by strong density variations inside the object, they would also have been visible in the absorption image, which is not the case. This observation also goes along with the theoretical relation between the noise level of φ and V [9]. The typically arising artifacts in the CT volume are streaks, which also degrade areas in the volume where the phase information is available. From a mathematical point of view one has to deal with an ill–posed problem which can only be solved using adequate *a priori* information.

The method presented in this paper will focus on handling image artifacts caused by low visibility areas in the projection images.

In reference [12] Thuering et al. presented an iterative approach for phase retrieval of differential phase contrast data with a focus on radiographic projection images. The approach presented here bases on this framework and extends it by using some additional *a priori* information.

II. METHOD

Let $\varphi(\vartheta, u, v)$ be the measured differential projection data. Here ϑ denotes the projection angle. The indices u and v represent the detector columns and rows. If the gratings are positioned parallel to the v-axis of the detector, the single phase steps are performed in u–direction. The corresponding extracted differential phase signal is

$$\varphi(\vartheta, u, v) = \frac{\partial q_P(\vartheta, u, v)}{\partial u}.$$

Here $q_P(\vartheta, u, v)$ is the phase signal, which is needed for tomographical reconstruction, because it can be regarded as a line integral consisting of phase information. The standard way to compute $q_P(\vartheta, u, v)$ is a simple numerical integration along u:

$$q_P(\vartheta, \hat{u}, v) = \int\limits_{u=0}^{u=\hat{u}} \varphi(\vartheta, u, v)\, du, \tag{1}$$

while this integral is realized as a summation of the measured discretized data. The method proposed here will handle this integration process as an optimization problem which can be solved iteratively. This enables us to include some prior knowledge which should compensate for the unwanted influence of the effects mentioned in the previous section. The cost function we like to optimize incorporates the attenuation information

$$q_A(\vartheta, u, v) = -\ln \frac{I(\vartheta, u, v)}{I_0(\vartheta, u, v)},$$

which is the logarithm of the normalized transmitted intensity, and the visibility map $V(\vartheta, u, v)$ into the calculation of $q_p(\vartheta, u, v)$ in form of a penalized weighted least square (PWLS) formulation. The cost function

$$C(q_P, q_A, V, \varphi) = C_1(q_P, V, \varphi) + \lambda \cdot C_2(q_P, q_A) \tag{2}$$

consists of two parts. Here

$$\begin{aligned} C_1(q_P, V, \varphi) &= ||\partial_u q_P(\vartheta, u, v) - \varphi(\vartheta, u, v)||_V^2 \\ &= \sum_{u,v,\vartheta} V^2(\vartheta, u, v)\,(\partial_u q_P(\vartheta, u, v) - \varphi(\vartheta, u, v))^2 \end{aligned}$$

is a weighted least square term. The minimizition of this term with respect to q_P leads to a weighted integration of $\varphi(\vartheta, u, v)$. The usage of $V^2(\vartheta, u, v)$ as diagonal elements of a weighting matrix reduces the significance of values with low visibility in the integrated image. The choice of V^2 can be motivated by the proportionality $\sigma_{\text{Phase}} \propto \frac{1}{V}$ [9] and the fact that weighting by the inverse variance $\frac{1}{\sigma^2}$ is the statistical optimal way to proceed.

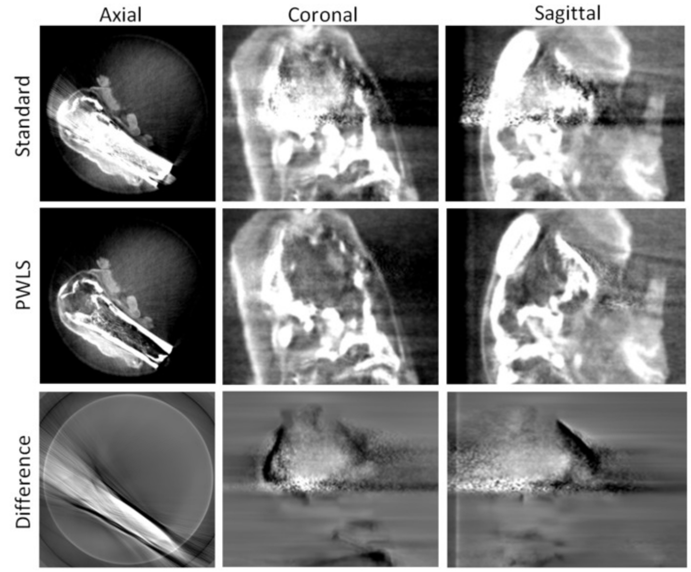

Fig. 3. Here axial, coronal and sagittal views of the reconstructed phase images are shown. Note the strong artifact reduction of the PWLS method compared to the standard reconstruction. All images are windowed $C = 50\%$ $W = 50\%$. The third row shows the difference images between the PWLS reconstruction and the standard reconstruction.

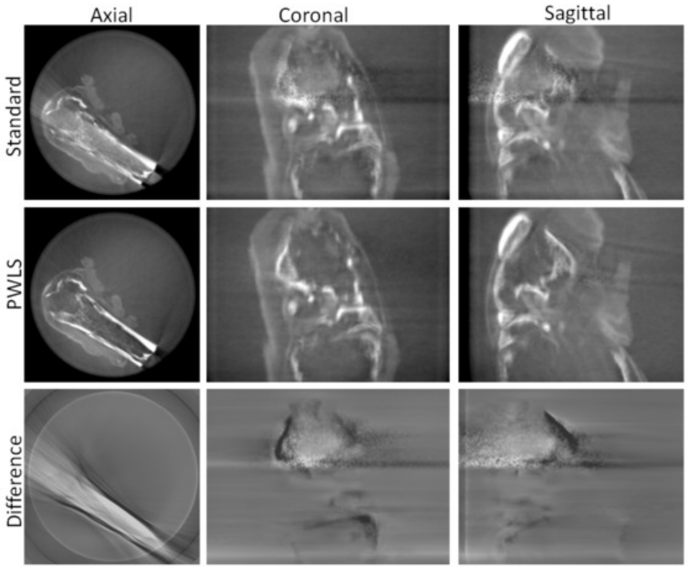

Fig. 4. Here the same slices as in Figure 3 are shown at a different window level ($C = 50\%$ $W = 100\%$).

The second term is an ℓ_1–norm prior as it is known from the compressed sensing [13] theory:

$$C_2(q_P, q_A) = (1-\alpha)||\nabla_{\vartheta,u,v}(q_P(\vartheta,u,v) - \gamma q_A(\vartheta,u,v))||_1 \\ + \alpha||\nabla_{\vartheta,u,v}(q_P(\vartheta,u,v)||_1$$

The first part enforces a similarity of edges in the absorption and the integrated phase image. The second part is a total variation prior [14]. It makes the solution more stable with respect to the unknown boundary conditions of the integration process, because the regularization in v– and ϑ–direction supresses high frequent fluctuations between neighboured detector rows and neighboured projection images. The factor γ matches the grayscales of $q_A(\vartheta,u,v)$ and $q_P(\vartheta,u,v)$ in a linear approximation. It was calculated in advance by minimizing

$$||\varphi(\vartheta,u,v) - \gamma\partial_u q_A(\vartheta,u,v)||_2^2.$$

For a correct calibrated system and a measured object consisting of only one material this factor should represent the mean relation between the real and the imaginary part of the refractive index. The parameter $0 \leq \alpha \leq 1$ is used as a linear weight between both prior functions. In this study $\alpha = 0.6$ was used.

The regularization parameter λ is a tuning parameter which controls the influence of the regularization function C_2. In this study it was evaluated empirically. The cost function was optimized using a standard conjugate gradient algorithm [15].

III. DATA PROCESSING

A. Data Acquisition

The method is evaluated using experimental tomographic grating–based DPC data. The measurements were conducted in the Radiation Physics Lab at the Erlangen Centre for Astroparticle Physics of the University of Erlangen–Nürnberg. The object scanned is a knee of a rat which was infiltrated by a tumor. The used tabletop system is a typical grating interferometer setup with a conventional x–ray tube including an absorption grating. The tube voltage during the measurements was set to 40 kV. To extract the phase and visibility information eight phase steps were performed for each view angle. The number of different projection views is 601. The exposure time per phase step was 6.6 s at a tube current of 50 mA.

B. Tomographic reconstruction

The reconstruction was performed using the standard Feldkamp-David-Kress (FDK) [16] algorithm. To compare the improvement of the PWLS–based integration method in the reconstructed images, we additionally performed a reconstruction based on the analytical integration formula (1). The iteration number of the PWLS integration was set to 100. At this iteration number only minor changes of the cost functional written in equation (2) were observed.

IV. RESULTS

In Figure 3 and 4 one can see the tomographical reconstruction of the acquired dataset. Here both integration techniques were used to enable a comparison. The reduction of streak artifacts which are caused by the strong scattering behaviour of the bone is clearly visible. The difference image shows, that there is no loss in spatial resolution or any corruption of soft tissue contrast. Figure 5 shows an enlarged area of the axial slice. Here it can obviously be seen, that the PWLS approach makes soft tissue areas visible which are otherwise corrupted by streak artifacts caused by the thick bone section aside.

V. DISCUSSION

To verify the robustness of the approach, further evaluations using different types of data sets have to be done. One assumption of the approach is that areas of low visibility still consist of

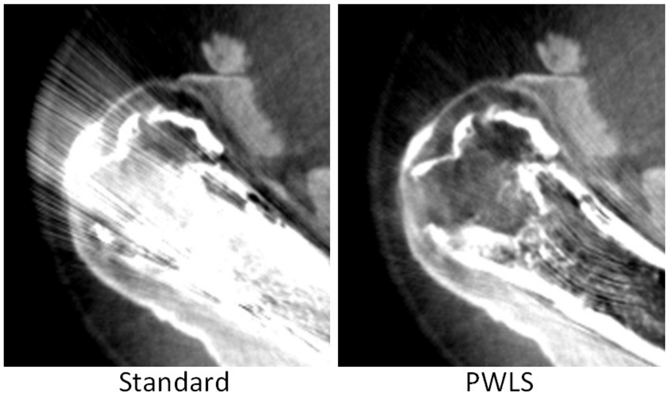

Standard PWLS

Fig. 5. Here an enlarged version of the axial slice is shown. Note the reduction of streak artifacts in the PWLS image which makes soft tissue structures more visible. The windowing is $C = 50\%$ $W = 50\%$.

information in the absorption image. In case of very low photon statistics, for example behind metal objects, this assumption does not hold any more. Handling such scenarios might be part of future investigations.

VI. CONCLUSION

To our knowledge the proposed method is the first, which tries to compensate for uncertainties in grating–based DPC tomography caused by partially low visibility of the input data. This incomplete data problem was compensated by the use of redundancies between the integrated phase image and the absorption image.

A part of future research will be finding other ways to use the dark field and absorption image for compensating incomplete or wrong phase information. One step will be the integration of the proposed framework into a fully iterative CT reconstruction algorithm which would enable the direct application of the penalty functions to the reconstructed volume.

We believe that this work is one important step towards *in vivo* grating–based DPC tomography of small animals because the corruption of the phase signal by strong scattering areas cannot be avoided.

ACKNOWLEDGMENTS

This work was supported by Ziehm Imaging GmbH, Nürnberg, Germany. The high–speed image reconstruction software RayConStruct–IR was provided by RayConStruct GmbH, Nürnberg, Germany. We thank the Intel Cooperation and Fujitsu Technology Solutions GmbH for providing their latest multicore hardware.

REFERENCES

[1] F. Pfeiffer, T. Weitkamp, O. Bunk and C. David, “Phase retrieval and differential phase-contrast imaging with low-brilliance x–ray sources,” *Nature Physics*, no. 2, pp. 258–261, 2006.

[2] S. Wilkins, T. Gureyev, D. Gao, A. Pogany and A. Stevenson, “Phase-contrast imaging using polychromatic hard x–rays,” *Nature*, no. 384, pp. 335-338, 1996.

[3] A. Momose, T. Takeda, Y. Itai and K. Hirano, “Phase-contrast x–ray computed tomography for observing biological soft tissues,” *Nature Medicine*, vol. 2, pp. 473-475, 1996.

[4] T. Davis, D. Gao, T. Gureyev, A. Stevenson and S. Wilkins, “Phase-contrast imaging of weakly absorbing materials using hard x–rays,” *Nature*, no. 373, pp. 595-598, 1995.

[5] T. Thuering, P. Modregger, T. Grund, J. Kenntner, C. David, M. Stampanoni , “High resolution, large field of view x–ray differential phase contrast imaging on a compact setup,” *Applied Physics Letters*, vol. 99, 2011.

[6] A. Tapfer, M. Bech, B. Pauwels, X. Liu, P. Bruyndonckx, A. Sasov, J. Kenntner, J. Mohr, M. Walter, J. Schulz, F. Pfeiffer, “Development of a prototype gantry system for preclinical x–ray phase-contrast computed tomography,” *Medical Physics*, vol. 38, no. 11, pp. 5910, 2011.

[7] F. Pfeiffer, O. Bunk, C. David, M. Bech, G. Le Duc, A. Bravin and P. Cloetens, “High-resolution brain tumor visualization using three-dimensional x–ray phase contrast tomography,” *Physics In Medicine and Biology*, vol. 52, no. 23, pp. 6923-6930, 2007.

[8] M. Bech, T. H. Jensen, R. Feidenhansï£¡l, O. Bunk, C. David and F.Pfeiffer, “ Soft–tissue phase–contrast tomography with x–ray tube sources,” *Physics in Medicine and Biology*, vol. 54, pp. 2747-2753, 2009.

[9] T. Weber, P. Bartl, F. Bayer, J. Durst, W. Haas, T. Michel, A. Ritter and G. Anton, “Noise in x-ray grating-based phase-contrast imaging,” *Medical Physics*, vol. 38, no. 7, pp. 4133-40, 2011.

[10] R. Raupach and T. Flohr, “Analytical evaluation of the signal and noise propagation in x–ray differential phase-contrast computed tomography,” *Physics In Medicine and Biology*, vol. 56, no. 7, pp. 2219, 2011.

[11] W. Haas, P. Bartl, F. Bayer, A. Ritter, T. Weber, G. Pelzer, J. Durst, T. Michel, M. Prümmer, and G. Anton, “Phase-unwrapping of differential phase-contrast data using attenuation information,” *Proceedings of SPIE*, pp. 79624R, 2011.

[12] T. Thüring, P. Modregger, B. R. Pinzer, Z. Wang and M. Stampanoni, “Non-linear regularized phase retrieval for unidirectional x–ray differential phase contrast radiography,” *Optics Express*, vol. 19, no. 25, pp. 25545, 2011.

[13] D. L. Donoho, “Compressd sensing,”*IEEE Trans. Inf. Theory*, vol. 52, no. 4, pp. 1289 - 1306, 2006.

[14] L. Rudin, S. Osher, and E. Fatemi, “Nonlinear total variation based noise removal algorithms”, *J. Phys. D*, vol. 60, pp. 259-268, 1992.

[15] S. Boyd and L. Vandenberghe. Convex Optimization. Cambridge University Press, 2004.

[16] L. Feldkamp, L. Davis, and J. Kress, “Practical cone beam algorithm,”*Journal of the Optical Society of America*, vol. 1, pp. 612-619, 1984.

A multi-modality software platform for image reconstruction

Samuel M. Johnston, G. Allan Johnson, and Cristian T. Badea*

Abstract—**We have developed a software platform for CT and MRI image reconstruction that combines GPU acceleration with a MATLAB interface. This platform enables the development of modality-general reconstruction algorithms composed of modality-specific modules. We describe one such algorithm, SART-BF, implement it with our platform, and apply it to data collected in simulations and in phantom studies with real CT and MRI systems. The results demonstrate that this implementation of SART-BF is sucessful at reducing noise while preserving edges in the reconstructed images from both CT and MRI data.**

Keywords-CT, MRI, reconstruction, GPU

I. INTRODUCTION

Medical imaging includes a diverse set of technologies, such as x-ray computed tomography (CT), positron emission tomography (PET), single photon emission computed tomography (SPECT), magnetic resonance imaging (MRI), and ultrasound (US). These modalities are based on a variety of different physical processes, and use sensors that measure these processes in a variety of formats. However, the algorithms for reconstructing images from the measured data share many common features. For example, many algorithms seek to iteratively maximize or minimize cost functions that quantify the agreement between the reconstructed image and the measured data, or the amount of noise or spurious features in the image. These algorithms require subroutines that map data between the measurement space and the image space, and these subroutines typically ev[*]ince a parallel structure that is an attractive target for optimization with parallel computer architectures.

Across all modalities, there is a perennial interest in developing new reconstruction algorithms to improve image quality, and to enable reductions in scan time, reconstruction time, and dosage of radiation and chemicals. However, this work is predominantly undertaken in modality-specific or device-specific contexts. While certain algorithmic patterns are shared by researchers in different modalities, code is rarely shared.

In recent years, there have been several efforts to address this problem. Dong *et al.* [1] present one such technology, a Unified Reconstruction Software Framework (URSF), and survey several other prior technologies, such as Software for Tomographic Image Reconstruction (STIR) (stir.sourceforge.net), Image Reconstruction Toolbox (IRT) (www.eecs.umich.edu/~fessler/code), and a sparse precomputed iterative reconstruction library (ASPIRE) (www.eecs.umich.edu/~fessler/aspire). These software frameworks differ in many ways, including their programming language, operating system, degree of parallelization, and applicable modalities.

In this study, we present our own work on a software platform for medical image reconstruction. This platform is written in C/C++ and exploits parallelization with a graphics processing unit (GPU). A MATLAB interface enables rapid algorithm development. Although originally designed for CT, we have used this platform for MRI reconstruction. We describe a typical iterative algorithm and measure its performance with simulated data and real data from CT and MRI.

II. ALGORITHM

Image reconstruction is an inverse problem. The interaction of the imaging device and the environment is given by a function A that maps the image vector $\mathbf{x}$ to the measurement vector $\mathbf{b}$.

$$A(\mathbf{x}) = \mathbf{b} \tag{1}$$

The goal of reconstruction is to find $\mathbf{x}$, given measurements $\mathbf{b}$ and prior system knowledge A. Some imaging modalities, such as CT and MRI, are well-approximated as linear systems, in which case $\mathbf{A}$ is a matrix.

$$\mathbf{Ax} = \mathbf{b} \tag{2}$$

In general, because of the size, shape, and conditioning of $\mathbf{A}$, neither the matrix inverse nor the pseudo-inverse are viable options. Instead, this problem can be solved iteratively. If we quantify the agreement between $\mathbf{x}$ and $\mathbf{b}$ with the data fidelity cost function K:

$$K = \left\| \mathbf{Ax} - \mathbf{b} \right\|_2 \tag{3}$$

then the following sequence is expected to converge to the $\mathbf{x}$ that minimizes K:

$$\mathbf{x}^{(n+1)} = \mathbf{x}^{(n)} + \mathbf{A}^{\mathrm{T}} \left(\mathbf{Ax}^{(n)} - \mathbf{b} \right) \tag{4}$$

The first element in the sequence, $\mathbf{x}^{(0)}$, can be produced by some other approximate reconstruction algorithm, or it can consist of some arbitrary values. The closer $\mathbf{x}^{(0)}$ is to the true value $\mathbf{x}$, the faster the convergence. To control the rate of convergence and improve numerical stability, a relaxation factor α is included:

$$\mathbf{x}^{(n+1)} = \mathbf{x}^{(n)} + \alpha \mathbf{A}^{\mathrm{T}} \left(\mathbf{Ax}^{(n)} - \mathbf{b} \right) \tag{5}$$

---

[*] Center for In Vivo Microscopy, Duke University, Durham, NC USA

This algorithm is generally known as gradient descent, but in the context of CT it is referred to as the simultaneous algebraic reconstruction technique (SART) [2].

While the sequence (5) is expected to improve the accuracy of **x**, it is agnostic with respect to the image statistics of **x**. In biological objects, we often expect to see a set of organs with a uniform composition over large regions, but distinct boundaries between these regions. For this reason, we introduce a regularization step that reduces variation within homogeneous regions while preserving boundaries between regions. In this study, we employ bilateral filtration (BF) [3], which replaces each pixel x_i with a weighted average of the neighboring pixels x_j:

$$F(x_i)=\frac{\sum_j \exp\left(-\frac{\left\|\mathbf{r}_i-\mathbf{r}_j\right\|_2}{2\sigma_d^2}\right)\exp\left(-\frac{x_i-x_j}{2\sigma_r^2}\right)x_j}{\sum_j \exp\left(-\frac{\left\|\mathbf{r}_i-\mathbf{r}_j\right\|_2}{2\sigma_d^2}\right)\exp\left(-\frac{x_i-x_j}{2\sigma_r^2}\right)} \tag{6}$$

Here, σ_d is the domain parameter, which weights the contributions of the neighboring pixels based on their distances $\left\|\mathbf{r}_i-\mathbf{r}_j\right\|_2$, and σ_r is the range parameter, which weights the contributions of the neighboring pixels based on differences in value x_i-x_j. The values of σ_d and σ_r are dependent on the particular imaging experiment. To control the strength of BF, we introduce another relaxation factor, β:

$$\mathbf{x}^{(n+1)}=\left(1-\beta\right)\mathbf{x}^{(n)}+\beta F\left(\mathbf{x}^{(n)}\right) \tag{7}$$

Putting these steps together, we have the following algorithm, SART-BF:

```
SART-BF
x := prior reconstruction
for each iteration
    $\mathbf{b}_{\text{expected}}$ := $\mathbf{Ax}$
    $\mathbf{b}_{\text{error}}$ := $\mathbf{b} - \mathbf{b}_{\text{expected}}$
    gradient := $\mathbf{A}^{\mathrm{T}}\mathbf{b}_{\text{error}}$
    x := x + $\alpha$*gradient
    $\mathbf{x}_{\text{filtered}}$ := $F(\mathbf{x})$
    x := (1 - $\beta$)*x + $\beta$*$\mathbf{x}_{\text{filtered}}$
```

The number of iterations, and the choice of relaxation factors α and β, are parameters that must be chosen by the user. There are various criteria that can be employed to determine optimal values, but we do not address that issue here.

So far, we have presented this algorithm as modality-general. However, two of the functions involved are modality-specific. Usually, **A** and $\mathbf{A}^{\mathrm{T}}$ are too large to be represented explicitly in memory, and must instead be implemented implicitly with functions that duplicate their behavior. In the case of CT, **A** is the projection operation (in our case, cone beam), and $\mathbf{A}^{\mathrm{T}}$ is the backprojection operation. The initial reconstruction is performed with filtered backprojection [2]. In the case of MRI with Cartesian sampling, **A** is the Fast Fourier Transform (FFT), and $\mathbf{A}^{\mathrm{T}}$ is the Inverse Fast Fourier Transform (IFFT). The initial reconstruction is the IFFT.

In our implementation, projection, backprojection, Fourier transforms, and bilateral filtration are written with CUDA in order to run on the GPU, and additional utility functions written in C enable input/output, manipulation, and arithmetic of large arrays. (The Fourier transforms are implemented by CUFFT, a library provided with CUDA.) At the uppermost level, the code for SART-BF is implemented in Matlab. The GPU used in this study is a GTX 285.

The SART-BF algorithm and GPU implementation presented here is similar to other recent developments in CT [4]. The key distinction here is that we can apply the same algorithm to both CT and MRI.

III. SIMULATIONS

To test SART-BF in simulations, we used the Moby digital mouse phantom [5], shown in Fig. 1. The version used here is 256 × 256 × 256 voxels, with each voxel 0.088 mm × 0.088 mm × 0.088 mm. A small cyclinder of water was placed next to the mouse to facilitate the measurement of image statistics. The CT simulation generated 200 projections with a step angle of 1.8°. The MRI simulation sampled the volume with the FFT. In both modalities, a sufficient amount of noise was added to the measured data so that a conventional reconstruction would produce images with an SNR around 5 in regions comprised of generic soft tissue.

For both modalities, we ran SART-BF for 10 iterations. The values used for the various parameters are shown in Table I. The total time for both was about 2 minutes. The reconstructed images are shown in Fig. 2.

After the initial reconstruction, and each subsequent iteration of SART-BF, we computed the normalized root mean squared error (RMSE) of the reconstructed image compared with the original phantom. We measured the mean and the standard deviation in the the interior of the water cylinder to compute the signal-to-noise ratio (SNR). To quantify the sharpness of the edges between regions, we calculated the modulation transfer function (MTF) from a radial line profile of the cylinder, and located the spatial frequency where the MTF equals 0.5. These image statistics are plotted in Fig. 3.

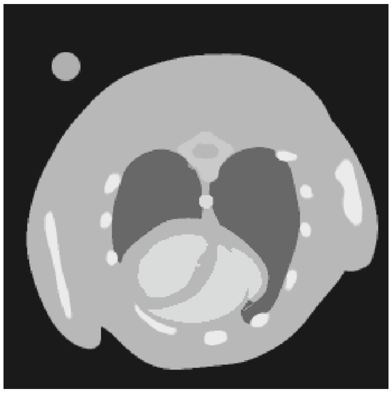

Figure 1. A slice from the Moby mouse phantom.

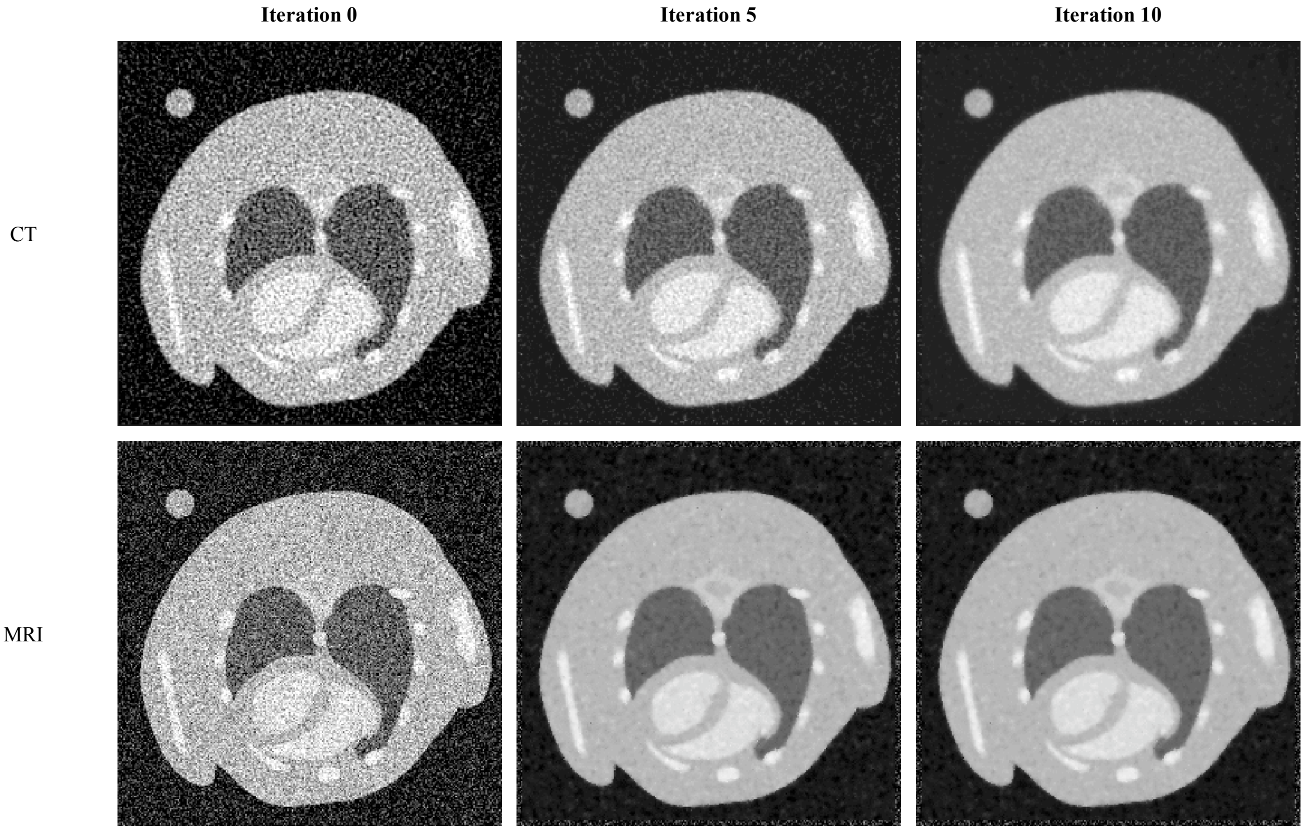

Figure 2. Images reconstructed with SART-BF from simulations

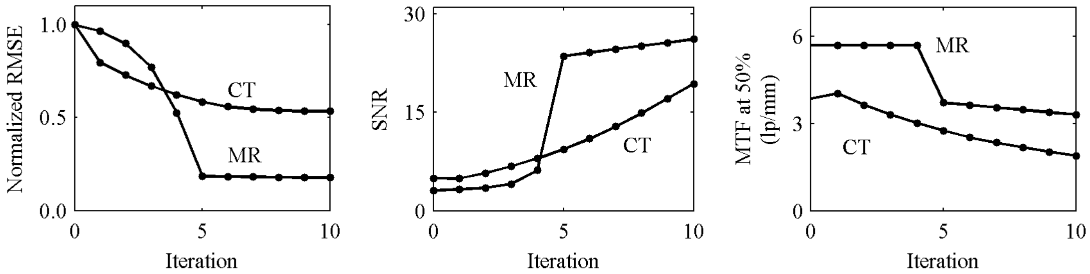

Figure 3. Image statistics at each iteration of SART-BF in the simulations.

TABLE I. RECONSTRUCTION PARAMETERS IN SIMULATIONS

	α	β	σ_d	σ_r
CT	0.2	0.2	1.5	0.0012
MRI	1.0	0.05	1.5	0.0012

IV. EXPERIMENTAL VALIDATION

To test SART-BF with real data, we scanned a plastic phantom containing holes and cylinders of various sizes with both CT and MRI. For the CT scan, we collected 200 projections with 1002 × 667 pixels of size 0.088 mm × 0.088 mm and a step angle of 1.8°, at 80 kVp, 40 mA, and 10 ms, on our custom micro-CT system [6]. These settings were chosen to approximate a densely-sampled but low-dose scan that might be desirable in the clinic but produces images that are unacceptably noisy in conventional reconstructions. For the MRI scan, we immersed the phantom in a copper sulfate solution. We performed a GRASS scan with an 8° flip angle over 512 × 512 × 512 samples on an isotropic Cartesian grid with an increment of 0.1 mm on our 2T GE SIGNA EXCITE system. Total scan time was about 4 minutes for the CT scan and 40 minutes for the MRI scan.

We then reconstructed the data with SART-BF. In each case 10 iterations were used, and the values used for the various parameters are shown in Table II. The CT images were reconstructed in a 512 × 512 × 256 volume and the MRI images in a 384 × 384 × 384 volume, but both sets were rotated, interpolated, and cropped to appear in the same orientation. The total time was 5 minutes for CT and 3 minutes for MRI. The reconstructed images are shown in Fig. 4.

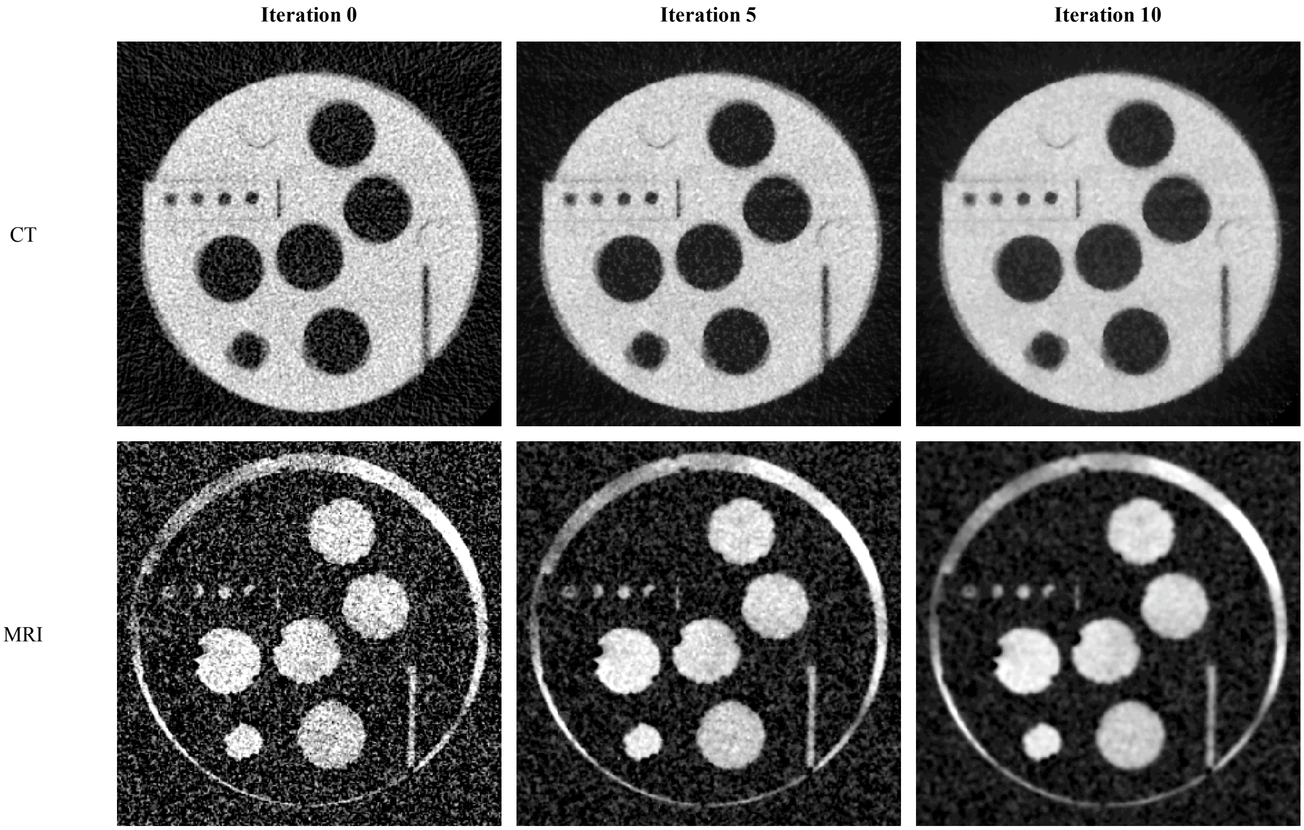

Figure 4. Images reconstructed with SART-BF from real data.

TABLE II. RECONSTRUCTION PARAMETERS FOR REAL DATA

	α	β	σ_d	σ_r
CT	0.2	0.2	1.5	0.012
MRI	0.03	0.4	1	0.3

V. CONCLUSION

The results from the simulations demonstrate that SART-BF improves the accuracy of the reconstruction, and delivers a large improvement in SNR for a relatively modest cost in spatial detail. The results from the real data affirm that SART-BF is sucessful at reducing noise while preserving edges in the reconstructed images. This algorithm depends on the user choice of several parameters that may vary depending on the particular scan.

But the more important result is that the same modality-general algorithm comprised of separate modality-specific modules can deliver an improvement in the quality of reconstructed images in different imaging modalities. Our software platform is capable of handling data from both CT and MRI, enabling efficient implementations of low-level and modality-specific modules on the GPU, and rapid development of new modality-general algorithms based on novel combinations of these modules in MATLAB. In future work we hope to extend this functionality beyond CT and MRI to include additional modalities.

ACKNOWLEDGMENTS

All work was performed at the Duke Center for In Vivo Microscopy, NCRR National Biomedical Technology Research Center (P41 RR005959), with additional support from NCI (U24 CA092656 and KO8 CA114176).

REFERENCES

[1] D. Dong, J. Tian, Y. Dai, G. Yan, F. Yang, and P. Wu, “Unified reconstruction framework for multi-modal medical imaging,” Journal of X-Ray Science and Technology, vol. 19, pp. 111-126, 2011.

[2] A. C. Kak and M. Slaney, Principles of Computerized Tomographic Imaging. Society of Industrial and Applied Mathematics, 2001.

[3] C. Tomasi and R. Manduchi, “Bilateral Filtering for Gray and Color Images,” Proceedings of the 1998 IEEE International Conference on Computer Vision, 1998.

[4] W. Xu and K. Mueller, “Accelerating regularized iterative CT reconstruction on commodity graphics hardware,” Proceedings of the 2009 IEEE International Symposium on Biomedical Imaging, pp. 1287-1290, 2009.

[5] W. P. Segars, B. M. W. Tsui, E. C. Frey, G. A. Johnson, and S. S. Berr, “Development of a 4-D digital mouse phantom for molecular imaging research,” Molecular Imaging and Biology, vol. 6(3), pp. 149-159, 2004.

[6] C. T. Badea, S. M. Johnston, B. Johnson, M. Lin, L. W. Hedlund, and G. A. Johnson, “A dual micro-CT system for small animal imaging,” Proceedings of the SPIE, vol. 6913, p. 91342, 2008.

Super Resolution CT Imaging Based on the Collimator

Yining Zhu, Defeng Chen, Peng Zhang

***Abstract*—When the ratio of the focal spot size to the detector cell size is relatively large, the spatial resolution of CT images is mainly dominated by the focal spot size. In order to improve the spatial resolution for such case, we divide a large x-ray focal spot into a set of discrete small virtual spots by means of a designed collimator, and propose an corresponding iterative algorithm to reconstruct a super resolution image from the data scanned under a set of narrow fan beams. The numerical experiments show that the proposed approach is validity to increase the resolution of the CT image significantly.**

***Keywords*—Super resolution; CT reconstruction; Collimator; Iterative algorithm.**

I. INTRODUCTION

The spatial resolution is one of the important indexes of a CT system, which reflects the capability of a CT system to distinguish details. The spatial resolution is theoretically described by MTF (Modulation Transfer Function). But, in practice, it is often specified in term of line pairs per millimeter (lp/mm) and directly measured with some typical models containing bar or hole patterns of various spatial frequencies. Generally the resolution is determined by the factors including the x-ray focal spot size, detector cell size, ratio of source-to-detector distance to source-to-iso distance, field of view, mechanical precision, reconstruction algorithm and so on.

The approaches of quarter-detector-offset, focal-spot-wobble [1] and the virtual-detector-based algorithms [2-5] were proposed to improve the spatial resolution of CT images. However, when the ratio of the focal spot size to the detector cell size is relatively large, the spatial resolution of CT images is mainly dominated by the focal spot size, and the approaches above become almost invalidation. For instance, the focal spot size of the x-ray tube for high energy industrial CT is typically about 3.0 to 6.5 mm as to the standard acc. EN12543, but the detector cell size is about 0.083 to 0.4 mm. In order to improve the spatial resolution for such situation, we design a collimator with a set of slits placed in the front of the x-ray source. The x-rays passing through the collimator consist of a set of narrow fan beams emitted from a set of discrete small virtual spots. We propose an iterative algorithm to reconstruct a super resolution CT image from such scanned data. The numerical experiments with typical test models show that the proposed approach is validity to increase the resolution of the CT image significantly.

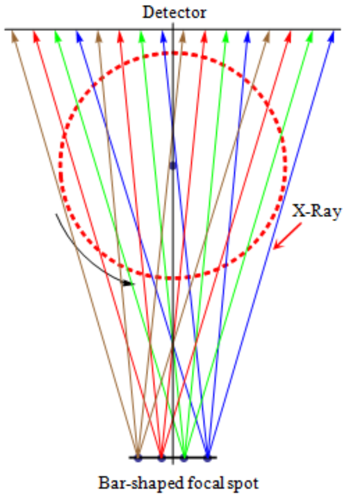

Fig. 1. Schematic diagram of CT scanning configuration with a bar-shaped focal spot.

II. DATA SCANNED WITH COLLIMATOR

In an ideal CT model, the x-ray focal spot is treated as an ideal point. Therefore, in the two dimensional ideal CT model, the rays emitted from the focal spot to the linear detector form a fan-beam. In reality, however, the focal spot size in some situations could not be ignored. In this paper, we treat the x-ray focal spot in two dimensional CT as a bar-shaped (i.e. short line segment) spot, because the variance of the focal spot is very small along the direction vertical to the detector, compared to the source-to-detector distance. Under this assumption, the x-rays emitted from the bar-shaped spot are shown in Fig. 1. In order to improve the spatial resolution, we place an arc-shaped collimator, shown in the Fig. 2, in the front of the x-ray focal spot. The collimator is made of tungsten or plumbum, and is of the arc radius r, the angle α and thickness k mm. A set of slits with width l mm are arranged on the collimator with equal radian.

For simplicity, we just consider the mono-energetic x-ray CT imaging. Then the data scanned with a collimator for a bar focal spot can be modeled as follows, if the scattering photons are ignored,

$$I(\beta,u)=\int_{s_0}^{s_1} I_0(s)e^{-\int\limits_{y\in L(s,u)} f(R(\beta)y,E_0)+\lambda(E_0)g(y)dL}\,ds, \tag{1}$$

where β denotes the rotation angle of the inspected object, $R(\beta)$ the relative rotation matrix, u the detector coordinate and $s\in[s_0,s_1]$ the position from which an x-ray is emitted

---

The authors are with The CT Laboratory, School of Mathematics, Capital Normal University, Beijing, 10048, China; email: zhumilan997@163.com

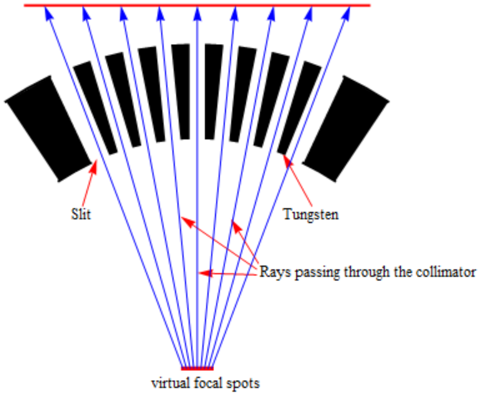

Fig. 2. Structure of the collimator.

respectively; let $I_0(s)$ be the photon intensity distribution with energy E_0 emitted from the position s, $L(s,u)$ an x-ray emitted from the position s to detector coordinate u, and $I(\beta,u)$ the remaining photons that penetrate the inspected object; $f(x,E_0)$ is the linear attenuation coefficient distribution of the inspected object at the point x related to energy E_0, $\lambda(E_0)$ linear attenuation coefficient of the collimator related to energy E_0, and $g(s)$ the thickness distribution of the collimator.

With the collimator described in Fig. 2, we can think that the x-ray focal spot consists of a set of discrete small virtual focuses. Then we can discrete the model (1) into the following form

$$I_n = \sum_{s=1}^{S} I_{0,s} \exp\left(-\sum_{j=1}^{J} a_{n,s,j} f_j - \lambda g_{n,s}\right), \tag{2}$$

where s denotes the index of the small virtual focuses, n the index of the scanned data, and j the index of image pixels; let $I_{0,s}$ be the total number of photons emitted from the s^{th} virtual focus, $a_{n,s,j}$ be the contribution factor of the ray emitted from the s^{th} virtual focus and passing through the j^{th} pixel to the n^{th} datum, and $g_{n,s}$ be the contribution factor of the ray emitted from the s^{th} virtual focus to the n^{th} datum. Specially, we can set $n = (n_1 \times N_2) + n_2$, $0 \le n_1 < N_1$, $0 \le n_2 < N_2$, where N_1 is the number of sampling angles, N_2 is the number of whole detector cells, and n_1,n_2 are indexes of detector and angle respectively.

Due to the obstruction of the collimator, only a narrow part of a fan beam emitted from a virtual focus can reach the inspected object. Therefore, the sinogram scanned with the designed collimator can be treated as a combination of data scanned under a set of narrow fan beams which are emitted from the virtual focuses and penetrate the collimator. We can choose the width of the slits, thickness of the collimator, and the ratio of the source-to-iso distance to the source-to-detector distance, to limit the number of the virtual focuses from which a single detector cell could receive the photons.

III. THE RECONSTRUCTION ALGORITHM

The CT image reconstruction problem for our model is to reconstruct f_j from data (2) under assumption that the $I^c_{0,n,s}$ are known for any n,s, where $I^c_{0,n,s} = I_{0,s}\exp(-\lambda g_{n,s})$.

Set

$$\begin{aligned} p_{n,s} &= -\ln \frac{I_{n,s}}{I^c_{0,n,s}} \\ &= \sum_{j=1}^{J} a_{n,s,j} f_j . \end{aligned}$$

Let F be the image vector, M the projection matrix, and P the projection data vector. Then we obtain the linear system

$$P = MF \tag{3}$$

where

$$P = \begin{pmatrix} P_1 \\ \vdots \\ P_s \\ \vdots \\ P_S \end{pmatrix}, P_s = \begin{pmatrix} p_{1,s} \\ \vdots \\ p_{n,s} \\ \vdots \\ p_{N,s} \end{pmatrix}; M = \begin{pmatrix} M_1 \\ \vdots \\ M_s \\ \vdots \\ M_S \end{pmatrix},$$

$$M_s = \begin{pmatrix} a_{1,1,1} & \cdots & a_{1,s,j} & \cdots & a_{1,1,J} \\ \vdots & \ddots & \vdots & \ddots & \vdots \\ a_{n,1,1} & \cdots & a_{n,s,j} & \cdots & a_{n,s,J} \\ \vdots & \ddots & \vdots & \ddots & \vdots \\ a_{N,1,1} & \cdots & a_{N,s,j} & \cdots & a_{N,S,J} \end{pmatrix}.$$

If $p_{n,s}$ are known for any n, s, then we can solve (3) using SART [6] as follows,

$$f_j^{(k+1)} = f_j^{(k)} + \frac{1}{\sum_{s=1}^{S}\sum_{n=1}^{N} a_{n,s,j}} \sum_{s=1}^{S}\sum_{n=1}^{N} a_{n,s,j} \frac{\delta^{(k)}_{n,s}}{\sum_{j=1}^{J} a_{n,s,j}}. \tag{4}$$

where $\delta^{(k)}_{n,s} = p_{n,s} - m_{n,s} \cdot F^{(k)}$ is the residual error for the k^{th} iteration and $m_{n,s}$ is the n^{th} row of matrix M_s. However, unfortunately, we could not directly measure $p_{n,s}$, and then could not calculate $\delta_{n,s}$ for any n, s.Therefore we could not apply the formula (4) to reconstruct image F.

What we could measure are I^c_0 and I_n for any n. Denoting $I^{(k)}_n$ as the total number of estimate photons calculated by forward-projection in the k^{th} iteration. Then we can calculate the total of the residual error of the n^{th} data $\delta^{(k)}_n$ from I^c_0 and $I^{(k)}_n$,

$$\begin{aligned} \delta^{(k)}_n &= -\ln(I_n/I^c_0) - (-\ln(I^{(k)}_n/I^c_0)) \\ &= \ln(I^{(k)}_n/I_n). \end{aligned} \tag{5}$$

On the other hand,

$$\delta^{(k)}_n = \sum_{s=1}^{S} \delta^{(k)}_{n,s}.$$

Setting u is the index of detector cells and

$$\omega_{u,s} = I^c_{0,u,s}/I^c_0.$$

As the $\omega_{u,s}$ is independence with the object, so

$$\begin{aligned} \omega_{n,s} &= \omega_{\bmod(n,N_2),s} \\ &= \omega_{u,s}, \end{aligned} \tag{6}$$

and we notice that

$$\sum_{s=1}^{S} \omega_{u,s} = 1. \tag{7}$$

Now substituting $w_{n,s}\delta_n^{(k)}$ for $\delta_{n,s}^{(k)}$ in formula (4), we obtain a new iterative formula which we call super resolution-SART (SR-SART),

$$f_j^{(k+1)} = f_j^{(k)} + \frac{1}{\sum\limits_{s=1}^{S}\sum\limits_{n=1}^{N} a_{n,s,j}} \sum_{s=1}^{S}\sum_{n=1}^{N} a_{n,s,j} \frac{\omega_{n,s}\delta_n^{(k)}}{\sum\limits_{j=1}^{J} a_{n,s,j}}. \tag{8}$$

It should be pointed that $I_{0,n,s}^{c}$ is a key parameter in SR-SART which is not only relative to the weights of assigning residual, but also is involved in computing the estimated value by forward-projection. However, in this paper, we just consider the ideal condition i.e. there is no error in scanning geometry and production of collimator. The investigation on estimating $I_{0,n,s}^{c}$ indirectly for real CT system will be a further work.

IV. EXPERIMENTS

To validate the effects of our approach, we use the pattern in Fig. 3 to test spatial resolution by numerical experiment. There are 4 line-pairs models in the pattern and their resolutions are: 1.9179 lp/mm (left), 1.4049 lp/mm (two in the middle), 1.1507 lp/mm(right). At the top left corner of the pattern, there are 5 concentric rings with a same thickness 0.2607 mm and distance 0.2607 mm between each one and there are some tiny squares meshed at the bottom right corner, of which width and interval both are 0.3476 mm.

The simulation parameters are the same as the industrial CT system in our laboratory: the source-to-detector distance is 1000 mm (SDD), the source-to-iso distance is 750 mm (SOD); The total of number of detector cells is 1800, of which width is 0.127 mm; The number of sampling angles is 720 and uniformly distribute in full directions. The size of focus is 6 mm and we divide it into 21 virtual focuses with the size 0.2857 mm. We assume the intensity of focuses obeys Gaussian function, according the distance to the centre of whole focus,

$$f(x) = \frac{1}{\sqrt{2\pi}} \exp(-x^2)$$

and each ray emits 10^6 photons with the energy 300 KeV.

Here we select tungsten as the materials for collimator with the density 19.35 g $\cdot$cm^{-3}. According to the reference data by National Institute of Standards and Technology (NIST) [7], the mass attenuation coefficient of tungsten is 0.3238 cm$^2 \cdot$ g^{-1} for 300 KeV. As mentioned in section 2, the parameters of collimator are listed in table 1.

TABLE I
THE PARAMETERS OF COLLIMATOR

r	k	h	l	α
150 mm	30 mm	120 mm	0.4 mm	12°

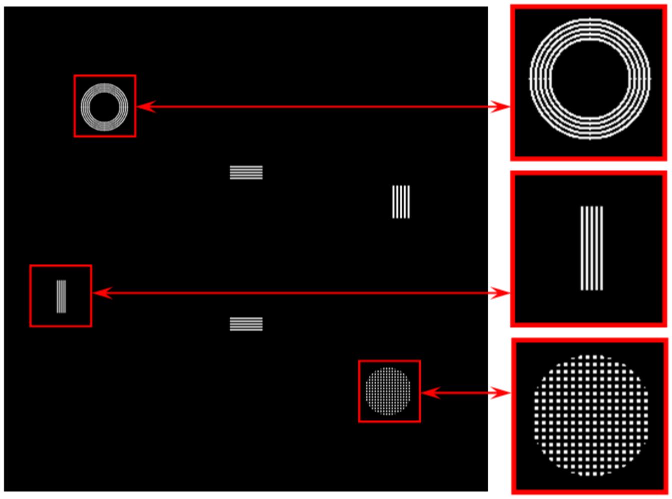

Fig. 3. The pattern for testing spatial resolution.

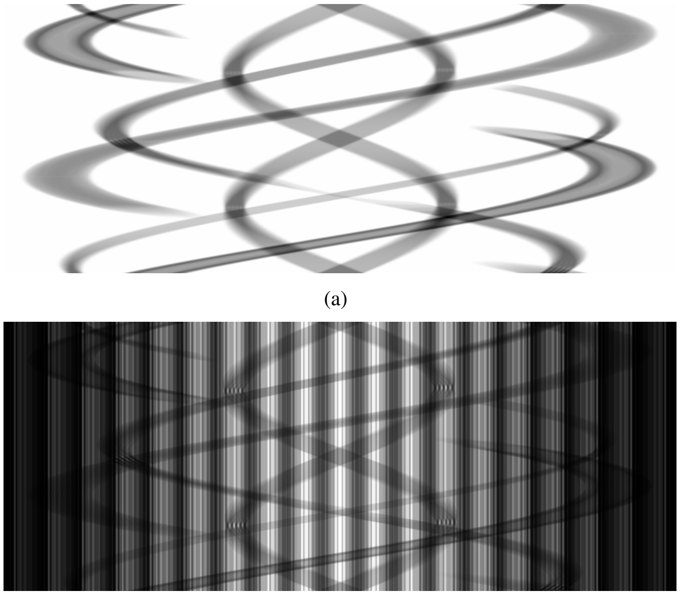

(a)

(b)

Fig. 4. The image of scanned data: (a) is scanned without collimator; (b) is scanned with collimator.

First, we process forward-projection at the phantom with and without collimator, respectively. The data scanned without collimator seems smooth(Fig. 4(a)) while The data scanned whith collimator have some band patterns of dark and light(Fig. 4(b)).

Fig. 5 is reconstructed from the the data scanned without collimator by Filter Back-Projection (FBP) algorithm. We zoom in the reconstructed CT image and find that all these patterns with high frequencies are blurred and unable to be distinguished such line-pairs and rings. Fig. 6 is reconstructed from the the data scanned with collimator by using the SR-SART reconstruction algorithm. Obviously, it has higher spatial resolution than Fig. 5. In the detail with enlarged scale, even the minimum line-pair 1.9179 lp/mm still can be distinguished clearly as well as rings and blocks.

We also did other experiments including low contrast phan-

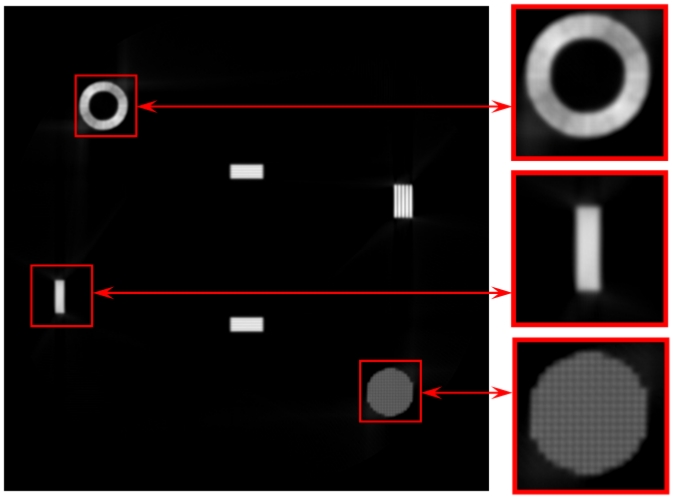

Fig. 5. The CT image reconstructed by FBP from data scanned without collimator.

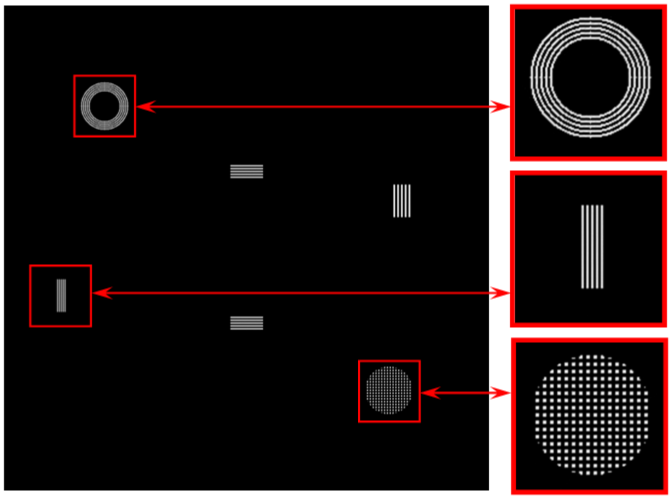

Fig. 6. The CT image reconstructed by SR-SART from data scanned with collimator.

tom reconstruction, geometric errors effects and so on. The results are satisfactory or positive. However, we could not describe them here, due to the limited space.

V. CONCLUSION

We have proposed a scanning configuration based on collimator and the corresponding reconstruction algorithm called Super Resolution-SART(SR-SART). The result of numerical experiments show our approach increases the resolution of CT images significantly. But for real CT system use of our approach, the estimate method for parameters $I_{0,u,s}^{c}$ should be investigated furthermore, since the geometric and machining errors are inevitable. The computational cost of SR-SART increases much more than conventional SART for the data scanned without a collimator. But the new computational techniques, such as GPU, make it possible for utilization.

ACKNOWLEDGMENT

This work was supported in part by the National Natural Science Foundation of China under the grants 60971131/F010404 and 60971131/F010404, Beijing Education Committee under the grants PHR20110509 and KZ201110028034.

REFERENCES

[1] Jiang Hsieh,Computed Tomography: principles, design, artifacts, and recent advances [M]. Washington USA: SPIE Press, 2002.

[2] Huitao Zhang, JuanTian, Ming Chen, Peng Zhang, A Novel Scanning Mode and Image Reconstruction Method on Super-Resolution CT [J],Chinese Journal of Stereology and Image Analysis, 2005,9:154-157.

[3] T.M.Peters, R.M.Lewitt, Computed tomography with fan-beam geometry, J.Comput.Assist.Tomogr., 1(4), 429-436(1977).

[4] A. H. Lonn, Computed tomography system with translatable focal spot, US Patent 5173852 (1990).

[5] J.Hsieh, M.F.Gard, and S.Gravelle, A reconstruction technique for focal spot wobbling, Proc. SPIE 1652, 175-182 (1992).

[6] Andersen, A.H.and A.C.kak, Simultaneous Algebraic Reconstruction Technique (Sart) - A Superior Implementation Of The Art Algorithm, Ultrasonic Imaging, 1984. 6(1): p. 81-94.

[7] J. H. Hubbell, S. M. Seltzer, Tables of X-Ray Mass Attenuation Coefficients and Mass Energy-Absorption Coefficients from 1 keV to 20 MeV for Elements Z = 1 to 92 and 48 Additional Substances of Dosimetric Interest, http://www.nist.gov/pml/data/xraycoef/.

Fat and iron quantification of the liver with dual-energy computed tomography in the presence of high atomic number elements

Benedek J. Kis, Zsolt Sarnyai, Róbert Kákonyi, Miklós Erdélyi, Gábor Szabó

Abstract **Liver fat and iron quantification in human liver is an active research area in dual-energy CT imaging. Basis material decomposition method can decompose any object into two basis materials, and three-material decomposition can be also performed with a constraint of volume or mass conservation. The most accurate technique for material decomposition relies on lookup tables (LUTs). LUTs can be pre-measured or calculated using appropriate material models. Any difference between the applied material model and the real sample introduces errors in the material quantification. In this paper the ICRU-44 compositions of soft tissue and adipose tissue were used to generate LUTs. The aim of the paper is to estimate the effect of further elements in liver, e.g. heavy metals on dual-energy liver decomposition accuracy for adipose tissue and iron. A computer simulated virtual abdomen phantom was used to test a pre-reconstruction three-material decomposition algorithm for liver fat and iron quantification. Two liver models were used in this work: the first contains only iron and ICRU-44 elements for liver tissue, which is free of higher atomic number elements. In the second model higher atomic number elements were added to the liver material composition. Iron and fat were selected as basis materials, and three-material decomposition was performed using the resulted iron and fat density images. Results of the study demonstrate that three-material decomposition detects the heavy metals as iron, thus the iron content will be overestimated if the higher atomic number elements are present, but the presence of these additional elements does not affect the quantification of fat.**

I. INTRODUCTION

Biopsy is the gold standard in the measurement of liver fat content. However the main drawback of biopsy is that the sample does not represent the entire liver. Cross-sectional imaging (CT, MR, and ultrasound) of the abdomen should be alternative methods to using liver biopsy, and can be used for mapping the whole liver. The main purpose of this paper is to examine the accuracy of pre-reconstruction three-material decomposition method using dual-energy CT in the presence of high atomic number elements in the liver. The compositions of soft- and adipose tissue of the ICRU Report 44 contain the following elements: H, C, N, O, Na, P, S, Cl, K [1]. Since the high atomic number elements have high density and absorption efficiency, even if their weight fractions in the liver are relative low it is essential to estimate their effect on fat, and iron quantification of the liver.

II. MATERIALS AND METHODS

A. Virtual abdomen phantoms

A computer simulated virtual phantom was generated with elliptic geometry and material compositions of ICRU-44. The phantom represents the fat layer of the skin (located in the subcutaneous layer of the tissue called the hypodermis), the ribs, the spine, the air regions close to the spine, and the liver region which was made up of fat, soft tissue, and iron. Two liver models were implemented: the first model (A) contains ICRU-44 elements and iron. In the second model (B) higher atomic number elements were added to the liver material composition. The phantom geometry contains different material regions (Fig.1).

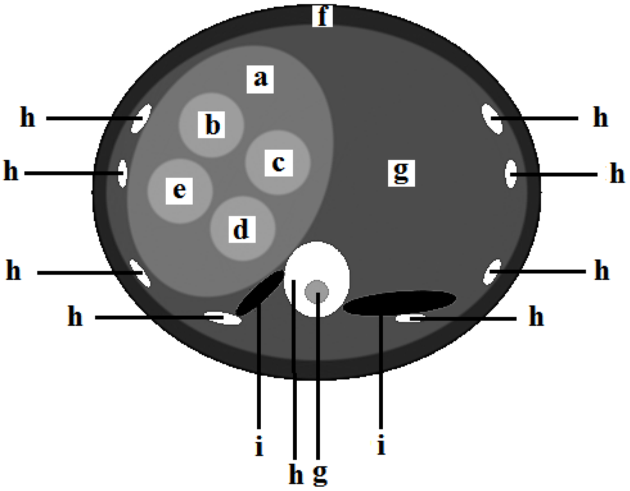

Fig. 1. Virtual abdomen phantom. Liver region a) contains only iron and soft tissue, while in regions b) c) and d) there is additional fat and iron with different concentrations. Region e) contains only iron and fat. Regions f), g), h) and i) contains 100% fat, soft tissue, bone and air, respectively.

To grade hepatic steatosis, pathologists use a five-point ordinal scale (0%-, 1%-, 5%-, 33%-, 66%-) [2]. These levels were used for the generation of the virtual fatty liver model.

2000 ppm iron was added to each liver region. This value corresponds to a liver with severe iron overload. The mean concentration of iron atoms present in a healthy liver is around 300 ppm, but the liver iron content in diseases such as hemochromatosis or thalassemia can be up to 9000 ppm.in the wet liver tissue [3].

The weight fractions of the constituent materials by each phantom region of the first liver model are listed in Table I.

Authors are with the Department of Optics and Quantum Electronics at the University of Szeged, Szeged, Hungary. Contact: kisjbenedek@gmail.com

TABLE I ELEMENTS IN THE ABDOMEN PHANTOM WITH THE LIVER MODEL 'A'

Phantom A regions	Soft tissue (w%)	Fat (w%)	Iron (w%)	Bone (w%)	Air (w%)
a	99.8	-	0.2	-	-
b	94.8	5	0.2	-	-
c	66.8	33	0.2	-	-
d	33.8	66	0.2	-	-
e	-	99.8	0.2	-	-
f	-	100	-	-	-
g	100	-	-	-	-
h	-	-	-	100	-
i	-	-	-	-	100

The upper limits (see Table II) of different higher atomic number elements in the wet liver were estimated by values can be found in the literature. Table II contains the upper limit values of different material levels in the liver.

TABLE II HIGHER ATOMIC NUMBER ELEMENTS IN THE HUMAN LIVER MODEL 'B'

Atomic number	Symbol	Density [g/cm3]	High level in liver [ppm]	Reference
13	Al	2.699	6.7	[4]
14	Si	2.33	29	[4]
23	V	6.11	0.86	[4]
24	Cr	7.18	0.97	[4]
25	Mn	7.44	2.5	[4]
27	Co	8.9	0.17	[5]
28	Ni	8.902	0.72	[4]
29	Cu	8.96	69.4*	[6]
30	Zn	7.133	204	[5]
33	As	5.73	5	[4]
34	Se	4.5	2.3	[4]
42	Mo	10.22	1.8	[4]
48	Cd	8.65	2.51	[7]
50	Sn	7.31	1.5	[4]
80	Hg	13.55	1.52	[8]
82	Pb	11.35	1.2	[4]

*value was calculated from dry weight value by dividing the dry weight fraction value by 3.6 [4].

The second liver model contains the same levels of fat and iron as model 'A'. The soft tissue levels differ, because model 'B' contains further elements listed in Table II.

B. *Simulation of the computed tomography system*

A simplified CT geometry was used during the simulations with the following parameters (Table III):

TABLE III GEOMETRIC PARAMETERS OF THE SIMULATION

Geometric parameter	Parameter value
Source to image distance	949 mm
Source to isocenter distance	541 mm
Field of view	500 mm
Number of detector pixels	912
Number of detector rows	1
Pixel size	1.0267 mm
Fan-beam angle	55.05°
Target-angle	7°

The direct photon flux on the detector was calculated by the exponential law of radiation attenuation (Beer-Lambert law). During simulations the Institute of Physics and Engineering in Medicine spectra of tungsten were applied [9]. The simulations were carried out with 80 kVp and 140 kVp spectra. The detector response function *D(E)* was estimated by the calculation of the absorption of a CsI column with a thickness of 500 µm [10,11]. Linear attenuation coefficients of the used materials were calculated via the database of XCOM from NIST [12]. Prefilters made of 0.1 mm copper and 3.25 mm aluminum were used to shape the source spectra. Noise- and scatter-free projections were used for calculations.

According to the Beer-Lambert law, the measured intensity signal can be written as

$$I=\int_E S(E)D(E)e^{-\int_L \mu(\vec{r},E)dl}\,dE \qquad (1)$$

where $S(E)$ is the incident spectrum, *D(E)* is the detector response function, and $\mu(\vec{r},E)$ is the spatially- and energy-dependent linear attenuation in the sample material. The measured intensity without sample $\int_E S(E)D(E)dE$ can be termed as the source intensity, I_0. Taking the logarithm of Eq. 1. provides a signal linearly related to the exponential term.

$$ln(I)=ln(I_0)-\int_L \mu(\vec{r},E)dl \qquad (2)$$

Rearranging the equation it can be seen that

$$-ln\left(\frac{I}{I_0}\right)=\int_L \mu(\vec{r},E)dl \qquad (3)$$

This value is referred to as CT signal, and can be normalized to the attenuation characteristics of water to obtain the Hounsfield unit (HU) values.

C. *Three-material decomposition*

Pre-reconstruction three-material decomposition was performed using the virtual abdomen phantom [13]. The most accurate technique for material decomposition is the application of pre-generated lookup tables (LUTs) [14]. Projection raw data of the phantom and lookup-tables (LUTs) for basis materials were simulated. The resolution of the used LUTs was 0.1 mm and interpolation was used by retrieving the detected signals. The obtained basis material thicknesses were used for filtered backprojection (FBP). FBP generated the density images, which were the input data of the three-material decomposition algorithm. Three-material specific images were calculated from the reconstructed basis material density images using the pre-calculated decomposition coefficients and volume conservation assumption.

The steps below (Fig. 2) comprise the basis material method using a CT system that can decompose objects into three material components.

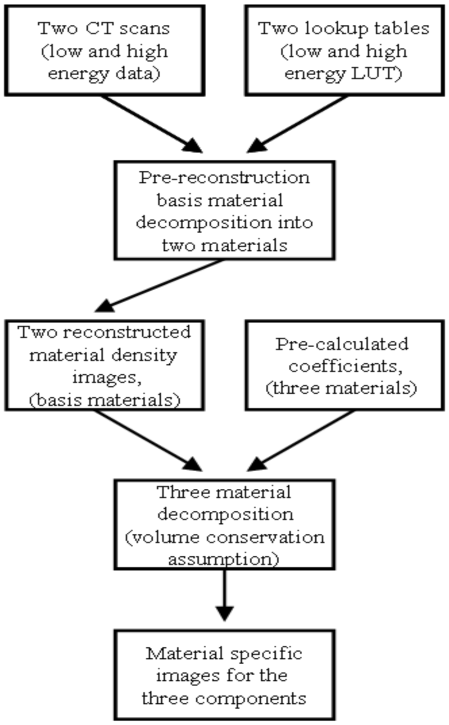
Two CT scans (low and high energy data)
Two lookup tables (low and high energy LUT)
Pre-reconstruction basis material decomposition into two materials
Two reconstructed material density images, (basis materials)
Pre-calculated coefficients, (three materials)
Three material decomposition (volume conservation assumption)
Material specific images for the three components

Fig. 2. Implementation scheme of pre-reconstruction three-material decomposition by means of basis material decomposition

Basis material decomposition method is based on the assumption that the attenuation of a material can be calculated as the sum of the linear combination of attenuations of the preselected two basis materials.

For material decomposition with dual-energy, two measurements are done one at high- and another at low-energy levels. According to the Beer-Lambert-law the measured intensities are:

$$I_{low} = \int_{E_{low}} S_{low}(E) D(E) \mathrm{e}^{(-\mu_1(E)d_1-\mu_2(E)d_2)} dE, \quad (4)$$

$$I_{high} = \int_{E_{high}} S_{high}(E) D(E) \mathrm{e}^{(-\mu_1(E)d_1-\mu_2(E)d_2)} dE, \quad (5)$$

where $S_{low}(E)$ and $S_{high}(E)$ are the prefiltered source spectra of the x-ray tube, $\mu_1(E)$ and $\mu_2(E)$ are the attenuation coefficients of the basis materials.

The measured CT projection values were assigned to the selected basis material thicknesses using the lookup tables. The resulted thickness values multiplied by the densities give the line integrals of the densities. These values were used for filtered backprojection to obtain the densities of the basis materials in each voxel. These density maps are used for three-material decomposition.

The mass attenuation of the three constituent materials ($\mu_1(E), \mu_2(E), \mu_3(E)$) can be decomposed to the linear combination of the mass attenuation of the two basis materials ($\mu_\mathrm{a}(E)$ and $\mu_\mathrm{b}(E)$) as follows

$$\mu_1(E) = a_1\mu_\mathrm{a}(E) + b_1\mu_\mathrm{b}(E), \quad (6)$$

$$\mu_2(E) = a_2\mu_\mathrm{a}(E) + b_2\mu_\mathrm{b}(E), \quad (7)$$

$$\mu_3(E) = a_3\mu_\mathrm{a}(E) + b_3\mu_\mathrm{b}(E). \quad (8)$$

The linear attenuation of the bases materials can be expressed as

$$\mu_a(E)\rho_a(\vec{r}) = a_1\mu_\mathrm{a}(E)\rho_1(\vec{r}) + a_2\mu_\mathrm{a}(E)\rho_2(\vec{r}) + a_3\mu_\mathrm{a}(E)\rho_3(\vec{r}), \quad (9)$$

$$\mu_b(E)\rho_b(\vec{r}) = b_1\mu_\mathrm{b}(E)\rho_1(\vec{r}) + b_2\mu_\mathrm{b}(E)\rho_2(\vec{r}) + b_3\mu_\mathrm{b}(E)\rho_3(\vec{r}) \cdot \quad (10)$$

The relation between decomposition coefficients and densities can be seen by dividing (9) by μ_a and (10) by μ_b:

$$\rho_a(\vec{r}) = a_1\rho_1(\vec{r}) + a_2\rho_2(\vec{r}) + a_3\rho_3(\vec{r}), \quad (11)$$

$$\rho_b(\vec{r}) = b_1\rho_1(\vec{r}) + b_2\rho_2(\vec{r}) + b_3\rho_3(\vec{r}). \quad (12)$$

Three-material decomposition can be performed with a constraint of volume or mass conservation. We applied volume conservation assumption, because the fat and soft tissue cells are separated in the liver tissue, and the concentrations of iron and higher atomic number elements are relatively low. In each voxel the sum of the material can be expressed as:

$$\frac{\rho_1(\vec{r})}{\rho_{1,0}} + \frac{\rho_2(\vec{r})}{\rho_{2,0}} + \frac{\rho_3(\vec{r})}{\rho_{3,0}} = 1 \quad (13)$$

where $\rho_{1,0}$, $\rho_{2,0}$ and $\rho_{3,0}$ are the densities of the three materials in their natural forms.

The decomposition coefficients a_1, a_2, a_3, b_1, b_2 and b_3 were calculated, and used for calculation of the fractions of the three materials.

III. RESULTS

Material density images of the basis materials (fat and iron) and volume conservation assumption were used to obtain three-material data. Fig. 3 shows the weight fractions of fat, soft tissue, and iron of model 'A'.

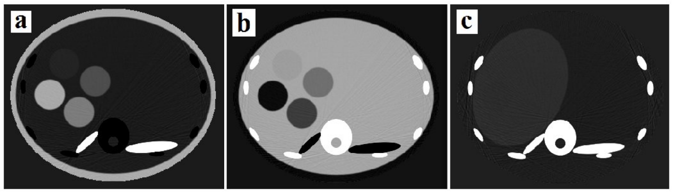

Fig. 3. The results of three-material decomposition. Material-specific weight fraction images: fat (a), soft tissue (b) and iron contents (c) of the phantom.

The results of the material decomposition are listed in Table IV.

TABLE IV CALCULATED WEIGHT FRACTIONS

Material	Fat (w%)			Iron (ppm)		
Region	Real value	model A	model B	Real value	model A	model B
a	***0***	0	0	***2000***	1530	2050
b	***5***	5.1	5.2	***2000***	1640	2120
c	***33***	36.2	36.1	***2000***	2130	2580
d	***66***	70.8	70.8	***2000***	2120	2590
e	***100***	100	100	***2000***	2150	2650

The simulation did not contain noise and scatter. Beam hardening and the filtered backprojection caused some errors in the calculation. These effects can be eliminated with the subtraction of the resulted values of the two models, because the geometry and hence the image artifacts in the two models were the same. The difference between the quantification results of the two liver models is caused by the presence of the higher atomic number elements. Table V contains the biases of the measured weight content values between the two models.

TABLE V ERROR OF THE MATERIAL QUANTIFICATION IN THE LIVER REGION

Bias caused by the added elements	Δ Soft tissue (w%)	Δ Fat (w%)	Δ Iron (ppm)
a	-0.3	0.2	520
b	-0.1	0.0	480
c	0.1	-0.1	450
d	0.0	-0.1	470
e	-0.1	0.1	500

IV. CONCLUSION

It was shown that the applied three-material decomposition method detects the higher atomic number elements as iron, thus the iron content is overestimated in the presence of the higher atomic number elements, However these additional elements do not affect the quantification of fat, because their attenuation coefficients are more similar to the attenuation of iron than the attenuation of soft tissue or fat. 330 ppm heavy metal concentration in liver causes ~500 ppm bias in iron measurement. These observed effects predict the difficulty of iron content measurement by dual-energy CT. To improve the accuracy of a future clinically used method, the liver soft tissue as one of the basis materials must be modeled with a material which contains no iron, but normal level elements with higher atomic numbers.

The results show that with an accurate CT system the method can be used to predict the condition of the liver.

ACKNOWLEDGMENT

The publication is supported by the European Union and co-funded by the European Social Fund. (Project title: “Broadening the knowledge base and supporting the long term professional sustainability of the Research University Centre of Excellence at the University of Szeged by ensuring the rising generation of excellent scientists.” Project number: TÁMOP-4.2.2/B-10/1-2010-0012).

REFERENCES

[1] ICRU (1989), “Tissue Substitutes in Radiation Dosimetry and Measurement”, Report 44 of the *International Commission on Radiation Units and Measurements* (Bethesda, MD).

[2] Hamer OW et al. “Fatty Liver: Imaging Patterns and Pitfalls”, *RadioGraphics*, vol. 26, pp. 1637-1653, 2006

[3] M. Marinelli et al. “Total Iron-Overload Measurement in the Human Liver Region by the Magnetic Iron Detector”. *IEEE Transactions on Biomedical Engineering*, vol. 57, pp. 2295-2303, 2010

[4] Y.C. Yoo et al. “Organ distribution of heavy metals in autopsy material from normal Korean”, *Journal of Health Science*, 2002, 48, 186-194.

[5] Y. Muramatsu and R.M. Parr, “Concentrations of Some Trace Elements in Hair, Liver and Kidney From Autopsy Subjects -- Relationship Between Hair and Internal Organs”, *The Science of the Total Environment*, vol. 76, pp. 29-40, 1988

[6] Ferenci P, Steindl-Munda P, Vogel W, et al. “Diagnostic value of quantitative hepatic copper determination in patients with Wilson‘s Disease”. *Clin Gastroenterol Hepatol* vol. 3, pp. 811–18, 2005

[7] J. L. Benedetti et al. “Levels of cadmium in kidney and liver tissues among a Canadian population (province of Quebec)”, *J Toxicol Environ Health A*, vol. 56 (3), pp. 145-163, 1999

[8] Poul Johansen, Gert Mulvad, Henning Sloth Pedersen, Jens C. Hansen, Frank Riget, Human accumulation of mercury in Greenland, *Science of the Total Environment* , vol. 377, pp. 173-178, 2007

[9] K. Cranley, B. J. Gilmore, G. W. A. Fogarty, and L. Desponds, “Catalogue of Diagnostic X-ray Spectra and Other Data”, *IPEM* Report 78, 1997

[10] Christoph R. Becker, Maximilian F. Reiser, Konstantin Nikolaou, Gary Glazer, “Multislice CT”, *Springer-Verlag Berlin Heidelberg*, 2009

[11] J. G. Rocha, J. H. Correia,, S. Lanceros-Mendez, “Modeling of the Performance of Scintillator Based X-ray Detectors”, *Proc of IEEE*, vol. 3, pp. 1257 – 1260, 2004

[12] M. J. Berger et al. “XCOM: Photon Cross Section Database version 1.3” (Gaithersburg, MD: *NIST*), 2005

[13] Lifeng Yu, Xin Liu, and Cynthia H. McCollough:. “Pre-reconstruction Three-material Decomposition in Dual-energy CT”, *Proc. of SPIE* Vol. 7258, 72583V, 2009

[14] K.S. Chuang and H.K. Huang, "Comparison of four dual energy image decomposition methods", *Physics in Medicine and Biology*, Vol. 33, pp. 455-466, 1988

Evaluation of mA Switching Method with Penalized Weighted Least-Square Noise Reduction for Low-dose CT

Yunjeong Lee, Hyekyun Chung, and Seungryong Cho

***Abstract* – Computed Tomography (CT) has been increasingly used in clinics for many purposes including diagnosis, intervention, and prognosis. Its image quality should be guaranteed for successful completion of such medical tasks, but at a minimal cost of radiation dose to the patients. There exist a host of approaches to realizing low-dose CT. For example, a low-dose CT can be achieved by lowering the x-ray tube current (mA) during a scan. However, lowering mAs may cause the image quality degradation owing to excessive x-ray quantum noise. Noise reduction techniques such as penalized weighted least-square (PWLS) method can reduce the quality degradation. In this work, we investigated whether mA switching during a scan can improve image quality after the PWLS noise reduction under a constraint of constant total exposure. A simulation study has been conducted, and a Gauss-Seidal update strategy was used to minimize the PWLS cost function. Line profiles of the reconstructed images were used to compare the performances qualitatively, and relative standard deviation and root mean square error (RMSE) were computed to quantitatively compare the results. In addition, the resolution-noise tradeoff curves were acquired using the edge image of a bone in the reconstructed images.**

***Index Terms*– mAs switching, low-dose, noise reduction, penalized weighted least-square, computed tomography**

I. INTRODUCTION

Much efforts have been made on achieving low-dose X-ray computed tomography (CT) for many clinical purposes since the risk of radiation damage to the patients due to CT scans may not be negligible. One possible way to lower radiation dose to the patients is to decrease the x-ray tube current (mA) or to make the x-ray exposure time shorter. However, reducing radiation exposure in CT will inevitably cause increase of the noise level in the sinogram mainly due to the excessive x-ray quantum noise, and will eventually degrade quality of the reconstructed images.

There are many approaches to mitigating the degradation of image quality [1-5]. Penalized weighted least-square (PWLS) noise reduction method is one of the popularly used techniques for sinogram denoising. Neighbor pixels in a sinogram are used to iteratively update a pixel value in the sinogram. Typically, horizontal neighbors and vertical (or angular) neighbors are weighted differently. Usually, horizontal neighbors are at the same noise level with the pixel under interest, but the vertical neighbors may be prepared to have different noise levels for example by modulating the mA from view to view. In such a case, the vertical weighting factors can be adjusted so that the high quality data are heavily used.

Tube current modulation techniques are actively used out there, which are aiming at low-dose high-quality CT imaging taking into account the patient anatomy. The tube current is relatively slowly modulated according to the axial and transverse anatomical path-length variations. Even in those techniques and in most conventional CT systems however, x-ray tube current time product (mAs) is maintained almost constant over many projections during the scan.

In this study, we numerically simulated mA switching and acquired projections: one at higher tube current time product setting (e.g., 14 mAs) and the other at lower tube current time product setting (e.g., 4 mAs) in an interweaving fashion. For comparison, we also acquired projections at a constant tube current setting (e.g., 9 mAs). Fast tube current switching is currently challenging, but may be readily available when cold cathode technique is used in the tube. We investigated whether the mA switching method can perform any better than a constant mA method under the PWLS algorithm. The PWLS cost function was set according to the Gaussian noise properties of the sinogram [6]. A theoretical formula that describes the relationship between data sample mean and variance was used [7], [8]. The minimizing process of the objective function follows the Gauss-Seidel update rule [9] and the reconstructed images were produced by use of the Feldkamp-Davis-Kress (FDK) algorithm [10], [11]. For a qualitative evaluation, line profiles of the reconstructed images were used and for a quantitative comparison, the relative standard deviation and root mean square error (RMSE) were computed in the selected regions of interest (ROIs) [12]. Full width half maximum (FWHM) of a bone edge image was calculated so as to evaluate the resolution of the reconstructed images and resolution-noise tradeoff curves [13] were obtained.

II. METHOD

A. Acquisition of the data sample

The XCAT phantom was used to simulate a human torso and we focused our study on the reconstruction of 2 dimensional slice of the abdominal region.

The CT project program was used and totally 360 projections were acquired with one rotation. We modified tube

---

The authors are with the department of nuclear and quantum engineering at KIAST, Korea. Correspondence to S. Cho (scho@kaist.ac.kr). The research was partly funded by NRF N01110154.

current time product (mAs), using 4 mAs and 14 mAs by turns in each projection. We also used 9 mAs in a fixed mode, which has the equivalent radiation dose to the mAs modulating case. Other geometry conditions are as follow: cone-beam projections onto a flat-panel detector with 512 channels and half fan-angle of 6.5 degrees. Distance from the x-ray source to the detector is 1510.4 mm, and the axis to the detector distance is 289.6 mm. We modeled a Poisson noise to each projection view according to the number of photons.

B. Penalized Weighted Least-Squares (PWLS) Noise Reduction

In this study, PWLS algorithm was applied to reducing the sinogram noise. The PWLS criterion can be used to estimate the corresponding ideal sinogram by minimizing the following cost function [6]

$$\Phi(q) = (\hat{y} - q)' \Sigma^{-1} (\hat{y} - q) + \beta R(q) \qquad (1)$$

Equation (1) is composed of two terms. The first term represents the weighted least-square (WLS) cost function; q is the vector of ideal projection data and $\hat{y}$ is the system-calibrated and log-transformed projection measurements. Σ is the diagonal variance matrix.

If the line integral of the object attenuation coefficients follows a Poisson distribution (if polyenergetic nature is not considered), theoretically the data mean and variance relation is valid [7], [8]

$$\sigma_i^2 \approx \frac{\exp(\mu_i)}{N_0} \qquad (2)$$

where N_0 is the numbers of detected photon in the absence of phantom in the field-of-view (FOV).

The second term describes roughness penalty and can be shown as follow:

$$R(q) = q' R q = \frac{1}{2} \sum_i \sum_{m \in N_i} w_{im} \left(q_i - q_m \right)^2 \qquad (3)$$

, where N_i represents the set of four nearest neighbors of the ith pixel in the sinogram. The parameter w_{im} was set to be 1 for the two horizontal neighbors and 0.25 for the vertical neighbors [7] when there is no modulation of x-ray tube current. We adjusted this parameter so that more weight is given to the 14 mAs projection views and less weight to the 4 mAs projection views. The smoothing parameter β determines the relative influence of these two terms.

We adapted the iterative Gauss-Seidel (GS) update algorithm [9]

$$q_i^{(n+1)} = \frac{y_i + \beta \sigma_i^2 \left(\sum_{m \in N_i^1} w_{im} q_m^{(n+1)} + \sum_{m \in N_i^2} w_{im} q_m^{(n)} \right)}{1 + \beta \sigma_i^2 \sum_{m \in N_i} w_{im}} \qquad (4)$$

, where index n indicates the iterative number, N_i^1 represents the upper and left pixels of q_i, N_i^2 denotes the right and lower pixels of q_i. The variance σ_j is determined according to (2).

In our simulation, 10 iterations were empirically found to be sufficient.

III. RESULTS AND DISCUSSIONS

Fig.1. shows the reconstructed images from the data acquired at 9 mAs scan (a), PWLS noise reduction applied (b), and from the data acquired mA switching scan after applying PWLS noise reduction (c). Fig.2. shows line profiles along the horizontal midline of the reconstructed images; dotted line corresponding to (a), solid to (b), and dashed to (c) in Fig.1.

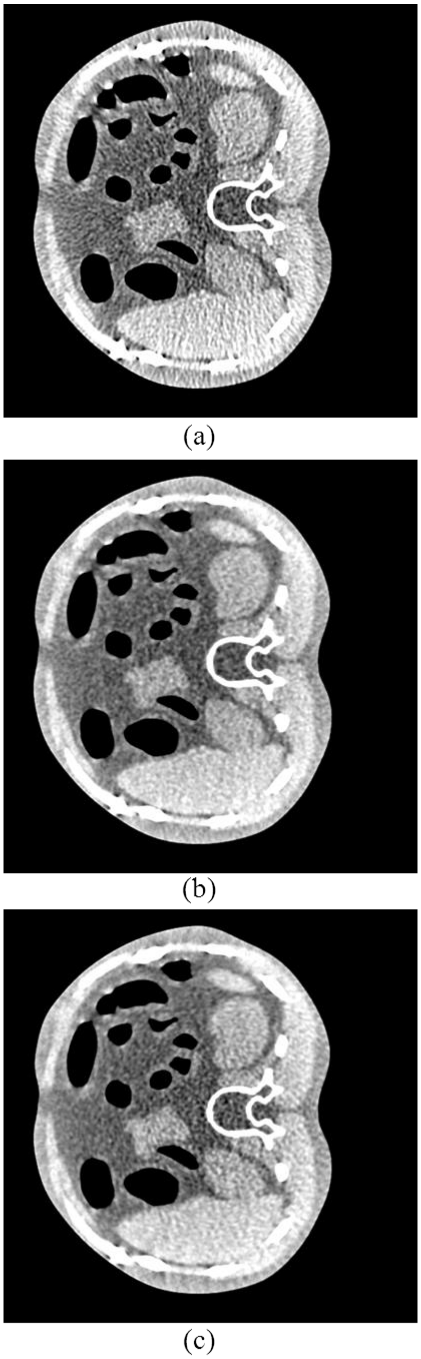

(a)

(b)

(c)

Fig. 1. Reconstructed images of XCAT phantom: (a) from projection images acquired with 9 mAs, (b) from PWLS noise reduction for 9 mAs projection images, and (c) from PWLS noise reduction for the shuffled 4 mAs and 14 mAs projection images.

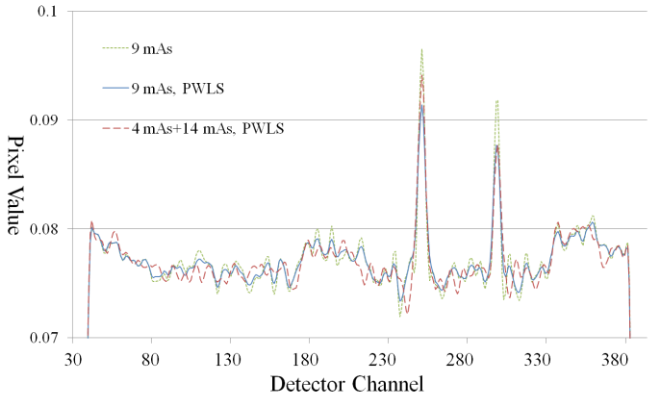

Fig. 2. 1 D profile along the horizontal midline of the reconstructed images in Fig. 1.

Fig.1. shows that the reconstructed images are smoothed both in 9 mAs and in mA switching case when the PWLS algorithm was applied. However, the noise characteristics are visually hard to distinguish.

Comparing the line profiles in Fig.2., it is seen that the image reconstructed from the mA switching method has different fluctuation tendency from 9 mAs reconstructed image. It is still difficult to say which one is less noisy however.

For a more quantitative analysis, the reconstructed image noise was characterized by the relative standard deviation, σ / μ, and the root mean square error (RMSE) of uniform regions of the phantom as shown in Fig. 3. The RMSE was calculated according to (5):

$$RMSE = \sqrt{\frac{1}{N}\sum_{i}^{N}(f_i - f_i^r)^2} \tag{5}$$

, where f and f^r indicate the reconstructed image and the reference image, respectively, and N is the number of pixels in each ROI. The computed values are summarized in Table I and Table II.

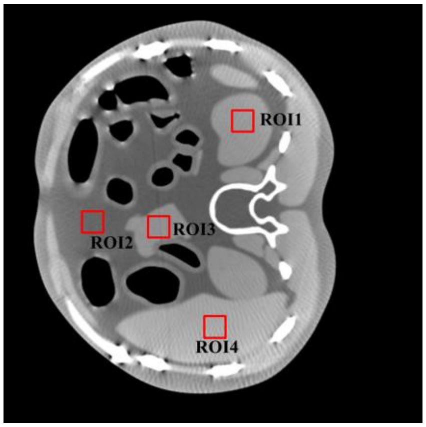

Fig. 3. Four regions of interest of the reconstructed image for the evaluation of the performance.

TABLE I. RMSE FOR REGIONS OF INTEREST

	ROI 1	ROI 2	ROI 3	ROI 4
9 mAs	10.695	8.551	10.246	8.644
9 mAs, PWLS	6.501	5.426	7.133	4.697
mixed , PWLS	6.666	5.203	8.289	4.841

TABLE II. RELATIVE STANDARD DEVIATION FOR REGIONS OF INTEREST ($\times 10^2$)

	ROI 1	ROI 2	ROI 3	ROI 4
9 mAs	1.357	1.123	1.305	1.078
9 mAs, PWLS	0.825	0.712	0.909	0.586
mixed , PWLS	0.845	0.684	1.068	0.604

The results of Table I and Table II represent that the noise in every ROI was reduced in both images reconstructed from the data acquired by the 9 mAs scanning method and the mA switching method after applying the PWLS. However, it cannot be said that the mA switching method outperforms the constant mA method.

Due to PWLS denoising, the reconstruction images may be blurred. Fig. 4. compares the images that are enlarged in one specific organ to check the edge blurring. It appears that the image from the data acquired by the mA switching method is blurrier.

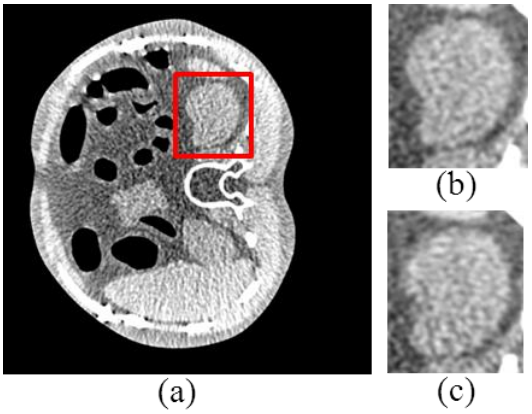

Fig. 4. (a) The reconstructed image from projections acquired at 9 mAs, (b) reconstructed image from 9 mAs projection with PWLS denoising, and (c) reconstructed image from mixed mAs projection with PWLS denoising.

By varying the smoothing parameter β of the PWLS algorithm, we acquired the noise-resolution tradeoff curve for the two scanned data sets. The noise-resolution tradeoff curves are shown in Fig. 5. We calculated the FWHM of a spinal bone edge in the horizontal midline of the reconstructed image.

In Fig.5., it is observed that the mA switching scan approach leads to higher noise levels at given resolutions than the constant 9 mAs scan method.

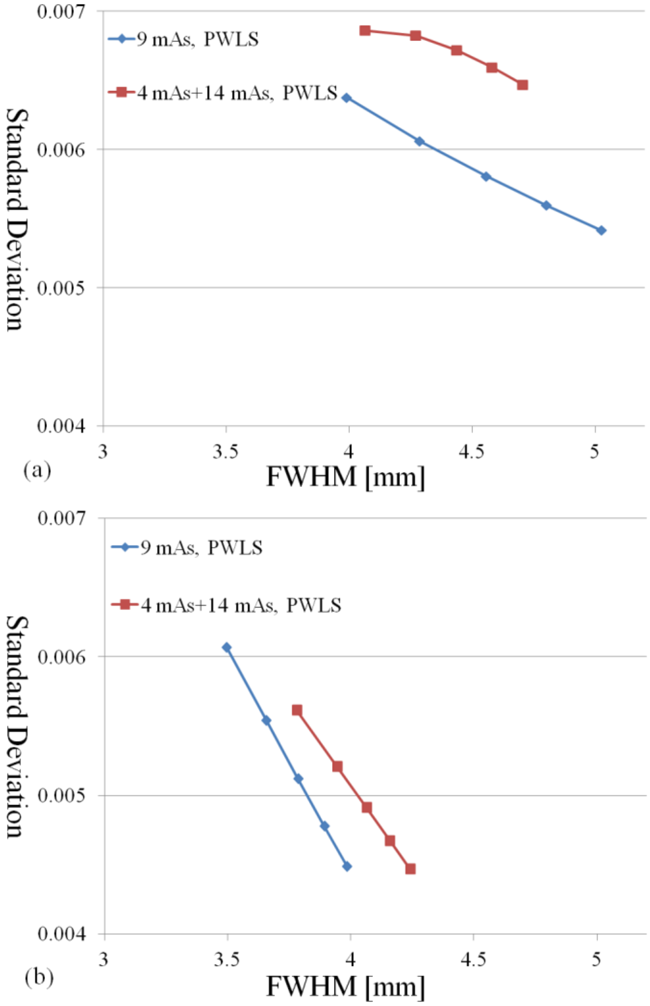

Fig. 5. The noise-resolution tradeoff curves for the 9 mAs CT scan with PWLS smoothing approach and the mAs modulated CT scan with PWLS smoothing approach: (a) the left bone edge and (b) the right edge of the bone in the horizontal midline of the reconstructed images in Fig.1 were analyzed.

IV. CONCLUSION

In this paper, tube current switching method for low-dose CT was simulated and penalized weighted least-square noise reduction approach was applied to improving the quality of reconstructed images. In addition, it was analyzed whether the mA switching CT scan method would be beneficial with the PWLS smoothing approach. Tube current time product of 14 mAs, which is normally used in conventional cone-beam CT based on flat-panel detector, and 4 mAs were numerically acquired alternatively at each projection. To better utilize the PWLS denoising, we used the data of higher tube current time product setting more heavily than those of lower tube current time product setting by adjusting the weight parameter. Constant tube current of 9 mAs, which has the equivalent dose to the previous case, was also simulated to compare the imaging performance.

The relative standard deviation and root mean square error at the selected ROIs did not show practical advantage of the mA switching CT scan method in terms of denoising. Additionally, the resolution-noise tradeoff curves imply that the PWLS denoising method does not selectively work better for the data acquired by the mA switching.

In the future study, other denoising approaches will be explored to seek better quality images from the data acquired by mA switching scan. Edge preserving techniques may be incorporated so as to prevent image blurring at the boundaries of organs.

REFERENCES

[1] Patrick J. La Rivière, "Penalized-likelihood sinogram smoothing for low-dose CT," *Med. Phys*. vol. 32, no. 6, pp. 1676-1683, June. 2005.

[2] Peter Forthmann, Thomas Köhler, Michel Defrise, and Patrick J. La Rivière, "Comparision of three sinogram restoration methods," *Proc, SPIE* vol. 6142, 61420Y, 2006.

[3] Vladimir Z. Mesarovic, Nikolas P. Galatsanos, and Miles N. Wernick, "Sinogram restoration from partially-known blur for tomographic reconstruction," *IEEE, Imaging Processing*, vol. 2, pp. 512-515, Oct. 1995.

[4] Trlet Le, Rick Chartrand, and Thomas J. Asaki, "A variational approach to reconstructing images corrupted by poisson noise," *J Math Imaging Vis 27*, pp. 257-263, 2007.

[5] Isabel Rodrigues, João Sanches, and José Bioucas-Dias, "Dinoising of medical images corrupted by poisson noise," *IEEE, Imaging Processing*, pp. 1756-1759. Oct. 2008.

[6] Jing Wang, Tianfang Li, Hongbing Lu, and Zhengrong Liang, "Penalized weighted least-square approach to sinogram noise reduction and image reconstruction for low-dose x-ray computed tomography," *IEEE Trans. Medical Imaging*, vol.25, no. 10, pp. 1272-1283, Oct. 2006.

[7] Tianfang Li, Xiang Li, Jing Wang, Junhai Wen, Hongbing Lu, Jiang Hsieh, and Zhengrong Liang, "Nonlinear sinogram smoothing for low-dose x-ray CT," *IEEE Trans. Nucl. Sci*., vol. 51, no. 5, pp. 2505-2513, Oct. 2004.

[8] Hongbing Lu, Ing-Tsung Hsiao, Xiang Li, and Zhengrong Liang, "Noise properties of low-dose CT projections and noise treatment by scale transformations," *Conf. Rec. IEEE NSS-MIC*, Nov. 2001.

[9] Ken Sauer and Charles Bouman, "A local update strategy for iterative reconstruction from projections," *IEEE Trans. Siganl Processing*, vol. 41, no. 2. Feb. 1993.

[10] L. A. Feldkamp, L. C. Davis, and J. W. Kress, "Practical cone-beam algorithm," *J. Opt. Soc.* Am. A/vol. 1, no.6, June. 1984.

[11] Thomas Rodet, Frédéric Noo, and Michel Defrise, "The cone-beam algorithm of Feldkamp, Davis, and Kress preserves oblique line integrals," Medical Physics, vol. 31, no.7, pp. 1972-1975. July. 2004.

[12] Lu Jiang, Khan Siddiqui, Bin Zhu, Yang Tao, and Eliot Siegel, "Sinogram restoration for ultra-low-dose x-ray multi-slice helical CT by nonparametric regression," *Proc. SPIE*, vol. 6510, 65105L, 2007

[13] Jing Wang, Hongbing Lu, Junhai Wen, and Zhengrong Liang, "Multislice penalized weighted least-squares sonogram restoration for low-dose x-ray computed tomography," *IEEE Trans. Biomedical Engineering*, vol. 55, no. 3, March. 2008.

Ultra-High Resolution Imaging by Archimedean Spiral on Radon Space

[1]Synho Do*, [1]Rajiv Gupta, [1]Tom Brady, and [2]W. Clem Karl

Abstract—**We presents an Archimedean spiral sampling method on Radon space to assess improvement in spatial resolution. In conventional systems, the system resolution is limited by the detector size and the angular step size. We hypothesize that the resolution of the proposed method is not determined by the detector size, but rather by the number of shifts, generating a spiral pattern(s) on Radon space. The exact mathematical form of this trajectory is derived by a modified Archimedean spiral. We show an iterative image reconstruction through accurate system modeling of this Archimedean spiral. Initial simulation results demonstrate a 16-fold resolution improvement.**

Keywords-component; Ultra-high resolution, Iterative reconstruciton technique, Radon space, Archimedean spiral, Compressed sensing, Sparse sampling

I. INTRODUCTION

There have been many advances in the physics of medical imaging systems, especially in X-ray detectors. Improvements in spectral sensitivity and the photon counting function of new detectors are essential to extend the applications of CT. Usually, the size of a prototype detector is bigger than the conventional detector element due to the additional circuits and physical limitation of detector. Thus systems are limited to acquire small Field of View (FOV) image or to generate coarse grid image. When the size of detector element is fixed, the resolution of system is fixed by circular nature of sampling pattern even though the quarter shift of detector and the Flying Focal Spot (FFS) can improve sampling density of CT systems.

Spiral sampling methods have been studied as a possible solution of conventional Magnetic Resonance Imaging (MRI) [1, 2], rapid MR imaging [3], and improving spatial resolution [4] of MRI. In this paper, we assess spiral sampling patterns to gain insights into the ultra-high resolution imaging in tomographic systems (i.e., SPECT, PET, and CT). Many proposals of the MRI image reconstruction aim to reduce data sampling by trying to mitigate under-sampling artifacts in k-space. In this paper, we try to overcome azimuthally under-sampling of bigger detector CT system by fractional shifts of detector. These fractional shifts of detector are modeled by Archimedean Spiral on Radon Space (ASRS).

In the ensuring sections, we review a general Archimedean spiral, derive exact formula for the proposed fractional shifts of detectors with modified Archimedean spiral, and examine iterative image reconstruction method for the proposed method. We demonstrate significant resolution improvement with simulation data.

II. METHODS

1) Archimedean Spiral

The Archimedean spiral, known as the arithmetic spiral, is the locus of points corresponding to the locations over time of a point moving away from a fixed point with a constant speed along a line, which rotates with constant angular [5]. The radial distance, r, is represented by a general form of Archimedean spiral is:

$$r = a + b\theta^{\frac{1}{k}} \tag{1}$$

where, θ is polar angle, and a and b are constant. When k change from -2 to 2, the spiral wraps tightly. Figure 1-(a) shows the trajectory of (θ, r) in Cartesian grid with $a = 0$, $b = 1$, and $0 \le \theta \le 540$. Figure 1-(b) shows zoomed spiral near origin (0, 0).

2) Modified Archimedean Spiral

We propose to shift detector system by *1/n* of detector size for *n* angular sampling positions to create Archimedean spiral (*k*=1) on Radon space. The schematic diagram of fractional shift is illustrated in Figure 2. At each angular sample, detector system shifts toward one direction. This proposed method to produce irregular sampling pattern on Radon space for each detector element is exactly described by the modified Archimedean spiral:

$$r = a + (b'/2n)\,\theta^{\frac{1}{k}} \tag{2}$$

where, a is initial detector location, b' is detector size, and n is rotation/180 degree. We use *k*=1 for our simulation. The modified Archimedean spiral can easily model multiple spirals from multiple detector elements.

---

[1]Dept. of Radiology, MGH and Harvard Medical School, Boston, MA, USA
[2]Dept. of ECE, Boston University, Boston, MA, USA
[*]sdo@nmr.mgh.harvard.edu

Figure 3 illustrates ASRS generated by each detector element with a = [-6, -2, 2, 6] and b'=4 by changing n (i.e., Figure 3-(a): 1, Figure 3-(b): 2, and Figure 3-(c): 3).

III. RESULTS

The detector shift method is simulated by using 64 by 64 pixels image as show in Figure 4-(a). We visually compare two sonograms in Figure 4. Figure 4-(c) is the conventional sinogram collected by 64-element detector system and Figure 4-(e) is the sinogram collected by 4-detector element detector system with fractional shifts, which is an unique way to create Archimedean spiral sampling on Radon space.

The sinogram generated by bigger detector element looks like compressed version of the normal sinogram. This compressed sensing has an under-sampling effect in the azimuthal direction. Therefore, the image reconstructed from compressed sinogram by conventional method results in a blurred image as show in Figure 5-(a). In contrast, the reconstructed image in Figure 5-(-b) that uses the compressed sinogram data that incorporates the fractional shifts in the system model, shows almost identical image resolution compared to ideal image in Figure 5-(b). Figure 5-(c) is the error map between ideal image and reconstructed image.

IV. DISCUSSIONS AND CONCLUSION

In this paper, we present a new image reconstruction method, which models fraction shifts of the detector exactly. The fraction shifts of the detector are derived by the modified Archimedean spiral on Radon space.

The approach to shift the detector and to reconstruct image accordingly is novel. The possible applications are:

- To increase resolution and to improve efficiency of detectors for conventional CT and other tomographic systems
- To implement expensive photon-counting detectors sparsely without losing resolution
- To utilize inhomogeneous detector sets (e.g., interleaved) for spectral imaging without losing resolution

The same effect of detector shifts can be realized by source shift (i.e., continuous FFS system without mechanical motion) or by both shifts (i.e., detector and source). In dual gamma camera SPECT, each gamma camera can create two interleaved Archimedean spirals of the same size. Also we can achieve super-resolution PET image by gentle motion (i.e. gantry wobbling or table motion) with accurate motion modeling.

In summary, the resolution of tomographic system is not limited by the detector size but by the sparseness of sampling on Radon space.

ACKNOWLEDGMENT

Authors would like to thank Dr. Karl Stierstorfer for a discussion at SPIE conference in 2012.

REFERENCES

1. Ljunggren, S., *A simple graphical representation of Fourier-based imaging methods.* J. Magn. Reson, 1983. **54**(2): p. 338-343.
2. Noll, D.C., et al., *Spiral K‐space MR imaging of cortical activation.* Journal of Magnetic Resonance Imaging, 1995. **5**(1): p. 49-56.
3. Ahn, C., J. Kim, and Z. Cho, *High-speed spiral-scan echo planar NMR imaging-I.* Medical Imaging, IEEE Transactions on, 1986. **5**(1): p. 2-7.
4. Meyer, C.H., et al., *Fast spiral coronary artery imaging.* Magnetic Resonance in Medicine, 1992. **28**(2): p. 202-213.
5. Lockwood, E.H., *A book of curves*. 1961: Cambridge University Press.

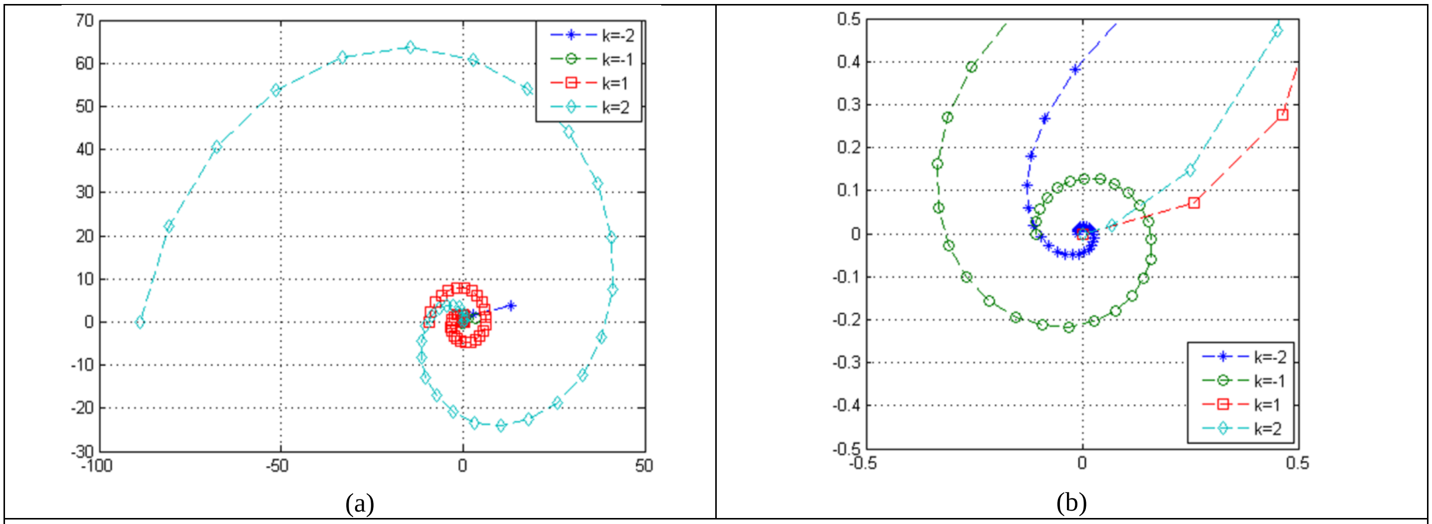

(a) (b)

Figure 1. A generalized Archimedean spiral with k=[-2,-1, 1, 2]: (a) Cartesian grid drawing of Eq.(1) with a=0, b=1, $0 \leq \vartheta \leq 540$, (b) Zoomed near origin (0,0).

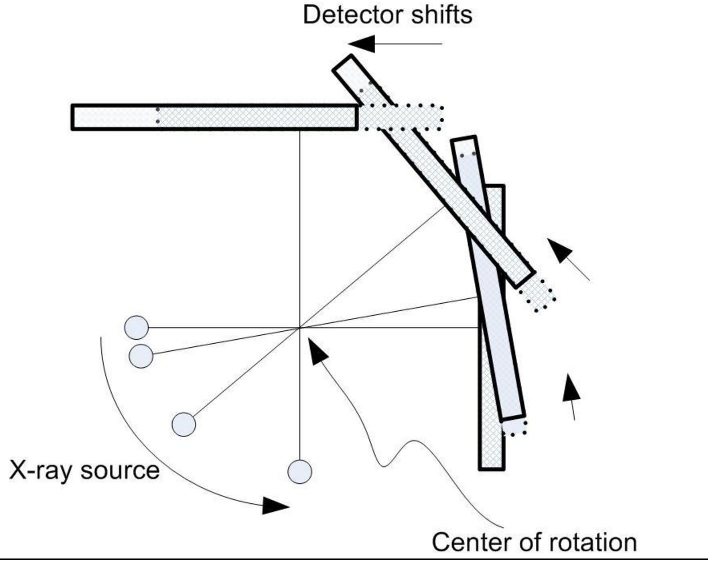

Figure 2, A diagram of fractional shift of detector systems. Detector system shifts *1/n* of detector size for *n* angular sampling position.

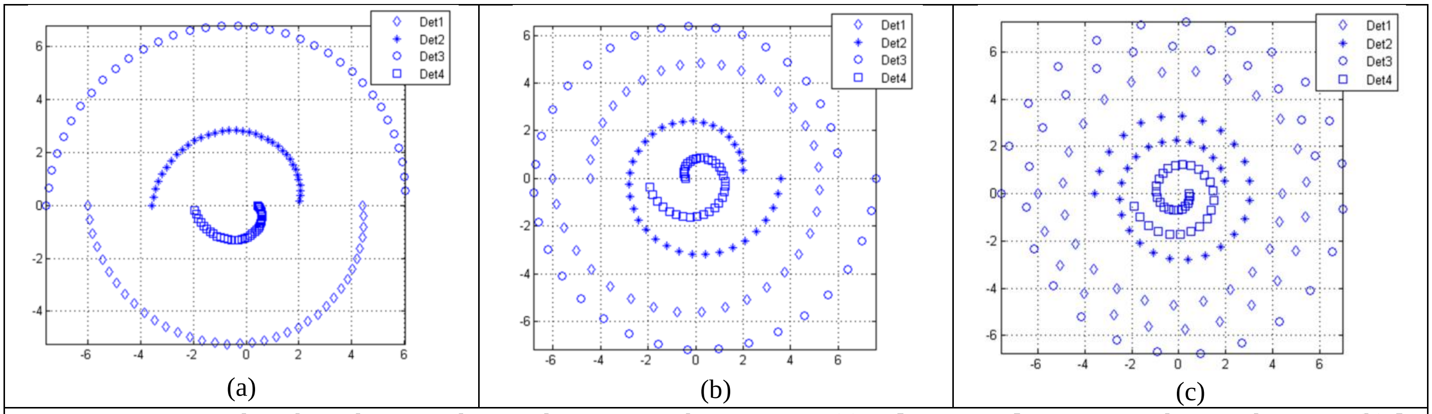

(a) (b) (c)

Figure 3, A proposed Archimedean spiral on Radon space with parameters (a) a=[-6 -2, 2, 6], rotation angle=180 deg, n=1, (b) [-6,-2, 2, 6], rotation angle=360, n=2, and (c) a=[-6,-2,2,6], rotation angle=540 deg, n=3.

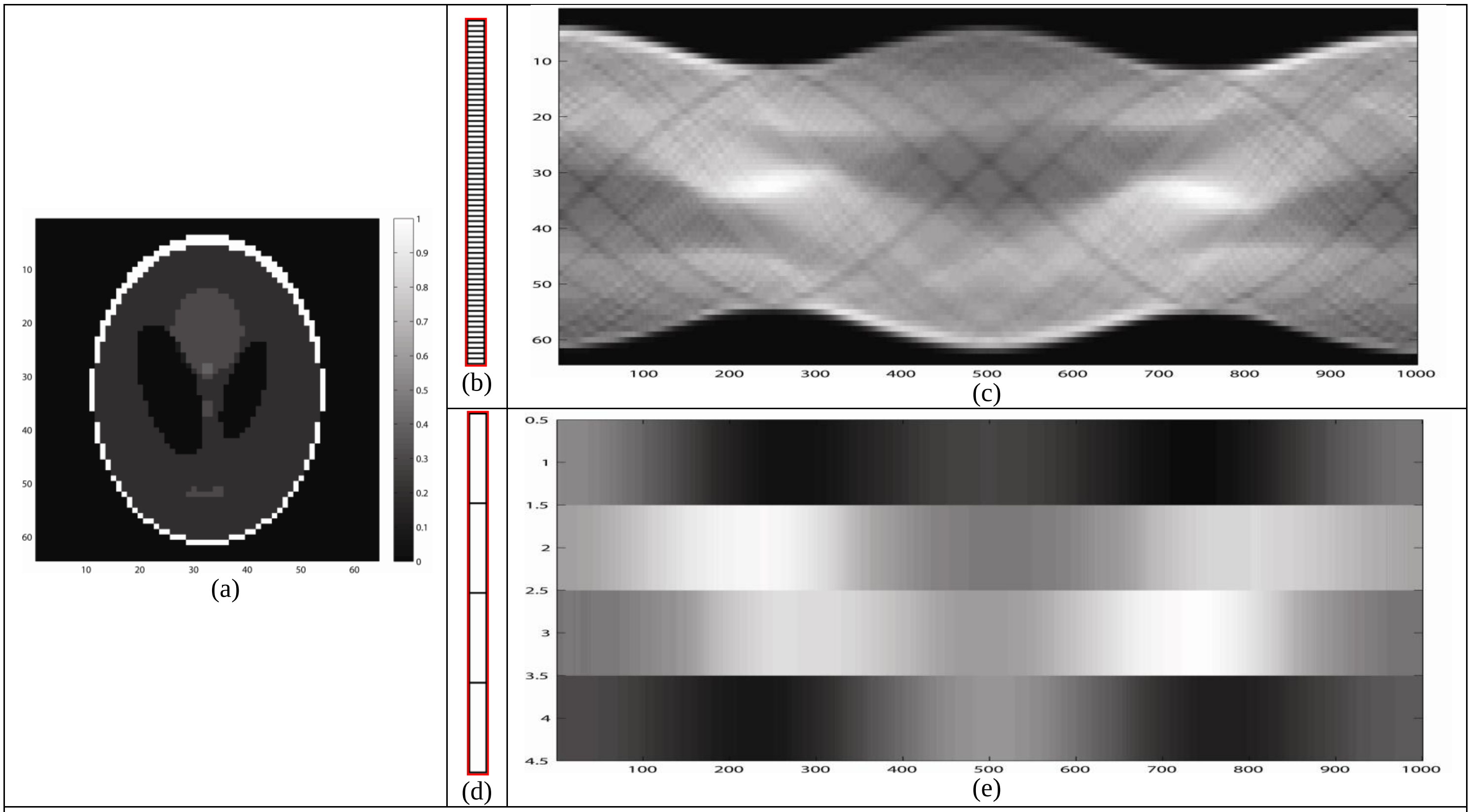
(a)
(b)
(c)
(d)
(e)
10
20
30
40
50
60
0
0.1
0.2
0.3
0.4
0.5
0.6
0.7
0.8
0.9
1
100
200
300
400
500
600
700
800
900
1000
0.5
1
1.5
2
2.5
3
3.5
4
4.5

Figure 4. A sinogram comparison from two detector sets (a) Ideal image (64 by 64), (b) 64-detector elements over 64 pixels, (c) conventional sinogram collected from detector set (b), (d) 4-detector elements over 64 pixels, and (e) sinogram collected from detector set (d), so called compressed sinogram.

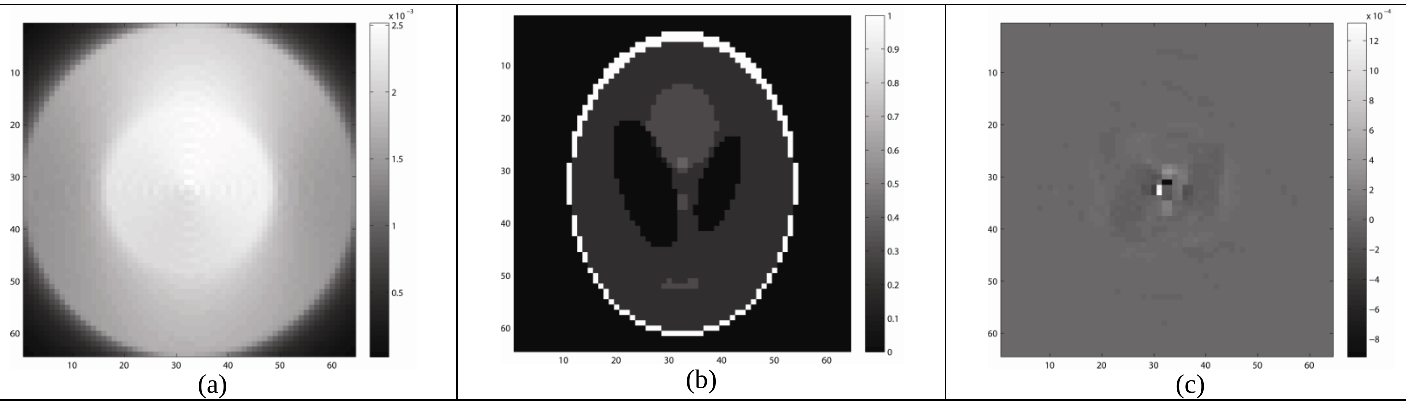
(a)
(b)
(c)
x 10⁻³
x 10⁻⁴
10
20
30
40
50
60
0.5
1
1.5
2
2.5
0
0.1
0.2
0.3
0.4
0.5
0.6
0.7
0.8
0.9
1
-8
-6
-4
-2
0
2
4
6
8
10
12

Figure 5, Reconstructed image (64 by 64) comparison by using the compressed sinogram in Figure 4-(e), (a) conventional TV solution without shift modeling in system matrix, (b) TV method with accurate detector shift model in system matrix, and (c) error map between Ideal image (Fig. 4-(a)) and (b)

Curvelet-based Inpainting for Metal Artifact Reduction in Computed Tomography

Matthias Kleine, Thorsten M. Buzug

Abstract—**We present an algorithm for metal artifact reduction in X-ray Computed Tomography which is based on an inpainting scheme. Inpainting tries to complete missing parts of an image by continuing information from outside consistently. The metal data is considered as missing part of the sinogram and the algorithm completes the absent projections. The inpainting scheme uses the fact that the sinogram can be approximated sparsely by its curvelet coefficients. Using ideas from compressed sensing, the sparse solution can be obtained by solving a convex optimization problem. The results obtained by inpainting are compared to the results received by linear interpolation. It is shown that the general error is reduced in the Radon space as well as in the reconstructed image. Furthermore, the error in the reconstructed image obtained by the inpainting scheme is smaller in regions of interest far-off the metal object.**

I. INTRODUCTION

The presence of metal objects as dental fillings or implants in the field of view of a CT scanner can cause severe artifacts in the reconstructed image. These artifacts can hinder correct diagnoses or even make the reconstructed images useless. Therefore, in many cases a strategy to reduce metal artifacts is needed. To improve image quality, the metal object is usually considered as opaque and the trace of the metal object is removed from the measured data. Dependent on the further processing, one can distinguish between two different groups of algorithms for metal artifact reduction. Iterative algorithms such as modified MLEM [1] can deal with incomplete data whereas interpolation methods try to complete the missing data by filling in synthetic values. This is required in order to use standard reconstruction methods like the Filtered Backprojection (FBP). We will pursue the second approach of filling in synthetic values here.

Kalender *et al.* [2] proposed in 1987 linear interpolation of the missing data in the Radon space. Since then, several methods have been proposed to replace the metal data in the sinogram. In the last decade, inpainting techniques have become very popular to restore missing parts of images. The original idea behind these techniques is to continue information smoothly along the isophote directions into the missing parts of the image. The term was first introduced by Bertalmio *et al.* [3] when they presented a PDE based method. Masnou and Morel [4] earlier used a variational approach for the inpainting problem in the field of computer vision. In 2005, Elad *et al.* [5] presented an inpainting algorithm which decomposes the image into a cartoon layer containing geometrical information and a texture layer. The different layers of an image are represented sparsely in dedicated bases. The problem of completing missing parts of an image is then formulated as a convex optimization problem. In the presented work we will follow the ideas from this paper and [6] to use an inpainting scheme for metal artifact reduction.

In the next section we will introduce the mathematical framework of the inpainting scheme and present the inpainting algorithm. The last two sections deal with the presentation and discussion of the inpainting and reconstruction results.

II. MATERIALS AND METHODS

For our experiments we use one 512x512 pixel slice of the XCAT Software phantom [7] where we add some artificial high values representing the metal object. The original slice serves as a ground truth for the evaluation of our results. We segment the metal in the image domain by a proper threshold. For the forward projection we simulate a system with parallel geometry and 1024 detector elements, rotating from 0 to 360 degrees in 0.5 degree steps. The segmented metal is forward projected into the Radon space. Afterwards, a binary mask M is created to exclude the metal data from the sinogram. To avoid ringing artifacts at the mask borders resulting from the curvelet transform we enlarge the sinogram by adding the 50 upper lines to the lower end and vice versa.

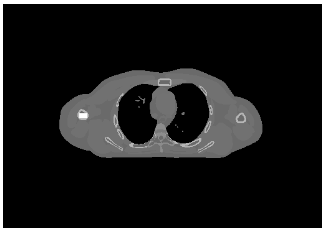
(a) CT-slice with manually inserted metal object

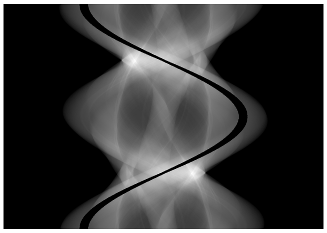
(b) The masked sinogram

We will express the sinogram sparsely in a dedicated frame (the curvelet frame) and formulate the inpainting task as an optimization problem. The mathematical theory for the problem of finding the sparsest representation of a signal in a given dictionary will be developed in the next section. The optimization problem is stated at the end of the section.

This work is part of MOIN - CC (Molecular Imaging North - Competence Centre), financially supported by the European Union and the State of Schleswig-Holstein (grant no. 122-09-053).

Matthias Kleine is with the Graduate School for Computing in Medicine and Life Sciences and Institute of Medical Engineering, University of Luebeck, Luebeck, Germany (e-mail: kleine@imt.uni-luebeck.de)

T. M. Buzug is with the Institute of Medical Engineering, University of Luebeck, Luebeck, Germany (e-mail: buzug@imt.uni-luebeck.de)

A. The optimization problem

Let our sinogram of size $n_1 \times n_2$ be represented by a 1D vector X of size $n = n_1 \times n_2$. We assume that we have a collection of vectors ϕ_i, $i = 1 \ldots m$ with $m > n$. Therefore, this set contains more elements than a basis for $\mathbb{R}^n$. We will call the set $\{\phi_i\}_i$ an overcomplete dictionary. The elements ϕ_i are called atoms.

We want to express the sinogram X with respect to the dictionary $\{\phi_i\}_i$ by a sparse coefficient vector $c = (c_1, \ldots, c_m)$, $X = \sum_{i=1}^{m} c_i \phi_i$. Sparse means here that the L_0-norm $||c||_0 := \#\{i : c_i \neq 0\}$ of the coefficient vector is small, hence the sinogram can be expressed by few coefficients c_i in the dictionary $\{\phi_i\}_i$.

If we arrange the atoms ϕ_i as columns in a matrix $\Phi \in \mathbb{R}^{n \times m}$, $m > n$, we can use matrix-vector notation to formulate the problem of finding a representation, $X = \Phi c$. We can see that the problem is underdetermined and therefore there is no unique solution. One has to remark that the transform Φ will usually not be implemented explicitly.

In order to find the sparsest representation c of our sinogram X, we have to solve the following minimization problem:

$$\min_c ||c||_0 \quad \text{s.t.} \quad X = \Phi c. \tag{1}$$

Unfortunately, this problem is combinatorial and therefore computationally intractable for larger signals X. From the theory of Compressed Sensing [8] it is well known that solving the convex optimization problem

$$\min_c ||c||_1 \quad \text{s.t.} \quad X = \Phi c. \tag{2}$$

in the L_1-norm $||c||_1 := \sum_{i=1}^{m} |c_i|$ leads also to the sparsest representation $\tilde{c}$. As the approach should also deal with noisy data, we demand only that the back-transform Φc of the sparse representation c approximates the sinogram X up to a small error σ (the noise level). A total variation (TV) penalty is added to suppress noise [9]. The TV term is the L_1-norm of the gradient of the image X and penalizes therefore images with are not piecewise constant. The TV penalty is implemented as in [6]: We compute the undecimated Haar wavelet transform [10] coefficients of our image X and soft-threshold these coefficients with threshold γ. Afterwards we reconstruct the image by the inverse undecimated wavelet transform.

We solve the following minimization problem

$$\min_c \{||c||_1 + \gamma \mathrm{TV}(\Phi c)\} \quad \text{s.t.} \quad ||X - \Phi c||_2 \leq \sigma \tag{3}$$

by using the adapted minimization algorithm from [5] or [6] below. The key step is the application of the soft-threshold on the coefficients c_i. This results in a shrinkage of the L_1-norm of c and therefore delivers a sparse representation of the sinogram. The component-wise soft-threshold is defined as follows: For a given threshold λ the update to the coefficient c_i is defined as

$$c_i = \begin{cases} c_i - \lambda, & \text{if } c_i \geq \lambda \\ 0, & \text{if } |c_i| \leq \lambda \\ c_i + \lambda, & \text{if } c_i \leq -\lambda \end{cases}$$

Algorithm 1 Minimization algorithm

```
Given a sinogram $X$ with gap, a binary mask $M$ and a dictionary $\Phi$.

Choose a maximum number of iterations $N$, the TV-parameter $\gamma$ and the stopping threshold $\lambda$.
  • Initialization:
      – Set $X_0 = 0$.
      – Set the residual $r_0 = X$.
      – Calculate $\Delta = \max ||\Phi^T X||_2$ and set threshold $\lambda_0 = \frac{\Delta}{N-1}$.
  • Main iteration: For t=1:N
      – Update the coefficients by soft-thresholding:
        $c_t = TH_{\lambda_t}(\Phi^T r_t)$.
      – Update the sinogram $X_t = \Phi c_t$.
      – Apply a TV penalty to $X_t$.
      – Update the residual $r_{t+1} = X - M X_t$.
      – Update the threshold $\lambda_{t+1}$ by a chosen scheme.

End iteration. Output: Inpainted image $\tilde{X} = \Phi c_N$.
```

As the sinogram contains almost no texture and can be well approximated by a piecewise smooth image, we use the curvelet frame to represent the sinogram in a sparse way.

B. The curvelet frame

The curvelet transform is a multiscale transform which is localized in direction and space. In contrast to wavelets which are only localized in space, curvelets have pronounced directions at higher scales. Whereas wavelets provide an optimal representation of signals with singularities at points, curvelets allow an almost optimal representation of objects having singularities along curves. More precisely, curvelets can represent objects which are in $\mathcal{C}^2$ (twice continuously differentiable) except at singularities along $\mathcal{C}^2$-curves in a sparse way. Two curvelets at two different scales are shown in figure 1.

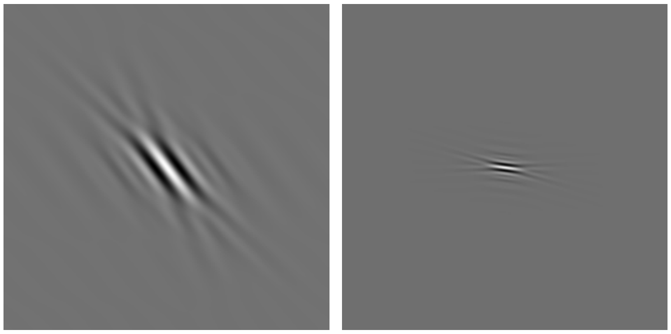

(a) Curvelet scale 2

(b) Curvelet scale 4

Fig. 1: Two different curvelets at two different scales in the image spaces.

The basic idea of the discrete curvelet transform is now as follows: the image is transferred into the Fourier-space and resampled there. The curvelets are constructed by an angular and a radial window function in frequency space, so that their support is on a circular wedge. Each of these wedges in frequency space is now transferred to the origin and wrapped that it covers a rectangle there. Finally, the 2D inverse Fourier transform is applied to each of these rectangles. Curvlets can represent smooth objects in a sparse way as only curvelet coefficients, which corresponds to curvelets aligned to edges in the image are large. Coefficients, which corresponds to curvelets that are not aligned with edges are close to zero. The curvelet transform is described in detail in [11] and [12]. The implemented curvelet transform is available at [13].

C. Experimental setup

For our experiments we choose a TV penalization parameter $\gamma = 0.1$. The iteration number is $N = 500$. The curvelet decomposition was made up to level 8. The threshold λ was chosen to be constant for all iterations. The stopping threshold was set to zero in our case.

III. RESULTS

We compare the results obtained by the sparsity-based inpainting scheme with the linear interpolation results. The comparison is done in the Radon space as well as in the image space. We use the root mean square error (RMSE) of two images U, V

$$\text{RMSE}(U,V) = \sqrt{\frac{1}{MN}\sum_{i,j}(U_{i,j} - V_{i,j})^2}, \quad U,V \in \mathbb{R}^{M\times N},$$

to compare the sinogram and the reconstructed images to the references. The visual impression of the sinogram after the inpainting process is good. In contrast to the results obtained by linear interpolation the gap is not noticeable anymore. A zoom of the same region of the sinogram for both interpolation methods is shown in figure 2.

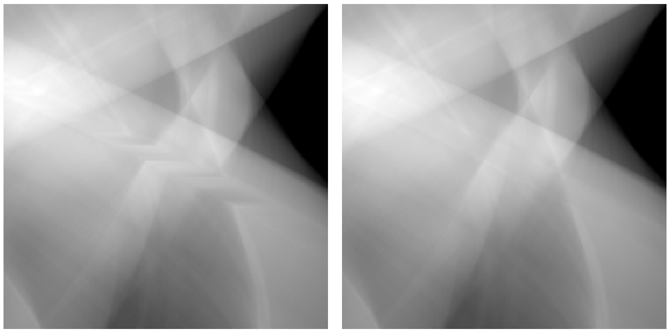
(a) Linear interpolation (b) Inpainting

Fig. 2: A zoom of the results of linear interpolation and the curvelet-based inpainting. The contrast is enhanced to make small structures visible.

The root mean square error between the completed sinograms and the reference sinogram is 0.2287 for linear interpolation and 0.1905 in case of the inpainting result. The absolute error to the reference image is shown in a small part of the sinogram in figure 3.

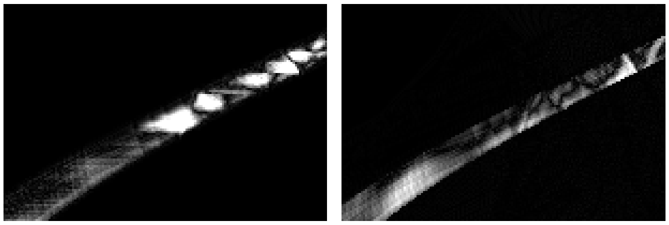
(a) Linear interpolation (b) Inpainting

Fig. 3: The absolute error at a small patch between the completed sinograms and the reference sinogram without metal. Both images are shown in the same gray value window.

We reconstruct the two sinograms obtained by linear interpolation and sparse-representation-based inpainting by using the filtered backprojection. The reconstructions are shown in figure 4 and figure 5. At regions farer away from the metal object artifacts are less visible in the inpainting-based result than in the result obtained by linear interpolation. However, the visual impression indicates that the result obtained by curvelet-based inpainting is worse than linear interpolation close to the metal object.

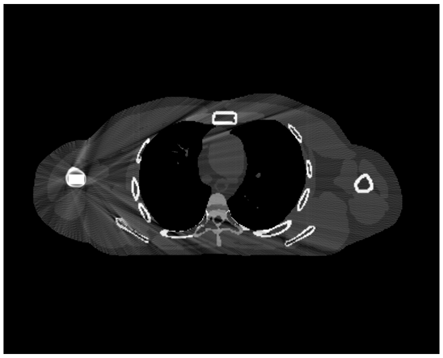
Fig. 4: Reconstruction results by linear interpolation

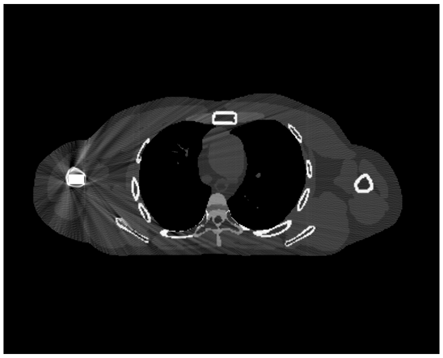
Fig. 5: Reconstruction results by curvelet inpainting

The root mean square error between the reconstructed images and the reference image is 2.4529e-3 for the linear interpolation result and 2.1892e-3 for the curvelet-based inpainting result.

We compare the reconstruction results at three different regions of interest. The regions of interest are shown in figure 6.

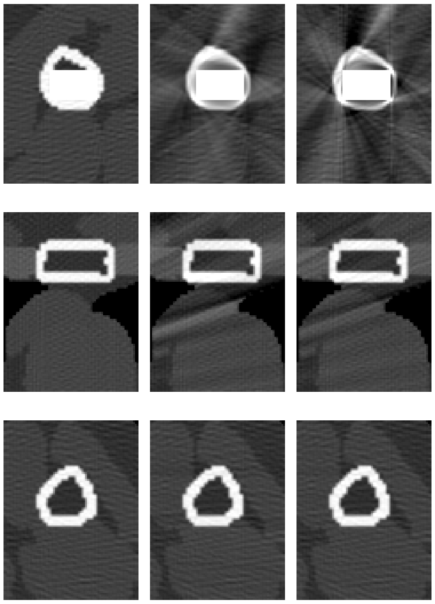
(a) Reference images (b) Linear interpolation (c) Curvelet-based inpainting

Fig. 6: The three different regions of interest. The first column is the reference reconstruction, the second column is the result obtained by linear interpolation and the third column is the curvelet-based inpainting result.

The root mean square errors between the three regions from top to bottom to the reference regions are shown in table I.

TABLE I: RMSE of three different regions of interest

	Linear interpolation	**Curvelet-based inpainting**
Region 1	8.1440e-3	1.1631e-2
Region 2	5.1843e-3	2.6900e-3
Region 3	9.5507e-4	7.6288e-4

The runtime of the inpainting process which is fully implemented in MATLAB takes about 15 minutes for 500 iterations.

IV. DISCUSSION

The results show that compared to linear interpolation the total error is reduced by the presented inpainting scheme in the Radon space as well as in the image domain. The visual impression of the reconstruction results matches the analysis of the RMSE. Even if the error in the region of interest close to the metal is smaller in the result received by linear interpolation, the total error and the error in the region of interest farer away from the metal is reduced by the curvelet-based inpainting scheme.

It is expected that the results can be further improved by optimizing parameters such as the finest scale or the number of different angles for the curvelet transform. The algorithm is suitable for a wide class of transforms such as the wavelet or ridgelet transform and can even deal with multiple transforms, each representing different layers of the image [6]. It is therefore planned to compare results obtained by different or additional transforms which can represent sparsely missing structures in the sinogram. Finally, the results should be compared to inpainting results obtained by different inpainting schemes.

REFERENCES

[1] M. Oehler and T. M. Buzug, “Modified MLEM algorithm for artifact suppression in CT,” in *Nuclear Science Symposium Conference Record, 2006. IEEE*, vol. 6. IEEE, 2006, pp. 3511–3518.

[2] W. Kalender and R. Hebel, “Reduction of CT artifacts caused by metallic implants,” *Radiology*, no. August, pp. 576–577, 1987.

[3] M. Bertalmio, G. Sapiro, and V. Caselles, “Image inpainting,” in *Proceedings of SIGGRAPH 2000*, 2000.

[4] S. Masnou and J. Morel, “Level lines based disocclusion,” in *Image Processing, 1998. ICIP 98. Proceedings. 1998 International Conference on*. IEEE, 1998, pp. 259–263.

[5] M. Elad, J. Starck, P. Querre, and D. Donoho, “Simultaneous cartoon and texture image inpainting using morphological component analysis (MCA),” *Applied and Computational Harmonic Analysis*, vol. 19, no. 3, pp. 340–358, Nov. 2005.

[6] J. Fadili, J. Starck, M. Elad, and D. Donoho, “Mcalab: Reproducible research in signal and image decomposition and inpainting,” *Computing in Science & Engineering*, vol. 12, no. 1, pp. 44–63, 2010.

[7] W. P. Segars, M. Mahesh, T. J. Beck, E. C. Frey, and B. M. W. Tsui, “Realistic CT simulation using the 4D XCAT phantom,” *Medical Physics*, vol. 35, no. 8, p. 3800, 2008.

[8] E. Candès, J. Romberg, and T. Tao, “Robust uncertainty principles: Exact signal reconstruction from highly incomplete frequency information,” *Information Theory, IEEE Transactions on*, vol. 52, pp. 489–509, 2006.

[9] L. Rudin, S. Osher, and E. Fatemi, “Nonlinear total variation based noise removal algorithms,” *Physica D: Nonlinear Phenomena*, vol. 60, no. 1-4, pp. 259–268, 1992.

[10] J.-L. Starck, J. Fadili, and F. Murtagh, “The undecimated wavelet decomposition and its reconstruction.” *IEEE transactions on image processing*, vol. 16, no. 2, pp. 297–309, Feb. 2007.

[11] E. Candès, “New tight frames of curvelets and optimal representations of objects with C2 singularities: Technical report,” vol. 72890, pp. 1–39, 2002.

[12] E. Candès, L. Demanet, D. Donoho, and L. Ying, “Fast discrete curvelet transforms,” *Multiscale modeling and simulation*, vol. 5, no. 3, pp. 861–899, 2007.

[13] E. Candès, L. Demanet, and L. Ying, “CurveLab Toolbox, Version 2.0. 3,” *Transform*, pp. 1–4, 2005. [Online]. Available: www.curvelet.org

A Translation-based Data Acquisition for Industrial Computed Tomography

Tobias Schön[1], Theobald Fuchs[2], Randolf Hanke[3] and Kilian Dremel[3]

***Abstract*—We propose a new method for CT data acquisition, which requires almost no rotational movement of the system, respectively the object. The new method is derived from the observation that both the direction (the angle) and the shortest of each ray with respect to the object change, when the distance between the X-ray source and the detector changes. Or, in other words: the rotational movement is substituted by one or more linear movements of the X-ray source towards the object to be inspected. We present a theoretical evaluation of the translational acquisition scheme. The issues of image reconstruction will be discussed and results from simulations with varying measurement parameters will be shown.**

I. INTRODUCTION

TODAY, X-ray Computed Tomography (CT) is widely used as a tool for industrial non-destructive testing (NDT). There is a manifold of applications in the laboratory [1], [2]. It is important to notice the following fact: Although, various CT data acquisition methods have been developed to meet the different applications, almost all systems are based on a rotation of the object. Alternatively, this can be achieved by rotating the detector and the source of x-rays around the object, which is mostly done in medical diagnostics.

Most CT systems use a fan-beam-type geometry and acquire projection data from several hundred to thousands of directions by employing multi-row (in 2-D) or flat-panel detectors (cone-beam for 3-D imaging). As mentioned above, the acquisition geometry relies on a rotational movement. The most widely utilized reconstruction algorithms, as for instance the well-known Feldkamp method [3], are based on filtered back projection (FBP). These algorithms afford a series of projection images out of an angular range of 180° in parallel geometry.

Nevertheless, in reality there are numerous objects which are desirable to be inspected by X-ray CT but do not allow for a rotational movement. These are non-portable or very heavy objects which cannot be accessed from all directions. For instance, such an object could be a tube, positioned directly in front of a wall or a cable channel located inside. (Figure 1).

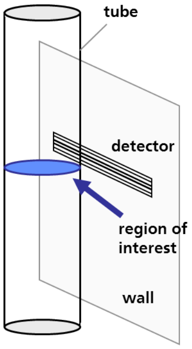

Fig. 1. A tube located close to a wall. This object is inaccessible to the conventional 180° view angle data acquisition by rotating an X-ray source and a detector, although it is feasible to insert a sensor into the gap between the object and the wall.

II. MATERIAL AND METHODS

The new technique [4] is based on a linear, translational-only movement of the X-ray source (Figure 2). The x-y-coordinate system is fixed with the object that is positioned within a circular field of measurement field of measurement (FoM). The radius of the field of measurement is R_M. The distance of the source to the edge of the field of measurement is denoted as x_S and is a positive number always. Given a certain distance of the source x_S to the object, each detector position y defines a different ray angle θ with respect to the object. This allows for acquiring a set of various view angles. The t-coordinate describes the shortest distance of the X-ray to the center of FoM.

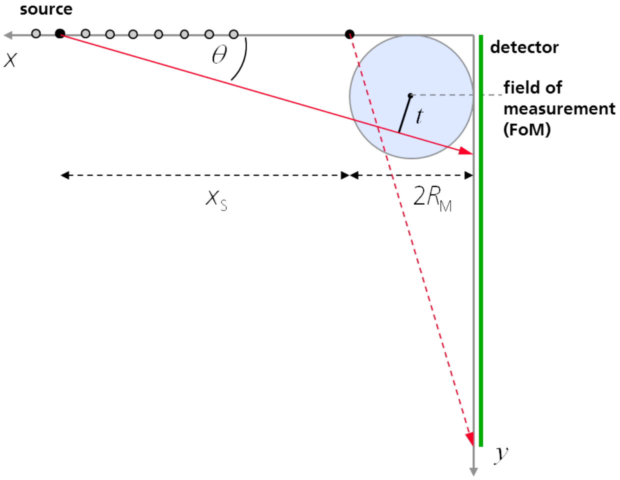

Fig. 2. Scheme of the basic principle of the translational CT data acquisition method. By changing the source-to-object distance x_S the angle of the ray measured at a fixed detector position changes accordingly.

In order to determine the range of ray parameters that is covered by the translational movement of the source with respect to the object the following equation for a single ray can be found.

---

[1] Process Integrated Inspection Systems, A Dept. of the Fraunhofer Institute for Integrated Circuits, Fürth, Germany; [2] Development Center for X-ray Technology (Fraunhofer-EZRT), A common Dept. of the Fraunhofer Institute for Integrated Circuits, Saarbrücken, Germany, and the Fraunhofer Institute for Non-destructive Testing, Fürth, Germany; [3] Chair for X-ray Microscopy, Julius-Maximilians-University, Würzburg

The new translational data acquisition scheme is mathematically described in a 2-D plane by the following two equations:

$$\tan\theta = \frac{y}{x_S + 2R_M},$$
$$t_\theta(x_S) = x_S \sin\theta + R_M(\sin\theta + \cos\theta) \qquad (1)$$

Each single ray is defined by the two parameters, t and θ. Using the two equations, the region within the complete parameter space, which is covered by the translational movement, can be determined.

The ray hitting the detector at exactly 90° is referred as the central ray of the X-ray source. The angle of the central ray with respect to the fixed object does not change while the source is translated, so no additional information is acquired. Deliberately, the central ray is shifted to the edge of the FoM. In consequence, the regions next to the central ray are expected to yield the poorest image quality.

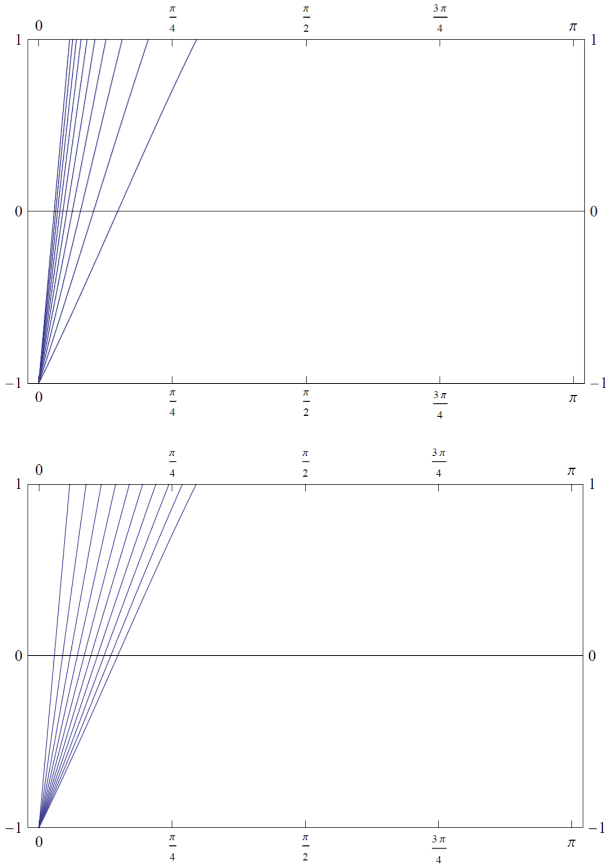

Fig. 3. The data range within the t-θ-coordinate space which can be filled by a single translational movement of the source. The parallel beam data of the full 180° angular range is required for a correct reconstruction by the filtered backprojection algorithm. A single translational movement of the source fills only a small part of the full 180° angular range. Top: data range covered with equidistant sampling of the focus position x_S, bottom: improved sampling

Figure 3 depicts Eq. (1) with $0 < x_S/R_M < 5$. The shaded area indicates the data range within the t-θ-coordinate space which can be filled by a single translational movement of the source. A reconstruction which is mathematically correct requires complete data from the rectangular region between $\theta = 0°$ and $\theta = 180°$ (the full rectangular area in Fig. 3). Besides the fact that a single translational movement of the source fills only a small part of the full 180° angular range, the spacing of data points within this triangular region is obviously very irregular. An advanced sampling ($n = 1, 2, \ldots$) of the source position according to $x_S(n) = \pi/2 * \cot(n\Delta\Phi)$ improves the distribution of the data points acquired by the single translation (Fig. 3, bottom). $\Delta\Phi$ is the angle between two projection datasets in the (t, θ) space belonging to two source positions in the translational movement.

In order to fill a larger fraction of the full 180° angular range, we implemented several extended data acquisition schemes employing more than one translation (Figure 4, Figure 5 and Figure 6). So, projection data can be derived, that yield almost complete 180° CT data.

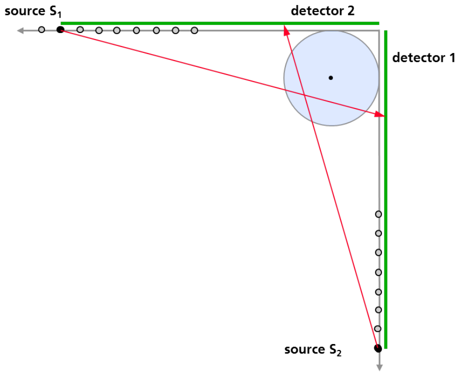

Fig. 4. Translational data acquisition scheme based on two orthogonal translations of the source. This method is denoted as "Two translations 90 degree" (2T90).

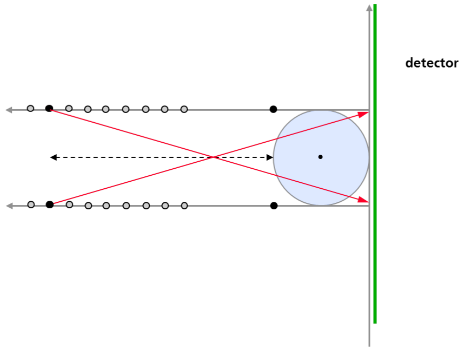

Fig. 5. Translational data acquisition scheme based on two translations parallel to each other (2Tpar).

A phantom was simulation which resembles a pipe with several details inside (Figure 7. For the simulation, the radius of the FoM is taken as unit: $R_M = 1$. During each linear translation of the X-ray source, 200 positions were sampled, with 0.1 spacing relative to the FoM. So, the source-to-object distance varied between 0 and 19.9. All simulations used an equidistant sampling of the source positions for each linear translation and not the improved non-equidistant sampling of Fig. 3, bottom. The detector was simulated with 512 pixel and 0.01 pixel size. Thus, the linear dimension of the detector is equivalent to approximately 2.5 times the object's diameter.

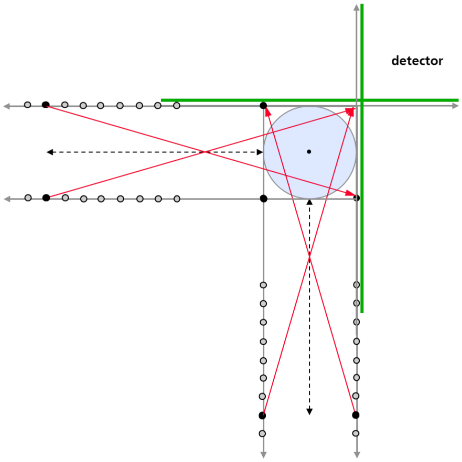

Fig. 6. A combination of 2T-par and 2T-90: 2(2Tpar)-90.

In the case of several linear movements (Figure 4, Figure 5 and Figure 6), each movement was generated with identical parameters, as described above.

For comparison, a complete set of data were simulated in parallel beam geometry. Explicitly, for each of 200 angular positions within 180° range the FoM (diameter 2 in arbitrary units) the attenuation profile was sampled by 256 parallel rays with a distance of 0.01. The reconstruction was made with a complete 180° data set and with reduced angular ranges of 120° and 90° degree. So, the degradation of image quality can be compared with the results of the translational technique.

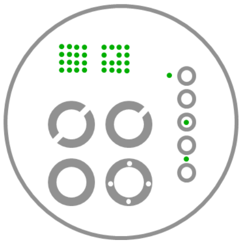

Fig. 7. A virtual tube comprising smaller pipes and cables was used for simulation.

A state-of-the art ART (algebraic reconstruction technique) algorithm was used for image, throughout the whole study [5]. All images have 256 by 256 pixels with 0.01 by 0.01 pixel size relative to the FoM.

III. RESULTS

In Fig. 8 reconstructions from a conventional rotation-based data acquisition in parallel beam geometry are shown. The image quality for the complete angular range of 180° is perfect, while rapidly degrading when the range is reduced to 120° and 90°.

The image quality obtained by a single translation is not sufficient (Figure 9, left hand side). By adding a second translation, parallel to each direction of source movement or shifted by 90°, the image quality improved significantly (Figure 9, right hand side and Figure 10 left hand side). Using translational data acquisition geometry by 2(2Tpar)-90 produces an image quality can be obtained with comparatively high quality.

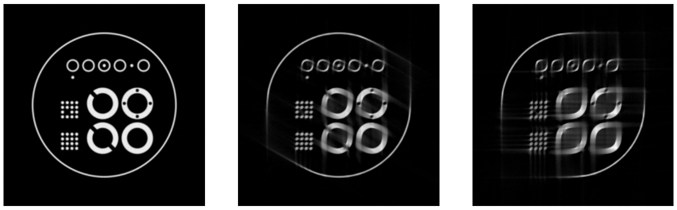

Fig. 8. Reconstructions in conventional parallel beam geometry angular range of 180°, 120° and 90° (from left to right).

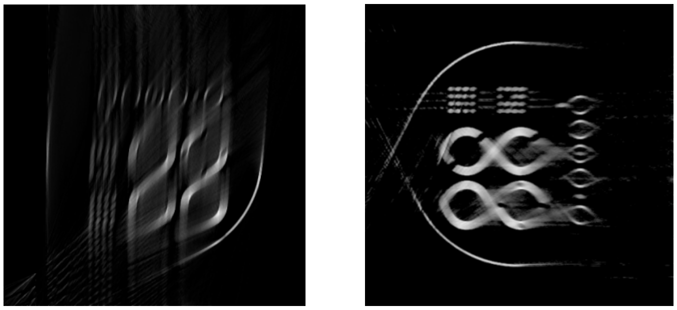

Fig. 9. Reconstructions in translational data acquisition geometry by one translation (left) and 2Tpar of Figure 5 (right).

For all images the same standard ART reconstruction was applied to all data-sets. There has not been made any optimization for the translational case, yet. Nevertheless, the results achieved with two translations are already comparable to a rotation about 90° angular range, which is equivalent to 100 projections according to the parameters used in this study.

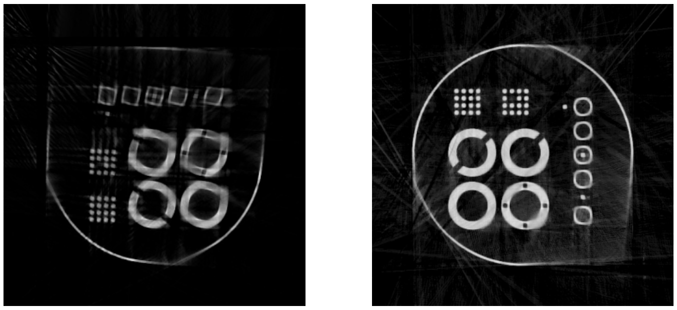

Fig. 10. Reconstructions in translational data acquisition geometry by and 2T90 of Figure 4 (left) and 2(2Tpar)-90 of Figure 6 (right).

IV. CONCLUSION AND FUTURE WORK

We proposed a new method for CT data acquisition, which requires almost no rotational movement of the system, respectively the object. We have shown by simulations that imaging of sections with Translational X-ray Computed Tomography is feasible. Substituting the rotational movements of the equipment respectively the object by linear movements of the source towards or away from the object allows for reconstructing images with comparatively high quality.

Several combinations of translational data acquisition schemes have been evaluated. Nevertheless, the image quality achieved by Translational CT method is worse compared to a complete parallel beam data set, measured during a 180° rotation of the object or the X-ray source and the detector, respectively.

Future efforts will be made in improving the quality of the Translational CT reconstructions by exploring several ways:

- Use of a-priori information about the objects to lead to further improvement of the image quality
- Further variations of the acquisition scheme will be implemented and evaluated
- Optimizing the translational scan parameters in general, i.e. necessary dimensions of the detector and the source travel distance
- Verification with real data is in progress
- Extension to fully 3-D imaging by investigating the translation in cone-beam geometry

REFERENCES

[1] T. Fuchs, T. Schön, R. Hanke, and et al., “Progress towards quantitative computed tomography as a tool for industrial inspection,” in *European Conference on Materials and Structures in Aerospace*, ser. VDI-Berichte 2028, 2008, pp. 425–430.

[2] T. Fuchs and R. Hanke, “Task-driven design of x-ray systems for industrial inspection,” in *IEEE Nuclear Science Symposium and Medical Imaging Conference, NSS/MIC 2008, Dresden, Germany*, 2008, pp. 523 – 527.

[3] L. Feldkamp, L. Davis, and J. Kress, “Practical cone-beam algorithm,” *J. Opt. Soc. Amer.*, vol. 1, pp. 612–619, 1984.

[4] T. Fuchs, T. Schön, and R. Hanke, “Translational computed tomography: A new data acquisition method for inspection of inaccessible objects,” in *10th European Conference on Non-destructive Testing ECNDT, Moscow*, 2010.

[5] G. Gordon, R. Bender, and G. T. Herman, “Algebraic reconstruction techniques (art) for three-dimensional electron microscopy and x-ray photography,” *J. Theoret. Biol.*, vol. 29, pp. 471–481, 1970.

GPU Implementation of Exact FBP and BPF Algorithms for Saddle and Circle-plus-line CT

Minji Lee, Kyung Sang Kim and Jong Chul Ye*

Abstract—**Exact cone-beam reconstruction algorithms have been developed for various scanning trajectories. Volumes scanned by saddle and circle-plus-line trajectories can be also reconstructed exactly with these algorithms. Generally, the exact cone-beam reconstruction algorithms are divided into two types, such as filtered backprojection (FBP) type and backprojection-filtration (BPF) type. For GPU implementation, the scanning with the saddle trajectory was reconstructed with the FBP method, and the scanning with the circle-plus-line trajectory was reconstructed with the BPF method. Usually, the reconstruction of CT contains repetitive tasks, so by parallelization, the computational time can be dramatically saved. These two GPU-based implementations are tested with the three-dimensional Shepp-Logan head phantom, and we compare the two trajectories both in terms of reconstruction quality and GPU implementation.**

I. INTRODUCTION

For a circular cone-beam CT scanner with a two dimensional detector, the Feldkamp-Devis-Kress (FDK) method has been used in most. However, it is an approximate reconstruction algorithm causing cone-beam artifacts. Exact cone-beam reconstruction algorithms can remove these artifacts though different scanning trajectories to cover the same field of view (FOV) with the FDK method. There are two types of the exact cone-beam reconstruction methods; filtered backprojection (FBP) method [1] and backprojection-filtration (BPF) method [2]. Both methods consist of same reconstruction steps; derivative, one-dimensional Hilbert filtration, and backprojection, but the orders are different. The FBP method reconstructs images by backprojection of filtered derivative scanning images, and the BPF method reconstructs images by filtering backprojection of derivative images. The exact cone-beam reconstructions with saddle and circle-plus-line trajectories can cover the same FOV with the FDK method, so these trajectories with the exact cone-beam reconstruction algorithms can replace the circular scanning trajectory.

In this paper, we implemented the exact cone-beam reconstruction algorithms of both FBP and BPF types for the saadle and circle-plus-line trajectories using graphics processing unit (GPU) for the case of saddle and circle-plus-line trajectories, respectively. GPU provides multi-core processors for parallelization and texture memories for fast interpolation [3]. The reconstruction algorithms need to compute a lot of repetitive tasks and interpolations, so the GPU implementation can make the reconstruction much faster than CPU.

II. EXACT CONE-BEAM RECONSTRUCTION

A. Cone-beam Projection

Projection of cone-beam CT with a three-dimensional density function $f(\vec{r})$ is given by

$$D(\vec{a},\vec{\theta}) = \int_0^\infty f(\vec{a}+t\vec{\theta})dt, \quad \vec{\theta} \in S^2 \tag{1}$$

where S^2 is a set of all unit vectors in three-dimensional space. The parameters of D, $\vec{a}$ and $\vec{\theta}$, mean a source position and a ray direction.

B. General Formulae of FBP and BPF

For FBP algorithm, the general formula $\mathcal{K}(\vec{r},\vec{e},\lambda^-,\lambda^+)$ is shown by Pack and Noo [1], which is

$$\mathcal{K}(\vec{r},\vec{e},\lambda^-,\lambda^+) = -\frac{1}{2\pi^2}\int_{\lambda^-}^{\lambda^+} \frac{d\lambda}{|\vec{r}-\vec{a}(\lambda)|} g_F(\lambda,\vec{r},\vec{e}) \tag{2}$$

where

$$g_F(\lambda,\vec{r},\vec{e}) = \int_{-\pi}^{\pi} \frac{d\gamma}{\sin\gamma}\frac{\partial}{\partial\mu} D(\vec{a}(\mu),\vec{\theta}(\lambda,\vec{r},\gamma,\vec{e}))\bigg|_{\mu=\lambda} \tag{3}$$

with

$$\vec{\theta}(\lambda,\vec{r},\gamma,\vec{e}) = \cos\gamma\vec{\alpha}(\lambda,\vec{r}) + \sin\gamma\vec{\beta}(\lambda,\vec{r},\vec{e}), \tag{4}$$

$$\vec{\alpha}(\lambda,\vec{r}) = \frac{\vec{r}-\vec{a}(\lambda)}{|\vec{r}-\vec{a}(\lambda)|}, \tag{5}$$

$$\vec{\beta}(\lambda,\vec{r},\vec{e}) = \frac{\vec{e}-\vec{\alpha}(\lambda,\vec{r})(\vec{e}\cdot\vec{\alpha}(\lambda,\vec{r}))}{|\vec{e}-\vec{\alpha}(\lambda,\vec{r})(\vec{e}\cdot\vec{\alpha}(\lambda,\vec{r}))|}. \tag{6}$$

This formula gives the reconstruction at $\vec{r}$ by the backprojection of filtered images $g_F(\lambda,\vec{r},\vec{e})$ from λ^- to λ^+ with given filtering direction $\vec{e}$ (Eq. (2)). $g_F(\lambda,\vec{r},\vec{e})$ can be obtained by filtering derivative images with respect to λ (Eq. (3)). To use this equation, $\vec{e}$, λ^-, and λ^+ are decided for a reconstruction point $\vec{r}$.

BPF reconstruction formula provides exact reconstruction on chord using cone-beam projection. A chord is the straight line connecting two points, $\vec{a}(\lambda_a)$ and $\vec{a}(\lambda_b)$, on a continuous trajectory. The BPF reconstruction on chords $f_c(x_c,\lambda_a,\lambda_b)$ are given by [2]

$$\begin{aligned} f_c(x_c,\lambda_a,\lambda_b) = \frac{1}{2\pi^2}&\frac{1}{\sqrt{(x_{c2}-x_c)(x_c-x_{c1})}} \\ \times\Bigg[\int_{x_{c1}}^{x_{c2}} &\frac{dx'_c}{x_c-x'_c}\sqrt{(x_{c2}-x'_c)(x'_c-x_{c1})} \\ &\times g_c(x'_c,\lambda_a,\lambda_b) + C\Bigg] \end{aligned} \tag{7}$$

M. Lee, K. S. Kim and J. C. Ye are with the Department of Bio & Brain Engineering, Korea Advanced Institute of Science & Technology (KAIST), 291 Deahak-ro, Yuseong-gu, Daejeon 305-701, Korea

where

$$C = 2\pi \int_{x_{c1}}^{x_{c2}} f_c(x_c, \lambda_a, \lambda_b) dx_c = 2\pi D(\vec{a}(\lambda_a), \vec{e}_c), \quad (8)$$

$$g_c(x_c, \lambda_a, \lambda_b) = \int_{\lambda_a}^{\lambda_b} \frac{d\lambda}{|\vec{r} - \vec{a}(\lambda)|} \frac{\partial}{\partial \mu} D(\vec{a}(\mu), \vec{\theta}) \bigg|_{\mu=\lambda}. \quad (9)$$

In Eq. (7), x_c indicates the position on the chord, and any x_{c1}, x_{c2} can be selected satisfying that $[x_{c1}, x_{c2}]$ covers all backprojection segment. C is a projection value at the intersection point of the detector with source location $\vec{a}(\lambda_a)$ and the chord line with λ_a, λ_b. The result of Eq. (9) is backprojection of derivative with only interval $[\lambda_a, \lambda_b]$.

C. FBP Algorithm for Saddle CT

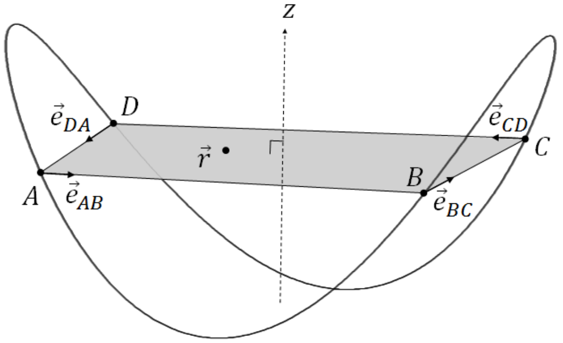

Fig. 1. FBP algorithm for saddle trajectory

The saddle trajectory is defined as [4]

$$\vec{a}(\lambda) = [R\cos\lambda, R\sin\lambda, H\cos 2\lambda], \quad \lambda \in [0, 2\pi]. \quad (10)$$

Here, R is a radius of a horizontal rotation, and H is a amplitude of vertical fluctuations. With this scanning trajectory, the reconstruction at $\vec{r}$ given by [5]

$$f(\vec{r}) = \frac{1}{2}\Big(\mathcal{K}(\vec{r}, \vec{e}_{AB}, \lambda_A, \lambda_B) + \mathcal{K}(\vec{r}, \vec{e}_{BC}, \lambda_B, \lambda_C) + \mathcal{K}(\vec{r}, \vec{e}_{CD}, \lambda_C, \lambda_D) + \mathcal{K}(\vec{r}, \vec{e}_{DA}, \lambda_D, \lambda_A)\Big). \quad (11)$$

If the reconstruction point is at $\vec{r}$, the plane containing $\vec{r}$ is determined, which is perpendicular to z axis, and 4 intersection points with the saddle trajectory are made. Then, the reconstruction at $\vec{r}$ is given by backprojecting filtration of derivative images with filtering direction $\vec{e}_{AB}$ for scanning trajectory from A to B, filtering direction $\vec{e}_{BC}$ for scanning trajectory from B to C, filtering direction $\vec{e}_{CD}$ for scanning trajectory from C to D, and filtering direction $\vec{e}_{DA}$ for scanning trajectory from D to A. The filtration with 4 kinds of filtering directions can be implemented only with the following two equations [5].

$$v = -\frac{\hat{z}\cos\lambda}{R\sin\lambda}u + \frac{D}{R}\hat{z}, \quad \hat{z} \geq 0 \quad (12)$$

$$v = \frac{\hat{z}\sin\lambda}{R\cos\lambda}u + \frac{D}{R}\hat{z}, \quad \hat{z} < 0. \quad (13)$$

These two equations represents filtering lines on the detector. Here, D is a distance from the source to the detector, and $\hat{z}$ is the parameter of the filtering lines which is decided by the point $(0, 0, H\cos 2\lambda + \hat{z})$. By sampling $\hat{z}$, the filtering lines can cover all detector plans, and the filtered images are computed by the Hilbert filtration along the filtering lines.

D. BPF Algorithm for Circle-plus-line CT

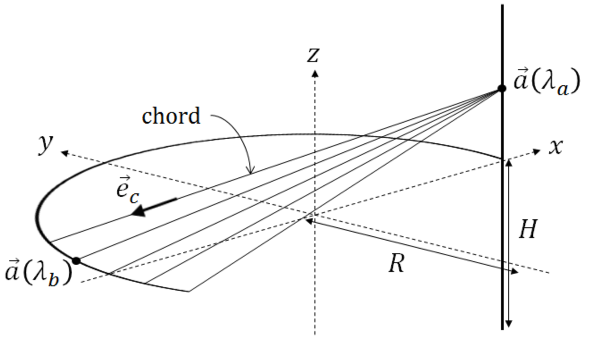

Fig. 2. Rebinned BPF algorithm for circle-plus-line trajectory

We define the configuration of the circle-plus-line source trajectory as

$$\vec{a}(\lambda) = \begin{cases} [R, 0, \frac{H}{\phi}\lambda], & \text{for } \lambda \in [-\phi, \phi] \\ [R\cos\lambda, R\sin\lambda, 0], & \text{for } \lambda \in [2\pi, 3\pi + \psi] \end{cases} \quad (14)$$

where $0 \leq \phi < 2\pi$, and it is shown in Fig.2.

Now we apply BPF reconstruction algorithm to the circle-plus-line cone-beam CT. To reconstruct a point on the chord of $\vec{a}(\lambda_a)$ and $\vec{a}(\lambda_b)$, derivative images of projections with source position from $\vec{a}(\lambda_a)$ to $\vec{a}(0)$ and from $\vec{a}(2\pi)$ to $\vec{a}(\lambda_b)$ are required, and the derivative images must be computed in this direction. After the first step of the BPF algorithm, backprojection is performed. BPF algorithm requires filtration along the chords after backprojection, thus the derivative images are backprojected onto the chords. This way makes the filtration step simple, but regridding process is required. The rebinned space can cover all region of interest varying $\vec{a}(\lambda_a)$ along the line trajectory and varying $\vec{a}(\lambda_b)$ along the circle trajectory. After the backprojection on chord line, it is filtered with proper x_{c1} and x_{c2} which cover backprojection segments as Eq. (7). The filtration result on chords is rebinned again into regularly grided Cartesian coordinate space.

III. GPU IMPLEMENTATION

In both FBP and BPF algorithms, the derivative step using chain rule is so simple, thus the GPU implementation is not necessary. For the filtration step, the FBP method needs the rebinning process for filtering lines, and its forward rebinning process can be implemented with texture memory providing fast interpolation of pixel values. The one-dimensional hilbert filtering was implemented by a fast Fourier transform (FFT) method, and a one-dimensional data was filtered by a thread. To avoid an out of memory problem, we copy images from

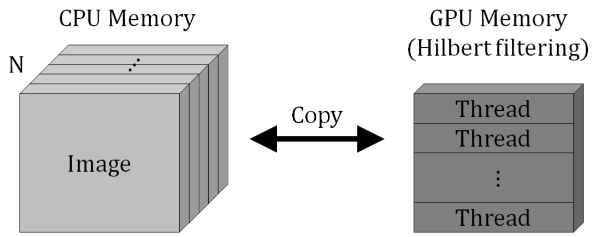

Fig. 3. Parallelization of filtration

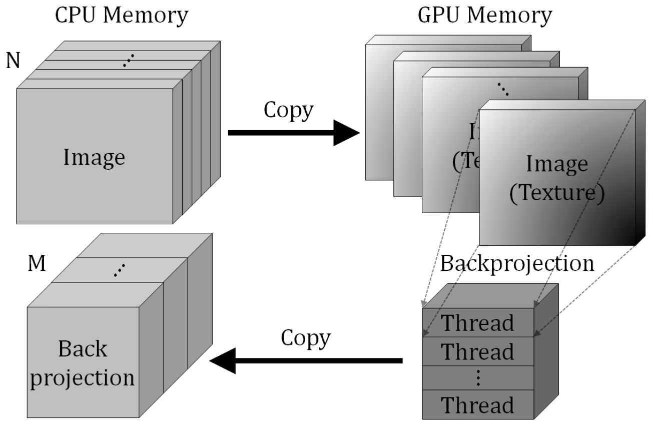

Fig. 4. Parallelization of backprojection

CPU memory to GPU memory dividing into several parts as shown in Fig.3. The backprojection step is the most time-consuming part, but it can be made fast by GPU implementation because it includes very repetitive tasks and interpolations. Fig.4 show GPU implementation of the backprojection step. Similar to the filtration, the GPU memory cannot be enough for all images and backprojection data, so we divide them into several parts and repeat the process. The images are copied to texture memory for fast interpolation, and in a thread, the images are backprojected into a one-dimensional space. If we divide all images into N parts and all backprojection space into M parts, $N \times M$ iterations are necessary.

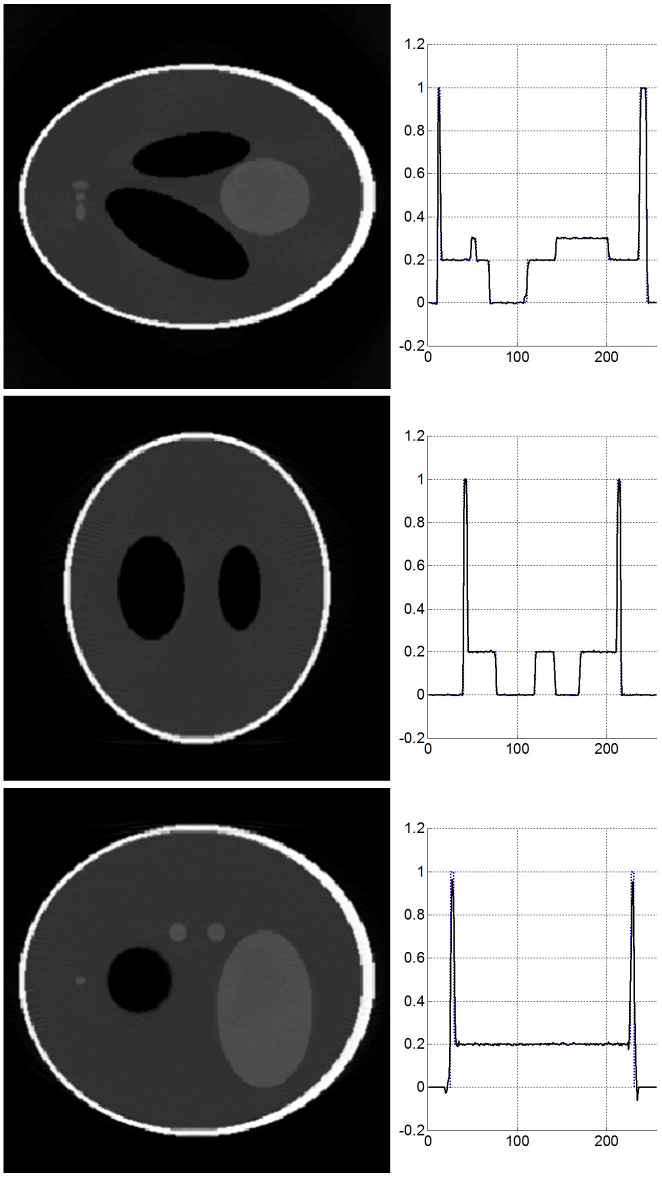

Fig. 5. FBP reconstruction result of saddle CT. Horizontal slice image and its row line profile (top), vertiacl slice image and its row line profile (middle), and vertical slice image and its column line profile (bottom).

IV. RESULT

The GPU implementations of the exact cone-beam reconstruction alorithms were evaluated using three-dimensional Shepp-Logan phantom. The object size is 256^3 voxels, and the voxel size is 0.5^3 mm^3. For scanning system, $R = 400$ mm, $D = 700$ mm. The GPU implementations were programmed by using compute unified device architecture (CUDA) which is a parallel computing architecture developed by Nvidia, and the implementations were tested with TESLA C1060.

For the saddle CT simulation, $H = 64$ mm to cover all object. Because of this pitch, we use the 512×1024 pixel size detector to cover all projections of the object inside the detector in any source position, and the pixel size is 0.5 mm. We generated 900 cone-beam projections as λ increases uniformly from 0 to 2π, and Fig.5 shows the reconstruction result. The reconstruction image quality of the horizontal slice is clear, but in the vertical slices, there are some artifact lines in a diagonal direction. These artifacts come from the pitch of the saddle trajectory, so it can be reduced by denser scanning. For the saddle CT simulation, the pitch of line trajectory was also decided to cover the object, which is about 153 mm, and the detector size was 512×512 pixels with 0.5 mm pixel size.

In the circle-plus-line CT, the detector does not need to cover all projections of the object when it was scanned in the line trajectory, thus it is smaller than the saddle CT. For simulation, 611 cone-beam projections in the line scanning part and 280 cone-beam projections in the circle scanning part were generated. As Fig.6, the reconstruction image quality of the horizontal slice is as almost same as saddle CT, but the vertical slices are clearer than saddle CT without artifacts. Even if the line profiles of the saddle and circle-plus-line CT are similar, the entire reconstruction image quality of the circle-plus-line CT is better than the saddle CT.

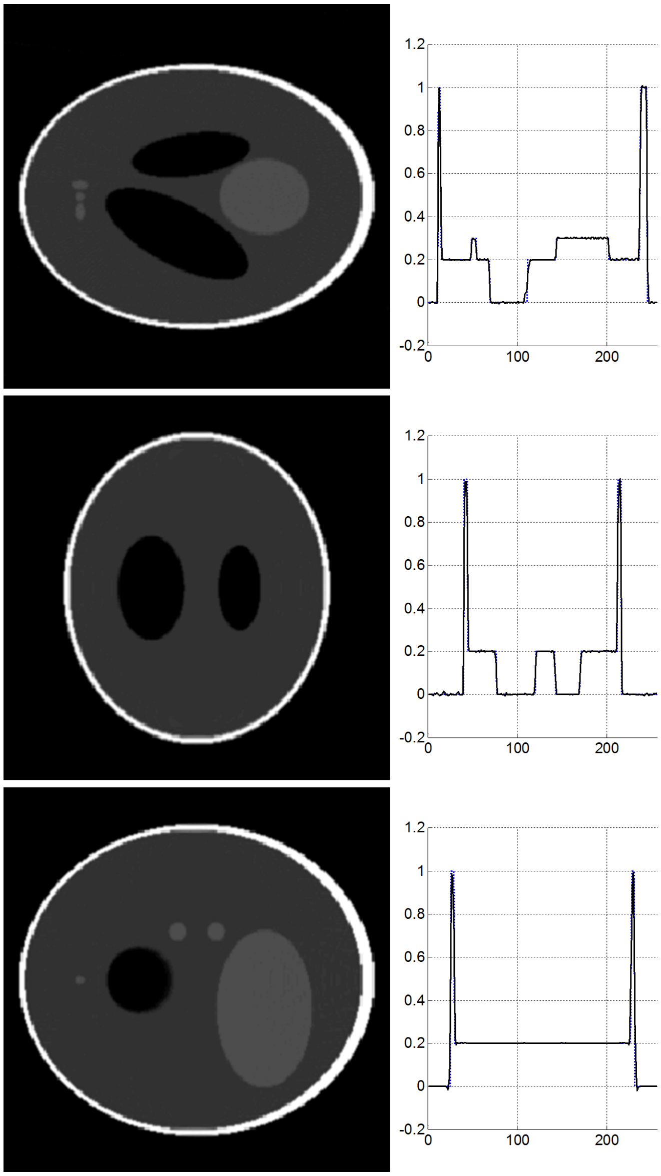

Fig. 6. BPF reconstruction result of circle-plus-line CT. Horizontal slice image and its row line profile (top), vertiacl slice image and its row line profile (middle), and vertical slice image and its column line profile (bottom).

TABLE I
COMPUTATION TIME

	Saddle	Circle-plus-line
Derivative	12.948 sec	3.415 sec
Filtration	5.631 sec	1.104 sec
Backprojection	10.172 sec	14.741 sec
Regridding		5.271 sec
total	28.751 sec	24.531 sec

Table I shows the computation time. Even if the number of projection views of two simulations were similar to each other (900 views for the saddle CT and 890 views for the circle-plus-line CT), the saddle CT used the much bigger detector than the circle-plus-line CT, so the derivative process of the saddle CT takes more time than the circle-plus-line CT. In the saddle CT, the filtration requires the forward and backward rebinning process, so it takes longer than circle-plus-line CT. For the backprojection step the circle-plus-line CT takes longer because the chord length in the rebinned space is almost twice longer than the object width for the filtration. Finally, the total computational times are similar.

V. CONCLUSION

In this paper, the exact cone-beam reconstruction with the FBP and BPF algorithms was implemented by GPU. From GPU implementation point of view, the FBP algorithm can be considered simpler than the BPF alorithms because it has no regridding process, but its filtration on the detector needs the forward and backward rebinning process. So, the FBP algorithm takes longer in filtering process. In the reconstruction results with two kinds of trajectories with the similar number of views, the line profiles looked similar, but the entire quality of circle-plus-line CT was clearer without artifacts. Moreover, the saddle CT requires the much bigger detector area than circle-plus-line CT to cover the object. Thus, the BPF reconstruction of circle-plus-line CT is more economical in practise than the FBP reconstruction of the saddle CT.

REFERENCES

[1] Jed D Pack and Frédéric Noo, "Cone-beam reconstruction using 1D filtering along the projection of M -lines," *Inverse Problems*, vol. 21, no. 3, pp. 1105–1120, June 2005.

[2] Yu Zou, Xiaochuan Pan, and Emil Y Sidky, "Theory and algorithms for image reconstruction on chords and within regions of interest," *America*, vol. 22, no. 11, pp. 2372–2384, 2005.

[3] Kyung Sang Kim and Jong Chul Ye, "Fully 3D iterative scatter-corrected OSEM for HRRT PET using a GPU.," *Physics in medicine and biology*, vol. 56, no. 15, pp. 4991–5009, Aug. 2011.

[4] Jed D Pack, Frédéric Noo, and H Kudo, "Investigation of saddle trajectories for cardiac CT imaging in cone-beam geometry," *Physics in Medicine and Biology*, vol. 49, no. 11, pp. 2317–2336, June 2004.

[5] Haiquan Yang, Meihua Li, Kazuhito Koizumi, and Hiroyuki Kudo, "Exact cone beam reconstruction for a saddle trajectory.," *Physics in medicine and biology*, vol. 51, no. 5, pp. 1157–72, Mar. 2006.

Iterative Image Reconstruction with Variable Resolution in Diagnostic CT

Zheng Zhang, Junguo Bian, Xiao Han, Daxin Shi, Alex Zamyatin, Patric Rogalla, Emil Y. Sidky and Xiaochuan Pan

***Abstract*—In tomographic imaging applications, it is not uncommon that one is interested in detailed information only about a region of interest (ROI) within an imaged subject, while rough knowledge outside the ROI may be sufficient. Therefore, it is of practical merit to develop algorithms that are capable of reconstructing an image with variable resolution, e.g., an image consists of high-resolution ROI reconstruction and coarse reconstruction outside the ROI. In this work, we investigate and develop optimization-based algorithms for image reconstruction with variable resolution and apply them to real patient and animal data collected with advanced diagnostic CT scanner. The results of our study demonstrate that optimization-based algorithms can be developed for yielding an image of which different parts can have different levels of spatial resolution. The work may have implications for reduction of computation memory and acceleration of computation speed. In the presence of data truncation, it may also provide an approach to obtaining an ROI image of high resolution with minimized truncation artifacts.**

I. INTRODUCTION

In tomographic imaging applications, it is not uncommon that one is interested in detailed information only about a region of interest (ROI) within an imaged subject. For example, in image-guided radiation therapy (IGRT) and image-guided surgery (IGS), one seeks to determine information about the location, size, shape, and contrast of tumors within an ROI, while rough knowledge outside the ROI may be sufficient. Therefore, it is of practical merit to develop a capability of reconstructing a high-resolution image within the ROI while yielding only a coarse image outside the ROI.

Based upon continuous-to-continuous (C-C) linear imaging models, analytic-based algorithms such as the FDK-based algorithms are designed for reconstructing continuous images from continuous data. Discrete forms of an analytic-based algorithm can be devised so that it can be applied to discrete data in realistic tomographic imaging. Because discretization is applied only to the data space, the algorithms can still yield continuous image reconstructions. Therefore, an image with regions of different resolutions can readily be reconstructed by use of analytic-based algorithms from discrete data.

Optimization-based (i.e., iterative) algorithms generally possesses a higher degree of flexibility than analytic-based algorithms in accommodating image reconstruction a wide variety of imaging conditions of practical significance. With the rapidly available computation power and significant advances in optimization theory for linear imaging models, there have been a substantially increased interest in developing and applying optimization-based algorithms for image reconstruction in tomographic imaging, particularly in computed tomography (CT).

In general, an optimization-based algorithm is developed based upon a discrete-to-discrete (D-D) imaging model in which both data and image are represented as discrete arrays. Since the algorithm reconstructs an image iteratively, reconstruction at a given iteration thus needs knowledge about reconstructions at previous iteration(s) on the *entire* image array, and current optimization-based algorithms are designed generally for image reconstruction on an image array consisting of identical voxels. Therefore, even if an ROI image of high resolution is desired, an optimization-based algorithm needs to reconstruct the entire image of high resolution, represented necessarily by a huge number of identical, small-size voxels, thus leading to a substantial demand on the computational memory and time.

In an attempt to minimize such a demand, we investigate and develop optimization-based algorithms for image reconstructions with variable resolution, and we apply the algorithms to image reconstruction with variable resolution from real patient and animal data collected with a Toshiba 320-slice diagnostic CT scanner. We considered in the investigation well-known iterative algorithms, including project-onto-convex-set (POCS), expectation-minimization (EM), simultaneous algebraic reconstruction technique (SART), and adaptive-steep-descent(ASD)-POCS algorithms. However, in this abstract, we include results obtained only with the ASD-POCS algorithm and will report results of other algorithms at the conference.

II. METHODS

We briefly describe the development of optimization-based algorithms for image reconstruction with variable resolution through the use of an image array consisting of voxels with different sizes.

A. Imaging model

One can obtain discrete representations of continuous data and image functions by using discrete basis sets to expand

---

Z. Zhang, J. Bian, X. Han, E. Y. Sidky and X. Pan are with the University of Chicago.

D. Shi and A. Zamyatin are with Toshiba Medical Research Institute USA.

P. Rogalla is with UHN Toronto General Hospital, Canada.

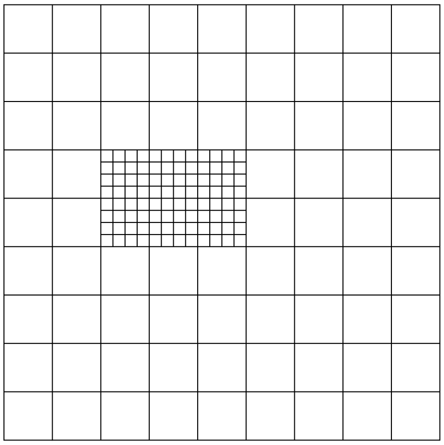

Figure 1. A variable-resolution array: It includes a rectangle-shaped ROI, consisting of pixels of size a, and the region surrounding the ROI, composing of pixels of size b. When $a < b$, different levels of resolution are obtained for the ROI and its surrounding region.

the functions. In this work, data and image functions are expanded in terms of M pixels and N voxels, and $\mathbf{g}_0$ and $\mathbf{f}$ denote the expansion coefficients, which we refer to as model-data and image vectors of sizes M and N. We now consider below a D-D imaging model for CT:

$$\mathbf{g}_0 = \mathcal{H}\mathbf{f}, \tag{1}$$

where $\mathcal{H}$ denotes a system matrix of size $M \times N$ that relates data and image vectors. It should be reminded that elements of system matrix $\mathcal{H}$ are determined not only by the selection of data and image vectors but also by the way as to how the discrete X-ray transform is calculated. The model data $\mathbf{g}_0$, which is consistent with the imaging model, differ from measured data $\mathbf{g}$, which always contains components inconsistent with the imaging model.

B. Uniform- and variable-resolution image arrays

In a practical optimization-based reconstruction, an image array consisting of voxels of identical sizes is generally used. We refer to such an array as *a uniform-resolution array*. In the work, instead, we develop optimization-based reconstructions that use an image array formed by voxels of different sizes, and thus refer to it as *a variable-resolution array*. In Fig. 1, we display a 2D version of a variable-resolution array, which includes a rectangle-shaped ROI consisting of pixels of size a, and the region surrounding the ROI composing of pixels of size b. Obviously, when $a = b$, a variable-resolution array becomes a uniform-resolution array. However, if $a \neq b$, different levels of resolution are obtained for the ROI and its surrounding region. In particular, when $a < b$, the array thus includes an ROI with resolution higher than that in the region surrounding the ROI. When a variable-resolution array is used, the calculation method of the system matrix remains largely unchanged except for that care should be taken for calculations involving voxels along boundaries between an ROI and its surrounding region.

C. Optimization programs

The inversion of Eq. (1) can be formulated into an optimization program to be solved by use of optimization-based algorithms. We first consider an optimization program

$$\mathbf{f}^* = \text{argmin} \parallel D(\mathbf{f}) \parallel, \tag{2}$$

where

$$D(\mathbf{f}) = \mid \mathcal{H}\mathbf{f} - \mathbf{g} \mid \tag{3}$$

denotes the Euclidean-data divergence between measured data $\mathbf{g}$ and imaging model $\mathcal{H}\mathbf{f}$. As discussed below, numerous algorithms can be used for solving this optimization program.

We then consider an optimization program:

$$\mathbf{f}^* = \text{argmin} \parallel \mathbf{f} \parallel_{\text{TV}} \quad \text{s.t.} \quad D(\mathbf{f}) \leq \epsilon, \tag{4}$$

where $\parallel \mathbf{f} \parallel_{\text{TV}}$, referred to as the image total variation (TV), denotes the ℓ_1-norm of the discrete gradient magnitude of the image, and ϵ is a pre-selected, positive parameter for accommodating inconsistencies between measured data $\mathbf{g}$ and imaging model $\mathcal{H}\mathbf{f}$. It should be noted that the calculation of both system matrix $\mathcal{H}$ and image TV $\parallel \mathbf{f} \parallel_{\text{TV}}$ depends critically on the design of an image array with variable resolution. Also, the often-used non-negativity constraint on reconstructed images is not considered in the two optimization programs described above because real data used in the study contain negative values as a result of the correction for physical factors by use of the method installed on the scanner.

We also consider an optimization program in which the Kullback-Liebler (KL) divergence $D(\mathbf{f})_{_{KL}}$ between measured data $\mathbf{g}$ and imaging model $\mathcal{H}\mathbf{f}$ is to be minimized.

D. Optimization-based algorithm

Numerous optimization-based algorithms can be used for solving the optimization program in Eq. (2). Specifically, in the absence of inconsistencies between data and imaging model, the POCS algorithm can solve the optimization program in Eq. (2). Also, the SART algorithm can minimize the objective function even in the presence of the inconsistencies. In this work, we have developed both POCS and SART algorithms for image reconstructions with variable resolution through solving Eq. (2).

We have also modified the ASD-POCS algorithm to solve the optimization program in Eq. (4). The main modifications include the calculation of the system matrix, image TV, and image-TV gradient when a variable-resolution array is used. We have also derived a necessary convergence condition for the ASD-POCS algorithm when an image-positivity constraint is not considered in Eq. (4).

Finally, it is well known that the EM algorithm minimizes the KL divergence $D(\mathbf{f})_{_{KL}}$. Therefore, we have also modified the standard EM algorithm for a uniform-resolution array to reconstruct for a variable-resolution array. In the EM reconstructions, negative values in real data are set to zero.

III. DATA ACQUISITION AND IMAGE ARRAYS

A. CT imaging system

In the work, we focus on image reconstruction from patient and swine data collected with a Toshiba 320-slice diagnostic CT scanner. In the CT scanner, the distance between the X-ray source and the center of rotation is 60 cm; the detector consists of 320 rows of bins, each of the 320 rows composes 896 bins, thus forming a fan angle of $49.2°$.

B. Data acquisition

The patient and swine data were collected at 1200 views over 2π. Specifically, in the patient study, the subject was scanned with X-ray energy of 135 kVp and current at 100 mAs, whereas for the swine study, the animal was scanned with X-ray energy of 100 kVp and current at 275 mAs. The projection data were corrected for scatter and beam-hardening by use of Toshiba's standard method installed on the scanner.

C. Selection of image arrays

In our studies below, without loss of generality, we consider four variable-resolution arrays determined by the selection of four different combinations of pixel sizes a and b, as shown in Fig. 1. Specifically, for the patient study, we select $a = 0.064$ cm to combine with $b = 0.064$ cm, 0.128 cm, 0.256 cm, and 0.512 cm, respectively. Clearly, the first combination yields a uniform-resolution array, whereas the other three combinations result in three variable-resolution arrays with a decreasing ratio between a and b. Similarly, for the swine study, four image arrays were determined by the four combinations of $a = 0.0625$ cm with $b = 0.0625$ cm, 0.125 cm, 0.250 cm, and 0.500 cm, respectively. Again, the first combination produces a uniform-resolution array, whereas the other three combinations result in three variable-resolution arrays, also with a decreasing ratio between a and b.

D. Inverse-crime studies

In an attempt to validate the optimization-based algorithms in Sec. II-D and their implementation, we first carried out an inverse-crime study in which simulation data were generated by use of a system matrix from a discrete image and images were reconstructed by use of the same system matrix in the reconstruction algorithms described above. In the study, data are completely consistent with the imaging model, and the same system matrix was used for data generation and image reconstruction. Therefore, it provides a validation of the algorithms under the ideal condition. We have used imaging parameters mimicking the Toshiba 320-slice diagnostic CT scanner to generate data from discrete images, and performed reconstructions from the generated data. Results of the study, which are not included in the abstract, validate that the algorithms described above can solve their corresponding optimization programs, respectively. We plan to report the inverse-crime study results at the conference.

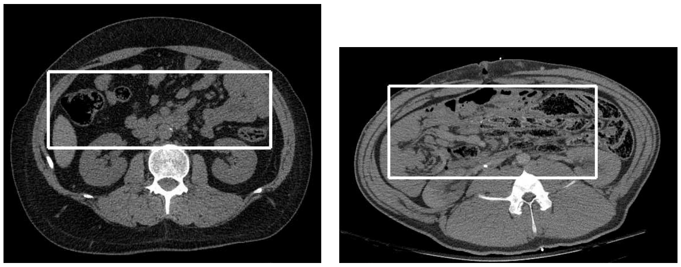

Figure 2. Patient (left) and swine (right) images reconstructed by use of the ASD-POCS algorithm in which ROIs are indicated by the white solid lines. The pixel sizes of 0.064 cm and 0.0625 cm are used in the uniform-resolutoin arrays, respectively, for the patient and swine reconstructions.

IV. RESULTS

We have used the POCS, SART, EM, and ASD-POCS algorithms to reconstruct images with uniform and variable resolution from both patient and swine data. We show below results obtained only with the ASD-POCS algorithm and will report results of other algorithms at the conference.

A. Reconstructions from patient data

1) Reconstruction on uniform-resolution arrays: We first performed optimization-based reconstructions on a uniform-resolution array consisting of pixels of size $a = 0.064$ cm, and show the ASD-POCS reconstruction in the left panel of Fig. 2. The ROI image enclosed by the white lines is also shown in a zoomed-in view in the first rows of Figs. 3-5, and it is used as a gold standard against which ROI reconstructions on variable-resolution arrays are compared. We then carried out ASD-POCS reconstructions on three additional uniform-resolution arrays with pixel sizes of 0.128 cm, 0.256 cm, and 0.512 cm, respectively, and display the corresponding ROI images in the second rows of Figs. 3-5. Clearly, reconstruction resolution decreases as the pixel size increases from 0.064 cm to 0.512 cm.

2) Reconstruction on variable-resolution arrays: We also performed optimization-based reconstructions on three different, variable-resolution arrays, in the patient study, as described in Sec. III-C. In row 3 of Figs. 3-5, we display the respective ROI images reconstructed by using the ASD-POCS algorithm.

Comparing ROI reconstructions of Figs. 3-5 with the gold standard in the row of Figs. 3-5, we observe that images within regions, which surround the ROI, with increased pixel sizes lose rapidly their resolution, as expected. However, image resolution within the ROI remains virtually unchanged, and is comparable to the gold standard resolution, even though the ratio between the pixel sizes within and outside the ROI has decreased considerably.

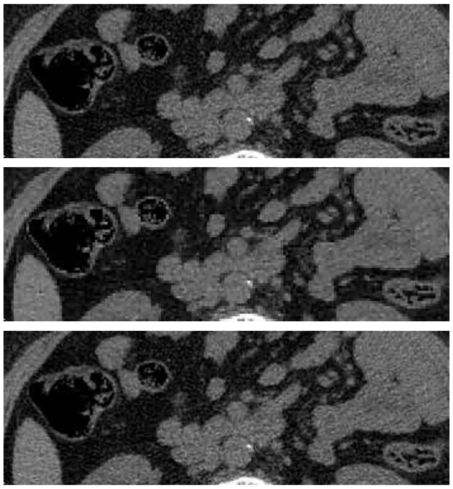

Figure 3. ROI images reconstructed by use of the ASD-POCS algorithm from patient data on a uniform-resolution array with pixel size 0.064 cm (row 1), a uniform-resolution array with pixel size 0.128 cm (row 2), and a variable-resolution array specified by the combination of $a = 0.064$ cm and $b = 0.128$ cm. A display window [-6, 13] is used.

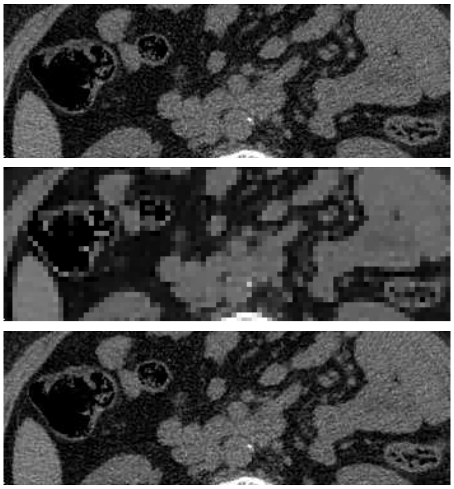

Figure 4. ROI images reconstructed by use of the ASD-POCS algorithm from patient data on a uniform-resolution array with pixel size 0.064 cm (row 1), a uniform-resolution array with pixel size 0.256 cm (row 2), and a variable-resolution array specified by the combination of $a = 0.064$ cm and $b = 0.256$ cm. A display window [-6, 13] is used.

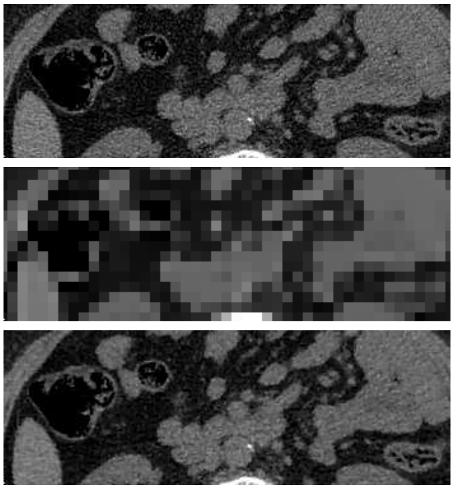

Figure 5. ROI images reconstructed by use of the ASD-POCS algorithm from patient data on a uniform-resolution array with pixel size 0.064 cm (row 1), a uniform-resolution array with pixel size 0.512 cm (row 2), and a variable-resolution array specified by the combination of $a = 0.064$ cm and $b = 0.512$ cm. A display window [-6, 13] is used.

B. *Reconstructions from swine data*

1) Reconstruction on uniform-resolution arrays: Again, we carried out optimization-based reconstructions on a uniform-resolution array consisting of pixels of size $a = 0.0625$ cm, and show the ASD-POCS reconstruction in the right panel of Fig. 2. The ROI image enclosed by the white lines is also shown in a zoomed-in view in the first rows of Figs. 6-8, and it is also used as a gold standard against which ROI reconstructions on variable-resolution arrays are compared. We also did ASD-POCS reconstructions on three uniform-resolution arrays with pixel sizes of 0.125 cm, 0.25 cm, and 0.5 cm, respectively, and display the ROI images in the second rows of Figs. 6-8. It can be observed that reconstruction resolution decreases as the pixel size increases from 0.0625 cm to 0.5 cm.

2) Reconstruction on variable-resolution arrays: We then performed optimization-based reconstructions on three different, variable-resolution arrays, in the swine study, as described in Sec. III-C. In row 3 of Figs. 6-8, we display the respective ROI images reconstructed by using the ASD-POCS reconstruction algorithm.

Comparison of ROI reconstructions in row 3 of Figs. 6-8. with the gold standard reconstruction displayed in row 1 of Figs. 6-8 reveals that observations similar to those made for the patient study above can also be made for the swine study.

V. DISCUSSIONS

In this work, we have investigated and developed optimization-based algorithms for image reconstruction with variable resolution and apply them to real patient and animal data collected with a diagnostic CT scanner. The results demonstrated that ROI images with quality comparable to that obtained with an image array with uniform, high resolution can be reconstructed through the use of image arrays with variable resolution by use of, e.g., the ASD-POCS algorithm. Results of this work may have implications for practical applications of iterative image-reconstruction algorithms as they can be exploited for reducing computation memory and time. They may also find applications for image reconstruction from severe truncated data.

VI. ACKNOWLEDGMENTS

This work was supported in part by the National Institutes of Health (NIH) under Grants CA120540, EB000225 and CA158446. The work of X. Han was supported in part by the Department of Defense (DoD) Predoctoral training Grants PC094510.

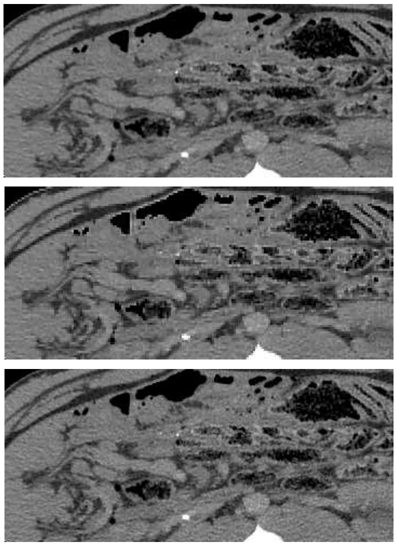

Figure 6. ROI images reconstructed by use of the ASD-POCS algorithm from swine data on a uniform-resolution array with pixel size 0.0625 cm (row 1), a uniform-resolution array with pixel size 0.125 cm (row 2), and a variable-resolution array specified by the combination of $a = 0.0625$ cm and $b = 0.125$ cm. A display window [-8.5, 16] is used.

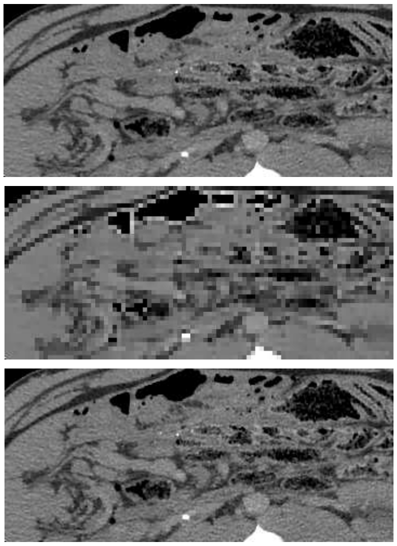

Figure 7. ROI images reconstructed by use of the ASD-POCS algorithm from swine data on a uniform-resolution array with pixel size 0.0625 cm (row 1), a uniform-resolution array with pixel size 0.25 cm (row 2), and a variable-resolution array specified by the combination of $a = 0.0625$ cm and $b = 0.25$ cm. A display window [-8.5, 16] is used.

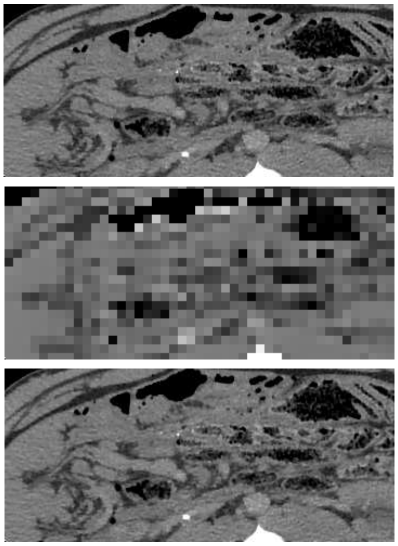

Figure 8. ROI images reconstructed by use of the ASD-POCS algorithm from swine data on a uniform-resolution array with pixel size 0.0625 cm (row 1), a uniform-resolution array with pixel size 0.5 cm (row 2), and a variable-resolution array specified by the combination of $a = 0.0625$ cm and $b = 0.5$ cm. A display window [-8.5, 16] is used.

Residual Motion Compensation in ECG-Gated Cardiac Vasculature Reconstruction

Chris Schwemmer, Christopher Rohkohl, Günter Lauritsch, Kerstin Müller and Joachim Hornegger

***Abstract*—Generating 3-D reconstructions of cardiac vasculature from angiographic C-arm CT (rotational angiography) data is a challenging problem. Currently, many approaches depend on a reconstruction from ECG-gated projection data either as a reference for further processing or as the final result. Due to imperfect gating, e.g. caused by irregular heart movement, residual motion corrupts these reconstructions.**

We present an algorithm to compensate for this residual motion. The approach is based on a deformable 2-D–2-D registration between the acquired projection data and a forward projection of the initial ECG-gated reconstruction. It does not depend on an explicit segmentation of vasculature or markers, and works without user interaction. The estimated 2-D deformation field is compensated for in the backprojection step of a subsequent reconstruction. The algorithm is evaluated on two clinical datasets, showing a clear decrease in artefact level and better visibility of structure in the compensated reconstructions.

I. INTRODUCTION

A. Purpose of this Work

Three-dimensional information during cardiac interventions can provide improved guidance and easier assessment for complex interventional procedures [1], [2]. Ideally, this 3-D imaging should be performed in the interventional suite using C-arm CT, avoiding the need to move the patient to a CT scanner or perform a prior diagnostic CT scan. Additionally, up-to-date information of the current state would be available. Currently, this approach is limited by the temporal resolution of available C-arm systems. Due to the long acquisition time of several seconds, heart motion corrupts a straightforward 3-D reconstruction. This results in motion blur, streak artefacts and reduced sharpness and visibility of structure.

Commonly, an ECG signal is recorded during the acquisition. This allows to retrospectively gate the available X-ray projection data so that only images from a specific heart phase contribute to the 3-D reconstruction [3]. However, ECG data does not necessarily correspond to the exact motion state of the heart [3]. A wider gating window is desirable to get a high signal-to-noise ratio and little undersampling artefacts, but then the residual motion in the gated projection data needs to be compensated for.

B. State of the Art

In the literature, several approaches have been proposed to account for residual motion due to non-ideal ECG-gating. A full 3-D estimation is a strongly ill-posed problem with high computational demands. However, due to the ECG-gating, the residual motion inside one window can be assumed to be reasonably small and an approximate 2-D motion estimation in projection space might be sufficient. This is demonstrated both by previous work [4]–[6] and the results shown below.

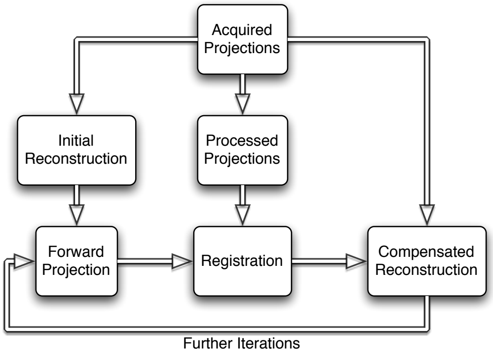

Figure 1: Illustration of the proposed algorithm.

A model-based learning approach was recently proposed, that registers a previously learnt motion model to the actual data [5]. Here, an extensive training phase is needed beforehand, and the application to patients with very irregular heart motion is difficult. A projection-based motion compensation was proposed in [6]. It requires a segmentation of vasculature centrelines in the acquired projection data, which is difficult [7].

C. Outline

In this paper, a method for compensation of residual motion in ECG-gated data is presented. Our method estimates residual motion by deformable 2-D–2-D registration in projection space without requiring complex image pre-processing steps.

In the next section, our algorithm and the experimental setup is discussed in detail. In Section III, the results are presented and both a qualitative and quantitative evaluation is performed.

II. MATERIALS AND METHODS

In the following, the individual steps of the algorithm as shown in Figure 1 are discussed in detail. First, an initial ECG-gated reconstruction is performed. A thresholding operation removes non-vascular tissue. Then, a forward projection (FwP) is generated. The original projections are pre-processed by automatic top-hat filtering and thresholding. The FwP is then registered to the pre-processed original projection data using

C. Schwemmer, K. Müller and J. Hornegger are with the Pattern Recognition Lab, Department of Computer Science, and the Erlangen Graduate School in Advanced Optical Technologies (SAOT), Friedrich-Alexander-Universität Erlangen-Nürnberg, Erlangen, Germany, email: chris.schwemmer@cs.fau.de. C. Rohkohl and G. Lauritsch are with the Siemens AG, Healthcare Sector, Forchheim, Germany.

a deformable 2-D–2-D registration algorithm. The resulting 2-D motion field is compensated for during the backprojection step of a subsequent ECG-gated reconstruction. The procedure may be repeated for additional refinement. In Section II-H, the experimental setup used for the evaluation is presented.

A. Initial Reconstruction

An initial ECG-gated reconstruction is performed by inserting a weighting function λ into a standard FDK-type algorithm [8], [9]. Let $h_r \in [0,1]$ be the heart phase at which reconstruction shall be carried out. The ECG-gated FDK reconstruction $f_{h_r} : \mathbb{R}^3 \mapsto \mathbb{R}$ at a voxel $\boldsymbol{x} \in \mathbb{R}^3$ is given by

$$f_{h_r}(\boldsymbol{x}) = \sum_{i=1}^{N} \lambda(i, h_r) \cdot w(i, \boldsymbol{x}) \cdot p_{\mathrm{F}}(i, \mathrm{A}(i, \boldsymbol{x})) \ , \quad (1)$$

where N is the number of projection images, $w : \mathbb{N} \times \mathbb{R}^3 \mapsto \mathbb{R}$ is the FDK distance weight and $p_{\mathrm{F}}(i, \boldsymbol{u}) : \mathbb{N} \times \mathbb{R}^2 \mapsto \mathbb{R}$ is the filtered and redundancy-weighted projection data of the i-th image at pixel position $\boldsymbol{u}$. The pixel position is determined by the perspective projection of voxel $\boldsymbol{x}$, $\mathrm{A} : \mathbb{N} \times \mathbb{R}^3 \mapsto \mathbb{R}^2, (i, \boldsymbol{x}) \mapsto \mathrm{A}(i, \boldsymbol{x}) = \boldsymbol{u}$. The weighting function λ is a cosine-window defined by

$$\lambda(i, h_r) = \begin{cases} \cos^a\left(\frac{d(h(i), h_r)}{\omega}\pi\right) & \text{if } d(h(i), h_r) \leq \frac{\omega}{2} \\ 0 & \text{otherwise} \end{cases} \ , \quad (2)$$

where $h(i)$ is the heart phase of the i-th projection image according to the ECG, $\omega \in [0,1]$ controls the width and $a \geq 0$ controls the shape of the gating window. The distance measure d is defined as $d(h_1, h_2) = \min_{j \in \{0,1,-1\}} |h_1 - h_2 + j|$.

Additionally, a streak reduction [9] is performed to reduce undersampling artefacts.

B. Thresholding and Forward Projection

Since the contrasted cardiac vasculature presents a high-contrast object, a simple thresholding operation can be used to remove background structure. It retains only the $t_r \in [0,1]$ percentile of the largest voxel values. Then, maximum intensity forward projections p_{fwp} are generated from the thresholded initial reconstruction using the original acquisition geometry.

C. Pre-Processing of Original Projections

A background reduction is performed on the original projection data. First, a morphological top-hat filtering using a kernel of radius r as in [10], then a thresholding that retains only the $t_p \in [0,1]$ percentile of the largest pixel values is done. This removes most of the non-vascular background while safely retaining vascular structure. The processed projection images are denoted p_{bgr} in the following.

D. Registration Method

Registration establishes a mapping between the space of the pre-processed projection data p_{bgr} and the FwP p_{fwp} so that $p_{\mathrm{bgr}}(i, \boldsymbol{u})$ is similar to $p_{\mathrm{fwp}}(i, \mathrm{M}(i, \boldsymbol{u}))$, where $\mathrm{M} : \mathbb{N} \times \mathbb{R}^2 \mapsto \mathbb{R}^2$ is the motion vector field for the i-th image. We chose a uniform cubic B-spline as a deformable motion model [11]. The mapping is parametrised by the number of B-spline control points c in each dimension. This model is very flexible, while containing an implicit smoothness constraint that avoids large local deformations for small values of c.

Mutual information [12] was used as a (multi-modality) similarity metric for the registration process. Mono-modal metrics like sum of squared differences cannot be used, since the grey values of p_{bgr} and p_{fwp} differ due to the maximum intensity FwP and data truncation. A gradient descent method was used to drive the registration process.

E. Motion Compensated Reconstruction

Using the motion vector field M, the estimated motion can be compensated for in the reconstruction step

$$f_{h_r,\mathrm{M}}(\boldsymbol{x}) = \sum_{i=1}^{N} \lambda(i, h_r) \cdot w(i, \boldsymbol{x}) \cdot p_{\mathrm{F}}(i, \mathrm{M}(i, \mathrm{A}(i, \boldsymbol{x}))) \ . \quad (3)$$

Motion compensation applies a 2-D deformation after the perspective projection instead of a 3-D deformation before the projection [8].

F. Further Iterations

The process can be repeated for an additional refinement of the motion compensation by using the output from Step II-E as input in Step II-B.

G. Considerations on Implementation

The main contribution to processing time is by the registration process. Since registration is performed on a per-image basis, the projection stack can be processed in parallel. In addition, only those images need to be considered that have a gating weight $\lambda > 0$. Using graphics hardware is work in process. An optimal parameter set for the mutual information calculation can be found using the methods presented in [13]. Backprojection can be implemented very efficiently on graphics hardware [14], as can be B-spline evaluation [15]. Therefore, the motion compensated backprojection can be carried out completely parallelised on the graphics card.

H. Experimental Setup

For evaluation, two clinical datasets were used, where a left (LCA) or a right (RCA) coronary artery was contrasted respectively. Patient heart rates were 103±7.0 bpm (LCA) and 68±1.5 bpm (RCA). All datasets were acquired using a five second rotational angiography with selective contrast agent administration (1-2 ml/s). Source-isocentre-distance was ~80 cm and source-detector-distance ~120 cm. The acquired 133 projection images per dataset had a size of 1240x960 pixels with a pixel size of 0.308 mm. The size of the 3-D volumes after reconstruction was 256x256 voxels with 224 (LCA) and 186 (RCA) slices and an isotropic voxel size of 0.48 (LCA) and 0.60 (RCA) mm.

The gating parameters were selected as $\omega = 0.4$ and $a = 4$, with $h_r = 0.47$ (LCA) and $h_r = 0.75$ (RCA). Therefore, 52 projection images were used for reconstruction of each dataset after gating. Thresholding was performed at $t_r = 0.005$

Table I: Estimated noise in HU around coronary tree.

Name	Initial	One Iter.	Two Iter.
LCA	12.02	11.71	10.65
RCA	25.55	21.97	21.80

and $t_p = 0.2$. The size of the morphological kernel was $r = 3.4\,\text{mm}$. The number of B-spline control points was set to $c = 5$ in each dimension. Two iterations of the algorithm were performed.

I. Evaluation

Qualitative evaluation was carried out visually. For a quantitative evaluation, image noise in the region of the reconstructed vessels was estimated [16] (on a sub-volume of $653\,\text{cm}^3$ (LCA) and $387\,\text{cm}^3$ (RCA) respectively). Additionally, vessel sharpness [17] was calculated for five different segments (cf. Figures 3a, 3d) along the coronary tree. To this end, one continuous branch of each tree was selected and 40 regularly spaced measurement sites were placed along each branch. At every site, 10 cross-sectional profiles equally distributed over 180° in the plane perpendicular to the vessel were used for the sharpness estimation. The values presented in Figures 3c and 3f are the average values of all sharpness measurements in the respective segments.

III. RESULTS AND DISCUSSION

Figure 2 shows an original and a pre-processed projection, and a chequerboard overlay of a pre-processed projection with a FwP before and after registration for dataset LCA. The displacement of vessel sections in the FwP compared to the original projection is significantly reduced by the registration step. In Figure 3, the resulting reconstructions both before and after two iterations of the proposed algorithm are shown. It can be seen that the artefact level is strongly decreased, while the visibility and sharpness of structure is increased when using our proposed algorithm. This observation is confirmed both by a decrease of image noise (cf. Table I) and an increase in vessel sharpness (cf. Figure 3c and 3f) after registration. The second iteration step increases image quality and vessel sharpness for most segments.

IV. CONCLUSION AND OUTLOOK

Due to non-ideal gating, residual motion corrupts ECG-gated cardiac reconstructions. We presented an algorithm that compensates residual motion. Motion is estimated by a deformable 2-D–2-D registration method. No explicit segmentation is needed for registration. Motion is directly compensated for in the backprojection step of image reconstruction. The method can be repeated in an iterative loop.

We showed that artefact level is greatly decreased, while sharpness and detail of structure is increased.

ACKNOWLEDGEMENTS

The authors gratefully acknowledge funding of the Erlangen Graduate School in Advanced Optical Technologies (SAOT) by the German Research Foundation (DFG) in the framework of the German excellence initiative. The authors also would like to thank Prof. Dr. D. Böcker and Dr. P. Skurzewski, St. Marienhospital Hamm, Germany for acquiring clinical data.

Disclaimer: The concepts and information presented in this paper are based on research and are not commercially available.

REFERENCES

[1] H. Hetterich, T. Redel, G. Lauritsch, C. Rohkohl, and J. Rieber, "New X-ray imaging modalities and their integration with intravascular imaging and interventions," *The International Journal of Cardiovascular Imaging (formerly Cardiac Imaging)*, vol. 26, no. 7, pp. 797–808, 2010.

[2] K.-J. Gutleben, G. Nölker, G. Ritscher, H. Rittger, C. Rohkohl, G. Lauritsch, J. Brachmann, and A. M. Sina, "Three-dimensional coronary sinus reconstruction-guided left ventricular lead implantation based on intraprocedural rotational angiography: a novel imaging modality in cardiac resynchronisation device implantation," *Europace*, vol. 13, no. 5, pp. 675–682, February 2011.

[3] B. Desjardins and E. Kazerooni, "ECG-gated cardiac CT," *American Journal of Roentgenology*, vol. 182, no. 4, pp. 993–1010, Apr. 2004.

[4] B. Perrenot, R. Vaillant, R. Prost, G. Finet, P. Douek, and F. Peyrin, "Motion correction for coronary stent reconstruction from rotational X-ray projection sequences," *IEEE Transactions on Medical Imaging*, vol. 26, no. 10, pp. 1412–1423, Oct. 2007.

[5] A. Lebois, R. Florent, and V. Auvray, "Geometry-constrained coronary arteries motion estimation from 2D angiograms – Application to injection side recognition," in *IEEE International Symposium on Biomedical Imaging: From Nano to Macro (ISBI)*, X. L. M. Wright, Steve; Pan, Ed. Chicago, IL, USA: IEEE, Mar. 2011, pp. 541–544.

[6] E. Hansis, D. Schäfer, O. Dössel, and M. Grass, "Projection-based motion compensation for gated coronary artery reconstruction from rotational x-ray angiograms," *Physics in Medicine and Biology*, vol. 53, no. 14, pp. 3807–3820, 2008.

[7] U. Jandt, D. Schäfer, M. Grass, and V. Rasche, "Automatic generation of time resolved motion vector fields of coronary arteries and 4D surface extraction using rotational x-ray angiography," *Physics in Medicine and Biology*, vol. 54, no. 1, pp. 45–64, Jan. 2009.

[8] D. Schäfer, J. Borgert, V. Rasche, and M. Grass, "Motion-compensated and gated cone beam filtered back-projection for 3-D rotational X-ray angiography," *IEEE Transactions on Medical Imaging*, vol. 25, no. 7, pp. 898–906, Jul. 2006.

[9] C. Rohkohl, G. Lauritsch, A. Nöttling, M. Prümmer, and J. Hornegger, "C-Arm CT: Reconstruction of Dynamic High Contrast Objects Applied to the Coronary Sinus," in *IEEE Nuclear Science Symposium and Medical Imaging Conference Record*, Dresden, Germany, Oct. 2008, pp. M10–328.

[10] E. Hansis, D. Schafer, O. Dossel, and M. Grass, "Evaluation of iterative sparse object reconstruction from few projections for 3-D rotational coronary angiography," *IEEE Transactions on Medical Imaging*, vol. 27, no. 11, pp. 1548–1555, Nov. 2008.

[11] M. Unser, "Splines: A Perfect Fit for Signal and Image Processing," *IEEE Signal Processing Magazine*, vol. 16, no. 6, pp. 22–38, Nov. 1999.

[12] D. Mattes, D. R. Haynor, H. Vesselle, T. K. Lewellyn, and W. Eubank, "Nonrigid multimodality image registration," in *Proceedings of SPIE*, M. Sonka and K. M. Hanson, Eds., vol. 4322, no. 1. San Diego, CA, USA: SPIE, Feb. 2001, pp. 1609–1620.

[13] D. Hahn, V. Daum, and J. Hornegger, "Automatic Parameter Selection for Multi-Modal Image Registration," *IEEE Transactions on Medical Imaging*, vol. 29, no. 5, pp. 1140–1155, May 2010.

[14] H. G. Hofmann, B. Keck, C. Rohkohl, and J. Hornegger, "Comparing performance of many-core CPUs and GPUs for static and motion compensated reconstruction of C-arm CT data," *Medical Physics*, vol. 38, no. 1, pp. 468–473, 2011.

[15] D. Ruijters, B. ter Haar Romeny, and P. Suetens, "Efficient GPU-Based Texture Interpolation using Uniform B-Splines," *Journal of Graphics, GPU, & Game Tools*, vol. 13, no. 4, pp. 61–69, 2008.

[16] S.-M. Yang and S.-C. Tai, "Fast and reliable image-noise estimation using a hybrid approach," *Journal of Electronic Imaging*, vol. 19, no. 3, pp. 033 007–1–15, July–September 2010.

[17] D. Li, J. Carr, S. Shea, J. Zheng, V. Deshpande, P. Wielopolski, and J. Finn, "Coronary Arteries: Magnetization-prepared Contrast-enhanced Threedimensional Volume-targeted Breath-hold MR Angiography," *Radiology*, vol. 219, no. 1, pp. 270–277, April 2001.

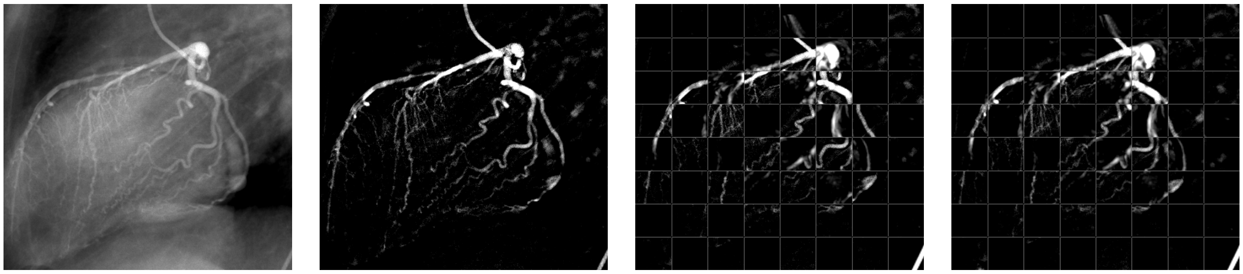

(a) Original Projection (b) Pre-processed Projection (c) Unregistered FwP (d) Registered FwP

Figure 2: Results of the registration algorithm for dataset LCA.
In Figures 2c and 2d, the pre-processed projection and the FwP are shown combined in a chequerboard pattern to visualise the registration result.

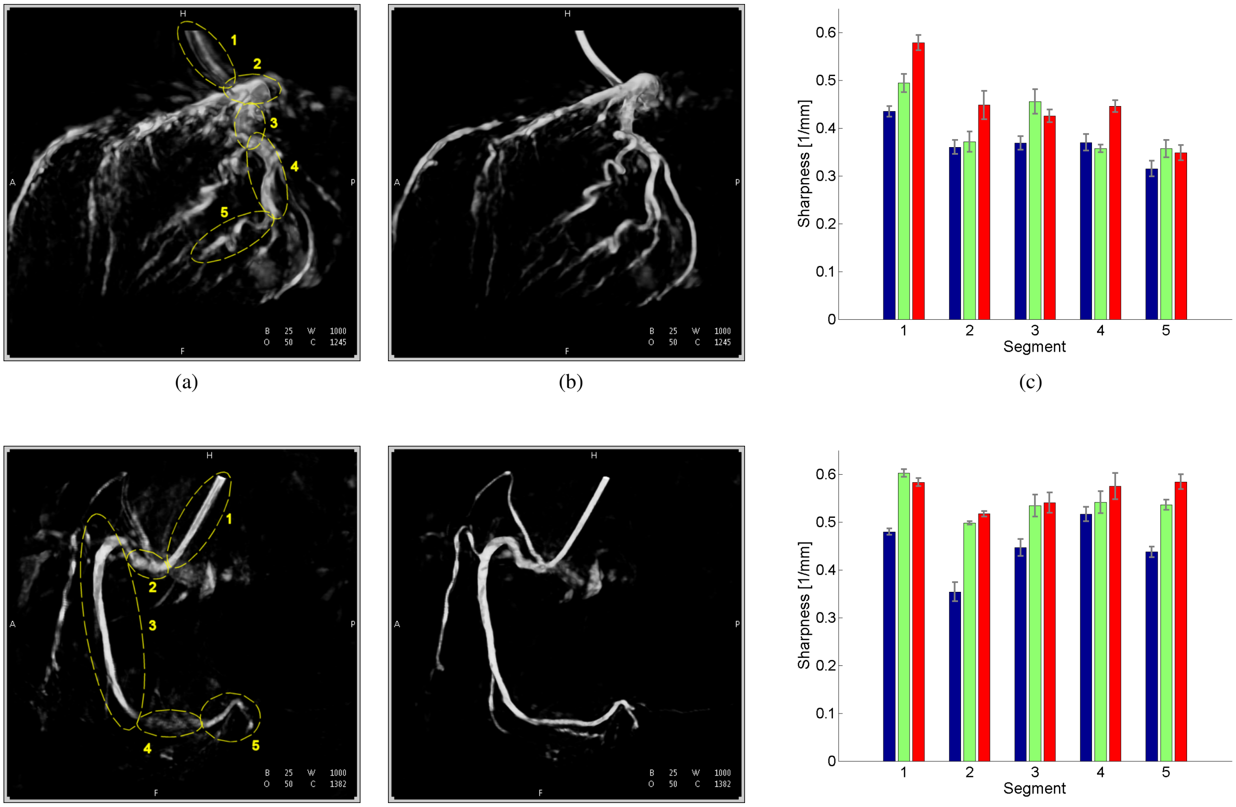

(a) (b) (c)

(d) (e) (f)

Figure 3: Reconstruction results without and after two iterations of the proposed algorithm.
Top row: LCA, bottom row: RCA. Left column: initial reconstruction (and segments for vessel sharpness measurements), middle column: compensated reconstruction, right column: vessel sharpness.
All volume renderings show a left sagittal view. The grey scale window was 1000. In the right column, the average vessel sharpness and standard deviation of the initial reconstruction (🟦), after one iteration (🟩) and after two iterations (🟥) are shown for each segment.

Noise Reduction With Low Dose CT Data Based On a Modified ROF Model

Mengliu Zhao, Yining Zhu, Hongwei Li, Peng Zhang

***Abstract*—A modified ROF model to denoise low dose CT measurement data in light of Poisson noise model is proposed. Experimental results indicate that the reconstructed CT images based on measurement data processed by our model are in better quality, compared to the original ROF model and bilateral filtering.**

***Keywords*—low dose CT; noise reduction; Poisson noise; modified ROF model.**

I. INTRODUCTION

Computed Tomography (CT) is crucial for clinical diagnosis. To reduce the risk of cancer [1], low dose CT has raised many interests in research community as well as in industry. One difficulty with the low dose CT is that the noise associated with the projection data is high, which leads to deterioration of the reconstructed CT images. Traditional denoising methods, such as FFT, wavelet and spatial filtering methods like Gaussian filtering and bilateral filtering, usually bring undesired blurring, and result in loss of resolution for the reconstructed images. This is the case for some more advanced denoising methods which are based on partial differential equations or variational principle, like the popular ROF model [2]. On the other hand, variational models enjoy some desired global smoothing properties which is unseen in traditional filtering methods.

In this paper, we propose a modified ROF model to filter the projection raw data (measurement data). The original ROF model has been proven effective for denoising images corrupted by additive white Gaussian noise. However, the projection raw data is assumed to obey the Poisson distribution [3], [4]. For our CT projection raw data, the noise is not exact Poisson. It's just poisson-like, which means that if we model the projection raw data by a random field, then its mean and variance are related to each other, but not equal. There are several approaches for denoising Poisson noise in the literature. Le *et al.* proposed a model in the framework of Bayesian inference [5], which fits well to Poisson noise. Other methods, like PURE-LET [6] and MS-VST [7], are based on wavelet transformation. However, it's not apparent how to adapt those approaches mentioned above to Poisson-like noise. The modified ROF model we propose here bares the Poisson nature of the projection raw data in mind, while it's easy to extend to Poisson-like noise.

II. NOISE MODEL AND THE ROF MODEL

For monoenergetic x-ray source, the number of photons collected by detectors obeys the Poisson distribution

$$I^d \sim \text{Poisson}\{I_0 \exp(-\int_{x\in L} f(x)dx)\}, \tag{1}$$

where I_0 indicates the number of emitted photons, I^d the number of photons collected, $f(x)$ the attenuation distribution of the object under examination and L the X-Ray trajectory. CT image reconstruction is an inverse problem, which is to solve $f(x)$ from a series of measurement data $\{I_1^d, I_2^d, ...I_n^d\}$. If the measurement data is noise free, we change formula (1) by logarithmic transformation for linearization

$$p_i = -\log(I_i^d/I_0) = \int_{L_i} f(x)dx, \tag{2}$$

and we call p_i the projection data. For formula (2), we usually use the Filter Back-Projection algorithm (FBP) [8] to compute $f(x)$. We do not intend to deal with p_i. Instead, we deal with the raw data I^d, which is named *projection raw data* in this paper, since I^d is less "polluted" than p_i because less mathematical computations are involved. For real CT systems, there are also two kinds of background noise–electrical thermal noise (i.i.d. gaussian) and round-off errors. Moreover, the monoenergetic source is just an ideal assumption. So the Poisson distribution is just an approximate model. Strictly, we can only say that the noise is Poisson-like.

The ROF model was proposed by Rudin, Osher and Fatemi [2] in 1992.

$$\left\{ \begin{array}{ll} \min \int_\Omega |\nabla u| d\Omega, & (3) \\ \frac{1}{|\Omega|} \int_\Omega (u-f)^2 d\Omega = \sigma^2. & (4) \end{array} \right.$$

It can be turned into a non-constrained minimization problem, with a suitable parameter λ

$$\min_u \left\{ J(u) + \frac{1}{2\lambda} \int_\Omega (u-f)^2 d\Omega \right\}, \tag{5}$$

where (for regular enough of u)

$$J(u) = \int_\Omega \sqrt{(\frac{\partial u}{\partial x})^2 + (\frac{\partial u}{\partial y})^2}\, d\Omega$$

In (5), Ω is the image domain, f is the input image which is assumed to contain additive white Gaussian noise.

The authors are with The CT Laboratory, School of Mathematics, Capital Normal University, Beijing, 10048, China; email: zhumilan997@163.com

III. THE MODIFIED ROF MODEL - POISSON-ROF

In the ROF model, Gaussian white noise is assumed, e.g.

$$f(x) = u(x) + n,$$

where n is a random variable that obeys $N(0, \sigma^2)$. Note that n doesn't depend on x. For digital images, it means that if we regard each pixel corresponding to a random variable, then all the random variables are independent of each other while share the same distribution. In this situation, the image pixels can be thought of as samplings to one single random variable. So the variance σ can be estimated as

$$\frac{1}{|\Omega|}\int_\Omega (u-f)^2 d\Omega = \sigma^2,$$

e.g.

$$\frac{1}{|\Omega|}\int_\Omega \frac{1}{\sigma^2}(u-f)^2 d\Omega = 1.$$

For the projection raw data, each "pixel" should be regarded as corresponding to a random variable of Poisson. Suppose $u(x)$ is the mean of $f(x)$, then the variance should be $\sqrt{u(x)}$. So if we would like to extend the ROF model to deal with Poisson noise, a heuristic choice for the data term is

$$\frac{1}{|\Omega|}\int_\Omega \frac{1}{u}(u-f)^2 d\Omega = 1. \tag{6}$$

Based on the above data term, we propose the following denoising model

$$\min_u \left\{ J(u) + \frac{1}{2\lambda}\int_\Omega \frac{1}{u}(u-f)^2 d\Omega \right\}, \tag{7}$$

which is named **Poisson-ROF** in this paper.

Remark 3.1: For our CT projection raw data, $u(x) = 0$ means that the X-Ray can not penetrate the object from some trajectory, and the associated information is lost. In this case, people usually increase the intensity of the X-Ray to avoid its happening. So for the CT projection raw data, one could think that $u(x) > 0$ holds true all the time.

Remark 3.2: It's easy to verify that if u is strictly greater than zero, then the minimization problem (7) is strictly convex. So the problem admits a single solution.

Remark 3.3: The deviation of the Poisson-ROF model is just formal. Due to space limit, a more strict statistical analysis is omitted here.

In the Poisson-ROF model, the data term is nonlinear with respect to u. To easy the problem, we do a iterative lineation of the data term.

$$\min_{u^{n+1}} \left\{ J(u^{n+1}) + \frac{1}{2\lambda}\int_\Omega \frac{1}{u^\star}(u^{n+1}-f)^2 d\Omega \right\},$$

where $u^\star$ takes u^n, u^{n-1} or u^{n-2} etc. The Chambolle's algorithm [9] can not be applied to the Poisson-ROF model directly. So we can introduce another variable v to relax the problem, just like in [10].

$$\min_{\{u,v\}} \left\{ J(u) + \frac{1}{2\theta}\int_\Omega (u-v)^2 d\Omega + \frac{1}{2\lambda}\int_\Omega \frac{1}{f_{NF}}(v-f)^2 d\Omega \right\} \tag{8}$$

Then we solve (8) by solving the following two subproblems alternatively

1) Minimization with u, for which Chambolle's method could be used, or one can adopt some more recently proposed fast algorithms such as the Split-Bregman [26];
2) Minimization with v, and replace f_{NF} by $\bar{u}$,

$$\frac{1}{\theta}(v-u) + \frac{1}{\lambda\bar{u}}(v-f) = 0 \Longrightarrow v = \frac{\lambda u\bar{u} + \theta f}{\lambda\bar{u} + \theta} \tag{9}$$

In our numerical simulations, θ is set to 0.1, v is updated for each 5 iterations.

The weighting parameter λ in (9) could be estimated in several ways. If we consider λ as coefficient of the Lagrange multiplier, then the choice of λ should always ensure that the Lagrange equation is equivalent. Gilboa *et al* suggested that λ should be updated according to the current SNR. However, fixed λ tends to smooth the image as the iteration number increases. Here we simply update λ to keep the Euler-Lagrange equation in equivalence, which means

$$\lambda = -\frac{\int_\Omega < div(p), \frac{1}{\bar{u}}(u-f) > d\Omega}{\int_\Omega |div(p)|^2 d\Omega} \tag{10}$$

IV. EXPERIMENTS

We compare our model with the original ROF and bilaterial filtering for simulation data as well as real CT data. The CT images reconstructed from the raw data processed by our model and other models will be shown and compared.

A. Simulation Data

The simulation data are produced by projecting the Shepp-Logan phantom using the ray-tracing algorithm. From Fig. 1(a)-(d), we see that the bilateral filtering can preserve the structures of the phantoms, while suppressing some portion of the noise. The ROF model could remove most of the noise, but the structures (edges) are also diffused, which is unacceptable in real applications. For the Poisson-ROF model, most of the noise are removed, while the details are also preserved.

B. Real CT Data

We get two sets of projection raw data from an Industrial CT system. The first group come from scanning some cylindroid object made of volcanic rock, and the second group are the results from scanning a line-pair phantom for testing spatial resolutions. The number of channels per view is 3710 with a total of 720 views evenly spanned on a circular track of 360 degrees. The length of detector bins is 0.083 mm, the distance from source to center of turntable is 800 mm and the source to the detectors is 1050 mm. All these raw data are denoised and then transformed to images by the famous FBP algorithm.

1) Volcanic rock at low dose: The cylinder of volcanic rock has a diameter of 100 mm, and we set the x-ray source to 160 KVp to acquire raw data. We first scanned the object with the current intensity 8 mA and reconstructed it as a high dose CT image as shown in Fig. 2, and then reduce the current to 1 mA to model a low dose CT, which decreases the dose to 12.5%. The reconstructed images are shown in Fig. 3. One can see that the bilateral filtering and ROF model tend to blur the regions that close to the edges, and our model can keep the fine structures while removing much of the noise.

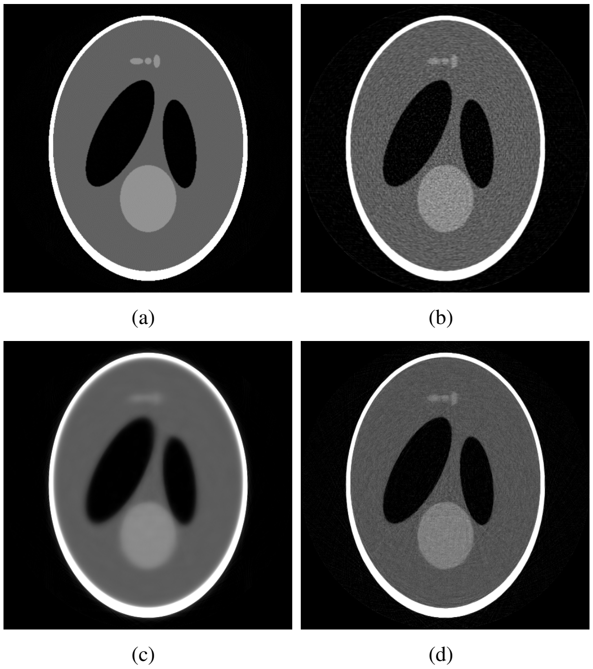
(a) (b) (c) (d)

Fig. 1. (a) the reference image, (b)-(d) are the corresponding reconstructed images for data filtered by bilateral filtering, ROF model and Poisson-ROF model respectively.

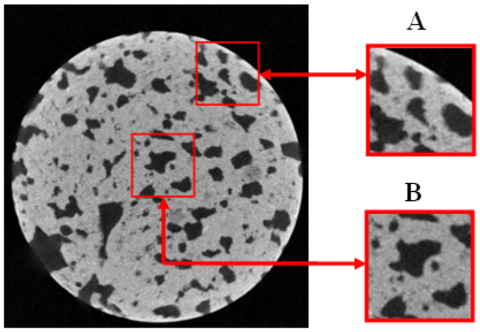

Fig. 2. The high dose CT image of volcanic rock

2) line-pairs phantom at low dose: To test the spatial resolution of our algorithm, we use a line-pairs phantom to scan in CT with 120 KVp and 4mA . The reconstructed image acts as an ideal resolution, as shown in Fig. 4. Then we decrease the current to 0.5mA and scan this phantom again. We then reconstruct images from the low dose data without denoising as well as denoised ones by the Poisson-ROF model. The results are shown in Fig. 5. As shown in Fig. 5(a), the CT image reconstructed from the low dose data without denoising almost cannot be distinguished by the bars. When the raw data are prepocessed by the Poisson-ROF model, the reconstructed images have better quality and resolution (See Fig. 5(b)).

V. CONCLUSION

In this paper, we propose a modified ROF model (Poisson-ROF) Experimental results compared with the original ROF and bilateral filtering validate the advantages of the proposed model.

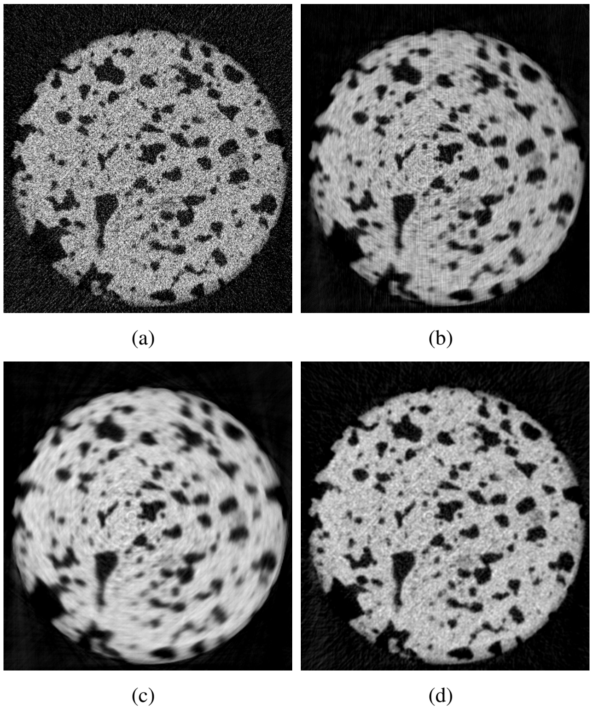
(a) (b) (c) (d)

Fig. 3. The (a) is CT image reconstructed without noise reduction in 12.5% dose of high dose data; from (b) to (d) are reconstructed results from raw data filtered by bilateral filtering, ROF model and Poisson-ROF model.

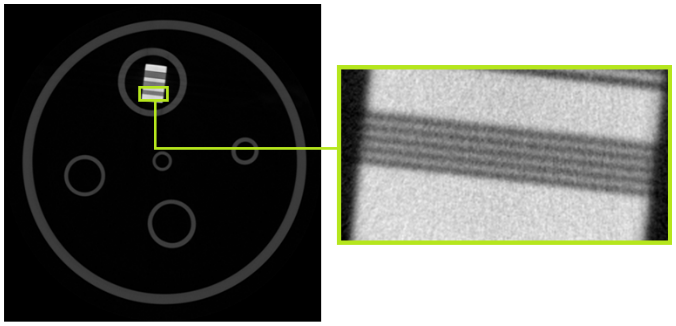

Fig. 4. The high dose CT image of line-pairs phantom.

ACKNOWLEDGMENT

This work was supported in part by the National Natural Science Foundation of China under the grants 60971131/F010404 and 60971131/F010404, Beijing Education Committee under the grants PHR20110509 and KZ201110028034.

REFERENCES

[1] A. B. Gonzalez, M. Mahesh and K. P. Kim *et al.*, "Projected cancer risks from computed tomographic scans performed in the United States in 2007", Arch.Intern.Med, Vol. 169, No. 22, pp.2071-2077, 2009.

[2] L. I. Rudin, S. Osher and E. Fetami, "Nonlinear total variation based noise removal algorithms", Physica D: Nonlinear Phenomena, Vol. 60, Issue 1-4, pp.259-268, 1992.

[3] J. Hsieh, "Computed Tomography: principles, design, artifacts, and recent advances", SPIE Publications, 2002.

[4] K. Lange and R. Carson, "EM reconstruction algorithms for emission and transmission tomography", Journal of Computer Assisted Tomography, Vol. 8, Issue. 2, 1984

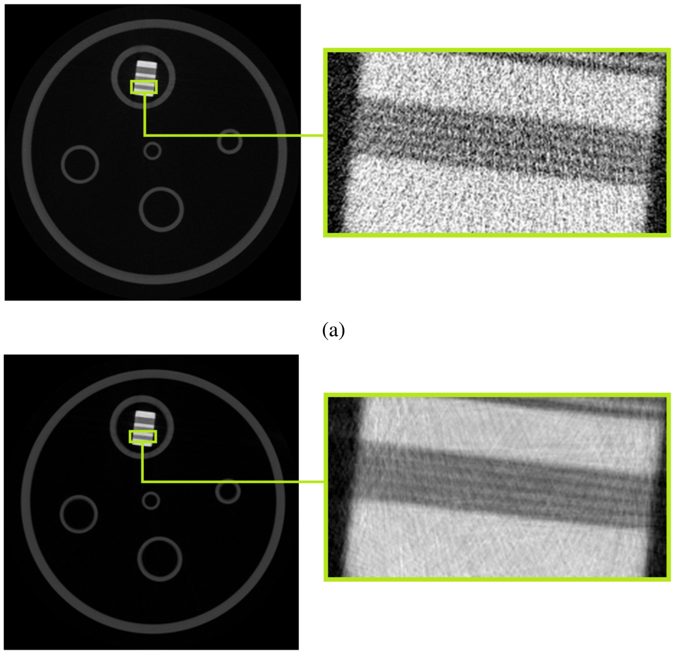
(a)

(b)

Fig. 5. (a) is CT image reconstructed from the raw data using 12.5% dose; (b) is CT image reconstructed from the same raw data processed by the Poisson-ROF model.

[5] T. Le, R. Chartrand and T. J. Asaki, ”A variational approach to reconstructing images corrupted by Poisson noise”, Journal of Mathematical Imaging and Vision, Vol. 27, Issue. 3, pp.257-263, 2007.

[6] F. Luisier, T. Blu and M. Unser, ”Image denoising in mixed Poisson-Gaussian noise”, Image Processing, IEEE Transactions on, Vol. 20, No. 3, pp. 696-708, 2011

[7] B. Zhang, J. M. Fadili and J. L. Starck, ”Wavelets, ridgelets, and curvelets for Poisson noise removal”, Image Processing, IEEE Transactions on, Vol. 17, No. 7, pp. 1093-1108, 2008

[8] A. C. Kak and Malcolm Slaney, ”Principles of Computerized Tomographic Imaging”, IEEE Press, 1988.

[9] A. Chambolle, ”An algorithm for total variation minimization and applications”, Journal of Mathematical Imaging and Vision, Vol. 20, pp.89-97, 2004.

[10] M. Unger, T. Pock and H. Bischof, ”Continuous globally optimal image segmentation with local constraints”, Computer Vision Winter Workshop 2008.

Robust Automated Regularization Factor Selection for Statistical Reconstructions

Frank Bergner[1], Bernhard Brendel[1], Peter B. Noel[2], Martin Dobritz[2],Thomas Koehler[1]

***Abstract*—Statistical, iterative reconstruction techniques have become a major research topic in the CT sector. These techniques promise a better system model, which is used for the inversion of the tomographic problem, and therefore better reconstruction results. Due to the ill–posedness of these problems, regularization is required in the cost functions in order to stabilize the algorithm and to reduce the noise in the resulting images. The strength of the regularization is usually changed by using an appropriate multiplicative factor, which in most cases has to be determined empirically with major efforts. This paper describes a new automated selection of this factor by using a quality criterion and a regulator, which controls the multiplicative factor over the iterations to a desired level. The method is light–weight, robust and also applicable for other iterative methods like de–noising.**

I. INTRODUCTION

For the reconstruction of computed tomography (CT) images filtered–backprojection (FBP) methods, which are based on analytical derivations, are the gold standard and well established in the clinical workflow as they offer a fast processing and acceptable image quality. In the last years the processing power of the reconstruction hardware has significantly increased, so also iterative reconstruction methods can be used in the clinical workflow. These introduce a better system and noise model compared to the analytic reconstruction, and therefore promise better reconstruction results with less noise and artifacts. In the statistical, iterative methods, which are based on noise models for the detected photons, regularization terms are used, which make the methods numerically stable and reduce the image noise down to some desired level. In most cases a regularization term is multiplied by a factor and then added to the cost function of the statistical reconstruction, which compares the projected image with the measured data. Some examples for these methods can be found in reference [1]. The main problem in the current iterative methods is the selection of the factor, which is data dependent and initially unknown. Most authors neglect this problem and leave the choice to the user, who, in the worst case, has to try different values in various reconstructions [2], [3]. The long reconstruction times make this approach infeasible for most clinical use cases. The choice of a correct regularization parameter is not limited to CT, and some methods have been proposed, which are depending on the used cost functions and to some extent hard to evaluate [4], [5]. In this paper a new, light–weight method for the automated selection for the regularization factor is proposed, which is independent of the used iterative method. It does not introduces changes into the cost function and can also be used for other problems like total variation de–noising, where the noise reducing term is steered by a multiplicative factor in a cost functions like

$$\mathrm{Cost}(\vec{\mu}) = \mathrm{RawdataTerm}(\vec{\mu}) + \beta\ \mathrm{RegularizationTerm}(\vec{\mu})$$

where $\vec{\mu}$ is the image vector.

Primarily the method presented here consists of two elements: A user chosen quality estimate, like the global noise level, and a controller, which steers β towards a user–chosen target quality level.

II. METHOD

In many iterative reconstruction methods intermediate images $\vec{\mu}(n)$ are available after the updates using the individual projection subsets. The proposed method examines the images according to a predefined quality metric and outputs a scalar value $q(n)$ which then is used for a controller to steer $\beta(n)$ towards the correct level. It is assumed that a reference image like an FBP image is available, which is used as a start image for the iterative method and for a reference quality level. The control flow is illustrated in Fig. 1.

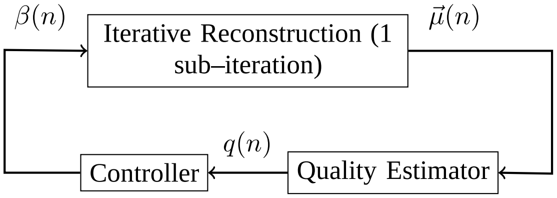

Fig. 1. Control flow of the proposed method. The parameter $\beta(n)$ is controlled in a closed loop of iterations and quality estimations.

A. Quality Measure

One part of the proposed method is the estimation of the quality of a given image. The quality can be the noise level or the artifact level, like streaks. In this paper the noise level is used as a metric. There, especially the noise within the homogeneous regions of the patient body is of interest. Edges shall not be part of the noise estimation. In this paper a simple noise estimation method is used. It uses a reference image, e.g. the FBP image, in order to extract the homogeneous regions within the body, in which later the local standard deviations are calculated as a noise estimate. The segmentation process and noise estimation is:

---

[1] Philips Technologie GmbH, Innovative Technologies, Research Laboratories, Hamburg, Germany
[2] Department of Radiology, Technische Universität München, Germany

- Denoising of the reference image by a large (7×7×7), edge preserving median filter
- Body segmentation by applying a threshold of -250 HU
- Edge removal: Application of the Sobel operator, followed by an edge detection using a threshold (10 HU) on the magnitude of the operator output
- Morphological erosion operation with a small kernel to further reduce the influence of edges on the estimate
- Calculation of the mean of the local standard deviations from the voxels within the segmentation

For the noise estimations over the iterations only the latter step has to be taken.

B. Controller and β Update

Controllers are well known in parts of our daily life, and can be found in various implementations and variations. One simple example is the thermostat of a heater, which tries to regulate the heating depending on the currently measured temperature and the user chosen temperature. The difference between both directly controls the heating, e.g. by a proportional mapping of the difference onto a change of the heating magnitude. If the difference is zero, then the controller does not change the heating as it is obviously at the correct level. In the proposed method a similar controller is used in a time–discrete manner. One popular example for such an controller is the so–called proportional-integrating-derivative (PID) controller, which does not only include the difference itself in the controlling but also its derivative and its integral [6]. At first an example for the update of β with a PID controller is given. For the actual algorithm a proportional–derivative (PD) controller is used.

Let the difference between the current quality level $q(n)$ and the desired quality level q_t be

$$e(n) = q(n) - q_\mathrm{t},$$

then a simple update formula for an PID controller is

$$\beta(n+1) = c_0(e(n) + c_1\Delta e(n) + c_2 E(n)) \qquad (1)$$

with

$$\Delta e(n) = e(n) - e(n-1)$$

and

$$E(n) = \sum_{m=0}^{n} e(m).$$

The constants c_0, c_1, and c_2 influence the controlling speed and accuracy and have to be adopted to the problem. The main problem that arises in this case is the unknown proportionality between $\beta(n)$ and $e(n)$, i.e. the correct choice of c_0. This can be circumvented by controlling the order of magnitude instead of the absolute value of β and by using a new update formula

$$\beta(n+1) = \beta(n) 2^{c_0(\tilde{e}(n) + c_1\Delta\tilde{e}(n) + c_2\tilde{E}(n))} \qquad (2)$$

where the normalized, relative quality

$$\tilde{q}(n) = \frac{q(n) - q_\mathrm{lo}}{q_\mathrm{hi} - q_\mathrm{lo}}$$

is introduced and accordingly $\tilde{e}(n)$, $\tilde{E}(n)$, and $\tilde{\Delta}e(n)$. In this case q_lo and q_hi are the upper and lower bounds between which the controller shall reach a certain level. For example for q_hi the quality of the FBP start image can be used. Thus, the noise estimation $\tilde{e}(n)$ naturally lies between 0 (no noise) and 1 (noise of the FBP image). Other metrics could require q_lo being non-zero if this level cannot be reached.

In the refined β update formula (2) all elements of the controller are unit-less and in a known order of magnitude. The constants c_0, c_1, and c_2 can be chosen more easily, e.g. for $c_0 = 100$ a positive, relative difference of 1% between the current quality and the target quality will double β. In the refined formulation also an integrating behavior is introduced by taking the previous value of $\beta(n)$ and changing it dependent on the error $\tilde{e}(n)$. The integration via c_2 is therefore redundant and might cause undesirable effects: If the set–point $\tilde{q}_\mathrm{t}$ is not achieved over several iterations then $\tilde{E}(n)$ will grow and required an overshoot of $\tilde{e}(n)$ in the other direction in order to reduce $\tilde{E}(n)$ again. As c_2 is not required in this approach to achieve and keep a correct level of $\beta(n)$ like in formula (1) it is therefore set to zero in the following sections resulting in a PD controller.

For a fixed $\tilde{q}_\mathrm{t}$ the initial difference can be quite large, leading to high β values if the slope is not limited by using the c_1 constant. Instead of using a fixed target quality the set point for the controller is exchanged by an iteration dependent set–point function, which the controller shall follow. By evaluation the quality curves in iterative reconstructions with fixed β values it was found that exponentially decaying curves match the characteristics of the quality over the iterations quite well. One possible explanation can be the step lengths of the noise reduction that get smaller with each iteration towards the minimum of the cost function. Therefore, an empirical choice for the set–point is

$$\tilde{q}_\mathrm{t}(n) = d_0 + e^{-d_1 n}$$

where the constants d_0 and d_1 are chosen such that the relative target level $\tilde{q}_\mathrm{t}$ is reached after N_t iterations up to a tolerance of e.g. of 1%. The constant c_1 can be used for a fine–tuning of the controller response. As there are no fast set–point changes due to the smooth exponential function, this constant only plays a secondary role and could also be set to zero.

C. Test Setup

The proposed regularization controlling method was evaluated using an separable paraboloid surrogate (SPS) iterative reconstruction with Gaussian noise model on the line integrals. Huber regularization with δ =2 HU was used. The update function was

$$\mu_j^{n+1} = \mu_j^n + \frac{\sum_i \frac{a_{ij}}{\sigma_i^2}(l_i - \sum_j a_{ij}\mu_j^n) + \beta \sum_k w_{kj}\dot{\Psi}_{kj}(\vec{\mu})}{\sum_i \frac{a_{ij}}{\sigma_i^2}\sum_j a_{ij} + \beta\sum_k w_{kj}\ddot{\Psi}_{kj}(\vec{\mu})}$$

where a_{ij} are the coefficients from the projection matrix, l_i are the projection data, σ_i^2 the variance estimates for each projection value, and $\dot{\Psi}_{kj}$ and $\ddot{\Psi}_{kj}$ the derivative and the curvature for the Huber regularization functions in each image position with individual weights w_{kj}.

The FBP image was used as an initial image. The data for the evaluation are helical CT scans with tube currents of 161 mA and 322 mA at 120 kV of an anesthetized pig using a Philips iCT and a pitch of 53.12 mm/360°. The iterations were done in equally distributed projection subsets (ordered subset (OS) operation) with 20 projections per 360°. For the reconstruction spherical, symmetric basis functions, also known as blobs, were used [7], [8].

For the controlling the upper quality level was the estimated noise level from the FBP image while the lower quality level was zero. The constants for the PD controller were c_0=10, c_1=0.01, and N_t=580, i.e. after 5 full OS SPS iterations the target level had to be approximately reached.

III. RESULTS

Fig. 2 shows the FBP reference image as well as the result for three controlled, iterative reconstructions with target noise level of 75%, 50%, and 25% for the 161 mA and the 322 mA scan. As expected the images qualitatively incorporate the noise reduction compared to the FBP images. The images show only approximately the same sagittal slice as no registration was applied between the images of the different scans. The overall image impression of the iterative reconstruction is much sharper than the FBP image. The noise in the iterative reconstruction has an artificial salt–and–pepper appearance in particular for small noise reductions which is mainly due to the Huber regularization. A better noise appearance could be obtained by fine–tuning the Huber parameter δ, which was not done here. In Table I and Table II noise level estimates for several regions of interest (ROI) in the reconstructed images are shown. The ROIs are located in different, homogeneous image regions, so that the noise can be estimated from the standard deviation within the ROIs. Apparently the noise levels in the ROIs show some small deviations compared to the desired target level and the FBP image noise levels. The quality estimator cannot take into account the different local noise levels, but it only sees the mean of the global noise distribution. Nevertheless, the noise in the ROIs matches the desired noise levels very well. Plots for the values of $\tilde{q}(n)$, $(\tilde{q}(n) - \tilde{q}_t(n))$, and $\beta(n)$ are shown in Fig. 3. The exponentially decaying curves of $\tilde{q}(n)$ clearly show that the controller behaves as expected. One can also see that the β values are different for both scans. The difference between the set–point $\tilde{q}_t(n)$ and the current, relative quality value shows that, apart from smaller oscillations, the controlled $\tilde{q}(n)$ sticks very tightly to the set–point. The oscillations get smaller over the iterations and come to a stable amplitude. They do not vanish but follow the natural, unequal changes of the quality in the images due to the ordered subset operation, apparent by the oscillation period of the number of subsets. The values for β appear in inverted order in the bottom plot, i.e. a higher β corresponds to a lower noise level. Here also some minor oscillations are visible after reaching the stable set–point. From the descending $\beta(n)$ one can see that the controller initially enforces a faster convergence to the final set–point by using higher β values. The iterative reconstruction is capable of changing the noise level this fast, nevertheless some more tuning of this behavior could be done by changing the target number of iterations N_t.

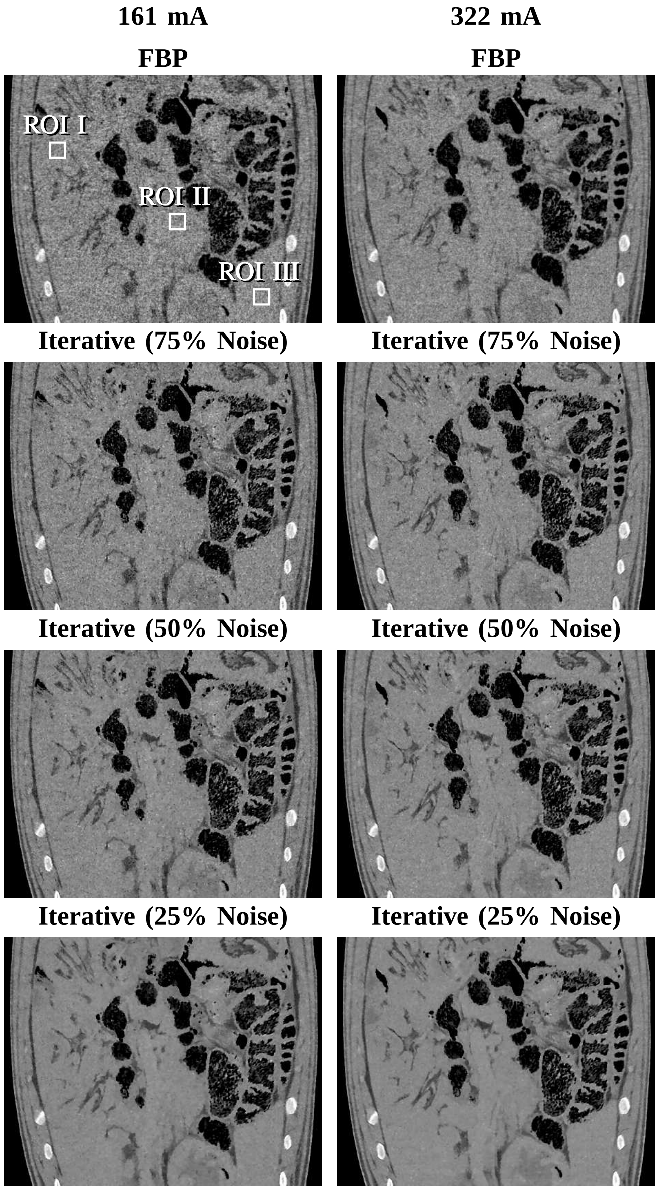

Fig. 2. Reference image and reconstruction results (sagittal slice) for 75%, 50%, and 25% estimated noise level relative to the estimated FBP noise level (C/W = 50/500 HU) for the 162 mA scan (left column) and the 322 mA scan (right column). The shown images are approximately at the same position for both scans.

161 mA	ROI I	ROI II	ROI III
FBP	32.2 HU	42.9 HU	40.0 HU
75%	28.7 HU	31.8 HU	27.8 HU
50%	21.8 HU	20.0 HU	19.2 HU
25%	12.4 HU	10.0 HU	9.4 HU

TABLE I
NOISE LEVELS ESTIMATED FROM THE STANDARD DEVIATION IN THE ROIS SHOWN IN FIG. 2 FOR THE 161 MA SCAN.

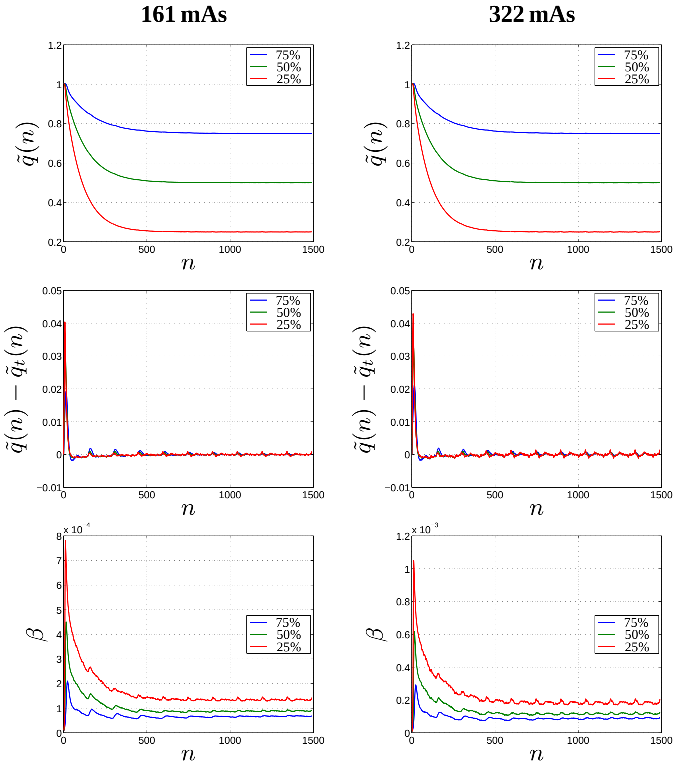
161 mAs

322 mAs

Fig. 3. Plots of the quality metric, the difference between the target quality and the iterate image quality, and the corresponding β values for the 162 mA scan (left column) and the 322 mA scan (right column).

322 mA	ROI I	ROI II	ROI III
FBP	28.3 HU	31.4 HU	27.8 HU
75%	20.2 HU	22.9 HU	21.8 HU
50%	13.9 HU	15.8 HU	15.4 HU
25%	7.8 HU	8.4 HU	7.8 HU

TABLE II
NOISE LEVELS ESTIMATED FROM THE STANDARD DEVIATION IN THE ROIS SHOWN IN FIG. 2 FOR THE 322 MA SCAN.

IV. DISCUSSION

In a practical approach for iterative reconstruction with regularization one could test different, fixed βs and select the images one likes best or use analysis methods like L–curves for this task [4]. Alternatively one could examine the image after each update and decide whether a bit more or less regularization is necessary in order to achieve a certain image quality. The latter approach is exactly what is done with the proposed controlling scheme. The results in this paper as well as some further testing with other datasets showed that the controlling is a robust method to alleviate the problem of selecting the correct regularization level through β. It maps β to a meaningful set of parameters which can be chosen quantitatively in accordance to the known capabilities of the selected iterative method. In general controllers are parametrized and analyzed with system models, which also allow a stability analysis of the closed controlled loop. Unfortunately a modeling of the highly non–linear iterative reconstruction process of arbitrary datasets is not possible, but using a controller with mainly proportional properties ($c_0 \gg c_1$) is known to be very stable for most applications. In conjunction with the chosen quality set–points the controller is very unlikely to become unstable. In the worst case when c_0 is chosen way too large the controlling process will end up in an on/off–behavior for the regularization, where only the number of regularized and non–regularized iterations is steered, which would be equivalent to an alternating minimization. Assuming that the subsets are large enough so that the alternating OS operation does not lead to undesired noise patterns, one would still get sensible results and the correct noise level. The reconstruction results showed that the method worked out–of–the–box and gave the expected mean noise levels. Local deviations from the mean level can be expected from the spatially dependent rawdata contributions from the statistical weighting in the reconstruction. Nevertheless, the target global noise level is achieved quite well. The evaluation of noise estimating techniques is out of scope for this work, but the operation range of the estimator has to be kept in mind especially if it is combined with a controller. The same is true for the used regularization method, which must be capable to change the used quality metric. If the iterative method cannot achieve e.g. 0% of noise due to some residual errors in the quality estimator, then the controller will wind up β to arbitrary high values if 0% is chosen as the target level. From this example it is also obvious that sensible, target quality values must be chosen.

V. CONCLUSION

The proposed method is a simple extension for iterative, regularized methods where an image quality can be estimated and then also changed by the regularization, and which has some practically known convergence properties. It is not bound to CT reconstructions, but can also be used for other applications, as it does not use portions from the iterative methods themselves. This is the case for most iterative CT reconstructions, which makes the proposed method a user friendly tool for the parameter selection in these algorithm classes.

REFERENCES

[1] J. A. Fessler, “Statistical image reconstruction methods for transmission tomography,” in *Handbook of Medical Imaging, Vol. 2*, M. Sonka and J. M. Fitzpatrick, Eds., chapter 1, pp. 1–70. SPIE Press, Bellingham, WA, 2000.

[2] H. Erdogan and J. A. Fessler, *IEEE Trans. Med. Imag.*, vol. 18, no. 9, pp. 801–814, 1999.

[3] J.-B. Thibault, K. D. Sauer, C. A. Bouman, and J. Hsieh, *Med. Phys.*, vol. 34, no. 11, pp. 4526–4544, 2007.

[4] P. Ch. Hansen, *SIAM Review*, vol. 34, no. 4, pp. 561 – 580, 1992.

[5] J. Fessler, *IEEE Sig. Proc. Mag.*, vol. 27, no. 4, pp. 81–89, 2010.

[6] K. H. Ang, G. Chong, and Y. Li, *IEEE Trans. on Control Syst. Tech.*, vol. 13, no. 4, pp. 559–576, 2005.

[7] R. M. Lewitt, *Phys. Med. Biol.*, vol. 37, no. 3, pp. 705–716, 1992.

[8] R. Bippus, T. Koehler, F. Bergner, B. Brendel, E. Hansis, and R. Proksa, in *Proceedings of the 3D’2011 Conference*, Potsdam, Germany, 2011, pp. 68–71.

The Potential Imaging Performance of Differential Phase-Contrast CT – *NPS(k)*, *MTF(k)* and *NEQ(k)*

Xiangyang Tang, *Senior Member, IEEE,* Yi Yang and Shaojie Tang

Abstract—**The grating-based x-ray differential phase contrast (DPC) CT is emerging as a new technology with the potential for preclinical and clinical applications. Via theoretical analysis, modeling and phantom simulation study, we investigate the signal and noise transfer properties of the DPC-CT, which are characterized by its modulation transfer function *MTF(k)*, noise power spectrum *NPS(k)* and spectrum of noise equivalent quanta *NEQ(k)*, and compare them with those of the conventional CT. Preliminary data show that, there exist little difference in the signal transfer behavior between the DPC-CT and conventional CT, because their *MTF(k)* are determined by detector cell dimension. Moreover, under the framework of ideal observer, even though the $NPS_p(k)$ of DPC-CT is of trait $1/|k|$ and the $NPS_a(k)$ of conventional CT is of trait $|k|$, the signal and noise transfer property of DPC-CT – $NEQ_p(k)$ – is virtually identical to the $NEQ_a(k)$ of conventional CT. Through such a thorough investigation, the imaging performance of grating DPC-CT and its potential over the conventional attenuation-based CT can be fully understood and appreciated, which may provide an insightful guidance on the design and optimization of DPC-CT for preclinical and eventually clinical applications.**

Keywords-CT; x-ray phase CT; x-ray differential phase contrast CT; modulation transfer function; MTF; noise power spectrum; NPS; noise equivalent quanta; NEQ

I. INTRODUCTION

The differential phase contrast CT (DPC-CT) implemented with x-ray tube and grating is emerging as a new technology to improve the contrast sensitivity in x-ray CT imaging [1-4]. The initial exploration was relatively qualitative, and a significant improvement in the soft tissue contrast in human tissue specimens or very small animals was demonstrated [1, 2]. Recently, the investigation has become increasingly quantitative. The noise property of the x-ray tube and grating based DPC-CT, such as the pixel-wise gross variance and contrast-to-noise ratio, have been reported [3]. However, it has been well acknowledged that the pixel-wise quality metrics are fundamentally flawed in assessing an imaging system's performance [5, 6]. The subject contrast of soft tissue in the x-ray tube and grating based DPC-CT is intrinsically determined by its interaction with the x-ray beam, while its imaging performance is dependent on its transfer properties of signal and noise [7]. The signal transfer property of a DPC-CT is dependent on its modulation transfer function *MTF(k)*, while its noise property can only be thoroughly characterized by the noise power spectrum *NPS(k)* [8, 9], i.e., the variation of noise intensity as a function over spatial frequency *k*. We have recently reported [4] that there exist a radical difference in the *NPS(k)* between DPC-CT and the conventional CT – the former manifests itself with the trait $1/|k|$, whereas that of the latter with the trait $|k|$. It also has been indicated that the root cause for such a radical difference is that the detected signal is the projection of the refractive coefficient's derivative, which results in a Hilbert filter, instead of the ramp filter, in reconstruction using the filtered back-projection algorithms.

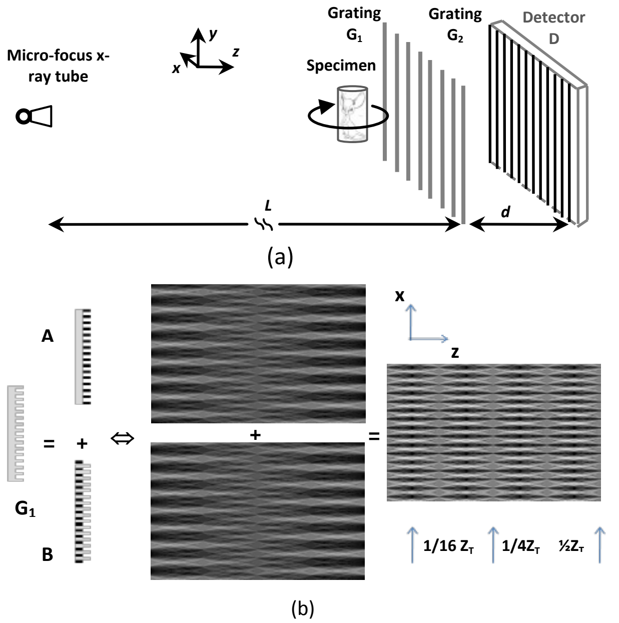

Figure 1. The schematic diagram of (a) x-ray tube and grating based DPC-CT and (b) the Talbot effect for phase retrieval.

Recognizing the important role played by the spectrum of noise equivalent quanta *NEQ(k)* in the figure of merit (FOM) to assess an imaging system's performance under the ideal observer framework [5, 6], we investigate the *NEQ(k)* of the x-ray tube and grating based DPC-CT in this work. In a way analogous to what has been conducted in investigating the conventional CT's *NEQ(k)*, we treat the DPC-CT as a linear and shift-invariant system. Furthermore, since a Gaussian distribution approaches the Poisson distribution if the number of detected x-ray photons is large, the Poisson noise in the DPC-CT can be modeled as Gaussian noise. Under the Bayesian ideal observer framework, we derive, analyze and evaluate the joint signal and noise transfer property of DPC-CT and compare it with that of the conventional CT, which provides an insightful understanding of the DPC-CT's potential imaging performance and the guidelines on its performance optimization for extensive applications.

II. CHRACTERISTICS OF SIGNAL AND NOISE

A. X-ray DPC-CT and its imaging mechanism

The architecture of a DPC-CT is shown in Fig. 1 (a). G_1 is a phase grating and G_2 an absorption grating. G_1 and G_2 work together as a shearing interferometer to detect the wavefront alteration caused by the object in x-ray beam, and an x-ray CCD detector is employed for data acquisition. The key component of the imaging chain is grating G_1, a diffraction interferometer based on the Talbot effect [10]. Fig. 1 (b) shows how G_1 works by virtually decomposing it into absorption gratings *A* and *B* [4]. The extra optical path of grating *B* relative to grating *A* is half wavelength, which is equivalent to a 180° or π phase shift. The beams corresponding to gratings *A* and *B* undergo different optical paths before they reach the gratings and recombine after they pass through them. An interference fringe appears if the refraction is different between the paths.

According to Fresnel analysis [11], the irradiance $I(x, z)$ in the CCD detector at location (x, z) is

$$I_{A+B}(x,z) \cong \frac{\partial\phi(x,y)}{\partial x}\Delta x \qquad (1)$$

where Δx is a displacement in *x*-direction, and $\phi(x, y)$ is the phase corresponding to Δx, which is the projection of the refractive coefficient along x-ray path *Z*

$$\phi(x,y) = \frac{2\pi}{\lambda}\int_Z \delta(x,y,z)dz\,. \qquad (2)$$

Eq. (1) shows that the irradiance depends on the derivative of phase variation along the x-axis. After the x-ray passes G_2, the irradiance at detector *D* is [12]

$$I_{d_x,d_y}(x) = a_0(d_x,d_y) + \sum_{m=1}^{\infty} a_m(d_x,d_y)\cos\left(\frac{2\pi mx}{g_2} + \varphi_m(d_x,d_y)\right), \qquad (3)$$

where (d_x, d_y) is the coordinate in the detector and g_2 the period of grating G_2. Since the object attenuates the x-ray beam, one needs to linearly shift G_2 along the x-axis for phase retrival. Via Fourier Analysis, one can determine $a_0(d_x, d_y)$, $a_1(d_x, d_y)$ $\varphi_1(d_x, d_y)$ from *eq*. (3). Then, one obtains

$$\frac{\partial\phi(x,y)}{\partial x} = \varphi_1(d_x,d_y)\, {g_2}\big/{\lambda z_T}\,, \qquad (4)$$

where $a_0(d_x, d_y)$ and $\partial\phi(x, y)/\partial x$ are the foundation of x-ray attenuation and DPC CT imaging, respectively. Substituting the $\phi(x, y)$ defined in *eq*. (2) into *eq*. (4), we further get

$$\varphi_1(d_x,d_y) = \frac{\lambda z_T}{g_2}\frac{\partial\phi(x,y)}{\partial x} = \frac{\lambda z_T}{g_2}\frac{\partial}{\partial x}\int_Z \delta(x,y,z)dz$$
$$= \frac{\lambda z_T}{g_2}\int_Z \frac{\partial}{\partial x}\delta(x,y,z)dz, \qquad (5)$$

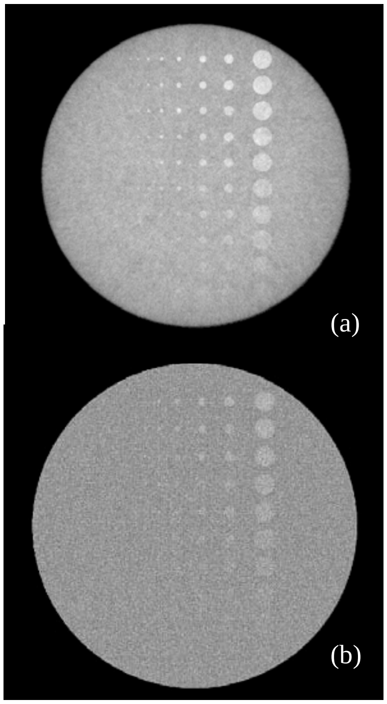

Figure 2. Transverse images of the contrast-detail phantom acquired with (a) DPC-CT and (b) conventional CT (exposure: 5×10^6 *photons/cm²·projection*; detector cell: 32×32 μm^2).

where λ is the wavelength of x-ray beam, z_T the fractional Talbot distance, and g_2 the period of grating G_2. This means that the phase retrieved through a Fourier Analysis of *eq*. (3) is the projection of the refractive coefficient's derivative, and this is the underlying reason that the CT implemented with x-ray tube and gratings is called the differential phase contrast CT [1]. Once $\partial\phi(x, y)/\partial x$ and $a_0(d_x, d_y)$ are acquired, the corresponding tomographic images of attenuation and refraction can be respectively reconstructed using the filtered back-projection (FBP) algorithms [13]. Since the reconstruction of refraction image can be carried out directly from phase derivative $\partial\phi(x, y)/\partial x$, the ramp kernel is replaced with the Hilbert kernel [14].

B. Noise equivalent quanta NEQ(k) of DPC-CT

The spectrum of noise equivalent quanta of the conventional CT has been given in the literature [8, 9, 15, 16]

$$NEQ_a(k) = \frac{\pi}{bNPS_a(k)} |k| |MTF_a(k)|^2 \qquad (6)$$

In parallel to *eq*. (6), we have derived the spectrum of noise equivalent quanta and noise power spectrum of the DPC-CT

$$NEQ_p(k) = \left(\frac{g_2}{\lambda z_T}\right)^2 \frac{(1-\varepsilon_2)}{2\pi\varepsilon_1^2 q_0 b |k| NPS_p(k)} MTF_p^2(k) \qquad (7)$$

$$\begin{aligned} NPS_p(k) &= \left(\frac{g_2}{\lambda z_T}\right)^2 \frac{a(1-\varepsilon_2)}{2\pi\varepsilon_1^2 |k| N_\theta M \overline{N}_0} MTF_p^2(k) \\ &= \left(\frac{g_2}{\lambda z_T}\right)^2 \frac{(1-\varepsilon_2)}{2\pi\varepsilon_1^2 q_0 b |k| NEQ_p} MTF_p^2(k) \end{aligned} \qquad (8)$$

where a is the detector cell pitch and b the cell height. $q_0=N_0/(abI_0)$ and I_0 is the measured photon flux. Parameters ε_1 and ε_2 are defined as the ratio of magnitude of the 1st- and 2nd-harmonic wave relative to that of the 0th harmonic wave. Both *eqs*. (6) and (7) show that the spectrum of noise equivalent quanta of an imaging system is jointly determined by its signal (*MTF(k)*) and noise (*NPS(k)*) transfer property. Note that factor $|k|$ is on the numerator of $NEQ_a(k)$, whereas it is on the denominator of $NEQ_p(k)$, owing to that $NPS_a(k)$ is of trait $|k|$, whereas $NPS_p(k)$ possesses trait $1/|k|$.

III. PRELIMINARY RESULTS

Computer simulation is carried out to evaluate the imaging performance of the DPC-CT and compare it with that of the conventional CT. The simulated x-ray exposure per projection view is approximately 5×10^6 *photon/cm*^{2}, which is comparable to that of a micro-CT for preclinical applications. The x-ray photons detected by each detector cell observe Poisson distribution. The simulated detector cell size is between 32×32 μm^2 and 128×128 μm^2. A mono-chromatic x-ray source with an infinitesimal focal spot at 30 *keV* is assumed in the simulation.

A cylindrical contrast-detail phantom is used to evaluate the accuracy of modeling in the DPC-CT. Presented in Fig. 2 (b) is the result compared with that of the conventional CT in Fig. 2 (a). It is observed that, given identical x-ray exposure, the DPC-CT implemented with x-ray tube and gratings outperforms the conventional CT in the contrast-to-noise ratio at high spatial resolution. It is also observed that the noise granularity of DPC-CT is quite different from that of the conventional CT, and this is the primary reason motivating us to further investigate the signal and noise transfer property of the DPC-CT.

A cylindrical air phantom at 37.68 *mm* diameter is used to study the *NPS(k)* of DPC-CT and compare it with that of the conventional CT. Approximately 360 regions, each at 128×128 matrix, are used to calculate the *NPS(k)* via 2D Fourier Transform. Shown in Fig. 3 (a) is the *NPS(k)* of DPC-CT, while that in Fig. 3 (b) is that of the conventional CT. It is observed that the *NPS(k)* of DPC-CT is of the trait $1/|k|$, whereas that of the conventional CT has the trait $|k|$. This is a radical difference in the noise property between the DPC-CT and the conventional CT.

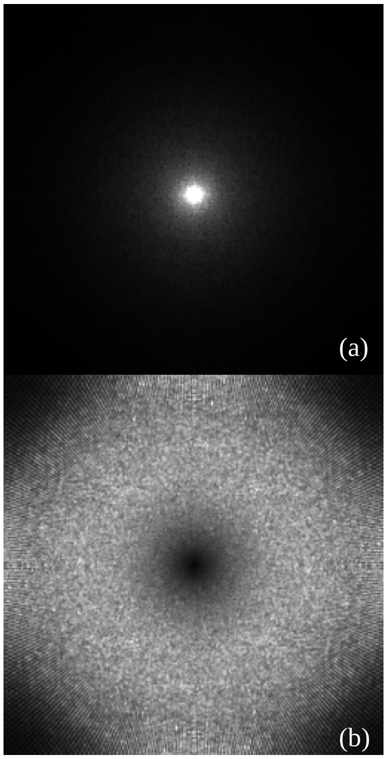

Figure 2. The noise power spectra *NPS(k)* of (a) DPC-CT and (b) the conventional CT(detector cell size: 32×32 μm^2).

A cylindrical water phantom at 5.0 *mm* diameter is used to evaluate the modulation transfer function *MTF(k)* of the DPC-CT and conventional CT, in which the strategy of ESF (edge spread function) → LSF (line spread function) → MTF is exercised. Presented in Fig. 4 are the examples at detector cell size 32 μm. It is observed that, though their imaging mechanisms are quite different, their signal transfer properties characterized by the *MTF(k)* are actually identical.

Once the noise power spectrum and modulation transfer function of the DPC CT and the conventional CT are obtained, their spectrum of noise equivalent quanta can be readily attained using *eqs*. (6) and (7). Presented in Fig. 5 are examples of the spectra of noise equivalent quanta of the DPC-CT and conventional CT at detector cell 32 μm. It is observed that the spectra of noise equivalent quanta of the DPC-CT and conventional CT are almost the same, i.e., their signal and noise transfer properties are virtually identical under the ideal observer framework.

IV. DISCUSSIONS AND CONCLUSIONS

Via theoretical analysis and computer simulation, we investigate the spectrum of noise equivalent quanta $NEQ(k)$ – the characteristics of signal ($MTF(k)$) and noise ($NPS(k)$) transfer property – in the DPC-CT and compare it with that of the conventional CT. To exclude the interference by other factors, the imaging chain of the x-ray tube and grating-based phase CT is assumed ideal. The preliminary data show that, given detector cell size, the signal and noise transfer property of DPC-CT – $NEQ_p(k)$ – is virtually identical to $NEQ_a(k)$ of the conventional CT, even though the $NPS_p(k)$ of DPC-CT is of trait $1/|k|$, but $NPS_a(k)$ of the conventional CT is of trait $|k|$. The reason underlying this fundamental fact is that, as shown in *eqs*. (6) and (7), under the ideal observer framework, the $1/|k|$ "color" in the $NPS_p(k)$ of DPC-CT and the $|k|$ "color" in $NPS_a(k)$ of the conventional CT are "pre-whitened" by the factor $|k|$ at the denominator of $NEQ_p(k)$ and the numerator of $NEQ_a(k)$, respectively. However, it should be pointed out and emphasized that, in reality, an observer is not ideal, and thus the fact that $NPS_p(k)$ of the DPC-CT is of trait $1/|k|$ but $NPS_a(k)$ of the conventional CT is of trait $|k|$ may result in a substantial difference in the square signal-to-noise ratio (detectability index) between the DPC-CT and conventional CT in the clinical and preclinical applications that demand a high spatial resolution.

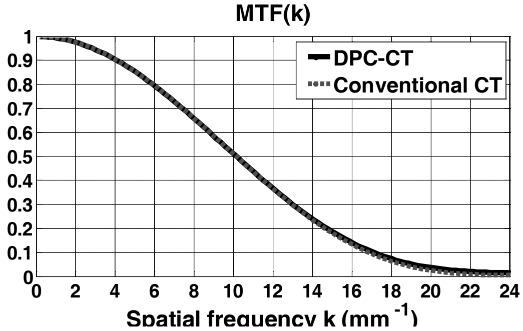

Figure 3. The modulation transfer function $MTF(k)$ of DPC-CT and the conventional CT (detector cell size: 32×32 μm^2).

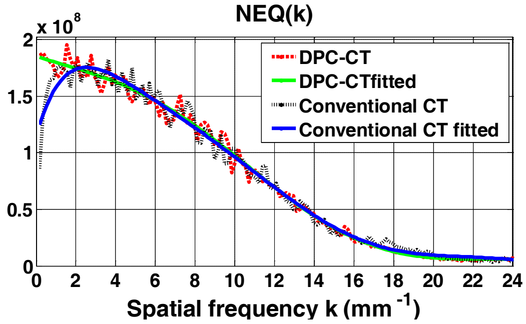

Figure 5. The noise equivalent quanta $NEQ(k)$ of DPC-CT and the conventional CT (detector cell size: 32×32 μm^2).

REFERENCES

[1] F Pfeiffer, T Weitkamp, O Bunk, C David, "Phase retrieval and differential phase-contrast imaging with low-brilliance x-ray sources," *Nature Phys.*, v.2, pp258-61, 2006.

[2] A Momose, W Yashiro, Y Takeda, Y Suzuki and T Hattori, "Phase tomography by x-ray Talbot interferometry for biological imaging," *Japan J. Applied Phys.*, v.45(6A), pp.5254-62, 2006.

[3] G Chen, J Zambelli, K Li, N Bevins and Z Qi, "Scaling law for noise variance and spatial resolution in differential phase contrast computed tomography," *Med. Phys.*, v.38, pp.584-88, 2011.

[4] X Tang, Y Yang and S Tang, "Characterization of imaging performance in differential phase contrast CT compared with the conventional CT–Noise power spectrum NPS(k)", *Med. Phys.*, v.38, pp.4386-95, 2011.

[5] H Barrett, "NEQ: its progenitors and progeny," SPIE Proc. v.7263, 72630F, 7 pages, doi: 10.1117/12.817795, 2009.

[6] CE Metz, RF Wagner, K Doi, DG Brown, RM Nishikawa and K Myers, "Toward consensus on quantitative assessment of medical imaging systems", *Med. Phys.*, v.27, pp.1057-61, 1995.

[7] JT Bushberg, JA Seibert, EM Leidholdt Jr. and JM Boone, *The Essential Physics of Medical Imaging*, 2nd ed., Philadelphia: Lippincott Williams & Wilkins, 2002.

[8] KM Hanson, "Detectability in computed tomography images," *Med. Phys.*, vol.6, pp.441-451, 1979.

[9] RF Wagner, DG Brown and MS Pastel, "Application of information theory to the assessment of computed tomography," *Med. Phys.*, v.6, pp.83-92, 1979.

[10] E Keren, O Kafri, "Diffraction effects in moiré deflectometry," *J. Opt. Soc. Am. A*, v.2, pp111-20, 1985.

[11] R Grella, "Fresnel propagation and diffraction and paraxial wave equation," *J. Optics (Paris)*, v.13, pp367-74, 1982.

[12] M Bech, TH Jensen, R Feidenhan'l, O Bunk, C David and F Pfeiffer, "Soft-tissue phase-contrast tomography with x-ray tube source," *Phys. Med. Biol.*, v.54, pp.2747-53, 2009

[13] X Tang, J Hsieh, RA Nilsen, A Hagiwara, J Thibault and E Drapkin, "A three-dimensional weighted cone beam filtered backprojection (CB-FBP) algorithm for image reconstruction in volumetric CT under a circular source trajectory," *Phys. Med. Biol.*, v.50, pp3889-905, 2005.

[14] Z Qi and G-H Chen, "Direct fan-beam reconstruction algorithm via filtered backprojection for differential phase-contrast computed tomography," *X-ray Opt. Instr.*, v.53, pp.1015-25, 2008.

[15] ICRU (International Commission on Radiation Units and Measurements), "Medical Imaging – The Assessment of Image Quality," *ICRU Report 54*, (Bethesda, MD: ICRU), pp.11-67, 1996.

[16] KL Boedeker, VN Cooper and MF McNitt-Gray, "Application of the noise power spectrum in modern diagnostic MDCT: part I. Measurement of noise power spectra and noise equivalent quanta," *Phys. Med. Biol.*, v.52, pp.4027-46, 2007.

Mobile C-arm CT for Minimally Invasive Surgery

Taylor Braun-Jones, Wendell Duncan, and Arvi Cheryauka

***Abstract*—Cone-beam CT is an emerging imaging mode on the mobile C-arm in the operating room, used to reconstruct 3-D volumes and enable 3-D surgical navigation. With the use of a model-based iterative reconstruction technique, we evaluate images and show enhancements in their quality compared to the results obtained with the analytical method. Based on early experiments for minimally invasive spine and cranial surgeries, we demonstrate the feasibility of our solution and relate it to the existing solutions.**

Keywords- cone beam, computer tomography, mobile C-arm, model-based iterative image reconstruction

I. INTRODUCTION

Over the past several decades, the mobile C-arm has become a central imaging tool and an integrated platform for image-guided interventions in the operating room (OR). Intraoperative imaging with C-arm systems conventionally produces 2-D real-time fluoroscopy data. The emerging imaging mode in the OR is cone-beam CT (CBCT) to produce 3-D anatomical reconstructions and perform 3-D surgical navigation [1]. Despite many advances in mobile C-arm design, 3-D imaging and anatomy tracking with a compact device poses substantial challenges in image formation, X-ray assembly position/orientation tracking, and computational performance [2]. We apply iterative CBCT image reconstruction techniques to mobile C-arm data and provide comparative views with analytical reconstruction results as well as with results by a conventional 360^0-degree scanning solution [3-4,6].

II. CBCT ON MOBILE C-ARM

A. *XRII-mounted C-arm*

A standard full-size non-isocentric C-arm is used to produce real-time high-resolution fluoroscopic images of human anatomy (Fig. 1). Electromagnetic (EM) navigation is used in lieu of mechanical encoders to track the position of the acquisition assembly [3].

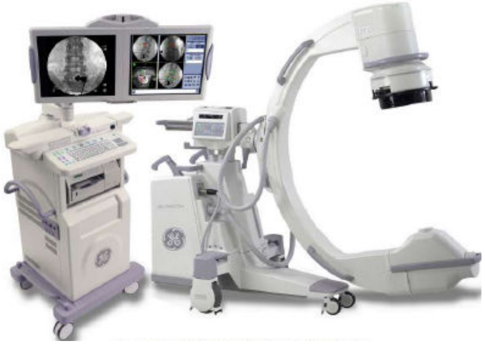

Fig. 1: GE OEC 9900 C-arm with integrated EM navigation.

B. *Anatomical cases*

The potential of cone-beam CT technology on a mobile C-arm lies in many surgical areas such as orthopedic, extremities, spine, sinus, neck, head, neuro, ear, breast, thoracic, interventional, brachytherapy, and pain management [2]. For example, minimally invasive spine procedures include vertebroplasty, pedicle screw, and cage placement. For further references in this paper, schematics of human lumbar spine and fluoroscopic image of L2-L4 pedicles are shown in Figure 2.

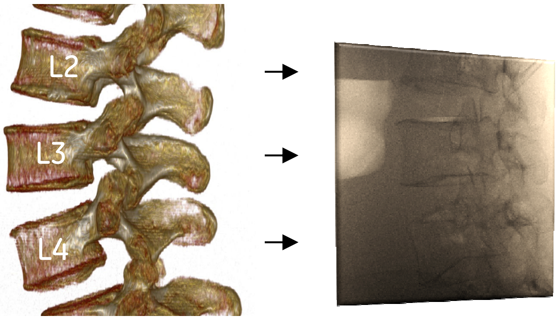

Fig. 2: Correspondence of L2, L3, and L4 pedicles to their fluoroscopic image.

T. Braun-Jones, W. Duncan, and A. Cheryauka are with GE Healthcare-Surgery, 384 Wright Brothers Drive,Salt Lake City, UT, USA

C. Methods

We use an iterative reconstruction technique (SART) to compensate for positioning irregularities [5-6]. Applying Total Variation (TV) regularization improves image quality, particularly with angular ranges that are significantly less than a traditional CT short scan. A multi-resolution scheme that dynamically adjusts the size of the voxel space and the pixel space where the reconstruction is occurring significantly improves performance time on the initial iterations.

A fast-converging gradient descent iterative optimization reduces the number of iterations needed [7]. The optimal step size required for the gradient descent method of TV minimization varies by orders of magnitudes as the SART algorithm converges to a solution. Therefore, empirically choosing a fixed value for the step size is not practical. To solve this problem, we adaptively compute the step size based on the median gradient of the input image. The median value is used so that the large gradients at the sharp anatomical edges do not skew the statistics. The result is good indication of the amount of noise which corresponds directly to the optimal step size. Empirically, we have found that applying a factor of about 0.15 to this median value gives a step size that produces images with reduced noise while still preserving edges and small anatomical details.

We implement the SART algorithm on a graphics processing unit (GPU) [6]. Reconstruction times of less than 60 seconds are feasible in the OR.

D. Results

Axial images of L3 pedicle obtained with the use of XRII-based C-arm and the lumbar spine phantom are shown in Figure 3.

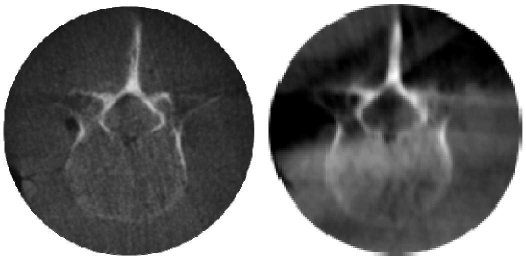

Fig. 3: An axial reconstruction slice using C-arm data, EM tracking, and Left: Filtered Backprojection (FBP) and an isocentric short scan Right: SART+TV iterative technique and 145^0 non-isocentric scan.

Experiments using alternatives to the asymmetric ray- and voxel-driven projectors has shown to reduce image artifacts. Figure 4 shows the results of using the distance-driven method comprising symmetric forward- and back-projectors [8]. The small FOV and non-isocentric acquisitions magnify the truncation artifacts, which also need to be addressed.

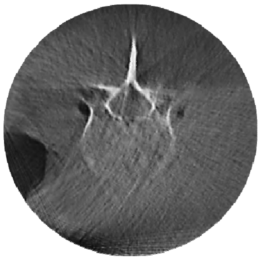

Fig. 4: An axial reconstruction slice using EM tracking, 145^0 non-isocentric scan, and distance-driven forward- and back-projectors.

E. FPD-mounted C-arm CT prototype

FPD-mounted system prototype has been built in our laboratory over the last few years (Fig. 5). We refer the reader to our earlier publications, where the description of the system setup and FBP imaging results can be found [3-4].

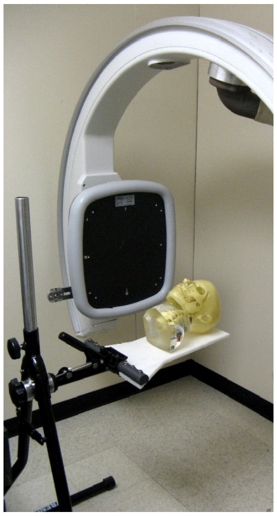

Fig. 5: FPD-based C-arm prototype, support stand, and anthropomorphic head phantom [4].

III. SKETCHING NEW TECHNIQUES

A. System components

Enhancements in the image acquisition capabilities comprise an improved X-ray source, a flat-panel detector of very low noise floor, fully integrated EM sensors, direct software access to high resolution data from imaging components, and GPU computational resources.

B. Iterative algorithm

Model-based iterative image reconstruction is capable of delivering superior image quality [9]. The volumetric attenuation function **f** is solved within a generalized deterministic algebraic reconstruction technique (ART) by minimizing the energy functional in Eq. 1 that can be schematically introduced as follows:

$$\underset{\Omega}{\operatorname{argmin}}\left(E_0(\mathbf{f})+\sum_{j>0}\lambda_j E_j(\mathbf{f})\right), \qquad (1)$$

where E_0 is a data misfit functional, E_j, are specific stabilizing functionals, λ_j are the regularization parameters, and $\boldsymbol{\Omega}$ is the optimization parameter support [10-12].

The data misfit term in Eq. 1 is defined, using the least squares norm, as follows:

$$E_0=\frac{1}{N_\theta S}\sum_{\theta}\ (\mathbf{D}^\theta\mathbf{f}-\mathbf{P}^\theta)^T\,\mathbf{W}_d^\theta\,(\mathbf{D}^\theta\mathbf{f}-\mathbf{P}^\theta), \qquad (2)$$

where $\mathbf{D}^\theta$ is the forward projection (compression capable) operator, $\mathbf{P}^\theta$ is the acquired projection, and $\mathbf{W}^\theta_d$ is the projection weighting matrix, S is the image detection area, and θ is the projection index.

The stabilizing terms, E_j, are introduced to incorporate edge preservation, denoising, deblurring, and other image enhancement features in to the reconstruction process. We use a TV stabilizer that is the popular choice for sharpening edges and reducing small-to-middle scale artifacts [6,10-11,13]. E_1 term is constructed, using the minimum norm, as follows:

$$E_1=\left\|\mathbf{W}_m\nabla\mathbf{f}\right\|_1, \qquad (3)$$

where $\mathbf{W}_m$ is the attenuation model weighting matrix, and $\boldsymbol{\nabla}$ is the gradient-type operator. Other non-linear stabilizing filters are investigated in [13].

The set of optimization parameters, $\boldsymbol{\Omega}$, in Eq. 1 consists of the attenuation vector-function **f**. Other model parameters are considered as prior known inputs. In particular, cone-beam projection geometry is independently obtained by online EM sensoring or, if gantry motion is repeatable, by offline calibration [3-4]. Non-negativity and upper bound (if a priori known) constraints are applied to the reconstructed data through the iterative process.

C. *Sensitivity analysis*

The gradient of the data misfit functional in Eq. 2 is calculated for three limited-angle acquisitions. Figure 6 shows the maps for the data simulated over the digital Shepp-Logan phantom.

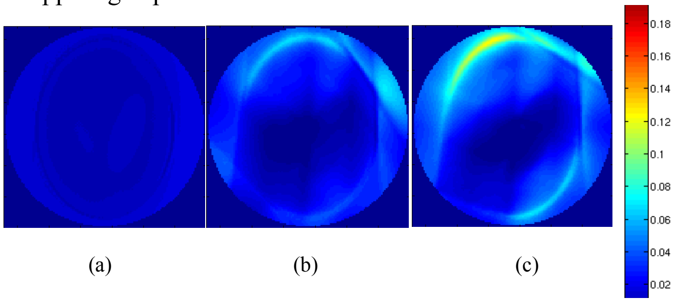

(a) (b) (c)

Fig. 6: Data misfit sensitivity maps of the data misfit functional (central axial slice) for (a) 180°+cone angle, (b) 145° and (c) 120° acquisitions.

The results in Figure 6 agree with their finite difference versions, and converge as distance between projections, pixel pitch, and voxel size are decreased. Since the Jacobian data defines direction and step size vectors in optimization engine, it provides a basis for formation of the weighting matrix $\mathbf{W}_\mathrm{m}$.

D. *Imaging results*

To evaluate the performance of this algorithm, we use the re-processed head phantom data under the selected acquisition configurations. These results are compared to the results computed by analytic method (FBP). The second ones are often used as an initial guess in the iterative process [6,10-12].

Figure 7 captures the differences in handling of quantum noise due to decrease of X-ray current (tube voltage of 80 kVp is constant) and, correspondingly, the number of photons. The iterative results show less graininess versus the FBP results.

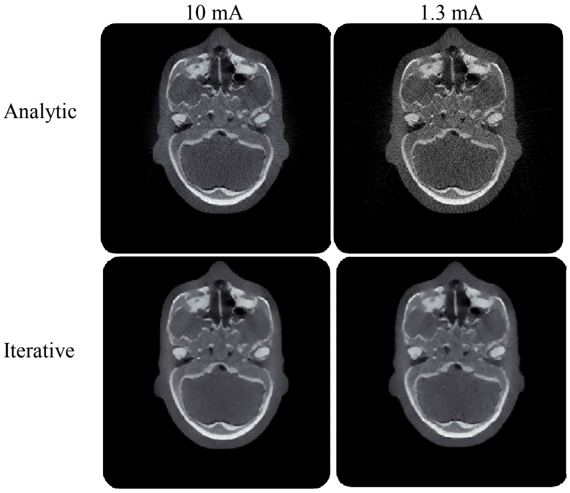

Fig. 7: Analytic and iterative reconstruction images for 8x difference in flux of X-ray photons.

Impact on spatial resolution and artifact appearance in the reconstructed imagery is shown in Figure 8.

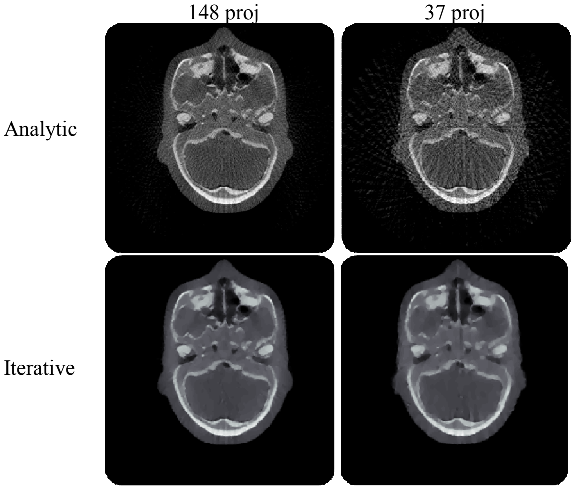

Fig. 8: Analytic and iterative reconstruction images for 4x difference in acquisition density.

The original projection dataset is reduced from 148 to 37 equiangular views (total angular range is kept equal to 180^0+cone angle). Iterative reconstruction better reduces the aliasing artifacts without degrading the edge details.

Narrowing the angular range in data acquisition generally results in global-scale streaking artifacts across the reconstructed imagery [10]. The reconstruction results for a complete short scan of 180^0+cone angle and a limited-angle scan of 145^0 (angular projection step of 1.3^0 is constant) are displayed in Figure 9.

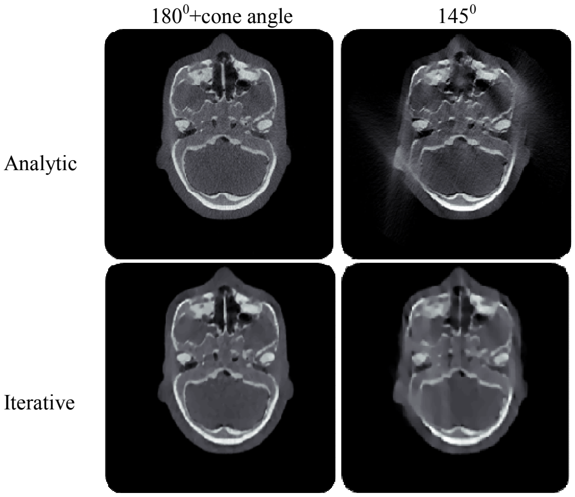

Fig. 9. Analytic and iterative reconstruction results for 1.4x difference in angular coverage.

Iterative approach produces less spatial artifacts and can be tuned to recover more object details.

Also, based on early experiments for minimally invasive spine surgery, we analyze side by side the imaging results obtained with a conventional 360-degree acquisition surgical scanner and a C-arm prototype (Fig. 10). The C-arm test setup comprises a stationary C-arm gantry and a programmable rotating stage enabling a similar 360^0 scanning trajectory.

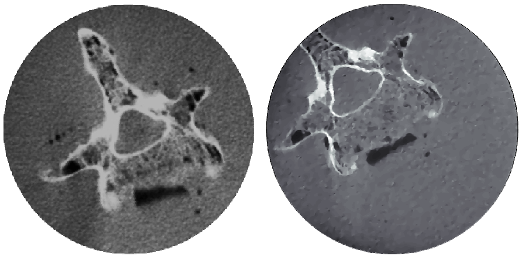

Fig. 10. The enlarged cross-view images of the L4 pedicle of the lumbar spine phantom obtained with mobile CT scanner (left) and C-arm prototype (right).

In both cases, we use an X-ray technique of 120 kVp/ 10 mA. Conventional scanner's high-definition mode consists of 340 projections. Our 30-second acquisition with 15 pulses per second totals in 450 projections, and, then, is rebinned to 340 views. We apply the iterative image reconstruction technique to our data, and, to match volumetric resolution, use 512^2 voxel dimension in the axial plane. The approximately co-registered axial slices of the L4 pedicle are shown in Figure 10.

IV. CONCLUSIONS

CBCT is prototyped on XRII- and FPD-mounted mobile C-arm platforms. EM tracking is used in lieu of mechanical encoders and offline positioning calibration. To handle challenges of performing CT on a low-cost mobile device, we apply a regularized iterative image reconstruction. The iterative results are compared with the analytic results in low power excitation, sparse acquisition, and limited-angle coverage scenarios for head and spine minimally invasive surgeries. Model-based iterative method has good potential in delivering superior and sustained image quality for interventional surgical procedures.

ACKNOWLEDGEMETNTS

The authors are grateful to Raghu Venkatram, Sam Maesato, Jon Lea, Laurent Node-Langlois, Dan Groszmann, Roger Anderson, Cristian Atria, and Jonathan Snyder for insightful discussions during the work on this paper.

REFERENCES

[1] R. Orth, M. Wallace, and M. Kuo, 2008, “C-arm Cone-beam CT: General Principles and Technical Considerations for Use in Interventional Radiology”, *J. Vasc. Interv. Radiol.*, v. 19, pp. 814–821.

[2] J.Siewerdsen, M. Daly, G. Bahar, D. Moseley, G. Bootsma, S. Chhabra, D. Jaffray, and J. Irish, 2007, “Multi-mode C-arm fluoroscopy, tomosynthesis, and cone-beam CT for image-guided interventions: From proof of principle to patient protocols,” *SPIE*, 65101A.

[3] A.Cheryauka, J.Barrett, Z. Wang, A. Litwin, A.Hamadeh, D. Beaudet, 2007, 3-D geometry calibration and markerless EM tracking with a mobile C-arm, *SPIE*, 650927.

[4] A. Cheryauka, D.Tubbs, V. Langille, P.Kalya, B. Smith, R. Cherone, CT imaging with a mobile C-arm prototype. 2008, *SPIE,* 69135C.

[5] B. Beck, H. Hofmann, H. Scherl, M. Kowarschik and J. Hornegger, 2009, GPU-accelerated SART reconstruction using CUDA programming environment, *SPIE*, 72582B.

[6] Y.Pan, R.Whitaker, A.Cheryauka, and D.Ferguson, 2010, TV-regulari-zed iterative image reconstruction on a mobile C-arm CT. *SPIE,* 7622L.

[7] K. Khare, B. Claus and J. Eberhard, 2011, Tomosynthesis imaging with 2D scanning trajectories, *SPIE,* 796115.

[8] B. DeMan and S.Basu, 2002, Distance-driven projection and backprojection, *IEEE Nucl. Sci. Symp.*, vol. 3, pp. 1477 –80.

[9] J.-B. Thibault, 2011, The model-based paradigm: A new frontier in image reconstruction, http://www.gehealthcare.com/usen/ct/products/docs/CT_Clarity_062411_pg63-65.pdf

[10] H. Langet, C.Ridell, Y.Trousset, A.Tenenhaurs, E.Lahalle, G.Fleury, and N. Paragios, 2011, Compressed sensing based 3D tomographic reconstruction for rotational angiography*, MICCAI*, pp. 97-104.

[11] X.Jia, Y. Lou, R. Li, W. Song, and S.Jiang, 2010, GPU-based fast cone beam CT reconstruction from undersampled and noisy projection via Toatl Variation, *Med. Phys,* 37(4), 1757-60.

[12] S.Schafer, S.Nithananiathan, D.Mirota, A.Uneri, J.Stayman, W.Zbijewski, C.Schmidgunst, G. Kleinszig, A.Khanna, and J.Siewerdsen, 2011, Mobile C-arm cone-beam CT for guidance of spibe surgery: Image quality, radiation dose, and integration with interventional guidance, *Med. Phys*., 38(8), 4563-74.

[13] W. Xu and K. Muller, 2010, Evaluaing popular non-linear image proces-sing filters for their use in regularized iterative CT. *IEEE Med Imag*.

Distortion Correction, Geometric Calibration, and Volume Reconstruction for an Isocentric C-Arm X-Ray System: Preliminary Studies

B. Spencer, R. Clackdoyle, C. Mennessier, T. Xu

***Abstract*—Preliminary evaluations were done on volume reconstructions attained from 100 projection images acquired from a C-arm image intensifier. Projection images were first corrected for distortion using a planar grid phantom before a custom geometric calibration phantom was imaged to calibrate every projection of the scan. The geometric parameters were then passed to an enhanced Feldkamp algorithm to perform shortscan reconstruction incorporating the known geometric fluctuations. The preliminary studies established the benefit of applying angle-dependent distortion correction to the projections before reconstruction.**

I. INTRODUCTION

Obtaining accurate 3D image reconstructions is a necessary component of the positron emission real-time tracking (PeTrack) project at the Carleton University department of Physics. The aim of PeTrack is to track objects in real time using very small implanted positron emission markers [1], with applications in image-guided radiation therapy and surgery. Accurate co-registration between the 3D positron tracking coordinates and a 3D anatomical image is essential.

The 3D imaging device is a Siemens Arcadis Orbic C-arm x-ray system. This system uses a 9 inch image intensifier (II) to collect projection images over 190° for shortscan image reconstruction of a (12 cm)^3 volume at the isocenter (see Fig. 1). To co-register the positron tracking system with the volume x-ray reconstructions we will be using a common 3D reference frame defined by a fixed set of markers. These markers will provide both global positioning information of the 3D reconstructed images, and positioning information for each angular position of the C-arm to also allow co-registration in fluoro-mode. In the context of the work presented here, these markers are the essential components of the geometric calibration phantom.

In this paper we describe only the 3D volume component of the PeTrack project. The isocentric C-arm system is used to collect shortscan projection views over 190°. We have developed and implemented several automated steps: distortion measurement and correction, geometric calibration, and volume reconstruction. The process of distortion measurement requires the use of a planar grid phantom imaged directly on the face of the II. Once this measurement is complete any image acquired under the same specifications can be automatically corrected. The process of geometric calibration uses a special 6-ball phantom to calibrate every projection individually. Once geometric calibration is achieved any image can be corrected and reconstructed automatically.

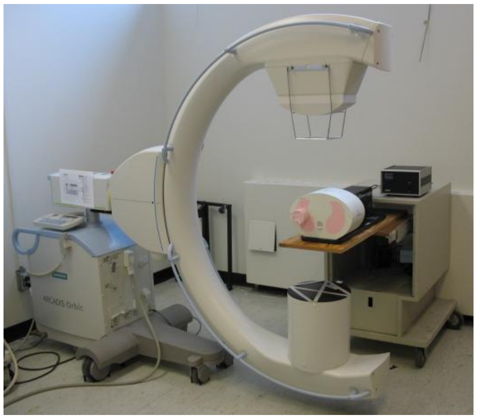

Figure 1. The Siemens Arcadis orbic C-arm Scanner

Our previous work [2] described our development of the distortion correction, calibration and reconstruction steps but tests were performed with a single projection of the C-arm with angular positions simulated using a rotating turntable. In this work, full view-by-view distortion correction was applied to each of the 100 angular views of the C-arm data. We are now able to operate the system in production mode, and have performed some preliminary evaluations.

The 3D reconstructed images obtained by this method have been compared to images reconstructed without first correcting for II distortion to give an indication of the effects of image distortion. Further images obtained using our reconstruction method have been compared with image reconstructions obtained by the Siemens Arcadis Orbic onboard reconstruction software. Comparisons of volume images or reconstructed slices of various phantoms was done to visually asses reconstructed image quality.

II. DISTORTION: MEASUREMENT AND CORRECTION

Image intensifier distortion is a combination of two effects: pin-cushion distortion and S-distortion. Pin-cushion distortion

B. Spencer and T. Xu are with Carleton University, 1125 Colonel By Drive Ottawa, Ontario K1S 5B6, Canada (e-mail: bspencer@physics.carleton.ca, txu@physics.carleton.ca

R. Clackdoyle is with the Laboratoire Hubert Curien, CNRS Unité Mixte de Recherche 5516, 42000 Saint Etienne, France (e-mail: rolf.clackdoyle@univ-st-etienne.fr).

C. Mennessier is with the Laboratoire Hubert Curien, CNRS Unité Mixte de Recherche 5516 and Ecole de Chimie Physique de Lyon, 69616 Villeurbanne, France (e-mail: mennessier@cpe.fr).

is simply the result of mapping of the curved input screen to the flat image. S-distortion on the other hand is dependent on the II's orientation and location relative to the earth's and other local magnetic fields. Because the II rotates 190° during image acquisition these magnetic fields introduce a significant amount of angle dependant S-distortion which is not usually compensated during scanner operation. The Siemens on-board C-arm software corrects for the (view independent) pin-cushion distortion but not for S-distortion. However, S-distortion can in principal be measured and corrected for each position and orientation.

Image intensifier distortion was measured by imaging a planar grid phantom placed directly on the front of the II. The x-ray system acquired 100 projection images of the grid phantom as it rotated 190° around the isocenter (see Fig. 2). Each of the 100 projections was processed using centroids of the ball images to define grid locations to subpixel resolution. The grid then partitions each projection into many small quadrilateral regions in which distortion can be identified and parameterized. Using a method adapted from [3], a polynomial function mapped the interior of each quadrilateral region from the distorted image to an ideal undistorted image. This method of distortion correction for a single projection was described in more detail in reference [2]. Following this procedure, all other distorted projection images were mapped back to the single ideal undistorted grid using their own set of polynomials for each region. The polynomials found for every region contained in all 100 projection images were stored to be used to correct the distortion in subsequent production scans.

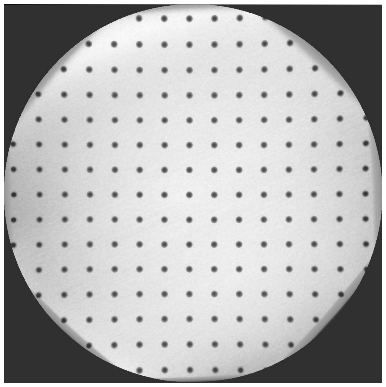

Figure 2. One of the projections of the planar grid phantom imaged directly on the II

The distortion correction of a single projection was evaluated and presented in [2]. The average RMS error in the distorted projection image was found to be 1.71 pixels while the average RMS error in the corrected image was improved to 0.63 pixels.

To inspect the degree of distortion incurred during a 190° scan the 100 projection images of the grid phantom before correction were observed and the distorted grid points of each projection were plotted as red circles superimposed on one of the corrected projection images (see Fig. 3). This image provides a visual description of the magnitude of the corrections.

The process of measuring distortion requires ImageJ [4] for image preprocessing, a non-linear χ^2 fitting program to define the ideal grid, and a Matlab program to find the polynomial coefficients used for mapping. This process required approximately 5 minutes of computer processing time and about 10 minutes of operator time for all 100 projection images. The distortion correction procedure was managed automatically using a Matlab program, taking approximately 25 seconds of computation time per projection, or about 42 minutes per scan.

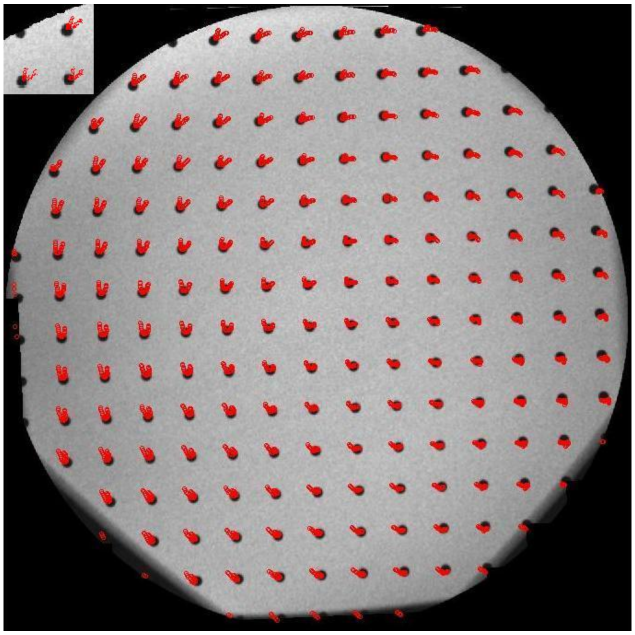

Figure 3. Distorted ball locations plotted on corrected projection image #50 to illustrate the magnitude of the distortion. The Inset shows a magnified view of the top left corner.

III. Geometric Calibration

Geometric calibration is the process of determining the exact detector and source locations and orientations during the scan. Once the geometry of the scanner is known the calibration information can be used by the image reconstruction software to process the projections of the production scans.

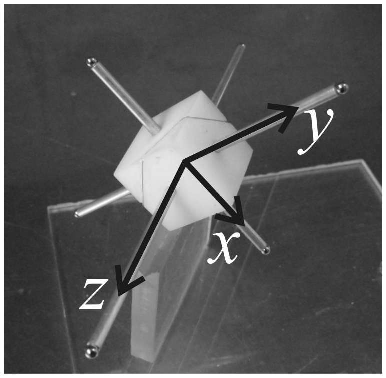

Figure 4. Geometric calibration phantom. The object is made from 6 balls suspended from the faces of a cube by aluminum rods with a thin copper wire around the center of the cube used for positioning.

The geometric calibration process has been adapted from reference [5] with a modified calibration phantom designed for our C-arm geometry. The phantom was composed of 6 steel balls extended from the center of a cube by aluminum rods of differing lengths k: $k_x = 30$mm $k_y = 40$mm $k_z = 50$mm (see Fig. 4). More information on the design of the calibration phantom and the principles of the calibration can be found in [6]. The calibration phantom was scanned using our standard protocol of 100 projections over 190° shortscan (see Fig. 5). The projections were corrected for distortion using the procedure described in section II above. Each projection was then processed to obtain 9 geometric parameters for the corresponding scanner position. These parameters were obtained in the reference frame defined by the phantom.

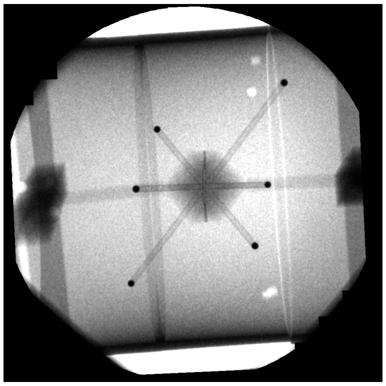

Figure 5. One of the projection images of the geometric calibration phantom suspended in a plastic cylindrical case

ImageJ [4] was again used for automated image processing to identify each ball and find the (u, v) detector positions for the 6 balls in each projection. The subsequent extraction of the 9 geometric parameters per view was performed automatically using direct mathematical formulas from the 6 detector positions (12 scalars). This geometric calibration process is fully automated such that the operator interaction time was negligible and CPU processing times to find the (u, v) ball locations and extract the geometric calibration parameters was virtually instantaneous.

IV. VOLUME RECONSTRUCTION

Volume reconstruction was accomplished using the Feldkamp algorithm [7] modified to use Parker shortscan weights [8]. The geometric calibration parameters used for reconstruction were first re-expressed from the calibration phantom reference frame to the circular trajectory reference frame by calculating the best circle through the x-ray source trajectory using an orthogonal least squares method. After this rotation, the calibration parameters were directly fed into the reconstruction program. As described in [9], the filtering steps of the reconstruction were not adjusted for the small perturbations measured by the calibration procedure, but each filtered projection view was backprojected precisely according to the geometric calibration parameters.

At this stage no compensation for transaxial truncation and no ROI reconstruction theory [9] was applied.

V. PRELIMINARY EVALUATIONS

Projection images of several phantoms have been acquired, corrected for distortion and reconstructed using the previously obtained geometric calibration parameters.

A high resolution image of the geometric calibration phantom has been reconstructed and shown in volume view representation to give an indication of the overall validity of the reconstruction(see Fig. 6). The figure can be visually compared with a photograph of the phantom in Fig. 4. The phantom was reconstructed using projection images with distortion correction as well as without correction to show the effects of distortion. These reconstructions were compared with the reconstruction done by the C-arm on-board system of the same scan. The slice view in the x direction of the three reconstructions is shown in Fig. 7 in which all reconstructions have the same voxel size. The on-board reconstruction applied a heavier smoothing filter, and indicates some truncation compensation (no bright ring). The effects of distortion can be clearly seen in both the reconstruction without correction and in the on-board Siemens reconstruction.

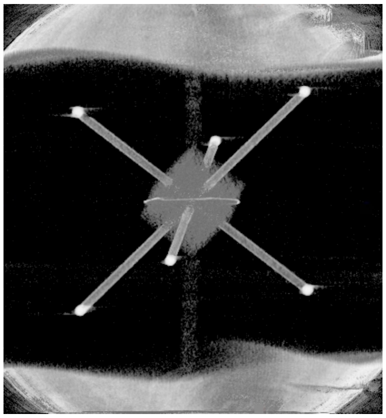

Figure 6. Volume view of a high resolution reconstruction of the geometric calibration phantom (Voxel size: $(0.245\text{mm})^3$)

A planar resolution phantom was also scanned and reconstructed using projection images both with and without distortion correction. Fig. 8 shows the slice view in the x direction of the phantom reconstructed with high resolution. The images in Fig. 8 are an average of a series of 23 sequential x slices in order to show the full depth of the planar resolution phantom. The vertical resolution pattern does not appear to have much difference, however, the horizontal pattern and the clarity of the number scale shows much improved quality in the reconstruction with distortion correction.

Lastly, a hand phantom was imaged and reconstructed to give an indication of the quality of the reconstruction of a clinical object. The hand phantom shown in Fig. 9 is composed of the bones of a human hand encased in Lucite to mimic tissue. A slice of the hand phantom reconstructed with distortion correction and reconstructed by the Siemens on-board system is shown in Fig. 10. The distortion corrected reconstructed slice is observed to have more clearly defined edges around the bones while the Siemens reconstructed image is visibly smoothed. The same reconstructions can be seen

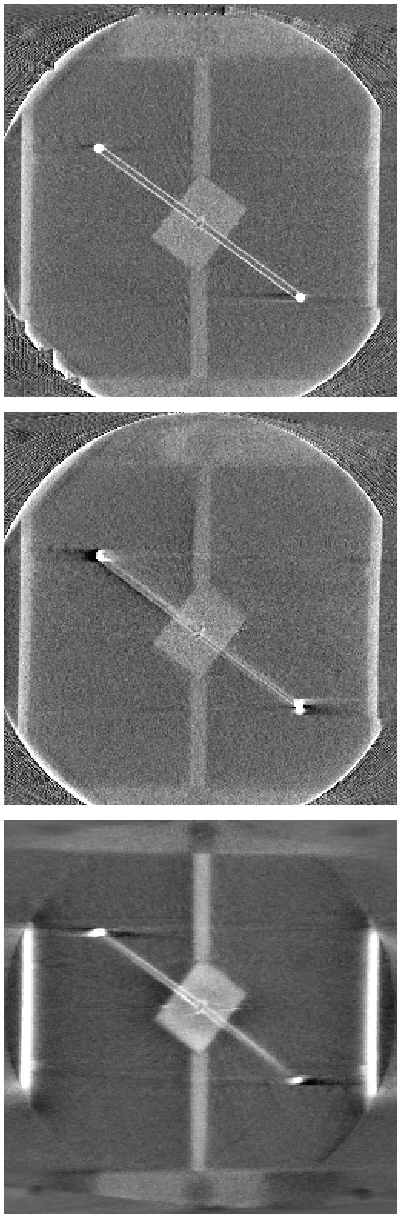

Figure 7. X direction slice view of the reconstructed geometric calibration phantom: (top) Reconstruction with distortion correction, (middle) Reconstruction without distortion correction, (bottom) Reconstruction done by on-board system (Voxel size: $(0.49\text{mm})^3$)

in volume view in Fig 11. In these images the same view of all the slices of the hand phantom are displayed to show the entire bone structure of the hand. All volume view image parameters were identical between the two images except the threshold level which was slightly adjusted to show only bone with little to no tissue. Improved resolution is apparent as the intricacy of the bone structure is much more visible in the distortion corrected reconstruction. The truncation effects around the edge of the field of view, however, are prominent in the distortion corrected reconstruction, which is seen as a bright partial ring around the image. The Siemens on-board reconstructed image in volume view is again smoothed with less obvious truncation effects observed as blurring of the image around its edges.

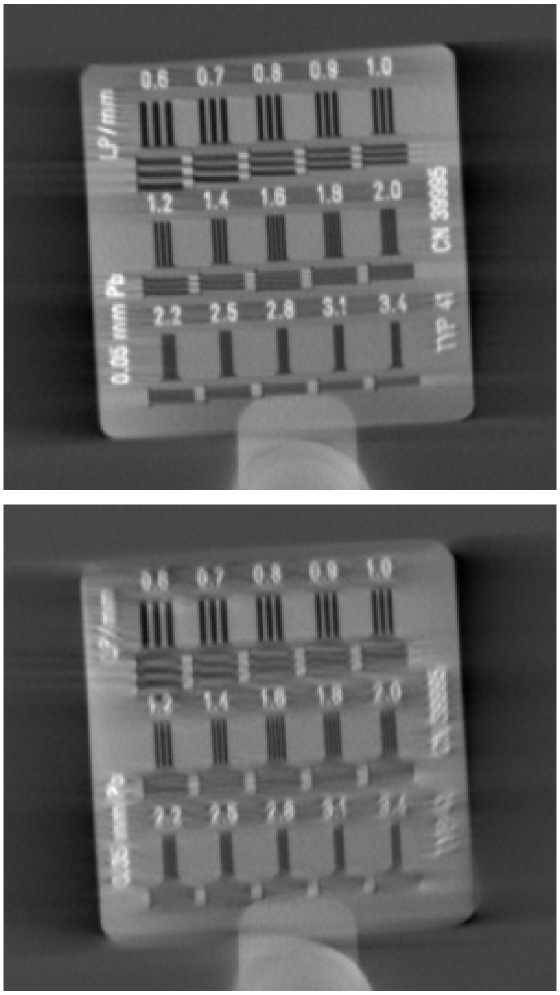

Figure 8. X direction slice view of the reconstructed resolution phantom: (top) Reconstruction with distortion correction, (bottom) Reconstruction without distortion correction (Voxel size: $(0.245\text{mm})^3$)

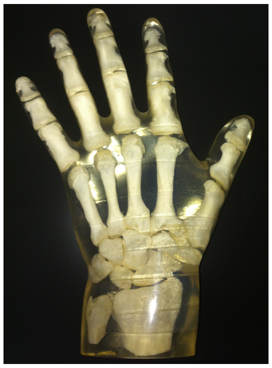

Figure 9. Hand phantom composed of bone encased in Lucite.

VI. CONCLUSION

Our preliminary evaluations have shown that distortion correction is required in order to achieve the best image quality. Our method of correcting for S-distortion is a process that the on-board Siemens system cannot do without a procedure to measure the local magnetic field strength of each individual scan. Consequently, improved resolution of reconstructed im-

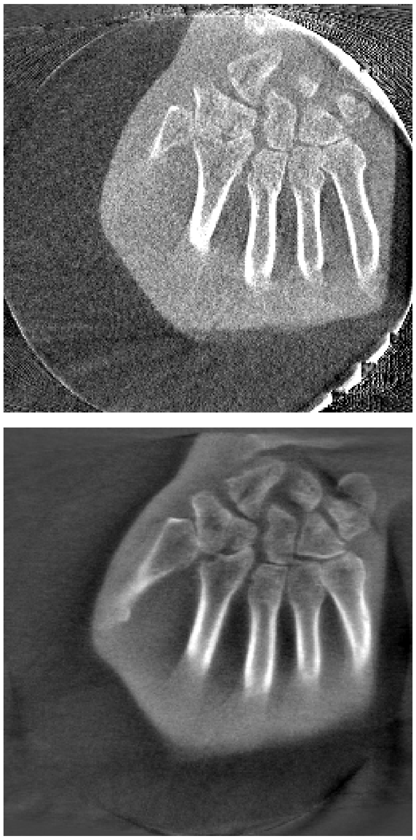

Figure 10. X direction slice view of the reconstruction of the hand phantom: (top) Reconstruction with distortion correction, (bottom) Reconstruction done by on-board system (Voxel size: (0.49mm)^3)

ages has been shown. Additionally, this work marks the first time this particular geometric calibration method [5] has been validated with real data.

The distortion correction process is a lengthy and time consuming procedure which has been reduced to a reasonable amount of time. The geometric calibration process is fully automated and the obtained parameters are fed directly into the Feldkamp reconstruction method. The automated data handling makes the process of distortion correction and geometric calibration computationally and logistically feasible for all prospective work.

Future work will involve increasing the speed of the correction process by using another programming language for execution. Further work will be done to attempt to reduce truncation effects by smoothing projection images around the field of view. The image quality desired for accurate co-registration and tracking with PeTrack has been achieved.

ACKNOWLEDGMENT

This work was partially supported by National Sciences and Engineering Research Council of Canada (NSERC) Discovery Grant (342079), Canada Foundation for Innovation and Ontario Research Fund (14034), and NSERC Idea to Innovation Grant (385574).

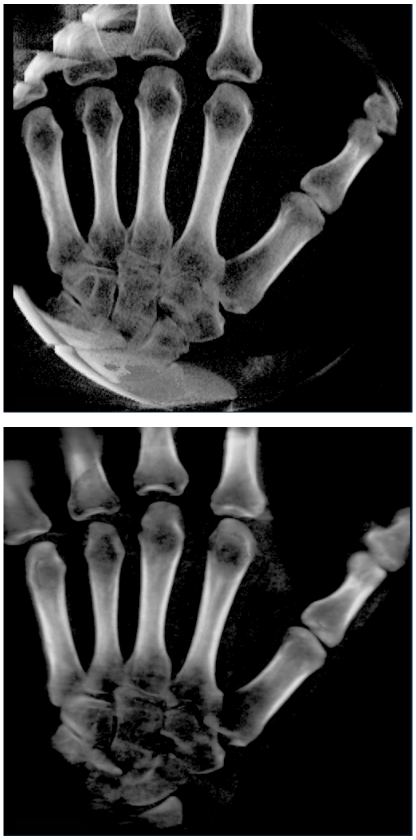

Figure 11. Volume view of hand phantom: (top) Reconstruction with distortion correction, (bottom) Reconstruction done by on-board system ((Voxel size: 0.49mm)^3)

REFERENCES

[1] M. Chamberland, R. Wassenaar, B. Spencer, T. Xu, "Performance evaluation of realtime motion tracking using positron emission fiducial markers," *Med. Phys. 38: 810-19, 2011*

[2] C. Mennessier, B. Spencer, R. Clackdoyle, A-C. Conneau, T. Xu, "Distortion Correction, Geometric Calibration, and Volume Reconstruction for an Isocentric C-Arm X-Ray System," *Conference Record of the 2011 IEEE Nuclear Science Symposium and Medical Imaging Conference. Valencia, Spain. (To appear)*

[3] X. Wang, R. Ning, "Accurate and efficient image intensifier distortion correction algorithm for volume tomographic angiography," *Opt. Eng. 37: 977-983, 1998*

[4] M.D. Abramoff, P.J. Magalhaes, S.J. Ram, "Image Processing with ImageJ," *Biophotonics International, volume 11, issue 7, pp. 36-42, 2004.*

[5] C. Mennessier, R. Clackdoyle, F. Noo, "Direct determination of geometric alignment parameters for cone-beam scanners," *Phys. Med. Biol. 54:1633-1660, 2009*

[6] C. Mennessier, R. Clackdoyle, "Automated Geometric Calibration and Reconstruction in Circular Cone-Beam Tomography," *Conference Record of the 2008 IEEE Nuclear Science Symposium and Medical Imaging Conference. Dresden, Germany. Pages: 5081-5085*

[7] L.A. Feldkamp, L.C. Davis, J.W. Kress, "Practical cone-beam algorithm," *JOSA 1 (6):612-619, 1984*

[8] D. Parker, "Optimal short scan convolution reconstruction for fan beam CT," *Med. Phys. 9 (2):254-258, 1982*

[9] R. Clackdoyle, M. Defrise, "Tomographic Reconstruction in the 21st Century. Region-of-interest reconstruction from incomplete data," *IEEE Signal Processing. 27(4), 60-80., 2010*

Low Dose Perfusion CT

Dominic J. Heuscher, Ph.D., Jeff Zhang, Ph.D., [†]Stanislav Zabic, Ph.D., Frederic Noo, Ph.D.
[*]UCAIR, University of Utah, Salt Lake City, Utah

Abstract– **Perfusion CT imaging, with today's multi-detector technology and rotation speed, has great potential to become extensively used for both diagnosis and treatment of diseases. However, high dose and the lack of standardization of protocols are limiting this potential. We would like to show that the x-ray dose of CT perfusion scans can be significantly reduced without sacrificing clinical accuracy. This would greatly facilitate the use of perfusion CT as a routine diagnostic tool, and would extend the applications of perfusion CT where dose is a limiting factor, e.g. cardiac perfusion. To significantly reduce the dose, we propose to use a novel dynamic collimator, a predictive sampling algorithm, and a predictive exposure algorithm. Combining these three approaches, we will show, as an example, in the case of kidney perfusion applications, that a 10:1 reduction in patient exposure can be achieved without sacrificing diagnostic accuracy. We think that, along with consistent protocols and further improvements in CT scan technology, this will enable perfusion CT to become a routine diagnostic tool.**

I. INTRODUCTION

With its widespread availability and experience, accessibility and ease of acquisition in acute settings, straightforward mathematical modeling, simple protocol modification, along with the advent of fast multi-slice scanning, perfusion CT should be in a great position to be used in clinical practice. Applications include stroke assessment[1], oncology[2,3], along with cardiac[4] and kidney function[5]. However, primarily due to the high dose, perfusion CT has not been routinely used for these applications. Current perfusion protocols scan the patient as often as once per second for a period of 70 seconds and expose the entire patient volume (up to 16 cm axially).

Our goal is to demonstrate that the dose in perfusion CT can be greatly reduced without impacting diagnostic accuracy. Three approaches are investigated, including:

1. Use dynamic collimation to expose the patient to just the area of interest
2. Use a predictive sampling algorithm based on the arterial input function (AIF) to acquire carefully-selected sparse samples of the perfusion curves
3. Use a predictive scan exposure algorithm based on the AIF to minimize the exposure of each scan to what is necessary

II. METHODOLOGY

Either repeated large area circular scans or helical scans are used to perform perfusion CT. In the case of helical scans, a dynamic collimator that limits the x-ray exposure, axially, at either end of the helical scan is already being utilized[6,7]. We propose to add a dynamic collimator (Fig.1) in the transverse plane in front of the x-ray source that further limits the x-ray exposure to just the region of interest (ROI), as illustrated in Fig. 2. Fig. 3 illustrates how this dynamic collimator can define the outline of the heart, limiting the x-ray exposure to just the heart itself.

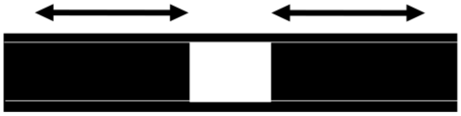

Fig. 1. Dynamic collimator with independent right and left leaves.

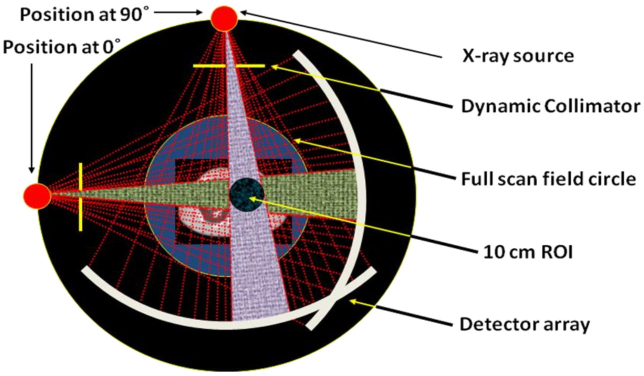

Fig. 2. Dynamic collimator positioned at 0 and 90 degrees for a 10 cm off-center ROI surrounding the heart.

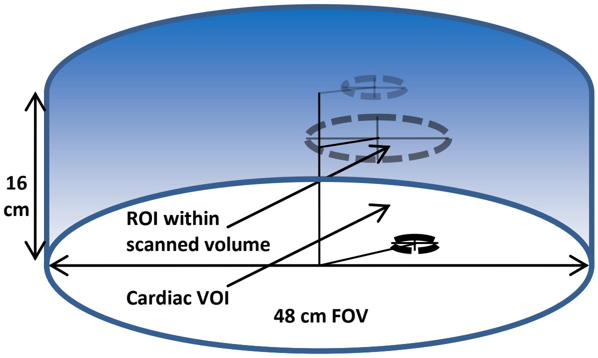

Fig. 3. Cardiac VOI defined by both the dynamic transverse and helical collimators.

After analyzing the dynamics[9], we feel it is feasible to build such a collimator, provided that it is placed close to the x-ray source (12 cm or less) and the motor controller is upgraded (about a factor of four faster than the helical collimator).

As illustrated in Fig. 4, attenuation information is necessary from the tissue surrounding the collimated ROI due to the extent of the convolution required to reconstruct the image. This can be accomplished in two recommended ways:

Manuscript received January 25, 2012. This work was partially supported by a Benning Foundation grant from the University of Utah and partially funded by NIH grants R01 EB007168 and R21 EB007236. Its contents are solely the responsibility of the authors.

[*]Authors are with [†]Philips Medical Systems, Highland Heights, Ohio, and the Utah Center for Advanced Imaging Research, Radiology Department, University of Utah, Salt Lake City, UT 84108 USA (e-mail: dheuscher@ucair.med.utah, telephone: 801-581-4418).

1. Use a previously-acquired very low dose scan (with registration) to measure the attenuation outside the VOI
2. Use heavily-attenuated rays through the outer portions of the collimator. This provides an estimate of the attenuation outside the VOI, provided the collimator attenuation is previously calibrated[8]

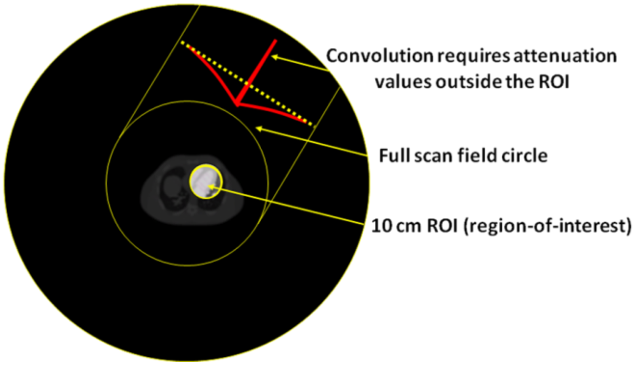
Convolution requires attenuation values outside the ROI
Full scan field circle
10 cm ROI (region-of-interest)

Fig. 4. To reconstruct the region-of-interest, attenuation values surrounding the ROI are required.

To calculate the reduction in exposure that can be achieved using transverse dynamic collimation, we approximate the boundaries of both the body and target ROI with ellipses, as illustrated in Fig. 5 for a cardiac scan in which the target ROI corresponds to the entire boundary of the heart. The scan is that of an XCAT phantom described by Zhicong et al[11].

The figure illustrates the geometry used to calculate the exposure at any designated point in the body, namely points along the boundary of the body and the point at the center of the target ROI. The boundary points are exposed either directly (top image), or exposed indirectly (middle image), with the body attenuating the x-rays by a path length (1-p) measured relative to the known path length p0. The point at the center of the target ROI (bottom image) is also exposed indirectly, with the body attenuating the x-rays by a path length (1-p) measured relative to the known path length from the source to the center of the ROI.

Given the source radius (57 cm), source angle, and point on the body ellipse, the path length p relative to the distance p0 can be calculated as a solution to a quadratic equation resulting from the condition that the entrance point of the ray also satisfies the equation for the body ellipse[10]. The exposure at the center of the target ROI is calculated as a reference for the skin exposure values. In this case, p0 corresponds to the path length to the point at the center of the target ellipse and p is calculated as the relative path length to the point on the body ellipse. Since the exposure is measured at the center of the target ellipse, the same value applies whether or not dynamic collimation is used.

A compensator in front of the X-ray source, used in most CT scans today, provides a more uniform signal to the detector and reduces the overall dose to the patient. We therefore modeled a compensator that perfectly compensates for a disc with a radius *rc* of 24 cm and an attenuation coefficient equal to water (.183/cm at 80 KeV, approximately the average energy for a typical CT system performing 120 KeV scans).

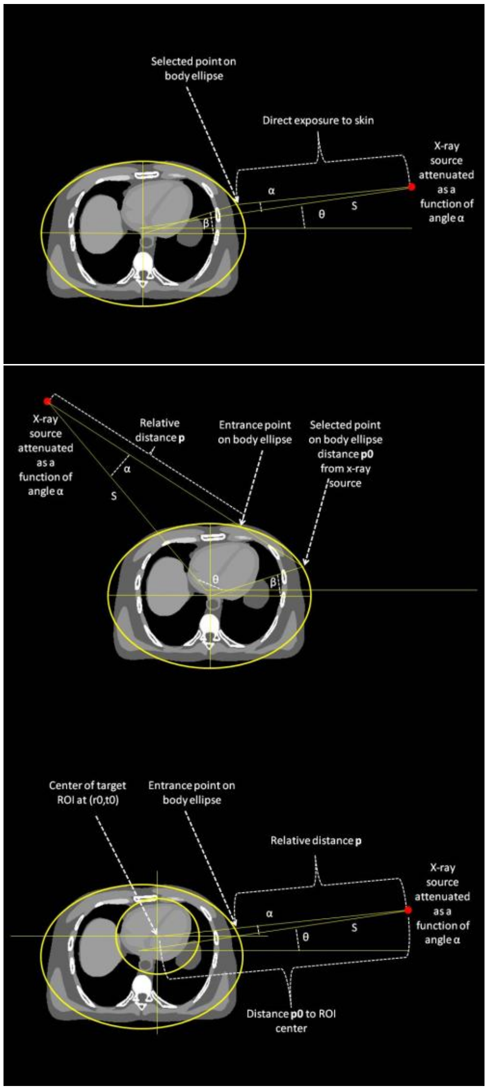
Selected point on body ellipse
Direct exposure to skin
X-ray source attenuated as a function of angle α
α
θ
S
β
X-ray source attenuated as a function of angle α
Relative distance p
Entrance point on body ellipse
Selected point on body ellipse distance p0 from x-ray source
α
S
θ
β
Center of target ROI at (r0,t0)
Entrance point on body ellipse
Relative distance p
X-ray source attenuated as a function of angle α
α
S
θ
Distance p0 to ROI center

Fig. 5. Geometry for a ray at angle α exposing the skin either directly (top image) or indirectly (middle image), or exposing the center of the target ROI (bottom image). The ray emanates from the x-ray source located at a distance S and angle θ with respect to scan center.

As an initial approximation, the water attenuation value of .183/cm was also assumed for all path lengths throughout the body. The exposure for each of 100 points equally spaced in angle β on the surface of the body ellipse was calculated for 1000 angular views, θ, of the source covering 360 degrees. These exposure values were then averaged over the 1000 views. Likewise, the exposure at the center of the target ROI, was averaged over 1000 views. This provided a reference for the skin exposure values. Thus all overall skin exposure values are measured as a ratio with respect to the exposure at the center of the target ROI.

The resulting skin exposure is then calculated as an average value over 360 degrees of the angular position (θ) of the x-ray source:

$$Exposure(\beta) = .001 \cdot \sum_{i=1}^{1000} intensity(\alpha(\beta,\theta_i)) \cdot att(\beta,\theta_i)$$

where:

β = the angle of the point on the body ellipse
θ = the source angle
α = fan angle of the ray intersecting the point on the body ellipse
$intensity(\alpha) = e^{2\cdot .183\cdot\left(\sqrt{rc^2-(S\cdot\sin\alpha)^2}-rc\right)}$
$att(\beta,\theta) = e^{-.183\cdot(1-p(\beta,\theta))\cdot p0(\beta,\theta)}$
p is the path length to the entrance point on the body ellipse relative to p0
p0 is the path length to the selected point on the body ellipse

The average relative skin exposure is then the average of the exposure for all points around the body ellipse divided by the exposure at the center of the target ROI.

For the average collimated exposure, the same exposure equation is used, but with the intensity set to zero for all ray angles whose fan angle exceeds that of the range of angles spanned by the two rays that intersect the tangents to the target ellipse, i.e.:

$$intensity\big(\alpha(\beta,\theta)\big) = 0\ if\ \alpha > AC(\theta)\ or\ \alpha < ACC(\theta)$$

AC is the clockwise angular position of the collimator leaf for source angle θ
ACC is the counter-clockwise angular position of the collimator leaf

With regards to the predictive sampling algorithm, the number of scan samples can typically be reduced by a factor of four as illustrated in Fig. 6 by using an algorithm that adaptively varies the sampling along the AIF which, in this example, corresponds to the Left Ventricular Input curve:

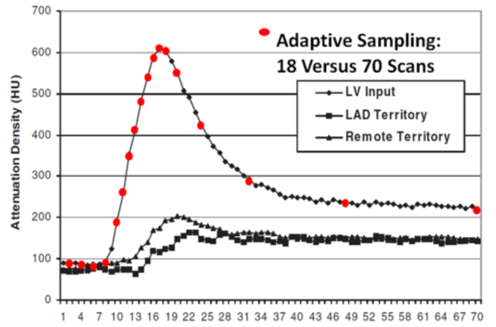

Fig. 6. Adaptive sampling using the LV Input curve.

The predictive algorithm is based on the following steps:

1. The first scan takes place at time t=0; proceed to scan every two seconds, looking for the rise in the arterial curve above a predefined threshold TH, e.g. 35 HU
2. After the rise in the curve, track the slope of the curve (using a finite difference) until the magnitude of the slope decreases
3. Scan every second until after the peak of the arterial curve (value of the slope becomes negative), then proceed to scan every 2 seconds
4. After the inflection point (when the magnitude of the slope again decreases), double the scan interval after each subsequent scan (since this is the slowly descending exponential portion of the curve, only very sparse sampling is required)
5. When the end of the predetermined scan period is reached, perform one final scan to complete the sampling of the arterial curve

The predictive scan exposure algorithm (illustrated in Fig. 7), also significantly reduces the overall exposure to the patient:

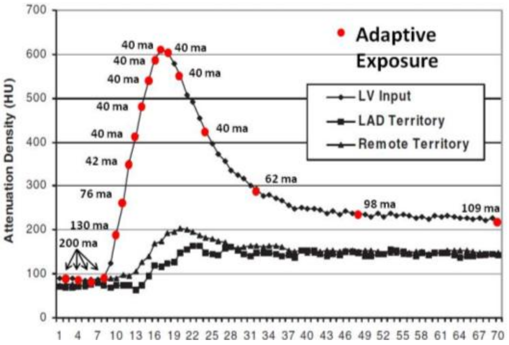

Fig. 7. Adaptive exposure control based on the LV Input curve.

Given the maximum and minimum ma allowed, the predictive scan exposure algorithm again follows a list of steps as follows:

1. Scan at the maximum current, e.g. 200 ma, until the rise in the arterial curve is detected (as described above)
2. Reduce the applied current (using the predetermined contrast detection threshold TH), by multiplying the maximum current by the following factor F:

$$F = e^{C\cdot(TH-\Delta\mathrm{HU})/TH}$$

where:
C = .25
(minimum allowable ma)/(maximum ma) < F < 1
ΔHU = the difference of the Houndsfield Unit value of the curve and the baseline value corresponding to the first HU value of the curve
(C is chosen such that if the arterial curve rises 10 times above the threshold TH (35 HU), the current is reduced by 10:1. For example, if the attenuation is 450 HU and the baseline is 100 HU (ΔHU=350), then the current will be decreased from a maximum of 400 ma to 40 ma)

3. Continue using the x-ray current determined by the above formula for the rest of the series

To validate the accuracy of the perfusion analysis after applying the sub-sampling algorithm, we have chosen to use a kidney perfusion study, originally acquired using 60 seconds of 8 cm circular scans, repeated every second. Each scan was acquired with a tube current of 200 ma. The derived perfusion parameters included the mean arterial transit time (MTT_a), the renal plasma flow (RPF), and the glomerular filtration rate (GFR). The ROIs chosen to generate the curves used to calculate these parameters included the cortex of the kidney and aorta. The parameters derived from the original data were compared to those derived from the sparsely-sampled data (using the above predictive algorithm). Finally, the overall exposure reduction was calculated using the exposure estimate based on the dynamically collimated ROI (an elliptical region surrounding both kidneys and aorta), the sparse sampling, and the average exposure due to the modulated tube current.

III. RESULTS

One of the cases used in the evaluation is shown in Fig. 8, including (left) the collimated ROI, the ROIs for the cortex and aorta, and (right) the 16 subsamples chosen out of 60. The minimum current was 40 ma, occurring at the peak of the AIF curve, and the maximum current was 200 ma, used at the beginning of the scan.

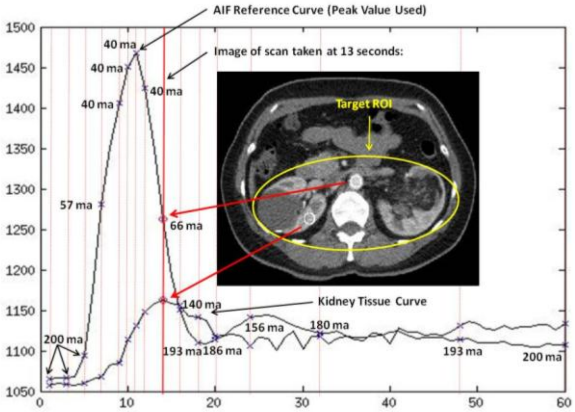

Fig. 8. Kidney perfusion evaluation showing ROIs, corresponding AIF and tissue curves, scan subsamples (vertical red lines), and dynamic ma values.

The following tables provide the results for the 2 kidney studies that were evaluated (maximum deviation in MTTa|RPF|GFR values is 5% and the average overall exposure reduction is 10.5:1):

Table 1a	**MTT_a/RPF/GFR**
Sub-sampling (Case I)	8.5|144|34 8.3|141|36

Table 1b	**Case I**	**Case II**
Sub-sampling Exposure Reduction	3.8:1	3.8:1
Current Modulation Exposure Reduction	1.5:1	1.5:1
Dynamic Collimation	1.6:1	2.1:1
Overall Reduction	9.1:1	12:1

Table 1a. Kidney perfusion evaluation comparing MTT_a/RPF/GFR values for fully-sampled (top) versus sub-sampled data (bottom). Table 1b. The calculated skin exposure reduction due to sub-sampling, current modulation, and dynamic collimation. The average overall reduction is 10.5:1

IV. DISCUSSION

The current protocol for the kidney studies used in this evaluation is as follows:

1. Perform low dose reference scan
2. Identify axial location and extent for perfusion series, insuring the required ROIs can be identified
3. Perform 60 second perfusion series, scanning every second for 60 seconds

The corresponding new low dose protocol would be as follows:

1. Perform low dose reference scan
2. Identify axial location and extent as well as the arterial VOI used to define the motion of the transverse dynamic collimator. Insure tissue ROI(s) can be identified.
3. Perform 60 second perfusion series, performing predictive sampling and current modulation based on the AIF as it is being acquired. The collimated regions can then be reconstructed using attenuation information from the surrounding tissue calculated from the original low dose reference scan.

Based on our results, this new protocol should provide comparable diagnostic results as the original protocol, with one-tenth the dose.

If possible, we recommend using VOIs that utilize more than one slice to provide the best statistics for the perfusion curves. To take care of motion that occurred between the reference scan and perfusion series, registration should be performed for the tissues containing the VOIs. Motion correction between all images acquired in the series could also significantly improve the quality and accuracy of the perfusion curves (note the oscillations in the tissue curve in Fig. 7 that repeat approximately every three seconds, most likely due to breathing motion). This should permit lowering the dose even further while retaining the statistical accuracy of the perfusion curves and achieving comparable diagnostic results.

V. CONCLUSION

Based on the techniques proposed, a 10:1 reduction in x-ray dose can be expected for kidney perfusion scans. Future work will include extending the evaluation to other perfusion applications, including the pancreas, liver, and heart. Additional dose-saving methodology will be explored, including the use of motion-correction to improve the accuracy of the low dose perfusion curves. Faster helical coverage using both dynamic transverse and helical collimators, along with sparse sampling and dynamic current modulation, should enable perfusion CT as a routine diagnostic tool.

ACKNOWLEDGMENT

This work is part of the low dose perfusion CT imaging project supported by a Benning Foundation grant from the University of Utah, with additional support from NIH grants R01 EB007168 and R21 EB007236.

REFERENCES

[1] A. Srinivasan, M. Goyal, F. Al Azri, Cheemun Lum, “State-of-the-Art Imaging of Acute Stroke”, RadioGraphics, October 2006, 26, S75-S95.
[2] Kandel S et al, “Whole-organ perfusion of the pancreas using dynamic volume CT in patients with primary pancreas carcinoma: acquisition technique, post-processing and initial results”, European Radiology 2009 [Epub ahead of print]
[3] Chaan S. Ng, X. Wang, S. Faria, E. Lin, C. Charnsangavej, N. Tannir, “Perfusion CT in Patients With Metastatic Renal Cell Carcinoma Treated With Interferon”, AJR January 2010; 194:166–171
[4] Gorka Bastarrika et al, “Adenosine-Stress Dynamic Myocardial CT Perfusion Imaging Initial Clinical Experience”, Investigative Radiology 45, Number 6, 2010, 306-313
[5] H. Zhao, J. Gong, “Renal hemodynamic changes with aging: a preliminary study using CT perfusion in the healthy elderly”, Clinical Imaging July 2010, 34:4, pp. 247-250
[6] J. A. Christner, V. A. Zavaletta, C. D. Eusemann, A. I. Walz-Flannigan, C. H. McCollough, "Dose Reduction in Helical CT: Dynamically Adjustable z-Axis X-Ray Beam Collimation" AJR:194, January 2010.
[7] Heuscher, "Dynamic Collimation in Cone Beam Computed Tomography to Reduce Patient Exposure", US Patent Application 20100246752, 2010.
[8] Nalcioglu et al, "Limited Field of View Reconstruction in Computerized Tomography", IEEE Transactions on Nuclear Science, vol. NS-26, No. 1, Feb. 1979.
[9] D. Heuscher, F. Noo, “CT Dose Reduction Using Dynamic Collimation”, MIC 23-29 October 2011, Conference Record.
[10] Y. Zhicong, F. Noo, F. Dennerlein, A. Wunderlich, G. Lauritsch, and J. Hornegger, “Simulation tools for two-dimensional experiments in x-ray computed tomography using the FORBILD head phantom”, 2012, Appendix I, (preprint: contact the first author at the Department of Radiology, University of Utah, Salt Lake City, UT, USA)
[11] W.P. Segars, M. Mahesh, T.J. Beck, E.C. Frey, B. M. Tsui, “Realistic CT simulation using the 4D XCAT phantom”, Medical Physics, 2008 August, 35(8), pp. 3800-3808.

Analysis of bias induced by various forward projection models in iterative reconstruction

K. Schmitt, H. Schöndube, K. Stierstorfer, J. Hornegger, F. Noo

***Abstract*—Discrete representation of the CT image is a major step in the design of iterative reconstruction algorithms, particularly because the decision being made at this level affects both bias and noise properties of the reconstruction, in addition to choices made later in the algorithm design. In this work, we examine the bias induced by popular image representation models, namely Joseph's method and the basis function approach relying on B-splines and blobs. Our preliminary results highlight a common weakness in terms of overshoot and undershoot artifacts at sharp boundaries. They also show that the Blobs may perform only as well as the B-spline of order two in terms of bias, and that Joseph's method tends to produce results that are fairly comparable to the B-spline of order one, with a slight advantage in favor of the latter.**

I. INTRODUCTION

Discrete representation of the CT image is a major step in the design of iterative reconstruction algorithms. Two commonly used techniques to represent the image with a finite number of unknowns are the sampling approach and the basis function approach. In the sampling approach, the image is represented by its values at a fixed number of locations that are typically equidistantly distributed in the direction of Cartesian coordinates. In the basis function approach, the image is represented by a finite linear combination of specific functions that are often selected as scaled and translated versions of a single function, called the mother function. Popular mother functions include the blobs [1] and the B-splines [2].

Since the basis function approach yields a continous model for the image, the definition of line integrals modelizing the CT measurements is straightforward when using this approach. For the sampling approach, the situation is different: defining line integrals with this approach requires the introduction of a numerical scheme. One widely-used scheme was suggested by Joseph [3]. Another more recent scheme that is gaining interest is the distance-driven technique suggested by De Man and Basu [4]. Note that both schemes process line integrals differently according to their slope, with the caveat that the involved approximation is usually less accurate for lines that are at 45 degrees relative to the Cartesian grid of samples used to represent the image.

Naturally, the performance of iterative reconstruction methods is affected by the choices made to represent the CT image and to model the CT measurements from this representation. Both bias and noise properties of the CT reconstruction can change dramatically according to these choices, as illustrated, for example, in [5], for the selection of parameters defining the blobs. In this work, we are interested in evaluating the bias induced by such choices. We will compare results obtained using blobs and B-splines together with results obtained using Joseph's method. The study is limited to two-dimensional CT imaging. In section II, we give a brief review on B-splines ans blobs. In section III, we present our experimental setting. Last, in section IV, we present and discuss preliminary results.

II. IMAGE REPRESENTATION USING BASIS FUNCTIONS

Here, we briefly review the basis function approach. Throughout this section and the rest of this abstract, we use $f(x, y)$ to denote the function that describes the linear attenuation coefficient of X-rays as a function of the position within the field-of-view of the scanner.

A. General concept

In the basis function approach, $f(x, y)$ is approximated by a linear combination of basis functions denoted as $f_a(x, y)$. When the basis functions are defined from a mother function, $b(x, y)$, the expression for $f_a(x, y)$ is as follows:

$$f_a(x, y) = \sum_{k,l} c_{kl} \cdot b((x - x_k)/\Delta x, (y - y_l)/\Delta y) \quad (1)$$

where the c_{kl} are the basis function coefficients to be estimated. In this expression, the locations $x_k = k\,\Delta x$ and $y_l = l\,\Delta y$ are samples on a Cartesian grid of size $N_x \times N_y$ with steps Δx and Δy in x and y, respectively. Often, Δx and Δy are selected to be equal. We make this assumption here and let $h = \Delta x = \Delta y$.

B. Line integrals

When using the basis function approach to represent $f(x, y)$, the Radon transform of f, denoted as $r(\theta, s)$, is simply approximated by the Radon transform of $f_a(x, y)$, denoted as $r_a(\theta, s)$. The linearity of the Radon transfrom yields

$$r_a(\theta, s) = \sum_{k,l} c_{kl} \cdot g(\theta, (s - x_k \cos\theta - y_l \sin\theta)/h) \quad (2)$$

where $g(\theta, s)$ is the Radon transform of $b(x, y)$.

K. Schmitt, H. Schöndube and K. Stierstorfer are with Siemens AG, Healthcare Sector. J. Hornegger is with the Pattern Recognition Lab, University of Erlangen-Nürnberg, Erlangen, Germany. F. Noo is with the Department of Radiology, University of Utah, Salt Lake City, Utah, USA.

The concepts presented in this paper are based on research and are not commercially available. This work was partially supported by NIH grant R01 EB007236; its content is solely the responsibility of the authors and do not necesarily represent the official views of the NIH.

C. B-splines

The B-splines are simple piecewise polynomial functions. They are defined by a single parameter: the degree, n, of the polynomial. The centered B-spline β_h^n of degree n and of width h is the $(n+1)$-th convolution of the normalized box function, β_h^0, with itself, i.e.,

$$\beta_h^n(x) = \beta_h^0 * \beta_h^{n-1}(x) = \underbrace{\beta_h^0 * \cdots * \beta_h^0}_{n+1 \text{factors}} \tag{3}$$

with

$$\beta_h^0(x) = \begin{cases} 1/h, & \text{if } -h/2 \le x \le h/2 \\ 0, & \text{otherwise} \end{cases} \tag{4}$$

Using B-splines in the basis function approach means that $b(x,y) = \beta_h^n(x)\,\beta_h^n(y)$ is chosen. Let the one-sided power function be defined by

$$x_+^m = \begin{cases} x^m, & x \ \ge \ 0 \text{ and } m > 0 \\ 1, & x \ \ge \ 0 \text{ and } m = 0 \\ 0, & \text{otherwise} \end{cases} \tag{5}$$

Using this definition, it was shown in [2] that the Radon transform of $b(x,y)$ is

$$g(\theta,s) = \sum_{i=0}^{n+1}\sum_{j=0}^{n+1}(-1)^{i+j}\binom{n+1}{i}\binom{n+1}{j} \cdot \frac{\left[s + (\frac{n+1}{2} - i)\cdot h_1(\theta) + (\frac{n+1}{2} - j)\cdot h_2(\theta)\right]_+^{2n+1}}{(2n+1)!\,(h_1(\theta)\,h_2(\theta))^{n+1}} \tag{6}$$

where $h_1(\theta) = h\,|\cos\theta|$ and $h_2(\theta) = h\,|\sin\theta|$. Note that using the B-spline of order $n = 0$ for image representation is equivalent to adopting the approach of Siddon [6].

D. Blobs

The blob function is given by the following one-dimensional expression

$$\gamma_{m,a,\alpha}(r) = \begin{cases} \left(1 - \frac{r^2}{a^2}\right)^{\frac{m}{2}} \frac{I_m\left(\alpha\sqrt{1-\frac{r^2}{a^2}}\right)}{I_m(\alpha)} & \text{if } 0 \le r \le a \\ 0 & \text{otherwise} \end{cases} \tag{7}$$

where r is the radial distance from the blob center, a is the radius of the basis function, α is a parameter controlling the blob shape, and I_m is the modified Bessel function of order m.

Using blobs in the basis function approach means that $b(x,y)$ is chosen as $\gamma_{m,a,\alpha}(r)$ with $r = \sqrt{x^2+y^2}$. Given this definition, $g(\theta,s)$ is independent of θ, zero for $|s| > a$, and expressed as

$$g(\theta,s) = \left(\frac{2a^2\pi}{\alpha}\right)^{\frac{1}{2}} \left(1 - \frac{s^2}{a^2}\right)^{\frac{m}{2}+\frac{1}{4}} \frac{I_{m+\frac{1}{2}}\left[\alpha\left(1-\frac{s^2}{a^2}\right)^{\frac{1}{2}}\right]}{I_m\left[\alpha\right]}. \tag{8}$$

for $|s| < a$. Following the recommendations in [5], we chose $m = 2$, $a = 2$ and $\alpha = 10.4$.

III. EXPERIMENTAL SETTING

In this section, we describe the setting used for evaluation of the reconstruction bias and thereby compare the accuracy of various image representation models.

A. Phantom and data geometry

The FORBILD head phantom was used for all our evaluations. Also, a parallel-beam data acquisition geometry was assumed. Each CT measurement was simulated as an average of five line integrals that were calculated each using analytical expressions. The average was introduced to model the finite detector response (disregarding non-linearity effects) and reduce thereby high-frequency errors in the reconstruction process. The parameters defining our simulations are given in Table I.

B. Iterative reconstruction technique

Evaluating the bias in iterative reconstruction is not straightforward when the algorithm is non-linear. To circumvent this difficulty, we adopted a statistical model with no prior term. More specifically, the CT measurements were modelled as independent Gaussian deviates, and we seeked the maximum likelihood solution of minimum norm. Also, we assumed that the noise was stationary, which is a reasonable assumption for brain imaging with tube current modulation and beam-shaping bowtie filter.

Let c be the vector of unknown image coefficients, let g be the vector grouping the CT measurements, and let A be the matrix that links c to the CT measurements. Using this notation, the desired reconstruction can be expressed as the minimum-norm minimizer of $\|Ac - g\|$. This reconstruction was seeked using the Landweber algorithm, i.e., using the following iterative procedure:

$$c^{(k+1)} = c^{(k)} + \lambda\, A^T(g - Ac^{(k)})\ , \tag{9}$$

where the convergence-controlling factor, λ, was chosen as 0.95 times $2/\sigma_{max}^2$, where σ_{max} is the maximum singular value of the projection matrix A. Thus, convergence was guaranteed and nearly as fast as possible. The quantity σ_{max} was computed using five iterations of the power method.

As it is well-known, resolution improves with the number of iterations, but discretization errors also increase at the same time, so that the maximum-likelihood reconstruction is not satisfactory. Hence, we focused on examining regularized reconstructions obtained by stopping the iterative process after a fixed number m of iterations.

C. Bias evaluation

Bias was evaluated using visual inspection of images and profiles, and also by calculing the reconstruction error over pixels located within the large central low-contrast ellipse within the phantom. The error was computed as the absolute difference between the reconstructed value and the true attenuation value for this ellipse, which is 1.045 ($45\ HU$).

D. Resolution measurement

As discussed earlier, resolution in the reconstruction typically improves with the number of iterations. To evaluate resolution, we opted for the modulation transfer function (MTF). Computation of this function was performed with the following steps: (i) a phantom that consists only of the

	image discretization	CT measurement
matrix size	350 × 350	700 × 380
	($N_y \times N_x$)	(views × rays-per-view)
sampling step	$\Delta x = \Delta y = 0.075$	$\Delta s = 0.075$

TABLE I
IMAGE REPRESENTATION AND CT MEASUREMENT PARAMETERS.

low-contrast ellipse within the FORBILD head phantom was defined, (ii) CT measurements for this ellipse were generated in the same way as measurements for the full phantom, (iii) reconstruction was performed from these measurements, (iv) an edge profile that gives the reconstructed value as a function of the distance from the ellipse was computed from the reconstruction, (v) the MTF was obtained as the Fourier transform of the edge profile.

Given the linearity of the chosen reconstruction method, the methodology above was suitable for assessment of the resolution achieved within the neighborhood of the large low-contrast ellipse in reconstructions of the FORBILD head phantom.

IV. PRELIMINARY RESULTS AND DISCUSSION

First, we examined the reconstructions obtained using both a small and a large number of iterations, which were chosen as 250 and 850. Figure 1 shows the reconstruction results obtained using 250 iterations, and Figure 2 shows a vertical profile through these results, which passes through the left eye. Figures 3 and 4 shows the reconstruction results and profiles for 850 iterations. These figures highlight significant differences between the different image representations. They also show that, irrespective of the selected representation, increasing the number of iterations amplifies the magnitude of overshoots and undershoots errors at the sharp boundaries while reducing their spread; note that these errors are present despite the low-pass filtering that was applied in the data simulation process.

Figure 5 shows the MTF curves corresponding to each image representation for both 250 and 850 iterations. From these plots, it can be seen that, not unexpectedly, resolution varies from one representation to the other and also changes at a different pace for each representation. For a fair comparison, it is needed to take these differences into account. An attempt at such a comparison is shown in Figure 6, where the bias metric discussed in section III.C is displayed as a function of the mean MTF value.

Under the assumption that the mean MTF value is acceptable as a summary measure for resolution, the following observations can be made from Figure 6, some of which were already well-known:

- The B-spline with $n = 0$ produces the largest bias.
- Joseph's method performs almost as well as the B-spline of order $n = 1$, with a slight difference in favor of the B-spline that is most likely due to Joseph's method yielding a reduced accuracy along lines that are at 45 degrees.
- The B-spline of order $n = 2$ performs as well as the blobs.

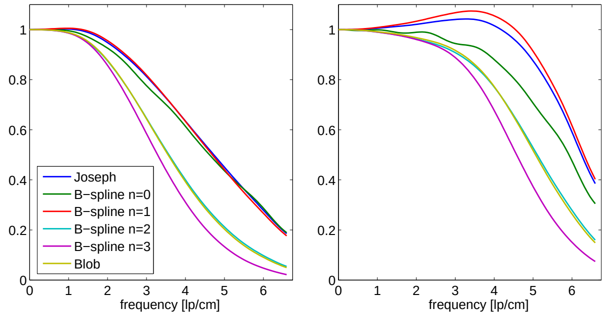

Fig. 5. *left:* Modulation transfer function (MTF) for reconstructions based on 250 and 850 iterations of the Landweber algorithm, using the basis function approach with the blobs and the B-splines, and also using Joseph's method.

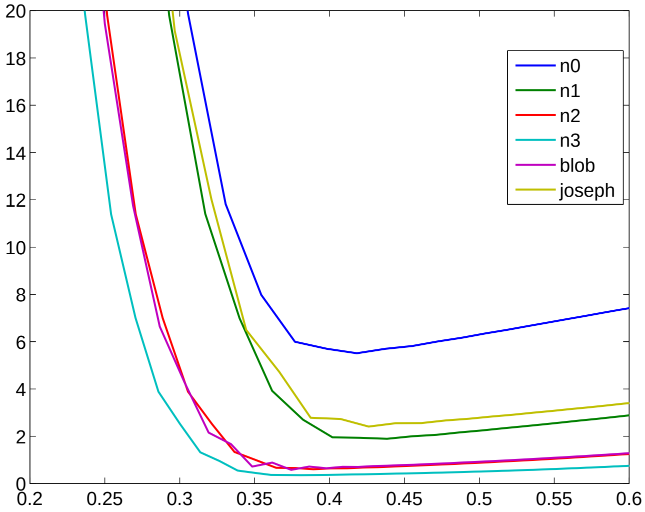

Fig. 6. *left:* Bias-versus-resolution curves obtained by varying the number of iterations by steps of 5. The bias is expressed in HU.

- The B-spline of order $n = 3$ outperforms the blobs.

In future work, we will examine closer the impact of the summary measure being chosen for the MTF curve, and we will also extend our study to include the distance-driven technique [4].

REFERENCES

[1] R. M. Lewitt, *Multidimensional digital image representations using generalized Kaiser-Bessel window functions*, J. Opt. Soc. am. a, 7(10), pp. 1834-46, 1990.

[2] S. Horbelt et al., *Discretization of the Radon Transform and of its Inverse by Spline Convolutions*, IEEE Transactions on Medical Imaging, 21(4), pp. 363-76, 2002.

[3] P. M. Joseph, *An Improved Algorithm for Reprojecting Rays Trough Pixel Images*, IEEE Transactions on Medical Imaging, 1(3), pp. 192-96, 1982.

[4] B. De Man, S. Basu, *Distance-driven projection and backprojection in three dimensions*, Physics in Medicine and Biology, 49, pp. 2463-75, 2004.

[5] S. Matej and R. M. Lewitt, *Practical considerations for 3-D image reconstruction using spherically symetric volume elements*, IEEE Transactions on Medical Imaging, 15(1), pp. 68-8, 1996.

[6] R. L. Siddon, *Fast calculation of the exact radiological path for a three-dimensional CT array*, Med. Phys., 12(2), pp. 252-55, 1985.

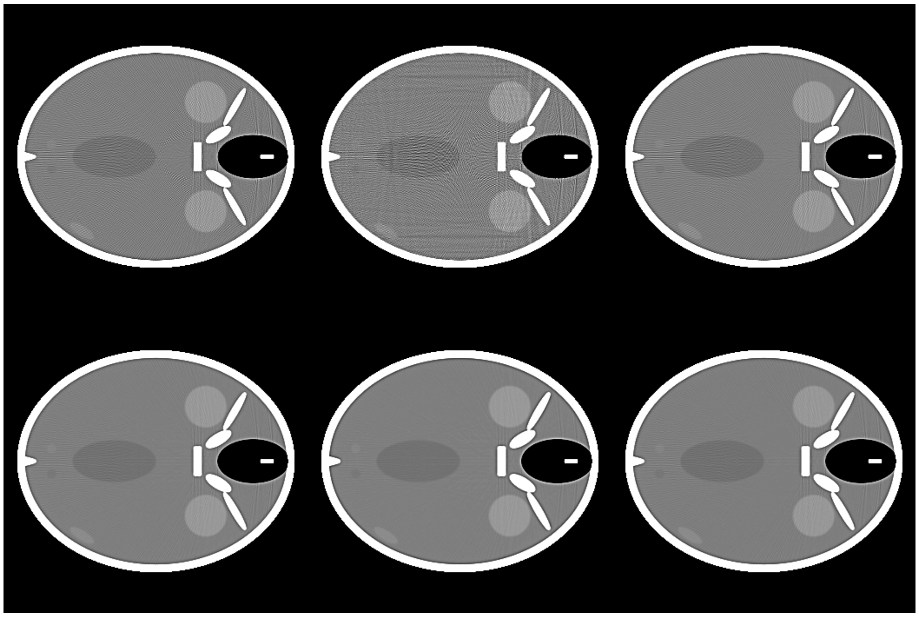

Fig. 1. Reconstruction using 250 iterations of the Landweber algorithm, using Joseph's method (top row, left image); using the B-splines of order $n = 0$ (top row, middle image), $n = 1$ (top row, right image), $n = 2$ (bottom rowm, left image) and $n = 3$ (bottom row, middle image); and using the blobs (bottom row, right image). Grayscale: [1,1.1].

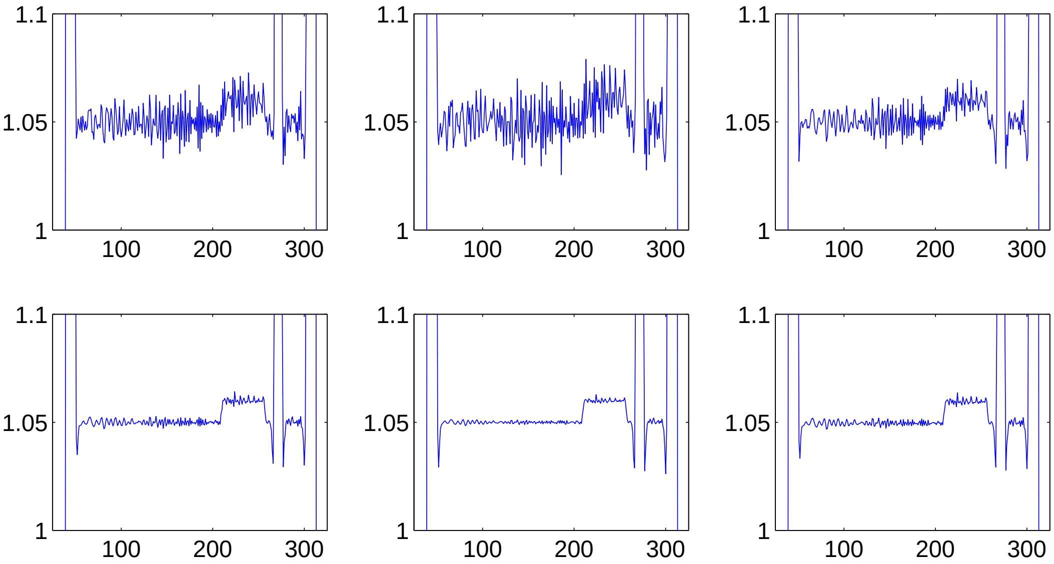

Fig. 2. Profile through the left eye for the reconstructions based on 250 iterations. Same arrangement is as in Fig. 1.

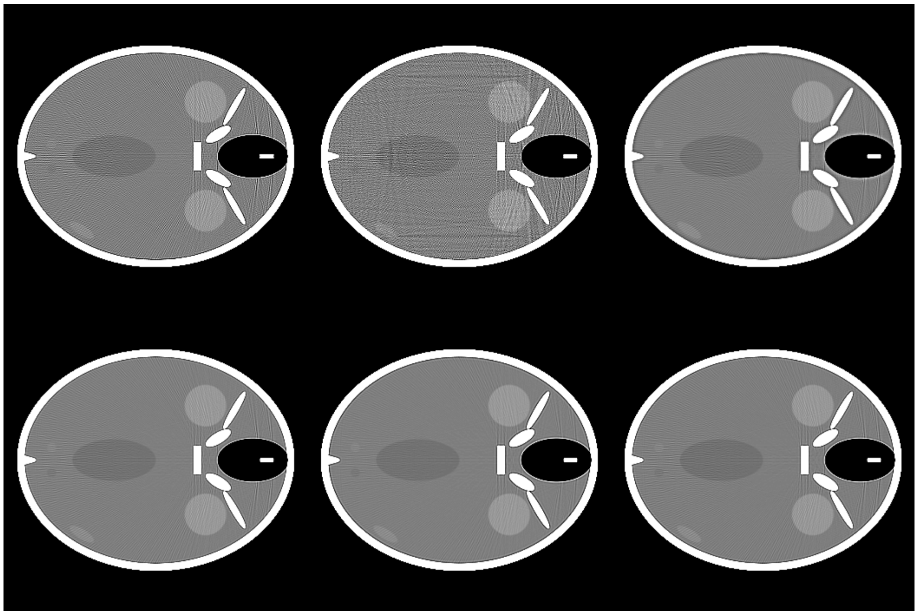

Fig. 3. Iterative reconstruction using 850 iterations of the Landweber algorithm. Grayscale: [1,1.1]. Same arrangement is as in Fig. 1.

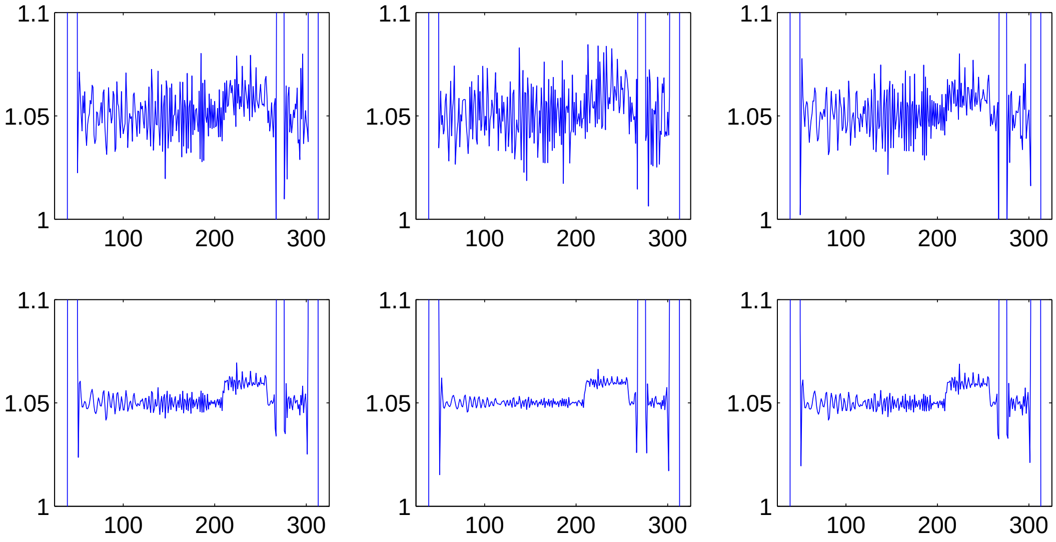

Fig. 4. Profile through the left eye for the reconstructions based on 850 iterations. Same arrangement is as in Fig. 1.

Visualizing the Segmentation Error of a Tomogram using the Residual Projection Error

Tom Roelandts, Kees Joost Batenburg and Jan Sijbers

Abstract—**Tomographic reconstructions are often segmented to quantify structure parameters. However, to our knowledge, no efforts have yet been made to visualize the accuracy of the segmentation result. This paper introduces a way to visualize the segmentation error, based on the residual projection error, which is the difference between the recorded data and the forward projection of the segmented tomogram. From the residual projection error, a segmentation error tomogram is reconstructed. This error tomogram allows to detect errors in the gray levels of the segmented tomogram, or to discriminate between reconstruction artifacts and actual features of the scanned object. The proposed technique is independent of the algorithms that were used to create and segment the tomogram.**

Index Terms—**Image segmentation, error reconstruction.**

I. INTRODUCTION

In many applications of tomography, the final tomographic reconstruction (the *tomogram*) must be segmented before the results can be analyzed. Segmentation amounts to the classification of image pixels into distinct classes, based on similarity with respect to some characteristic. Image segmentation is a well established field, and a range of methods has been developed, using diverse techniques such as global or local thresholding, region growing, and clustering [1], [2].

Most image segmentation methods are not specific towards the modality that was used to acquire the image. As a result, such methods do not exploit the raw data (X-ray radiographs in case of CT imaging) from which the image was reconstructed. Recently, global and local thresholding methods were proposed that do use the projection data to improve the selection of threshold parameters [3], [4]. In addition, reconstruction methods were recently developed in which the segmentation was directly incorporated into the reconstruction algorithm [5]–[8].

In this paper, the projection data is used to examine the *quality* of the segmentation. The proposed method assumes that the scanned object consists of homogeneous regions, and then determines how well a given segmentation represents that object. Moreover, the method can also be used to test for object homogeneity, since it generates large errors for non-homogeneous objects. The technique is independent of the reconstruction and segmentation algorithms.

The structure of this paper is as follows. In Section II, the method is introduced. Section III describes the simulation experiments that were performed to validate it. The results are discussed and a conclusion is reached in Section IV.

II. METHOD

The projection process in tomography can be modeled as a linear operator that is determined by the projection geometry. This leads to a system of linear equations,

$$\boldsymbol{W}\boldsymbol{x} = \boldsymbol{p}, \tag{1}$$

where $\boldsymbol{p} \in \mathbb{R}^m$ contains the projection data and $\boldsymbol{x} \in \mathbb{R}^n$ corresponds to the image. The linear operator is represented by the $m \times n$ matrix $\boldsymbol{W}$, the *projection matrix*. An approximate solution $\hat{\boldsymbol{x}} \in \mathbb{R}^n$ of (1) can then be computed, in practice often by minimizing some norm $\|\boldsymbol{W}\boldsymbol{x} - \boldsymbol{p}\|$. The image $\hat{\boldsymbol{x}}$ can then be segmented.

A segmentation method essentially partitions the pixels of an image into sets $Y_1, \ldots, Y_d$, where d is the number of classes (or gray levels) in the segmented image. Since we assume that the scanned object consists of homogeneous regions, the segmented image should have the same gray level for all pixels in a set Y_k. From $\hat{\boldsymbol{x}}$, we create a segmented image $\boldsymbol{s} \in \mathbb{R}^n$ by assigning a gray level $\rho_k \in \mathbb{R}$ to all pixels in a set Y_k, for each $k \in \{1, \ldots, d\}$. The values of $\rho_1, \ldots, \rho_d$ are not known a priori. Moreover, most of the segmentation algorithms that are commonly used, do not have these gray levels as an output. In such case, we use the mean of all pixel values in a class as an estimate,

$$\rho_k = \frac{1}{|Y_k|} \sum_{\hat{y} \in Y_k} \hat{y}, \text{ for each } k \in \{1, \ldots, d\}. \tag{2}$$

We now define the residual projection error. The segmented image $\boldsymbol{s}$ is forward projected to give $\boldsymbol{p_s} \in \mathbb{R}^m$, so $\boldsymbol{p_s} = \boldsymbol{W}\boldsymbol{s}$. The *residual projection error* $\boldsymbol{e} \in \mathbb{R}^m$ is then defined as

$$\boldsymbol{e} = \boldsymbol{p} - \boldsymbol{p_s}. \tag{3}$$

This projection error is then reconstructed by solving the system $\boldsymbol{W}\boldsymbol{y} = \boldsymbol{e}$, where $\boldsymbol{y} \in \mathbb{R}^n$ corresponds to the (unknown) error image. This results in an approximate solution $\hat{\boldsymbol{y}} \in \mathbb{R}^n$, the *reconstructed residual error*.

As mentioned in the introduction, this procedure does not depend on any particular reconstruction or segmentation algorithm. To create the segmented reconstructions, we use filtered backprojection (FBP), with a Ram-Lak filter, as an example of an analytical method. We use the simultaneous iterative reconstruction technique (SIRT) [9] as an example of an

---

This work was financially supported by the FWO (The Research Foundation - Flanders, Belgium) and by the NWO (the Netherlands Organisation for Scientific Research - The Netherlands, research programme 639.072.005).

Tom Roelandts, Kees Joost Batenburg and Jan Sijbers are with the IBBT-Vision Lab, University of Antwerp, Universiteitsplein 1, 2610 Wilrijk, Belgium.

Kees Joost Batenburg is with the Centrum Wiskunde & Informatica (CWI), Science Park 123, 1098 XG Amsterdam, The Netherlands.

Corresponding author: Tom Roelandts, E-mail: tom.roelandts@ua.ac.be.

iterative method. The reconstructions are globally thresholded using Otsu's method [10]. The residual projection error is reconstructed using SIRT.

III. SIMULATION EXPERIMENTS

All simulation experiments were performed on a square reconstruction grid of 512×512 pixels. Three *phantom images* were created, as shown in Fig. 1. The size of each phantom is 2048×2048 pixels. The phantoms are much larger than the reconstruction grid, to reduce the effect of the pixelation on the reconstructions.

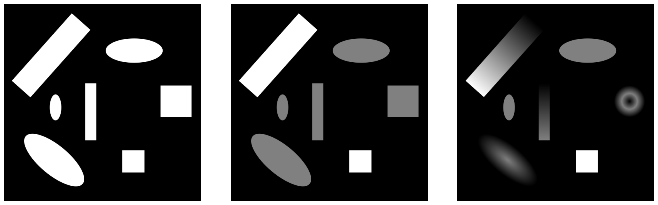

(a) Phantom 1 (b) Phantom 2 (c) Phantom 3

Fig. 1: Phantom images: (a) two gray levels, (b) three gray levels, (c) continuous grayscale.

A. Optimally Segmented Reconstructions

In the first simulation experiment, the residual projection error was reconstructed for a dataset with no noise and a large number of projections. This demonstrates the result of the proposed technique with minimal hindrance from reconstruction artifacts. From Phantom 1, which is a binary phantom, a synthetic dataset was created using 360 parallel beam projections, evenly spaced at 0.5° intervals. A detector with 512 pixels was used, to simulate the practical situation where the detector pixel size equals the width of the reconstruction grid. The "ideal" segmented reconstruction was approximated by binning Phantom 1 to a 512×512 grid, and then segmenting it using a threshold of 0.5.

The "ideal" segmented reconstruction was then forward projected, and the difference with the original projections computed. This results in the residual projection error, which was then reconstructed using 300 iterations of SIRT. Fig. 2a shows the result. The true error (Fig. 2b) was computed as the difference between the original phantom (Fig. 1a) and an upscaled version of the ideal segmented reconstruction. For comparison, the true error is shown downscaled to the same resolution as Fig. 2a. The true error is only nonzero at the edges of the different structures, where errors are unavoidable, since the original phantom is not pixelated at the size of the reconstruction. The reconstructed residual error (Fig. 2a) is very close to the true error.

B. Reconstructions with Homogeneous Regions

The second simulation experiment is based on Phantom 2 (Fig. 1b), which contains three gray levels. Reconstructions of Phantom 2 should consist of homogeneous regions, since the ground truth object is divided into several such regions (compare with Phantom 3 (Fig. 1c), where this is clearly not the case). From Phantom 2, a synthetic dataset was created using 90 parallel beam projections, evenly spaced at 2° intervals. A detector with 512 pixels was again used. This synthetic dataset was then reconstructed twice, once using FBP and once using 300 iterations of SIRT. These reconstructions were then segmented using Otsu's method. The final segmented reconstructions are shown in Fig. 3. Due to the relatively low number of projection angles, a number of streaks are visible, especially in the FBP reconstruction of Fig. 3a.

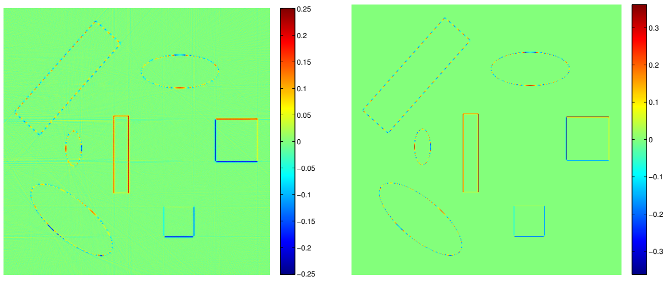

(a) (b)

Fig. 2: (a) Reconstructed residual error for Phantom 1. (b) True error for Phantom 1, at the resolution of Fig. 2a.

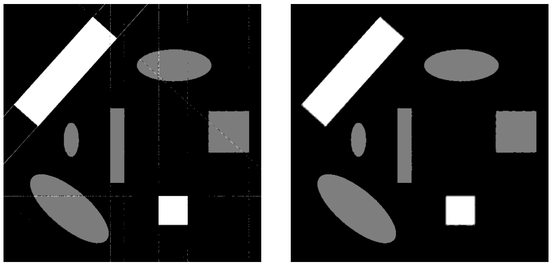

(a) FBP (b) SIRT

Fig. 3: Reconstructions of Phantom 2, segmented using Otsu's method.

The segmented reconstructions were then forward projected, and the difference with the original projections computed, resulting in the residual projection error. This was then reconstructed using 300 iterations of SIRT. Figs. 4a (FBP) and 5a (SIRT) show the result. For comparison, the true error is also shown, in Figs. 4b and 5b. As before, there seems to be a close correspondence between the reconstructed error and the true error. The streaks from the FBP reconstruction are clearly visible in the reconstructed residual error (Fig. 4a). Hence, the error tomogram can be used to discriminate between this type of artifact and actual features of the scanned object. Apart from these streaks, the largest errors are again situated at the edges of the different structures. Figs. 4a and 5a further suggest that the gray levels of the different objects are underestimated, since the error is clearly positive and relatively uniform inside the objects. This is also confirmed by the true error.

Table I shows this quantitatively. It contains an overview of a number of parameters that were determined from the reconstructions, while the true gray levels were taken from Phantom 2. The computed gray levels were determined from the segmented reconstructions (Fig. 3), from which they were

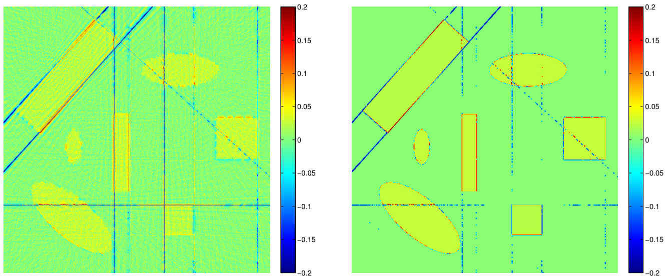

(a) (b)

Fig. 4: (a) Reconstructed residual error for the FBP reconstruction of Phantom 2. (b) True error for that reconstruction, at the resolution of Fig. 4a. The scales have been limited to $[-0.2, 0.2]$ to keep the smaller errors from disappearing.

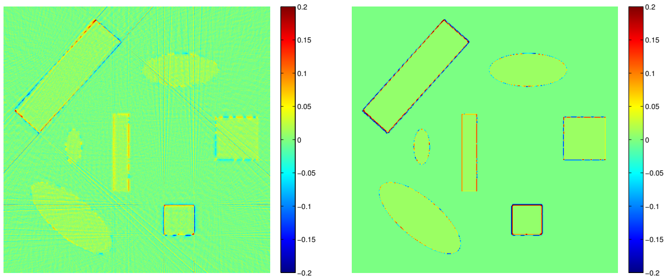

(a) (b)

Fig. 5: (a) Reconstructed residual error for the SIRT reconstruction of Phantom 2. (b) True error for that reconstruction, at the resolution of Fig. 5a. The scales have been limited to $[-0.2, 0.2]$ to keep the smaller errors from disappearing.

computed using (2). The gray level errors were computed from Figs. 4a and 5a, using the same procedure. To verify the accuracy of the gray level errors, the last lines for each algorithm in Table I show the corrected gray levels, i.e., the sum of the computed gray levels and the gray level errors. The last lines show that the gray level error is a good estimate of the difference between the true gray level and the computed gray level, and that it can be used to correct the computed gray level. This result could potentially be improved even further by recreating the reconstructed residual error, starting with a segmented reconstruction that uses the corrected gray levels.

TABLE I: Estimated and true gray levels, noiseless dataset.

Algorithm	Parameter	ρ_1	ρ_2	ρ_3
FBP	True gray level	0.000	0.502	1.000
	Computed gray level	−0.004	0.476	0.979
	Gray level error	0.003	0.018	0.017
	Corrected gray level	−0.001	0.494	0.996
SIRT	True gray level	0.000	0.502	1.000
	Computed gray level	0.002	0.491	0.994
	Gray level error	−0.002	0.010	0.009
	Corrected gray level	−0.000	0.502	1.002

We also ran these experiments with Poisson noise applied to the synthetic dataset. The results are shown in Figs. 6 and 7, and in Table II. The quality of the FBP reconstruction (Fig. 6a) has suffered more from the noise than that of the SIRT reconstruction (Fig. 7a). In the reconstructed residual error (Figs. 6b and 7b), the noise from the original projections is apparent. The results in Table II, however, are still largely comparable with those from Table I. This means that the gray level errors in Figs. 6b and 7b, which seem drowned by the noise, are still quite accurate when averaged. This implies that we can decide, from the reconstructions of the residual error in Figs. 6b and 7b, that the segmentation from Fig. 7a is more accurate than that from Fig. 6a.

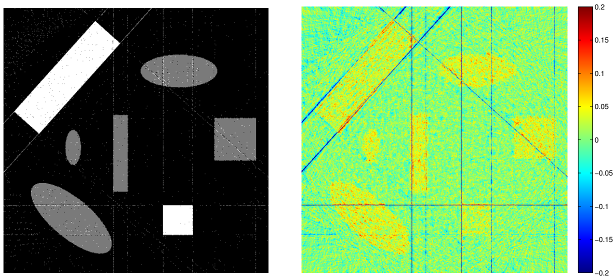

(a) (b)

Fig. 6: (a) FBP Reconstruction of Phantom 2, segmented using Otsu's method. Poisson noise was applied to the synthetic dataset. (b) Reconstructed residual error. The scale has been limited to $[-0.2, 0.2]$ to make it the same as in Fig. 4.

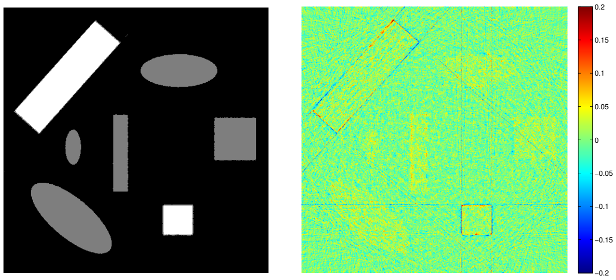

(a) (b)

Fig. 7: (a) SIRT Reconstruction of Phantom 2, segmented using Otsu's method. Poisson noise was applied to the synthetic dataset. (b) Reconstructed residual error. The scale has been limited to $[-0.2, 0.2]$ to make it the same as in Fig. 5.

TABLE II: Estimated and true gray levels, dataset with noise.

Algorithm	Parameter	ρ_1	ρ_2	ρ_3
FBP	True gray level	0.000	0.502	1.000
	Computed gray level	−0.006	0.467	0.979
	Gray level error	0.002	0.022	0.020
	Corrected gray level	−0.004	0.489	0.999
SIRT	True gray level	0.000	0.502	1.000
	Computed gray level	0.002	0.491	0.994
	Gray level error	−0.002	0.010	0.009
	Corrected gray level	−0.000	0.502	1.003

C. Reconstructions with Non-Homogeneous Regions

The last simulation experiment is based on Phantom 3 (Fig. 1c), in which some of the homogeneous objects of

Phantom 2 are replaced by objects with a continuously varying intensity. Reconstructions of Phantom 3 are not expected to consist of homogeneous regions, since the ground truth object is not a collection of such regions. From Phantom 3, a synthetic dataset was again created using 90 parallel beam projections, evenly spaced at 2° intervals. This synthetic dataset was reconstructed using FBP and SIRT, and segmented using Otsu's method. The result is shown in Fig. 8.

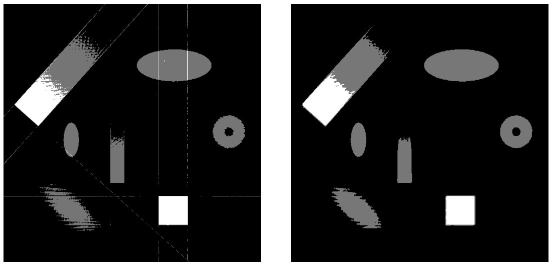
(a) FBP (b) SIRT

Fig. 8: Reconstructions of Phantom 3, segmented using Otsu's method.

As before, the residual projection error was computed and reconstructed using 300 iterations of SIRT. The result is shown in Figs. 9a (FBP) and 10a (SIRT). Both figures show that the reconstructed residual error is useful to discriminate between objects that can be reconstructed as a homogeneous region (the homogeneous objects from Phantom 3), and those that cannot (the objects with continuously varying intensity, which have large structured errors in Fig. 9a and 10a). The reconstructed residual error is again quite close to the true error (Figs. 9b and 10b).

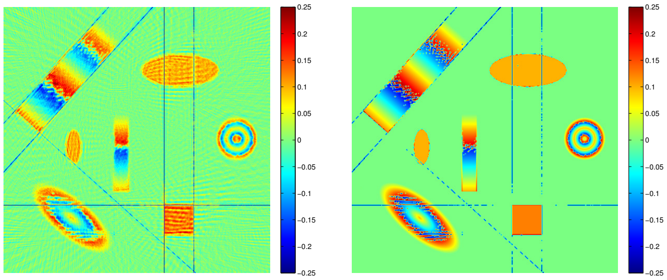

(a) (b)

Fig. 9: (a) Reconstructed residual error for the FBP reconstruction of Phantom 3. (b) True error for that reconstruction, at the resolution of Fig. 9a.

IV. Discussion and Conclusion

If tomograms are segmented without exploiting the projection data, which is often the case, the reconstructed residual error can still provide information on the quality of the segmentation.

The result for the ideal segmented reconstruction from Section III-A shows that the reconstructed residual error is a good approximation of the true error. For objects that consist of homogeneous regions, the experiments from Section III-B show that the proposed method can detect errors in the gray levels of the segmented reconstruction, even if those are quite small (Fig. 5), and in the presence of noise. The experiment from Section III-C shows that the technique can discriminate between homogeneous and non-homogeneous objects, without this knowledge being available a priori. Several experiments also show that artifacts that are visible in the segmented reconstruction, are also visible in the reconstructed residual error (e.g., Figs. 4a and 9a). Together, the simulation experiments demonstrate that the reconstructed residual error can be used as a visual map of the errors in the segmentation.

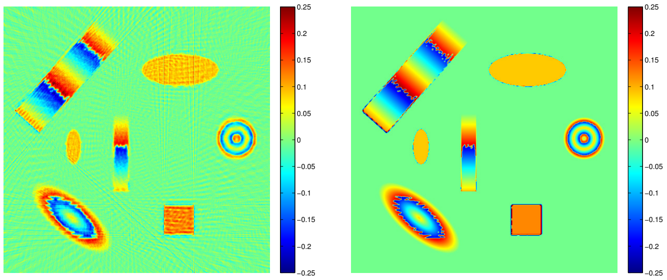

(a) (b)

Fig. 10: (a) Reconstructed residual error for the SIRT reconstruction of Phantom 3. (b) True error for that reconstruction, at the resolution of Fig. 10a.

Reconstructing the residual projection error is a simple way to visualize the segmentation error of a tomogram. The technique is trivial to implement, since the only necessary tools are a forward projector and a reconstruction algorithm. The computational cost is modest, since only a single forward projection and a single reconstruction are needed.

References

[1] N. R. Pal and S. K. Pal, "A review on image segmentation techniques," *Pattern Recogn.*, no. 9, pp. 1277–1294, 1993.

[2] D. L. Pham, C. Xu, and J. L. Prince, "Current methods in medical image segmentation," *Annu. Rev. Biomed. Eng.*, pp. 315–337, 2000.

[3] K. J. Batenburg and J. Sijbers, "Optimal threshold selection for tomogram segmentation by projection distance minimization," *IEEE Trans. Med. Imag.*, vol. 28, no. 5, pp. 676–686, 2009.

[4] W. van Aarle, K. J. Batenburg, and J. Sijbers, "Optimal threshold selection for segmentation of dense homogeneous objects in tomographic reconstructions," *IEEE Trans. Med. Imag.*, vol. 30, no. 4, pp. 980–989, 2011.

[5] K. J. Batenburg, S. Bals, J. Sijbers, C. Kübel, P. A. Midgley, J. C. Hernandez, U. Kaiser, E. R. Encina, E. A. Coronado, and G. Van Tendeloo, "3D imaging of nanomaterials by discrete tomography," *Ultramicroscopy*, vol. 109, no. 6, pp. 730–740, 2009.

[6] K. J. Batenburg and J. Sijbers, "DART: A practical reconstruction algorithm for discrete tomography," *IEEE Trans. Image Process.*, vol. 20, no. 9, pp. 2542–2553, 2011.

[7] T. Roelandts, K. J. Batenburg, and J. Sijbers, "PDART: A partially discrete algorithm for the reconstruction of dense particles," in *Proc. of the 11th International Meeting on Fully Three-Dimensional Image Reconstruction in Radiology and Nuclear Medicine (Fully 3D)*, Potsdam, Germany, 2011.

[8] T. Roelandts, K. J. Batenburg, E. Biermans, C. Kübel, S. Bals, and J. Sijbers, "Accurate segmentation of dense nanoparticles by partially discrete electron tomography," *Ultramicroscopy*, In Press, doi:10.1016/j.ultramic.2011.12.003.

[9] J. Gregor and T. Benson, "Computational analysis and improvement of SIRT," *IEEE Trans. Med. Imag.*, vol. 27, no. 7, pp. 918–924, 2008.

[10] N. Otsu, "A threshold selection method from gray-level histograms," *IEEE Trans. Syst., Man, Cybern.*, vol. 9, no. 1, pp. 62–66, 1979.

A Model-Based 3D Multi-slice Helical CT Reconstruction Algorithm for Transportation Security Application

Pengchong Jin*, Eri Haneda*, Charles A. Bouman*, Ken D. Sauer †
*School of Electrical and Computer Engineering, Purdue University, West Lafayette, IN 47907-0501
†Department of Electrical Engineering, University of Notre Dame, 275 Fitzpatrick, Notre Dame, IN 46556-5637

Abstract—**Multi-slice helical CT is widely used for baggage inspection in transportation security due to its fast acquisition speed and large scan coverage. In addition, recent studies indicate that model-based reconstruction has the potential to improve image quality and reduce artifacts relative to traditional filtered backprojection (FBP) method. In this paper, we present the results of a 3D model-based reconstruction algorithm on a multi-slice helical scan of actual baggage with high and low density objects, acquired on a medical CT system. We compared our reconstruction results to conventional FBP reconstructions and illustrated the potential value of our algorithm in terms of image quality and artifact reduction.**

I. INTRODUCTION

Computed tomography (CT) is widely used in transportation security applications [1], [2]. Among various CT scanner geometries, multi-slice helical CT has come into wide use due to its fast acquisition and large scan coverage. In fact, many airports have installed multi-slice helical CT systems as a central component of baggage screening. However, the more complex geometry of multi-slice helical CT also poses challenges in reconstruction. For example, as cone angles become wider, there is an increasing need to use true 3D reconstruction methods in order to avoid the image artifacts introduced by 2D approximations.

Moreover, the task in transportation security is quite different from the medical problem. In the medical application, it is critical to preserve fine details of soft tissue structure; however, in the security application, typically it is more important to obtain precise estimates of object boundary and its average density. Also, in security, the objects typically have densities that are substantially greater than water.

Recently, model-based reconstruction (MBR) algorithms have been shown to be effective in the reconstruction of multislice helical scan CT data [3]. These algorithms have the advantage that they can incorporate more detailed models of both the scanner and the objects being reconstructed. In addition, they offer flexibility in the application of transportation security since they allow for more accurate reconstruction for nontraditional geometries, such as with limited view data [4]. Model-based algorithms have the potential to more accurately account for a wide array of scanner characteristics including photon counting and electronic noise, beam hardening, metal attenuation and scatter, and the detector point-spread function. More accurate modeling of the scanner can be used to reduce streaking artifacts from high density objects, which arise in many CT applications. In addition, the MBR method incorporates a prior model that can be tuned to the characteristics of typical objects and the performance metrics of interest.

In this paper, we apply the methods of 3D model-based reconstruction (MBR) to the problem of transportation security imaging. Our approach is based on maximum a posterior (MAP) reconstruction along with the iterative coordinate descent (ICD) optimization method. We also describe how our algorithm can be parallelized on multicore processing hardware.

In our results, we present 3D MBR cross-sections from real multislice helical scan data of travel bags packed with a variety of high and low density objects, imaged on a medical scanner. Our results indicate that MBR has the potential to produce reconstructions with fewer artifacts than analytic reconstruction methods.

II. STATISTICAL MODEL FOR IMAGE RECONSTRUCTION

Let $x \in \mathbb{R}^M$ be the image vector, and let $y \in \mathbb{R}^N$ be the vector of projection measurements. We assume x and y are related by a linear sparse matrix operator A,

$$y = Ax \tag{1}$$

The matrix coefficient A_{ij} reflects the formation of i-th projection by j-th voxel.

In the Bayesian statistical framework, both x and y are considered as random, and the reconstruction is most commonly computed as the maximum a posterior (MAP) estimate given by

$$\hat{x} = \arg\min_{x \geq 0} \{-\log p(y|x) - \log p(x)\} \tag{2}$$

where $p(y|x)$ is the likelihood term corresponding to the forward projection model and $p(x)$ is the prior distribution of x. Also notice that we impose a positivity constraint on the image.

Given the image x, the received photon count λ_i of the i-th projection follows a Poisson distribution with mean $\lambda_{T,i} e^{-A_{i*}x}$ where $\lambda_{T,i}$ is the photon count of the i-th projection obtained in an air calibration scan. The line integral

---

This research was supported by ALERT DHS center Northeastern University.

of i-th projection can then be obtained by $y_i = \log\left(\frac{\lambda_{T,i}}{\lambda_i}\right)$. Using the second order Taylor expansion, the log likelihood term can be approximated by a quadratic function [5],

$$\log p(y|x) \approx -\frac{1}{2}(y - Ax)^T D(y - Ax) + c(y) \qquad (3)$$

where D is the diagonal matrix with diagonal elements $D_{i,i}$ which are proportional to the photon counts λ_i, and $c(y)$ is a term depending only on y. Notice that in this case, a smaller value of λ_i indicates that the associate projection is less heavily weighted.

The prior distribution $p(x)$ incorporates knowledge about the object being reconstructed, x. We will describe the prior model in detail in the next section.

III. METHOD AND ALGORITHM

A. 3D Forward Projection Model

To calculate the projection matrix A, we use the distance-driven (DD) model [6]. Figure 1 illustrates how the 3D projection geometry is decomposed into the z axis that falls along the object's translation direction, and the xy-plane, which is perpendicular to z [3]. Each voxel is flattened along the dimension most parallel to the detector, and the coefficient A_{ij} is calculated as the product of xy-plane projection, B_{ij}, and z-direction projection, C_{ij}.

$$A_{ij} = B_{ij} \times C_{ij} \qquad (4)$$

The coefficients B_{ij} and C_{ij} are calculated as the convolution of the detector response and the flattened voxel profile to yield

$$B_{ij} = \frac{\Delta_{xy}}{\Delta d_c \cos\tilde{\theta}} clip\left[0, \frac{W_c + \Delta d_c}{2} - |\delta_c|, \min(W_c, \Delta d_c)\right] \qquad (5)$$

$$C_{ij} = \frac{1}{\Delta d_r \cos\phi} clip\left[0, \frac{W_r + \Delta d_r}{2} - |\delta_r|, \min(W_r, \Delta d_r)\right] \qquad (6)$$

where W denotes the voxel's width when projected onto the detector, Δd denotes the detector width, subscript c and r denote channel and row respectively, θ and ϕ are the ray angles in xy-plane and z-direction, and $\tilde{\theta}$ is the adjusted ray angle defined by

$$\tilde{\theta} = \left(\theta + \frac{\pi}{4}\right) \ mod\ \frac{\pi}{2} - \frac{\pi}{4} \ . \qquad (7)$$

The function $clip$ is defined by $clip[a, b, c] = \min(\max(a, b), c)$.

B. Prior Model

We model the image x as a Markov random field, with a 26-point 3D neighborhood and the following distribution

$$p(x) = \frac{1}{z}\exp\left\{-\sum_{\{s,r\}\in\mathcal{C}} b_{s,r}\rho(x_s - x_r)\right\} \qquad (8)$$

where ρ is the positive and symmetric potential function and $\mathcal{C}$ is the set of all pairwise cliques.

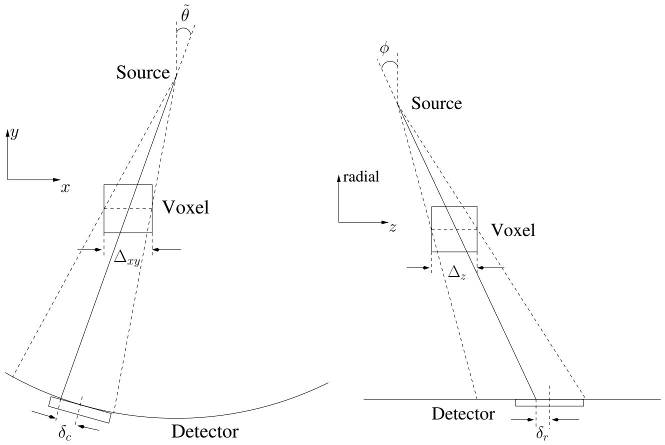

Fig. 1. 3D forward projection geometry used for the distance driven projector.

We studied two different potential functions, given by the l_1 norm prior, which is a special case of generalized Gaussian MRF (GGMRF) [7] when $p = 1$,

$$\rho(\Delta) = |\Delta| \ , \qquad (9)$$

and the q-generalized Gaussian MRF (q-GGMRF) [3].

$$\rho(\Delta) = \frac{|\Delta|^q}{1 + |\Delta/c|^{q-p}} \qquad (10)$$

The q-GGMRF allows more degrees of freedom to control both low-contrast and high-contrast edge characteristics. If $|\Delta| \ll c$, $\rho(\Delta) \approx |\Delta|^q$ and if $|\Delta| \gg c$, $\rho(\Delta) \approx |\Delta/c|^p$ where c is the parameter determining the transition between the two cases. Normally, we will set $q = 2$ and $1 < p < q$. It ensures the overall cost to be convex and, therefore, allows global convergence.

C. Optimization

The overall cost function, obtained by combining the approximate log-likelihood and the prior, is

$$\hat{x} = \arg\min_{x\geq 0}\left\{\frac{1}{2}\|y - Ax\|_D^2 + \sum_{\{s,r\}\in\mathcal{C}} b_{s,r}\rho(x_s - x_r)\right\} \qquad (11)$$

We solve this optimization problem using the iterative coordinate descent (ICD) algorithm [5] in which we scan over all voxels and sequentially optimize each voxel while fixing the others. In order to solve the 1D optimization problem resulting from each pixel update, we design a quadratic substitute functional $q(\Delta;\Delta')$ that upper bounds $\rho(\Delta)$ and optimize the cost with $\rho(\Delta)$ replaced by $q(\Delta;\Delta')$ [8]. In particular,

$$q(\Delta;\Delta') = \frac{\rho'(\Delta')}{2\Delta'}\Delta^2 \qquad (12)$$

where Δ' denotes the voxel difference before this update. In this way, the original 1D line search is converted into a quadratic optimization and the closed form solution can be derived. Since the substitute cost is always an upper bound of the original cost, minimizing the substitute will also produce a

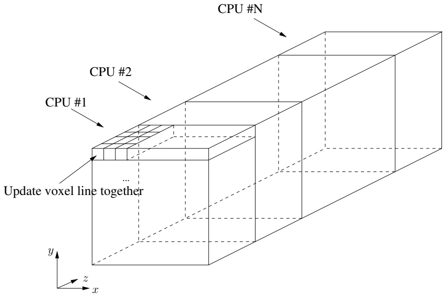

Fig. 2. Parallelized ICD scheme

decreasing sequence of original cost and iterative optimization will lead to the optimal solution of the original problem.

In order to further speed convergence, we also use the non-homogeneous ICD (NHICD) method of [8]. The idea is to focus computation on voxels which tend to generate significant updates. In NHICD, we alternated between a full scan and a partial scan which involves only those voxels which have significant updates at the previous iteration. This scheme provides a further speedup of approximately a factor of three.

D. Parallelization

To utilize multi-core processing and speed up the reconstruction for large image volumes, we implemented a parallelized ICD update scheme. In this scheme, the full image volume is cut into N boxes along the z-direction as shown in Figure 2 and each processor is responsible for updating voxels in one box. Different processors are synchronized once they finish the work; therefore, one synchronization is made per full scan. This will assign each processor a fairly large amount of work to do in parallel and workload is roughly balanced for different processors in order to reduce processor waiting time. Also, since the image is stored with the index in z-direction as the fastest-changing variable, the processors update voxels along z-direction first in order to create better cache efficiency. Moreover, the voxels being updated are selected to be far apart so that they do not share the same sinogram entry, and therefore, can be updated independently.

IV. RESULTS

In this study, we used scan data acquired on a medical scanner and provided by the ALERT (Awareness and Localization of Explosives-Related Threats) Center, at Northeastern University, to conduct our experiments. The reconstructed image is of size $512 \times 512 \times 840$ and the voxel width is 0.975 mm in cross-section in the xy-plane and the slice thickness is 1.25 mm in z-direction. Figure 3 illustrates some of the objects contained in the bag used in our experiment.

Figure 6 demonstrates the quality of different reconstruction algorithms. The FBP reconstruction is blurred, as we can see on the feet of the toy Mr. Potato Head in (a). The shape of some objects are distorted. For example, in the center of (a) and (b), the steel bar, which is of high density and supposed to be a rectangular shape, has been distorted. Also, we can see the severe streaking artifacts, such as the region around the high-density objects in (b). The model-based algorithms, on the other hand, provide better reconstructions. The overall image is sharper and shapes of objects are more accurately recovered. Moreover, the model-based algorithm reduces the structured artifacts as compared to the FBP method. These advantages suggest that the model-based algorithm has the ability to provide more detailed and accurate rendering, which could possibly lead to better detection performance.

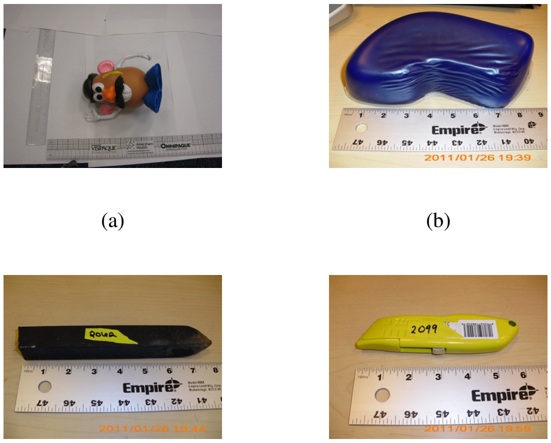

(a) (b)

(c) (d)

Fig. 3. Objects contained in the baggage (a) toy Mr. Potato Head (b) gel pad (c) steel bar (d) box cutter

We further quantify the reconstruction quality by measuring the noise variance on the uniform region. In Figure 4, a target object, which is a plastic bottle of water, is shown. The streaking artifact caused by the nearby high-density metal object can be easily identified in the FBP reconstruction. In Figure 5, we plot the CT voxel values along the line passing through the bottle of water vertically. We observe that the curve of the FBP reconstruction fluctuates more significantly than the curve of the other two model-based reconstructions. We further calculate the noise variances with different reconstructions along the line and the result is listed in Table I. The FBP reconstruction leads to the largest noise variance, which is the result of the streaking artifacts. It also shows that q-GGMRF gives the smallest noise variance. This is due to the fact that q-GGMRF has more smoothing effects than the l_1 norm prior.

TABLE I
NOISE VARIANCE ON UNIFORM REGION

Method	FBP	l_1 norm prior	q-GGMRF
Noise variance	3042.8	836.0	496.5

V. CONCLUSION

In this work, we developed a model-based image reconstruction algorithm and tested it on the data taken from actual

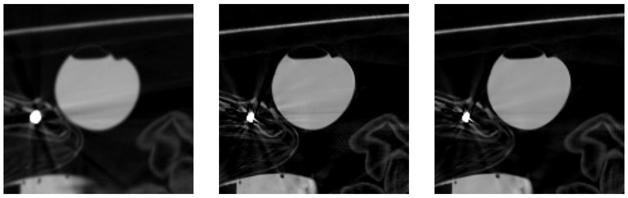

(a) (b) (c)

Fig. 4. Reconstructions zoomed to the target area using (a) FBP, (b) l_1 norm prior, and (c) q-GGMRF The round object is the plastic bottle of water.

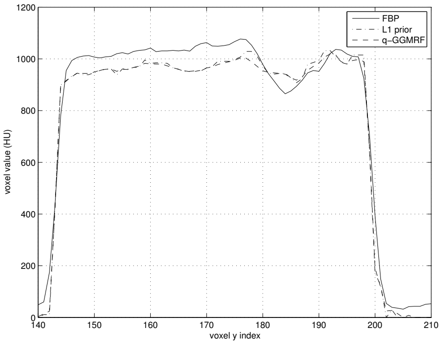

(a)

Fig. 5. CT values for voxels along the line through the center of the target region in Figure 4

baggage. Our algorithm depends on a statistical framework involving a forward model and a prior model. We compared our reconstructions using two different priors, l_1 norm prior and q-GGMRF prior, to the standard FBP algorithm. The model-based algorithms provide better reconstructions and reduce structured artifacts, which suggests potential advantages over the FBP approach.

REFERENCES

[1] R. C. Smith and J. M. Connelly, *Aspects of Explosive Detection*. Elsevier, 2009, ch. 7.

[2] Z. Ying, R. Naidu, and C. Crawford, "Dual energy computed tomography for explosive detection," *J. X-Ray Sci. and Tech.*, vol. 14, no. 4, pp. 235–256, 2006.

[3] J.-B. Thibault, K. Sauer, C. Bouman, and J. Hsieh, "A three-dimensional statistical approach to improved image quality for multi-slice helical CT," *Med. Phys.*, vol. 34, no. 11, pp. 4526–4544, 2007.

[4] S. J. Kisner, E. Haneda, and C. Bouman, "Limited view angle iterative ct reconstruction," in *Proc. SPIE*, vol. 8296, 2012, p. 82960F.

[5] K. Sauer and C. Bouman, "A local update strategy for iterative reconstruction from projections," *IEEE Trans. Signal Process.*, vol. 41, pp. 534–548, Feb. 1993.

[6] B. D. Man and S. Basu, "Distance-driven projection and backprojection in three dimensions," pp. 2463–2475, 2004.

[7] C. Bouman and K. Sauer, "A generalized gaussian image model for edge-preserving MAP estimation," *IEEE Trans. Image Process.*, vol. 2, pp. 296–310, 1993.

[8] Z. Yu, J.-B. Thibault, C. Bouman, K. Sauer, and J. Hsieh, "Fast model-based X-ray CT reconstruction using spatially non-homogeneous icd optimization," *IEEE Trans. Image Process.*, vol. 20, pp. 161–175, Jan. 2011.

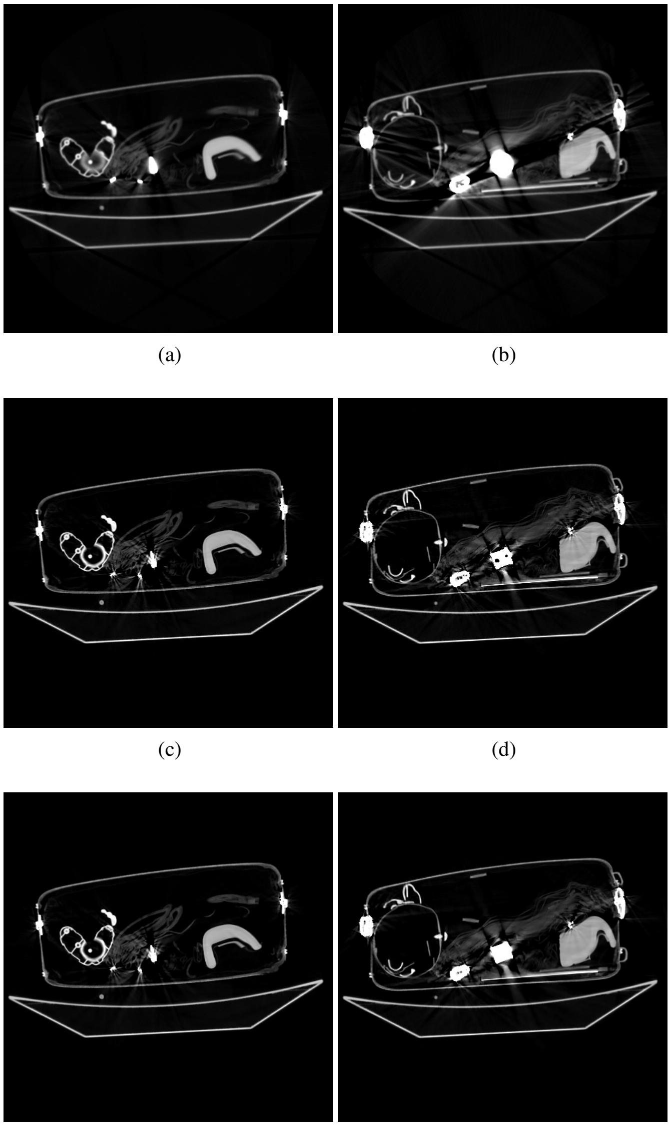

(a) (b) (c) (d) (e) (f)

Fig. 6. Reconstruction of the ALERT baggage security data using (a, b) FBP, (c, d) l_1 norm prior, and (e, f) q-GGMRF. The gray scale is in offset Hounsfield Unit (HU), where air $= 0$ HU and the scale range for all results shown is in $[0, 1600]$ HU.

Design of the Discrete Skew Geometry and Iterative Reconstruction of the MV3D Scanner

Andrew D. Foland

Abstract— Design considerations for airport security volumetric imaging scanners differ significantly from those for medical CT scanners, despite the much they have in common. We describe what drives these differences, then describe how we account for these considerations with a combination of an innovative "discrete skew" geometry and iterative reconstruction in the new L-3 MV3D security scanner product.

***Index Terms*— discrete skew, fixed-gantry, image reconstruction, iterative algorithms, national security**

I. Introduction

While medical CT scanners clearly share crucial overlap with airport security scanners, significant differences in the use considerations drive differences in design decisions. Security scanners face a variety of challenges relative to medical scanners that, from an engineering standpoint, cannot yet be considered as fully solved as medical engineering challenges [1]. These considerations may make security scanners a receptive ground for advanced applications in fully three dimensional reconstruction.

Medical scanners are designed primarily [1] for a tradeoff between cost and generally theoretically well-defined image quality metrics[2]. Security scanner design, on the other hand, must from the very start consider fiercer compromises among cost, "image quality", bag throughput, and target range with an important secondary focus on durability and maintainability. Complicating the design is that in security scanner design "image quality" cannot as easily be captured by a technically well-defined metric.

We describe how the skew geometry and the iterative volumetric reconstruction of the L-3 MV3D meets the design considerations.

II. Design Considerations

A. Microbombs Make Microexplosions

Many medical CT scanner designs are driven by spatial resolution, trying to detect ever smaller and smaller features. This is one area in which security scanners have an easier task than medical CT scanners. While a microcalcification might one day become a cancer [3], a minimum mass of ungrowing explosive is needed in order to pose a threat to an airliner. Furthermore, explosive materials must satisfy various geometrical requirements in order to actually detonate [4]. Fortunately, this minimum mass is sufficiently large that typical medical spatial resolutions of hundreds or even tens of microns are not required for detection of detonable threats. Similarly, because explosive threats are large enough to comprise many voxels, individual voxel density resolution is very much a secondary consideration, once density is averaged over all object voxels.

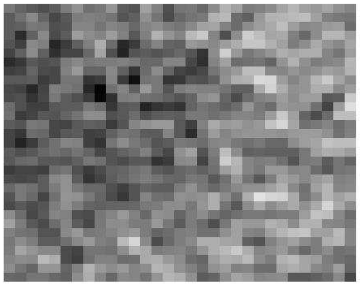

Fig. 1: The central region of a slice through a reconstruction of a bulk object of known constant density near water. The grayscale window is ±35 HU (70 HU total) around the known density. The scanner producing this reconstruction is certified to detect threats: voxel-to-voxel variation of tens of HU need present no barrier to security effectiveness.

Some of these issues are illustrated in fig. 1. The image is of the central region of a large bulk object of constant density. The image is taken from a machine that has passed regulator certification for threat detection. As the image shows, voxel-to-voxel variation of tens of HU need present no barrier to security detection, even if such variation might have more impact in a medical setting.

B. Patients Per Hour

A single one of the worlds largest airports, for instance Hart airport in Atlanta, can expect to process 200,000 bags or more on a typical day. Based on estimates of worldwide CT use [5], one recognizes that one single such airport already exceeds the *entire worldwide* daily use of medical CT scanners. In the United States, for every patient scanned by a medical CT, roughly 60 checked passenger bags undergo volumetric scans in airports. At the same time, only a tiny portion of the cost of a single few-hundred-dollar airline ticket can be dedicated to scanning costs. A medical CT scan typically charges thousands of dollars per patient. Given typical machine and maintenance costs, the hardware and maintenance cost per bag scan is generally held under one US dollar.

A.D. Foland is with L-3 Communications, Security and Detection Systems, Woburn, MA 01801 USA (phone: 781-939-3893; email andrew.foland@l-3com.com).

C. *Cancer Can't Take Countermeasures*

One unyielding challenge of security scanners is that the target list can be dynamic; and that the target can take countermeasures to any publicly revealed details. Cancer, on the other hand, cannot read specifications or patents. Machines are designed to robust to countermeasures, and regulators specifically test the machines against a variety of countermeasures. (This is why, for instance, MV3D images in this abstract may have been intentionally degraded to obscure our capabilities.)

This has led the security industry, in general, to rely on trade (and governmental) secrecy in design of its machines. This prevents some of the cooperation (such as cross-licensing [6]) that has been seen in the medical field.

D. *What's In a Bag?*

Medical targets consist largely of near-water organ and flesh materials, and bones, in relatively predictable configurations. Metal, while occasionally present as implants, is generally of lesser importance. Baggage contains significant metal content with probability near 1. Even unremarkable baggage contains a very wide array of materials and objects: clothing, shampoos, shoes, gels, small electronics, glass bottles, food, and books. Less usual but still commonplace are items such as golf clubs, ski equipment, prosthetic devices, cookware, power tools, and medical equipment.

E. *Who Makes the Call?*

The images produced by a medical CT scanner is generally reviewed by a radiologist or other highly-trained medical professional, who, with knowledge of patient history and possibly in consultation with other experts, can interpret the images and decide whether there is any threat. Security scanners, on the other hand, generally operate an "EDS" (explosion detection system) algorithm on a computing device that renders an automated decision . In general no other knowledge about the bag or passenger is known

F. *Are We There Yet?*

Security scanner quality is defined in the end solely by a largely binary regulator test. The test must demonstrate the ability to detect, with a challengingly high regulator-defined probability, threat objects, while maintaining at the same time a challengingly low false-alarm. The translation of technically well-defined measures into P_D / P_{FA} on the space of passenger bags is in general not straightforward. For instance, artifacts that a human radiologist might judge unacceptable are often easily overcome by automated detection algorithms, while issues a human eye easily recognizes can require considerable effort for an automated detection scheme to resolve.

G. *Baggage Handling*

The baggage handling systems where security scanners are installed are typically in exposed conditions on or near the runways, and must function over a wide range of temperatures. They must be unaffected by an unclean environment, running flat out for up to 20 hours a day. Due to the compact spaces into which they must fit, typical baggage handling- conveyor systems in airports must divert a suspect bag off of the main track within seconds of having been scanned. This enforces a very fast processing, reconstruction, and automated detection time on security scanning machine, measured in seconds.

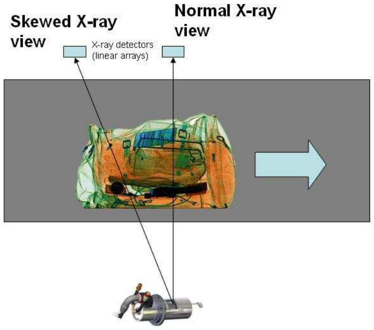

Fig. 2: A depiction of the skew-angle geometry used in the MV3D system. As the conveyor progresses forward, the skewed rays exiting the X-ray tube provide a radiograph taken from a different angle from the normal X-ray views.

III. DESIGN IMPLICATIONS

As described in [1], for most purposes, medical CT scanners can consider that they have reached a very good compromise between cost and the image quality metrics—which, for most medical machines, are the main considerations. While specialized medical machines may have other considerations[7]-[8], the specialization allows the CT engineer to define a narrowly focused design target [9].

Many of the foregoing considerations point towards the value of nonrotating gantries, with minimal moving parts and high throughput, for security machines. On the other side, rotating gantries are a well-proven technique that is known to be effective in security design, and nonrotating gantry machines must be judged against that record of success.

From an engineering perspective, a three-order-of-magnitude cost (per scan) differential also forces very different design considerations. Three design elements are key to meeting the cost goals: simplified operational controls, automated decision making, and low cost hardware. A limited number of commodity hardware items must be used.

IV. THE L-3 MV3D

A. *Device Overview*

The L-3 machine is a limited-angle, limited-view security scanner that iteratively reconstructs three-dimensional images of bags that pass through it on a conveyor. There has been considerable recent work on this kind of reconstruction over the past five years [11],[12]. Timely reconstruction is made possible by recent advances in computational hardware speed [13],[14], as well as by proprietary L-3 computational methods.

The geometrical freedom inherent in iterative reconstruction allows for a handful of fixed, unmoving, nonexotic sources, making use of "skew" views, to obtain bag information sufficient to reconstruct in three dimensions.

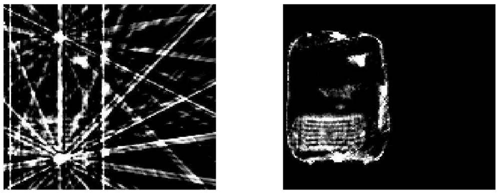

Fig. 3: A slice through a reconstruction of a bag. (Left) Filtered backprojection (see text for details). (Right) MV3D iterative volumetric algorithm with skew views reconstructing the same slice. The power of the MV3D skew geometry combined with iterative volumetric reconstruction is apparent. Note that image quality may have been intentionally degraded in the MV3D image.

The nonnecessity of a rotating gantry, and the simplicity of the X-ray tube sources, are key to meeting the cost challenges. Of course, reconstruction of such a geometry is flatly impossible using standard direct methods such as filtered backprojection [15] or cone-beam techniques [16],[17].

B. *Discrete Skew Tomography*

The patented L-3 geometry uses views oriented at a substantial angle to the direction of belt motion in order to obtain additional information about the bag volume. Though it is not perfectly analogous, in some ways it functions similarly to having a very large cone beam angle. A depiction of the geometry is shown in fig. 2. The skew angles in the MV3D are substantially larger than can be accommodated in any standard cone-beam algorithm[15],[16]. For this reason, and because no simple factorization of the volume into 2-D slices exists, we found the need for an iterative algebraic technique functioned on the entire 3D volume at once.

The skew geometry is chosen because it allows a single source to provide nonoverlapping information in multiple views as the bag passes. This is key to obtaining sufficient information to reconstruct the bag from a limited (and therefore cost-effective) number of sources.

The bag is reconstructed iteratively by forward-projecting the current volumetric density estimate into line integrals on each of the skew and normal view directions. This is done using a geometric model of the machine. The geometric model is modified by calibration measurements of the machine made *in situ* to account for registration imperfection.

After forward projection of the density distribution onto the view directions, the current estimate projection is compared (after suitable corrections) to the actual data measured in the projection. Differences are noted and used to produce an update to the estimate of the volumetric density. Many different update equations are possible and have been described in the literature [18]-[23].

As an example, letting k be the iteration number, x_j be the density in voxel j, b_i be the i^{th} measurement, and a_{ij} be a coefficient representing the geometric interaction of the i^{th} ray with the j^{th} voxel, a well-known update equation is:

$$x_j^{(k+1)} = x_j^{(k)} + \frac{\sum_i \left[a_{ij} \frac{b_i - a^T \cdot x^{(k)}}{\sum_j a_{ij}} \right]}{\sum_i a_{ij}}$$

In this SART equation [24], an average residual of the rays is additively projected back into the volume.

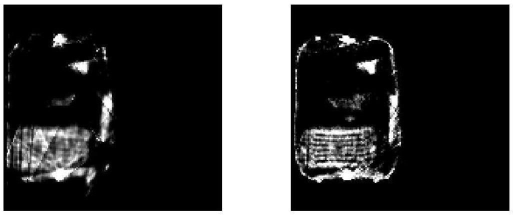

Figure 4: A slice through a reconstruction of a bag. (Left) Reconstruction of the bag using the MV3D volumetric iterative algorithm, but using only normal views and none of the skew view hardware. (Right) The MV3D reconstruction of the same slice, using all views (same as previous image.) Note that image quality may have been intentionally (but identically) degraded in these images.Comparisons left and right, and to previous image, allow isolation of relative contributions of skew view geometry and the MV3D iterative volumetric reconstruction technique.

The advantage of an iterative reconstruction, from the point of view of engineering constraint reduction, is that any computable set of a_{ij}'s may be employed. That said, the geometry cannot be wholly arbitrary. It must nonetheless be sufficient to provide reliable inversion of the Radon transform.

Limited-angle and limited-view machines can suffer from precisely this instability in transform inversion [11]. Regulation is often crucial in limited-angle and limited-view reconstructions, where the dimensionality of the volumetric space can exceed the dimensionality of the measurement space. Many different forms of regulation have been described in the literature [11],[25]-[30]. (Note that "compressed sensing" schemes [31] can be thought of as a form of implicit regulation.) L-3 considered numerous different forms of regulation before a final choice was made for the MV3D scanner.

C. *Design Process*

The L3 MV3D scanner geometry was designed in simulation first. The simulation used was a combination of GEANT4 [32], NIST tables [33], and discrete approximations to generate simulated detector readings from discretized phantoms. Over time, modules were added to modify the simulated readings to simulate other physics effects. The simulations were validated against data taken on existing L-3 scanners.

At the same time, L-3 engineers designed an iterative reconstruction engine that could read in simulated data in the same format expected to come from the scanner data, and render a reconstruction. In the design stage, the reconstruction is of the discretized phantom that was input to the simulation. For baggage reconstruction targets, we found exceedingly strong differences among the effectiveness of many standard forms of iterative schemes, both simultaneous and block iterative [18]-[23],[34]. We hypothesize this is due to the very wide dynamic range of relevant densities, and prevalence inside bags of large low-density voids. We also considered many possible forms of regulation [11],[25]-[31] in order to obtain the best possible image quality.

We were also able, with the simulation suite, to generate "data" for consideration of a wide array of geometries. Geometry considerations were number of sources and their tunnel bore. Combinations of geometry and algorithm were

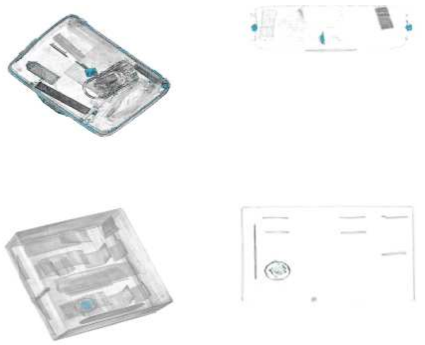

Fig. 5: Reconstruction examples of two bags. (Top) a mockup passenger bag, (Top Left) a 3-d volume rendering of the reconstruction (Top right) a transverse slice (Bottom) a mockup bag containing many sheet-like geometries. (Bottom left) a 3-d volume rendering of the reconstruction (Bottom right) a coronal slice through multiple of the slices, including a speaker cone. Note that image quality may have been intentionally degraded in these MV3D images.

evaluated for their ability to yield an acceptable reconstruction in the limited seconds alotted. We found significant variation in image quality with arrangement of the sources.

Many iterative algorithms work in a block-iterative or subset fashion [34],[35]. We (to our surprise) generally found negligible dependence of convergence speed on the subset ordering, even between a "worst" order and a widely-accepted near-optimal ordering choice [34].

D. Results and Images

As shown in the following figures, we get more than adequate results on even very challenging targets. In fig. 3 we show a comparison of a single slice of a volumetric reconstruction of a bag phantom. The MV3D reconstruction makes use of all skew angles. We also show a single-slice 2D filtered backprojection using limited in-plane sources, arranged around the bag as the geometry of the MV3D. The power of the MV3D approach is apparent.

In fig. 4 we show the same slice using an iterative reconstruction using only the normal (non-skew) views. The result is intermediate between the two results of fig. 3. This allows the reader to isolate the relative contributions of iterative reconstruction and skew view geometry.

In fig. 5 we show perspective renderings and selected slices of a reconstructed mockup bag and a multi-sheet phantom that presents sheets at many different positions and orientations.

We measure that the MV3D system achieves volumetric image quality comparable or superior to existing certified CT systems, when evaluated on a standard quantity such as PSF on standard phantoms.

EXPORT STATEMENT

This technical data is considered Technology Software Publicly Available (TSPA) as defined in Export Administration Regulations (EAR) Part 734.7-11.

ACKNOWLEDGMENT

A.D. Foland thanks the L-3 MV3D team, and M. Kachelriess, for assistance in preparation and review.

REFERENCES

[1] X. Pan, et al, "Why do commercial CT scanners still employ traditional, filtered back-projection for image recon?", Inv*erse Problems* **25** 2009.

[2] H.H Barrett and K. J. Myers, *Foundations of Image Science*, Wiley & Sons, Hoboken, NJ, 2004.

[3] E.Y. Sidky, et al "Enhanced imaging of microcalcifications in digital breast tomosynthesis" *Med. Phys.* **36** 4920, 2004.

[4] M. Marshall and J.C. Oxley, eds "Explosives: the threats and the materials", in *Aspects of Explosives Detectors*, Elsevier, 2009.

[5] D.J. Brenner and E.J. Hall "Computed Tomography - An increasing source of radiation exposure." *N. Engl. J. Med.* **357**:2277-2284, 2007.

[6] C. Crawford, personal communication.

[7] E.Y. Sidky and X. Pan, "In-depth analysis of cone-beam CT image reconstruction*", IEEE Med. Im. Conf. Rec.*, Dresden, M10-358, 2008.

[8] A. Wunderlich and F. Noo, "Image covariance and lesion detectiblity in fan-beam computed tomography", *Phys. Med. Biol.*, vol. 53, 2471 2008.

[9] C.E. Metz, "ROC methoed. in rad. imaging", Inv. Rad. 21 720, 1986.

[10] G. Moore, "Cramming more components on ICs", Elec. 38 18, 1965.

[11] E.Y. Sidky, et al, "Accurate image recon. from few-views and limited-angle data in divergent-beam CT", *J. X-Ray Sci. Tech.* 14 119, 2006.

[12] S. J. LaRoque, E. Y. Sidky, and X. Pan, "Accurate image reconstruction from few-views and limited-angle data in divergent-beam CT", *J. Opt Soc Am.A* 25 1772, 2007.

[13] M. Kachelriess, M. Knaup, and O. Bockenboch, "Hyperfast parallel-beam and cone-beam backprojection using the cell general-purpose hardware", *Med. Phys*., 34 1474 2007.

[14] F. Xu and K. Mueller, "Real-time 3D computed tomographic reconstruction w. commodity hardware", *Phys Med Biol*, 52 3405 2007.

[15] H. Turbell, *Cone Beam Reconstruction Using Filtered Backprojection*, PhD thesis, Linkoeping University, 2001.

[16] L. A. Feldkamp, L.C. Davis, and J.W. Kress, "Practical Cone-beam algorithm", *J. Opt. Soc. Am*, A1 612, 1984.

[17] A. Katsevich, "Theoretically exact FBP-type inversion algorithm for spiral-CT" SIAM J. Appl. Math, 62 2012, 2002.

[18] R. Gordon, et al, "Algebraic Reconstruction Techniques for 3-D electron microspcopy and X-ray photography", J. Theor. Biol. 29 471, 1970.

[19] D.C. Youla and H. Webb, "Image restoration by the method of convex projections: Part I-theory", IEEE Trans. Med. Imaging, 1 81, 1982.

[20] Y. Censor and S. A. Zenios, Parallel optimization-Theory, Algorithms, and Applications, Oxford University Press, Oxford, 1997.

[21] A.P. Dempster, N.M. Laird, and D.B. Rubin, "Max. likelihood from incomplete data via the EM algorithm", J. Roy. Stat. Soc. B39 1, 1977.

[22] K. Lange and R. Carson, "EM reconstruction algorithms for emission and transmission tomography", J. Computed. Ass.Tom. 8 306, 1984.

[23] J.A. Fessler and A. Hero, "Sapce-alternating generalized expectation-maximization algorithm", IEEE Trans Sig. Proc. 42 2664, 1994.

[24] Kak and Slaney, "Principles of Computed Tomography"

[25] E. Y. Sidky and X. Pan, "Image recon. in circular cone-beam CT by constrained, total-variation minimization", Phys Med. Biol. 53 2008.

[26] R. Chartrand, "Exact reconstruction of sparse signals via nonconvex minimization", IEEE Signal Process. Lett., 14 707 2007.

[27] G.H. Chen, J. Tang, and S. Leng, "Prior image constrained compressed sensing (PICCS)", Med. Phys., 35 660, 2008.

[28] J. Song, et al, "Sparseness prior based iterative image reconstruction for retrospectively gated cardiac micro-CT", Med Phys 34 4476 2007.

[29] A. H. Delany and Y. Bresler, "Globally convergent edge-preserving regularized reconstruction", IEEE Trans. Image Proc., 7 204 1998.

[30] W.H. Press, S.A. Teukolsky, W. T. Vetterling, B.P. Flannery, "Numerical Recipes in C", Cambridge Univ. Press, Cambridge, 1992.

[31] E.J. Candes and M.B. Wakin, "An introduction to compressive sampling", IEEE Signal Process. Mag. 25 21, 2008.

[32] A. Agostinelli et all, "G4-a simulation toolkit, NIM A506 250, 2003.

[33] J.H. Hubbell and S. M. Seltzer, "Tables of X-ray mass coefficients and mass-energy absorption coefficients", NISTIR 5632**,** National Institute of Standards and Technology, Gaithersburg, MD (1995).

[34] H.Hudson, and R. Larkin, "Accelerated Image Reconstruction using ordered subsets of projection data", IEEE Tran. Med. Im. 13 601, 1994.

[35] S. Sra and J. A. Tropp, "Row-action methods for compressed sensing", in ICASP 2006 Proceedings 3, 2006.

Ray-weighted constrained-conjugate-gradient tomographic reconstruction for security applications

Jeffrey S. Kallman and Stephen G. Azevedo

Abstract—**Computed tomography (CT) reconstruction of objects in luggage is affected by surrounding clutter, which can contribute artifacts such as streaking and beam hardening. We have been investigating a constrained conjugate gradient (CCG) algorithm for CT reconstruction. We have found that the time required to perform each iteration of the CCG can be reduced by a factor of 10 or more by using an approximation to the error in the minimization line search. We have also found that ray weighting can alleviate streak artifacts.**

Index Terms—**Gradient methods, Least squares methods, Reconstruction algorithms, X-ray tomography**

I. INTRODUCTION

COMPUTED tomography (CT) reconstruction of many objects of interest is affected by surrounding clutter. The clutter may contribute scatter, beam hardening and photon starvation [1]. This case is particularly important in security applications such as checked baggage scanning, where quantitative data are used to decide whether a bag contains a threat. Clutter can significantly alter the reconstructed attenuation of a material or create false alarms. Iterative reconstruction techniques offer a number of possible ways to alleviate many of these environmental effects, including incorporation of prior knowledge, regularization and weighting of rays.

An example of environmental effects is shielding, which occurs when a highly-attenuating material blocks many of the projections of a less attenuating material. An example of this effect is a steel bar lying across a bottle of jelly in an airport bin (Fig 1). If reconstructed using filtered back-projection [2] (as in 1a), beam hardening and photon starvation make the bar appear hollow and some of the streaks in air have higher image intensity than the jelly. The streaks in the jelly change its mean attenuation. Many of the effects of shielding can be alleviated by using a ray-weighted iterative reconstruction (as in 1b).

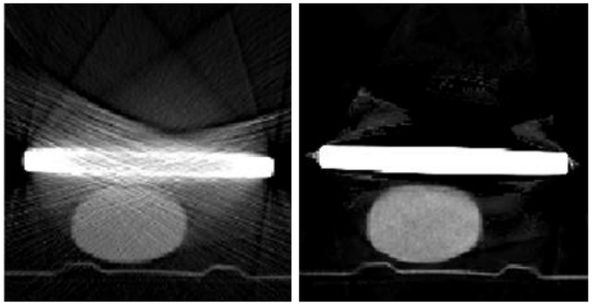
(a) (b)

Fig. 1. (a) Filtered backprojection reconstruction of a steel bar lying over a bottle of jelly in an airport bin. Note that the streaks in empty air have points of higher intensity than the jelly, blur the space between the bar and the jelly, and that the bar appears to be hollow. (b) Ray-weighted iterative reconstruction. Note that the streaks have been diminished, there is a clear separation between the jelly and the bar, and the jelly is more uniform.

Scatter, beam hardening and photon starvation act to change the x-ray features of materials in luggage. If a particular set of features is used for explosive detection, these changes require enlarging the regions of feature space where it is necessary to raise an alarm and thus increase the false alarm rate (Fig 2). The goal of our iterative reconstruction work is to show that the effects of containers and concealment can be reduced.

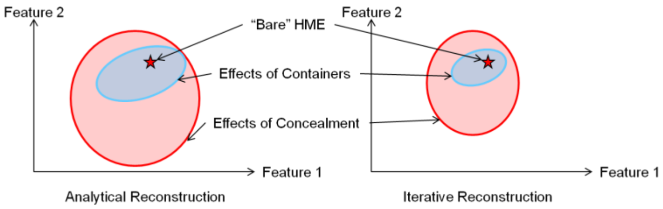

Fig. 2. The goal of our iterative reconstruction work is to show a reduction in the size of the feature space where an alarm must be raised. Features may include x-ray attenuation coefficients, effective atomic number, density, texture, etc. "Bare" is the object scanned as is without clutter.

One of the drawbacks of iterative reconstruction techniques is the amount of computer memory and time they require. We have been examining acceleration techniques for constrained conjugate gradient reconstruction and have found that using an approximation to the error can

Manuscript (LLNL-JRNL-560413) received June 12, 2012. This work performed under the auspices of the U. S. Department of Energy by Lawrence Livermore National Laboratory under Contract DE-AC52-07NA27344. This work was funded under DHS Interagency Agreement HSHQPM-10-X-00034/P00002.

J. S. Kallman is with the Lawrence Livermore National Laboratory, Livermore, CA 94551 USA: 925-423-2447; (e-mail: kallman1@ llnl.gov).

S. G. Azevedo is with the Lawrence Livermore National Laboratory, Livermore, CA 94551 USA (e-mail: azevedo3@llnl.gov).

accelerate the reconstruction by more than an order of magnitude.

The purpose of this work is to report on our results to date using a ray-weighted constrained-conjugate-gradient iterative reconstruction technique.

II. RECONSTRUCTION ALGORITHM

A. *High Level Overview*

We first generate a model to fill space. This model may be comprised of blobs, regular voxels, or pieces (if we have prior knowledge of the object to be scanned). We determine the interaction of the model with all the rays and prune those parts of the model that are un-attenuating. The reconstruction approach we use is to minimize the mean-square error function of the model for all attenuated rays. We use the adjoint method to find the gradient of the error function for every voxel [3]. This gradient is used in a constrained conjugate gradient algorithm [4] to determine the search direction for error minimization. An iteration of the method consists of:

- For each ray:
    - Execute the forward model,
    - Determine the mismatch between the forward model and the data,
    - Distribute the error gradient to the parts of the model that interact with the ray.
- Generate an appropriate direction given the error gradient, regularization, and the previous descent direction.
- Perform line minimization to find the minimum error in the chosen direction.
- If the error is small enough, exit, otherwise perform another conjugate gradient iteration.

B. *Adjoint Method as a Source of the Gradient*

We use the adjoint method on the one dimensional ray equation to determine the error function gradient for the voxels along the ray. We represent position along the ray by s, modeled intensity along the ray at any point by *I(s)*, and modeled attenuation at any point along the ray by $\mu(s)$. The initial intensity of the ray is given by $I(0) = I_0$. The one dimensional equation for intensity along the ray is

$$\frac{dI}{ds} + \mu(s)I(s) = -I_0\delta(s) \tag{1}$$

where in this case $\delta(s)$ is a Dirac delta function. We define the error functional of the attenuation distribution as

$$E[\mu(s)] = \frac{1}{2}\left[I(s_{final}) - I_{obs}(s_{final})\right]^2 \tag{2}$$

where s_{final} is at the detector and I_{obs} is the detected intensity.

We want the gradient of the error with respect to the modeled attenuation distribution. This gradient, when integrated with the variation in the attenuation, gives the variation of the error:

$$\Delta E[\mu(s)] = \int \nabla E(S)\Delta\mu(s)ds \tag{3}$$

here the Δ indicates variation. The variation of the ray equation is given by

$$\frac{d\Delta I}{ds} + \mu(s)\Delta I(s) + I(s)\Delta\mu(s) = 0 \tag{4}$$

and the variation of the error is given by

$$\Delta E[\mu(s)] = \left[I(s_{final}) - I_{obs}(s_{final})\right]\Delta I(s_{final}). \tag{5}$$

The forward ray equation represents forward projection through the model. The adjoint ray equation describes the backward projection of the error between the model and the observed data:

$$-\frac{d\tilde{I}}{ds} + \tilde{I}(s)\mu(s) = -\tilde{S}(s) \tag{6}$$

where the source term $\tilde{S}(s)$ is, in effect, an initial condition:

$$\tilde{S}(s) = \left[I(s_{final}) - I_{obs}(s_{final})\right]\delta(s - s_{final}) \tag{7}$$

and thus the variation of the error is given by

$$\Delta E[\mu(s)] = \int \tilde{S}\,\Delta I ds = \int \left[-\frac{d\tilde{I}}{ds} + \tilde{I}(s)\mu(s)\right]\Delta I ds. \tag{8}$$

Using the identity

$$\Delta I\frac{d\tilde{I}}{ds} = -\tilde{I}\frac{d\Delta I}{ds} + \frac{d}{ds}(\tilde{I}\Delta I) \tag{9}$$

and realizing that we can disregard the right hand term of (9) because it is zero at the endpoints, we find (8) becomes

$$\Delta E[\mu(s)] = -\int \left[\frac{d\Delta I}{ds} + \Delta I(s)\mu(s)\right]\tilde{I}ds. \tag{10}$$

Substituting (4) into (10) yields a form of the variation of the error from which we can easily extract the gradient:

$$\Delta E[\mu(s)] = \int I(s)\tilde{I}(s)\Delta\mu(s)ds = \int \nabla E(s)\Delta\mu(s)ds. \tag{11}$$

The gradient is thus

$$\nabla E(s) = I(s)\tilde{I}(s). \tag{12}$$

Evaluating the Gradient Along a Ray

Given the gradient of the error as a function of position along the ray, how do we evaluate it? For simplicity, assume a uniform attenuation distribution, $\mu(s) = \mu$. Over the course of the forward projection, the intensity at any position is then:

$$I(s) = I_0 e^{-\int \mu(t)dt} = I_0 e^{-\mu s}. \tag{13}$$

Suppose the result of the forward projection is not the same as the observed intensity. The difference is the initial condition on the back projection. Over the course of the back projection, the intensity at any position is:

$$\tilde{I}(s) = \left[I(s_{final}) - I_{obs}(s_{final})\right]e^{-\mu(s_{final} - s)} \tag{14}$$

and the resultant product at any position is

$$I(s)\tilde{I}(s) = \left[I(s_{final}) - I_{obs}(s_{final})\right]I(s_{final}). \tag{15}$$

Equation (15) holds for any distribution of attenuation along the ray for the simple attenuation model.

Evaluating the Gradient Along a Ray for a Voxel

If the attenuation distribution to be found is represented by the sum of *N* basis functions $\phi_i(s)$ with weightings p_i

$$\mu(s) = \sum_{i=1}^{N} p_i\phi_i(s) \tag{16}$$

then the finite-dimensional gradient is given by

$$\frac{\partial E}{\partial p_i} = \int I(s)\tilde{I}(s)\,\phi_i(s)ds = I(s_{final})\tilde{I}(s_{final})P_i \tag{17}$$

where P_i is the projection of the ray through the basis function.

Evaluating the Total Gradient for a Voxel

We extend the error for a ray to the error over the entire reconstruction as follows:

$$E[\mu(\vec{r})] = \frac{1}{2}\sum_{m=1}^{M} w_m\left[I_m\left(s_{final}\right) - I_{m,obs}\left(s_{final}\right)\right]^2 + \beta \iiint \sqrt{\nabla\mu(\vec{r})\cdot\nabla\mu(\vec{r})}\,d^3r \tag{18}$$

where m is the ray index, β determines the balance between the pure error term and the total variation regularization term, and w_m is used to weight the rays. The gradient for the ith voxel is then

$$\nabla E(\vec{r}_i) = \sum_{m=1}^{M} w_m\, I_m\left(s_{final}\right)\tilde{I}_m\left(s_{final}\right)P_{i,m} - \beta\,\frac{\nabla^2\mu(\vec{r}_i)}{\sqrt{\nabla\mu(\vec{r})\cdot\nabla\mu(\vec{r})}} \tag{19}$$

where $P_{i,m}$ is the projection of the mth ray through the ith voxel.

C. Model Pruning

In many cases there are regions of the model that are intersected by rays that are un-attenuated. It is a waste of computational resources, and a potential source of error, to let those parts of the model affect the calculation. The way we determine which parts of the model to eliminate is to count both the number of ray interactions that each part of the model experiences as well as the number of those interactions that occur with un-attenuated rays.

If the number of un-attenuated interactions is greater than a chosen ratio of the total number of interactions (we use 0.25), then that piece of the model is eliminated. One problem that we have encountered is defining the threshold for an un-attenuated ray.

D. Approximate Error

One of the most time-consuming steps of many descent methods, for example the conjugate gradient algorithm, is the search for the minimum in the descent direction. This can involve tens of evaluations of the forward model and error function for the problem. For even a modest problem involving 1000 rays in 1000 views interacting with approximately 1000 voxels apiece, there are on the order of 1e9 multiply-adds per forward modeling and error evaluation.

There is a long history in the conjugate gradient solver community of trying to cut computational effort by using inexact line searches [5,6,7]. In all of these efforts the line search is stopped before it finally converges. Another way of using these results is not to stop the line search before it converges, but to use an approximation to the error. If we take a random sample of the set of all rays for each conjugate gradient iteration and use that to approximate the behavior of the error in the minimization step, we can cut the computational effort significantly. The approximate error we use is the squared error of a random subset of the rays that have at least 0.1% mismatch between the modeled ray intensity and the detected ray intensity. The actual value of the approximate error does not matter as long as the minimum of the approximate error occurs near the minimum of the true error (as defined in [5], [6], and [7]). One full forward model and error computation must be performed before the line search in order to generate the gradient for the entire problem. This cuts the computational effort of the line search down to less than two full evaluations of the forward model (and resultant error) and consequently speeds the algorithm by a factor of between 10 and 40 times.

The problems we have observed using this technique are that close to the converged solution it becomes difficult to select an appropriate set of rays with which to approximate the error. At this point it is reasonable to switch to the full error conjugate gradient. Depending on when this switch occurs it may significantly reduce the time savings of the method. Another drawback is that the same data will yield different results depending on which random sets of rays are used in the line searches. This drawback can be alleviated by switching to the full error minimization as the problem nears convergence.

E. Ray Weighting

One of the strengths of iterative methods is that rays can be weighted in importance. A ray that is heavily attenuated will have more Poisson noise and be more sensitive to scatter and beam hardening. By adjusting the weights of the rays we can incorporate our knowledge of these noise sources. In [8] a case is made for weighting by the ray transmission, I_{obs}/I_0. We examined two ray weighting policies:

$$w_m = \left(\frac{I_{obs}}{I_0}\right)^p \tag{20}$$

which weights a ray by the transmission to a power p, and

$$w_m = \frac{1}{2} + \frac{1}{\sqrt{\pi}}\int_0^{s\left(\frac{I_{obs}}{I_0}-x\right)} e^{-t^2}dt = \frac{1}{2} + \frac{1}{2}erf\left(s\left(\frac{I_{obs}}{I_0} - x\right)\right) \tag{21}$$

which weights rays by a sigmoidal function, erf, centered around x with a sharpness s. These weighting policies are illustrated in Fig. 3.

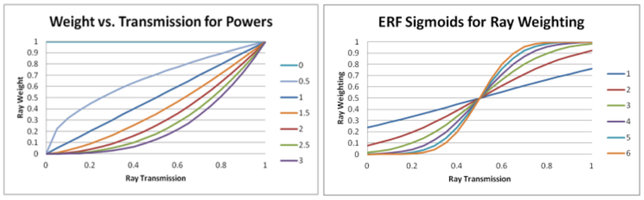

(a) (b)

Fig. 3. (a) Ray weighting by powers of transmission. Each curve represents the weighting by transmission to a different power. (b) Ray weighting by a sigmoidal function of ray transmission. Here $x = 0.5$ is fixed and each curve illustrates the effect of a different s.

We use the situation of the bar of steel suspended over the container of jelly (Fig. 1.) as our sample problem. One metric for performance is the difference between the mean jelly attenuation in this situation as compared to the mean jelly attenuation when it is scanned alone (bare) in a bin. Another metric is the flatness of the attenuation along the length of the steel bar. For this problem we are not using regularization, so $\beta = 0$. In this situation we have found that ray weighting by powers of transmission yields better results than ray weighting by sigmoidal functions. This is illustrated by Figs. 4-9. In Figs. 5-9 attenuation is measured in Livermore Modified Hounsfield Units (LMHU) which assigns the attenuation of air to 0 and water to 1000.

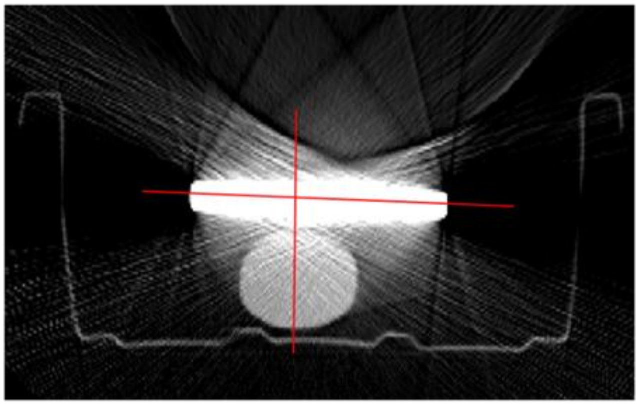

Fig. 4. Lineouts taken along steel bar and through bar and jelly to determine the performance of the reconstruction as a function of ray weighting.

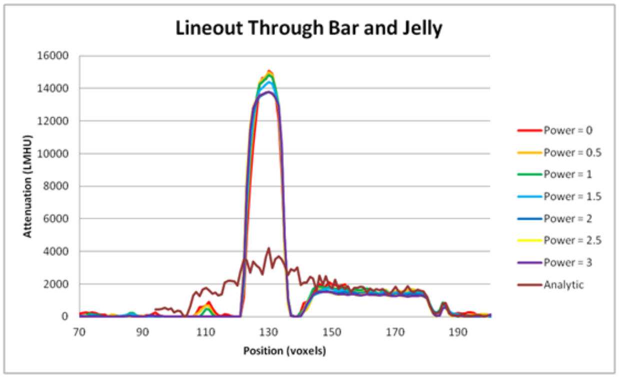

Fig. 5. Lineouts through steel bar and jelly for analytic and iterative reconstruction with transmission power ray weighting.

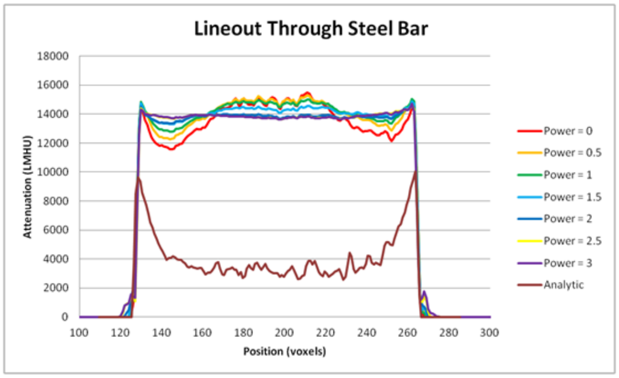

Fig. 6. Lineouts through steel bar for analytic and iterative reconstruction with transmission power ray weighting.

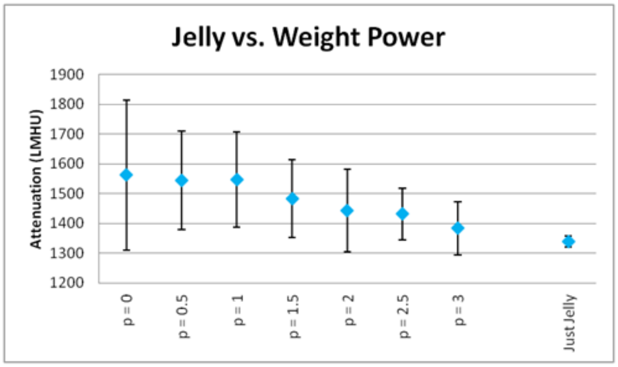

Fig. 7. Mean and standard deviation of jelly as a function of transmission power ray weighting compared to jelly alone (bare) in an airport bin.

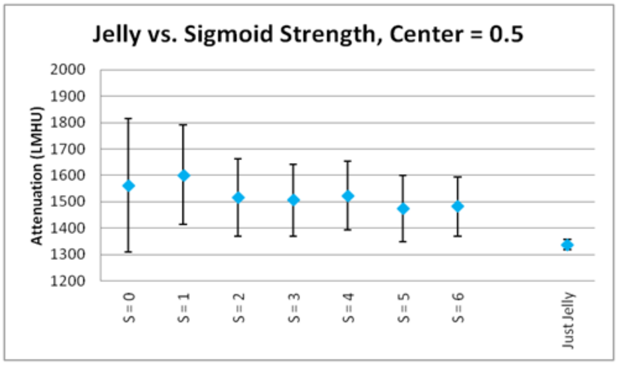

Fig. 8. Mean and standard deviation of jelly as a function of the strength of sigmoidal ray weighting. The center of the sigmoid was chosen to be 0.5.

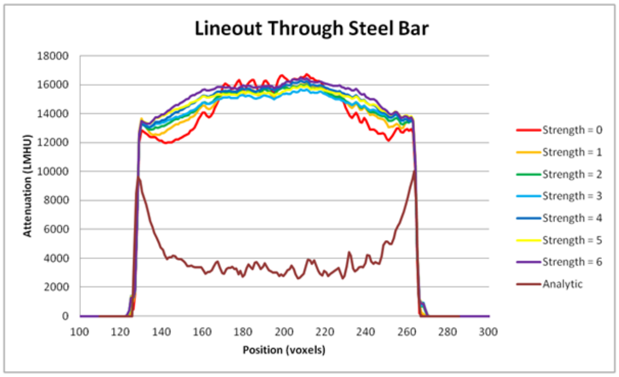

Fig. 9. Lineouts through steel bar for analytic and iterative reconstruction with signoidal power ray weighting. The sigmoidal center was set at 0.5 while the strength was varied.

III. FUTURE WORK

There are several directions for future work. We now need to apply these techniques to a wide variety of data to determine when they are applicable and whether the effects of containment, clutter and concealment can be reduced in the feature spaces that automatic threat detection are performed in.

ACKNOWLEDGMENT

We are grateful for the flexibility of the conference organizers in allowing us to get our paper in post-deadline.

REFERENCES

[1] G. Wang, D. L. Snyder, J. A. O'Sullivan, and M. W. Vannier, "Iterative Deblurring for CT Metal Artifact Reduction," IEEE Trans. Med. Imaging., vol. 15, no. 5, pp. 657-664, October 1996.

[2] A. C. Kak and M. Slaney, *Principles of Computerized Tomographic Imaging*, IEEE Press, New York 1988.

[3] S. J. Norton, "Iterative inverse scattering algorithms: Methods of computing Frechet derivatives," J. Acoust. Soc. Am., vol. 106, no. 5, pp. 2653-2660, Nov. 1999.

[4] D. M. Goodman, E. M. Johansson and T. W. Lawrence, *Multivariate Analysis: Future Directions,* C. R. Rao, editor Elsevier Science Publishers, 1993, pp. 209–232.

[5] P. Wolfe, "Convergence Conditions for Ascent Methods," SIAM Review, vol. 11, no. 2, pp. 226-235, April 1969.

[6] M. L. Lenard, "convergence Conditions for Restarted Conjugate Gradient Methods with Inaccurate Line Searches," Mathematical Programming, vol. 10, pp. 32-51, 1976.

[7] D. F. Shanno, "On the convergence of a new conjugate gradient algorithm," SIAM J. Numer. Anal., vol. 15, no. 6, pp. 1247-1257, Dec. 1978.

[8] K. Sauer and C. Bouman, "A Local Update Strategy for Iterative Reconstruction from Projections," IEEE Trans. Sig. Proc., vol. 41, no. 2, pp. 534-548, Feb. 1993.

Automatic Segmentation of CT Scans of Checked Baggage

David F. Wiley, Deboshmita Ghosh, and Christian Woodhouse

Abstract—**We adapted our novel segmentation method, called Stratovan Tumbler, to automatically segment objects from CT scans of checked baggage at airports. Our segmentation method handles problems with CT scans such as streaking and noise and is able to make difficult splitting and merging decisions for touching objects. Our methodology produces an object hierarchy describing the relationship of baggage objects to one another that can be used during the explosive detection stage in airport security for the purpose of identifying threats. The main benefits of our method are (i) tolerance of CT reconstruction artifacts, (ii) works well on objects of any shape, and (iii) can handle both homogeneous and heterogeneous materials.**

Index Terms—**Segmentation, Automatic object segmentation, Computed tomography, Baggage screening, Airport security, Automated threat recognition, Explosive detection**

I. INTRODUCTION

EXPLOSIVE detection in airport security involves automatically analyzing x-ray computed tomography (CT) scans of checked baggage [6]. The goal of this detection process is to identify possible explosive material signatures within baggage contents prior to their being transported on a plane. The detection process involves numerous steps, with one possible step being that of image segmentation to delineate individual objects, such as a bottle of liquid, so that object characteristics can be extracted and fed into a threat recognition system to determine whether or not the object matches an explosive signature [5]. The challenge in this environment is that x-ray CT scans inherently suffer from image quality problems such as low-resolution, noise, poor contrast, and streaking artifacts to name a few. These problems adversely affect the segmentation step by, for example, incorrectly merging touching objects or by splitting an object into too many pieces to the extent that extracted characteristics are compromised to the subsequent explosive detection step.

We adapted a medical segmentation technology called Stratovan Tumbler [7] to the problem of delineating objects from CT scans of checked baggage. Tumbler is a flexible region-growing segmentation method which delineates objects irrespective of shape, topology, and orientation. We made no assumption in object shape, type, density, or composition in an effort to develop a robust system that could automatically delineate most objects. The result of this effort is Stratovan Decorum, a software tool for automatically delineating and analyzing objects from CT scans of baggage. Our work in this area was initiated by the Department of Homeland Security and focuses on improving segmentation of all objects above a minimum intensity threshold, 500 modified Hounsfield units (MHU), where water is calibrated at 1000 MHU [1].

II. TUMBLER SEGMENTATION

A. *Overview*

Tumbler uses a kernel that virtually moves in three dimensions in a flood-fill manner. The kernel starts inside the object and iteratively moves outward until it meets the object's boundary. Tumbler can also simulate the outside-inward process with proper setup.

Our algorithm begins by defining the kernel shape and size, and positioning it inside the object being segmented. We move the kernel outward in a flood-fill fashion while the newly traversed voxel intensities continue to satisfy predetermined criteria (e.g., mean value is above some threshold). The size and shape of the kernel prevents it from escaping through holes in ill-defined boundaries.

B. *Process Details*

We implement the Tumbler process by:

1. **Defining a 3D kernel**: in most cases, a sphere suffices. The kernel is always smaller than the object to be segmented and bigger than any expected holes in the object's boundary.
2. **Determine movement criteria**. Each time the kernel moves, we pre-compute the minimum, maximum, mean, and standard deviation **{min, max, mean, std}** of the "to be" traversed voxels. Based on these parameters, one must determine the criteria required to decide whether or not to accept or reject the new position. This can be as simple as comparing the mean value to a constant threshold or more complicated as needed.
3. **Choose a start location**. This can either be done manually or by some automatic process. Once established, the

---

Manuscript received June 15, 2012. This work was funded by the Northeastern University ALERT program under the CT Segmentation Initiative.

D. Wiley is the founder and CEO of Stratovan Corporation, Sacramento, CA 95826, USA (phone: 916-813-7233; e-mail: wiley@stratovan.com).

D. Ghosh is with Stratovan Corporation, Sacramento, CA 95826, USA (email: dghosh@stratovan.com).

C. Woodhouse is with Stratovan Corporation, Sacramento, CA 95826, USA (email: woodhouse@stratovan.com).

neighboring voxel coordinates and direction of movement from the current position *{i, j, k, dir}* are placed in a queue that drives the flood-fill process.

4. **Flood-fill process**:
    a. Remove a position from the queue and compute the **{min, max, mean, std}** values of the voxel intensities.
    b. Compare the **{min, max, mean, std}** to the criteria established in Step 2 and decide whether these new voxels are acceptable or not.
    c. If not acceptable, do nothing more. If acceptable, move the kernel to this new position, mark all voxels covered by the kernel as the "object," and add all of its non-traversed neighbors to the flood-fill queue.
    d. Repeat Step 4a.
5. **Completion**. The process stops when the flood-fill queue is empty. The voxels traversed by the kernel represent the object.

This process is illustrated in Fig. **1**.

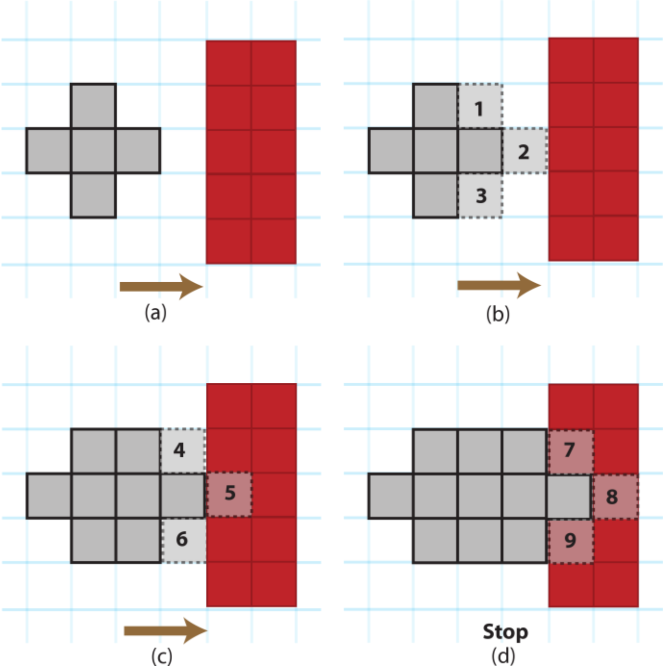

Fig. 1. Illustration of the Tumbler process. In each image, red pixels indicate the object's boundary while the white pixels indicate the object. Image (a) shows the initial condition having a "+" shaped kernel, as indicated by the gray pixels. Image (b) shows that to move the kernel one position to the right, pixels 1, 2, and 3 must satisfy some predetermined criteria; such as their average value must be below some threshold. Assuming that this criteria is met, image (c) indicates the completed move and tries another by evaluating the intensity values of pixels 4, 5, and 6. Assuming that the average of these intensity values continues to satisfy the guiding criteria, image (d) indicates the completed move and now evaluates the average intensity of pixels 7, 8, and 9. In case (d) we find that the average value is now above our threshold, preventing further movement to the right. (The algorithm would then continue in the remaining directions.)

C. *Algorithm Variables*

Parameters that control the Tumbler process are:

- **Kernel size and shape**. A bigger kernel is more tolerant to noise but can consume fine detail internal to an object and at its boundary. A smaller kernel results in better detail but is susceptible to noise and, if objects are touching, the flood-fill process can spill into neighboring objects. The rule of thumb is that the kernel must be smaller than the object of interest yet bigger than any holes in its boundary.
- **Start position**. The tumbler kernel must start inside an object of interest. Choice of start location within the object can affect segmentation results in some cases and must be evaluated on a case-by-case basis during segmentation training in order to determine optimal starting position requirements.
- **Guiding criteria**. Each object of interest must be evaluated to determine acceptable parameters for **{min, max, mean, std}** voxel intensities. This information constrains the flood-fill movement of the kernel at each iteration.
- **Voxel spacing**. Tumbler performs better with near uniform voxel spacing. Additionally, Tumbler performs substantially better with a kernel larger than a single voxel. The spacing between each voxel imposes a lower bound on the kernel size and ultimately on the smallest extracted objects. Resampling data to a finer resolution can, in some cases, better identify thin objects.

D. *Adapting Tumbler to Aviation Security*

Our focus during the project period with the Northeastern University ALERT CT Segmentation Initiative was to develop a fully automated system for segmenting baggage scans. This involved automating various steps and refining techniques used at various stages to improve segmentation quality. These improvements are described in the following sections.

1) *Algorithm Automation*

We devised methods for automatic selection of Tumbler parameters in order to automatically analyze baggage scans:

Kernel Shape and Size: We were able to devise a robust method for automatically choosing a kernel size for any point within a CT scan. This is important since we must choose a kernel size that is smaller than the object being delineated yet larger than any expected holes in the object boundary. We were able to determine kernel size (1-, 2-, 3-, or 4-mm radius sphere) based on an analysis of image gradient near each voxel, which implies the amount of "clutter" at any given point. More clutter demanded a smaller kernel while less clutter permitted a larger kernel since the surrounding area represented a relatively homogeneous region.

Start Position: We were able to devise an ordering method for each voxel to choose seed points for starting each object delineation process. We found that considering the following circumstances enabled the automatic determination of seed point priority:

- Run large kernel sizes first and smaller sizes last.
- Run high-intensity voxels first and low-intensity voxels last.
- Start in the middle of objects rather than on the edges.

- Increase the priority of voxels within "thin" objects, since thins objects tended to be sorted last, but we still needed to delineate them.

Guiding Criteria: We setup a training process for determining guiding criteria used when moving the kernel from one voxel to the next. Initially, this consisted of choosing minimum and maximum thresholds that bounded the mean intensity computed from the kernel when placed at each seed point (i.e., choosing 0.98*mean and 1.02*mean for the minimum and maximum thresholds, respectively). We were able to mature this process by manually improving errant segmentations (by either increasing or decreasing the thresholds) and adding each improvement to a central training file which eventually replaced our initial, crude estimate. We fit a polynomial function to the training points while considering mean intensity, standard deviation, minimum intensity, maximum intensity, and gradient information within the kernel as placed at the seed location. The trained polynomial was then used to automatically determine guiding criteria at any voxel location within the CT scan. Furthermore, we tracked error metrics associated with the training function to maintain integrity of the system. In general, we found that the training process converged quickly with minimal to no un-intended side effects as training points were added. In total, we used just over seventy training points from around twenty training bags.

2) *Splitting*

We found that our method works rather well at splitting objects into distinct and relatively homogeneous parts. We also found that our training process converged quickly when correcting splitting errors and was able to separate almost any touching objects if there existed a gradient boundary between them. Also, in many cases, *our system is able to separate touching objects when there does not exist a gradient boundary*. This is possible with our multi-voxel kernel since the larger kernel does not slip through the touching region. By manipulating the kernel size and the guiding criteria we are able to separate touching objects, for example, a lotion and gel pad, as shown in Fig. **2**.

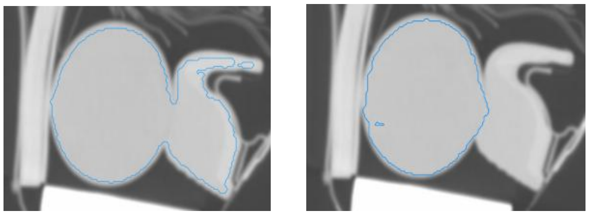
(a) (b)

Fig. 2. Segmentation result of two touching objects (bottle of lotion and gel pad) with kernel radius 2mm (a) and 4mm (b). By using a larger kernel we are able to identify the slight gradient boundary between the two objects, as indicted by the blue outline.

3) *Merging*

Our process tends to split objects into relatively homogeneous parts. For example, a cell phone is split into its internal electronics, plastic case, leather case, and belt buckle. This introduces the problem of *object philosophy*. The object philosophy problem is simply: how does one represent something like a cell phone in their segmentation results: *Is it a single object or is it multiple component parts?*

By determining a tree hierarchy that defines how each part relates to the others, the object philosophy problem is averted since a cell phone exists both as component parts and a single composite object depending upon how one traverses the parts tree.

We computed a hierarchical representation of segmented parts by evaluating overlap between each delineated part and *merging* two parts in our tree that meet certain criteria. (We initially based this decision on whether two parts overlapped by 10% or more voxels which worked well for most cases.) Our merging process takes advantage of a side-effect of our Tumbler segmentation which results in overlapping object segmentations, as indicated by the arrows in Fig. **3**.

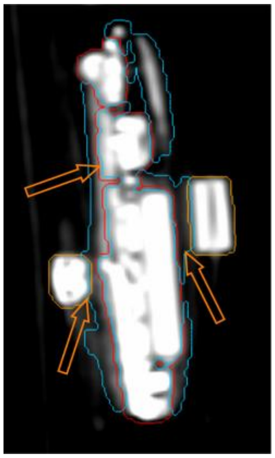

Fig. 3. Segmentation of a cell phone into overlapping component parts: internal electronics, plastic case, belt buckle, etc. Arrows indicate overlapping voxels between parts implying connectedness.

Fig. **4** shows the merged components of a candle (wax inside a metal container with lid) and a camera tripod (constituting over forty individually segmented parts).

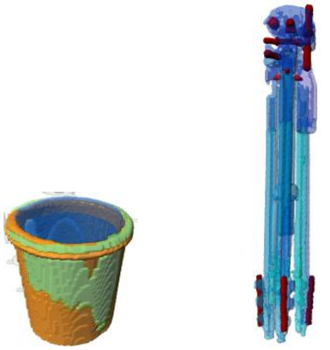
(a) (b)

Fig. 4 Results of our merging process on a candle (a) and a tripod (b).

III. RESULTS

We tested our software on over thirty baggage CT scans provided to us by the Northeastern University ALERT CT Segmentation Initiative [1]. Each scan was captured on a medical grade CT scanner and had a resolution of 0.98 x 0.98 x 1.29 mm with water calibrated at a value of 1000 MHU.

Our Tumbler segmentation method is effective in delineating many different kinds of objects from CT scans of baggage. Bulk or homogeneous objects such as a bottle of water, honey, rubbing alcohol, hydrogen peroxide, nylon phantom, and rolls of tape are generally composed of a single material. We are able to segment nearly all objects in this category accurately, as shown in Fig. **5** and Fig. **6**.

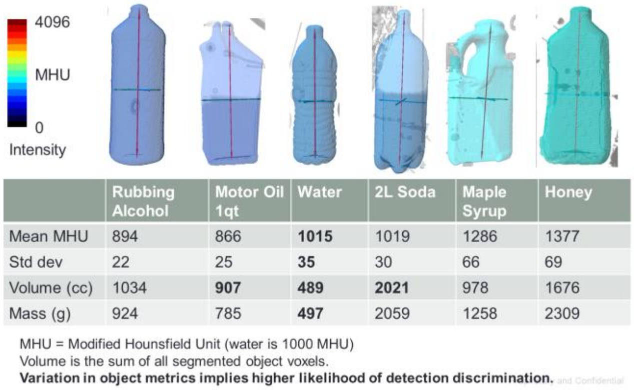

	Rubbing Alcohol	Motor Oil 1qt	Water	2L Soda	Maple Syrup	Honey
Mean MHU	894	866	**1015**	1019	1286	1377
Std dev	22	25	**35**	30	66	69
Volume (cc)	1034	**907**	**489**	**2021**	978	1676
Mass (g)	924	785	**497**	2059	1258	2309

MHU = Modified Hounsfield Unit (water is 1000 MHU)
Volume is the sum of all segmented object voxels.
Variation in object metrics implies higher likelihood of detection discrimination.

Fig. 5. Segmentation result of liquids with varying intensities. Examples include bottles of rubbing alcohol, motor oil, water, honey, soda, maple syrup, and honey. The mean intensities, volume, and mass are computed from our segmentation results.

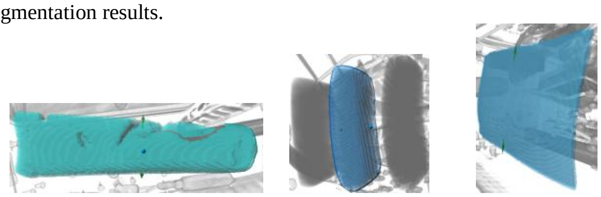
(a) (b) (c)

Fig. 6. Segmentation results of (a) toothpaste, (b) soap and (c) rubber sheet. We are able to delineate all objects that are generally composed of a single material with reasonably well defined boundaries (even if these objects are touching other objects).

We are able to easily separate touching objects since we use a large kernel size allowing us to effectively detect ill-defined object boundaries (i.e., the touching region even when there is no gradient boundary between objects).

In the case of heterogeneous objects, including cell phones, laptops, hard drives, etc., we delineate the components parts of the object and merge those together into a parts tree describing the connectedness of the parts (see Fig. **4** and Fig. **7**).

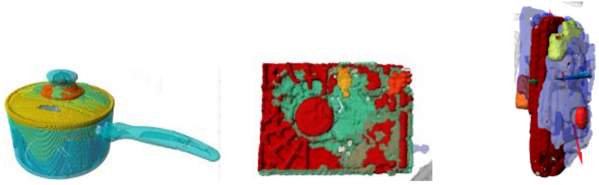
(a) (b) (c)

Fig. 7. Segmentation results of (a) metal pot with lid, (b) harddrive and (c) cell phone. Objects that are composed of heterogeneous parts (i.e., materials of different density) are delineated as separate parts and later combined in the merging step.

Thin objects with low intensity are poorly represented by CT due to lower contrast at the lower intensity. Sometimes these objects touch high-intensity objects like the neoprene sheet sitting on top of a Costco package of 48 AA batteries in Fig. **8**, which destroys the gradient boundary information making it challenging for any segmentation method to delineate accurately. Such CT artifacts cause segmentations to result in multiple parts, which we recombine later in the merging step.

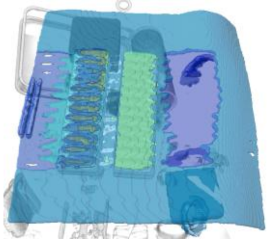

Fig. 8. Segmentation result of neoprene sitting on top of a package of 48 AA batteries. Here we are unable to delineate the sheet into a single segmentation since streak artifacts from the high-intensity batteries destroy the gradient boundary and erroneously changing the neoprene intensity in various regions.

IV. CONCLUSIONS

Tumbler segmentation tolerates common problems inherent in image segmentation and those caused by CT reconstruction artifacts such as noise, streaking, shading, and poor representation of object boundaries. It employs a multi-voxel kernel which considers several voxel intensities when deciding whether to connect neighboring voxels in a region-growing step. This allows the Tumbler method to tolerate noise, streaks, shading, and most importantly to detect ill-defined object boundaries in the case of touching objects.

We are currently improving performance of our Tumbler algorithm (currently runs about 40 min) by adapting it to the GPGPU and also improving our parts tree merging process. We are also investigating the impact our improved segmentation technique has on explosive detection quality.

REFERENCES

[1] C.R. Crawford, H.E. Martz, and H. Pien, "Segmentation of Objects from Volumetric CT Data," Northeastern University, Boston. This report can be found at: https://myfiles.neu.edu/groups/ALERT/strategic_studies/SegmentationInitiativeFinalReport.pdf

[2] Z. Lin, J. Jin, and H. Talbot, "Unseeded region growing for 3D image segmentation," Selected papers from Pan-Sydney Workshop on Visual Information Processing, Sydney, Australia, 2001.

[3] K.R. Peschmann and J. Harmann, "Automatic Concealed Object Detection System Having a Pre-Scan Stage," US Patent 5,182,764, January 26, 1993.

[4] T. Shen, H. Li, Z. Qian, and X. Huang, "Active Volume Models for 3D Medical Image Segmentation," Computer Vision and Pattern Recognition, 707-714, 2009.

[5] S. Simanovsky, I.M. Bechwati, M. Hiraoglu and C.R. Crawford, "Apparatus and method for detecting sheet objects in computed tomography data," US Patent 6,026,143, February 15, 2000.

[6] S. Singh and M. Singh, "Explosives detection systems (EDS) for aviation security," Signal Processing 83 (2003), 31-55.

[7] D. Wiley, "Analysis of Anatomic Regions Delineated from Image Data," US Patent 8,194,964 (US App. No. 12/430,545), filed April 27, 2009.

An iterative reconstruction method for spectral CT with tensor-based formulation and nuclear norm regularization

Oguz Semerci, Ning Hao, Misha E. Kilmer and Eric L. Miller

***Abstract*—Spectral computed tomography (CT) has become possible with the development of photon counting X-ray detector technology. Energy selective measurement capabilities of these devices open the doors to many exciting directions in CT research. In this work we assume perfect energy resolution at detectors, which results in a family of monochromatic CT problems. We propose a tensor based iterative algorithm that simultaneously reconstructs the X-ray attenuation distribution for each energy level. Specifically, we model the multi-spectral unknown as a 3rd order tensor where first two dimensions are in space and the 3rd dimension is in energy. This approach allows the design of a regularizer based on low rank assumptions on the multi-spectral unknown where we apply tensor spectral norm penalties. The solution to the convex optimization problem is obtained using the alternating direction method of multipliers (ADMM). Simulation results show that the proposed regularizer is applicable to the spectral CT problem and reliable in recovering a multi-linear structures in an inverse problem set up. In addition, when accompanied to TV it enhances the regularization capability and provide superior reconstructions.**

***Index Terms*—Computed tomography, spectral CT, photon counting detectors, low-rank modelling, spectral regularization, tensor rank, inverse problems, iterative reconstruction**

I. INTRODUCTION

A CONVENTIONAL computed tomography (CT) imaging system utilizes energy integrating detector technology [1] and provides a monochromatic reconstruction of the linear attenuation coefficient distribution of an object under investigation. The polychromatic nature of the X-ray spectra is either neglected [2], [3] or incorporated into the model in an iterative reconstruction method to achieve more accurate results [4], [5]. Energy resolving (photon counting) detector technology [6], on the other hand, provides the possibility of energy selective measurement and opens the door to spectral CT technology. Spectral CT promises improved diagnostic imaging [7], [8] and applicability to the security domain [9] due to the contrast enhancement and material characterization capabilities.

In this work, we propose an iterative reconstruction method for the spectral CT problem where we model the multi spectral unknown as a low rank 3rd order tensor. Recently, there has been considerable work on recovering corrupted matrices or tensors based on low-rank and sparse decomposition [10] or solely on low-rank assumptions [11], [12], [13], [14]. Our goal here is to adopt the generalized tensor rank formulation [15] to regularize the spectral CT problem. Similar studies where the multi spectral unknown is modelled as a superposition of low rank and sparse matrices had been conducted for 4D cone beam CT [16] and spectral tomography [17]. In these approaches, the multi spectral unknown is represented as a matrix with row dimension in space and column dimension in energy. Applying the low rank prior to the multi spectral matrix is a special case of our tensor model where only the unfolding in the energy dimension is considered. However, more powerful regularization can be achieved, especially when the number of energy bins is limited, if the redundancy in the spatial dimensions is exploited with the incorporation of unfoldings in spatial dimensions [14]. One of the purposes of this work is to investigate the effect of low-rank assumptions on the unfoldings in the spatial dimensions.

The paper is organized as follows: Section II describes the measurement and noise model. Section III describes the multi-spectral phantom and Section IV provides the details of the tensor based modelling of the unknown and mathematical details about the nuclear norm regularizer. Section V shows simulation results and Section VII gives concluding remarks and future directions.

II. MEASUREMENT MODEL

At the photon counting detectors the photons in the polychromatic spectrum are classified into energy bins. If we assume perfect energy resolution (i.e., infinitesimal bin width) the polychromatic X-ray CT problem reduces to N_E linear monochromatic problems :

$$\mathbf{A}\mathbf{x}_i = \mathbf{y}_i + \mathbf{n}_i, \quad i = 1, \dots, N_E. \tag{1}$$

Here $\mathbf{A}$ is the CT system matrix discretizing the Radon transform, $\mathbf{x}_i$ is the vectorized 2D linear attenuation coefficient image, $\mathbf{n}_i$ is the noise[1] vector and $\mathbf{y}_i$ is the measurement vector for the i^{th} energy bin.

III. THE MULTI-SPECTRAL UNKNOWN AS A TENSOR

Let us define the 3rd order tensor $\chi \in \mathbb{R}^{N_1 \times N_2 \times N_E}$ where N_1 and N_2 are the number of pixels in spatial dimensions. Note that $\mathbf{x}_i \in \mathbb{R}^{N_1 N_2}$ can be obtained by lexicographical ordering of the $N_1 \times N_2$ attenuation distribution (frontal slice)

This work was supported by the U.S. Department of Homeland Security under Award 2008-ST-061-ED0001.

O. Semerci and E.L. Miller are with the Department of Electrical and Computer Engineering, Misha Kilmer and Ning Hao are with Mathematics Department of Tufts University, Medford, MA, 02155 USA.

[1] Ideally, the measurements in spectral CT should be modelled as Poisson random variables [8]. However, we assume additive Gaussian noise in this proof of concept study

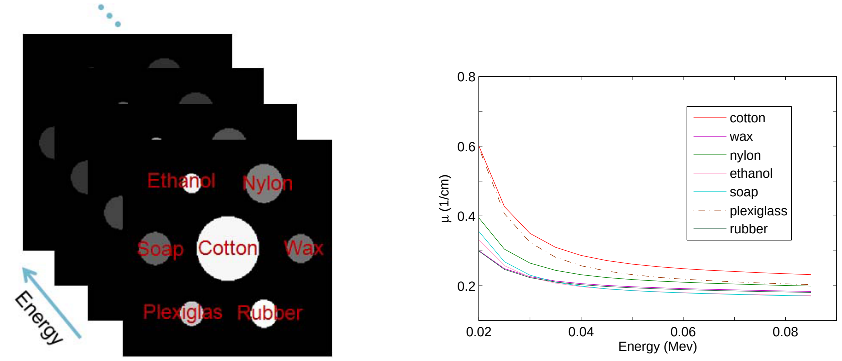

Fig. 1. Multi-spectral phantom and the attenuation curves for existing materials.

at the i^{th} energy. A depiction of the multi-spectral phantom used in this study along with the corresponding attenuation curves are given in Figure 1. With this notation we can define the forward operator K in a block diagonal form as follows:

$$K(\chi) := \begin{bmatrix} \mathbf{A} & & \\ & \ddots & \\ & & \mathbf{A} \end{bmatrix} \begin{bmatrix} \mathbf{x}_1 \\ \vdots \\ \mathbf{x}_{N_E} \end{bmatrix}. \tag{2}$$

IV. PRELIMINARIES ON TENSORS AND THE NUCLEAR NORM REGULARIZER

We start with the definition of the unfolding (matricization) operation: For the tensor, $\chi \in \mathbb{R}^{N_1 \times N_2 \times \dots N_K}$, the mode-$k$ unfolding $\mathbf{X}_{(k)} \in \mathbb{R}^{N_k \times \prod_{k' \neq k} N_k}$ is a matrix whose columns are mode-k fibers, where mode-k fibers are vectors in $\mathbb{R}^{N_k}$ that are obtained by varying the index in k^{th} dimension and fixing the others [18]. It is easy to visualize unfolding operations in terms of fronral, horizontal and lateral slices. Figure 2 depicts the 1st and 2nd unfoldings for a 3rd order tensor.

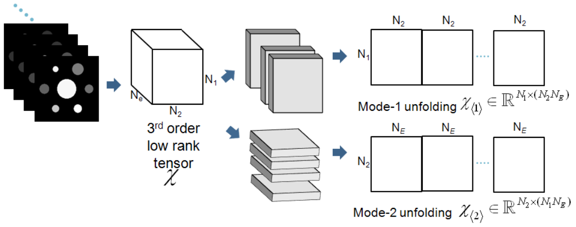
N_2
N_1
N_e
3rd order
low rank
tensor
χ
N_E
Mode-1 unfolding $\chi_{\langle 1 \rangle} \in \mathbb{R}^{N_1 \times (N_2 N_E)}$
Mode-2 unfolding $\chi_{\langle 2 \rangle} \in \mathbb{R}^{N_2 \times (N_1 N_E)}$

Fig. 2. First two unfoldings of a 3rd order tensor

The nuclear norm of a matrix $\mathbf{X}$ is defined as $\|\mathbf{X}\|_* := \sum_i \sigma_i(\mathbf{X})$, where σ_i's are the singular values. It is shown that the nuclear norm provides the tightest convex relaxation for the rank operation in matrices [12]. Consequently, convex optimization methods for low-rank matrix completion and rank estimation via minimization of the nuclear norm [12], [19] were proposed. This idea has been generalized to tensors for an N-way tensor [15], [14] as

$$\|\chi\|_* := \frac{1}{N} \sum_{k=1}^{N} \|\chi_{(k)}\|_* \tag{3}$$

We refer the reader to [15] for a thorough discussion about the relation of (3) to Tucker decomposition and Shatten 1-norm of matrices.

Except for K-edge materials X-ray attenuation at neighbouring energies are highly correlated. Therefore, for spectral CT, one expects the third unfolding, $\chi_{(3)}$ to be low-rank [17]. However, structural redundancies can also be exploited by enforcing low-rank structure on other two unfoldings. To this end, we use a more general form [13] of the tensor nuclear norm given in 3 as a regularizer:

$$R(\chi) = \sum_{k=1}^{3} \gamma_k \|\chi_{(k)}\|_*, \tag{4}$$

where γ_k tunes the importance of each each unfolding.

V. INVERSE PROBLEM FORMULATION

We seek a solution for the spectral CT problem via a convex optimization problem:

$$\underset{\chi}{\text{minimize}} \quad \frac{1}{2}\|K(\chi) - \mathbf{y}\|^2 + \lambda_1 R(\chi) + TV(\chi) \tag{5}$$

The total variation regularizer $TV(\chi)$ considered here is the weighted superposition of isotropic TV operator applied to frontal slices of χ as

$$TV(\chi) := \sum_{k=1}^{N_E} \alpha_i \sum_{\substack{i<N_1, \\ j<N_2}} |(\nabla \mathbf{x}_k)_{i,j}|. \tag{6}$$

The optimization problem given in (5) can be solved with alternating direction method of multipliers (ADMM) [20], where the problem is reformulated as

$$\begin{aligned} \underset{\chi, Z_1, Z_2, Z_3}{\text{minimize}} \quad & \frac{1}{2}\|K(\chi) - \mathbf{y}\|^2 + \lambda_1 \sum_{k=1}^{3} \gamma_k \|Z_k\|_* + TV(\chi) \\ \text{subject to} \quad & Z_k = \chi_{(k)}, \ \text{for } k = 1, 2, 3. \end{aligned} \tag{7}$$

To solve (7) we form the augmented Lagrangian as

$$\begin{aligned} L_\eta(\chi, \{Z_k\}, \{Y_k\}) = & \frac{1}{2}\|K(\chi) - \mathbf{y}\|^2 + \lambda_1 \sum_{k=1}^{3} \gamma_k \|Z_k\|_* + TV(\chi) \\ & + \sum_{k=1}^{3} < Y_k, \chi_{(k)} - Z_k > + \frac{\eta}{2}\|\chi_{(k)} - Z_k\|_F^2, \end{aligned} \tag{8}$$

where Y_k's are dual variables, $\eta > 0$ is the penalty term and $< . >$ is the inner product in the sense of Frobenius norm. ADMM minimizes (8) for χ and Z_k's in an alternating manner and then updates the dual variables:

$$\begin{aligned} \chi^{n+1} &:= \underset{\chi}{\operatorname{argmin}}\, L_\eta\left(\chi, \{Z_k\}^n, \{Y_k\}^n\right), \\ Z_k^{n+1} &:= \underset{Z_k}{\operatorname{argmin}}\, L_\eta\left(\chi^{n+1}, \{Z_k\}, \{Y_k\}^n\right), \text{ for } k = 1, 2, 3, \\ Y_k^{n+1} &:= Y_k^n + \eta(\chi_{(k)}^{n+1} - Z_k^{n+1}), \text{ for } k = 1, 2, 3. \end{aligned} \tag{9}$$

The χ update in (9) can be decoupled and each frontal face (energy) can be treated separately. We used FISTA [21] to solve the arising total variation regularized quadratic problems. With a straightforward reformulation one finds that the Z_k updates can be obtained via proximity operator of nuclear norm as

$$\begin{aligned} Z_k^{n+1} &:= \underset{Z_k}{\operatorname{argmin}}\, \|Z_k\|_* + \frac{\eta}{2\lambda_1}\left\|\frac{Y_k^n}{\eta} + \chi_{(k)}^{n+1}\right\|_* \\ &:= \underset{\|\cdot\|_*, \frac{\lambda_1}{\eta}}{\operatorname{prox}} \left(\frac{Y_k^n}{\eta} + \chi_{(k)}^{n+1}\right) \end{aligned} \tag{10}$$

which has an analytical solution via singular value shrinkage operator [11]. Specifically, $\underset{\|\cdot\|_*, \rho}{\operatorname{prox}}(\mathbf{X}) = \mathbf{U} S_\rho(\mathbf{\Sigma}) V^{\mathbf{T}}$, where $\mathbf{X} = \mathbf{U}\mathbf{\Sigma}V^{\mathbf{T}}$ is the singular value decomposition of $\mathbf{X}$ and $S\rho(\mathbf{\Sigma}) = \operatorname{diag}(\{(\sigma_i - \rho)_+\})$ is a shrinkage operator with $t_+ = \max(t, 0)$ applied to the singular values. Finally, the dual variable (Y_k's) update with the step length η keeps the updates dual feasible [20].

VI. RECONSTRUCTION EXAMPLES

We compared following methods in our simulations:

1. Filtered back projection (FBP) [22] algorithm applied to each energy bin separately.
2. Only TV regularization at each energy bin separately (i.e., $\lambda_1 = 0$ in (5)).
3. Only nuclear norm regularization (i.e., $\lambda_2 = 0$).
4. TV and nuclear norm regularization.
5. Nuclear norm regularization where only the unfolding in the energy dimension is considered (i.e., $\gamma_1, \gamma_2 = 0$).

We simulated multi-spectral data for 12 energies between 20 and 80 keV with 60dB SNR for 16 uniformly distributed angles between 0 and 180 degrees. We have added some texture on the objects and a small linear variation to the background of the phantom (128x128 pixels) given in Figure 1. The ground truth images for 20 and 80 keV bins are given in Fig. 3.

In all examples we set $\eta, \gamma_1, \gamma_2, \gamma_3 = 1$ and $\lambda_1 = 0.1$ with the exception of the last example where $\gamma_1, \gamma_2 = 0$. We let α_i's reduce from 0.1 to 0.03 with a quadratic manner. Intuitively, X-ray attenuation reduces as energy increases and it is sensible to reduce the amount of TV regularization in a similar manner. Fig. 4 shows reconstruction results for 20 and 80 keV images. Firstly, observing the last example, we realize that relying solely on spectral redundancy is ineffective and does not provide

VII. CONCLUSIONS

In this proof of concept work, we provided an algorithmic framework for iterative spectral CT and showed that generalized tensor nuclear norm ideas can be used to regularizers. Ideas presented here can be extended to inverse problems where a multi-linear description of the unknown is possible. Future research will be directed to combining the nuclear norm ideas with quadratic edge preserving regularizer such as weighted $L2$ for faster and more accurate reconstructions. Quantifying redundancy and automatic determination of regularization parameters of the nuclear norm regularizer is also an important direction to extend the current approach.

REFERENCES

[1] B. Whiting, P. Massoumzadeh, O. Earl, J. OSullivan, D. Snyder, and J. Williamson, "Properties of preprocessed sinogram data in x-ray computed tomography," *Medical physics*, vol. 33, p. 3290, 2006.

[2] C. Bouman and K. Sauer, "A unified approach to statistical tomography using coordinate descent optimization," *Image Processing, IEEE Transactions on*, vol. 5, no. 3, pp. 480–492, mar 1996.

[3] X. Pan, E. Sidky, and M. Vannier, "Why do commercial ct scanners still employ traditional, filtered back-projection for image reconstruction?" *Inverse problems*, vol. 25, p. 123009, 2009.

[4] I. Elbakri and J. Fessler, "Statistical image reconstruction for polyenergetic x-ray computed tomography," *Medical Imaging, IEEE Transactions on*, vol. 21, no. 2, pp. 89–99, 2002.

[5] O. Semerci and E. Miller, "A parametric level-set approach to simultaneous object identification and background reconstruction for dual-energy computed tomography," *Image Processing, IEEE Transactions on*, vol. 21, no. 5, pp. 2719 –2734, may 2012.

[6] P. Shikhaliev, "Energy-resolved computed tomography: first experimental results," *Physics in medicine and biology*, vol. 53, p. 5595, 2008.

[7] P. Shikhaliev and S. Fritz, "Photon counting spectral ct versus conventional ct: comparative evaluation for breast imaging application," *Physics in medicine and biology*, vol. 56, p. 1905, 2011.

[8] J. Schlomka, E. Roessl, R. Dorscheid, S. Dill, G. Martens, T. Istel, C. Bäumer, C. Herrmann, R. Steadman, G. Zeitler *et al.*, "Experimental feasibility of multi-energy photon-counting k-edge imaging in pre-clinical computed tomography," *Physics in medicine and biology*, vol. 53, p. 4031, 2008.

[9] V. Ivakhnenko, "A novel quasi-linearization method for ct image reconstruction in scanners with a multi-energy detector system," *Nuclear Science, IEEE Transactions on*, vol. 57, no. 2, pp. 870–879, 2010.

[10] E. Candes, X. Li, Y. Ma, and J. Wright, "Robust principal component analysis?" *Arxiv preprint ArXiv:0912.3599*, 2009.

[11] J. Cai, E. Candes, and Z. Shen, "A singular value thresholding algorithm for matrix completion," *Arxiv preprint Arxiv:0810.3286*, 2008.

[12] E. Candès and B. Recht, "Exact matrix completion via convex optimization," *Foundations of Computational Mathematics*, vol. 9, no. 6, pp. 717–772, 2009.

[13] R. Tomioka, K. Hayashi, and H. Kashima, "Estimation of low-rank tensors via convex optimization," *Arxiv preprint arXiv:1010.0789*, 2010.

[14] J. Liu, P. Musialski, P. Wonka, and J. Ye, "Tensor completion for estimating missing values in visual data," in *Computer Vision, 2009 IEEE 12th International Conference on*. IEEE, 2009, pp. 2114–2121.

[15] M. Signoretto, L. De Lathauwer, and J. Suykens, "Nuclear norms for tensors and their use for convex multilinear estimation," *Technical Report 10-186, ESAT-SISTA, K.U.Leuven*, 2010.

[16] J. Cai, X. Jia, H. Gao, S. Jiang, Z. Shen, and H. Zhao, "Cine cone beam ct reconstruction using low-rank matrix factorization: algorithm and a proof-of-princple study," *Arxiv preprint arXiv:1204.3595*, 2012.

[17] H. Gao, H. Yu, S. Osher, and G. Wang, "Multi-energy ct based on a prior rank, intensity and sparsity model (prism)," *Inverse problems*, vol. 27, p. 115012, 2011.

[18] T. Kolda and B. Bader, "Tensor decompositions and applications," *SIAM review*, vol. 51, no. 3, p. 455, 2009.

[19] S. Ma, D. Goldfarb, and L. Chen, "Fixed point and bregman iterative methods for matrix rank minimization," *Mathematical Programming*, vol. 128, no. 1, pp. 321–353, 2011.

[20] S. Boyd, N. Parikh, E. Chu, B. Peleato, and J. Eckstein, *Distributed optimization and statistical learning via the alternating direction method of multipliers*. Now Publishers, 2011.

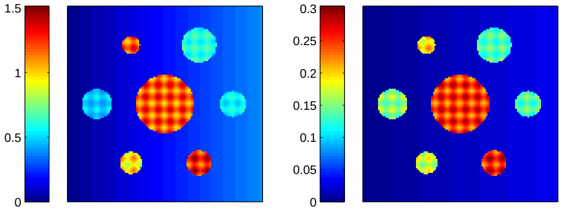

Fig. 3. Left: Ground truth for 20 keV. Right: Ground truth for 80 keV

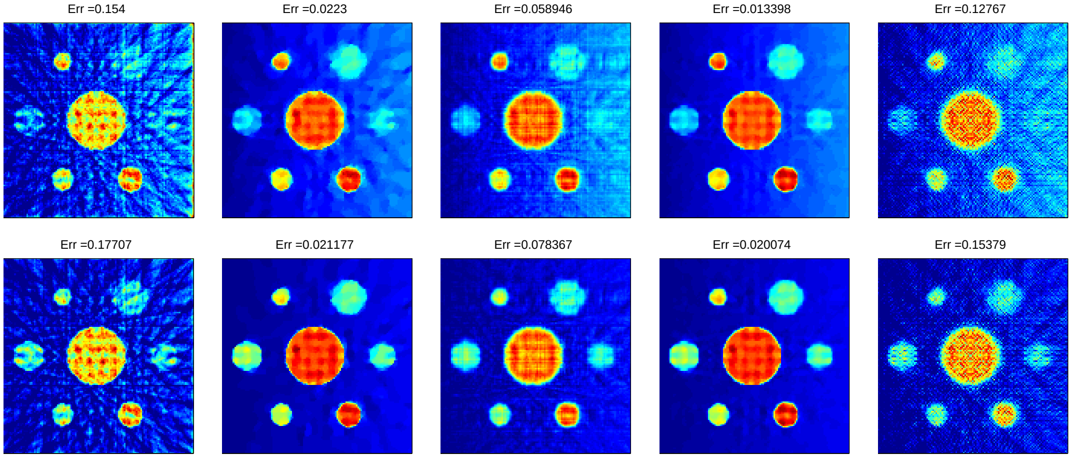

Fig. 4. First row: Reconstruction for 20 keV. Second Row: Reconstruction for 80 keV. Columns: Reconstructions results with methods given in the order above.

[21] A. Beck and M. Teboulle, “A fast iterative shrinkage-thresholding algorithm for linear inverse problems,” *SIAM Journal on Imaging Sciences*, vol. 2, no. 1, pp. 183–202, 2009.
[22] M. Slaney and A. Kak, “Principles of computerized tomographic imaging,” *SIAM, Philadelphia*, 1988.

Dynamic tomography, mass preservation and ROI reconstruction

Laurent Desbat, Catherine Mennessier and Rolf Clackdoyle

Abstract—**In this paper we consider the mass preservation in dynamic tomography. We present an analytic compensation of deformations preserving the mass and the acquisition line geometry. We show 2D ROI reconstructions of truncated dynamic data.**

I. INTRODUCTION

A. Tomography and notations

We consider the attenuation function μ of an object in $\mathbb{R}^d, d \in \mathbb{N}, d \geq 2$ (in practice we restrict the dimension d to $d = 2$ for single slice tomography, $d = 3$ for 3D reconstruction). We suppose that $\mu : \mathbb{R}^d \to \mathbb{R}$ is a bounded function of compact support Ω. Thus $\mu \in L^q\left(\mathbb{R}^d\right), \forall q \in \mathbb{N}^\star$.

Let $\vec{v} \in \mathbb{R}^d$ denotes a point (an X-ray source position in X-ray CT), and $\vec{\zeta} \in \mathbb{S}^{d-1}$ a unit vector (in the direction from the source to the detector in X-ray CT), the Divergent Beam transform is defined by

$$\mathcal{D}\mu\left(\vec{v},\vec{\zeta}\right) \overset{\text{def}}{=} \int_0^{+\infty} \mu\left(\vec{v}+l\vec{\zeta}\right) dl \tag{1}$$

Generally (in particular in X-ray CT) the data are acquired from multiple source positions and the source describe a trajectory, i.e. a curve $\mathcal{C} = \{\vec{v}(t), t \in T \subset \mathbb{R}\}$ in $\mathbb{R}^d$. We will suppose in the following that the curve $\mathcal{C}$ is outside of the convex hull of Ω, the support of μ. In practice, the source trajectory is sampled. The number $n_p \in \mathbb{N}$ of x ray projections is bounded. Thus we deal with a finite number of vertexes, $\vec{v}_i \in \mathbb{R}^d, i = 1, \ldots, n_p$ (and $\vec{v}_i = \vec{v}(t_i), t_i \in T$ is the sampling of the source trajectory). In this work, we concentrate on 2D image reconstruction ($\mu \in \mathbb{L}^q\left(\mathbb{R}^2\right)$) even if many results can be extended to 3D. In 2D, the fan beam data can be parametrized

$$d(t,\alpha) = \mathcal{D}\mu\left(\vec{v}(t),\vec{\zeta}(\alpha)\right) \tag{2}$$

with $\vec{\zeta}(\alpha) = (\cos\alpha, \sin\alpha)$, $\alpha \in [0, 2\pi[$.

B. Dynamic tomography

In dynamic tomography or 3D reconstruction, we can no more suppose that the function μ is not changing during the acquisition. This problem arises for example when measuring X-ray projections from the thorax region with a relative slow acquisition system like a C-arm [1] or in nuclear imaging acquisition (PET or SPECT) . Indeed, respiration motion and/or patient movements occur. Fast moving organs like the heart yield also artifacts, see [2], [3].Let t the source trajectory parameter be also the time, then μ is both a function of t and the space variable $\vec{x}$, $\mu(t,\vec{x})$ (and we suppose that $\mu \in L^q\left(T \times \mathbb{R}^d\right), \forall q \in \mathbb{N}^\star$).

Gating methods [4], [5], [6] have been proposed, in particular to improve cardiac imaging. The assumption that the object movement is quasi periodic is made (respiration, beating heart) and information on the object phase at acquisition time t is collected from external devices (such as an electrocardiograph in cardiac CT [7]). Then all data acquired at the same phase are gathered in order to reconstruct the object at this phase. The drawback of gating methods is their necessity to acquire complete data for each movement phase to be reconstructed. In practice, this means high dose to the patient and long time acquisition compare to static tomography.

When the variations of μ during the acquisition is occurring just because of movements or time dependent space deformations, the assumption that $\mu(t,\vec{x})$ behaves like $\mu\left(\vec{\Gamma}_t\left(\vec{x}\right)\right)$ can be made, where μ is the attenuation function at a reference time, for example $t = 0$, and $\vec{\Gamma}_t$ is a time dependent diffeomorphic[1] deformation, i.e. a smooth bijective mapping on the space $\mathbb{R}^d$, $d \in \{2,3\}$:

$$\begin{array}{rccc} \vec{\Gamma}_t : & \mathbb{R}^d & \longrightarrow & \mathbb{R}^d \\ & \vec{x} & \longrightarrow & \vec{\Gamma}_t(\vec{x}) \end{array} . \tag{3}$$

Thus $\vec{\Gamma}_t(\vec{x})$ maps $\vec{x}$ at time t to its position at the reference time. Such kind of modeling was introduced by Crawford et al [8].Note that this model take care only for space deformations during the acquisition (for example introduction of new materials in the FOV during the acquisition is not modeled this way).

It is reasonable to add the assumption that the deformation is preserving the mass. The mass is preserved on any set Ω of $\mathbb{R}^d$ when performing the change of variable $\vec{y} = \vec{\Gamma}_t(\vec{x})$ thanks to

$$\int_\Omega \mu\left(\vec{\Gamma}_t\left(\vec{x}\right)\right) |\det J_{\vec{\Gamma}_t}(\vec{x})| d\vec{x} = \int_{\vec{\Gamma}_t(\Omega)} \mu\left(\vec{y}\right) d\vec{y}$$

where $\det J_{\vec{\Gamma}_t}(\vec{x})$ is the determinant of $J_{\vec{\Gamma}_t}(\vec{x})$ the Jacobian matrix of $\vec{\Gamma}_t$ at $\vec{x}$. Thus we define the diffeomorphic deformation of μ by $\vec{\Gamma}_t$ with mass conservation by

$$\mu_{\vec{\Gamma}_t}\left(\vec{x}\right) \overset{\text{def}}{=} \mu\left(\vec{\Gamma}_t\left(\vec{x}\right)\right) |\det J_{\vec{\Gamma}_t}(\vec{x})| \tag{4}$$

L. Desbat is with UJF-Grenoble 1, CNRS, TIMC-IMAG, UMR 5525, Grenoble University ; C. Mennessier and R. Clackdoyle are with LHC, UMR 5516, St Etienne, France (C.M. is also with CPE Lyon) ; emails: laurent.desbat@imag.fr, catherine.mennessier@cpe.fr, rolf.clackdoyle@univ-st-etienne.fr

[1] If $\vec{\Gamma}_t$ and $\vec{\Gamma}_t^{-1}$ are r times continuously differentiable, $\vec{\Gamma}_t$ is called a C^r-diffeomorphism. We will suppose that $\vec{\Gamma}_t$ is at least a C^1-diffeomorphism

and we suppose from now that $\mu(t,\vec{x}) = \mu_{\vec{\Gamma}_t}(\vec{x})$. Thus, in dynamic tomography, we have to identify μ from

$$\mathcal{D}\mu_{\vec{\Gamma}_t}(\vec{v}(t),\vec{\zeta}) = \int_{\mathbb{R}} \mu\left(\vec{\Gamma}_t\left(\vec{v}(t)+l\vec{\zeta}\right)\right)|\det J_{\vec{\Gamma}_t}(\vec{v}(t)+l\vec{\zeta})|dl \tag{5}$$

for some source trajectory $\vec{v}(t), t \in T$, line directions $\vec{\zeta} \in \mathbb{S}^{d-1}$ and $\vec{\Gamma}_t$.

An advantage of this model compare to gating methods is that all the data contribute to the reconstruction of one function $\mu_{\vec{\Gamma}_t}$ or equivalently μ when $\vec{\Gamma}_t$ is known. A (big) disadvantage is that $\vec{\Gamma}_t$ must be measured or estimated from the available data or extra ones. In all the following approaches we will assume that $\vec{\Gamma}_t$ is known. For general smooth bijective deformations no inversion formula exists and usually algebraic approaches are used for general dynamic tomography reconstruction, see for exemple [9]. Approximate analytic inversions have also been proposed [10]. Singularity surfaces of μ can be reconstructed from projections of $\mu_{\vec{\Gamma}_t}(\vec{x})$ (Eq. (5)) and $\vec{\Gamma}_t$, thanks to an exact local approach, see [11].

In the following we want to reconstruct μ from the knowledge of $\vec{\Gamma}_t$ and projections of $\mu_{\vec{\Gamma}_t}(\vec{x})$, see Eq. (5). Following [8], we proposed in [12] a generalization of the analytic deformation compensation to the class of deformations preserving the acquisition line geometry with the restriction to linear deformations along each line. This last restriction is suppressed in this work thanks to the mass conservation of the deformation.

We first consider deformations preserving the projection line geometry. More precisely we consider $\vec{\Gamma}_t$ mapping the set of convergent measurement lines at time t onto a set of convergent lines at the reference time. Indeed, preserving the measurement line geometry allow to stay within tomographic problems and thus to propose analytic solutions. The parallel geometry can be treated similarly.

II. DIVERGENT GEOMETRY AND MASS PRESERVATION

A. Divergent geometry preservation

The deformation $\vec{\Gamma}_t$ preserves a divergent geometry if it transforms the acquisition fan lines (respectively conical lines in 3D) into another set of fan lines (respectively conical lines in 3D). Let $\vec{v}(t) + \mathbb{R}\vec{\zeta}$ be such a line with $\vec{v}(t)$ the source vertex and $\vec{\zeta} \in \mathbb{S}^{d-1}$ the line direction. First the source $\vec{v}(t)$ is transform into a concurrent point $\vec{\Gamma}_t(\vec{v}(t))$ of all the transforms lines $\vec{\Gamma}_t\left(\vec{v}(t)+\mathbb{R}\vec{\zeta}\right)$. Second, each line direction $\vec{\zeta}$ is transformed into a new direction denoted $\vec{\Sigma}_t(\vec{\zeta})$ where $\vec{\Sigma}_t$ is a diffeomorphism on the unit sphere (bi-smooth bijection on the sphere):

$$\begin{array}{rccc} \vec{\Sigma}_t: & \mathbb{S}^{d-1} & \longrightarrow & \mathbb{S}^{d-1} \\ & \vec{\zeta} & \longrightarrow & \vec{\Sigma}_t(\vec{\zeta}) \end{array}. \tag{6}$$

Thus a deformation preserving the divergent geometry satisfies

$$\vec{\Gamma}_t\left(\vec{v}(t)+\mathbb{R}\vec{\zeta}\right) = \vec{\Gamma}_t\left(\vec{v}(t)\right) + \mathbb{R}\vec{\Sigma}_t(\vec{\zeta}).$$

We can remark that the divergent line geometry is preserved, i.e. $\forall\vec{\zeta} \in \mathbb{S}^{d-1}$ the half line $\vec{v}(t)+l\vec{\zeta}, l \in \mathbb{R}^+$ is mapped to an other half line because $\vec{\Sigma}_t$ does not depend on the variable l (the position on the line). To complete the modeling of the time dependent deformation preserving the divergent geometry, we have to precise the deformation along each line. Obviously, it may differ from line to line, thus it may depend on $\vec{\zeta}$ (and t). We introduce $\gamma_{t,\vec{\zeta}}$ the deformation function along each half line $\vec{v}(t)+l\vec{\zeta}, l \in \mathbb{R}^+$:

$$\begin{array}{rccc} \gamma_{t,\vec{\zeta}}: & \mathbb{R}^+ & \longrightarrow & \mathbb{R}^+ \\ & l & \longrightarrow & \gamma_{t,\vec{\zeta}}(l) \end{array}. \tag{7}$$

We have, $\forall l \in \mathbb{R}^+$, $\forall\vec{\zeta} \in \mathbb{S}^{d-1}$,

$$\vec{\Gamma}_t\left(\vec{v}(t)+l\vec{\zeta}\right) = \vec{\Gamma}_t\left(\vec{v}(t)\right) + \gamma_{t,\vec{\zeta}}(l)\vec{\Sigma}_t(\vec{\zeta}). \tag{8}$$

Clearly for $\vec{\Gamma}_t$ to be smooth and bijective, $\gamma_{t,\vec{\zeta}}$ must be a strictly monotonic smooth function and $\gamma_{t,\vec{\zeta}}(0) = 0$.

B. Geometry and mass preservation

Proposition II.1. *A time dependent deformation $\vec{\Gamma}_t$ preserving the divergent geometry in the form of Eq. (8) such that*

$$\begin{aligned} &\mu_{\vec{\Gamma}_t}\left(\vec{v}(t)+l\vec{\zeta}\right) \\ =&\mu\left(\vec{\Gamma}_t\left(\vec{v}(t)\right)+\gamma_{t,\vec{\zeta}}(l)\vec{\Sigma}_t(\vec{\zeta})\right)|\gamma'_{t,\vec{\zeta}}(l)||J_{\vec{\Sigma}_t}(\vec{\zeta})|\frac{\gamma^{d-1}_{t,\vec{\zeta}}(l)}{l^{d-1}} \end{aligned} \tag{9}$$

preserves also the mass of μ.

Proof: $\vec{\Gamma}_t$ is a change of variable on $\mathbb{R}^d$ and $\left(\gamma_{t,\vec{\zeta}}, \vec{\Sigma}_t\right)$ is the corresponding change of variable on the spherical variable $(l,\vec{\zeta}) \in \mathbb{R}^+ \times \mathbb{S}^{d-1}$ centered on $\vec{v}(t)$ to the spherical variables $(u,\vec{\vartheta}) \in \mathbb{R}^+ \times \mathbb{S}^{d-1}$ centered on $\vec{\Gamma}_t(\vec{v}(t))$ with $\vec{\Gamma}_t(\vec{v}(t)) + u\vec{\vartheta} = \vec{\Gamma}_t(\vec{v}(t)) + \gamma_{t,\vec{\zeta}}(l)\vec{\Sigma}_t(\vec{\zeta})$, i.e., $(u,\vec{\vartheta}) = (\gamma_{t,\vec{\zeta}}(l), \vec{\Sigma}_t(\vec{\zeta}))$. We have

$$\begin{aligned} &\int_{[l_1,l_2]\times\Omega_S} \mu_{\vec{\Gamma}_t}\left(\vec{v}(t)+l\vec{\zeta}\right)l^{d-1}dld\vec{\zeta} \\ &= \int_{[l_1,l_2]\times\Omega_S} \mu\left(\vec{\Gamma}_t\left(\vec{v}(t)\right)+\gamma_{t,\vec{\zeta}}(l)\vec{\Sigma}_t(\vec{\zeta})\right) \\ &\qquad |\gamma'_{t,\vec{\zeta}}(l)||J_{\vec{\Sigma}_t}(\vec{\zeta})|\frac{\gamma^{d-1}_{t,\vec{\zeta}}(l)}{l^{d-1}}l^{d-1}dld\vec{\zeta} \\ &= \int_{[\gamma_{t,\vec{\zeta}}(l_1),\gamma_{t,\vec{\zeta}}(l_2)]\times\vec{\Sigma}_t(\Omega_S)} \mu\left(\vec{\Gamma}_t\left(\vec{v}(t)\right)+u\vec{\vartheta}\right)u^{d-1}dud\vec{\vartheta} \end{aligned}$$

■

Because in practice the X-ray source is not really punctual, it is quite realistic to suppose that the x-ray beam between the source and the detector is some region $\Omega_{\vec{v}(t),\vec{\zeta}}$ of approximately constant photon flux, in cross section perpendicular to $\vec{\zeta}$ close and around the line $\vec{v}(t)+\mathbb{R}^+\vec{\zeta}$ (at least during the travel in the patient region (and for no attenuation)). $\vec{\Gamma}_t$ transforms the region $\Omega_{\vec{v}(t),\vec{\zeta}}$ around the line $\vec{v}(t)+\mathbb{R}^+\vec{\zeta}$ into $\vec{\Gamma}_t\left(\Omega_{\vec{v}(t),\vec{\zeta}}\right)$ around the line $\vec{\Gamma}_t(\vec{v}(t)) + \mathbb{R}^+\vec{\Sigma}_t(\vec{\zeta})$. Because we suppose that the photon flux in $\Omega_{\vec{v}(t),\vec{\zeta}}$ in sections perpendicular to the direction $\vec{\zeta}$ are essentially constant, we can write

$$\begin{aligned}
& \int_{\mathbb{R}+} \mu_{\vec{\Gamma}_t}\left(\vec{v}(t)+l\vec{\zeta}\right) dl \\
\approx\ & K \int_{\Omega_{\vec{v}(t),\vec{\zeta}}} \mu_{\vec{\Gamma}_t}\left(\vec{v}(t)+l\vec{\zeta}\right) l^{d-1} dl d\vec{\zeta} \\
=\ & K \int_{\vec{\Gamma}_t\left(\Omega_{\vec{v}(t),\vec{\zeta}}\right)} \mu\left(\vec{\Gamma}_t\left(\vec{v}(t)\right)+u\vec{\vartheta}\right) u^{d-1} du d\vec{\vartheta} \\
\approx\ & \int_{\mathbb{R}+} \mu\left(\vec{\Gamma}_t\left(\vec{v}(t)\right)+l\vec{\Sigma}_t(\vec{\zeta})\right) dl
\end{aligned}$$

We remark that in the previous equations the proportionality coefficients K should be the same in both approximations because the real photon flux on $\Omega_{\vec{v}(t),\vec{\zeta}}$ is the same as on the virtual transformed on $\vec{\Gamma}_t\left(\Omega_{\vec{v}(t),\vec{\zeta}}\right)$. We can deduce from the previous development that we can assume for deformations preserving the mass and the the divergent geometry that

$$\int_{\mathbb{R}+} \mu_{\vec{\Gamma}_t}\left(\vec{v}(t)+l\vec{\zeta}\right) dl = \int_{\mathbb{R}+} \mu\left(\vec{\Gamma}_t\left(\vec{v}(t)\right)+l\vec{\Sigma}_t(\vec{\zeta})\right) dl \tag{10}$$

and the following rebinning formula

Proposition II.2 (Dynamic DB rebinning Formula). *If $\vec{\Gamma}_t$ preserves both the divergent geometry and the mass (Eq. (9)) then*

$$\mathcal{D}\mu_{\vec{\Gamma}_t}\left(\vec{v}(t),\vec{\zeta}\right) = \mathcal{D}\mu\left(\vec{\Gamma}_t\left(\vec{v}(t)\right),\vec{\Sigma}_t(\vec{\zeta})\right) \tag{11}$$

(the equality being strictly verified only for volumic measurement model)

C. Density, mass and acquisition geometry preservation

As solid and fluid can be generally considered as incompressible in many applications (organ movements in CT for example: soft and hard tissue can be considered as incompressible), the question of deformation $\vec{\Gamma}_t$ preserving the density, the mass and the acquisition geometry is of interest. In this case we want $\vec{\Gamma}_t$ to fulfill (density conservation)

$$\mu_{\vec{\Gamma}_t}\left(\vec{x}\right) = \mu\left(\vec{\Gamma}_t\left(\vec{x}\right)\right)$$

Deformations conserving the mass and the divergent geometry (Eq. (9)) preserve the density if

$$|\gamma'_{t,\vec{\zeta}}(l)||J_{\vec{\Sigma}_t}(\vec{\zeta})|\frac{\gamma^{d-1}_{t,\vec{\zeta}}(l)}{l^{d-1}} = 1 \tag{12}$$

In 2D (i.e. $d=1$), $\vec{\zeta}$ is parametrized by an angle α, let say $\vec{\zeta}(\alpha) = (\cos\alpha, \sin\alpha)$ and thus $\vec{\Sigma}_t$ is a function on the unit circle. $\vec{\Sigma}_t$ can be represented by a bijective periodic function ψ_t from $[0,2\pi)$ to $\psi_t([0,2\pi))$ such that $\vec{\Sigma}_t\left(\vec{\zeta}(\alpha)\right) = \vec{\zeta}\left(\psi_t(\alpha)\right)$ with $\psi_t(2\pi) = \psi_t(0)+2\pi$ (the functions $\gamma_{t,\vec{\zeta}}$ and ψ_t must be strictly monotonic and for the sake of simplicity we suppose both of them increasing). Thus Eq. (12) is equivalent to

$$\gamma'_{t,\vec{\zeta}}(l)\gamma_{t,\vec{\zeta}}(l)\psi'_t(\alpha) = l$$

integrating over l and considering $\gamma_{t,\vec{\zeta}}(0) = 0$ yields

$$\gamma^2_{t,\vec{\zeta}}(l)\psi'_t(\alpha) = l^2$$

From any of both previous equations we remark that for ψ_t being independent of l (which is a characterization for preserving the divergent geometry in 2D) we need to have $\gamma_{t,\vec{\zeta}}(l) = c_t(\alpha)l$ with $c_t(\alpha) > 0$ thus the deformations along the lines must be linear and $\psi'_t(\alpha) = \frac{1}{c_t^2(\alpha)}$. As ψ_t is 2π-periodic smooth so must be $c_t(\alpha)$ and $\psi_t(2\pi) - \psi_t(0) = 2\pi$ yields $\int_0^{2\pi} \frac{d\alpha}{c_t^2(\alpha)} = 2\pi$.

Proposition II.3. *A time dependent deformation in the form of Eq. (9) preserving the divergent geometry and the mass preserves also the density if*

$$\gamma_{t,\vec{\zeta}}(l) = c_t(\alpha)l \text{ and } \psi'_t(\alpha) = \frac{1}{c_t^2(\alpha)} \tag{13}$$

with $c_t(\alpha) > 0$ some 2π-periodic smooth function such that $\int_0^{2\pi} \frac{d\alpha}{c_t^2(\alpha)} = 2\pi$.

III. ANALYTIC 2D RECONSTRUCTION FROM DYNAMIC DATA

In our numerical experiments we consider dynamic data combined with ROI reconstruction methods, see [13]. Indeed, in practical applications such as interventional imaging, detectors are often too small and we have to deal with data truncations. 2D ROI reconstruction methods, such as Virtual Fan Beam (VFB) (deriving from the original work [14]) or Differentiated BackProjection (DBP) (see [15], [16]) can be quite easily adapted to dynamic tomography with deformation preserving the fan beam geometry and the mass, i.e., of the form (8) such that (9) is satisfied. Indeed with (11) we can rebin the dynamic data $\mathcal{D}\mu_{\vec{\Gamma}_t}$ on $\vec{v}(t)$ and $\zeta \in S_t$ ($\subset \mathbb{S}^{d-1}$)), $\forall t \in T$ into static data $\mathcal{D}\mu$ acquired on a virtual trajectory $\vec{\Gamma}_t\left(\vec{v}(t)\right)$ with a moving virtual detector described by $\vec{\Sigma}_t(\vec{\zeta}) \in \vec{\Sigma}_t(S_t)$, $\forall t \in T$. To know which ROI of μ can be reconstructed we have to consider the virtual trajectory $\vec{\Gamma}_t\left(\vec{v}(t)\right), t \in T$ and the virtual available directions $\vec{\Sigma}_t(\vec{\zeta})$, see [13].

In our first numerical experiments we have considered an essentially parallel geometry. The phantom is a sum of two ellipses (respectively centered on (0,0) and (-0.0147,0), with long semi-axis 0.736 and 0.6992 with short semi-axis 0.552 and 0.5299 and with density 1 and -0,98) and two disks of density 1 (respectively centered on (-0.2044, 0.2195) and (0.62,0), with radius 0.08 and 0.05). The trajectory of the source is a circle of radius $R = 1000$ and 386 source positions were regularly sampled on $[0,\pi[$. We define the fan angle as $2\alpha_F$ with $\alpha_F = \arcsin(1/R)$. The fan angle was sampled with 256 values (with a regular angular sampling of $\Delta\alpha = 2\alpha_F/256$). However, for the truncated data we suppose here that only around 60% of the fan angle can be seen from the detector in the central region with 154 lines (instead of 256 for the complete data) with the same angular sampling $\Delta\alpha$).

The deformation is of type (8). In our simple example we chose $\vec{\Gamma}_t\left(\vec{v}(t)\right) = \vec{v}(t)$, $\gamma_{t,\vec{\zeta}}(l) = l$ and $\vec{\Sigma}_t\left(\vec{\zeta}(\alpha)\right) = \vec{\zeta}\left(\psi_t(\alpha)\right)$ with ψ_t is piecewise linear from $[-\alpha_F, \alpha_F]$ to $[-\alpha_F, \alpha_F]$ and defined by $\psi_t(-\alpha_F) = -\alpha_F$, $\psi_t(-\alpha_F/2) = -1.2\alpha_F/2$, $\psi_t(\alpha_F/2) = 1.1\alpha_F/2$, $\psi_t(\alpha_F) = \alpha_F$ (and linear between these 4 control angular knots). We show in Fig. 1 the effect of the deformation on the phantom and we show the truncated data and the rebinned truncated data using (11) (the motion compensated data). We show in Fig. 2 the reconstruction from truncated and complete data from both motion corrupted data and motion compensated data.

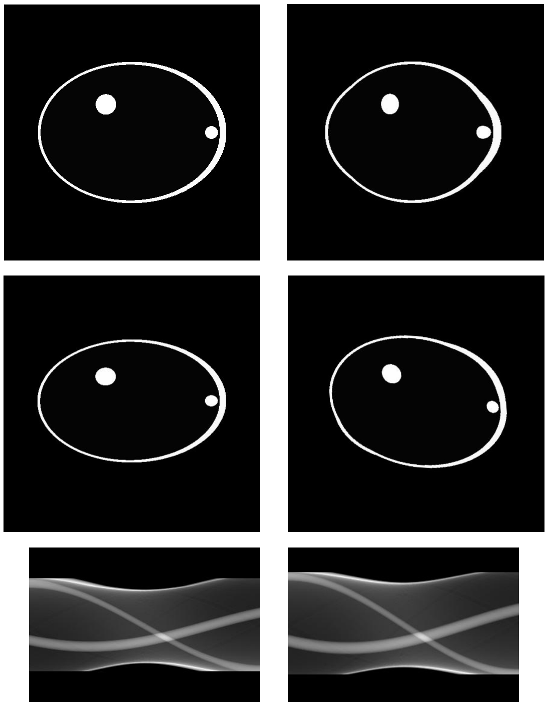

Fig. 1. Phantom and 3 three deformations at projection 0 (first line right) and (second line) 190 (left) and 285 (right). Third line: motion corrupted truncated sinogram (left), motion corrected truncated sinogram (right).

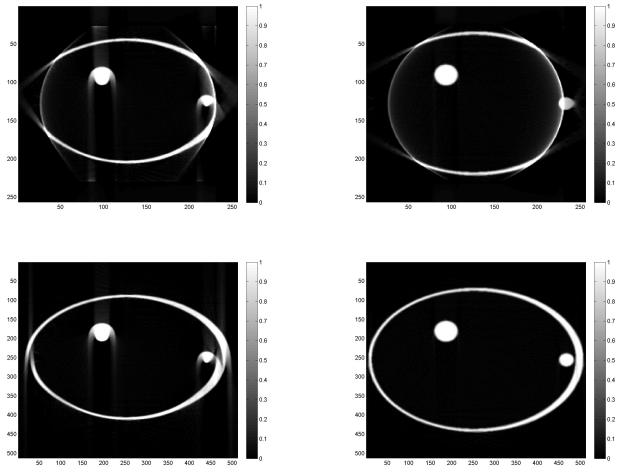

Fig. 2. First line: reconstruction from truncated data with the DBP approach on motion corrupted data (right) and on motion compensated data (left). Second line: corresponding FBP reconstruction with complete projections.

IV. CONCLUSION

We have shown very preliminary results of ROI reconstructions from analytic compensation of deformations preserving the mass and the divergent geometry in dynamic tomography.

REFERENCES

[1] S. Krimski and et al, "Respiratory correlated cone-beam computed tomography on an isocentric c-arm," *Phys. Med. Biol.*, vol. 50, no. 22, pp. 5263–80, November 2005.

[2] J. Li, R. J. Jaszczak, H. Wang, and R. Coleman, "A filtered-backprojection algorithm for fan-beam SPECT which corrects for patient motion," *Phys. Med. Biol.*, vol. 40, pp. 283–294, 1995.

[3] P. Grangeat, A. Koenig, T. Rodet, and S. Bonnet, "Theoretical framework for a dynamic cone-beam reconstruction algorithm based on a dynamic particle model," *Phys. Med. Biol.*, vol. 47, no. 15, pp. 2611–2625, August 2002.

[4] M. Kachelriess and W. A. Kalender, "Electrocardiogram-correlated image reconstruction from subsecond spiral computed tomography scans of the heart," *Medical Physics*, vol. 25(12), pp. 2417–2431, December 1998.

[5] T. Flohr and B. Ohnesorge, "Heart rate adaptative optimization of spatial and temporal resolution for electrocardiogram-gated multislice spiral CT of the heart," *Journal of Computer Assisted Tomography*, vol. 25(6), pp. 907–923, 2001.

[6] D. R. Gilland, B. A. Mair, J. E. Bowsher, and R. J. Jaszczak, "Simultaneous reconstruction and motion estimation for gated cardiac ECT," *IEEE Transactions on Nuclear Sciences*, vol. 49, pp. 2344–2349, October 2002.

[7] M. Kachelriess, S. Ulzeimer, and W. A. Kalender, "Ecg-correlated reconstruction from subsecond multi-slice spiral CT scans of the heart," *Medical Physics*, vol. 27(5), pp. 1881–1902, August 2000.

[8] C. Crawford, K. King, C. Ritchie, and J. Godwin, "Respiratory compensation in projection imaging using a magnification and displacement model," *IEEE Transactions on Medical Imaging*, vol. 15, pp. 327 –332, 1996.

[9] S. Rit, D. Sarrut, and L. Desbat, "Comparison of analytic and algebraic methods for motion-compensated cone-beam ct reconstruction of the thorax," *IEEE Transactions on Medical Imaging*, vol. 28, no. 10, pp. 1513–25, 2009.

[10] K. Taguchi and H. Kudo, "Motion compensated fan-beam reconstruction for nonrigid transformation," *IEEE Transactions on Medical Imaging*, vol. 27, no. 7, pp. 907– 917, 2008.

[11] A. Katsevich, "Motion compensated local tomography," *Inverse Problems*, vol. 24, no. 4, 2008.

[12] L. Desbat, S. Roux, and P. Grangeat, "Compensation of some time dependent deformations in tomography," *IEEE transaction on Medical Imaging*, vol. 26, no. 2, pp. 261–269, 2007.

[13] R. Clackdoyle and M. Defrise, "Tomographic reconstruction in the 21st century," *IEEE Signal Processing Magazine*, vol. 27, no. 4, pp. 60–80, 2010.

[14] F. Noo, M. Defrise, R. Clackdoyle, and H. Kudo, "Image reconstruction from fan-beam projections on less than a short-scan," *Phys. Med. Biol.*, vol. 47, pp. 2525–2546, July 2002.

[15] F. Noo, R. Clackdoyle, and J. Pack, "A two step hilbert transform method for 2d image reconstruction," *Phys. Med. Biol.*, vol. 49, no. 17, pp. 2525–2546, 2004.

[16] M. Defrise, F. Noo, R. Clackdoyle, and H. Kudo, "Truncated hilbert transform and image reconstruction from limited tomographic data," *Inverse Problems*, vol. 22, no. 3, pp. 1037–53, 2006.

An analysis of motion artifacts in CT and implications for motion compensation

Jed D. Pack and Bernhard Claus

***Abstract*—Motion artifacts continue to present a challenge in diagnostic CT. Algorithmic correction of motion artifacts is emerging as a valuable tool, but widespread use requires computational efficiency. An analysis of how the characteristics of motion artifacts depend both on the reconstruction algorithm and on the object dynamics is given. The findings are used to motivate a backproject-then-warp motion compensation strategy that provides computational advantages over the more traditional warp-then-backproject approach.**

***Index Terms*—motion compensation, cardiac CT**

I. INTRODUCTION

Algorithmic corrections for motion artifacts in diagnostic CT have long been sought after as such artifacts contribute to the low positive predictive value (PPV) of coronary CTA. A solution to the cardiac motion problem, therefore, has the potential to reduce the number of diagnostic cath procedures and thus reduce cost and improve quality of cardiac care. Often, approaches to solve this problem have taken a (sometimes iterative) two-step approach: i) estimate the motion of the heart and ii) compensate for the motion [1], [2], [3]. Arguably, the motion estimation is the more challenging problem, and advances in motion estimation are the key element in the success of emerging commercially available motion correction algorithms. Nevertheless, the choice of compensation approach can have a very significant impact on computational requirements and should, therefore, be carefully considered. This work begins with an analysis of the cause and nature of motion artifacts and proceeds to motivate a motion compensation technique that is computationally efficient.

A. Motion Artifact Analysis

To provide context for our motion artifact analysis, it is worth a brief review of how the simplest of CT reconstructions works. Consider a simple backprojection of an unfiltered 2D parallel-beam 180 degree sinogram. The resulting image is a blurred version of the original image because the data in each view is spread uniformly along the paths of the measured rays during backprojection. For example, if our original image is a delta function at the origin, our unfiltered backprojection image (over all 180 degrees) will decay inversely with distance from the origin. Use of a ramp filter allows each view to help cancel out the unwanted portions of the backprojection of every other view. Consider in our example a point that is sufficiently far from the origin (say on the y-axis). During backprojection, this point will receive a positive contribution only for the view (and a small set of nearby views, depending on sampling, apodization, etc.) that has rays parallel to the y-axis since it shares a ray with our delta function only in this view. For other views, the contribution will be negative. The sum of all the contributions over a 180 degree range is zero. This fact is why filtered backprojection works: the point spread function of forward projection and ramp-filtered backprojection is zero away from the origin, thus blurring is eliminated and a good representation of the true image results.

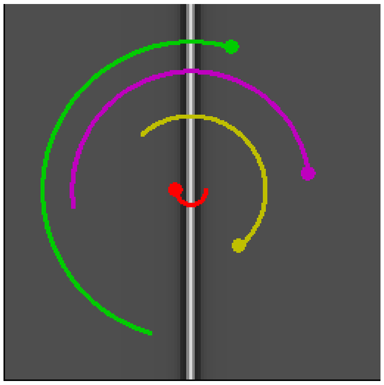

Fig. 1. Integration on any semicircle centered on the backprojected ramp filter kernel gives zero. This is why the ramp filter solves the blurring induced by projection/backprojection over 180 degrees.

The above framework can be used to analyze how this cancellation fails when there is motion, but it is useful to first recast the problem as follows: The summation over view for our point on the y-axis can also be thought of as an integration along a semicircle of the (single view) backprojection of the ramp filter kernel as shown in figure 1–that is to say, rotating the point is equivalent to sweeping the view angle. Note that the background image in figure 1 and other similar figures herein is the backprojection of the ramp filter kernel. It is worth noting that most of the cancellation for the positive contribution from the view along the y-axis comes from other views that are nearby since the highest amplitude negative taps of the ramp filter are all very close to the positive center. We can build up the point spread function of our system by performing the integrations on all semicircles—points farther from the origin have larger radii and points away from the y-axis would have different angular centers (as shown in the figure). All such integrations produce zero (provided the radius is sufficiently large).

It is now time to ask what would happen if our delta function moved around somewhat during the data acquisition. The answer is that the integrations would no longer be over a semicircle, but over a path that is perturbed from the semicircle based on the motion of the delta function. Carrying out all

---

J. D. Pack and B. Claus are with GE Global Research Center Niskayuna, NY 12309, Email: pack@ge.com

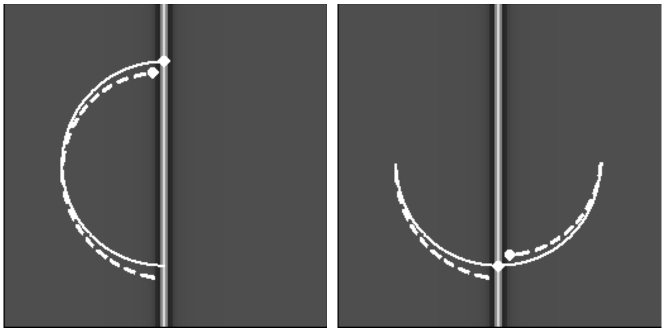

Fig. 2. Motion corrupts our point spread function by distorting the semicircle of integration. In this case, there are negative, but no positive contributions to the integration.

these integrations (over the various perturbed semicircles) would give us the various values of the point spread function of the motion corrupted system. As the ramp filter is fairly flat in most locations the point spread function will still approximately cancel out in most locations (assuming that the motion is smooth and not too large). There are two exceptions to this. Points that are very close to the origin spend a lot of time in the region of the ramp filter that is very steep since they move along a perturbed semicircle with a small radius (like the smallest semicircle in figure 1). Also, points with semicircles that have endpoints near the central spike of the ramp filter kernel can be strongly affected by small perturbations of the semicircular path. Thus, the motion corrupted point spread function can contain values that are far from zero near the origin and also along one particular line through the origin. The direction of this line is the projection direction of the first (or last) view.

Consider one example. In figure 2 the left image shows a perturbation (dashed line) of a semicircle (solid line). The dashed line represents linear motion. At the start of the path (top) the point is at a smaller radius than it is at the end, implying that the delta function has moved away from the point. Also, both endpoints of the dashed semicircle are on the same side of the ramp filter kernel, which means that the delta function has also moved to the side. It is useful to reflect each point in one half of each (perturbed) semicircle about the origin as shown in the right hand image. This does not affect the integration since the ramp filter is symmetric. The (reflected) unperturbed path is still a semicircle, so we know it integrates to 0 for this (no motion) case. There is a small range of strong positive contributions at the center and the contributions are negative elsewhere since the ramp filter kernel only has positive values near the central tap. In the case of the dashed line, the negative contributions are similar, but the entire positive portion of the ramp filter is skipped over due to the motion. On the other hand if the motion had been in the opposite direction (this case is not shown) the positive portion would have been counted twice. In either case, the integration would clearly not be zero as it is in the motion-free case. The key observation here is that although the motion is very smooth in time (it is linear), it is not smooth when parameterized by backprojection ray orientation (which is periodic) since there is a discontinuity between the beginning and the end of the scan. Recall that the bulk of the cancellation for unwanted backprojection from any particular view is done by the neighboring views. If these neighboring views see the object in a very different motion state, this cancellation may not occur properly.

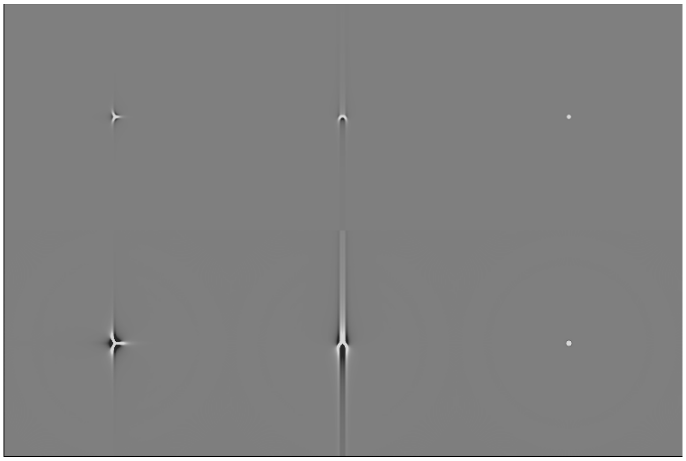

Fig. 3. Six images of point spread functions (psf) are shown. Top row (left to right): psf for a right-then-left zig-zag motion, psf for a motion to the right only, psf for the stationary case. Bottom row: same as top row, but with a grayscale window that is 10x tighter.

One can conclude from the preceding analysis that our motion corrupted point spread function will be more compact if the motion is such that the object returns to its original state by the end of the 180 degree acquisition. Indeed, figure 3 shows the integrals of our ramp image over the (perturbed) semicircles for an entire grid of pixels. These can be interpreted as (motion-corrupted) point spread functions. The images on the left correspond to a delta function that moves linearly to the right at a fixed rate of speed during the first 90 degrees and then moves linearly to the left at the same rate during the last 90 degrees, thus returning to its original location. The images in the center correspond to a delta function that moves to the right the entire time at half the rate such that the maximum displacement is the same. The images on the right are for a stationary delta function.

B. Backproject-then-warp

Let us now consider what happens if the reconstruction grid is moved in order to compensate for the motion of the object. For the simple case of rigid motion during a 2D parallel-beam acquisition, shifting the grid exactly compensates for the motion of the object. Furthermore, if the grid is shifted incorrectly, the motion artifacts that result match those that would have been seen with no motion compensation had the motion path been equal to the difference between the true motion and the assumed motion. For example, if the true motion were to the right at a rate of 20 mm/sec and the assumed motion was to the right at a rate of 15 mm/sec, the result of compensating for the motion by shifting the grid based on this assumption would be the same as what one would get without any compensation in the case where the motion is 5 mm/sec to the right.

Although these observations do not hold true for the case of non-rigid motion, they are good approximations of what

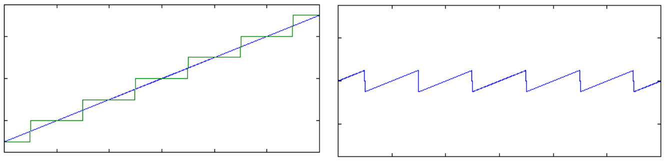

Fig. 4. Left: A piecewise constant approximation to linear motion (sampling every 30 degrees). Right: The residual motion due to sampling.

happens locally. Unfortunately, warping the grid every view according to a known non-rigid motion field can be quite computationally intensive. Two modifications can make the problem much more tractable. First, the motion fields are approximated as being step-like in time. In other words, the true (continuous) motion path at any location is sampled somewhat coarsely in time (for example, six samples might be taken over the time it takes to acquire 180 degrees worth of data). At any other time the motion state is assumed (approximated) to match that of the nearest sampled time point. Second, the warping is done after backprojection. Each step along our path must be backprojected into a separate image. These images can then be warped (each according to the corresponding motion field) before being added together. This backproject-then-warp approach to motion compensation is similar to an idea presented in [4].

The impact of these two modifications can now be analysed using the framework laid out in the previous section. The impact of warping after backprojection is theoretically nothing as these processes are linear and can be switched. With discrete sampling, however, there is an interpolation required in the warping in addition to the interpolation in the backprojection. This may have a smoothing effect, but if a good interpolator is used (e.g. tri-cubic instead of tri-linear) the impact will be neglibible, provided that the image sampling is sufficient to capture the inplane resolution well—it typically is in cardiac CT. The impact of sampling the motion path is that the compensation produces an image that is very much like the image that would have been produced without compensation had the motion been equal to the residual error in the motion due to sampling. For linear motion, this residual motion error is a sawtooth function as shown in figure 4. Note that when one considers the motion as a function of backprojected ray angle, the original linear motion was also a sawtooth function due to the inconsistency in the object state at the beginning and end of the acquisition. The difference is that the jumps in the new function are 6 times smaller than in the original function (and there are 6 times as many). The motion corrupted point spread function for this new case can be analysed as above. Our perturbed semicircles will have six small discontinuities. Wherever these discontinuities cause the semicircles to jump near the central spike of the ramp filter the integral may be far from zero. Figure 5 shows the result. The motion has been exaggerated in the top figure since it would otherwise be difficult to see the perturbed (dashed) path as distinct from the non-perturbed (solid) one.

A key improvement to this motion compensation approach is now introduced. As described briefly in [3], our partial backprojection ranges (each corresponding to one sample of our motion path) can be overlapped by a factor of two. An additional view weight can be incorporated such that each view is represented in two consecutive chunks and the sum of the two weights is one. Also, the views near the center of each chunk should be given the largest weight. For example, the view weighting can be a triangle function that goes linearly from 0 to 1 and back to zero. This requires a relatively modest change to the backprojection routine—it requires far fewer than twice the number of computations as a standard backprojection with non-overlapping view ranges. The result of this modification is shown in figure 6 (the motion magnitude has again been exaggerated so that the perturbed paths can be seen). The psf is much cleaner with this improvement and this will be reflected in reduced streak artifacts in the reconstructed images. Note that the triangular weighting function essentially does a linear interpolation to produce a net effect that is very similar to what a piecewise linear path would produce (rather than a piecewise constant path). Also, the integration is now a weighted integration with path segments that overlap substantially, thus eliminating the opportunity for creating significant artifacts as a result of sharp changes near the center of the ramp kernel.

Choosing the number of time samples can be a tradeoff between matching the performance of the warp-then-backproject approach (when the sampling is dense) and the computational efficiency of only needing to warp a small number of image volumes (when the sampling is sparse). In our experience, the temporal sampling does not need to be very high to see very dramatic reductions in motion artifacts, given a good estimate of the true motion fields. Warping this number of volumes is not a high computational cost.

It was mentioned above that in the case of non-rigid motion, the psf computed using the residual motion path may not be valid far from the point. It is better to compute the psf based on the difference in the assumed motion of the center point and the true motion of the point at which the kernel is being computed. This motion path is generally fairly smooth except at the transition between the beginning and ending of the data range (in view angle). One solution is to acquire more data than 180 degrees and to again introduce blending. In fact, this is a more realistic scenario than the 180 degree case as it is common today to reconstruct from a short-scan or more and use a view weighting to blend out the transition [5]. It should be pointed out that streaky motion artifacts have been observed in the past when using exact reconstruction techniques with fairly discontinuous view weights [7] [8]. Both of these papers proposed doing multiple reconstructions and averaging them appropriately (with the purpose of also reducing noise).

It is important to note that while the blending introduced between the start and end of the scan will eliminate streaks, there can be residual low frequency artifacts that are induced at a given location due to an object at another location that is moving in a different way. This is equally true for the backproject-then-warp approach and for the warp-then-backproject approach (it is also true for non-motion compensated reconstruction). Dealing with these artifacts is a topic that is beyond the scope of this paper, although we believe the framework described herein to be useful for this problem as well.

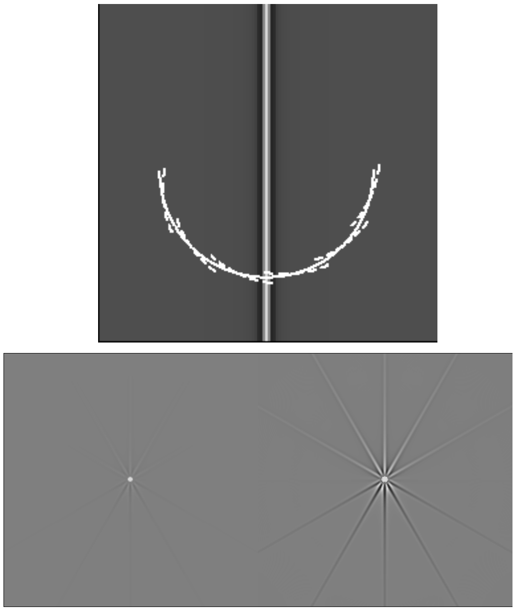

Fig. 5. Top: Perturbed semicircle. Bottom: psf corrupted by residual motion for the case of a non-optimized backproject-then-warp compensation. The grayscale windows used in the two images match those used in other psf figures (the one on the right is 10x tighter).

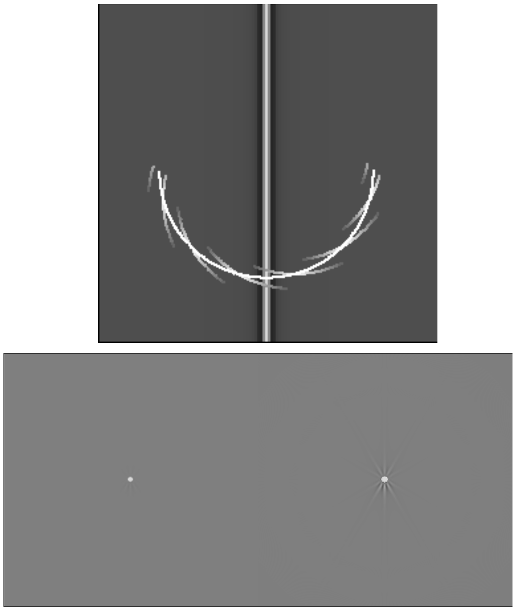

Fig. 6. Top: Perturbed semicircle (weighting of the integration is indicated by different graylevels). Bottom: psf corrupted by residual motion for the case of a better (blended) backproject-then-warp compensation.

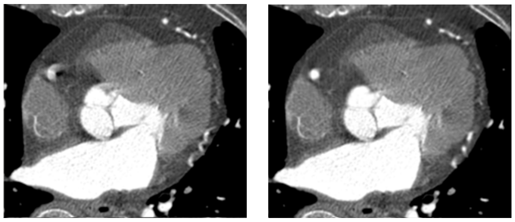

Fig. 7. Illustration of the capabilities of backproject-then-warp (non-rigid) motion compensation. Nine (partial reconstruction) image volumes were warped and added to produce the image on the right. Adding these nine volumes without any warp is equivalent to a standard reconstruction image (as shown on the left).

II. CONCLUSION

It can be concluded that the backproject-then-warp strategy for motion compensation is a very good approximation of the more traditional warp-then-backproject approach. While neither compensates perfectly for non-rigid motion (particularly at the low frequencies), either one is highly effective at properly restoring edges and other high frequency content. Further, the computational advantages of the backproject-then-warp approach are quite attractive. This is particularly true when one considers the investments that have been made in optimizations of the traditional fixed-grid backprojection. For example, using an inner loop in the z direction can cut down on the number of operations that each elementary backprojection requires when the grid is composed of uniform stacks of voxels along that direction (e.g., a standard Cartesian grid) [6]. Also, many existing optimizations to GPU code break down when the grid is warped prior to backprojection. Finally, if an iterative motion correction framework is used wherein the compensated images are fed back into the the motion estimation step in a loop, the backproject-then-warp method has a further computational advantage over the warp-then-backproject approach: backprojection only needs to be done once regardless of the number of iterations used since this step is not dependent on the estimated motion fields.

The motion artifact analysis is also instructive and highlights one advantage of continuing to use a smooth view weighting function like the well known Parker weighting even for non-compensated 3D reconstruction when scanning objects that are likely to move. In such cases, the benefits of constraining large scale motion artifacts to the lower frequencies can outweigh the benefits of theoretical exactness offered by some of the approaches that have developed in the past decade (in particular, those that effectively use a much more discontinuous view weight).

ACKNOWLEDGMENT

The authors would like to thank Roshni Bhagalia and Maria Iatrou for valuable discussions on this topic.

REFERENCES

[1] Q. Tang, J. Cammin, and K. Taguchi, “A fully four-dimensional, iterative motion estimation and compensation for cardiac x-ray computed tomography,” *11th International Meeting on Fully Three-Dimensional Image Reconstruction*, 470-3 (2011).

[2] A. A. Isola, M. Grass, and W. J. Niessen, “Fully automatic non-rigid registration-based local motion estimation for motion-corrected iterative cardiac CT reconstruction,” *Med. Phys.*, 37, 1093-1109 (2010).

[3] M. Iatrou, J. D. Pack, R. Bhagalia, D. Beque, and J. Seamans, “Coronary artery motion estimation and compensation: A feasibility study,” *IEEE NSS/MIC Conf. Record* (2010) pp. 2819-21.

[4] P. Grangeat, A. Koenig, T. Rodet, and S. Bonnet, “Theoretical framework for a dynamic cone-beam reconstruction algorithm based on a dynamic particle model,” *Phys. Med. Biol.*, 47, 2611-26, (2002).

[5] D. L. Parker, “Optimal short scan convolution reconstruction for fan beam CT,” *Med. Phys.* 9, 254 (1982).

[6] F. Noo, J. Pack, and D. Heuscher, “Exact helical reconstruction using native cone-beam geomatries,” *Phys. Med. Biol*, 48, 3787 (2003).

[7] H. Schondube, K. Stierstorfer, and F. Noo, “Accurate helical cone-beam CT reconstruction with redundant data,” *Phys. Med. Biol*, 54, 4625 (2009).

[8] T. Kohler, C. Bontus, and R. Proska, “BPF reconstruction for helical CT using all data” *IEEE NSS/MIC Conf. Record* (2008), pp 4154-6 (2008).

A novel motion estimation algorithm

Alexander Katsevich, Alexander Zamyatin and Mike Silver

***Abstract*—We continue investigation of a novel, simple and robust motion estimation algorithm proposed in [5]. The algorithm works with a sufficiently short time window, which is typically equivalent to that of a short scan. The center of the window is taken as reference time. The problem is to estimate motion within the window relative to the reference time. The proposed algorithm is based on quasi-exact motion-compensated reconstruction. If there is some uncompensated motion in f, the edges of f and of the reconstructed function f_{rec} in general do not coincide. Practically this means that if motion is not known (or, is known incorrectly), edges in the reconstructed image spread out. A single edge in f produces multiple edges in f_{rec} at random locations. Consequently, the reconstructed image will look "chaotic". We can use a measure of chaos in the reconstructed image f_{rec} to tell us whether our motion model is accurate or not. Our main idea is to iteratively refine the motion model, so that the chaos in f_{rec} is as small as possible. The results of testing the algorithm on real cardiac data show significant improvement of image quality.**

***Index Terms*—motion estimation, motion compensation, quasi-exact reconstruction, cardiac CT.**

I. INTRODUCTION

Motion estimation is a very important challenge in Computed Tomography (CT). Two major groups of approaches are available for solving this problem: voxel-based nonrigid image registration and surface-model-based segmentation [1], [2], [9], [10], [8]. As pointed out in [10], image registration methods suffer from strong artifacts. Model-based segmentation methods are more robust, but they are quite a bit more complicated.

In this paper we continue investigation of a novel, simple and robust motion estimation algorithm proposed in [5]. The algorithm is local in time, because it works with a sufficiently short time window. The length of the window is typically equivalent to that of a short scan. The center of the window is taken as reference time. The problem is to estimate motion within the window relative to the reference time. Here we describe some improvements compared to the algorithm in [5] and show the results of testing on real cardiac data.

II. DESCRIPTION OF THE ALGORITHM

The proposed algorithm is based on a simplified quasi-exact filtered-backprojection type motion-compensated reconstruction. Let f_{rec} be the reconstructed function. If there is some uncompensated motion in f, the edges of f and f_{rec} in general no longer coincide [4]. Practically this means that if motion is not known (or, is known incorrectly), edges in the reconstructed image spread out. A single edge produces multiple edges at random locations. Consequently, the reconstructed image will look "chaotic". We can use a measure of chaos in the reconstructed image f_{rec} to tell us whether our motion model is accurate or not. Using this idea, we summarize the proposed motion estimation algorithm as follows.

1) Assume some motion model;
2) Perform motion-compensated image reconstruction using the current motion model;
3) Compute the measure of chaos in the reconstructed image;
4) If chaos is low (i.e., image quality is good), stop. If chaos is high, change the motion model and go to step 2.

A similar idea was used in [7] for misalignment correction in circular cone beam CT. The main novelty of our approach is that we use a new criterion for estimating image quality instead of conventional entropy. We also came up with a sufficiently general motion model, that allows a speed-up of the algorithm. We now describe the algorithm in more detail.

A. Motion model

Let $[t_l, t_r]$ be a time window, which is used for motion estimation. The center point $t_0 = (t_l + t_r)/2$ is taken as reference time. The primary purpose of the algorithm is to perform local (in time) motion estimation, thus the width of the window $T := t_r - t_l$ is usually rather short. In our experiments T is typically less than one gantry rotation. Let D denote the region where motion takes place. We assume that D is a rectangular parallelepiped, i.e. $D := \{(x, y, z) : x_l < x < x_r, y_l < y < y_r, z_b < z < z_t\}$. To represent motion, we consider a rectangular grid over D. The grid planes are

$$\begin{aligned} x &= x_i = x_l + i\Delta x,\ 0 \le i \le N_x + 1, \\ y &= y_j = y_l + j\Delta y,\ 0 \le j \le N_y + 1, \\ z &= z_k = z_b + k\Delta z,\ 0 \le k \le N_z + 1, \end{aligned} \tag{1}$$

where $\Delta x = (x_r - x_l)/(N_x + 1)$, $\Delta y = (y_r - y_l)/(N_y + 1)$, and $\Delta z = (z_t - z_b)/(N_z + 1)$. Thus, grid (1) has $N_x N_y N_z$ interior nodes. Because of motion, the grid planes are deformed over time:

$$\begin{aligned} x &= x_i + a_i(t)\phi[(y - y_l)/(y_r - y_l)]\phi[(z - z_b)/(z_t - z_b)], \\ y &= y_j + b_j(t)\phi[(x - x_l)/(x_r - x_l)]\phi[(z - z_b)/(z_t - z_b)], \\ z &= z_k + c_j(t)\phi[(x - x_l)/(x_r - x_l)]\phi[(y - y_l)/(y_r - y_l)], \\ & 1 \le i \le N_x,\ 1 \le j \le N_y,\ 1 \le k \le N_z. \end{aligned} \tag{2}$$

We assume that motion equals zero at the boundary of D, so the boundary grid planes (i.e. those corresponding to $i = 0, N_x + 1$, $j = 0, N_y + 1$, and $k = 0, N_z + 1$ do not change. In (2), the function ϕ is smooth, defined on the interval $[0, 1]$, and

---

Department of Mathematics, University of Central Florida, Orlando, FL 32816. Corresponding author: Alexander Katsevich, E-mail: Alexander.Katsevich@ucf.edu

Toshiba Medical Researc Institute USA, Inc, Vernon Hills, IL 60061.

equals zero at both endpoints of the interval. Since the time window T is sufficiently short, we assume that the functions $a_i(t)$, $b_j(t)$, and $c_k(t)$, are linear:

$$\begin{aligned} &a_i(t)=a_i(t-t_0)/(0.5T), b_j(t)=b_j(t-t_0)/(0.5T),\\ &c_k(t)=c_k(t-t_0)/(0.5T), \end{aligned} \tag{3}$$

where $a_i, 1 \leq i \leq N_x$, $b_j, 1 \leq j \leq N_y$, $c_k, 1 \leq k \leq N_z$, are constants to be determined. Note that substituting $t=t_0$ into (2) gives rectangular grid (1). Equations (2) and (3) allow us to describe motion of every point in D. To determine where a grid node (x_i, y_j, z_k) is located at time t, we find the intersection of the corresponding i-th, j-th, and k-th deformed grid planes in (2) at time t. Location of all other pixels is computed using trilinear interpolation.

B. *Motion compensated reconstruction and edge entropy*

Let C be a smooth curve in $\mathbb{R}^3$

$$\mathbb{R} \ni s \to r_c(s) \in \mathbb{R}^3,\ |\dot{r}_c(s)| \neq 0. \tag{4}$$

Here the dot denotes the derivative with respect to s. Usually the source moves along C with constant speed, so we identify s with time variable. To simplify notations, the model of motion described in the preceding section is denoted simply by $\psi(s,r)$, $r:=(x,y,z)$. More precisely, $r'=\psi(s,r)$ is the position of the particle at time s, which is located at r at the reference time $s=t_0$. In the absence of motion, theoretically exact image reconstruction in the case of helical trajectory is achieved by the formula [3]:

$$\begin{aligned} f(r)&=-\frac{1}{2\pi^2}\int_{I_{PI}(r)}\frac{1}{|r-r_c(s)|}\Psi(s,r)ds,\\ \Psi(s,r)&:=\int_0^{2\pi}\frac{\partial}{\partial q}D_f(r_c(q),\Theta(s,r,\gamma))\bigg|_{q=s}\frac{d\gamma}{\sin\gamma}. \end{aligned} \tag{5}$$

Here $I_{PI}(r)$ is the PI-interval of r, $\beta(s,r):=\frac{r-r_c(s)}{|r-r_c(s)|}$, and $D_f(r_c,\beta)$ is the cone beam transform of f:

$$D_f(r_c,\Theta):=\int_0^\infty f(r_c+\Theta t)dt. \tag{6}$$

Also, $e(s,r):=\beta(s,r)\times u(s,r)$, $\Theta(s,r,\gamma):=\cos\gamma\beta(s,r)+\sin\gamma e(s,r)$, and $u(s,r)$ is a vector function chosen in a special way (see e.g., [3]). At the stage of motion estimation our goal is not to come up with the best possible image reconstruction. Instead, we seek an efficient algorithm, which reproduces edges accurately. Thus, to speed up the calculations, we make the following simplifications in (5): (a) Filtering, which is represented by the second equation in (5), is done along detector rows, instead of tilted lines determined by the vector-function u; (b) Motion is ignored during the filtering step, and is taken into account only during back-projection. More precisely, the first integral in (5) is replaced by

$$f_{rec}(r)=-\frac{1}{2\pi^2}\int_{I_{PI}(r)}\frac{1}{|\psi(s,r)-r_c(s)|}\Psi(s,\psi(s,r))ds. \tag{7}$$

(c) Finally, the interval $I_{PI}(r)$ is replaced by the interval of the source trajectory corresponding to the time window $[t_l,t_r]$. To compensate for the possible artifacts caused by the sharp truncation at t_l and t_r, we insert in (7) a smooth cut-off function, which is based on the idea of PI-partners of [6]. The cut-off function also is computed by ignoring motion.

Next we describe a proposed measure of "chaos" in an image, which we call "edge entropy". Suppose f_{rec} is computed on a regular grid $r_{mnp}:=(x_m,y_n,z_p), 1\leq m\leq M, 1\leq n\leq N, 1\leq p\leq P$, which covers D. Of course, this grid should be much more dense than the one in (1). We also need a shifted grid with nodes $\bar{r}_{mnp}:=(\bar{x}_m,\bar{y}_n,\bar{z}_p)$, where $\bar{x}_m=x_m+\Delta x/2$, $1\leq m\leq M-1$, and $\bar{y}_n,\bar{z}_p$ are defined similarly. Introduce the distance function:

$$\text{dist}(\bar{r}_{m_1n_1p_1},\bar{x}_{m_2n_2p_2})=\max(|m_1-m_2|,|n_1-n_2|,|p_1-p_2|). \tag{8}$$

Calculation of edge entropy consists of several steps. Let a parameter $\kappa, 0<\kappa<1$, be fixed.

1) Using finite differences, compute the norm of the gradient $|\nabla f_{rec}(x_{m'},y_{n'},z_{p'})|$, where primes denote a shift of half a pixel;
2) Compute the empirical histogram of the norm of the gradient;
3) Using the histogram, estimate the value M such that $|\nabla f_{rec}(x_{m'},y_{n'},z_{p'})|>M$ for 100κ percent of the pixels (such pixels are called "bright");
4) By running a sliding window over the image compute the total number of points $\bar{r}_{mnp}$ whose distance (in the sense of (8)) to the closest bright point equals either 2, 3, or 4;
5) Divide this number by the total number of nodes in the grid and multiply by 100 (to get percents). The result is the edge entropy of the image f_{rec}.

C. *Remarks on implementation*

In this subsection we describe various tricks, that help deal with instability and improve overall efficiency.

1) Since the filtering step is motion-independent, it is performed only once at the beginning of iterations;
2) For simplicity, each of the parameters a_j,b_j,c_k in (3) can take only three values: $-h$, 0, or h, where $h>0$ is a predetermined constant;
3) The coordinate planes (1), (2) split D into a collection of smaller sub-regions D_{ijk}. The deformation of each such sub-region depends only on six parameters, that describe the planes that form its faces. It does not depend on all other parameters. Each of the six relevant parameters can take only three different values. Thus, each sub-cube is precomputed 3^6 times and stored;
4) The minimum of edge entropy is found by looping over all possible combinations of parameters in the following way. First, we create the volume D by combining the appropriate versions of the sub-volumes D_{ijk} based on the current values of the parameters corresponding to its faces. Note that no image reconstruction needs to be done at this stage. Then, edge entropy is computed for D. If it is less than the current minumum, the new minimum is retained and the current comination of parameters is called optimal.

III. EVALUATION

We use clinical data from Charite Hospital, Berlin. The source trajectory is circular. As a baseline for comparison, we use an FBP short scan reconstruction. Both FBP and proposed methods use a subset of 800 views. Number of views per rotation is 900. Rotation time is 0.35 ms. The heartbeat is 56 bpm for the first patient and 52 bpm for the second patient. Typically cardiac reconstruction uses cardiac phases where cardiac motion is minimal, such as end-systole (33% of R-R interval) or mid-diastole (75% of R-R interval). To illustrate the potential of our approach, we selected a midsystole phase (20% of the R-R interval for the first patient and 15% for the second patient), where the ventricles rapidly contract to pump blood to the body and lungs. Results are shown in Figures 1 and 2. The proposed approach shows significant reduction of motion artifacts. In particular, small high-contrast objects near the center become better localized and less distorted, organ shape becomes more continuous, and organ boundaries become clearly separated.

IV. CONCLUSION

We propose a robust motion estimation algorithm. Evaluation shows reduction of motion artifacts and improved image quality. One of our concerns was performance with noisy clinical data. Evaluation shows that the proposed approach is stable to data noise. Currently we are working on evaluation with more datasets and quantitative measurement of temporal resolution improvement with the proposed approach.

ACKNOWLEDGMENT

The work of AK was supported by NSF grant DMS-0806304 and Toshiba Medical Research Institute, USA. We thank Satoru Nakanishi of Toshiba Medical System Corp., Japan, for help with this investigation.

REFERENCES

[1] C. Blondel, R. Vaillant, G. Malandain, and N. Ayache. 3D tomographic reconstruction of coronary arteries using a precomputed 4D motion field. *Physics in Medicine and Biology*, 49:2197–2208, 2004.

[2] U. Jandt, D. Schafer, M. Grass, and V. Rasche. Automatic generation of time-resolved 4D motion vector fields of coronary arteries. In *Proceedings of the IXth International Conference on Fully 3D Reconstruction in Radiology and Nuclear Medicine. Lindau, Germany. July 9 - 13, 2007*, pages 249–252, 2007.

[3] A. Katsevich. Analysis of an exact inversion algorithm for spiral cone-beam CT. *Physics in Medicine and Biology*, 47:2583–2598, 2002.

[4] A. Katsevich. Motion compensated local tomography. *Inverse Problems*, 24, 2008. article ID 045013 (21 pp).

[5] A. Katsevich, M. Silver, and A. Zamyatin. Local tomography and the motion estimation problem. *SIAM Journal on Imaging Sciences*, 4:200–219, 2011.

[6] Th. Köhler, C. Bontus, and P. Koken. The Radon-split method for helical cone-beam CT and its application to nongated reconstruction. *IEEE Transactions on Medical Imaging*, 25:882–897, 2006.

[7] Y Kyriakou, R. M. Lapp, L. Hillebrand, D. Ertel, and W.A. Kalender. Simultaneous misalignment correction for approximate circular cone-beam computed tomography. *Physics in Medicine and Biology*, 53:6267–6289, 2008.

[8] K. Taguchi, W. P. Segars, G. Fung, and B. M.W. Tsui. Toward time resolved 4D cardiac CT imaging with patient dose reduction: estimating the global heart motion. In M. J. Flynn and J. Hsieh, editors, *Proc. Medical Imaging 2006: Physics of Medical Imaging*, pages 61420J–9, 2006. Proceedings SPIE-6142.

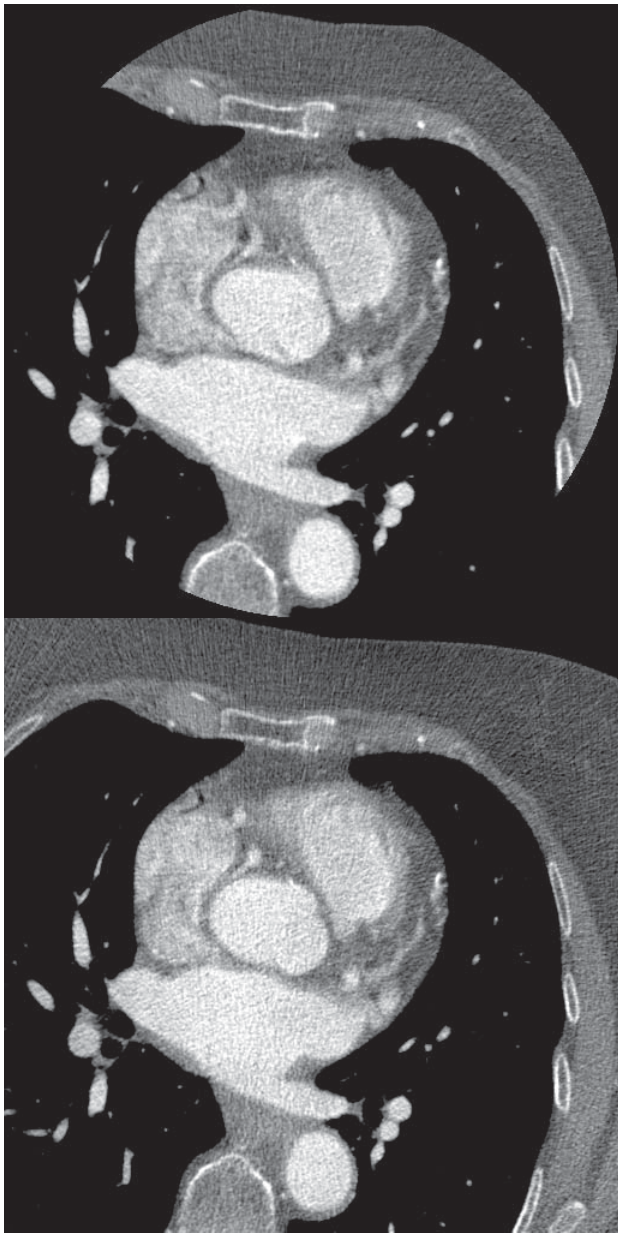

Fig. 1. Evaluation of the proposed method with the first clinical dataset. Top panel: FBP-Short Scan Reconstruction, bottom panel: proposed method. W/L = 800/200 HU.

[9] U. van Stevendaal, C. Lorenz, J. von Berg, and M. Grass. Motion-compensated reconstruction in helical cardiac CT. In *Proceedings of the IXth International Conference on Fully 3D Reconstruction in Radiology and Nuclear Medicine. Lindau, Germany. July 9 - 13, 2007*, pages 437–440, 2007.

[10] U. van Stevendaal, J. von Berg, C. Lorenz, and M. Grass. A motion-compensated scheme for helical cone-beam reconstruction in cardiac CT angiography. *Medical Physics*, 35:3239–3251, 2008.

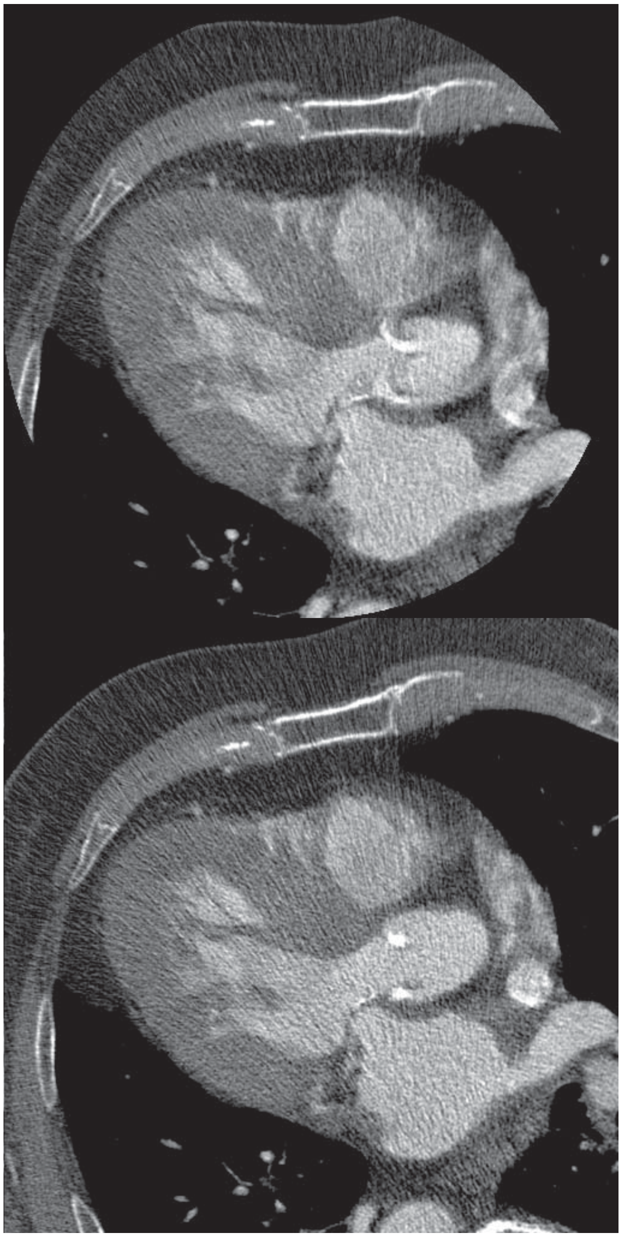

Fig. 2. Evaluation of the proposed method with the second clinical dataset. Top panel: FBP-Short Scan Reconstruction, bottom panel: proposed method. W/L = 800/200 HU.

MOTION-COMPENSATED IMAGE RECONSTRUCTION WITH ALTERNATING MINIMIZATION

Jang Hwan Cho, Sathish Ramani and Jeffrey A. Fessler

ABSTRACT

Cardiac computed tomography (CT) is important for its use in diagnosing heart disease. Motion artifacts are a significant issue for cardiac CT image reconstruction. Motion-compensated image reconstruction (MCIR) has the potential to overcome the drawbacks of conventional gated reconstruction methods by exploiting all the measurement data and using motion information. However, MCIR methods are computationally expensive: the system matrix has both the forward-projector and the warp matrices that make it hard to precondition or to apply block iterative algorithms such as ordered-subsets (OS). In this study, we propose a novel approach to solve the image reconstruction part of the MCIR method more efficiently. We use a variable-splitting technique to dissociate the original problem into a number of simpler problems. The proposed method is amenable to preconditioning, parallelization, and application of block iterative algorithms to sub-problems. We demonstrated through a phantom simulation that with simple diagonal or circulant preconditioners, the proposed method shows good convergence rate compared to conjugate gradient (CG) method.

1. INTRODUCTION

Even with the fast acquisition speed of commercial scanners, motion artifacts such as blurring and streaks are still a significant issue in CT image reconstruction, especially for cardiac CT imaging. Various methods have been proposed to address this problem [1, 2]. Many of these are gated reconstruction methods that use only the projection data corresponding to approximately the same motion state. Such methods can provide promising results in terms of image quality and processing time. However, they suffer from limitations such as dose inefficiency and limited temporal resolution. Especially for fast and arhythmic cardiac motion, such methods may be subjected to residual motion artifacts [3].

To overcome the limitations of gated reconstruction, a variety of motion-compensated image reconstruction methods (MCIR) have been proposed in the literature [3, 4]. MCIR methods can exploit all collected data and motion information to obtain reconstructed images with better dose efficiency. In general, MCIR methods consist of two main steps: estimating the motion and reconstructing the image using the estimated motion. The quality of the reconstructed image is significantly affected by the accuracy of the estimated motion, and thus many researchers have focussed on improving motion estimates. However, the image reconstruction part is also very important for practical use of MCIR methods. Since the system model in MCIR methods has both the forward-projector and the warp matrices, it becomes computationally very expensive to use iterative algorithms for MCIR. Unlike conventional CT image reconstruction problems, designing a proper preconditioner for MCIR is not trivial due to the complexity of the system model. Ordered-subset (OS) type of algorithms are not efficient for MCIR, especially when when warping is computationally expensive.

In this paper, we propose a novel approach to solve the image reconstruction part of MCIR method more efficiently. We use a variable-splitting technique to dissociate the original problem into a number of simpler problems that are then solved individually.

2. MOTION-COMPENSATED IMAGE RECONSTRUCTION FOR CT

2.1. Measurement Model

Let $\boldsymbol{x}(\boldsymbol{r}, t)$ denote the time-dependent attenuation coefficient distribution of the unknown object, where $\boldsymbol{r}$ is the spatial location and t is time. Let t_m be the time of mth frame at which the measurements, $\boldsymbol{y}_m$, corresponding to the motion-free state of the objects are acquired. We assume that the measurements consist of N_f scans, $\boldsymbol{y} = [\boldsymbol{y}_1, \cdots, \boldsymbol{y}_{N_f}]$. The measurements were assumed to be linearly related to the object $\boldsymbol{x}_m = \boldsymbol{x}(\cdot, t_m)$ as follows:

$$\boldsymbol{y}_m = \boldsymbol{A}_m \boldsymbol{x}_m + \epsilon_m, \quad m = 1, \cdots, N_f, \tag{1}$$

where $\boldsymbol{A}_m$ is the system model for mth frame and ϵ_m is the noise. The goal is to reconstruct $\{\boldsymbol{x}_m\}$ from $\{\boldsymbol{y}_m\}$ using a motion model. Here we assume $\boldsymbol{x}_m = \boldsymbol{T}_m \boldsymbol{x}$ where $\boldsymbol{T}_m$ is a warp matrix based on motion estimates that are determined separately.

This work is supported by GE Healthcare.

The authors are with the Electrical Engineering and Computer Science Department, University of Michigan, Ann Arbor, MI 48109-2122 USA

2.2. Problem Formulation

Consider a penalized-likelihood least squares (PWLS) formulation of motion-compensated CT image reconstruction:

$$\hat{\boldsymbol{x}} = \arg\min_{\boldsymbol{x}} \{\Psi(\boldsymbol{x}) \triangleq \mathsf{L}(\boldsymbol{x}) + \mathsf{R}(\boldsymbol{C}\boldsymbol{x})\}, \tag{2}$$

$$\mathsf{L}(\boldsymbol{x}) = \frac{1}{2}\|\boldsymbol{y} - \boldsymbol{A}\boldsymbol{T}\boldsymbol{x}\|_{\boldsymbol{W}}^2, \quad \mathsf{R}(\boldsymbol{C}\boldsymbol{x}) = \beta \sum_{k=1}^{K} \kappa_k \, \psi_k([\boldsymbol{C}\boldsymbol{x}]_k),$$

$$\boldsymbol{A} = \mathrm{diag}\{\boldsymbol{A}_1, \cdots, \boldsymbol{A}_{N_f}\}, \quad \boldsymbol{T} = [\boldsymbol{T}_1' \ldots \boldsymbol{T}_{N_f}']',$$

where $\boldsymbol{A}$ is the system matrix, $\boldsymbol{x} \in \mathbb{R}^N$ is the discretized version of the object being reconstructed, $\boldsymbol{W} = \mathrm{diag}\{w_i\}$ is a statistical weighting matrix, β is the regularization parameter, κ_k is the user-defined weight for controlling spatial resolution in the reconstructed image, ψ_k is the potential function, $\boldsymbol{C}$ is a matrix that performs finite differences between neighboring voxels, K is the number of neighbors, and $\boldsymbol{T}$ is the warp matrix. The minimization problem (2) is challenging due to the warp matrix $\boldsymbol{T}$ in the system model.

3. PROPOSED METHOD

We apply a variable splitting approach to the problem. The basic idea of variable splitting method is to introduce auxiliary constraint variables so that coupled parts in the cost function can be separated [5]. The original problem is transformed into an equivalent constrained optimization problem, and then alternating minimization methods are applied to efficiently solve the problem. Previous works have focussed on splitting the regularization term and also the statistical weighting [6]. In this work, in addition to those splittings, we focus on splitting the warp matrix from the forward-projector in the system matrix.

3.1. Equivalent Constrained Optimization Problem

We introduce auxiliary constraint variables $\boldsymbol{u}$, $\boldsymbol{v}$, $\boldsymbol{z}$, and $\boldsymbol{s}$, and write (2) as the following equivalent constrained problem:

$$\arg\min_{\boldsymbol{x},\boldsymbol{u},\boldsymbol{v},\boldsymbol{z},\boldsymbol{s}} \Psi(\boldsymbol{x},\boldsymbol{u},\boldsymbol{v},\boldsymbol{z},\boldsymbol{s}) = \frac{1}{2}\|\boldsymbol{y} - \boldsymbol{v}\|_{\boldsymbol{W}}^2 + \mathsf{R}(\boldsymbol{z}),$$

$$s.t. \quad \boldsymbol{u} = \boldsymbol{T}\boldsymbol{x}, \quad \boldsymbol{v} = \boldsymbol{A}\boldsymbol{u}, \quad \boldsymbol{z} = \boldsymbol{C}\boldsymbol{s}, \quad \boldsymbol{s} = \boldsymbol{x}, \tag{3}$$

where $\boldsymbol{u} \in \mathbb{R}^{NN_f}$ separates the system matrix from the warp matrix, $\boldsymbol{v} \in \mathbb{R}^M$ separates the effect of the weighting matrix, $\boldsymbol{W}$, on $\boldsymbol{A}\boldsymbol{x}$, $\boldsymbol{z} \in \mathbb{R}^{NK}$ and $\boldsymbol{s} \in \mathbb{R}^N$ detach the warp matrix from the regularizer.

3.2. Method of Multipliers

We used the framework of method of multipliers [7] to solve (3), and constructed an augmented Lagrangian function as follows:

$$\begin{aligned} L(\boldsymbol{x},\boldsymbol{u},\boldsymbol{v},\boldsymbol{z},\boldsymbol{s}) &\triangleq \frac{1}{2}\|\boldsymbol{y} - \boldsymbol{v}\|_{\boldsymbol{W}}^2 + \mathsf{R}(\boldsymbol{z}) \\ &+ \frac{\mu_{\boldsymbol{u}}}{2}\|\boldsymbol{u} - \boldsymbol{T}\boldsymbol{x} - \eta_{\boldsymbol{u}}\|^2 + \frac{\mu_{\boldsymbol{v}}}{2}\|\boldsymbol{v} - \boldsymbol{A}\boldsymbol{u} - \eta_{\boldsymbol{v}}\|^2 \\ &+ \frac{\mu_{\boldsymbol{z}}}{2}\|\boldsymbol{z} - \boldsymbol{C}\boldsymbol{s} - \eta_{\boldsymbol{z}}\|^2 + \frac{\mu_{\boldsymbol{s}}}{2}\|\boldsymbol{s} - \boldsymbol{x} - \eta_{\boldsymbol{s}}\|^2, \end{aligned} \tag{4}$$

where η's are Lagrange-multiplier-like vectors and μ's are the AL penalty parameters (see [6] for details).

Solving (3) using the AL function would require jointly minimizing (4) with respect to all variables which is computationally expensive. So we apply to alternating minimization [6].

3.3. Alternating Direction Minimization

At the jth iteration, we update each vector in turn as follows:

$$\begin{aligned} \boldsymbol{x}^{(j+1)} &= \arg\min_{\boldsymbol{x}} \frac{\mu_{\boldsymbol{u}}}{2}\left\|\boldsymbol{u}^{(j)} - \boldsymbol{T}\boldsymbol{x} - \eta_{\boldsymbol{u}}^{(j)}\right\|^2 \\ &\quad + \frac{\mu_{\boldsymbol{s}}}{2}\left\|\boldsymbol{s}^{(j)} - \boldsymbol{x} - \eta_{\boldsymbol{s}}^{(j)}\right\|^2, && (5) \\ \boldsymbol{u}^{(j+1)} &= \arg\min_{\boldsymbol{u}} \frac{\mu_{\boldsymbol{u}}}{2}\left\|\boldsymbol{u} - \boldsymbol{T}\boldsymbol{x}^{(j+1)} - \eta_{\boldsymbol{u}}^{(j)}\right\|^2 \\ &\quad + \frac{\mu_{\boldsymbol{v}}}{2}\left\|\boldsymbol{v}^{(j)} - \boldsymbol{A}\boldsymbol{u} - \eta_{\boldsymbol{v}}^{(j)}\right\|^2, && (6) \\ \boldsymbol{v}^{(j+1)} &= \arg\min_{\boldsymbol{v}} \frac{1}{2}\|\boldsymbol{y} - \boldsymbol{v}\|_{\boldsymbol{W}}^2 \\ &\quad + \frac{\mu_{\boldsymbol{v}}}{2}\left\|\boldsymbol{v} - \boldsymbol{A}\boldsymbol{u}^{(j+1)} - \eta_{\boldsymbol{v}}^{(j)}\right\|^2, && (7) \\ \boldsymbol{s}^{(j+1)} &= \arg\min_{\boldsymbol{s}} \frac{\mu_{\boldsymbol{z}}}{2}\left\|\boldsymbol{z}^{(j)} - \boldsymbol{C}\boldsymbol{s} - \eta_{\boldsymbol{z}}^{(j)}\right\|^2 \\ &\quad + \frac{\mu_{\boldsymbol{s}}}{2}\left\|\boldsymbol{s} - \boldsymbol{x}^{(j+1)} - \eta_{\boldsymbol{s}}^{(j)}\right\|^2, && (8) \\ \boldsymbol{z}^{(j+1)} &= \arg\min_{\boldsymbol{z}} \mathsf{R}(\boldsymbol{z}) \\ &\quad + \frac{\mu_{\boldsymbol{z}}}{2}\left\|\boldsymbol{z} - \boldsymbol{C}\boldsymbol{s}^{(j+1)} - \eta_{\boldsymbol{z}}^{(j)}\right\|^2, && (9) \\ \eta_{\boldsymbol{u}}^{(j+1)} &= \eta_{\boldsymbol{u}}^{(j)} - (\boldsymbol{u}^{(j+1)} - \boldsymbol{T}\boldsymbol{x}^{(j+1)}), && (10) \\ \eta_{\boldsymbol{v}}^{(j+1)} &= \eta_{\boldsymbol{v}}^{(j)} - (\boldsymbol{v}^{(j+1)} - \boldsymbol{A}\boldsymbol{u}^{(j+1)}), && (11) \\ \eta_{\boldsymbol{s}}^{(j+1)} &= \eta_{\boldsymbol{s}}^{(j)} - (\boldsymbol{s}^{(j+1)} - \boldsymbol{x}^{(j+1)}), && (12) \\ \eta_{\boldsymbol{z}}^{(j+1)} &= \eta_{\boldsymbol{z}}^{(j)} - (\boldsymbol{z}^{(j+1)} - \boldsymbol{C}\boldsymbol{s}^{(j+1)}), && (13) \end{aligned}$$

The sub-problems (5) to (8) are all quadratic problems for which analytical solutions exist. However, (5) and (6) cannot be implemented explicitly due to the enormous sizes of the matrices involved. We employ the iterative CG-solver for these sub-problems.

Sub-problem (5) is an image-registration-type problem, which has the following analytical solution:

$$\boldsymbol{x}^{(j+1)} = \boldsymbol{H}^{-1}(\mu_{\boldsymbol{u}}\boldsymbol{T}'(\boldsymbol{u}^{(j)} - \eta_{\boldsymbol{u}}^{(j)}) + \mu_{\boldsymbol{s}}(\boldsymbol{s}^{(j)} - \eta_{\boldsymbol{s}}^{(j)})), \tag{14}$$

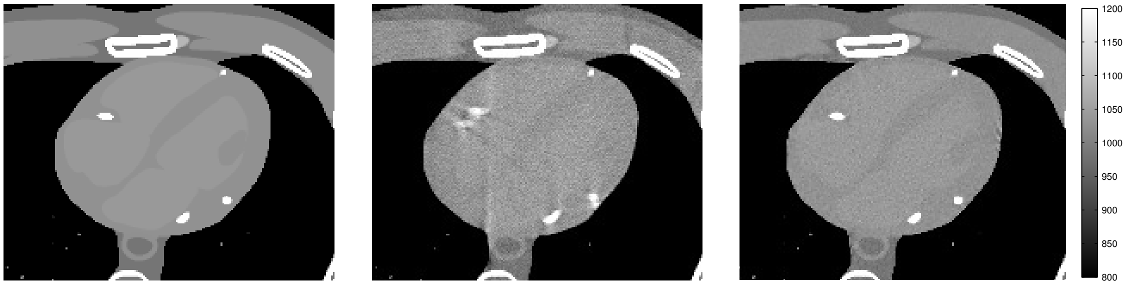

(a) (b) (c)

Fig. 1. Images in the ROI of (a) XCAT phantom, (b) FBP reconstruction with Hanning filter (also the initial guess $\boldsymbol{x}^{(0)}$), (c) Converged Image $\boldsymbol{x}^{(\infty)}$.

where $\boldsymbol{H} = \mu_{\boldsymbol{u}}\boldsymbol{T}'\boldsymbol{T} + \mu_{\boldsymbol{s}}\boldsymbol{I}_N$. We accelerate the CG-solver for (14) by using a suitable preconditioner for $\boldsymbol{H}$. Since $\boldsymbol{H}$ is much simpler than the Hessian of the original data term in (2), it is more amenable to preconditioning.

We now consider (6), which is a tomography problem with the following solution:

$$\boldsymbol{u}^{(j+1)} = \boldsymbol{G}^{-1}(\mu_{\boldsymbol{u}}(\boldsymbol{T}\boldsymbol{x}^{(j+1)} + \eta_{\boldsymbol{u}}^{(j)}) + \mu_{\boldsymbol{v}}\boldsymbol{A}'(\boldsymbol{v}^{(j)} - \eta_{\boldsymbol{v}}^{(j)})),$$

where $\boldsymbol{G} = \mu_{\boldsymbol{v}}\boldsymbol{A}'\boldsymbol{A} + \mu_{\boldsymbol{u}}\boldsymbol{I}_{NN_f}$. We preconditioned this term with a circulant matrix to obtain faster convergence [6, 8]. This sub-problem can be further parallelized into N_f problems. Each parallelized problem can be efficiently solved by preconditioned CG or ordered-subsets type algorithms, which are less efficient for the original problem.

Sub-problems (7) - (9) can be solved much more easily compared to above two sub-problems. Sub-problem (7) has a simple analytical solution, and (8) is exactly solvable with Fourier transform if we use $\boldsymbol{C}$ with periodic end condition. Finally, (9) can be solved easily with iterative algorithms or exactly solved for a variety of potential functions. Here, we consider one of the edge-preserving regularization using the Fair potential function. For this regularizer, (9) separates into 1D minimization problems and has an exact solution (See [6] for details). The AL parameters, μ's, mainly govern the convergence speed of the proposed splitting method [6]; we selected them empirically to achieve good convergence speed.

4. RESULTS

The proposed algorithm was investigated on a 2D CT image reconstruction problem with cardiac motion for simulated data. We simulated a 3rd-generation fan-beam CT system using the separable footprint projector [9]. The simulated system has 888 channels per view spaced 1.0239 mm apart, and 984 evenly spaced view angles over 360°. The image was reconstructed to a 512×512 grid of 0.9766 mm pixels. We generated seven frames of the XCAT phantom for a heart rate of 75 bpm. The motion between the frames was estimated directly from XCAT images using nonrigid image registration.

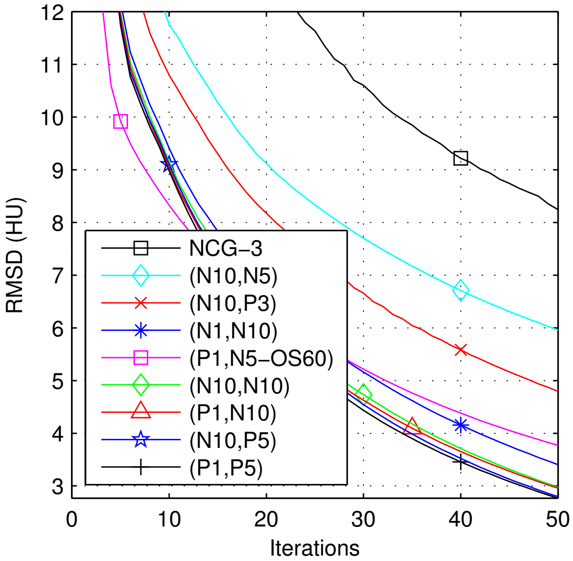

Fig. 2. Plot of RMSD versus iteration for various settings of the proposed method compared to the conventional CG method. For the proposed method, (N10,P5) indicates 10 iterations for sub-problem (5) without preconditioner for $\boldsymbol{H}$ and 5 iterations for sub-problem (6) with a preconditioner for $\boldsymbol{G}$. OS60 indicates that ordered subsets method with 60 subsets was used instead of CG.

Estimating motion parameters from true images is unrealistic, but our focus is not on obtaining reasonable motion estimates. We only focus on the image reconstruction part of MCIR. For the regularizer, we used a Fair potential function to provide edge-preservation and a certainty-based penalty to obtain more uniform resolution. The sinogram was generated with Poisson noise, and the weights in the data-fit term in (2) were chosen as $w_i = \exp(-[\boldsymbol{A}\boldsymbol{x}]_i)$. We selected the regularization parameter β such that the target PSF has a full-width at half-maximum (FWHM) of approximately 1.3 mm.

For comparison, we used the (nonlinear) conjugate gradient algorithm to solve the original problem (2). To analyze the convergence speed of the proposed method we computed the root mean squared (RMS) difference between the image estimate at the nth iteration, $\boldsymbol{x}^{(n)}$, with the "fully" converged solution, $\boldsymbol{x}^{\infty}$. For the Fair potential, the original MCIR problem is strictly convex and thus has a unique minimizer, $\boldsymbol{x}^{\infty}$. We numerically approximated $\boldsymbol{x}^{\infty}$ as the mean of the images reconstructed (assuming convergence) by running 1000 iterations of CG and 700 iterations of the proposed method with (10,10) sub-iterations.

Fig. 1 illustrates that the conventional filtered backprojection (FBP) method gives a reconstructed image with severe motion artifacts but the motion-compensated image, on the contrary, contains much less motion artifacts. Some residual motion artifacts still exist due to imperfect motion estimates even though they were obtained directly from the true XCAT images.

Fig. 2 illustrates that the proposed method converges much faster in iterations compared to the conventional CG method when we use enough sub-iterations with obvious computation overhead. This result suggests that if we have a proper preconditioner for each sub-problem, we can still obtain fast convergence. We also investigated different options for the proposed method summarized in Fig. 2. Using a preconditioner for sub-problems helped reduce the number of sub-iterations while achieving fast convergence speed.

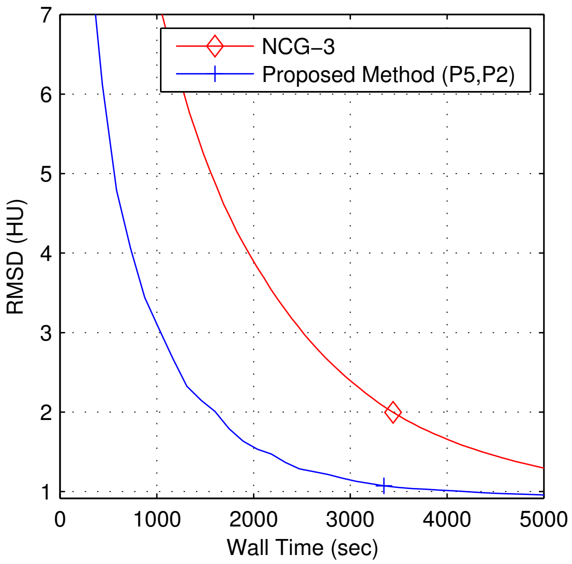

Fig. 3. Plot of RMSD versus wall time for the proposed method compared to the conventional CG method with 3 line-search iterations. A diagonal preconditioner and a circulant preconditioner were used for sub-problems (5) and (6) respectively.

In Fig. 3, we provided the proposed method with sub-optimal preconditioners. We used a simple diagonal preconditioner for (5) based on the diagonal elements of $\boldsymbol{H}$ and a circulant preconditioner for (6) using the fact that $\boldsymbol{G}$ contains $\boldsymbol{A}_m'\boldsymbol{A}_m$, which is approximately shift invariant [6]. The proposed method shows faster convergence speed compared to CG method. While the proposed method as implemented in MATLAB provides marginal improvement in convergence speed over CG, we believe its ability to parallelize some of the update steps can further improve its efficiency.

5. DISCUSSION

We applied a variable splitting approach to the motion-compensated image reconstruction problem. The proposed method has faster convergence speed to conjugate gradient method, and offers the potential for parallelizabilty and preconditioning of sub-problems. Some of the sub-problems can be solved simultaneously or further divided into smaller problems. By using more sophisticated preconditioners for the sub-problems, the performance of the proposed method can be further improved. In this study, we focussed on the image reconstruction part of MCIR, but our method also can be extended to the joint estimation framework. Our future work will focus on improving the convergence speed of the proposed method and on applying it to 3-D CT.

6. REFERENCES

[1] M. Grass, R. Manzke, T. Nielsen, P. Koken, R. Proksa, M. Natanzon, and G. Shechter, "Helical cardiac cone beam reconstruction using retrospective ECG gating," *Phys. Med. Biol.*, vol. 48, no. 18, pp. 3069–84, Sep. 2003.

[2] E. Hansis, D. Schäfer, O. Dössel, and M. Grass, "Projection-based motion compensation for gated coronary artery reconstruction from rotational x-ray angiograms," *Phys. Med. Biol.*, vol. 53, no. 14, pp. 3807–20, Jul. 2008.

[3] A. A. Isola, A. Ziegler, T. Koehler, W. J. Niessen, and M. Grass, "Motion-compensated iterative cone-beam CT image reconstruction with adapted blobs as basis functions," *Phys. Med. Biol.*, vol. 53, no. 23, pp. 6777–98, Dec. 2008.

[4] Q. Tang, J. Cammin, and K. Taguchi, "A fully four-dimensional, iterative motion estimation and compensation for cardiac x-ray computed tomography," in *Proc. Intl. Mtg. on Fully 3D Image Recon. in Rad. and Nuc. Med*, 2011, pp. 470–3.

[5] T. Goldstein and S. Osher, "The split Bregman method for L1-regularized problems," *SIAM J. Imaging Sci.*, vol. 2, no. 2, pp. 323–43, 2009.

[6] S. Ramani and J. A. Fessler, "A splitting-based iterative algorithm for accelerated statistical X-ray CT reconstruction," *IEEE Trans. Med. Imag.*, vol. 31, no. 3, pp. 677–88, Mar. 2012.

[7] J. Nocedal and S. J. Wright, *Numerical optimization*. New York: Springer, 1999.

[8] N. H. Clinthorne, T. S. Pan, P. C. Chiao, W. L. Rogers, and J. A. Stamos, "Preconditioning methods for improved convergence rates in iterative reconstructions," *IEEE Trans. Med. Imag.*, vol. 12, no. 1, pp. 78–83, Mar. 1993.

[9] Y. Long, J. A. Fessler, and J. M. Balter, "3D forward and back-projection for X-ray CT using separable footprints," *IEEE Trans. Med. Imag.*, vol. 29, no. 11, pp. 1839–50, Nov. 2010.

Information Propagation in Prior-Image-Based Reconstruction

J. Webster Stayman, Jerry L. Prince, Jeffrey H. Siewerdsen

Abstract—**Advanced reconstruction methods for computed tomography include sophisticated forward models of the imaging system that capture the pertinent physical processes affecting the signal and noise in projection measurements. However, most do little to integrate prior knowledge of the subject – often relying only on very general notions of local smoothness or edges. In many cases, as in longitudinal surveillance or interventional imaging, a patient has undergone a sequence of studies prior to the current image acquisition that hold a wealth of prior information on patient-specific anatomy. While traditional techniques tend to treat each data acquisition as an isolated event and disregard such valuable patient-specific prior information, some reconstruction methods, such as PICCS[1] and PIR-PLE[2], can incorporate prior images into a reconstruction objective function. Inclusion of such information allows for dramatic reduction in the data fidelity requirements and more robustly accommodate substantial undersampling and exposure reduction with consequent benefits to imaging speed and reduced radiation dose. While such prior-image-based methods offer tremendous promise, the introduction of prior information in the reconstruction raises significant concern regarding the accurate representation of features in the image and whether those features arise from the current data acquisition or from the prior images. In this work we propose a novel framework to analyze the propagation of information in prior-image-based reconstruction by decomposing the estimation into distinct components supported by the current data acquisition and by the prior image. This decomposition quantifies the contributions from prior and current data as a spatial map and can trace specific features in the image to their source. Such "information source maps" can potentially be used as a check on confidence that a given image feature arises from the current data or from the prior and to more quantitatively guide the selection of parameter values affecting the strength of prior information in the resulting image.**

Index Terms—**CT Reconstruction, Prior Image, Penalized-Likelihood Estimation.**

I. INTRODUCTION

A great deal of effort on the development of advanced tomographic reconstruction approaches has focused on increasingly sophisticated and accurate models for the data acquisition and noise associated with the measurements. Statistical methods using such advanced forward models have demonstrated a dramatically improved tradeoff between radiation dose and image quality [3] and such model-based techniques are being adopted for more widespread use in clinical diagnostic imaging. Despite these advances, most approaches use very little prior information about the anatomical structure of the patient. Typical model-based approaches use only very general concepts including image smoothness or edges [4] to encourage desirable image features.

In many cases, a great deal of knowledge about the object is available. Consider the case of interventional imaging. Prior to an image-guided intervention, a patient typically has one or more imaging studies conducted for purposes of diagnosis and treatment planning. Other sequential imaging situations include longitudinal surveillance of disease progression or therapy response. Traditionally, imaging systems treat each acquisition in isolation even though previous scans contain a wealth of patient-specific prior information.

While such knowledge is typically ignored (even in model-based reconstructors), two methods that integrate prior images include PICCS [1] and PIR-PLE [2]. Both use compressive sensing notions and use prior images to construct a sparse domain and apply sparsity encouraging metrics (e.g. the ℓ_1 norm). The methods differ in that PICCS does not include a noise model and relies on a linear constraint related to the data (requiring a linearizable forward model); whereas PIR-PLE uses a likelihood-based objective and forward model similar to other statistical, model-based methods. Both methods have demonstrated good image quality even under conditions of dramatic data undersampling, and PIR-PLE shows promise even under conditions of simultaneous undersampling and photon starvation.[5]

Despite these strengths, methods that integrate prior images into the reconstruction should be able to address a fundamental question if they are to find widespread adoption: to what extent are the features in the image the result of the newly acquired data, and to what extent are they the result of the prior image? For example, if a prior image is included in the reconstruction process, how can one determine if a reconstructed feature is "real" and supported by the current data collection, versus features that appear only because they were in the prior image. The question is complicated further in that such methods include parameters that can be tuned to adjust the strength of the prior images, allowing features to be selectively eliminated or reinforced in the resulting image. How, therefore, can one quantitatively select or justify these parameter values?

In this paper we investigate a novel framework that tracks the propagation of information from both the current measurement data and from the prior image portions of the reconstruction objective function in an attempt to begin answering these important questions. This investigation leverages the mathematical form of the PIR-PLE objective function where prior images are

J. Webster Stayman is with the Department of Biomedical Engineering, Johns Hopkins University, Baltimore, MD 21212 USA (phone: 410-955-1314; fax: 410-955-1115; e-mail: web.stayman@jhu.edu).

Jerry L. Prince is with the Department of Electrical and Computer Engineering, Johns Hopkins University, Baltimore, MD.

Jeffrey H. Siewerdsen is with the Department of Biomedical Engineering, Johns Hopkins University, Baltimore, MD.

This work supported in part by NIH grant 2R01-CA-112163.

included as a penalty term and is extensible to PICCS as well. The work is somewhat similar in spirit to previous regularization analysis [6] where quantitative measures of the influence of regularization (e.g., on spatial resolution) have been developed. The current work is distinct, and identifies a method by which the contribution of prior and current data can be estimated for each image voxel.

II. METHODS

A. Review of Prior Image Reconstruction Methods

We adopt the following forward model where the mean transmission measurements are written as

$$\bar{y} = \mathbf{D}\{b\}\exp(-\mathbf{A}\mu) + r \tag{1}$$

where **D** represents an operator that forms a diagonal matrix from a vector, b is a vector comprising detector pixel-dependent photon levels and detector sensitivity effects, μ is a vector of the discretized attenuation volume we wish to estimate, r is a vector of the (presumed known) scatter contribution, and **A** represents the so-called system matrix that carries out the projection operation. (Note that $\mathbf{A}^T$ represents the matched backprojection operation.)

From this forward model, it is straightforward to adopt a noise model and derive a likelihood-based objective function to estimate the attenuation volume. Choosing a Poisson noise model results in the following log-likelihood function

$$\begin{aligned} L(\mu; y) &= \sum_i h_i\left([\mathbf{A}\mu]_i\right) \\ h_i(l_i) &= y_i \log\left(b_i e^{-l_i} + r_i\right) - \left(b_i e^{-l_i} + r_i\right) \end{aligned} \tag{2}$$

where h_i is the marginal log-likelihood for the i^{th} measurement.

Consider the general form of the PIR-PLE reconstruction technique introduced in [2] but without the simultaneous registration of the prior image. This estimator may be written

$$\hat{\mu} = \arg\max L(\mu; y) - \beta_R \left\|\mathbf{\Psi}_R \mu\right\|^{p_R} - \beta_P \left\|\mathbf{\Psi}_P(\mu - \mu_P)\right\|^{p_P} \tag{3}$$

The objective has three terms: 1) The first term is the log-likelihood function that enforces a fit between the attenuation estimate and the data, and that incorporates the relative data fidelity of different measurements. 2) The second term is a generalized image penalty that typically discourages roughness in the reconstruction through the use of a gradient (or other sparsifying) operator $\mathbf{\Psi}_R$ applied to the image volume and a p-norm metric. 3) The third term encourages similarity with a previously obtained prior image, μ_P, and may also use a sparsifying operator $\mathbf{\Psi}_P$. We have allowed for potentially different sparsifiers and p-norms for each of the two penalty terms (as indicated by subscripts), and the relative strength of the roughness and prior-image penalties are controlled by the regularization parameters, β_R and β_P, respectively. The implicit estimator described by (3) does not appear to have a closed-form solution, and solutions are found iteratively[2].

The PICCS methodology [1] is another promising approach that leverages information from prior images. Recall the general form of the PICCS objective function and constraint:

$$\begin{aligned} &\hat{\mu} = \arg\min \Omega(\mu) \quad s.t. \quad \mathbf{A}\mu = \hat{l}(y) \\ &\Omega(\mu) = \alpha\left\|\mathbf{\Psi}_P(\mu - \mu_P)\right\|^p + (1-\alpha)\left\|\mathbf{\Psi}_R \mu\right\|^p. \end{aligned} \tag{4}$$

Here, the objective is comprised of terms that are analogous to the prior image penalty and general image penalty terms in (3) with a control parameter α, but the data enters through a linear constraint based on an estimate of the line integrals. Again, solutions are computed iteratively. The relationship between PICCS and PIR-PLE can be elucidated somewhat by rewriting the PICCS estimator in an unconstrained form:

$$\begin{aligned} \hat{\mu} &= \arg\min \Theta(\mu) \\ \Theta(\mu) &= \lim_{\beta\to\infty}\left\{\alpha\left\|\mathbf{\Psi}_P(\mu - \mu_P)\right\|^p + (1-\alpha)\left\|\mathbf{\Psi}_R \mu\right\|^p + \beta\left\|\mathbf{A}\mu - \hat{l}\right\|^2\right\} \\ &= \lim_{\beta\to\infty}\left\{\left\|\mathbf{A}\mu - \hat{l}\right\|^2 + \frac{(1-\alpha)}{\beta}\left\|\mathbf{\Psi}_R \mu\right\|^p + \frac{\alpha}{\beta}\left\|\mathbf{\Psi}_P(\mu - \mu_P)\right\|^p\right\}. \end{aligned} \tag{5}$$

Thus, PICCS and PIR-PLE are alike in a sense, but the latter uses an unweighted norm for the data fit term, and regularization parameters $\beta_R = (1 - \alpha)/\beta$ and $\beta_P = \alpha/\beta$ with large β values.

B. Analysis of Prior-Image Reconstruction Approaches

Direct analysis of (3) is difficult due to the nonlinearities of the likelihood function and the use of p-norms. One approximation that has previously been applied is to use a second-order Taylor approximation of the likelihood [7] about an estimate of the line integrals, so that the objective may be re-written approximately as

$$\hat{\mu} \approx \arg\min \left\|\mathbf{A}\mu - \hat{l}\right\|_{\mathbf{W}}^2 + \beta_R\left\|\mathbf{\Psi}_R \mu\right\|^{p_R} + \beta_P\left\|\mathbf{\Psi}_P(\mu - \mu_P)\right\|^{p_P} \tag{6}$$

where we have adopted a weighted norm for the first term and

$$\mathbf{W} = \mathbf{D}\left\{\frac{(y-r)^2}{y}\right\} \quad \hat{l}_i(y) = -\ln\left(\frac{y_i - r_i}{b_i}\right). \tag{7}$$

The special case of quadratic penalties ($p_R = 2$ and $p_P = 2$) yields the closed-form:

$$\begin{aligned} &\hat{\mu} \approx \arg\min \left\|\mathbf{A}\mu - \hat{l}\right\|_{\mathbf{W}}^2 - \beta_R\left\|\mathbf{\Psi}_R \mu\right\|^2 - \beta_P\left\|\mathbf{\Psi}_P(\mu - \mu_P)\right\|^2 \\ &= \left(\mathbf{A}^T\mathbf{W}\mathbf{A} + \beta_R\mathbf{\Psi}_R^T\mathbf{\Psi}_R + \beta_P\mathbf{\Psi}_P^T\mathbf{\Psi}_P\right)^{-1}\left(\mathbf{A}^T\mathbf{W}\hat{l} + \beta_2\mathbf{\Psi}_P^T\mathbf{\Psi}_P\mu_P\right). \end{aligned} \tag{8}$$

Equation (8) is interesting since it implies a decomposition

$$\hat{\mu}_D = F(y) + G(\mu_P) \tag{9}$$

$$\begin{aligned} F(y) &= \left(\mathbf{A}^T\mathbf{W}\mathbf{A} + \beta_R\mathbf{\Psi}_R^T\mathbf{\Psi}_R + \beta_P\mathbf{\Psi}_P^T\mathbf{\Psi}_P\right)^{-1}\mathbf{A}^T\mathbf{W}\hat{l}(y) \\ G(\mu_P) &= \left(\mathbf{A}^T\mathbf{W}\mathbf{A} + \beta_R\mathbf{\Psi}_R^T\mathbf{\Psi}_R + \beta_P\mathbf{\Psi}_P^T\mathbf{\Psi}_P\right)^{-1}\beta_P\mathbf{\Psi}_P^T\mathbf{\Psi}_P\mu_P. \end{aligned} \tag{10}$$

The first term, $F(y)$, is a function of only the current data and the second term, $G(\mu_P)$ is a function of only the prior image. This additive form suggests two distinct attenuation domain volumes whose source can be traced to either the current data or the prior image. Analysis of these volumes should reflect how information is transferred from the two sources to the resulting image. The extent to which specific image features arise from a given information source can be identified in a spatially varying manner – an *information source map*. Note that we differentiate between the approximate "decomposition" reconstruction, $\hat{\mu}_D$, and the solution to (6), $\hat{\mu}$. With valid approximations, we expect these terms to be nearly identical.

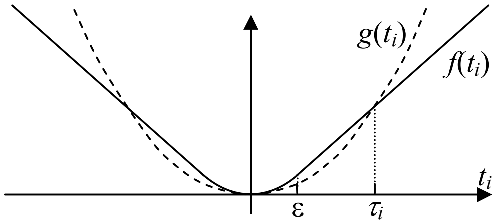

Fig. 1. Consider a prior image reconstruction that uses the modified norm that includes $f(t_i)$. Finding a suitable operating point, τ_i, we may approximate $f(t_i)$ with a quadratic function, $g(t_i)$, that intersects at $f(\tau_i)$.

Unfortunately, while the selection of quadratic penalties terms in (6) allows for the simple decomposition in (10), reconstructions with quadratic penalties provide a fairly poor integration of prior image information. That is, the real power of PIR-PLE and PICCS approaches lies in the use of lower p-values that encourage similarity to a prior image, but include a small enough penalty for larger differences that significant changes are still permitted in the reconstruction. The following section illustrates a decomposition methodology for accommodating nonquadratic penalties.

C. Additional Approximation for Nonquadratic Penalties

The additive decomposition in (9) is compelling, but raises questions about how to extend the decomposition to more general values of p. Consider the typical selection of $p = 1$ that can be difficult for some reconstruction algorithms and that is often replaced by a modified norm that is "rounded" near the origin and differentiable at zero. For example,

$$\|t\|^1 \approx \sum_i f(t_i) \quad f(t_i) = \begin{cases} \frac{1}{2\varepsilon} t_i^2 & |t_i| < \varepsilon \\ \left|t_i - \frac{\varepsilon}{2}\right| & |t_i| \geq \varepsilon \end{cases}. \tag{11}$$

As illustrated in Figure 1, given a suitable operating point, τ, we approximate the modified norm using a quadratic function

$$g(t_i) = \kappa_i(\tau_i) t_i^2 \quad \kappa_i(\tau_i) = \begin{cases} \frac{1}{2\varepsilon} & |\tau_i| < \varepsilon \\ \frac{\left|\tau_i - \frac{\varepsilon}{2}\right|}{\tau_i^2} & |\tau_i| \geq \varepsilon \end{cases} \tag{12}$$

such that

$$\|t\|^1 \approx \sum_i g(t_i) = (t)^T \mathbf{D}\{\kappa(\tau)\}(t). \tag{13}$$

Applying this approximation to (6) for the case of $p_R = 1$ and $p_P = 1$ yields an approximate decomposition:

$$\begin{aligned} F(y) &= \left(\mathbf{A}^T\mathbf{W}\mathbf{A} + \beta_R \mathbf{\Psi}_R^T \mathbf{D}_R \mathbf{\Psi}_R + \beta_P \mathbf{\Psi}_P^T \mathbf{D}_P \mathbf{\Psi}_P\right)^{-1} \mathbf{A}^T \mathbf{W} \hat{l}(y) \\ G(\mu_P) &= \left(\mathbf{A}^T\mathbf{W}\mathbf{A} + \beta_R \mathbf{\Psi}_R^T \mathbf{D}_R \mathbf{\Psi}_R + \beta_P \mathbf{\Psi}_P^T \mathbf{D}_P \mathbf{\Psi}_P\right)^{-1} \cdot \\ &\qquad \beta_P \mathbf{\Psi}_P^T \mathbf{D}_P \mathbf{\Psi}_P \mu_P. \end{aligned} \tag{14}$$

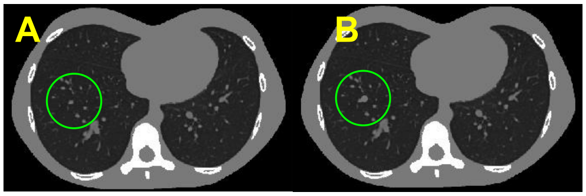

Fig. 2. Illustration of the prior image (A) and the true follow-up image (B) used to form current acquisition data (i.e., ROI or angularly undersampled). The images are the same except for the addition of a simulated lung nodule in the follow-up (green circle).

It remains to choose an operating point for the approximation. In our analysis, we presume that the reconstruction in (3) has already been performed, allowing us to choose an operating point based on the solution, $\hat{\mu}$. This means the diagonal matrices in (14) may be defined as

$$\begin{aligned} \mathbf{D}_R &= \mathbf{D}\left\{\kappa\left(\mathbf{\Psi}_R \hat{\mu}\right)\right\} \\ \mathbf{D}_P &= \mathbf{D}\left\{\kappa\left(\mathbf{\Psi}_P \left(\hat{\mu} - \mu_P\right)\right)\right\}. \end{aligned} \tag{15}$$

Note the close relation between (10) and (14) with equality if the diagonal matrices in (15) are identity. Moreover, it is straightforward to extend this methodology for other p-values. We note that the same decomposition may be applied to PICCS by leveraging the unconstrained form in (5). This necessitates setting $\mathbf{W} = \mathbf{I}$ and choosing a sufficiently large β.

Since the system matrix is typically not computed explicitly and is too large to store, we adopt a conjugate gradient approach for approximating the terms $F(y)$ and $G(\mu_P)$ in (14) to decompose a prior-image-based reconstruction (PIR-PLE or PICCS) into data- and prior-image-supported components.

III. RESULTS/DISCUSSION

To investigate the data and prior image decomposition framework described in the previous section we adopted the imaging scenario illustrated in Figure 2. The experiment presumes the availability of a reconstructed prior image and data for a follow-up image that includes a change (viz., enlargement of a nodule feature in the right lung). The follow-up acquisition involves highly sparse data. We investigate two acquisition strategies using a simulated C-arm geometry: 1) a **region-of-interest (ROI) scan** that acquires 60 laterally truncated projections over 360° (dashed white circle in Fig. 3); and 2) an **angularly subsampled scan** that acquires 20 untruncated projections over 360°. All experiments used 0.776 mm detector pixels, 0.8 mm isotropic voxels, and a

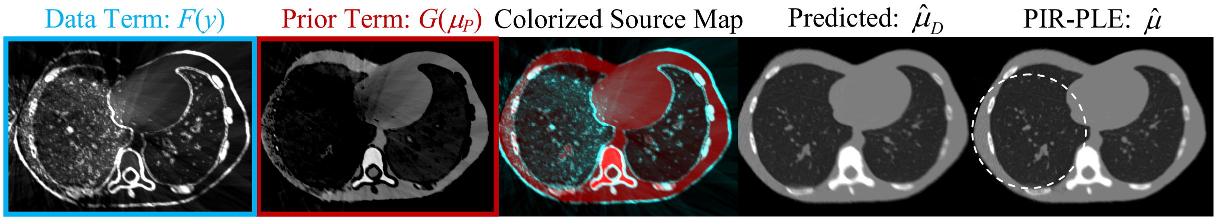

Fig. 3. The information source decomposition applied to the ROI experiment using PIR-PLE. The two decomposition terms $F(y)$ and $G(\mu_P)$ along with their sum (the predicted reconstruction, $\hat{\mu}_D$). The colorized source map combining $F(y)$ and $G(\mu_P)$ in a single image conveys which features arise mainly from the prior image (red) and which arise largely from the newly acquired data (cyan/gray). The reconstruction is seen to rely more heavily on prior image information in regions outside the scanned region-of-interest (indicated by the dashed white circle).

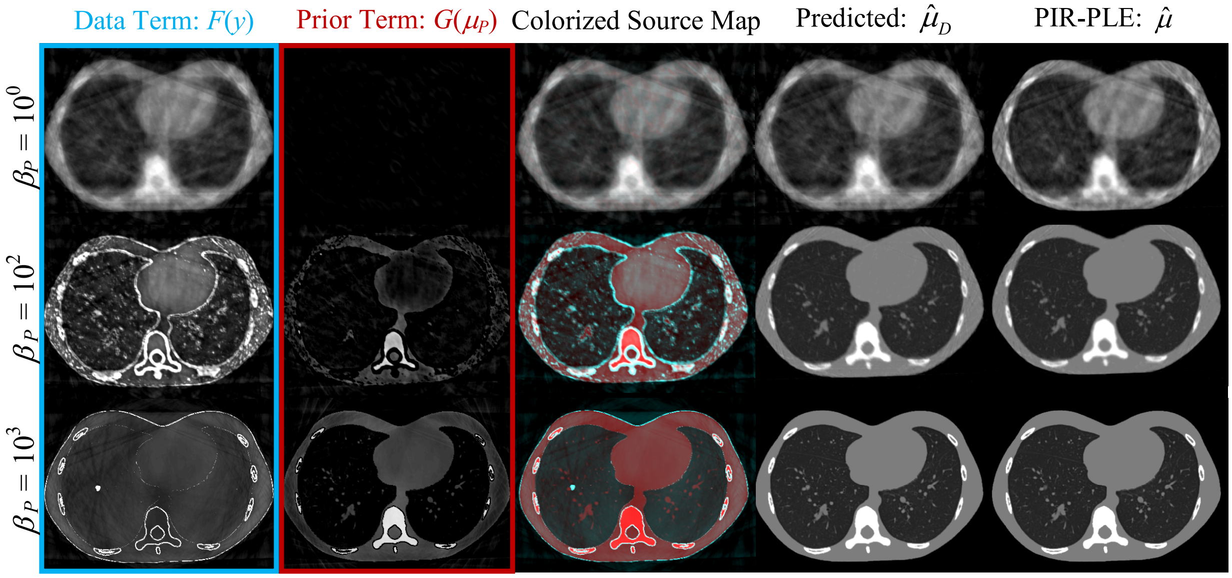

Fig. 4. Information source mapping applied to angularly undersampled data using PIR-PLE. Each row represents a different prior image penalty strength (β_P). The direct relationship between prior image penalty strength and the influence of the prior image is clear. Low β_P values result in a negligible G component and produce images similar to traditional penalized-likelihood with no prior image contribution. High β_P values yield greater similarity with the prior image, and the changes supported by the newly acquired data are readily apparent in the F component and the colorized source maps – most notably, the solitary lung nodule.

monoenergetic x-ray beam with 10^5 photons per detector element in the unattenuated beam. Both PIR-PLE and PICCS reconstructions are investigated.

We illustrate the application of the decomposition approach applied to the ROI acquisition experiment in Figure 3. A PIR-PLE reconstruction was formed (using $p_R = 2$ and $p_P = 1$), and both the data-based (F) and the prior-image-based (G) terms of the decomposition are shown. Moreover, the sum of the individual terms are presented as a check on the validity of the approximations leading to (9). (I.e., $\hat{\mu} \approx \hat{\mu}_D$ which is qualitatively confirmed by the results.) A colorized *information source map* is also shown that identifies regions of the estimate that arise predominantly from either the current data (cyan/white) or the prior image (red). As one might expect, in this ROI scenario we see increasing contribution from the prior image in regions outside the scanned ROI. Moreover, the anatomical change (i.e., the simulated lung nodule) occurring between the prior image and follow-up can be clearly traced to the F term representing the newly acquired data.

A second experiment considered the angularly undersampled case in which reconstructions were performed using both PIR-PLE ($p_R = 2$, $p_P = 1$) and PICCS ($p = 1$) over a range of reconstruction parameters. Specifically, we performed a sweep over the prior image penalty strength (β_P) for PIR-PLE and a sweep of the α parameter in PICCS. The results are summarized in Figures 4 and 5, respectively. In both cases, the relationship between parameter strength and the strength of the prior image is clearly reflected in the decomposition. Moreover, the presence of the lung nodule is consistently represented in the data decomposition term, F. Interestingly, similar image reconstructions do not necessarily have similar decompositions – most evident in the reconstructions at higher levels of β_P and α. This suggests that even though the images appear very similar, they are actually relying on different sources of information transferred from the prior and newly acquired data, suggesting different conclusions regarding what might have changed in the image, and what is supported by the data.

The ability to trace the source of information offers a potentially very important tool in beginning to understand how information propagates in prior-image-based reconstruction and how data and prior information are integrated in the resulting image. It also suggests a quantitative method by which one might justify the selection of penalty strengths and could even provide a basis by which one could design penalties that enforce a specific balance of information usage.

Simiarly, such a framework helps to illustrate the relationship between methods like PICCS and PIR-PLE and the particular information balance that is reached by either approach. Ongoing work includes analysis of such a relationship, the extent to which the *information source map* is quantitatively valid, and how such a framework could be implemented in systems employing prior-image-based reconstruction to communicate confidence levels to the observer that a perceived image feature arises from the prior or from the newly acquired data.

REFERENCES

[1] G. H. Chen, *et al.*, "Prior image constrained compressed sensing (PICCS): a method to accurately reconstruct dynamic CT images from highly undersampled projection data sets," *Med Phys*, vol. 35, pp. 660-3, Feb 2008.
[2] J. Stayman, *et al.*, "Penalized-likelihood reconstruction for sparse data acquisitions with unregistered prior images and compressed sensing penalties," in *SPIE Medical Imaging*, 2011.
[3] J. B. Thibault, *et al.*, "A three-dimensional statistical approach to improved image quality for multislice helical CT," *Med Phys*, vol. 34, pp. 4526-44, Nov 2007.

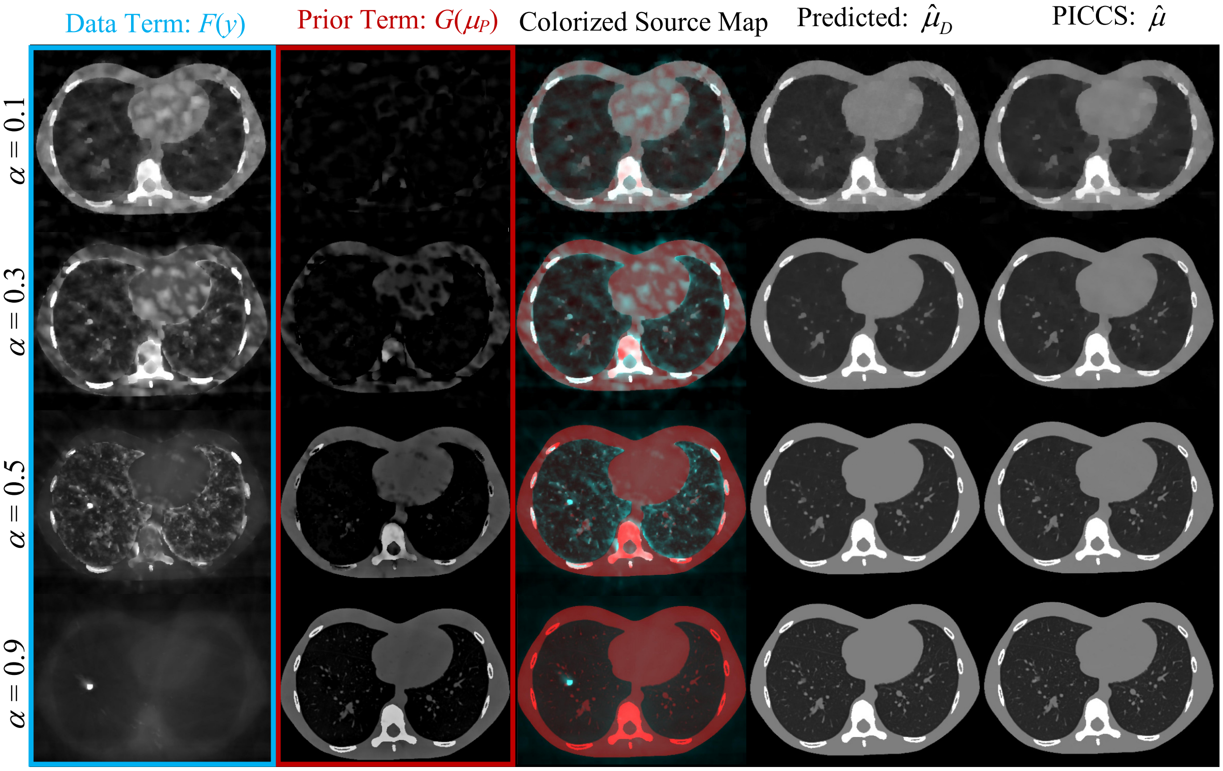
Data Term: $F(y)$
Prior Term: $G(\mu_P)$
Colorized Source Map
Predicted: $\hat{\mu}_D$
PICCS: $\hat{\mu}$
$\alpha = 0.1$
$\alpha = 0.3$
$\alpha = 0.5$
$\alpha = 0.9$

Fig. 5. Information source mapping applied to the angular undersampling case and PICCS reconstruction. Each row represents a different choice of α, with larger α yielding increased reliance on the prior image and smaller α yielding increased reliance on the roughness penalty.

[4] K. Lange, "Convergence of EM image reconstruction algorithms with Gibbs smoothing," *IEEE Trans Med Imaging,* vol. 9, pp. 439-46, 1990.

[5] Y. Ding, *et al.*, "Incorporation of Noise and Prior Images in Penalized-Likelihood Reconstruction of Sparse Data," in *SPIE Medical Imaging*, San Diego, CA, 2012.

[6] J. A. Fessler and W. L. Rogers, "Spatial resolution properties of penalized-likelihood image reconstruction: space-invariant tomographs," *IEEE Trans Image Process,* vol. 5, pp. 1346-58, 1996.

[7] K. Sauer and C. Bouman, "A Local Update Strategy for Iterative Reconstruction from Projections," *Ieee Transactions on Signal Processing,* vol. 41, pp. 534-548, Feb 1993.

Iterative Helical Cone-Beam CT Reconstruction using Fast Hierarchical Backprojection/Reprojection Operators

Jeffrey Brokish*, Hongbin Guo*, Paul Sack*, Daniel B. Keesing* and Yoram Bresler*†
*InstaRecon, Inc., Champaign, IL USA 61820
†Dept. of Electrical and Computer Engineering, University of Illinois at Urbana-Champaign

***Abstract*—This is the first report on a new fast iterative CT reconstruction algorithm for helical cone beam scans, accelerated by InstaRecon's fast $O(N^3logN)$ hierarchical cone beam backprojection and reprojection algorithms. We report on the results of image quality evaluations for dose reduction on iterative algorithms, demonstrating that the iterative algorithm introduced here can provide image quality indistinguishable from an iterative algorithm using conventional BP/RP operators. We further show the iterative algorithm providing image quality comparable to a high-dose FBP reconstruction but with only 25% of the dose. Finally, run-time statistics are reported for a version of the algorithm using GPU implementations of the hierarchical operators. The combined algorithmic and hardware acceleration provides a reconstruction engine with sufficient throughput to be viable as the default modality for typical clinical workflow, but with very modest hardware requirements.**

I. INTRODUCTION

Incorporating statistical and physical models of the data acquisition, iterative CT reconstruction algorithms reduce noise and artifacts in images, which is a key enabler for reduced dose imaging. However, iterative algorithms are computationally expensive, as each iteration requires a forward and backward projection operation. These backprojection/reprojection (BP/RP) operators, which are $O(N^4)$ for 3D cone-beam scans, are the computational bottleneck of iterative reconstruction, just as the BP operation is the bottleneck of standard filtered backprojection (FBP). Hierarchical algorithms reduce the complexity of these operators to $O(N^3logN)$, offering the potential to greatly accelerate the reconstruction throughput. In this paper, we report on the performance of an iterative algorithm for the 3D helical cone-beam case using fast hierarchical algorithms [1].

II. ITERATIVE ALGORITHM FRAMEWORK

A. Cost Function

The iterative reconstruction framework plays a key role in determining image quality, dose reduction, and computational requirements. There are various methods for implementing an iterative reconstruction scheme: the choice of a cost function, regularization, and optimization strategy. For this work we chose a penalized weighted least squares cost function [?] of the form

$$J(f) = \|y - Rf\|_W^2 + \beta C(f) \tag{1}$$

In this cost function, f is the current estimate of the image, y is the measured projection data, R computes the forward projection of its argument, and $C(f)$ is a non-quadratic regularization term that favors smooth regions in f while preserving sharp transitions, with relative weight β. The W indicates a weighted norm of the difference between the measured values y and estimated projections Rf. The form of this cost function lends itself to conjugate gradient (CG)-based minimization strategies, which are the most amenable to acceleration by InstaRecon fast hierarchical operators.

B. System Model

There are many options for the implementation of the conventional reprojector R that depend on the representation of the image f. The choice of the image representation (basis function) has a significant influence on the performance of the iterative algorithm, both in terms of runtime and resulting image quality. Based on the ideas presented in [4] we implemented a higher order separable footprint for each voxel. For computational efficiency, the footprint integration is calculated not on the detector panel, but rather detector boundaries are brought to image 'slabs' and integration is performed in the image domain. The choice between x-z or y-z image slabs is based on which direction is most orthogonal to the line between the source and center of rotation. Such a voxel representation is useful in reducing aliasing artifacts in the reprojection step, which may not be suppressed by an iterative algorithm. Additionally, reprojectors with a large amount of aliased energy are more challenging for the hierarchical algorithms to handle accurately.

III. FAST HIERARCHICAL OPERATORS

The fast 3D conebeam BP/RP algorithms used in this work reduce the computational complexity from $O(N^4)$ to $O(N^3logN)$ by a hierarchical decomposition of the image volume. The hierarchical reprojection algorithm is briefly described here. The hierarchical reprojection algorithm is based on two main concepts. The first concept is divide and conquer, in which the volume is successively divided into smaller non-overlapping volumes, and the reprojection operation is applied to these subvolumes. An example of this decomposition used for 3D volumes is shown in Figure 1. By itself this does not provide any reduction in computational cost.

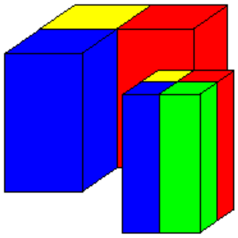

Fig. 1: Recursive Pillar Decomposition

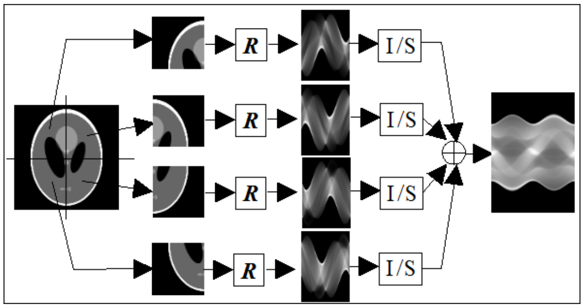

Fig. 2: Reprojection Decomposition (1 level)

The second concept invokes sampling conditions, where the number of views required to accurately sample the projections of a bandlimited subvolume at the center of the source of rotation is proportional to the size of the subvolume. For the projections of a half-size subvolume, the projection data set can initially be reprojected at a sparser set of P/2 projections and then angularly interpolated by a factor of 2, yielding projection data with comparable quality.

These two concepts are combined to form the hierarchical algorithm. Subvolumes are approximately 'centered' through shifts in the projection data to position the center of the subvolume's shadow with the detector isocenter. This sufficiently reduces the angular sampling requirements of the subregion that it can be reprojected at a coarser set of views, then interpolated to a higher angular sampling rate. Projection data for groups of neighboring subvolumes are then added together to form data for larger subvolumes, which is again interpolated to a higher number of views. This process continues until the entire volume has been reconstituted.

An example demonstrating one level of this process for a 2D example is shown in Figure 2. The image is broken down into small subregions, which are reprojected (R) at a sparse set of view angles. These projection sets are shifted and interpolated (S/I) to a larger projection count and merged together to form projection sets of larger subregions.

The fast hierarchical backprojector is constructed as the adjoint of this operation, with the appropriate flow reversal of each step in the algorithm. It is analogous in form to the fast hierarchical backprojection algorithms [**?**] that have been developed for filtered backprojection reconstruction (FBP). An FBP reconstruction is typically used to form the initial guess in the iterative algorithm, so this step can also be accelerated by hierarchical methods.

IV. GPU IMPLEMENTATION

The primary processing element of an Nvidia GPU is organized as an array of simple processing units (SP) grouped together into multiprocessor units (MP). A GPU consists of several such multiprocessors operating in parallel. Typical GPUs have a combined SP count in the hundreds. Each multiprocessor contains a small amount of local shared memory and a set of registers that are shared among all of the simple processing units in that multiprocessor. Additionally, each multiprocessor has a dedicated texture unit, which can perform array lookup and interpolation operations.

While GPUs offer tremendous computational resources, care must still be taken in programming the computation kernels. Extracting high performance requires taking into account architectural features of the GPU. A sufficient number of parallel threads of execution must be available to keep all the SP units busy and tolerant of any delays in computation or memory accesses. The resources (registers and shared memory) required by each thread must be minimized to enable a large number of threads to run on an MP.

Conventional filtered backprojection (FBP) has a very obvious parallel structure, where each voxel can be reconstructed independently. The GPU is particularly amenable to an FBP implementation, as a key component of the algorithm is linear interpolation of projection data. The texture unit serves as a data cache that provides linear interpolation in hardware, offloading a good portion of the work required by the FBP kernel. Implementation on the GPU of a reprojector, on the other hand, is substantially more complicated and does not map as elegantly to the GPU, especially for system models that incorporate some form of basis representation along with detector integration.

Our approach to implementation of hierarchical operators on the GPU platform involved looking at the decomposition in 'stages' (e.g. kernel launches). This first stage is comprised of taking the reconstruction volume and dividing it into the set of smallest subvolumes (after all recursive decompositions have been applied), performing the reprojection operation on each subregion using the conventional reprojector at a projection set with sparse angular sampling. Each successive stage then involves interpolation of each dataset to a higher angular sampling rate, followed by a shifting operation (the I/S operation from Figure 2). Finally, the projection data for groups of four subvolumes are added together to form the projection dataset of the 'parent' subvolume.

It turns out that this process does not map to the GPU architecture as elegantly (or simply) as the traditional FBP. Different subvolumes will have different sized decimated projection datasets (dependent on the rays that intersect the subvolume) leading to challenges in packing data efficiently and effectively assigning worker threads to the decimated projection detectors in a regular manner. We developed a scheduling mechanism to prevent the creation of idle threads in a thread block due to this irregularity. Other GPU hardware features are also leveraged to improve efficiency, including storing intermediate calculations in Shared Memory, and using the texture units as a memory caching mechanism for accessing the decimated projection data.

One other challenging issue was the data set sizes encountered in helical geometries, where a scan may consist of many revolutions. It becomes very easy to exhaust the available memory on the GPU cards we were using (around 1GB of onboard memory). We devised a set of strategies which partition the problem into a sequence of manageable subproblems that can fit on the GPU. We leverage the asynchronous operational mode of the GPU to overlap transfers and computation as much as possible.

V. RESULTS

A. Equivalence of Hierarchical and Conventional Operators

Figure 3 demonstrates reconstructions for simulated data for a 64 row detector panel with helical pitch 1. The iterative algorithm is able to reduce noise and suppress artifacts in the image (i.e. streaks emanating from the air cells in the temporal bone). The low contrast features are very apparent while the sharpness of the image (air cells, bone) is maintained. Most importantly, the good agreement between hierarchical and conventional operator based iterative algorithms is confirmed.

B. Low Dose Imaging

Figure 4 shows a comparison of reconstruction methods at different dose levels. Noise was added to the clinical dataset to simulate a reduction of dose to 25% of the full dose level. The following reconstructions were performed: FBP using high dose data, FBP using low dose data, and Iterative using low dose data. The iterative algorithm is able to bring back the image quality to a level comparable to that of the high-dose FBP reconstruction.

C. Iterative Reconstruction Throughput

The CPU platform used here is a quad-core Core i7 processor running at 2.66 GHz with 24 GB of RAM. The GPU used is the nVidia GTX 470, a modest gaming-class graphics card, with 448 cores running at 1215 MHz and 1280 MB of on-board memory. The hierarchical BP/RP operators are run on the GPU, the remaining aspects of the iterative framework (regularization term, etc) are run on the CPU. The CPU code is written in C++ and uses thread parallelism to leverage all available processing cores and when possible extracts data level parallelism using the SSE vector instruction set.

Table I lists results from two clinical datasets with different helical pitches and region of interest (ROI) sizes. In both of these cases we achieve a reconstruction rate of 2 seconds per slice or better, which is a rate viable for a typical clinical workflow (6 patients per hour, 300 slices per scan). This throughput is also competitive with other commercially available iterative reconstruction packages employing the model-based techniques used here, but does so on vastly lower powered hardware.

TABLE I: Iterative Algorithm Throughput

Dataset	Pitch	ROI Diameter (mm)	Slice Count	Sec / Slice
896 x 16 x 6840	0.75	220	340	1.35
896 x 16 x 9960	1.00	500	330	2.04

Further gains in reconstruction rates could be had by porting the remainder of the iterative framework to the GPU. While such aspects are fairly minor overhead for an iterative algorithm using conventional operators, after the BP/RP operators have been accelerated by both the hierarchical algorithm and the GPU, the extra computation is a non-trivial component of the total runtime. With a modest 4x acceleration of these components by running them on the GPU, we estimate potential improvement of 15-30% in system throughput. The newer 500 series of graphics cards can also provide a significant performance boost over the GTX 470 used in this evaluation.

VI. CONCLUSION

In this paper, we reported on results in evaluating an iterative reconstruction framework for dose reduction, accelerated by the combination of the algorithmic techniques of InstaRecon hierarchical backprojection/ reprojection operators along with hardware acceleration on the GPU platform. This is the first time that an algorithmically-accelerated iterative reconstruction engine for 3D CCB/HCB geometries has been demonstrated.

The iterative reconstruction engine delivers significant decrease in dose (a factor of 4 reduction) at a throughput that enables iterative reconstruction as the default reconstruction mode without impacting workflow. Further, the modest hardware requirements enables the possibility of including low-dose scanning in the value segment of the CT market. In addition, the delivered acceleration enables to incorporate, with additional development, additional enhanced physical modeling at reduced cost, to facilitate even greater dose reductions in the future.

ACKNOWLEDGMENT

The project described was supported by a Phase II SBIR Award Number R44EB005576 from the National Institute of Biomedical Imaging and Bioengineering to InstaRecon, Inc. The content of this publication is solely the responsibility of the authors and does not necessarily represent the official views of the National Institute of Biomedical Imaging and Bioengineering or the National Institutes of Health.

REFERENCES

[1] J. Brokish, D. Keesing, and Y. Bresler, "Iterative Circular Cone-Beam CT Reconstruction using Fast Hierarchical Backprojection/Reprojection Operators", *SPIE Physics of Medical Imaging Conference*, Feb 2010.

[2] J. Fessler and S. Booth, "Conjugate-Gradient Preconditioning Methods for Shift-Variant PET Image Reconstruction," *IEEE Trans Image Processing*, May 1999.

[3] Y. Bresler and J. Brokish, "A hierarchical algorithm for fast backprojection in helical cone-beam tomography,", *Proc. 2nd IEEE Int. Symp. Biomedical Imaging*, 2004.

[4] J. Sunnegardh and P.E. Danielsson, "A New Anti-Aliased Projection Operator for Iterative CT Reconstruction," *9th International Meeting on Fully Three-Dimensional Image Reconstruction*, 2009.

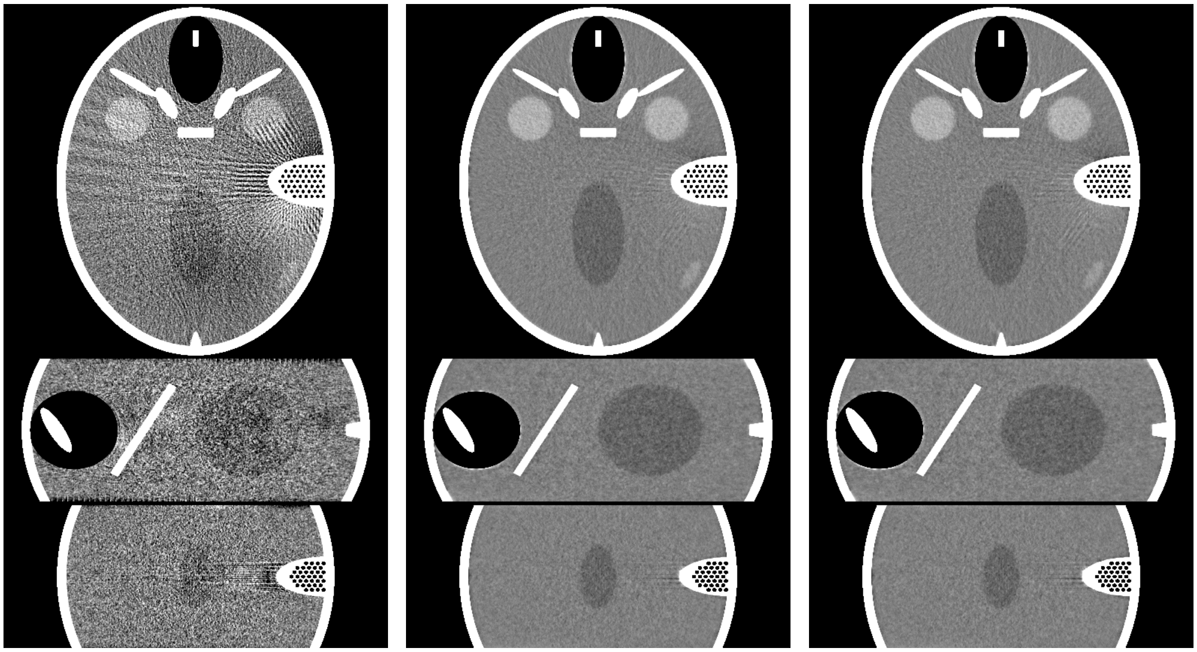
(a) (b) (c)

Fig. 3: Slices through reconstruction of simulated phantom dataset comparing (a) FBP with (b) Iterative using conventional operators and (c) Iterative using hierarchical operators

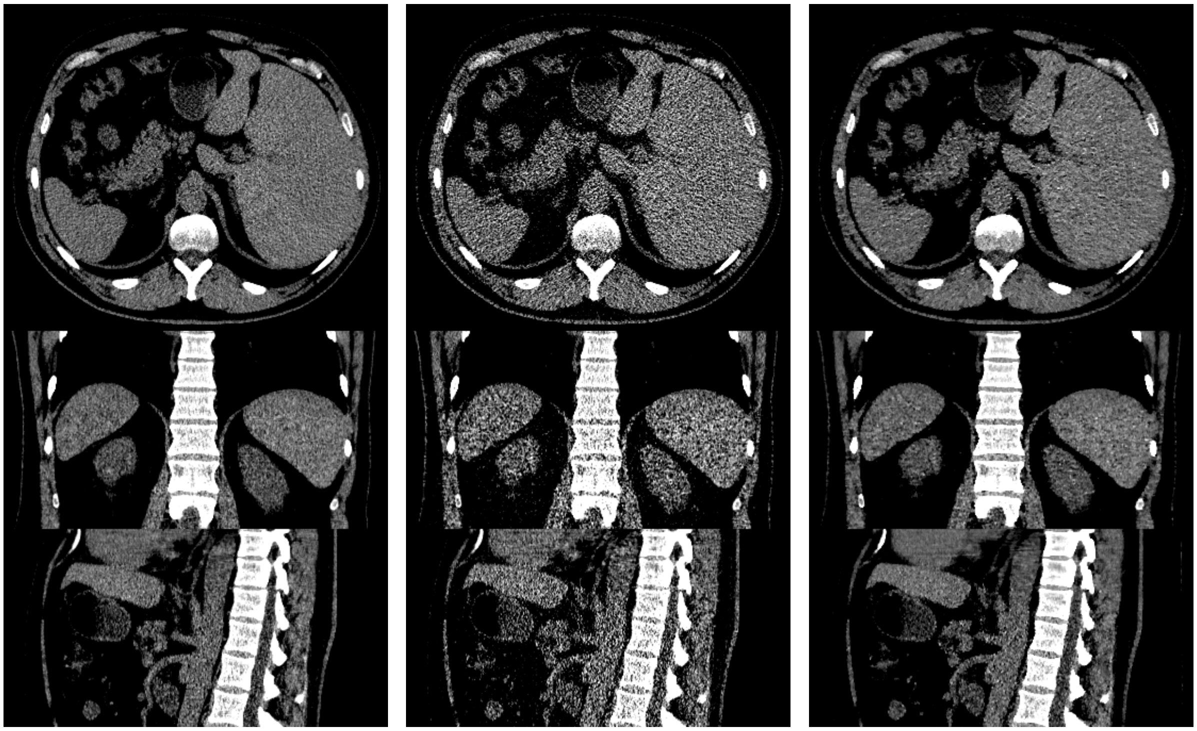
(a) (b) (c)

Fig. 4: Comparison of reconstructions of clinical dataset from FBP with high dose data (a), FBP with low dose data (b), and iterative with low dose data (c)

Convex optimization prototyping for iterative image reconstruction in X-ray CT

Emil Y. Sidky[1], Jakob H. Jørgensen[2], and Xiaochuan Pan[1]

***Abstract*—It is demonstrated how the primal-dual optimization algorithm developed by Chambolle and Pock (CP), 2011, can be used as a flexible framework for prototyping a variety of convex optimization problems of potential interest in computed tomography (CT) image reconstruction. The algorithm is useful for investigative purposes, because it covers a wide range of applicability to convex optimization including non-smooth functions and the various instances of the CP algorithm can be derived by well-defined mechanical operations. As a result, a given convex optimization problem for CT image reconstruction can be rapidly prototyped. The CP methodology is reviewed, and its application to convex convex optimization problems of interest to CT is illustrated by deriving an algorithm instance for non-negativity-constrained total-variation-regularized least squares minimization.**

I. INTRODUCTION

Many iterative image reconstruction algorithms for CT are derived from convex optimization problems, either minimizing an unconstrained, convex objective function directly or minimizing a given objective subject to convex constraints. Investigating the utility of various optimization problems is often hindered by the lack of a practical algorithm for solving them. Simple algorithms such as generic forms of gradient descent, conjugate gradients, and expectation-maximization may not be directly applicable, particularly in the case of non-smooth objectives, or they may be unacceptably inefficient. These well-known algorithms can often be adapted to a particular problem of interest, but they may require expert knowledge on specific methods for attaining efficiency gains and many weeks of development time. The enthusiasm for pursuing novel optimization formulations for CT image reconstruction may, as a result, be dampened by this algorithmic barrier.

Recently, Chambolle and Pock [1] have introduced a series of algorithms for solving a generic convex optimization problem that can cover many specific forms of potential interest for image reconstruction in CT. Non-smooth terms can be included, which allows for constraints and for sparsity-enhancing ℓ_1-based norms. The algorithms are primal-dual; namely, they solve the original primal minimization problem together with its corresponding dual maximization problem. Accordingly, the primal-dual nature of the algorithm comes with a generic convergence check that the primal-dual gap tends to zero as the iterates approach the solutions of their respective optimization problems. In a recent report [2] we have found that this algorithm is very well suited to optimization problem prototyping for CT image reconstruction because: many of the optimization problems investigated for this application fit into the general CP form; it comes with its own convergence check; and, a specific form of the CP algorithm *with no free parameters* suffices to obtain the solution.

This conference contribution begins by summarizing the background of the CP algorithm and presenting the algorithm in a generic form in Sec. II. A specific instance of the CP algorithm is illustrated for total-variation (TV) based image reconstruction for CT. A numerical example is shown in Sec. IV.

II. THE GENERIC OPTIMIZATION PROBLEM AND CP ALGORITHM

The generic CP algorithm, which we investigate here, solves the following minimization problem:

$$\min_x \ \phi_{\text{primal}}(x); \ \ \phi_{\text{primal}}(x) = F(Kx) + G(x), \tag{1}$$

where x is a N-dimensional vector; K is a linear transform from R^N to R^M; and F and G are convex functions of R^M and R^N, respectively. For CT image reconstruction, x can represent, for example image

---

[1] The University of Chicago, Department of Radiology MC-2026, 5841 S. Maryland Avenue, Chicago IL, 60637.

[2] Department of Informatics and Mathematical Modeling, Technical University of Denmark, Richard Petersens Plads, Building 321, 2800 Kgs. Lyngby, Denmark.

pixel values, and the matrix K could model the X-ray transform. In addition to this minimization the CP algorithm solves the associated dual maximization:

$$\max_y \; \phi_{\text{dual}}(y); \;\; \phi_{\text{dual}}(y) = -F^*(y) - G^*(-K^T y), \tag{2}$$

where K^T is the transpose of K; y is a vector in R^M; and the *-superscript indicates convex conjugation. The convex conjugate is arrived at through the Legendre transform:

$$H^*(y) = \max_{y'} \; \langle y, y' \rangle - H(y'), \tag{3}$$

$$H(y') = \max_{y} \; \langle y', y \rangle - H^*(y), \tag{4}$$

where $\langle \cdot, \cdot \rangle$ denotes the inner product. Under some not very restrictive conditions the vectors x' and y' are solutions, respectively, to the primal minimization and dual maximization when the primal-dual gap is zero: $\phi_{\text{primal}}(x') - \phi_{\text{dual}}(y') = 0$, and this gap is always non-negative.

The generic CP algorithm for solving Eqs. (1) and (2) is presented in Algorithm 1. This algorithm is the same as the first algorithm presented in Ref. [1] with the exception that there are no free algorithmic parameters. As presented in Ref. [1], σ and τ are parameters of the CP algorithm, which should satisfy $L^2 \sigma \tau < 1$ where $L = \|K\|_2$ is the largest singular value of the matrix K. The largest singular value of K can be computed by the power method. We have found that the choice of $\sigma = \tau = 1/L$ suffices for observing convergence in numerical experiments we have performed for image reconstruction in CT, and fixing these parameters simplifies the implementation for the purpose of optimization problem prototyping. We do point out, however, that this choice technically does not satisfy the inequality for which the proof of convergence applies. Despite this, we have not encountered a case where convergence fails with this setting of σ and τ.

Algorithm 1 Pseudocode for N_0-steps of the basic Chambolle-Pock algorithm. See text for definition of variables and the operators $prox_\sigma[F^*]$ and $prox_\tau[G]$.

```
$L \leftarrow \|K\|_2;\ \tau \leftarrow 1/L;\ \sigma \leftarrow 1/L;\ \theta \leftarrow 1;\ n \leftarrow 0$
initialize $x_0$ and $y_0$ to zero values
$\bar{x}_0 \leftarrow x_0$
repeat
    $y_{n+1} \leftarrow prox_\sigma[F^*](y_n + \sigma K \bar{x}_n)$
    $x_{n+1} \leftarrow prox_\tau[G](x_n - \tau K^T y_{n+1})$
    $\bar{x}_{n+1} \leftarrow x_{n+1} + \theta(x_{n+1} - x_n)$
    $n \leftarrow n + 1$
until $n \geq N_0$
```

The only additional ingredients, needed to realize CP algorithm instances, are the proximal mappings $prox_\sigma[F^*]$ and $prox_\tau[G]$. The proximal mapping is used to generate a descent direction for the convex function F and it is obtained by the following minimization:

$$prox_\sigma[H](y) = \arg\min_{y'} H(y') + \frac{\|y - y'\|_2^2}{2\sigma}. \tag{5}$$

This operation admits non-smooth convex functions, but F needs to be simple enough that the above minimization can be solved in closed form. For CT applications the ability to handle non-smooth F and G allows the study of many optimization problems of interest. In particular, below, we introduce a CP algorithm instance TV-regularized least-squares minimization with a non-negativity constraint.

Before presenting this CP instance, we need one more ingredient, which is particularly useful for including constraints for the primal minimization. Namely, the indicator function $\delta_S(x)$

$$\delta_S(x) \equiv \begin{cases} 0 & x \in S \\ \infty & x \notin S \end{cases}, \tag{6}$$

where S is a convex set, is also a convex function which fits into the CP framework. Below, we employ the indicator for enforcing non-negativity by having S be the set of images with non-negative pixel values, which is convex. The indicator can be used for more complex constraints such as a hard, data-error constraint (see Ref. [2]).

III. A CP ALGORITHM INSTANCE FOR TV-REGULARIZED, NON-NEGATIVITY CONSTRAINED, LEAST-SQUARES MINIMIZATION

We take the linear, discrete-to-discrete (DD) model for the CT model:

$$Au = g,$$

where u represents the image pixel coefficients, g the projection data, and A is the DD approximation to the continuous X-ray transform. The minimization problem of interest is

$$\min_u \; \frac{1}{2}\|Au - g\|_2^2 + \lambda \, \|(|\nabla u|)\|_1 + \delta_P(u), \tag{7}$$

where ∇ is a matrix representing the discrete form of the image gradient (the ℓ_1-norm of the gradient-magnitude image is the TV semi-norm); $|\cdot|$ is the pixel-wise Euclidean norm of the gradient components (thus

$|\nabla u|$ yield the gradient magnitude image of u); λ is a parameter controlling the strength of the regularization; the set P consists of the non-negative image vectors so the last term enforces the non-negativity constraint. Accurate solution of this particular minimization problem has garnered recent interest for CT. An algorithm employing parabolic surrogates was reported in Ref. [3], and another work taking advantage of recent developments in first-order methods was reported in Ref. [4]. In order to apply the CP algorithm, we match this minimization with the generic form in Eq. (1). We recognize in Eq. (7) that the first two terms involve a linear transform, while the third term involves the untransformed image. Accordingly, the first two terms can be written in the form $F(Kx)$ and the last term takes the form of $G(x)$ with the following assignments:

$$F(y,z) = F_1(y) + F_2(z),$$

$$F_1(y) = \frac{1}{2}\|y-g\|_2^2, \quad F_2(z) = \lambda \left\| (|z|) \right\|_1, \tag{8}$$

$$G(x) = \delta_P(x), \tag{9}$$

$$x = u, \;\; y = Au, \;\; z = \nabla u, \tag{10}$$

$$K = \begin{pmatrix} A \\ \nabla \end{pmatrix}. \tag{11}$$

Note that $F(y,z)$ is convex because it is the sum of two convex functions. Also the linear transform K takes an image x, yielding a combined vector containing a data vector y and an image gradient vector z. The transpose of K, $K^T = (A^T, -div)$, produces an image vector from the combined data vector y and image-gradient vector z; $-div$, the transpose of the matrix ∇, is a discrete approximation to the negative divergence of an image-gradient, and A^T is the back-projector corresponding to the matrix transpose of A.

The conjugates of F and G, obtained through the Legendre transform, are:

$$F^*(p,q) = \frac{1}{2}\|p\|_2^2 + \langle p, g\rangle + \delta_{Box(\lambda)}(|q|), \tag{12}$$

$$G^*(r) = \delta_P(-r), \tag{13}$$

where $Box(\lambda)$ indicates the set of image vectors whose pixel values are bounded in absolute value by λ. Substituting these conjugate functions into Eq. (2) yields the maximization problem dual to Eq. (7):

$$\max_{p,q} \; -\frac{1}{2}\|p\|_2^2 - \langle p, g\rangle - \delta_{Box(\lambda)}(|q|) - \delta_P(A^T p - div\, q). \tag{14}$$

The dual objective is needed for computing the primal-dial gap, which provides the convergence check. An important aspect to computing this gap is to handle the indicator functions separately, as they are valued at ∞ if their argument is not a member of the indicated convex set. The final piece needed for putting together the CP algorithm instance for Eq. (7) is the proximal mapping:

$$prox_\sigma[F^*](y,z) = \left(\frac{y - \sigma g}{1+\sigma}, \frac{\lambda z}{\max(\lambda, |z|)} \right), \tag{15}$$

$$prox_\tau[G](x) = pos(x), \tag{16}$$

where $pos(x)$ thresholds negative values of x to 0.

With the necessary pieces in place, the CP algorithm instance for Eq. (7) can be written down in Algorithm 2. The resulting algorithm will be demonstrated on a breast CT simulation.

Algorithm 2 Pseudocode for N_0 steps of the TV-regularized,least-squares CP algorithm instance, included a non-negativity constraint.

```
$L \leftarrow \|(A;\nabla)\|_2$; $\tau \leftarrow 1/L$; $\sigma \leftarrow 1/L$;
$\theta \leftarrow 1$; $n \leftarrow 0$
initialize $u_0$, $p_0$, and $q_0$ to zero values
$\bar{u}_0 \leftarrow u_0$
repeat
    $p_{n+1} \leftarrow (p_n + \sigma(A\bar{u}_n - g))/(1+\sigma)$
    $q_{n+1} \leftarrow \lambda(q_n + \sigma\nabla\bar{u}_n)/\max(\lambda, |q_n + \sigma\nabla\bar{u}_n|)$
    $u_{n+1} \leftarrow pos(u_n - \tau A^T p_{n+1} + \tau div\, q_{n+1})$
    $\bar{u}_{n+1} \leftarrow u_{n+1} + \theta(u_{n+1} - u_n)$
    $n \leftarrow n + 1$
until $n \geq N_0$
```

IV. RESULTS

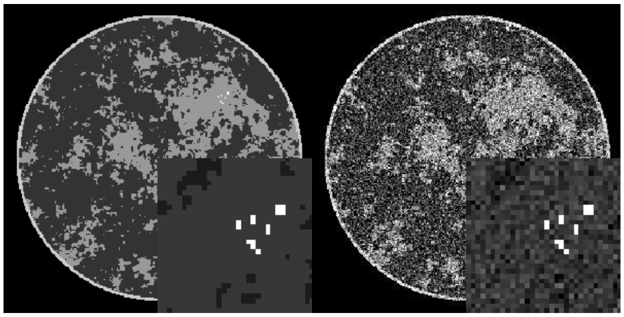

Fig. 1. Breast phantom for CT and FBP reconstructed image for a 512-view noisy data set. Left is the phantom in the gray scale window [0.95,1.15] with a blow-up on the micro-calcification ROI displayed in the gray scale window [0.9,1.8]; and right is the FBP image reconstructed from the noisy data. The middle panel is the reference for all image reconstruction algorithm results. The FBP image is shown only to provide a sense of the noise level.

For the following demonstration of the above CP algorithm instance, we employ a digital 256 × 256 breast phantom, described in Ref. [5]. For the present case, we focus on circular, fan-beam scanning with 60 projections equally distributed over a full 360° angular range. The detector sampling consists of 512 bins. For this phantom under ideal conditions, we have found that accurate recovery is possible with constrained, TV-minimization with as few as 50 projections [6]. In the present study, we add noise to the data model at a level consistent with what might be expect in a typical breast CT scan. For reference, the phantom is shown in Fig. 1. To have a sense of the noise level, a standard fan-beam filtered back-projection reconstruction is shown for a 512-view data set simulated for the same exposure level. Shown in Fig. 2, are two reconstructions from the above CP algorithm instance for two values of λ.

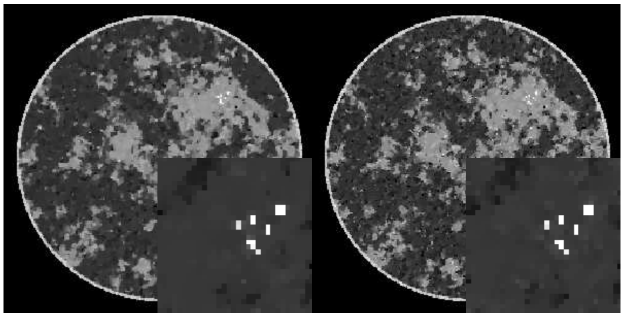

Fig. 2. Images reconstructed from 60-view simulated, noisy projection data. The images result from minimizing the objective in Eq. (7) for $\lambda = 1 \times 10^{-4}$, and 5×10^{-5}.

Although this particular example is motivated by our recent interest in investigating the trade-off between number-of-views and noise-level-per-view [5], The results here are meant to demonstrate the CP algorithm; thus we do not attempt to assess the quality of the TV-regularized reconstructed images in comparison with other methods. We are more interested in the ability of prototyping the optimization problems for iterative image reconstruction in CT. To demonstrate that the images in Fig. (2) are actually solutions of Eq. (7), we plot the primal-dual gap as a function of iteration number in Fig. 3. Shown in this figure are the curves corresponding to the two values of λ, yielding the images in Fig. 2. The primal-dual gap is computed as the difference between the objectives of Eq. (7) and Eq. (14) ignoring the indicator functions of both objectives. The non-negativity indicator function of Eq. (7) is automatically respected; the $pos(\cdot)$ function at line 8 of the CP algorithm instance guarantees that the image iterates u will have no negative components. The indicator function in the dual maximization is more complex and it must be checked separately that the argument does indeed respect non-negativity. For the present example, we have verified that the image iterates quickly respect this indicator, and as can be seen in Fig. 3, the primal-dual gap numerically converges to zero.

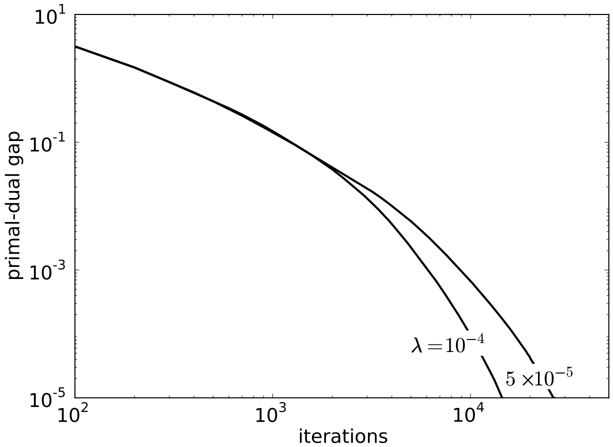

Fig. 3. Convergence of the primal-dual gap for the CP algorithm instance solving Eq. (7) for different values of λ.

V. SUMMARY

In summary, we have shown how to apply the Chambolle-Pock algorithm to solving an optimization problem of interest for image reconstruction in CT. Although we have shown only one particular instance of the CP algorithm applied to TV-regularized least-squares with a non-negativity constraint, we point out that the CP methodology can be rapidly applied to other convex objectives. Indeed, in Ref. [2] we have derived CP instances using alternative data-error norms based on ℓ_1 and the Kullback-Leibler divergence. Moreover, constraints can be incorporated by designing the appropriate indicator function. The only requirement of any particular convex objective, is that the functions F and G be simple enough that their convex conjugate and corresponding proximal mappings can be computed. Within these restrictions, the CP framework provides a means for rapid prototyping of optimization problems for CT image reconstruction and it comes with a convergence check which is important for both simulation studies and real data studies where the underlying object is not known.

VI. ACKNOWLEDGMENT

This work is part of the project CSI: Computational Science in Imaging, and J.H.J. is supported by grant 274-07-0065 from the Danish Research Council for Technology and Production Sciences. E.Y.S. and X.P. were supported in part by NIH R01 Grant Nos. CA158446, CA120540, and EB000225. The contents of this article are solely the responsibility of the authors and do not necessarily represent the official views of the National Institutes of Health.

REFERENCES

[1] A. Chambolle and T. Pock, "A first-order primal-dual algorithm for convex problems with applications to imaging," *J. Math. Imag. Vis.*, vol. 40, pp. 120–145, 2011.
[2] E. Y. Sidky, J. H. Jørgensen, and X. Pan, "Convex optimization problem prototyping for image reconstruction in computed tomography with the Chambolle-Pock algorithm," *Phys. Med. Biol.*, vol. 57, pp. 3065–3091, 2012.
[3] M. Defrise, C. Vanhove, and X. Liu, "An algorithm for total variation regularization in high-dimensional linear problems," *Inv. Prob.*, vol. 27, pp. 065002, 2011.
[4] S. Ramani and J. Fessler, "A splitting-based iterative algorithm for accelerated statistical X-ray CT reconstruction," *IEEE Trans. Med. Imag.*, 2011, available online at IEEE TMI - early access.
[5] J. H. Jørgensen, P. C. Hansen, E. Y. Sidky, I. S. Reiser, and X. Pan, "Toward optimal X-ray flux utilization in breast CT," in *Proceedings of the 11th International Meeting on Three-Dimensional Image Reconstruction in Radiology and Nuclear Medicine*, 2011, arxiv preprint arxiv:1104.1588 (http://arxiv.org/abs/1104.1588).
[6] J. H. Jørgensen, E. Y. Sidky, and X. Pan, "Analysis of discrete-to-discrete imaging models for iterative tomographic image reconstruction and compressive sensing," 2011, arxiv preprint arxiv:1109.0629 (http://arxiv.org/abs/1109.0629).

A Hybrid Regularizer Combining Orthonormal Wavelets and Finite Differences for Statistical Reconstruction in 3-D CT

Sathish Ramani and Jeffrey A. Fessler

***Abstract*—Statistical reconstruction methods for X-ray CT rely on regularization to yield good quality images. We propose and investigate a specific type of nonquadratic regularization for 3-D CT reconstruction that corresponds to applying a 2-D orthonormal wavelet transform (OWT) on trans-axial slices and finite differences (FD) along the axial direction. We use an iterative variable-splitting-based *alternating direction method of multipliers* (ADMM) reconstruction algorithm that effectively handles the proposed regularizer. We also present a simple procedure to incorporate iteration-dependent random shifting to circumvent the shift-variance of OWT and to reduce block artifacts. The proposed regularizer requires less memory compared to those that use FDs and is thus advantageous for ADMM that stores and manipulates auxiliary variables related to the regularizer. We demonstrate using simulation with a 3-D XCAT phantom that the proposed regularizer yields images that are visually comparable in quality to those obtained using a regularizer composed of FDs.**

***Index Terms*—X-ray CT imaging, statistical image reconstruction, nonquadratic regularization, alternating direction method of multipliers, orthonormal wavelet transform.**

I. INTRODUCTION

Regularized reconstruction methods for X-ray CT can provide good image quality at the expense of increased computation compared to unregularized noniterative methods such as FBP. Nonquadratic regularizers that preserve edges [1] or those that promote sparsity are particularly appealing for CT reconstruction [2]. Such regularizers are usually composed of shift-invariant operators such as finite differences (FD) [1] or frames [2]. Wavelet frames are especially attractive due to their multiresolution nature and have been employed for CT [2], [3]; they may also be interpreted as multiresolution extensions of finite differences. However, for 3-D CT, frames can increase computation (due to calculation of frame coefficients during reconstruction) compared to FDs and would require a significant memory overhead when used with some algorithms like *iterative shrinkage thresholding* (IST) [4], [5] or *alternating direction method of multipliers* (ADMM) [2].

An orthonormal wavelet transform (OWT) is a computation- and memory-efficient alternative to a wavelet frame. OWTs retain the multiresolution aspect of wavelet frames and have been successfully used in reconstruction problems in image processing [4] and magnetic resonance imaging [5]. In this work, we investigate the use of OWT for 3-D CT reconstruction. Specifically, we propose a hybrid nonquadratic regularizer that is composed of 2-D OWTs (applied on the trans-axial slices) and FDs (applied along the axial direction). We used the ADMM algorithm [2], for performing reconstruction as it can easily handle the proposed regularizer. Based on our previous work [6], we also present a simple strategy to integrate iteration-dependent random shifting (IDRS) in ADMM to compensate for the shift-variance of OWT and to reduce block-artifacts therefrom. We illustrate using simulations with a 3-D XCAT phantom [7] that the proposed approach is able to provide reconstruction results that are qualitatively similar to those obtained using a regularizer with FDs. Our method can be easily extended for use with 3-D OWTs and can be readily applied to axial and helical CT.

II. STATISTICAL X-RAY CT RECONSTRUCTION

A. Problem Formulation

We consider a penalized weighted least-squares formulation of statistical 3-D X-ray CT reconstruction [1],

$$\arg\min_{\mathbf{x}} \left\{ \frac{1}{2}\|\mathbf{y}-\mathbf{A}\mathbf{x}\|_{\mathbf{W}}^2 + \Psi(\boldsymbol{\mathcal{B}}\mathbf{x}) \right\}, \tag{1}$$

where $\mathbf{x} \in \mathbb{R}^N$ is a vector representing the 3-D volume (of size $N = N_1 \times N_2 \times N_3$) being reconstructed, $\mathbf{y} \in \mathbb{R}^M$ is the logarithm of raw transmission data, $\mathbf{W} \in \mathbb{R}_+^{M\times M}$ is a diagonal matrix consisting of statistical weights [1], [2], $\mathbf{A} \in \mathbb{R}^{M\times N}$ is the system matrix so that $\mathbf{A}\mathbf{x}$ represents line integrals. We consider a regularizer of the form

$$\Psi(\boldsymbol{\mathcal{B}}\mathbf{x}) = \lambda \sum_r \kappa_r \Phi(|[\boldsymbol{\mathcal{B}}\mathbf{x}]_r|), \tag{2}$$

where $\boldsymbol{\mathcal{B}}$ represents the regularization operator, Φ is a potential function, $\lambda > 0$ is the regularization parameter and $\kappa_r > 0$ are weights that govern the spatial resolution [8] in the reconstructed result.

B. Regularization Operator

While common choices for $\boldsymbol{\mathcal{B}}$ in 3-D CT are finite differences (FD) along 3 orthogonal directions, or more comprehensively, along 13 nearest-neighbor-directions [1], we explore the use of an orthonormal wavelet transform (OWT) for (1) in this work. OWTs posses several attractive properties including regularity, sparsity / compressibility and their ability to represent an image at multiple scales and have been widely used in image-processing applications, e.g., restoration [4], and magnetic resonance image reconstruction [5]. There are several ways to incorporate OWTs for 3-D CT reconstruction, e.g., one could consider (a) an entirely wavelet-based regularizer using a 3-D OWT, or (b) some combination of OWTs and FDs for $\boldsymbol{\mathcal{B}}$ in (2). The advantage of (b) is that it allows for simultaneous utilization of wavelet-properties and shift-invariance of FDs,

---

This work was supported by the National Institutes of Health under Grant R01-HL-098686.

Sathish Ramani and Jeffrey A. Fessler are with the Electrical Engineering and Computer Science Department, University of Michigan, Ann Arbor, MI, USA.

so we specifically choose to investigate the following hybrid-form for $\boldsymbol{\mathcal{B}}$:

$$\boldsymbol{\mathcal{B}} = \left[\begin{array}{c} \boldsymbol{\mathcal{V}} \\ \boldsymbol{\mathcal{C}} \end{array} \right], \tag{3}$$

where $\boldsymbol{\mathcal{V}} = \mathbf{I}_{N_3} \otimes \boldsymbol{\mathcal{W}}$, $\boldsymbol{\mathcal{C}} = \mathbf{R} \otimes \mathbf{I}_{N_1 N_2}$, $\otimes$ represents Kronecker product, and $\mathbf{I}_M$ is the identity matrix of size M. The operator $\boldsymbol{\mathcal{B}}$ in (3) thus corresponds to applying a 2-D OWT, represented by $\boldsymbol{\mathcal{W}} \in \mathbb{R}^{N_1 N_2 \times N_1 N_2}$, on each trans-axial slice and nearest-neighbor-differences, represented by $\mathbf{R} \in \mathbb{R}^{N_3 \times N_3}$, along the axial direction (perpendicular to the trans-axial slices). Moreover, as the axial direction is handled separately in $\boldsymbol{\mathcal{B}}$ (3), it allows for the use of varying regularization strength along that direction to account for the cylindrical nature of CT scanner geometries [1].

III. A Splitting-Based Iterative Method

IST-type algorithms [4], [5] are a common choice for solving inverse problems like (1) with entirely wavelet-based regularizers. However, the inclusion of FDs in $\boldsymbol{\mathcal{B}}$ (3) precludes the use of IST-type algorithms for (1). Gradient-descent algorithms like nonlinear conjugate gradient (NCG) can be readily applied for (1), but they are difficult to precondition due to the highly shift-variant nature of the Hessian, $\mathbf{A}^\top \mathbf{W} \mathbf{A}$, of the data-fidelity term in (1) [2] and thus may converge slowly.

Recently, we proposed an iterative variable-splitting-based ADMM algorithm [2] for solving (1). ADMM employs auxiliary constraint variables to separate $\mathbf{A}$ from the data-fidelity term and $\boldsymbol{\mathcal{B}}$ from the regularization term in (1) [2]. The resulting effect of these variables is that ADMM involves simple update steps [2] that correspond to inverting a diagonal matrix, minimizing 1-D denoising cost functions that can be achieved analytically and solving a linear system of equations that is amenable to iterative solvers (e.g., preconditioned conjugate gradient) with effective preconditioning using circulant matrices (e.g., associated with cone-type filters [2]). These features enable fast convergence of ADMM compared to contemporary methods for CT [2] and also allow it to tackle a variety of regularization criteria [2] including the proposed one (2)-(3).

A. ADMM Algorithm

For solving (1) using ADMM, we employ constraints of the form $\mathbf{u} = \mathbf{A}\mathbf{x}$ and $\mathbf{v} = \boldsymbol{\mathcal{B}}\mathbf{x}$, where for ease of analysis, we decompose $\mathbf{v} = [\mathbf{v}_1^\top \mathbf{v}_2^\top]^\top$, so that $\mathbf{v}_1 = \boldsymbol{\mathcal{V}}\mathbf{x}$ and $\mathbf{v}_2 = \boldsymbol{\mathcal{C}}\mathbf{x}$ for $\boldsymbol{\mathcal{B}}$ in (3). Through a derivation similar to that in [2, Sec. III], we obtain the following ADMM algorithm, where at iteration j, we perform the following sequence of operations:

$$\mathbf{x}^{(j+1)} = \mathbf{G}_\nu^{-1} \left(\mathbf{A}^\top (\mathbf{u}^{(j)} - \boldsymbol{\eta}_{\mathbf{u}}^{(j)}) \begin{array}{l} + \nu \boldsymbol{\mathcal{V}}^\top (\mathbf{v}_1^{(j)} - \boldsymbol{\eta}_{\mathbf{v}_1}^{(j)}) \\ + \nu \boldsymbol{\mathcal{C}}^\top (\mathbf{v}_2^{(j)} - \boldsymbol{\eta}_{\mathbf{v}_2}^{(j)}) \end{array} \right), \tag{4}$$

$$\mathbf{u}^{(j+1)} = \mathbf{D}_\mu^{-1} (\mathbf{W}\mathbf{y} + \mu [\mathbf{A}\mathbf{x}^{(j+1)} + \boldsymbol{\eta}_{\mathbf{u}}^{(j)}]), \tag{5}$$

$$\mathbf{v}_1^{(j+1)} = \arg\min_{\mathbf{v}_1} \left\{ \Psi(\mathbf{v}_1) + \frac{\mu\nu}{2} \left\| \mathbf{v}_1 - [\boldsymbol{\mathcal{V}}\mathbf{x}^{(j+1)} + \boldsymbol{\eta}_{\mathbf{v}_1}^{(j)}] \right\|_2^2 \right\}, \tag{6}$$

$$\mathbf{v}_2^{(j+1)} = \arg\min_{\mathbf{v}_2} \left\{ \Psi(\mathbf{v}_2) + \frac{\mu\nu}{2} \left\| \mathbf{v}_2 - [\boldsymbol{\mathcal{C}}\mathbf{x}^{(j+1)} + \boldsymbol{\eta}_{\mathbf{v}_2}^{(j)}] \right\|_2^2 \right\}, \tag{7}$$

$$\boldsymbol{\eta}_{\mathbf{u}}^{(j+1)} = \boldsymbol{\eta}_{\mathbf{u}}^{(j)} - (\mathbf{u}^{(j+1)} - \mathbf{A}\mathbf{x}^{(j+1)}), \tag{8}$$

$$\boldsymbol{\eta}_{\mathbf{v}_1}^{(j+1)} = \boldsymbol{\eta}_{\mathbf{v}_1}^{(j)} - (\mathbf{v}_1^{(j+1)} - \boldsymbol{\mathcal{V}}\mathbf{x}^{(j+1)}), \tag{9}$$

$$\boldsymbol{\eta}_{\mathbf{v}_2}^{(j+1)} = \boldsymbol{\eta}_{\mathbf{v}_2}^{(j)} - (\mathbf{v}_2^{(j+1)} - \boldsymbol{\mathcal{C}}\mathbf{x}^{(j+1)}). \tag{10}$$

The Lagrange-multiplier-like vectors $\boldsymbol{\eta}_{\mathbf{u}}^{(\cdot)}$, $\boldsymbol{\eta}_{\mathbf{v}_1}^{(\cdot)}$ and $\boldsymbol{\eta}_{\mathbf{v}_2}^{(\cdot)}$ are associated with the constraint variables $\mathbf{u}$, $\mathbf{v}_1$ and $\mathbf{v}_2$, respectively. The penalty parameters $\mu > 0$, $\nu > 0$ govern only the convergence speed of ADMM and were chosen as described in [2, Sec. III.E], and

$$\mathbf{G}_\nu \triangleq \mathbf{A}^\top \mathbf{A} + \nu (\boldsymbol{\mathcal{V}}^\top \boldsymbol{\mathcal{V}} + \boldsymbol{\mathcal{C}}^\top \boldsymbol{\mathcal{C}}) = \mathbf{A}^\top \mathbf{A} + \nu (\mathbf{I}_N + \boldsymbol{\mathcal{C}}^\top \boldsymbol{\mathcal{C}}), \tag{11}$$

where we have used the orthonormality of $\boldsymbol{\mathcal{W}}$ and $\boldsymbol{\mathcal{V}}$ in (11):

$$\boldsymbol{\mathcal{W}}^\top \boldsymbol{\mathcal{W}} = \boldsymbol{\mathcal{W}} \boldsymbol{\mathcal{W}}^\top = \mathbf{I}_{N_1 N_2} \implies \boldsymbol{\mathcal{V}}^\top \boldsymbol{\mathcal{V}} = \boldsymbol{\mathcal{V}} \boldsymbol{\mathcal{V}}^\top = \mathbf{I}_N. \tag{12}$$

Since $\mathbf{A}^\top \mathbf{A}$ is "more" shift-invariant than $\mathbf{A}^\top \mathbf{W} \mathbf{A}$ [2] and because $\boldsymbol{\mathcal{C}}^\top \boldsymbol{\mathcal{C}} = \mathbf{R}^\top \mathbf{R} \otimes \mathbf{I}_{N_1 N_2}$ is shift-invariant ($\mathbf{R}$ is a finite differencing matrix), a CG-solver for (4) is amenable to FFT-based preconditioning using suitable cone-type filters [2]. The updates corresponding to $\boldsymbol{\eta}_{\mathbf{u}}^{(\cdot)}$, $\boldsymbol{\eta}_{\mathbf{v}_1}^{(\cdot)}$, $\boldsymbol{\eta}_{\mathbf{v}_2}^{(\cdot)}$ (8)-(10) are trivial. The matrix $\mathbf{D}_\mu \triangleq \mathbf{W} + \mu \mathbf{I}_M$ is diagonal and can be inverted exactly in (5).

The minimizations in (6)-(7) each decouple in to $2N$ scalar denoising problems in terms of the components $\{v_{i,r}\}_{r=1}^N$ of $\mathbf{v}_i$, $i = 1, 2$, for the regularization Ψ in (2). Writing, $\boldsymbol{\varrho}_{\mathbf{v}_1}^{(j)} \triangleq \boldsymbol{\mathcal{V}}\mathbf{x}^{(j+1)} + \boldsymbol{\eta}_{\mathbf{v}_1}^{(j)}$, $\boldsymbol{\varrho}_{\mathbf{v}_2}^{(j)} \triangleq \boldsymbol{\mathcal{C}}\mathbf{x}^{(j+1)} + \boldsymbol{\eta}_{\mathbf{v}_2}^{(j)}$, we have that

$$v_{i,r}^{(j+1)} = \arg\min_v \left\{ \Psi(v) + \frac{\mu\nu}{2} (v - \varrho_{\mathbf{v}_i,r}^{(j)})^2 \right\}, \tag{13}$$

$\varrho_{\mathbf{v}_i,r}^{(j)}$ is the r-th component of $\boldsymbol{\varrho}_{\mathbf{v}_i}^{(j)}$, $i = 1, 2$, $r = 1, \ldots, N$. The 1-D problem (13) admits analytical closed-form solution for a variety of potential functions Φ [2]. For simplicity, we focus on the Fair potential (smoothed-Laplacian)

$$\Phi(x) = \Phi_{\mathrm{FP}}(x) \triangleq x/\delta - \log(1 + x/\delta), \tag{14}$$

$\delta > 0$, that has been used successfully for CT [2], [6]. For Φ_{FP}, (13) leads to [2]

$$v_{i,r}^{(j+1)} = \mathrm{sign}\{\varrho_{\mathbf{v}_i,r}^{(j)}\} \frac{\zeta_{\mathbf{v}_i,r}^{(j)} + \sqrt{(\zeta_{\mathbf{v}_i,r}^{(j)})^2 + 4\delta |\varrho_{\mathbf{v}_i,r}^{(j)}|}}{2}, \tag{15}$$

where $\zeta_{\mathbf{v}_i,r}^{(j)} \triangleq |\varrho_{\mathbf{v}_i,r}^{(j)}| - \delta - \lambda \kappa_r / (\delta \mu \nu)$, $i = 1, 2$.

B. Memory Requirement

Compared to other iterative methods like NCG or IST-type algorithms, ADMM requires more memory as it needs to store $\mathbf{u}^{(\cdot)}$, $\mathbf{v}^{(\cdot)}$ and associated Lagrange-multiplier-like vectors. Depending on the regularization, memory requirement for $\mathbf{v}^{(\cdot)}$ may overshoot that of $\mathbf{u}^{(\cdot)}$ and represent a significant memory-overhead for 3-D CT; this is particularly the case with FDs when all 13 nearest-neighbour directions are used [2]. As an alternative, FDs in 3 orthogonal directions may be considered, which will only require a total of 6 image-volumes for storing $\mathbf{v}^{(\cdot)}$ and its Lagrange-multiplier vector (significantly less than 26 image-volumes required for the 13-neighborhood case). In comparison, ADMM for the proposed regularization operator $\boldsymbol{\mathcal{B}}$ (3) requires even less memory, a total of only 4 image-volumes for storing $\mathbf{v}^{(\cdot)}$ and its Lagrange-multiplier vector, due to the use of the OWT $\boldsymbol{\mathcal{W}}$ in $\boldsymbol{\mathcal{B}}$; the proposed $\boldsymbol{\mathcal{B}}$ (3) is thus advantageous for ADMM-based 3-D CT reconstruction.

IV. ITERATION-DEPENDENT RANDOM SHIFTING

Memory efficiency of an OWT comes at the expense of its shift-variant nature that can lead to block-artifacts in the reconstructed image [5], [6]. Iteration dependent random shifting (IDRS) [4] is a cost-effective technique for partially compensating the shift-variance of OWT and has been successfully used for image restoration [4] and MRI reconstruction [5] with iterative shrinkage-thresholding (IST) type methods. We proposed a simple strategy recently to incorporate IDRS in ADMM for statistical 2-D CT reconstruction using regularization composed entirely of OWT [6]. The basic idea there is to apply an iteration-varying random translation to the estimate $\mathbf{x}^{(j)}$ before solving a denoising problem akin to (6) and then to undo the translation later in the sequence of updates in ADMM. The same idea can be readily extended to the OWT-part of the proposed $\boldsymbol{\mathcal{B}}$ (3) and the update equation (6) for corresponding constraint variable $\mathbf{v}_1$.

Before proceeding, it is useful to introduce $\widetilde{\mathbf{v}}_1 \triangleq \boldsymbol{\mathcal{V}}^\top \mathbf{v}_1$ and $\boldsymbol{\eta}_{\widetilde{\mathbf{v}}_1} \triangleq \boldsymbol{\mathcal{V}}^\top \boldsymbol{\eta}_{\mathbf{v}_1}$. Then the updates that depend on $\boldsymbol{\mathcal{V}}$, (4), (6) and (9), respectively, become

$$\mathbf{x}^{(j+1)} = \mathbf{G}_\nu^{-1} \left(\mathbf{A}^\top (\mathbf{u}^{(j)} - \boldsymbol{\eta}_{\mathbf{u}}^{(j)}) \begin{array}{c} +\nu(\widetilde{\mathbf{v}}_1^{(j)} - \boldsymbol{\eta}_{\widetilde{\mathbf{v}}_1}^{(j)}) \\ +\nu\boldsymbol{\mathcal{C}}^\top(\mathbf{v}_2^{(j)} - \boldsymbol{\eta}_{\mathbf{v}_2}^{(j)}) \end{array} \right), \tag{16}$$

$$\widetilde{\mathbf{v}}_1^{(j+1)} = \boldsymbol{\mathcal{V}}^\top \left(\arg\min_{\mathbf{v}_1} \left\{ \begin{array}{l} \Psi(\mathbf{v}_1) + \\ \frac{\mu\nu}{2} \left\| \mathbf{v}_1 - \boldsymbol{\mathcal{V}}[\mathbf{x}^{(j+1)} + \widetilde{\boldsymbol{\eta}}_{\mathbf{v}_1}^{(j)}] \right\|_2^2 \end{array} \right\} \right), \tag{17}$$

$$\boldsymbol{\eta}_{\widetilde{\mathbf{v}}_1}^{(j+1)} = \boldsymbol{\eta}_{\widetilde{\mathbf{v}}_1}^{(j)} - (\widetilde{\mathbf{v}}_1^{(j+1)} - \mathbf{x}^{(j+1)}), \tag{18}$$

where we have used the orthonormality of $\boldsymbol{\mathcal{V}}$ in (17) and (18). Thus the only step in ADMM where $\boldsymbol{\mathcal{V}}$ (i.e., OWT) appears now is (17), so we need only focus on (17) for incorporating IDRS. Since we want to promote shift-invariance, at each iteration j, we consider $\boldsymbol{\mathcal{S}}^{(j)} \triangleq \mathrm{diag}\{\boldsymbol{\mathcal{S}}_1^{(j)} \cdots \boldsymbol{\mathcal{S}}_{N_3}^{(j)}\}$, where $\{\boldsymbol{\mathcal{S}}_i^{(j)}\}_{i=1}^{N_3}$ are $N_1 N_2 \times N_1 N_2$ block permutation matrices, such that the action of $\boldsymbol{\mathcal{S}}^{(j)}$ on $\mathbf{x}^{(j)}$ randomly translates each trans-axial slice by different amounts. Then applying IDRS simply amounts to using $\widetilde{\boldsymbol{\mathcal{V}}}^{(j)} \triangleq \boldsymbol{\mathcal{V}}\boldsymbol{\mathcal{S}}^{(j)}$ in (17), i.e., $\widetilde{\mathbf{v}}_1^{(j+1)} =$

$$\widetilde{\boldsymbol{\mathcal{V}}}^{(j)\top} \left(\arg\min_{\mathbf{v}_1} \left\{ \begin{array}{l} \Psi(\mathbf{v}_1) + \\ \frac{\mu\nu}{2} \left\| \mathbf{v} - \widetilde{\boldsymbol{\mathcal{V}}}^{(j)} [\mathbf{x}^{(j+1)} + \widetilde{\boldsymbol{\eta}}_{\mathbf{v}_1}^{(j)}] \right\|_2^2 \end{array} \right\} \right), \tag{19}$$

that is, IDRS is first applied to the input $(\mathbf{x}^{(j+1)} + \widetilde{\boldsymbol{\eta}}_{\mathbf{v}_1}^{(j)})$ to the denoising step (19) via $\widetilde{\boldsymbol{\mathcal{V}}}^{(j)}$, the denoising operation [minimization in (19)] is performed similar to (13)-(15), and IDRS is undone later in the same step via $\widetilde{\boldsymbol{\mathcal{V}}}^{(j)\top}$. This is similar to how IDRS is also applied in IST-type algorithms [4], [5]. We summarize below our ADMM-IDRS scheme for 3-D CT reconstruction assuming we have a sequence of random translations represented by $\{\boldsymbol{\mathcal{S}}^{(j)}\}$.

ADMM-IDRS for 3-D CT Reconstruction

1. Initialization: $\mathbf{x}^{(1)}$; Set $\boldsymbol{\eta}_{\mathbf{u}}^{(0)} = \boldsymbol{\eta}_{\widetilde{\mathbf{v}}_1}^{(0)} = \boldsymbol{\eta}_{\mathbf{v}_2}^{(0)} = \boldsymbol{\eta}_{\mathbf{u}}^{(1)} = \boldsymbol{\eta}_{\widetilde{\mathbf{v}}_1}^{(1)} = \boldsymbol{\eta}_{\mathbf{v}_2}^{(1)} = \mathbf{0}$; Compute $\mathbf{u}^{(1)}$ using (5); obtain $\widetilde{\mathbf{v}}_1^{(1)}$, $\mathbf{v}_2^{(1)}$, respectively, using (19), (7), (13)-(15); set $j = 1$.
2. Apply (P)CG for partially solving (16) to obtain $\mathbf{x}^{(j+1)}$.
3. Compute $\mathbf{u}^{(j+1)}$ using (5).
4. Obtain $\widetilde{\mathbf{v}}_1^{(j+1)}$, $\mathbf{v}_2^{(j+1)}$ using (19), (7) and (13)-(15).
5. Update $\boldsymbol{\eta}_{\mathbf{u}}^{(j+1)}$, $\boldsymbol{\eta}_{\widetilde{\mathbf{v}}_1}^{(j+1)}$, $\boldsymbol{\eta}_{\mathbf{v}_2}^{(j+1)}$ using (8), (18), (10).
6. Set $j \leftarrow j+1$; Repeat Steps 2-6 till stop criterion is met.

IDRS as applied to ADMM above for 3-D CT reconstruction is computationally efficient since it only requires trivial translation operations and provides image quality comparable to that obtained using FDs as demonstrated next.

V. EXPERIMENTAL SETUP & RESULTS

We performed simulations with a 3-D XCAT phantom [7] of size $1024 \times 1024 \times 188$. We generated a $888 \times 984 \times 64$ noisy sinogram with GE LightSpeed fan-beam geometry [2] (axial scan) corresponding to a monoenergetic source with 5×10^5 incident photons per ray and no background events. We reconstructed $512 \times 512 \times 92$ image-volumes (that include a padding of 28 trans-axial slices to account for the "long object problem" of the scanner geometry) whose trans-axial FOV was 50 cm and whose axial FOV of the region of interest was 4 cm. We used the separable-footprints (SF-TR) projector [9] (implemented in C) for computing matrix-vector products such as $\mathbf{A}\mathbf{x}$, $\mathbf{A}^\top\mathbf{u}$ and initialized ADMM [2] and the proposed ADMM-IDRS with the image-volume reconstructed using FDK with Hanning filter. We applied 5 CG iterations with a cone-filter-type preconditioner [2] for "solving" (16). We compared reconstruction quality yielded by the regularizer in (2) with Φ_{FP} [$\delta = 10$ HU (14)] using (a) finite differences (FD) in 3 orthogonal directions and (b) the proposed operator $\boldsymbol{\mathcal{B}}$ (3) employing 3 levels of the orthonormal Haar wavelet transform for $\boldsymbol{\mathcal{W}}$. Computation times of ADMM [2] for case (a) and the proposed ADMM-IDRS for case (b) were dominated by products with $\mathbf{A}$ and $\mathbf{A}^\top$ and were similar (≈ 3 minutes / iteration in Matlab running on a 12-core PC with 2.80 GHz Intel Xeon CPUs and 24 GB RAM).

We set $\kappa_r = \sqrt{[\mathbf{A}^\top\mathbf{W}\mathbf{1}]_r / [\mathbf{A}^\top\mathbf{1}]_r}$ [8] wherever FDs were involved (including those in $\boldsymbol{\mathcal{B}}$). For the OWT part in $\boldsymbol{\mathcal{B}}$, we first applied IDRS, i.e., $\boldsymbol{\mathcal{S}}^{(\cdot)}$, to $\boldsymbol{\kappa} = \{\kappa_r\}$ and propagated the resulting vector through the wavelet decomposition tree without employing the wavelet-filtering steps to obtain a set of subband-dependent weights that replaced κ_r in (15) for ($i = 1$) the OWT part of $\boldsymbol{\mathcal{B}}$. We also set the weights corresponding to the approximation coefficients to zero (i.e., they were not thresholded since they are not sparse in general [4]–[6]). We chose the regularization parameter λ so as to roughly compromise between smoothing and reduction of noise and artifacts. Figs. 1-3 present reconstruction results for our simulation. Both regularized reconstruction results (third and fourth columns in all figures) provide improved quality over the FDK result along the trans-axial, coronal and sagittal views. Moreover, the proposed method [ADMM-IDRS with $\boldsymbol{\mathcal{B}}$ (3)] yields reconstructed images (fourth column in Figs. 1-3) that are visually comparable to those obtained using finite differences in 3 orthogonal directions (third column in Figs. 1-3) indicating the potential of orthonormal wavelets and IDRS for 3-D CT reconstruction.

VI. CONCLUSION & DISCUSSION

We proposed a hybrid nonquadratic regularizer (2) for statistical 3-D CT reconstruction with an operator $\boldsymbol{\mathcal{B}}$ (3) that applies a 2-D orthonormal wavelet transform (OWT) on trans-axial

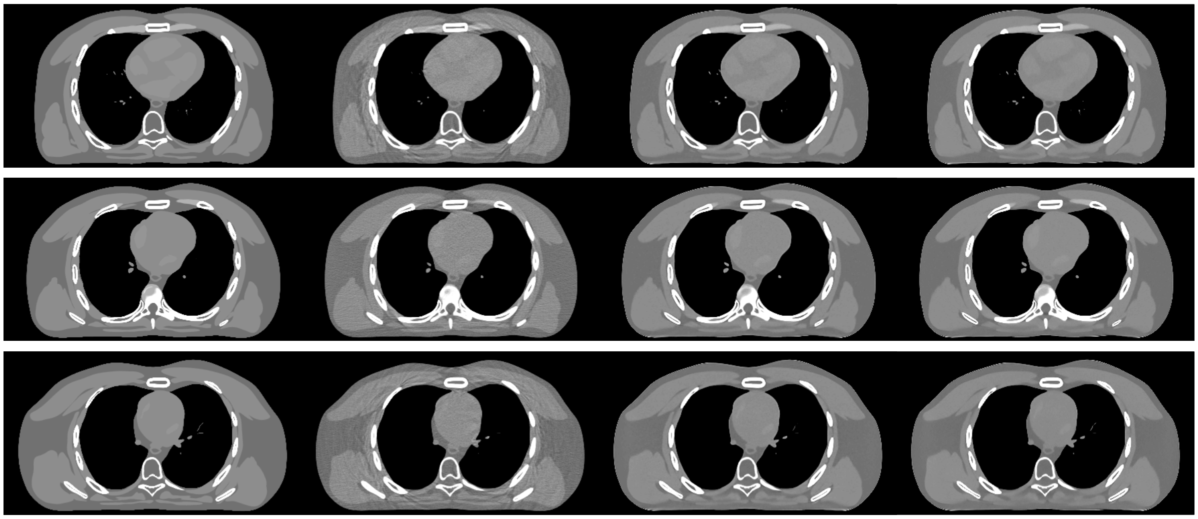

Fig. 1. Simulation with a 3-D XCAT phantom. Zoomed slices in **trans-axial view** (444×242). **First row:** Slice 26, **Second row:** Slice 46 and **Third row:** Slice 66. **First column:** Noisefree phantom; **Second column:** FDK result with Hanning filter; **Third column:** ADMM result for Φ_{FP} (14) with finite differences in 3 orthogonal directions; **Fourth column:** ADMM-IDRS result for Φ_{FP} (14) with proposed operator $\boldsymbol{\mathcal{B}}$ (3) involving OWT. Images are displayed in Hounsfield units in the range of [800, 1200].

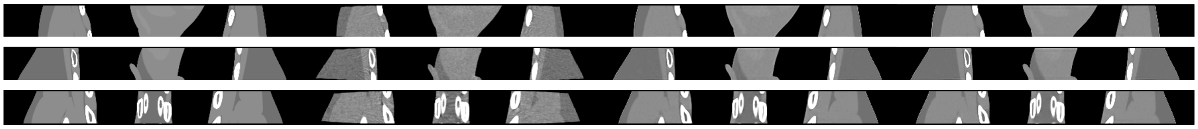

Fig. 2. Simulation with a 3-D XCAT phantom. Zoomed slices in **coronal view** (444×50). **First row:** Slice 197, **Second row:** Slice 257 and **Third row:** Slice 317. **First column:** Noisefree phantom; **Second column:** FDK result with Hanning filter; **Third column:** ADMM result for Φ_{FP} (14) with finite differences in 3 orthogonal directions; **Fourth column:** ADMM-IDRS result for Φ_{FP} (14) with proposed operator $\boldsymbol{\mathcal{B}}$ (3) involving OWT. Images are displayed in Hounsfield units in the range of [800, 1200].

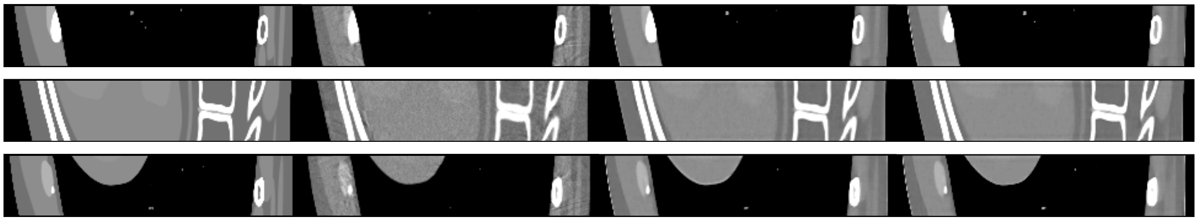

Fig. 3. Simulation with a 3-D XCAT phantom. Zoomed slices in **sagittal view** (242×50). **First row:** Slice 197, **Second row:** Slice 257 and **Third row:** Slice 317. **First column:** Noisefree phantom; **Second column:** FDK result with Hanning filter; **Third column:** ADMM result for Φ_{FP} (14) with finite differences in 3 orthogonal directions; **Fourth column:** ADMM-IDRS result for Φ_{FP} (14) with proposed operator $\boldsymbol{\mathcal{B}}$ (3) involving OWT. Images are displayed in Hounsfield units in the range of [800, 1200].

slices and finite differences (FD) along the axial direction. We developed a simple scheme to incorporate iteration-dependent random shifting (IDRS) [4]–[6] in the ADMM reconstruction algorithm [2] to compensate for the shift-variance of the OWT part of the proposed operator $\boldsymbol{\mathcal{B}}$ (3). Simulations with a 3-D XCAT phantom indicate that the proposed method, i.e., ADMM-IDRS with the hybrid regularizer (2)-(3), yields reconstructed images that are qualitatively similar to those obtained using a regularizer composed of FDs in 3 orthogonal directions. We are currently evaluating improved choices for subband-dependent weights for the OWT part of the proposed regularizer (2)-(3). The next step is to compare the proposed regularizer (2)-(3) against one that uses FDs in all 13 nearest-neighbour directions [1] in 3-D. We also plan to investigate regularization criteria that use 3-D OWT for 3-D CT reconstruction with application to helical CT.

REFERENCES

[1] J-B. Thibault, K. Sauer, C. Bouman, and J. Hsieh, "A three-dimensional statistical approach to improved image quality for multi-slice helical CT," *Med. Phys.*, vol. 34, no. 11, pp. 4526–44, Nov. 2007.

[2] S. Ramani and J. A. Fessler, "A splitting-based iterative algorithm for accelerated statistical X-ray CT reconstruction," *IEEE Trans. Med. Imag.*, vol. 3, no.3, pp. 677–88, Mar. 2012.

[3] X. Jia, B.Dong, Y.Lou, and S. B. Jiang, "GPU-based iterative cone-beam CT reconstruction using tight frame regularization," *Phys. Med. Biol.*, vol. 56, pp. 3787–807, 2011.

[4] M. A. T. Figueiredo and R. D. Nowak, "An EM algorithm for wavelet-based image restoration," *IEEE Trans. Im. Proc.*, vol. 12, no. 8, pp. 906–16, Aug. 2003.

[5] M. Guerquin-Kern, M. Haberlin, K.P. Pruessmann, and M. Unser, "A fast wavelet-based reconstruction method for magnetic resonance imaging," *IEEE Trans. Med. Imag.*, vol. 30, no. 9, pp. 1649–1660, 2011.

[6] S. Ramani and J. A. Fessler, "Statistical X-ray CT reconstruction using a splitting-based iterative algorithm with orthonormal wavelets," *Proc. IEEE Intl. Symp. Biomed. Imag.*, pp. 1008-11, Barcelona, Spain, 2012.

[7] W. P. Segars, M. Mahesh, T. J. Beck, E. C. Frey, and B. M. W. Tsui, "Realistic CT simulation using the 4D XCAT phantom," *Med. Phys.*, vol. 35, no. 8, pp. 3800–8, Aug. 2008.

[8] J. A. Fessler and W. L. Rogers, "Spatial resolution properties of penalized-likelihood image reconstruction methods: Space-invariant tomographs," *IEEE Trans. Im. Proc.*, vol. 5, no. 9, pp. 1346–58, Sept. 1996.

[9] Y. Long, J. A. Fessler, and J. M. Balter, "3D forward and back-projection for X-ray CT using separable footprints," *IEEE Trans. Med. Imag.*, vol. 29, no. 11, pp. 1839–50, Nov. 2010.

Statistical CT Reconstruction from Limited Views with Probabilistic Atlas Prior

Essam A. Rashed and Hiroyuki Kudo

Abstract—**Statistical iterative reconstruction (SIR) methods are known to achieve superior image quality compared to conventional methods derived from analytical inversion formulae. Effective noise modeling and possibilities to incorporate priors in the image reconstruction problem are the main advantages of the SIR methods. The compressed sensing principal provides an interesting framework for possible reconstruction of artifacts-free images from highly down-sampled projection data. In this paper, we introduce a new image reconstruction algorithm from limited view data based on prior information obtained from probabilistic atlas. A data set collected from screening chest CT for several patients was used to construct a 3D atlas with Laplace mixture model. The mixture parameters are estimated using the expectation maximization (EM) algorithm. Later, the prior information obtained from the probabilistic atlas is used to formulate the image reconstruction cost function. Experimental studies indicate that the probabilistic atlas prior is a practically promising approach for low-dose CT imaging.**

I. INTRODUCTION

X-ray computed tomography (CT) has evolved into an essential imaging modality in clinical routines. It is hardly to find a hospital has no in-duty CT imaging equipment worldwide. The side effects of the radiation dose generated from CT scans become an interesting topic to be investigated. Though, it is not yet strictly proved that regular CT scans may lead to a malignancy, it is estimated that a rough of 2% of cancers may eventually be caused by the average radiation dose currently used in clinical CT [1]. The optimization of hardware factors such as scanning geometry, tube current and pitch factor would probably lead to a dose reduction. However, it is always preferable to obtain standard imaging techniques that minimize the patient dose with acceptable image quality. The conventional image reconstruction methods based on analytical inversion formulae still the fundamental choice for clinical equipment. Though, statistical iterative reconstruction (SIR) methods are known to provide a higher image quality due to noise modeling and possibilities to incorporate prior information in the image reconstruction problem.

This work investigates the problem of image reconstruction from small number of projection views (Fig. 1) as a potential approach for tomographic imaging with diminished patient dose. The angular sampling rate has a large influence on the accuracy and stability of the image reconstruction inverse problem. While reducing the projection views might contribute to the patient dose reduction, this assumption is known to generate streak artifacts in the reconstructed image [2]. This classical problem had been studied since the invention of tomographic imaging. Nevertheless, the basic mathematical principal behind this problem concludes that when the projection data is highly down-sampled, the image reconstruction becomes underdetermined problem and the achievement of exact reconstruction is not theoretically possible [3]. Supplementary information, added to the image reconstruction cost function, would probably lead to a more accurate reconstruction. Recently, the principal of compressed sensing [4], [5] becomes the essential framework of several image reconstruction approaches that handle data limitations in tomographic imaging (e.g. [6]–[9]).

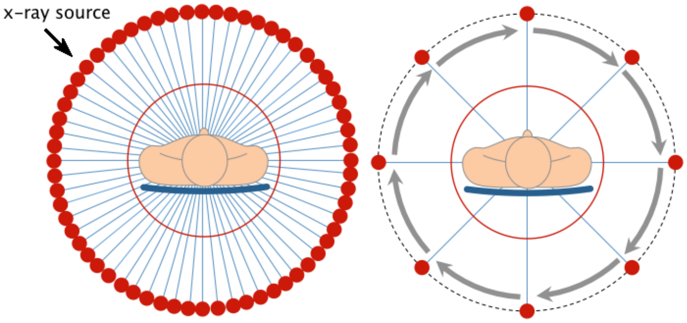

Fig. 1. CT imaging configurations. The positions of x-ray source in data acquisition for full scan (left) and limited views (right).

A principal approach to solve the problem of image reconstruction from limited views is the incorporation of *a priori* known information (e.g. [10], [11]). The cost function and prior information required for theoretically exact reconstruction is still unknown [12]. Thus, it is interesting to quantitatively investigate how different types of prior information contribute to image quality. Generally, we can classify the possible prior information into the following three categories: (1) complete reference image (intensity and spatial information), (2) boundaries and support information (spatial information only), and (3) attenuation information (intensity values only). The first category considers the case where the prior information is obtained from a reference image generated prior to reconstruction. The second category includes the use of prior information corresponding to the boundaries of uniform regions such as the well-known quadratic smoothing penalty. The third category corresponds to the case where the prior information is limited to a set of intensity values representing

---

This work was partially supported by Grant-in-Aid from the Japan Society for the Promotion of Science (JSPS). Grant for foreign Post-doctoral fellows (ID No. P10052). E.A.Rashed and H.Kudo are with the Division of Information Engineering, Faculty of Engineering, Information and Systems, University of Tsukuba, Tsukuba 305-8573, Japan. E.A.Rashed is also with the Department of Mathematics, Faculty of Science, Suez Canal University, Ismailia 41522, Egypt (e-mail: essam@imagelab.cs.tsukuba.ac.jp).

uniform regions inside the object. Recently, we have developed image reconstruction algorithm from small number of projection views, named intensity-based MAP (iMAP) [13]. A penalty term based on prior information limited to a small number of intensity values was introduced. The penalty term, named *intensity prior*, is computed using the average intensity values of uniform regions in the scanned object and it leads to a considerable improvement of image quality.

In this paper, we propose a new statistical iterative reconstruction (SIR) method using prior information obtained from probabilistic atlas. First, we use a set of reconstructed volumes obtained from previous scans of several patients to construct a probabilistic atlas using Laplace mixture model (LMM). The mixture parameters are estimated using the expectation maximization (EM) algorithm. Probabilistic atlas and mixture model parameters are then used to formulate the image reconstruction cost function from limited view data. Although, the use of finite mixture models is a common and popular approach in the context of image segmentation, to the best of our knowledge, the use of probabilistic atlas have not been investigated to solve the concerned problem before. The developed method can be considered as an extension of the iMAP algorithm [13] that enable automatic robust estimation of required parameters. The main contribution of this paper is to emphasis that the spatial information provided from a probabilistic atlas leads to a more accurate reconstruction.

II. METHODS

A. Image reconstruction with intensity priors

The transmission x-ray CT imaging can be described in a discrete form using the following statistical model:

$$y_i = \text{Poisson}(b_i \exp(-\langle \vec{a_i}, \vec{x} \rangle)), \tag{1}$$

where $\vec{x} = (x_1, \dots, x_n)$ is the image vector representing the attenuation coefficients of the image object, $\vec{y} = (y_1, \dots, y_m)$ is a vector represents the raw detector measurements with the corresponding blank scan $\vec{b} = (b_1, \dots, b_m)$, $A = \{a_{ij}\}$ is the $m \times n$ system matrix that models the imaging system, and $\langle \vec{a_i}, \vec{x} \rangle = \sum_{j=1}^{n} a_{ij} x_j$ is the inner product of the ith row of matrix A and image vector $\vec{x}$. In iMAP algorithm, the solution of image reconstruction problem is found through the following cost function:

$$\min_{\vec{x} \geq 0} f(\vec{x}) = L(\vec{x}) + \beta D(\vec{x}, \vec{z}), \tag{2}$$

$$L(\vec{x}) = \sum_{i=1}^{m} \left[b_i \exp(-\langle \vec{a_i}, \vec{x} \rangle) + y_i \langle \vec{a_i}, \vec{x} \rangle \right], \tag{3}$$

$$D(\vec{x}, \vec{z}) = \sum_{j=1}^{n} \min_{l=1}^{L} \left(w_l |x_j - z_l| \right). \tag{4}$$

The term $L(\vec{x})$ is the negative log-likelihood and $D(\vec{x}, \vec{z})$ is a distance function controlled by a hyper-parameter β, $\vec{z} = (z_1, \dots, z_L)$ is a set of *a priori* known intensity values in ascending order, and $w_1, \dots, w_L$ represent empirically determined parameters that quantitatively represent the corresponding intensity values.

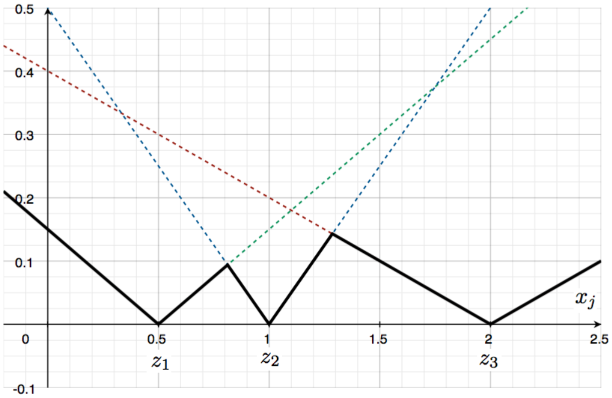

Fig. 2. The penalty function in (4) with $L = 3$, $\vec{z} = (0.5, 1.0, 2.0)$, w_1=0.3, $w_2 = 0.5$, and $w_3 = 0.2$.

An illustration of the intensity prior function in (4) is shown in Fig. 2. Each value of *a priori* known intensity values z_l intuitively represents the mean intensity value corresponding to a uniform region expected in the scanned object. The main challenge in minimizing the cost function in (2) is that the penalty term is based on ℓ_1-norm distance, which is neither convex nor differentiable. Therefore it is not possible to employ ordinary gradient-type iterative method to minimize the cost function. Instead, the majorizarion-minimization (MM) strategy [14], [15] is used to derive a separable quadratic function $\tilde{f}(\vec{x}, \vec{x}^k)$. At each iteration k, the non-separable part of the cost function is approximated by a separable quadratic function around $\vec{x} = \vec{x}^k$ given by:

$$\tilde{f}(\vec{x}; \vec{x}^k) = \sum_{j=1}^{n} \beta w_l \left[c_{j,l}(x_j - p_j)^2 + |x_j - z_l| \right] + T(\vec{x}^k),$$

$$l = \{ |x_j - z_l| \leq |x_j, z_t|, t = (1, \dots, L) \}, \tag{5}$$

where $T(\vec{x}^k)$ is the term independent of $\vec{x}$ and p_j, $c_{j,l}$ are computed as follow:

$$p_j = x_j^k + x_j^k \frac{\sum_{i=1}^{m} a_{ij} \left(b_i \exp(-\langle \vec{a_i}, \vec{x}^k \rangle) - y_i \right)}{\sum_{i=1}^{m} a_{ij} \langle \vec{a_i}, \vec{x}^k \rangle b_i \exp(-\langle \vec{a_i}, \vec{x}^k \rangle)}, \tag{6}$$

$$c_{j,l} = \frac{1}{2\beta \omega_l x_j^k} \sum_{i=1}^{m} a_{ij} \langle \vec{a_i}, \vec{x}^k \rangle b_i \exp(-\langle \vec{a_i}, \vec{x}^k \rangle). \tag{7}$$

The final form of the iMAP algorithm is as follow:

(i) *Initialization*: Estimate the intensity prior $\vec{z}$, set initial image $\vec{x}^0$ to a uniform value and initialize iteration number $k = 0$.

(ii) *Majorization*: The cost function $f(\vec{x})$ is majorized around the current estimate $\vec{x}^k$.

(iii) *Minimization*: The separable cost function $\tilde{f}(\vec{x}; \vec{x}^k)$ is minimized over $\vec{x} \geq 0$ to obtain the image estimate for next iterate:

$$q = \arg\min_{\vec{x} \geq 0} \tilde{f}(\vec{x}; \vec{x}^k), \quad x_j^{k+1} = \max(q_j, \epsilon) \tag{8}$$

where ϵ is a small value to guarantee that $x_j^{k+1} > 0$.

(iv) *Iterate condition*: Set iteration number $k = k + 1$ and repeat steps (i)-(iii) until reaching to a stopping criterion.

The minimization in (8) is implemented through the following multi-thresholding function:

$$q_j = \begin{cases} p_{j,l}^{+} & (s_{l-1} < p_j < z_{j,l}^{-}) \\ z_l & (\max(z_{j,l}^{-}, s_{l-1}) \leq p_j \leq \min(z_{j,l}^{+}, s_l)) \\ p_{j,l}^{-} & (z_{j,l}^{+} < p_j \leq s_l) \end{cases} , \qquad (l = 1, \dots, L). \quad (9)$$

with $p_{j,l}^{+} = p_j + 1/(2c_{j,l})$, $p_{j,l}^{-} = p_j - 1/(2c_{j,l})$, $z_{j,l}^{+} = z_l + 1/(2c_{j,l})$, $z_{j,l}^{-} = z_l - 1/(2c_{j,l})$, $s_l = (\omega_l z_l + \omega_{l+1} z_{l+1})/(\omega_l + \omega_{l+1}), s_0 = -\infty$ and $s_L = \infty$. The multi-thresholding function in (9), can be expressed as a combination of multiple successive soft-thresholding functions, each is implemented around a single value of the *a priori* known intensity values $z_l, l = (1, \dots, L)$. The practical interpretation of this thresholding operation is as follows. If the computed pixel value p_j is closed to the intensity value z_l, the pixel value is trimmed to z_l. Otherwise, the pixel value p_j is shifted softly towards the closest value of z_l.

During the practical implementation of the iMAP method, we have found the major challenge stationed in how to estimate the parameters. Moreover, the thresholding function in (9) is based on the current image estimate with no pixel spatial information. In this paper, we extend the iMAP algorithm by including additional information obtained from a probabilistic atlas generated using reconstructed volumes obtained from different patients.

B. Construction of the Probabilistic Atlas

The probabilistic atlas presented in this paper is used to provide a complete spatial distribution of probabilities that a voxel belong to one or more uniform regions (organs). Each image voxel is assigned to L-vector, where L denotes the number of regions in the modeling system. To create the atlas, the LMM is used to segment the data set into L number of regions. The parameters of the LMM are estimated using the EM algorithm [16]. Finally, the probabilistic atlas parameters are used to identify the parameters for image reconstruction problem in (2).

The LMM is a statistical model for multivariate data mixture that is widely used in the context of robust clustering such as image segmentation. The LMM [17], [18] assumes that the density function at an observation x_j is given by:

$$p(x_j) = \sum_{l=1}^{L} \pi_l p(x_j | \Omega_l), \quad (10)$$

where π_l is the prior distribution of the pixel x_j belongs to the class Ω_l, which satisfy the constraints:

$$0 \leq \pi_l \leq 1 \quad \text{and} \quad \sum_{l=1}^{L} \pi_l = 1. \quad (11)$$

Each Laplacian distribution $p(x_j | \Omega_l)$, called a component of the mixture, and the probability density function (pdf) is given by:

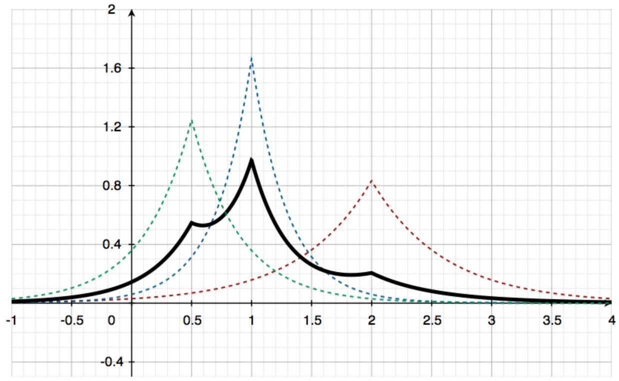

Fig. 3. Plot of probability Laplacian density function of three components with parameters (μ, λ) = (0.5, 0.4), (1.0, 0.3) and (2.0, 0.6) is in dotted lines. The mixture density corresponding to proportions of 0.3, 0.5 and 0.2, respectively, is in solid line.

$$p(x_j | \Omega_l) = \frac{1}{2\lambda_l} \exp\left(-\frac{|x_j - \mu_l|}{\lambda_l} \right) \quad (12)$$

with $\lambda_l > 0$ is a width control parameter and μ_l is the median of mixture component Ω_l. An example of the mixture density function is plotted in Fig. 3.

C. Image Reconstruction with Probabilistic Atlas Prior

Considering the probabilistic atlas, the median value of mixture components μ_l is modeled as the known intensity values z_l in the iMAP method. Also, the mixture weight π_l is modeled as the weighting parameter w_l. As the probabilistic atlas is computed from different patients the mixture weight parameter can be computed as a pixel-dependant value π_{lj}. The probabilistic atlas prior can be formulated as:

$$D_{LMM}(\vec{x}) = \sum_{j=1}^{n} \left(\pi_{lj} \; |x_j - \mu_l| \right), x_j \in \Omega_l \quad (13)$$

III. EXPERIMENTAL STUDIES

A. Compute 3D Probabilistic Atlas

The data sets used to construct the probabilistic atlas is obtained from a clinical screening chest CT volumes for different patients [19]. The data set consists of 68 volumes each of 25 to 31 slices with slice grid of 320×320 pixels and pixel size 1×1 mm. A subset of 28 volumes were selected to create the atlas. A single volume is arbitrarily selected as a reference and the remanning 27 volumes are registered onto the reference volume using non-rigid registration with a single control point located at the center region of the spinal cord. The EM algorithm is used to estimate the LMM parameters (λ_l, μ_l, π_l) and thus the posterior probability function.

B. Image Reconstruction Results

A single volume from the data set, which is not included in the construction of the atlas, was used to evaluate the proposed method. The central slice is forward-projected into 48 projection views over 180° and reconstruction was implemented using standard filtered back-projection (FBP), iMAP

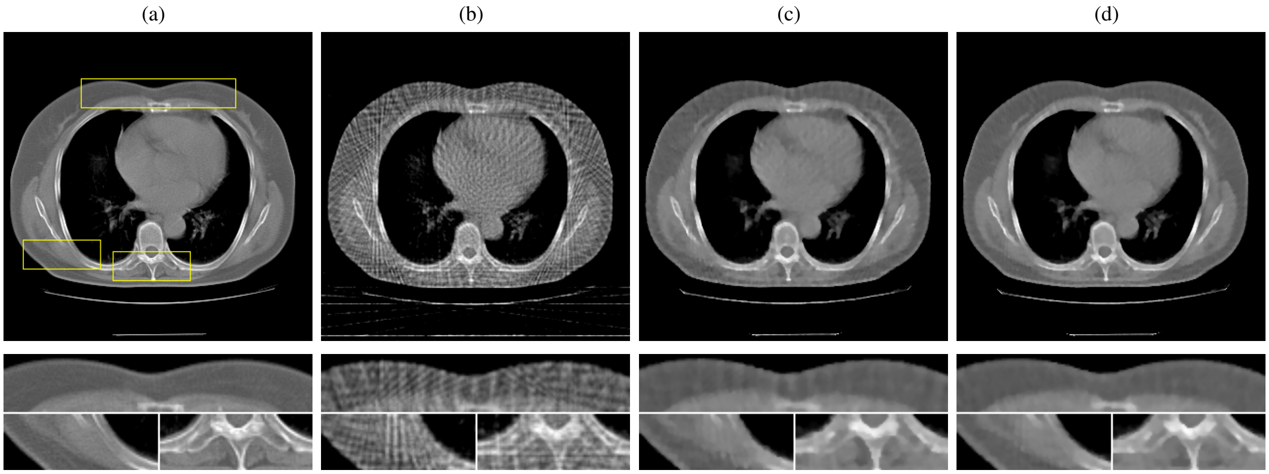

Fig. 4. Central slice of patient number 15 of the chest CT data set. Original slice image in (a) and reconstructions from 48 projection using (b) FBP, (c) iMAP and (d) proposed methods. A magnification display of marked regions in (a) are shown below each image. Display gray scale is (0.51, 1.55) cm^{-1}.

and proposed methods. The model assumes that the image is a mixture of six components intuitively represents air, patient bed, lungs, fatty-tissues, muscles and bones. The LMM mixture parameters represents the median value of the mixture components (μ_l) is used as the known intensity values for the iMAP algorithm. The same values with other mixture parameters are used in the proposed method. The iterative reconstruction was implemented using 500 iterations and the central reconstructed slices from different methods are shown in Fig. 4. The FBP image suffers from strong streak artifacts which is effectively reduced by using the iMAP and the proposed methods. However, it is observed that image quality is improved by using additional spatial information in the proposed method. As the probabilistic atlas used in this study is roughly computed, a more sophisticated registration is expected to contribute to image quality.

IV. CONCLUSION

This paper presents a new image reconstruction algorithm from small number of projection views. The main contribution is the use of prior information obtained from probabilistic atlas. The formulation of image reconstruction cost function is based on the fact that, in many CT imaging applications, the attenuation coefficients within the same region (organ) are almost uniform and can be *a priori* known within a specific range that slightly varies based on the imaging application. Reconstructed volumes are used to formulate a probabilistic atlas using Laplace mixture model. The model parameters that represent the prior information were estimated using the EM algorithm. The proposed method is evaluated using chest screening CT data set and results indicate that the use of probabilistic atlas prior is a promising approach to reconstruct a high quality image from limited views data. The spatial information provided from a probabilistic atlas contributes to image quality in this limited data problem. '

REFERENCES

[1] D. J. Brenner and E. J. Hall, "Computed Tomography - An increasing source of radiation exposure," *N. Engl. J. Med.*, vol. 357, pp. 2277-2284, 2007.

[2] F. Natterer, *The Mathematics of Computerized Tomography*. Philadelphia, PA: Wiley, 1986.

[3] G. T. Herman and R. Davidi, "Image reconstruction from a small number of projections," *Inverse Problems*, vol. 24, pp. 045011, 2008.

[4] D. L. Donoho, "Compressed sensing," *IEEE Trans. Inf. Theory*, vol. 52, pp. 1289-1306, 2006.

[5] E. J. Candès, J. Romberg, and T. Tao, "Robust uncertainty principles: exact signal reconstruction from highly incomplete frequency information," *IEEE Trans. Inf. Theory*, vol. 52, pp. 489-509, 2006.

[6] G.-H. Chen, J. Tang, and S. Leng, "Prior image constrained compressed sensing (PICCS): A method to accurately reconstruct dynamic CT images from highly undersampled projection data sets," *Med. Phys.*, vol. 35, pp. 660-663, 2008.

[7] E. Y. Sidky and X. Pan, "Image reconstruction in circular cone-beam computed tomography by constrained, total-variation minimization," *Phys. Med. Biol.*, vol. 53, pp. 4777-4807, 2008.

[8] H. Yu and G. Wang, "A soft-threshold filtering approach for reconstruction from a limited number of projections, *Phys. Med. Biol.*, vol. 55, pp. 3905-3916, 2010.

[9] E. A. Rashed and H. Kudo, "Iterative thresholding framework for row-action reconstruction from sparse projection data," in *Proc. 2011 IEEE Nuclear Science Symposium and Medical Imaging Conference*, Valencia, Spain, Paper no. MIC21-204, 2011.

[10] K. Sauer, J. Sachs Jr., and C. Klifa, "Bayesian estimation of 3-D objects from few radiographs," *IEEE Trans. Nucl. Sci.*, vol. 41, pp. 1780-1790, 1994.

[11] V. Kolehmainen, S. Siltanen, S. Järvenpää, J. P. Kaipio, P. Koistinen, M. Lassas, J. Pirttilä, and E. Somersalo, "Statistical inversion for medical x-ray tomography with few radiographs: II. Application to dental radiology," *Phys. Med. Biol.*, vol. 48, pp. 1465-1490, 2003.

[12] E. Garduño, G. T. Herman, and R. Dividi, "Reconstruction from a few projections by ℓ_1-minimization of the Haar transform," *Inverse Problems*, vol. 27, pp. 055006, 2011.

[13] E. A. Rashed and H. Kudo, "Statistical image reconstruction from limited projection data with intensity priors," *Phys. Med. Biol.*, vol. 57, pp. 2039-2061, 2012.

[14] J. A. Fessler and A. O. Hero, "Penalized maximum-likelihood image reconstruction using spacealternating generalized EM algorithms," *IEEE Trans. Image Process.*, vol. 4, pp. 1417-1429, 1995.

[15] I. Daubechies, M. Defrise, and C. De Mol, "An Iterative thresholding algorithm for linear inverse problems with a sparsity constraint," *Comm. Pure Appl. Math.*, vol. 57, pp. 1413-1457, 2004.

[16] A. P. Dempster, N. M. Laird, and D. B. Rubin, "Maximum likelihood from incomplete data via the EM algorithm," *J. Royal Statistical Soc.*, vol. 39, pp. 1-38, 1977.

[17] G. J. McLachlan and D. Peel, *Finite Mixture Models*. New York: Wiley, 2000.

[18] A. Cord, C. Ambroise, and J.-P. Cocquerez, "Feature selection in robust clustering based on Laplace mixture," *Pattern Recong. Lett.*, vol. 27, pp. 627-635, 2006.

[19] Medical image database, The Japanese Society of Medical Imaging Technology (JAMIT) (http://www.jamit.jp/cad-committe/caddbinfo)

Coding Ants: Using Ant Colony Optimization to Accelerate CT Reconstruction

Eric Papenhausen, Ziyi Zheng and Klaus Mueller

Abstract –**There is no one size fits all solution when it comes to CT reconstruction. Many different CT reconstruction algorithms and implementations have been devised in an attempt to solve the problem of producing an image under a specific set of constraints. One optimal CT reconstruction implementation can look very different from another optimal implementation; depending on the data, quality, and time constraints. In this paper, we present a framework that is able to dynamically create and compile new implementations that optimize the multiple objectives contained in CT reconstruction. We then show the results of this framework when applied to a GPU accelerated version of the FDK back-projection algorithm.**

***Index Terms*—CT reconstruction, GPU, ant colony optimization, Filtered backprojection**

I. INTRODUCTION

Any CT reconstruction algorithm can be identified as a multi-objective optimization problem. The optimal result will provide the highest quality reconstruction in the shortest time. Many algorithms have been developed and extended, and good parameter settings have been identified to solve this problem under specific conditions [1][4][7]. However, if the boundary conditions change (i.e. noisier projections, different numbers of projections, stricter time constraint, anatomy and pathology, etc.), the existing implementation is rendered sub-optimal, and in some cases, useless.

In this paper, we use swarm optimization to determine an optimal CT reconstruction implementation for any given set of parameters. More specifically, we use the ant colony optimization algorithm to find an optimal implementation of a GPU accelerated FDK back-projection, described in [5].

In this paper, we begin in Section II by discussing related work. Section III gives a brief description of the ant colony system optimization algorithm. Section IV presents the details of the coding ants framework. Section V gives a brief description of the graphics hardware used in our experiments and the structure of a CUDA program. Section VI presents the results of our experiments. Section VII presents future work and Section VIII concludes the paper.

II. RELATED WORK

Recent work has focused on finding good algorithmic parameters for iterative CT reconstruction [9]. Parameter tuning is critical in finding a good balance between image quality and reconstruction speed. The use of GPUs in accelerating CT reconstruction has also become very popular in decreasing reconstruction time [5][8][10]. However, not all GPUs are created equally; and there are many parameters to consider when creating a GPU accelerated program.

Whereas [9] focused on tuning algorithmic parameters, we focus on tuning system level parameters. Our optimizations come from creating a framework that will find an optimal implementation by directly manipulating source code. The optimal implementation may change across different machines and this framework will be able to produce a machine dependent optimal implementation without direct programmer intervention.

III. ANT COLONY SYSTEM

The ant colony system optimization algorithm is a part of the family of swarm optimization algorithms. It is a modification of the ant system algorithm which was designed to mimic the way ants find the shortest path from the ant nest to a food source. Initially ants will choose paths randomly. Once an ant finds food, it will travel back to the nest and emit pheromones so other ants can follow that path to the food source. As other ants follow the pheromone trail, they emit pheromones as well which reinforces the trail. After some time, however, the pheromone trail will evaporate. Given multiple paths to a food source, the pheromones on the shortest path will have the least amount of time to evaporate before being reinforced by another ant. Over time, the ants will converge to the shortest path.

The ant colony system was presented in [2] and was applied to the traveling salesman problem. It modifies the ant system algorithm [3] in several ways to lead to a faster convergence rate. After an ant crosses an edge, the pheromone value of that edge is decayed according to equation 1:

Eric Papenhausen, Ziyi Zheng and Klaus Mueller are with the Computer Science Department, Stony Brook University, Stony Brook, NY 11777 USA(e-mail: {epapenhausen, zizhen, mueller}@cs.sunysb.edu).

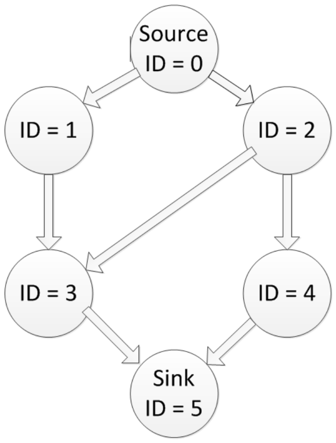

(a)

```
/*#{id=1, path=0}*/
        If(A==B)
/*#{end 1}*/
/*#{id=2, path=0}*/
        If(A!=B)
/*#{end 2}*/
/*#{id=3, path=1:2}*/
        A+=B;
/*#{end 3}
/*#{id=4, path=2}*/
        A*=B;
/*#{end 4}
/*#{id=5, path=3:4, sink)*/
        return A;
/*#{end 5}*/
```

(b)

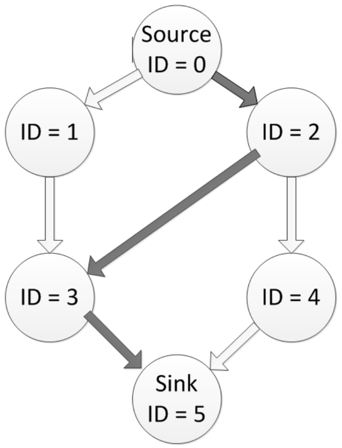

(c)

```
    If(A!=B)
        A+=B;

    return A;
```

(d)

Figure 1. An illustration of the framework presented in this paper. (a) a graph representing all possible implementations of a program. (b) the super source file represented by the graph in (a). (c) a path is selected through the graph. (d) source code corresponding to the path selected in (c).

$$\tau_{ij} = (1-\varphi)\cdot\tau_{ij} + \varphi\cdot\tau_0 \qquad (1)$$

where τ_{ij} denotes the pheromone quantity on the edge from state *i* to state *j*. The pheromone decay coefficient, φ, determines how much pheromone is decayed after an ant choses the edge from *i* to *j*. The initial pheromone value, $\tau_{0,}$ is the value every edge has at the beginning of the program. Equation 1 reduces the probability of multiple ants choosing the same path.

After all ants have chosen a path, the pheromone of each edge is updated as follows:

$$\tau_{ij} = (1-\rho)\cdot\tau_{ij} + \rho\cdot\Delta\tau_{ij}^{best} \qquad (2)$$

The variable τ_{ij} has the same meaning as equation 1. The variable $\Delta\tau_{ij}^{best}$ evaluates to the inverse of the length of the best path if the edge from *i* to *j* was taken by the ant with the best path; otherwise it evaluates to zero. The variable ρ represents the evaporation rate. This leads to a pheromone increase on the edges taken by the ant that produced the best solution; while decaying the pheromones on all other edges. When transitioning from one state to another, the edge is selected probabilistically according to the following probability:

$$p_{ij}^{k} = \frac{\left(\tau_{ij}^{\alpha}\right)\left(\eta_{ij}^{\beta}\right)}{\Sigma\left(\tau_{ij}^{\alpha}\right)\left(\eta_{ij}^{\beta}\right)} \qquad (3)$$

where τ_{ij} determines the amount of pheromone on the edge from *i* to *j*, and η_{ij} defines some predetermined desirability of that edge (e.g. the inverse of the edge weight). The variables α and β are weighting factors for τ_{ij} and η_{ij} respectively. The variable p_{ij}^{k} is the probability that an ant will select an edge that goes from state *i* to state *j* during the *k*th iteration.

IV. IMPLEMENTATION

We use the ant colony system described in the previous section to find and create an optimal implementation for a specific set of constraints. In order to do so we define the structure of a program as a directed graph with a single source, at which every ant will start, and a single sink, where every ant will finish. The nodes of the graph correspond to source code snippets. A path from source to sink corresponds to a candidate implementation that can be compiled and executed. The output of the candidate implementation can then be measured and ranked among the other candidate implementations to find the ant with the shortest path for that iteration. The shortest path can be defined as a function of image quality and reconstruction time.

The graph is constructed by creating a super source file. This super source file contains annotated sections of code. These annotations specify node id and incoming edges. Figure 1(a) and 1(b) show the graph and its corresponding super source file. Figure 1(c) and 1(d) show a potential path through the graph, and the corresponding candidate implementation. This super source file is then submitted as input to our program, which converts it to its graph representation and runs the ant colony system algorithm to produce an optimal implementation.

One aspect of our program differs from the traditional ant colony system algorithm. There is no predetermined desirability, η. There is no way of determining edge weight before running the algorithm. We can still apply the ant colony system algorithm by only considering the pheromone value, τ, when looking at an edge. This is equivalent to setting η to one, for all edges. Equation 4 shows how edges are selected by ants. Our experiments indicate that this still converges to an optimal solution.

$$p_{ij}^{k} = \frac{\left(\tau_{ij}^{\alpha}\right)}{\Sigma\left(\tau_{ij}^{\alpha}\right)} \qquad (4)$$

Since graphics hardware plays such a prominent role in CT reconstruction, our framework provides the option of expanding the graph provided in the super source file to account for different grid and thread block sizes. This is done by copying the code snippets that contain the threads unique ID and offsetting the ID by the grid dimension. This allows the framework to implicitly increase the workload for each thread. Figure 2 shows an example of this. The grid and thread block dimensions determine the granularity of each thread. The smaller the grid and block size, the more work each thread will perform.

```
int tid = blockIdx.x * blockDim.x + threadIdx.x;
                              .
                           <code>
                              .
F_L[tid] = result;
```

(a)

```
int tid = blockIdx.x * blockDim.x + threadIdx.x;
                              .
                           <code>
                              .
F_L[tid] = result;
                              .
                           <code>
                              .
F_L[(blockIdx.x + 8) * blockDim.x + threadIdx.x] = result;
```

(b)

Figure 2. Sample code demonstrating how thread granularity can be increased implicitly. (a) Source code representing a thread granularity of one (e.g. grid = 16, thread block = 16). (b) Source code representing a thread granularity of two (e.g. grid = 8, thread block = 16).

In this specific example a thread in Figure 2b computes two final results and stores them into the respective target locations in memory.

V. GRAPHICS HARDWARE

Modern GPUs follow a “Single Instruction Multiple Thread” (SIMT) model of parallel execution. In this model of execution, every thread executes the same instruction, but over different data. The implementation we attempt to optimize in our experiments use a C-like API called CUDA (Compute Unified Device Architecture) to program NVIDIA GPUs.

The GPU used in our experiments was the NVIDIA GeForce GTX 480. This graphics card contains 15 streaming multiprocessors. Each streaming multiprocessor contains 32 cores. Theoretical computing power of this graphics card is 1.3 TFLOPS. Like all NVIDIA graphics cards, this card has both on-chip and off-chip memory. Off-chip memory includes global, texture, and constant memory and typically incurs a latency of 400 to 600 clock cycles. On-chip memory includes shared memory as well as cache for texture and constant memory and is much faster than off-chip memory. The GTX 480 has a peak memory bandwidth of 177.4 GB/s for its 1.5 GB DDR5 device memory.

When accessing global memory, it is critical to performance that the access is coalesced. A coalesced memory access will allow multiple memory addresses to be returned with a single memory access; increasing memory bandwidth. A coalesced memory access typically requires every thread in a warp to access consecutive memory addresses. This constraint is relaxed, however, in devices with compute capability of 1.2 and higher. As long as the memory access of each thread is within a 32, 64, or 128 byte segment, depending on the data type, a coalesced memory access is performed.

GPU accelerated applications have a large number of parameters that can be tuned for optimal performance. Occupancy, thread granularity, and memory bandwidth are all examples of the types of parameters that can have a large impact on performance. Tuning one parameter too much can often lead to a sudden decrease in performance in some other aspect of the application. This is what is known as a performance cliff.

VI. EXPERIMENT AND RESULTS

We used the framework presented in this paper to create an optimal GPU accelerated implementation of the FDK back-projection algorithm described in [4]. This back-projection implementation is then tested with the help of the RabbitCT framework [6]. We chose to compose the graph out of the three major implementations presented in [5]. An ant’s path from the source to the sink represents either the first, second, or third configuration presented in [5], or some combination of the three. In this graph we also added a fourth configuration in which two projections are loaded per kernel call.

We ran our framework with 30 ants for 5 iterations. Our super source file described a graph that contained 25 nodes. This graph, however, is replicated for 16 different grid and thread block dimensions; creating a graph that contains 400 nodes. Table 1 shows a comparison of the timings of the FDK implementations that were produced through our framework with the results presented in [5] which were obtained by manually optimizing the code. For the 256^3 implementation we found a faster implementation. This configuration loads two projections per kernel invocation and has a thread granularity of two in the x direction. For the 512^3 implementation, our framework produced the same code as in [5]. Figure 3 shows a slice of the reconstructed volume. The quality of the reconstruction for the implementations produced by this framework was the same as the quality produced in [5].

TABLE I
RUNTIMES OF BEST KNOWN AND FRAMEWORK PRODUCED IMPLEMENTATIONS

Configuration	Volume	Time (s)
Framework	256^3	2.54
Best Known	256^3	2.71
Framework	512^3	6.07
Best Known	512^3	6.07

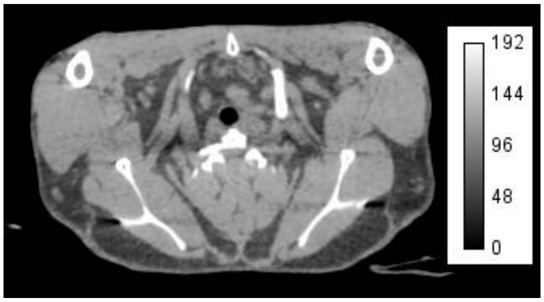

Figure 3. Slice of the reconstructed image.

The run time of our framework is dependent on the scale of the application it is trying to produce. For each ant, source code is generated, compiled, and executed. For the experiments that we ran, it took approximately 2 hours for all 30 ants to complete 5 iterations. The graph could have been pruned, however, by eliminating nodes that correlate to configurations that we know have bad performance. In our experiments, we included the naïve configuration explained in [5], as a possible implementation. By pruning the graph of bad implementations, we could reduce the number of ants; thus greatly reducing the amount of time required by our framework.

We wish to add that the code produced by the ant colony optimization can be re-used for any new CT reconstruction task with the same boundary conditions the code was generated for. Therefore the optimization overhead is well amortized.

VII. FUTURE WORK

One direction of future work for this framework is to develop a visual interface that is much more user friendly. At its current state, this framework requires the input to be an annotated source file. As the size of this source file grows, it can become difficult to keep track of the graph structure. In the future, we would like to develop a visual interface that clearly shows the graph. Nodes can be easily added or removed from this graph. Source code can be easily added or modified inside a node; and the information that is currently stored in the annotations can be abstracted away.

Another direction of future work, involves using this framework to build an all-encompassing CT reconstruction builder. This would incorporate different CT reconstruction algorithms and implementations. Given a set of parameters, this CT reconstruction builder would produce an optimal implementation.

VIII. CONCLUSION

In this paper we presented a novel framework for producing an optimal code structure using an ant colony optimization algorithm. Through our experiments in applying our framework to the RabbitCT platform, we have discovered a better implementation for the 256^3 volume reconstruction, while producing the same results as [5] for the 512^3 implementation.

Although we apply this framework to GPU accelerated CT reconstruction, it is in no way restricted to that field of study. The graph structure that the framework works off of ensures that this framework can be applied to produce an optimal implementation of any type of application.

REFERENCES

[1] A. Andersen and A. Kak, “Simultaneous algebraic reconstruction technique (SART): A superior implementation of the ART algorithm,” Ultrason. Imaging, 6:81–94, 1984

[2] M. Dorigo and L. M. Gambardella. “Ant Colony System: A cooperative learning approach to the traveling salesman problem.” IEEE Transactions on Evolutionary Computation, 1(1):53–66,

[3] M. Dorigo, V. Maniezzo, and A. Colorni. “Ant System: Optimization by a colony of cooperating agents.” IEEE Transactions on Systems, Man, and Cybernetics – Part B, 26(1):29–41, 1996.

[4] L. Feldkamp, L. Davis, and J. Kress, “Practical cone-beam algorithm,” J. Opt. Soc. Am. Vol 1, No. A6, 612–619 , 1984

[5] E. Papenhausen, Z. Zheng, and K. Mueller, "GPU-Accelerated Back-Projecting Revisited: Squeezing Performance by Careful Tuning," Fully Three-Dimensional Image Reconstruction in Radiology and Nuclear Medicine (Potsdam, Germany, 2011)

[6] C. Rohkohl, B. Keck, H. G. Hofmann and J. Hornegger, “RabbitCT---an open platform for benchmarking 3D cone-beam reconstruction algorithms,” Medical Physics, 36:3940, 2009.

[7] L. Shepp and Y. Vardi, “Maximum likelihood reconstruction for emission tomography,” IEEE Trans. Med. Imag., 1(2):113–122, 1982.

[8] H. Scherl, B. Keck, M. Kowarschik, J. Hornegger, “Fast GPU-based CT reconstruction using the Common Unified Device Architecture (CUDA),” IEEE Medical Imaging Conference, 6: 4464-4466, Honolulu, HI, 2007.

[9] W. Xu, K.Mueller "Learning Effective Parameter Settings for Iterative CT Reconstruction Algorithms," Fully 3D Image Reconstruction in Radiology and Nuclear Medicine (Beijing, China, 2009)

[10] Z. Zheng, K. Mueller “Cache-Aware GPU Memory Scheduling Scheme for CT Back-Projection,” *IEEE Medical Imaging Conference*, Oct. 2010.

An inversion formula for the cone-beam transform for arbitrary source trajectories

Birsen Yazıcı, *Senior Member IEEE*, Zhengmin Li and Jed Pack

***Abstract*—We introduce a forward model for the cone-beam X-ray Computed Tomography projection data measured in native geometries as a Fourier Integral Operator and present a corresponding filtered-backprojection type inversion formula. Our model and inversion formula can accommodate arbitrary source trajectories, arbitrary detector plane orientation, detector surface geometries, and other system related parameters. When the model parameters are chosen such that the forward model is equivalent to the cone-beam transform with helical or circular source trajectory, the inversion formula leads to the well-known Feldkamp's method with the one-dimensional filtering in the tangential direction. In the final version of the manuscript we will present validation of the inversion formula using the cone-beam projection data generated using GE's software package CatSim.**

I. INTRODUCTION

In practice, most of the existing cone-beam reconstruction methods are designed for the circular and helical source trajectories. They utilize a standard data acquisition geometry, in which the detector plane is perpendicular to the central ray, and parallel to the axial-axis. However, reconstruction methods for more general source trajectories and detector plane orientations are desirable in various applications [1] [2] [3]. In this paper, we introduce a new analytic forward model for the cone-beam projection data obtained in its native geometries in the form of a Fourier Integral Operator (FIO). The model reduces to the standard cone-beam transform when the amplitude term of the FIO is set to a certain function. We, next, introduce a filtered-backprojection (FBP) type inversion method for the new forward model. The model and the associated inversion method can accommodate arbitrary source trajectories, detector surface geometry and orientation, and other system related parameters, such as the physical detector size and the focal spot size. When the source trajectory is restricted to a helix and when the detector surface is planar with the cone axis perpendicular to the detector plane, our inversion formula reduces to the Feldkamp's (FDK) formula for the helical trajectory with one-dimensional tangential filtering.

Our approach has several advantages as compared to the idealized X-ray transform and associated inversion methods: 1) The new forward model can provide a more realistic representation of the cone-beam CT projection data than the idealized X-ray transform. As a result, our inversion method can provide a better reconstruction method than that of approximate or exact X-ray transform inversion methods. 2) Our model and inversion method can accommodate arbitrary imaging geometries including source trajectory, detector surface geometries and orientations. 3) Our model and inversion formula are both analytic and can be implemented computationally efficiently with the computational complexity of fast-backprojection algorithms [4]. 4) The measurement noise and a priori object statistics can be incorporated into our model and reconstruction formula [5]. 5) The point spread function of our reconstruction formula can be studied by microlocal analysis.

The paper is organized as follows: In Section II, we introduce the cone-beam transform for arbitrary source trajectories and briefly describe the general FIO-based model for cone-beam projection data. In Section III, we present our FBP-type inversion formula. In Section IV, we show the equivalence of our inversion formula with the FDK's method for the circular source trajectory and comment on the relationship of our method to other methods. Section IV concludes our discussion. In the final version of the manuscript, we will present simulation results using the X-ray CT simulation package CatSim developed by GE.

II. CONE-BEAM TRANSFORM AS A FOURIER INTEGRAL OPERATOR IN ITS NATIVE GEOMETRY

We consider the imaging geometry shown in Fig.1. We assume a coordinate system where the x_-axis is perpendicular to the axial plane spanned by the unit vectors along x_1- and x_2-axes shown in Fig.1. We assume that the detector plane is perpendicular to the axial plane. Furthermore, we assume that the horizontal axis of the detector plane remains parallel to the tangent vector of the source trajectory; and the cone axis

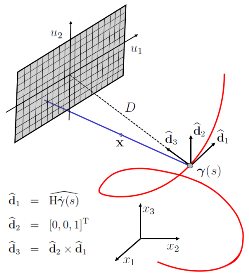
u_2
u_1
D
$\mathbf{x}$
$\widehat{\mathbf{d}}_3$
$\widehat{\mathbf{d}}_2$
$\widehat{\mathbf{d}}_1$
$\gamma(s)$
$\widehat{\mathbf{d}}_1 = \widehat{\mathrm{H}\dot{\gamma}(s)}$
$\widehat{\mathbf{d}}_2 = [0,0,1]^{\mathrm{T}}$
$\widehat{\mathbf{d}}_3 = \widehat{\mathbf{d}}_2 \times \widehat{\mathbf{d}}_1$
x_3
x_2
x_1

Fig. 1: Local coordinate system for the cone-beam projection measurements for a planar detector geometry. Vectors $\widehat{\mathbf{d}}_1$ and $\widehat{\mathbf{d}}_2$ are parallel to the u_1 and u_2 axis of the detector plane, and the vector $\widehat{\mathbf{d}}_3$ is orthogonal to the detector plane. $\widehat{\mathbf{d}}_3$ is the unit vector pointing from the source location $\gamma(s)$ to the point whose location is $(0,0)$ on the detector plane.

is perpendicular to the detector plane. These assumptions are all consistent with the practical X-ray CT systems.

Let $\boldsymbol{\gamma}(s) \in \mathbb{R}^3$, $s \in [s_0,\ s_1]$, be a smooth trajectory for the X-ray source, and S^2 be the unit sphere in $\mathbb{R}^3$. Let $\hat{\mathbf{r}} \in S^2$ be the unit vector originating from the source position $\boldsymbol{\gamma}(s)$. We define the local coordinate system shown in Fig.1 as follows:

$$\begin{aligned} \widehat{\mathbf{d}}_1 &= \widehat{\mathrm{H}\dot{\boldsymbol{\gamma}}(s)} \\ \widehat{\mathbf{d}}_2 &= [0,0,1]^{\mathrm{T}} \\ \widehat{\mathbf{d}}_3 &= \widehat{\mathbf{d}}_2 \times \widehat{\mathbf{d}}_1 \end{aligned} \tag{1}$$

where $\mathrm{H} = \begin{bmatrix} 1 & 0 & 0 \\ 0 & 1 & 0 \\ 0 & 0 & 0 \end{bmatrix}$.

We assume that the detector array consists of $N_r \times N_c$ detector units. We use the pair $[u_1, u_2]$ to indicate the detector position, which are signed distances along $\widehat{\mathbf{d}}_1$ and $\widehat{\mathbf{d}}_2$. We assume that the axis of the cone when the source is at $\boldsymbol{\gamma}(s)$ intersects the detector plane at the $[u_1, u_2] = (0,0)$ of the detector plane. Let D be the distance between the source and the detector plane. Given the source location and the distance D, $[u_1, u_2]$ can be determined by the rotation angle s.

The line equation of the X-ray, which goes through $\mathbf{x}$ and projects onto $[u_1, u_2]$ in the detector plane, can be defined as the intersection of the following two planes:

$$u_1 = D\frac{(\mathbf{x}-\boldsymbol{\gamma}(s))\cdot\widehat{\mathbf{d}}_1}{(\mathbf{x}-\boldsymbol{\gamma}(s))\cdot\widehat{\mathbf{d}}_3} \tag{2}$$

$$u_2 = D\frac{(\mathbf{x}-\boldsymbol{\gamma}(s))\cdot\widehat{\mathbf{d}}_2}{(\mathbf{x}-\boldsymbol{\gamma}(s))\cdot\widehat{\mathbf{d}}_3}. \tag{3}$$

Thus, we write the cone-beam transform as follows:

$$\begin{aligned} d(u_1,u_2,s) &= \int \delta\Big(u_1 - D\frac{(\mathbf{x}-\boldsymbol{\gamma}(s))\cdot\widehat{\mathbf{d}}_1}{(\mathbf{x}-\boldsymbol{\gamma}(s))\cdot\widehat{\mathbf{d}}_3}\Big) \\ &\quad \delta\Big(u_2 - D\frac{(\mathbf{x}-\boldsymbol{\gamma}(s))\cdot\widehat{\mathbf{d}}_2}{(\mathbf{x}-\boldsymbol{\gamma}(s))\cdot\widehat{\mathbf{d}}_3}\Big) \\ &\quad \times \frac{D^2|\mathbf{x}-\boldsymbol{\gamma}(s)|}{((\mathbf{x}-\boldsymbol{\gamma}(s))\cdot\widehat{\mathbf{d}}_1)^3} f(\mathbf{x})\mathrm{d}\mathbf{x}. \end{aligned} \tag{4}$$

To simplify our notation we define

$$\begin{aligned} \rho_1(\mathbf{x},s) &:= D\frac{(\mathbf{x}-\boldsymbol{\gamma}(s))\cdot\widehat{\mathbf{d}}_1}{(\mathbf{x}-\boldsymbol{\gamma}(s))\cdot\widehat{\mathbf{d}}_3} \\ \rho_2(\mathbf{x},s) &:= D\frac{(\mathbf{x}-\boldsymbol{\gamma}(s))\cdot\widehat{\mathbf{d}}_2}{(\mathbf{x}-\boldsymbol{\gamma}(s))\cdot\widehat{\mathbf{d}}_3} \\ \boldsymbol{\rho}(\mathbf{x},s) &:= [\rho_1(\mathbf{x},s),\ \rho_2(\mathbf{x},s)] \end{aligned}$$

and

$$\begin{aligned} \boldsymbol{u} &:= [u_1,\ u_2] \\ A(\mathbf{x},s) &:= \frac{D^2|\mathbf{x}-\boldsymbol{\gamma}(s)|}{((\mathbf{x}-\boldsymbol{\gamma}(s))\cdot\widehat{\mathbf{d}}_1)^3}. \end{aligned}$$

We rewrite Eq. (4) as follows:

$$d(\boldsymbol{u},s) = \int \delta(\boldsymbol{u}-\boldsymbol{\rho}(\mathbf{x},s))A(\mathbf{x},s)f(\mathbf{x})\mathrm{d}\mathbf{x}. \tag{5}$$

Alternatively, we can express (5) as:

$$\begin{aligned} d(\boldsymbol{u},s) &= \mathcal{F}[f](\mathbf{u},s) \\ &:= \frac{1}{4\pi^2}\int \mathrm{e}^{\mathrm{i}\boldsymbol{\omega}\cdot(\boldsymbol{u}-\boldsymbol{\rho}(\mathbf{x},s))}A(\mathbf{x},s)f(\mathbf{x})\mathrm{d}\boldsymbol{\omega}\mathrm{d}\mathbf{x}. \end{aligned} \tag{6}$$

Eq. (6) shows that the cone-beam transform $\mathcal{F}$ is an FIO [6] with its phase term equal to

$$\phi(\boldsymbol{\omega},\mathbf{x},\boldsymbol{u},s) = \boldsymbol{\omega}\cdot(\boldsymbol{u}-\boldsymbol{\rho}(\mathbf{x},s)) \tag{7}$$

and its amplitude term equal to

$$A(\mathbf{x},s) = \frac{D^2|\mathbf{x}-\boldsymbol{\gamma}(s)|}{((\mathbf{x}-\boldsymbol{\gamma}(s))\cdot\widehat{\mathbf{d}}_1)^3}.$$

Since the critical points of the model in (7) are given by the line passing through the source and the point $[u_1, u_2]$ on the detector plane, we define the general forward model for the cone-beam projection data by the following model:

$$\begin{aligned} d(\boldsymbol{u},s) &= \mathcal{F}[f](\mathbf{u},s) \\ &= \frac{1}{4\pi^2}\int \mathrm{e}^{\mathrm{i}\boldsymbol{\omega}\cdot(\boldsymbol{u}-\boldsymbol{\rho}(\mathbf{x},s))}A(\boldsymbol{\omega},\mathbf{x},\boldsymbol{u},s)f(\mathbf{x})\mathrm{d}\boldsymbol{\omega}\mathrm{d}\mathbf{x} \end{aligned} \tag{8}$$

where the amplitude factor A is a slowly decaying function that depends on the underlying system parameters and geometric correction factors. Note that the amplitude factor in (8) depends not only on $\mathbf{x}$ and s, but also on $\boldsymbol{\omega}$ and $\boldsymbol{u}$.

III. A FBP-TYPE INVERSION OF THE CONE-BEAM TRANSFORM

We form an image by means of a filtered-backprojection operator as follows:

$$\begin{aligned} I(\mathbf{z}) &= \mathcal{K}[d](\mathbf{z}) \\ &= \int \mathrm{e}^{-\mathrm{i}\phi(\boldsymbol{\omega},\mathbf{z},\boldsymbol{u},s)}Q(\boldsymbol{\omega},\mathbf{z},s)d(\boldsymbol{u},s)\mathrm{d}\boldsymbol{\omega}\mathrm{d}\boldsymbol{u}\mathrm{d}s \end{aligned} \tag{9}$$

where $I(\mathbf{z})$ is the reconstructed image, $\mathcal{K}$ is the filtered-backprojection operator, and Q is the filter to be determined below.

Substituting (6) into (9), we obtain

$$I(\mathbf{z}) = \mathcal{K}\mathcal{F}[f](\mathbf{z}) = \int L(\mathbf{z},\mathbf{x})f(\mathbf{x})\mathrm{d}\mathbf{x} \tag{10}$$

where

$$\begin{aligned} L(\mathbf{z},\mathbf{x}) &= \int \mathrm{e}^{\mathrm{i}\left(\phi(\boldsymbol{\omega},\mathbf{x},\boldsymbol{u},s)-\phi(\boldsymbol{\omega}',\mathbf{z},\boldsymbol{u},s)\right)}A(\mathbf{x},s) \\ &\quad Q(\boldsymbol{\omega}',\mathbf{z},s)\mathrm{d}\boldsymbol{\omega}\mathrm{d}\boldsymbol{\omega}'\mathrm{d}\boldsymbol{u}\mathrm{d}s. \end{aligned} \tag{11}$$

Applying the method of stationary phase and evaluating the $\mathrm{d}\boldsymbol{u}$ integration above, we obtain

$$L(\mathbf{z},\mathbf{x}) = \int \mathrm{e}^{\mathrm{i}\boldsymbol{\omega}\cdot(\boldsymbol{\rho}(\mathbf{x},s)-\boldsymbol{\rho}(\mathbf{z},s))}A(\mathbf{x},s)Q(\boldsymbol{\omega},\mathbf{z},s)\mathrm{d}\boldsymbol{\omega}\mathrm{d}s. \tag{12}$$

The kernel L of $\mathcal{K}\mathcal{F}$ is the point spread function (PSF) of the imaging operator $\mathcal{K}$. $L(\mathbf{z},\mathbf{x})$ represents the reconstructed image at pixel $\mathbf{z}$ due to a point object located at $\mathbf{x}$.

Let

$$\varphi(\mathbf{z},\mathbf{x},\boldsymbol{\omega},s) = \boldsymbol{\omega}\cdot(\boldsymbol{\rho}(\mathbf{x},s)-\boldsymbol{\rho}(\mathbf{z},s)). \tag{13}$$

The main contributions to $L(\mathbf{z},\mathbf{x})$ come from the critical points of the phase of $\mathcal{KF}$, satisfying the following conditions:

$$\frac{\partial\varphi}{\partial\boldsymbol{\omega}} = 0 \quad\Rightarrow\quad \boldsymbol{\rho}(\mathbf{x},s)=\boldsymbol{\rho}(\mathbf{z},s) \tag{14}$$

$$\frac{\partial\varphi}{\partial s} = 0 \quad\Rightarrow\quad \partial_s\boldsymbol{\rho}(\mathbf{x},s)=\partial_s\boldsymbol{\rho}(\mathbf{z},s). \tag{15}$$

Thus, we recover the singularities of the object at the intersection of the locus points of the two three-dimensional manifolds defined above.

Assuming that the only contribution to the pixel at $\mathbf{z}$ comes from $\mathbf{x}$, we approximate φ as follows:

$$\begin{aligned}\varphi(\mathbf{z},\mathbf{x},\boldsymbol{\omega},s) &\approx (\mathbf{z}-\mathbf{x})\cdot\nabla\varphi(\mathbf{z},\mathbf{x},\boldsymbol{\omega},s)\\ &= (\mathbf{z}-\mathbf{x})\cdot\nabla\boldsymbol{\omega}\cdot\boldsymbol{\rho}(\mathbf{z},s)|_{\mathbf{z}=\mathbf{x}}.\end{aligned} \tag{16}$$

Let

$$\boldsymbol{\xi} = \nabla\boldsymbol{\omega}\cdot\boldsymbol{\rho}(\mathbf{z},s)|_{\mathbf{z}=\mathbf{x}}. \tag{17}$$

We now make the following change of variables:

$$(\boldsymbol{\omega},s)\rightarrow\boldsymbol{\xi}$$

and obtain

$$\begin{aligned}I(\mathbf{z}) \approx & \int_{\Omega_{\mathbf{z}}} \mathrm{e}^{\mathrm{i}(\mathbf{z}-\mathbf{x})\cdot\boldsymbol{\xi}}\,|\frac{\partial(\boldsymbol{\omega},s)}{\partial\boldsymbol{\xi}}|\,A(\mathbf{z},s(\boldsymbol{\xi}))\\ & Q(\boldsymbol{\omega}(\boldsymbol{\xi}),\mathbf{z},s(\boldsymbol{\xi}))f(\mathbf{x})\mathrm{d}\boldsymbol{\xi}\mathrm{d}\mathbf{x}\end{aligned} \tag{18}$$

where $|\frac{\partial(\boldsymbol{\omega},s)}{\partial\boldsymbol{\xi}}|$ is the determinant of the Jacobian that comes from the change of variables in (17), and $s(\boldsymbol{\xi})$ and $\boldsymbol{\omega}(\boldsymbol{\xi})$ represent s and $\boldsymbol{\omega}$ in terms of $\boldsymbol{\xi}$; and $\Omega_{\mathbf{z}}$ is the data collection manifold defined as

$$\Omega_{\mathbf{z}} = \{\boldsymbol{\xi}=\nabla\boldsymbol{\omega}\cdot\boldsymbol{\rho}(\mathbf{x},s)|_{\mathbf{x}=\mathbf{z}} \mid |\frac{\partial(\boldsymbol{\omega},s)}{\partial\boldsymbol{\xi}}|\neq 0 \;\&\; A(\boldsymbol{\omega},\mathbf{z})\neq 0\}. \tag{19}$$

We determine the filter Q so that the kernel L of the PSF is approximately a Dirac-delta function, i.e.,

$$L(\mathbf{x},\mathbf{z})\approx\delta(\mathbf{x}-\mathbf{z}).$$

We set

$$Q(\boldsymbol{\xi},\mathbf{z}) = \frac{\chi\Omega}{A(s(\boldsymbol{\xi}),\mathbf{z})}|\frac{\partial\boldsymbol{\xi}}{\partial(\boldsymbol{\omega},s)}|, \quad \boldsymbol{\xi}\in\Omega_{\mathbf{z}} \tag{20}$$

where $\chi_{\Omega_{\mathbf{z}}}$ is a smooth cut-off function that prevents division by zero.

With this choice of filtering, the inverse map $\mathcal{K}$ reconstructs the visible singularities of the object not only at the right location and orientation, but also at the right strength.

The $\boldsymbol{\xi}$ vector is given as follows:

$$\begin{aligned}\boldsymbol{\xi} &= \nabla\boldsymbol{\omega}\cdot\boldsymbol{\rho}(\mathbf{x},s)|_{\mathbf{x}=\mathbf{z}}\\ &= \frac{D}{C_3^2(\mathbf{x},s)}\boldsymbol{\omega}\cdot\begin{bmatrix}\widehat{\mathbf{d}}_1C_3(\mathbf{x},s)-\widehat{\mathbf{d}}_3C_1(\mathbf{x},s)\\ \widehat{\mathbf{d}}_2C_3(\mathbf{x},s)-\widehat{\mathbf{d}}_3C_2(\mathbf{x},s)\end{bmatrix}\\ &= D\{\frac{\omega_1}{C_3(\mathbf{x},s)}\widehat{\mathbf{d}}_1+\frac{\omega_2}{C_3(\mathbf{x},s)}\widehat{\mathbf{d}}_2\\ &\quad -[\frac{\omega_1C_1(\mathbf{x},s)+\omega_2C_2(\mathbf{x},s)}{C_3^2(\mathbf{x},s)}]\widehat{\mathbf{d}}_3\}\end{aligned} \tag{21}$$

where $C_i(\mathbf{x},s) = (\mathbf{x}-\boldsymbol{\gamma}(s))\cdot\widehat{\mathbf{d}}_i,\ i=1,2,3$. Note that $C_3(\mathbf{x},s)=0$ corresponds to the case when the cone angle is 90 degrees, which is an unrealistic setting for all practical purposes. The vector $\boldsymbol{\xi}$ can be viewed as the Fourier component that contributes to the reconstruction of the pixel at $\mathbf{z}$ when the source is at $\boldsymbol{\gamma}(s)$. The vector $\boldsymbol{\xi}$ and the data collection manifold $\Omega_{\mathbf{z}}$ determine the resolution as well as many of the properties of the reconstructed image. Fig. 2 illustrates the $\boldsymbol{\xi}$ vector.

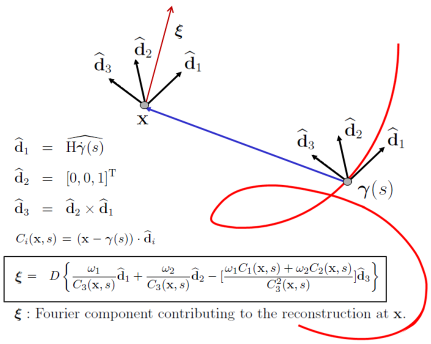
ξ
$\widehat{\mathrm{d}}_2$
$\widehat{\mathrm{d}}_3$
$\widehat{\mathrm{d}}_1$
x
$\widehat{\mathrm{d}}_3$
$\widehat{\mathrm{d}}_2$
$\widehat{\mathrm{d}}_1$
$\gamma(s)$
$\widehat{\mathrm{d}}_1 = \widehat{\mathrm{H}\dot{\gamma}(s)}$
$\widehat{\mathrm{d}}_2 = [0,0,1]^{\mathrm{T}}$
$\widehat{\mathrm{d}}_3 = \widehat{\mathrm{d}}_2\times\widehat{\mathrm{d}}_1$
$C_i(\mathrm{x},s) = (\mathrm{x}-\gamma(s))\cdot\widehat{\mathrm{d}}_i$
$\xi = D\left\{\frac{\omega_1}{C_3(\mathrm{x},s)}\widehat{\mathrm{d}}_1+\frac{\omega_2}{C_3(\mathrm{x},s)}\widehat{\mathrm{d}}_2-[\frac{\omega_1C_1(\mathrm{x},s)+\omega_2C_2(\mathrm{x},s)}{C_3^2(\mathrm{x},s)}]\widehat{\mathrm{d}}_3\right\}$
ξ : Fourier component contributing to the reconstruction at x.

Fig. 2: The vector $\boldsymbol{\xi}$ represents the Fourier component contributing to the reconstruction of the object at $\mathbf{x}$.

IV. INVERSION FORMULA FOR THE CIRCULAR SOURCE TRAJECTORY

In this section, we discuss the equivalence of our inversion method to the existing approximate methods [7] for the circular source trajectory.

For the circular trajectory, $\boldsymbol{\gamma}(s)$ is given as follows:

$$\boldsymbol{\gamma}(s) = [R\cos(s),\ R\sin(s),\ 0],\ \ s\in\mathbb{R}^3, \tag{22}$$

where R denotes the radius of the circle. Substituting Eq. (22) and its derivative into Eq. (1), we obtain

$$\begin{bmatrix}\widehat{\mathbf{d}}_1\\ \widehat{\mathbf{d}}_2\\ \widehat{\mathbf{d}}_3\end{bmatrix} = \begin{bmatrix}-\sin(s) & \cos(s) & 0\\ 0 & 0 & 1\\ -\cos(s) & -\sin(s) & 0\end{bmatrix}.$$

Thus, for the circular trajectory, the filter in Eq. (20) becomes

$$Q(\boldsymbol{\omega},\mathbf{z},s) = \frac{DR}{C_3(\mathbf{z},s)|\mathbf{z}-\boldsymbol{\gamma}(s)|}|\omega_1|. \tag{23}$$

Substituting Q into Eq. (9), we obtain the FBP-type inversion formula for the circular source trajectory given as

$$\begin{aligned}I(\mathbf{z}) = & \int \mathrm{e}^{\mathrm{i}(\omega_1D\frac{(\mathbf{z}-\boldsymbol{\gamma}(s))\cdot\hat{\mathbf{d}}_1}{(\mathbf{z}-\boldsymbol{\gamma}(s))\cdot\hat{\mathbf{d}}_3}+\omega_2D\frac{(\mathbf{z}-\boldsymbol{\gamma}(s))\cdot\hat{\mathbf{d}}_2}{(\mathbf{z}-\boldsymbol{\gamma}(s))\cdot\hat{\mathbf{d}}_3})}\\ & \frac{DR}{C_3^2(\mathbf{z},s)|\mathbf{z}-\boldsymbol{\gamma}(s)|}|\omega_1|\hat{d}_{12}(\omega_1,\omega_2,s)dsd\omega_1\end{aligned}$$

where

$$\hat{d}_{12}(\omega_1,\omega_2,s) = \int d(u_1,u_2,s)\mathrm{e}^{-\mathrm{i}(\omega_1u_1+\omega_2u_2)}du_1du_2 \tag{24}$$

is the Fourier transform of $d(u_1,u_2,s)$ with respect to u_1,u_2 variables.

We rewrite the original FDK's formula using the local coordinate system introduced above and obtain:

$$
\begin{aligned}
I(\mathbf{z}) &= \int \mathrm{e}^{\mathrm{i}(\omega_1 u_1+\omega_2 u_2)} \frac{RD^2}{\sqrt{D^2+u_1^2+u_2^2}[R+\mathbf{z}\cdot\widehat{\mathbf{d}}_3]^2} \\
&\quad \hat{d}_{12}(\omega_1,\omega_2,s)|\omega_1|\mathrm{d}\omega_1\mathrm{d}\omega_2\mathrm{d}s \qquad (25)
\end{aligned}
$$

where u_1 and u_2 indicate the projection location on the planar detector plane of the reconstructed point $\mathbf{z}$, which are given as

$$u_1(\mathbf{z}) = \frac{D\mathbf{z}\cdot\widehat{\mathbf{d}}_1}{R+\mathbf{z}\cdot\widehat{\mathbf{d}}_3}$$

$$u_2(\mathbf{z}) = \frac{D\mathbf{z}\cdot\widehat{\mathbf{d}}_2}{R+\mathbf{z}\cdot\widehat{\mathbf{d}}_3}.$$

We now compare the weighting factor and the one-dimensional filter of the FDK's formula to the filter in our inversion formula. From the CT scanner geometry, we have

$$\frac{C_3(\mathbf{x},s)}{D} = \frac{|\mathbf{x}-\boldsymbol{\gamma}(s)|}{\sqrt{D^2+u_1^2+u_2^2}} \qquad (26)$$

$$|\mathbf{x}-\boldsymbol{\gamma}(s)| = \frac{C_3(\mathbf{x},s)\sqrt{D^2+u_1^2+u_2^2}}{D} \qquad (27)$$

$$C_3(\mathbf{x},s) = R+\mathbf{z}\cdot\widehat{\mathbf{d}}_3. \qquad (28)$$

Inserting the above three relationships into our filter, we obtain the familiar weighting factor and the one-dimensional filter in the FDK's formula:

$$
\begin{aligned}
Q(\boldsymbol{\omega},\mathbf{z},s) &= \frac{D}{C_3(\mathbf{x},s)|\mathbf{x}-\boldsymbol{\gamma}(s)|}|R\omega_1| \\
&= \frac{D^2R}{[R+\mathbf{z}\cdot\widehat{\mathbf{d}}_3]^2\sqrt{D^2+u_1^2+u_2^2}}|\omega_1|. \qquad (29)
\end{aligned}
$$

V. SIMULATION STUDY OF THE INVERSION FORMULA

To validate our analytic derivation, we performed the reconstruction of the FORBILD-like thorax phantom using our formula. The simulation results will be included in the final manuscript.The number of views per rotation: 984; the number of detector columns: 888; the detector size: 1 mm×1 mm; the thickness of each slice in z- direction: 0.625 mm; the distance from source to detector: 949 mm; and the distance from the origin to the detector plane: 545 mm.

The reconstructed image size is 512×512, and the pixel size in each slice is 0.25 mm×0.25 mm.

The reconstructed image is are shown in Fig. 3. The visual comparison and the comparison of the cross section of the reconstructed images show that t our inversion formula produce the acceptable images.

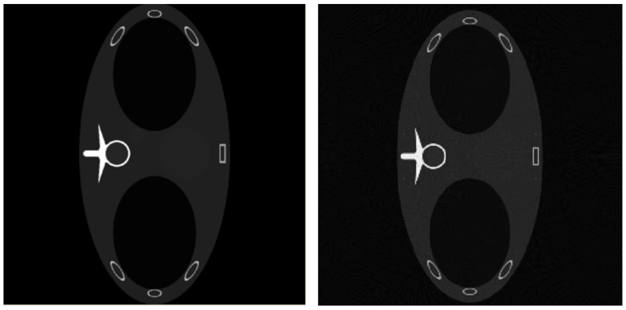

Fig. 3: Left: original center slice. Right :the reconstructed thorax phantom using our formula

VI. CONCLUSION

We present a new model for the cone-beam projection data in its native geometries and an FBP-type analytic reconstruction method for the model. Our model and inversion formula can accommodate arbitrary source trajectories, arbitrary detector orientation, detector surface geometry and other system related parameters. We showed the equivalency of our inversion formula to the FDK's formula for the circular trajectory both analytically and numerically.

In the final version of the manuscript we will present validation of the inversion formula using the cone-beam projection data generated using GE's software package CatSim.

REFERENCES

[1] P. M. Shikhaliev, *Tilted angle CZT detector for photon counting/energy weighting x-ray and CT imaging,* Phys. Med. Biol., Vol.51, pp. 4267-4287, 2006

[2] J. D. Pack, F. Noo and H. Kudo, *Investigation of saddle trajectories for cardiac CT imaging in cone-beam geometry*, Phys. Med. Biol., Vol. 49, No. 11, pp. 2317-2336, 2004

[3] Z. Yu, *et al*, *Line plus arc source trajectories and their R-line coverage for long-object cone-beam imaging with a C-arm system,* Phys. Med. Biol., Vol.56 , pp. 3447-3471, 2011

[4] E. Candes, *et al*, *Fast computation of Fourier integral operators,* Applied and computational mathematics, Caltech, Pasadena, CA, 2006

[5] B. Yazici, M. Cheney and C.E. Yarman, *Synthetic aperture inversion in the presence of noise and clutter,* Inverse Problems, Vol. 22, pp. 1705-1729, 2006.

[6] F. Treves, *Introduction to Pseudodifferential and Fourier Integral Operators,* Vol. 1 and 2 Plemum Press, New York, 1980

[7] L.A. Feldkamp, L.C. Davis and J.W. Kress, *Practical cone-beam algorithm*, J.Opt.Soc. Am., Vol.1, No. 6, pp. 612-619, 1984

[8] G. Wang, *et al*, *A general cone-beam recosntruction algorithm,* IEEE Trans. on Med. Imag., Vol. 12, No. 3, pp. 486-495, 1993

[9] X. Yan and R. M Leahy, *Cone beam tomography with circular, elliptical and spiral orbits,* Phys. Med. Biol., Vol. 37, No. 3, pp. 493-506, 1992

[10] X. Yan and R. M Leahy, *Derivation and Analysis of a Filtered Backprojection Algorithm for Cone Beam Projection Data,*IEEE Trans. on Med. Imag., Vol.10. No. 3, pp. 462-412, 1991

First Experimental Results on Long-object Imaging using a Reverse Helical Trajectory with a C-arm System

Zhicong Yu, Andreas Maier, Manfred Schönborn, Florian Vogt, Christoph Köhler,
Günter Lauritsch, Joachim Hornegger, and Frédéric Noo

***Abstract*—3D imaging with C-arm systems has become a crucial tool in the interventional room. In this work, we present a methodology and first experimental results for long-object imaging using a reverse helical trajectory with a modified Artis zeego system. First the raw data was preprocessed by the Siemens pipeline, and the scan positions were obtained through a calibration process. After trajectory registration and fitting, preprocessed data was rebinned, and image reconstructions were obtained through the Fusion-RFDK method. The reconstruction results are encouraging and effectively demonstrate that long-object imaging using a reverse helical trajectory is feasible in the interventional room.**

I. INTRODUCTION

3D imaging with C-arm systems has become a crucial tool in the interventional room. It has allowed significant improvements in clinical workflow, and it has also enabled new interventional procedures as well as refinements in existing procedures. In this work, we seek to further improve the capabilities of this 3D imaging tool by allowing smooth, long-object scanning using a reverse helix [1] for data acquisition. The reverse helix is well-suited for C-arm systems, particularly since such systems are open and do not include slip-ring technology.

This work presents a methodology and first experimental results for long-object imaging using a reverse helical trajectory with multi-turns using a modified Artis zeego system (Siemens AG, Healthcare Sector, Forchheim, Germany). The methodology involved the following five steps: i) a calibration method [2] to assess the exact geometrical position of the source and the detector during data acquisition, ii) the computation of a rigid transformation to register these positions into a conventional reverse helix geometry, iii) a geometrical fitting process to find an analytical reverse helix to match the registered trajectory, iv) a rebinning step to interpolate the measured data into the fitted geometry, and v) an application of the Fusion-RFDK [3] method for reconstruction from the rebinned data. Using this methodology, we were able to produce satisfactory reconstructions of two physical objects that extend over a 300 mm long volume. These reconstructions were obtained from real data collected over five turns.

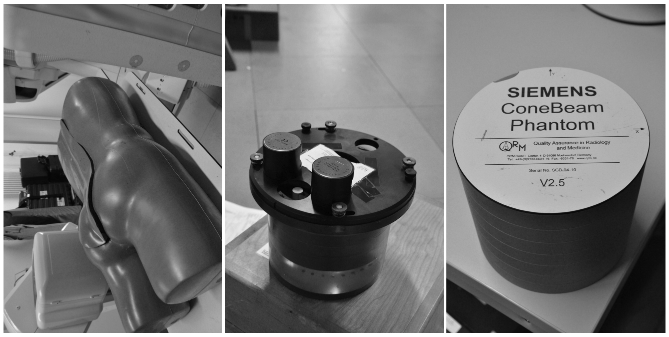

Fig. 1. Left: TORSO with SAWBONES spine. Middle: CATPHAN phantom. Right: Siemens Cone-Beam phantom. The CATPHAN and Siemens CB phantoms were scanned in-line to simulate a single long object.

II. DATA ACQUISITION

A. System configuration and data correction

As a prototype, the reverse helical trajectory was successfully implemented on the modified Artis zeego system by rotating and translating the C-arm gantry around a stationary patient table. We avoided any table motion because patients are usually connected to several medical instruments so that translating them poses health risks. The trajectory achieved in this experiment consists of five turns, and each turn was configured with the same angular coverage ($240°$ of step-size $0.35°$) and the same axial height (60 mm). This configuration yielded 681 projections per turn, with each projection acquired on a 300×400 mm^2 flat-panel detector of binned pixel size 0.308 mm$\times 0.308$ mm. The detector was set in the landscape mode (shorter side in the axial direction) so as to maximize the radius of the field-of-view (FOV) (about 130 mm) in the trans-axial direction. The rotation radius was about 785 mm, and the source-to-detector distance was about 1199 mm.

Three phantoms were scanned: the anthropomorphic torso phantom containing a SAWBONES spine [4], the CATPHAN phantom [5] and the Siemens Cone-Beam (CB) phantom [6] (QRM, Möhrendorf, Germany), as shown in Figure 1. The torso phantom is of length 550 mm, width 400 mm and

---

Zhicong Yu and Frederic Noo are with Department of Radiology, University of Utah, Salt Lake City, UT, USA; Andreas Maier, Manfred Schönborn, Florian Vogt, Christoph Köhler and Günter Lauritsch are with Siemens AG, Healthcare Sector, Forchheim, Germany; Zhicong Yu and Joachim Hornegger are with The Chair of Pattern Recognition, University of Erlangen-Nuremberg, Erlangen, Germany. This work was partially supported by a grant of Siemens AG, Healthcare Sector and by the U.S. National Institutes of Health (NIH) under grant R21 EB009168. The concepts presented in this paper are based on research and are not commercially available. Its contents are solely the responsibility of the authors and do not necessarily represent the official views of the NIH.

thickness 200 mm, and the inserted spine is of length 360 mm and of diameter 180 mm. This phantom was placed parallel to the patient table so that the entire spine was located within the FOV. Due to the large transversal size, the torso phantom suffered from trans-axial data truncation, which was not the case for the CATPHAN and Siemens CB phantoms, since they had small enough radii to be wholly contained within the FOV. On the other side, the CATPHAN and Siemens CB phantoms are too short to test long-object imaging, and thus they were scanned in-line so as to define a long object.

Preprocessed projection data was obtained by converting the photon number to line integrals using the Siemens pipeline, the major steps of which included I_0 correction for the automatic exposure control (an analog is reported in [7]), beam-hardening and scatter correction as described in [8], [9]. As an example, several preprocessed projections of the torso phantom are shown in Figure 2.

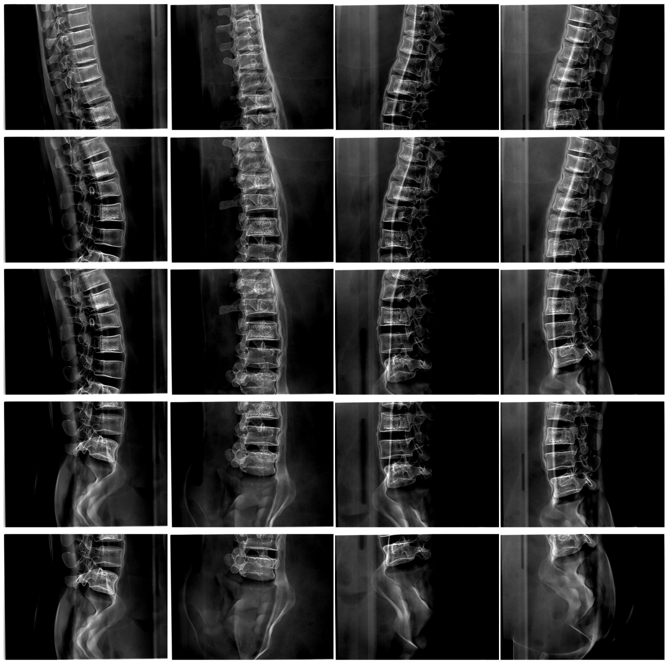

Fig. 2. Illustration of the preprocessed projections of the torso phantom. Top to bottom: 1st to 5th turn. Polar angle from left to right: $0°$, $-80°$, $-160°$ and $-230°$.

B. Trajectory calibration

Due to the open design, a C-arm system is not capable of producing a perfect source trajectory. To assess the exact geometrical positions and detector orientations, a calibration process is necessary. We have solved this calibration problem by using the robust technique presented in [2] with a new calibration phantom that was specifically designed to accommodate our long-object imaging needs. This new phantom was designed as an extension of the 206 mm long PDS-2 phantom (see [10] for an illustration), which consists of 108 beads of various size arranged on a helix with an 8-bit encoding scheme, so that identification of beads in the projection data is straightforward. The extended PDS-2 phantom is 500 mm and uses beads arranged with a 10-bit encoding scheme; see Figure 3 (upper left). The calibration process provided the source positions as well as the detector orientations in a calibration coordinate system, denoted as (xc, yc, zc), which was attached to the extended PDS-2 phantom. The calibrated trajectory is shown in Figure 3. Note that the reverse helix moves downwards opposite to the zc-axis.

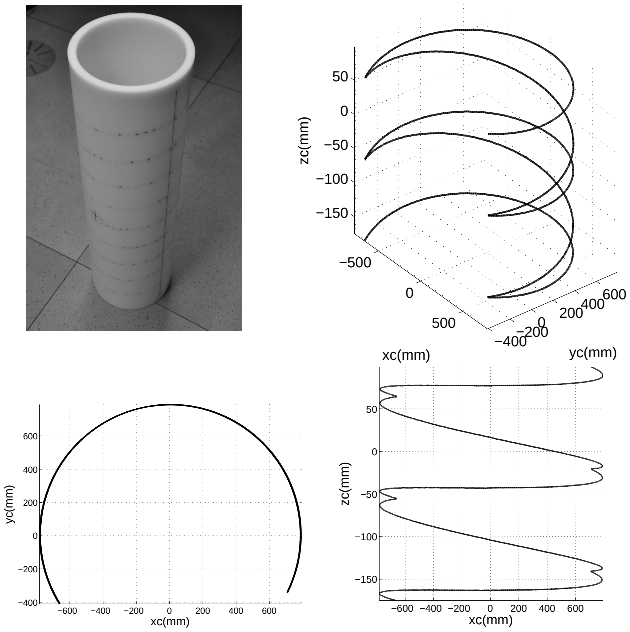

Fig. 3. Upper left: the 500 mm Siemens 10 digits PDS-2 calibration phantom. Upper right: calibrated source trajectory in the same Cartesian coordinate system as that of the calibration phantom. Lower left: projection of the calibrated trajectory onto the (xc, yc)-plane. Lower right: projection of the calibrated trajectory onto the (xc, zc)-plane.

C. Trajectory registration

In practice, it is impossible for the axial direction of the reverse helix to be parallel to the zc-axis of the calibration coordinate system, since the latter is specified by a simple manual placement of the calibration phantom on the patient table. To make the projection data appropriate for the Fusion-RFDK method, the reverse helix was first registered. This registration process transformed the trajectory from the calibration coordinate system to a Cartesian coordinate system that was defined with the (x, y, z)-axes such that i) the axial direction of the reverse helix lies on the z-axis, i.e., the projections of the vertex points onto the (x, y)-plane form a curve that is close to a circular arc, ii) the first source position lies in the (x, z)-plane.

The registered trajectory is shown in Figure 4; note in the right figure that, instead of the configured uniform axial height of 60 mm for each helical turn, the axial height of the 1st, 3rd and 5th turns is around 66 mm and that of the 2nd and 4th is about 53 mm. Various reasons could be responsible for this inconsistency, and they will be analyzed in the future. The registered trajectory is very close to a conventional reverse helix, as demonstrated in Figure 5 where the rotation radius,

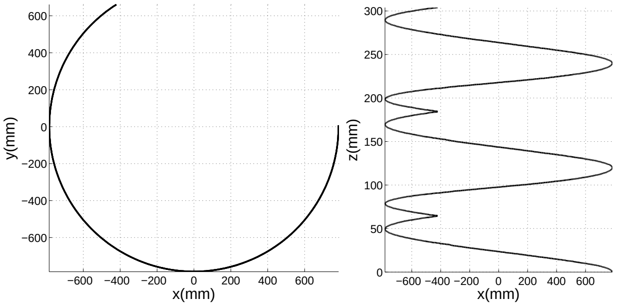

Fig. 4. Illustration of the registered trajectory. Left: projection of the registered trajectory onto the (x, y)-plane. Right: projection of the registered trajectory onto the (x, z)-plane.

the source-to-detector distance, the rotation angle and the z coordinate of each source position are displayed. Observe that the noise of both the scan radius and source-to-detector distance contains two components, i.e., white noise and low frequency noise, and we believe the former comes from the calibration process, whereas the latter stems from the effect of the gravity.

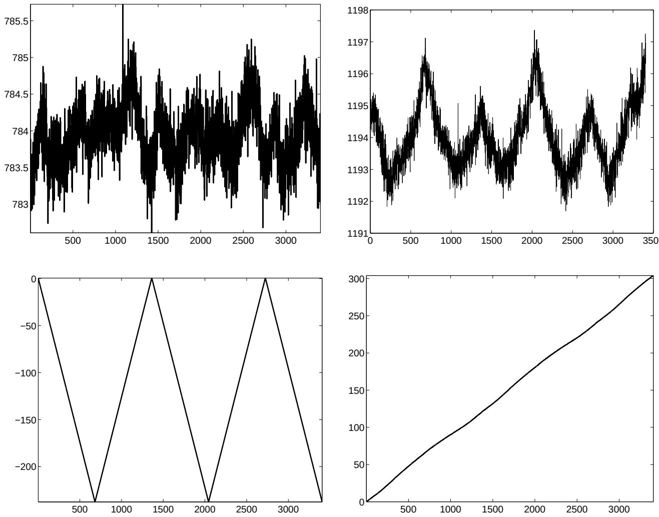

Fig. 5. Illustration of the parameters of the registered trajectory. The horizontal axis indicates the index of the source positions along the reverse helix. Upper left: rotation radius (mm); upper right: source-to-detector distance (mm); lower left: rotation angle (degree); lower right: z position (mm).

III. IMAGE RECONSTRUCTION THEORY

To create projection data that is suitable for reconstruction with the Fusion-RFDK method, we determined an analytically defined trajectory that fitted the registered trajectory as well as possible, and created projection data for each source position along the fitted trajectory through a rebinning process using data from the registered trajectory.

A. Trajectory fitting

Fusion-RFDK performs reconstructions independently for each helical turn, and the global results are then obtained by a fusion process. Therefore, the trajectory fitting was achieved by respectively finding an optimal analytical helix for each turn with constant step sizes in rotation angles and z positions. The fitting was such that the total distance between each pair of source points of the fitted and registered helices was minimized. The fitted result for the first helical turn is shown in Figure 6. The top and bottom right figures indicate good agreements between the fitted and registered trajectories. However, the relative angular difference between the fitted and registered trajectories was considerable.

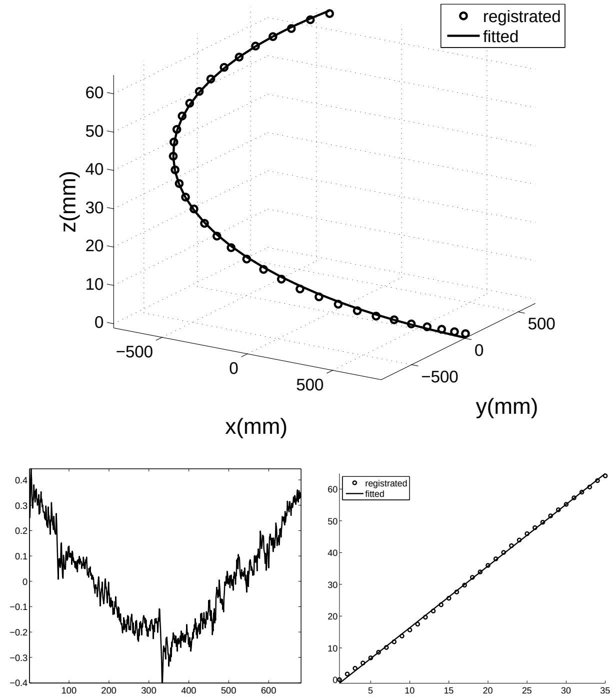

Fig. 6. Illustration of the curve fitting for the first sweep of the reverse helix. Upper: 3D view; lower left: relative angular difference for each pair of source points from the fitted and registered trajectories; lower right: illustration of z positions of both registered and fitted trajectories (mm).

B. Rebinning

To create projection data for the fitted trajectory, a rebinning approach was employed for each source position. Let $\mathcal{L}(\lambda_k, \underline{\alpha_k})$, with λ_k as the rotation angle, be the divergent beam pointing from the source point $\underline{a}(\lambda_k)$ on the fitted reverse helix in the direction $\underline{\alpha_k}$; and let $\underline{m}$ be the middle point of the two intersections between $\mathcal{L}(\lambda_k, \underline{\alpha_k})$ and the central FOV cylinder surface, as shown in Figure 7. Also, let $\underline{b}(\gamma_i)$ and $\underline{b}(\gamma_j)$, with angular positions γ_i and γ_j, be the two points on the registered trajectory that were closest to $\underline{a}(\lambda_k)$. Then the line integral along $\mathcal{L}(\lambda_k, \underline{\alpha_k})$ can be obtained through a linear interpolation (respect to the rotation angle) between the line integrals along the lines connecting $\underline{b}(\gamma_i)$ and $\underline{m}$, and $\underline{b}(\gamma_j)$ and $\underline{m}$. One rebinned slice is shown in Figure 8, note that the different orientation of the spine in the rebinned slice is due to different detector coordinate systems being used for the registered and fitted trajectories.

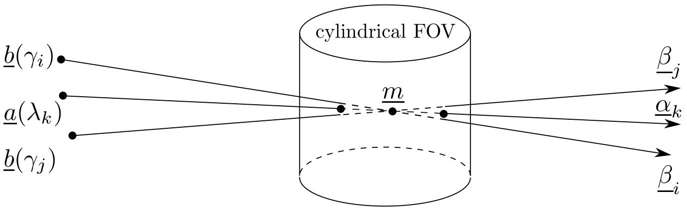

Fig. 7. Projection rebinning scheme. Source point $\underline{a}(\lambda_k)$ belongs to the fitted trajectory, and $\underline{b}(\gamma_i)$ and $\underline{b}(\gamma_j)$ are two points on the registered trajectory.

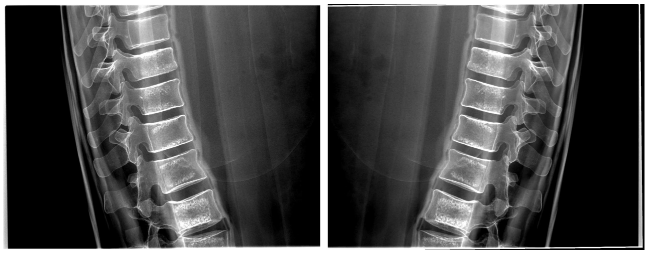

Fig. 8. The 50th rebinned projection of the torso phantom from the first sweep. Left: preprocessed; right: rebinned.

C. Reconstruction

A Fusion-RFDK reconstruction consists of four steps: i) CB length correction and Parker like weighting; ii) horizontal ramp filtering; iii) backprojection; iv) fusion. For more details, see Section III-A in [3]. Based upon those four steps, five volumes were reconstructed using the rebinned data from each turn of the fitted reverse helix separately, then all those volumes were combined by a fusion process.

In practice, two aspects need to be specified. First, we have to define kink planes, which are through the connecting point of any two successive helical turns and perpendicular to the axial axis of the reverse helix. In this work, take the kink plane of the 2nd and 3rd helices as an example, the z location of the kink plane for this portion of the reverse helix was chosen to be the average of the z positions of the last point of the 2nd turn and the first point of the 3rd turn. Other kink planes were defined in a similar way. Second, the fusion length needs to be defined. Given the radius of the FOV, $r = 130$ mm, the height of the detector (in z), 300 mm, and the maximum height of all fitted sweeps, 66 mm, a fusion length of 30 mm was chosen.

IV. RECONSTRUCTION RESULTS

Reconstructions were obtained for both the torso and the combined CATPHAN and Siemens CB phantoms with a hamming window in ramp filtering and a fusion length of 30 mm. The accuracy of the results was verified using CT images. The reconstruction of the torso phantom consists of $200 \times 200 \times 1021$ voxels of size 0.7910 mm$\times 0.7910$ mm$\times 0.3$ mm as shown in Figure 9. For the CATPHAN and Siemens CB combined phantom, we performed two reconstructions of different voxel sizes. The reconstruction for the CATPHAN is composed of $478 \times 478 \times 1021$ voxels of size 0.3770 mm$\times 0.3770$ mm$\times 0.3$ mm (see Figure 10 (a) and (b)), whereas the reconstruction for the Siemens CB phantom consists of $512 \times 512 \times 1021$ voxels of size

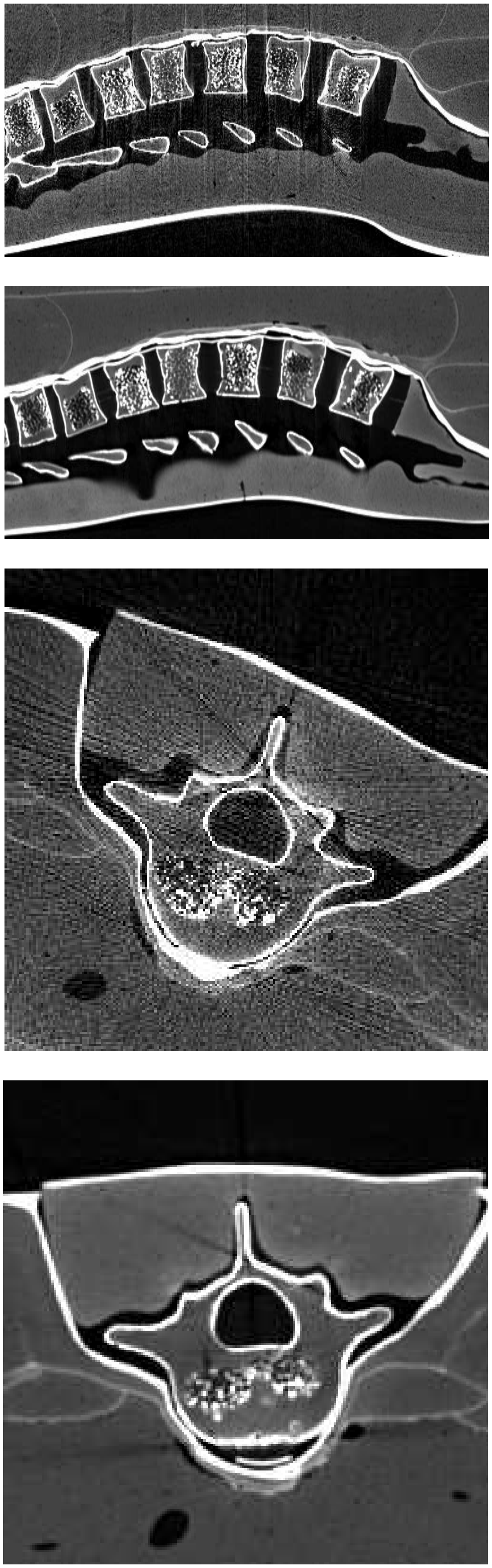

Fig. 9. Reconstruction results of the torso phantom. Display window: $(-1000, -200)$ HU. The first and second rows: sagittal view of the results from Fusion-RFDK and CT, respectively. The third and fourth rows: transversal view of the results from Fusion-RFDK and CT.

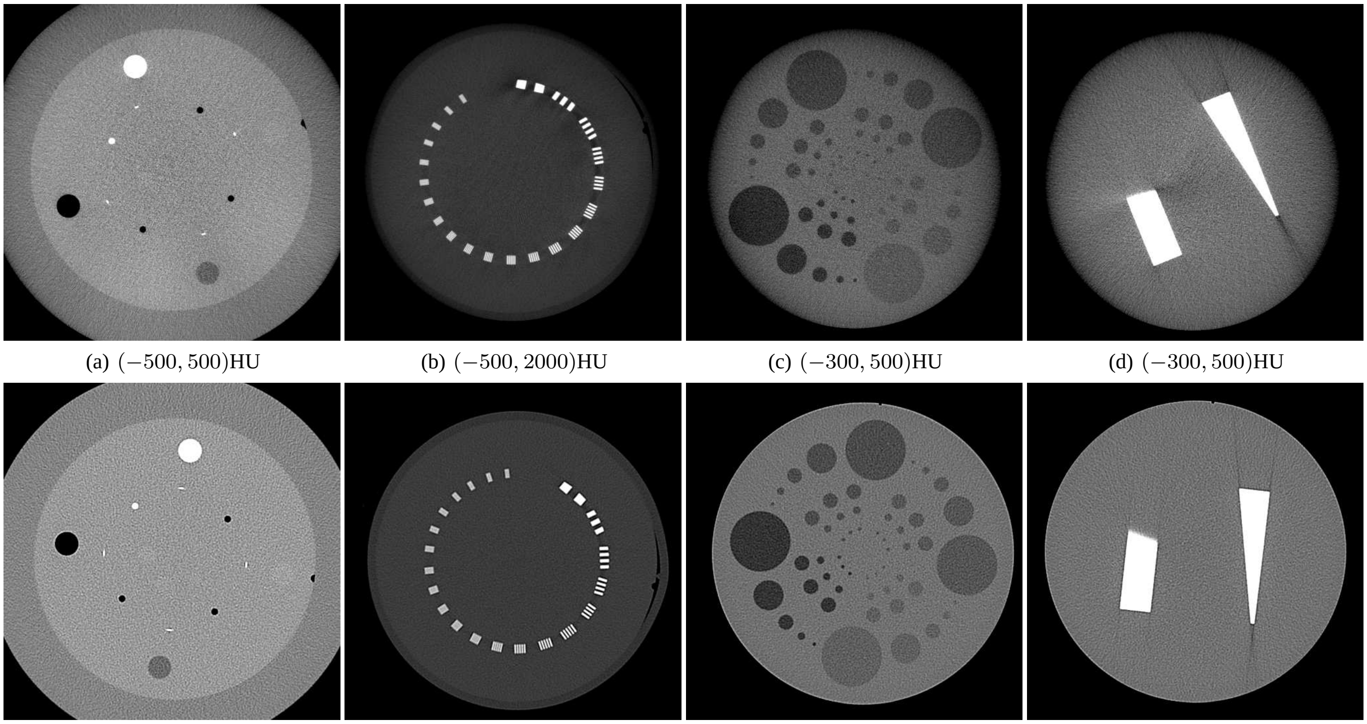

(a) $(-500, 500)\mathrm{HU}$ (b) $(-500, 2000)\mathrm{HU}$ (c) $(-300, 500)\mathrm{HU}$ (d) $(-300, 500)\mathrm{HU}$

Fig. 10. Reconstruction results of the CATPHAN (a, b) and Siemens CB phantoms (c, d). Upper row: C-arm; lower row: CT.

$0.3477\ \mathrm{mm}\times 0.3477\ \mathrm{mm}\times 0.3\ \mathrm{mm}$ (see Figure 10 (c) and (d)). Note that the voxel sizes used for Fusion-RFDK were matched with that of the CT images, and the attenuation coefficients were brought to the same level for both modalities using a linear mapping. It is also necessary to point out that the x-ray beam energy for the C-arm scans was $85\mathrm{kVp}$, whereas the energy for the CT scans was $120\mathrm{kVp}$.

Figures 9 and 10 indicate good agreement between our reconstution results and the CT images. Be aware that the images from the two modalities are not registered to the same coordinate system. As preliminary results, the reconstruction images from all three phantoms are largely encouraging.

V. SUMMARY AND OUTLOOOK

We have demonstrated that long-object imaging using a reverse helical trajectory in the interventional room is feasible using a C-arm system with large motion flexibility such as the Artis zeego system. To process the real data, the calibrated trajectory was first registered to the (x, y, z)-coordinate system, and then an analytical trajectory was found to fit the registered trajectory and its projections were obtained through a rebinning process. Reconstruction results of the torso, CATPHAN and Siemens CB phantoms from the Fusion-RFDK method are encouraging. Note that the modified Artis zeego system is capable of producing a reverse helix consisting of more than five turns, and thus a longer volume is possible.

As mentioned in III-A, the relative angular difference between the fitted and registered trajectories was considerable, and this could yield innegligible resolution loss in the data rebinning step. An alternative approach would be to modify Fusion-RFDK to allow direct usage of the preprocessed registered data for reconstruction. A comparison between this method and the one in this work is the topic of future investigations.

REFERENCES

[1] S. Cho, D. Xia, C. A. Pellizzari, and X. Pan, “A BPF-FBP tandem algorithm for image reconstruction in reverse helical cone-beam CT,” *Med. Phys.*, vol. 37, no. 1, pp. 32–39, Jan 2010.

[2] N. Strobel, B. Heigl, T. Brunner, O. Schuetz, M. Mitschke, K. Wiesent, and T. Mertelmeier, “Improving 3d image quality of x-ray c-arm imaging systems by using properly designed pose determination systems for calibrating the projection geometry,” in *Proceedings of SPIE*, vol. 5030, 2003, pp. 943–54.

[3] Z. Yu, F. Noo, F. Dennerlein, G. Lauritsch, and J. Hornegger, “FDK-type reconstruction algorithms for the reverse helical trajectory,” in *Proc. IEEE Nuc. Sci. Symp.*, 2011, pp. 3980–3985.

[4] http://www.sawbones.com/products/ortho/category.aspx?9.

[5] http://www.phantomlab.com/products/catphan.php.

[6] http://www.qrm.de/content/products/imagequality/conebeam.htm.

[7] C. Schwemmer, “High-density object removal from x-ray projection images,” Master’s thesis, Friedrich-Alexander University Erlangen-Nuremberg, 2010.

[8] M. Zellerhoff, B. Scholz, E. Rührnschopf, and T. Brunner, “Low contrast 3D reconstruction from C-arm data,” in *Proceedings of SPIE*, vol. 5745, 2005, pp. 646–55.

[9] N. Strobel, O. Meissner, J. Boese, T. Brunner, B. Heigl, M. Hoheisel, G. Lauritsch, M. Nagel, M. Pfister, E. Rührnschopf, *et al.*, “3D imaging with flat-detector C-arm systems,” *Multislice CT*, pp. 33–51, 2009.

[10] S. Hoppe, F. Noo, F. Dennerlein, G. Lauritsch, and J. Hornegger, “Geometric calibration of the circle-plus-arc trajectory,” *Phys. Med. Biol.*, vol. 52, pp. 6943–60, 2007.

Cone Beam X-Ray Luminescence Computed Tomography: A Preliminary Experimental Study

Shouping Zhu, Dongmei Chen, Huangjian Yi, Xianghan Zhang, Jimin Liang and Jie Tian*

Abstract—**The appearance of X-ray luminescence computed tomography (XLCT) opens new possibilities to perform molecular imaging by X-ray. In this paper, we propose a new cone beam XLCT method. Compared with the previous narrow beam XLCT, the cone beam XLCT can more fully utilize the X-ray dose and the scanning time will be shorten significantly. Photons scattering in biological tissue makes it an ill-posed problem to reconstruct the 3D distribution of the X-ray luminescent materials in cone beam XLCT. In order to overcome this issue, we use diffusion approximation (DA) model to describe the photons propagation in tissue, employ the sparse regularization method for reconstruction and utilize permissible source region strategy as *a priori* knowledge to ensure the uniqueness and stability of the reconstruction result. Phantom experiments have demonstrated the validity of the new cone beam XLCT method.**

I. INTRODUCTION

As the first trans-axial tomography model, X-ray computed tomography (CT) has revolutionized radiographic imaging and promoted the development of other tomographic modalities since its introduction in 1970s [1]. However, the contrast mechanism of all the mainstream X-ray CT imaging has been attenuation based, and its use in molecular imaging remains limited due to lack of high sensitive X-ray molecular agents [2].

Based on nanophosphors or other similar materials, X-ray luminescence imaging opens new possibilities for the use of X-ray imaging in molecular tracers *in vivo*. When excited with X-rays, some materials produce visible or near infrared (NIR) luminescence which can be measured by sensitive photo detectors [3]. Nanophosphors are able to target with biological processes specifically. Therefore, such materials can be used as molecular imaging agents during X-ray imaging. Compared with optical methods, the use of X-ray excitation eliminates the autofluorescence in optical fluorescence imaging.

Recently a novel molecular imaging modality, X-ray luminescence computed tomography (XLCT) was proposed [4][5][6][7]. In such a modality, a selective excitation strategy has been utilized. The sample is irradiated by a sequence of narrow X-ray beams, and the X-ray luminescence is measured by a high sensitive charge coupled device (CCD) camera. No matter where the photons are detected, it is known that those photons were emitted from somewhere on the path of the X-ray beam. Regarded the CCD camera as a "single-pixel detector", a projection sinogram of XLCT is formed by summing all the pixels together [4]. Reconstructed images can be obtained by back-projecting the sinogram along the X-ray beam path, as the conventional CT dose. Since the projection number is relative small in XLCT imaging, iterative reconstruction strategy has been adopted for reconstruction. In such scheme, the reconstruction results are not affected by the scatting of photons, and the spatial resolution is determined by the beam size and sampling [4].

As it utilizes a narrow beam, the scanning of XLCT is very similar to the first generation of CT scanners, which use a pencil beam and work in a translation-rotation mode. This results in a long sampling time. In addition, restricting the X-ray to a narrow beam means most of the X-ray photons have been wasted during scanning. In order to overcome these drawbacks, we propose a cone beam luminescence computed tomography strategy, in which cone beam X-ray is adopted to illuminate samples and a high sensitive CCD camera is utilized to acquire luminescent photons emitted from the samples. Compared with the above narrow beam XLCT, cone beam XLCT can fully utilize the X-ray dose and the scanning time will be shorten significantly. However, the scattering of the luminescent photos will play an important role during imaging, as is done in bioluminescence tomography (BLT) [8] and fluorescence molecular tomography (FMT) [9]. In this case, we employ diffusion approximation (DA) model to describe the photons propagation in tissue, and the sparse regularization is adopted to reconstruct the luminescent materials. Permissible source region strategy is adopted to provide *a priori* knowledge for the uniqueness and stability of reconstruction results [10][11].

The paper is organized as follows. The next section presents our experimental setup, cone beam XLCT imaging model and reconstruction method. Phantom experiments and results are shown in Section III to demonstrate the feasibility of the cone beam XLCT modality. Finally, we conclude the paper and discuss relevant issues in Section IV.

II. METHODS

A. Experimental Setup

The prototype cone beam XLCT system was built based on a micro-CT system in our lab. Fig. 1 shows the photograph of the experimental setup, which consists of a microfocus X-ray source (Apogee, Oxford Instruments, USA), a X-ray flat panel

---

This work was supported in part by the National Basic Research Program of China (973 Program) under Grant No. 2011CB707702, the Natural Science Foundation of China under Grant Nos.81090272, 81101084, and the Fundamental Research Funds for the Central Universities.

Asterisk indicates corresponding author.

Shouping Zhu, Dongmei Chen, Huangjian Yi, Xianghan Zhang, Jimin Liang and Jie Tian are with the School of Life Sciences and Technology, Xidian University, Xi'an, Shaanxi 710071, China. Jie Tian is also with the Intelligent Medical Research Center, Institute of Automation, Chinese Academy of Sciences, Beijing 100190, China. (Email: tian@ieee.org)

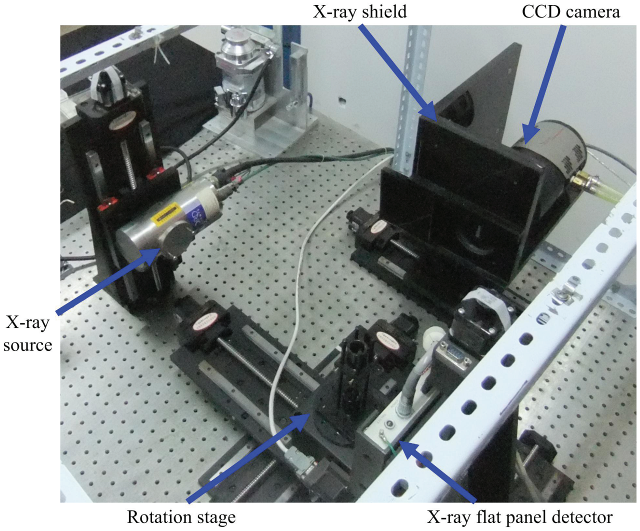

Fig. 1. Photograph of the experimental setup including the CCD camera, the X-ray source and detector, and the rotation stage.

detector (C7921CA-02, Hamamatsu, Japan), a motorized rotation stage, and a liquid-cooled backilluminated CCD camera (PIXIS 2048B, Princeton Instruments, USA) with a focus lens (Micro-Nikkor 55mm f/2.8, Nikon, Japan). A lead-made X-ray shield is used to to protect the CCD chip from X-ray directly irradiation.

This system can perform not only cone beam XLCT imaging, but also conventional cone beam micro-CT imaging. Fix the sample on the rotation stage, and irradiate it by the X-ray source. If we want to carry out XLCT experiment, we can collect the emitted luminescence by the CCD camera. If using the X-ray flat panel detector to collect the transmitted X-rays, X-ray CT projections will be obtained by the system. An ideal case is to perform both XLCT and conventional micro-CT imaging *simultaneously*. However, limited by the hardware performances, we have to carry out XLCT and micro-CT imaging sequentially using the current system. How to perform these two modalities *simultaneously* will be studied in future.

B. Imaging Model

The light transport in the biological soft tissue can be accurately modeled by the radiative transfer equation (RTE). For the highly scattering and weakly absorbing properties of the soft tissue in the NIR spectral region, RTE is usually replaced by diffusion approximation. Considering the X-rays propagation in tissue, the imaging model can be expressed as

$$S(\mathbf{r}) = \varepsilon I(\mathbf{r})\rho(\mathbf{r}), \tag{1}$$

$$-\nabla \cdot [D(\mathbf{r})\nabla\Phi(\mathbf{r})] + \mu_a(\mathbf{r})\Phi(\mathbf{r}) = S(\mathbf{r}), \quad \mathbf{r} \in \Omega \tag{2}$$

where $\mathbf{r}$ is the position vector and Ω is the domain under consideration. $D(\mathbf{r}) = (3(\mu_a(\mathbf{r}) + (1-g)\mu_s(\mathbf{r})))^{-1}$ is the diffusion coefficient with $\mu_a(\mathbf{r})$ as the absorption coefficient, g as the anisotropy parameter and $\mu_s(\mathbf{r})$ as the scattering coefficient. $\Phi(\mathbf{r})$ is the photon flux density and $S(\mathbf{r})$ is the source. $I(\mathbf{r})$ is the X-ray intensity, and $\rho(\mathbf{r})$ is the nanophosphor density at position $\mathbf{r}$. ε is the light yield. Assuming no photon travels across the boundary $\partial\Omega$ into the tissue domain Ω, then the Robin boundary can be constrained DA as

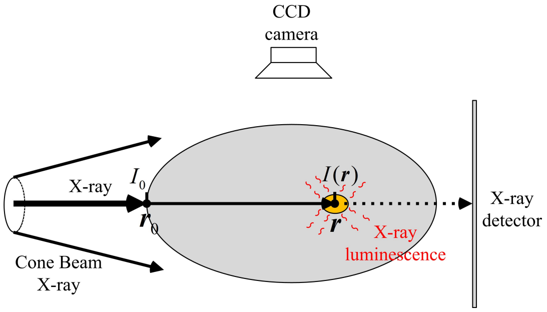

Fig. 2. Schematic diagram of X-ray propagation in tissue.

$$\Phi(\mathbf{r}) + 2\kappa(\mathbf{r}, n, n')D(\mathbf{r})[\mathbf{v}(\mathbf{r}) \cdot \nabla\Phi(\mathbf{r})] = 0, \quad \mathbf{r} \in \partial\Omega \tag{3}$$

where $\mathbf{v}(\mathbf{r})$ is the outward unit normal vector on $\partial\Omega$, and $\kappa(\mathbf{r}, n, n')$ is the boundary mismatch factor, which depends on the refractive indices n within Ω and n' in the surrounding medium. The measured photon flux on the surface of the object is expressed as

$$\Phi(\mathbf{r}) = -D(\mathbf{r})[\mathbf{v}(\mathbf{r}) \cdot \nabla\Phi(\mathbf{r})], \quad \mathbf{r} \in \partial\Omega. \tag{4}$$

In our imaging model, we assume that the X-rays propagate along a straight line in tissue, as shown in Fig. 2, then the X-ray intensity distribution $I(\mathbf{r})$ is expressed as follows

$$I(\mathbf{r}) = I_0 \exp\{-\int_{\mathbf{r}_0}^{\mathbf{r}} \mu_t(\boldsymbol{\tau})d\boldsymbol{\tau}\}, \tag{5}$$

where I_0 is the X-ray source intensity, and $\mu_t(\mathbf{r})$ is the X-ray attenuation coefficient at position $\mathbf{r}$. A more complex X-ray transport model, which has considered the X-rays scattering effect, can be found in [12].

C. Reconstruction

The diffusion equation (2) and its boundary condition (3) can be formulated into a matrix equation using the finite element method as follows [12]

$$\mathbf{M} \cdot \boldsymbol{\Phi} = \mathbf{F} \cdot \boldsymbol{\rho}. \tag{6}$$

Since the matrix $\mathbf{M}$ above is positive definited, we have

$$\boldsymbol{\Phi} = (\mathbf{M}^{-1}\mathbf{F}) \cdot \boldsymbol{\rho} = \mathbf{A} \cdot \boldsymbol{\rho}, \tag{7}$$

which is a linear relationship between the nanophosphor distribution and the NIR measurement. The reconstruction of the luminescence source is to recover the nanophosphor density $\boldsymbol{\rho}$ from the measured photon flux density $\boldsymbol{\Phi}$ on $\partial\Omega$. Since the ill-poseness of the problem and the measured data on the surface are usually noisy, it is impractical to solve for $\boldsymbol{\rho}$ directly in (7). In most biological applications, the nanoparticles are sparsely distributed in the tissue, hence the sparse regularization method can be employed to find

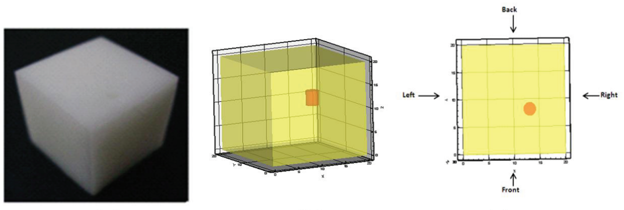

(a) (b) (c)

Fig. 3. Experimental phantom. (a) The homogeneous physical phantom; (b) The 3D view of the single fluorescent target in the cubic phantom; (c) The x-y view on the z=10mm plane, where the black dots represent the excitation point source positions. Four degrees show the direction of the CCD camera during data acquisition.

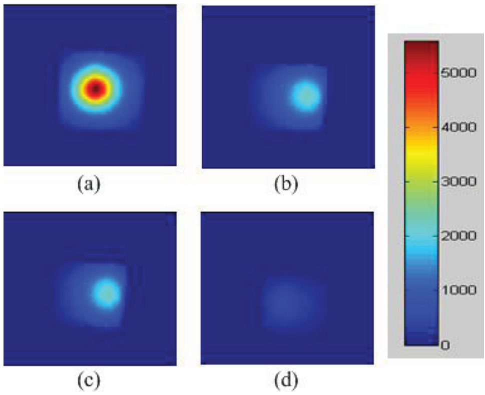

Fig. 4. Surface images acquired by CCD camera from four views. (a) front view; (b) right view; (c) back view; (d) left view.

a regularized solution by minimizing the following object function

$$\min\{\|\mathbf{A}\boldsymbol{\rho}-\boldsymbol{\Phi}\|_2^2+\lambda\|\boldsymbol{\rho}\|_1\}, \tag{8}$$

where λ is the regularization parameter. Here we solve this minimization problem by primal-dual interior-point method [13]. In order to ensure the uniqueness of the reconstruction result, permissible source region strategy is also adopted in reconstruction [11].

III. EXPERIMENTS AND RESULTS

In the experiments, an europium (III) oxide ($\mathrm{Eu_2O_3}$) precursor was used as a luminescence activator. As [3] reported, Eu^{3+} emission peaks were at 597 nm, 615 nm, and 692 nm due to the $^5\mathrm{D}_0 \rightarrow {}^7\mathrm{F}_1$, $^5\mathrm{D}_0 \rightarrow {}^7\mathrm{F}_2$, and $^5\mathrm{D}_0 \rightarrow {}^7\mathrm{F}_4$ transitions under X-ray irradiation, respectively. We used a polyoxymethylene made cubic phantom with a length of 20 mm to mimic biological tissue, as shown in Fig. 3(a). The optical parameters of this phantom is $\mu_a = 0.0025\mathrm{mm}^{-1}$ and $\mu_s = 11.15\mathrm{mm}^{-1}$. A glass capillary with a 1 mm radius was embedded in the phantom, which was used to contain X-ray luminescent materials. The center of the materials in the capillary was (13.05 mm, 8.25 mm, 10.15 mm) with a 2 mm height, as shown in Fig. 3(b). The X-ray luminescent materials were excited by X-ray source from four different directions with 90° intervals and the luminescent photons emitted from the phantom were acquired by the CCD camera. In the experiment, the voltage of X-ray source was set to 50 kVp, and the current was 1.0 mA. The CCD camera was cooled to $-70°\mathrm{C}$ to reduce the effect of the electronic noises, and 4×4 binning operation was employed to improve signal noise ratio (SNR). The image acquisition system was enclosed in a light-tight environment to avoid outside light effect. Fig. 4 shows fours views luminescence images with the exposure time 60 seconds and lens numerical aperture NA = 2.8. The micro-CT scanning was also performed (50 kVp, 1.0 mA, 360 views with 1° intervals) in the experiment to to get the attenuation coefficient. The CT result was reconstructed by filter backprojection (FBP) method [14]. Fig. 5 shows a longitudinal view of the result, in which the bright parts denote the luminescent materials.

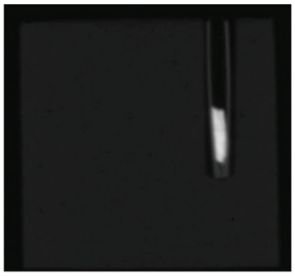

Fig. 5. Micro-CT reconstruction result of the phantom.

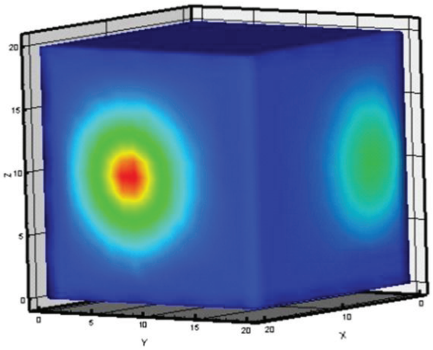

Fig. 6. Surface flux density distribution of the phantom.

In the inverse reconstruction, the cubic phantom was discretized into 24576 tetrahedral-elements and 4913 nodes. Fig. 6 shows the surface flux density distribution of the phantom, which was mapping from the acquired four images shown in Fig. 4. From the measured data, the distribution of luminescent materials can be reconstructed by the method described in the last section. In the reconstruction, permissible source region was set to $\{(x,y,z)|12\mathrm{mm} \le x \le 15\mathrm{mm}, 5\mathrm{mm} \le y \le 10\mathrm{mm}, 8\mathrm{mm} \le z \le 13\mathrm{mm}, (x,y,z) \in \partial\Omega\}$.

The final results are shown in Figs. 7(a) and (b) with the maximum reconstructed value at (12.50 mm, 10.00 mm, 10.00 mm) and location error 1.84 mm. Fig. 7(a) is the perpendicular cross sections of the reconstruction. Fig. 7(b) is the transverse view of the reconstruction at the z = 10 mm plane, and the black circle represents the real position of the luminescent materials.From this results we can see 3D reconstruction the X-ray luminescent materials distribution by cone beam XLCT strategy is feasible.

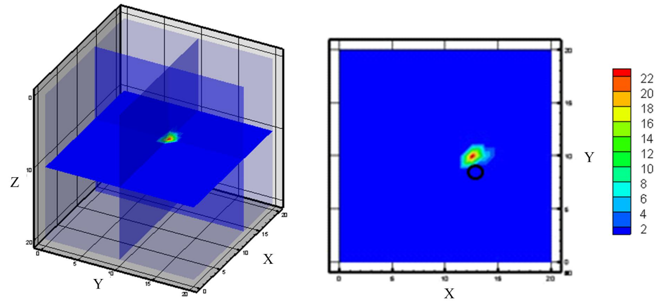

(a) (b)

Fig. 7. X-ray luminescence reconstruction results.

IV. Conclusion and Discussion

In view of the drawbacks of the previous narrow beam XLCT imaging and the development of the optical 3D reconstruction of BLT and FMT, we propose a new cone beam XLCT method in this paper, which can improve the efficiency of X-rays utilization and reduce the scanning time significantly. In our method, we use diffusion approximation model to describe the photos propagation in tissue, and employ the sparse regularization method for reconstruction. The permissible source region strategy, which is widely used in BLT reconstruction [11], is also used as *a priori* knowledge to ensure the uniqueness and stability of the reconstruction result. The validity of the method has been demonstrated by phantom experiments.

Due to the photons scattering in biological tissue, the spatial resolution of cone beam XLCT is lower than narrow beam XLCT, in which the spatial resolution is determined by the beam width and sampling. As the 3D reconstruction of cone beam XLCT is very similar to BLT and FMT, we believe that the spatial resolution which can be achieved by cone beam XLCT should be in the same level as BLT and FMT do, on the millimetre or sub-millimetre level as reported [9][11]. The experiment results in our paper has proved this point. Other imaging strategies, such as adding scanning angles, multi-spectrum measurement, can be used to improve our spatial resolution further. In our XLCT imaging, only four angles cone beam scanning were used, and the exposure time for each angle was 60 seconds. For the previous narrow beam XLCT, for example, a phantom scanning needs to translate 26 times and rotate 24 times with 1 second exposure [4]. The small exposure time in their experiment is caused by the use of a large X-ray tube current (30 mA). In contrast, X-ray tube current in our experiment is only 1.0 mA. Nonetheless, our scanning time is still much shorter than the narrow beam XLCT strategy. The improvement in scanning speed will contribute to the practice application of the XLCT technique.

In summary, we propose a novel cone beam XLCT method and demonstrate the preliminary experimental results in this paper. The results are valuable to design and implement a cone beam XLCT system for small animals imaging, which will be studied in future.

References

[1] G. Wang, H. Y. Yu, and B. De Man, "An outlook on x-ray CT research and development," *Med. Phys.*, vol. 35, no. 3, pp. 1051-1064, 2008.

[2] S. R. Cherry, "In vivo molecular and genomic imaging: new challenges for imaging physics," *Phys. Med. Biol.*, vol. 49, pp. R13-R48, 2004.

[3] C. Sun, G. Pratx, C. M. Carpenter, H. Liu, Z. Cheng, S. S. Gambhir, and L. Xing, "Synthesis and Radioluminescence of PEGylated Eu^{3+}-doped Nanophosphors as Bioimaging Probes," *Adv. Mater.*, vol. 23, pp. H195-H199, 2011.

[4] G. Pratx, C. M. Carpenter, C. Sun, R. P. Rao, and L. Xing, "Tomographic molecular imaging of x-ray-excitable nanoparticles," *Opt. Lett.*, vol. 35, no. 20, pp. 3345-3347, 2010.

[5] C. Carpenter, G. Pratx, C. Sun, and L. Xing, "Hybrid x-ray/optical luminescence imaging: characterization of experimental conditions," *Med. Phys.*, vol. 37, no. 8, pp. 4011-4018, 2010.

[6] G. Pratx, C. Carpenter, C. Sun, and L. Xing, "X-ray luminescence computed tomography via selective excitation: a feasibility study," *IEEE Trans. Med. Imaging*, vol. 29, no. 12, pp. 1992-1999, 2010.

[7] C. M. Carpenter, G. Pratx, C. Sun and L. Xing, "Limited-angle x-ray luminescence tomography: methodology and feasibility study," *Phys. Med. Biol.*, vol. 56, pp. 3487-3502, 2011.

[8] W. Cong, G. Wang, D. Kumar, Y. Liu, M. Jiang, L.Wang, E. Hoffan, G. McLennan, P. McCray, J. Zabner, and A. Cong, "Practical reconstruction method for bioluminescence tomography," *Opt. Express*, vol. 13, no. 18, pp. 6756-6771, 2005.

[9] V. Ntziachristos, "Fluorescence molecular imaging," *Annu. Rev. Biomed. Eng.*, vol. 8, no. 1, pp.1-33, 2006.

[10] G. Wang, Y. Li, and M. Jiang, "Uniqueness theorems in bioluminescence tomography," *Med. Phys.*, vol. 31, no. 8, pp. 2289-2299, 2004.

[11] C. Qin, S. Zhu, J. Feng, J. Zhong, X. Ma, P. Wu, and J. Tian, "Comparison of permissible source region and multispectral data using efficient bioluminescence tomography method," *J. Biophotonics*, vol.4, no. 11-12, pp. 824-39, 2011.

[12] W. Cong, H. Shen, and G. Wang, "Spectrally resolving and scattering-compensated x-ray luminescence/fluorescence computed tomography," *J. Biomed. Opt.*, Vol. 16, no. 6, pp. 066014, 2011.

[13] Q. Zhang, H.Zhao, D. Chen, X. Qu, X. Chen, X. He, W. Li, Z. Hu, J. Liu, J. Liang, and J. Tian, "Source sparsity based primal-dual interior-point method for three-dimensional bioluminescence tomography," *Opt. Commun.*, vol. 284, no. 24, pp. 5871-5876, 2011.

[14] J. Hsien, Computed Tomography Principles, Design, Artifacts, SPIE Press, Bellingham, Wash, USA, 2003.

A small-animal phase-contrast CT scanner

P. Bruyndonckx[1], B. Pauwels[1], X. Liu[1], A. Tapfer[2], M. Bech[2,3], A. Velroyen[2], A. Sasov[1], F. Pfeiffer[2]

[1] Skyscan, Kontich, Belgium, [2] Technische Universität München, Garching bei München, Germany, [3] Medical Radiation Physics, Clinical Sciences, Lund University, Lund, Sweden

Abstract—**Due to the phase shift x-rays undergo while passing through matter, a minute angular refraction occurs. This process offers two new contrast modalities in addition to the classical absorption contrast: Differential Phase-Contrast Imaging (DPC) and Dark Field Imaging (DFI). We developed a compact in-vivo CT system with a rotating gantry that relies on Talbot-Lau interferometry to extract the three imaging contrasts during a single scan.**

Scans of biological samples have demonstrated that phase-contrast and dark-field contrast x-ray tomography is possible in a system with a rotating gantry. The images displayed an improved or complementary soft-tissue contrast.

I. INTRODUCTION

Standard attenuation-based x-ray imaging of biological samples often yields poor soft-tissue contrast. The wave-like character of x-rays can be exploited to generate other forms of imaging contrast besides the usual absorption contrast. The interaction of x-rays with an object is determined by the complex index of refraction n(λ) of the material constituting the object:

$$n(\lambda) = 1 - \delta(\lambda) + i\beta(\lambda) \qquad (1)$$

with

$$\beta = \frac{\rho_a \sigma_a(\lambda,Z)}{2k} \qquad (2)$$

$$\delta = \frac{\rho_a\, p(\lambda,Z)}{k} \qquad (3)$$

where ρ_a is the atomic number density, σ_a is the absorption cross-section, p is the phase-shift cross-section and $k=2\pi/\lambda$ is the magnitude of the wave vector of the incoming x-rays. The imaginary part β is related to the transmission T(x) of x-rays through a sample:

$$T(x) = e^{-\int_0^L \frac{4\pi}{\lambda}\beta(x,y)dy} = e^{-\int_0^L \mu(x,y)dy} \qquad (4)$$

where L is the path length through the sample. The real term δ relates to the phase-shift Φ(x) the x-rays undergo when passing through the material :

$$\Phi(x) = \frac{2\pi}{\lambda}\int_0^L \delta(x,y)dy \qquad (5)$$

The impact of the phase shift presents itself as a very small angular refraction α of the x-rays:

$$\alpha(x) = \frac{\lambda}{2\pi}\frac{\partial\Phi(x)}{\partial x} \qquad (6)$$

Combining (5) and (6) yields

$$\alpha(x) = \int_0^d \frac{\partial\delta(x,y)}{\partial x}dy \qquad (7)$$

In addition to absorption and phase shifting, x-rays can also undergo small angle scattering and multiple refraction. In [1] it was proposed to describe these processes using a linear diffusion coefficient ε.

II. PRINCIPLE OF GRATING BASED PHASE CONTRAST EXTRACTION

One way of detecting the deflection caused by the phase shift is with the aid of a grating interferometer implemented according to the scheme described in [2,3,4] (fig 1).

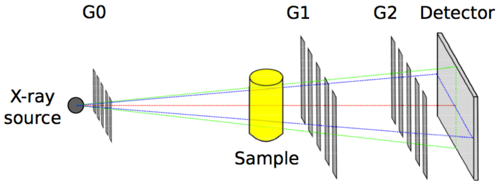

Figure 1: Scheme of the Talbot-Lau grating interferometer

The set-up consists of three gratings: a source grating G_0, a phase grating G_1 and an analyzer grating G_2. When no object is in the x-ray beam, an enlarged image of the G_1 grating will appear at certain distances (Talbot effect). When an x-ray detector is placed at a position where the self-images emerge, it is usually not possible to image this intensity pattern directly because the pitch in the grid image is much smaller than the detector pixel size. To overcome this problem, an absorbing analyzer grating is added with the same pitch as the G_1 grating self-image. The intensity distribution generated by a Gaussian x-ray spot and the combined effect of the G_1 and G_2 grating can be approximated by a sinusoidal function [3]:

$$I_{p_x,p_y}(x_g) \cong A_0(p_x,p_y) + A_1(p_x,p_y)cos\left(\frac{2\pi x_g}{g_2} + \phi(p_x,p_y)\right) \qquad (8)$$

where $I_{px,py}(x_g)$ is the intensity measured in pixel (p_x,p_y) when the analyzer grating is at position x_g and g_2 is the pitch of the analyzer grating (fig. 2a). When the analyzer grating is moved in small steps over a distance of one period g_2 (i.e. phase stepping) and the intensity $I_{px,py}(x_g)$ is measured, the three unknown parameters $A_0(p_x,p_y)$, $A_1(p_x,p_y)$ and $\phi(p_x,p_y)$ in eq. 8 can be determined. The value of $A_0(p_x,p_y)$ relates to the classical x-ray absorption, $\phi(p_x,p_y)$ relates to the x-ray phase shift and the amplitude $A_1(p_x,p_y)$ conveys information about the small angle scattering. The latter is usually called the dark field signal.

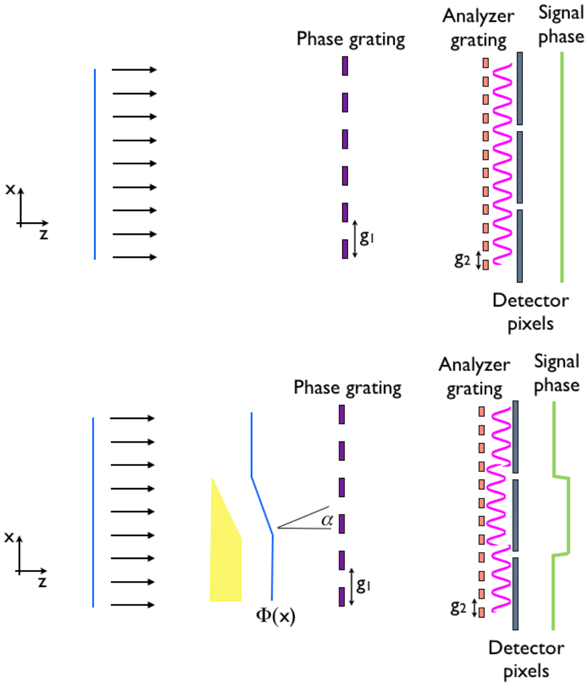

Figure 2: (a) The combination of a phase grating and analyzer grating generates a sinusoidal intensity pattern at specific Talbot distances. The mean, amplitude and phase can be measured by moving the analyzer grating over small steps over a distance g_2. (b) Introducing an object in the x-ray beam creates an x-ray phase shift, resulting in a small deflection α of the x-rays that can be quantified by measuring the local phase shift in the sinusoidal intensity signal.

These are easily obtained by computing the first two components of the discrete Fourier transform of the measured data $I_{px,py}$.

When an object is inserted in the FOV, the x-rays passing through the object can undergo absorption, phase shifting and small angle scattering. The refraction angle α of the x-rays due to the phase shift they undergo results in a lateral shift of the interference pattern (fig 2b). This lateral shift S is observed as a phase shift of the sinusoidal signal obtained after a phase stepping procedure:

$$\alpha(p_x,p_y)=\frac{S(p_x,p_y)}{d}=\frac{\phi(p_x,p_y)-\phi^{FF}(p_x,p_y)}{d}\frac{g_2}{2\pi} \tag{13}$$

where d is the distance between the G_1 and G_2 grating and the index FF stands for flat-field, i.e. signals measured without an object in x-ray beam.

Small angle scattering and multiple refractions reduce the dark field contrast. The dark field contrast is usually quantified as the ratio $A_1(p_x,p_y)/A_0(p_x,p_y)$ and normalized such that the dark field contrast in the flat field is 100%. The relation between the dark field contrast V(x) and the linear diffusion coefficient is given by [1]

$$V(x)=e^{-\frac{2\pi^2 d^2}{g_2}\int_0^L \varepsilon(x,y)dy} \tag{14}$$

The projections along an x-ray path of the physical parameters responsible for x-ray attenuation, phase shift and small angle scattering $\varepsilon(x,y)$ are then given by

$$\int_0^L \frac{4\pi}{\lambda}\beta(x,y)dy=-\log\left(\frac{A_0(p_x,p_y)}{A_0^{FF}(p_x,p_y)}\right) \tag{15}$$

$$\int_0^L \frac{\partial\delta(x,y)}{\partial x}dy=\frac{g_2}{2\pi d}\left(\phi(p_x,p_y)-\phi^{FF}(p_x,p_y)\right) \tag{16}$$

$$\int_0^L \varepsilon(x,y)dy=-\frac{g_2}{2\pi^2 d}log\left(\frac{A_1(p_x,p_y)}{A_0(p_x,p_y)}\frac{A_0^{FF}(p_x,p_y)}{A_1^{FF}(p_x,p_y)}\right) \tag{17}$$

3D distributions of the absorption coefficients and dark-field contrast component can be obtained from resp. eq. 15 and eq. 17 using the standard Feldkamp reconstruction. To create a 3D phase contrast image, the Feldkamp algorithm needs to be modified because eq. 16 only yields the projection of the derivative of the x-ray phase shift and not the projection of the phase shift itself. This problem can be solved by replacing the standard ramp filter with a complex filter $h(\nu)$ in the FBP reconstruction algorithm [5]:

$$h(\nu)=\begin{cases}\frac{1}{2\pi i}sgn(\nu) & |\nu|\le \upsilon_{Nyquist}\\ 0 & |\nu|>\upsilon_{Nyquist}\end{cases} \tag{18}$$

III. PROTOTYPE SYSTEM

To study the feasibility of grating interferometry as a means of phase shift detection in a small animal in-vivo CT system with a rotating gantry, a prototype was built (fig. 3). The grating design and their relative positions depend on the mean energy of the x-rays. All parameters in our prototype were chosen for a design energy of 23 keV [6]. The gratings were produced in the LIGA process involving x-ray lithography and electroplating.

The G_0 grating consists of 35 µm high Au structures with a period of 10.0 µm and is positioned close to the x-ray source (RTW, tungsten target, 20-50 kVp, 50 W) to create an array of individually coherent cone-beam x-ray sources. This eliminates the need for a micro focus x-ray source.

The phase grating G_1 is made from 4 µm thick Ni structures (3.24 µm period) that introduce a phase of $\pi/2$ for the x-rays passing through them. It is placed 50 mm behind the sample stage.

Finally, the analyzer grating G_2 with 25 µm high Au structures (period 4.80 µm) is mounted just in front of the camera, which is placed at the first Talbot distance. The x-rays are detected by a 5 mega-pixel Hamamatsu flat panel device (50 µm pixel size).

The total length of the interferometer is 47 cm and the scanner is operated at an x-ray energy of 50 kVp. The bed of the scanner is optimized for mice, with a gantry opening of 70 mm. The FOV of 40 mm x 15 mm results in a reconstructed volume of 40×40×15 mm^3 with an image voxel size of 30×30×30 μm^3.

In theory each of the three gratings can be used for the phase stepping. In the prototype the G_0 grating was used because it has the largest pitch and hence requires the lowest accuracy on the stepping movement.

A shutter was installed in front of the x-ray source. It only opens when the camera is actually acquiring images. During all other times (e.g. moving the gratings, rotating the gantry, moving the animal in and out for flat-field measurement) it shields the animal from the x-ray source.

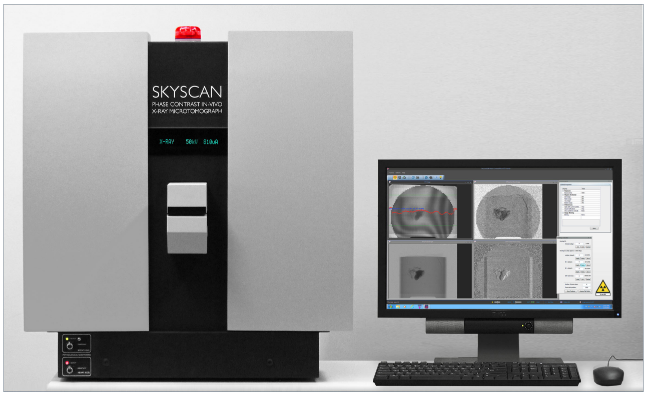

Figure 3: Phase contrast CT imaging prototype

IV. PHASE STABILITY

Minute changes in the gratings during a scan (e.g. due to temperature changes, mechanical vibrations, gravity) cause the obtained value of the signal phase $\phi(p_x,p_y)$ in each pixel to drift. This results in a wrong estimate of the differential x-ray phase shift $\partial\Phi(p_x,p_y)/\partial x$ introduced by the object.

The blue curve in fig. 4 shows the signal phase drift in a small air-filled ROI during a rotation over 360°. Ideally it should remain constant. Because the signal phase shift drifts smoothly as a function of the gantry position, it can be compensated by acquiring additional phase flat-fields during the scan. For each acquired projection, the flat-fields used in eq. 15-17 were interpolated from two flat-field images measured at projection angles closest to the projection angle of the projection being processed. It was found that the drift was mainly due to movement of the G_1 grating during gantry rotation. To stabilize the G_1 grating, positioning mechanics were preloaded by a spring to keep its position and all alignment drives use backlash-free motor gear head assemblies. The red curve in figure 4 shows the signal phase drift during a rotation over 360° after the change. The maximum drift difference has been reduced from about 14π to 4π. This reduced drift results in fewer flat-fields that need to be acquired during the scan.

The signal phase also drifts as a function of temperature. After the initial warm-up period of the x-ray source, the phase fluctuations over a 48-hour period were less then ± 0.5 radians.

V. DATA PREPROCESSING

Once the flat-field corrected signal phase shifts have been computed for each pixel, they should be identical when no object is in the FOV. However, a 2D phase ramp was observed in the signal phase image (fig. 5). To remove this phase ramp when an object is present, a signal phase gradient in the x and y direction was computed from the signal phase in "air filled" pixels at the edges of the FOV. The interpolated values along the inclined 2D signal phase plane were then subtracted from the differential phase projection image.

Next, the phase of "air filled" pixels is set to zero. This is accomplished by looking for an "air filled" ROI at the edge of the FOV in the phase ramp corrected image and subtracting the average phase in that ROI from the differential phase in each of the pixels.

Finally the projection of the differential x-ray phase shift is computed for each pixel using eq. 16.

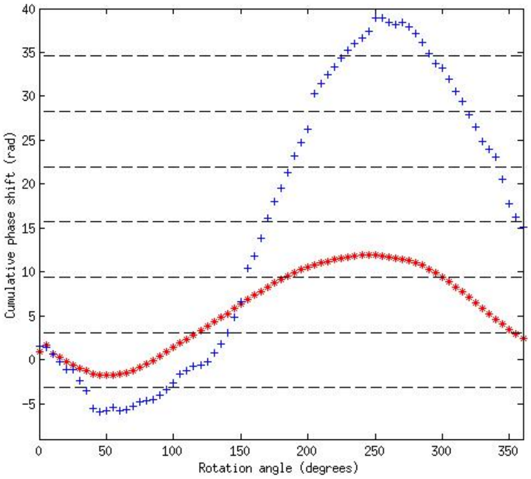

Fig. 4: Drift of the differential phase during a 360° rotation, without (blue curve) and with (red curve) G_1 grating stabilization.

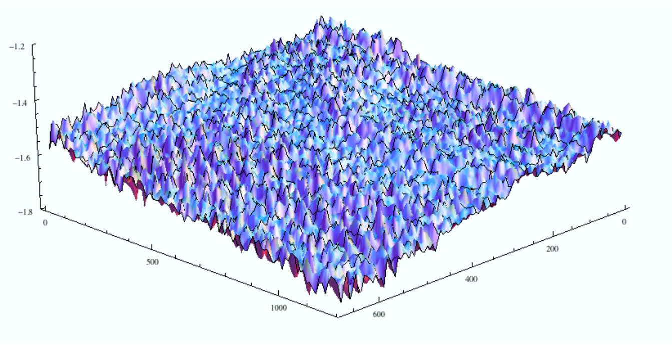

Fig. 5: After subtracting the phase reference of each pixel, a 2D phase ramp remains in the image.

VI. QUALITY OF THE INTERFEROMETER

The quality of the interferometer is evaluated by the visibility of the interference pattern:

$$Q_{vis} = \frac{I_{max}-I_{min}}{2\,I_{mean}} = \frac{A_1^{FF}}{A_0^{FF}} \qquad (19)$$

This number should be as high as possible. It depends on a number of instrumental parameters such as the grating quality, grating alignment and monochromaticity of the x-ray beam. Table I shows the visibility that could be achieved at different x-ray tube voltages. The visibility is highest at 30 kVp and decreases for high x-ray tube voltages. This is due to the fact that the gratings and the interferometer were designed for a mean energy of 23 keV. In addition, the absorption gratings become more transparent with increasing energy. This also lowers Q_{vis}.

The last column in table I shows the mean energy for each of the x-ray tube settings used. At 30 kVp the mean energy is close to the design energy but at 50 kVp the mean energy is already 30% higher than the design energy. This has a clear impact on the quality of the interference pattern and is reflected by a much lower visibility.

Table I: Visibility and mean x-ray beam energy as a function of the x-ray tube voltage

X-ray tube voltage (kVp)	Q_{vis} (%)	Mean X-ray energy (keV)
30	24.8	24.2
35	18.9	26.0
40	14.8	27.9
45	12.7	29.0
50	10.1	30.2

VII. EXAMPLE IMAGES

Figure 6 shows one slice of the reconstructed volume of the absorption image (left), phase image (middle) and dark field image (right) of a gold fish in ethanol. The images where taken at 40 kVp with projections taken every 0.7°. At each projection angle, six G_0 grating positions were used. Intermediate flat-field were acquired every 20 projections. The dark field image tends to enhance the edges and sometimes shows very small structure that have a low or no contrast in the absorption image. The phase image on the other hand improves the contrast in some soft tissue. This can be seen in the area indicated by the green square. Figure 7 shows an enlarged image of this ROI. The phase contrast image shows some additional soft tissue towards the middle of the image. This tissue is barely visible in the attenuation image.

Figure 8 shows 3D rendered images of a spider. The left image is the classical absorption image. The middle image shows a color-coded representation of the phase shift introduced by the spider. The dark field image on the right clearly shows the very thin leg structures that are barely visible in the absorption image.

VIII. CONCLUSION AND FUTURE WORK

We have built an in-vivo CT system that allows acquiring absorption images, phase contrast images and dark field images in a single scan. The first reconstruction results from this prototype show that a combination of mechanical stabilization and data pre-correction makes it possible to obtain good phase contrast and dark-field images.

We are looking into ways to increase the sensitivity such as thinning the grating support structure (less absorption). This will help to keep the animal dose to an acceptable level and reduce the total scan time.

Using higher grating structures in G_0 and G_2 will allow us to work at higher x-ray tube voltages while maintaining sufficient absorption power. This will move the mean x-ray beam energy closer to the design energy of the gratings and consequently improve the visibility of the interference patterns.

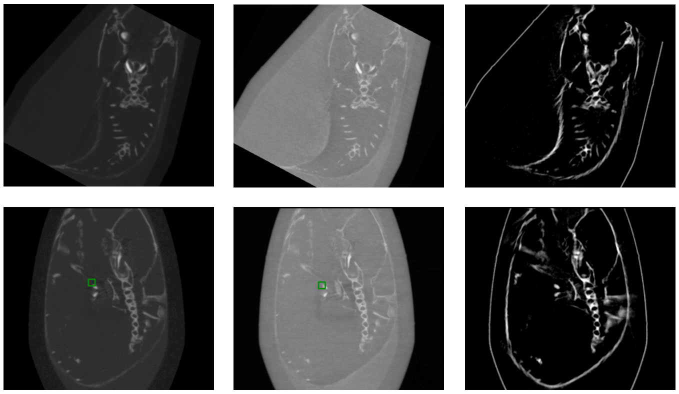

Fig. 6: Virtual slices through the reconstructed absorption image (left), phase image (middle) and dark field image (right) of a gold fish.

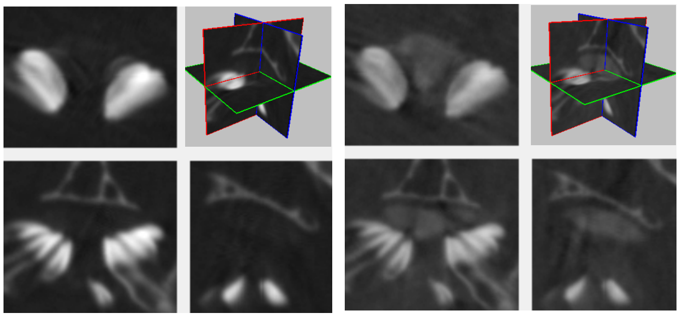

Fig. 7: Three orthogonal slices in the green box drawn on the absorption image and phase image of the gold fish.

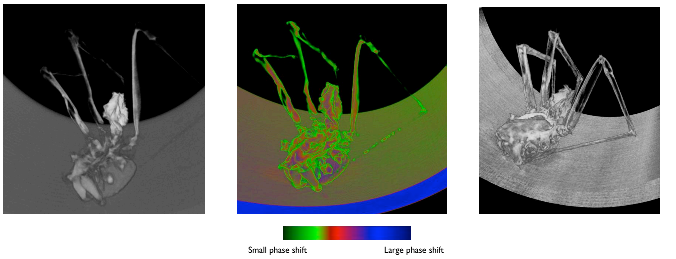

Fig. 8: 3D rendering of the reconstructed absorption image (left), color-coded phase contrast image (middle) and dark field image (left) of a spider.

REFERENCES

[1] M. Bech et al., Phys. Med. Biol 55 (2010), 5529-5539

[2] F. Pfeiffer, T. Weitkamp, O. Bunk, and C. David, *Nature Phys.* **2** (2006) 258-261.

[3] F. Pfeiffer, M. Bech, O. Bunk, P. Kraft, E.F. Eikenberry, C. Brönnimann, C. Grünzweig, and C. David, *Nature Mat.* **7**, (2008) 134-137.

[4] Engelhardt et al., Journal of microscopy (2008),145-157

[5] F. Pfeiffer et al., Nuclear Instruments and Methods in Physics Research A 580 (2007) 925–928
[6] A.Tapfer et al., Medical Physics 38 (2011), 5910-5916

Improved ordered subsets algorithm for 3D X-ray CT image reconstruction

Donghwan Kim, Debashish Pal, Jean-Baptiste Thibault, and Jeffrey A. Fessler

***Abstract*—Statistical image reconstruction methods improve image quality in X-ray CT, but long compute times are a drawback. Ordered subsets (OS) algorithms can accelerate convergence in the early iterations (by a factor of about the number of subsets) provided suitable "subset balance" conditions hold. OS algorithms are most effective when a properly scaled gradient of each subset data-fit term can approximate the gradient of the full data-fidelity term. Unfortunately, this property can fail in the slices outside a region-of-interest (ROI) of 3D CT geometries where sampling becomes limited, particularly for large numbers of subsets, leading to undesirable results. This paper describes a new approach to scaling the subset gradient for a regularized OS algorithm so that it better approximates the full gradient outside the ROI. We demonstrate that the new scaling factors improve stability and image quality in helical CT geometry, even for a very large number of subsets.**

I. INTRODUCTION

Statistical image reconstruction methods can improve resolution and reduce noise and artifacts by minimizing a cost function that models the physics and statistics in X-ray CT [1]. The primary drawback of these methods is their computationally expensive iterative algorithms. Ordered subsets (OS) algorithms group the projection data into (ordered) subsets and update the image each sub-iteration using one forward and back projection of just one subset [2], [3]. OS methods can accelerate convergence (by a factor of about L, the number of subsets) in the early iterations, so it is desirable to use many subsets[1]. OS methods are most effective when suitable "subset balance" conditions hold. Unfortunately, the "long object problem" in CT hampers subset balance, particularly for large L. This paper describes a new approach that improves OS methods for helical CT with large L (many subsets).

In CT, the user defines a target region-of-interest (ROI) for reconstruction. Iterative reconstruction algorithms must estimate more voxels than the ROI to model the measured data completely. In particular, in helical CT, extra slices are needed at each end of the volume (expanding the z dimension) due to the "long-object problem" [5]. Estimating correctly these slices outside the ROI is important as they may impact the estimation of voxels inside the ROI. In helical CT, these extra slices are only sparsely sampled by the projection views (see Fig. 1(a)). This sparse sampling can lead to very imbalanced subsets, particularly for large L, which can destabilize standard OS methods, degrading image quality.

The idea underlying regularized OS algorithms for CT is to use the gradient of a subset of the data fidelity term to approximate the gradient of the full data-fit term. Standard regularized OS algorithms simply scale the subset gradient by the constant L [3]. This works fine in 2D, but does not account for the sampling geometry outside ROI in helical CT, leading to degraded images particularly for large L. Section II-C proposes new scaling factors that stabilize the regularized OS algorithm for helical CT. The idea may be translated to other geometries with non-uniform geometric sampling. Like standard OS algorithms, the proposed approach is not guaranteed to converge (except for the one subset version).

OS algorithms can be modified so that they converge by introducing relaxation [6], reducing L, or by incremental optimization transfer [7]. The new scaling factors could be combined with such methods. Unfortunately, such methods converge slower than standard OS algorithms. Section III investigates practical methods for improving image quality of regularized OS algorithms without slowing initial convergence.

Results with real helical CT data illustrate that the proposed approach provides improved image quality and better convergence behavior than the ordinary OS algorithm in [3].

II. THEORY

We reconstruct an image $x = (x_1, \ldots, x_N) \in \mathbb{R}^N$ from noisy measurement data $y \in \mathbb{R}^M$ by minimizing a penalized weighted least-squares cost function [1]:

$$\begin{aligned}\Psi(x) = Q(x) + \beta R(x) &= \frac{1}{2}||y - Ax||_W^2 + \beta R(x) \\ &= \sum_{i=1}^{M} q_i([Ax]_i) + \beta \sum_{k=1}^{K} \psi_k([Cx]_k), \end{aligned} \tag{1}$$

where $A = \{a_{ij}\}$ is a projection matrix, $C = \{c_{kj}\}$ is a finite differencing matrix, the diagonal matrix $W = \mathsf{diag}\{w_i\}$ provides statistical weighting, and $q_i(t) = \frac{1}{2}w_i(t - y_i)^2$, each $\psi_k(t)$ is a potential function, and β is a regularization parameter.

A. Separable quadratic surrogate (SQS) algorithm

In this paper, we consider OS algorithms for minimizing the cost function (1) that are based on separable quadratic surrogate (SQS) methods [3] that update all voxels simultaneously:

$$x_j^{(n+1)} = x_j^{(n)} - \frac{1}{d_j}\left([A'W(Ax^{(n)} - y)]_j + \beta \frac{\partial}{\partial x_j} R(x^{(n)})\right), \tag{2}$$

D. Kim and J. A. Fessler are with the Dept. of Electrical Engineering and Computer Science, University of Michigan, Ann Arbor, MI 48109 USA (e-mail:kimdongh@umich.edu, fessler@umich.edu).

D. Pal and J.-B. Thibault are with GE Healthcare, Waukesha, WI 53188 USA (e-mail:debashish.pal@ge.com, jean-baptiste.thibault@med.ge.com).

Supported in part by GE Healthcare and NIH grant R01-HL-098686.

[1] Regularized OS algorithms with large L will have increased compute time per iteration due to repeated computation of the regularizer gradient, but this problem has been reduced in [4].

where we use a precomputed denominator d_j [3]. The denominator $d_j = d_j^Q + \beta d_j^R$ consists of $d_j^Q = [A'WA1]_j$ for the data-fit term and $d_j^R = [|C|'\Lambda|C|1]_j$ for the regularizer using maximum penalty curvature in [3], where $|C| = \{|c_{kj}|\}$ and $\Lambda = \mathsf{diag}\left\{\max_t \ddot{\psi}_k(t)\right\}$. This paper focuses on OS-SQS algorithms, but the proposed ideas are applicable to other OS algorithms.

B. Ordered subsets (OS) algorithm

An OS algorithm for accelerating the SQS update (2) has the following lth sub-iteration at the nth iteration:

$$x_j^{(n+\frac{l+1}{L})} = x_j^{(n+\frac{l}{L})} - \frac{1}{d_j}\left(\hat{\gamma}_j^{(n+\frac{l}{L})}[A_l'W_l(A_l x^{(n+\frac{l}{L})} - y_l)]_j + \beta\frac{\partial}{\partial x_j}R(x^{(n+\frac{l}{L})})\right), \tag{3}$$

where l is the subset index. We count one iteration when all subsets are used once.

The update (3) would accelerate the SQS algorithm by exactly L if the scaling factor $\hat{\gamma}_j^{(n+\frac{l}{L})}$ satisfied the condition:

$$\hat{\gamma}_j^{(n+\frac{l}{L})} = \frac{[A'W(Ax^{(n+\frac{l}{L})} - y)]_j}{[A_l'W_l(A_l x^{(n+\frac{l}{L})} - y_l)]_j}. \tag{4}$$

This factor would be expensive to compute, so the conventional OS approach is to simply use the constant $\gamma = L$. This "approximation" often works well in the early iterations when the subsets are suitably "balanced," but in general the errors caused by the differences between $\hat{\gamma}_j^{(n+\frac{l}{L})}$ and γ cause OS methods to approach a limit-cycle that loops around the optimum of the objective function (1) [6], [7]. The next section describes a new approximation to the scaling factor $\hat{\gamma}_j^{(n+\frac{l}{L})}$ in (4) that stabilizes OS for helical CT.

C. OS algorithm with proposed scaling factors

The constant scaling factor $\gamma = L$ used in the ordinary regularized OS algorithm is reasonable when all the voxels are sampled uniformly by the projection views in all the subsets. But in geometries like helical CT, the voxels are non-uniformly sampled. In particular, voxels outside the ROI are sampled by fewer projection views than voxels within the ROI (see Fig. 1(a)). We propose to use a voxel-based scaling factor γ_j that considers the sampling rather than a constant factor γ. After investigating several candidates, we focused on the following scaling factor:

$$\gamma_j = \sum_{l=1}^{L} I_{\{[A_l'W_l A_l 1]_j > 0\}}, \tag{5}$$

where $I_{\{B\}} = 1$ if B is true or 0 otherwise. As expected, $\gamma_j < L$ for voxels outside the ROI and $\gamma_j = L$ for voxels within the ROI.

Fig. 1(b) shows that the OS algorithm using the proposed scaling factors (5) provides better image quality than the ordinary OS approach which does not converge outside the ROI. The instability seen with the ordinary OS approach may also degrade image quality within the ROI as seen by the noise standard deviations in Fig. 1(b). Fig. 2 further shows that the ordinary OS algorithm within ROI is unstabilized due to the instability outside ROI, whereas the proposed OS algorithm being robust.

We precompute (5) and the data-fit denominator $d_j^Q \triangleq [A'WA1]_j = \sum_{l=1}^{L}[A_l'W_l A_l 1]_j$ simultaneously to minimize the overhead of computing (5). We store (5) as a short integer for each voxel outside the ROI only, so it does not require significant memory.

III. FURTHER REFINEMENTS OF OS ALGORITHM

Although the new scaling factors (5) stabilize OS and improve image quality, the final image quality still is worse than a convergent algorithm (see Fig. 1(b)) because any OS method with constant scaling factors will not converge. This section discusses some practical methods that can improve image quality while maintaining reasonably fast convergence rates. These approaches help the OS algorithm come closer to

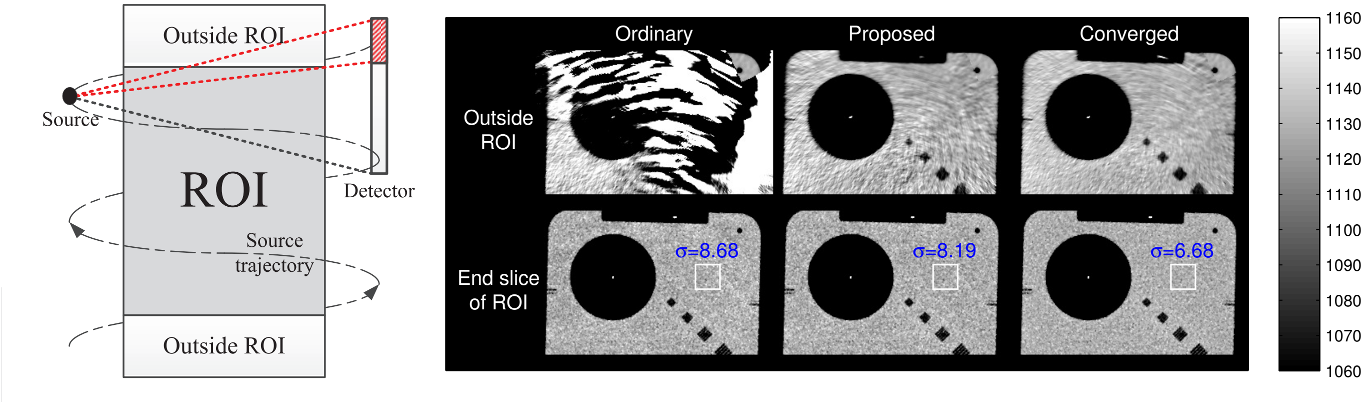

(a) (b)

Fig. 1. Helical geometry and reconstructed images in the geometry: (a) Diagram of helical geometry. A (red) dashed region indicates the detector which acquires measurement data contributed by both voxels in ROI and voxels outside ROI. (b) Effect of gradient scaling in regularized OS-SQS algorithm with GE performance phantom (GEPP) in helical geometry: Each image is reconstructed after running 30 iterations of OS algorithm with 328 subsets, using ordinary and proposed scaling approaches. Standard deviation σ of a uniform region (in white box) is computed for comparison. (Several iterations of a convergent algorithm as a reference)

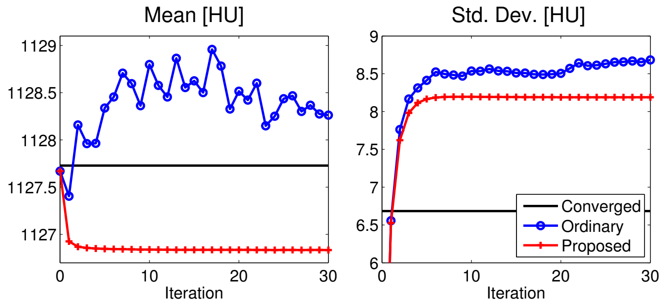

Fig. 2. Mean and standard deviation within an uniform region of end slice of ROI (See Fig. 1(b)) vs. iteration, showing the instability of ordinary OS approach compared with the proposed OS approach.

the converged image, reducing the undesirable noise in images reconstructed using OS algorithms with large L.

We investigated these methods using helical CT scans of the GE performance phantom (GEPP), shown in Fig. 4. We used mean and standard deviation of an uniform region to measure noise, full width at half maximum (FWHM) of a tungsten wire to measure resolution, and a root mean square difference (RMSD) between the OS image and a converged reference image.

A. Transition to small number of subsets

OS algorithm with large L is preferred for faster convergence, but it approaches a limit cycle leading to noisier images than to a converged solution. Using fewer subsets leads to images closer to the solution but slower convergence. A practical solution is to have fast initial convergence with many subsets and subsequently switch to fewer subsets to achieve a desirable final image. SQS converges slower for high spatial frequencies [8], and Table. I shows that an impulsive wire converges slowly for fewer subsets. Thus, the transition point must be chosen carefully to achieve fast convergence and desirable image quality. We found that 20 iterations with 328 subsets followed by 10 iterations with 82 subsets provided a reasonable balance between resolution and noise.

Because (5) depends on L, the transitioning approach requires computing another set of γ_j factors for the smaller number of subsets. For the choice of switching from 328 to 82 subsets, we can precompute both $\gamma_{j,328}$ and $\gamma_{j,82}$ efficiently along with the precomputed data-fit denominator using the following equations:

$$\gamma_{j,328} = \sum_{p=1}^{82} \sum_{l=4p-3}^{4p} I_{\{[A_l' W_l A_l 1]_j > 0\}}$$

$$\gamma_{j,82} = \sum_{p=1}^{82} I_{\{\sum_{l=4p-3}^{4p} I_{\{[A_l' W_l A_l 1]_j > 0\}} > 0\}}. \qquad (6)$$

Because 328 is divisible by 82, each group of 4 consecutive subsets out of 328 subsets matches one of the 82 subsets.

B. Averaging sub-iterations at termination

To ensure convergence, [7] proposed to average previous sub-iterations, but the greatly increased memory space required has prevented its application in 3D X-ray CT. As a practical alternative, we investigated an approach where the final image is formed by averaging all of the sub-iterations of the final iteration of the OS algorithm (after it approaches its

	Smoothed	Number of subsets			Suggested approaches			Conv.
	FBP	82	246	328	Trans.	Aver.	Tr.&Av.	
Mean [HU]	1126.2	1126.2	1125.4	1125.2	1126.2	1126.3	1126.4	1126.4
Std. Dev. [HU]	2.22	6.91	7.58	8.02	7.01	7.38	6.97	6.81
FWHM [mm]	1.36	0.72	0.61	0.60	0.61	0.60	0.61	0.59
RMSD [HU]	18.48	2.20	2.99	4.03	1.58	2.31	1.36	·

TABLE I
NOISE, RESOLUTION AND RMSD BEHAVIOR OF OS ALGORITHM FOR EACH APPROACHES AFTER 30 ITERATIONS, COMPARED WITH SMOOTHED FBP AND CONVERGED IMAGE.

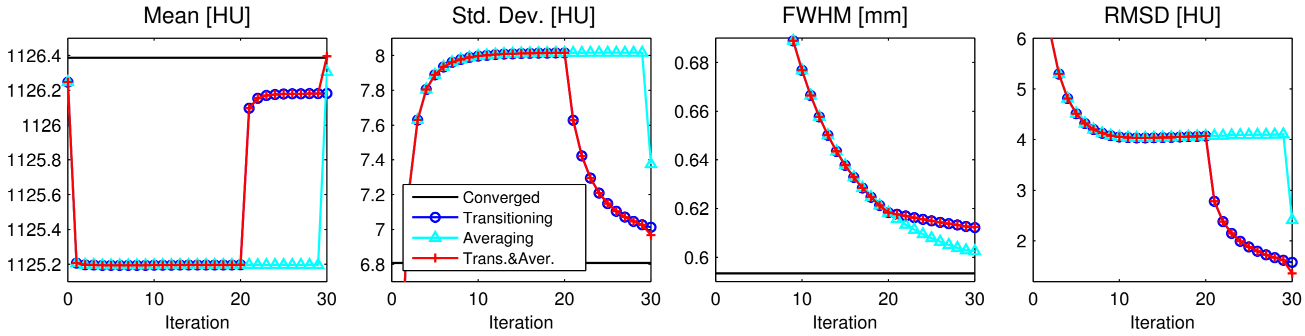

Fig. 3. Noise (mean and std. dev.), resolution (FWHM) and RMSD of OS-SQS with three suggested approaches vs. iteration. Three methods improved image quality of OS algorithm without slowing down the fast convergence rate.

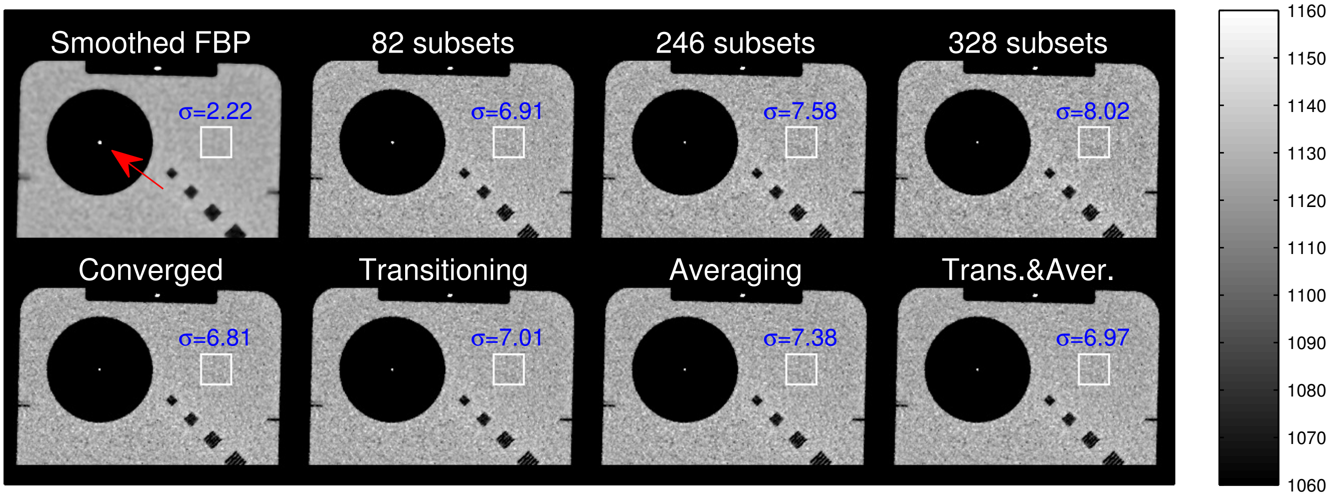

Fig. 4. Smoothed FBP, converged image and OS-SQS reconstructed images after 30 iterations. We used the uniform region within the white box to measure the noise level and σ indicates the standard deviation of the uniform region. We computed the FWHM of a wire (red arrow) to measure the resolution.

limit cycle). We ran 30 iterations of 328 subsets and averaged the 328 sub-iterations of the final iteration. A memory-efficient implementation of this approach uses a recursive in-place calculation:

$$\bar{x}^{(\frac{l+1}{L})} = \frac{l}{l+1}\bar{x}^{(\frac{l}{L})} + \frac{1}{l+1}x^{(\frac{l+1}{L})}, \qquad (7)$$

where $\bar{x}^{(1)}$ is the final averaged image.

We also investigated the combination of transitioning and averaging approaches. We averaged the 82 sub-iterations of the final iteration, after running 20 iteration of 328 subsets and 10 iterations of 82 subsets.

C. Results

We examined the effects of the three suggested methods applied to OS algorithms with 328 subsets. Fig. 4 shows the smoothed filtered back-projection (FBP) image and converged reference image, where we use the smoothed FBP image as the initial condition for the iterative algorithms. Table. I, Fig. 3 and Fig. 4 show that all methods help improve overall image quality, whereas the resolution slightly degraded compared with solely using 328 subsets. Both transitioning and averaging greatly helped reducing the noise in the images.

Transitioning to small number of subsets decreased the noise level but using fewer subsets impacted somewhat the convergence of high-frequency structures in the image. In contrast, averaging sub-iterations over the last iteration maintained the resolution level but the noise did not decrease as much as the transitioning approach. A combination of both the approaches compensates for the drawbacks of each and is a feasible solution.

IV. DISCUSSION

We proposed a new scaling approach (5) for a regularized OS algorithm that provides an efficient solution for non-uniformity in the sampling geometry such as in helical CT. This approach reverts to the standard regularized OS algorithm in the middle of the ROI where the voxels are all well sampled, but stabilizes the images in the slices outside of the ROI where the standard constant scaling factor leads to over-correction, particularly when using many subsets. In addition, we investigated some practical approaches for improving the image quality after OS approaches a limit cycle, namely, transitioning to fewer subsets and averaging the sub-iterations of the final iteration. Preliminary results suggest that these methods can improve the overall image quality of OS algorithms when using numerous subsets without unduly affecting the convergence rate. Future work includes seeking a theoretical justification for the proposed scaling factors (5).

REFERENCES

[1] J-B. Thibault, K. Sauer, C. Bouman, and J. Hsieh, "A three-dimensional statistical approach to improved image quality for multi-slice helical CT," *Med. Phys.*, vol. 34, no. 11, pp. 4526–44, Nov. 2007.
[2] H. M. Hudson and R. S. Larkin, "Accelerated image reconstruction using ordered subsets of projection data," *IEEE Trans. Med. Imag.*, vol. 13, no. 4, pp. 601–9, Dec. 1994.
[3] H. Erdoğan and J. A. Fessler, "Ordered subsets algorithms for transmission tomography," *Phys. Med. Biol.*, vol. 44, no. 11, pp. 2835–51, Nov. 1999.
[4] J. H. Cho and J. A. Fessler, "Accelerating ordered-subsets image reconstruction for X-ray CT using double surrogates," in *Proc. SPIE 8313, Medical Imaging 2012: Phys. Med. Im.*, 2012, To appear at 8313-69.
[5] M. Defrise, F. Noo, and H. Kudo, "A solution to the long-object problem in helical cone-beam tomography," *Phys. Med. Biol.*, vol. 45, no. 3, pp. 623–43, Mar. 2000.
[6] S. Ahn and J. A. Fessler, "Globally convergent image reconstruction for emission tomography using relaxed ordered subsets algorithms," *IEEE Trans. Med. Imag.*, vol. 22, no. 5, pp. 613–26, May 2003.
[7] S. Ahn, J. A. Fessler, D. Blatt, and A. O. Hero, "Convergent incremental optimization transfer algorithms: Application to tomography," *IEEE Trans. Med. Imag.*, vol. 25, no. 3, pp. 283–96, Mar. 2006.
[8] K. Sauer and C. Bouman, "A local update strategy for iterative reconstruction from projections," *IEEE Trans. Sig. Proc.*, vol. 41, no. 2, pp. 534–48, Feb. 1993.

Distance-driven binning for proton CT filtered backprojection along most likely paths

Simon Rit and Nicolas Freud and David Sarrut and Jean-Michel Létang

***Abstract*—We propose to account for curved most likely paths of protons in proton CT using an approximate adaptation of filtered backprojection algorithms. The protons are first binned in several proton radiographies at different distances to the source of protons. The adequate radiography is then used during backprojection depending on the distance to the source. The efficiency of the distance-driven binning on spatial resolution is demonstrated on a Monte Carlo simulated phantom with a circular trajectory and a cone-beam of protons.**

I. INTRODUCTION

Proton computed tomography (pCT) has been considered very early in the history of CT [1] with a continuous development until the beginning of the eighties. This development was then slowed down because the ratio between benefits and cost was too low compared to photon CT scanners. In the nineties, the development of proton therapy has triggered new developments on pCT scanners [2].

There are indeed a few advantages of pCT over photon CT that are foreseen. The main expectation is the reduction of the uncertainty in the proton therapy planning due to the lack of accuracy of the proton stopping power computed from Hounsfield units [3]. Another potential benefit is the reduction of the imaging dose thanks to the Bragg curve characterizing the dose deposit of protons in matter [4], [5]. Finally, pCT is an additional modality which could have its own advantages for improving the diagnostic [6].

However, pCT has also one major drawback, its lack of spatial resolution. Indeed, protons traversing matter undergo multiple deflections due to Multiple Coulomb Scattering (MCS), resulting in curved trajectories and blurred proton radiographies [7]. Therefore, in the past decade, most efforts have focused on improving the spatial resolution of pCT by constructing most likely proton paths [5], [8], [9]. So far, these estimates have either been used to reconstruct pCT images using iterative algorithms [10], or to eliminate protons that had not followed straight lines before applying filtered backprojection (FBP) algorithms [4]. Indeed, to our knowledge, it is always claimed in pCT that FBP can only be applied to straight acquisition lines, probably because exact FBP has only been proposed along straight acquisition lines [11].

In this article, we propose a new FBP algorithm for pCT using curved most likely paths of protons. We have previously shown [12], as well as others, that approximate FBP algorithms for motion compensation along curved acquisition lines are efficient. The assumption of those algorithms is that local compensation of the deformation corrects for the motion blur and improves spatial resolution. In pCT, the problem is different because one records individual proton information which requires specific handling. We propose a distance-driven binning of protons in several radiographies located at different distances to the source to adapt the binning depending on the intersection of proton paths with each radiography.

II. PCT RECONSTRUCTION PROBLEM

Along its path, a proton loses most of its energy via inelastic collisions if it does not undergo nuclear interactions [13]. The local energy loss dE at point $\boldsymbol{x} \in \mathbb{R}^3$ is given by

$$-\frac{dE}{dx}(\boldsymbol{x}) = \eta(\boldsymbol{x}) S(I(\boldsymbol{x}), E(\boldsymbol{x})) \tag{1}$$

where $\eta : \mathbb{R}^3 \to \mathbb{R}$ is the relative electron density with respect to a reference medium (water in this study), $S : \mathbb{R}^2 \to \mathbb{R}$ is the proton stopping power in water given by the Bethe-Bloch equation [14] and $I : \mathbb{R}^3 \to \mathbb{R}$ is the ionization potential which depends on the tissue characteristics.

The ionization potential I varies moderately in human tissues and has a limited effect on S so, in pCT, it is typically approximated to that of water, i.e., $I(\boldsymbol{x}) = I_{water} = 69\,\text{eV}\ \forall \boldsymbol{x} \in \mathbb{R}^3$ in our simulations. Under this assumption, integrating Equation 1 leads to the line integral

$$\int_{\boldsymbol{\Gamma}_i} \eta(\boldsymbol{x}) d\boldsymbol{x} = \int_{E_i^{out}}^{E_i^{in}} \frac{1}{S(I_{water}, E)} dE = G(E_i^{in}, E_i^{out}) \tag{2}$$

with $\boldsymbol{\Gamma}_i(t) \in \mathbb{R}^3$ the curved trajectory of the proton, function of time $t \in \mathbb{R}$, $i \in \mathbf{I} \subset \mathbb{Z}$ the proton index, E_i^{in}, E_i^{out} the entrance and exit energies of the proton, and $G : \mathbb{R}^2 \to \mathbb{R}$ the function that computes the energy integral from E_i^{in} and E_i^{out}, defined for simpler notations in the following. Finding η from E_i^{in}, E_i^{out} and an estimate of the path $\boldsymbol{\Gamma}_i$ for a set $\mathbf{I}$ of protons is the pCT reconstruction problem.

Proton path estimation is a crucial problem in pCT reconstruction because it directly influences the spatial resolution [7]. Several solutions have been proposed to the problem of most likely path (MLP) estimation [5], [8], [9]. These recent works on MLP estimation rely on pCT scanners such as the apparatus described in [2] which measures the position and the direction of each proton, before and after traversing the object. Similarly, we assumed a cone-beam pCT scanner with a proton source following a circular trajectory $\boldsymbol{a}(t) \in \mathbb{R}^3$ around the axis defined by the isocenter $\boldsymbol{o} \in \mathbb{R}^3$ and the

---

S. Rit, N. Freud, D. Sarrut and J.-M. Létang are with the Université de Lyon, CREATIS; CNRS UMR5220; Inserm U1044; INSA-Lyon; Université Lyon 1; Centre Léon Bérard, France (e-mail: simon.rit@creatis.insa-lyon.fr). This work is supported by the grant ProTom of the *ITMO Cancer et Technologie* in the *Plan Cancer 2009-2013* program.

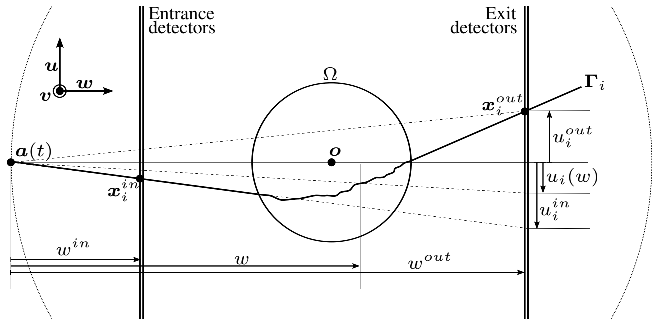

Fig. 1. Schematic top view of the pCT scanner used in this study. The signed distances w^{out}, w^{in}, w and u_i^{out}, u_i^{in}, $u_i(w)$ are used in Equation 4, 5 and 6, respectively.

unit axis $\boldsymbol{v} \in \mathbb{R}^3$, and two pairs of flat panels located before and after the scanned object to record their entrance and exit positions and directions $\boldsymbol{x}_i^{in}, \boldsymbol{x}_i^{out}, \dot{\boldsymbol{x}}_i^{in}, \dot{\boldsymbol{x}}_i^{out} \in \mathbb{R}^3$ (Figure 1). We define the unit vectors $\boldsymbol{u}, \boldsymbol{w} : \mathbb{R}^3 \to \mathbb{R}^3$ depending on the source position, with $\boldsymbol{w}(\boldsymbol{a}(t)) = -\boldsymbol{a}(t)/\|\boldsymbol{a}(t)\|_2$ and $\boldsymbol{u}(\boldsymbol{a}(t)) = \boldsymbol{v} \times \boldsymbol{w}(\boldsymbol{a}(t))$, to have a 3D Cartesian coordinate system $\{\boldsymbol{u}, \boldsymbol{v}, \boldsymbol{w}\}$ rotating with the source and the detectors. We also assumed that the convex hull of the object $\Omega \subset \mathbb{R}^3$ was known which can practically be measured with a surface scanner or a rough initial reconstruction. The algorithm proposed in this work is applicable to any MLP estimation from measured spatial information ($\boldsymbol{x}_i^{in}$, $\dot{\boldsymbol{x}}_i^{in}$, $\boldsymbol{x}_i^{out}$, $\dot{\boldsymbol{x}}_i^{out}$ and Ω).

III. DISTANCE-DRIVEN BINNING

Our objective is to adapt existing filtered backprojection algorithms for pCT reconstruction. So far, previous works in that direction have binned proton information in virtual proton radiographies. Let $j \in \mathbf{J} \subset \mathbb{Z}^2$ be a set of spatial indices corresponding to a grid of pixels of the exit panel and $h : \mathbb{R}^2 \to \mathbb{R}$ their indicators,

$$h_j(\boldsymbol{y}) = \begin{cases} 1 & \text{if } \boldsymbol{y} \in \mathbb{R}^2 \text{ is in the } j^{\text{th}} \text{ pixel,} \\ 0 & \text{else.} \end{cases} \tag{3}$$

The virtual proton radiography binned at the exit detector for a subset of protons $\mathbf{I}_a \subset \mathbf{I}$ emitted from a same source position $\boldsymbol{a}$ is

$$g_{j,\boldsymbol{a}}^{out} = \frac{\sum_{i \in \mathbf{I}_a} h_j(u_i^{out}, v_i^{out}) G(E_i^{in}, E_i^{out})}{\sum_i h_j(u_i^{out}, v_i^{out})} \tag{4}$$

with $u_i^{out} = (\boldsymbol{x}_i^{out} - \boldsymbol{a}) \cdot \boldsymbol{u}(\boldsymbol{a})$ and $v_i^{out} = (\boldsymbol{x}_i^{out} - \boldsymbol{a}) \cdot \boldsymbol{v}$ (Figure 1). Repeating this operation for several source positions, one obtains a typical set of projection images g^{out} that can be used in a standard filtered-backprojection algorithm.

We observe that one could also use the entrance positions $\boldsymbol{x}_i^{in}$ to bin projection images on the exit detector assuming a straight path going through $\boldsymbol{x}_i^{in}$ and the source $\boldsymbol{a}$, i.e.

$$g_{j,\boldsymbol{a}}^{in} = \frac{\sum_{i \in \mathbf{I}_a} h_j(u_i^{in}, v_i^{in}) G(E_i^{in}, E_i^{out})}{\sum_i h_j(u_i^{in}, v_i^{in})} \tag{5}$$

with the distances illustrated in Figure 1

$$\begin{cases} u_i^{in} = \frac{w^{out}}{w^{in}} \left((\boldsymbol{x}_i^{in} - \boldsymbol{a}) \cdot \boldsymbol{u}(\boldsymbol{a})\right), & w^{in} = (\boldsymbol{x}_i^{in} - \boldsymbol{a}) \cdot \boldsymbol{w}(\boldsymbol{a}), \\ v_i^{in} = \frac{w^{out}}{w^{in}} \left((\boldsymbol{x}_i^{in} - \boldsymbol{a}) \cdot \boldsymbol{v}\right) & , w^{out} = (\boldsymbol{x}_i^{out} - \boldsymbol{a}) \cdot \boldsymbol{w}(\boldsymbol{a}). \end{cases}$$

The ratio $\frac{w^{out}}{w^{in}}$ is the constant magnification from the entrance to the exit detection plane produced by a cone-beam focused on $\boldsymbol{a}$ to obtain the coordinates on the exit flat panel. Therefore, if protons were travelling along straight paths, g^{in} and g^{out} would be equal. They are actually different due to MCS.

From this observation, we introduce the concept of distance-driven binning given by

$$g_{j,\boldsymbol{a}}(w) = \frac{\sum_{i \in \mathbf{I}_{\boldsymbol{a}}} h_j(u_i(w), v_i(w)) G(E_i^{in}, E_i^{out})}{\sum_i h_j(u_i(w), v_i(w))} \tag{6}$$

with the distances illustrated in Figure 1

$$\begin{cases} u_i(w) = \frac{w^{out}}{w} \left((\boldsymbol{\Gamma}_i(t_{i,w}) - \boldsymbol{a}) \cdot \boldsymbol{u}(\boldsymbol{a})\right), \\ v_i(w) = \frac{w^{out}}{w} \left((\boldsymbol{\Gamma}_i(t_{i,w}) - \boldsymbol{a}) \cdot \boldsymbol{v}\right). \end{cases}$$

$t_{i,w}$ is the time at which proton i crosses the plane parallel to the detectors at distance w from the source, i.e. , $(\boldsymbol{\Gamma}_i(t_{i,w}) - \boldsymbol{a}) \cdot \boldsymbol{w}(\boldsymbol{a}) = w$. Equation 6 is the extension of Equation 4 and 5 to any distance w using the most likely path $\boldsymbol{\Gamma}_i$ of proton i to interpolate intermediate positions between entrance and exit positions $\boldsymbol{x}_i^{in}$ and $\boldsymbol{x}_i^{out}$. Indeed, as the trajectory $\boldsymbol{\Gamma}_i$ crosses the detectors at positions $\boldsymbol{x}_i^{in}$ and $\boldsymbol{x}_i^{out}$, we have $g(w^{out}) = g^{out}$ and $g(w^{in}) = g^{in}$.

In practice, g is computed at a finite number of distances in the $\boldsymbol{w}$ direction and linear interpolation is used between voxels g_j. In combination with bilinear interpolation between spatial indices j, we obtain a 4D sinogram $g : \mathbb{R}^3 \times \mathbb{Z} \to \mathbb{R}$ instead of the conventional 3D sinogram, e.g. $g^{out} : \mathbb{R}^2 \times \mathbb{Z} \to \mathbb{R}$, where the last dimension is the index of projection images.

IV. DISTANCE-DRIVEN BACKPROJECTION

We use the distance-driven binning in a filtered backprojection algorithm adapted from the Feldkamp-Davis-Kress (FDK) algorithm [15]. As in approximate motion-compensated cone-beam CT [12], we do not modify the 2D processing of projections in the FDK algorithm (the 2D weighting and the ramp filtering) but we repeat it for every depth w. We call $\tilde{g}_{\boldsymbol{a}}$ this 3D filtered projection at position source $\boldsymbol{a}$ corresponding to a source angle $\theta_{\boldsymbol{a}} \in \mathbb{R}$. We use this filtered distance-driven sinogram by accounting during backprojection for the distance to the source of the voxel being backprojected to select the adequate part of the distance-binned sinogram, i.e.

$$\eta(\boldsymbol{x}) = \int_0^{2\pi} \left(\frac{\|\boldsymbol{a}\|_2}{w(\boldsymbol{x})}\right)^2 \tilde{g}_{\boldsymbol{a}}\left(u(\boldsymbol{x}), v(\boldsymbol{x}), w(\boldsymbol{x})\right) d\theta_{\boldsymbol{a}} \tag{7}$$

with $u(\boldsymbol{x}) = \frac{w^{out}}{w(\boldsymbol{x})}((\boldsymbol{x} - \boldsymbol{a}) \cdot \boldsymbol{u})$, $v(\boldsymbol{x}) = \frac{w^{out}}{w(\boldsymbol{x})}((\boldsymbol{x} - \boldsymbol{a}) \cdot \boldsymbol{v})$ and $w(\boldsymbol{x}) = (\boldsymbol{x} - \boldsymbol{a}) \cdot \boldsymbol{w}$. It is worth noting that both the backprojection and its FDK weighting are driven by the same distance to the source $w(\boldsymbol{x})$.

V. EXPERIMENTS

The algorithm was evaluated with Monte-Carlo simulations using the latest release of GATE [16], an end-user software using the Geant4 toolkit [17]. GATE was run on the EGEE computing grid with the GateLab applet [18]. An ideal pCT scanner was simulated: a $200\,\text{MeV}$ mono-energetic point source was placed at distance $w^s = -100\,\text{cm}$ from the

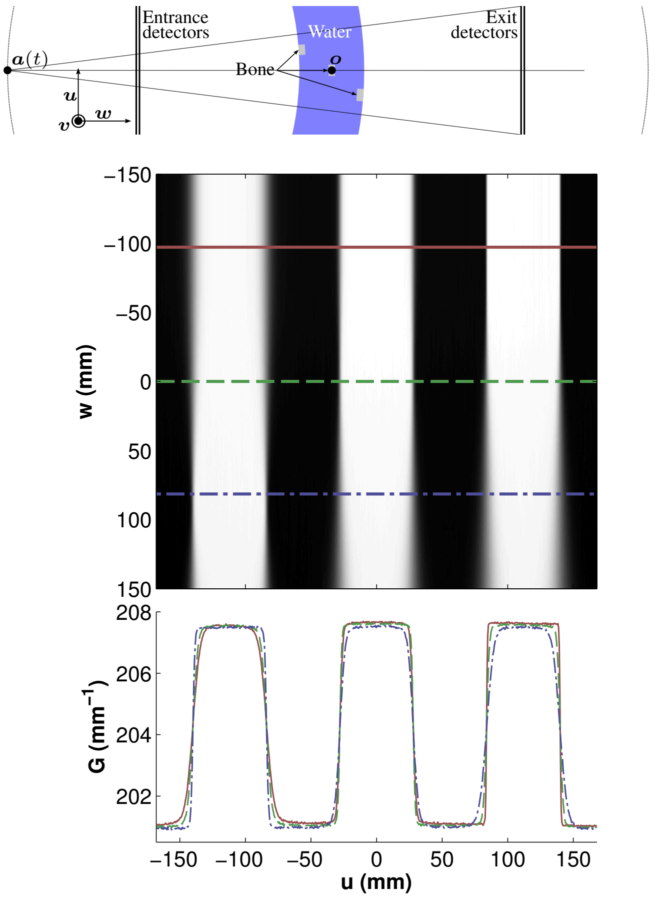

Fig. 2. Experiment 1. Top: drawing of the object. Middle: axial slice at the isocenter of the distance driven binning. Bottom: profiles along the three lines drawn on the top image.

isocenter and the characteristics (E_i^{in}, E_i^{out}, $\boldsymbol{x}_i^{in}$, $\dot{\boldsymbol{x}}_i^{in}$, $\boldsymbol{x}_i^{out}$ and $\dot{\boldsymbol{x}}_i^{out}$) of protons traversing the planes $w^{in} = -60\,\mathrm{cm}$ and $w^{out} = 60\,\mathrm{cm}$ were recorded.

Standard 3σ cuts on energy and angle were applied to eliminate nuclear interactions [13]. Most likely paths $\boldsymbol{\Gamma}_i$ were estimated as straight paths outside Ω and curved paths in Ω according to the maximum likelihood formalism of Schulte *et al* [9]. The object was assumed to be homogeneous and made of water. We closely followed their work for its parameterization.

A. Experiment 1

The first experiment was designed to provide the reader with insights into the effect of the distance-driven binning by looking at one projection image only. We centered a spherical shell of water with radii $90\,\mathrm{cm}$ and $110\,\mathrm{cm}$ around the proton source, therefore placing the isocenter in the middle of the water layer (Figure 2, top). Three spherical bone inserts with identical solid angles were placed in the water sphere with regular radii from the source ($90/92\,\mathrm{cm}$, $99/101\,\mathrm{cm}$ and $108/110\,\mathrm{cm}$). Since all objects are portions of hollow spheres centered on the source, the projection image for particles travelling along straight lines crossing the source would be a rectangular function with one rectangle per insert.

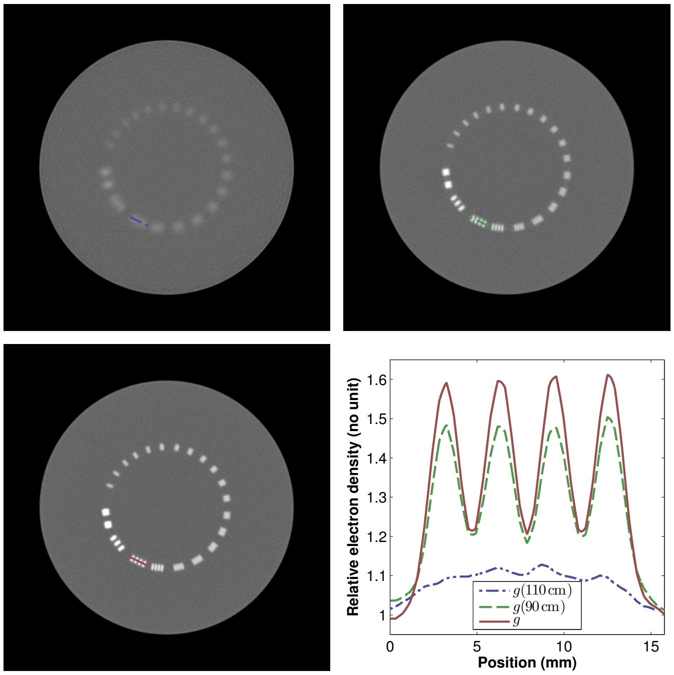

Fig. 3. Experiment 2, full scan. Top-left: axial slice at the isocenter of the standard FDK reconstruction using the 2D set of projection images $g(110\,\mathrm{cm})$ binned according to the position of protons at the exit of the object. Gray window: [0.6,1.6]. Top-right: idem with the sinogram $g(90\,\mathrm{cm})$ at the entrance of the object. Bottom-left: distance-driven FDK reconstruction using the complete set of 3D projections g. Bottom-right: profile along the three segments drawn on each slice.

B. Experiment 2

The second experiment was designed to evaluate the spatial resolution of reconstructed pCT images (Figure 3). We used a resolution phantom similar to the CTP528 high-resolution module of the Catphan phantom (The Phantom Laboratory, Salem NY, USA): various resolution gauges made of $2\,\mathrm{mm}$-thick aluminium sheets were placed on a circle ($\varnothing 10\,\mathrm{cm}$) in a water cylinder ($\varnothing 20\,\mathrm{cm}$).

VI. RESULTS

A. Experiment 1

Figure 2 is an illustration of the effect of distance-driven binning in the projection space. The effect of MCS depended on the distance to the source and the position of the inserts. The edges of the bone inserts were the sharpest at the distance which corresponds to their location in space, i.e. at the level of each line profile (Figure 2, bottom). The loss of sharpness increased with the distance to their location. We also observed that the middle insert was not as sharp on the central profile as the entrance and exit insert on their respective profile because the uncertainty on the estimate of the proton path was higher in the middle of the object than on the borders of the object.

B. Experiment 2

The effect on the reconstruction is shown in Figure 3. The spatial resolution improved with the distance binning compared to the spatial resolution of reconstruction using a

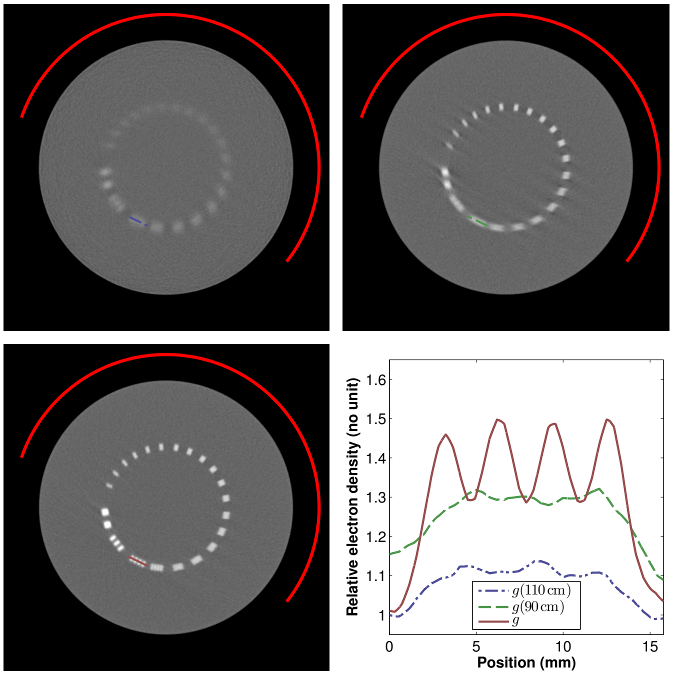

Fig. 4. Experiment 2, short scan. Idem as Figure 3 with an additional circle arc indicating the source trajectory at a false scale ($\varnothing 24\,\mathrm{cm}$ on the figure instead of $\varnothing 200\,\mathrm{cm}$).

standard set of binned projections (Figure 3, bottom left vs. top). We also observed that using the binning g^{in} according to the position of protons before the object is more efficient than using the binning g^{out} according to their exit position (Figure 3, top right vs. top left).

The effect is emphasized when only a subset of projection images is used which corresponds to a short scan (Figure 4). Parker weighting [19] was used to account for the short scan in the reconstructions of Figure 4.

VII. Discussion and Conclusion

We have proposed an algorithm to use curved most likely paths in a pCT filtered backprojection algorithm. Our solution uses a distance driven binning in order to recover sharp edges at the distance where the edge is located in space (Figure 2). During backprojection, the spatial position of each voxel is translated to a distance to the source and the corresponding position of the distance-driven binning is used so that, at the location of each edge, its sharpest binning is used.

This FBP algorithm is as approximate as other FBP algorithms used in pCT since there is no exact solution for curved trajectories. We observed an improved spatial resolution without apparent loss in density resolution (Figure 3) because the algorithm only modifies high frequencies of the sinogram without modifying low frequencies. The algorithm is inspired by our experience in approximate motion compensated FBP reconstruction where limited differences have been observed with iterative reconstruction [12]. However, comparison with existing pCT iterative algorithms will provide a better quantification of the effect of this approximation.

The major advantage of our algorithm over iterative pCT algorithms is faster and on-the-fly reconstruction. These assets could become essential for their use in proton therapy treatment rooms when the reconstructed image is required to check the patient anatomy prior to starting the treatment. In this context, a short scan could also greatly reduce the acquisition time and the imaging dose, for which the use of most likely paths seems crucial.

References

[1] A.M. Cormack, “Representation of a function by its line integrals, with some radiological applications,” *Journal of Applied Physics*, vol. 34, no. 9, pp. 2722–2727, 1963.

[2] R. Schulte *et al.*, “Conceptual design of a proton computed tomography system for applications in proton radiation therapy,” *IEEE Transactions on Nuclear Science*, vol. 51, no. 3, pp. 866–872, 2004.

[3] B. Schaffner and E. Pedroni, “The precision of proton range calculations in proton radiotherapy treatment planning: experimental verification of the relation between CT-HU and proton stopping power,” *Phys Med Biol*, vol. 43, no. 6, pp. 1579–1592, 1998.

[4] G.A.P. Cirrone *et al.*, “Monte carlo evaluation of the filtered back projection method for image reconstruction in proton computed tomography,” *Nucl Inst Meth A*, vol. 658, no. 1, pp. 78–83, 2011.

[5] D. Wang, T.R. Mackie, and W.A. Tomé, “Bragg peak prediction from quantitative proton computed tomography using different path estimates,” *Phys Med Biol*, vol. 56, no. 3, pp. 587–599, 2011.

[6] N. Depauw and J. Seco, “Sensitivity study of proton radiography and comparison with kV and MV x-ray imaging using GEANT4 monte carlo simulations.” *Phys Med Biol*, vol. 56, no. 8, pp. 2407–2421, 2011.

[7] U. Schneider and E. Pedroni, “Multiple coulomb scattering and spatial resolution in proton radiography,” *Med Phys*, vol. 21, no. 11, pp. 1657–1663, 1994.

[8] D.C. Williams, “The most likely path of an energetic charged particle through a uniform medium,” *Phys Med Biol*, vol. 49, no. 13, pp. 2899–2911, 2004.

[9] R. W. Schulte, S. N. Penfold, J. T. Tafas, and K. E. Schubert, “A maximum likelihood proton path formalism for application in proton computed tomography.” *Med Phys*, vol. 35, no. 11, pp. 4849–4856, 2008.

[10] S. Penfold, “Image reconstruction and monte carlo simulations in the development of proton computed tomography for applications in proton radiation therapy,” Ph.D. dissertation, University of Wollongong, 2010.

[11] L. Desbat, S. Roux, and P. Grangeat, “Compensation of some time dependent deformations in tomography,” *IEEE Trans Med Imaging*, vol. 26, no. 2, pp. 261–269, 2007.

[12] S. Rit, D. Sarrut, and L. Desbat, “Comparison of analytic and algebraic methods for motion-compensated cone-beam CT reconstruction of the thorax,” *IEEE Trans Med Imag*, vol. 28, no. 10, pp. 1513–1525, 2009.

[13] R.W. Schulte, V. Bashkirov, M.C. Loss Klock, T. Li, A.J. Wroe, I. Evseev, D.C. Williams, and T. Satogata, “Density resolution of proton computed tomography,” *Med Phys*, vol. 32, no. 4, pp. 1035–1046, 2005.

[14] K Nakamura and Particle Data Group, “Review of particle physics,” *Journal of Physics G: Nuclear and Particle Physics*, vol. 37, no. 7A, p. 075021, 2010.

[15] L.A. Feldkamp, L.C. Davis, and J.W. Kress, “Practical cone-beam algorithm,” *J Opt Soc Am A*, vol. 1, no. 6, pp. 612–619, 1984.

[16] S. Jan *et al.*, “GATE V6: a major enhancement of the GATE simulation platform enabling modelling of CT and radiotherapy.” *Phys Med Biol*, vol. 56, no. 4, pp. 881–901, 2011.

[17] S. Agostinelli *et al.*, “Geant4-a simulation toolkit,” *Nuclear Instruments and Methods in Physics Research Section A: Accelerators, Spectrometers, Detectors and Associated Equipment*, vol. 506, no. 3, pp. 250–303, 2003.

[18] S. Camarasu-Pop, T. Glatard, J.T. Moscicki, H. Benoit-Cattin, and D. Sarrut, “Dynamic partitioning of GATE monte-carlo simulations on EGEE,” *Journal of Grid Computing*, vol. 8, no. 2, pp. 241–259, 2010.

[19] D.L. Parker, “Optimal short scan convolution reconstruction for fanbeam CT,” *Med Phys*, vol. 9, no. 2, pp. 254–257, 1982.

Micro-CT Artifacts Reduction Based on Detector Random Shifting and 3D-Data Inpainting

Yining Zhu, MengLliu Zhao, Hongwei Li, Peng Zhang

***Abstract*—The scanning data errors will lead to heavy artifacts in reconstructed CT images. In the micro-CT systems based on optical coupling detectors, the data errors are mainly caused by the defects of the scintillator and the CCD-camera. In this paper, we propose a data preprocessing method that combines the detector random shifting and the 3D-data inpainting. The proposed method can effectively reduce the artifacts in micro-CT images, which is verified by both the simulation and real micro-CT data.**

***Keywords*—Micro-CT; Detector defects; Artifacts reduction; Detector random shifting; 3D-Data inpainting.**

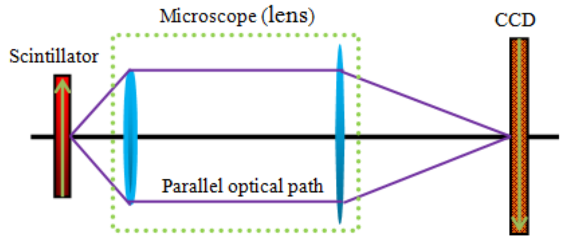

Fig. 1. The structure of OCD for X-ray imaging.

I. INTRODUCTION

In recent years Micro-CT systems have been applied to many areas such as biomedicine, materials, MEMS (Micro-Electromechanical Systems) and CMOS chip, etc. Two kinds of detectors, flat panel detector (FPD) and optical coupling detector (OCD) are typically used in Micro-CT systems. The FPD consists of an x-ray scintillator and amorphous-silicon photodiodes, while the OCD consists of an x-ray scintillator, a set of optical lenses and CCD-camera (See Fig.1) [1]. Generally, the resolution of the OCD is much higher than that of the FPD. However, the efficiency of OCD is much lower than that of FPD.

In this paper, we consider the OCD-based Micro-CT system. In an OCD-type detector, the role of the scintillator is to convert x-ray into visible light, the role of the set of optical lenses is to magnify the visible light image, and the role of the CCD-camera is to convert the magnified visible light image into digital image. In order to obtain a digital image with high resolution by the OCD, the scintillator slice in the OCD should be made very thin. Due to technical and material reasons, there often exist some defects in the scintillator slice. Beside, the CCD-camera may also have bad cells. The defects of the scintillator and the CCD-camera can cause heavy artifacts in the reconstructed 3D CT images.

In this paper, we propose a data preprocessing method that combines the detector random shifting and the 3D-data inpainting. Due to the reason that the OCD-type detector random shifting, the set of the defect areas in 2D images related to full views could not form regular 3D regions. Hence, it is complicated to use 3D-based interpolation method to inpainting the 3D scanned data. The data inpainting algorithm that we employed in this paper is based on PDE (Partial Differential Equations), which can inpainting such scanned in 3D form effectively. The proposed method is verified by both the simulation and real Micro-CT data. The results we obtained by the proposed method are quite satisfied in the artifact reduction.

II. DATA SCANNED BY OCD-TYPE DETECTOR

In an OCD-based Micro-CT system, the x-ray photons emitted from x-ray tube first interact with the inspect object, after penetrating the object the remaining x-ray photons will hit the thin scintillator slice and produce a visible image on the thin slice, and then the visible image on the thin slice is magnified by a set of lens, last is converted into a digital image by CCD-camera [2]. When the object is rotated on the turn table step by step, the images are scanned frame by frame, i.e., the CT data scanned by OCD-type detector.

As mentioned in the introduction, the scintillator may have some defects, due to technical and material reasons. The CCD-camera may also have bad cells. These will lead to some bright speckles when data scanning. In Fig. 2, two images show the typical speckles. The top one is scanned when no object is on the turntable, while the bottom one is scanned when an oil core on the turntable. These speckles will disrupt the projection data, and result in heavy artifacts in the CT images reconstructed by the FDK algorithm.

III. METHOD

The scintillator related to the bright speckle areas could not convert the photons into visible light correctly, which means that the corresponding projection data may be wrong. The FDK algorithm [3] is unable to reconstruct a good quality CT images from such data. The iterative algorithm is flexible to deal with such data. One way is to avoid using the wrong data in iterative processing. However, the number of voxels for a typical 3D CT image are very huge, about 2^{30} to 2^{33}. From such huge data to reconstruct 3D CT images by the iterative algorithm is still a great challenge to practice applications

The authors are with The CT Laboratory, School of Mathematics, Capital Normal University, Beijing, 10048, China; email: zhumilan997@163.com

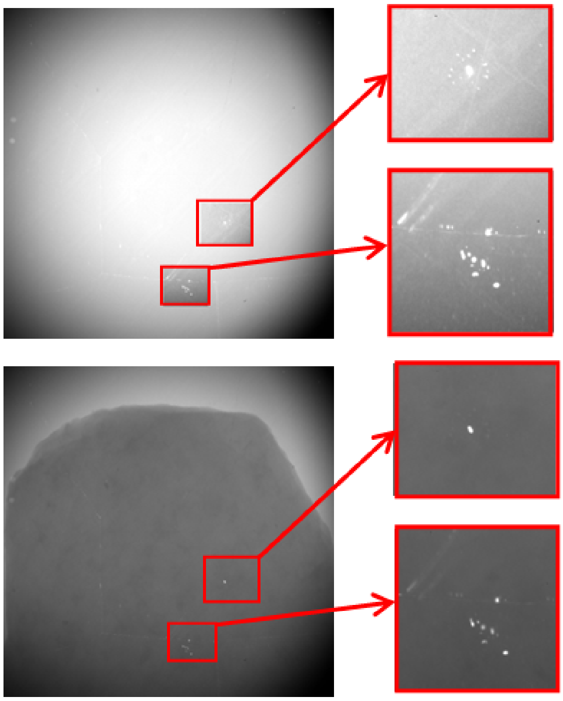

Fig. 2. The imaged by OCD type detector: The top one is scanned when there is no object on turn table; The bottom one is scanned when an oil core on turn table in one view.

because of its huge computational cost. Therefore, we have to choose analytic kind algorithms, such as the FDK, for huge 3D image reconstruction. In order to reducing the artifacts caused by the defects of the scintillator and CCD, we propose a data preprocessing method that combines the detector random shifting and the 3D-data inpainting.

A. Detector random shifting

When the geometric relation between source and the OCD type detector is fixed, and cone-beam data are scanned with a circular source trajectory, then the defect areas in 2D images related to each view will stack some columns in 3D cone-beam data space (See Fig.3(b)). To inpainting the bad data, only the 2D interpolation method could be used. Then inpainting errors become large as the bad data areas increase.

In order to avoid the bad data columns, we let the detector random shift (See Fig.3(a)). But the set of the defect areas in 2D images related to full views could not form regular 3D regions (See Fig.3(c)). Hence, it is complicated to use 3D-based interpolation method to inpainting the bad data.

B. 3D-data inpainting

To overcome the difficulty that the defect areas distribute irregularly (See Fig. 3(c)), we employ PDE (Partial Differential Equations) -based data inpainting algorithm in this paper, which is able to inpainting effectively such irregular 3D bad regions. Digital image inpainting was first introduced by Bertalmio et al. [5] in 1999. Since then, many methods have been proposed. One of the most popular methods proposed by Chan and Shen [6] is TV inpainting, which is close related to the TV restoration model (ROF) [4]. The TV inpainting method is effective for repairing small holes.

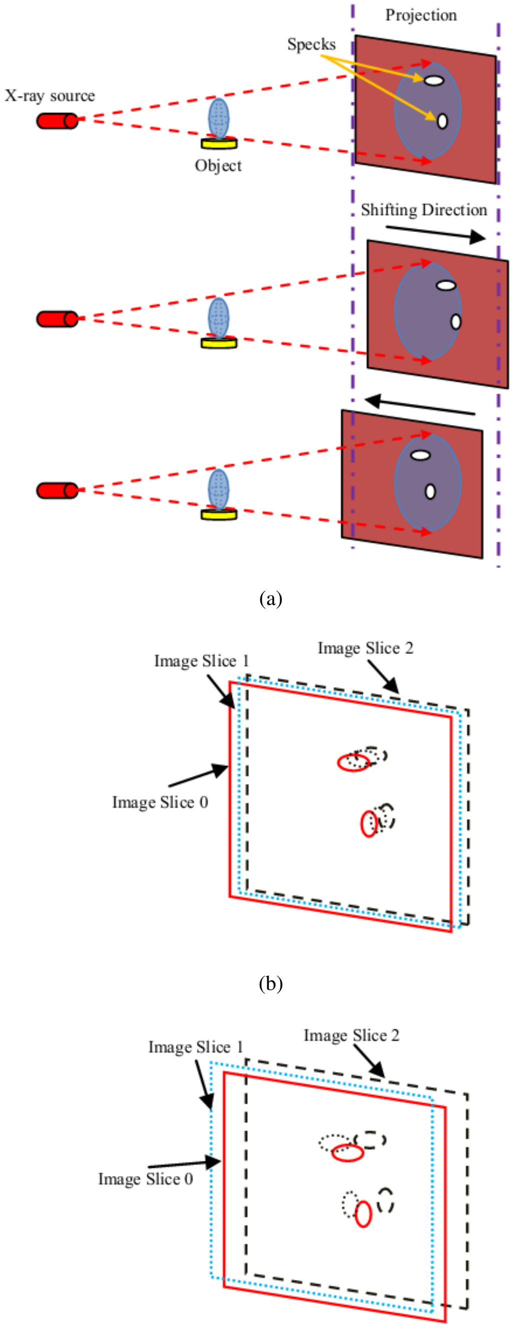

(a)

(b)

(c)

Fig. 3. The schematic diagram of detector random shifting.

Denote the region to be inpainted by D, the neighborhood region of D by E, the original image by u_0, and the inpainting image by u. The TV inpainting model could be written as follows

$$\min \int_E \left[|\nabla u| + \frac{1-\chi_D}{2\lambda}(u-u_0)^2 \right], \qquad (1)$$

where χ_D is the characteristic function of D.

The above minimization problem can be solved by running

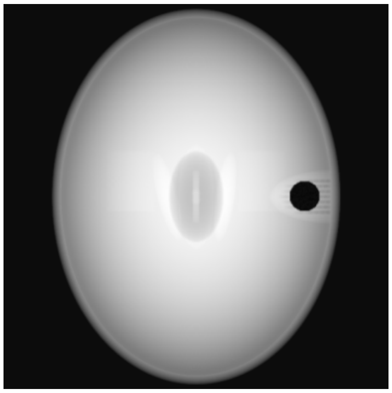

Fig. 4. The simulation projection data with a dug region.

the following equation to steady state

$$u_t = \nabla \cdot \left(\frac{\nabla u}{|\nabla u|_\alpha} \right) - \frac{1-\chi_D}{\lambda}(u - u_0), \qquad (2)$$

where the term $|\nabla u|_\alpha$ is a regularization version of $|\nabla u|$, which is defined as

$$|s|_\alpha = \sqrt{s^2 + \alpha}.$$

IV. EXPERIMENTS

To verify our method, we use two sets of projection data, simulation and real CT data, to carry out the experiments.

A. Images reconstructed from simulation data

We simulate two set of projection data by using the FORBILD head phantom [8] with analytical method. One is simulated with fixed relation between the X-ray source and the detector, the other is simulated with detector random shifting vertical to the normal of the detector. As shown in Fig. 4, all of the projection data are dug a small part with a circle shape. We make a circular trajectory scanning with 360 views. The total number of detector bins is 512 × 512, and the bin size is 10 um × 10 um. The distance from source to object (SOD) is 30 mm, and from source to detector (SDD) is 60 mm.

Fig. 5 is a comparison that show the images reconstructed by FDK algorithm from the different scanning modes and data preprocessing methods. Fig. 5(b) is reconstructed from the data without processing. With inpainting, Fig.5(d) has a much better quality. Fig. 5(e) shows the result reconstructed from the data with both inpainting and random shifting preprocessing, which is the method proposed in this paper. We can see that our method produces the most desired image, which reduces both the ring artifacts and the artifacts caused by the speckles to a large extent.

B. Images reconstructed from real Data

For the real CT data, the size of projection data is 2048 × 2048 × 720, the SOD is 105 mm, the SDD is 120 mm, the magnification factor of microscope is 4 and the size of units in CCD is 13.5 um × 13.5 um (which means the size of virtual pixel in scintillator is 3.375 um × 3.375 um). We also scan two set of data for an oil core with the micro-CT. One is sacnned with fixed relation between the X-ray source and the detector, the other is scanned with detector random shifting within the range of 60 um vertical to the normal of the detector. The slices of reconstructed CT images are shown in Fig. 6. It is obvious that the quality of the image (Fig.6(d)) reconstructed from the data preprocessed by our method is much better than the others.

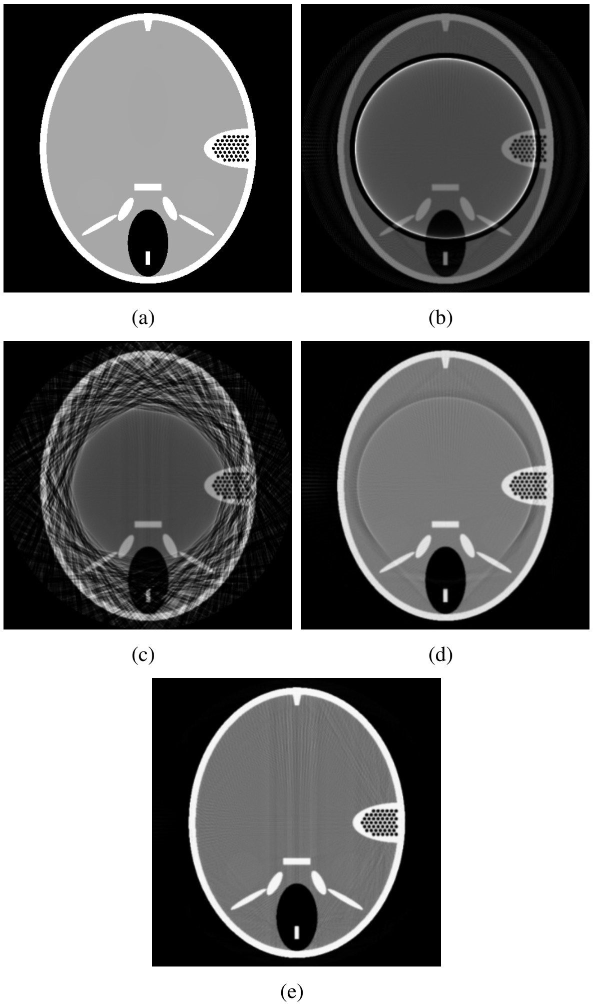

(a) (b)

(c) (d)

(e)

Fig. 5. The comparison that show the transverse section images reconstructed by FDK algorithm from the different scanning modes and data preprocessing methods: (a) ideal image, (b),(c),(d) and (e) are: without processing, detector random shifting only, inpainting only and detector random shifting plus inpainting respectively.

V. CONCLUSION

We have proposed a data preprocessing method that combines the detector random shifting and the 3D-data inpainting. The two techniques are complementary in reducing the artifacts. The experiment results for both simulation and real CT data are quite satisfied in artifacts reduction. The PDE-based inpainting models and especially their fast implementations need to be investigated furthermore.

ACKNOWLEDGMENT

This work was supported in part by the National Natural Science Foundation of China under the grants 60971131 and

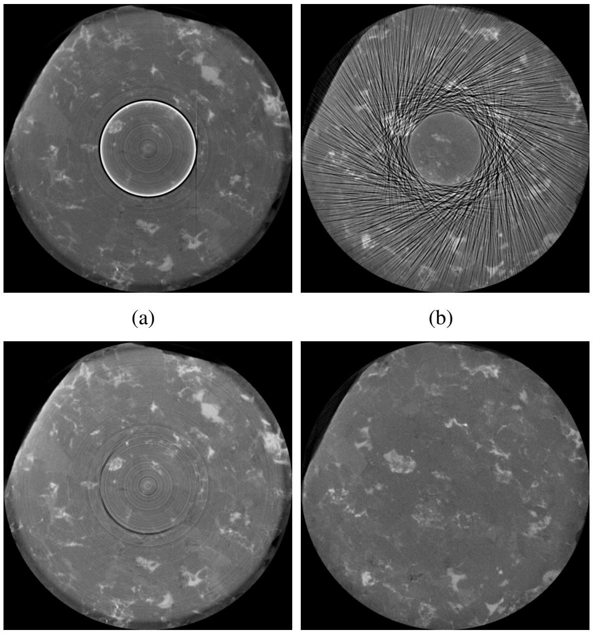

(a) (b)

(c) (d)

Fig. 6. The comparison that show the transverse section images reconstructed by FDK algorithm from the different scanning modes and data preprocessing methods.(a), (b),(c) and (d) are: without processing, detector random shifting only, inpainting only and detector random shifting plus inpainting respectively.

60971131, Beijing Education Committee under the grants PHR20110509 and KZ201110028034.

REFERENCES

- [1] Knoll G F, ”Radiation Detection and Measurement”, 2000, New York: Wiley.
- [2] M Nikl, ”Scintillation detectors for x-rays”, Measurement Science and Technology, 17, R36-R45, 2006.
- [3] I. A. Feldkamp, L. C. Davis, and J. D. Kress, ”Practical cone beam algorithm,” Journal of Optical Society of America A, vol.1, no.6, pp.612-619, 1984.
- [4] L. Rudin, S. Osher and E. Fatemi, ”Nonlinear total variation based noise removal algorithms”, Physica D, 60:250-268, 1992.
- [5] M. Bertalmio, G. Sapiro, V. Caselles and C. Balleser, ”Image Inpainting”, Technical report, ECE-University of Minnesota, 1999.
- [6] T. Chan and J. Shen, ”Mathematical models for local non-texture inpaintings”, SIAM Journal on Applied Mathematics, 62: 1019-1043, 200.
- [7] Jan Sijbers, Andrei Postnov, ”Reduction of ring artifacts in high resolution micro-CT reconstructions”, Physics in Medicine and Biology, Vol.49, Nr.14, 2004.
- [8] H. Bruder et al, http://www.imp.uni-erlangen.de/phantoms.

Optimization-based Extrapolation for Truncation Correction

Andreas Maier [1] , Bernhard Scholz [1] , and Frank Dennerlein [2]

Abstract—**A general approach to correct for lateral data truncation in cone-beam CT is presented in which the correction is achieved by minimizing a specific objective function in the projection domain. We suggest an efficient objective function and derive, from the general approach, an iterative truncation correction algorithm. This algorithm is initialized with a water-cylinder-model-based fan-beam extrapolation as it is employed in a clinical product. Compared to using the model-based extrapolation alone, our iterative algorithm improves image quality in the artifact regions at the boundaries of the field-of-view, particularly where the water-cylinder assumptions are not fulfilled. In that case, first quantitative evaluations on a clinical data set indicate an improvement in the root mean square error of up to 18 %.**

Keywords-image reconstruction; truncation; extrapolation; optimization

I. INTRODUCTION

The X-ray dose that the patient receives during a CT exam is proportional to the volume that is irradiated during the scan. Several medical applications require only a small volume to be imaged, so that the irradiated area can be highly restricted. Fig. 1 shows a follow-up scan of a cochlear implant. In this case, a scan with a full field of view was performed although only the small area, indicated by the circle, is of diagnostic interest. Hence, a restriction of the X-ray irradiation to only that area would have been possible to significantly reduce radiation dose.

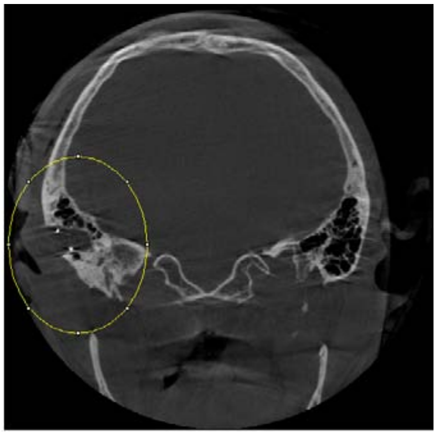

Figure 1: In many diagnostic exams, only a part of the scanned volume is of diagnostic interest. The image shows a follow-up scan of a cochlear implant. The area of interest is marked with an ellipse.

Several practical methods have been suggested for volume-of-interest tomography. Some of them require prior knowledge about the reconstructed object [1] or irradiate parts of the scan at a lower dose [2]. In this paper, however, we will only focus on methods that are able to reconstruct without any other means of prior knowledge.

Reconstruction from laterally severely truncated projection data is an algorithmic challenge. Iterative methods are computationally demanding but might provide solutions if only a part of the object is truncated [3]. In case of bilateral truncation in all views, practically useful results are often obtained by estimating the missing data using heuristic extrapolation methods, e.g. [4]. A good overview on such methods is given in [5]. It is also possible to reconstruct without using any explicit extrapolation scheme [6]. Results are visually satisfying, but generally also approximate.

In this paper, we follow a different approach to solve the truncation problem: We formulate the extrapolation of the missing data as an optimization problem in the projection domain that may involve data before and after filtering. In order to do so, we setup an objective function that describes desired properties of this extrapolation. Then we search for extrapolation values that minimize this objective function using water-cylinder-based fan beam extrapolation values as start values [7]. In the following, we will describe a few properties of truncated and complete filtered projections and will subsequently derive different components of an objective function. Using this objective function, we calculate extrapolation data, and use them for reconstructions and compare their results with reconstruction results from the clinically used extrapolation algorithm using the water-cylinder-based fan beam extrapolation. At the end of this paper, we discuss the properties of the proposed extrapolation algorithm and describe future improvements of the algorithm.

II. EXTRAPOLATION AS OPTIMIZATION PROBLEM

The limited size of the field of measurement can be formulated by a multiplication of the complete row signal $p^*(u,\lambda)$ with a function that describes the size of the field of measurement $d(u,\lambda)$, where $u \in [0, U-1]$ is the index of the detector column, u_{min} and u_{max} are the smallest and the highest detector column indices that are still observed, and λ is the current projection angle:

$$d(u,\lambda) = \begin{cases} 1 & u_{min} \le u \le u_{max} \\ 0 & else \end{cases}$$

The observed row signal $p(u,\lambda)$ is then found as the multiplication of both:

$$p(u,\lambda) = p^*(u,\lambda) \cdot d(u,\lambda)$$

The idea of extrapolation adds new coefficients $x(u)$ to the observed values yielding an extrapolated projection $p'(u,\lambda)$:

$$p'(u,\lambda) = \begin{cases} p(u,\lambda) & u_{min} < u < u_{max} \\ x(u) & else \end{cases}$$

The extrapolated values can be summarized in the vector $\boldsymbol{X}$

$$\boldsymbol{X} = [x(0) \dots x(u_{min}-1)\; x(u_{max}+1) \dots x(U-1)].$$

$\boldsymbol{X}$ is found as the solution to a minimization problem

$$\boldsymbol{X} \leftarrow \mathrm{argmin}_{\boldsymbol{X}}\, f(\boldsymbol{X}).$$

The challenge to perform an optimal extrapolation is thus the challenge to find an objective function $f(\boldsymbol{X})$ that leads to an extrapolation, which would coincide best with the missing data if they could be measured. In the following, we describe a few properties that are suitable for inclusion in such an objective function.

A. High Frequency Artifact

The predominant artifact that is caused by truncation is a bright ring that is generated at the boundary of the field of view of the reconstructed image. The artifact is caused by the distortion that is introduced into the signal by the convolution of $P^*(\omega,\lambda)$ with $D(\omega,\lambda)$which are the Fourier transforms of $p^*(u,\lambda)$ and $d(u,\lambda)$. The filtered projection data after extrapolation is denoted by $g'(u,\lambda)$ in the following.

The relevant property of the artifact is that it contains high frequencies. We use this to build the following constraint: The signal should only have few high frequency components in Fourier domain. The amount of high frequencies can be described using the 1D frequency representation $G'(\omega,\lambda)$ of $g'(u,\lambda)$

$$c_1 = \sqrt{\sum_{\omega\in\Omega_{high}} G'(\omega,\lambda)^2},$$

where Ω_{high} represents the coefficients of the spectrum that contains the N highest frequencies.

Another relevant property of the filtered projection is that the extrapolated values do not introduce additional signal. This observation is used to design a second term:

$$c_2 = \sqrt{\sum_{u=0}^{U-1} g'(u,\lambda)^2}$$

B. Constant Extrapolation in Reconstruction Domain

As we do not know the object outside the field of measurement, its shape is difficult to describe in a constraint. In most applications, we image objects that are homogenous to some extent. Hence, we can assume that the average absorption coefficient in reconstruction domain at the end of the field of measurement stays in the same range during extrapolation. In order to achieve this constant behavior after backprojection, we also require the filtered projection to be a constant continuation of the known part. Furthermore, we assume that there is only little deviation from this constant continuation. Subtraction of the average value should yield a signal with many zeros, i.e. a sparse signal.

These postulates yield the following constraint:

$$c_3 = \sum_{j=u_{min}-R}^{u_{min}-1} |\overline{g_{min}} - g'(j,\lambda)|_1 + \sum_{j=u_{max}+1}^{u_{max}+R} |\overline{g_{max}} - g'(j,\lambda)|_1$$

with

$$\overline{g_{min}} = \frac{1}{Q}\sum_{j=u_{min}}^{u_{min}+Q-1} g'(j,\lambda)$$

$$\overline{g_{max}} = \frac{1}{Q}\sum_{j=u_{max}-Q+1}^{u_{max}} g'(j,\lambda)$$

where $\overline{g_{min}}$ and $\overline{g_{max}}$ are average values over the left and right end of the filtered projection over an area of Q values and $|\cdot|_1$ describes the L1 norm that promotes sparsity. R denotes the area in which this constant behavior is required.

C. Optimization

Using the criteria defined above, we are now able to define our optimization problem using the following objective function:

$$f(\boldsymbol{X}) = \alpha c_1 + \beta c_2 + \gamma c_3,$$

where α, β, and γ are constants that are used to weigh the influence of each of the constraints.

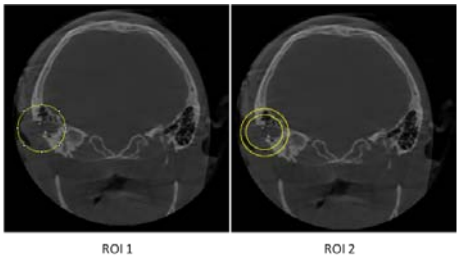

Figure 2: The root mean square error was evaluated over the complete reconstructable area and in an area close to the boundary.

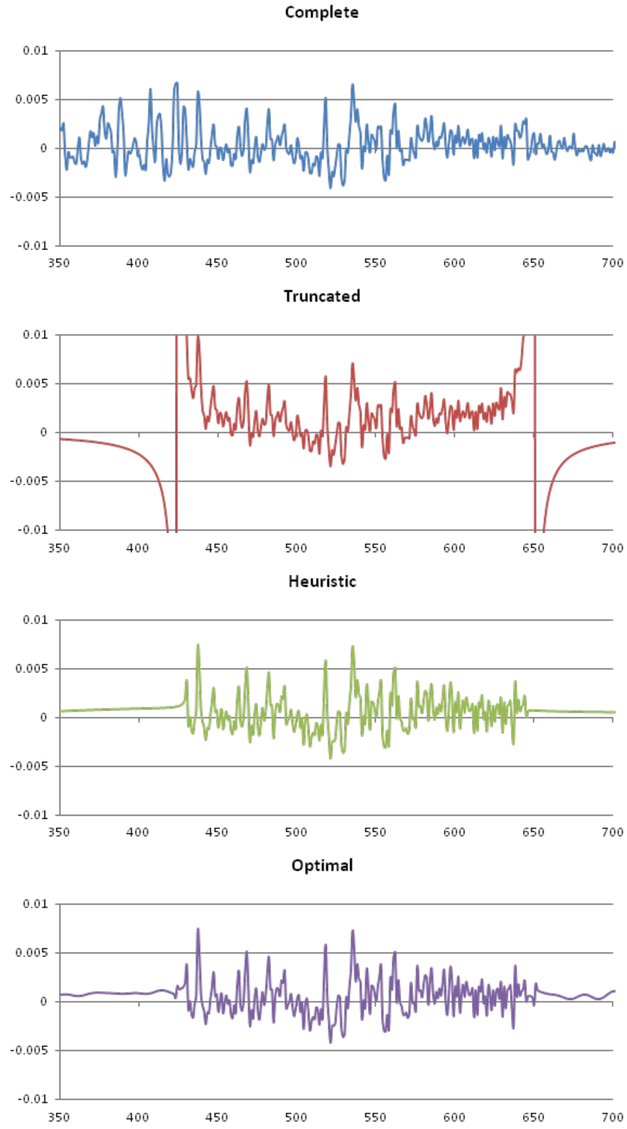

Figure 3: **Truncation introduces additional frequencies into the signal that are amplified after filtering. While heuristics can help to reduce this effect, they often suffer from the problem that the remaining signal has a certain slope as seen in the left side of this example. By definition of a constant region at the boundary of the field of view (here R=Q=64), this effect is reduced.**

III. EXPERIMENTAL VALIDATION

The scope of this paper is more of an exploratory nature, and to investigate the properties of such a compound objective function. We involve an iterative coordinate-descent for optimization and initialize the iterations using a water-cylinder based fan-beam extrapolation. This model-based extrapolation is also used as a baseline result in the experimental validation.

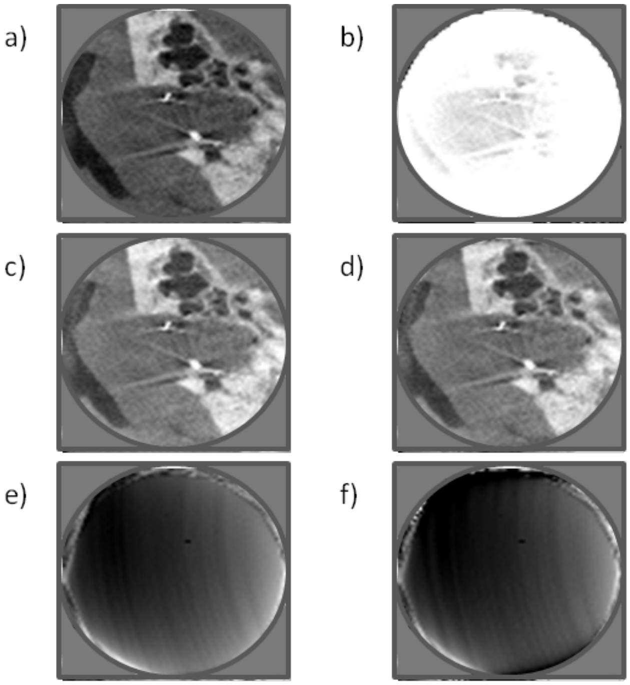

Figure 4: The reconstruction with the complete data is shown in subfigure a). The effect of the truncation is shown in b). Subfigure c) was reconstructed with the heuristic approach. Subfigure d) shows the effect of the optimization ($\alpha = 0.5$, $\beta = 0.0005$, and $\gamma = 0.4995$). Subfigures e) and f) show the absolute differences between images and a) and c) and a) and d). The darker the image is, the lower the error. The top and the bottom of f) show that the match between a) and d) is improved by the optimization process. The visualization window in Subfigures a-d is [-1000, 2500] HU. In subfigures e) and f) the window is [350, 1000] HU.

In order to speed up the computation, we solved the problems on a multi-resolution grid that started with a very coarse resolution of 64 bins. In each step of the grid search, we increased resolution by a factor of 2 and used the result of the previous iteration as initial value for the optimization problem. In each iteration, we reduced the search space towards the boundary of the field of measurement to speed up computation time further. The optimization parameters were chosen as α=0.5, β=0.0005, γ=0.4995, and $R = Q = 64$.

The reconstruction scenario was the truncated reconstruction of the cochlear implant in Fig.1. The scan was acquired with 496 projections at 1280x960 pixels. Reconstruction was performed at 512^3 voxels with a Shepp-Logan kernel. We chose to evaluate the proposed extrapolation with real data that was truncated artificially. In this manner, we are able to compare the extrapolation result with the reconstruction from the complete signal. The reconstructions are evaluated using the root mean square error (RMSE) on the reconstructable part of the image (ROI 1) and within an area close to the boundary of the field of view (ROI 2, cf. Fig. 2).

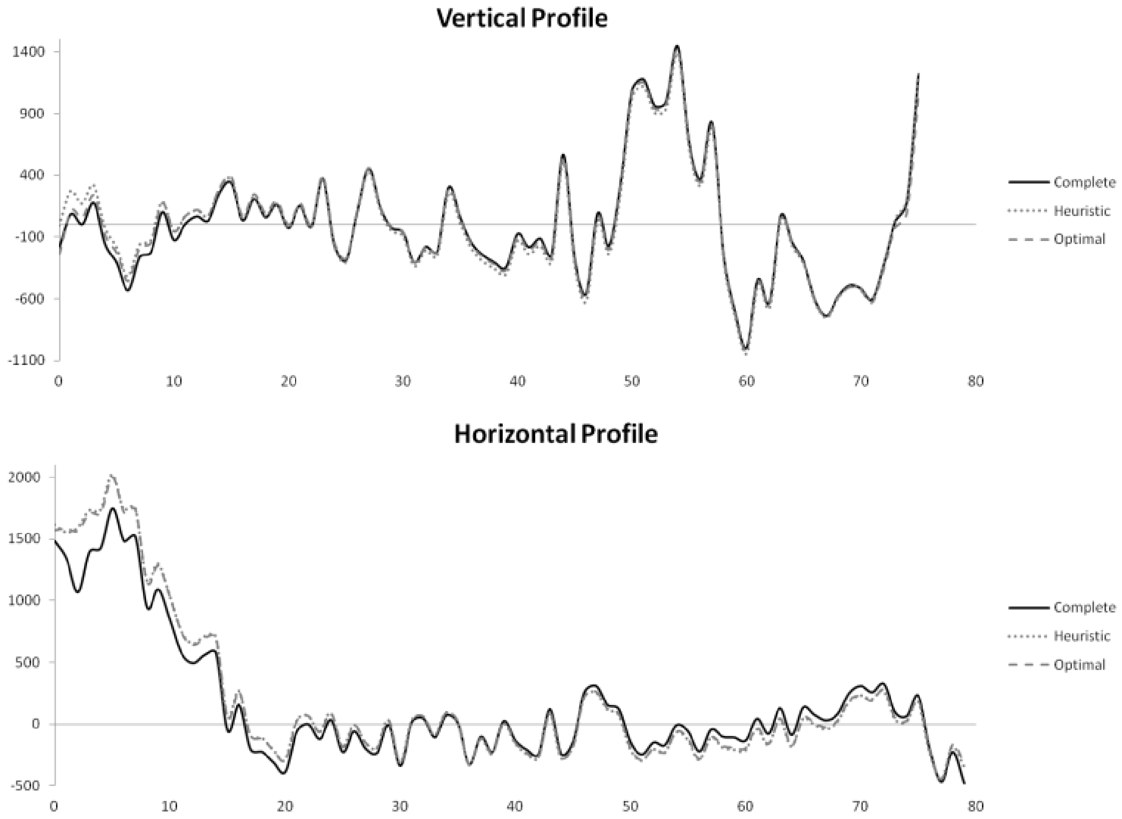

Figure 5: The graphs display two profiles through the reconstructed image. The vertical profile shows an improvement towards the end of the field of measurement. In the horizontal profile no further improvement was obtained compared to the heuristic extrapolation. We subtracted the mean value of each profile to reduce the effect of the offset error.

In Fig. 3 we show the effect of the extrapolation after a Shepp-Logan ramp filter was applied. The optimized signal shows the characteristics that were postulated in the objective function. The signal remains constant in the defined area, has few additional frequencies, and has a low norm.

Fig. 4 shows a comparison between the different reconstructions obtained from the signals from Fig. 4. Subfigure a) shows the reference signal and Subfigure b) the effect of the truncation. In Subfigure c) the reconstruction with the heuristic method is shown. Due to the truncation, the lateral extent of the projection is small, making the fit of a water-cylinder model difficult. The extrapolation is thus degraded and all observed values are increased by an offset. The RMSE for ROI 1 is 557 HU. In ROI 2, the error is even larger with 628 HU. Subfigure d) shows the reconstruction with the optimized extrapolation. Its average RMSE is 500 HU which is lower than in the heuristic extrapolation. At the boundary an average RMSE of 531 HU is obtained. This is only a little higher than the average of the complete ROI, i.e. the reconstruction shows fewer artifacts at the boundary than the heuristic method. The absolute difference images are shown in subfigures e) and f). The error is reduced at the top and the bottom of the image, i.e. in the areas where bones are at the edge of the field of measurement in the projection images. In these areas, the heuristic water cylinder assumption is violated which causes a reduction in image quality. The optimization helps to reduce this artifact.

Fig. 5 shows the effect of the different compensation algorithms on vertical and horizontal profiles through the reconstruction. In order to diminish the offset error, we subtracted the mean values of each of the profiles in the visualization. On the vertical profile, the optimally compensated reconstruction matches the complete reconstruction better. This is especially the case towards the end of the field of measurement. In the horizontal profile, we do not see an improvement compared to the heuristic extrapolation.

IV. DISCUSSION

The results indicate that the presented method is able to improve image quality. The error introduced by the truncation artifact is reduced by 18%. The method seems to be able to yield better extrapolation results in cases where the assumptions of the water cylinder model are not valid. When bone passes through the end of the detector, the heuristic truncation correction algorithm is not able to find a very good solution since the model assumption is invalid. In these cases, the optimization-based method is able to outperform the heuristic method.

In cases that match the water cylinder assumption well, it is difficult to find a better solution with the presented objective function. The optimization-based method then presents the same result as the heuristic method (cf. Fig. 5).

The presented method has an interesting property: As we define parts of the objective function after the filtering step, the optimization is dependent on the used filter kernel. If a smoother kernel is applied, a different extrapolation result is obtained. In the present paper, we employ the method in a Feldkamp-type reconstruction method [8]. In principle, the same method could also be applied to different analytic reconstruction methods that require a completely different filtering step.

The first results indicate that criterion c_2 did not show a lot of importance. A value of $\beta = 0.0005$ was sufficient in our first experiments. The other two criteria were almost balanced with $\alpha = 0.5$ and $\gamma = 0.4995$.

The runtime of the algorithm could be reduced to a feasible amount as we employed multi-grid methods and only applied few iterations (N=5) in the present study. It helped to reduce the search space dramatically, but also limited the solution to one that is rather close to the initial value. This implies that the result of the computation is somewhat dependent on the initialization. At the present state, we decided that the investigation of the objective function was more important than finding an algorithm that is robust of different initializations. We expect this to improve with a more efficient optimization strategy. With respect to the objective function, we could not observe a deterioration that was caused by the method compared to the baseline result.

V. CONCLUSION AND OUTLOOK

We presented a truncation correction method that was inspired by the optimization of an objective function. In a first investigation, we could achieve an improved image quality compared to a water cylinder extrapolation-based algorithm. In an area towards the end of the field of measurement, a reduction of the truncation error of 18 % was obtained. The method could mainly contribute in areas where the water cylinder assumption was violated. This is quite surprising, as only simple assumptions were used in the objective function.

In future work, we will investigate additional constraints that can be used in the objective function. One main concern is that the reconstruction still suffers from an offset error that needs to be reduced. This could be achieved, if the correct size of the object were supplied to the truncation correction method. Improvements of the optimization method are also scope of our current work.

ACKNOWLEDGMENT

The authors wish to thank the Dept. of Neuroradiology, University of Heidelberg, Medical Center, for providing the patient data.

Disclaimer: The concepts and information presented in this paper are based on research and are not commercially available.

REFERENCES

[1] D. Kolditz, Y. Kyriakou, W.A. Kalender, "Volume-of-interest (VOI) imaging in C-arm flat-detector CT for high image quality at reduced dose," *Med Phys*, vol. 37, no. 6, pp. 2719-2730, 2010.

[2] R. Chityala, K.R. Hoffman, D. R. Bednarek, S. Rudin, "Region of Interest (ROI) Computed Tomograpy," in *Proc. SPIE*, 2004, p. 534.

[3] H. Kunze, W. Härer, K. Stierstorfer, "Iterative extended field of view reconstruction," in *Proc. SPIE*, 2007, p. 6510SX.

[4] Ohnesorge B, Flohr T, Schwarz K, Heiken JP, Bae KT, "Efficient correction for CT image artifacts caused by objects extending outside the scan field of view.," *Med Phys*, vol. 27, no. 1, pp. 39-46, 2000.

[5] G.V. Gompel, *Towards accurate image reconstruction from truncated X-ray CT projections*. Antwerpen, Belgium: University Antwerpen, 2009.

[6] F. Dennerlein, A. Maier, "Region-Of-Interest Reconstruction on medical C-arms with the ATRACT Algorithm," in *Proc. SPIE*, 2012, p. to appear.

[7] B. Scholz, J. Boese, "Correction of Truncation Artifacts in C-Arm CT Images by Fan-Beam Extrapolation Using Savitzky-Golay Filtering," in *RSNA*, 2008, pp. Session SSJ24-06.

[8] A. C. Kak, M. Slaney, *Principles of Computerized Tomographic Imaging*. Piscataway, NJ, United States: IEEE Service Center, 1988.

[9] G. Lauritsch, J. Boese, L. Wigström, H. Kemeth, and R. Fahrig, "Towards cardiac C-arm computed tomography," *IEEE Trans Med Imaging*, vol. 25, pp. 922-34, 2006.

[10] A. Maier, L. Wigström, H. G. Hofmann, J. Hornegger, L. Zhu, N. Strobel, R. Fahrig, "Three-dimensional Anisotropic Adaptive Filter-ing of Projection Data for Noise Reduction in Cone Beam CT," *Med Phys*, vol. 38, no. 11, pp. 5896-5909, 2011.

[11] J. Hsieh, E. Chao. J. Thibault, B. Grekowicz, A. Horst, S. McOlash, "A novel reconstruction algorithm to extend the CT scan field-of-view," *Med Phys*, vol. 31, no. 9, pp. 2385-2391, 2004.

Comparison of Image Features for Misalignment Correction in Flat-Detector CT

Julia Wicklein, Holger Kunze, Willi A. Kalender and Yiannis Kyriakou

***Abstract*—Generally the geometrical parameters, which are essential for reconstruction are provided by preceding calibration routines. These procedures are time consuming and the later use of stored parameters is sensitive towards external impacts or patient movement. The method of choice in a clinical environment would be a marker-less online-calibration procedure, that allows flexible scan trajectories and simultaneously corrects misalignment and motion artifacts during the reconstruction process. Therefore, different image features were evaluated according to their capability of quantifying misalignment. Projections of the FORBILD Head and Thorax Phantom were simulated. Additionally, acquisitions of a head phantom and patient data were used for evaluation. For the reconstruction different sources and magnitudes of misalignment were introduced in the geometry description. The resulting volumes were analyzed by entropy criteria based on the gray-level histogram and Gabor filters. Additionally we evaluated total variation approaches.**

***Index Terms*—flat-detector CT (FDCT), misalignment correction, image quality.**

I. INTRODUCTION

For artifact-free reconstruction, precise knowledge of the detector position and orientation as well as the position of the x-ray source are required for every projection. It is common practice to determine the geometry parameters for certain scan protocols with the aid of dedicated calibration phantoms and store them ([1]). Later these stored parameters are used for reconstruction. This procedure is time consuming and works only on pre-defined scan trajectories. Due to external impacts, the actual geometry during acquisition might differ from the geometry used for reconstruction. These geometrical inaccuracies, the so-called misalignment, as well as patient movement during acquisition lead to specific artifacts in the reconstructed volume. Up to now, several approaches for reducing misalignment artifacts were followed. Most algorithms focus on optimizing the preceding calibration procedure ([2]) or follow a marker-based approach ([3]). The method of choice in a clinical environment would be a marker-less online-calibration procedure. This would overcome the drawbacks of using offline acquired geometry parameters for pre-defined scan protocols. In Ref. [4], a calibration algorithm which is independent of the measuring system was introduced. It analyzes the image entropy inside the field of measurement without knowledge of spatial characteristics or other a priori knowledge. During an optimization routine, the geometry parameters are adjusted by minimizing the entropy calculated from the gray-level histogram. Additionally we evaluated an entropy criterion based on Gabor filters. TV-norm minimization has become very popular for medical imaging tasks during the last two decades ([5],[6]). Therefore, we decided to evaluate TV-norm for misalignment correction. In Ref. [7] the authors introduces an online-calibration procedure that uses the L_2-norm of the image gradient to increase sharpness. The back-projection mismatch (BPM) is used to create the ground-truth for feature evaluation [8]. It is an object-independent measure for comparing different geometry parameters.

II. GEOMETRY CALIBRATION

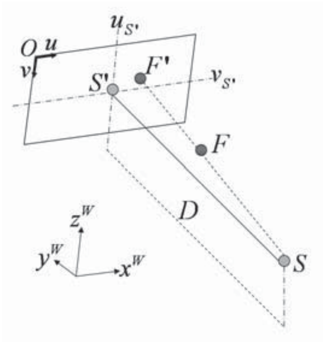

Fig. 1. Perspective projection of a point F on the detector plane (F'). S is the position of the source and S' it‘s projection. D is the source-detector distance.

Fig. 1 shows the basic constitution of the flat-detector CT geometry. It illustrates the perspective projection of a point F on the detector plane (F'). S is the x-ray source and S' it's projection. D is the source-detector distance, O is the origin point of the detector and u and v it‘s column- and row-vector. $u_{S'}$ and $v_{S'}$ are the detector coordinates of the source projection S'. It is common practice to estimate the intrinsic and extrinsic parameters of the acquisition system via calibration, providing information about its optical parameters, position and orientation (see Ref. [9]). This is done by calculating a projection matrix for each position of the trajectory, including the geometrical parameters of the system. One possibility for the calibration is introduced in Ref. [1]. The described phantom consists of an empty cylinder with several markers of known positions. After detecting the 2D marker positions in the projected image, the 2D/3D correspondences are used for determining the projection matrix **P**. This is done for each projection image of the trajectory and combined

---

Julia Wicklein and Willi A. Kalender are with the Institute of Medical Physics (IMP), University of Erlangen–Nürnberg, Henkestraße 91, 91052 Erlangen. Holger Kunze and Yiannis Kyriakou are with Siemens AG, Healthcare Sector, Forchheim, Germany. Corresponding author: Julia Wicklein, E-mail: julia.wicklein@imp.uni-erlangen.de.

to one table of projection matrices. The projection matrix **P** describes compactly how a 3D point $F = (x_F^w, y_F^w, z_F^w)$, given in homogeneous coordinates is mapped onto a 2D point on the detector plane (see Fig. 1).

$$\mathbf{p}(\mathbf{P}, F) = \begin{pmatrix} p_x/p_z \\ p_y\ p_z \end{pmatrix} = \begin{pmatrix} u_{F'} \\ v_{F'} \end{pmatrix} = F'$$

defines the projection function of F.

III. HISTOGRAM ENTROPY

The histogram (H) of the intensity values q provides a global description of an image. Entropy using the gray level histogram H is calculated according to:

$$E = -\sum_{q=0}^{Q} (h(q) \cdot log\ h(q)),$$

with

$$h(q) = \frac{H(q)}{N},$$

where Q is the maximum intensity value, h is the normalized histogram or probability distribution of the image and N is the number of image pixels.

IV. TOTAL VARIATION

Total Variation (TV) based algorithms became very popular within the scopes of image denoising ([10],[11]) or image reconstruction ([5], [6]) during the last two decades. In ([10]), an iterative, edge preserving method of TV-norm minimization is introduced to remove noise from images, given the TV-norm definition for two-dimensional functions:

$$TV(I) = \int_\Omega |\nabla I| dudv = \int_\Omega \sqrt{\left[\frac{\partial}{\partial u} I\right]^2 + \left[\frac{\partial}{\partial v} I\right]^2} dudv.$$

where $u, v \in \Omega$ are the pixel indices of image I. In most of numerical implementations, a discrete version of TV-norm based on the discretization of the gradient opertator ∇ is used. The simplest gradient operator is defined:

$$g_u = \begin{pmatrix} -1 & 1 \\ 0 & 0 \end{pmatrix} \qquad g_v = \begin{pmatrix} -1 & 0 \\ 1 & 0 \end{pmatrix},$$

with $\frac{\partial}{\partial u} I = g_u * I$ and $\frac{\partial}{\partial v} I = g_v * I$.

An automatic alignment by passive auto-focus is presented in Ref. [7]. The basic procedure includes the reconstruction of a set of 2D slices of the 3D tomogram to cover the range of misalignments and selecting the image, that looks the best. The authors decided to use the L_2-norm as fitness function, representing the sharpness of the image:

$$S(I) = \sum_u \sum_v |\nabla I(u, v)|^2.$$

V. TEXTURE FEATURES BASED ON GABOR FILTERS

Gabor features are commonly used in several image analysis applications, like texture classification and segmentation ([12]), image registration ([13]), face recognition ([14]) and motion tracking ([15]). Concerning medical applications, they have already been successfully applied for content-based mammogram retrieval ([16]). Gabor filters are constructed of a Gaussian function modulated by a planar cosine. They are defined by a certain frequency f and orientation θ:

$$g_{f,\theta}(x, y) = \frac{1}{2\pi\sigma^2} exp\left(\frac{x^2 + y^2}{2\sigma^2}\right) cos\left(2\pi(fxcos\theta + fysin\theta)\right).$$

The reconstructed CT image I is filtered with a set of Gabor filters $g_{f,\theta}$:

$$G_{f,\theta} = I * g_{f,\theta}.$$

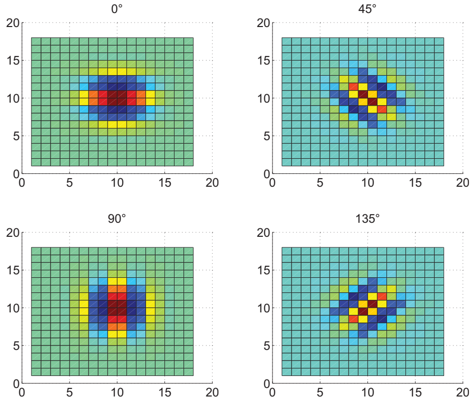

Fig. 2. Gabor filter set with four different orientations $\theta_i = (0°, 45°, 90°, 135°)$ and frequency $f = 1/4$.

Fig. 2 shows the used filter set with frequency $f = 1/4$ and four different orientations $\theta_i = (0°, 45°, 90°, 135°)$. A probability matrix $P^{G_{f,\theta}}$ is calculated from every filter result, forming the basis for entropy calculation:

$$P^{G_{f,\theta}}(u, v) = \frac{G^2_{f,\theta}(u, v)}{\int\int G^2_{f,\theta}(\tilde{u}, \tilde{v})\, d\tilde{u} d\tilde{v}}.$$

VI. SIMULATIONS AND MEASUREMENTS

We use the FORBILD head and thorax phantoms (FHP and FTP) for the evaluation of the features ([17]). Simulations of two different scan types were adapted to both phantoms, based on the geometry of FDCT systems ([18]). A circular 360°scan with 360 projections and 616 pixels × 480 pixels of size 616 μm × 616 μm [see Fig. 3(a)] and a circular partial scan with an angular range of 200°, performing 133 projections with 1240 pixels × 960 pixels and a pixel size of 308 μm × 308 μm [see Fig. 3(b)] . The radius of the source trajectory was set to 785 mm and the source-detector distance to 1200 mm. We reconstructed three transverse slices with a

Shepp-Logan convolution kernel for images of size 512 pixels × 512 pixels. The pixel size was set to $0.5\ mm \times 0.5\ mm$ for the FHP, and $1.0\ mm \times 1.0\ mm$ for the FTP [see Figs. 3(c) and (d)].

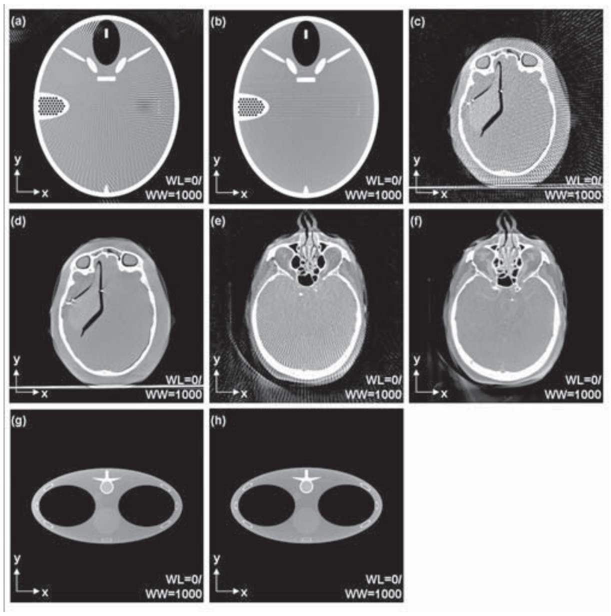

Fig. 3. The central transverse slices (z=0) of all evaluated datasets. (a) shows the simulation of the FHP with 133 projections over 200°. (b) shows the simulation of the FHP, performed with 360 projections for a full rotation. (c) shows the reconstruction result of the MHP, performed with 133 projections over 200°. (d) shows the reconstruction result of the MHP, performed with 496 projections over 200°. (e) shows the reconstruction result of the PAD with 133 projections over 200°. (f) shows the reconstruction result of the PAD, performed with 496 projections over 200°. (g) shows the simulation of the FTP, performed with 133 projections over 200°. (h) shows the simulation of the FTP, performed ith 360 projections for a full rotation.

Measurements of a head phantom (MHP) and a patient (PAD) were acquired with SIEMENS Artis Zeego. This system is equipped with a flat detector of $40\ cm \times 30\ cm$ with 2480 pixels × 1920 pixels and a pixel size of $154\ \mu m \times 154\ \mu m$. All scans were conducted in a circular partial scan with an angular range of 200 which is typically used in FDCT ([18]). Scans with 133 [see Fig. 3(c) and (e)] and 496 [see Fig. 3(d) and (f)] projections with a 2 × 2 pixel binning were performed. In account with the simulation data, the radius of the source trajectory was set to $785\ mm$ and the source-detector distance to $1200\ mm$. We reconstructed the three central slices for images of size 512 pixels × 512 pixels with a pixel size of $0.5\ mm \times 0.5\ mm$.

VII. EVALUATION

Our aim in this paper is to evaluate the presented image features in terms of their capability of quantifying misalignment. In cases of the gray-level histogram based entropy, we converted the reconstructed images to 8 bit to achieve a 256 bins histogram. Therefore, we regarded the images using a classical bone window with a window level of 300 HU and a window width of 1500 HU. All other features were evaluated using the full bit-depth and min-max scaling. For the following operations we used the BPM with a virtual object including 200 points arranged in a sphere of radius around the isocenter. We defined a ground truth, including nine misalignment levels according to the back-projection mismatch (BPM). This was achieved by manipulating the ideal geometry (BPM=0) of each dataset with a combination of detector translations and rotations in a proper magnitude. Fig. 4 illustrates the central transverse slices of all nine levels in ascending order from 0 to 3 pixels for MHP with 496 projections (MHP 496). This BPM order, including nine misalignment levels builds the ground truth for the resulting feature sequences.

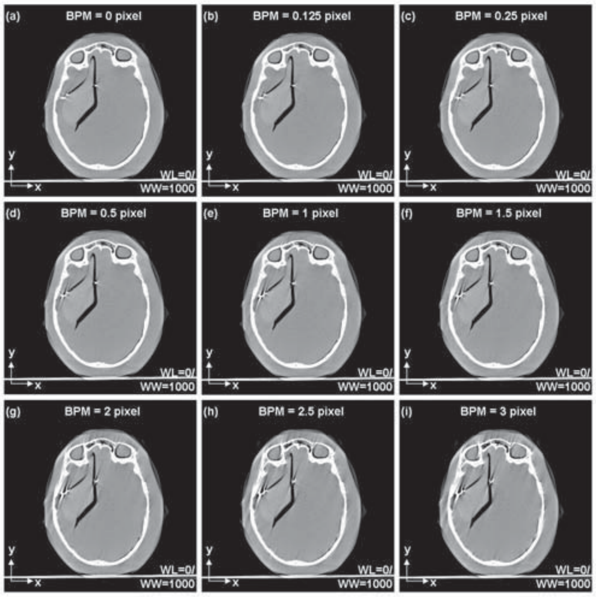

Fig. 4. The transverse cuts ($z = 0$) of the reconstruction result of the MHP, performed with 496 projections over 200°. The images (a)-(i) show the evaluated misalignment levels from 0 to 3 pixels, quantified by the BPM.

For each misalignment level and dataset the feature values are calculated for three different transverse slices ($z = 0$, $z = 6.16\ mm$ and $z = -6.16\ mm$) and averaged to obtain one value. We use a min-max-scaling of the feature values for a specific dataset, for an easier comparison of the different methods. Fig. 5 shows three examples of possible feature sequences with a percentage of 100, 92 and 28, visualising the analogy to the curve progression of the underlying ground truth. The ideal image feature produces the same sequence of misalignment levels as the corresponding BPMs and thus is strictly monotonic increasing. Linearity is not necessary here. For an efficient optimization method it is important to provide local minima differing from the parameter adjustment with minimal BPM, which forms the only global minimum. For that reason, we focus on the sequence of the feature values for evaluation. To improve comparability, we converted the resulting curves into one significant percentage, using the well-known BubbleSort algorithm ([19]). The number of permutations for an increasing arithmetic of each feature vector was enumerated, which gives an adequate approximation of the degree of analogy with the ideal feature sequence. This resulted in a value between zero and 36 for a maximum number of permutations with nine vector elements. Therefore, we achieved the percentage of the corresponding feature by dividing the enumeration result by 0.36 and subtract that from 100.

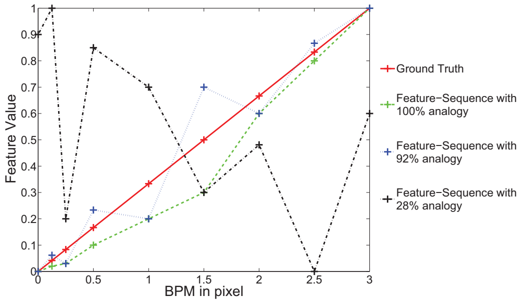

Fig. 5. Ground truth for feature evaluation complemented by three examples of feature sequences with 100%, 92% and 28% of analogy to the ideal sequence.

VIII. RESULTS

We present the feature results according to the percentage evaluation, introduced in chapter VI. Fig. 6 illustrates the achieved accuracy values for all regarded image features.

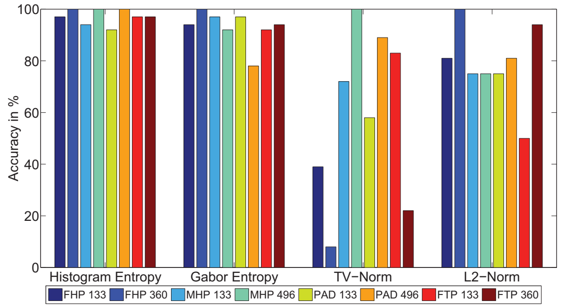

Fig. 6. Accuracy of the histogram-based entropy, the Gabor entropy, the TV-norm and the L_2-norm.

IX. DISCUSSION AND CONCLUSIONS

For our evaluation we use the BPM as ground truth for the quantification of misalignment. In Ref. [8] we have shown that for increasing shifts and detector rotation the value of the BPM also increases. In addition, the visual inspections have shown a very good correlation of the strength of misalignment and the BPM. Therefore, and lacking an alternative quantification method for misalignment, we used the BPM to appraise the quality of the different feature extraction methods.

Regarding Fig. 6, it becomes obvious that the gray-level histogram based entropy meets these conditions the best. With a 256 bins histogram and a classical bone window setting it achieved high accuracy values for all simulated scans. It shows small weakness in the case of 133 projections scans, but exceeds the 90% accuracy level for all evaluated datasets. The minimal value for the measured head phantom was at 0.125 pixel BPM, for the patient data at 0.25 pixel BPM [see Fig. 4(b) and (c)]. The entropy calculated from the Gabor filtered images shows also good results, apart from the patient scan with 496 projections. A big drawback of this method is the noticeably inferior performance compared to the histogram based entropy calculation. TV-norm minimization shows good results for some of the regarded scans. Nonetheless it shows considerable differences over all evaluated scans. This high quality fluctuation makes TV-norm improper for a general misalignment correction approach. The L_2-norm maximization works quite well on the simulated datasets for a full circular scan. It shows considerable inadequateness in the case of 200°angle range. The authors of Ref. [7] proposed to pre filter the images with a low pass to overcome the influences of noise or under sampling. Our evaluations did not show improvements with that approach. The same is true with respect to the alternative convolution kernels.

REFERENCES

[1] N. Strobel et. al., *Improving 3D Image Quality of X-Ray C-Arm Imaging Systems by Using Properly designed Pose Determination Systems for Calibrating the Projection Geometry*, Proc. of SPIE, vol. 5030, pp.943-954, 2003.

[2] L. v. Smekal et. al., *Geometric misalignment and calibration in cone-beam tomography*, Med. Phys., Vol. 31, Issue 12, pp. 3242-3266, (2004).

[3] L. Smith et. al., *Automatic detection of fiducial markers in fluoroscopy images for on-line calibration*, Med. Phys., Vol. 32, Issue 6, pp. 1521-1523, (2005).

[4] Y. Kyriakou et. al., *Simultanious misalignment correction for approximate circular cone-beam computed tomography*, Phys. Med. Biol. 53, pp.6267-6289, 2008.

[5] E. Y. Sidky, and X. Pan, *Image reconstruction in circular cone-beam computed tomography by constrained, total variation minimization*, Phys. Med. Biol., Vol. 53, pp. 4777-4807, (2008).

[6] M. Persson et. al., *Total variation norm for three-dimensional iterative reconstruction in limited view angle tomography*, Phys. Med. Biol., Vol. 46, pp.853-866, (2001).

[7] A. Kingston et. al., *Reliable automatic alignment of tomographic projection data by passive auto-focus*, Med. Phys., Vol. 38, Issue 9, pp. 4934-4945, (2011).

[8] J. Wicklein et. al., *An Object-Independent Measure for Improving Misalignment Correction in C-Arm CT*, Proc. of Fully3D Meeting 2011 Potsdam, pp. 148-151, 2011.

[9] F. Noo et. al., *Analytic method based on identification of ellipse parameters for scanner calibration in cone-beam tomography*, Phys. Med. Biol., Vol. 45, pp. 3489-3508, (2000).

[10] L. I. Rudin et. al., *Nonlinear total variation based noise removal algorithms*, Physica D: Nonlinear Phenomena, Vol. 60, Issues 1-4, pp. 259-268, (1992).

[11] C. R. Vogel, and M. E. Oman, *Iterative methods for total variation denoising*, SIAM J. Sci. Comput., Vol. 17, pp. 227-238, (1996).

[12] T. P. Weldon et. al., *Efficient Gabor filter design for texture segmentation*, Pattern Recognition, Vol. 29, Issue 12, pp. 2005-2015, (1996).

[13] Q. Zheng, and R. Chellappa, *A computational vision approach to image registration*, IEEE Transactions on Image Processing, Vol. 2, Issue 3, pp.311-326, (1993).

[14] C. Liu, and H. Wechsler, *Gabor feature based classification using the enhanced fisher linear discriminant model for face recognition*, IEEE Transactions on Medical Image Processing, Vol. 11, Issue 4, pp. 467-476, (2002).

[15] B. S. Manjunath et. al., *A new approach to image feature detection with applications*, Pattern Recognition, Vol. 29, Issue 4, pp. 627-640, (1996).

[16] C. H. Wei et. al., *Effective Extraction of Gabor Features for Adaptive Mammogram Retrieval*, IEEE International Conference on Multimedia and Expo 2007, pp. 1503-1506, (Beijing, 2007).

[17] Description of the FORBILD Phantom Database, online at http://www.imp.uni-erlangen.de/phantoms/index.htm.

[18] W. A. Kalender and Y. Kyriakou, *Flat-detector computed tomography (FD-CT)*, Eur. Radiol. Vol. 17, Issue 11, pp.2767-2779, (2007).

[19] D. E. Knuth, *The Art of Computer Programming: Sorting and Searching*, Vol. 3, 2nd edition, Addison-Wesley, (1998).

An analytical geometric calibration method for circular cone-beam CT geometry

Jingyan Xu and Benjamin M.W. Tsui

I. INTRODUCTION

GEOMETRIC calibration in cone-beam x-ray CT and SPECT or pinhole SPECT[1] aims to determine the complete imaging parameters that are crucial for artifact-free image reconstruction. The importance of accurate geometrical information is evidenced by the extensive literature on this topic, not only in computed tomography [1]–[3], but also in diverse fields such as robotics [4] and computer vision [5].

It is well known that seven parameters completely describe the geometry of a circular cone-beam imaging system [3], [6]. Different but equivalent 7-parameter sets have been used in the literature [6]–[8]. We use the following definition in this work.

- D, the focal length or the perpendicular distance from the x-ray source or pinhole aperture to the detector;
- R, the radius of rotation or the distance from the focal point to the rotational axis $\underline{e}_z$;
- η, θ, ϕ, the 3 rotation angles that define the detector orientation, in which η is the in-plane rotation, ϕ the detector slant angle, and θ the detector tilt angle. If $\theta \neq 0$, then the detector plane is not parallel to $\underline{e}_z$. In the object coordinate system, the detector axes are defined by [6]:

$$\begin{aligned} \underline{e}_w &= (\cos\theta\cos\phi, \cos\theta\sin\phi, \sin\theta); && (1)\\ \underline{e}_u &= \cos\eta\underline{\alpha} + \sin\eta\underline{\beta}, && (2)\\ \underline{e}_v &= -\sin\eta\underline{\alpha} + \cos\eta\underline{\beta} && (3)\\ \underline{\alpha} &= (-\sin\phi, \cos\phi, 0) && (4)\\ \underline{\beta} &= (-\sin\theta\cos\phi, -\sin\theta\sin\phi, \cos\theta) && (5) \end{aligned}$$

- (u_c, v_c), the cone-beam projection of the object space origin on the detector.

The first 5 parameters are identical to those in many publications, *e.g.*, [6], [9]. When these 5 parameters are determined, there is a simple translation to convert between the last two parameters (u_c, v_c) and the perpendicular intersection from the focal point to the detector (u_0, v_0) (the principal point) that are used in other published works. The parameter definitions are illustrated in Fig. 1.

This paper is a continuation of our recent work on determining the in-plane rotation angle using a graphical procedure [10]. Here we use the cone-beam projection correspondence established in [10] to determine the other 6 parameters. Our method is general in that we do not assume any parameters, especially the two out-of-plane angles, θ and ϕ, to be zero. The proposed method uses a minimum of 3 point objects with known distances to calculate all 7 geometrical parameters. The method is exact in the noise-free case. It can accommodate shorter scan ranges ($\leq 360°$) and some projection trucation in the calibration scan without affecting its accuracy.

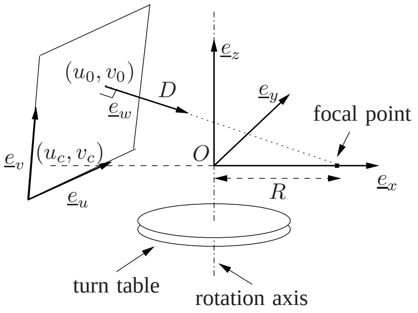

Fig. 1. The coordinate system definition. The detector orientation, defined by the axes $\underline{e}_w$, $\underline{e}_u$, and $\underline{e}_v$, are specified by three rotation angles, θ, η, ϕ, with respect to the object space. The other 4 parameters to be determined are D, R, and (u_c, v_c).

II. METHOD

We first provide a brief summary of the geometric construction that finds the in-plane rotation angle η [10]. A by-product of the graphical method is a set of point correspondence between some characteristic points in the object space and their cone-beam projection on the detector.

A. A graphical procedure for finding η

To determine the complete set of 7 parameters we need a minimum of 3 point objects ($p = 3$), but for η, the geometric construction uses a minimum of 2 point objects ($p = 2$). The projection of different point objects traces out different ellipses on the detector, from which we can calculate the following [6]:

- the fitted ellipses $\mathcal{E}_k$, $k = 1, \cdots, p$;
- the projection of the rotational axis $\underline{e}'_z$;
- the two points on $\underline{e}'_z$, $(\hat{u}_k, \hat{v}_k)$, $k = 1, \cdots, p$ from the intersections of the radial or opposing pairs of point projections;
- the 2 intersection points between each ellipse and $\underline{e}'_z$, $(u^{\pm}_k, v^{\pm}_k)$, $k = 1, \cdots, p$.

Using the above elements, we perform the following steps.

1) Draw lines that are tangent to the ellipse $\mathcal{E}_k$ at $(u^{\pm}_k, v^{\pm}_k)$. These lines, denoted by $L^{\|y,\pm}_k$ in Fig. 2, $k = 1, \cdots, p$, should converge to the same point $(u_{\rm ch}, v_{\rm ch}) \overset{\triangle}{=} P_\phi$. This is the "converging point" in [11] due to $\phi \neq 0$.
2) Connect P_ϕ with $(\hat{u}_k, \hat{v}_k)$ on the rotational axis $\underline{e}'_z$. Each line, denoted by $L^{\|y,0}_k$, intersects with the ellipses $\mathcal{E}_k$ at two points $(u_{k,\pm}, v_{k,\pm})$ [Fig. 2].
3) Draw lines that are tangent to the ellipse $\mathcal{E}_k$ at $(u_{k,\pm}, v_{k,\pm})$. These "vertical tangent" lines, denoted by $L^{\|x,\pm}_k$ in Fig. 2, and the rotational axis $\underline{e}'_z$ have a common intersection point O', which is the projection of the origin O on the detector [Fig. 2].
4) Connect O' with P_ϕ from step 1. Its slope is $-\tan\eta$.

When $\phi = 0$, the "horizontal tangent" lines $L^{\|y,\pm}_k$ in step 1 are parallel and P_ϕ is at infinity. In this case, the slope of

---

J Xu and Benjamin M W Tsui are with the Division of Medical Physics, Department of Radiology, Johns Hopkins University. {jxu,btsui}@jhmi.edu.

[1] Subsequently we use cone-beam CT to include all these modalities and may not mention them individually each time.

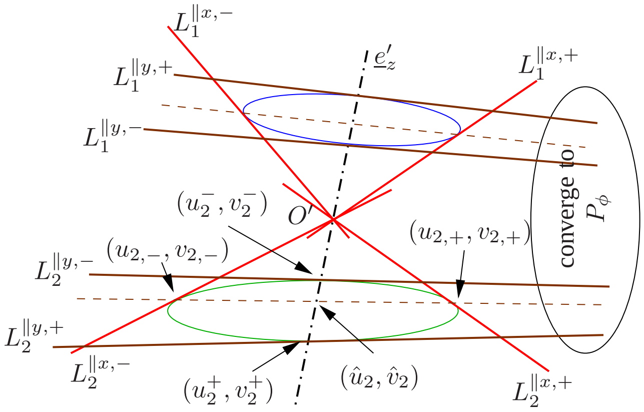

Fig. 2. The graphical procedure for finding η. The left panel is on the detector. The right panel is the object space.

$L_k^{\|y,\pm}$ is equal to $-\tan\eta$. In order to determine the point correspondence for finding other parameters, we modify the above step 2 as follows.

2m) In case $L_k^{\|y,\pm}$ are parallel with each other, $L_k^{\|y,0}$ then passes $(\hat{u}_k, \hat{v}_k)$ and is parallel to $L_k^{\|y,\pm}$. Each $L_k^{\|y,0}$ intersects with the ellipses $\mathcal{E}_k$ at 2 points $(u_{k,\pm}, v_{k,\pm})$.

Once η is obtained, the projection image can be rotated by η and subsequent analysis can proceed as if η were zero [6].

B. *Finding the other six parameters*

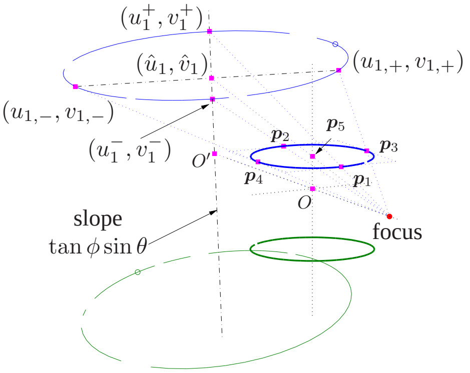

Fig. 3. The characteristic positions $\boldsymbol{p}_k$, $k = 1, \cdots, 5$ of one point object and their cone-beam projections. These are the projection locations of object points with at least one of their (x, y, z) coordinates equal to zero. For instance, $(u_{k,\pm}, v_{k,\pm})$ are projections of $(0, \pm r, z)$. Similar positions are identified for all other point objects. Their drawings are omitted to avoid cluttering.

Figure 3 summarizes the established correspondence from the graphical procedure and introduces additional notations for subsequent derivations. We define 5 characteristic positions for each point object k and include the origin of the object space in the point correspondence.

- $(\pm r_k, 0, z_k) \overset{p}{\leftrightarrow} (u_k^\pm, v_k^\pm)$;
- $(0, \pm r_k, z_k) \overset{p}{\leftrightarrow} (u_{k,\pm}, v_{k,\pm})$;
- $(0, 0, z_k) \overset{p}{\leftrightarrow} (\hat{u}_k, \hat{v}_k)$
- $O \triangleq (0, 0, 0) \overset{p}{\leftrightarrow} O' = (u_c, v_c)$

The notation $\overset{p}{\leftrightarrow}$ means that the left and right entities are associated by the cone-beam projection. From the above correspondence, we calculate the following quantities.

$$\begin{aligned} \check{b}_{k,\pm} &\triangleq v_k^\pm - v_c,\ \check{b}_{k,0} = \hat{v}_k - v_c, && (6) \\ \check{a}_{k,\pm} &\triangleq u_{k,\pm} - \hat{u}_k, && \\ c_k &= \frac{\check{b}_{k,+}}{\check{b}_{k,+} - \check{b}_{k,0}} = \frac{\check{b}_{k,-}}{\check{b}_{k,0} - \check{b}_{k,-}} && (7) \end{aligned}$$

A consequence of eqn. (7) is that $\check{b}_{k,0}$ is the harmonic mean of $\check{b}_{k,+}$ and $\check{b}_{k,-}$, *i.e.*,

$$\frac{2}{\check{b}_{k,0}} = \frac{1}{\check{b}_{k,+}} + \frac{1}{\check{b}_{k,-}}, \forall k. \tag{8}$$

Note that $\check{a}_{k,+} > 0$ and $\check{a}_{k,-} < 0$ by definition. The cone-beam geometric parameters are calculated by a sequential evaluation of eqns. (9) – (13).

$$\begin{aligned} \tan\phi &= c_k \left(\frac{\check{a}_{k,+} + \check{a}_{k,-}}{\check{a}_{k,+} - \check{a}_{k,-}} \right) && (9) \\ \sin\theta &= \frac{1}{\tan\phi} \frac{\hat{u}_k - \hat{u}_j}{\hat{v}_k - \hat{v}_j}, \quad k \neq j && (10) \\ \frac{D}{\cos\theta} &= -\check{b}_{k,0} \sin\theta \sin^2\phi - \frac{2\check{a}_{k,+}\check{a}_{k,-} c_k \cos^2\phi}{\check{a}_{k,+} - \check{a}_{k,-}} && (11) \\ u_0 &= u_c - \frac{D\tan\phi}{\cos\theta}, && (12) \\ v_0 &= v_c - D\tan\theta. && (13) \end{aligned}$$

For now we assume $\phi \neq 0$ in eqn. (10). The point object locations, r_k, z_k, in units of the radius of rotation R, can be obtained as follows.

$$\tilde{r}_k \triangleq \frac{r_k}{R} = \frac{1}{c_k} \frac{D/\cos\theta}{D/\cos\theta + \check{b}_{k,0}\sin\theta}. \tag{14}$$

$$\tilde{z}_k \triangleq \frac{z_k}{R} = \frac{\check{v}_0 \cos\phi\cos\theta}{\frac{D}{\cos\theta} + \check{b}_{k,0}\sin\theta} \tag{15}$$

The radius of rotation R can be determined if the distance between a pair of point objects is known. The method is similar to that described in [6], with the consideration that $\theta \neq 0$. We define the following quantities for each point object k at each projection view i,

$$\begin{aligned} \tilde{I}_k^{(i)} &\triangleq \frac{\tilde{z}_k}{(v_k^{(i)} - v_0)\cos\theta - D\sin\theta}, \\ \tilde{U}_k^{(i)} &\triangleq \frac{\tilde{z}_k(u_k^{(i)} - u_0)}{(v_k^{(i)} - v_0)\cos\theta - D\sin\theta} = \tilde{I}_k^{(i)}(u_k^{(i)} - u_0), \\ \tilde{V}_k &\triangleq \frac{\tilde{z}_k(v_k^{(i)} - v_0)}{(v_k^{(i)} - v_0)\cos\theta - D\sin\theta} = \tilde{I}_k^{(i)}(v_k^{(i)} - v_0), \end{aligned}$$

where $D, \theta, u_0, v_0, \tilde{z}_k$ are the estimated geometric parameters as given in (10) – (15), and $(u_k^{(i)}, v_k^{(i)})$ denotes the projected center location of the point object k at projection view i. Let d_{kj} be the distance between 2 point objects k and j, $k \neq j$, then we can show that

$$\begin{aligned} \frac{d_{kj}^2}{R^2} &= (\tilde{U}_k^{(i)} - \tilde{U}_j^{(i)})^2 + +[\tilde{I}_k^{(i)} - \tilde{I}_j^{(i)}]^2 D^2 \cos^2\theta \\ &\quad +(\tilde{z}_k - \tilde{z}_j)^2 + (\tilde{V}_k^{(i)} - \tilde{V}_j^{(i)})^2 \sin^2\theta \\ &\quad +2(\tilde{V}_k^{(i)} - \tilde{V}_j^{(i)})(\tilde{I}_k^{(i)} - \tilde{I}_j^{(i)}) D\sin\theta\cos\theta \quad (16) \end{aligned}$$

holds for all projection view index i. The right-hand-side (RHS) of eqn. (16) are all known values. R can then be obtained from an averaged RHS and the known d_{kj} [6].

Although not explicitly used for calculating the geometric parameters, a relationship that we have rely on heavily in the derivations is

$$\tilde{z}_k \tan\theta = (1 - c_k \tilde{r}_k)\cos\phi. \tag{17}$$

We omit all derivations due to space limitations. The generic expressions eqns. (9) – (15) simplify when $\theta = 0$. When $\phi \neq 0$, we need a minimum of two point objects to determine the geometric parameters since eqn. (10) needs 2 point objects, and all the other equations need one each. However when $\tan\phi = 0$, θ cannot be determined using eqn. (10) and subsequent evaluations can not proceed. Another issue that we find in numerical simulations is that even when $\tan\phi \neq 0$, calculating θ from eqn. (10) results in a large variation and affects subsequent parameter evaluations. Next we start by considering the issue $\tan\phi = 0$ first. Through the process, we also discover a more stable way of estimating θ to replace eqn. (10).

C. Finding θ

Examining the general equations (11) – (13), we observe that the following parameters can still be obtained when $\phi = 0$.

$$\frac{D}{\cos\theta} = c_k \check{a}_{k,+}, \tag{18}$$

$$u_0 = u_c. \tag{19}$$

Eqn. (18) is obtained from eqn. (11), and that $\phi = 0$ which results from $\check{a}_{k,+} + \check{a}_{k,-} = 0$.

Among the remaining relationships, namely eqns. (14), (15), and (17), only 2 are independent for each k. Counting $D/\cos\theta$ as known, there are 3 unknowns ($\tilde{r}_k$, $\tilde{z}_k$, and $\sin\theta$) in the two independent equations. If we consider using more point objects, then each additional object will bring two more equations but also two more unknowns of the object location ($\tilde{r}_k$ and $\tilde{z}_k$), hence will not help the situation.

To reduce the number of unknowns, we must have some prior information on the point object locations. Suppose we have 3 colinear objects such that the middle one is at a known relative distance to the other two, then there will be in total 6 equations (two for each k) and also 6 unknowns (θ, $\tilde{r}_{1,2,3}$ and $\tilde{z}_{1,3}$, since by assumption

$$\tilde{z}_2 = \lambda\tilde{z}_1 + (1-\lambda)\tilde{z}_3, \ 0 < \lambda < 1, \lambda \text{ known}. \tag{20}$$

The detector tilt angle θ can then be unambiguously resolved, and so are all other parameters. Therefore a minimal of 3 point objects are needed when $\phi = 0$. Moreover, using such 3-point configurations, we can obtain an alternative, more stable expression for $\sin\theta$ even when $\phi \neq 0$ to replace eqn. (10). The following two expressions for $\sin\theta$ can be derived.

$$\sin\theta = \frac{\frac{D}{\cos\theta}}{\prod_{k=1}^{3} \check{b}_{k,0}} \left(\frac{\lambda \check{b}_{1,0} + (1-\lambda)\check{b}_{3,0} - \check{b}_{2,0}}{\frac{\lambda}{\check{b}_{1,0}} + \frac{1-\lambda}{\check{b}_{3,0}} - \frac{1}{\check{b}_{2,0}}} \right) \tag{21}$$

for $\phi = 0$ and

$$\sin\theta = \frac{\prod_{k=1}^{3} A_k}{\prod_{k=1}^{3} \check{b}_{k,0}} \left(\frac{\lambda \frac{\check{b}_{1,0}}{A_1} + (1-\lambda)\frac{\check{b}_{3,0}}{A_3} - \frac{\check{b}_{2,0}}{A_2}}{\lambda \frac{A_1}{\check{b}_{1,0}} + (1-\lambda)\frac{A_3}{\check{b}_{3,0}} - \frac{A_2}{\check{b}_{2,0}}} \right) \tag{22}$$

for $\phi \neq 0$. In both eqns. (21) and (22), $\check{b}_{k,0}$, for $k = 1, 2, 3$ are as defined in eqn.(6), and A_k in eqn. (22) are defined as

$$A_k \overset{\triangle}{=} -\frac{2\check{a}_{k,+}\check{a}_{k,-}c_k}{\check{a}_{k,+} - \check{a}_{k,-}}, \ k = 1, 2, 3. \tag{23}$$

The quantity λ is the known relative distance between the middle point and the two side ones [cf. eqn. (20)]. It is easy to see that eqn. (21) is a special case of eqn. (22) since when $\phi = 0$, from eqn. (11) we have

$$\frac{D}{\cos\theta} = -\frac{2\check{a}_{k,+}\check{a}_{k,-}c_k}{\check{a}_{k,+} - \check{a}_{k,-}} \equiv A_k, \ \forall k. \tag{24}$$

Replacing eqn. (10) with either eqn. (21) or the general case eqn. (22), we obtain the complete parameters from eqns. (9), (11) – (16). We also need to know the distance between any 2 point objects to calculate R by eqn. (16).

D. Summary of the method

We summarize the calibration method using the recipe in Fig. 4. We start by the graphical procedure determining the in-plane rotation angle η [10]. A byproduct is that we also determine the projections of 5 characteristic positions for each point object. The locations of these characteristic positions, *i.e.*, at least one of their (x, y, z) coordinates is zero, simplifies the equations that link the unknown geometric parameters with their projection and subsequently enable a simple inversion.

1) Use the graphical procedure to determine η;
2) Perform in-plane rotation by η, the rotation center can be arbitrary, *e.g.*, $(0, 0)$;
3) Locate the projection of the characteristic positions $(\hat{u}_k, \hat{v}_k)$, $(u_k^{\pm}, v_k^{\pm})$, $(u_{k,\pm}, v_{k,\pm})$, (u_c, v_c), for all k;
4) Calculate quantities $a_{k,\pm}, b_{k,0}, c_k$, for all k;
5) Use eqn. (22) to calculate θ;
6) Use eqn. (9) to calculate ϕ;
7) Use eqn. (11) to calculate $D/\cos\theta$, and D;
8) Use eqn. (19) to calculte u_0 ;
9) Use eqn. (13) to calculate v_0
10) Use eqns. (14), (15), and (16) to calculate R.
11) Perform in-plane rotation by $-\eta$ to obtain u_c, v_c, or u_0, v_0.

Fig. 4. Step-by-step recipe of the proposed geometric calibration method.

As has been observed in other publications, *e.g.* [6], [7], [12], we find a 2-point object configuration is not enough to resolve the parameter ambiguity when the detector slant angle $\phi = 0$. When $\phi \neq 0$, although a 2-point configuration theoretically suffices to calculate all unkonwns, our numerical studies show that the estimate of θ using eqn. (10) is not stable. A 3-point colinear configuration with known relative distance is proposed to estimate θ more reliably whether $\phi = 0$ or not. The *colinear* requirement is an easy and practical way to ensure the relative distance condition (20).

Both [6] and our method rely on ellipse fitting. Our parameterization is more ”aligned” with the object space coordinate system hence the inversion process is simpler. One property of these ellipse-fitting base methods is that the calibration results depend on the input point object projection only through the fitted ellipse parameters. In this sense, partial data acquisition range, *i.e.*, a short scan, or projection truncation can be handled naturally as long as ellipse fitting can be performed. How well it works in these partial projection situations may depend on the specific data acquisition geometry and the noise in the projection data, and is one of the problems we study next.

III. NUMERICAL STUDIES

We focus on two properties of the proposed method, (1) the robustness against noise in the projection data; and (2) the robustness against the angular acquisition range in the calibration scan.

The parameters in Table I are used in the simulations. We simulate cone-beam projection of 3 ideal (of radius 0) colinear point objects at 0.5° interval over 360° acquisition range. The objects are arranged such that $\lambda = 1/3$ in eqn. (20). The simulated detector has 616 elements in the transaxial direction (u) and 480 elements in the axial direction v. The flat detector has square pixels of side length 0.616 mm. To approximate effects of noise in the projection data, the projection location of the point object is perturbed by Gaussian noise of standard deviations 0.01 and 0.1 in pixel size unit. To calculate R [cf. eqn. (16)], estimates of the object distance d_{12} and d_{23} are obtained by perturbing their true distances (114.92 mm and 57.462 mm) with the same level Gaussian noise of 0.01 and 0.1 (pixel unit) standard deviations. These estimated distances also provide an estimate of λ. From the 720 projection views in a full 360° scan, we extract three data sets that correspond to 200°, 270°, and the full 360° angular range. The shortest acquisition interval 200° can be used as a short scan for objects of 23 cm or smaller.

TABLE I
PARAMETERS USED IN COMPUTER SIMULATIONS.

θ [deg]	ϕ [deg]	D [mm]	R [mm]
2.5	-2.2	1200.0	750.0
u_c [mm]	v_c [mm]	η [deg]	# of views
-33.338	44.736	3	200°, 270°, 360° @ 0.5°

In our simulations, the detector tilt angle θ and the slant angle ϕ are fixed at 2.5° and -2.2°, respectively. We apply the recipe in Fig. 4 to obtain the complete set of parameters. In all cases, *i.e.*, different noise level in projection data and different data acquisition range, we calculate the mean and the standard deviation of the estimated parameters using 50 independent noise realizations. The parameter estimation results are provided in Fig. 5.

IV. RESULTS

In Fig. 5 we tabulate the estimation results. At each noise level, the standard deviation of the estimated parameters increase as the data acuqisition range shortens. Generally speaking, shorter acqusition range and higher noise in projection data have similar effects on the parameter variation. We notice at the higher noise level (0.1 pixel standard deviation) and the 200° angular range, there is a sharp increase in the standard deviation of the estimated parameters.

V. CONCLUSIONS

We have proposed a geometrical calibration method to estimate the seven parameters in circular cone beam geometry. The method is analytical and exact in the noise-free case. The calibration scan requires a minimum of 3 point objects with known distances between any 2-point combinations. A 3-point colinear configuration can be an easy and practical way to satisfy these requirements.

The initial steps of the calibration method are highly graphical in nature, which involves ellipse fitting, and calculation of line-ellipse intersections and tangencies. The results of these calculations are summarized by the projection locations of 5 characteristic positions for each point object and the projection of the origin. The subsequent analytical calculation of the geometrical parameters is straightforward. Due to space limitations, the derviations of all equations are omitted.

In the noise-free case, the accuracy of the proposed method is not affected by the angular range in the calibration scan as long as ellipse-fitting can be performed. It could be a full 360° acquisition, partial scans or with calibration projection truncation. In the presence of noise, our numerical evaluations demonstrate that the effects of partial scans on parameter accuracy are similar to increased noise level in projection data.

REFERENCES

[1] G. T. Gullberg, B. M. W. Tsui, C. R. Crawford, and E. R. Edgerton, “Estimation of geometrical parameters for fan beam tomography,” *Physics in Medicine and Biology*, vol. 32, no. 12, p. 1581, 1987.

[2] G. T. Gullberg, B. M. W. Tsui, C. R. Crawford, J. G. Ballard, and J. T. Hagius, “Estimation of geometrical parameters and collimator evaluation for cone beam tomography,” *Medical Physics*, vol. 17, no. 2, pp. 264–272, 1990.

[3] P. Rizo, P. Grangeat, and R. Guillemaud, “Geometric calibration method for multiple-head cone-beam SPECT system,” *Nuclear Science, IEEE Transactions on*, vol. 41, pp. 2748 –2757, dec 1994.

[4] R. Tsai, “A versatile camera calibration technique for high-accuracy 3D machine vision metrology using off-the-shelf TV cameras and lenses,” *Robotics and Automation, IEEE Journal of*, vol. 3, pp. 323 –344, august 1987.

[5] J. Heikkila, “Geometric camera calibration using circular control points,” *Pattern Analysis and Machine Intelligence, IEEE Transactions on*, vol. 22, pp. 1066 – 1077, oct 2000.

[6] F. Noo, R. Clackdoyle, C. Mennessier, T. A. White, and T. J. Roney, “Analytic method based on identification of ellipse parameters for scanner calibration in cone-beam tomography,” *Physics in Medicine and Biology*, vol. 45, no. 11, pp. 3489–3508, 2000.

[7] D. Beque, J. Nuyts, G. Bormans, P. Suetens, and P. Dupont, “Characterization of pinhole SPECT acquisition geometry,” *Medical Imaging, IEEE Transactions on*, vol. 22, pp. 599–612, May 2003.

[8] Y. Wang and B. Tsui, “Pinhole SPECT with different data acquisition geometries: Usefulness of unified projection operators in homogeneous coordinates,” *Medical Imaging, IEEE Transactions on*, vol. 26, pp. 298–308, March 2007.

[9] K. Yang, A. L. C. Kwan, D. F. Miller, and J. M. Boone, “A geometric calibration method for cone beam CT systems,” *Medical Physics*, vol. 33, no. 6, pp. 1695–1706, 2006.

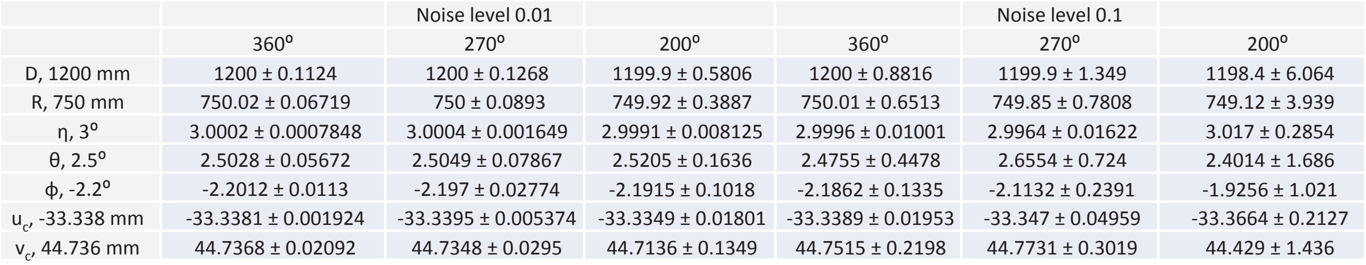

		Noise level 0.01			Noise level 0.1	
	360°	270°	200°	360°	270°	200°
D, 1200 mm	1200 ± 0.1124	1200 ± 0.1268	1199.9 ± 0.5806	1200 ± 0.8816	1199.9 ± 1.349	1198.4 ± 6.064
R, 750 mm	750.02 ± 0.06719	750 ± 0.0893	749.92 ± 0.3887	750.01 ± 0.6513	749.85 ± 0.7808	749.12 ± 3.939
η, 3°	3.0002 ± 0.0007848	3.0004 ± 0.001649	2.9991 ± 0.008125	2.9996 ± 0.01001	2.9964 ± 0.01622	3.017 ± 0.2854
θ, 2.5°	2.5028 ± 0.05672	2.5049 ± 0.07867	2.5205 ± 0.1636	2.4755 ± 0.4478	2.6554 ± 0.724	2.4014 ± 1.686
ϕ, -2.2°	-2.2012 ± 0.0113	-2.197 ± 0.02774	-2.1915 ± 0.1018	-2.1862 ± 0.1335	-2.1132 ± 0.2391	-1.9256 ± 1.021
u_c, -33.338 mm	-33.3381 ± 0.001924	-33.3395 ± 0.005374	-33.3349 ± 0.01801	-33.3389 ± 0.01953	-33.347 ± 0.04959	-33.3664 ± 0.2127
v_c, 44.736 mm	44.7368 ± 0.02092	44.7348 ± 0.0295	44.7136 ± 0.1349	44.7515 ± 0.2198	44.7731 ± 0.3019	44.429 ± 1.436

Fig. 5. Calibration results for different noise levels in the projection data and different angular acquisition range.

[10] J. Xu and B. M. Tsui, “A graphical method for determining the in-plane rotation angle in geometric calibration of circular cone-beam CT systems,” *IEEE Transactions on Medical Imaging*, vol. 31, pp. 825–833, march 2012.

[11] Y. Cho, D. J. Moseley, J. H. Siewerdsen, and D. A. Jaffray, “Accurate technique for complete geometric calibration of cone-beam computed tomography systems,” *Medical Physics*, vol. 32, no. 4, pp. 968–983, 2005.

[12] L. von Smekal, M. Kachelrieß, E. Stepina, and W. A. Kalender, “Geometric misalignment and calibration in cone-beam tomography,” *Medical Physics*, vol. 31, no. 12, pp. 3242–3266, 2004.

Hybrid Scatter Correction for CT Imaging

Matthias Baer and Marc Kachelrieß, *Member, IEEE*

***Abstract*—The purpose of this study was to develop and evaluate a hybrid scatter correction (HSC) for CT imaging. Therefore two established ways to perform scatter correction, physical scatter correction based on Monte Carlo simulations and a convolution–based scatter correction algorithm, were combined in order to perform an object–dependent, fast and accurate scatter correction.**

Based on a reconstructed CT image, patient–specific scatter intensity is estimated by a coarse Monte Carlo simulation that uses a reduced amount of simulated photons in order to reduce simulation time. In a second step this high noise estimate of the scatter intensity is used to calibrate the open parameters in a convolution–based algorithm which is then used to correct measured intensities for scatter.

Results show that with HSC scatter artifacts in CT images can be strongly reduced. While the error between images corrected with HSC and scatter–free reference images reduces to about 10% for simulations and measurments, simulation time can be reduced by about a factor of 50 $\approx$ 100 as compared to a low noise Monte Carlo scatter correction.

Keywords: CT imaging, Monte Carlo simulation, scatter correction, Convolution–based scatter correction

I. INTRODUCTION

In the literature there exists a great amount of scatter correction algorithms which either aim to produce estimates of the scatter portion in the measured intensities or try to heuristically correct images based on the well known structure of scatter artifacts (cupping and streaks).

Recently Rührnschopf et al. [1, 2] published a review article about scatter correction algorithms and interested reader may refer to these publications to get a general overview of available scatter correction algorithms.

Here we want to introduce an algorithm for a hybrid scatter correction (HSC) of CT images that combines two different scatter estimation methods: Physical scatter estimation based on Monte Carlo simulation and convolution–based scatter estimation. Each of these methods has its certain disadvantages which we want to avoid by combining the two approaches.

Physical scatter estimation based on Monte Carlo simulation of photon transport through the object is considered to be very accurate since real physics are incorporated in the model. The drawback of these methods is their high computational complexity as compared to other scatter methods [2].

Scatter estimation methods which have less computational needs are convolution–based methods. The principle of convolution–based algorithms is that based on measured intensities I_{ps}, a so–called scatter potential $\Phi = f(I_{\mathrm{ps}})$ is calculated which is convolved by a scatter kernel K in order to generate an estimate of the scatter intensity I_{s}. Different models for calculating Φ and K are given in [3, 4, 5, 6, 7, 8].

The drawback of convolution–based methods is that the models contain parameters for the shape of the scatter kernel K and the scatter potential Φ which need to be calibrated in advance.

The HSC algorithm which we introduce here combines Monte Carlo–based scatter correction with a convolution–based algorithm to do a fast, accurate, and object–dependent scatter correction that needs no extra calibration measurements or simulations. Thereby the principle of HSC is that based on a coarse Monte Carlo simulation of the scatter intensity open parameters in a convolution–based algorithm are determined. The Monte Carlo–calibrated convolution–based algorithm is then used to correct measured intensities for scatter.

II. MATERIALS AND METHODS

In the following the projection angle will be denoted by α while the angles in the fan and cone are parameterized by β and γ. Let $q_{\mathrm{ps}}(\alpha,\beta,\gamma)$ be the measured projection value including scatter, i.e. $q_{\mathrm{ps}}(\alpha,\beta,\gamma)$ is given by

$$q_{\mathrm{ps}}(\alpha,\beta,\gamma) = -\ln \frac{I_p(\alpha,\beta,\gamma) + I_s(\alpha,\beta,\gamma)}{I_0(\alpha,\beta,\gamma)}.$$

Here $I_{\mathrm{p}}(\alpha,\beta,\gamma)$, $I_{\mathrm{s}}(\alpha,\beta,\gamma)$, and $I_0(\alpha,\beta,\gamma)$ are the primary, scattered and unattenuated intensity. The dependency on α, β, and γ will be dropped in the following for convenience.

Given that we have an algorithm to generate an estimate $\hat{I}_{\mathrm{s}}$ of the real scatter intensity I_{s} we can compute a scatter corrected projection value

$$\hat{q}_{\mathrm{p}} = -\ln \frac{I_{\mathrm{p}} + I_{\mathrm{s}} - \hat{I}_{\mathrm{s}}}{I_0}$$

that is an estimate of the real scatter–free projection value $q_{\mathrm{p}} = -\ln I_{\mathrm{p}}/I_0$.

Note that $\hat{q}_{\mathrm{p}}$ is only corrected for scatter and therefore images reconstructed from $\hat{q}_{\mathrm{p}}$ will still contain artifacts that arise from the polychromatic source spectrum of the x–ray tube, i.e. cupping and beam hardening artifacts. To correct those artifacts we used the Empirical Cupping Correction (ECC) algorithm [9] for water precorrection and the Empirical Beam Hardening Correction (EBHC) algorithm [10] to remove beam hardening artifacts.

Matthias Baer, Prof. Dr. Marc Kachelrieß: Institute of Medical Physics (IMP), University of Erlangen–Nürnberg, Henkestr. 91, 91052 Erlangen, Germany.

Matthias Baer, Prof. Dr. Marc Kachelrieß: German Cancer Research Center (DKFZ), Im Neuenheimer Feld 280, 69120 Heidelberg, Germany.

Corresponding author: matthias.baer@imp.uni-erlangen.de

A. Monte Carlo Simulation Tool

For HSC we used an in–house Monte Carlo simulation tool. Based on tabulated data for the attenuation coefficient and the cross sections of Compton scattering, Rayleigh scattering and photo effect, photon histories through the scanned object are simulated in order to compute a Monte Carlo estimate $\hat{I}_\mathrm{s}^\mathrm{MC}$ of the scatter intensity. To reduce the computational costs of the photon transport the Woodcock tracking algorithm [11] for path length sampling is used. In order to further decrease the simulation time of the Monte Carlo scatter signal the fixed splitting technique [12] and the Richardson–Lucy algorithm as described in [13] are implemented and used in the software.

B. Convolution–Based Algorithm

The convolution–based algorithm we used for HSC is the one published by Ohnesorge et al. [5]. According to this model scatter intensity can be estimated by scaling measured x–ray intensities with the scatter potential

$$\Phi(q_\mathrm{ps}, c_0, c_1) = c_0 + c_1 \cdot q_\mathrm{ps}\, e^{-q_\mathrm{ps}},$$

followed by a convolution with the scatter kernel K. Therefore with the convolution–based model an estimate $\hat{I}_\mathrm{s}^\mathrm{CB}$ of the scatter intensity along a certain ray may be estimated using

$$\hat{I}_\mathrm{s}^\mathrm{CB}(q_\mathrm{ps}, \boldsymbol{c}) = \Phi(q_\mathrm{ps}, c_0, c_1) * K(q_\mathrm{ps}, c_2, c_3, c_4, c_5)$$

with the scatter kernel

$$K(q_\mathrm{ps}) = \left(\sum_{\pm} e^{-c_2(\beta \pm c_3)^2} \cdot \sum_{\pm} e^{-c_4(\gamma \pm c_5)^2} \right).$$

In the original paper [5] the open parameters $c_i,\ i = 0, \ldots, 5$ were determined by calibration measurements. With HSC the open parameters are determined without prior calibration but by using a coarse Monte Carlo simulation of the scatter intensity based on a reconstruction of the scanned object.

C. Hybrid Scatter Correction (HSC)

Since the simulation time of Monte Carlo simulations depends on the number of simulated photons one way to reduce simulation time is to decrease the number of simulated photons. The drawback of this approach is that it comes at the cost of a higher noise level in the simulated scatter signal. With HSC we overcome this by using the high noise Monte Carlo signal only to calibrate the open parameters in a convolution–based algorithm which is then used for the scatter correction. As compared to other approaches were the open paramteres are calibrated by prior calibration measurements [14] or Monte Carlo simlations of calibration objects [15, 6, 8], we here use an estimate of the scatter intensity that is computed based on the scanned object itself to determine the open paramters.

The calibration of the convolution–based algorithm is then done by minimizing the quadratic error between the high noise Monte Carlo estimate $\hat{I}_\mathrm{s}^\mathrm{MC}$ and the estimate $\hat{I}_\mathrm{s}^\mathrm{CB}$ of the convolution–based algorithm, i.e. we have to solve

$$\boldsymbol{c}(\alpha) = \arg\min_{\boldsymbol{c}(\alpha)} \int d\beta\, d\gamma \left(\hat{I}_\mathrm{s}^\mathrm{MC}(\alpha, \beta, \gamma) - \hat{I}_\mathrm{s}^\mathrm{CB}(\alpha, \beta, \gamma, \boldsymbol{c}) \right)^2. \tag{1}$$

Here $\boldsymbol{c}(\alpha) = \big(c_0(\alpha), \ldots, c_5(\alpha)\big)$ is a vector containing all open parameters of the convolution–based algorithm which may depend on the projection angle α.

Equation (1) can be solved by using any standard numerical nonlinear minimization algorithm. We here used a multidimensional downhill simplex algorithm [16].

Note that HSC is not restricted to the usage of a certain convolution–based algorithm. As long as a convolution–based algorithm contains a set of open parameters to model the scatter potential Φ and the scatter kernel K that need to be calibrated in advance, it can be used in HSC. The investigation which of the numerous convolution–based algorithms that exist in literature fits best to HSC is beyond the scope of this paper since here we only want to show the general applicability of HSC.

D. Simulations

To validate our new method we performed simulations in a clinical CT geometry. A typical prefiltration and typical detector efficiencies corresponding to a clinical CT scanner were taken into account. Additionally a one dimensional anti scatter grid was placed on top of the detector. Simulations were performed for a monochromatic and a polychromatic source spectrum in order to clearly distinguish between artifacts arising from scatter and artifacts caused by the spectrum of the x–ray source. The polychromatic source spectrum was modeled according to Tucker et al. [17]. Polychromatic simulations were done at a typical tube voltage of U =120 kV whereas monochromatic simulations were performed at an energy of E =70 keV. All simulations were done for the Forbild thorax phantom (http://www.imp.uni-erlangen.de/phantoms/).

1) Monochromatic Source Model: In a first experiment the number of calibration steps N_cal needed to achieve an accurate scatter correction was determined. The projection angles $\alpha_n = \alpha_0 + n \cdot 2\pi/N_\mathrm{cal}$ for which a new parameter vector $\boldsymbol{c}(\alpha_n)$ was calibrated were distributed equally spaced over 360 degree starting at the p.a. direction ($\alpha_0 = 0$). The parameter vector $\boldsymbol{c}(\alpha)$ between two calibration angles was computed by linear interpolation. In order to facilitate the analysis of the pure scatter correction potential of HSC as a function of N_cal, calibration was done based on a low noise Monte Carlo simulation.

To determine the number of photons N_Ph needed in the Monte Carlo simulation step of HSC, scatter intensity was simulated with reduced amounts of photons. The convolution–based algorithm was calibrated based on these coarse Monte Carlo simulations and the accuracy of the scatter correction as a function of N_Ph was investigated.

As a quantitative measure of the scatter correction potential we use the relative error E defined as

$$E = \sqrt{\int d\boldsymbol{r}\,\left(f_{\text{ref}}(\boldsymbol{r}) - \hat{f}(\boldsymbol{r})\right)^2 \Big/ \int d\boldsymbol{r}\,\left(f_{\text{ref}}(\boldsymbol{r}) - f(\boldsymbol{r})\right)^2}. \tag{2}$$

Here, f_{ref} is the reference image reconstructed from primary radiation only, f is the uncorrected image with scatter, and $\hat{f}$ is the scatter–corrected image. The material composition and density distribution needed for the Monte Carlo simulations were taken from the known phantom composition.

2) Polychromatic Source Model: Based on the results for N_{cal} and N_{Ph} from the preceding sections the scatter correction potential of HSC was investigated in a more realistic simulation setup using polychromatic projection data. The density and material information for the Monte Carlo simulation were taken from a water–precorrected reconstruction that included beam hardening and scatter artifacts. Again artifact reduction was determined by measuring the error E (equation (2)).

E. Measurements

To evaluate the scatter correction potential of HSC for measured data a scan of an head phantom was performed with the Varian OBI CT scanner, Varian Medical Systems, Palo Alto, USA. Tube voltage was set to 120 kV and density and material information of the head phantom was extracted from a water–precorrected reconstruction. For the measurements no scatter–free reference reconstruction was available. Therefore we used an image corrected with a low noise Monte Carlo simulation on which we applied EBHC as reference. In analogy to equation (2) the error between this reference and the corrected image was used as a measure of artifact correction.

III. RESULTS

A. Monochromatic Source Model

Figure 1 shows the results for the scatter reduction potential of HSC as a function of calibration steps N_{cal}. For $N_{\text{cal}} \geq 16$ only minor changes can be observed. Based on this result all further experiments were performed with $N_{\text{cal}} = 16$.

The error between an image reconstructed from primary radiation only and an image reconstructed from scatter–corrected projection data as a function of the number of simulated Monte Carlo photons is depicted in figure 1. The error increases only slightly up to a relative photon number of $N_{\text{Ph}}/N_{\text{Ph, ref}} = 0.01$, where $N_{\text{Ph, ref}}$ is the number of photons used in a low noise reference Monte Carlo simulation. If the photon number is further reduced a strong increase in the error can be observed. Therefore all succeeding experiments were performed with with $N_{\text{Ph}}/N_{\text{Ph, ref}} = 0.01$.

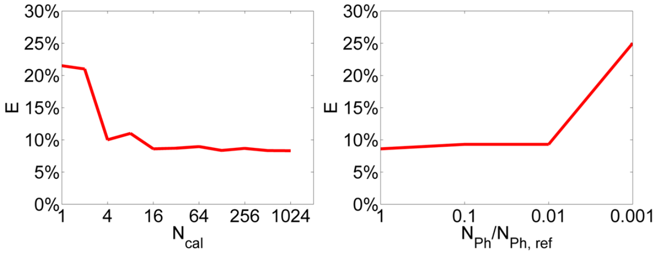

Fig. 1. Left: Error in scatter–corrected images as a function of N_{cal}. The analysis for N_{cal} was done based on a low noise Monte Carlo simulation using $N_{\text{Ph, ref}}$ photons. For $N_{\text{cal}} \geq 16$ only minor changes can be observed. A total of 1024 projections were simulated. Right: Error in scatter–corrected images as a function of the relative photon number $N_{\text{Ph}}/N_{\text{Ph, ref}}$ with $N_{\text{Ph, ref}}$ being the number of photons in a low noise reference Monte Carlo simulation and N_{Ph} being the number of photons used to calibrate the convolution–based algorithm. The analysis was done with $N_{\text{cal}} = 16$.

B. Polychromatic Source Model

The results for the scatter correction potential of HSC in case of polychromatic projection data are shown in figure 2. With HSC scatter artifacts are strongly reduced. Since HSC addresses only scattered radiation beam hardening artifacts remain in the corrected image. After performing EBHC on top of HSC the error in the corrected image stays under 15%.

C. Measurements

Results for the measurements are shown in figure 2. Compared to the uncorrected image scatter and beam hardening artifacts are strongly reduced by using HSC and EBHC. The difference image shows only minor differences between the reference image corrected with the full blown Monte Carlo simulation and the HSC corrected image (figure 2).

IV. SUMMARY AND CONCLUSION

As shown, four simulated Monte Carlo projections are sufficient to achieve an accurate scatter correction. Let us assume that during a standard CT scan in the order of 1000 projections are acquired. Further assume that the simulation time for one low noise Monte Carlo scatter projection is given by t_{MC}. As shown, with HSC we need to do the Monte Carlo simulation only for four projections and the photon number in the Monte Carlo simulation can be decreased by about a factor of 100 while still achieving a good scatter correction. The computation time t_{CB} for fitting the open parameters in the convolution–based algorithm was in the same order as the simulation time t_{MC} for one low noise Monte Carlo scatter projection. Therefore the total speed up due to HSC as compared to a full low noise Monte Carlo simulation of the scatter signal can be estimated by

$$\text{SpeedUp} = \frac{1000 \cdot t_{\text{MC}}}{16 \cdot 0.01 \cdot t_{\text{MC}} + 16 \cdot \underbrace{t_{\text{CB}}}_{\approx t_{\text{MC}}}} \approx 50 \text{ to } 100.$$

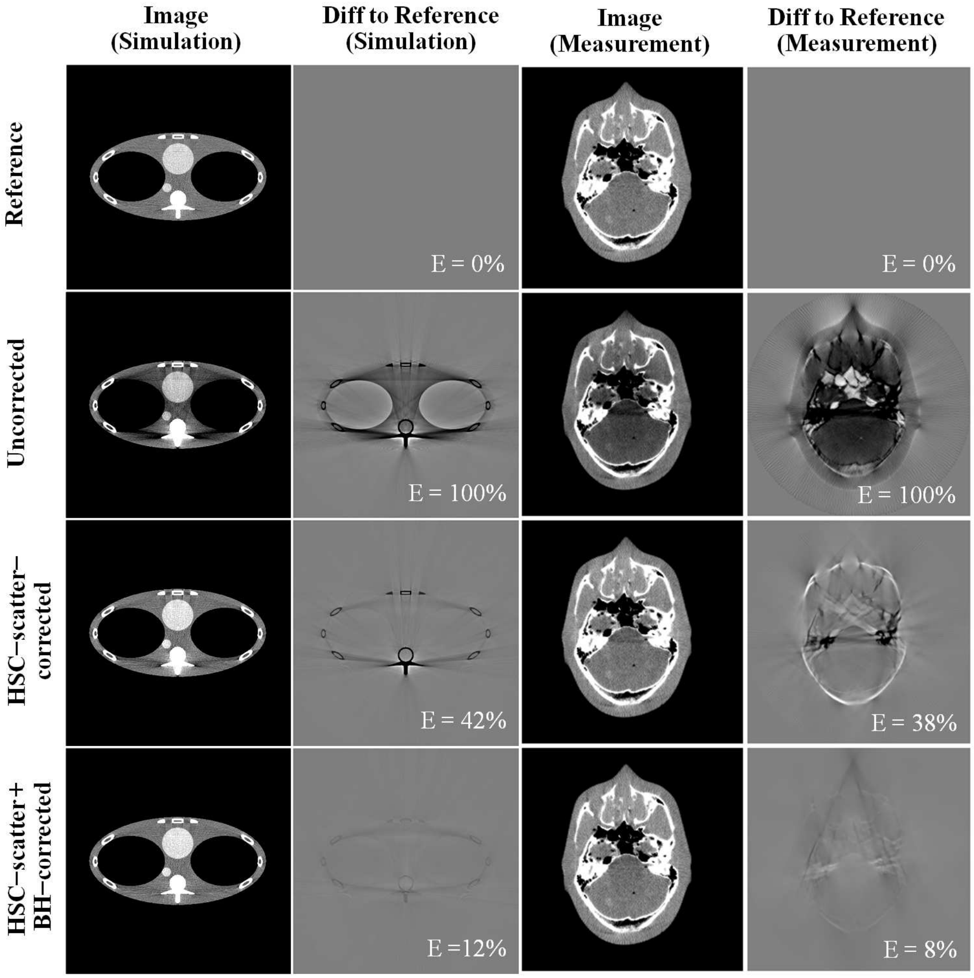

Fig. 2. First and second column depict the results of the simulation study. First column top to bottom: EBHC–corrected image reconstructed from scatter free projection data, uncorrected image containing scatter and beam hardening artifacts, image corrected for scatter with HSC, scatter– and beam hardening–corrected image. All images are depicted at the same window setting (C=0 HU / W=200 HU). Second column: Difference to reference image. Windowing: C=0 HU / W=200 HU. Results of the measurements are depicted in third and fourth row. Third column top to bottom: Scatter– (low noise Monte Carlo) and EBHC–corrected reference image, uncorrected image containing scatter and beam hardening artifacts, image corrected for scatter with HSC, scatter– and beam hardening–corrected image. All images are depicted at the same window setting (C=50 HU / W=400 HU). Fourth column: Difference to refernce image. Windowing: C=0 HU / W=300 HU.

So in conclusion with HSC we propose a method that exhibits the possibility to do a Monte Carlo–based, object–dependent scatter correction with highly reduced computational needs as compared to pure Monte Carlo–based scatter correction while still achieving a good scatter artifact correction.

V. ACKNOWLEDGMENTS

This study was supported by a grant from the Intel Corporation. Parts of the reconstruction software were provided by RayConStruct® GmbH, Nürnberg, Germany.

REFERENCES

[1] Ernst-Peter Rührnschopf and Klaus Klingenbeck. A general framework and review of scatter correction methods in x–ray cone–beam computerized tomography. Part 1: Scatter compensation approaches. *Med. Phys.*, 38(7):4296–4311, July 2011.
[2] Ernst-Peter Rührnschopf and Klaus Klingenbeck. A general framework and review of scatter correction methods in cone beam CT. Part 2: Scatter estimation approaches. *Med. Phys.*, 38(9):5186–5199, September 2011.
[3] W. Swindell and P. M. Evans. Scattered radiation in portal images: A Monte Carlo simulation and simple physical model. *Med. Phys.*, 23(1):63–67, 1996.
[4] V. N. Hansen, W. Swindell, and P. M. Evans. Extraction of primary signal from EPIDs using only forward convolution. *Med. Phys.*, 24(9):1477–1484, 1997.
[5] Bernd Ohnesorge, Thomas Flohr, and Klaus Klingenbeck-Regn. Efficient object scatter correction algorithm for third and fourth generation CT scanners. *European Radiology*, 9:563–569, 1999.
[6] J. S. Maltz, B. Gangadharan, S. Bose, D. H. Hristov, B. A. Faddegon, A. Paidi, and A. R. Bani-Hashemi. Algorithm for x–ray scatter, beam–hardening, and beam profile correction in diagnstic (kilovoltage) and treatment (megavoltage) cone beam CT. *IEEE Transactions on Medical Imaging*, 27(12):1791–1810, 2008.
[7] Michael Meyer, Willi A. Kalender, and Yiannis Kyriakou. A fast and pragmatic approach for scatter correction in flat–detector CT using elliptic modeling and iterative optimization. *Phys. Med. Biol.*, 55(1):99–120, Janurary 2010.
[8] M. Sun and J. M. Star-Lack. Improved scatter correction using adaptive scatter kernel superposition. *Phys. Med. Biol.*, 55(22):6695–6720, October 2010.

[9] Marc Kachelrieß, Katia Sourbelle, and Willi A. Kalender. Empirical cupping correction: A first order rawdata precorrection for cone–beam computed tomography. *Med. Phys.*, 33(5):1269–1274, May 2006.

[10] Yiannis Kyriakou, Esther Meyer, Daniel Prell, and Marc Kachelrieß. Empirical beam hardening correction (EBHC) for CT. *Med. Phys.*, 37(10):5179–5187, October 2010.

[11] E. Woodcock. Techniques used in the GEM code for Monte Carlo neutronics calculations in reactors and other systems of complex geometry. *Proc. Conf. on Apll. Of Compution Methods to Reactor Problems, Argonne National Laboratories Report*, 1965.

[12] Ernesto Mainegra-Hing and Iwan Kawrakow. Variance reduction techniques for fast Monte Carlo CBCT scatter correction calculations. *Phys. Med. Biol.*, 55(16):4495–4507, July 2010.

[13] Wojciech Zbijewski and Freek J. Beekmann. Efficient Monte Carlo based scatter artifact reduction in cone–beam micro–CT. *IEEE Transactions on Medical Imaging*, 25(7):817–827, 2006.

[14] Li Heng, Radhe Mohan, and X Ronland Zhu. Scatter kernel estimation with an edge–spread function method for cone–beam computed tomography imaging. *Phys. Med. Biol.*, 53(23):6729–6748, 2008.

[15] L Spiess, M. Ebert, B. A. Groh, B. M. Hesse, and T. Bortfeld. Correction of scatter in mega voltage cone–beam CT. *Phys. Med. Biol.*, 46(3):821–833, 2001.

[16] William H. Press, Saul A. Teukolsky, William T. Vetterling, and Brian P. Flannery. *Numerical Recipes in C*. Cambridge University Press, 1992.

[17] Douglas M. Tucker, Gary T. Barnes, and Dev P. Chakraborty. Semiempirical model for generating tungsten target x–ray spectra. *Med. Phys.*, 18(3):211–218, March/April 1991.

Calculation and Comparison of Figures of Merit for Spectral CT

David S. Rigie and Patrick J. La Rivière

Abstract—**In recent years, there has been a renewed interest in spectral CT. Advances in detector technology and post-processing methods have made concepts which were described as early as the 1970s realizable in the clinic today. Still, there is divergence in the field as to which approach to spectral CT is optimal, with major vendors exploring dual-source imaging, fast kV switching, dual-layer detectors, and photon counting detectors. In this paper we propose two figures of merit for quantitatively comparing these techniques: a physical SNR that is a direct measure of the data quality, and a clinical SNR that quantifies a systems ability to perform a clinical decision task. We believe these metrics will be useful both in guiding the design of a spectral CT system as well as choosing optimal parameters when performing a clinical scan based upon the task that is being performed.**

I. INTRODUCTION

There has been a great deal of interest in spectral CT over the last few years due partly to the development of clinical systems by major vendors and also because of the recent advances made in photon-counting detectors. Though the mathematical framework has been around for several decades [1], the technology has only recently seen clinical adoption. It has been shown that spectral CT can provide better contrast-to-noise than conventional CT without additional dose cost [4], and there is an ever-growing list of clinical applications, which have been discussed extensively elsewhere [5].

The usefulness of spectral CT is unquestionable, however the general criteria for acquiring spectral information are quite loose, and so many different approaches have been studied, each with its own advantages and disadvantages. In this paper, we seek to outline some methods for evaluating the relative performance of different spectral CT systems. Specifically, we have looked at kV switching, dual-source imaging, multilayer detection, and photon-counting schemes. All of the methods discussed are readily generalizable to generic spectral CT systems. We discuss two different figures of merit for evaluating the performance of a specified system: a physical SNR, which quantifies the quality of the measured data with regard to a specific decomposition task, and a clinical SNR which quantifies a system's utility in making a stated clinical decision. The physical SNR also serves as a useful metric for optimizing a system over a range of parameters, such as the energy thresholds in a photon-counting system. We believe these tools will be useful in aiding design choices during the development of a spectral CT system as well as helping an operator choose optimal parameters on an already existent system.

II. OBJECT MODEL

As described by Alvarez et al. [1] we first assume that the object function $\mu(\mathbf{r}, E)$ can be represented by some set of basis functions.

$$\mu(\mathbf{r}, E) = \sum_{i=1}^{N} \rho_i(\mathbf{r}) f_i(E) \tag{1}$$

One option is to use the mass-attenuation coefficients of the materials comprising the object. In this case, $\rho_i(\mathbf{r})$ would be the physical density distribution of the i^{th} material and $f_i(E)$ would be its mass attenuation at energy E. Next, we assume that multiple, spectrally distinct measurements are acquired. The j^{th} such measurement along a given ray through the object is

$$M_j = \int S_j(E) D_j(E) \exp\left\{ - \sum_{i=1}^{N} A_i f_i(E) \right\} dE \tag{2}$$

where $S_j(E)$ and $D_j(E)$ represent the energy dependence of the incident x-ray spectrum and the detector response, respectively. $A_i \equiv \int \rho_i(\mathbf{r}) d\ell$ is the integrated density of the i^{th} material along the measured ray. If the number of spectrally distinct measurements is at least as great as the number of basis materials, one can solve for the A_i and if this process is repeated for all of the rays in the CT projection data, one obtains the Radon transforms of the $\rho_i(\mathbf{r})$ for each material. Standard reconstruction methods can be applied to obtain true density maps.

III. PHYSICAL FIGURE OF MERIT

The inversion of (2) to get A, the line integral of the material densities, is affected by noise in the measurements M. Given the statistical fluctuations in M, we are only able to get a noisy estimate of the true values of A. The amount of noise in this estimate is largely affected by how well-posed the inverse problem is. It is straight-forward to show that the maximum-likelihood estimator of A, denoted by $\hat{A}$, is simply the value that satisfies (2), if the noise corrupted measurements are plugged in for M_j. While it is extremely difficult to calculate the probability distribution of $\hat{A}_i$, one can easily find the Cramer-Rao lower bound on the variance of $\hat{A}_i$ [3]. In most practical situations, the CRLB is achieved [1], and we obtain the true value of the variance of $\hat{A}_i$. We define the physical SNR for a given decompositon task as

$$\text{SNR}_{\text{P}} \equiv \frac{A_i}{\sigma_{\hat{A}_i}} \tag{3}$$

David Rigie and Patrick J. La Rivière are with the Department of Radiology at the University of Chicago

where $\sigma_{\hat{A}_i}$ is the standard deviation of $\hat{A}_i$. This physical SNR quantifies the minimum uncertainty we can achieve in a sinogram-domain material decomposition for a given projection line. It depends on the magnitude of the noise in our raw measurements as well as the amount of unique energy information provided by the spectral measurements.

IV. CLINICAL FIGURE OF MERIT

The clinical figure of merit seeks to assess the information content of the spectral CT data with respect to performing a specified clinical task. We've used the ideal observer formalism to evaluate the quality of the raw transmission data [2]. The task is to discriminate two nonrandom signals in additive Gaussian or Poisson noise. In spectral CT, it is often the case that the "shape" of the signal is known or discernable (e.g. a blood vessel), and the goal is to determine which of two known materials is present (e.g., Calcium or Iodine).

Mathematically, we are trying to discriminate between two hypotheses.

$$\begin{aligned} H_1 &: \ g = \mathbf{H} f_1 + n \\ H_2 &: \ g = \mathbf{H} f_2 + n \end{aligned} \tag{4}$$

Here, g is a vector containing our two different noise-corrupted, spectral measurements. The ideal observer decides in favor of hypothesis 1 when the likelihood ratio is greater than 1. Using the log-likelihood ratio as a test statistic, Λ, we can define a signal-to-noise ratio as

$$\mathrm{SNR}_{\mathrm{C}}^2 \equiv \frac{\left(\overline{\Lambda}_1 - \overline{\Lambda}_2\right)^2}{\frac{1}{2}\sigma_{\Lambda_1}^2 + \frac{1}{2}\sigma_{\Lambda_2}^2} \tag{5}$$

where $\overline{\Lambda_j}$ and $\sigma_{\Lambda_j}^2$ are the mean and variance, respectively, of the test-statistic under hypothesis j. The SNR quantifies how well the test-statistic is able to separate the two different hypotheses for given measurements. For the case of meausrements corrupted by Poisson noise, we get the following expression:

$$\mathrm{SNR}^2 = \frac{\left[\sum_i (\overline{g}_{1i} - \overline{g}_{2i}) \ln \frac{\overline{g}_{1i}}{\overline{g}_{2i}}\right]}{\frac{1}{2}\sum_i (\overline{g}_{1i} + \overline{g}_{2i}) \ln^2 \frac{\overline{g}_{1i}}{\overline{g}_{2i}}}. \tag{6}$$

Using the clinical and physical SNRs we will compare the performance of several different types of CT systems at distinguishing materials of clinical interest.

V. SOURCE AND DETECTOR MODELS

For all of the following models, it was assumed that multiple measurements were made along the same ray through the object. In practice, this may not be true for kV switching or dual-source imaging, so this idealization could artifically boost the performance of these techniques. All x-ray tube spectra were generated using the well-benchmarked Tucker model [6], and overall tube outputs were adjusted so that all spectral CT approaches would be evaluated at equal dose.

A. Dual-layer detection

Our model of the dual-layer detector is highly flexible in terms of material types and thicknesses. However, since it is not possible to change the composition of the detector on the fly for different imaging tasks, we assumed a 1mm front layer of ZnSe and a 2mm rear layer of GOS. The measurements from the two layers were considered to be completely independent, which in practice is difficult to achieve due to optical and electronic cross-talk. A 120 kVp spectrum was used with 2.7mm Al filtration, and its output was scaled so that one million photons would be incident on the object for a single projection line.

B. Fast kV Switching

To simulate fast kV switching, we used 140 and 80 kVp spectra with 2.7mm Al filtration. It was assumed that the 80 kVp measurement was taken with twice the integration time of the 140 kVp measurement. This is commonly done in practice to partially compensate for differences in tube output.

C. Dual-source Imaging

Dual-source imaging was modeled in the same manner as the kV switching case, except the high kVp spectrum had an additional 0.4mm tin filter for greater spectral separation. The relative outputs of the two tubes was also left as a free parameter, and for comparison purposes, it was optimized for each task according to physical SNR.

D. Photon Counting

Using the same tube spectrum as in the dual-layer detector case, the photon counting detector was assumed to have perfect energy windowing based on defined thresholds. Though we have not incorporated it into our model, it is straight-forward to model bin overlap caused by imperfect energy resolution. We used three energy bins with thresholds optimized for each imaging task based on physical SNR.

We have compared the photon-counting system to the others under the assumption of equal dose, which is usually unachievable due to low count-rate capabilities of photon-counting detectors at present. In practical situations, this would require a very long imaging time, so the strong performance of the photon-counting system should be interpreted with this caveat in mind.

VI. PRELIMINARY RESULTS

A. Physical SNR

To compare the above systems, we calculated the physical SNR associated with the determination of the integrated concentration of a "contrast" material within 30g/cm^2 of water background. Specifically, we looked at calcium, iodine, gold, gadolinium, uric acid, and struvite. Plots of the physical SNR as a function of the mass-thickness of contrast material are seen in fig. 1 and fig. 2. Table I gives a cross-section of such curves for all of the materials we looked at for 0.05g/cm^2 of contrast.

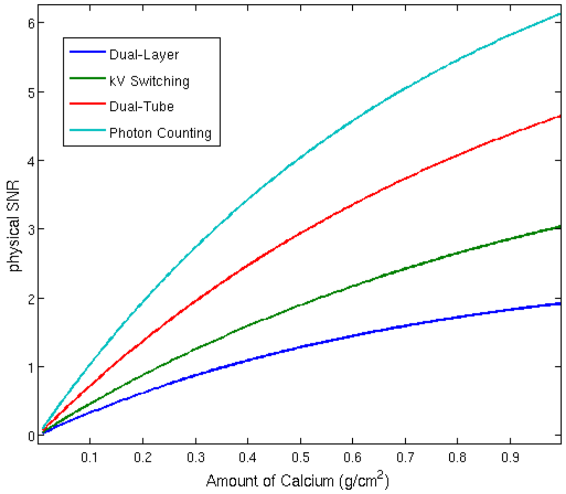

Fig. 1. Plot of physical SNR for varying amounts of Calcium in 30 g/cm^2 water background

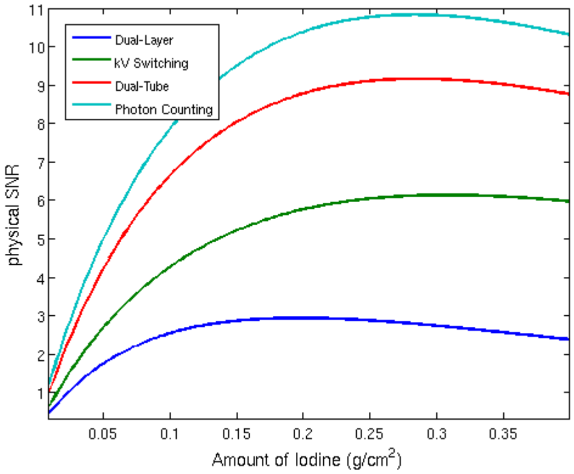

Fig. 2. Plot of physical SNR for varying amounts of Iodine in 30 g/cm^2 water background

TABLE I
PHYSICAL SNR OF CONTRAST MATERIALS

Contrast Material	Dual Layer	kV Switch	Dual Source	Photon Counting
Calcium	1.28	1.77	2.81	4.03
Iodine	2.00	5.16	7.96	9.70
Gold	0.58	1.17	2.10	8.14
Gadolinium	1.12	2.67	4.17	5.76
Uric Acid	0.05	0.02	0.03	0.05
Struvite	0.10	0.13	0.21	0.32

The relative ranking of these systems matches our intuition. Systems with greater degree of spectral separation between measurements perform better.

B. *Clinical SNR*

Using (6) for the photon-counting systems and an analogous Gaussian noise formula for the others, we looked at the task of distinguishing two materials of known amounts. Here, the task is not to distinguish contrast from background, but rather to determine which of two contrast materials is present. Table II gives the clinical SNR assuming 0.5 cm of contrast material in 30cm of water background. Figure 3 shows how the clinical SNR varies with the amount of contrast material for the case of the uric acid/calcium identification task.

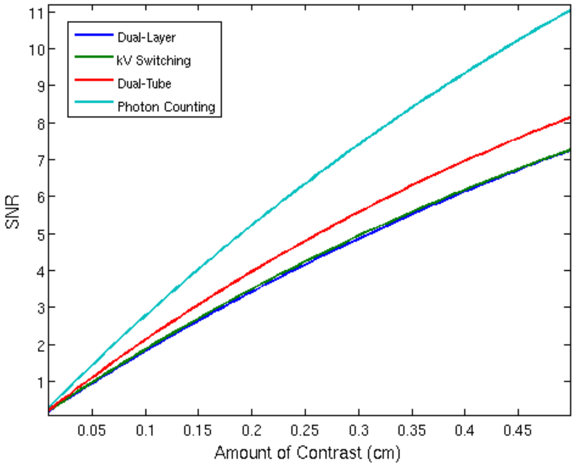

Fig. 3. Uric Acid / Calcium identification task: plot of clinical SNR for varying amounts of contrast in 30cm water background

TABLE II
CLINICAL SNR FOR IDEAL OBSERVER TASK

Contrast Material	Dual Layer	kV Switch	Dual Source	Photon Counting
Ca vs. I	23.11	10.38	13.64	43.28
Ca vs. Uric Acid	7.27	7.30	8.22	11.06
Uric Acid vs Ca	0.40	0.47	0.56	0.79

Again, we see the same relative performance ranking among systems considered.

C. *Image Domain Analysis*

The ideal observer model for clinical SNR does provide some useful information, but it is a bit restrictive. Another approach that may be more illuminating is to map the physical SNR into the image domain. Here, we will show how this can be done for parallel-beam geometry.

Let the integrated density of the i^{th} material along the line parametrized by (ξ, ϕ) be denoted by $A_i(\xi, \phi)$. These values are the ones that are solved for when doing the dual energy decomposition by inverting (2). The material density can be obtained by performing filtered back projection,

$$\rho_i(\mathbf{r}) = \int_0^{\pi} \int_{-\infty}^{\infty} h(\xi') A_i(\xi - \xi', \phi) d\xi' \qquad (7)$$

where $h(\xi')$ is the conventional ramp filter. Therefore, the variance of the density at position $\mathbf{r}$ is simply

$$\mathrm{var}\left\{\rho_i(\mathbf{r})\right\} \int_0^{\pi} \int_{-\infty}^{\infty} h^2(\xi')\sigma^2_{A_i}(\xi-\xi',\phi)d\xi' \tag{8}$$

where $\sigma^2_{A_i}$ is the same variance used in (5) obtained from the CRLB. We can use (8) to calculate the variance images for any arbitrary phantom. Figure 4 shows a 2D water phantom with four disks made of calcium and associated SNR images.

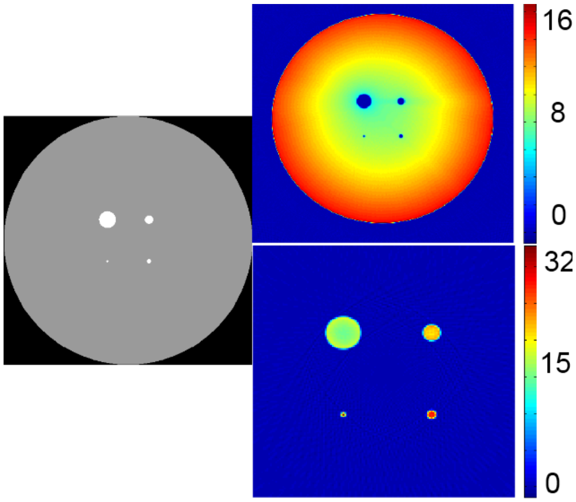

Fig. 4. (Left) 30 cm water phantom with 2cm, 1cm, 0.5cm and 0.25cm diameter calcium disks. (Top Right) SNR image for water density. (Bottom Right) SNR image for calcium density

This approach can easily be extended to a more realistic beam geometry.

VII. CONCLUSIONS AND FUTURE WORK

The simple physical SNR presented here is a useful tool for quantitatively comparing different spectral CT systems, and it can be mapped into the image domain for a more intuitive evaluation of performance. The fact that it can be calculated rapidly for different system parameters makes it suitable for optimization studies.

We found that the dual-source and photon-counting systems performed the best in every task we evaluated. This is to be expected because of the excellent spectral separation provided by these modalities.

In the future we would like to create a more realistic photon counting model that accounts for bin overlap and pulse pile-up. Furthermore, we plan on extending the 2D simulation to model a fan-beam geometry and include other relevant features, such as a bow-tie filter and electronic noise in the detector. Eventually, it may be necessary to resort to Monte Carlo simulations to account for scatter and other higher order effects. These considerations will be important for determining absolute performance capabilities, but we do not anticipate that they will drastically affect the relative performance rankings we are seeing. We are also working on developing better clinical performance metrics.

VIII. ACKNOWLEDGEMENT

We acknowledge research support and useful discussions from Toshiba Medical Research Institute USA. Patrick La Riviére was partly supported by NIH grant R01CA134680.

REFERENCES

[1] R.E. Alvarez and A. Macovski. Energy-selective reconstructions in x-ray computerised tomography. *Physics in Medicine and Biology*, 21:733–744, 1976.

[2] H. Barrett and K. Myers. *Foundations of Image Science*. Wiley-Interscience, 2004.

[3] C. Hermann E. Roessl. Cramer-rao lower bound of bases image noise in multiple-energy x-ray imaging. *Physics in Medicine and Biology*, 54.5:1307–1318, 2009.

[4] K. Neumaier G. Michalski U. Lechel K. Nikolaou C. Becker M. Resier J. Schenzle, W. Sommer and T. Johnson. Dual energy ct of the chest: how about the dose? *Invest Radiol*, 45.6:347–353, 2010.

[5] S.O. Schoenberg M.F. Resier T.R.C. Johnson, C. Fink, editor. *Dual Energy CT in Clinical Practice*. Springer, 2011.

[6] D.M. Tucker and G.T. Barnes. Semiempirical model for generating tungsten target x-ray spectra. *Medical Physics*, 18.2:211–218, 1991.

Multi-Material Decomposition Using Statistical Image Reconstruction in X-Ray CT

Yong Long and Jeffrey A. Fessler

Abstract—**Dual-energy (DE) CT scans provide two sets of measurements at two different source energies. In principle, two materials can be accurately decomposed from DECT measurements. For triple-material decomposition, a third constraint, such as volume or mass conservation, is required to solve three sets of unknowns from two sets of measurements. An image-domain (ID) method [1] has been proposed recently to reconstruct multiple materials using DECT. This method assumes each pixel contains at most three materials out of several possible materials and decomposes a mixture pixel by pixel. We propose a penalized-likelihood (PL) method with edge-preserving regularizers for each material to reconstruct multi-material images using a similar constraint. Comparing with the image-domain method the PL method greatly reduced noise, streak and cross-talk artifacts, and achieved much smaller root-mean-square (RMS) errors.**

Index Terms—**Computed tomography, dual energy, multi-material decomposition, statistical image reconstruction**

I. INTRODUCTION

Dual-energy (DE) CT reconstruction methods typically reconstruct images of two basis materials (*e.g.*, soft-tissue and bone) from two sets of measurements at two different X-ray source potential. However, some applications desire three or more component images [1], [2]. When quantifying the concentration of iron in a fatty liver, images of three constitute materials, iron, fat and tissue, are required [2]. For the purpose of radiotherapy, in addition to soft-tissue and bone it is also useful to know the distribution(s) of other materials, such as calcium, metal (*e.g.*, gold) and iodine.

A third criteria, such as volume conservation [1] or mass conservation [2], can enable reconstructing three basis materials from DECT measurements. Volume (mass) conservation assumes the sum of the volumes (masses) of the three constituent materials is equivalent to the volume (mass) of the mixture.

Mendonca *et al.* [1] proposed an image-domain method to reconstruct multiple materials pixel by pixel from a DECT scan. In addition to volume conservation assumption, this method assumes that each pixel contains a mixture of at most three materials and the material types can vary between pixels. It establishes a material library containing all the possible triplets of basis materials for a specific application. It obtains a dual-material-density pair through projection-based decomposition approach from DECT measurements, and then generates a linear-attenuation-coefficient (LAC) pair for each pixel at two selected distinct energies. Given a LAC pair, a material triplet and the volume conservation assumption, triple material decomposition is solvable for each pixel. This method sequentially decompose each pixel into different triplets in the material library, and collects solutions of volume fractions that satisfy a box constraint ([0 1]). If there are multiple solutions, it determines the optimal triplet as the one which has the smallest sum of distances between the original LAC pair and three LAC pairs of its constituent materials at the two selected distinct energies. If there is no feasible solution, it finds a unique multi-material decomposition by solving a mixed least-square optimization problem with volume conservation constraint.

Inspired by the image-domain method [1], we propose a penalized-likelihood (PL) method with edge-preserving regularizers for each material to reconstruct multi-material images. It is well known that statistical image reconstruction methods based on physical models of the CT system and a statistical model can obtain lower noise images. The proposed PL method considers each material image as a whole, instead of pixel by pixel, so prior knowledge, such as piecewise smoothness, can be used to help solve the reconstruction problem.

We evaluated the proposed PL method on a simulated object containing fat, blood, omnipaque300 (a common contrast agent), cortical bone and air. Comparing with the image-domain method, the PL method was able to reconstruct component images with lower noise, greatly reduce streak artifacts, and effectively alleviate the cross-talk phenomenon where a component of one material appearing in the image of another material. The RMS errors of the PL method were about 40% lower for fat, blood, omnipaque300 and cortical bone compared to the image-domain method.

The organization of this paper is as follows, Section 2 introduces the physical model and the PL method, Section 3 shows the results and Section 4 presents conclusions.

II. METHOD

A. Physical Models

1) Measurement Model: We use the following general model to describe the measurement physics for X-ray CT. The detector measures X-ray photon emerging from the object at $M_0 \geq 1$ different incident spectra. Let Y_{im} denote the measurement for the ray $\mathcal{L}_{im}$ which is the ith ray for the mth energy scan, where $m = 1, \ldots, M_0$, $i = 1, \ldots, N_{\mathrm{d}}$, and N_{d} is the number of rays. For a ray $\mathcal{L}_{im}$ of infinitesimal width, the mean of the projection measurements could be expressed

---

This work was supported in part by NIH grant HL-098686.

Y. Long and J. Fessler are with Dept. of Electrical Engineering and Computer Science, University of Michigan, Ann Arbor, MI 48109.

as:

$$\bar{y}_{im} \triangleq \int I_{im}(\mathcal{E}) \exp\left(-\int_{\mathcal{L}_{im}} \mu(\vec{x}, \mathcal{E})\, \mathrm{d}\ell\right) \mathrm{d}\mathcal{E} + r_{im}, \quad (1)$$

where $\mu(\vec{x}, \mathcal{E})$ denotes the 3D unknown spatially- and energy-dependent attenuation distribution, $\int_{\mathcal{L}_{im}} \cdot\, \mathrm{d}\ell$ denotes the "line integral" function along line $\mathcal{L}_{im}$, the incident X-ray intensity $I_{im}(\mathcal{E})$ incorporates the source spectrum and the detector gain, and r_{im} denotes the ensemble mean of background signals. We treat each $I_{im}(\mathcal{E})$ and r_{im} as known nonnegative quantities.

2) Object Model: Assuming volume conservation [1] that volume of a mixture equals to the sum of volumes of its constituent parts, the volume fraction of the lth material at the jth pixel is $x_{lj} = V_{lj} / \sum_{l=1}^{L_0} V_{lj}$, where V_{lj} denotes the volume of the lth material at the jth pixel and L_0 denotes the number of materials of interest. We also assume that each pixel contains no more than three materials and the material types can be different among pixels. Let Θ be the triplet library containing all physically meaningful triplets formed from L_0 pre-selected materials of interest.

We describe the object model as

$$\mu(\vec{x}, \mathcal{E}) = \sum_{l=1}^{L_0} \sum_{j=1}^{N_\mathrm{p}} \mu_l(\mathcal{E})\, b_j(\vec{x})\, x_{lj}, \quad (2)$$

subject to

$$\begin{cases} \sum_{l=1}^{L_0} x_{lj} = 1, & \forall j, \\ \sum_{l=1}^{L_0} \mathbb{1}_{\{x_{lj} \neq 0\}} \leq 3, & \forall j \\ 0 \leq x_{lj} \leq 1, & \forall l, j \end{cases} \quad (3)$$

where $\mu_l(\mathcal{E})$ is the energy-dependent LAC of the lth material type and $b_j(\vec{x})$ denotes spatial basis functions (*e.g.*, pixels).

Let $\boldsymbol{x}$ denote the image vector $\boldsymbol{x} = (\boldsymbol{x}_1, \ldots, \boldsymbol{x}_l, \ldots, \boldsymbol{x}_{L_0}) \in \mathbb{R}^{N_\mathrm{p} \times L_0}$ for $\boldsymbol{x}_l = (x_{l1}, \ldots, x_{lj}, \ldots, x_{lN_\mathrm{p}})$ of the lth material. Combining the general measurement model (1) and the object model (2), the mean of the projection measurements $\bar{y}_{im}(\boldsymbol{x})$ is a function of $\boldsymbol{x}$. The goal of the proposed reconstruction method is to estimate $\boldsymbol{x}$ for $L_0 > 3$ subject to (3) from noisy measurements Y_{im} with $M_0 = 2$.

B. Penalized-Likelihood (PL) Reconstruction

For the case of normal clinical exposures, the X-ray CT measurements are often modeled as independently Poisson random variables with means (1), *i.e.*

$$Y_{im} \sim \mathsf{Poisson}\{\bar{y}_{im}(\boldsymbol{x})\}\,.$$

The corresponding negative log-likelihood for independent measurements Y_{im} has the form

$$-L(\boldsymbol{x}) \equiv \sum_{m=1}^{M_0} \sum_{i=1}^{N_\mathrm{d}} \bar{y}_{im}(\boldsymbol{x}) - Y_{im} \log \bar{y}_{im}(\boldsymbol{x}), \quad (4)$$

where $\equiv$ means "equal to within irrelevant constants independent of $\boldsymbol{x}$."

Component images are estimated from the noisy measurements Y_{im} by minimizing a Penalized-Likelihood (PL) cost function subject to constraints given in (3) on the elements of $\boldsymbol{x}$ as follows:

$$\hat{\boldsymbol{x}} = \underset{\boldsymbol{x} \text{ subject to } (3)}{\arg\min}\ \Psi(\boldsymbol{x}) \quad (5)$$

$$\Psi(\boldsymbol{x}) \triangleq -L(\boldsymbol{x}) + R(\boldsymbol{x}). \quad (6)$$

The edge-preserving regularization term $R(\boldsymbol{x})$ is

$$R(\boldsymbol{x}) = \sum_{l=1}^{L_0} \beta_l R_l(\boldsymbol{x}_l), \quad (7)$$

where the regularizer for the lth material is

$$R_l(\boldsymbol{x}_l) = \sum_{j=1}^{N_\mathrm{p}} \sum_{k \in \mathcal{N}_{lj}} \kappa_{lj} \kappa_{lk} \psi_l(x_{lj} - x_{lk}) \quad (8)$$

$$\psi_l(t) = \frac{\delta_l^2}{3} \left(\sqrt{1 + 3\left(\frac{t}{\delta_l}\right)^2} - 1 \right), \quad (9)$$

where κ_{lj} and κ_{lk} are parameters encouraging uniform spatial resolution [3] and $\mathcal{N}_{lj}$ is some neighborhood of voxel x_{lj}. The regularization parameters β_l and δ_l can be chosen differently for different materials according to their properties.

Because the cost function $\Psi(\boldsymbol{x})$ in (6) is difficult to minimize directly, we apply optimization transfer principles to develop an algorithm that monotonically decreases $\Psi(\boldsymbol{x})$ each iteration [4]. We first find pixel-wise separable quadratic surrogates of the cost function, and then minimize them under constraints given in (3). We loop over all triplets in the predetermined material library, minimize the surrogates under box and sum-to-one constraints in (3), and determine the optimal triplet for each pixel as the one making the surrogate of that pixel smallest. To obtain a good initialization for the iterative optimization, we use the images reconstructed by the image-domain method [1]. We use the ordered subsets approach to accelerate the "convergence" to a good local minimum [4].

III. RESULTS

To evaluate the proposed PL method for multi-material decomposition purpose, we reconstructed volume fractions of a NCAT chest phantom [5] containing fat, blood, omnipaque300, cortical bone and air from a simulated DECT scan.

Fig. 1 shows true volume fractions and monoenergetic image at 70 keV of the simulated NCAT chest phantom. We simulated the geometry of a GE LightSpeed X-ray CT fan-beam system with an arc detector of 888 detector channels by 984 views over 360°. The size of each detector cell was 1.0239 mm. The source to detector distance was $D_\mathrm{sd} = 949.075$mm, and the source to rotation center distance was $D_\mathrm{s0} = 541$mm. We included a quarter detector offset to reduce aliasing. We used the distance-driven (DD) projector [6] to generate projections of the true object. We simulated two incident spectra of the X-ray tube voltages at 140 kVp and 80 kVp. Their corresponding effective energies were 69 keV and 47 keV. We generated noiseless measurements $\bar{y}_{im}$ of the simulated NCAT phantom using (1) and the simulated spectra. The simulated true images were 1024×1024 and the pixel size was 0.49 mm, while the reconstructed images were

512×512 and the pixel size was 0.98 mm. We introduced this model mismatch deliberately to test the multi-material decomposition methods. To the noiseless measurements $\bar{y}_{im}$, we added Poisson distributed noise corresponding to 2×10^5 incident photons per ray for rays corresponding to the 140 kVp spectrum. For the 80 kVp spectrum, we added Poisson noise corresponding to $2 \times 10^5 \cdot I_{i2}/I_{i1} = 6 \times 10^4$ incident photons per ray where I_{i1} and I_{i2} denote the total intensity of the ith ray for the 140 kVp and 80 kVp spectrum respectively.

For this simulation we let the triplet material library Θ contain seven triplets which formed from pre-selected five materials: fat, blood, omnipaque300, cortical bone and air, and which exclude the combination of omnipaque300 and cortical bone (This is based on the fact that contrast agent does not spread into the cortical bone area). We implemented the image-domain method as described in [1] to initialize the PL method. We used the conventional DE projection-based method with polynomial approximation [7] followed by FBP to reconstruct water-iodine density images and chose 70 keV and 140 keV to yield LAC pairs for the image-domain method. We also tried a more sophisticated dual-material decomposition method, the statistical sinogram restoration method proposed in [8], but the final reconstructed component images were very similar to those of using polynominal approximation. For the PL method we chose $\beta_l = 2^8, 2^{11}, 2^{11}, 2^8, 2^4$ and $\delta_l = 0.01, 0.01, 0.005, 0.01, 0.1$ for fat, blood, omnipaque300, cortical bone and air, respectively. We ran 1000 iterations of the optimization transfer algorithm with 41 subsets to accelerate the convergence. Note that (5) is a nonconvex problem so the algorithm finds a local minimum.

Fig. 2, Fig. 3, Fig. 4, Fig. 5 and Fig. 6 show estimated volume fractions of the five materials reconstructed by the PL method and the image-domain method. The grayscale values represent volume fractions of each material. The big white disks Fig. 6 were due to the elliptical reconstruction support. The streak-like artifacts in the reconstructed images by the image-domain method were very similar to those in Figure 4 in [1]. The PL method greatly reduces these streak-like artifacts. The cross-talk phenomenon is evident in the image-domain results. Fat went into the cortical bone image Fig. 5, while cortical bone presented in the blood image Fig. 3. The PL method alleviated this cross-talk phenomenon very effectively. Fig. 4 shows the horizontal profiles through the upper disk of the reconstructed omnipaque300 images on the right. The PL method corrected the positive bias introduced by the image-domain method. In addition, the PL method reconstruct component images with lower noise.

We down-sampled the simulated true component images to the sizes of the reconstructed images by linearly averaging, and then calculated the root-mean-square (RMS) error of the component fractions, $\sqrt{\frac{1}{N_\mathrm{p}} \sum_{j=1}^{N_\mathrm{p}} (\hat{x}_{lj} - x_{lj})}$ within the reconstruct support for each material based on the down-sampled images. Table I shows RMS errors of the component images reconstructed by the image-domain method and the PL method. The errors were scaled by 10^3 for easy comparison. Comparing with the image-domain method, the PL method lowered the RMS errors by about 40% for fat, blood, omnipaque300 and cortical bone.

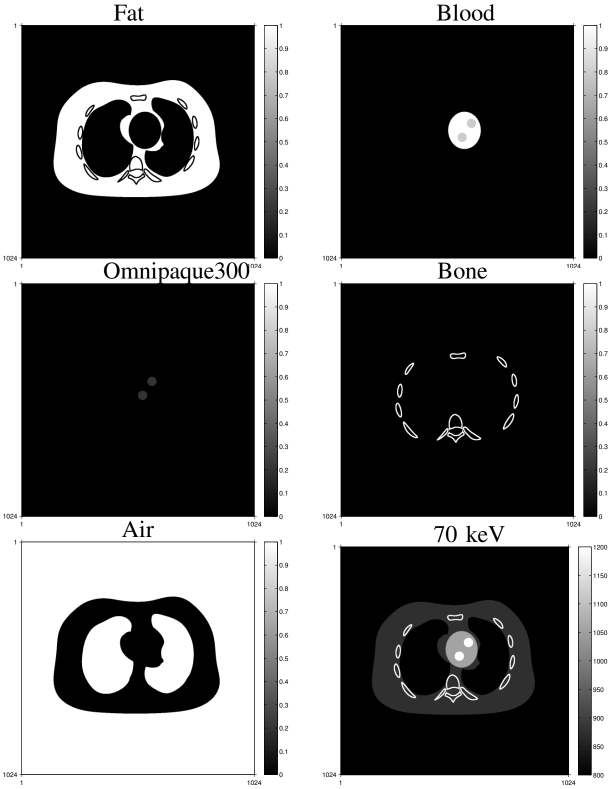

Fig. 1. True volume fractions and monoenergetic image at 70 keV.

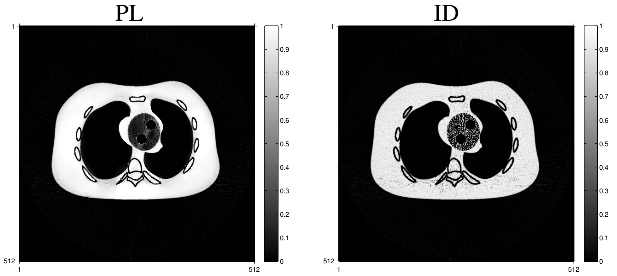

Fig. 2. Fat component results.

Method	fat	blood	omnipaque	bone	air
ID	93	73	4.4	36	46
PL	60	40	2.9	22	46

TABLE I

RMS ERROR COMPARISON OF THE RECONSTRUCTED IMAGES BY THE IMAGE-DOMAIN (ID) METHOD AND THE PL METHOD. THE ERRORS WERE UNITLESS AND ENLARGED BY 10^3.

IV. CONCLUSIONS

We proposed a statistical image reconstruction method with a PL cost function containing a negative log-likelihood term and edge-preserving regularizers for each material to decompose a mixture into multiple materials using DECT measurements. We adopted the volume conservation assumption and assumed each pixel contains no more than three materials to help solve the multi-material reconstruction problem.

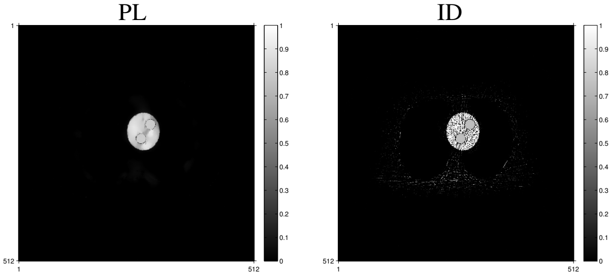

(a) Field of view (FOV) images

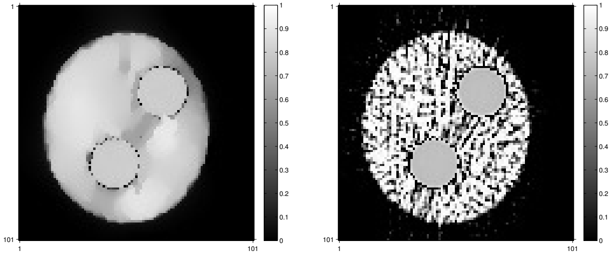

(b) Region of interest (ROI) images

Fig. 3. Bone component results.

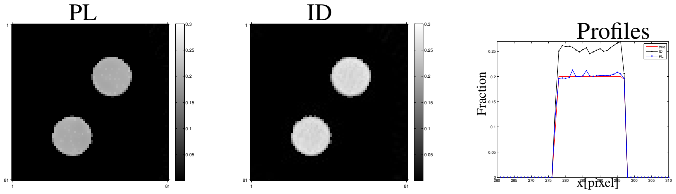

Fig. 4. Omnipaque300 component results. The right figure shows the horizontal profiles through the upper disk. The red, black and blue line denote the true, PL and ID image respectively.

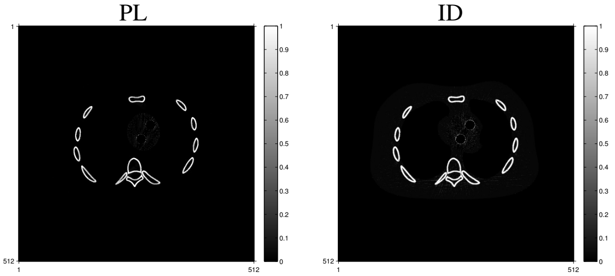

(a) Display window [0, 1]

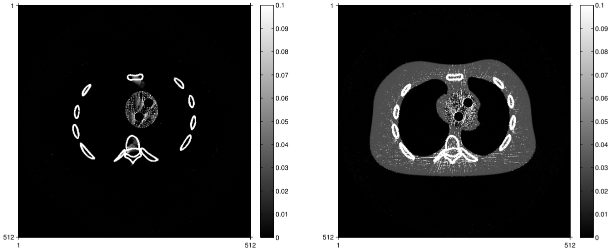

(b) Display window [0, 0.1]

Fig. 5. Cortical bone component results.

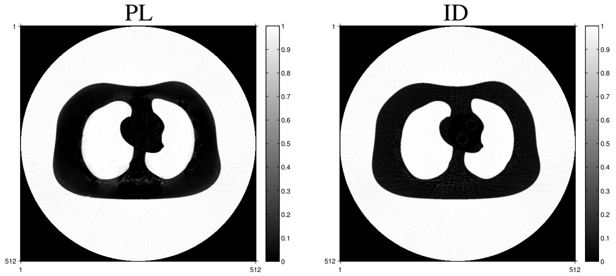

Fig. 6. Air component results.

Comparing with the image-domain method [1] that makes the same assumptions, the proposed PL method reconstructed component images with reduced noise, streak artifacts and cross-talk. The PL method was able to lower the RMS error by about 40% for fat, blood, omnipaque300 and cortical bone, compared to the image-domain method.

The PL cost function has two parameters, one regularizer coefficient β_l and one edge-preserving parameter δ_l for each material. We found that the choice of parameters for one material component influenced the reconstructed image of another component. An appropriate combination of parameters needs to be carefully determined for each application. It is also desirable for the regularizer to provide approximately uniform, isotropic and material-independent spatial resolution. Choosing regularizers for the PL method and optimizing there parameters needs further investigation.

Future work also includes applying the PL method to real data to decompose materials as many as the application needs. Since the PL cost function is non-convex, a good initialization is very important for the PL method. Future work would investigate image domain “statistica” method which is more practical than the PL method in terms of computation.

REFERENCES

[1] P. R. S. Mendonca, R. Bhotika, B. W. Thomsen, P. E. Licato, and M. C. Joshi, “Multi-material decomposition of dual-energy CT data,” in *spie*, vol. 7622, 2010, p. 76221W. [Online]. Available: http://dx.doi.org/10.1117/12.844531

[2] X. Liu, L. Yu, A. N. Primak, and C. H. McCollough, “Quantitative imaging of element composition and mass fraction using dual-energy CT: Three-material decomposition,” *Med. Phys.*, vol. 36, no. 5, pp. 1602–9, Apr. 2009.

[3] J. A. Fessler and W. L. Rogers, “Spatial resolution properties of penalized-likelihood image reconstruction methods: Space-invariant tomographs,” *IEEE Trans. Im. Proc.*, vol. 5, no. 9, pp. 1346–58, Sep. 1996.

[4] H. Erdoğan and J. A. Fessler, “Monotonic algorithms for transmission tomography,” *IEEE Trans. Med. Imag.*, vol. 18, no. 9, pp. 801–14, Sep. 1999.

[5] W. P. Segars and B. M. W. Tsui, “Study of the efficacy of respiratory gating in myocardial SPECT using the new 4-D NCAT phantom,” *IEEE Trans. Nuc. Sci.*, vol. 49, no. 3, pp. 675–9, Jun. 2002.

[6] B. De Man and S. Basu, “Distance-driven projection and backprojection in three dimensions,” *Phys. Med. Biol.*, vol. 49, no. 11, pp. 2463–75, Jun. 2004.

[7] R. E. Alvarez and A. Macovski, “Energy-selective reconstructions in X-ray computed tomography,” *Phys. Med. Biol.*, vol. 21, no. 5, pp. 733–44, Sep. 1976.

[8] J. Noh, J. A. Fessler, and P. E. Kinahan, “Statistical sinogram restoration in dual-energy CT for PET attenuation correction,” *IEEE Trans. Med. Imag.*, vol. 28, no. 11, pp. 1688–702, Nov. 2009.

Quantitative Soft Tissue Characterization from Multi-Energy Photon Counting CT

Adam M Alessio and Lawrence R MacDonald

***Abstract*—The goal of this project is to quantify the concentration of soft-tissue components through the decomposition of the x-ray spectral signatures in multi-energy CT images. Decomposition of dual-energy and multi-energy x-ray data into basis materials can be performed in the data domain, image domain, or during image reconstruction. In this work, we evaluate the ability to decompose multi-energy x-ray data in the image domain for the application of subtle soft-tissue characterization. We apply several proposed methods and a novel content-aware image-based method to measured multi-energy images. Methods were applied to measured data from a prototype photon counting CT system with CdTe detectors and a microfocus x-ray source. Data from phantom and ex-vivo specimens were evaluated. Results suggest that content-aware image-based decomposition is preferable when the number and type of basis materials in a region can be limited based on *a priori* knowledge or classification strategies. Bias in the estimation of the concentration of water and oil components in a phantom study was <0.16±0.15 g/cc. Decomposition of ex-vivo carotid endarterectomy specimens demonstrates the presence of water, lipid, and calcium deposits in the plaque walls. Results suggest that multi-energy CT can be used to classify and quantify soft-tissue components.**

I. INTRODUCTION

Several multi-energy CT systems have been proposed and constructed for use in small animal imaging [1], whole-body clinical systems [2], and breast CT [3]. These systems are based on on CdTe or CdZnTe detectors, which offer high energy resolution and the potential to discriminate multiple energy bands during a single acquisition.

Our current work is particularly motivated by the need to assess atherosclerotic plaque. The detection and quantification of vulnerable plaque is widely accepted as one of the leading challenges in diagnostics. Clinical in-vivo imaging of atherosclerosis primarily focuses on assessment of lumen diameter, which is a poor measure of risk and plaque vulnerability. As such, the conventional imaging modalities have a limited role in detailed plaque characterization. An ideal plaque imaging device would a) have high resolution to measure plaque morphology, b) offer multiple tissue classification (lipid, loose fibrous matrix, calcium, dense fibrous tissue) to investigate plaque composition, and c) be safe for serial studies. While conventional dual-energy CT can provide high resolution, it is not able to provide soft tissue classification [4] and requires relatively high dose levels limiting its use for serial evaluation.

Multi-energy CT offers the potential to decompose spectral information for tissue classification and quantification. Multi-energy CT has been applied to plaque imaging in the context of quantifying the concentration of contrast agents [5]. In particular, gadolinium and gold contrast agents have been quantified in phantom and mouse studies [6], [7]. Little effort to date has been applied to quantifying soft tissue components in plaques in the absence of contrast agents, based on the prevailing assumption that soft-tissue components, such as lipid versus water, do not have sufficient differences in their mass attenuation coefficients to enable discrimination. This work attempts to develop methods to classify and quantify soft tissue components of water, lipid, and calcium.

Along with tissue classification, photon counting x-ray detectors offer the potential of improved sensitivity over conventional energy integrating detectors. This sensitivity could be translated to reduced flux/dose acquisitions leading to photon-counting CT as a more safe device for serial evaluation.

II. METHODS

A. Description of CT System

We have built a prototype photon-counting CT system for the interrogation of single carotid arteries. The geometry of the system and prototype device are presented in Figure 1. The prototype system uses a CdTe detector (Hamamatsu Photonics, Shimokanzo, Japan) with a 64 mm linear array of 64 pixels of 0.8 mm width (0.5mm depth, 1mm height) with pitch of 1mm. The detector electronics support simultaneous acquisition of 5 energy thresholds. The microfocus x-ray source (L8121-03, Hamamatsu Photonics) was operated at 120kVp with a 20μm focal spot. The central platform rotates and translates (1mm steps) to support step-and-shoot acquisition of multiple slices.

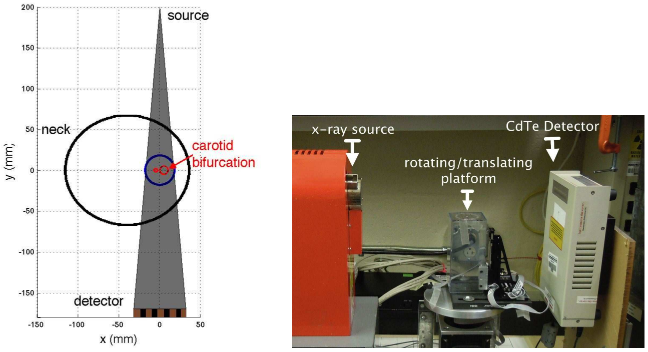

Fig. 1. Diagram and photograph of prototype carotid CT system.

B. Phantom Acquisitions

All objects in this study were scanned with 12 0kVp and 7 μA in a tomographic mode with 64 radial bins and 160

A. Alessio and L. MacDonald are with the University of Washington, Seattle, WA, USA. aalessio@u.washington.edu; http://faculty.washington.edu/aalessio/

azimuthal angles per 360°. The low tube current was selected to minimize the effects of pulse-pileup, deadtime, and energy response distortion [2]. The ability to scan with low current is one of the benefits of carotid-specific imaging. Counts of x-rays above five energy thresholds were subtracted to acquire the energy windows: 30-45, 45-60, 60-80, 80-100, and >100 keV. All images were reconstructed with a fan-beam FBP method with the ramp filter.

C. *Iodine Phantom*

We imaged a phantom consisting of increasing dilutions of iodine based contrast in saline (Dilutions of [0, 1/80, 1/40, 1/20] of Omnipaque contrast agent) and poppyseed oil (Dilutions of [0, 1/80, 1/40, 1/20] of Lipiodol). In addition, the phantom contained additional control regions of water and poppyseed oil (for a total of 2 water and 2 oil only regions) and two $CaCl_2$ solutions with density of 1.1 g/cc and 1.2 g/cc.

D. *Carotid Plaque Specimens*

Two plaque specimens obtained from carotid endarterectomy surgery were scanned to determine the ability to provide tissue discrimination. Each slice was acquired for 35 seconds; Multiple slices were acquired with 1 mm spacing (total acquisition time was 27 minutes).

E. *Separation of Materials*

We evaluated the theoretical and measured ability to separate two solutions. Using a method proposed by Wang et al [8], we determined the angle of separation of two materials. With the vector of linear attenuation coefficients defined as $\vec{\boldsymbol{\mu}}_{\boldsymbol{m}} = (\mu_{e=1}, \mu_{e=2}, ..., \mu_{e=E})_m$ for each energy bin, e, of a total of E bins, the angle of separation between material, m, 1 and 2 is

$$\theta_{1,2} = \arccos\left(\vec{\boldsymbol{\mu}}_{\boldsymbol{m=1}} \cdot \vec{\boldsymbol{\mu}}_{\boldsymbol{m=2}} / |\vec{\boldsymbol{\mu}}_{\boldsymbol{m=1}}||\vec{\boldsymbol{\mu}}_{\boldsymbol{m=2}}|\right)$$

Vectors were theoretically determined from known concentrations and material properties in the iodine phantom. These vectors were based on an estimate of the spectra in each energy window. The vectors from the measured data were determined from reconstructed images of linear attenuation at each energy bin.

F. *Decomposition of Images*

The linear attenuation at each location in the image, $\vec{x}$, can be represented as a linear combination of the mass attenuation coefficients of each component material, $f_m(e)$, as $\mu(e, \vec{x}) = \sum_{m=1}^{E} \rho_m(\vec{x}) f_m(e)$. The goal of decomposition is to estimate the concentration of materials at each location, $\rho_m(\vec{x})$. An approach that can be applied directly to the image based on weighted least squares optimization is

$$\hat{\rho}_m(\vec{x}) = \arg\min \sum_{e=1}^{E} (\hat{\mu}(e, \vec{x}) - \rho_m(\vec{x}) f_m(e))^2 W_e$$

where $\hat{\mu}(e, \vec{x})$ is an estimate of the linear attenuation coefficient at energy bin e from the reconstructed multi-energy images images. This approach, without a weighting component, was proposed previously [9]. The weights, W_e, can account for variable confidence in information from each energy bin.

Prior work by Le and Molloi, and our initial application of this least-squares estimation, found that direct decomposition of multiple, closely related materials from multi-energy data is not successful [9]. They proposed a decoupled strategy where the images are first segmented into different materials and then least-squares estimation is used to determine the material concentration. In their work, each location in the image can only be a single material. We propose a variant of this in which the images are first segmented into classes, which can contain a few materials (for example 1-3 materials). Then the weight least-squares estimation can determine the concentration in this limited set of possible materials. This approach benefits from content-aware, dimensionality reduction in which each estimated concentration is derived from a limited set of possible bases. For example, instead of estimating 4-5 unknown concentrations from 4-5 energy bands, this approach can estimate 2 unknown concentrations from 4-5 energy bands at each location and the particular materials varies by location in the image based on *a priori* knowledge or an initial automatic classification.

III. RESULTS

A. *Separation of Materials*

The angle of separation between water and each region in the iodine phantom are presented in figure 2. This plot contains the theoretical and measured separation angle based on the energy bands used during acquisition and the assumption of a non-overlapping energy response. Of particular importance, is that water and oil can be separated both in theory and with the measurements. The dependence of separability and the number of energy bins is presented in figure 3.

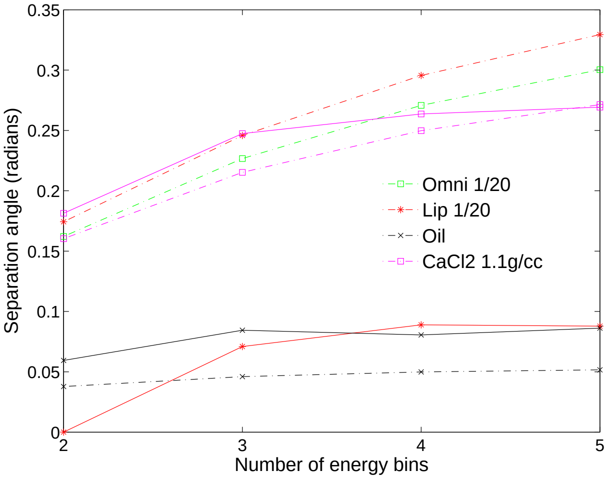

Fig. 3. Separation angle between water basis material and four materials versus the number of energy bins. As the number of energy bins decreases, the separability between the materials decreases. The measured separation is plotted in solid lines, the theoretical separation is plotted in dashed lines.

B. *Decomposition*

We applied the decoupled decomposition strategy discussed above. The initial classification was performed with a novel

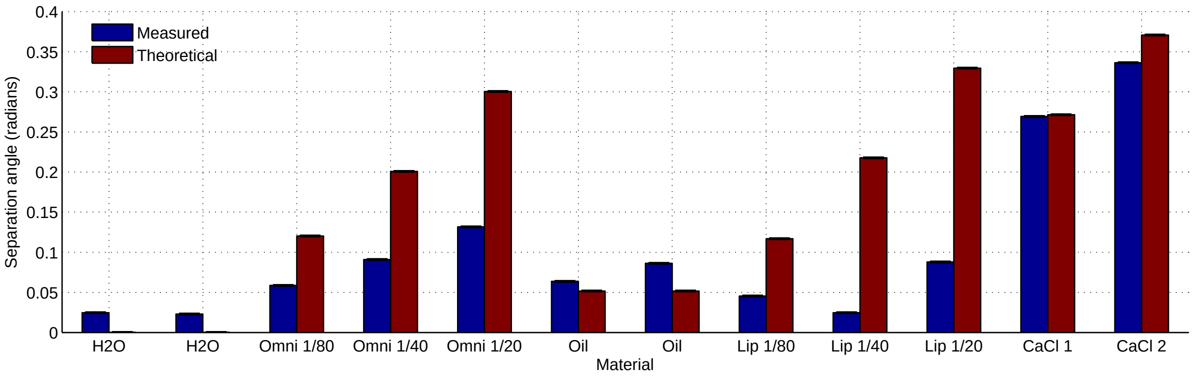

Fig. 2. Separation angle between water basis material and each solution in the iodine phantom. The measured separation angle is plotted in blue and the theoretical separation angle, based on theoretical mass attenuation coefficients for approximate spectra, is plotted in red. The solutions include water+omnipaque (IV contrast) and oil+lipiodol (oil-based contrast) in different dilutions. Two concentrations of CaCl2 are included.

simple classifier based on the differences in measured linear attenuation coefficients at each energy band as presented in figure 4. Based on this classification scheme, each voxel in the image was classified as either a combination of Oil-Water, Water-Iodine, or Bone-Water.

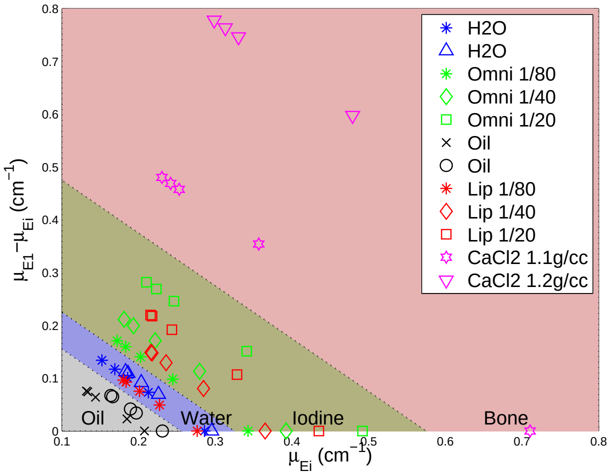

Fig. 4. Proposed simple difference classifier shown with linear attenuation coefficients from iodine phantom. The difference between the current energy bin and the lowest energy bin is plotted versus the current energy bin. Materials lie within linear bands with negative slopes.

The measured multi-energy images of the iodine phantom are presented in figure 5. These images are quantitative maps of linear attenuation coefficients at each energy level and the mean bias, compared to theoretical, is 3±4 %. The classification image followed by weighted least squares estimation of each concentration is presented in figure 6. The absolute error between the estimated densities and true densities in the water vials was 0.15±0.14 g/cc, oil vials was 0.16±0.16 g/cc, Omnipaque solutions was 0.08±0.01 g/cc, Lipiodol solutions was 0.49±0.09 g/cc, and the CaCl2 was 0.64±0.02 g/cc.

Images from one of the plaque specimens are presented in figure 7. These multi-energy images lead to the classified and decomposed image in figure 8.

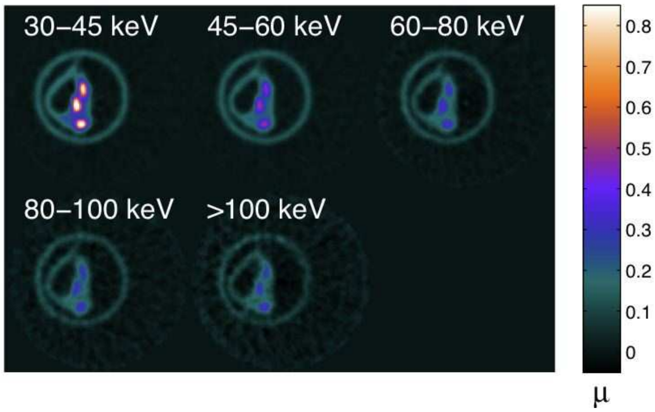

Fig. 7. Transaxial view of plaque specimen B at 5 energy levels acquired simultaneously on prototype system.

IV. DISCUSSION

We developed and acquired data from a multi-energy CT imaging platform. We proposed an image-based decomposition method based on first classifying each voxel into a limited set of basis functions and then concentration estimation based on weighted least squares optimization. Initial application to an iodine phantom was partially successful. The oil only regions (in the absence of iodine) were able to be separated from water and quantified. The regions of the phantom containing both iodine + oil (lipiodol) was not able to be distinguished from iodine + water regions. The decomposition failed in the Lipiodol solutions partially because these vials were near the edge of the FOV, leading to some truncation artifacts in that portion of the image. Also, the simple classifier we used assumed that any region with iodine also contained water (not oil). In short, this particular implementation does not allow for iodine contrast in oil solutions.

The application to plaque specimens, which do not contain iodine agents, suggests that this method is translatable to biologic tissue. The decomposition of plaque specimens reveals regions of adipose tissue (oil/fat), water, and Ca2.

This method would benefit from extension to a more desirable application in the data-domain or during image reconstruction. The initial classification could be performed in

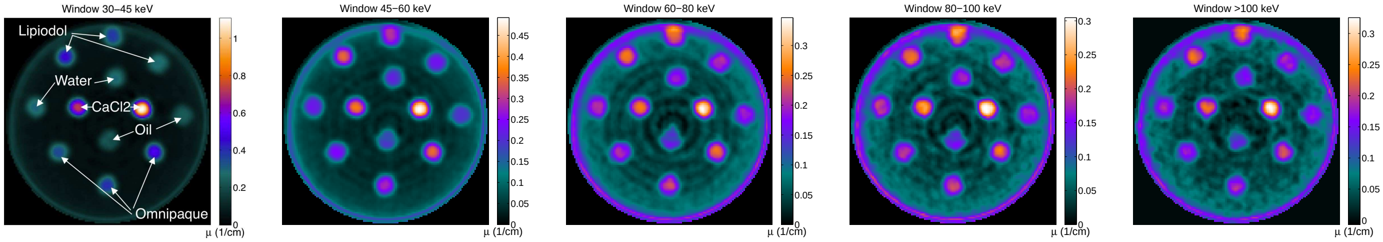
Window 30–45 keV
Lipiodol
Water
CaCl2
Oil
Omnipaque
1
0.8
0.6
0.4
0.2
0
μ (1/cm)
Window 45–60 keV
0.45
0.4
0.35
0.3
0.25
0.2
0.15
0.1
0.05
0
μ (1/cm)
Window 60–80 keV
0.3
0.25
0.2
0.15
0.1
0.05
0
μ (1/cm)
Window 80–100 keV
0.3
0.25
0.2
0.15
0.1
0.05
0
μ (1/cm)
Window >100 keV
0.3
0.25
0.2
0.15
0.1
0.05
0
μ (1/cm)

Fig. 5. Transaxial slices of phantom study at each energy level showing quantitative maps of linear attenuation coefficients in units of 1/cm.

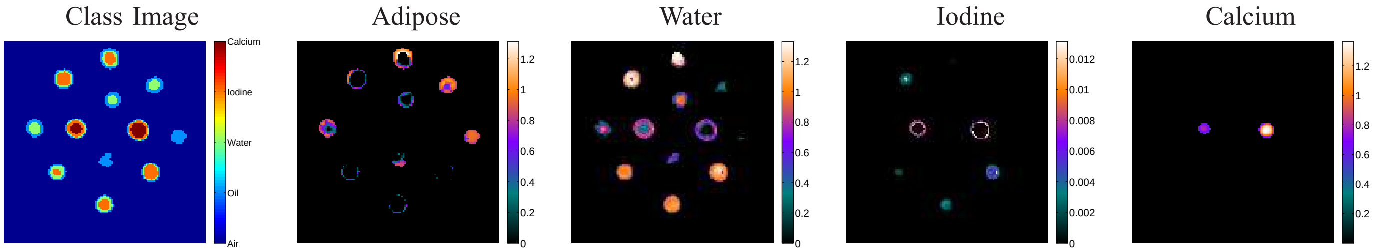
Class Image
Calcium
Iodine
Water
Oil
Air
Adipose
1.2
1
0.8
0.6
0.4
0.2
0
Water
1.2
1
0.8
0.6
0.4
0.2
0
Iodine
0.012
0.01
0.008
0.006
0.004
0.002
0
Calcium
1.2
1
0.8
0.6
0.4
0.2

Fig. 6. Decomposition of iodine phantom. Classification image on left derived from proposed difference classifier. Material images are quantitative estimates of material concentration in units of g/ml.

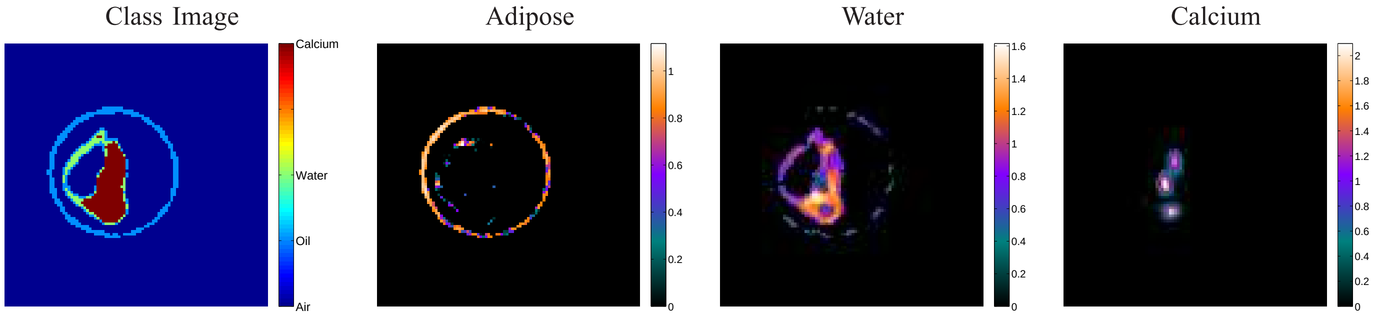
Class Image
Calcium
Water
Oil
Air
Adipose
1
0.8
0.6
0.4
0.2
0
Water
1.6
1.4
1.2
1
0.8
0.6
0.4
0.2
0
Calcium
2
1.8
1.6
1.4
1.2
1
0.8
0.6
0.4
0.2
0

Fig. 8. Decomposition of plaque specimen B. Classification image on left derived from proposed difference classifier. Material images are quantitative estimates of material concentration in units of g/ml.

the image-domain and these classes could be forward projected in the data domain for limited material decomposition prior to reconstruction of decomposed images.

Acknowledgments: This work is supported by the National Heart, Lung, And Blood Institute of the NIH under grant K25-HL086713. Authors are grateful to Roshan Patel and Hamamatsu Photonics for the x-ray source and detector components. We thank Chun Yuan, Marina Ferguson, and Thomas Hatsukami for access to carotid endarterectomy samples.

REFERENCES

[1] JP Schlomka, E Roessl, R Dorscheid, S Dill, G Martens, T Istel, C Baumer, C Herrmann, R Steadman, G Zeitler, A Livne, and R Proksa. Experimental feasibility of multi-energy photon-counting k-edge imaging in pre-clinical computed tomography. *Phys Med Biol*, 53(15):4031–4047, 2008.

[2] K Taguchi, M Zhang, EC Frey, X Wang, JS Iwanczyk, E Nygard, NE Hartsough, BMW Tsui, and WC Barber. Modeling the performance of a photon counting x-ray detector for CT: Energy response and pulse pileup effects. *Med. Phys.*, 38(2):1089–1102, 2011.

[3] Huy Q., L and S Molloi. Segmentation and quantification of materials with energy discriminating computed tomography: A phantom study. *Med. Phys.*, 38(1):228–237, 2011.

[4] M Barreto, P Schoenhagen, A Nair, S Amatangelo, M Milite, NA Obuchowski, ML Lieber, and SS Halliburton. Potential of dual-energy computed tomography to characterize atherosclerotic plaque: ex vivo assessment of human coronary arteries in comparison to histology. *J Cardiovasc Comput Tomogr*, 2(4):234–242, 2008.

[5] JW Bulte. Science to practice: can CT be performed for multicolor molecular imaging? *Radiology*, 256(3):675–676, 2010.

[6] S Feuerlein, E Roessl, R Proksa, G Martens, O Klass, M Jeltsch, V Rasche, HJ Brambs, MH Hoffmann, and JP Schlomka. Multienergy photon-counting k-edge imaging: potential for improved luminal depiction in vascular imaging. *Radiology*, 249(3):1010–1016, 2008.

[7] E Roessl, D Cormode, B Brendel, Klaus Jrgen, E, G Martens, A Thran, Z Fayad, and R Proksa. Preclinical spectral computed tomography of gold nano-particles. *Nuclear Instruments and Methods in Physics Research*, In Press, Corrected Proof, 2011.

[8] X Wang, D Meier, K Taguchi, DJ Wagenaar, BE Patt, and EC Frey. Material separation in x-ray CT with energy resolved photon-counting detectors. *Med. Phys.*, 38(3):1534–1546, 2011.

[9] Huy Q., L and S Molloi. Least squares parameter estimation methods for material decomposition with energy discriminating detectors. *Med. Phys.*, 38(1):245–255, 2011.

Image Reconstruction for Hybrid True-Color Micro-CT

Qiong Xu, Hengyong Yu*, James Bennett, Peng He, Rafidah Zainon, Robert Doesburg, Alex Opie,
Mike Walsh, Haiou Shen, Anthony Butler, Phillip Butler, Xuanqin Mou, Ge Wang*

***Abstract*—X-ray micro-CT is an important imaging tool for biomedical researchers. Our group recently proposed a hybrid ‘true-color’ micro-CT system to improve contrast resolution with lower system cost and radiation dose. The system incorporates an energy-resolved photon-counting true color detector into a conventional micro-CT configuration, and can be used for material decomposition. In this paper, we develop an interior color-CT image reconstruction algorithm for this hybrid true-color micro-CT system. A compressive sensing-based statistical interior tomography (CS-SIT) method is employed to reconstruct each channel in the local spectral imaging chain, where a reconstructed global gray-scale image from the conventional imaging chain served as the initial guess. Principal component analysis was used to map the spectral reconstructions into the color space. The proposed algorithm was evaluated by numerical simulation and animal study. The results confirm the merits of the proposed algorithm, and demonstrate the feasibility of the hybrid true-color micro-CT system. Additionally, a “color diffusion” phenomenon was observed whereby high quality true-color images are produced not only inside the region of interest (ROI), but also in neighboring regions.**

***Index Terms*—Micro-CT, color/spectral-CT, photon-counting, statistical interior tomography, principal component analysis**

I. INTRODUCTION

X-ray micro-CT is an important imaging tool for biomedical researchers. However, a major limitation of current micro-CT scanners is insufficient contrast resolution for soft-tissue due to the energy-integrating detectors[1]. In contrast, recently developed energy-resolved photon-counting detectors can resolve individual photons and their associated energies [2]. These photon-counting detectors have been used to develop true-color CT systems that dramatically improve contrast resolution [3-6]. True-color CT is also referred to as spectral, multi-energy, spectroscopic, energy-selective or energy-sensitive CT.

Given innumerable potential applications of spectral x-ray CT, the transition from gray-scale to true-color is almost certain to occur sooner or later. However, there are two major challenges in this process: detector cost and radiation dose. First, the spectral detection technology is not yet mature for large area, and the replacement of a gray-scale x-ray detector array with a true-color spectral detector will be rather expensive in the near future. Second, x-ray spectral detection would requires much higher radiation dosage if each spectral channel requires the same exposure as that for a corresponding energy-integrating detector.

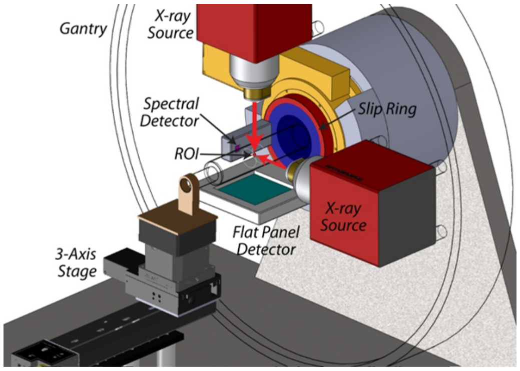

Fig. 1. A 3D rendering of the hybrid true-color micro-CT system. A wide-beam gray-scale imaging chain and a narrow-beam true-color.

While classic CT theory targets exact reconstruction of the sample’s entire cross-section from complete projections, biomedical applications of CT and micro-CT often focus on smaller, internal regions of interest (ROIs). We propose that the detector cost and radiation dose problems of x-ray spectral micro-CT can be solved by applying interior tomography. Recently, we designed a hybrid true-color micro-CT system that incorporates spectral imaging and interior tomography to improve micro-CT performance [7]. Our design adds a

This work was supported in part by NIH/NIBIB grant EB011785 and a seed grant from Wake Forest Institute for Regenerative Medicine.

Qiong Xu is with the Institute of Image Processing and Pattern Recognition, Xi'an Jiaotong University, Xi'an, Shaanxi 710049, China & the Division of Radiologic Sciences, Wake Forest University Health Sciences (WFUHS), Winston-Salem, NC, 27157, USA.

Hengyong Yu and Ge Wang are with the Division of Radiologic Sciences, WFUHS, Winston-Salem, NC, 27157, USA & Biomedical Imaging Division, VT-WFU School of Biomedical Engineering and Sciences, WFUHS, Winston-Salem, NC, 27157, USA & Virginia Tech, Blacksburg, VA 24061, USA. (e-mail: Hengyong-yu@ieee.org, ge-wang@ieee.org).

James Bennett, Peng He and Haiou Shen are with Biomedical Imaging Division, VT-WFU School of Biomedical Engineering and Sciences, Virginia Tech, Blacksburg, VA 24061, USA.

Rafidah Zainon and Robert Doesburg are with the Department of Physics and Astronomy, University of Canterbury, Private Bag 4800, Christchurch 8140, New Zealand.

A. Opie is with the Department of Electrical and Computer Engineering, University of Canterbury, Christchurch 8140, New Zealand (e-mail: alex.opie@pg.canterbury.ac.nz).

Mike Walsh is with the Department of Radiology, University of Otago, P.O. Box 4345 Christchurch, New Zealand.

Anthony Butler is with the Department of Radiology, University of Otago, P.O. Box 4345 Christchurch, New Zealand & the European Organization for Nuclear Research (CERN), Geneva, Switzerland.

Phillip Butler is with the Department of Physics and Astronomy, University of Canterbury, Private Bag 4800, Christchurch 8140, New Zealand & the CERN, Geneva, Switzerland.

Xuanqin Mou is with the Institute of Image Processing and Pattern Recognition, Xi'an Jiaotong University, Xi'an, Shaanxi 710049, P.R. China.

narrow-beam true-color imaging chain in the current micro-CT system using a small energy-resolved photon-counting detector (Figs.1 & 2). In this paper, we demonstrate an interior color-CT image reconstruction algorithm developed for this hybrid imaging system.

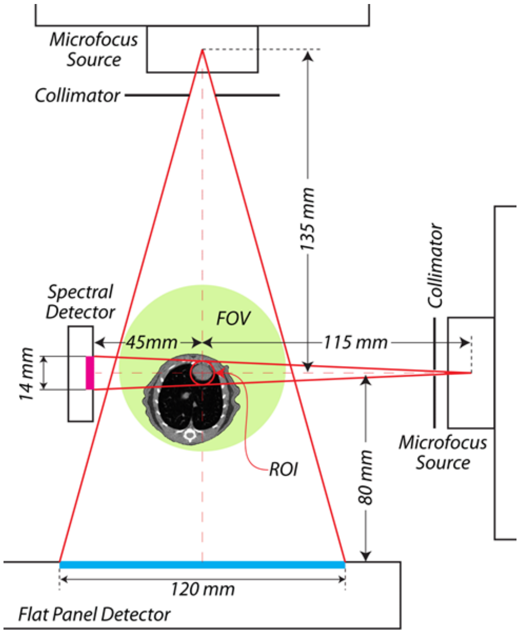

Fig. 2. 2D sketch of the hybrid true-color micro-CT system. A wide-beam gray-scale imaging chain and a narrow-beam true-color imaging chain are combined on a rotating gantry.

II. METHODOLOGY

A. *CS-based Statistical Interior Tomography*

We used CS-based statistical interior tomography (CS-SIT) algorithm [8] to reconstruct each spectral channel (energy threshold). First, it does not need a known sub-region within the ROI, which is required by landmark-based methods and usually difficult to be exactly obtained, especially for determining the exact attenuations of a sub-region on a different spectral channel. Second, it better accommodates the statistical property of the projections and performs better with noisy data, which is important for multi-energy data due to the lower counts and higher noise in each spectral channel.

The detected photons of each spectral channel s ($s=1,\cdots,S$, S is the number of spectral channels) can be approximately modeled as a Poisson distribution,

$$y_i^s \sim Poisson\left\{b_i^s \exp\left(-l_i^s\right)+r_i^s\right\},\quad i=1,\cdots,I \qquad (1)$$

where y_i^s is the measured data of the spectral channel s along the i^{th} x-ray path, b_i^s is the blank scan factor, $l_i^s=\sum_{j=1}^{J}a_{ij}\mu_i^s=\left[\mathbf{A}\boldsymbol{\mu}^s\right]_i$ is the integral of the x-ray linear attenuation coefficients, $\mathbf{A}=\left\{a_{ij}\right\}$ is the system matrix, $\boldsymbol{\mu}^s=\left(\mu_1^s,\cdots,\mu_J^s\right)^T$ is a distribution of linear attenuation coefficients, r_i^s accounts for read-out noise, and I and J are the number of projections and pixels.

According to the CS-based interior tomography theory, a piecewise constant ROI can be exactly reconstructed from the locally truncated projections by minimizing the image total-variation (TV). Combining the Poisson property of projection data and the TV regularization in the maximization of *a posterior* (MAP) framework, an ROI image on each spectral channel s can be exactly reconstructed via minimizing the following objective function,

$$\Phi\left(\boldsymbol{\mu}^s\right)=\sum_{i=1}^{I}\frac{w_i^s}{2}\left(\left[\mathbf{A}\boldsymbol{\mu}^s\right]_i-\hat{l}_i^s\right)^2+\beta^s TV\left(\boldsymbol{\mu}^s\right),\quad s=1,\cdots,S \qquad (2)$$

where $w_i^s=\left(y_i^s-r_i^s\right)^2/y_i^s$ is the statistical weight for each x-ray path, $\hat{l}_i^s=\ln\left(b_i^s/\left(y_i^s-r_i^s\right)\right)$ is the estimated line integral, β^s is the regularization parameter to balance the data fidelity and TV terms, and $TV\left(\boldsymbol{\mu}^s\right)$ is the operator of computing TV of the reconstructed image.

B. *Principle Component Analysis*

The sample's attenuation coefficients are embedded in each spectral channel from the spectral image set $\left\{\boldsymbol{\mu}^s\right\}_{s=1}^{S}$. Identical materials should have the same pattern of attenuation change from one spectral channel to another (i.e. different energy thresholds). We aim to discriminate different materials by identifying these patterns through the Principle component analysis (PCA) method [5, 9], which will be briefly described.

Introduce a matrix $\mathbf{M}=\left\{M_{sj}\right\}\in\mathbb{R}^{S\times J}$, $M_{sj}=\mu_j^s-\frac{1}{S}\sum_{s=1}^{S}\mu_j^s$, and the covariance of the images set $\left\{\boldsymbol{\mu}^s\right\}_{s=1}^{S}$ in spectral domain is $\mathbf{C}=\frac{1}{S-1}\mathbf{M}\mathbf{M}^T$ (the superscript " T " is the transpose operator). Applying singular value decomposition to $\mathbf{C}$ and arranging the eigenvalues in decreasing order, the corresponding eigenvectors $\left\{\mathbf{v}_s\right\}_{s=1}^{S}$ form a new basis, which are called principal components. The matrix $\mathbf{M}$ can be transformed by this basis to form the principal components image (PC-image) set $\left\{\mathbf{P}_k\right\}_{k=1}^{S}$, $\mathbf{P}_k^T=\mathbf{v}_k^T\mathbf{M}$. We can use the first N PC-images $\left\{\mathbf{P}_k\right\}_{k=1}^{N}$ to discriminate between various materials.

C. *Overall workflow*

The overall workflow of the hybrid imaging system reconstruction algorithm is shown in Fig. 3. Global projection data is denoted as $\left\{y_i^G\right\}_{i=1}^{I_G}$ and I_G is the number of global projections. In this case, the statistical iterative reconstruction method with a TV regularization constraint (SIR-TV) is used to reconstruct the gray-scale global image $\boldsymbol{\mu}^{\mathrm{G}}$ due to better performance for low count data. Moreover, SIR-TV and CS-SIT are identical except for the input data type.

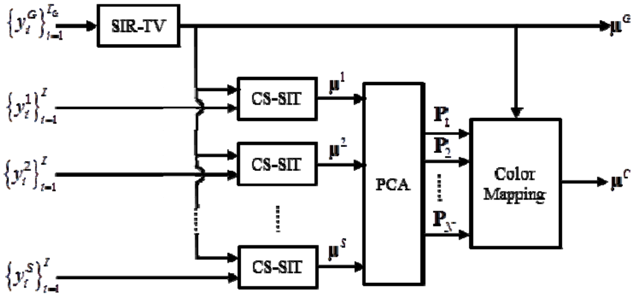

Fig. 3. Image reconstruction workflow for the hybrid true-color micro-CT system

On each spectral channel, the image μ^s is reconstructed by the CS-SIT with μ^G as the initial image. Then a PCA is performed on this set of spectral results $\{\mu^s\}_{s=1}^{S}$. The first N PC-images $\{P_k\}_{k=1}^{N}$ are selected and combined with the global reconstruction μ^G to render a color image μ^C.

III. EXPERIMENTAL RESULTS

A. *Numerical Simulation*

In this simulation, a cylindrical phantom was designed to evaluate the spatial and contrast resolution of the proposed hybrid system and reconstruction methodology; it contains several cylindrical inclusions of various radii and seven materials with different energy attenuation properties. The phantom parameters in transverse plane are shown in Fig. 4.

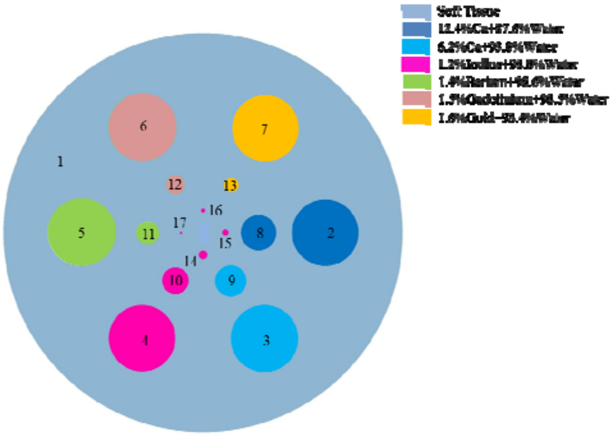

Fig. 4. Transverse plane of the cylindrical phantom with seven materials

Both the wide-beam gray-scale imaging chain and narrow-beam color-scale imaging chain were simulated with a fan-beam geometry and equidistant detector. The virtual detectors were centered at the system origin and perpendicular to the lines from the system origin to its corresponding x-ray source. The distance from each source to the system origin was 115mm. The wide-beam and narrow-beam imaging chain detectors have 540 and 256 detector elements, respectively, with an element width of 0.04mm. 600 equiangular projections were collected over 360°. The x-ray tube voltage was assumed as 120kVp; its normalized emission spectrum is shown in Fig. 6. Taking into account the k-edges of materials in this phantom, which are iodine (33 keV), barium (37.4 keV), gadolinium (50.2 keV) and gold (80.7 keV), five spectral channels were selected in the color-scale imaging chain: ≤32keV, 33keV~37keV, 38keV~42keV, 51keV~56keV and ≥81keV. In order to simulate various noisy scenarios, both imaging chains were simulated with emitted photon counts along each x-ray path as 10^5, 5×10^4, 2×10^4 and 10^4. The emitted photon counts of the true-color imaging chain were calculated by weighting the tube spectrum distribution; thus, each spectral channel contained only about 10% of the total photons and resulted in more noise in the projection data.

The reconstructed images are 600×600 pixels covering a region of 10×10mm; the iteration count was fixed at 20. The results are shown in Figs. 5. The gray-scale images are reconstructed from global projections via the SIR-TV method. In these gray-scale results, the materials “12.4%Ca+87.6%Water”, “1.4%Barium+98.6%Water”, “1.2%Iodine+98.8%Water”, “1.5%Gadolinium+98.5%Water” and “1.6%Gold+98.4%Water” have similar gray-scales, which cannot be discriminated between each other. However, in the true-color interior reconstructions, different materials are mapped into different colors and can be easily distinguished. Therefore, we can see that spectral scanning can provide color reconstructions with much higher contrast. At the same time, it can be seen that the true-color interior ROIs have the same noise and spatial resolution as the gray-scale reconstructions. When the emitted photon count decreases from 10^5 to 10^4, both the gray-scale and true-color results have increased noise and decreased spatial resolution. In the cases of 2×10^4 and 10^4 photons, the smallest inclusion is contaminated by the severe noise and cannot be recognized. It is worth noting that although the spectral scanning is only performed in the ROI, high quality true-color reconstruction can be produced not only inside the ROI but also in neighboring regions.

B. *GNP Mice Study*

To evaluate the feasibility of the designed hybrid true-color micro-CT system for GNP based applications, two euthanized mice were scanned on the MARS micro-CT with a Medipix MXR CdTe layer detector. One mouse was injected with 0.2 mL of 15 nm Aurovist II GNP (Nanoparticles; Yaphank, NY) into the tail vein and was alive for ~3 hours between injection and euthanasia. The second mouse was injected with 0.2 mL of 15 nm Aurovist II GNP in a direct cardiac puncture injection and immediate euthanasia. The distances from source to system origin and source to detector are 158mm and 255mm, respectively. 371 equiangular projections were collected over 360° to form a full scan. 13 energy bins were collected with the source tube operated with 120 kVp and 175mA. The detector chip was moved horizontally with overlapped pixels to cover a

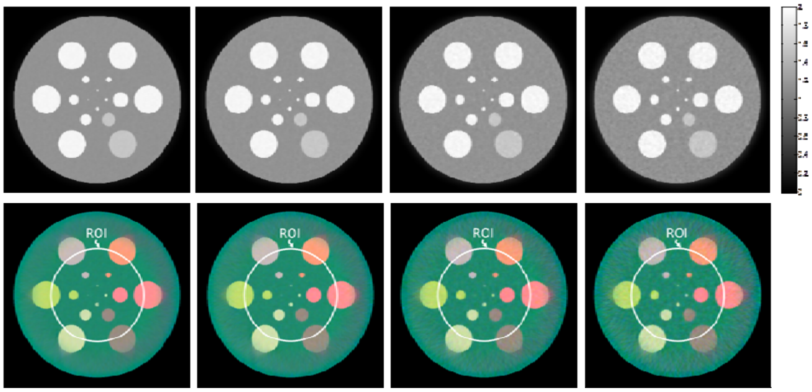

Fig. 5. Reconstructed images in numerical simulation. The 1st and 2nd rows are the global gray-scale reconstructions and the true-color interior reconstructions, respectively. From 1st to 4th columns are the results from the projections assuming 10^5, 5×10^4, 2×10^4, and 10^4 photons, respectively.

wider FOV of 34.89 mm diameter and correct for production defects in the detector sensor layer. Since there was significant noise in the sinogram, neighboring detector bins were merged to form a new sinogram of size 512×371. The dataset with the lowest energy threshold was assumed to be the gray-scale projection from the global imaging chain. Other datasets were truncated to simulate spectral ROI scanning; the ROIs are indicated in Figs. 6 with a radius of 3.4 mm.

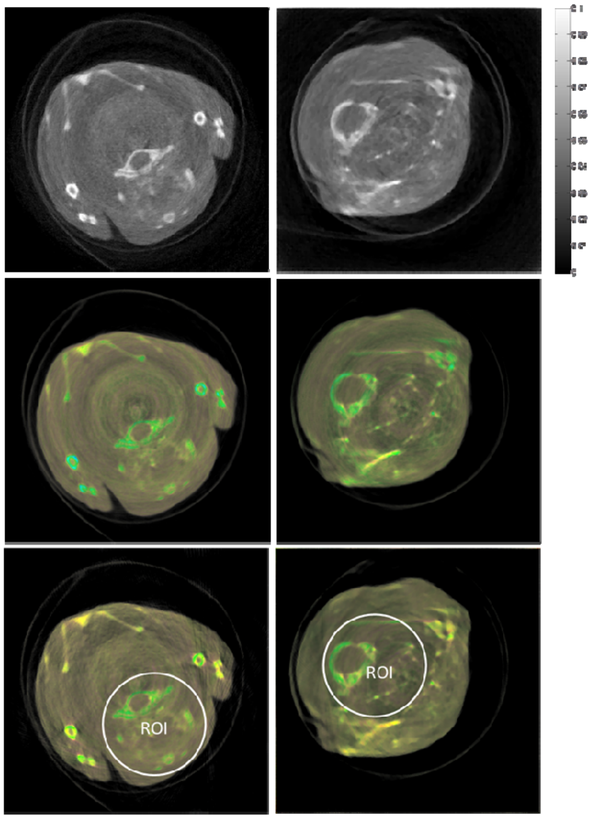

Fig. 6. The results from GNP mice studies. The 1st and 2nd rows are the global gray-scale and true-color reconstruction results; and the 3rd row is the color interior reconstructions. The left and right column are the central slices from the mouse with tail vein injection of GNP and with direct cardiac puncture injection of GNP, respectively.

The reconstructed images are 512×512 pixels covering a region of 18.41×18.41mm. The reconstructed results were shown in Fig. 5. These image slices are of the mouse upper thorax and include the front limbs, thoracic vertebra, and scapula. The true-color reconstructions demonstrate the GNP was present within the vascular structures of the upper thorax. It can be seen that the color interior tomography can nearly reproduce the same color result in ROI as with global reconstruction. The calcium in the bones and injected GNP have varying energy specific attenuation properties compared to the background soft tissues which is represented as color variation in the PCA images.

IV. CONCLUSION

In conclusion, we proposed an image reconstruction method for a hybrid true-color micro-CT system, which has an additional spectral imaging chain based on a conventional micro-CT configuration. The spectral imaging chain incorporates an energy-resolving photon counting detector and interior tomography reconstruction technique. With the proposed reconstruction method, this system can provide a low noise, high spatial and contrast resolution true-color images with low system cost and radiation dose. Furthermore, the observed color diffusion can help to reduce the color detector size for a given ROI to further reduce system cost and radiation dose.

REFERENCES

[1] R. E. Alvarez and A. Macovski, "Energy-selective reconstructions in x-ray computerised tomography," *Physics in medicine and biology,* vol. 21, p. 733, 1976.

[2] J. Jakůbek, "Semiconductor Pixel detectors and their applications in life sciences," *Journal of Instrumentation,* vol. 4, p. P03013, 2009.

[3] E. Roessl and R. Proksa, "K-edge imaging in x-ray computed tomography using multi-bin photon counting detectors," *Physics in medicine and biology,* vol. 52, p. 4679, 2007.

[4] J. Schlomka, *et al.*, "Experimental feasibility of multi-energy photon-counting K-edge imaging in pre-clinical computed tomography," *Physics in medicine and biology,* vol. 53, p. 4031, 2008.

[5] N. Anderson, *et al.*, "Spectroscopic (multi-energy) CT distinguishes iodine and barium contrast material in MICE," *European radiology,* vol. 20, pp. 2126-2134, 2010.

[6] X. Wang, *et al.*, "MicroCT with energy-resolved photon-counting detectors," *Physics in medicine and biology,* vol. 56, p. 2791, 2011.

[7] G. Wang, "Computed tomography based imaging systems, VTIP-40-10147-US," 2010.

[8] Q. Xu, *et al.*, "Statistical interior tomography," *IEEE Transactions on Medical Imaging,* vol. 30, pp. 1116-1128, 2011.

[9] J. Butzer, *et al.*, "Medipix Imaging-evaluation of datasets with PCA," 2008, pp. 1-6.

Differentiation of Uric Acid vs Non Uric Acid Urinary Stones in the Presence of Iodine Contrast Using Dual-Energy CT

Jia Wang, Mingliang Qu, Xinhui Duan, Naoki Takahashi, Akira Kawashima, Shuai Leng, Cynthia H. McCollough
Department of Radiology, Mayo Clinic, Rochester, MN 55905

***Abstract*—The objective of this study was to develop a dual-energy CT method for characterizing urinary stone composition in the presence of iodine contrast. A total of 75 urinary stones were included in this phantom study. Each stone was placed in a 1.5-mL vial, which was filled first with saline and then with increasing concentrations of iodine contrast solution (20, 40, 60, 80, and 100 mgI/mL). For each condition, the tubes were put in a 35-cm water phantom and scanned on a dual-source CT system at 100 and 140 kV with tin filtration applied on the 140 kV beam. Virtual noncontrast images created from scans of stones in iodine-containing solutions provided position and volume information. The stone map was then used to calculate a CT number ratio (CTR, the ratio of the CT numbers of a stone at 100 kV and 140 kV) for each stone to differentiate its composition. A region-growing method was developed to improve the ability to differentiate between UA and non-UA stones in iodine contrast.**

I. INTRODUCTION

DECT has been used in CT urograms to create virtual non-contrast (VNC) images for stone detection from pyelographic phase scans, where urinary stones are not distinguishable from iodine contrast since they both appear bright in CT images [1, 2]. In this work, we extended the application of urinary stone detection in DECT urogram to stone composition differentiation in iodine contrast. The challenge in stone differentiation in the presence of iodine was investigated and a region-growing correction method was developed to achieve reliable stone characterization.

II. MATERIALS AND METHODS

A. Urinary stone samples

A total of seventy five urinary stones, each collected from a different patient, were used in this phantom study: 30 uric acid (UA), 15 cystine (CYS), 15 calcium oxalate (COX), and 15 calcium hydroxyapatite (APA). The stone compositions were determined with Fourier transform infrared spectroscopy in our institutional mineral analysis laboratory. For each stone, the component of interest was required to be 90% or more so that it can be considered as a single type composition. The effective diameters of stones range from 3 to 9 mm based on volume measurement from CT images.

Five concentrations of iodine solutions were prepared by diluting iodine contrast medium (iodexol, Omnipaque 350, GE healthcare) with saline: 20, 40, 60, 80 and 100 mg/ml, which correspond to approximately 510, 905, 1300, 1696 and 2092 HU at 100 kV. Each stone was placed in a 1.5 ml plastic tube and each tube was filled with either saline or one of the five different concentration iodine solutions. All tubes were then placed

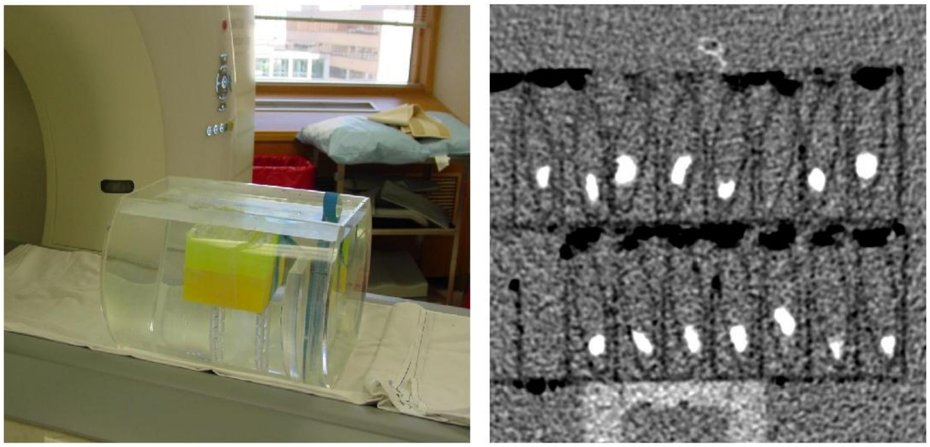

Figure 1. Left: Stone samples were immersed into 35-cm water phantom for DECT scan. Right: CT images of Stones immersed in saline scanned at 100 kV.

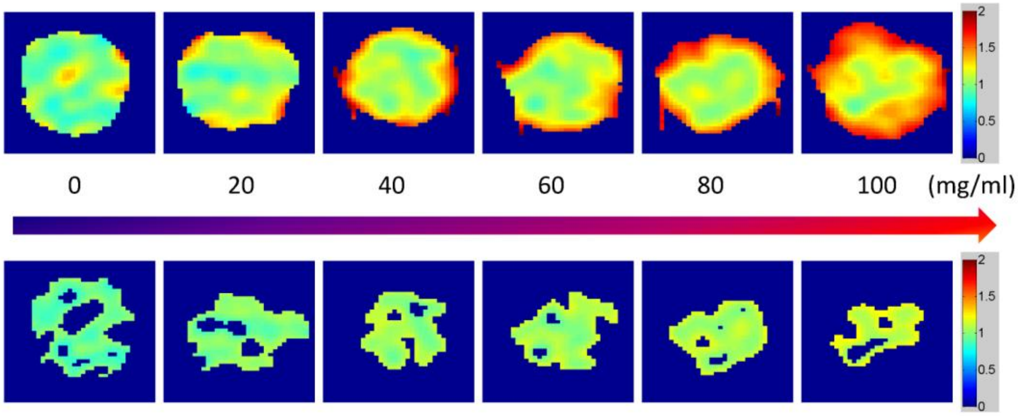

Figure 2. The top row shows CTR map of a uric acid stone in saline, 20, 40, 60, 80 and 100 mg/ml iodine solution; the bottom row shows the pixels of CTR identified by region growing correction method.

in a 35-cm water phantom to simulate realistic attenuation of a standard size patient. All stones were hydrated in distilled water for 24 hours prior to scanning.

B. *Dual energy CT acquisitions*

The phantom was scanned with a dual-source CT system (Definition Flash, Siemens Healthcare, Forchheim, Germany), as shown in Fig.1. Based on our clinical DECT stone composition protocol, dual energy scanning was performed at tube voltages of 100 and 140 kV with tin filtration applied on 140 kV. Auto exposure control (CareDose 4D, Siemens Healthcare) was used with quality reference mAs of 240 for 100 kV and 185 for 140 kV. Other scanning parameters including: beam collimation is 32*0.6 mm, pitch is 0.6, and rotation time is 0.5 s.

A non-contrast scanning was first performed with each tube filled with saline. The scan was then repeated five times with tubes filled with iodine solution at each of the five concentrations (20, 40, 60, 80 and 100 mg/ml). Same scanning parameters were used for all six scans. Images were reconstructed at 1 mm thickness and 0.8 mm increment, with a 150 mm field of view and a medium smooth kernel (D30). Linearly mixed images were also generated with equal weighting (0.5) of two energies.

C. *Post-scan image processing*

Following our routine pyelographic phase DECT procedure, iodine-substraction VNC images were generated using commercial software (Syngo, Dual Energy Viewer, Siemens Healthcare) from images of 100 and 140 kV for scans with stones in iodine solutions.

Stone segmentation was performed using mixed images from the non-contrast scan and VNC images from the scans with iodine solutions. The threshold of CT number was chosen at 200 HU for all images, which is the default value in our clinical urinary stone study. A commercial image processing software (Analyze 10.0, Mayo Clinic, Rochester, MN) was used for stone segmentation. The segmentation results were then mapped to images at 100 and 140 kV of the non-contrast and contrast scans for further CT number ratio (CTR) calculation. The CTR at every pixel of each stone was calculated as: CT_100kV/CT_140kV, where CT_100(140)kV is the CT number at 100(140)kV images. CTR of all pixels of each stone were averaged to represent the CTR of the whole stone.

Table 1. Average CTR of each stone type calculated from images of low and high energies.

CTR	Non-contrast	20 mgI/ml	40 mgI/ml	60 mgI/ml	80 mgI/ml	100 mgI/ml
UA	0.99 ± 0.03	1.21 ± 0.04	1.33 ± 0.04	1.41 ± 0.05	1.46 ± 0.05	1.54 ± 0.05
CYS	1.31 ± 0.04	1.36 ± 0.04	1.43 ± 0.04	1.47 ± 0.05	1.52 ± 0.04	1.57 ± 0.06
COX	1.46 ± 0.05	1.46 ± 0.02 *	1.48 ± 0.02	1.51 ± 0.03	1.58 ± 0.03	1.61 ± 0.04
APA	1.52 ± 0.04	1.51 ± 0.03 *	1.55 ± 0.03	1.58 ± 0.02	1.63 ± 0.02	1.65 ± 0.03

* means results are not statistically different from that from non-contrast scan.

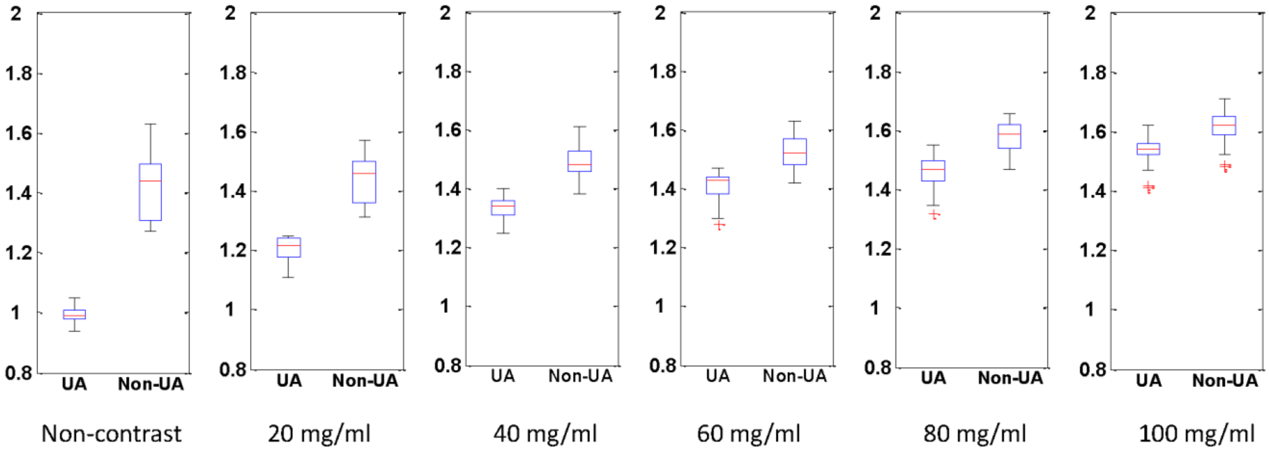

Figure 3. CTR of UA and Non-UA stones in saline and iodine solutions of five different concentrations (CTR was calculated by averaging over the whole stone volume).

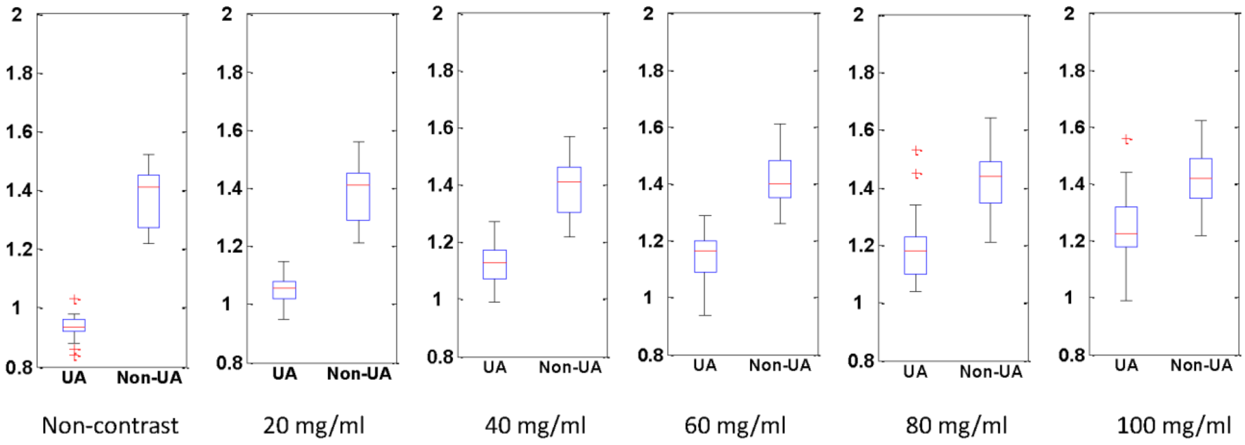

Figure 4. Using region growing correction method, CTR of all stones in saline and iodine solutions showed substantial reduced overlap.

When stones are immersed into iodine contrast, the CT number around its boundary can be affected by surrounding iodine solution due to the partial volume effect. This can lead to inaccurate results of CTR calculation and hence stone differentiation. To correct the influence of iodine solution on CTR values of stones, a region-growing method was developed to identify the pixels which are not "contaminated" by iodine in stone CTR map. By assuming the CTR of a urinary stone is homogeneous and only pixels around stone boundary were changed by iodine solution, the region growing method finds pixels in the central part of the stone (Fig.2). This method is implemented with matlab based program (Matlab 7.11.0, The MathWorks, Inc.) and is fully automatic.

D. Statistical analysis

A two-tailed, unequal variance t test (Statistical toolbox, Matlab, The MathWorks, Inc.) was used to analyze two groups of data for each stone composition: 1. Calculated CTR of each stone from non-contrast images versus that from contrast scans; 2. Calculated CTR of each stone from non-contrast scan versus CTR of contrast scans with region-growing correction method. The differentiation between UA and non-UA stones has been reported with same DECT scanners and scanning protocols (100 and 140kV) and the optimized threshold was determined through ROC analysis [3]. In this work, the same threshold was used to calculate the sensitivity and specificity of differentiating UA stones from non-UA stones for the non-contrast scan and contrast scans of five iodine concentrations.

Table 2. Calculated CTR of each stone type using region-growing method.

CTR	Non-contrast	20 mgI/ml	40 mgI/ml	60 mgI/ml	80 mgI/ml	100 mgI/ml
UA	0.93 ±0.04	1.05 ±0.05	1.12 ±0.07	1.15 ±0.08	1.18 ±0.11	1.25 ±0.11
CYS	1.26 ±0.05	1.28 ±0.05	1.29 ±0.05	1.33 ±0.07	1.32 ±0.08	1.34 ±0.08
COX	1.41 ±0.03	1.42 ±0.03 *	1.41 ±0.04 *	1.4 ±0.03 *	1.42 ±0.03 *	1.41 ±0.06 *
APA	1.47 ±0.04	1.47 ±0.04 *	1.48 ±0.05 *	1.49 ±0.05 *	1.52 ±0.05	1.52 ±0.07

* means results are not statistically different from that from non-contrast scan.

III. RESULTS

In non-contrast scan, average CTR of four stone types (UA, CYS, COX and APA) was 0.99, 1.31, 1.46 and 1.52, respectively (Table 1). Except the COX and APA stones in 20 mgI/ml solution, CTR of all stones was increased ($p<0.05$) when stones were immersed into iodine solution (CTRiodine = 2.01) and the error increased as the iodine concentration. Even in the lowest iodine concentration 20 mg/ml, the average CTR of uric acid stones were enhanced to 1.21, which is quite close to the true CTR values of CYS stones from the non-contrast scan. The influence of iodine solutions on the stone CTR values leads to substantial overlap between UA and non-UA stones (Fig.3). With threshold CTR at 1.17, the sensitivity for differentiating UA stones is 100% for non-contrast scan, and fell to 18% with 20 mg/ml iodine solution and 0 for all higher concentrations.

Using region-growing correction method, the error caused by iodine solution was largely reduced (Table 2). The overlap of CTR between UA and Non-UA stones were substantially reduced (Fig.4). Using the same threshold, the sensitivity for detecting UA stones was increased to 100%, 82%, 57%, 50% and 21%, for iodine solution at concentrations 20, 40, 60, 80 and 100 mg/ml.

Differentiation of urinary stone composition using DECT is based on the ratio of CT numbers of the stone at the low and high energies. Non-uric acid stones with high atomic number elements such as calcium present higher CTR than uric acid stones [4]. However, this differentiation mechanism is challenged when iodine is onboard, because iodine has higher CTR than both uric acid and non-uric acid stones. Due to the partial volume effect, outer part of the stones could display substantially enhanced CTR (Fig.2) when surrounded by iodine. The region growing method was used in this work to correct this error by only counting the image pixels not influenced by iodine.

Our results showed 100% specificity for differentiating UA stones, which indicates a reliable strategy of identifying UA stones. As the iodine concentration increases, the error in CTR of UA stones can not be completely eliminated even after region growing correction (Table 2), however our results showed that even in the highest iodine concentration (100 mgI/ml), the corrected CTR of UA stones is about 1.25, which is close to the true CTR of CYS stones (around 1.3), but still well below the true CTR of calcified stones (from 1.4 to 1.5). CYS stones are much rarer compared to UA stones and these two types can be reliably differentiated through urine test. Thus in practice, if the CTR of a UA stone falls in the range between UA and CYS using our region growing method, it is still possible to identify its true composition by ruling out the possibility of CYS. This can be beneficial in renal stone management since UA stones can be dissolved through urinary alkalinization, instead of shockwave lithotripsy for other stone types.

In this study, stone differentiation was limited to separation between UA and non-UA stones. Differentiation of non-UA stone compositions can be achieved by increasing the spectral separation between two tube energies in DECT [4]. The energy pair (100 and 140 kV) used in this work is our standard clinical protocol for CT urogram. The spectral separation can be further increased by using the tube energies of 80 and 140 kV. However, it is not clear whether this improvement will benefit the stone differentiation in iodine. With enhanced spectral separation, the CTR of iodine is also substantially increased, so is the error of CTR of stones caused by iodine. The overall effect of increased spectral separation and CTR error requires further investigation.

IV. CONCLUSIONS

In this study, the potential to characterize urinary stones in the presence of iodine with DECT was investigated. Due to the partial volume effect, the CTR of stone was falsely enhanced by surrounding iodine. We developed a region growing correction method to identify the uncontaminated stone pixels so that the differentiation between UA and non-UA stones is possible.

REFERENCE

1. Scheffel H, Stolzmann P, Frauenfelder T, Schertler T, Desbiolles L, Leschka S, Marincek B, Alkadhi H: Dual-Energy Contrast-Enhanced Computed Tomography for the Detection of Urinary Stone Disease. Investigative Radiology 2007, 42(12):823-829 810.1097/RLI.1090b1013e3181379bac.
2. Takahashi N, Hartman RP, Vrtiska TJ, Kawashima A, Primak AN, Dzyubak OP, Mandrekar JN, Fletcher JG, McCollough CH: Dual-Energy CT Iodine-Subtraction Virtual Unenhanced Technique to Detect Urinary Stones in an Iodine-Filled Collecting System: A Phantom Study. Am J Roentgenol 2008, 190(5):1169-1173.
3. Qu M, Ramirez-Giraldo JC, Wang J, Duan X, Vrieze TJ, Leng S, McCollough CH: Advanced Dual-energy image processing algorithm to improve the discrimination of renal stones in phantoms of large size patients using dual-energy dual-source CT. In: RSNA. Chicago, IL; 2010.
4. Boll DT, Patil NA, Paulson EK, Merkle EM, Simmons WN, Pierre SA, Preminger GM: Renal Stone Assessment with Dual-Energy Multidetector CT and Advanced Postprocessing Techniques: Improved Characterization of Renal Stone Composition—Pilot Study1. Radiology 2009, 250(3):813-820

Incorporation of Bone Beam Hardening Correction into Statistical Iterative CT Reconstruction

Bernhard Brendel[a], Thomas Koehler[a], Yoad Yagil[b], and Richard Thomson[c]

***Abstract*—A number of different methods for post reconstruction bone beam hardening (BBH) correction are available for conventional FBP reconstruction and are used in commercially available products. An incorporation of these existing methods into statistical iterative reconstruction for CT would be desirable. There are two ways imaginable to incorporate the BBH correction into iterative reconstruction: The first option is to use the beam hardening corrected projections as input for the statistical iterative reconstruction. For this it has to be considered that the noise level in the projection data changes due to the correction. The second option is to incorporate the inverse of the beam hardening correction into the forward projection of the cost function, and derive an update equation from this modified cost function. Both methods are implemented and compared based on simulated data with respect to artifact suppression, image noise, and speed of convergence.**

I. INTRODUCTION

In recent years, the attention to iterative reconstruction methods for CT has grown considerably, since the increasing power of todays computation hardware decreased reconstruction times to a tolerable level. Iterative reconstruction methods have the advantage as compared to conventional filtered back projection (FBP) that image quality can be increased significantly. The incorporation of a statistical model for the noise in the acquired data, the application of a detailed geometrical model, and the consideration of a priori knowledge about the image decrease noise and increase resolution in the image [1].

To further improve image quality, also other important physical effects (apart from noise) influencing the data acquisition should be modeled in the iterative reconstruction process. In conventional FBP reconstruction, a number of these effects are already considered in pre- and postprocessing steps. One of these effects is beam hardening, which may lead to artifacts if it is not handled properly during reconstruction [2]. In FBP based methods, it is corrected in two steps: The beam hardening due to soft tissue is corrected in a preprocessing step, while the beam hardening due to bone is accounted for in a postprocessing step, which itself includes normally at least one forward projection step and one reconstruction step [3], [4].

Due to the sometimes severe artifacts introduced by beam hardening, it is necessary to consider it also in iterative reconstruction. A number of methods have been introduced to avoid beam hardening artifacts in iterative reconstruction [5], [6]. Most of them defer significantly from the methods used in the pre- and postprocessing of conventional FBP reconstruction, and extensively use knowledge about the spectral properties of tube, detector, and scanned object. Thus, an application of these methods may results in additional effort regarding implementation, spectral characterization of the CT system, and testing.

To avoid this, we discuss in the following two ways to incorporate a beam hardening correction scheme originally designed for FBP based reconstruction, into iterative reconstruction. The first way is to use the beam hardening corrected projection data as input for the iterative reconstruction. For this scenario, it has to be considered that the noise level of the projection data changes during the correction, and the noise assumptions for the iterative reconstruction have to be adapted accordingly. This can be done by propagating the noise through the correction steps. The second way is to incorporate the inverse of the correction steps in the forward projection of the cost function for the iterative reconstruction, and derive an update equation from this modified cost function. Both ways are explained in the following section in detail, along with the applied beam hardening correction scheme.

II. METHOD

Conventional FBP reconstruction is based on the assumption that the input data represents line integrals of the X-ray attenuation μ of an object:

$$l_i = \int_{L_i} \mu(\mathbf{x})\,\mathrm{d}l \tag{1}$$

Here, l_i denotes the line integral of the $i\mathrm{th}$ measurement along ray L_i. A calculation of these line integrals is easy, if the X-ray radiation used for data acquisition is monochromatic. According to Beer's law, the measured intensities I_i at the detector are then

$$I_i = I_0 \cdot \mathrm{e}^{-\int_{L_i} \mu(\mathbf{x})\mathrm{d}l}, \tag{2}$$

with I_0 being the intensity of the X-ray radiation before the object. The line integrals can then simply be determined by

$$l_i = \log \frac{I_0}{I_i}. \tag{3}$$

In reality however, the applied X-ray radiation covers a broad spectrum of energies, and the X-ray attenuation

---

[a] Philips Technologie GmbH, Innovative Technologies, Research Laboratories, Hamburg, Germany
[b] Philips Healthcare, Haifa, Israel
[c] Philips Healthcare, Cleveland, OH

depends on the energy E of the photons. Thus, the measured intensities are modeled as follows:

$$I_i = I_0 \cdot \int S\left(E\right) \mathrm{e}^{-\int_{L_i} \mu(\mathbf{x},E)\mathrm{d}l} \mathrm{d}E \tag{4}$$

Here, $S(E)$ is the probability, that a detected photon has the energy E.

For a first step, we assume, that the object consists of only one material (e.g., water), with attenuation spectrum $\mu_{\mathrm{w}}(E)$. Furthermore, it is assumed that the material distribution is spatially varying and modeled by $\rho_{\mathrm{w}}(\mathbf{x})$, which stands here for the volume fraction containing water at location $\mathbf{x}$. The energy dependent attenuation in each location is then given by $\mu\left(\mathbf{x}, E\right) = \mu_{\mathrm{w}}(E)\rho_{\mathrm{w}}(\mathbf{x})$, and Eq. (4) can be written as

$$I_i = I_0 \cdot \int S\left(E\right) \mathrm{e}^{-T_{\mathrm{w}i}\mu_{\mathrm{w}}(E)} \mathrm{d}E, \tag{5}$$

with $T_{\mathrm{w}i} = \int_{L_i} \rho_{\mathrm{w}}(\mathbf{x})\mathrm{d}\mathbf{x}$ being the path length of water along the ray. The line integral we are looking for is $l_i = \mu_{\mathrm{w}}(\overline{E}) \cdot T_{\mathrm{w}i}$, with $\overline{E}$ being a "mean energy", derived from $S(E)$ [3]. As one can see, the relationship between l_i and $\log(I_0/I_i)$ is not trivial, and depends on the spectra $S(E)$ and $\mu_{\mathrm{w}}(E)$. Nevertheless, $\log(I_0/I_i)$ is a monotonic and only weakly nonlinear function in $T_{\mathrm{w}i}$. Thus, the mapping of $\log(I_0/I_i)$ onto l_i can be approximated by a low order polynomial. This is conventionally done in the water beam hardening (WBH) correction step [3]. The coefficients of the polynomial can be calculated from Eq. (5) or derived from a calibration measurement.

This correction step eliminates beam hardening artifacts due to water and soft tissue, but if the object contains additionally bone, artifacts remain due to the fact that the attenuation spectrum of bone $\mu_{\mathrm{b}}(E)$ differs significantly from water. To solve this problem, we have to consider Eq. (4) for two materials:

$$I_i = I_0 \cdot \int S\left(E\right) \mathrm{e}^{-T_{\mathrm{w}i}\mu_{\mathrm{w}}(E) - T_{\mathrm{b}i}\mu_{\mathrm{b}}(E)} \mathrm{d}E. \tag{6}$$

Now, the line integral we are looking for is $l_i = \mu_{\mathrm{w}}(\overline{E}) \cdot T_{\mathrm{w}i} + \mu_{\mathrm{b}}(\overline{E}) \cdot T_{\mathrm{b}i}$, but a mapping of $\log(I_0/I_i)$ onto l_i is no longer possible. For a certain value of I_i, different combinations of $T_{\mathrm{w}i}$ and $T_{\mathrm{b}i}$ fulfill Eq. (6), but they lead to different values for l_i. Thus, one common way to correct the beam hardening for two materials is to estimate in a preliminary image (e.g., reconstructed with WBH corrected projection data) for each pixel $\rho_{\mathrm{w}}(\mathbf{x})$ and $\rho_{\mathrm{b}}(\mathbf{x})$ based on the reconstructed attenuation value [4]. $\rho_{\mathrm{w}}(\mathbf{x})$ and $\rho_{\mathrm{b}}(\mathbf{x})$ can then be forward projected to get an estimate of $T_{\mathrm{w}i}$ and $T_{\mathrm{b}i}$. One of both or both are then utilized in combination with Eq. (6) to estimate l_i.

There are different methods described to estimate l_i in a two material scenario [3], [4], [7]. We use here one, which has similarities with [7]. It is based on the idea, that we can do a correction similar to the WBH correction for any given attenuation spectrum. For example, a measurement with a certain fraction of attenuation by water with respect to the complete attenuation $R = T_{\mathrm{w}i} \cdot \mu_{\mathrm{w}}(\overline{E}) / (T_{\mathrm{b}i} \cdot \mu_{\mathrm{b}}(\overline{E}) + T_{\mathrm{w}i} \cdot \mu_{\mathrm{w}}(\overline{E}))$ has the effective normalized attenuation spectrum $m_R(E) = R \cdot \mu_{\mathrm{w}}(E)/\mu_{\mathrm{w}}(\overline{E}) + (1 - R) \cdot \mu_{\mathrm{b}}(E)/\mu_{\mathrm{b}}(\overline{E})$. With this, Eq. (6) becomes

$$I_i = I_0 \cdot \int S\left(E\right) \mathrm{e}^{-l_i m_R(E)} \mathrm{d}E. \tag{7}$$

Since $m_R(E)$ is constant for a given R, $\log(I_0/I_i)$ can unambiguously be mapped onto l_i using Eq. (7) if R is known.

Thus, if for a number of fraction values R polynomials $f_R(\log(I_0/I))$ are estimated based on Eq. (7) or on calibration measurements, these can be applied to correct the projection data.

$$l_i = f_{R_i}\left(\log \frac{I_0}{I_i}\right) = \sum_{n=0}^{N} \alpha_{R_i,n} \cdot \log^n \frac{I_0}{I_i} \tag{8}$$

Here, R_i is the fraction value for measurements i, which is estimated based on preliminary reconstructions as explained above. The correction can be applied iteratively, i.e., the reconstruction based on the corrected data can be used to refine the values R_i for an improved correction of the data and so on.

The next step is to combine the correction of Eq. (8) with an iterative reconstruction scheme. We use a log-likelihood approach assuming Gaussian noise on the line integral data, resulting in the cost function [1]

$$C = \|\mathbf{D}(\mathbf{A}\mu - \mathbf{l})\|^2 = \sum_{i=1}^{M} d_{ii}^2 \cdot \left(\sum_{j=1}^{J} a_{ij}\mu_j - l_i\right)^2 . \tag{9}$$

μ is a vector with entries μ_j containing a discretized version of the image to reconstruct, $\mathbf{A}$ is the forward projection matrix, $\mathbf{l}$ is the vector with the line integral data l_i, and $\mathbf{D}$ is a diagonal weighting matrix with the inverse standard deviations of the line integral data l_i as entries d_{ii}. Sums are running over all J image pixels and over all M measurements.

For the monochromatic case, the entries l_i of $\mathbf{l}$ are simply $\log(I_0/I_i)$. Based on the assumption that the standard deviations of the measured intensities are $\sigma_{I_i} = \sqrt{I_i}$, and according to error propagation the standard deviations of the line integrals are $\sigma_{l_i} = 1/\sqrt{I_i}$, and thus the diagonal Matrix $\mathbf{D}$ has entries $d_{ii} = 1/\sigma_{l_i} = \sqrt{I_i}$ (see also [1]).

There are now two options to incorporate the beam hardening correction as given in Eq. (8) in the cost function (9). First, we can use the corrected projection data l_i instead of $\log(I_0/I_i)$ in vector $\mathbf{l}$. For this case, Eq. (9) is still valid, but we have to choose the entries of $\mathbf{D}$ properly. Neglecting the influence of the projection noise on the estimation of the values R_i (and thus on the choice of the coefficients for the correction polynomial), we can determine them as $d_{ii} = \sqrt{I_i} / \sum_n \alpha_{R_i,n} \cdot n \cdot \log^{n-1}(I_0/I_i)$.

Second, we can estimate polynomials $f_{R_i}^{-1}$ solving the inverse problem of mapping l_i onto $\log(I_0/I_i)$, and apply these inverse polynomials to the forward projected values $\mathbf{A}\mu$. The cost function is then given by

$$C = \sum_i I_i \cdot \left(f_{R_i}^{-1}\left(\sum_j a_{ij}\mu_j\right) - \log \frac{I_0}{I_i}\right)^2 . \tag{10}$$

For both cost functions we derived SPS-like update equations according to [8]. Since Eq. (9) is quadratic and Eq. (10) is almost quadratic (with the valid assumption that $f_{R_i}^{-1}$ is only weakly nonlinear), we calculate the update as Newton-Raphson steps of a separable surrogate function of the respective cost function. To keep equations short, we abbreviate $h_i = \log(I_0/I_i)$ in the following. The update equation for cost function (9) can be written as

$$\mu_j^{(k+1)} = \mu_j^{(k)} - \frac{\sum_i a_{ij} \cdot d_{ii}^2 \cdot \left(\sum_{j'} a_{ij'} \mu_{j'}^{(k)} - f_{R_i}\left(h_i\right)\right)}{\sum_i a_{ij} \cdot d_{ii}^2 \cdot \sum_{j'} a_{ij'}} \tag{11}$$

with $d_{ii} = \sqrt{I_i} / \sum_n \alpha_{R_i,n} \cdot n \cdot h_i^{n-1}$ (see above). $\mu_j^{(k)}$ are the image values in the kth iteration step. For the cost function (10) the update equation is given by

$$\mu_j^{(k+1)} = \mu_j^{(k)} - \frac{\sum_i a_{ij} \cdot I_i \cdot \left(f_{R_i}^{-1}\left(\sum_{j'} a_{ij'} \mu_{j'}^{(k)}\right) - h_i\right) \cdot \dot{f}_{R_i}^{-1}(h_i)}{\sum_i a_{ij} \cdot I_i \cdot \sum_{j'} a_{ij'} \cdot \left(\dot{f}_{R_i}^{-1}(h_i)^2 + f_{R_i}^{-1}(h_i) \ddot{f}_{R_i}^{-1}(h_i)\right)} \tag{12}$$

with $\dot{f}_{R_i}^{-1}(h_i)$ and $\ddot{f}_{R_i}^{-1}(h_i)$ being the first and second derivative of $f_{R_i}^{-1}$ with respect to h_i.

We extended the update equations to include ordered subsets and regularization (see [8] for details). We then implemented both iterative reconstruction methods. The Polynomials f_R and f_R^{-1} are estimated using a least square fit based on Eq. (7) with a polynomial order of 11 for 500 equidistantly spaced values of R.

For the method based on Eq. (11) we do the beam hardening correction before iterative reconstruction, with the "conventional" approach as follows: A FBP reconstruction is performed based on WBH corrected projection data. The reconstructed image is used to calculate $\rho_{\mathrm{w}}(\mathbf{x})$ and $\rho_{\mathrm{b}}(\mathbf{x})$. Based on that the values R_i are estimated and projection data is BBH corrected using Eq. (8). This process is repeated a second time using the BBH corrected projection data as input (but the observed improvement is very low). Then, the values of d_{ii} are calculated. The corrected projection data of the second step as well as the values d_{ii} are the input for the iterative reconstruction method, i.e., the values of R_i are not updated during the reconstruction. This method is named "BBH external" in the following.

For the method based on Eq. (12) uncorrected projection data is used as input. The values R_i are calculated during reconstruction. This leads to one additional forward projection per update to determine $T_{\mathrm{b}i}$ from $\rho_{\mathrm{b}}(\mathbf{x})$, increasing computation time substantially. The method is called "BBH internal" in the following.

Both methods are evaluated based on simulated 2D spectral data of the FORBILD head phantom. We simulated an axial CT scan of a single-row detector with 672 elements, a source-detector distance of 1040 mm, source iso–center distance of 570 mm, fan–angle of 52.138°, and 2320 views over 360°. The tube spectrum is a 120kV tungsten spectrum, filtered by 0.6 mm Titanium and 0.8 mm Aluminum. The detector is assumed to be ideal energy integrating. The absorption spectra of soft tissue and bone are taken from [9], [10].

III. RESULTS

We analyze the reconstructions of the simulated data with respect to artifacts, noise, and speed of convergence.

For the analysis of the artifacts, we use noise free simulated data. Nevertheless, the noise model described above is used for iterative reconstruction. In Fig. 1 the FBP reconstructions of the WBH corrected data and of the BBH corrected data are given. One can clearly see that the BBH correction suppresses the BBH artifacts, however there are some weak remaining artifacts (marked by arrows).

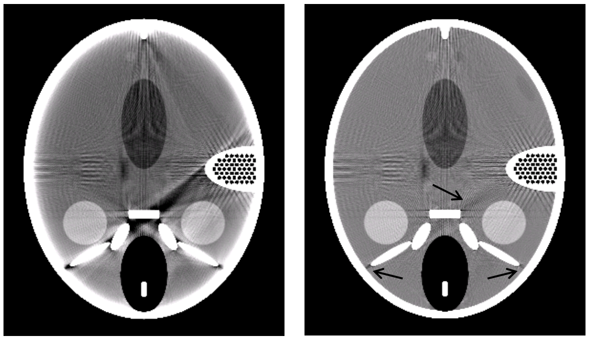

Fig. 1. FBP reconstructions. Left: WBH corrected projection data. Right: BBH corrected projection data. (Window/Level: 50/100 HU)

Iterative reconstructions are performed with 116 equally distributed projection subsets. For the noise free case, a weak Huber regularization is applied to suppress aliasing artifacts (δ = 1 HU). For both methods the BBH corrected FBP image is used as start image. In Fig. 2, reconstruction results after 100 iterations are shown. While, as expected, the BBH external reconstruction has weak remaining artifacts similar to the BBH corrected FBP reconstruction (Fig. 1, right), the BBH internal reconstruction suppresses bone artifacts even better. This is due to the repeated refinement of the R_i values during reconstruction. However, the improvement of the artifact suppression is a rather slow converging process, as can be seen in Fig. 3. Here the reconstructed attenuation value of one image pixel within one of the artifact regions

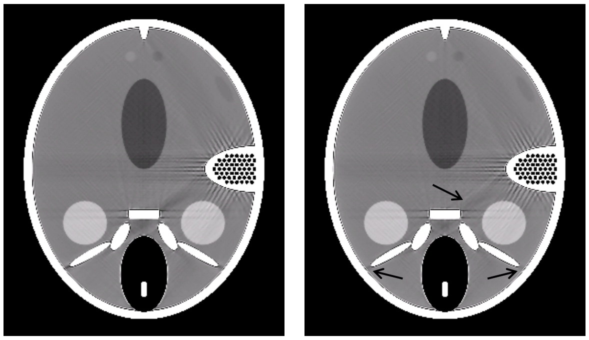

Fig. 2. Iterative reconstructions with BBH corrected start image. Left: BBH external method. Right: BBH internal method. Window/Level: 50/100 HU

is shown over the first 200 iterations. It takes roughly 100 iterations (corresponding to 11,600 updates of the R_i values) until the final improved artifact level is reached. The intermediate results degrade if a WBH corrected FBP image is used as start image.

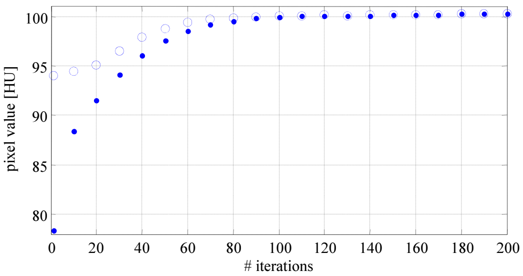

Fig. 3. Value of one image pixel in the artifact region denoted by the bottom right arrow in Fig. 2 over the number of iterations for the BBH internal method. Circles: BBH corrected FBP image as start image. Dots: WBH corrected FBP image as start image.

To analyze the noise in the reconstructed images, Poisson noise was added to the simulated intensity data. For the reconstructions the regularization strength was a bit increased to avoid salt-and-pepper noise in the images. Reconstruction results are shown in Fig. 4 for 100 iterations. In the difference image it becomes obvious, that the main differences between the two images are due to the different artifact suppression level, while differences in the noise pattern are very weak, even in the representation with a 5 HU window. This is verified by SNR measurements in homogeneous regions, which show a roughly 5 % better SNR for the BBH external method. The differences in the bone regions are due to differences in the BBH suppression, but it has to be kept in mind, that the window of 5 HU is extremely low as compared to the absolute attenuation values of bone.

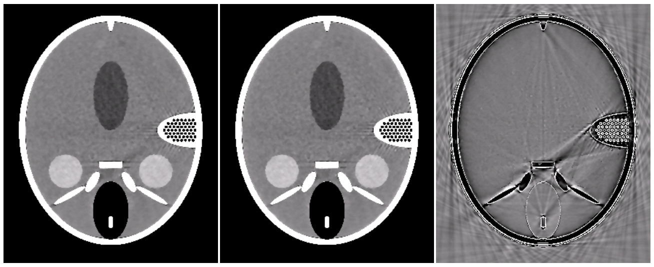

Fig. 4. Iterative reconstructions from noisy projection data. Left: BBH external method. Middle: BBH internal method. (Window/Level: 50/100 HU) Right: Difference image. (Window: 5 HU)

To analyze the convergence, we compared the differences between the reconstructions of the two methods after 100 iterations (when the improvement of the bone artifact suppression for the BBH internal is nearly finished) and after 1000 iterations:

$$\Delta = \mu^{1000}_{\text{internal}} - \mu^{1000}_{\text{external}} - (\mu^{100}_{\text{internal}} - \mu^{100}_{\text{external}}) \qquad (13)$$

Here $\mu^{n}_{\text{internal}}$ denotes the reconstruction of the BBH internal method after n iterations ("external" analogous). This has the advantage that the progress over 900 iterations can be compared, while the differences between the reconstruction methods due to the different BBH suppression is widely eliminated. The Δ-image is visualized in Fig. 5. Apart from the outer rim of the skull, the differences are below a few HU, indicating that the convergence of both methods is very similar. The larger differences at the outer rim of the skull can be explained by the different bone artifact suppression, resulting especially in different attenuation values at the outer rim of the skull (see also Fig. 4). The different contrast between air and skull leads to different amplitudes of overshoots for the two methods, and in consequence to the differences observed here.

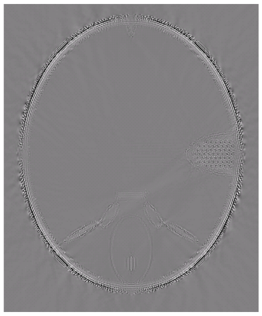

Fig. 5. The Δ-image as defined by Eq. (13). (Window: 20 HU)

IV. DISCUSSION

We introduced and compared two methods to incorporate a BBH correction method, which is originally designed for FBP based reconstruction methods, in an iterative reconstruction scheme. Both perform very similar with respect to noise and speed of convergence. The BBH internal method has the advantage that it suppresses BBH artifacts slightly better, but the reduction of the BBH artifacts converges quite slowly. The advantage of the BBH external method on the other hand is the clearly reduced computational effort due to the avoidance of an additional forward projection per update step.

The idea introduced here is not only applicable to BBH correction, but also to the correction of other physical effects in pre- or postprocessing steps of conventional FBP methods.

REFERENCES

[1] Jean-Baptiste Thibault, Ken D Sauer, Charles A Bouman, and Jiang Hsieh, *Med. Phys.*, vol. 34, no. 11, pp. 4526–4544, 2007.
[2] J. Hsieh, *Computed Tomography - Principles, Design, Artifacts, and Recent Advances*, SPIE, Bellingham, Washington, 2003.
[3] G. T. Herman, *IEEE Trans. Med. Imag.*, vol. MI-2, no. 3, pp. 128–135, 1983.
[4] P. K. Kijewski and B. E. Bjärngard, *Med. Phys.*, vol. 5, no. 3, pp. 209–214, 1978.
[5] B. De Man, J. Nuyts, P. Dupont, G. Marchal, and P. Suetens, *IEEE Trans. Med. Imag.*, vol. 20, no. 10, pp. 999–1008, 2001.
[6] M. Abella and J.A. Fessler, in *IEEE International Symposium on Biomedical Imaging*, 2009, pp. 165–168.
[7] X. Mou, S. Tang, T. Luo, Y. Zhang, and H. Yu, in *Medical Imaging 2008*, 2008.
[8] J. A. Fessler, "Statistical image reconstruction methods for transmission tomography," in *Handbook of Medical Imaging, Vol. 2*, M. Sonka and J. M. Fitzpatrick, Eds., chapter 1, pp. 1–70. SPIE Press, Bellingham, WA, 2000.
[9] *ICRU Report 44*, 1989.
[10] *ICRU Report 46*, 1992.

CT Reconstruction Using Spectral and Morphological Prior Knowledge: Application to Imaging the Prosthetic Knee

Wojciech Zbijewski, J. Webster Stayman, Abdullah Muhit, John Yorkston,
John A. Carrino and Jeffrey H. Siewerdsen

***Abstract*—Imaging in the presence of prosthetic implants presents a notoriously difficult challenge to CT reconstrucion. Such hardware is made of alloys that are highly attenuating (e.g., Co-Cr-Mo) and impart severe degradation in image quality due to photon starvation, beam hardening, etc. An important clinical example is in the proliferation of total knee replacement, increasing the need for technologies capable of imaging in the presence of knee prostheses. The usefulness of CT in follow-up to knee replacement surgery is, however, extremely limited due to severe artifacts associated with the implant. Recent developments in likelihood-based CT reconstruction offer a potential solution to the problem. In particular, we exploit the fact that exact models of the shape and composition of prostheses are often available. A framework is proposed that extends earlier work [1,2] on known component reconstruction (KCR) to account for polyenergetic beam hardening and apply to the case of a large, highly attenuating object such as a knee implant. The proposed algorithm uses a polyenergetic object model to simultaneously estimate the unknown background density volume and the position and orientation of the known implant. We test the approach in studies emulating a recently developed, dedicated cone-beam CT scanner for extremities imaging. The results indicate substantial reduction of image artifacts and significant improvements in the visualization of areas adjacent to the implant. The KCR approach is found to outperform traditional filtered-backprojection and penalized-likelihood methods that do not account for the implant model or polyenergetic object attenuation. The method suggests promising new capability to assess implant integrity, loosening, and tissue disease (osteolysis and soft-tissue derangement).**

***Index Terms*—CT Reconstruction, Extremities Imaging, Implant Imaging, Metal Artifact Reduction, Penalized-Likelihood Estimation.**

I. INTRODUCTION

The prevalence on knee replacement surgery is rapidly increasing, with some predictions suggesting over a million replacements per year by 2015 [3]. Consequently, there is a growing need for imaging technologies that enable follow-up of knee prostheses, which requires reliable visualization in the direct vicinity of the implant. X-ray CT would be a compelling candidate thanks to its excellent spatial resolution and numerous existing applications in orthopedic radiology. However, its application to implant imaging remains a major and largely unsolved challenge due to severe artifacts caused primarily by beam hardening and photon starvation. An example knee implant is shown in Fig. 1(A), along with CT images of a prosthetic knee in (B) and (C), clearly demonstrating the magnitude of the associated artifacts. (CT images are courtesy of E. Fishman, MD, [4]). As illustrated in Fig. 1(D), typical alloys used in manufacturing knee prostheses (Co-Cr-Mo, consisting of ~60% Co, ~30% Cr and ~5% Mo) are significantly more attenuating to diagnostic x-rays than other common highly x-ray opaque materials, such as Ti or cortical bone. As a result, x-ray beams traversing even a short pathlength (~1-2 mm) in such alloys suffer not only from severe photon starvation but also significant beam hardening. This is shown in Fig. 1(E), where 110 kVp x-ray spectra are attenuated by 2 mm of cortical bone, Ti, and Co-Cr-Mo, with the spectrum attenuated by Co-Cr-Mo exhibiting the most significant shift to high energies.

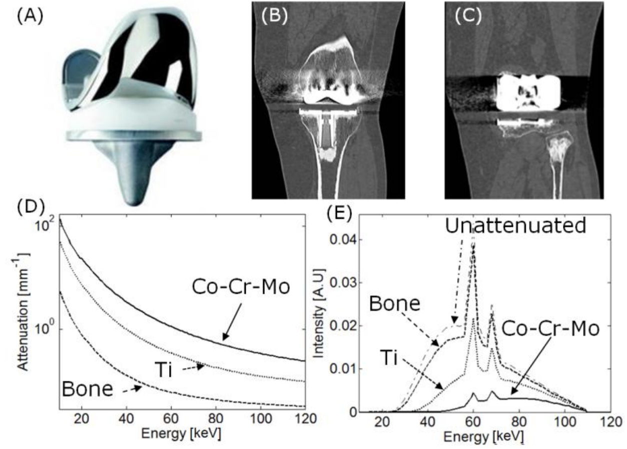

Fig. 1. (A) Example of a knee implant: DePuy Sigma [5]. Such prostheses present a large volume of highly x-ray attenuating alloy, often Cr-Co-Mo containing ~60% Cobalt, and thus pose a major challenge for x-ray CT. Artifacts associated with the presence of knee implants in CT scans are shown in (B) and (C) [4]. In (D), x-ray attenuation of Co-Cr-Mo (solid line) is compared to Titanium (dotted line) and cortical bone (dashed line). Significant loss of photon flux and substantial beam hardening are observed even for short path lengths through the alloy, as shown in (E), where x-ray spectra attenuated by 2 mm of Co-Cr-Mo (solid line), Ti (dotted line) and cortical bone (dashed line) are compared to the un-attenuated 110 kVp beam.

This work was supported in part by academic-industry partnership with Carestream Health (Rochester NY) and by NIH 2R01-CA-112163.

W. Zbijewski, J. W. Stayman, A. Muhit and J. H. Siewerdsen are with the Department of Biomedical Engineering, Johns Hopkins University, Baltimore, MD 21212 USA (phone: 410-955-1305; fax: 410-955-1115; e-mail: wzbijewski@jhu.edu).
J. Yorkston is with Carestream Health, Rochester, NY.
J. A. Carrino is with Department of Radiology, Johns Hopkins University, Baltimore, MD

These extremely strong attenuation characteristics of the Co-Cr-Mo alloy, combined with the large size of the implants [Fig. 1(A)] lead to large areas of missing data (zero or near-zero counts) and low signal-to-noise ratio in the projections. They are thus extremely challenging for conventional metal artifact reduction methods, such as those based on interpolation in the projection domain [6].

While the development of CT-compatible implants is an area of ongoing research, the ability to image heavy metallic prosthetics would be of significant immediate benefit to a growing population of patients.

The ability to image the prosthetic knee could be especially beneficial in the context of recently introduced dedicated cone-beam CT (CBCT) systems for extremities, such as the prototype shown in Fig. 2 [7]. Providing novel capabilities (e.g., load-bearing imaging), these systems promise to significantly expand the scope and quality of CT applications in orthopedics. Increasing prevalence of knee replacement implies that the ability to image in the presence of implants will be an important aspect of broad utilization of such dedicated devices. Moreover, the open system architecture of the prototype in Fig. 2 provides an ideal platform for development of novel reconstruction algorithms.

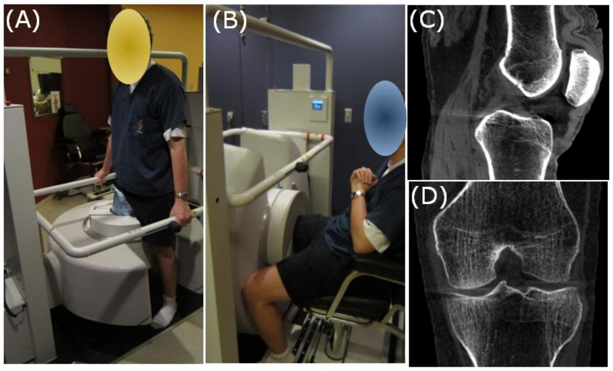

Fig. 2. The recently developed flat-panel cone-beam CT system for extremities imaging. The scanner allows for scanning in both a weight-bearing, standing (A) configuration and in a non-weight-bearing, sitting (B) configuration. Studies in cadaveric specimens indicate soft-tissue visibility comparable to conventional CT (C) and exquisite spatial resolution (D). Images in (C) and (D) were obtained from a single 80 kVp, 9 mGy acquisition using soft-tissue and bone reconstruction kernels, respectively.

One of the unique features of implant imaging is that the knowledge of their shape and composition is often available (e.g., from CAD models). If properly leveraged in the reconstruction, such prior knowledge can be used to alleviate the effects of missing data and low signal-to-noise ratio. This is especially true if combined with a penalized-likelihood (PL) approach, which properly accounts for projection noise, such as in the recently proposed Known Component Reconstruction (KCR) [1,2]. In KCR, the position of the known components is estimated jointly with the unknown background image (i.e., the underlying anatomy) using an alternating joint optimization method. This algorithm has been shown to yield excellent, near artifact-free reconstructions in imaging of pedicle screws under conditions of severe photon starvation. KCR has been previously developed under the assumption of a monoenergetic x-ray beam, which may be sufficient when polyenergetic effects in the object under consideration are relatively weak. However, as illustrated above, the heavy alloys used in knee implants exhibit significant beam hardening, and thus the KCR algorithm needs to be expanded to polyenergetic beams and energy-dependent attenuation. A number of approaches to include spectral effects in penalized-likelihood reconstruction have been proposed [8-10]. Here, we combine the algorithm of Elbakri et al. [9] with KCR and apply the resulting method to imaging in the presence of a knee prostheses.

II. METHODS

A. Forward Model

We assume an energy-integrating x-ray detector with uniform detection efficiency and write the measured projection value for detector element *i*:

$$y_i = \int \varepsilon \cdot Poisson\left\{q(\varepsilon) I_{0i} e^{-\int \mu_M(\varepsilon,x)\rho(x)dx}\right\} d\varepsilon \quad (1)$$

where I_{0i} is the total photon flux for pixel *i*, ε is the x-ray energy, $q(\varepsilon)$ is the spectral density of the x-ray beam, $\mu_M(\varepsilon,x)$ is the mass-attenuation coefficient of the object, $\rho(x)$ is the object density, and *x* is the spatial dimension. We express the line integral in (1) for a voxelized object following Elbakri et al. [9], where we assume that the object consists of *K* materials (mass-attenuation of *k-th* material given by $\mu_M^k(\varepsilon)$) and that the fraction of *k-th* material in voxel *j* is known and denoted by f_j^k. The mean signal at pixel *i* is then:

$$\bar{y}_i = \int \tilde{I}_{0i}(\varepsilon) e^{-l_i(\varepsilon,\rho)} d\,\varepsilon$$

$$\tilde{I}_{0i}(\varepsilon) = \varepsilon q(\varepsilon) I_{0i} \quad l_i(\varepsilon,\rho) = \sum_j \sum_k a_{ij} f_j^k \mu_M^k(\varepsilon)\rho_j \quad (2)$$

where $\mathbf{A} = \{a_{ij}\}$ is the system matrix. By assuming that the fraction f_j^k is known throughout the volume, the formulation in (2) allows the likelihood-based objective function for image reconstruction to have only one unknown per voxel, namely the density ρ_j (as opposed to a number of unknowns equal to the number of energy bins without this simplification). Elbakri et al. [9] assumed that the material fractions are known from segmentation of an initial FBP reconstruction.

Analogous to KCR, we will now further parameterize the object as a superposition of an unknown background image, given by density distribution ρ^*, and a known implant volume $\mu^I(\varepsilon)$ undergoing an arbitrary transformation (registration) $\mathbf{W}(\cdot,\lambda)$. The implant transformation is characterized by an unknown vector λ (e.g., rotation and translation). This leads to the following substitution in (2):

$$l_i(\varepsilon,\rho^*,\lambda) = \sum_j a_{ij} \left(\begin{array}{c} \left(\sum_k f_j^k \mu_M^k(\varepsilon)\rho_j^*\right)[\mathbf{W}(m,\lambda)]_j + \\ [\mathbf{W}(\mu^I(\varepsilon),\lambda)]_j \end{array} \right) \quad (3)$$

where *m* is a mask representing the support of the implant.

B. Reconstruction algorithms

Equation (2) with the line integral $l_i(\varepsilon,\rho^*,\lambda)$ given by (3) provides a relationship between mean measurement at pixel i and the object volume. To estimate the background density ρ^* and the parameters of the implant transformation λ, we invoke a Poisson noise model and write the log-likelihood:

$$L(\rho^*,\lambda;y) = \sum_i y_i \log\left(\int \tilde{I}_{0i} e^{-l_i(\varepsilon,\rho^*,\lambda)} d\,\varepsilon\right) - \int \tilde{I}_{0i}(\varepsilon) e^{-l_i(\varepsilon,\rho^*,\lambda)} d\,\varepsilon \qquad (4)$$

The unknowns can be estimated by maximizing the penalized-likelihood estimator:

$$\{\hat{\rho}^*,\hat{\lambda}\} = \operatorname{argmax}_{\rho^*,\lambda} L(\rho^*,\lambda;y) - \beta\cdot R(\rho^*) \qquad (5)$$

where $R(\cdot)$ is a regularization term to penalize noisy images (e.g., a pair-wise quadratic penalty). The estimator in (5) provides a general form that encompasses a variety of reconstruction object models (mono and polyenergetic, with and without the known components). Different iterative algorithms are used to solve (5), depending on the exact choice of the reconstruction object model. The simulated projection data in this study were obtained using the full spectral model. We consider the following cases:

- **PL-Mono**: if the x-ray spectrum is assumed to be monoenergetic ($q(\varepsilon) = \delta(\varepsilon_0)$) and no implant is included in the reconstruction model, (5) becomes the familiar penalized-likelihood estimator for monoenergetic x-ray CT, which is solved iteratively as in [11].
- **KCR-Mono**: in this case, the spectrum is still assumed monoenergetic, but the implant volume is included in the model, as in (3). Since polyenergetic effects are neglected, the implant attenuation is assumed equal to its attenuation at 90 keV, chosen to reflect the beam hardening effect of the Co alloy for the 110 kVp beam. The KCR algorithm of Stayman et al. [1,2] is used to solve this objective by an alternating minimization of λ and ρ^*.
- **PL-Poly**: when the reconstruction uses a polyenergetic object model, but without knowledge of the implant volume, the segmentation-based polyenergetic PL algorithm of Elbakri et al. [9] is employed. Two cases are considered: PL-Poly-Single, where the segmentation (f_j^k in (2)) assumes that all the voxels are composed of soft-tissue (represented by $\mu_M(\varepsilon)$ of muscle) and PL-Poly-Full with oracle segmentation into soft tissue, bone, and implant. Obtaining such segmentation from the initial FBP corrupted by artifacts caused by the prosthesis may be difficult; thus, PL-Poly-Full provides an upper bound on the performance of PL-Poly for such data.
- **KCR-Poly**: the full model of (3) is assumed. We estimate the unknown background density volume and the position of the known implant using a polyenergetic model of x-ray transmission. The same update equation as in PL-Poly is employed, but with the terms depending on the forward projection $\bar{y}_i$ computed using the separation of the volume into the density map ρ^* and the registered implant volume $\mathbf{W}(\mu^I(\varepsilon),\lambda)$, as in (3). This extension of the KCR methodology (aside from application to extremity imaging) is the main novel contribution of the current work. Similar to PL-Poly, segmentation needs to be provided to constrain the estimation of ρ^*. Note however that the segmentation of the implant is no longer required in KCR since the *a priori* knowledge of the implant is now part of the object model. Two approaches are tested: a simple segmentation assuming that all voxels consist of soft tissue (KCR-Poly-Single) and oracle segmentation into soft tissue and bone (KCR-Poly-Full, again providing the upper bound on algorithm performance).

The initial studies were performed under the assumption that the implant transformation **W** is fixed - i.e., that the implant location is known. The minimization over λ in (5) is therefore omitted. While this is a simplification, the results presented in [1,2] indicate that the registration step is extremely robust for a wide range of conditions, including the presence of multiple known objects. We therefore expect that inclusion of this step in KCR-Poly (ongoing work) will not alter the conclusions.

C. Phantoms, simulations, and reconstruction settings

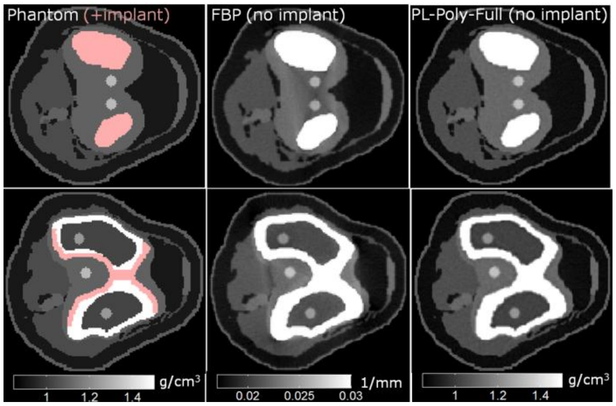

Fig. 3. (left) Phantoms used in the study. The knee implant (pink overlay) was simulated by replacing bone voxels with the Co-based alloy. Note the circular soft-tissue contrast inserts in the joint spaces and inside the condyles. (center) FBP reconstruction of the phantom with no implant, illustrating the magnitude of beam hardening due to bone. (right) Beam hardening artifacts are efficiently removed with the polyenergetic PL algorithm of Elbakri et al. [10] This algorithm was combined with Known-Component Reconstruction (KCR) [1,2] to yield a polyenergetic algorithm robust to the presence of implants.

Fig. 3 (left) demonstrates the phantoms used in this study. Two slices through segmented knee volumes from the Virtual Population dataset [12] were used. The base materials included four soft tissues (skin, fat, muscle, and cartilage), bone marrow, and cortical bone. Circular soft tissue contrast inserts (4 mm radius) were placed inside the joint space and inside the condyles; each insert was made from the same material as its background, but at a 1.2x higher density. The knee implant was simulated by replacing a region of bone voxels with a Co-Cr-Mo alloy, shown as pink overlay in Fig. 3. Following the basic geometry of such implants (Fig. 1), all bone voxels were replaced with the alloy in the distal region of the condyles (top row of Fig. 2); in the proximal region of the condyles (bottom row) only the inner and anterior bone surfaces were replaced with the alloy.

The geometry of the extremities CBCT scanner (Fig. 2) was simulated. For simplicity, a single slice, fan-beam acquisition was considered in this preliminary study. The SDD was 550 mm, and the SAD was 430 mm; there were 384 detector pixels at 0.776 mm pitch. A circular orbit with 360 projections at 1^{o} increment was assumed. The voxel size was 1 mm. Polyenergetic projections were simulated using Eq. (1) with 10^6 photons per detector element. The x-ray spectrum for a 110 kVp beam with 2 mm Al and 0.2 mm Cu filtration (as in the prototype scanner) was computed using SPEKTR [13].

Reconstruction by the PL and KCR methods above involved the same x-ray spectrum, pixel size, and voxel size as in the simulation. 200 iterations with 60 subsets were performed in each case. The regularization parameter β was varied to achieve similar resolution in all reconstructions. Matched forward- and back-projector based on separable footprints [14] were implemented in a CUDA-based library for nVidia GPUs.

III. RESULTS

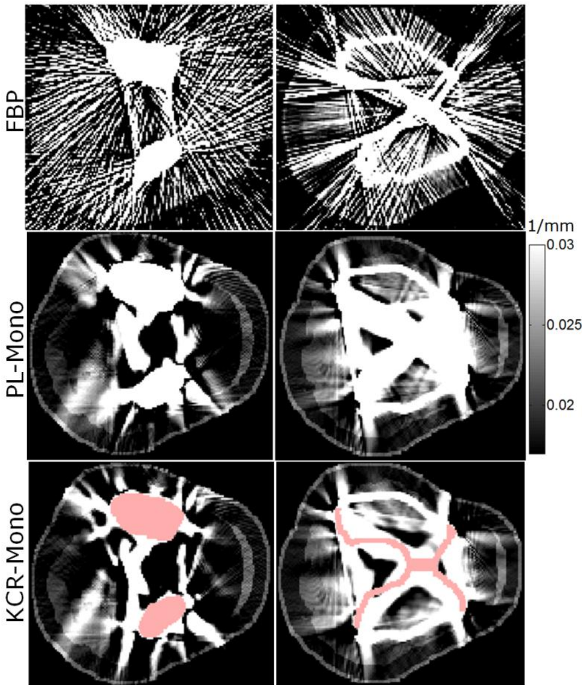

Fig. 4. Monoenergetic reconstructions (from polyenergetic projection data) in the presence of a knee implant. (top) FBP, showing severe streaks due to photon starvation and beam-hardening in the presence of the implant. (center) PL-Mono reconstruction, demonstrating a degree of improvement in artifacts caused by poor photon statistics; however, significant streak artifacts are persistent. (bottom) KCR-Mono reconstruction, where the implant (pink overlay) was modeled using its attenuation at 90 keV. Neglecting spectral effects results in little or no improvement over PL-Mono.

FBP and PL-Poly reconstructions of the two phantoms without the prostheses are shown Fig. 3 (center and right), demonstrating the strength of PL-Poly in addressing beam hardening from common materials such as cortical bone. In Fig. 4, reconstructions of polyenergetic projections of the phantoms with the implant included are compared for monoenergetic algorithms. The FBP images are severely compromised by streak artifacts. These artifacts are somewhat alleviated when a likelihood-based algorithm is used (PL-Mono). This demonstrates the value of including a noise model that penalizes low-count projections in the reconstruction. Nevertheless, the areas surrounding the implant are still plagued by artifacts. Including knowledge of the implant morphology (KCR-Mono) is not sufficient to reduce the artifacts because of the mismatch between the monoenergetic model of implant attenuation and the polyenergetic nature of the measured data.

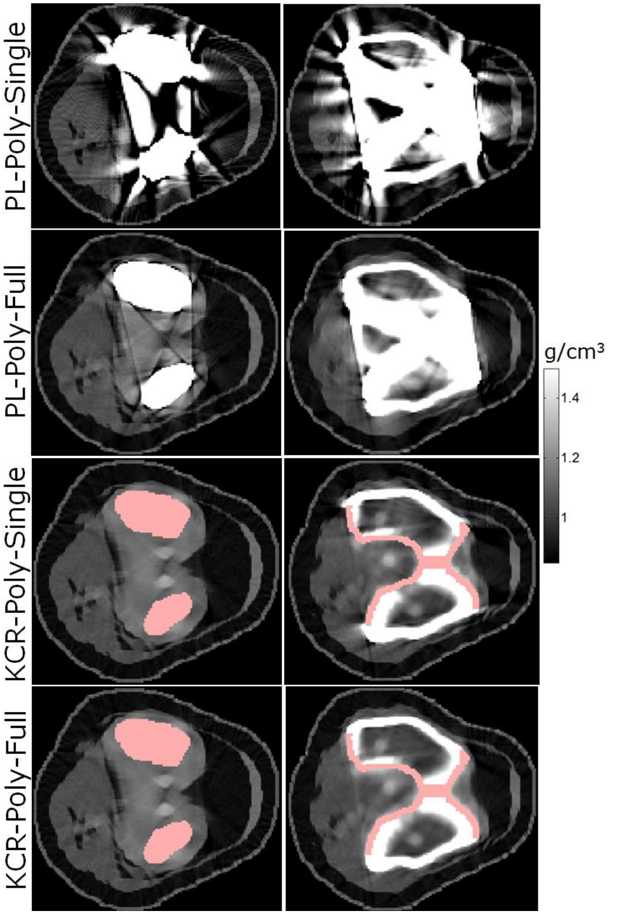

Fig. 5. Polyenergetic PL and KCR reconstructions. (top) PL-Poly reconstruction of the implanted knee, where object segmentation consisted of only soft tissue. The single-component model is not sufficient to suppress streak artifacts. (second row) PL-Poly with oracle segmentation that included soft tissue, bone, and the implant. While significantly improved from either PL-Mono or PL-Poly-Single, the image still suffers from artifacts. Such artifacts are largely removed with KCR-Poly-Single (third row), which applies knowledge of the material and morphological characteristics of the implant and estimates the unknown underlying anatomy simultaneously with the position of the known implant. (bottom) KCR-Poly-Full gives further improvement by including segmentation of bone and soft tissue.

In Fig. 5, reconstruction algorithms that employ a polyenergetic object model are compared for the same projection data. A simple model of object attenuation used in PL-Poly-Single (all voxels consisting of soft-tissue) fails to produce significant reduction in artifacts. Even when the implant is included in the initial segmentation (PL-Poly-Full), artifacts persist in the vicinity of the prosthesis. They are significantly reduced with KCR-Poly-Single (third row in Fig. 5), as evident by the improved visualization of the contrast inserts. The artifacts are further diminished when bone is also included in segmentation (KCR-Poly-Full, bottom row on Fig. 5). While traditional algorithms attempt to extract information from data with very few or zero counts (in effect a data null-space), KCR uses *a priori* implant knowledge to better condition the problem and select solutions from within potential null-spaces. Note also that KCR-Poly-Single achieves excellent artifact reduction while not requiring a complete segmentation of the object, which is likely difficult to obtain in the presence of artifacts caused by the prosthesis.

IV. DISCUSSION

A novel reconstruction algorithm (KCR-Poly) that combines the knowledge of the material and morphological characteristics of the prosthesis with a polyenergetic model of x-ray propagation was introduced. The algorithm was shown to yield excellent results in reduction of severe image artifacts around such implants in conventional reconstructions. The success of KCR-Poly owes to both the use of *a priori* knowledge of the implant and the account of the polyenergetic nature of object attenuation, as indicated by the persistence of artifacts for the monoenergetic version of KCR.

Ongoing work includes inclusion of the implant registration step as part of the joint optimization [1,2] in KCR, extension to segmentation-free polyenergetic reconstruction [10], and testing in real data, including an analysis of the effects of scatter [15]. The algorithm will be tested on the prototype extremities scanner in realistic scenarios and extended to other applications involving large metallic implants.

REFERENCES

[1] Stayman J. W., Otake Y., Prince J. L., Siewerdsen J. H., "Likelihood-based CT Reconstruction of Objects Containing Known Components," *Int'l Mtg. Fully 3D Image Recon.*, (2011).

[2] Stayman J. W., Otake Y., Prince J. L., Siewerdsen J. H., "Model-Based Tomographic Reconstruction of Objects Containing Known Components", *IEEE Trans. Med. Im.*, in press (2012).

[3] Kim, S., "Changes in Surgical Loads and Economic Burden of Hip and Knee Replacements in the US: 1997–2004," *Arthritis & Rheumatism (Arthritis Care & Research),* 59(4):481–488 (2008).

[4] Fishman E. K., "Case 3563: Total Knee Replacement," www.ctisus.com.

[5] DePuy Companies, "Sigma Rotating Platform Knee," www.depuy.com.

[6] Kalender W. A., Hebel R., Ebersberger J., "Reduction of CT artifacts caused by metallic implants," *Radiology,* 164:576–577 (1987).

[7] Zbijewski, W., De Jean P., Prakash P., Ding Y., Stayman J. W., Packard N., Senn R., Yang D., Yorkston J., Machado A., Carrino J. A., Siewerdsen J. H., "A dedicated cone-beam CT system for musculoskeletal extremities imaging: Design, optimization, and initial performance characterization," *Med. Phys.* 38(8):4700 - 4713 (2011)

[8] De Man, B., Nuyts, J., Dupont, P., Marchal, G., Suetens, P., "An iterative maximum-likelihood polychromatic algorithm for CT," *IEEE Trans. Med. Im.,* 20(10):999-1008 (2001).

[9] Elbakri, I. A., Fessler, J. A., "Statistical image reconstruction for polyenergetic X-ray computed tomography," *IEEE Trans. Med. Im.* 21(2):89-99 (2002).

[10] Elbakri, I. A., Fessler, J. A., " Segmentation-free statistical image reconstruction for polyenergetic X-ray computed tomography with experimental validation," *Phys. Med. Biol.*, 48(15):2543-78 (2003)

[11] Erdogan, H., Fessler, J. A., "Ordered subsets algorithms for transmission tomography," *Phys. Med. Biol.* 44:2835-51 (1999).

[12] IT'IS Foundation, "The Virtual Population," www.itis.ethz.ch.

[13] Siewerdsen, J. H., Waese, A. M., Moseley, D. J., Richard, S., Jaffray, D. A., " Spektr: A computational tool for x-ray spectral analysis and imaging system optimization," *Med. Phys.*, 31:3057 (2004).

[14] Long, Y., Fessler, J. A., Balter, J. M., "3D forward and back-projection or X-ray CT using separable footprints," *IEEE Trans. Med. Im.*, 29:1839-50 (2010).

[15] Zbijewski, W., Sisniega, A., Vaquero, J. J., Packard, N., Senn, R., Yang, D., J. Yorkston, Carrino, J. A., Siewerdsen, J. H., "Dose and Scatter Characteristics of a Novel Cone Beam CT system for Musculoskeletal Extremities," *Proc. of SPIE Medical Imaging* (2011).

A Model-Based Iterative Algorithm for Dual-Energy X-Ray CT Reconstruction

Ruoqiao Zhang, Jean-Baptiste Thibault, *Member*, *IEEE*, Charles A. Bouman, *Fellow*, *IEEE*,
Ken D. Sauer, *Member*, *IEEE*, and Jiang Hsieh, *Senior Member*, *IEEE*

***Abstract*—Recent developments in dual-energy X-ray CT have shown a number of benefits over standard CT for object separation, contrast enhancement, artifact reduction, and material composition assessment. As with traditional CT, model-based iterative approaches to reconstruction offer the opportunity to reduce noise and artifacts in dual energy reconstructions. However, previous approaches to model-based dual energy reconstruction have not fully modeled the statistical dependencies in the material-decomposed data. In this paper, we present a method for model-based iterative reconstruction which accounts for both the statistical dependency in the material decomposed sinogram components, and fast-switching approaches to dual-energy sampling. Our method also incorporates a positivity constraint in the space domain which accurately accounts for the true physical constraint of positive X-ray attenuation and is computationally simple to implement. Both phantom and clinical results show that the proposed model produces images which compare favorably to FBP in overall image quality.**

I. INTRODUCTION

Acquiring X-ray CT exposures at two distinct energy levels can help distinguish different material types, which is of great importance in disease diagnosis and security inspection. Dual-energy CT reconstruction typically works by reconstructing two density maps for two basis materials. The cross-sectional attenuation map at any given energy can then be computed as a linear combination of the two material density maps [1].

A typical approach to dual-energy reconstruction works by first transforming the low and high energy photon counts into quantities that are proportional to the integral of the material density for two basis materials. This material-decomposed sinogram can then be directly reconstructed using FBP to form the material density maps in image space. The transformation from photon counts to integral projections is performed by a material-decomposition function, which can then be experimentally measured through a scanner calibration procedure. However, the processes of applying this material-decomposition function changes the statistics of the measured data, which results in reconstructions that have statistically correlated noise properties.

Statistical iterative methods have the natural advantage that they can explicitly build data statistics into the dual-energy problem description, and account for the significant changes occurring during material decomposition. Some statistical approaches [2], [3] have been proposed from a rigorous theoretical perspective to reconstruct the material images directly from the low- and high-energy projections. On the other hand, Model-Based Iterative Reconstruction (MBIR), which views the reconstruction problem as the solution of a Maximum *A Posteriori* (MAP) estimation formulation, has been found to be very effective in reconstruction of single-energy CT images [4], [5].

In this paper, we propose an approach for applying MBIR to the dual-energy X-ray CT problem. Our approach explicitly accounts for the correlation of scanner noise caused by the material-decomposition process, and it also allows for accurate modeling of data collected using kV switching techniques, in which low and high energy measurements are used at alternating views. The MBIR approach incorporates a prior model that accounts for the separation into materials, and includes a simple positivity constraint that accurately accounts for the true physical constraint of positive X-ray attenuation.

II. PROBLEM FORMULATION AND PROPOSED SOLUTION

A. Problem Formulation

The linear attenuation coefficient $x(E)$ of any material as a function of energy E can be expressed as a linear combination of mass attenuation coefficients of two basis materials [1]. Without loss of generality, in this paper we choose the basis materials as water and iodine. Then the relationship can be described as

$$x_j(E) = m_j \cdot \mu^T(E), \tag{1}$$

where j is the index of the voxel, $m_j \triangleq [m_{j,W},\ m_{j,I}]$ represents the water-equivalent and iodine-equivalent densities at voxel j and $\mu(E) \triangleq [\mu_W(E),\ \mu_I(E)]$ represents the known mass attenuation coefficients for water and iodine. The task is to reconstruct the material densities from the measurements obtained from dual-energy acquisition.

Let $m \in \Re^{N\times 2}$ represent the reconstructed images for the selected material basis pair, where each row is given by $m_j = [m_{j,W},\ m_{j,I}]$. Furthermore, let $y \in \Re^{M\times 2}$ be the set of dual-energy sinogram measurements, where each row given by, $y_i = [y_{i,l},\ y_{i,h}]$, specifies the low and high energy measurements for the i^{th} projection.

Then the reconstruction problem can be formulated as computing the MAP estimate given by

$$\hat{m} = \arg\max_{m\in\Omega^N} \{\log P(y|m) + \log P(m)\}, \tag{2}$$

This work was supported by GE Healthcare.

R. Zhang and C. A. Bouman are with the School of Electrical and Computer Engineering, Purdue University, West lafayette, IN 47907-0501 USA (email: zhang393@purdue.edu; bouman@ecn.purdue.edu).

J.-B. Thibault and J. Hsieh are with GE Healthcare Technologies, Waukesha, WI 53188 USA (email: jean-baptiste.thibault@med.ge.com; jiang.hsieh@med.ge.com).

K. D. Sauer is with the Department of Electrical Engineering, University of Notre Dame, Notre Dame, IN 46556-5637 USA (email: sauer@nd.edu).

where $P(y|m)$ is the conditional distribution of y given m, $P(m)$ is the prior distribution of m, and Ω is the constrained set for each voxel.

B. Forward Model

Let $p \in \Re^{M \times 2}$ be the forward projection of the material reconstruction, with its i^{th} row given by

$$p_i \triangleq \left[\int\limits_{ray\ i} m_{*,W}(r)dr, \quad \int\limits_{ray\ i} m_{*,I}(r)dr \right] \tag{3}$$

Then p can be expressed as $p = Am$ where A is the forward projecting matrix for the CT system.

Furthermore, we may define a vector-valued function $h_i : \Re^2 \rightarrow \Re^2$, which transfers the material projections to the expected photon attenuation along the i^{th} ray, as

$$h_i(p_i) \triangleq -\log \left(\int\limits_{\mathbb{R}} s_i(\mathcal{E}) \exp\left\{ -p_i \mu^T(\mathcal{E}) \right\} d\mathcal{E} \right), \tag{4}$$

where $\mathcal{E}$ denotes the X-ray photon energy, vector $s_i(\mathcal{E})$ represents the two normalized source/detector spectra for the i^{th} ray. Assuming h_i is invertible, the corresponding inverse function h_i^{-1} is defined as

$$h_i^{-1}(h_i(p_i)) \triangleq p_i \ . \tag{5}$$

Assume that for each detector, a measurement is made of the photon counts for both the low and high energy case. Then we can compute the associated low and high attenuation measurement as

$$y_i \triangleq \left[-\log\left(\frac{\lambda_{i,l}}{\lambda_{i,o,l}} \right), -\log\left(\frac{\lambda_{i,h}}{\lambda_{i,o,h}} \right) \right], \tag{6}$$

where $\lambda_{i,l}$ and $\lambda_{i,h}$ represent the measured photon counts along the i^{th} ray at low and high energies, respectively, and $\lambda_{i,o,l}$ and $\lambda_{i,o,h}$ represent the expected air-scanned photon rate. Then y_i has approximate mean $h_i(p_i)$ and approximate inverse covariance W_i as

$$W_i = diag\left\{ w_{i,l},\ w_{i,h} \right\}. \tag{7}$$

The diagonal elements $w_{i,l}$ and $w_{i,h}$ give the inverse variances of $y_{i,l}$ and $y_{i,h}$ respectively. Zero off-diagonal entries come from the assumption that the incident rays with different energy levels are mutually independent. The values of $w_{i,l}$ and $w_{i,h}$ can be estimated by using the photon count measurement λ_i [6], [7], as

$$w_{i,l} = \frac{\lambda_{i,l}^2}{\lambda_{i,l} + \sigma_e^2}, \tag{8}$$

$$w_{i,h} = \frac{\lambda_{i,h}^2}{\lambda_{i,h} + \sigma_e^2}, \tag{9}$$

where σ_e^2 represents the variance of electronic noise in the data acquisition [8]. The log-likelihood term can then be approximated by a second-order Taylor series expansion using a Poisson-Gaussian noise model [6], [7], which yields the quadratic expression:

$$\begin{aligned} &-\log P(y|m) \\ &\approx \frac{1}{2} \sum_i \left(y_i - h_i(A_{i,*}m) \right) W_i \left(y_i - h_i(A_{i,*}m) \right)^T + f(y), \end{aligned} \tag{10}$$

where $f(y)$ is a function depending on data y only. Define $\hat{p}_i$ as an estimate of the material projection p_i, which is obtained via the h_i^{-1} function,

$$\hat{p}_i \triangleq h_i^{-1}(y_i). \tag{11}$$

Then by a first order approximation, the likelihood term can be written as

$$-\log P(y|m) \approx \frac{1}{2} \sum_i \left(\hat{p}_i - A_{i,*}m \right) B_i \left(\hat{p}_i - A_{i,*}m \right)^T, \tag{12}$$

where the weighting matrix B_i is given by

$$B_i \triangleq [\nabla h_i^{-1}(y_i)]^{-1} W_i [\nabla h_i^{-1}(y_i)]^{-T}. \tag{13}$$

Each B_i is a 2×2 symmetric matrix which represents the inverse covariance of the estimated material projections $\hat{p}_i$. The off-diagonal entries of B_i provide information about the correlation between the calculated projections of distinct materials.

This formulation also works for the fast kVp switching data acquisition mode, in which the effective source voltage changes from view to view. In this case, each projection only contains one of the low- or high-kV measurements. So if a low measurement is made, then $w_{i,h} = 0$, and if a high measurement is made, then $w_{i,l} = 0$. The missing components for the values of y_i are then computed by interpolation. However, these interpolated values are only used to compute the gradient $\nabla h_i^{-1}(y_i)$, which consequently only have a small effect the value of B_i. Moreover, the matrix B_i is always rank deficient in this case, with a zero eigenvalue in the direction of the missing information.

In practice, the h_i^{-1} can be the same material decomposition function used in FBP reconstruction, and it can be empirically measured from the physical system.

C. Prior Model

We employ a Markov random field (MRF) as our prior model with the form

$$-\log P(m) = \sum_{s \in \{W,I\}} \sum_{\{j,k\} \in \mathcal{C}} b_{jk,s} \rho(m_{j,s} - m_{k,s}), \tag{14}$$

where s is the index of material type, $\mathcal{C}$ represents the set of all neighboring voxel pairs, $b_{jk,s}$ are regularization weights and $\rho(.)$ is the potential function. Our particular choice of penalty here is the q-generalized Gaussian MRF (q-GGMRF) [4]:

$$\rho(\Delta) = \frac{|\Delta|^p}{1 + |\Delta/c|^{p-q}}. \tag{15}$$

with $1 < q \leq p \leq 2$, which guarantees strict convexity and therefore global convergence of the cost function. The parameter c balances the performance between noise reduction and edge preservation [4]. We choose here to perform this regularization independently on each of the material density images.

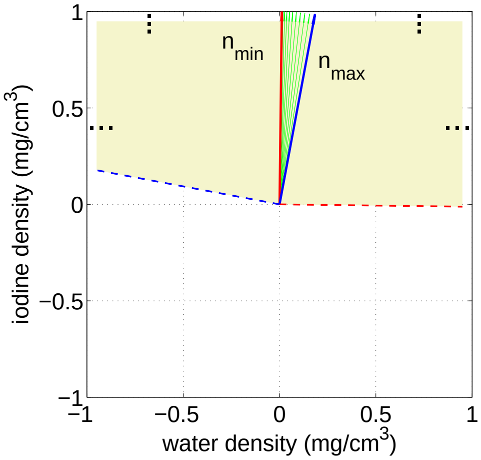

Fig. 1. This figure illustrates the feasible values of a pixel $m_j = [m_{j,W}, m_{j,I}]$. The set is formed by the intersection of only two half planes, one defined by n_{max} and the other by n_{min}.

D. Constrained Optimization

An important physical constraint to the solution is that the attenuation at every energy must be non-negative. More precisely for all $E \in [40, 140]$ keV, we know that

$$x_j(E) = m_j \cdot \mu^T(E) \geq 0 \ , \tag{16}$$

where the photon energy range [40, 140] keV is of particular interest for medical imaging and is above the k-edge of iodine. This constraint is then equivalent to the constraint that

$$m_j \cdot n^T(E) \geq 0 \ , \tag{17}$$

where $n(E) = \frac{\mu(E)}{||\mu(E)||}$ is the normalized mass attenuation vector. The constraint set is then given by $m_j \in \Omega$ where

$$\Omega = \cap_{E \in [40,140]} \{ m_j \in \Re^2 : m_j \cdot n^T(E) \geq 0 \} \ . \tag{18}$$

So Ω is formed by the intersection of an infinite number of half planes. However, the form of Ω can be dramatically simplified by noticing that the direction of $n(E)$ moves continuously with E, therefore the constraint can be represented much more simply by the intersection of two planes corresponding to the minimum and maximum values of $n(E)$ as n_{min} and n_{max}, with

$$\Omega = \left\{ m : m_j \cdot n^T_{\text{min}} \geq 0 \text{ and } m_j \cdot n^T_{\text{max}} \geq 0 \right\} . \tag{19}$$

The constraint set and the associated vectors are illustrated graphically in Fig. 1.

Combining the log likelihood in (12) and the prior in (14) with the above constraints, the MAP estimate of m can be obtained by solving the following constrained optimization:

$$\begin{aligned} \hat{m} = \arg \min_{m \in \Omega^N} \Bigg\{ & \frac{1}{2} \sum_i \left(\hat{p}_i - A_{i,*} m \right) B_i \left(\hat{p}_i - A_{i,*} m \right)^T \\ & + \sum_{s \in \{W,I\}} \sum_{\{j,k\} \in \mathcal{C}} b_{jk,s} \rho(m_{j,s} - m_{k,s}) \Bigg\} \ . \end{aligned} \tag{20}$$

We use iterative coordinate descent (ICD) algorithm with an FBP initial condition to solve the problem in (20), and with each ICD voxel update, we compute the exact solution to the constrained voxel update with the Karush-Kuhn-Tucker (KKT) conditions.

TABLE I

COMPARISON OF FBP AND MBIR FOR MEASUREMENT OF NOISE AND IN-PLANE MTF, FOR THE IMAGES IN FIG. 2. THE 10% MTF IS CHOSEN SINCE IT GENERALLY REPRESENTS THE VISUAL RESOLUTION OF THE IMAGE.

	Noise Std. Dev. (mg/cc)		10% MTF (lp/cm)	
	FBP	MBIR	FBP	MBIR
Water	21.21	9.68	6.15	11.80
Iodine	0.60	0.38	5.81	10.59
70keV Mono	14.18	13.69	6.60	11.70

III. RESULTS

In this section, we apply the dual-energy MBIR algorithm to both phantom and clinical reconstructions. Data is acquired on a Discovery CT750 HD scanner (GE Healthcare, WI) in dual-energy fast switching acquisition mode, rapidly alternating source voltage between 80 kVp and 140 kVp from view to view in 540 mAs. Each reconstructed 512×512 axial image has a prescribed thickness of 0.625mm. The reconstructed pixel value represents the water-equivalent or iodine-equivalent densities in units of mg/cm^3. The prior parameters are empirically chosen to be $p = 2.0$, $q = 1.2$, and $c = 10$. We will compare our method with a generic FBP method with a standard reconstruction filter kernel, which improves the FBP image quality via a correlation-based noise management [9]. Our method has not been optimized to yield a particular desired image quality performance.

Fig. 2 presents reconstructions of a GE Performance Phantom with 984 views per rotation for each kVp with pitch 0.938:1. As shown in the figures, MBIR creates smoother texture over FBP in flat regions. Fig. 3 shows the improvement in visual resolution brought by MBIR in the monochromatic image. Quantitative measurements also indicate that MBIR has the ability to improve the in-plane resolution with reduced noise over FBP, as illustrated in Table I.

Fig. 4 shows reconstructions of a clinical scan of the abdomen with 984 views per rotation for each kVp at a helical pitch of 0.984:1. By visual comparison to FBP, MBIR improves the water image by reducing noise and enhancing the overall contrast. The bone structures in the MBIR images exhibit less blooming and sharper edges than FBP, and the texture of the liver area is also improved. Some small lesions in the liver area and some fine structures are also enhanced in the MBIR images compared to the FBP images. The overall contrast enhancement by MBIR can also be observed in the monochromatic images. These results illustrate some potential diagnostic benefits of iterative reconstruction from dual-energy CT data.

IV. CONCLUSION

In this paper, we have presented a model-based iterative reconstruction approach for dual-energy X-ray CT reconstruction. The method combines a forward model to account for correlation between material decomposed projections with

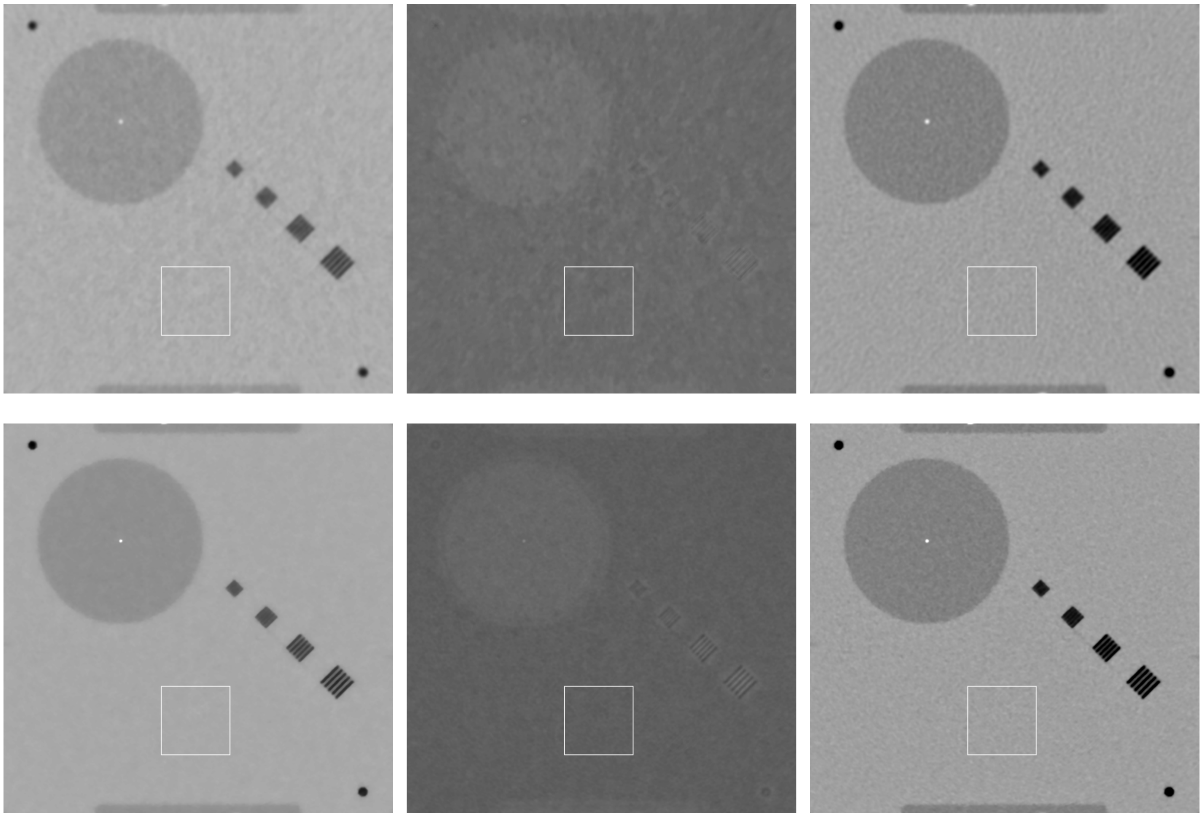

Fig. 2. Comparison of generic FBP vs MBIR performance on a GE Performance Phantom. All the images represent the same imaging plane in the 3D volume. Top left: FBP water image; top middle: FBP iodine image; top right: 70keV monochromatic FBP image. Bottom left: MBIR water image; bottom middle: MBIR iodine image; bottom right: 70keV monochromatic MBIR image. Display window for the water images: WW 1600mg/cm^3 and WL 900mg/cm^3; for iodine images: WW 40mg/cm^3 and WL 3mg/cm^3; for mono images: WW 1000HU and WL 0HU. The monochromatic image at a particular photon energy is generated by linearly combining water and iodine images with the corresponding mass attenuation coefficients at the given photon energy, according to equation in (1). The white box in the image indicates the region where the noise standard deviation is evaluated.

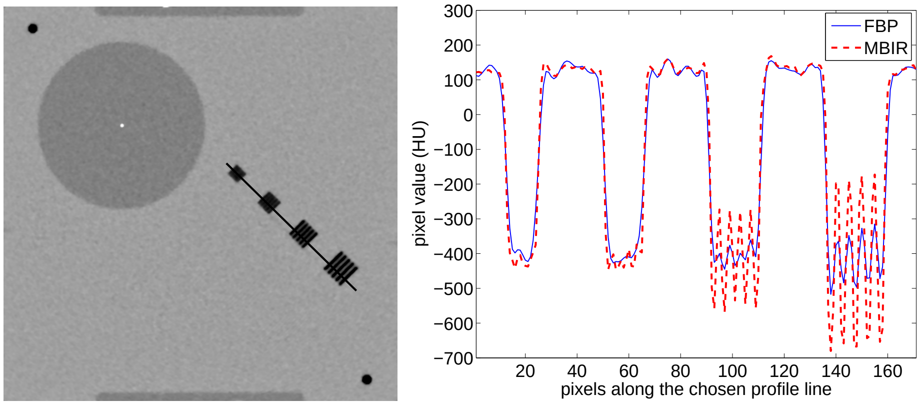

Fig. 3. Profile plot across the resolution bars on a GE Performance Phantom for FBP and MBIR images. Image on the LHS indicates the location of the profile line, which passes through the resolution bars perpendicularly. Image on the RHS shows the pixel values along that particular line in FBP (blue) and MBIR (red) images. It can be seen in the figure that the spikes in the MBIR image are much more enhanced than those in the FBP image, which makes the resolution bars more spatially separable.

MRF regularization, and features an additional physical constraint over the reconstructed linear attenuation coefficients. The proposed method has better performance than FBP in terms of noise reduction and spatial resolution. Further investigation will assess how to further improve material separation performance and investigate potential clinical benefits.

REFERENCES

[1] R. Alvarez and A. Macovski, “Energy-selective reconstructions in X-ray computerized tomography,” *Med. Phys.*, vol. 21, no. 5, pp. 733–744, 1976.

[2] J. Fessler, I. Elbakri, P. Sukovic, and N. Clinthorn, “Maximum-likelihood dual-energy tomographic image reconstruction,” in *Proc. SPIE4684, Medical Imaging 2002: Image Proc.*, vol. 1, 2002, pp. 38–49.

[3] J. O’Sullivan and J. Benac, “Alternating minimization algorithms for

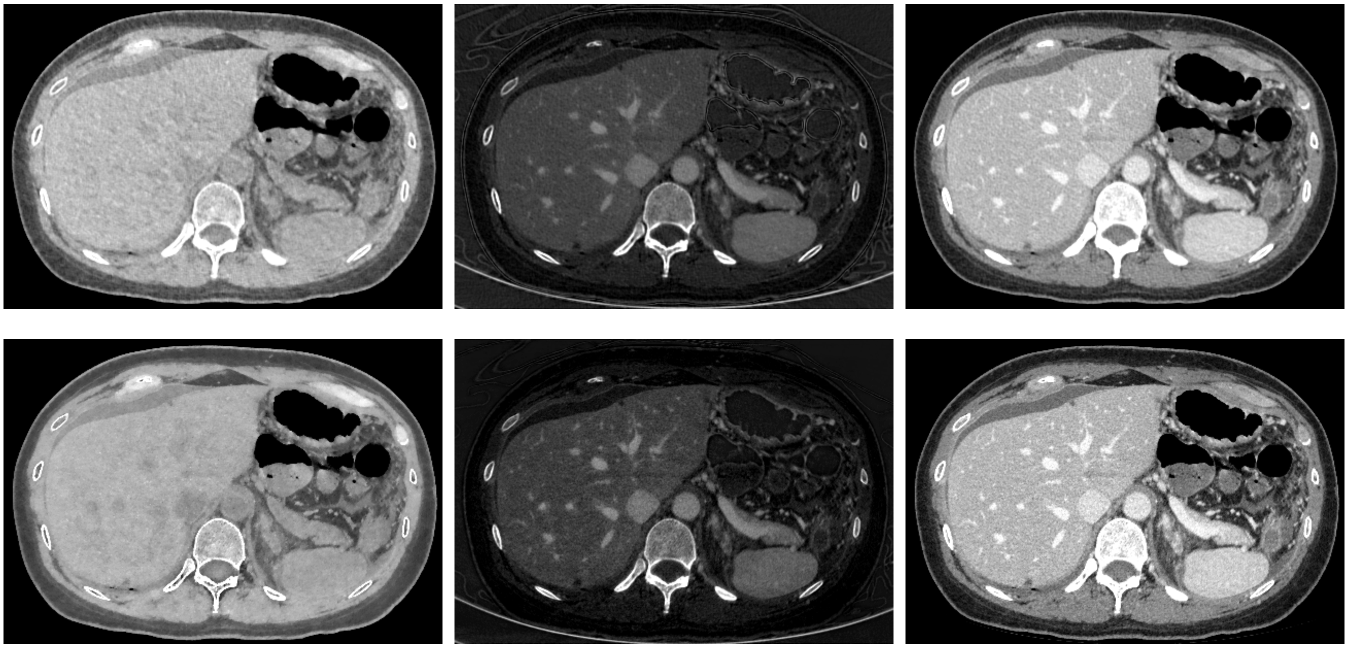

Fig. 4. Comparison of generic FBP vs MBIR performance on an abdominal clinical scan. All the images represent the same imaging plane in the 3D volume. Top left: FBP water image; top middle: FBP iodine image; top right: 70keV monochromatic FBP image. Bottom left: MBIR water image; bottom middle: MBIR iodine image; bottom right: 70keV monochromatic MBIR image. Display window for the water images: WW 300mg/cm^3 and WL 1000mg/cm^3; for iodine images: WW 17.5mg/cm^3 and WL 7.5mg/cm^3; for mono images: WW 400HU and WL 40HU.

transmission tomography," *IEEE Trans. on Medical Imaging*, vol. 26, no. 3, pp. 283–297, Mar. 2007.

[4] J.-B. Thibault, K. Sauer, J. Hsieh, and C. Bouman, "A three-dimensional statistical approach to improve image quality for multislice helical CT," *Med. Phys.*, vol. 34, no. 11, pp. 4526–4544, 2007.

[5] Z. Yu, J.-B. Thibault, C. Bouman, K. Sauer, and J. Hsieh, "Fast model-based X-ray CT reconstruction using spatially nonhomogeneous ICD optimization," *IEEE Trans. on Image Processing*, vol. 20, no. 1, pp. 161–175, January 2011.

[6] C. Bouman and K. Sauer, "A unified approach to statistical tomography using coordinate descent optimization," *IEEE Trans. on Image Processing*, vol. 5, no. 3, pp. 480–492, March 1996.

[7] K. Sauer and C. Bouman, "A local update strategy for iterative reconstruction from projections," *IEEE Trans. on Signal Processing*, vol. 41, no. 2, pp. 534–548, February 1993.

[8] J.-B. Thibault, C. Bouman, K. Sauer, and J. Hsieh, "A recursive filter for noise reduction in statistical tomographic imaging," in *Proc. SPIE/IS&T Symp. Comput. Imag. IV*, vol. 6065, San Jose, CA, Jan. 16-18, 2006.

[9] W. Kalendar, E. Klotz, and L. Kostaridou, "An algorithm for noise suppression in dual energy CT material density images," *IEEE Trans. on Medical Imaging*, vol. 7, no. 3, pp. 218–224, Sep. 1988.

Model-based CT Reconstruction from Sparse Views

Sherman J. Kisner, Eri Haneda, Charles A. Bouman, Sondre Skatter, Mikhail Kourinny, and Simon Bedford

***Abstract*—In this paper, we investigate the use of model-based CT reconstruction in conjunction with limited-view scanning architectures, and we illustrate the value of these methods using transportation security examples. The advantage of limited view architectures is that it has the potential to reduce the cost and complexity of a scanning system, but its disadvantage is that limited-view data can result in structured artifacts in reconstructed images. Our method of reconstruction depends on the formulation of both a forward projection model for the system, and a prior model that accounts for the contents and densities of typical baggage. In order to evaluate our new method, we use realistic models of baggage with randomly inserted simple simulated objects. Using this approach, we show that model-based reconstruction can substantially reduce artifacts and improve important metrics of image quality such as the accuracy of the estimated CT numbers.**

I. INTRODUCTION

While *computed tomography* (CT) has developed primarily in the context of medical applications, there has been increasing utilizing of CT systems for transportation security. For example, many airports have deployed X-ray CT systems as a central component of baggage screening. While the underlying theory is largely the same as for medical CT, a different set of constraints are associated with security CT systems, such as the physical size and diversity of the scanned objects, the maximum acceptable X-ray energy, and the scan time requirements. Such constraints present some new opportunities and challenges for the CT reconstruction problem.

Scan time is a particularly important constraint for many security screening systems in order to handle the large volume associated with a transportation environment. One strategy to reduce scan time in a CT system is to simply take measurements at a fewer number of view angles, but this is generally to the detriment of reconstruction quality due to the ill-posed nature of the inversion problem [1]. For example, the traditional *filtered backprojection* (FBP) algorithm typically produces severe streaking artifacts in the limited view problem, which can in turn affect the later stages of security screening.

Recently, there has been growing interest in the use of model-based reconstruction techniques in CT security systems. Their potential to produce high-quality reconstructions is facilitated by their ability to incorporate knowledge of the physical and statistical properties of both the scanner and the targets. These include modeling of system geometry, uncertainty in the measurements, and prior knowledge about the solution. In particular, the modeling of the underlying image plays an important role in compensating for the missing data in the limited view problem.

One established class of model-based techniques applies a regularization on the solution through a *Markov random field* (MRF) prior model, describing the statistical distribution of a voxel given its neighbors. Such methods formulate the reconstruction as a maximization of the *posterior* distribution (of the image, given the measurements), or a *MAP* estimate. The optimization is typically solved using an iterative strategy [2] such as *iterative coordinate descent* (ICD).

The particular choice of MRF prior model has a strong influence on the character of the solution. A quadratic, or Gaussian MRF (GMRF) prior, provides for fast convergence but tends to over-regularize the solution. The *generalized Gaussian MRF* [3] (GGMRF) provides noise suppression while preserving edges in the image. A further generalization called the *q-generalized Gaussian MRF* [4] (qGGMRF) is even more controllable while providing for fast convergence [5].

At present, only a small number of published studies have been dedicated to CT reconstruction for transportation security [6], [7], including the application of FBP [8] and algebraic reconstruction (ART) [9]. In this paper, we evaluate the performance of model-based reconstruction for parallel beam CT in the context of transportation security. We investigate the effect of reconstruction with a limited number of projection angles, as well as the effect of background clutter on the accuracy of the attenuation coefficient estimates. The FBP algorithm is used as a baseline for comparison.

II. METHODS

A. Projection Model

We assume a linear forward projection model in which, in the noiseless case, the object density image, $x \in \mathbb{R}^M$, and the projections, $y \in \mathbb{R}^N$, are related by a sparse matrix operator A,

$$y = Ax \ . \tag{1}$$

The matrix coefficient A_{ij} represents the contribution of voxel j in forming projection element i. In a line-beam model, A_{ij} is calculated as the length of beam i that intersects voxel j. In a wide-beam model [10], which accounts for the fact that photons are collected over a detector *area*, the coefficient A_{ij} is computed as the inner product of the projection of voxel j onto the face of sensor i, with a detector efficiency kernel which is typically a simple indicator function. All results presented in this study use the wide-beam model.

S.J. Kisner, E. Haneda, and C.A. Bouman are with the School of Electrical and Computer Engineering, Purdue University, West Lafayette, IN, USA.

S. Skatter and M. Kourinny are with Morpho Detection Inc., Newark, CA, USA.

S. Bedford is with Astrophysics Inc., City of Industry, CA, USA.

This work was supported by the Department of Homeland Security, Science and Technology Directorate (Explosives Division and Transportation Security Laboratory).

B. Iterative MAP reconstruction

In the statistical framework, we consider the image, x, and the projection measurements, y, as random vectors, and our goal is to reconstruct the image by computing the maximum *a posteriori* (MAP) estimate given by

$$\hat{x} = \underset{x \geq 0}{\text{argmin}} \{ -\log p(y|x) - \log p(x) \} \tag{2}$$

where $p(y|x)$ is the likelihood function associated with the data model, and $p(x)$ is the prior distribution of x. Note we also include a positivity constraint on the solution.

In general, the received photon count, λ_i, corresponding to projection i follows a Poisson distribution with mean $\bar{\lambda}_i = \lambda_{T,i} e^{-A_{i*}x}$, where $\lambda_{T,i}$ denotes the input photon count for projection i, and A_{i*} denotes the i^{th} row of the projection matrix. Starting from the Poisson model, a second-order Taylor expansion can be used to approximate the log likelihood term by the following [2],

$$\log p(y|x) \approx -\frac{1}{2}(y - Ax)^T D (y - Ax) + f(y) \tag{3}$$

where A is the forward projection matrix, D is a diagonal weighting matrix given by diag$\{\lambda_1, ..., \lambda_N\}$, and $f(y)$ is a function which depends on measurement data only. Note in this form, the photon count, λ_i, acts as a weighting coefficient for the error, $(y_i - A_{i*}x)^2$, associated with projection i (i.e. smaller photon counts are less reliable, so are weighted less in the cost framework).

We will consider a Markov random field for the prior model, $p(x)$, where we use a standard 8-point neighborhood. An MRF distribution is often defined implicitly in terms of conditional densities, but the Hammersley-Clifford theorem allows the joint density to be expressed as a Gibbs distribution of the following form,

$$p(x) = \frac{1}{z} \exp \left\{ - \sum_{\{s,r\} \in \mathcal{C}} b_{s,r} \rho(x_s - x_r) \right\} \tag{4}$$

where ρ is a positive and symmetric function called the *potential function*, $\mathcal{C}$ is the set of all pairwise cliques and z is a normalizing constant. The MAP solution then becomes,

$$\hat{x} = \underset{x \geq 0}{\text{argmin}} \left\{ \frac{1}{2} \|y - Ax\|_D^2 + \sum_{\{s,r\} \in \mathcal{C}} b_{s,r} \rho(x_s - x_r) \right\} . \tag{5}$$

In this study, we consider two different potential functions, $\rho(\cdot)$. The first is a quadratic, which corresponds to a Gaussian Markov random field (GMRF). So defining $\Delta = x_s - x_r$, we have $\rho(\Delta) = \Delta^2$. The second, is a q-generalized Gaussian MRF, or qGGMRF [4], which has the form,

$$\rho(\Delta) = \frac{|\Delta|^p}{1 + |\Delta / c|^{p-q}} . \tag{6}$$

Generally, the qGGMRF potential allows more control over the behavior since $\rho(\Delta) \approx |\Delta|^p$ for small values of Δ (small voxel differences), and is proportional to $|\Delta|^q$ for large values of Δ. The c parameter controls the "transition point" between these two cases. Of particular interest are the cases where $1 \leq q \leq p$, which ensures convexity of the potential function. Common values to use are $p = 2$ (quadratic near zero), and q close to 1.

The reconstruction is computed by minimizing the expression in Eq. (5). We compute the solution by iterative coordinate descent (ICD) which minimizes the cost with respect to each voxel serially. Note because of our choice of priors, the global cost function is convex and ICD is ensured to converge to the global minimum.

III. RESULTS

This section will present both qualitative and quantitative analyses on the accuracy of model-based reconstruction. So that we can evaluate with respect to ground truth, projection data was simulated by applying a linear wide-beam projector to a clean high-resolution scan of a duffel bag (see Figure 2(b)). Sinograms were generated with various numbers of views ({64,32,16,8} views, at 800 samples per view.) Since we are principally interested in examining the effect of a reduced number of view angles, and the effect of clutter in the image, no photon noise is incorporated for this study. All images were reconstructed at 800x800 pixel resolution, and the qGGMRF model parameters were (p=2.0, q=1.0, c=15HU).

For comparison, reconstructions are also computed using *filtered backprojection*. The filter employed in these reconstructions has a ramp frequency response multiplied by a Hamming window, and a cutoff frequency of 0.8 times the Nyquist rate. Source code for this reconstruction software is available for download (See Ref. 11).

A. Effect of Limited View Angles

Figure 1 shows the reconstructions after forward projecting a ground truth bag scan at a limited number of equally spaced view angles between 0 and 180 degrees. Illustrated is the effect of reducing the number of view angles on reconstruction by filtered backprojection (FBP), and by iterative model-based reconstruction using a Gaussian Markov random field (GMRF) prior, and a q-generalized Gaussian MRF prior (qGGMRF). The corresponding *root mean square error* (RMSE) from ground truth for each of these reconstructions is listed in Table I. The RMSE was computed from only those voxels having a density greater than air in the ground truth image.

TABLE I
ROOT MEAN SQUARE ERROR OF RECONSTRUCTIONS IN FIG. 1. UNITS ARE OFFSET HOUNSFIELD (AIR=0).

no. of views	FBP	GMRF	qGGMRF
64	481.0	237.8	112.8
32	628.4	361.1	277.1
16	746.2	498.9	453.8
8	854.4	607.1	598.5

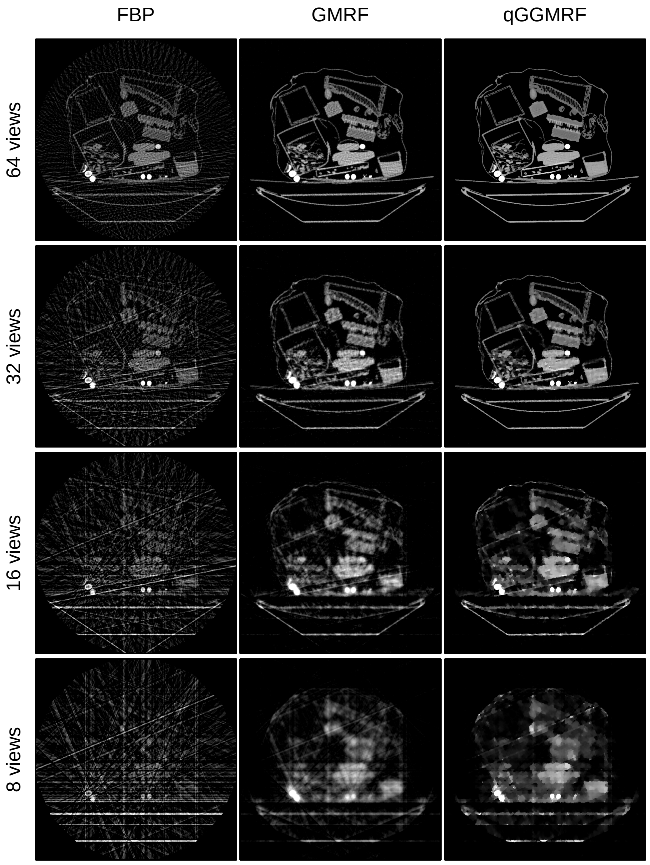

Fig. 1. Image reconstructions from limited view angle projection data. Four parallel projection data sets are considered, containing 64, 32, 16, and 8 view angles, uniformly spaced between 0 and 180 degrees. Reconstructions include filtered backprojection (FBP) and iterative MAP reconstruction using a Gaussian Markov random field prior (GMRF), and a q-generalized Gaussian MRF prior (qGGMRF). The gray scale range for all results shown is [0,2000] HU.

B. Effect of Clutter on CT Accuracy

To examine the effect of image “clutter” on the accuracy of CT number estimates, we modified the ground truth image in two respects. First, the contents of the bag scan were masked out to produce a *low clutter* scene, and we consider the original image as a *high clutter* scene. Second, we inserted a single round 1.7 cm diameter target of a known uniform CT value (1400 HU) somewhere inside the perimeter of the bag. Figures 2(a) and 2(b) illustrate this for the low and high clutter scenes.

Two experiments were performed. In the first, we produced 32 view angle parallel projection data from the images shown in Figures 2(a) and 2(b) (without the highlighting box). Reconstructions were computed using FBP and iterative MAP reconstruction using the GMRF and qGGMRF priors. A close-up of the reconstructions around the target region are shown in Figure 3. Figure 4 shows the reconstructed CT numbers for voxels along the reference line through the target.

In the second experiment we calculated the average accuracy of the reconstructed target voxels after placing the target at various locations in the bag. Specifically, in each trial we (1) place the synthetic target at a random location inside the bag perimeter, (2) forward project to produce a 32 view angle sinogram, (3) reconstruct, and (4) calculate the average deviation of the target voxels from the true value, as well as the root mean square of the deviations. Table II summarizes the results of this procedure averaged over 60 trials of random placement.

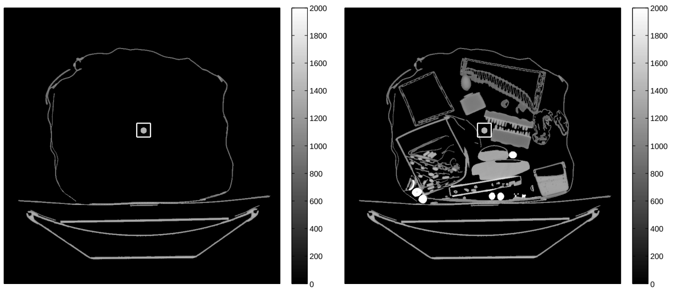

(a) Low clutter scene (b) High clutter scene

Fig. 2. Ground truth images for investigating the effect of clutter on CT reconstruction accuracy. The bag contents from the ground truth image have been masked out to create a *low clutter* scene in (a). For evaluation, a synthetic target of uniform value (1400 HU) has been added, as highlighted by the box near the center of the low and high clutter scenes. A close-up of the target in (c) also shows a reference line highlighting voxels that will be examined in the experiment.

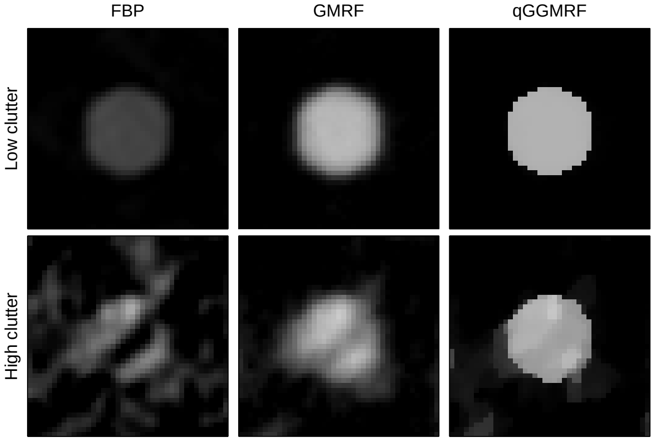

Fig. 3. Reconstructions zoomed to the target area indicated in Figs. 2(a) and 2(b). All results are from 32 view angle parallel projection data, the top row generated from the low clutter scene of Fig. 2(a), and the bottom row from the high clutter scene of Fig. 2(b).

TABLE II

RECONSTRUCTED CT NUMBERS FOR A RANDOMLY PLACED SYNTHETIC TARGET. THE *Dev.* IS THE AVERAGE DEVIATION OF RECONSTRUCTED TARGET VOXELS FROM THE TRUE VALUE. SIMILARLY, THE *RMSE* IS THE ROOT MEAN SQUARE DEVIATION FROM THE TRUE TARGET VALUE. ALL VALUES ARE IN OFFSET HOUNSFIELD UNITS (AIR=0).

	Low clutter		High clutter	
	Dev.	RMSE	Dev.	RMSE
FBP	-895.1	899.1	-647.8	702.7
GMRF	-157.2	280.4	-179.8	332.7
qGGMRF	-14.2	25.8	-87.3	209.2

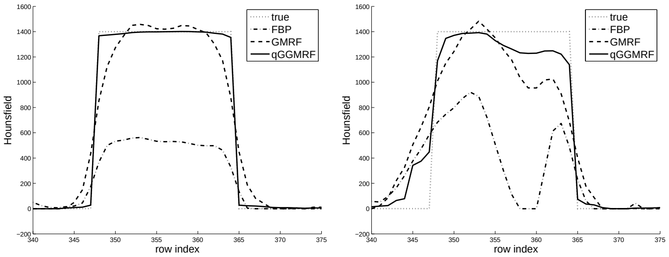

(a) Low clutter (b) High clutter

Fig. 4. CT values from limited view reconstructions of Fig. 3 for voxels along a line through the center of the target region. Also shown are the true voxel values from ground truth.

IV. DISCUSSION

The most apparent advantage of model-based reconstruction from Figure 1 is a reduced susceptibility to streaking artifacts, whereas FBP quickly devolves into streaks as the number of views becomes small. While streaking patterns can be seen in dense regions of the MAP-GMRF result at 64 views, the spatial extent of the streaks is much more localized than in FBP, and the regularization of the qGGMRF prior further reduces these dramatically.

In fact, for each data set in Figure 1 the qGGMRF prior produces a result with less structured error and a clearer edges that the GMRF prior. However, for extremely low view angles such as the 8-views case, the advantage of the qGGMRF over GMRF is minimal because the edge locations are not always accurate. These points are also reflected in the RMSE values listed in Table I. In each case, the qGGMRF RMSE is smaller than the GMRF RMSE, with the difference becoming less significant as the number of views decreases.

Of note in Table I is the result that, in the mean square sense, MAP-qGGMRF produces a more accurate reconstruction than FBP using only a quarter of the number of views. Specifically, the RMSE of qGGMRF at 16 views is smaller than that of FBP at 64 views, and qGGMRF at 8 views is smaller than FBP at 32 views. If this result generalizes, this is a particularly significant consideration since the number of views can have a direct correlation to system cost, scan time, and reconstruction time. Of course this marked difference in RMSE does not necessarily translate in the qualitative sense because visual inspection can somewhat compensate for the streaking in FBP. It should also be noted that one reason for the relatively high RMSE in the FBP reconstructions is a general underestimation of the CT numbers (which is apparent in Figure 1) partly due to image energy dispersal in the streaking. Presumably an appropriate image-dependent rescaling could be employed to provide a degree of compensation for this.

The 32-view synthetic target experiment of Figs. 3 and 4 reinforces several of the above observations. Namely, MAP-qGGMRF produces a much more accurate reconstruction in terms of both CT numbers overall, and in terms of edge clarity. The low clutter scene results in effectively no visible streaking in any case, with qGGMRF producing very accurate CT numbers and very little blurring of the target boundary. In the high clutter scene, FBP fully splits the target into two disjoint objects, while the GMRF prior produces a recognizable object but with highly non-uniform CT numbers. The qGGMRF prior produces a significantly more uniform reconstruction of the target and reproduces the edges with remarkable accuracy by comparison.

The results of the random placement experiment summarized by Table II are a more general confirmation of the observations about the reconstructions in Fig. 3. Since the target position is allowed to vary, the results are not strongly dependent on any particularly strong streaking artifacts caused by the metallic objects in the image. Of note is the factor of 10 improvement in the accuracy in the low clutter scene, going from the GMRF to the qGGMRF prior. As observed in Fig. 4(a), this is due to the much more accurate edge reconstruction afforded by the qGGMRF model. Similar, while not as dramatic, improvements are produced for the high clutter scene.

V. CONCLUSION

This paper presented the application of iterative model-based reconstruction on limited view angle parallel projection data, generated from a typical bag scan. We compared MAP reconstructions using two different prior models, a Gaussian Markov random field (GMRF) and a q-generalized Gaussian Markov random field (qGGMRF), to the standard filtered backprojection algorithm. Qualitative and quantitative measures demonstrated potentially great strengths in model-based reconstruction applied to transportation security, both in terms of reconstruction of form and in the CT number accuracy.

REFERENCES

[1] M. E. Davison, “The ill-conditioned nature of the limited angle tomography problem,” *SIAM J. Appl. Math.*, vol. 43, pp. 428–448, 1983.

[2] K. Sauer and C. Bouman, “A local update strategy for iterative reconstruction from projections,” *IEEE Trans. on Signal Processing*, vol. 41, no. 2, pp. 534–548, 1993.

[3] C. Bouman and K. Sauer, “A generalized Gaussian image model for edge-preserving MAP estimation,” *IEEE Trans. on Image Processing*, vol. 2, no. 3, pp. 296–310, 1993.

[4] J.-B. Thibault, K. Sauer, C. Bouman, and J. Hsieh, “A three-dimensional statistical approach to improved image quality for multi-slice helical CT,” *Medical Physics*, vol. 34, no. 11, pp. 4526–4544, 2007.

[5] Z. Yu, J. Thibault, C. Bouman, K. Sauer, and J. Hsieh, “Fast model-based X-Ray CT reconstruction using spatially non-homogeneous ICD optimization,” *IEEE Trans. on Image Processing*, vol. 20, no. 1, pp. 161–175, 2011.

[6] R. C. Smith and J. M. Connelly, *Aspects of Explosives Detection, Chapter 7 - CT Technologies*. Elsevier, 2009.

[7] Z. Ying, R. Naidu, and C. Crawford, “Dual energy computed tomography for explosive detection,” *Journal of X-Ray Science and Technology*, vol. 14, no. 4, pp. 235–256, 2006.

[8] E. Riveros, “The digital radiographic and computed tomography imaging of two types of explosive devices,” *Applied Radiation and Isotopes*, vol. 57, no. 6, pp. 861–865, 2002.

[9] H. Zhang, Y. Sun, and L. Wei, “Explosives detection method based on improved algebraic reconstruction technique,” in *Intelligent Control and Automation, 2008*, June 2008, pp. 1764–1767.

[10] T. Buzug, *Computed Tomography: From Photon Statistics to Modern Cone-Beam CT*. Springer, 2010.

[11] C. A. Bouman, “Tomography software,” 2011, available from http://www.ece.purdue.edu/~bouman/software/tomography.

AUTHOR INDEX

Author Index

A

Alessio A 79, 417
Allmendiger T 135
Anton G 218
Azevedo S G 305

B

Badea C T 222
Baer M 404
Barkhausen J 46
Bartling S 127
Bartolac S 119
Batenburg K J 170, 293
Bäuerle T 218
Bayer F 218
Bech M 373
Becker J-M 157
Bedford S 444
Bennett J 421
Bergner F 267
Berkus T 131
Bian J 50, 165, 254
Bögel M 13
Bouman C A 297, 439, 444
Brady T 238
Braun-Jones T 275
Brehm M 91
Brendel B 29, 267, 430
Bresler Y 339
Brokish J 339
Brown K M 29, 61
Bruder H 1, 107, 135
Bruyndonckx P 373
Butler A 421
Butler P 421
Buzug T M 46, 210, 242

C

Callstrom M R 140
Cammin J 186
Carrino J A 434
Carvalho L 131
Chang Y-B 9
Chen Defeng 226
Chen Dongmei 369
Chen L 74
Cheryauka A 275
Cho J H 330
Cho S 234
Choi K 198
Chung H 234
Clackdoyle R 279, 318
Claus B 322
Conover D 70
Crane J A 87

D

De Man B 198
Denis L 157
Dennerlein F 390
Desbat L 157, 318
Deuerling-Zheng Y 123
Dinu M P 57
Do S 238
Dobritz M 267
Doesburg R 421
Dremel K 246
Duan X 202, 425
Duncan W 275
Durst J 218
Duschka R L 46

E

Erdelyi M 230

F

Fahrig R 5, 13, 206
Fan Y 190
Fessler J A 33, 194, 330, 348, 378, 413
Fieselmann A 123
Fishman E K 95
Flohr T 1, 66
Foland A D 301
Freud N 382
Fu L 198
Fuchs T 246
Fung G S K 66, 95, 186

G

Ghosh D 310
Gödel K 218
Goossens B 37
Guo H 339
Gupta R 238

H

Ha S 111, 174, 178
Haas W 218
Han X 50, 165, 254
Haneda E 297, 444
Hanke R 246
He P 421
Heilbrun M 153
Heuscher D J 83, 115, 284
Higuchi T 95
Hofmann C 17
Hofmann H 13, 206
Hornegger J 5, 13, 206, 259, 288, 364
Hsieh J 439

J

Jaffray D 119
Jerebko A 21
Jin P 297
Johnson G A 222
Johnston S M 222
Jorgensen J H 161, 343

K

Kachelrieß M 17, 91, 127, 214, 218, 404
Kaiser F 210
Kakonyi R 230
Kalender W A 395
Kallman J S 305
Kappler S 135
Karellas A 70
Karl W C 238
Katsevich A 326
Kawashima A 425
Keesing D B 339
Kigure T 95
Kim D 33, 378
Kim J K 194
Kim K S 250
Kinahan P E 79
Kis B J 230
Kisner S J 444
Kleine M 242
Knaup M 17, 127, 214
Knudsen B 140
Koehler T 29, 267, 430
Kofler J M 74
Köhler C 364
Kourinny M 444
Kudo H 352
Kuntz J 127
Kunz P 91
Kunze H 395
Kyriakou Y 395

L

La Rivière P J 409
Lauritsch G 5, 259, 364
Lee M 250
Lee Y 234
Leng S 74, 87, 425
Lerman L O 87
Létang J-M 382
Levakhina Y 46, 210
Li H 263, 386
Li Z 360
Liang J 369
Liang Z 41, 190
Lionheart, W R B 99
Liu B 25
Liu X 373
Liu Y 41, 190
Long Y 413
Lu H 190

M

Ma J 41, 190
MacDonald L R 417
Maier A 5, 13, 206, 364, 390
Manhart M 123
McCollough C H 74, 87, 140, 202, 425
Mennessier C 157, 279, 318
Miao C 25
Michel T 218

Michielsen K 21
Miller E L 314
Momey F 157
Morton E J 99
Mou X 421
Mueller J 46, 210
Mueller Kl 111, 174, 178, 182, 356
Muhit A 434
Müller Ke 5, 259
Myers K J 148

N

Noel P B 267
Noo F 83, 115, 153, 284, 288, 364
Nuyts J 21

O

O'Connell A M 70
Oelhafen M 91, 131
Oishi S 9
Opie A 421

P

Pack J 322, 360
Pal D 378
Palenstijn W J 170
Pan X 50, 144, 161, 165, 254, 343
Papenhausen E 182, 356
Pauwels B 373
Pavkovich J 131
Paysan P 91
Pelzer G 218
Petersilka M 107
Pfeiffer F 373
Pi J 174, 178
Pižurica A 37
Plantagie L 170
Popescu, L M 148
Prince J L 334

Q

Qu M 425

R

Ramani S 330, 348
Ramirez-Giraldo J C 87, 140
Rashed E A 352
Raupach R 107
Rieger J 218
Rigie D 409
Rit S 382
Ritschl L 214, 218
Ritter A 218
Roelandts T 293
Rogalla P 50, 254
Rohkohl C 1, 5, 259
Rui X 198

S

Sack P 339
Sanchez A A 144
Sarnyai Z 230
Sarrut D 382
Sasov A 373
Satow T 9
Sauer K D 297, 439
Sawall S 127, 218
Schmitt K 83, 288
Schoendube H 135, 288
Scholz B 390
Schön T 246
Schönborn M 364
Schüller S 218
Schwemmer C 5, 259
Segars W P 66
Semerci O 314
Shao L 165
Shen H 421
Shi D 50, 57, 254
Shi L 70
Sidky E Y 50, 144, 161, 165, 254, 343
Siewerdsen J 334, 434
Sijbers J 170, 293
Silver M 9, 326
Skatter S 444
Socher M 127
Spencer B 279
Srivastava S 186
Staelens S 37
Star-Lack J 131
Stayman J W 334, 434
Stierstorfer K 1, 66, 107, 135, 288

Stille M 210
Sun M 131
Sunnegårdh J 107
Szabo G 230

T

Taguchi K 66, 95, 186
Takahashi N 425
Tang Q 95
Tang S 271
Tang X 271
Tapfer A 373
Thibault J-B 378, 439
Thiebaut E 157
Thompson S 140
Thompson W M 99
Thomson R 430
Tian J 369
Tsui B M W 66, 399

V

Van Holen R 37
Van Slambrouck K 21
Vandeghinste B 37
Vandenberghe S 37
Vanhove C 37
Vedantham S 70
Velroyen A 373
Vogt F 46, 364

W

Walsh M 421
Wang G 421
Wang Jia 202, 425
Wang Jing 41
Wang Jiong 165
Wang Q 61
Weber T 218
Weyers I 210
Wicklein J 395
Wiley D F 310
Woodhouse C 310
Woodrum D A 140
Wu H 206
Wucherer L 218
Wunderlich A 83, 153

X

Xia T 79
Xu J 399
Xu Q 25, 421
Xu T 279
Xu W 111

Y

Yagil Y 430
Yamada M 9
Yang Y 271
Yazıcı B 360
Ye J C 250
Yi H 369
Yokoyama H 9
Yorkston J 434
Yu H 25, 421
Yu L 74, 87, 140, 202
Yu Z 83, 364

Z

Žabić S 61, 284
Zainon R 421
Zamyatin A 50, 57, 254, 326
Zbijewski W 434
Zeng G L 103
Zeng K 198
Zhang H 41
Zhang J 284
Zhang P 226, 263, 386
Zhang R 439
Zhang X 369
Zhang Zheng 50, 254
Zhang Zhengya 194
Zhao M 263, 386
Zheng Y 5
Zheng Z 182, 356
Zhu S 369
Zhu Y 226, 263, 386